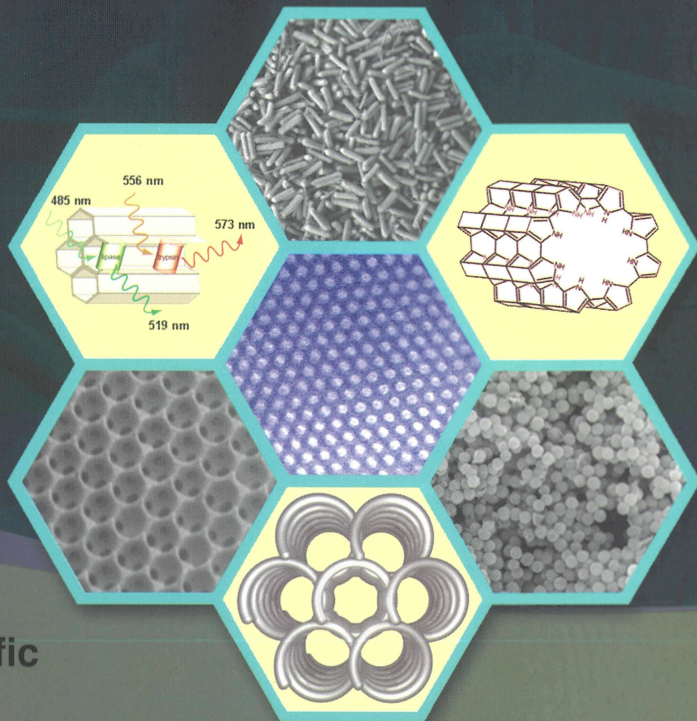


Abdelhamid Sayari
Mietek Jaroniec
Editors

Nanoporous Materials

Proceedings of the 5th International Symposium



Nanoporous Materials

Proceedings of the 5th International Symposium

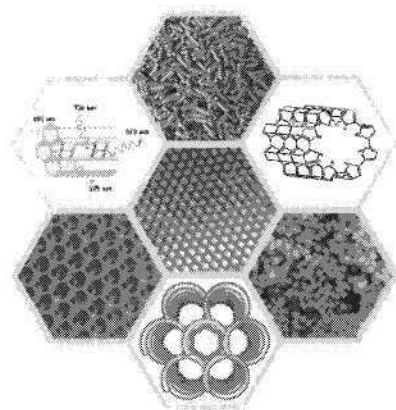
This page intentionally left blank

Nanoporous Materials

Proceedings of the 5th International Symposium

Vancouver, Canada

25 - 28 May 2008



Editors

Abdelhamid Sayari

University of Ottawa, Canada

Mietek Jaroniec

Kent State University, USA

 **World Scientific**

NEW JERSEY • LONDON • SINGAPORE • BEIJING • SHANGHAI • HONG KONG • TAIPEI • CHENNAI

Published by

World Scientific Publishing Co. Pte. Ltd.

5 Toh Tuck Link, Singapore 596224

USA office: 27 Warren Street, Suite 401-402, Hackensack, NJ 07601

UK office: 57 Shelton Street, Covent Garden, London WC2H 9HE

British Library Cataloguing-in-Publication Data

A catalogue record for this book is available from the British Library

NANOPOROUS MATERIALS

Proceedings of the 5th International Symposium

Copyright © 2008 by World Scientific Publishing Co. Pte. Ltd.

All rights reserved. This book, or parts thereof, may not be reproduced in any form or by any means, electronic or mechanical, including photocopying, recording or any information storage and retrieval system now known or to be invented, without written permission from the Publisher.

For photocopying of material in this volume, please pay a copying fee through the Copyright Clearance Center, Inc., 222 Rosewood Drive, Danvers, MA 01923, USA. In this case permission to photocopy is not required from the publisher.

ISBN-13 978-981-277-915-1

ISBN-10 981-277-915-9

Printed in Singapore by World Scientific Printers

PREFACE

Following the breakthrough discovery of the so-called M41S silica mesostructures in the early nineties, the area of periodic mesoporous materials has been growing steadily. Important findings appear in the literature on a regular basis, providing new impetus for further innovations, as well as creating new areas of research. Remarkable progress has been made in the area of material synthesis, marked by the following key discoveries: (i) generalization of synthesis strategies involving van der Waals, electrostatic and covalent interactions between the amphiphile and the inorganic species, (ii) framework and surface modified silicas via direct synthesis and post-synthesis modification, (iii) non-silica mesostructured materials via supramolecular templating pathways (e.g., metals, transition metal oxides and chalcogenides), and via silica or carbon mesophase casting (e.g., mesoporous carbons, oxides, metals, alloys and polymers), (iv) mesoporous organosilicates, and (v) assembly of zeolite nanocrystals into mesoporous structures. Furthermore, a wide variety of potential applications in catalysis, adsorption, separations, environmental cleanup, controlled drug delivery, sensing and optoelectronics are reported on a regular basis.

Though dominated by silica-based mesoporous materials, this series of international symposia “*Nanoporous Materials*” deals with a variety of other mesoporous materials, including clays, carbon molecular sieves, porous polymers, sol-gel, and imprinted materials, as well as self-assembled organic and organometallic zeolite-like materials. Now in its fifth round, *Nanoporous Materials V* will provide an international platform for leading scientists and newcomers alike to discuss recent advances in the areas of synthesis, characterization and applications of organic, inorganic and hybrid porous materials.

Nanoporous Materials V will feature three plenary lectures and seven keynote lectures covering a wide range of porous materials, including porous silicas, organosilicas, carbons and semiconductors, as well as metal oxides, zeolites and metal-organic frameworks. In addition, more than 200 oral and poster presentations will be given both by world-class experts and young scientists. Based on the wide range of these contributions and their high quality, the Organizing Committee is confident that the *Nanoporous Materials V*

Symposium to be held in Vancouver, Canada on May 25-28, 2008, will be as successful as its predecessors.

The current volume represents a sampling of the oral and poster peer-reviewed presentations to be made at the ***Nanoporous Materials V Symposium***. It includes 73 contributions divided into 13 chapters dealing with specific topics within the three broad themes of interest: (i) synthesis of mesoporous silicas and related materials, (ii) synthesis of non-silica based nanoporous and nanostructured materials, and (iii) characterization and applications of nanoporous materials.

Certainly the current volume of proceedings does not cover all topics in the area of nanoporous materials; however, it reflects the recent trends and advances in this rapidly growing field, which continues to attract the attention of materials scientists, chemists, chemical engineers and physicists around the globe. We hope that this proceedings volume will benefit both newcomers as well as researchers from academia, national laboratories and industry working in the synthesis, characterization and applications of nanoporous materials.

Abdel Sayari

University of Ottawa, Canada

Mietek Jaroniec

Kent State University, USA

December 2007

CONTENTS

1. Mesoporous Silicas

New Routes for Improving Hydrothermal Stability of Ordered Mesoporous Materials and Synthesis of Mesoporous Zeolites 1
Feng-Shou Xiao

Porous Structure of SBA-15 Synthesized by Evaporation Induced Self-Assembly Process 9
Akira Endo, Yuki Inagi and Takao Ohmori

Effect of the Lower Consolute Temperature on the Structure of Mesoporous Materials 17
J.L. Blin, F. Michaux and M.J. Stebe

Tailoring Porous Silica Particle and Pore Size Using a Modified Ströber, Fink, Bohn (SFB) System and Post-Synthesis Hydrothermal Treatment 27
Donal Keane, John Hanrahan, Mark Copley, Justin Holmes and Michael Morris

2. Si-Containing Mesoporous Inorganic Frameworks

Three Dimensional Mesoporous FeSBA-1 Catalysts for Alkylation and Acylation of Aromatics 37
Veerappan V. Balasubramanian, Josena Justus and Ajayan Vinu

Incorporation of Al into Cage-Type Mesoporous Silica Molecular Sieves 47
Pavuluri Srinivasu, Dhanashiri P. Sawant, Josena Justus, Veerappan V. Balasubramanian and Ajayan Vinu

Deposition and Characterization of Functional Nanoparticles of Lead-Zirconia Titanate (PZT) in Matrices of Mesoporous Silica of MCM-48-type Structure 55
Vijay Narkhede and Hermann Gies

Characterization of a Germanium Analog of the Tubular Aluminosilicate, Imogolite 63
Masashi Ookawa, Yoshihiro Hirao, Hiroshi Yamashita, Takashi Maekawa and Keiichi Inukai

3. Mesoporous Zeolites

Synthesis of Zeolite ZSM-5 Composites with a Single Template 71
Jia Wang, Johan C. Groen, Marc-Olivier Coppens, Wenbo Yue and Wuzong Zhou

Synthesis of Nano-Sized β -Zeolite by Dry-Gel Conversion (DGC) Method without the Use of Sodium Hydroxide 79
Ayyamperumal Sakthivel, Akira Iida, Yoichi Nishimura, Kenichi Komura, Yoshihiro Sugi, Sung J. Cho, Jong-Ho Kim and Gon Seo

Generation of Hierarchical Porosity in Zeolites by Seed Silanization 89
D.P. Serrano, J. Aguado, R. Sanz, P. Pizarro, J.M. Rodríguez, A. Peral and I. Moreno

Synthesis and Characterization of Y/ β Composite Zeolite and its Hydrocracking Performance 99
Xiwen Zhang, Qun Guo, Zhizhi Zhang, Fengxiang Ling, Wanfu Sun, and Ruifeng Li

4. Mesoporous Organosilicas

Photoresponsive Mesoporous Organosilica with Molecular Order in the Pore Walls 109
Krystyna Czechura and Abdelhamid Sayari

- Ultra-Fast Hydrothermal Synthesis of Diastereoselective Pure
Ethenylene-Bridged Periodic Mesoporous Organosilicas 117
Carl Vercaemst, Matthias Ide, Francis Verpoort and Pascal Van Der Voort
- Structural Investigation of Ordered Mesoporous Silicas Functionalized
by Direct Synthesis with Cyclam Derivatives 129
*Fabrice Gaslain, Anne-Catherine Faust, Claire Marichal,
B n dicte Lebeau, Yoann Rousselin, Franck Denat, Mathieu Etienne
and Alain Walcarius*
- Facile Synthesis of Free-Standing PMO Films with Amorphous and
Crystal-Like Wall Structure 139
Sung S. Park and Chang-Sik Ha
- Synthesis and Characterization of Periodic Mesoporous Organosilicas
with Disulfide and Mercaptopropyl Groups 149
B. E. Grabicka, R. M. Grudzien, I. P. Blitz and M. Jaroniec
- Textural Investigations of Highly Proton Conductive Functionalized
Mesoporous SiO₂ 159
*Roland Marschall, Michael Wark, Jiř  Rathousk y and Michaela
Wilhelm*
- 5. Non-siliceous Inorganic Nanomaterials**
- Mesoporous Ceria by Structure Replication from Various Porous
Matrices 169
Jan Roggenbuck and Michael Tiemann
- Synthesis of Vanadium Oxide Nanoclusters in Confined Environment
via a Template-Exchange Method 179
Parasuraman. Selvam, Vidya Krishna and Arunasish Layek
- Synthesis of Co₃O₄, NiO Nanoparticles with Mesoporous Structure
and Their Electrochemical Capacitive Behaviors 187
*Ming-Bo Zheng, Yu Zhao, Jian Cao, Jin-Song Liu, Hai-Jun Zhao,
Jie-Ming Cao, Guang-Bin Ji, Hai-Yan Wang and Jie Tao*

Synthesis and Characterization of Nanoporous CO_3O_4 via Solvothermal-Annealing Route <i>Hai-Jun Zhao, Ming-Bo Zheng, Dong-Mei Liu, Jing-Song Liu, Xi-Hua Jiang, Jie Tao and Jie-Ming Cao</i>	195
Synthesis of Niobia Nanostructures and their Catalytic and Photocatalytic Activity <i>I. Nowak, A. Feliczak, K. Walczak, M. Darul and M. Jaroniec</i>	203
6. Porous Polymers and Polymer/Inorganic Nanocomposites	
Soft Microporous Frameworks Based on Oligopeptides <i>D.V. Soldatov</i>	213
Mesoporous Polymers with Controlled Porosity and Functionality Derived from Semi-Degradable Diblock Copolymers <i>B. Gorzolnik, J. Penelle, D. Grande, R. Séguéla, V. Mirri, P. Davidson and R. Denoyel</i>	225
Mesostructured Polypyrrole Synthesized by Anionic Surfactant Templating Route <i>Mahasweta Nandi, Asim Bhaumik, Nawal K. Mal and Masahiro Fujiwara</i>	235
Synthesis and Characterization of Thermo-Sensitive Nanocomposite PNIPAAm / SBA-15 <i>Boshi Tian and Chun Yang</i>	245
Synthesis and Preparation of Novel Polyoxometalate-Functionalized Mesoporous Hybrid Materials <i>Rongfang Zhang, Chun Yang</i>	255
Synthesis of a Microporous Organic-Inorganic Hybrid Layered Nanocomposite with Bis(methyldichlorosilyl)biphenyl and Silicic Acid of Ilerite <i>Ryo Ishii, Takuji Ikeda, Tetsuji Itoh, Toshirou Yokoyama, Taka-Aki Hanaoka and Fujio Mizukami</i>	265

7. Mesoporous Carbons

- Preparation of Three-Dimensionally Interconnected Ordered Mesoporous Carbons by Using Novel Silica Nanospheres as Template *Toshiyuki Yokoi, Ryota Watanabe, Seigo Ohta, Junko. N. Kondo, Takashi Tatsumi and Tatsuya Okubo* 275
- Porous Carbon Materials via Chemical Vapour Deposition Using As-Synthesised Zeolites as Template: Synthesis and Hydrogen Storage Properties *Alexandra Pacuła and Robert Mokaya* 283
- Effect of Carbonisation Heating Ramp Rate on the Properties of Ordered Mesoporous Carbons *Zhuxian Yang and Robert Mokaya* 293
- Novel Mesoporous Nitrides and Nitrogen Doped Carbon Materials with Different Structure, Pore Diameters, and Nitrogen Contents *Ajayan Vinu* 303
- Carboxyl, Amine and Thiol Functionalized Mesoporous Carbon Materials *Dhanashri P. Sawant, Josena Justus and Ajayan Vinu* 313
- Control of Pore Size Distribution and Conductivity of Ordered Mesoporous Carbon *Chanho Pak, Sang H. Joo, Dae J. You, Hyuk Chang, Hyung I. Lee, Jin H. Kim and Ji M. Kim* 323
- SBA-15-Templating Synthesis and Properties of Pyrrole-Based Ordered Mesoporous Carbons *Joanna Gorka and Mietek Jaroniec* 333
- Mono and Bimodal Porosity by Pyrolysis of Block Copolymer-Phenolic Resin Complexes *Antti Soininen, Sami Valkama, Harri Kosonen, Antti Nykänen, Ramasubbu Ramani, Olli Ikkala, Janne Ruokolainen, Filip Tuomisto, Peter Engelhard and Gerrit Ten Brinke* 347

Uniform Porosity in Modified Carbon Cryogels 355
Saghar Sepehri, Betzaida B. García, Qifeng Zhang and Guozhong Cao

Effect of Pore Morphology on the Electrochemical Properties of 365
 Electric Double Layer Carbon Cryogel Supercapacitors
Betzaida B. Garcia, Aaron M. Feaver, Guozhong Cao, Gerald T. Seidler, Tim T. Fister and Ken P. Nagle

8. Nanoparticles Assembly

Shaped Metal Oxide-Phosphate Composite Nanoparticles Synthesized 377
 by Templated Disassembly
Fan Li, Sarah A. Delo and Andreas Stein

Metal Oxide Nanoparticles as Building Blocks for Periodic 385
 Mesoporous Materials: Application in Nanotechnology
Carmela Aprile, Mercedes Alvaro and Hermenegildo Garcia

Responsive Nanoporous Organic-Inorganic Colloidal Films 395
Andrew K. Bohaty, Julie Cichelli, Olga Schepelina and Ilya Zharov

9. Adsorption on Nanostructured Materials

Computer Simulation Study in Adsorption of Water in Carbon 407
 Nanotubes
Atichat Wongkoblap and Duong D. Do

Adsorptions of CH₄ and C₂H₄ on MOP-28 Based Clusters: 423
 A Combined QM and QM/MM Study
Saowapak Choomwattana, Pipat Khongpracha and Jumras Limtrakul

Effects of the Framework on the Adsorption of Methane on IRMOF-1, 431
 IRMOF-2 and IRMOF-6 Metal-Organic Frameworks: A Combined
 QM and MM Study
Bundet Boekfa, Saowapak Choomwattana, Chularat Wattanakit, Pailin Limtrakul, Piboon Pantu, Pipat Khongpracha and Jumras Limtrakul

Adsorptions of CO and NO Molecules on MOF-11: A QM/MM Study 439
Pipat Khongpracha, Supawadee Namuangruk and Jumras Limtrakul

Thermal Anomaly and Molecular Motion of Organic Molecules 445
Confined in the Nanocavity of Metal-Organic Frameworks IRMOF-1
Takahiro Ueda, Kenji Kurokawa, Yoshinori Kawamura, Keisuke Miyakubo and Taro Eguchi

10. Nanostructured Catalysts

Spray Drying: a Versatile Route for the Preparation of New Acidic 457
Mesostructured Powders
S. Pega, A. Coupe, C. Boissiere, T. Azais, D. Grosso, C. Sanchez, J. Blanchard, D. Massiot and A. Chaumonnot

Lewis Acidity of Mesoporous Molecular Sieves for Acylation 477
Reactions
Martina Bejblová, Josef Vlk, Dana Procházková, Helena Šiklová and Jiří Čejka

Formation of Superbasic Sites under Mild Condition through 487
Dispersion and Redox of Neutral Potassium Nitrate Salt on Alumina
Lin B. Sun, Fang N. Gu, Ling Gao, Jing Yang, Jia H. Kou, Yuan Chun, Ying Wang, Jian H. Zhu and Zhi G. Zou

Efficient and Selective Nanoporous Catalysts by Placing Multiple 497
Site-Isolated Functional Groups on Mesoporous Materials
Tewodros Asefa, Krishna K. Sharma, Abhishek Anan, Rajyalakshmi Vathyam, Robert P. Buckley, Hieu M. Dam, Youwei Xie, Sean Quinlivan, Gang Wang and Cole Duncan

Polymeric Activated Carbon-Supported Copper and Magnesium for 509
Ethylbenzene Dehydrogenation with Carbon Dioxide
Sérgio Botelho de Oliveira, Danns Pereira Barbosa, Maria do Carmo Rangel and Denilson Rabelo

- Iron Oxide Magnetic Nanoparticles Confined in Mesoporous Silica and Carbon Materials 519
Sher Alam, Sujit K. Mondal, Jonathan P. Hill and Ajayan Vinu
- Functionalized Mesoporous Materials for Gold Catalysis 529
Zhen Ma, Haoguo Zhu, Wenfu Yan, Steven H. Overbury and Sheng Dai
- Electrodeposition of Gold Structures in Mesoporous TiO₂ Sol-Gel Films 543
Inga Bannat, Katrin Wessels, Torsten Oekermann and Michael Wark
- 11. Catalytic Applications of Nanoporous Materials**
- Mesoporous Layers of TiO₂ as Highly Efficient Photocatalysts for Clean Environment 553
Vít Kalousek, Jiří Rathouský, Jessica Tschirch and Detlef Bahnemann
- Quinoline-Carboimine Palladium Complex Immobilized on MCM-41 as a Versatile Catalyst for Sonogashira Cross-Coupling Reaction 561
Hideki Nakamura, Kenichi Komura and Yoshihiro Sugi
- Soy Oil Degradation over Highly Ordered Al-MCM-41 571
Marcelo J.B. Souza, Gicelia Rodrigues, Antonio S. Araujo, Anne M. G. Pedrosa and Stevie H. Lima
- Biodiesel Production by Heterogeneous Catalysis in the Presence of CaO Supported on Mesoporous Silica 577
Mônica C. G. Albuquerque, Diana C. S. Azevedo, Célio L. Cavalcante Jr., Inmaculada Jiménez Urbistondo, José Santamaría Gonzalez, Josefa M. Mérida Robles, Enrique Rodríguez Castellon, Antonio Jiménez Lopez and Pedro Maireles Torres
- Polymeric Activated Carbon-Supported Vanadium and Magnesium Oxides for Styrene Production 589
Raphael Dias Holtz, Maria do Carmo Rangel and Sérgio Botelho de Oliveira

- Two Step Synthesis Procedure of Beta Zeolites: Mesoporosity and Performance as Acidic Catalysts 599
Saulo de Tarso Figueiredo Grecco, Paulo Sérgio Santana Nobre, Ernesto Antônio Urquieta-González and Maria do Carmo Rangel
- Activated Carbon-Supported Copper-Doped Iron Oxide for Ethylbenzene Dehydrogenation 607
Dannis Percira Barbosa, Maria do Carmo Rangel and Denilson Rabelo
- Catalytic Properties of Platinum (II) Exchanged Zirconium Phosphate for WGSR 617
Alexilda Oliveira de Souza, Maria do Carmo Rangel and Oswaldo Luiz Alves
- 12. Environmental Applications of Nanoporous Materials**
- Amine-Functionalized SBA-15 Silica for the Adsorption of Carbon Dioxide 625
H. Šiklová, A. Zukal, J. Čejka and V. Zelenák
- Adsorption of Volatile Organic Compounds on Pore Expanded Mesoporous Materials 633
Rodrigo Serna-Guerrero and Abdelhamid Sayari
- Removal of Low Vapour Pressure Toxic Substances by Nanoporous Materials 643
J.M. Meneses, R. Denoyel and J. Rouquerol
- Improvement of Mesoporous Silica as an Adsorbent for Nitrosamines by Development of Hierarchical Structure 653
Fang N. Gu, Jing J. Wen, Ting T. Zhuang, Jia H. Xu, Wei Huang, Chun F. Zhou and Jian H. Zhu
- Application of Mesoporous Organosilicas with Sulfur- and Nitrogen-Containing Ligands for Adsorption of Mercury Ions 665
Rafal M. Grudzien, Bogna E. Grabicka, Oksana Olkhoviyk, Mietek Jaroniec and Jonathan P. Blitz

Separation of High Surface Area Mineral Solids from Suncor Coke Fly Ash <i>Abdul Majid, Steve Argue, David Kingston, Stephen Lang and James Margeson</i>	677
---	-----

13. Bio-related Applications of Mesoporous Materials

Direct Visualization of Enzymes Encapsulated in Mesoporous Materials <i>Shun-Ichi Matsuura, Tetsuji Itoh, Ryo Ishii, Tatsuo Tsunoda, Satoshi Hamakawa, Taka-Aki Hanaoka and Fujio Mizukami</i>	687
Urease Immobilization on Pore-Expanded Mesoporous Silica and Its Catalytic Effect on Hydrolysis of Urea <i>Kazi-Zakir Hossain, Abdelhamid Sayari and Carlos M. Monreal</i>	697
Entrapment of Glucose Oxidase into Mesostructured Silica <i>J.L. Blin, R. Bleta, M.J. Stebe and C. Carteret</i>	709
Influence of the Preparation Method on the Ampicillin Incorporation in Hydrotalcite-Like Compounds <i>Rodica Zăvoianu, Octavian D. Pavel, Anca Cruceanu, Mihaela Florea, Ruxandra Bîrjega, Andrei Rotaru, Corina Bradu and Petre Rotaru</i>	717
Author Index	729
Subject Index	735

NEW ROUTES FOR IMPROVING HYDROTHERMAL STABILITY OF ORDERED MESOPOROUS MATERIALS AND SYNTHESIS OF MESOPOROUS ZEOLITES

FENG-SHOU XIAO

College of Chemistry, Jilin University, Changchun 130012, China

In comparison to industrial zeolite catalysts, ordered mesoporous materials exhibit relatively low hydrothermal stability, which severely hinders their practical applications in industrial catalytic reactions such as petroleum refining. In this paper, several new routes for improving hydrothermal stability of ordered mesoporous materials are summarized, including (1) hydrothermally stable mesoporous aluminosilicates and titanosilicates assembled from preformed zeolite precursors; (2) high-temperature synthesis of ordered mesoporous silica-based materials with high silica condensation; (3) introduction of promoters for silica condensation in the synthesis of ordered mesoporous materials. Furthermore, we focus on synthesis of mesoporous zeolites because mesoporous zeolites have the advantages of both zeolites and mesoporous materials. In this paper, a facile route for synthesis of mesoporous zeolites from cationic polymers is described.

1. Introduction

Since the first discovery of ordered mesoporous materials by Mobil scientists [1], a series of novel ordered mesoporous materials have been successfully synthesized [2-10]. However, compared with zeolites, these mesoporous materials exhibit low catalytic activity and hydrothermal stability due to their amorphous walls [2]. Therefore, increasing catalytic activity and hydrothermal stability are great tasks for rational synthesis of ordered mesoporous materials. In this work, we have mainly reviewed our recent development for synthesis of ordered mesoporous materials with improved hydrothermal stability, which include (1) catalytically active and hydrothermally stable mesoporous aluminosilicates and titanosilicates assembled from preformed zeolite precursors; (2) high-temperature synthesis of ordered mesoporous silica-based materials with high silica condensation; (3) introduction of promoters for silica condensation in the synthesis of ordered mesoporous materials.

Additionally, mesoporous zeolites are also a hot topic for synthesis of porous materials recently [15] because the mesoporousity in zeolites is favorable for mass transfer. Very importantly, these crystalline mesoporous zeolites exhibit

much higher hydrothermal stability than the amorphous mesoporous materials. In this work, we also show a facile synthesis of mesoporous zeolites from mesoscale template of cationic polymer in the presence of small organic ammonium salts [15.].

2. Improving Hydrothermal Stability of Ordered Mesoporous Materials

2.1. *Strongly Acidic and Hydrothermally Stable Ordered Mesoporous Aluminosilicates from Preformed Aluminosilicate Zeolite Precursors*

It is well known that zeolites are hydrothermally stable and catalytically active, and one of reasons for their excellent properties is the existence of primary and secondary zeolite building units (PSBU) in zeolites [16]. Of course, the preformed zeolite precursors contain PSBU. Fortunately, when preformed aluminosilicate zeolite precursors are assembled with the templating micelle, strongly acidic and hydrothermally stable ordered mesoporous aluminosilicates have been synthesized successfully [19-24]. The early works for synthesis of ordered mesoporous aluminosilicates are carried out in alkaline media [19-21]. However, under alkaline media, mixed phases would often be obtained if the synthetic conditions are not controlled very well. In order to prevent the formation of mixed phases, the assembly of preformed zeolite precursors with the templating micelle is explored to strongly acidic media. Under this condition, crystallization of zeolites will be avoided, and the products therefore would be pure mesoporous materials [22-24].

It is worthy to mention that the quality of preformed zeolite precursors play a key role for the synthesis of strongly acidic and hydrothermally stable ordered mesoporous aluminosilicates. If the sizes of the preformed zeolite precursors are too big, it is difficult to form an ordered mesostructure due to the rigidity of nanocluster assembly. If the sizes of the preformed zeolite precursors are too small, it is difficult to obtain strongly acidic and hydrothermally stable mesoporous aluminosilicates due to a significant increase of amorphous silica in the samples. In our case, the quality of the preformed zeolite precursors (zeolite seeds solution) is usually checked by the synthesis of zeolites in the absence of organic template. For example, addition of a small amount of the preformed Beta zeolite precursors with a good quality into alumina-silica gel at 140 °C for 2-4 days led to Beta zeolite with high crystallinity in the absence of organic templates [25]. The preformed aluminosilicate precursors appear to serve as seeds for the crystallization of Beta zeolite.

Recently, various types of the preformed zeolite precursors such as MFI and L nanoclusters was also used to synthesize ordered mesoporous aluminosilicates, and these mesoporous materials also exhibit higher hydrothermal stability and acidity than conventional MCM-41 [26, 27].

2.2. Catalytically Active and Hydrothermally Stable Ordered Mesoporous Titanosilicates from Preformed Titanosilicate Precursors

Since the discovery of TS-1 zeolite by Enichem Company [28], a series of microporous crystals of titanosilicates, have been reported which have remarkable catalytic properties. However, the pore sizes (<0.8 nm) of these microporous titanosilicates too small for access by bulky reactants of the kind important in fine chemical and pharmaceutical industries. The solution for this problem is to synthesize mesoporous titanosilicates with pore sizes of 3~8 nm [29]. Unfortunately, when compared with TS-1, the oxidation ability and hydrothermal stability are relatively low, which severely hinders their practical applications. The relatively low oxidation ability and hydrothermal stability, e.g. of Ti-MCM-41, can be attributed to the difference in the titanium coordination environment (amorphous nature of the mesoporous wall) [2]. In our case, an ordered mesoporous titanosilicate (MTS-9) has been assembled from the preformed TS-1 precursors in strongly acidic media, and its mesostructure is hydrothermally stable [30], compared with that of Ti-MCM-41. For hydroxylation of phenol with hydrogen peroxide, the activity and selectivity are similar to TS-1. However, for hydroxylation of bulky molecules like trimethylphenol, TS-1 is inactive, while mesoporous MTS-9 has very high activity. The increased activities, especially for bulky reactants, and higher stability are novel catalytic properties that may lead to new applications [30].

Recently, the synthesis of ordered mesoporous titanosilicates from the preformed TS-1 precursors is extended to alkaline media [31, 32], and obtained products exhibit excellent properties for the conversion of bulky reactants. For example, in non-aqueous solvent decane epoxidation of cyclohexene was tested and compared with conventional Ti-MCM-41 and TS-1. It is clear that the much higher conversion cyclohexene to the epoxidation product of the mesoporous materials assembled from the preformed TS-1 precursors, demonstrating their superiority of catalytic properties [32]. Furthermore, ordered mesoporous ferrosilicates are also synthesized from the assembly of the preformed ferrosilicate zeolite precursors with surfactant micelle in strongly acidic media, and obtained products exhibit much higher hydrothermal stability than Fe-MCM-41 [32]. Obviously, the assembly of the preformed zeolite precursors with the templating

micelle is a good route for synthesis of catalytically active and hydrothermally stable ordered mesoporous materials.

2.3. High-temperature Synthesis of Hydrothermally Stable Ordered Mesoporous Silica-based Materials with High Silica Condensation

It has been reported that a critical factor in increasing hydrothermal stability is to have more silica condensation on the mesoporous walls [33]. Conventionally, the synthesis of ordered mesoporous materials is at low temperatures (80-150 °C) because there is no surfactant that can be used as template at high temperature (160-220 °C). The low-temperature synthesis usually results in imperfect silica condensation of mesoporous materials with a large amount of terminal OH group which make the mesostructure unstable [2]. Fortunately, when the mixture of an ordered polymer surfactant micelle (P123) with a fluorocarbon surfactant (FC-4, $C_3F_7O(CFCF_3CF_2O)_2CFCF_3CONH(CH_2)_3N^+(C_2H_5)_2CH_3I$) is used as a template, ordered hexagonal mesoporous silica-based materials with good hydrothermal stability, designated JLU-20, are successfully synthesized in strong acidic media at high temperature (160-220 °C) [34]. XRD pattern of calcined JLU-20 generally shows four clearly well-resolved peaks that can be indexed as the (100), (110), (200), and (210) diffractions associated with the $P6mm$ hexagonal symmetry, and TEM images of JLU-20 sample confirm this mesostructure. Interestingly, JLU-20 is much more hydrothermally stable than SBA-15. Upon hydrothermal treatment, JLU-20 remains well-ordered, whereas SBA-15 loses most of its mesostructure. Furthermore, the ^{29}Si MAS NMR spectrum of the as-synthesized JLU-20 provides direct evidence of the extent of silica condensation. JLU-20 is primarily made up of fully condensed Q^4 silica units (-112 ppm) with a small contribution from incompletely cross-linked Q^3 (-102 ppm), giving very high Q^4/Q^3 ratio (6.5). In contrast, SBA-15 has typical peaks correspond to Q^2 , Q^3 , and Q^4 silica species respectively, and the ratio of Q^4/Q^3+Q^2 is 1.9, suggesting the presence of large amounts of terminal hydroxyl group in the mesoporous walls. These results demonstrate that JLU-20 has fully condensed mesoporous silica walls, which should be attributed directly to the contribution of high-temperature synthesis [34].

Recently, the synthesis of JLU-20 at high-temperatures was investigated by 1H , ^{13}C , and ^{19}F NMR spectroscopy, and obtained results show that the ammonium head in the mixture of FC-4 and P123 play a key role for the high-temperature synthesis. Accordingly, it is suggested that ordered silica mesoporous materials could be synthesized at high temperature without the use of fluorocarbon chains. Therefore, we can design fluorocarbon-free templates for the synthesis of ordered mesoporous silica materials at high temperatures (>180°C). Fortunately, when a mixture of tetraethylammonium hydroxide (TEAOH) with P123 is used as a template, ordered hexagonal silica-based

materials (JLU-20-TEA) is successfully synthesized at high-temperature (180 °C). The ^{29}Si MAS NMR spectrum of the as-synthesized JLU-20-TEA shows high Q^4/Q^3 ratio at 4.2, and hydrothermal treatments of the samples show that JLU-20-TEA is more stable than conventional mesoporous silica of SBA-15.

2.4. Introduction of Promoters for Silica Condensation in the Synthesis

SBA-15 is a first example of ordered mesoporous silica materials templated from triblock copolymer surfactant in strongly acidic media, and its good features such as thicker walls and larger pore sizes are very favorable for improvement of hydrothermal stability and diffusion of bulky molecules [3]. However, the relatively low silica condensation in SBA-15 is still a problem for improving its hydrothermal stability. Recently, we systemically investigate the effect of anions on silica condensation in acidic, neutral, and alkaline conditions at conventional temperatures such as 100 °C, and it is found that sulfate is a good promoter for silica condensation in aqueous solution under neutral condition. Therefore, when an inorganic anion of sulfate is added into the starting gel for synthesis of SBA-15 under neutral condition, hydrothermally stable and well ordered hexagonal mesoporous SBA-15 materials (SBA-15-SO_4^{2-}) have been successfully synthesized at conventional temperature (100 °C). As we have expected, as-synthesized SBA-15-SO_4^{2-} exhibit very high degree of silica condensation, giving Q^4/Q^3 ratio of 6.3. Interestingly, after treatment in 100% steaming at 780 °C for 3 h, SBA-15-SO_4^{2-} still shows three clear peaks assigned to (100), (110) and (200) reflections of hexagonally ordered mesostructure. In contrast, the treated SBA-15 gives rise to a broad peak assigned to (100) reflection. These results confirm that the hydrothermal stability of SBA-15-SO_4^{2-} is significantly improved, compared with that of SBA-15. Furthermore, this approach has been extended to synthesize hydrothermally stable mesoporous materials with various substituted heteroatoms such as aluminum, zirconium, titanium, iron, tin, and vanadium. For example, ordered hexagonal Al-SBA-15 synthesized in the presence of urea exhibits much higher hydrothermal stability than conventional Al-SBA-15.

3. Mesoporous Zeolites Templated with a Mixture of Small Organic Ammonium and Mesoscale Cationic Polymer

Although those mesoporous materials mentioned above have much improved stability, they are less hydrothermally stable than zeolites. Therefore, our group is to develop new route to synthesize mesoporous zeolites. Mesoporous zeolites should have the advantages of both mesoporous materials for fast diffusion of

molecules and microporous zeolites for highly active sites [11, 12]. Generally, microporous crystals of zeolites such as Beta and ZSM-5 are synthesized from small organic templates such as tetraethylammonium hydroxide (TEAOH) and tetrapropyl ammonium hydroxide (TPAOH). Recently, mesoporous zeolites are successfully templated from nanosized carbon templates in the presence of small organic templates [13, 14], but their industrial applications are limited due to the complexity of synthetic procedure and hydrophobicity of carbon templates. In our case, we show a unique, facile, controllable, and universal route for the synthesis of hierarchical mesoporous zeolites templated from a mixture of both small organic ammonium and mesoscale cationic polymer [15], which are well characterized by HR TEM, nitrogen isotherms, HR SEM, XRD, and probing catalytic reactions. In this route, the choice of mesoscale template of cationic polymer is one of keys for the formation of mesoporous zeolites, which is mainly related to three points in the following: (1) good thermal and hydrothermal stability in the temperatures (up to 200 °C) under the condition of zeolitic synthesis; (2) very low cost; and (3) very strong interaction between cationic polymers with negative silica species in alkaline media.

Figure 1 shows TEM image of mesoporous ZSM-5 zeolite synthesized from cationic polymer. Obviously, there is hierarchical mesoporosity in the range of about 10-30 nm for the sample. Notably, this route is “one-step” hydrothermal synthesis, and the template mixture is homogeneously dispersed into synthetic gel. Notably, these novel mesoporous zeolites exhibit excellently catalytic properties, compared with conventional zeolites. For example, while there is a little activity for cracking of triisopropylbenzene in conventional ZSM-5, high conversion was obtained with mesoporous ZSM-5 zeolite. Very interestingly, one-pot synthesis of mesoporous zeolites is also successful from various mesoscale organic templates such as silane-functionalized polymer [35] and organic-inorganic hybrid surfactant [36] recently.

Additionally, when palladium species were loaded into mesoporous Beta zeolite (Beta-H), the Pd particles could be located in both mesopores and micropores (Pd/Beta-H). The presence of Pd particles in the mesopores offers an opportunity for catalytic hydrotreating of bulky molecules. As a model reaction, the deep hydrogenation of bulky aromatic pyrene shows that the Pd/Beta-H exhibits much higher activity and selectivity for products of deep hydrogenation than a conventional Beta zeolite-supported Pd catalyst (Pd/Beta) and Pd catalysts supported on MCM-41 (Pd/Al-MCM-41), which is greatly important for increasing fuel quality and controlling the undesirable emissions in exhaust gases [37].

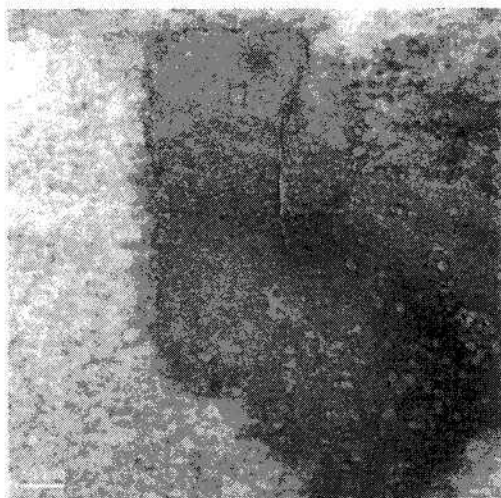


Figure 1. TEM of hierarchical mesoporous ZSM-5 zeolite templated from cationic polymer in the presence of TPAOH.

Acknowledgments

This work was supported by State Basic Research Project of China (2004CB217804) and Natural Science Foundation of China (20573044).

References

1. C. T. Kresge, M. E. Leonowicz, W. J. Roth, J. C. Vartuli and J. S. Beck, *Nature*, 352, 710 (1992).
2. A. Corma, *Chem. Rev.* 97, 2373 (1997).
3. D. Zhao, J. Feng, Q. Huo, N. Melosh, G. H. Fredrickson, B. F. Chmelka and G. D. Stucky, *Science* 279, 548 (1998).
4. S. S. Kim, W. Zhang and T. J. Pinnavaia, *Science* 282, 1032 (1998).
5. R. Ryoo, J. M. Kim and C. H. Shin, *J. Phys. Chem.* 100, 17718 (1996).
6. R. Mokaya, *Angew. Chem. Int. Ed.*, 38, 2930 (1999).
7. P. D. Yang, D. Y. Zhao, D. I. Margolese, B. F. Chmelka and G. D. Stucky, *Nature* 396, 152 (1998).
8. D. M. Antonelli and J. Y. Ying, *Curr. Opin. Colloid Interface Sci.* 1, 529 (1996).
9. D. Khushalani, A. Kuperman, N. Coombs and G. A. Ozin, *Chem. Mater.* 8, 2188 (1996).
10. X. S. Zhao and G. Q. Lu, *J. Phys. Chem. B* 102, 1556 (1998).
11. M. E. Davis, *Nature* 417, 813 (2002).

12. M. Hartmann, *Angew. Chem. Int. Ed.* **43**, 5880 (2004).
13. C. J. H. Jacobsen, C. Madsen, J. Houzvicka, I. Schmidt, A. Carlsson, *J. Am. Chem. Soc.* **122**, 7116 (2000).
14. Y. Tao, H. Kanoh and K. Kaneko, *J. Am. Chem. Soc.* **125**, 6044 (2003).
15. F.-S. Xiao, L. Wang, C. Yin, K. Lin, Y. Di, J. Li, R. Xu, D. S. Su, R. Schlögl, T. i Yokoi, T. Tatsum, *Angew. Chem. Int. Ed.* **45**, 3090 (2006).
16. H. Van Bekkum, E. M. Flanigen, P. A. Jacobs, J. C. Jansen, Introduction to Zeolite Science and Practice (Eds.), Elsevier, Amsterdam, 2001.
17. H. Robson, *ACS Symp. Ser.* **398**, 436 (1989).
18. Q. Zhou, W. Pang, S. Qiu and M. Jia, *CN Patent*, ZL 93 1 17593.3, 1996.
19. Y. Liu, W. Z. Zhang, T. J. Pinnavaia, *J. Am. Chem. Soc.*, **122**, 8791 (2000).
20. Y. Liu, W. Z. Zhang, T. J. Pinnavaia, *Angew. Chem. Int. Ed.* **40**, 1255 (2001).
21. Z. Zhang, Y. Han, L. Zhu, R. Wang, Y Yu, S. Qiu, D. Zhao, F.-S. Xiao, *Angew. Chem. Int. Ed.* **40**, 1258 (2001).
22. Y. Han, F.-S. Xiao, W. Wu, Y. Sun, X. Meng, D. Li, S. Lin, F. Deng, X. Ai, *J. Phys. Chem. B* **105**, 7963 (2001).
23. Y. Liu, T. J. Pinnavaia, *Chem. Mater.* **14**, 3 (2002).
24. Y. Han, S. Wu, Y. Sun, D. Li, F.-S. Xiao, J. Liu, X. Zhang, *Chem. Mater.* **14**, 1144 (2002).
25. Q. Zhou, Ph. D. Thesis, Jilin Univ., 1996.
26. P.-C. Shih, H.-P. Lin, C.-Y. Mou, *Stud. Surf. Sci. Catal.*, **146**, 557 (2003).
27. Y. Di, Y. Yu, Y. Y. Sun, X. Y. Yang, S. Lin S, M. Y. Zhang, S. G. Li, F.-S. Xiao, *Microporous Mesoporous Mater.*, **62**, 221(2003).
28. M. Taramasso, G. Perego and B. Notari, *US Patent* 4410501 (1983).
29. W. Zhang, J. Wang, P. T. Tanev and T. J. Pinnavia, *Chem. Commun.* 979 (1996).
30. F.-S. Xiao, Y. Han, Y. Yu, X. J. Meng, M. Yang, S. Wu, *J. Am. Chem. Soc.*, **124**, 888 (2002); X.-J. Meng, D.-F. Li, X. Y. Yang, Y. Yu, S. Wu, Y. Han, Q. Yang, D. Z. Jiang, F.-S. Xiao, *J. Phys. Chem.* **107**, 8972 (2003).
31. K. F. Lin, Z. H. Sun, D. Z. Jiang and F.-S. Xiao, *Microporous Mesoporous Mater.*, **72**, 193 (2004).
32. M. Reichinger, H. Gies, M. Van den Berg, W. Grunert and Chr. Kirschhock, *Stud. Surf. Sci. Catal.*, **170**, 276 (2007).
33. R. Mokaya, *J. Phys. Chem. B*, **103**, 10204 (1999).
34. Y. Han, D. Li, L. Zhao, J. Song, X. Yang, N. Li, Y. Di, C. Li, S. Wu, X. Xu, X. Meng, K. Lin, F.-S. Xiao, *Angew. Chem. Int. Ed.*, **42**, 3633 (2003).
35. H. Wang and T. J. Pinnavaia, *Angew. Chem. Int. Ed.* **45** (2006) 7603.
36. M. Choi, H. Cho, R. Srivastava, C. Venkatesan, D. Choi, R. Ryoo, *Nat. Mater.* **5**, 718 (2006).
37. T. D. Tang, C. Y. Yin, L. F. Wang, Y. Y. Ji, and F.-S. Xiao, *J. Catal.* **249**, 111 (2007).

POROUS STRUCTURE OF SBA-15 SYNTHESIZED BY EVAPORATION INDUCED SELF-ASSEMBLY PROCESS

AKIRA ENDO, YUKI INAGI, TAKAO OHMORI

*Research Institute for Innovation in Sustainable Chemistry,
National Institute of Advanced Industrial Science and Technology (AIST),
1-1-1 Higashi, Tsukuba Central 5
Tsukuba, Ibaraki 305-8565, Japan*

The Evaporation Induced Self-Assembly (EISA) process is one of the most promising routes for the large scale synthesis of ordered mesoporous materials, because of some advantages over the hydrothermal synthesis such as short synthesis time, easiness of controlling silica/metal ratio, possibility of continuous synthesis. In the present study, SBA-15 materials were synthesized by three different kinds of methods, i) spray-drying, ii) vacuum-assisted solvent evaporation, and iii) conventional hydrothermal reaction. SBA-15 materials via EISA process possessed the different pore structure compared with conventional SBA-15, smaller BET surface and thinner pore wall thickness.

1. Introduction

Mesoporous inorganic materials templated by surfactant molecular assemblies have attracted a great deal of attention because of their potential applications as catalysts, adsorbents, molecular sieves, sensors, etc. There are two major pathways by which these ordered mesoporous materials are synthesized. One is a hydrothermal synthesis in which the products precipitate from inorganic surfactant aqueous solutions under alkaline or acidic conditions. The other is an evaporation induced self-assembly (EISA) process in which the source solution is concentrated with the evaporation of the solvent to form an ordered inorganic surfactant mesostructure. The EISA process is one of the most promising route for the large scale synthesis of ordered mesoporous materials, because of some advantages over the hydrothermal synthesis such as short synthesis time, easiness of controlling silica/metal ratio, possibility of continuous synthesis. Although some reports on the synthesis of SBA-15 powder through EISA process have been published [1,2], the meso- and microporous structure has not been clarified well. In the present study, SBA-15 materials were synthesized by three different kinds of method, i) spray-drying (SD), ii) vacuum-assisted solvent evaporation (VASE) [3], iii) conventional

hydrothermal reaction (HT) [4] and we discuss the difference of the porous structure.

2. Experimental

In the present study, SBA-15 materials were synthesized by three different kinds of method, i) spray-drying (SD), ii) vacuum-assisted solvent evaporation (VASE), and iii) conventional hydrothermal reaction (HT). Tetraethyl orthosilicate (TEOS), ethanol, and hydrochloric acid were used as received from Junsei Chemical Co. Ltd., Japan. An amphiphilic triblock copolymer (BASF Pluronic P123, $\text{EO}_{20}\text{PO}_{70}\text{EO}_{20}$) was used as a structure-directing material. The obtained are referred to as SD-SBA-15, VASE-SBA-15 and HT-SBA-15 in this paper, where SD, VASE and HT designate the synthesis method as described above, respectively.

2.1. *Synthesis of SBA-15 by spray drying (SD) Method*

TEOS and P123 were dissolved into ethanol. After HCl aqueous solution was added to the mixture, obtained solution was stirred at room temperature for 20 minutes to hydrolyze the TEOS. The typical molar ratio of the starting solution was 1 TEOS : 0.01-0.02 P123 : 10 EtOH : 1.8×10^{-3} HCl : 10 H_2O . The solvent was then transferred to a round-bottom flask and evaporated using a vacuum rotary evaporator at 145 hPa for 30 minutes. Then, the solution was spray dried using the spray dryer GS310 (Yamato Kagaku Co. Ltd.). The inlet temperature was 403-433K and the gas pressure 0.07MPa. The resulting solid, a silica-template composite, was calcined at 773K for 6 hours to remove the structure directing agents.

2.2. *Synthesis of SBA-15 by vacuum-assisted solvent evaporation (VASE) method*

TEOS and templates were mixed with HCl, H_2O , and ethanol in the synthesis. The molar composition of the starting solution was 1 TEOS : 0.02 P123 : 10EtOH 1.8×10^{-2} HCl : 10 H_2O . The solution was stirred for 20minutes at room temperature, and then the solvent was removed under a reduced pressure of 1.145 hPa at 313K using a vacuum rotary evaporator. Once the solution had reached a paste-like consistency, the pressure was reduced to 2×10^3 Pa and maintained for 30 min. This resulted in the viscous, paste-like liquid changing to a white wet solid with slight bubbling. The temperature was then increased to 333 K and maintained for 30 min to evaporate the remaining solvent. The

obtained solid was calcined at 773K for 6 h to remove the structure directing agents.

2.3. Characterization of SBA-15

To characterize the obtained SBA-15, small-angle X-ray diffraction (XRD) patterns were measured using a Bruker AXS D8 Advance diffractometer (Cu-K α radiation, $\lambda=0.154$ nm, operated at 40 kV and 40 mA). The TEM observations of the obtained samples were carried out using a Hitachi HF-2000 field emission transmission electron microscope with an electron acceleration of 200 kV. The adsorption/desorption isotherms of N₂ at 77 K were measured using an automatic gas adsorption analyzer (BELSORP-mini, BEL Japan, Inc.) after outgassing the samples at 573 K for 5 h in vacuum. The pore-size distribution curve (PSD) was calculated from the desorption branch using the NLDFT N₂ zeolite/silica equilibrium transition kernel at 77 K based on a cylindrical pore model [5]. The pore volume and surface area corresponding to a mesopore were determined from the curves obtained by the cumulative plots. The amount of micropore was calculated by the *t*-plot analysis.

3. Results and Discussion

3.1. Characterization of SBA-15

Table 1 shows the optimized synthesis conditions for the SD and VASE method. As reported in our previous paper[3], there are two rate processes in the EISA process. The one is the rate of the solvent evaporation, which induces the self-assembly of the surfactant micelles, and the other is the rate of the polycondensation of the silicate species. It is considered that the well-ordered mesostructure can be obtained only when these two rate processes are well balanced. Thus, P123/TEOS molar ratio, reaction temperature, stirring time, solvent evaporation time should be optimized for each synthesis method.

Table 1 Optimized synthesis conditions for three kinds of synthesis method.

Sample	P123/ TEOS[-]	Temp. [K]	Stir. time[min]	Total time	Solvent	HCl [M]
HT	0.016	313-353	1200	5days	H ₂ O	2
VASE	0.020	313	20	5hours	EtOH	0.1
SD@403K	0.010	403	20	2hours	EtOH	0.01
SD@433K	0.010	433	20	2hours	EtOH	0.01

Figure 1 shows the XRD patterns of the SD-SBA-15 prepared at a drying temperature at 403K with a variety of P123/TEOS ratios. The other conditions are same as listed in Table 1. The lowering of the order was observed with increasing the P123/TEOS ratio and the XRD peaks almost disappeared at the P123/TEOS=0.015 or less, which is the typical ratio in the hydrothermal synthesis of SBA-15 as reported elsewhere [4,6]. In the SD synthesis, the smaller amount of P123 and HCl was preferred to obtain the highly ordered structure. The porous structure of obtained by N_2 adsorption measurements will be discussed later compared with the VASE and HT-SBA-15 samples. The SD-SBA-15 and VASE-SBA-15 samples synthesized in the optimized condition exhibited one intense (100) peak around 1.0 degree and 1-2 peaks for (110) and (200) of 2 to 6 degrees in a 2θ angle range, which are associated with $p6mm$ hexagonal symmetry as shown in Figure 2. The (100) peaks of these sample is relatively broad and (210) peak was not observed, indicating the less ordered structure compared to conventional SBA-15 materials synthesized by hydrothermal reaction (HT-SBA-15).

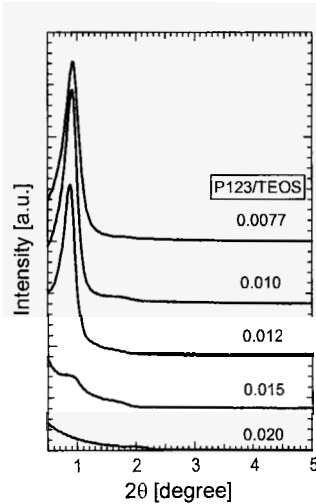


Figure 1 Small-angle XRD patterns of Spray-dried SBA-15.

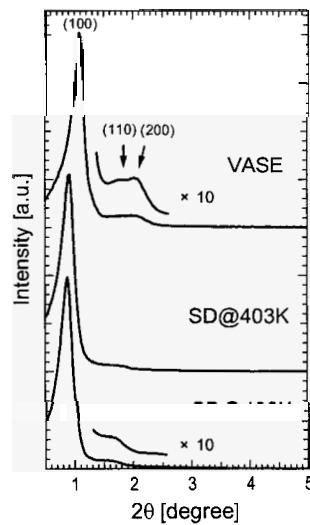


Figure 2 Small-angle XRD patterns of SD and VASE SBA-15.

The N_2 adsorption/desorption isotherms (Figure 3) were typical Type IV in the IUPAC classification, clearly indicating the mesoporous structure. From the N_2 adsorption measurements, the BET surface area was about $300\text{m}^2/\text{g}$ for SD samples and $515\text{m}^2/\text{g}$ for VASE sample, respectively. These values are relatively

smaller than conventional HT-SBA-15, whose BET surface area is typically over $800\text{m}^2/\text{g}$. The reason for smaller BET surface area is discussed in the next section. The other parameters (lattice parameter, pore size, thickness of pore wall, meso- and micropore volume) calculated from XRD and N_2 adsorption measurements are summarized in Table 2. From the XRD patterns, N_2 adsorption/desorption isotherms and the TEM observation (Figure 4); we confirmed that all the SBA-15 samples had a highly ordered hexagonal mesostructure.

Table 2 Porous properties of synthesized SBA-15.

Sample	d_{100} [nm]	d_p [nm] ^a	d_w [nm] ^b	V_{meso} [cc/g] ^c	v_{micro} [cc/g] ^d	S_{BET} [m ² /g]
HT	10.0	7.9	3.7	0.80	0.1	912
VASE	7.9	7.3	1.8	0.72	<0.01	515
SD@403K	9.7	7.6	3.6	0.39	<0.01	302
SD@433K	10.0	8.5	3.1	0.42	<0.01	304

^{a, c} calculated from adsorption branch using NLDFT analysis. ^b $2d_{100}/1.732$ - ^d calculated by the t -plot method.

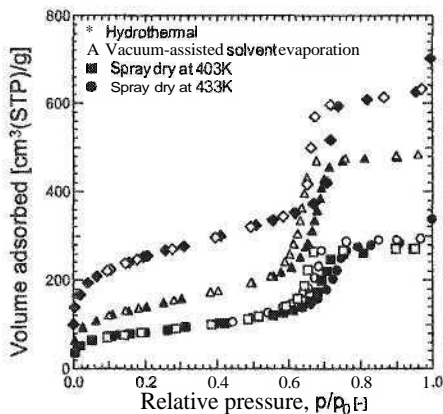


Figure 3. N_2 adsorption/desorption isotherms measured at 77K. Open symbols denote adsorption and closed symbols denote desorption.

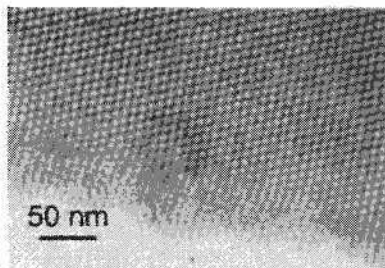


Figure 4. TEM image of SBA-15 synthesized by vacuum-assisted solvent evaporation method.

3.2. Porous structure of SBA-15

The N_2 adsorption/desorption isotherms were measured at 77K (Figure 3) and pore structure was evaluated by NLDFT and t -plot analysis. The porosity data determined based on the N_2 adsorption/desorption isotherms are

summarized in Table 2. The most common pore size (d_p) for the synthesized SBA-15 were ranged from 7.3 to 8.5 nm, depending on the synthesis method and conditions. A noticeable feature is the thin pore wall of VASE sample (1.8nm), which is thicker than 3.5nm for SD and HT samples. The mesopore volume (V_{meso}) synthesized by SD method is less than that of the samples synthesized by VASE and HT. This is mainly because the smaller amount of the block copolymer (P123/TEOS=0.01) in the optimized synthesis solution for SD-SBA-15 samples (P123/TEOS=0.01) compared to those of HT-SBA-15 (P123/TEOS=0.016) and VASE-SBA-15 (P123/TEOS=0.02) samples. As described previously, the increase of P123 amount in the synthesis solution for SD resulted in the formation of less ordered structure.

There have been some reports on the synthesis of SBA-15 by spray drying method. Anderson et al., reported that formation of 2D hexagonal mesoporous silica using Pluronic P123 block copolymer as templates, whose BET surface area is 316m²/g and mesopore volume is 0.54cc/g [2]. Baccile et al. also reported the formation of mesoporous silica using Pluronic P123 template, whose BET surface area is 540m²/g and mesopore volume is 0.69cc/g [1]. Although their sample showed larger mesopore volume than ours, the shape of N₂ adsorption isotherm had larger hysteresis loop like SBA-16, indicating the bottlenecks between pore arrays. At the present, the synthesis of SBA-15 with same quality as hydrothermally synthesized one via EISA process has not been reported and the further optimization of synthesis conditions is needed.

3.3. Comparison with conventional SBA-15

As described above, the SBA-15 samples synthesized via EISA process have smaller BET surface area than that of common SBA-15 materials. The main reason for the smaller BET surface area is the extreme reduction of micropores. It should be noted that the mesoporous SBA-15 synthesized by a hydrothermal reaction possesses micropores that interconnect the primary mesopores as reported in many studies [7,8]. Figure 5 shows the t-plots calculated from N₂ adsorption isotherms using the reference isotherm for non-porous silica. The t-plots for all the samples synthesized via EISA process (SD and VASE) provided straight lines at $t = 0.25-0.7$ and the extrapolation line went through the origin, indicating the absence of micropores. In fact, the calculated micropore volume are approximately zero for the samples synthesized via EISA process, whereas that for HT-SBA-15, is 0.1cc/g (the extrapolation line of t-plot cut the y-axis at 70 cm³ (STP)/g in Figure 5).

The synthesis of micropore-free SBA-15 or control of the micropore volume in the hydrothermal synthesis has been reported by several research groups. It is considered that the formation of micropores are due to the penetration of EO chains into silica network, and the amount and size of micropore depend on the synthesis condition such as temperature, P123 concentration, solvent. Miyazawa and Inagaki reported the increase of synthesis temperature and surfactant/TEOS ratio result in the decrease of the amount of micropore[9]. Newalkar et al. reported the addition of inorganic salt into the synthesis solution is effective for the formation of micropore-free SBA-15[8]. They also reported that the use of co-solvent (ethanol) with the addition of minimum amount of inorganic salt results in the formation of micropore-free SBA-15[10].

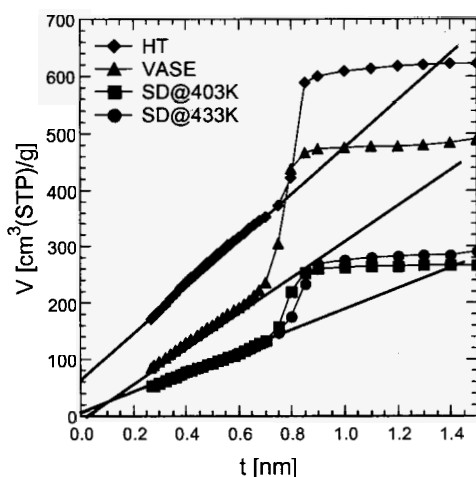


Figure 5 t -plots for SD, VASE and HT-SBA-15 samples.

In our SD and VASE synthesis, the solidification of the solution during spray-drying finish in very short (typically shorter than few seconds). In addition ethanol is used as a main solvent. This is probably the reason for the absence of micropores, although the SD synthesis temperature is relatively high (403-433K) or the P123/TEOS molar ratio in the VASE synthesis is higher than that of hydrothermal synthesis.

4. Conclusions

In this study, the synthesis of SBA-15 materials via evaporation induced self-assembly (EISA) process was investigated. Optimizing the synthesis

conditions, SBA-15 materials with 2D hexagonal pore arrangement were successfully synthesized by two kinds of evaporation induced self-assembly process, namely spray-drying method and vacuum-assisted solvent evaporation method. SBA-15 materials via EISA process possessed smaller BET surface area than hydrothermally synthesized SBA-15, mainly due to the significant reduction of microporosity interconnecting the primary mesopores. SBA-15 synthesized spray drying method had smaller mesopore volume than hydrothermally synthesized SBA-15 at this moment and the further optimization of synthesis conditions is needed.

References

1. N. Baccile, D. Grosso, C. Sanchez, *J. Mater. Chem.* **13**, 3011(2003).
2. N. Andersson, P. C. A. Alberius, J. S. Pedersen, L. Bergstrom, *Micropor. Mesopor. Mater.* **72**, 175(2004).
3. A. Endo, Y. Inagi, S. Fujisaki, T. Yamamoto, T. Ohmori, M. Nakaiwa, K. Iwakabe, *AIChE J.* **52**, 1275(2006).
4. D. Zhao, Q. Huo, J. Feng, B. F. Chmelka, G. D. Stucky, *J. Am. Chem. Soc.* **120**, 6024(1998).
5. P. I. Ravikovitch, A. V. Neimark, *J. Phys. Chem. B* **105**, 6817(2001).
6. A. Galarneau, C. Cambon, F. Di Renzo, R. Ryoo, M. Choi, F. Fajula, *New J. Chem.* **27**, 73(2003).
7. M. Imperor-Clerc, P. Davidson, A. Davidson, *J. Am. Chem. Soc.* **122**, 11925(2000).
8. B. L. Newalkar, S. Komarneni, *Chem. Mater.* **13**, 4573(2001).
9. K. Miyazawa, S. Inagaki, *Chem. Commun.* **2000**, 2121.
10. B. L. Newalkar, S. Komarneni, *Chem. Commun.* **2002**, 1774.

EFFECT OF THE LOWER CONSOLUTE TEMPERATURE ON THE STRUCTURE OF MESOPOROUS MATERIALS

J.L. BLIN, F. MICHAUX AND M.J. STEBE

*Equipe Physico-chimie des Colloïdes, UMR SRSMC N° 7565 Université Nancy 1/CNRS,
Faculté des Sciences, BP 239
F-54506, Vandoeuvre-les-Nancy cedex, France*

We have investigated the phase behavior of the $C_7F_{15}C_2H_4(OC_2H_4)_8OH$ [$R^F_7(EO)_8$] nonionic fluorinated surfactant in water as well as the effect of the presence of additives. Results show that the lower consolute temperature is increased upon addition of sodium iodide or of a hydrogenated nonionic surfactant. As regards the mesoporous syntheses, the self assembly mechanism are not favored if the lower consolute temperature is near the temperature at which the silica precursor is added to the micellar solution.

1. Introduction

One of the main characteristics of the nonionic surfactants-based system is that a miscibility gap is often encountered in the phase diagrams. The miscibility curve that determines the gap is called the lower consolute boundary (lcb). Below this curve a micellar phase L_1 exists, whereas above the lower consolute boundary the solution separates into two phases, one is rich in micelles (L'_1) and the other one is poor in micelles (L''_1). The minimal temperature at which the appearance of the micellar solution becomes turbid defined the value of the cloud point (CP), also labeled the lower consolute temperature. In the case of nonionic polyoxyethylene alkyl ether surfactants [$C_m(EO)_n$], this phenomenon is related to the fact that water around the polyoxyethylene chain is more structured than bulk water and it is associated to a strong entropy dominance [1,2] The value of CP depends strongly on the Hydrophilic-Lipophilic Balance (HLB) of the surfactant, but also on the presence of additives, which affects the intermicellar interactions [4]. Among the nonionic surfactants, the fluorinated ones are of particular interest. Indeed, linear fluorocarbon chains are less flexible than the hydrocarbon ones and, thus, present high melting points and as a consequence fluorinated surfactants have a higher thermal stability than their hydrogenated analogous. As hydrogenated nonionic surfactants, fluorinated ones can be used for the preparation of mesoporous materials through the self assembly mechanism. Moreover, it appears that the characteristics of the recovered materials, such as

the structure and the pore diameter are strongly related to the properties of the surfactant used for their preparation [3]. Even if in the literature many papers deal with the lower consolute temperature of nonionic surfactants, to the best of our knowledge, no detail investigation concerning the relation between the location of the lower consolute boundary and the structure of mesoporous materials is reported. Here, we have focused our investigations on the $C_{7F_{15}}C_2H_4(OC_2H_4)_8OH$ surfactant. The lower consolute temperature has been shifted by adding salts or a hydrogenated nonionic surfactant.

2. Materials and Methods

The used fluorinated surfactant, which was provided by DuPont, had an average chemical structure of $C_7F_{15}C_2H_4(OC_2H_4)_8OH$, labeled as $R^F_{7}(EO)_8$. The hydrogenated surfactant $C_{18}H_{35}(OC_2H_4)_{10}$, labeled as $R^H_{18}(EO)_{10}$ was purchased from Aldrich (Brij 97). In both cases, the hydrophilic chain moiety exhibited a Gaussian chain length distribution.

2.1. Determination of the surfactant properties

The samples were prepared by weighting the required amounts of surfactant and water or salt solutions in well-closed glass vials to avoid evaporation. They were left at controlled temperature for some hours in order to reach equilibrium. Micellar and liquid crystal domains were identified by visual observations. The lower consolute boundary was determined visually by noting the temperature at which the turbidity of the surfactant solutions was observed. In order to get this curve (lcb), these temperatures were plotted as a function of the surfactant concentration.

2.2. Mesoporous materials preparation and characterization

A micellar solution containing 10 wt.% of surfactant in water or in an aqueous electrolyte solution was prepared. The pH value of the solution was kept to 7.0. Tetramethoxysilane (TMOS), used as the silica source, was added dropwise into the micellar solution at different temperatures. The surfactant/silica molar ratio was adjusted to 0.5. The obtained samples were sealed in Teflon autoclaves and heated for 1 day at 80°C. The final products were recovered after ethanol extraction with a soxhlet apparatus during 48 hours.

X-ray measurements were carried out using a home-built apparatus, equipped with a classical tube ($\lambda = 1.54\text{\AA}$). The X-ray beam was focused by means of a curved gold/silica mirror on the detector placed at 527 mm from the

sample holder. Nitrogen adsorption – desorption isotherms were obtained at -196°C over a wide relative pressure range from 0.01 to 0.995 with a volumetric adsorption analyzer TRISTAR 3000 manufactured by Micromeritics. The samples were degassed further under vacuum for several hours at 320°C before nitrogen adsorption measurements. The pore diameter and the pore size distribution were determined by the BJH (Barret, Joyner, Halenda) method.

3. Results and discussion

3.1. The $R^F_7(\text{EO})_8$ /water binary system

The binary surfactant/water phase diagram (Fig. 1), that has been established between 20°C and 65°C , evidenced that $R^F_7(\text{EO})_8$ presents a cloud point at 34°C for 1 wt.% of surfactant. The isotropic micellar phase L_1 is found to be present over a wide range of surfactant compositions going up to 52.5 wt% at 20°C . The liquid crystal domain contains only a lamellar (L_a) phase which is stable over a temperature range going up to 57.5°C . At concentrations of $R^F_7(\text{EO})_8$ higher than 95%, a reverse micellar phase L_2 is formed.

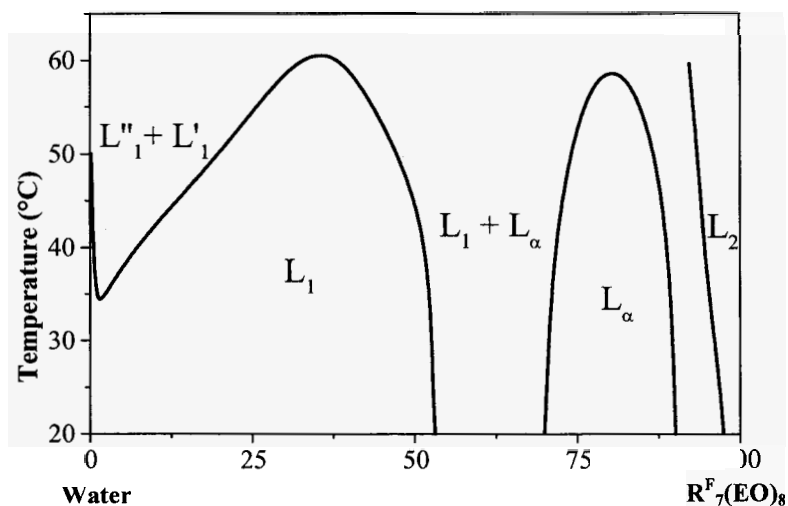


Figure 1. Temperature-composition phase diagram of $R^F_7(\text{EO})_8$ in water.

Mesoporous silica material has been prepared from a micellar solution of $R^F_7(\text{EO})_8$ at 10 wt.% in water, it should be noted that the demixion temperature of this solution is equal to 42.5°C . The silica precursor has been added to the

micellar solution at 20°C. The SAXS patterns of the material exhibits a single broad reflexion at 5.2 nm (Fig. 2a), which indicates the formation of a disordered structure. A type IV isotherm is obtained by nitrogen adsorption-desorption analysis (Fig. 2b). The specific surface area value is 697 m²/g. The pore diameter distribution is quite narrow and centered at 3.9 nm (Fig. 2b insert).

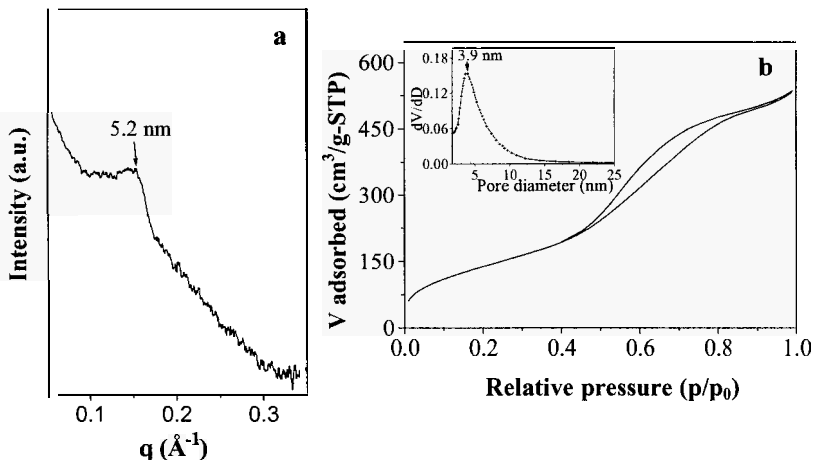


Figure 2. SAXS pattern (a) and the nitrogen adsorption-desorption isotherm (b) with the corresponding BJH pore size distribution curve (insert) of the silica obtained from the $\text{R}^{\text{F}}_7(\text{EO})_8/\text{water}$ system.

3.2. Effect of sodium iodide addition

The variation of the lower consolute boundary position with the addition of NaI is shown in Figure 3. We can observe that with the increase of the NaI concentration the lcb is shifted toward higher temperature (salting in effect) and the surfactant concentration, at which CP appears, is modified. For example at 10 wt.% of $\text{R}^{\text{F}}_7(\text{EO})_8$ the demixion temperature varies from 42.5 to 70°C, when the NaI concentration is raised from 0 to 3 mol.L⁻¹. These changes in the lcb's are mainly attributed to the anion. Indeed, even if the changes produced by individual ions are additive algebraically, the cations does not compete with ethylene oxide groups for water or hydration. Due to its low electronegativity, high polarizability and weak electrostatic field I^- disrupts the association of water molecules, which surround the micelles of surfactant. Thus I^- belongs to the chaotropic family. This kind of anion increases the concentration of single water

molecules, which are able to form hydrogen bonds with the ethylene oxide groups of nonionic surfactants. Hence, it raises the CP [5].

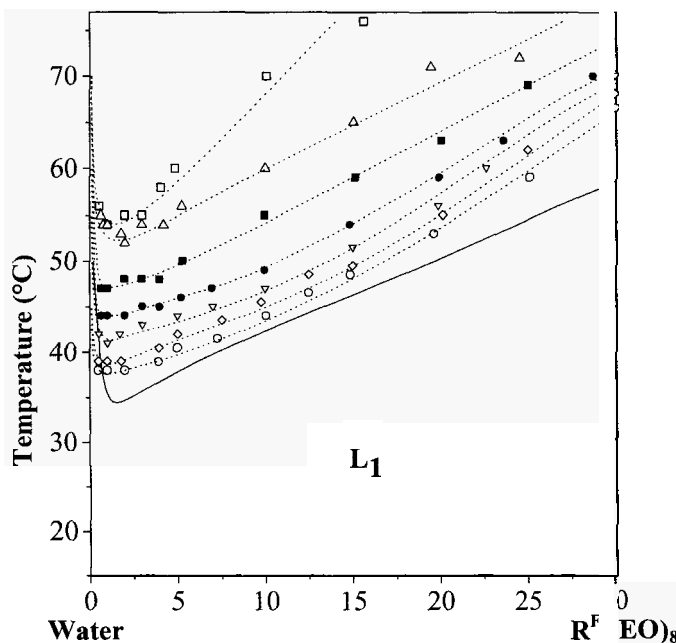


Figure 3. Lower consolute boundary location, of the $R_7^F(EO)_8$ surfactant in water (solid line) and in NaI aqueous solution \circ : 0.05; \diamond : 0.1; ∇ : 0.25; \bullet : 0.5; \blacksquare : 1; \triangle : 2 and \square : 3 mol.L⁻¹.

Then mesoporous materials have been prepared by adding the silica precursor to the micellar solution, containing NaI, at 20°C. By contrast to the sample obtained from the free salt system, when the concentration of the aqueous electrolyte solution is higher or equal to 0.1 mol.L⁻¹, in addition to a sharp peak at 4.9 nm, two peaks at 2.8 and 2.4 nm are detected on the SAXS patterns, (Fig. 4Ab-g). The presence of these two last peaks is suggestive of a hexagonal organization of the channels. Increasing the NaI concentration from 0.1 to 3 mol.L⁻¹ does not vary significantly the position of the first peak. According to Bragg's law, the unit cell dimension ($a_0=2d_{100}/\sqrt{3}$), which corresponds to the sum of the pore diameter and the thickness of the pore wall, can be calculated and its value is found equal to 5.6 nm. Therefore, we can conclude that, when the silica source is added at 20°C, in the investigated range of salt concentrations,

the presence of NaI, which increases the lower consolute temperature, involves a regular channel arrangement.

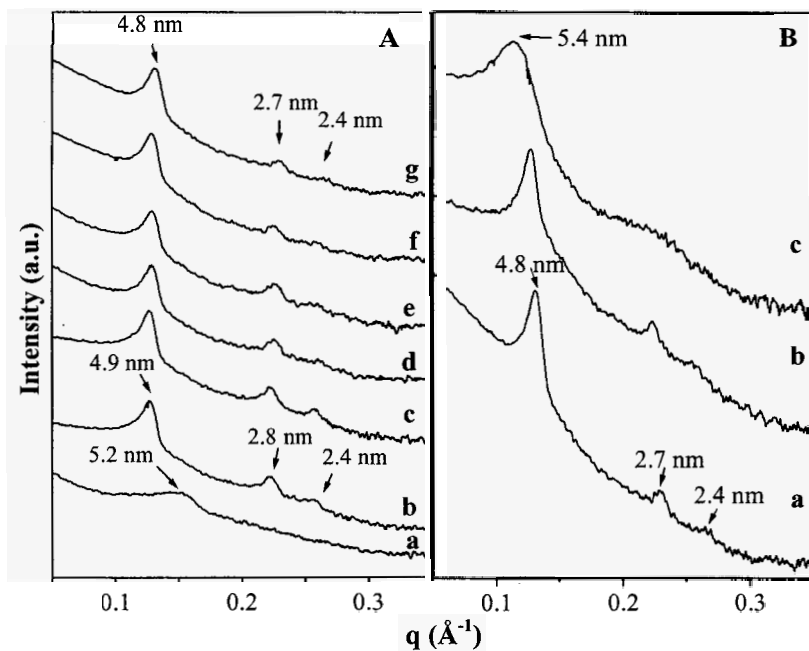


Figure 4. A : SAXS patterns of samples synthesized from NaI aqueous solutions a : 0.05; c : 0.1; c : 0.25; d : 0.5; e : 1; f : 2 and g : 3 mol.L⁻¹. The silica precursor has been added at 20°C. B : SAXS patterns of samples synthesized from a 2 mol.L⁻¹ NaI aqueous solution and by adding the silica precursor at a : 20, b : 30 and c : 40°C.

Nevertheless, the ordered structure is lost if the temperature at which the TMOS is incorporated to the 10 wt.% R^F₇(EO)₈ solution is too close to the lcb. As an example for the materials prepared from a 2 mol.L⁻¹ sodium iodide aqueous solution, the addition of the TMOS at 20 or 30°C leads to a hexagonal channel arrangement (Fig.4Ba,b), whereas only wormhole-like structure is obtained when TMOS is added at 40°C; i.e. at 20°C below the lcb (Fig. 4Bc). Indeed, while the 3 reflexions, characteristic of the hexagonal structure are evidenced on Figures 4Ba and 4Bb, only one broad peak is detected on Figure 4Bc, this reflects the lost of the mesopore ordering.

Whatever the synthesis conditions, a type IV isotherm (not shown), characteristic of mesoporous materials is obtained. When the transition from a

disordered to a hexagonal channel array occurs, the pore size distribution becomes narrower and the specific surface area increases. For example, when the concentration of NaI is changed from 0 to 0.1 mol.L⁻¹, the value of the specific area is raised from 697 to 913 m²/g. The mean pore diameter does not vary and the maximum of the pore size distribution remains centered at 3.9 nm.

From the results reported above it appears that to obtain ordered mesoporous materials the temperature, at which the silica precursor is added to the surfactant solution, has to be moved from the lower consolute boundary.

3.3. Effect of R^H₁₈(EO)₁₀ addition

Another way to shift the lower consolute temperature consists in mixing surfactants. Indeed, generally the physico-chemical properties of the mixtures are modified from that of homogeneous surfactant solutions. So, in order to confirm the above results, we have mixed the R^H₁₈(EO)₁₀ surfactant with the R^F₇(EO)₈ one. The hydrogenated surfactant has been selected according to various criterions. First, according to the literature it exhibits a CP at 75°C [6]. Secondly, at pH = 7 well ordered mesostructured silica can be synthesized from a micellar solution of R^H₁₈(EO)₁₀ at 10 wt.% in water, in which the TMOS is added either at 20 or 40°C [7]. The overall surfactant concentration in the solution was kept equal to 10wt.% and the content of R^H₁₈(EO)₁₀ in the mixture was varied from 0 to 5%. By this we can shift the lcb as a function R^H₁₈(EO)₁₀ content in the surfactant solution. An increase of the demixion temperature is noted with the incorporation of the hydrogenated surfactant (Fig. 5A). For example when the content of R^H₁₈(EO)₁₀ is changed from 0 to 5 wt.% the demixion temperature is varied from 42.5 to 63°C

After the determination of the lower consolute boundary the fluorinated-hydrogenated mixture has been employed for the design of mesoporous materials. As R^H₁₈(EO)₁₀ and R^F₇(EO)₈ bear ethylene oxide in their head groups we can assume that in the investigated range of concentrations, the mix of both surfactants leads to the formation of mixed micelles in all proportion [8]. Thus, mesoporous materials are prepared from only one type of micelles. The silica precursor has been added to the fluorinated-hydrogenated mixture at 40°C. From Figure 5B we can note that once again, the pore ordering occurs when the demixion temperature is raised. Indeed, while disordered silica is prepared from a 10 wt.% of R^F₇(EO)₈ well ordered mesostructure with uniform pore diameter is recovered if the surfactant solution contains 2wt.% of R^H₁₈(EO)₁₀ (Fig. 5Bb); i.e. when the lcb has been shifted to 50°C.

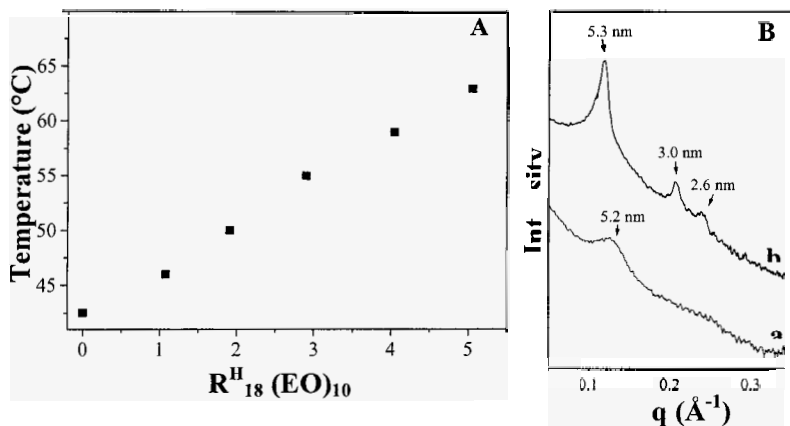


Figure 5. Evolution of the demixion temperature with the weight percent of $R^H_{18}(EO)_{10}$ for an overall surfactant concentration equal to 10 wt.% (A) and SAXS pattern of sample prepared from the $R^H_{18}(EO)_{10}$ - $R^F_7(EO)_8$ mixture (B). The loading of the hydrogenated surfactant in the mixture is equal to 0 wt.%(a) and to 2 wt.%(b).

3.4. Discussion

According to the phase diagram of the $R^F_7(EO)_8$ /water system for a surfactant concentration equal to 10 wt.%, micelles are formed at 20°C. So, the formation of disordered mesostructures when syntheses are carried out from the system without salt can not be related to the perturbation of the self assembly mechanism since, all conditions are together in order that such a mechanism occurs. Looking at the salting in effect of NaI or at the increase of the demixion temperature in the presence of $R^H_{18}(EO)_{10}$, we rather consider the location of the lower consolute boundary in order to explain this behavior. Indeed, adding sodium iodide or $R^H_{18}(EO)_{10}$ involves a shift of the lcb toward higher temperature and hexagonal mesostructures with a uniform pore size distribution are recovered in the same synthesis conditions. The self assembly mechanism is not favored if the lower consolute temperature is too low.

This tendency is confirmed by the investigation of the $C_8F_{17}C_2H_4(OC_2H_4)_9OH$ [$R^F_8(EO)_9$]/water system, which displays a CP higher than 90°C and leads to ordered mesoporous materials [4]. A shift of the lcb toward lower temperatures is evidenced with the addition of NaCl, which is known to be a kosmotropic anion; i.e. it decreases the CP [5]. For 10 wt.% of $R^F_8(EO)_9$ in a 3 mol.L⁻¹ sodium chloride solution the demixion temperature is decreased to 48°C. As regards the SAXS patterns of the molecular sieves

prepared from a 3 mol.L^{-1} NaCl aqueous solution, it is obvious that the hexagonal structure is maintained when TMOS is added at 40°C (Fig. 6Aa), but only disordered structures are recovered when the silica precursor is incorporated to the surfactant solution at 45 and 50°C (Fig. 6Abc). Actually, when the temperature, at which TMOS is added to the micellar solution, is increased; the secondary reflexions disappear and the shape of the nitrogen isotherm is modified. As it can be seen in Figure 6B, the capillary condensation is spread out over a larger range of relative pressures, meaning that compounds become less homogeneous in pore sizes. This is confirmed by the pore diameter distribution, which evidences the presence of micropores and shows a low dV/dD value in the mesopore range (Fig. 6Bb-c insert). These observations reflect the disorganization of the mesopore network.

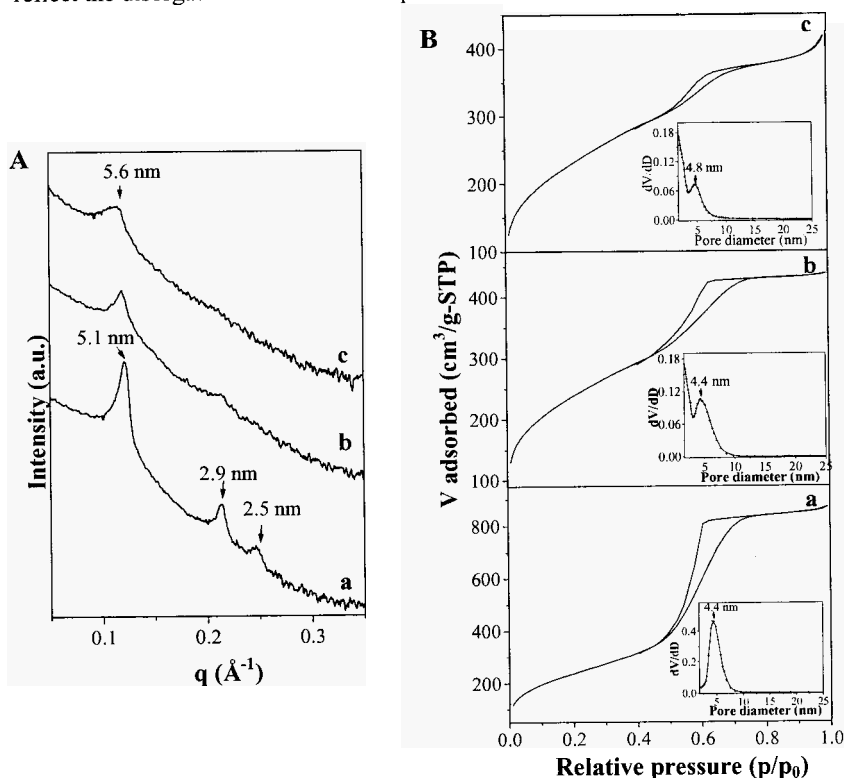


Figure 6. SAXS pattern (A) and the nitrogen adsorption-desorption isotherm with the corresponding BJH pore size distribution curve (insert) (B) of samples prepared from 10 wt.% of $R_f^s(\text{EO})_9$ in a 3 mol.L^{-1} NaCl aqueous solution; the silica precursor has been added at a : 40; b : 45; c : 50°C .

Moreover, this conclusion is supported by the experiments made by Zhao *et al.* [9]. The authors have synthesized silica mesostructures, in strong acid medium, by using the triblock copolymer P85 ($\text{EO}_{26}\text{PO}_{39}\text{EO}_{20}$) and P65 ($\text{E}_{20}\text{PO}_{30}\text{EO}_{20}$) as structuring agent and tetraethyloxysilane (TEOS) as silica precursor. Both P85 and P65 have a CP value of 82°C in water. These authors claim that ordered mesoporous silicates can only be obtained at a temperature higher than 90°C . To explain this tendency they assume that the high concentration of H^{+} and the ethanol released by the hydrolysis of TEOS have increased the CP of the triblock copolymer to a temperature higher than 100°C . However, they have not performed a detail study.

4. Conclusion

The $\text{R}^{\text{F}}_7(\text{EO})_8/\text{water}$ system presents a CP at 34°C and the addition of NaI shifts the lower consolute boundary toward higher temperature (salting in effect). While only disordered mesostructured are recovered from this system, well ordered mesostructure are synthesized from aqueous solutions of sodium iodide. The self assembly mechanism is not favored if the lcb is situated at low temperature is not increased or if demixion temperature is near the temperature at which the silica source is added to the micellar solution. This result is further confirmed by using a hydrogenated-fluorinated surfactant mixture as template for the preparation of the silica mesoporous materials

References

1. J. Sjöblom, P. Stenius and I. Danielsson In *Nonionic Surfactant Physical Chemistry*; M.J. Schick, Ed; Surfactant Science Series, **Vol. 23**; M. Dekker : New York, (1987) pp 369.
2. T. Inoue, H. Ohmura and D. Murata, *J. Colloid Interface Sci.* **258**, 374 (2003).
3. W.N.J. Maclay, *J. Colloid Interface Sci.* **11**, 272 (1956).
4. J.L. Blin and M.J. Stébé, *J.Phys.Chem.B.* **108**, 11399 (2004).
5. H. Schott, *J. Colloid Interface Sci.* **189**, 117 (1997).
6. K. Shigeta, M. Suzuki and H. Kunieda, *Progr. Colloid. Polymer. Sci.* **106**, 49 (1997).
7. F. Michaux, J.L. Blin and M.J. Stébé, *Langmuir* **23**, 2138 (2007).
8. W. Guo, E.K. Guzman, S.D. Heavin, Z. Li, B.M. Fung and S.D. Christian, *Langmuir* **8**, 2368 (1992).
9. M. Yuan, J. Tang, C. Yu, Y. Chen, B.Tu and D. Zhao, *Chem. Lett.* **32**, 660 (2003).

TAILORING POROUS SILICA PARTICLE AND PORE SIZE USING A MODIFIED STÖBER, FINK, BOHN (SFB) SYSTEM AND POST-SYNTHESIS HYDROTHERMAL TREATMENTS

DONAL KEANE, JOHN HANRAHAN, MARK COPLEY, JUSTIN HOLMES,
MICHAEL MORRIS

*Department of Chemistry, Materials Section, University College Cork,
Cork, Ireland*

Porous silica microspheres in the 1-2 μm range with low size deviation were synthesized by ammonia catalysed hydrolysis and condensation of tetraethylorthosilicate using methanol as co-solvent and cetyltrimethylammonium bromide as surfactant. The mesopore diameter was subsequently expanded from $<20 \text{ \AA}$ to $\sim 200 \text{ \AA}$ by a postsynthesis hydrothermal treatment in a water-amine emulsion system followed by controlled dissolution in aqueous sodium hydroxide. XRD, TEM, and N_2 sorption measurements were used to characterize pore properties. ESZ technique in conjunction with SEM was used to establish morphology and measure particle size and size distribution. Particle aggregation and scale up reproducibility are discussed. Preliminary chromatographic results are presented which demonstrate the applicability of these particles in Ultra Performance Liquid Chromatography (UPLC).

1. Introduction

Since the first report of surfactant-templated silica (STS) in the early nineties [1], much effort has been made to control its bulk morphology. Various morphologies can be generated utilising sol-gel processing techniques [2]. In particular, the synthesis of spherical mesoporous silica with well defined particle and pore size has been a strong focus because of chromatographic separation applications [3].

High-performance liquid chromatography (HPLC) is currently the most commonly applied technique for separating and analysing multi-component mixtures. Development in pumping technology (allowing higher pressures to be attained at reasonable cost) and more available high sensitive mass spectrometer-based detection systems means that UPLC [4] may be realised provided that column technologies improve. The improved resolution, sensitivity and speed of

analysis offered by UPLC are conditional on the delivery of porous ($>70 \text{ \AA}$) monodispersed sub-2 micron particle stationary phases.

Spherical STS in the micron size range can be precipitated from both acidic and alkaline solution. Zhao *et al.* [5] synthesized mesoporous SBA-15 spheres ($\sim 1 \text{ \mu m}$) in acidic conditions. In alkaline solution, the process is commonly labeled as a modification of a popular system reported by Stöber, Fink and Bohn (SFB) in the late 1960's which results in monodisperse silica spheres in the micron size range by ammonia catalysed reactions of alkyl silicates in alcoholic solutions [6]. In 1997, Grun *et al.* [7] combined the SFB method with the surfactant templating approach to produce mesoporous MCM-41 silica microspheres in the micron size range. This so called 'modified' SFB (m-SFB) system consists of five reagents: a silica source, water, an alkaline catalyst, alcohol and a surfactant. By empirically relating the initial synthesis conditions to the final product, silica particles with varying morphology, size, size distribution, degree of aggregation, pore size and phase have been produced [8-12]. Thus, particle and pore size may be 'tailored' by relating reactant stoichiometry and experimental conditions to final silica properties rather than design through understanding the complex physical and chemical processes involved. In general, 'tailoring' monodisperse precipitates [13] and porous materials [14] has progressed in this manner.

Various methods are available to modify the pore size of STS. However, the application of many of these methods to the m-SFB system result in loss of control of particle size or cause particle aggregation rendering them useless for chromatographic separations. For example, techniques used to achieve a larger pore size in direct synthesis (prior to addition of silica source) is a major challenge as any change to an established system is likely to effect particle growth and final size.

Hydrothermal treatments of uncalcined non-spherical CTAB templated MCM-41 silica have been found to increase the pore size whilst maintaining pore structure [15-17]. Sayari *et al.* [18,19] subsequently increased the degree of expansion by using amines as swelling agents in direct and post-synthesis hydrothermal treatments, albeit with a loss of structural order. The post-synthesis hydrothermal treatments in particular, may be applied to the m-SFB system to increase the pore size without causing particle aggregation [20].

We show here that the pore size may be further increased by controlled silica dissolution in aqueous NaOH. Although silica is well known to be soluble in alkali and the chemical processes involved have been described [21], this technique is not common for the pore expansion of STS.

The specific goal of this work was to produce monodisperse mesoporous silica microspheres with a particle diameter in the 1-2 μm range and mesopore size greater than 70 \AA to find application in UPLC. A process patent has been subsequently filed [22].

2. Experimental

2.1. Materials and methods

Tetraethylorthosilicate (TEOS) and hexadecyltrimethylammonium bromide (CTAB) were obtained from Fluka. N,N-Dimethyldecylamine (DMDA) =90%, Ammonium hydroxide solution 28.0-30.0% (NH_4OH) and sodium hydroxide (NaOH), reagent grade, =98%, pellets (anhydrous) were obtained from Sigma-Aldrich. All chemicals were used without further purification.

Nitrogen sorption measurements were performed on a Micromeritics Gemini 2375 volumetric analyzer. Prior to measurement, samples were degassed at 200 $^\circ\text{C}$ for 12 hours. The specific surface area was calculated using the BET (Brunauer-Emmett-Teller) method. The pore size distribution (PSD) was calculated from adsorption data using the BJH (Barrett-Joyner-Halenda) method. The average pore size (w_{BJH}) is defined as the maximum of the PSD. Scanning electron microscopy (JEOL JSM – 5510) was used to obtain images of the silica microspheres. Transmission electron microscopy (JEOL JEM – 2000) investigations were made on crushed samples deposited on copper grids by ultrasonication. Powder X-ray diffraction data (PXRD) were collected using a Philips Accelerator apparatus (40kV, 40 mA) equipped with a conventional Cu anode at step size $0.02^\circ \text{ s}^{-1}$ 2θ . Particle size distributions (PaSD) were measured using the electrical sensing zone (ESZ) technique on a Beckmann Multisizer 3 Coulter Counter.

2.2. Synthesis of mesoporous silica microspheres

Mesoporous silica microspheres were synthesized using a similar system as that reported by Shimura *et al.* [12] in a simple batch process at room temperature. In a typical preparation, 1.2g CTAB is first dissolved in 500ml of methanol. 32 ml NH_4OH and 90 ml of water are added to the mixture and stirred for 15 minutes before the one step addition of 1.8 ml TEOS resulting in a sol with the following molar ratio: 1TEOS:0.4CTAB:773 H_2O :1524MeOH:62 NH_3 . The sol is allowed to stir at 300 rpm for one day. The silica precipitate is separated by filtration and dried at room temperature.

2.3. Pore Size Expansion

An emulsion of DMDA in H₂O (3.3% v/v) was stirred for 1 hr. As synthesized uncalcined silica powder (2.5% w/w) was added to the emulsion and stirred for a further hour and treated statically under autogenous pressure in a Schott borosilicate bottle at 110 °C for 48 hours. The surfactants were removed by calcination at 550 °C for 10 hours. The DMDA treated calcined silica (1% w/w) was then stirred in 0.05M sodium hydroxide at room temperature for 1 hour. The silica was separated by filtration and the wet slurry was dried at 200 °C.

3. Results and discussion

3.1. Particle size control

Figure 1 shows a PaSD with SEM images (inset) of silica particles synthesized from the m-SFB method. The average particle size measured by ESZ is 1.41 μm which is in good agreement with particles measured from SEM. However, ESZ analysis typically reveals a smaller secondary peak at slightly larger size which is attributed to particle aggregation during growth. Figure 1 shows doublets, triplets and larger aggregates commonly observed by SEM. Particle aggregation is common in less dilute m-SFB sols which is not surprising considering that long chain alkyl substituted quaternary ammonium salts such as CTAB are strong flocculating agents for colloidal silica [21].

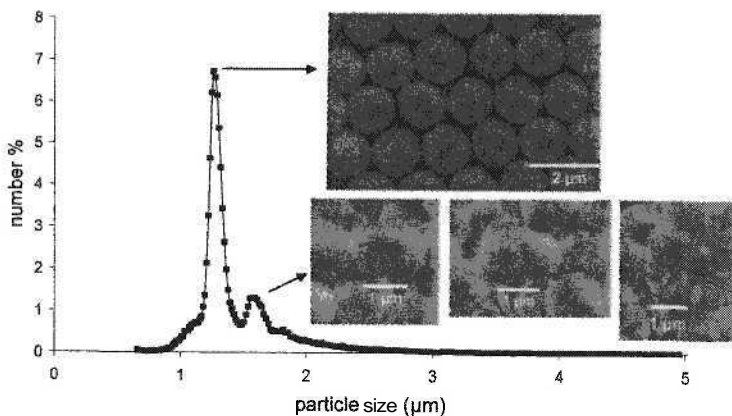


Figure 1. Particle size distribution and SEM images (inset) of m-SFB silica

The limitations of microscopy as a particle sizing technique are evident in this system. Even if particle sizes of a large number of particles are taken this may

not be representative of the entire sample. Furthermore, the procedure is tedious and time consuming and not trivial when an image analysis program is used [23]. Thus, despite reports of particle size and particle size distributions using this direct method being common in the literature, it is clear SEM is not a quantifiable analytical tool (particularly when aggregates are common).

It is useful to compare the processing and particle size control of the m-SFB method with the original SFB method. Stöber *et al.* [6] systematically varied reaction parameters so that silica particles could be tailored from 0.05 μm to 2 μm in diameter. Bogush *et al.* [24] extended this work, focusing on the TEOS, EtOH, NH_3 , H_2O system and established concentration ranges in which monodispersity is maintained. We found the m-SFB synthesis used here to be too sensitive to experimental conditions for similar relationships to be established. For example, unlike SFB silica, particle size and size deviation was found to be dependent on factors such as batch size and stirring speed. As is the case with many monodisperse precipitates, the sensitivity of the particle properties to the experimental conditions puts special demand on engineers who wish to scale up [13], and experimental protocols are necessary to achieve reproducibility.

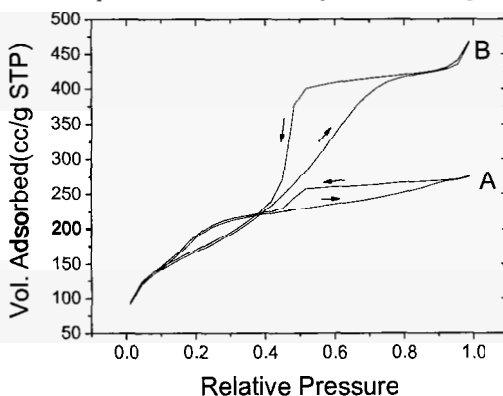


Figure 2. N_2 sorption isotherms of untreated (A) and amine treated (B) silica

3.2. Pore Size Expansion

As-synthesized particles display one broad low angle x-ray diffraction peak of low intensity characteristic of a disordered pore structure. This is due to the methanol content in the mixture being greater than 60% w/w [25]. The pore diameter is typically below 20 \AA which is too small for UPLC. The pore size may be expanded by a hydrothermal treatment of uncalcined silica in a water-

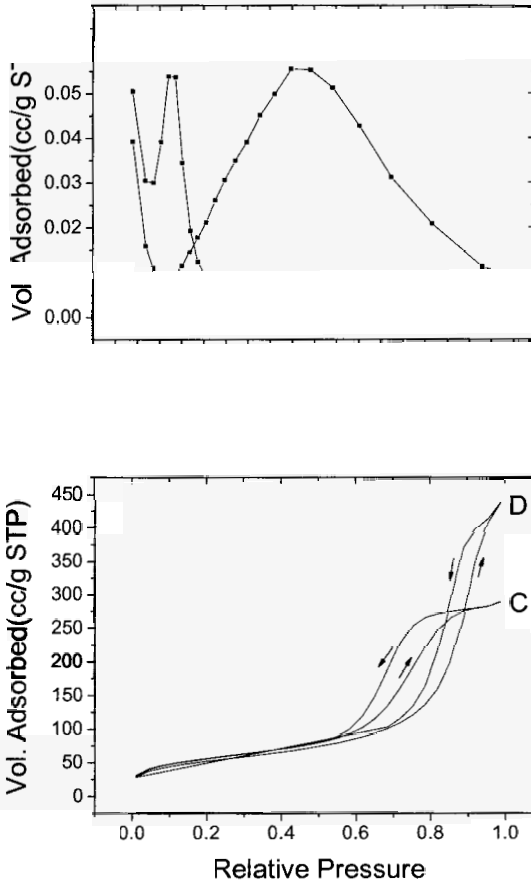


Figure 4. N₂ sorption isotherms of single etched (C) and double etched (D) silica

The pore size may be further increased by hydrothermally treating the calcined amine treated silica in aqueous NaOH in single or multiple steps. Figure 4 shows nitrogen sorption isotherms of single and double etched particles. Pore size and pore size distribution both increase as shown in Figure 5. The large

pore system is visible by TEM as shown in Figure 6. ESZ analysis showed that the particle size decreased and the size deviation increased. However, the morphology remains spherical as shown by TEM. The etching conditions described here are not critical to achieve pore expansion. What is important is that the rate of silica dissolution is controlled, and this is dependant on many factors [21]. Treatment effect on particle size must also be considered. The porosity measurements at each stage of the process are shown in Table 1.

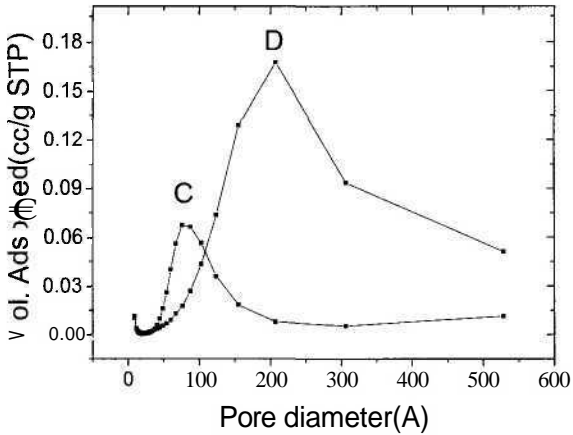


Figure 5. PSDs of single etched (C) and double etched (D) silica

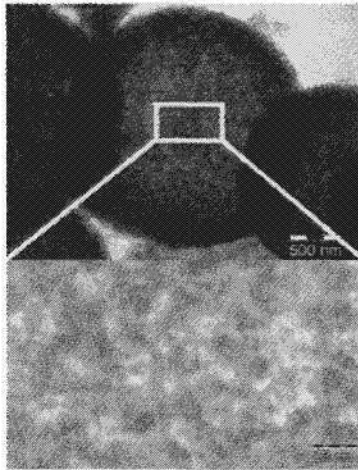


Figure 6. TEM images of single etched particles

Table 1. Porosity measurements of untreated (A), amine treated (B), single etched (C) and double etched (D) silica

	$S_{\text{BET}}/\text{m}^2\text{g}^{-1}$	$w_{\text{BJH}}/\text{\AA}$	$V_{\text{BJH}}/\text{cm}^3\text{g}^{-1}$
A	704	18	0.45
B	599	47	0.60
C	197	81	0.45
D	179	206	0.67

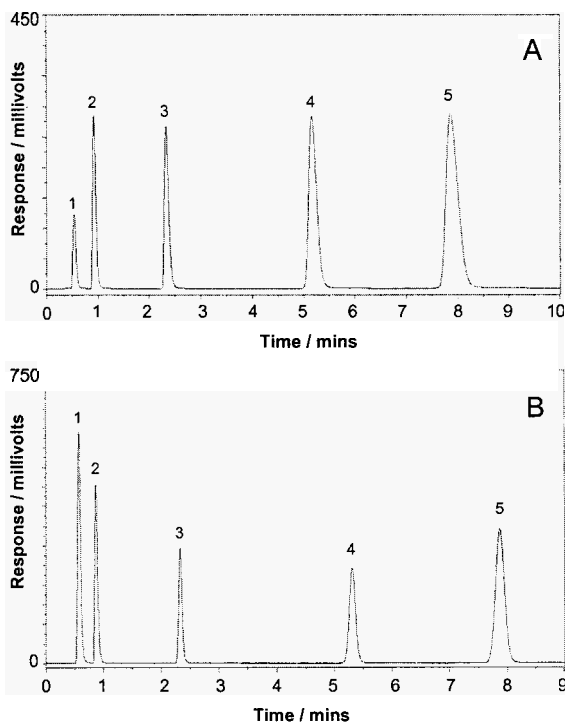


Figure 7. Separation of 1) Uracil 2) Dimethyl phthalate 3) Toluene 4) Biphenyl 5) Phenanthrene on (A) C-18 modified m-SFB SiO_2 and (B) commercial sub-2 μm SiO_2

3.3. Chromatography

The treated silica was C-18 modified, packed into a 50×2.1 mm column and compared to a commercial Sub 2 μm reference (Zorbax XDB 1.8 μm C-18). Tests were performed to separate non-polar and polar molecules. Results of a non-polar separation are shown in Figure 7. M-SFB silica shows similar retention times but greater peak asymmetry and poorer column efficiency. The

back pressure was approximately double that of a commercial column. Separation of polar analytes showed increased retention times and peak tailing characteristic of a low purity (high metal content) silica. Metal ions activate surface silanol groups, increasing polarity. A further treatment to remove the sodium or replacing NaOH with HF in the pore expansion is necessary for successful separation of polar molecules.

4. Conclusions

(1) Large pore (~200 Å) silica microspheres in the 1-2 µm range have been produced by a m-SFB process and post-synthesis hydrothermal treatments ; in a water amine emulsion and in aqueous NaOH.

(2) ESZ particle size distributions typically shows a satellite peak which has been attributed to particle aggregation during growth. This highlights the limitations of microscopy as a primary particle sizing technique. The m-SFB method is more sensitive than the original SFB method and protocols are necessary for particle size reproducibility.

(3) The pore size is increased threefold by hydrothermal treatment of uncalcined particles in a water-DMDA emulsion and further increased by etching calcined particles in aqueous NaOH. The pore size distribution increases in both cases. The particle size distribution is maintained after the amine treatment. There is a decrease in particle size and an increase in size distribution after etching.

(4) Preliminary separations of non-polar analytes show similar performance to commercial columns. Future research includes controlling the particle size through systematic optimization/particle sizing and replacement of NaOH with HF as etchant to increase purity for the separation of polar analytes.

Acknowledgments

We wish to thank Enterprise Ireland for financial support under their proof of concept (EI/POC/04/304) grant allocation scheme. We would also like to thank Dr. Stephane Constantin (ThermoFisher Scientific) for ESZ particle sizing and Andy Smith (Hichrom Limited) for packing and chromatographic testing of the columns. Helpful insights were provided by both.

References

1. J. S. Beck, J. C. Vartuli, W. J. Roth, M. E. Leonowicz, C. T. Kresge, K. D. Schmitt, C. T. W. Chu, D. H. Olson, E. W. Sheppard, S. B. McCullen, J. B. Higgins and J. L. Schlenker, *J. Am. Chem. Soc.* **114**, 10834 (1992).

2. P. Selvam, S. K. Bhatia and C. G. Sonwane, *Ind. Eng. Chem. Res.* **40**, 3237 (2001).
3. K. K. Unger, D. Kumar, M. Grun, G. Buchel, S. Ludtke, T. Adam, K. Schumacher and S. Renker, *J. Chromatogr. A.* **892**, 47 (2000).
4. M. E. Swartz, *J. Liq. Chromatogr. R. T.* **28**, 1253 (2005).
5. D. Zhao, J. Sun, Q. Li and G. D. Stucky, *Chem. Mater.* **12**, 275 (2000).
6. W. Stöber, A. Fink and E. Bohn, *J. Colloid. Interf. Sci.* **26**, 62 (1968).
7. M. Grun, I. Lauer and K. K. Unger, *Adv. Mater.* **9**, 254 (1997).
8. G. Buchel, M. Grun, K. K. Unger, A. Matsumoto and K. Tsutsumi, *Supramol. Sci.* **5**, 253 (1998).
9. Q. Cai, Z. S. Luo, W. Q. Pang, Y. W. Fan, X. H. Chen and F. Z. Cui, *Chem. Mater.* **13**, 258 (2001).
10. R. I. Nooney, D. Thirunavukkarasu, Y. M. Chen, R. Josephs and A. E. Ostafin, *Chem. Mater.* **14**, 4721 (2002).
11. K. Yano and Y. Fukushima, *J. Mater. Chem.* **13**, 2577 (2003).
12. N. Shimura and M. Ogawa, *Bull. Chem. Soc. Jpn.* **78**, 1154 (2005).
13. E. Matijevic, *Chem. Mater.* **5**, 412 (1993).
14. T. J. Barton, L. M. Bull, W. G. Klemperer, D. A. Loy, B. McEnaney, M. Misono, P. A. Monson, G. Pez, G. W. Scherer, J. C. Vartuli and O. M. Yaghi, *Chem. Mater.* **11**, 2633 (1999).
15. D. Khushalani, A. Kuperman, G. A. Ozin, K. Tanaka, J. Garces, M. M. Olken and N. Coombs, *Adv. Mater.* **7**, 842 (1995).
16. Q. S. Huo, D. I. Margolese and G. D. Stucky, *Chem. Mater.* **8**, 1147 (1996).
17. C. F. Cheng, W. Z. Zhou, D. H. Park, J. Klinowski, M. Hargreaves and L. F. Gladden, *J. Chem. Soc. Faraday. T.* **93**, 359 (1997).
18. A. Sayari, M. Kruk, M. Jaroniec and I. L. Moudrakovski, *Adv. Mater.* **10**, 1376 (1998).
19. A. Sayari, *Angew. Chem. Int. Edit.* **39**, 2920 (2000).
20. M. Grun, C. Buchel, D. Kumar, K. Schumacher, B. Bidlingmaier and K. K. Unger, *Stud. Surf. Sci. Catal.* **128**, 155 (2000).
21. R. K. Iler, *The Chemistry of Silica*, Wiley, New York (1979).
22. J. P. Hanrahan, D. A. Keane, M. P. Copley, J. D. Holmes and M. A. Morris, *Patent pending* (2007).
23. J. L. Bass, *Surfactant Science Series (Colloidal Silica)* **131**, 535 (2006).
24. G. H. Bogush, M. A. Tracy and C. F. Zukoski, *J. Non-Cryst. Solids.* **104**, 95 (1988).
25. M. T. Anderson, J. E. Martin, J. G. Odinek and P. P. Newcomer, *Chem. Mater.* **10**, 1490 (1998).

THREE DIMENSIONAL MESOPOROUS FeSBA-1 CATALYSTS FOR ALKYLATION AND ACYLATION OF AROMATICS

VEERAPPAN VAITHILINGAM BALASUBRAMANIAN, JOSENA JUSTUS,
AJAYAN VINU*

*WPI Center for Materials Nanoarchitectonics, National Institute for Materials Science,
1-1, Namiki, Tsukuba, 305-0044, Japan. Email: vinu.ajayan@nims.go.jp*

Three dimensional cage type mesoporous ferrosilicate materials with different n_{Si}/n_{Fe} ratios have been prepared through soft templating technique using cetyltriethylammonium bromide as a surfactant in a highly acidic medium. All the materials were evidently characterized by AAS, XRD, N_2 adsorption, and XPS. The catalytic activities of these catalysts in the isopropylation of m-cresol and acylation of toluene were investigated and the results are compared with one dimensional mesoporous catalysts. The influence of various reaction parameters such as reaction temperature and reactant feed ratio was also studied. Among these catalysts, FeSBA-1(36) gave excellent conversion on both m-cresol and toluene as compared to those of the uni-dimensional mesoporous catalysts.

1. Introduction

Mesoporous molecular sieves has attracted considerable attention in the recent years because of their potential applications in many fields including adsorption, separation, catalysis, and nanotechnology owing to their excellent textural characteristics such as high surface area, pore volume, and well ordered pore structure [1-12]. These materials were first discovered by Mobil Oil Corporation researchers and named as M41S materials, which have been further classified into three sub-groups: a hexagonal (MCM-41), a cubic (MCM-48) and a lamellar phase (MCM-50) [1,2]. Among these materials, the materials with the three dimensional (3D) pore systems are more advantageous than the uni-dimensional materials for many catalytic applications because the 3D pore structures support the easy and faster diffusion of reactant molecules and restrict the pore damage or locking due to the coke formation [13-15]. Huo et al. synthesized a novel mesoporous silica materials with a three dimensional cubic structure of uniform pore size, denoted SBA-1 formed by counter ion-mediated ($S^+ X^- I^-$) pathway [cationic surfactants (S^+), halogen anions (X^-) and cationic silicic acid species (I^-)] having a cage-type structure with open windows [16, 17]. However, the pure silica materials possess neutral framework, which does not provide acid sites required for the catalytic applications. Consequently, they are

considered to be unsuitable as catalysts for various industrially important organic bulky molecule transformations. In order to make them available for catalytic applications, it is extremely necessary to incorporate di or trivalent metal ions in the silica framework of SBA-1. However, the incorporation of metal atoms in the silica materials synthesized in a highly acidic medium has never been easy because of the high solubility of the metal source in the harsh condition. Tatsumi et al. investigated the synthesis of V- and Mo-containing SBA-1 and gained control of the crystal morphology [18-20]. Subsequently, Vinu et al. reported the direct synthesis of AlSBA-1 containing exclusively tetrahedral coordinated aluminum and the catalytic activity of this material in the isomerization of *n*-decane, as well as the synthesis of cobalt-containing SBA-1 [21, 22].

Friedel-Crafts alkylation and acylation of phenols are industrially important reaction because many alkyl or arylphenols are used as intermediates in the manufacture of antioxidants, ultraviolet absorbers, phenolic resins, polymerization inhibitors and heat stabilizers [23]. These reactions have been extensively studied by many researchers using AlCl_3 , FeCl_3 , BF_3 , HF, H_3PO_4 , H_2SO_4 , silica-alumina, cation exchange resins and microporous molecular sieves. However, the utilization of these catalysts is connected with a numerous drawbacks and technical difficulties, such as high toxicity, corrosion, disposal and dangerous by products production. In this context, it is obligatory for the development of new types of acid catalysts being able to transform aromatic alcohols and aromatic hydrocarbons into the alkylated aromatic alcohols and alkyl-aryl or aryl-aryl ketones respectively and also it is a challenge in the present day research in heterogeneous catalysis [24].

Iron containing microporous molecular sieves have attracted considerable attention due to their remarkable activity as catalysts for the reduction of nitrous oxides [25], oxidation of benzene to phenol [26] and the selective oxidation of methane [27]. However, they are not useful for treating heavier feeds and the production of more bulky fine chemicals, owing to their small pore size. These problems can be overcome by using the iron substituted mesoporous catalysts. Very recently, Vinu et al. have reported the direct synthesis of FeSBA-1 materials with different iron contents and studied their catalytic activity in the alkylation of phenol [14-15]. It was demonstrated that the FeSBA-1 catalysts are highly active for the alkylation reaction [14-15].

Here we demonstrate the catalytic activities of FeSBA-1 catalysts with different $n_{\text{Si}}/n_{\text{Fe}}$ ratios in the isopropylation of *m*-cresol and the acylation of toluene. FeSBA-1 materials with different $n_{\text{Si}}/n_{\text{Fe}}$ ratios were synthesized through a soft templating technique using cetyltriethylammonium bromide as a surfactant in a highly acidic medium. All the materials were unambiguously characterized

by AAS, XRD, N₂ adsorption, and XPS. The isopropylation of *m*-cresol and the acylation of toluene were carried out over FeSBA-1 catalysts in the vapor phase. The influence of various reaction parameters such as reaction temperature, reactant feed ratio, and weight hourly space velocity affecting the activity and selectivity of FeSBA-1 were also studied. Under the optimized reaction conditions, the FeSBA-1(36) catalyst showed superior catalytic performance for both the reactions as compared to the uni-dimensional mesoporous catalysts.

2. Experimental Section

Iron containing SBA-1 was synthesized under acidic conditions using cetyltriethylammonium bromide (CTEABr) as the surfactant, tetraethylorthosilicate (TEOS) as the silica source and ferric nitrate nonahydrate as the iron source. A typical synthesis procedure for FeSBA-1 is as follows: Solution A was prepared by adding 0.812 g of CTEABr to an appropriate amount of the aqueous solution of 4.4M HCl ($n_{\text{HCl}}/n_{\text{H}_2\text{O}}$ ratio was fixed to 0.08). The solution thus obtained was cooled to 0 °C and homogenized for 30 min. TEOS and Fe(NO₃)₃ · 9 H₂O were precooled to 0 °C and then added to solution A under vigorous stirring and continued the stirring for another 5 h at 0 °C. Thereafter, the reaction mixture was heated to 100 °C for one hour. A sequence of samples was prepared by changing the $n_{\text{Si}}/n_{\text{Fe}}$ ratio in the gel and the $n_{\text{HCl}}/n_{\text{Si}}$ ratio was fixed to 10. The samples were labeled FeSBA-1(x) where x denotes the $n_{\text{Si}}/n_{\text{Fe}}$ molar ratio. The solid product was recovered by filtration and dried in an oven at 100 °C overnight. The molar composition of the gel was 1 TEOS: 0.0025 - 0.025 Fe₂O₃: 0.2 CTEABr : 10 - 56 HCl : 125 - 700 H₂O. The as-synthesized material was then calcined in air by raising the temperature from 20 to 550 °C with a heating rate of 1.8 °C/min and keeping the sample at the final temperature for 10 h.

The powder X-ray diffraction patterns of FeSBA-1 materials were collected on a Siemens D5005 diffractometer using CuK α ($\lambda = 0.154$ nm) radiation. The diffractograms were recorded in the 2θ range of 0.8 to 10 ° with a 2θ step size of 0.01 ° and a step time of 10 seconds.

The X-ray photoelectron spectroscopy (XPS) measurements were carried out in a PHI 5400 instrument with a 200 W MgK α probe beam to characterize the samples. The spectrometer was configured to operate at high resolution with pass energy of 20 eV. Prior to the analysis, the samples were evacuated at high vacuum and then introduced into the analysis chamber. Survey and multiregion spectra were recorded at O_{1s}, Si_{2p}, and Fe_{2p} photoelectron peaks. Each spectra

region of photoelectron interest was scanned several times to obtain good signal-to-noise ratios.

Nitrogen adsorption and desorption isotherms were measured at $-196\text{ }^{\circ}\text{C}$ on a Quantachrome Autosorb 1 sorption analyzer. Before analysis, all samples were out gassed for 3 hours at $250\text{ }^{\circ}\text{C}$ under vacuum ($p < 10^{-5}\text{ hPa}$) in the degas port of the adsorption analyzer. The specific surface area was calculated using the BET model. The pore size was obtained from the adsorption branch of the nitrogen isotherms using the corrected form of the Kelvin equation by means of the Barrett-Joyner-Halenda method as proposed by Kruk et al.[28]

$$r(p/p_0) = \frac{2\gamma VL}{RT \ln[p_0/p]} + t(p/p_0) + 0.3\text{ nm} \quad (1)$$

In equation (1), VL is the molar volume of the liquid adsorbate, γ is its surface tension ($8.88 \cdot 10^{-3}\text{ N/m}$), R is the gas constant ($8.314\text{ J/(mol}\cdot\text{K)}$), and T is the absolute temperature (77 K). $t(p/p_0)$ is the statistical film thickness of nitrogen adsorbate in pores of the SBA-1 as a function of the relative pressure p/p_0 .

The vapour phase alkylation of *m*-cresol with isopropanol was carried out in a continuous fixed-bed down flow reactor made up of a quartz glass tube with a length of 40 cm and an internal diameter of 2 cm. About 0.5 g of catalyst was placed in the reactor and supported on either side with a thin layer of quartz wool and ceramic beads. The needed temperature is attained with the help of a tubular furnace and the temperature is controlled by a temperature controller. Reactants were fed into the reactor using a 20 ml glass syringe attached with infusion pump to maintain the space velocity. The bottom of the reactor was connected to a spiral condenser and receiver to collect the products. In all catalytic runs the products collected at the first 15 minutes were decanted in order to set right the reaction conditions and the product collected after one hour was analyzed for identification.

The liquid phase acetylation of toluene with acetic anhydride (AA) was carried out in an oil bath using 50 ml two necked flask connected with condenser and septum. The reaction mixture is stirred well by magnetic stirrer equipped with heating plate and the temperature controller. Samples were withdrawn at regular intervals of time by glass syringe through septum and analyzed immediately.

For both alkylation and acetylation reaction, the analysis is done by a Shimadzu gas chromatograph GC-17A using a DB-5 capillary column. Product identification was achieved by co-injection and GC-MS. The catalysts were activated in air at $500\text{ }^{\circ}\text{C}$ for 4 h with a flow rate of 50 ml/min and cooled to room temperature prior to their use in the reaction.

3. Results and Discussion

The powder XRD patterns of FeSBA-1 samples prepared with various ratios of $n_{\text{Si}}/n_{\text{Fe}}$ are depicted in Figure 1. All the samples exhibit an intense (210) reflection with smaller (200) and (211) reflections confirming the characteristic XRD patterns of the SBA-1 cubic phase which can be indexed to $Pm\bar{3}n$ space group, matches well with those reported in the literatures [6,7,16,17]. It is interesting to note that the intensity of the (210) peak increase with increasing Fe content of the material, which could be mainly due to the presence of nitrate ions (from the Fe source, ferric nitrate) in the synthesis gel mixture which would catalyze the condensation of iron hydroxo species and helps the formation of thicker walls and well ordered structure. Moreover, it is interesting to note that the unit cell parameter increases from 7.6 to 7.9 nm with increasing Fe content (Table 1).

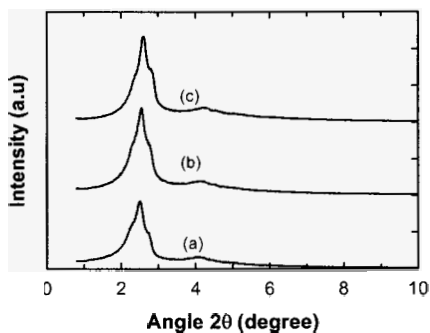


Figure 1: XRD powder patterns of calcined FeSBA-1 samples: (a) FeSBA-1(36), (b) FeSBA-1(90), and (c) FeSBA-1(120).

XPS was used to analyze the nature and coordination of the elements present in FeSBA-1 samples using their respective binding energy values. Figure 2A shows the survey spectrum of FeSBA-1 samples with different $n_{\text{Si}}/n_{\text{Fe}}$ ratios. All the samples exhibit five sharp peaks which are indicative of $\text{Fe}_{2\text{p}}$, $\text{O}_{1\text{s}}$, $\text{C}_{1\text{s}}$, $\text{Si}_{2\text{s}}$ and $\text{Si}_{2\text{p}}$. The $\text{C}_{1\text{s}}$ peak can be assigned to the adventitious carbon for calibrating binding energy as a reference. The elemental composition of, mainly Si and Fe of all the samples from their survey spectrum is in close agreement with the results obtained from the elementary analysis. The $\text{Fe}_{2\text{p}}$ spectra of the FeSBA-1 sample with different iron content are shown in Figure 2B. As can be seen in the Figure 2B, all the samples had two sharp peaks with binding energy values of 710.9 and 723.7 eV. In the case of FeSBA-1(36), a shoulder peak with the binding energy of 712.9 eV was observed. The $\text{Fe}_{2\text{p}}$ peak at 710.0 eV is

typically assigned for iron atom with +3 coordination state. Further, the shoulder peak in the FeSBA-1(36) at 712.9 eV can be assigned to small iron oxide particles which normally have binding energy values of 710.7 and 712 eV. This reveals that the FeSBA-1(36) sample contain a little amount of octahedral coordinated iron atoms. In addition, the broad peak which is centered at 723.7 eV may be assigned to iron atoms coordinated to hydroxyl groups or water molecules in the samples.

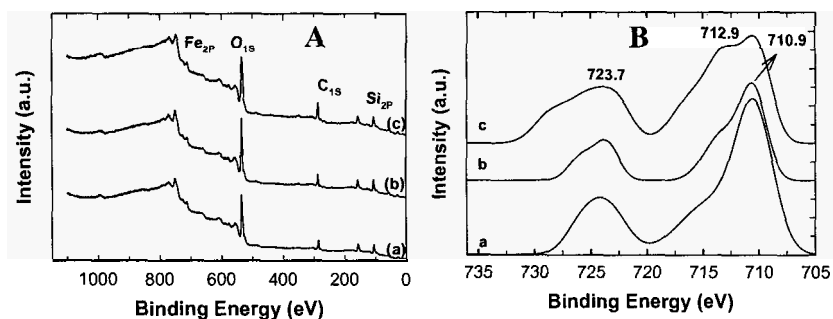


Figure 2: The XPS (A) survey and (B) Fe_{2p} spectra of FeSBA-1 samples with different n_{Si}/n_{Fe} ratio (a) FeSBA-1(36), (b) FeSBA-1(90) and (c) FeSBA-1(120)

The textural parameters of all FeSBA-1 samples prepared with various n_{Si}/n_{Fe} ratios at the molar hydrochloric acid to silica (n_{HCl}/n_{Si}) ratio of 10 is summarized in Table 1. The specific surface area decreases from 1390 m²/g for FeSBA-1(120) to 1280 m²/g for FeSBA-1(36) whereas the pore diameter calculated from the adsorption branch of the isotherm increases from 2.4 for FeSBA-1(120) to 2.5 nm for FeSBA-1(36). Moreover, the specific pore volume increases from 0.70 cm³/g to 0.71 cm³/g upto n_{Si}/n_{Fe} ratio of 90, and then decreases to 0.69 cm³/g for n_{Si}/n_{Fe} ratio of 36. The increase in pore diameter of FeSBA-1 with increasing Fe content indicates that Fe atoms are occupying framework positions in SBA-1. Moreover, the high specific surface area and pore volume even at high Fe loading indicate that high quality FeSBA-1 can be obtained (Table 1). It should be noted that the synthesis of FeSBA-1 with higher Fe content is extremely difficult as the structure of the FeSBA-1 is completely collapsed below the n_{Si}/n_{Fe} ratio of 36.

The alkylation of m-cresol using isopropanol (IPA) was carried out over FeSBA-1 catalysts with different n_{Si}/n_{Fe} ratios (36, 90 and 120) at a reaction temperature of 200 °C, at WHSV of 3.46 h⁻¹ and $n_{IPA}/n_{m-cresol}$ ratio = 3 and the products obtained are 2-isopropyl-5-methylphenol (2I-5MP), 2,6-diisopropyl-5-

methyl phenol (2,6-DI-5MP), and 2,4-diisopropyl-5-methyl phenol (2,4-DI-5MP). *m*-Cresol conversion and products selectivity over FeSBA-1 catalysts with different n_{Si}/n_{Fe} is presented in Figure 3. FeSBA-1 catalysts show a non-linear response of conversion with increase in temperature. Conversion at lower temperatures is higher than at higher temperatures. The less conversion at higher temperature is due to coke formation. Moreover, a rapid decrease in the conversion of *m*-cresol is observed for FeSBA-1(36), which could be mainly attributed to presence of strong acid sites. This could enhance the coke formation at higher temperature due to cracking of the reactant molecules.

Table 1: Textural parameters of FeSBA-1 samples prepared at n_{Si}/n_{Fe} ratios.

Catalysts	n_{Si}/n_{Fe}		n_{HCl}/n_{Si}	ao (nm)	A,BET ($\pm 5 \text{ m}^2/\text{g}$)	dp, BJH (nm)	Vp, (cm^3/g)
	Gel	Product					
FeSBA-1(36)	20	36	10	7.9	1280	2.5	0.69
FeSBA-1(90)	40	90	10	7.8	1350	2.4	0.71
FeSBA-1(120)	67	120	10	7.6	1390	2.4	0.70

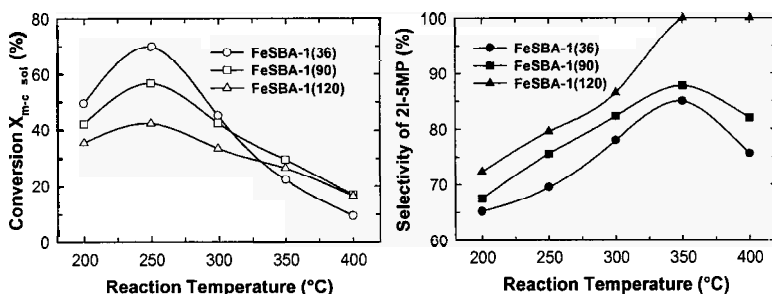


Figure 3: Effect of the (A) n_{Si}/n_{Fe} ratio on the *m*-cresol conversion and (B) selectivity of 2I-5MP over FeSBA-1 catalysts with different iron contents at different temperatures: WHSV of 3.46 h^{-1} , $n_{IPA}/n_{m-cresol} = 5$.

A maximum *m*-cresol conversion of 69.9 % was observed for the FeSBA-1(36) catalyst at a reaction temperature of 250 °C. The change in the selectivity of the products with increasing the n_{Si}/n_{Fe} is mainly due to the difference in the acid strength and the number of Lewis acid sites. It has been found that the activity of the catalysts changes in the following order: FeSBA-1(36) > FeSBA-1(90) > FeSBA-1(120). FeSBA-1(36) exhibits the best performance with a *m*-

cresol conversion of 69.9 % and 2I-5MP selectivity of 69.5 % which are significantly higher as compared to other mono- and/or bimetal substituted uni-dimensional mesoporous materials such as H-AlMCM-41 which show only 59.6 % of *m*-cresol conversion and the selectivity to 2I-5MP of 46 % under optimized reaction conditions. The effect of feed ratio on the reaction was studied over FeSBA-1(36) at 250 °C with a WHSV of 3.5 h⁻¹ and $n_{\text{IPA}}/n_{m\text{-cresol}}$ ratio 3, 5 and 7 (not shown). The $n_{\text{IPA}}/n_{m\text{-cresol}}$ ratio 5 gives higher conversion than 7 and 3. The higher conversion at the $n_{\text{IPA}}/n_{m\text{-cresol}}$ ratio of 5 than 3 is due to more adsorption of IPA on the active sites of the catalyst. It also shows more adsorption of *m*-cresol on the catalyst surface at $n_{\text{IPA}}/n_{m\text{-cresol}}$ ratio 3. But the less conversion at $n_{\text{IPA}}/n_{m\text{-cresol}}$ ratio 7 might be due to more dilution of *m*-cresol in the vapor phase.

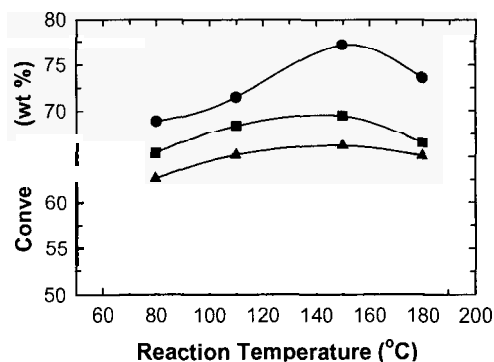


Figure 4: Effect of temperature on the toluene conversion over FeSBA-1 catalysts with various $n_{\text{Si}}/n_{\text{Fe}}$ ratios: (●) FeSBA-1 (36), (◻) FeSBA-1 (90) and (▲) FeSBA-1 (120).

Acylation of toluene was carried out over FeSBA-1 catalyst with different $n_{\text{Si}}/n_{\text{Fe}}$ ratios in the temperature range 80-180 °C for time-on-stream of 1-6 h. The optimized conditions for these reactions are a) molar ratio of AA to toluene ($n_{\text{AA}}/n_{\text{Toluene}}$) = 2 and catalyst weight = 0.1 g, which is 3.3 wt% of total reaction mixture. Under the same reaction conditions, the conversion of toluene over FeSBA-1(36) is much higher as compared to those obtained for other FeSBA-1 catalysts (Figure 4). FeSBA-1(36) shows the toluene conversion of 77.2%. When the conversion of toluene and the product selectivities of different catalysts used in this study are compared under the same reaction conditions, as shown in the Figure 4, the conversion of toluene decreases in the following order: FeSBA-1(36) > FeSBA-1(90) > FeSBA-1(120). The observed increase in toluene conversion with increasing incorporation of iron content could be due to the additional increase in Brönsted and Lewis acidity leading to high density of acid sites generated by iron incorporation. As FeSBA-1(36) shows the maximum

toluene conversion and the catalytic activity can be altered to a greater extent by changing the reaction conditions. FeSBA-1 catalysts are found to be highly active for both the alkylation of *m*-cresol and acylation of toluene and give higher product selectivities as compared to that of AIMCM-41. The observed higher activity of FeSBA-1 is tentatively ascribed to its three-dimensional cage-type pore structure resulting in a higher number of accessible active sites, acid strength, and excellent textural parameters such as very high surface area and pore volume.

4. Conclusions

FeSBA-1 materials with different $n_{\text{Si}}/n_{\text{Fe}}$ ratios have been prepared using cationic surfactant in a highly acidic medium. All the catalysts were thoroughly characterized by XRD, XPS and N_2 adsorption. XRD results reveal that the FeSBA-1 materials possess three dimensional structure with cage type pore system. The catalytic activities of the FeSBA-1 catalysts were tested in the isopropylation of *m*-cresol and acylation of toluene. Among the catalysts studied, FeSBA-1(36) gave the outstanding catalytic activities, such as substrate conversion as well as product selectivities, and the catalyst activities decrease in the following order: FeSBA-1(36) > FeSBA-1(90) > FeSBA-1(120). For both *m*-cresol alkylation and toluene acylation, FeSBA-1(36) was found to be more active than previously studied systems such as AIMCM-41.

References

1. C.T. Kresge, M.E. Leonowicz, W.J. Roth, J.C. Vartuli and J.S. Beck, *Nature* **359**, 710 (1992).
2. J.S. Beck, J.C. Vartuli, W.J. Roth, M.E. Leonowicz, C.T. Kresge, K.D. Schmitt, C.T.-W. Chu, D.H. Olson, E.W. Sheppard, S.B. McCullen, J.B. Higgins and J.L. Schlenker, *J. Am. Chem. Soc.* **114**, 10834 (1992).
3. D. Zhao, Q. Huo, J. Feng, B.F. Chmelka and G.D. Stucky, *J. Am. Chem. Soc.* **120**, 6024 (1998).
4. M. Hartmann and A. Vinu, *Langmuir* **18**, 8010 (2002).
5. A. Vinu, V. Murugesan and M. Hartmann, *J. Phys. Chem. B* **108**, 7323 (2004).
6. Q. Huo, D.I. Margolese, U. Ciesla, P. Feng, T.E. Gier, P. Sieger, R. Leon, P.M. Petroff, F. Schu"th and G.D. Stucky, *Nature* **368**, 317 (1994).
7. Q. Huo, R. Leon, P.M. Petroff and G.D. Stucky, *Science* **268**, 1324 (1995).
8. A. Vinu, V. Murugesan, O. Tangermann and M. Hartmann, *Chem. Mater.* **16**, 3056 (2004).

9. A. Vinu, V. Murugesan, W. Bohlmann and M. Hartmann, *J. Phys. Chem. B* **108**, 11496 (2004).
10. Y. Sakamoto, M. Kaneda, O. Terasaki, D. Zhao, J.M. Kim, G.D. Stucky, H.J. Shin and R. Ryoo, *Nature*, **408**, 449 (2000).
11. P. Yang, D. Zhao, D. Margolese, B.F. Chmelka and G.D. Stucky, *Nature* **396**, 152 (1998).
12. P. Yang, D. Zhao, D. Margolese, B.F. Chmelka and G.D. Stucky, *Chem. Mater.* **11**, 2831 (1999).
13. A. Vinu, V. Murugesan and M. Hartmann, *Chem. Mater.* **15**, 1385 (2003).
14. A. Vinu, T. Krithiga, V.V. Balasubramaniam, A. Anjana, P. Srinivasu, T. Mori, K. Ariga, G. Ramanath and P.G. Ganesan, *J. Phys. Chem. B* **110**, 11924 (2006).
15. A. Vinu, T. Krithiga, V. Murugesan and M. Hartmann, *Adv. Mater.* **16**, 1817 (2004).
16. Q. Huo, D.I. Margolese, U. Ciesla, P. Feng, T.E. Gier, P. Sieger, R. Leon, P.M. Petroff, F. Schuth and G.D. Stucky, *Nature* **368**, 317 (1994).
17. Q. Huo, R. Leon, P.M. Petroff and G.D. Stucky, *Science* **268**, 1324 (1995).
18. L.-X. Dai, K. Tabata, E. Suzuki and T. Tatsumi, *Chem. Mater.* **13**, 208 (2001).
19. L.-X. Dai, Y.-H. Teng, K. Tabata, E. Suzuki, T. Tatsumi, *Chem. Lett.* **795** (2000).
20. S. Che, Y. Sakamoto, O. Terasaki and T. Tatsumi, *Chem. Mater.* **13** 2237 (2001).
21. M. Hartmann, A. Vinu, S.P. Elangovan, V. Murugesan and W. Bohlmann, *Chem. Commun.* **11**, 1238 (2002).
22. A. Vinu, J. Dedecek, V. Murugesan and M. Hartmann, *Chem. Mater.* **14**, 2433 (2002).
23. A. Knop and L.A. Pilato, *Phenolic resin chemistry*, Springer, Berlin, (1985).
24. P. Métivier, R.A. Sheldon and H. van Bekkum (Eds.), *Fine Chemicals through Heterogeneous Catalysis*, Wiley-VCH, Weinheim, 161-175 (2001).
25. H.-Y. Chen and W.M.H. Sachtler, *Catal. Today* **42**, 73 (1998).
26. A. E. Shilov and G.B. Shulpin, *Chem. Rev.* **97**, 2879 (1997).
27. J. Valyon, W.S. Millman and W.K. Hall, *Catal. Lett.* **24**, 215 (1994).
28. M. Kruk, M. Jaroniec and A. Sayari, *Langmuir* **13**, 6267 (1997).

INCORPORATION OF Al INTO CAGE-TYPE MESOPOROUS SILICA MOLECULAR SIEVES

PAVULURI SRINIVASU, DHANASHRI P. SAWANT, JOSENA JUSTUS,
VEERAPPAN VAITHILINGAM BALASUBRAMANIAN, AJAYAN VINU*

*WPI Center for Materials Nanoarchitectonics, National Institute for Materials Science
Tsukuba, Ibaraki 305-0044, Japan, Email: vinu.ajayan@nims.go.jp*

Highly ordered three dimensional mesoporous aluminosilicates (AIKIT-5) with tunable pore diameters have been successfully prepared using Pluronic F127 as a surfactant by simply adjusting the molar water to hydrochloric acid ($n_{\text{H}_2\text{O}}/n_{\text{HCl}}$) ratio in the synthesis mixture. All the materials have been characterized by x-ray diffraction (XRD), N_2 adsorption-desorption isotherms, high resolution scanning electron microscopy (HRSEM), high resolution transmission electron microscopy (HRTEM), and inductively coupled plasma (ICP) spectrometry. The amount of Al incorporation in KIT-5 materials increased with increasing $n_{\text{H}_2\text{O}}/n_{\text{HCl}}$ ratio in the synthesis gel. The Al incorporation, morphology and textural parameters of the resulting aluminosilicate materials can also be controlled by varying the $n_{\text{H}_2\text{O}}/n_{\text{HCl}}$ ratio. It has been found that the specific surface area and pore diameter of the aluminosilicates significantly increase upon increasing the Al loading and the detailed mechanism has been explained in detail. HRTEM, XRD, and ICP analyses reveal that high amount of Al atoms can be introduced into the framework of AIKIT-5 under acidic conditions without affecting their structural order and textural parameters.

1. Introduction

Mesoporous materials have received considerable attention due to their high surface area, regular frameworks, narrow pore size distributions, and the highly valuable potential applications mainly in catalysis, adsorption of bulky organic molecules, and electrode materials [1-14]. There are numerous reports which deal with the preparation of various types of one and three dimensional mesoporous materials, such as MCM-41, MCM-48, SBA-1, SBA-15, AMS, HMS, MSU etc [2-14]. Among these materials, mesoporous silica materials consisting of interconnected large pore cage type mesoporous system with three-dimensional porous network are highly interesting and believed to be more advantageous and superior to materials having hexagonal pore structure with an uni-dimensional array of pores for several potential applications involving transformation of bulky molecules through catalysis, and adsorption and separation of large biomolecules such as proteins, vitamins, amino acids, bulky dyes, etc, and as inorganic templates. These peculiar characteristics are mainly

attributed by the fact that the materials with three-dimensional cage type pore arrangements are more resistant to pore blocking, allow faster diffusion of reactants, and provide more adsorption sites, which can be easily accessible through three dimensional pore channels. In spite of these interesting features, surprisingly, the majority of studies published so far deal with phases having a one-dimensional pore system, viz. MCM-41 and SBA-15 [3, 11-13].

Recently, Kleitz et al. have reported the preparation of mesoporous silica KIT-5 materials using tetraethyl orthosilicate (TEOS) as a silica source and Pluronic F127 as a structure directing agent in a highly acidic medium [15]. Pure silica mesoporous materials possess a neutral framework, which limits their applications in catalysis and adsorption. It is difficult to prepare heteroatom-introduced mesoporous silica under strong acid conditions. This is because, under such conditions, metals exist only in the cationic form rather than their corresponding oxo species and therefore heteroatoms cannot be introduced into the mesoporous walls via a condensation process with silicon species. Recently, Vinu et al. successfully reported a facile method to incorporate hetero-atoms, such as Al, Fe, and Ti in mesoporous SBA-15 and SBA-1 materials, which normally require highly acidic medium for obtaining highly ordered structure by altering various synthesis parameters [10-13]. However, unfortunately, there has been no report available in the literature on the direct synthesis of the Al incorporated KIT-5 materials. Thus, it is highly imperative to have a one-step or a direct synthesis method for the preparation of Al substituted mesoporous KIT-5 in a highly acidic medium. Here, we strikingly demonstrate a facile direct synthesis route for the preparation of Al substituted KIT-5 materials by the simple adjustment of the molar water to hydrochloric acid ($n_{\text{H}_2\text{O}}/n_{\text{HCl}}$) ratio of the synthesis gel via templating with a Pluronic F127 in a highly acidic medium.

2. Experimental Section

AlKIT-5 samples were synthesized by changing the molar water to hydrochloric acid ($n_{\text{H}_2\text{O}}/n_{\text{HCl}}$) ratio using Al isopropoxide as an aluminum source, tetraethyl orthosilicate as a silica source and Pluronic F127 as a template and the samples were denoted as AlKIT-5($x\text{H}$) where x denotes the $n_{\text{H}_2\text{O}}/n_{\text{HCl}}$ ratio. In a typical synthesis, 5.0 g of F127 is dissolved in the required amount of HCl (35 wt%) and 240 g of distilled water. To this mixture, 24.0 g of TEOS and the required amount of the Al isopropoxide were added, and the resulting mixture was stirred for 24 h at 100 °C. Subsequently, the reaction mixture was heated for 24 h at 100 °C under static condition for hydrothermal treatment. The solid product was filtered off and then dried at 100 °C without washing. The product

was calcined at 540 °C for 10 h. Pure siliceous KIT-5 was prepared using the same procedure with the $n_{\text{H}_2\text{O}}/n_{\text{HCl}}$ of 463 in the absence of Al.

Powder X-ray diffraction patterns were collected on a Rigaku diffractometer using $\text{CuK}\alpha$ ($\lambda = 0.15406$ nm) radiation, operated at 40 kV and 40 mA. The diffractograms were recorded in the 2θ range of 0.7 to 10 ° with a 2θ step size of 0.01 ° and a step time of 6 seconds. N_2 adsorption-desorption isotherms were measured at -196 °C on a Quantachrome Autosorb 1 volumetric adsorption analyzer. Before the adsorption measurements, all samples were outgassed for 3 h at 250 °C under vacuum in the degas port of the sorption analyzer. The specific surface area was obtained from the adsorption branch of the isotherm in the relative pressure range of 0.05-0.18 using the BET equation. The total pore volume was estimated from the amount of nitrogen gas adsorbed at a relative pressure of 0.95. The position of the maximum on pore size distribution is referred to as the pore diameter, which was calculated from the adsorption branch of the nitrogen isotherms using the Barrett-Joyner-Halenda (BJH) method. The HRTEM images were obtained with JEOL JEM-2100F. The preparation of samples for HRTEM analysis involved sonication in ethanol for 5 min and deposition on a copper grid. The accelerating voltage of the electron beam was 200 kV.

The morphology of the materials was obtained with Hitachi S-4800 HR-FESEM using an acceleration voltage of 15 kV. The diameter of the cages in AlKIT-5 materials is calculated using equation (1) which was recently proposed by Ravikovitch et al [16].

$$D_{\text{me}} = a \cdot (6\epsilon_{\text{me}}/\pi v)^{1/3} \quad (1)$$

In equation (1), D_{me} is the diameter of the cavity of a cubic unit cell of length a , ϵ_{me} is the volume fraction of a regular cavity and v is the number of cavities present in the unit cell (for $Fm\bar{3}m$ space group, $v = 4$). The average wall thickness of the materials (h) was calculated using the equation (2) which was derived from the mesoporosity and D_{me}

$$h = (D_{\text{me}}/3) (1 - \epsilon_{\text{me}}) / \epsilon_{\text{me}} \quad (2)$$

3. Results and Discussion

Highly acidic condition required for the synthesis of KIT-5 limits the direct incorporation of metal ions into the neutral silica framework because of the facile dissociation of Al-O-Si bonds under strong acidic conditions. Here, we demonstrate a novel technique to incorporate high amount of Al atom into KIT-5 framework by simply adjusting the $n_{\text{H}_2\text{O}}/n_{\text{HCl}}$ ratio in the synthesis mixture. The

powder XRD patterns of as-synthesized and calcined AIKIT-5 materials prepared at different $n_{\text{H}_2\text{O}}/n_{\text{HCl}}$ ratios are shown in Figure 1 and 2, respectively. As shown in Figure 1 and 2, all AIKIT-5 samples prepared at different $n_{\text{H}_2\text{O}}/n_{\text{HCl}}$ ratios exhibit the typical XRD patterns of three dimensional highly ordered large-cage mesoporous silica with cubic $Fm\bar{3}m$ close packed structure, similar to the siliceous KIT-5 material described by Kleitz et al. [15]. Three peaks which correspond to the (111), (200), and (220) are well-resolved and can be indexed in the cubic space group $Fm\bar{3}m$. A significant improvement in the intensity and the peak shift towards higher angle were observed for AIKIT-5 materials prepared at different $n_{\text{H}_2\text{O}}/n_{\text{HCl}}$ ratios upon the calcination. This can be attributed to the occurrence of the atomic arrangements in the Al-O-Si framework of the mesoporous walls during the calcination process. The length of the cubic cell (a_0) is calculated using the formula $a_0 = d_{111} (3)^{1/2}$ (Table 1).

Table 1: Structural parameters of AIKIT-5 samples prepared at different $n_{\text{H}_2\text{O}}/n_{\text{HCl}}$ ratio

Sample	$n_{\text{H}_2\text{O}}/n_{\text{HCl}}$	$n_{\text{Si}}/n_{\text{Al}}$	a_0 (nm)	A_{BET} (m^2/g)	V_p (cm^3/g)	dp_{ads} , BJH (nm)	Cage diameter (nm)	Wall thickness (nm)
AIKIT-5(132H)	132	435	16.39	614	0.39	5.0	9.6	4.3
AIKIT-5(198H)	198	294	16.54	634	0.41	5.0	9.8	4.2
AIKIT-5(278H)	278	181	16.74	648	0.42	5.1	10.0	4.1
AIKIT-5(463H)	463	44	16.97	713	0.45	5.2	10.3	4.0
KIT-5	463	-	16.60	622	0.41	5.0	9.9	4.2

The observed d spacing is compatible with the cubic $Fm\bar{3}m$ space group. It can also be seen from the Figure 2 that the XRD patterns of the AIKIT-5 materials are better resolved as compared to that of the pure silica KIT-5 material prepared at the $n_{\text{H}_2\text{O}}/n_{\text{HCl}}$ ratio of 463. Moreover, the XRD peaks of AIKIT-5 samples are significantly shifted towards lower angle with increasing the $n_{\text{H}_2\text{O}}/n_{\text{HCl}}$ ratio, which corresponds to an increased length of the unit cell a_0 from 16.39 to 16.97 nm. The increase of Al content (ICP results) and the unit cell constant with increasing the $n_{\text{H}_2\text{O}}/n_{\text{HCl}}$ ratio suggests the formation of Al-O-Si bond occasioned by the substitution of Al for Si in the framework of AIKIT-5. These interesting features can be explained in terms of the size of the Al and Si atoms. The atomic radius of Al^{3+} (0.53 Å) is larger as compared to that of the Si^{4+} (0.40 Å) by assuming the coordination number of both the atoms is 4, leading to a longer Al-O distance, which results in the expansion of the distance between the two nearest pore centers. These results undoubtedly confirm that the

interaction between the Al oxo species and the silica species is significantly improved at higher $n_{\text{H}_2\text{O}}/n_{\text{HCl}}$ ratio, which results in a significant increase in the Al incorporation and the expansion of the unit cell size.

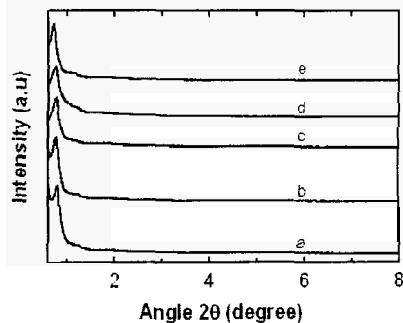


Figure 1. The powder XRD patterns of the as-synthesized AIKIT-5 samples prepared at different $n_{\text{H}_2\text{O}}/n_{\text{HCl}}$ ratios: (a) KIT-5, (b) AIKIT-5(132H), (c) AIKIT-5(198H), (d) AIKIT-5(278H), and (e) AIKIT-5(463H).

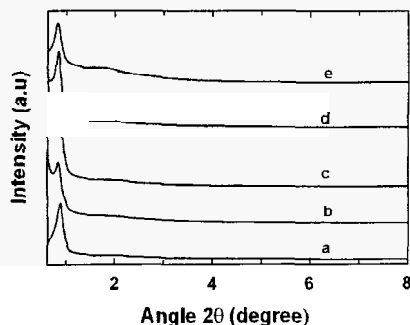


Figure 2. The powder XRD patterns of the calcined AIKIT-5 samples prepared at different $n_{\text{H}_2\text{O}}/n_{\text{HCl}}$ ratios: (a) KIT-5, (b) AIKIT-5(132H), (c) AIKIT-5(198H), (d) AIKIT-5(278H), and (e) AIKIT-5(463H).

The textural properties of AIKIT-5 materials prepared at different $n_{\text{H}_2\text{O}}/n_{\text{HCl}}$ ratio are depicted in Table 1. All isotherms display typical type IV curves with a sharp capillary condensation step and a broad H2-type hysteresis loop, which is indicative of large uniform cage-type pores [15]. The capillary condensation step of the isotherms of AIKIT-5 samples is sharp, which is shifted toward the higher relative pressure with increasing the $n_{\text{H}_2\text{O}}/n_{\text{HCl}}$ ratio, indicating that the nitrogen condensation occurs within the cage type three dimensional mesopores and the samples possess better mesostructure ordering and pores are highly uniform even after the Al incorporation. In addition, the specific surface area and specific pore volume systematically increase with increasing the $n_{\text{H}_2\text{O}}/n_{\text{HCl}}$ ratio. The specific surface area amounts to $614 \text{ m}^2/\text{g}$ for AIKIT-5(132H) and increases to $713 \text{ m}^2/\text{g}$ for AIKIT-5(463H), while the specific pore volume increases from 0.39 to $0.45 \text{ cm}^3/\text{g}$ for the same samples. It is worthwhile to note that the pore diameter of the materials increases with the concomitant increase of the cage diameter with increasing the $n_{\text{H}_2\text{O}}/n_{\text{HCl}}$ ratios in the synthesis mixture.

The pore diameter of AIKIT-5(463H) is 5.2 nm , which is 0.2 nm higher than the sample prepared at lower $n_{\text{H}_2\text{O}}/n_{\text{HCl}}$ ratio. The results are in quite agreement with the unit cell constant data obtained from the XRD analysis. It should be stressed here that the specific surface area, specific pore volume and pore diameter of AIKIT-5(463H) are higher as compared to those of pure silica KIT-5

material. The wall thickness of the A1KIT-5 samples prepared at different $n_{\text{H}_2\text{O}}/n_{\text{HCl}}$ ratio, calculated from the cage diameter and the mesopores volume using the equation (2) (see the experimental section), is given in Table 1. Interestingly, the wall thickness of the samples after Al incorporation declines from 4.3 to 4 with increasing the $n_{\text{H}_2\text{O}}/n_{\text{HCl}}$ ratio from 132 to 463. This shows that the presence of high concentration of local H^+ ion in the synthesis gel i.e. $n_{\text{H}_2\text{O}}/n_{\text{HCl}}$ ratio of 132, which is required for the silanol groups condensation, suppresses the interaction between the silanol groups and the Al oxo species, but enhances the rate of silanol groups condensation which results in an increase in the number of silicate layers around the surfactant micelles. As a consequence, the wall thickness of the A1KIT-5 materials prepared at lower $n_{\text{H}_2\text{O}}/n_{\text{HCl}}$ ratio increases.

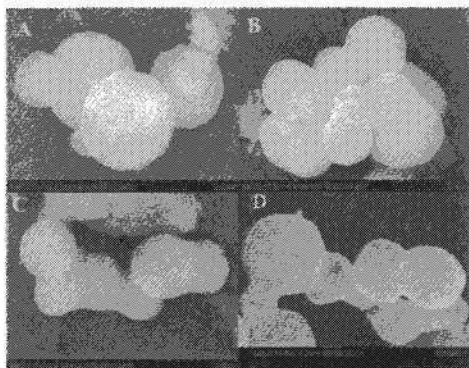


Figure 3. HRSEM images of the calcined A1KIT-5 samples prepared at different $n_{\text{H}_2\text{O}}/n_{\text{HCl}}$ ratios: (A) A1KIT-5(132H), (B) A1KIT-5(198H), (C) A1KIT-5(278H), and (D) A1KIT-5(463H).

To investigate the effect of the $n_{\text{H}_2\text{O}}/n_{\text{HCl}}$ ratios on the Al content, the morphology, and the topology of the A1KIT-5 materials the samples were characterized by HRSEM and HRTEM measurements. Figure 3 shows the HRSEM images of A1KIT-5 materials with different $n_{\text{H}_2\text{O}}/n_{\text{HCl}}$ ratios. The pure silica KIT-5 is composed of uniform sized spherical particles with a regular shape. The size of the particles is in the range 3.2 to 3.5 μm . However, with increasing $n_{\text{H}_2\text{O}}/n_{\text{HCl}}$ ratio, a significant change in the shape of the particle is observed. When the $n_{\text{H}_2\text{O}}/n_{\text{HCl}}$ ratio in the final product is 132 (A1KIT-5(132H)), the spherical particles with regular shape are observed, though the size of the particle is somewhat smaller than that of the pure silica samples (0.82 to 1.2 μm). On the other hand, the spherical particles or aggregated small round shape particles (0.55 to 0.71 μm) with irregular shape are observed for A1KIT-5(463H). It can be also seen that the size of the particles decreases gradually

with increasing the $n_{\text{H}_2\text{O}}/n_{\text{HCl}}$ ratio. This could be due to the difference in the spontaneous curvature of the micelles before and after the Al addition. It was demonstrated previously that the adsorption or condensation or the formation of polymeric silica species around the micelles controls the length of the micelles because it reduces the spontaneous curvature of the micelles [17-18]. When the Al isopropoxide is added in the synthesis mixture, the generation of a lot of isopropanol molecules from the Al source and the Al atoms may disturb the adsorption of the inorganic precursors on the bare surfactant micelles and the condensation reaction between the inorganic species. We surmise that this process may inhibit the charge neutralization process, which is critical for reducing the electrostatic repulsion among the surfactant head groups for obtaining longer micelles, leading to small size spherical particles. When excess amount of Al isopropoxide is added, this effect may be more pronounced, and hence, the spherical particles with irregular shape are observed for the AlKIT-5(463H) sample.

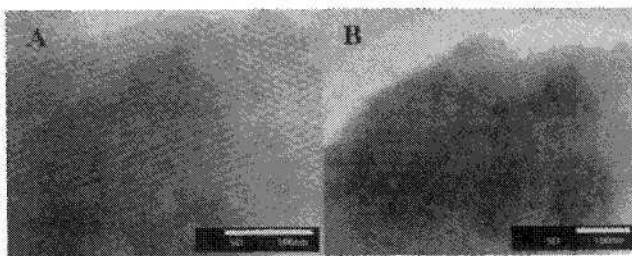


Figure 4. HRTEM images of (A) AlKIT-5(278H) and (B) AlKIT-5(463H)

HRTEM images of the AlKIT-5(278H) and AlKIT-5(463H) samples were produced (Figure 4), to have better understanding of the structural order after the incorporation of Al. The excellent three-dimensional mesoscopic order of AlKIT-5 was confirmed by HRTEM. The AlKIT-5(278H) and AlKIT-5(463H) clearly exhibits highly ordered mesoporous networks with a linear array of mesopores and walls, which is characteristics of well-ordered KIT-5 mesoporous silica. Based on the HRTEM image, it is suggested the occurrence of well ordered mesopores with a three dimensional cubic mesoporous structure in AlKIT-5(463H).

4. Conclusions

We demonstrated the preparation of novel three dimensional cubic $Fm\bar{3}m$ mesoporous aluminosilicates (AlKIT-5) with very high structural order and unprecedented Al incorporation by simply adjusting the molar water to

hydrochloric acid ratio ($n_{\text{H}_2\text{O}}/n_{\text{HCl}}$) in the synthesis mixture. The obtained materials have been unambiguously characterized by several sophisticated techniques such as XRD, N_2 adsorption, HRTEM and HRSEM. It has been found that the amount of Al incorporation in the silica framework can easily be controlled by simply varying the $n_{\text{H}_2\text{O}}/n_{\text{HCl}}$ in the synthesis gel.

References

1. C. T. Kresge, M. E. Leonowicz, W. J. Roth, J. C. Vartuli and J. S. Beck, *Nature* **359**, 710 (1992).
2. A. Corma, *Chem. Rev.* **97**, 2373 (1997).
3. M. Hartmann and A. Vinu, *Langmuir* **18**, 8010 (2002).
4. A. Vinu, V. Murugesan and M. Hartmann, *J. Phys. Chem. B* **108**, 7323 (2004).
5. D. Zhao, Q. Huo, J. Feng, B. F. Chmelka and G. D. Stucky, *J. Am. Chem. Soc.* **120**, 6024 (1998).
6. Q. Zhang, K. Ariga, A. Okabe and T. Aida, *J. Am. Chem. Soc.* **126**, 988 (2004).
7. Q. Huo, R. Leon, P. M. Petroff and G. D. Stucky, *Science* **268**, 1324 (1995).
8. A. Vinu, V. Murugesan, O. Tangermann and M. Hartmann, *Chem. Mater.* **16**, 3056 (2004).
9. A. Vinu, V. Murugesan and M. Hartmann, *Chem. Mater.* **15**, 1385 (2003).
10. A. Vinu, T. Krithiga, V. Murugesan and M. Hartmann, *Adv. Mater.* **16**, 1817 (2004).
11. A. Vinu, V. Murugesan, W. Bohlmann and M. Hartmann, *J. Phys. Chem. B* **108**, 11496 (2004).
12. A. Vinu, D. P. Sawant, K. Ariga, K. Z. Hossain, S. B. Halligudi, M. Hartmann and M. Nomura, *Chem. Mater.* **17**, 5339 (2005).
13. A. Vinu, P. Srinivasu, M. Miyahara and K. Ariga, *J. Phys. Chem. B* **110**, 801 (2006).
14. D. Zhao, J. Feng, Q. Huo, N. Melosh, G. H. Fredrickson, B. F. Chmelka and G. D. Stucky, *Science* **279**, 548 (1998).
15. F. Kleitz, D. Liu, G. M. Anilkumar, I.-S. Park, L. A. Solovyov, A. N. Shmakov and R. Ryoo, *J. Phys. Chem. B* **107**, 14296 (2003).
16. P. I. Ravikovitch and A. V. Neimark, *Langmuir* **18**, 1550 (2002).
17. A. Zilman, S. A. Safran, T. Sottmann and R. Strey, *Langmuir* **20**, 2199 (2004).
18. O. Regev, *Langmuir* **12**, 4940 (1996).

DEPOSITION AND CHARACTERIZATION OF FUNCTIONAL NANOPARTICLES OF LEAD-ZIROCNIA TITANATE (PZT) IN MATRICES OF MESOPOROUS SILICA OF MCM-48-TYPE STRUCTURE*

VIJAY NARKHEDE AND HERMANN GIES[†]

*Chair of crystallography
Inst. of Geology, Mineralogy and Geophysics
Ruhr-University Bochum, 44780 Bochum
Germany*

For the first time MCM-48 was used as the matrix for size-confined lead zirconate-titanate $\text{PbZr}_x\text{Ti}_{(1-x)}\text{O}_3$ (PZT), where x is varied from 0 to 1. PZT gel prepared using a co-precipitation method was introduced into the channels of MCM-48 by dip wet impregnation technique. Calcination in air led to the formation of PZT in the pores of MCM-48. All the synthesized composites were characterized by means of XRD, TEM, BET and AAS. No Bragg-peak due to the PZT was observed in the wide angle XRD pattern, indicating the particle size of the encapsulated PZT is below 2 nm. TEM and N_2 adsorption measurements further confirm the deposition of nanosized PZT particles inside the pores of the mesoporous matrix without destroying their integrity. AAS analyses reveal both the metal composition and the loading of ca. 11 to 16 wt% of the encapsulated PZT.

1. Introduction

In recent years the preparation of nanocrystalline lead zirconate-titanate (PZT) powders has attracted much attention due to their unique piezoelectric and ferroelectric properties [1]. PZT-based piezoelectric materials exhibit excellent electromechanical properties and are widely used as ultrasonic resonators, ceramic filters, high-power transducers, actuators, and so on [2]. Because of fundamental and technological importance of PZT, few chemical methods have been developed to lower the reaction temperature and get nanocrystalline PZT materials of chemical homogeneity, which cannot be obtained by conventional solid-state method [3-5]. To obtain the materials with desired electrical properties, a perovskite structure is required. One of the necessary conditions for

* This work is supported by DFG under a grant within the frame of the Collaborative Research Project 558: "Metal-support interactions in heterogeneous catalysis"

[†] Corresponding author's e-mail: hermann.gies@rub.de

maintaining the perovskite structure is to maintain the stoichiometric composition of perovskite. However, the volatile PbO tends to be deficient in the PZT materials when annealed at high temperatures. In order to solve this problem, a decrease in the powder calcination temperature or sintering temperature could be effective, besides adding excess lead to the precursor to compensate for the loss of lead oxide. To avoid the loss of Pb, the matrices of porous material can also be used to confine such a piezoelectric material.

Since the discovery of novel class of mesoporous M41S materials by Mobil researchers [6,7], much application oriented research has been performed in order to find innovative uses for these new materials. Because of their narrow pore size distribution and composition related to zeolites, most inspiration for the research activity came from the zeolite community. The composition of the M41S family of materials is restricted to silicate frameworks; and MCM-41 (with hexagonal honeycomb symmetry), MCM-48 (with cubic $Ia\bar{3}m$ symmetry) and MCM-50 (a lamellar phase) are the three main mesoporous silicate host structures of this family. The properties of these materials were explored for sorption, separation and catalytic processes. Several review articles are available in the literature on these activities [8,9].

Another area of application-oriented interest for the M41S family of materials could be their use as carriers or matrices for functional molecules or nanoparticles [10-12]. Because of their transparency, high thermal and chemical stability, and their mechanical robustness the silica-based mesoporous materials have attracted much attention. In the past we have studied composites of MCM-41/48 with hyper-polarizable molecules such as p-nitroaniline [11], conducting polymers such as poly-pyrrole [13], large molecules such as C60 and C70 [14]. Recently we have explored the use of MCM-48 as a matrix for metal/metal oxides with catalytic activity such as TiO_2 , Au/ TiO_2 , ZnO, Cu/ZnO [15-17]. Herein we, for the first time, report on the deposition of Pb, Zr and Ti hydroxides within the pore system of the cubic MCM-48 and their subsequent decomposition to their oxide clusters PZT. The composites underwent thorough characterization by means of X-ray powder diffraction (XRD), Transmission Electron Microscopy (TEM), N_2 adsorption and Atomic Absorption Spectroscopy (AAS).

2. Experimental

The flow diagram of the synthesis of the composite material is shown in Fig. 1. Pure silica MCM-48 was obtained following the method described by Gies et al. [15]. In a typical synthesis, 1.0 M NaOH was taken in a polypropylene bottle,

and cetyltrimethylammonium-chloride (CTACl, Aldrich, 25% solution in water) was added drop-wise under continuous stirring. After that, tetraethoxysilane, (TEOS Merck), was added dropwise until the gel was homogeneous. The final molar gel composition of the synthesis mixture was 1 (TEOS):0.70 (CTACl):0.5 (NaOH):64 (H₂O). The sealed bottle was transferred to an oven heated at 90 °C where the gel was kept for 4 days. Thereafter, the sample was thoroughly washed with water and dried overnight at room temperature. The dried product was calcined at 540 °C for 5 h with a heating rate of 1 K/min.

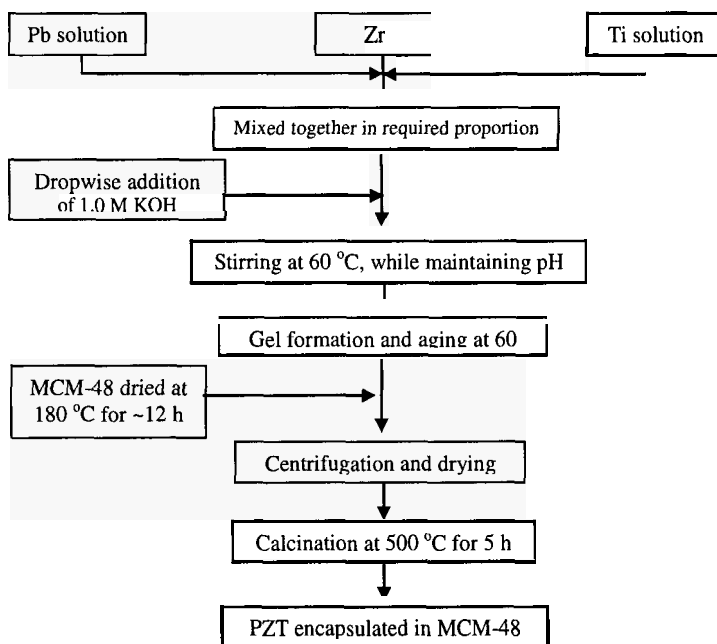


Figure 1. Flow diagram for the preparation procedure of PZT powder and PZT/MCM-48 composites. Nanocrystalline PZT material can be obtained using this co-precipitation method, if the step of addition of MCM-48 is neglected.

The precursors used for the preparation of PZT were lead acetate ((CH₃COO)₂Pb.3H₂O, Merck), zirconium oxynitrate hydrate (ZrO(NO₃)₂.xH₂O, Aldrich), titanylacetylacetonate (TiO(acac)₂, Merck) and were used without any further purification. The preparation of PZT/MCM-48 was carried using a co-precipitation method in which only the amount of the reactants was varied and all other conditions were the same for all the preparations. For instance, the synthesis of a PbZr_{0.5}Ti_{0.5}O₃/MCM-48 (sample code: Zr050) was performed as follows: first aqueous solutions containing 97 mg (0.256 mmol) Pb precursor,

29.6 mg (0.128 mmol) Zr precursor and 33.5 mg (0.128 mmol) Ti precursor in 50 ml of distilled water was prepared. The second solution was potassium hydroxide (0.1 M). These two solutions were added dropwise into a flask containing deionized water (10 ml) under vigorous stirring at 60 °C, while maintaining a constant pH of 8-10. The resulting gel-like material was aged for 0.5 h and then MCM-48 (0.5 g) dried at 180 °C for ~12 h was added and again stirred for an hour. The resulting composite was centrifuged, carefully washed with distilled water and dried overnight at 60 °C. For calcination the sample was heated at 500 °C for 5 h with a heating rate of 1 K/min. (The sample codes were designated based on the amount of Zr taken during the preparation of a sample, e.g. the code for sample $\text{PbZr}_{0.25}\text{Ti}_{0.75}\text{O}_3/\text{MCM-48}$ is Zr025).

X-ray powder diffraction experiments were carried out using a Siemens diffractometer with Cu K α radiation in Bragg–Brentano geometry on flat plate sample holders. Atomic absorption analysis was carried using Varian spectrAA 220 spectrometer. The N₂ adsorption measurements were performed with a Quantachrome Autosorb automated gas sorption system using the Autosorb software. Transmission electron microscopy (TEM) was performed using a Hitachi H-8100 instrument operating at 200 kV.

3. Results and Discussion

Conventional hydrothermal procedure was utilized to synthesize pure silica MCM-48 materials. Before using the material as matrix for PZT, it was characterized by means of XRD and N₂ adsorption techniques. Both the characterization methods showed that MCM-48 material was with excellent periodicity. After that PZT nanoparticles were introduced into the mesoporous MCM-48 matrix using the dip impregnation technique, as presented in Fig. 1. It is worth to mention that during the preparation of PZT/MCM-48 pH of the gel should be controlled in the given range because of lead hydroxide can dissolve at pH value lower than 8 and higher than 10.

XRD measurements (not shown) in the 2θ range of 2–80° were performed for all the PZT/MCM-48 composites. Low-angle powder XRD patterns showed that the parent structure of the mesoporous host was maintained after loading with PZT. However, because of the strong reduction of scattering contrast between wall and pore due to impregnation of nanoparticles, the resulting XRD signal from mesoporous carrier was only very weak [18]. In the high-angle region, there was no signal in the XRD patterns, indicating the PZT nanoparticles inside the host are below 2 nm. To confirm the interpretation of the XRD measurements, TEM studies of the composite samples were performed

confirming that no isolated, external PZT-particles had formed and that the structure of MCM-48 as support was intact after impregnation and heat treatment.

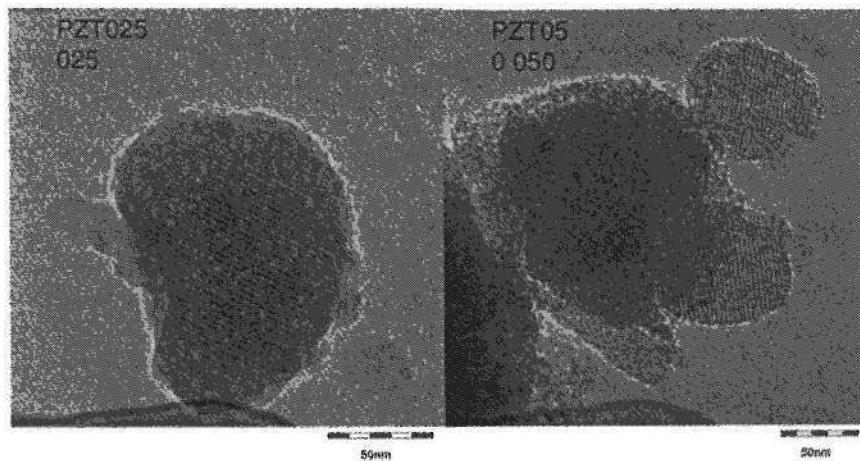


Figure 2. TEM images of the PZT/MCM-48 composites: PZT025 ($\text{PbZr}_{0.25}\text{Ti}_{0.75}\text{O}_3$) and PZT050 ($\text{PbZr}_{0.50}\text{Ti}_{0.50}\text{O}_3$). The periodic ordering of the mesoporous MCM-48 solid clearly shows up. The periodic pattern reveals the homogeneity of the order in the samples.

In Figure 2, TEM images (PZT025 and PZT050) of a well-aligned MCM-48 particle after dip wet impregnation of PZT are shown. The lattice fringes of this well-ordered crystallite have a d spacing of 2.5 nm corresponding to (110) planes. The regular contrast variation in the TEM image shows the intact MCM-48 silicate framework. For all imaged PZT/MCM-48 composites, no damage of the periodic structure of the silicate framework was observed. Therefore, it can be concluded that the impregnation procedure and the consecutive thermal treatment does not damage the MCM-48 silica host framework. In the course of the TEM measurements of a large number of isolated MCM-48 particles as well as aggregates, we have not observed any large PZT particles situated outside of the silicate framework. The TEM and EDX results indicate that PZT is incorporated inside MCM-48. However, no isolated PZT particles inside the MCM-matrix could be resolved and analyzed in the TEM experiments. Selected area electron diffraction experiments of well-resolved parts of MCM-48 loaded with PZT are under investigation to gain a detailed knowledge on PZT structural parameters.

Adsorption isotherms are used as a macroscopic average measurement for exploring the surface area, the pore diameter, and the pore volume of all the composites. Prior to the sorption experiments, the materials were dehydrated by

evacuation under standardized conditions, 300 °C, 2 h. Fig. 3 shows selected isotherms of the parent MCM-48 materials and of 2 samples after loading of titania and metal salts and successive calcination. Table 1 summarizes the measurements of the different MCM-48 samples without and with PZT. Using the BET method for the analysis of the isotherms, the surface area of calcined MCM-48 was determined to be 1069 m²/g with 2.5 nm pore diameter and 1.02 cm³/g pore volume. This is in agreement with data published in the literature [13] and confirms the good quality of the MCM-48 sample. Further loading and calcination of PZT in MCM-48 pores leads to decrease of an average surface of 293 m²/g, of an average pore volume of 0.35 cm³/g and of the average pore diameter of 14 Å. The results of the surface measurements agree well with the formation of particles inside the matrices which reduce surface area, pore volume and pore diameter. This finding is consistent with our recent reports, where Cu/ZnO and TiO₂ nanoparticles were loaded inside the channels of MCM-48 [15,17].

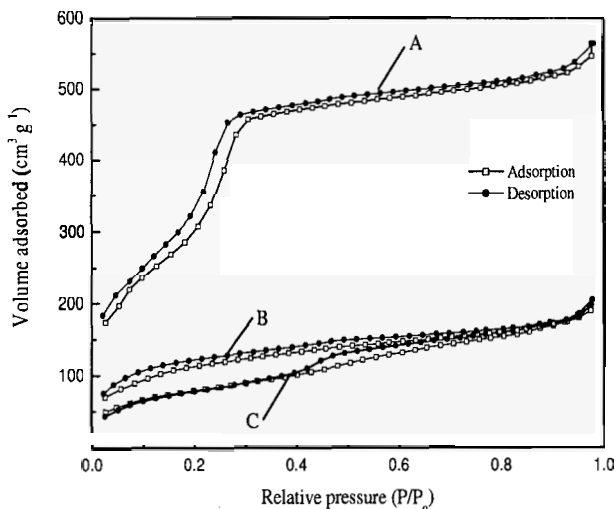


Figure 3. Selected nitrogen adsorption / desorption isotherms of (A) MCM-48, (B) Zr025 and (C) Zr050 samples are shown.

AAS results reveal the content of lead, zirconium and titanium present in all the composites. The data are presented in Table 2. The overall loading of PZT was in the range of 11-16 %. Nearly all of the synthesized materials have metal content similar to the ideal composition, indicating there was no loss of metal during synthesis or subsequent decomposition at higher temperature. Therefore, it can be concluded that this method of the preparation of PZT nano particles in

confined space is beneficial over a conventional solid-state preparation method. In particular, sintering of particles and subsequent increase of particle size is avoided inside the MCM-48 support. On the other hand, the thermal and chemical resistance together with the favorable optical properties of silica-MCM-48 allow for interesting applications. One particular open question, however, is the atomic structure and shape of the nanoparticle. To investigate these particle properties, pair distribution function analysis of the powder pattern is in progress.

Table 1. Results of Nitrogen adsorption measurements of a calcined reference MCM-48 and PZT/MCM-48 composites. After loading with PZT particles reduced pore volume, surface area and also pore size is realized.

Sample	Pore diameter (Å)	Pore volume (cm ³ /g)	Surface area (m ² /g)
MCM-48	25	1.02	1069
Zr100	15	0.39	333
Zr075	14	0.41	239
Zr050	16	0.32	419
Zr025	14	0.42	276
Zr000	13	0.30	196

Table 2. Results of atomic absorption analysis measurements of representative PZT/MCM-48 composites. Between 10 and 14 wt% of metal content was analyzed after final calcination.

Sample	wt % of Pb	wt % of Zr	wt % of Ti
Zr100	7.34	2.96	
Zr075	7.74	2.31	0.50
Zr050	7.54	1.58	0.82
Zr025	8.63	0.96	1.46
Zr000	11.1	-	2.52

The example demonstrates once more the feasibility to use size confinement of mesoporous silicas for the production and preservation of nanoparticles of general composition within the chemical and size limitations of the mesoporous host system.

In summary the three-dimensional channel system of silica MCM-48 was successfully used to deposit nano-sized PZT materials, which were characterized by means of XRD, TEM, N₂ adsorption and AAS analysis. The combination of these characterization techniques reveals that the silica-MCM-48 support can be used as container for nanoparticles. The materials are stable and retain their structural integrity after loading and calcination procedures. PZT nanoparticles are formed and deposited inside the mesoporous MCM-48 material without

blocking the mesoporous pore system.

Acknowledgements

We acknowledge financial support by the Deutsche Forschungsgemeinschaft in the frame of the Sonderforschungsbereich SFB 558. The authors are grateful to Dr. A. Birkner for TEM measurements and Dr. V. Hagen for measuring the nitrogen isotherms.

References

1. E.K. Akdogan, W. Mayo, A. Safari, *Ferroelectrics* **223**, 11(1999).
2. G.W. Taylor, J.J. Gagnepain, T. Nakamura, L. Shuvlaov (Eds.), *Piezoelectricity, Vol. 4*, Gordon & Breach, 1992.
3. B. Guiffard, M. Trccaz, *Mater. Res. Bull.* **33**, 1759(1998).
4. S.D. Pradhan, S.D. Sathaye, K.R. Patil, A. Mitra, *Mater. Lett.* **48**, 351(2001).
5. G. Xu, W. Weng, J. Yao, P. Du, G. Han, *Microelectronic Engineering* **66**, 568(2003).
6. J.S. Beck, J.C. Vartuli, W.J. Roth, M.E. Leonowicz, C.T. Kresge, K.D. Schmitt, J.L. Higgins, J.L. Schlenker, *J. Am. Chem. Soc.* **114**, 10834(1992).
7. C.T. Kresge, M.E. Leonowicz, W.J. Roth, J.C. Vartuli, J.S. Beck, *Nature* **359**, 710(1992).
8. A. Sayari, *Chem. Commun.* **8**, 1840(1996).
9. A. Corma, *Chem. Rev.* **97** (6), 2373(1997).
10. R. Hoppe, A. Ortlam, J. Rathousky, G. Schulz-Ekloff, A. Zukal, *Microporous Mater.* **8**, 267(1997).
11. I. Kinski, H. Gies, F. Marlow, *Zeolites* **19**, 375(1997).
12. G. Schulz-Ekloff, D. Woehrle, B. van Duffel, R.A. Schoonheydt, *Microporous Mesoporous Mater.* **51**, 91(2002).
13. I. Kinski, Diploma Thesis, Ruhr-University Bochum, 1994.
14. H. Gies, J. Rius, J. Veciana, *Proceedings of the 9th German Zeolite Meeting*, PO2, (1997).
15. H. Gies, S. Grabowski, M. Bandyopadhyay, W. Gruenert, O.P. Tkachenko, K.V. Klementiev, A. Birkner, *Microporous Mesoporous Mater.* **60**, 31(2003).
16. M. Bandyopadhyay, O. Korsak, M.W.E. van den Berg, W. Gruenert, A. Birkner, W. Li, F. Schueth, H. Gies, *Microporous Mesoporous Mater.* **89**, 15(2006).
17. M. Bandyopadhyay, A. Birkner, M.W.E. van den Berg, K.V. Klementiev, W. Schmidt, W. Gruenert, H. Gies, *Chem. Mater.* **17**, 3820(2005).
18. B. Marler, U. Oberhagemann, S. Vortmann, H. Gies, *Microporous Materials* **6**, 375(1996).

CHARACTERIZATION OF A GERMANIUM ANALOG OF THE TUBULAR ALUMINOSILICATE, IMOGOLITE

MASASHI OOKAWA, YOSHIHIRO HIRAO, HIROSHI YAMASHITA,
TAKASHI MAEKAWA

*Department of Materials Science and Biotechnology, Graduate School of Science
and Engineering, Ehime University, Matsuyama 790-8577, JAPAN*

KEIICHI INUKAI

*National Institute of Advanced Industrial Science and Technology (AIST), Nagoya,
463-8560, JAPAN*

The imogolite composites in which Si was substituted by Ge (Ge-substituted imogolite) were prepared from a concentrated solution with dissolved GeO_2 and were characterized by using atomic force microscopy, IR and Raman spectroscopy. IR and Raman spectra of these materials are the same as previous results prepared from a dilute inorganic solution. Thermal transformation of Ge-substituted imogolite was investigated by using thermal analysis, ^{27}Al solid-state nuclear magnetic resonance and X-ray diffraction. Two endothermic peaks (110°C and 400°C) and an exothermic peak (906°C) were shown by differential thermal analysis. Ge-substituted imogolite changed into an amorphous phase by dehydration and transformed $\text{Al}_6\text{Ge}_2\text{O}_{13}$ crystals at ca. 900°C. $\text{Al}_2\text{Ge}_2\text{O}_7$ crystals were formed as a new phase at 1300°C from Ge-substituted imogolite.

1. Introduction

Imogolite is a hydrous aluminosilicate clay mineral with a unique fibrous structure, which was discovered in a glassy volcanic ash soil in Kyushu, Japan, in 1962 [1]. The structure model of imogolite [2] with typical chemical composition of $(\text{OH})_3\text{Al}_2\text{O}_3\text{SiOH}$ is shown in Figure 1. The tube walls consist of a single continuous gibbsite sheet and orthosilicate anions. Imogolite has an outer diameter of ca. 2 nm and an inner diameter of 1 nm. Thermal transformation of natural imogolite was investigated using solid-state nuclear magnetic resonance (NMR), thermal analysis and X-ray powder diffraction (XRD) [3]. Imogolite changed to an amorphous phase with a collapse of the tubular structure due to dehydroxylation with increasing heat treatment temperature and to crystalline mullite above 960°C.

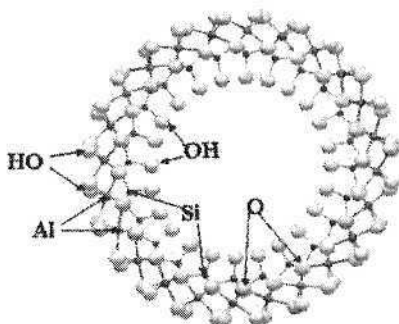


Figure 1. Structural model of imogolite.

Wada and Wada [4] synthesized an imogolite composite in which Si was substituted by Ge from a dilute inorganic solution containing GeCl_4 as the source of germanium. In this paper, we call this material "Ge-substituted imogolite" whose typical chemical composition is $(\text{OH})_3\text{Al}_2\text{O}_3\text{GeOH}$. The material substituted by Ge was shorter than synthetic imogolite, and its diameter increased with an increase in the degree of substitution of germanium. Recently, Mukherjee *et al.* [5] investigated the formation process of single-walled aluminogermanate nanotubes (Ge-substituted imogolite) prepared based on a method reported by Wada and Wada [4] by transmission electron microscopy (TEM), electron diffraction, XRD and dynamics light scattering (DLS). In addition, the formation mechanism of aluminogermanate nanotubes from a dilute solution containing $\text{Ge}(\text{OC}_2\text{H}_5)_4$ and AlCl_3 was also examined by DLS, UV absorption spectroscopy, Raman spectroscopy and Infrared (IR) spectroscopy [6].

It is difficult to obtain a large amount of Ge-substituted imogolite using the previous synthetic method [4, 5] because it is formed from a dilute solution in order to prevent the condensation of orthogermanic acid. Recently, a synthetic technique to form imogolite from a concentrated inorganic solution was developed [8]. In this technique, which was an improvement of the former one, we synthesized Ge-substituted imogolite from a concentrated solution by dissolving GeO_2 and characterized it by XRD, IR, TEM and Atomic force microscopy (AFM) [9].

In this study, we investigated the structure of Ge-substituted imogolite and its structural changes with heat treatment using AFM, IR, thermal analysis, Raman spectroscopy, ^{27}Al solid state NMR and XRD.

2. Experimental

GeO_2 (99.99%, Nacalai Tesque), $\text{AlCl}_3 \cdot 6\text{H}_2\text{O}$ (98.0%, Nacalai Tesque), NaOH (97.0%, Wako) were used as starting materials. At first, a mixture composed of 0.01 mol of GeO_2 and 0.04 mol of NaOH was dissolved in 100 ml of deionized water. This solution and 100 ml of 0.15 M AlCl_3 aqueous solution were mixed and stirred for 1.5h. The precursor was obtained by adding 0.1 M NaOH aqueous solution slowly until pH 5.5. The salt-free precursor was obtained by centrifugal separation twice and was then dispersed in 2,000 ml of water. After adding 40 ml of 0.1 M HCl , it was aged at 100°C for 48h. After cooling to room temperature, concentrated ammonia water was added until the pH 9.5. The gel-like sample was separated from the solution by centrifugation. The final product i.e., Ge-substituted imogolite was obtained by drying at 100°C . The heat treatment of Ge-substituted imogolite sample was then performed at various temperatures.

The Ge-substituted imogolite sample was characterized by AFM, IR spectroscopy, FT-Raman spectroscopy, differential thermal analysis (DTA) and thermogravimetric analysis (TGA). AFM images were recorded at room temperature under air with a Nanoscope(R) IIIa scanning probe microscope (Digital Instruments). A tapping mode technique was used. After diluting the aging solution 1,000 times with extra-pure water, the aqueous solution was placed onto a clean mica surface and then dried overnight at room temperature in a desiccator with dried silica gels. The measurements of IR spectra were carried out with a KBr pellet using a JASCO FT-IR 460 Plus. FT-Raman spectra were collected using a JASCO FT-IR 800 with an RFT-800 Raman attachment. The 1064 nm line of a Nd:YAG laser was used as an excitation light source. DTA and TGA were performed using a DTG-50 (SHIMADZU) in static air at a heating rate of $10^\circ\text{C min}^{-1}$ with α -alumina as a reference.

The thermal transformations of Ge-substituted imogolite were investigated by XRD and solid-state ^{27}Al magic angle spinning (MAS) NMR. The XRD were carried out using an Ultima-III diffractometer (RIGAKU). The ^{27}Al MAS NMR spectra were obtained by a JEOL JNM-CMX 300 spectrometer operating at 78.34 MHz with a MAS rates of 4 kHz. The chemical shift of ^{27}Al was determined by using 1 M $\text{Al}(\text{NO}_3)_3$ aqueous solution as a secondary standard.

3. Results and discussion

3.1. Characterization of Ge-substituted imogolite

The tapping mode AFM image of Ge-substituted imogolite is shown in Figure 2. A small cylindrical morphology was observed. As a result of section analysis, we found that the tube diameter was almost uniform and estimated to be ca. 4.0 nm in any tubes. In the AFM image of synthetic imogolite [8] that is not shown here, fibrous materials with 100 - 400 nm of length and ca. 2.2 - 2.4 nm in diameter can be observed. These results indicate that Ge-substituted imogolite is shorter and wider than synthetic imogolite.

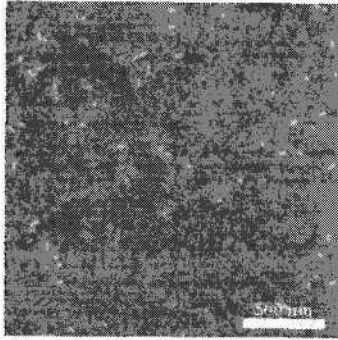


Figure 2. Tapping mode AFM image of Ge-substituted imogolite

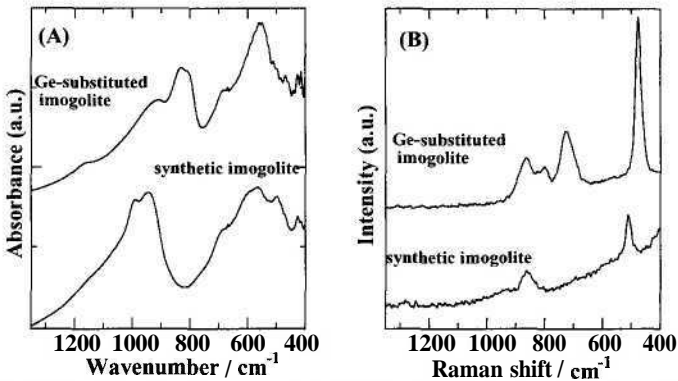


Figure 3. IR spectra (A) and FT-Raman spectra (B) of Ge-substituted and synthetic imogolite.

FT-IR spectra of Ge-substituted and synthetic imogolite are shown in Figure 3(a). Characteristic absorption bands were observed near 900 cm^{-1} and

500 cm^{-1} in Ge-substituted imogolite and near 1000 cm^{-1} and 500 cm^{-1} in imogolite. These absorptions of Ge-substituted imogolite were attributed to “Ge-O and Ge-O-Al stretching” and “various Al-O vibrations”, respectively [4]. On the other hand, four Raman bands at 478, 729, 802 and 866 cm^{-1} were shown in the spectrum of Ge-substituted imogolite (Figure 3(b)). Imogolite indicated two Raman bands at 511 and 864 cm^{-1} in this region. The assignment of Raman bands of imogolite or Ge-substituted imogolite has not yet been adequately established because structural studies using Raman spectroscopy are fewer than those using IR spectroscopy. Mukherjee *et al.* [6] more recently reported Raman spectra of aluminogermanate nanotubes and classified them into three regions namely, “Al-O-Al bends”, “Al-O-Al stretches” and “Al-O-Ge and Ge-O stretches”. The Raman spectrum of Ge-substituted imogolite obtained in this study was almost the same as that of an aluminogermanate nanotube. According to Mukherjee *et al.*'s classification, the Raman bands at 478 cm^{-1} and 729 cm^{-1} are assigned as Al-O-Al bends and Al-O-Al stretches, respectively, and other bands are assigned as Al-O-Ge and Ge-O stretches.

3.2. Thermal transformation of Ge-substituted imogolite

The DTA and TGA traces of Ge-substituted imogolite are shown in Figure. 4. Two broad endothermic peaks with a weight loss and an exothermic peak without a weight change were observed. Each peak was assigned based on previous literature [3, 4]. The endothermic peaks at 110°C and 400°C were attributed to the loss of adsorbed water and dehydroxylation, respectively. The exothermic peak at 906°C was attributed to crystallization. The heat treatment of Ge-substituted imogolite was carried out at 200°C, 500°C and 950°C referred to this result of thermal analysis.

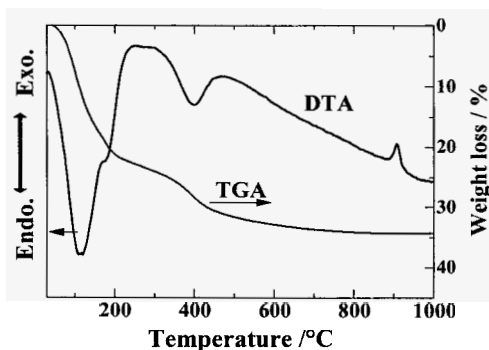


Figure 4. Thermal analysis of Ge-substituted imogolite (differential thermal analysis and thermogravimetric analysis).

^{27}Al MAS NMR spectra of heat treated samples are shown in Figure 5. The ^{27}Al spectrum of unheated Ge-substituted imogolite (Figure 5 -(a)) indicates six coordinated octahedral Al^{3+} ($\text{Al}(\text{oct})$), the same as imogolite. There were no spectrum changes with heat treatment at 200°C , except for the S/N ratio. In the sample heated at 500°C , the peak of $\text{Al}(\text{oct})$ near 0 ppm was broader and a very small peak, which is not attributed to a spinning side band but rather to a tetrahedral Al^{3+} ($\text{Al}(\text{tet})$), appeared at 55.3 ppm. At 950°C (Figure 5 -(d)), the peak intensity of $\text{Al}(\text{tet})$ increased and the peak near 0 ppm had lower symmetry and became broader.

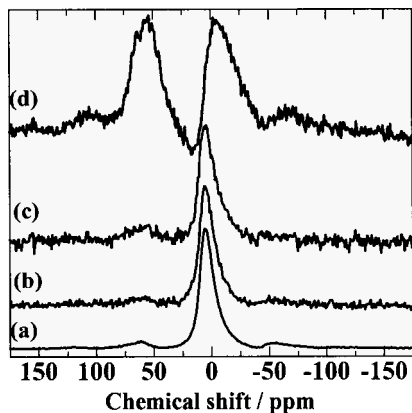


Figure 5. ^{27}Al MAS NMR spectra of (a) Ge-substituted imogolite and heat treated sample at (b) 200°C , (c) 500°C and (d) 950°C .

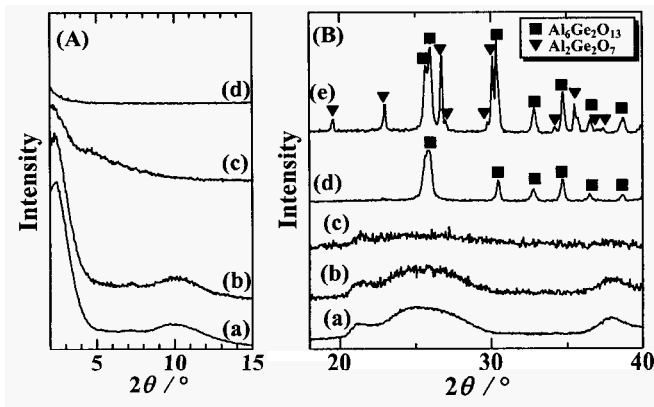


Figure 6. XRD profiles of (a) Ge-imogolite and heat treated sample at (b) 200°C , (c) 500°C , (d) 950°C and (e) 1300°C . (A): low angle region ($2^\circ < 2\theta < 15^\circ$). (B): high angle region ($16^\circ < 2\theta < 40^\circ$).

The X-ray diffraction profiles were created from Ge-substituted imogolite heat treated at three given temperatures and the results are given in Figure 6. The characteristic peaks of Ge-substituted imogolite were observed at $2\theta = 2.5^\circ$, 10° with a small shoulder at 7° , 21° , 25° and 38° . These peaks were kept until 200°C , however, they disappeared with heat treatment at 500°C except for small angle scattering shown in the angle below 5° (Figure 6 (A)-(c)). New crystalline peaks appeared with heat treatment at 950°C , which corresponded to $\text{Al}_6\text{Ge}_2\text{O}_{13}$ (germanium-mullite) crystal.

We now develop our discussion about the thermal transformation of Ge-substituted imogolite using these results and previous literatures [3, 4]. The above-mentioned, physically adsorbed water was desorbed without a structural change up to 200°C . The endotherm caused by dehydroxylation was observed in the temperature range from 300°C to 500°C in which Ge-substituted imogolite changed to an amorphous phase. Amorphism of imogolite and formation of Al(tet) occurred in the same temperature range [3]. MacKenzie *et al.* showed the formation of 10% of Al(tet) at 500°C in the case of natural imogolite, although there was only a slight formation of Al(tet) in the case of Ge-substituted imogolite in this study. The exothermic peak observed at 906°C in DTA was assigned as crystallization of germanium-mullite similar to a previous result [4]. Germanium-mullite has two kinds of Al site which are Al(tet) and Al(oct) [9]. It was found that increasing the intensity of Al(tet) was caused by the formation of germanium-mullite. Since the Al/Ge atomic ratio of Ge-substituted imogolite (= 2) is different to that of germanium-mullite (= 3), another amorphous component was present in this sample. Donkai *et al.* [10] investigated thermal transformation of natural imogolite up to 1600°C using XRD and IR and reported the formation of tridymite (SiO_2) with mullite ($\text{Al}_6\text{Si}_2\text{O}_{13}$) crystal above 1200°C .

Furthermore, the heat treatment of Ge-substituted imogolite was carried out at 1300°C for 2h. This result is shown in Figure 6(B)-(e). The diffraction peaks of germanium-mullite were sharpened with a new crystalline phase and this was attributed to the $\text{Al}_2\text{Ge}_2\text{O}_7$ crystal. The $\text{Al}_2\text{Ge}_2\text{O}_7$ crystal is a digermanate group (Ge_2O_7) with a unique structure characterized by AlO_5 bipyramids with two common edges forming $(\text{AlO}_3)_8$ chains [11]. We attempted to measure this sample by ^{27}Al MAS NMR. Unfortunately, we could not detect five coordinated Al species because of a low S/N ration and poor resolution of the ^{27}Al NMR spectrum.

The behavior of thermal transformation of Ge-substituted imogolite below 1000°C was similar to that of natural imogolite. However, GeO_2 , which appeared in the phase diagram, was not formed by heat treatment at high temperature while the transformation, similar to a disproportionation reaction, occurred. It is clear that at first $\text{Al}_2\text{Ge}_2\text{O}_7$ crystal was formed as a new phase at 1300°C from Ge-substituted imogolite.

4. Conclusion

The Ge-substituted imogolite samples were prepared from a concentrated solution by dissolving GeO_2 and were characterized by a 4 nm diameter when assessed by AFM. The Raman spectrum was the same as that of sample prepared from a dilute inorganic solution. Thermal transformation of Ge-substituted imogolite was investigated by using thermal analysis, ^{27}Al solid-state nuclear magnetic resonance and X-ray diffraction. Two endothermic peaks (110°C and 400°C) with weight loss and an exothermic peak (900°C) without weight change were observed in DTA. Up to 200°C, the structure of Ge-substituted imogolite was maintained. Above this temperature, amorphism caused by the dehydroxylation and crystallization of $\text{Al}_6\text{Ge}_2\text{O}_{13}$ occurred at ca. 900°C. We found that $\text{Al}_2\text{Ge}_2\text{O}_7$ crystal formed as a new phase at 1300°C from Ge-substituted imogolite.

References

1. N. Yoshinaga and S. Aomine, *Soil Sci. Plant Nutr.* **8**, 114 (1962).
2. P. D. G. Cradwick, V. C. Farmer, J. D. Rucell, C. R. Masson, K. Wada and N. Yoshinaga, *Nature Phys. Sci.* **240**, 187 (1972).
3. K. J. D. MacKenzie, M. E. Bowden, I. W. M. Brown and R. H. Meinhold, *Clays Clay Miner.* **37**, 317(1989).
4. S. -I.Wada and K.Wada, *Clays Clay Miner.* **30**, 123 (1982).
5. S. Mukherjee, V. M. Bartlow and S. Nair, *Chem. Mater.* **17**, 4900 (2005).
6. S. Mukherjee, K. Kim and S. Nair, *J. Am. Chem. Soc.* **129**, 6820 (2007).
7. M. Suzuki, F. Ohashi, K. Inukai, M. Maeda, and S. Tomura, *Nendo Kagaku*, **40**, 1 (2000).
8. M. Ookawa, Y. Hirao, M. Watanabe, T. Maekawa, K. Inukai, S. Miyamoto and T. Yamaguchi, *Clay Sci.* **13**, 69 (2006).
9. L. H. Merwin, A. Sebald, H. Rager and H. Schneider, *Phys. Chem. Miner.* **18**, 47 (1991).
10. N. Donkai, T. Miyamoto, T. Kokubo and H. Tanei, *J. Mater. Sci.*, **27**, 6193 (1992).
11. V. Agafonov, A. Kahn, D. Michel and M. Perez Y Jorba, *J. Solid State Chem.* **62**, 402 (1986).

SYNTHESIS OF ZEOLITE ZSM-5 COMPOSITES WITH A SINGLE TEMPLATE*

JIA WANG, JOHAN C. GROEN, MARC-OLIVIER COPPENS[§]

*DelftChemTech, Delft University of Technology, Julianalaan 136, Delft, 2628 BL,
The Netherlands*

*and [§]Dept. of Chemical and Biological Engineering, Rensselaer Polytechnic Institute,
110 8th Street, Troy NY12180, U.S.A.*

WENBO YUE, WUZONG ZHOU

School of Chemistry, University of St Andrews, St Andrews, KY16 9ST, United Kingdom

Hierarchically structured composites (TUD-C) with ZSM-5 crystals embedded in a well-connected amorphous mesoporous aluminosilicate matrix were synthesized by employing only one organic templating/scaffolding molecule (TPAOH). Micro- and mesopores form separately under different conditions, allowing a high degree of controllability. Solid state NMR reveals that the aluminum species are all in framework positions. This new type of composite displays the typical Brønsted acidity and high hydrothermal stability of zeolites. The scaffolding mechanism at the basis of the mesostructure is not limited to TPAOH. Other zeolite/meso-structure composites could also be synthesized based on the same concept.

1. Introduction

Zeolites are microporous, crystalline aluminosilicates used extensively in the petroleum industry, separation processes and adsorption applications.[1,2] Their strong solid acidity, high surface area and hydrothermal stability are excellent properties for heterogeneous catalysis. The narrow micropores (typically < 1.5 nm) are responsible for the shape selectivity that results in preferential formation of desired products. However, these narrow pores also impose diffusion limitations that hinder transport of molecules to and from active sites that are normally inside zeolite crystals. Heavy products formed within the micropores can lead to pore blockage and thus deactivate the catalysts.[3] A well-connected system of wide pores may reduce transport limitations.[4] In industrial applications of zeolites, meso- and macropores are often introduced in an empirical, poorly controlled manner.[1] Performance could be improved by

* This work is supported by Delft Research Centre for Sustainable Industrial Processes and the Dutch National Science Foundation NOW by a CW/PIONIER grant.

rationally designing the broad pore channel network with a good connectivity, but this requires the ability to easily control the broad channel sizes.[5]

Great progress has been made in the synthesis of hierarchically structured zeolites by combining ordered mesopores and zeolitic structures.[6-8] One of the important synthesis routes is to grow zeolite crystals inside of a mesoporous matrix. However, the meso-structure deteriorates easily since the force exerted during zeolite crystal formation is much greater than that during meso-structure formation. To overcome this challenge hard templates [9,10] and specially designed supra-molecular templates [11,12] have been introduced to preserve the meso-structure during crystallization. Jacobsen *et al.* [9] proposed an elegant route using carbon black to create intra-crystalline mesopores. Other templates, such as CMKs [10] and TPHAC [11], accurately control the mesoporosity, but tend to be expensive, and the synthesis routes are rather involved.

Here we present a single-template route to synthesize a material with zeolite nano-crystals dispersed in a mesoporous matrix of tunable porosity. By applying different conditions to the synthesis mixture we use the same templating/scaffolding molecule (tetrapropylammonium hydroxide, TPAOH) to direct both micro- and mesopore formation. Thus, no additional supra-molecular template is needed and the synthesis can be performed in one pot. This method requires only four raw materials including water, which is even one element less (no NaOH) than a typical lab-based ZSM-5 synthesis. The simplicity, flexibility, and tunability of this method are the most attractive features when compared to existing routes.

2. Experimental

A series of samples (denoted as TUD-C) with Si/Al=30 were prepared by a two-step procedure. In the first step, a homogeneous synthesis solution was prepared from TPAOH (1M in water), tetraethyl orthosilicate (TEOS), and aluminium isopropoxide [Al(iPrO)₃]. The molar composition was 60 SiO₂: Al₂O₃: 14 TPAOH: 1800 H₂O. This solution was aged at room temperature under controlled evaporation for 10 days to obtain a transparent solid gel. In the second step, 0.3 g of the solid gel and 0.4 ml water were transferred into a specially designed autoclave, in which the solid phase was separated from the aqueous phase. During the crystallization, the solid was only in contact with steam, which is an essential difference compared to traditional zeolite synthesis. A series of samples was obtained upon heating at 130 °C for different durations. The products were dried at 80 °C, and subsequently calcined in air at 550 °C for 6 h to remove the organic materials. All resulting samples were monolithic.

3. Results and Discussions

In the first step, TPAOH acts as a scaffold under the mild conditions, forming the meso-structure. This has been investigated previously. [13] In Figure 1, the N_2 adsorption isotherms and the corresponding pore size distribution (0 h sample) have confirmed the formation of mesopores. The near-linear uptake of the isotherm over the range $P/P_0 = 0.10$ to 0.50 indicates the presence of small mesopores in the solid gel. This solid gel has a high BET surface area ($734 \text{ m}^2\text{g}^{-1}$, Table 1), which is comparable to SBA-15 mesoporous materials. ZSM-5 crystals are formed during the second step, where TPAOH acts as the well-known zeolite template at high temperatures. [7] This is a solid-phase crystallization process assisted by steam. [14] X-ray diffraction shows the characteristic peaks of ZSM-5 (Figure 2). The intensity of the peaks increases from 0 h to 4.5 h, which shows the gradual conversion of the amorphous structure of the starting gel into a crystalline phase. The enhanced zeolite crystallinity is also indicated by an increase in micropore volume to $0.13 \text{ cm}^3/\text{g}$ after 15 h (Table 1).

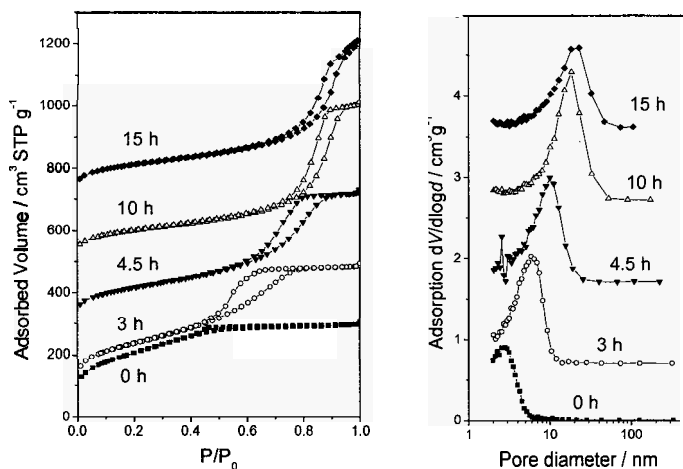


Figure 1. Analysis of the pores by N_2 adsorption and desorption. (Left) The isotherms of TUD-C samples with different crystallization times. Samples 3 h, 4.5 h, 10 h, and 15 h were vertically offset by 50, 250, 450, 650 $\text{cm}^3 \text{STP g}^{-1}$, respectively. (Right) Pore size distributions corresponding to the adsorption isotherms. Samples 3 h, 4.5 h, 10 h, and 15 h were vertically offset by 0.7, 1.7, 2.7, 3.5 cm^3g^{-1} , respectively. (Adapted from ref. 15)

One of the important features of our new synthesis route is the ability to tune the mesopore size. The isotherms from 3 h to 15 h (Figure 1) show that the

zeolite crystal growth does not lead to the deterioration of the mesopores. On the contrary, by controlling the crystallization time, the mesopore size can be systematically varied. As Figure 1 shows, the average pore size increases from 3 nm in the starting dry gel to about 20 nm in the 15 h sample. A more detailed analysis (Table 1) reveals that the external surface area decreases with crystallization time, but remains very high even after 15 h. The possibility of maintaining a high external surface area is attractive for catalytic applications involving large molecules, since in many cases the surface inside the micropores is not easily accessed.

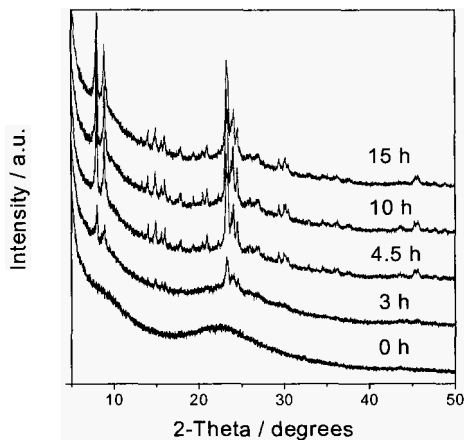


Figure 2. XRD patterns of calcined TUD-C samples with different crystallization times. (Adapted from ref. 15)

Table 1. Texture of the samples corresponding to Figure 1. (Adapted from ref. 15)

Samples	S_{BET}	S_{external}	V_{micro}	V_{meso}	D_{meso}
Time (h)	($\text{m}^2 \text{g}^{-1}$)	($\text{m}^2 \text{g}^{-1}$)	($\text{cm}^3 \text{g}^{-1}$)	($\text{cm}^3 \text{g}^{-1}$)	(nm)
0	734	-*	-*	0.42	3
3	658	571	0.040	0.64	6
4.5	602	392	0.085	0.64	10
10	535	266	0.114	0.75	18
15	580	269	0.130	0.71	20

* t-plot is not applicable because of the continuous distribution of pore sizes around 2 nm.

To obtain insight into the local structure of the amorphous and crystalline phases we have selected samples to perform high-resolution transmission

electron microscopy (TEM). Figure 3a shows that the 3 h sample is a composite with small zeolite crystals embedded in a mesoporous matrix. The crystals have a fairly uniform size of 120-150 nm in diameter. Not surprisingly, the 10 h sample contains larger crystals than the 3 h sample, i.e., 150 to 250 nm in size (Figure 3c). These results are in quantitative agreement with calculations based on the application of Scherrer's equation to the XRD peaks. A high-resolution image (figure 3b) of an interface between the zeolite crystal and the amorphous mesoporous matrix clearly confirms the combined micro- and meso-structures. The disordered mesopores of uniform size are well connected as the carbon replica of TUD-C 0 h sample (Figure 3d) showed 3-D mesoporous structures that are stable upon the removal of silica/alumina. The mesoporous connectivity would ensure efficient diffusion pathways to access the active sites of the zeolite crystals. Because of the disordered nature of the mesopores it is not straightforward to directly link the pore sizes observed in TEM with the results of N₂ adsorption. We are investigating the reasons why the mesopores can be tuned by prolonging the crystallization time. The structure of TUD-C shows similarities to that of recently reported zeolite/mesoporous matrix materials by Waller *et al.* [16] and Gagea *et al.*[17] However, TUD-C has a tunable mesopore size in a wider range, and requires fewer starting materials.

The structural configuration and the location of Al atoms were investigated by ²⁷Al MAS NMR spectroscopy (Figure 4 left). The absence of the peak at 0 ppm and the single, pronounced peak at 56.7 ppm in the TUD-C 15 h sample demonstrate that Al is entirely incorporated in the framework. We also performed measurements on the sample 0 h (amorphous solid gel). NMR showed similar results of Al completely incorporated in the framework. This reveals that in both crystalline phase and amorphous phase Al is present in tetrahedral coordination. With a similar approach to obtain the amorphous solid gel, Corma *et al.* also reported Al present entirely as framework species. [18] FTIR measurements (Figure 4 right) further confirm the acidity of sample 15 h. The absorption band at 3610 cm⁻¹ is characteristic of Brønsted acid sites [19], where the Si-O(H)-Al bond is present. This is a promising feature for applications of TUD-C as a solid acid catalyst, e.g. for catalytic cracking or alkylation.

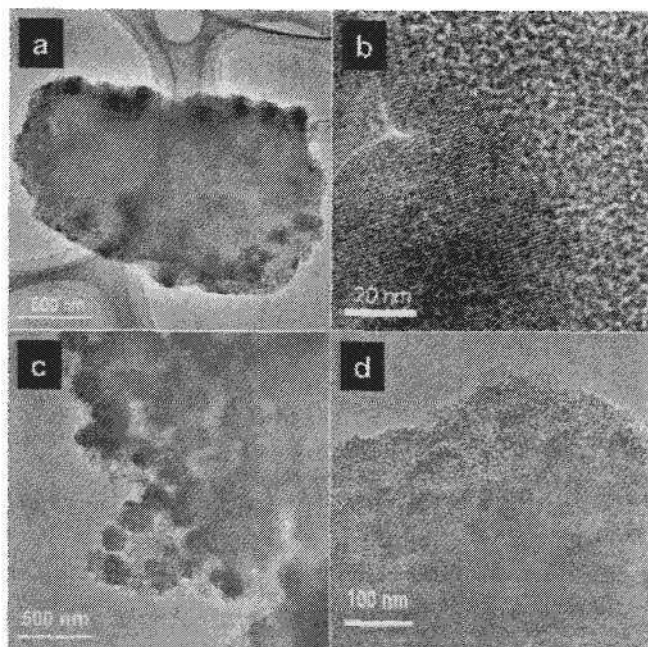


Figure 3. TEM images of selected samples a) sample 3 h, an entire particle; b) sample 3 h, a bordering area between micro- and meso-phases; c) sample 10 h; d) carbon replica of sample 0 h, disordered mesoporous structure.

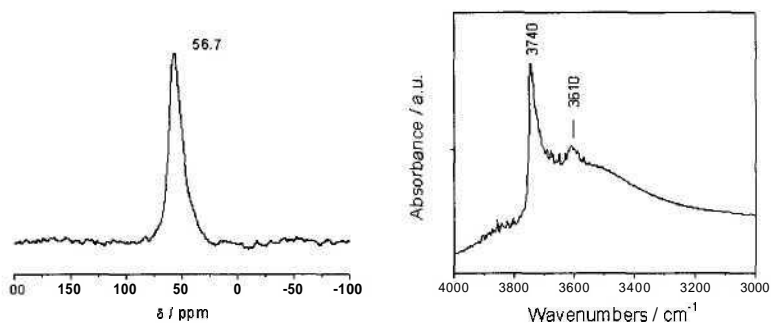


Figure 4. ^{27}Al MAS NMR spectra (left) and FTIR spectrum (right) of sample TUD-C 15 h. The adsorption band at 3610 cm^{-1} is characteristic of Brønsted acid sites. (Adapted from ref. 15)

Though TUD-C does not have a fully crystalline structure, severe hydrothermal treatment (800 °C with 20 % steam for 2 h) only had a minor effect on the pore structure. There was no significant difference of the mesopore structures after the hydrothermal treatment. The micropore volume dropped slightly after the treatment. This demonstrates a remarkable stability of our material. It was reported that solid-phase conversion leads to a better thermal stability compared to zeolites prepared by traditional methods. [14]

4. Conclusions

We have developed a new and facile one-pot synthesis route to obtain a ZSM-5 zeolite/meso-structure composite with a minimum number of starting materials. Assemblies of TPAOH serve as a scaffold for the meso-structure at a much lower temperature than that of the typical ZSM-5 synthesis. The zeolite crystals (micropore phase) are embedded in a well-connected amorphous mesoporous aluminosilicate framework with a tunable pore size in a wide range. The crystal sizes increase over the crystallization time, which is in agreement with XRD results. Since the scaffolding mechanism of the TUD-C mesopore formation is not restricted to TPAOH [13], and more zeolites are synthesized by the solid-phase crystallization technique, we can envision extensions of our synthesis route to other types of zeolites and mesoporous materials. To improve the present synthesis route, we are investigating the influence of the Si/Al ratio and the temperatures applied in both steps, as well as the formation mechanism of the mesopores. Without need for separate mesopore templates, our synthesis method is unique in its remarkable simplicity. The demonstrated controllability of the mesopore size should allow optimizing zeolite performance in a more rational way [5].

Acknowledgments

We thank Mr. S. Brouwer, Mrs. K. Djanashvili and Dr. W. T. Fu (Univ Leiden) for N₂ adsorption, NMR and XRD measurements, respectively.

References

1. S. van Donk, A. H. Janssen, J. H. Bitter and K. P. de Jong, *Cat. Rev. – Sci. Eng.* **45**, 297 (2003).
2. J. Choi, G. Ghosh, Z.-P. Lai and M. Tsapatsis, *Angew. Chem. Int. Ed.* **45**, 1154 (2006).
3. G. F. Froment, *Appl. Catal. A* **212**, 117 (2001).

4. P. Kortunov, S. Vasenkov, J. Kärger, R. Valiulin, P. Gottschalk, M. Fé Elia, M. Perez, M. Stöcker, B. Drescher, G. McElhiney, C. Berger, R. Gläser and J. Weitkamp, *J. Am. Chem. Soc.* **127**, 13055 (2005).
5. E. Johannessen, G. Wang and M.-O. Coppens, *Ind. Eng. Chem. Res.* **46**, 4245 (2007).
6. Y. Liu and T. J. Pinnavaia, *J. Mater. Chem.* **12**, 3179 (2002).
7. D. Trong On and S. Kaliaguine, *Angew. Chem. Int. Ed.* **40**, 3251 (2001).
8. J. Pérez-Pariente, I. Díaz and J. Agúndez, *C.R.Chimie* **8**, 569 (2005).
9. C. J. H. Jacobsen, C. Madsen, J. Houzvicka, I. Schmidt and A. Carlsson, *J. Am. Chem. Soc.* **122**, 7116 (2000).
10. Y.-M. Fang and H.-Q. Hu, *J. Am. Chem. Soc.* **128**, 10636 (2006).
11. M. Choi, H. S. Cho, R. Srivastava, C. Venkatesan, D.-H. Choi and R. Ryoo, *Nature Mater.* **5**, 718 (2006).
12. H. Wang, T. J. Pinnavaia, *Angew. Chem. Int. Ed.* **45**, 7603 (2006).
13. M. R. S. Manton and J. C. Davidtz, *J. Catal.* **60**, 156 (1979).
14. M. Matsukata, M. Ogura, T. Osaki, P. R. H. P. Rao, M. Nomura and E. Kikuchi, *Top. Catal.* **9**, 77 (1999).
15. J. Wang, J. C. Groen, W. Yue, W. Zhou and M.-O. Coppens, *Chem. Commun.* (2007) Accepted.
16. P. Waller, Z.-P. Shan, L. Marchese, G. Tartaglione, W.-Z. Zhou, J. C. Jansen and T. Maschmeyer, *Chem. Eur. J.* **10**, 4970 (2004).
17. B. C. Gagea, D. Liang, G. van Tendeloo, J. A. Martens and P. A. Jacobs, *Stud. Surf. Sci. Cat.* **162**, 259 (2006).
18. A. Corma, J. Pérez-Pariente, V. Fornés, F. Rey and D. Rawlence, *Appl. Catal.* **63**, 145 (1990).
19. J. C. Groen, L. A. A. Peffer, J. A. Moulijn and J. Pérez-Ramírez, *Chem. Eur. J.* **11**, 4983 (2005).

SYNTHESIS OF NANO-SIZED β -ZEOLITE BY DRY-GEL CONVERSION (DGC) METHOD WITHOUT THE USE OF SODIUM HYDROXIDE*

AYYAMPERUMAL SAKTHIVEL, AKIRA IIDA, YOICHI NISHIMURA,
KENICHI KOMURA, AND YOSHIHIRO SUGI†

*Department of Materials Science and Technology, Faculty of Engineering,
Gifu University Gifu 501-1193, Japan*

SUNG JUNE CHO, JONG-HO KIM, AND GON SEO

*School of Applied Chemical Engineering and The Research Institute for Catalysis,
Chonnam National University, Gwangju, 500-757, Korea*

β -Zeolite was synthesized first time from steaming dry-gel precursors without the use of sodium hydroxide. The dry gel precursor was obtained by varying tetraethylammonium hydroxide (TEAOH)/SiO₂ ratio of 0.5 to 0.9. The resultant β -zeolite had uniform particle size of 40–80 nm with BET surface areas in the range of 530–590 m²·g⁻¹, the external surface area of 198–242 m²·g⁻¹, and cumulative surface areas were in the range of 757–858 m²·g⁻¹. The zeolites were applied for the catalysts of the isomerization and cracking of hexane. Further, the β -zeolites modified with Ca, Ce, and La were synthesized by the introduction of their salts during the gel preparation, and applied for the isomerization.

1. Introduction

Zeolites and their related molecular sieves have been used for various catalytic applications, because they have uniform pore and channel sizes, unique shape-selectivity, as well as strong acidity and good thermal/hydrothermal stabilities [1-3]. In particular, β -zeolite with a three dimensional large-pore system is one of potential catalysts used in petrorefining and other chemical industries [4]. β -Zeolite was usually synthesized in the presence of alkali cations [5,6]. The alkali cations strongly affect the phase and kinetics of crystallization [7]. In some cases, the presence of alkali cations was claimed to be necessary for crystallization of a desired zeolite phase [5].

* A part of this work was financially supported by Grant Aid for Scientific Research (B) 16310056 and 19061107, the Japan Society for the Promotion of Science (JSPS). A. Sakthivel is grateful to the JSPS for the postdoctoral fellowship.

†Corresponding author. E-mail: ysugi@gifu-u.ac.jp.

Recently, there have been several works on the synthesis of β -zeolite without the use of alkaline hydroxide [9-13]. Pure β -zeolite was obtained by fluoride media only in the absence of alkali cations when its seed was added to gel mixtures [8]. Cambor *et al.* first synthesized pure β -zeolites without the use of alkali cations [9]. They demonstrated alkali cations were not essential for the nucleation and crystal growth of β -zeolite, resulting in the successful synthesis of β -zeolite with a particle size of *ca.* 10 nm. Interestingly, so far, most of β -zeolites with particle sizes smaller than 100 nm have been synthesized without the use of alkali cations [9-13]. From these situations, the efficient synthesis of nano-sized zeolites is of great significance due to important application in the preparation of zeolite films which is expected as membranes, catalysts, sensors, and components for optical and electronic devices, *etc* [14-16].

Dry-gel conversion (DGC) method, in which a gel dried in advance is crystallized into a zeolitic phase in water steam environment, has been much interested as a synthetic method for zeolites materials in recent years [17-20]. However, there has been no report on the synthesis of β -zeolite by DGC method without the use of alkali cations. It is interesting, particularly, to use DGC method for efficient synthesis of nano-sized β -zeolite without the use of NaOH.

Here, we first time apply a novel method to synthesize β -zeolite by DGC method without the use of sodium hydroxide, in which TEAOH is used as structure directing agent (SDA) as well as the base. An advantage of present method is the efficient synthesis of proton form β -zeolite by very short time and immediately after calcination of as-synthesized sample without the cation exchange procedures. We also examine the isomerization and cracking of hexane to evaluate catalytic properties of β -zeolite in this work.

2. Experimental

2.1. Synthesis procedure

The gel composition was used for the synthesis of β -zeolite: 1 SiO_2 : x tetraethylammonium hydroxide (TEAOH): 0.02 Al_2O_3 : 17 H_2O , where x = 0.5 to 0.9. A typical synthesis procedure is as follows: 21.1–37.9 g (50–90 mmol) of TEAOH solution (35 wt.%) was mixed with 15.02 g colloidal silica (Ludox HS-40 (40 wt%)) containing 6.01 g (100 mmol) of SiO_2 . Then, the mixture was stirred for 30 min. An appropriate amount of $\text{Al}_2(\text{SO}_4)_3 \cdot 6\text{H}_2\text{O}$ (0.684 g) dissolved in 10.18 ml of warm distilled water was added to the mixture, and the resultant mixture was stirred for further 1 h. The gel was then dried for about 4–6 h over an oil bath at 100 °C with continuous stirring. The dry-gel was transferred to a Teflon cup (55 mm x 37 mm I.D.), and placed in a Teflon-lined

autoclave (100 ml) by supporting with a Teflon holder in the presence of a small amount of external bulk water (ca. 0.2 g per 1 g of dry gel) at the bottom of the autoclave [17-20]. The crystallization of the dry-gel was carried out at 175 °C for 1 d. The as-synthesized materials were collected and washed well with distilled water, and their calcination at 550 °C for 6 h gave β -zeolite.

The modification of β -zeolite with alkaline earth and rare earth metals, such as calcium (Ca), lanthanum (La), and cerium (Ce) was examined by introduction of their salts during dry-gel preparation. The synthesis of the β -zeolite was carried out by 3 d crystallization period according to previous method.

β -Zeolites with different TEAOH/SiO₂ ratios were abbreviated as ZB x - y , where x is SiO₂/Al₂O₃ ratio; y is TEAOH/SiO₂ ratio). β -Zeolite with alkaline earth and rare earth metals are abbreviated as ZB x - y -M, where M is rare earth and alkaline earth metals with SiO₂/M = 100.

2.2. Characterization of Catalysts

Powder X-ray diffraction was measured by Shimadzu XRD-6000 with Ka radiation ($a = 1.5418 \text{ \AA}$). Elemental analysis was performed using an inductive coupled plasma spectrophotometer (JICP-PS-1000 UV Leeman Labs Inc.) after destruction of the samples by potassium carbonate. Crystal size and morphology of zeolites were determined by a Hitachi S-4300 FE-SEM microscope. TEM images were taken on a JEOL JEM-2000FXII microscope. Nitrogen adsorption measurements were carried out on a Belsorp 28SA (Bel Japan, Inc.). NH₃ temperature programmed desorption (NH₃-TPD) was measured using a Bel TPD-66 apparatus: the catalyst was evacuated at 400 °C for 1 h, and NH₃ was adsorbed at 100 °C followed by further evacuation for 1 h. Then, the sample was heated from 100 to 710 °C with a temperature- programmed rate of 10 °C/min in a helium stream. TG analyses were carried out by using a Shimadzu DTG-50 analyzer with programmed rate of 10 °C/min in air stream. ²⁷Al spectra of zeolites were recorded at room temperature under magic angle spinning (MAS) by using 4 mm diameter zirconia rotors spinning at 15 kHz on a JEOL ECA-500 NMR spectrometer.

2.3. The Isomerization and Cracking of Hexane

The isomerization and cracking of hexane was carried out in a 9 mm (ID) quartz tubular flow micro-reactor loaded with 1 g of nano-sized β -zeolite (SiO₂/Al₂O₃ = 50; 20–32 mesh). The zeolite was placed between two layers of quartz wool. After loading the catalyst in reactor, it was heated in a stream of dry nitrogen, 20 ml/min at 550 °C for 1 h before introducing hexane. The reactions were

performed at 350 °C for 4 h. The reaction products were analyzed using two Shimadzu 14C and 18A chromatographs equipped with 2 different columns: CP-Al₂O₃/KCl (Agilent, 50 m x 0.53 mm, 10 μm film thickness) for the analysis of C1 to C6 hydrocarbons and HR-1 column (GL Sciences, 30 m x 0.53 mm, 5 μm film thickness) for the analysis of C7⁺ hydrocarbons including BTX.

3. Results and Discussion

The recently developed DGC method for synthesis of zeolite has great interest on zeolite research, since DGC method requires short crystallization period to get high crystallinity [17-20]. Further, zeolite precursors such as SDA (template) and silica have very close proximity during the synthesis process of DGC method, which can be easily obtained to form desired phase efficiently.

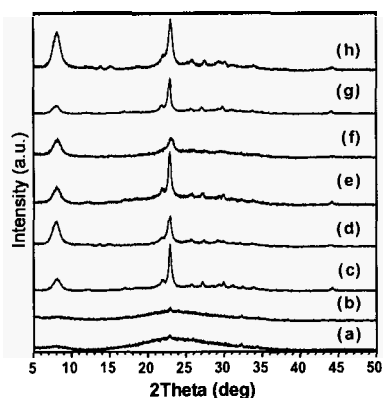


Figure 1. Powder XRD pattern of (a) ZB50-0.5as; (b) ZB50-0.5ca; (c) ZB50-0.6as; (d) ZB50-0.6ca; (e) ZB50-0.75as; (f) ZB50-0.75ca; (g) ZB50-0.9as; and (h) ZB50-0.9ca. as: as-synthesized. ca: calcined.

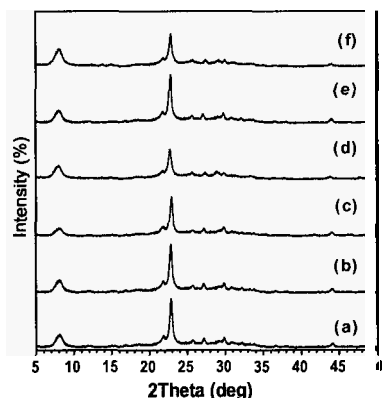


Figure 2. Powder XRD pattern of (a) ZB50-0.6as-Ca100; (b) ZB50-0.6ca-Ca100; (c) ZB50-0.6as-Ce100; (d) ZB50-0.6ca-Ce100; (e) ZB50-0.6as-La100; (f) ZB50-0.6ca-La100. as: as-synthesized. ca: calcined.

Figure 1 shows the XRD patterns of β -zeolite synthesized by DGC method with different TEAOH/SiO₂ molar ratios. The ratio of 0.5 results in the formation of amorphous phase with few very weak peaks, which corresponds to semi-crystalline β -zeolite precursors. However, the increase of TEAOH concentration (TEAOH/SiO₂ molar ratios of 0.6, 0.75 and 0.9) results in the formation of nano-sized β -zeolite with high crystallinity. The enhancement of the nano-sized β -zeolite at higher TEAOH concentration may be mostly due to

complete dissolution of aluminosilicate species and to the formation of uniform synthesis gel [12].

The XRD patterns of β -zeolite synthesized in the presence of rare earth and alkaline earth metal salts (Ca, La, and Ce) also showed the patterns of pure phase with high crystallinity, where any patterns of these metal oxides were not observed (Figure 2). The introduction of Ca, La, and Ce salts on the synthesis gel does not affect the crystallinity of β -zeolite, because these metals are finely dispersed as oxides.

Figure 3 shows TG profiles of as-synthesized samples. A total weight loss of β -zeolite (ZB50-0.6) to 800 °C was about 46 wt.%, which is higher than a β -zeolite synthesized in the presence of sodium hydroxide (ZB-Na). In both the cases, the observed weight loss occurred in two stages, (i) initial weight loss from physisorbed water molecules which is about 20 wt.% for ZB50-0.6 and 10 wt.% for ZB-Na observed in the range of 100–200 °C; (ii) the second stage weight loss is about 25 wt.% for ZB50-0.6 and 20 wt.% for ZB-Na in the range of 200–450 °C was due to the decomposition of TEAOH. The observed weight loss in ZB50-0.6 corresponds to the amounts of TEAOH as SDA and TEA^+ as charge balancing cation. These TG profiles also indicate that β -zeolite synthesized without the use of sodium hydroxide has relatively hydrophilic nature (13 wt.% loss of calcined sample) than β -zeolite synthesized in the presence of sodium hydroxide (10 wt.% loss) because of smaller particle sizes of ZB50-0.6 sample.

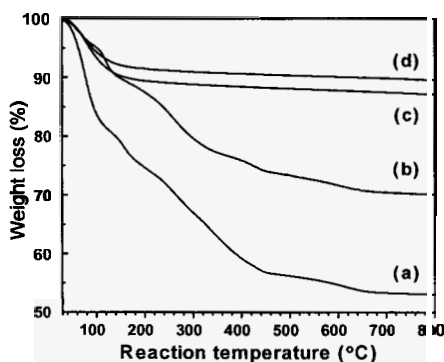


Figure 3. TGA profiles of (a) ZB50-0.6as; (b) β -zeolite-with NaOH-as; (c) ZB50-0.6ca; and (d) β -zeolite-with NaOH-ca; as: as-synthesized. ca: calcined.

The SEM image of β -zeolite (ZB50-0.6) showed particle size of ca. 40–80 nm (Figure 4a). The β -zeolite synthesized in the present studies have smaller

particle size compared to the zeolites by Matsukata et al. [19,20], where they used sodium hydroxide as basic media and obtained B-zeolite structure with an average particle size of 300-400 nm. Further, Ca, La, and Ce species introduced on the synthesis gel resulted in segregated fine particles (Figure 4b-4d). These metal salts may form oxy-hydroxide species during the synthesis, which may hinder the growth of particles, by occupying as counter anion in aluminum sites.

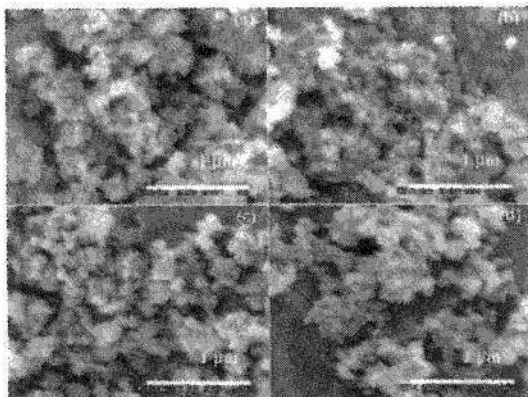


Figure 4. SEM images of (a) ZB50-0.6; (b) ZB50-0.6-Ca100; (c) ZB50-0.6-Ce100; (d) ZB50-0.6-La100.

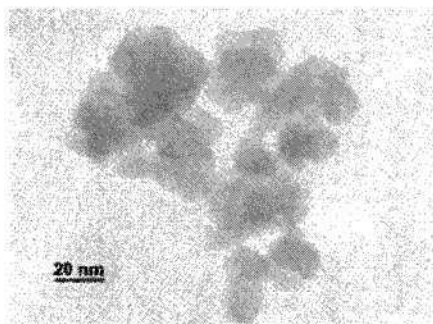


Figure 5. TEM image of β -zeolite (ZB50-0.6) sample.

The TEM image of B-zeolite (ZB50-0.6) again confirmed the very uniform fine particles of B-zeolite with an average particle size of 40-80 nm (Figure 5). Table 1 summarizes the textural properties and ICP analysis of unmodified and Ca, Ce, and La containing β -zeolites. The ICP analysis shows that all the zeolites have the $\text{SiO}_2/\text{Al}_2\text{O}_3$ and SiO_2/M (M= Ca, Ce, and La) ratios similar to initial gel composition.

Table 1. Properties of β -zeolite synthesized in the absence of sodiumhydroxide

Sample	TEAOH /SiO ₂ ratio	Acid amount (mmol·g ⁻¹)	SiO ₂ /Al ₂ O ₃ (MO) ratio		Surface area ^b (m ² ·g ⁻¹)	External Surface area ^c (m ² ·g ⁻¹)	Total Surface area ^c (m ² ·g ⁻¹)	Pore volume (cm ³ ·g ⁻¹)
			Initial	Product ^a				
ZB50-0.5	0.5	0.306	50	55.9	410	118	513	0.407
ZB50-0.6	0.6	0.371	50	57.4	644	205	811	0.748
ZB50-0.75	0.75	0.349	50	54.1	585	182	773	0.625
ZB50-0.9	0.9	0.337	50	56.2	591	242	859	0.730
ZB50-0.6Ca	0.6	0.145	50(100) ^d	56.5(116) ^d	577	166	810	0.685
ZB50-0.6Ce	0.6	0.132	50(100) ^d	54.3(108) ^d	596	160	737	0.668
ZB50-0.6La	0.6	0.130	50(100) ^d	54.9(94.5) ^d	417	122	556	0.399

^a measured by ICP; ^b BET method; ^c *t*-plot method. ^d SiO₂/M ratio; (M = Ca, Ce, and La

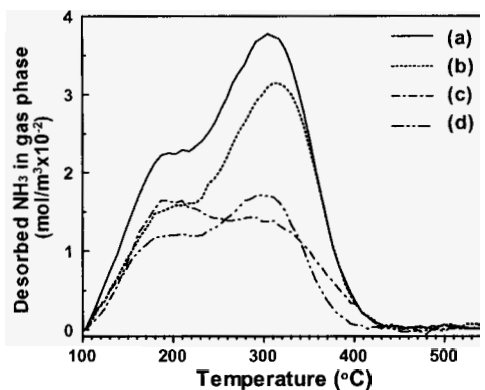


Figure 6. NH₃ TPD profiles of (a) ZB50-0.6; (b) ZB50-0.6-Ca100; (c) ZB50-0.6-Ce100; and (d) ZB50-0.6La100.

The total surface area calculated based on nitrogen gas adsorbed at the external surface as well as condensed in the zeolite pores, which are determined by *t*-plot method, and the results are presented in Table 1 along with BET surface area. Their BET surface areas were in the range of 410–644 m²·g⁻¹, the external surface areas of 117–242 m²·g⁻¹, and their cumulative surface areas were in the range of 513–859 m²·g⁻¹. The observed high surface areas of β -zeolite are mainly due to its particle size. The external surface area of the β -zeolites also increased with the increase in TEAOH/SiO₂ ratio, mainly due to the formation of smaller particle sizes. However, the introduction of Ca, Ce, and La results in the decreasing surface areas and pore volume: the decreases are mainly due to the

cations remain as charge balancing cation on the aluminum sites, thus it may block the microporous channel.

NH_3 -TPD profiles of proton-formed β -zeolites showed two stages of NH_3 desorption peaks appeared at around 160 °C and 300 °C similar to conventional β -zeolite (Figure 6). The first peak (*l*-peak) is due to the desorption of physisorbed NH_3 , and the second peak (*h*-peak) is due to NH_3 desorption from Brønsted acid sites. As expected, the amount of acid sites drastically decreased by the introduction of Ca, Ce, and La species. The decrease suggests that mostly these metal ions are present as counter-ions on the Al-sites.

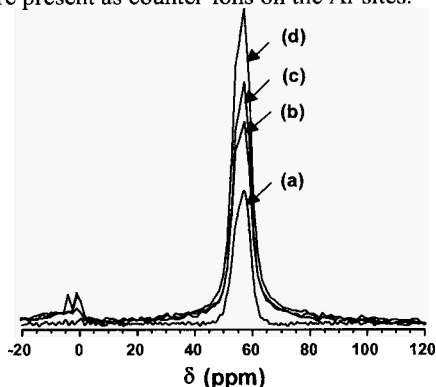


Figure 7. ^{27}Al MAS-NMR spectra of (a) ZB50-0.6; (b) ZB50-0.6-Ca100; (c) ZB50-0.6-Ce100; (e) ZB50-0.6La100.

^{27}Al MAS-NMR spectrum of calcined β -zeolite (ZB50-0.6) shows only one symmetrical signal at around -57 ppm, which is characteristic of tetrahedral Al^{3+} species in the framework (Figure 7a). However, there are no octahedral Al^{3+} species in the zeolite. However, when Ca, Ce, and La species were introduced during the synthesis, a weak signal around 0 ppm appeared due to very small amount of octahedral Al^{3+} species present as non-framework species (Figure 7b-7d). Further ^{139}La MAS NMR spectra of ZB50-0.6La have only a very broad signal around 0 ppm: this indicates that the lanthanum highly dispersed on the zeolite framework as oxide.

The β -zeolite and Ca, Ce, and La containing β -zeolites were applied for the isomerization of hexane at 350 °C, and the results are shown in Figures 8 and 9. Comparable conversion with the selectivity for the C_6 -isomerized products (viz. 2- and 3-methylpentanes and 2,2-dimethylbutane) in the range of 65–74% was obtained. However, cracking products in the range of 33–24% with about 1% of aromatic hydrocarbons (benzene, toluene, and xylenes) were formed

accompanying the isomerization. All zeolites deactivated in the initial hours mainly due to coke formation on the strong acid sites.

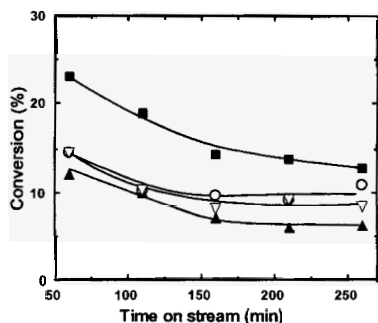


Figure 8. The influence of time on stream on catalytic activity of β -zeolites in the isomerization and cracking of hexane: Reaction conditions: catalyst: 1 g; reaction temperature: 350 °C; W/F = 8.17 g·h/mol. zeolite: □: ZB50-0.6; ○: ZB50-0.6-Ca100; ▲: ZB50-0.6-Ce100; S: ZB50-0.6-La100.

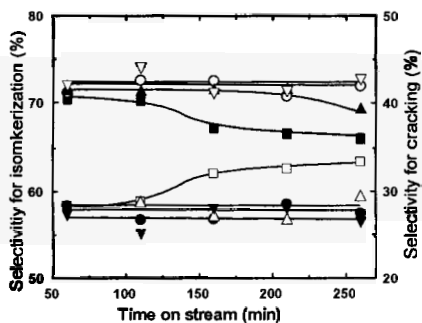


Figure 9. The influence of time on stream on the selectivity for the isomerization and cracking of hexane over β -zeolites: Reaction conditions: see Figure 6. Selectivity of isomerization: □: ZB50-0.6; ○: ZB50-0.6-Ca100; ▲: ZB50-0.6-Ce100; S: ZB50-0.6-La100. Selectivity of cracking: □: ZB50-0.6; ●: ZB50-0.6-Ca100; ◻: ZB50-0.6-Ce100; ◼: ZB50-0.6-La100.

Ca, and La containing β -zeolites were less deactivated than the parent β -zeolite. Although the conversion of hexane decreased in the case of Ca, Ce, and La containing β -zeolite, the selectivity for the isomerization was improved slightly from 65 to 73%. These results suggest that Ca, Ce, and La species were located on the strong active sites. However, further studies are necessary to understand the exact role of these metal ions on the catalytic properties.

4. Conclusion

A series of nano-sized β -zeolite with $\text{SiO}_2/\text{Al}_2\text{O}_3 = 50$ was synthesized without the use of sodium hydroxide by varying TEAOH concentration. Proton-form of β -zeolites with particle size of 30–80 nm was obtained only by calcination of as-synthesized zeolites without cationic exchange, where TEAOH worked SDA as well as the base. Further, alkali earth metal and rare earth metals were introduced to β -zeolites during the synthesis, and the resultant materials have higher surface area.

The isomerization and the cracking of hexane were studied to know catalytic properties of the β -zeolites. They are active for the isomerization of hexane with

good selectivity for branched isomers. The role of Ca, La, and Ce metals in catalytic behavior will be discussed in near future.

References

- 1 W. E. Farneth and R. J. Gorte, *Chem. Rev.*, **95**, 615 (1995).
- 2 C. S. Cundy and P. A. Cox, *Chem. Rev.*, **103**, 663 (2003).
- 3 A. de Angelis, P. Ingallina, and C. Perego, *Ind. Eng. Chem. Res.*, **43**, 1169 (2004).
- 4 G. Bellussi, G. Pazzuconi, C. Perego, G. Girotti, and G. Terzoni, *J. Catal.*, **157**, 227 (1995).
- 5 M. A. Camblor and J. Perez-Pariente, *Zeolites* **11**, 202 (1991).
- 6 J. Warzywoda, R. D. Edelman, and R. W. Thompson, *Zeolites*, **9**, 187 (1989).
- 7 R.M. Barrer, *Hydrothermal Chemistry of Zeolites*, Academic Press, London, p. 133 (1982).
- 8 P. Caullet, J. L. Hazm, J. F. Joly, J. Lynch, and F. Raatz, *Zeolites* **12**, 240 (1992).
- 9 M.A. Camblor, A. Corma, A. Mifsud, J. Perez-Pariente, and S. Valencia, *Stud. Surf. Sci. Catal.*, **105**, 341 (1997).
- 10 M. A. Camblor, A. Corma, and S. Valencia, *Microporous Mesoporous Mater.*, **25**, 89 (1998).
- 11 L. Tosheva and V.P. Valtchev, *Chem. Mater.*, **17**, 2494 (2005).
- 12 L. Ding and Y. Zheng, *Microporous Mesoporous Mater.*, **103**, 94 (2007).
- 13 M. V. Landau, D. Tavor, O. Regev, M. L. Kaliya, and M. Herskowitz, *Chem. Mater.*, **11**, 2030 (1999).
- 14 N. B. Castagnola and P. K. Dutta, *J. Phys. Chem. B*, **102**, 1696 (1998).
- 15 M. Lassinantti, J. Hedlund, and J. Sterte, *Microporous Mesoporous Mater.*, **38**, 25 (2000).
- 16 S. Mintova, S. Mo, and T. Bein, *Chem. Mater.*, **10**, 4030 (1998).
- 17 R. Bandyopadhyay, R. K. Ahedi, Y. Kubota, M. Ogawa, Y. Goto, Y. Fukushima, and Y. Sugi, *J. Mater. Chem.*, **11**, 1869 (2001)
- 18 A. Sakthivel, K. Komura, and Y. Sugi, *Chem. Lett.*, **36**, 894 (2007).
- 19 P. R. H. Prasad Rao and M. Matsukata, *Chem. Commun.*, 1441 (1996).
- 20 M. Matsukata, T. Osaki, M. Ogura, and E. Kikuchi, *Microporous Mesoporous Mater.*, **56**, 1 (2002).

GENERATION OF HIERARCHICAL POROSITY IN ZEOLITES BY SEED SILANIZATION

D. P. SERRANO*, J. AGUADO, R. SANZ, P. PIZARRO, J. M. RODRIGUEZ,
A. PERAL, I. MORENO

*Department of Chemical and Environmental Technology, ESCET, Universidad Rey Juan
Carlos, c/ Tulipán s/n, 28933, Móstoles, Madrid, Spain*

Seed silanization is a novel strategy for the synthesis of zeolites with hierarchical porosity and enhanced textural properties. This strategy is based on the organic functionalization of the protozeolitic units by anchoring of a silanization agent, which perturbs the growth of the zeolite crystals and avoids their further aggregation. This new method has been successfully applied to the synthesis of a variety of zeolites. The present work reports the results obtained when this procedure is employed to obtain ZSM-5 and TS-1 zeolites with hierarchical porosity.

1. Introduction

Zeolites are microporous crystalline metasilicates featured by exhibiting molecular sieve and shape selective properties. Zeolites have found a wide variety of applications in adsorption, ion exchange and as catalysts in oil refining, petrochemistry and fine chemistry [1]. However, the intracrystalline diffusion rate in zeolites is usually limited by the existence of micropores, especially in those processes involving large molecules [2]. To overcome this limitation, intensive research has been undertaken in the last years towards the synthesis of materials with enhanced accessibility by means of a number of methods: generation of secondary porosity by dealumination or desilication [3,4], confined space synthesis [5-7], preparation of nanozeolites [8], delaminated zeolites [9] and mesoporous zeolitic materials [10,11], or synthesis of hybrid zeolitic-ordered mesoporous materials [12,13]. The term hierarchical zeolites has been applied for designating zeolites containing a bimodal porosity, showing reduced steric and diffusional restrictions [14].

In this work, we report a novel strategy for the synthesis of zeolites with hierarchical porosity which exhibit excellent textural properties and enhanced accessibility to the zeolitic micropores. This method is based on the organic functionalization of the zeolitic seeds by reaction with a silanization agent. The formation of the zeolitic seeds occurs during an initial precrystallization step.

The silanization agent is added over the precrystallized gel and grafted onto the external surface of protozeolitic units forming a protective barrier against aggregation. Finally, a hydrothermal treatment is carried out in order to obtain highly crystalline materials. The presence of the organic moiety hinders the crystal growth by aggregation and avoids a complete fusion of the zeolitic seeds [15]. The zeolitic materials obtained by this method present an additional secondary porosity, in the range of supermicro/mesopores, originated from the space occupied by the silanization agent.

This novel strategy can be considered as a general method, as it has been successfully applied to the crystallization of different zeolitic materials with hierarchical porosity [16]. Here we show the results obtained when this new method is employed to synthesize the aluminosilicate and titanosilicate form of the MFI zeolite structure, which correspond with ZSM-5 and TS-1 zeolites.

2. Experimental Section

2.1. Samples Preparation

Hierarchical ZSM-5 samples were prepared from clear solutions with the following molar composition: $\text{Al}_2\text{O}_3:60\text{SiO}_2:11.5\text{TPAOH}:1500\text{H}_2\text{O}$. Tetraethoxysilane (TEOS, 98%; Aldrich), tetrapropylammonium hydroxide (TPAOH, 40%; Alfa), aluminum isopropoxide (AIP; Aldrich) and distilled water were used as starting materials. First, the aluminum source was added to an aqueous solution of TPAOH. The mixture was stirred at 0°C to obtain a clear solution. Then the silica source was added and the final mixture was stirred at room temperature for several hours to hydrolyze TEOS completely. Thereafter, the alcohols formed were removed under vacuum at 40°C. The precursor solution was precrystallized in a reflux system under stirring at 90°C for 20 h. Thereafter, the silanization agent, phenylaminopropyl-trimethoxysilane (PHAPTMS; Aldrich) was added in different quantities (8 and 12 mol% in regards to the total silica content in the gel), and the functionalization reaction was performed under stirring at 90°C for 6h. Finally, crystallization was carried out in a Teflon-lined stainless-steel autoclave under autogenous pressure at 170°C for 7 days.

Hierarchical TS-1 samples were obtained by adapting the method initially developed by Taramasso et al. [17]. First, the silica source (TEOS, Alfa) and the titanium source (TEOT, Alfa) were mixed at 30°C. Subsequently, this mixture was cooled at 0°C and a 1 M TPAOH aqueous solution was added dropwise. This reagent was synthesized alkali free by reaction of TPABr (98%, Aldrich)

with Ag_2O (Alfa). The resulting solution was heated at 80°C to remove the alcohols formed. The molar composition of the final solution so obtained was as follows: $\text{SiO}_2:0.0163\text{TiO}_2:0.44\text{TPAOH}:28.5\text{H}_2\text{O}$. The precrystallization and silanization steps were carried out analogously to the synthesis of hierarchical ZSM-5, with a precrystallization time of 24 hours, using 5 and 8 mol% of silanization agent in regards to the total silica content in the gel. The final crystallization treatment was carried out by microwave heating at 170°C for 8 h.

In all cases, the solid products obtained after crystallization were separated by centrifugation, washed several times with distilled water, dried overnight at 110°C and calcined in air at 550°C for 5 h.

Reference ZSM-5 and TS-1 zeolites were prepared applying the methods described above but omitting the silanization step.

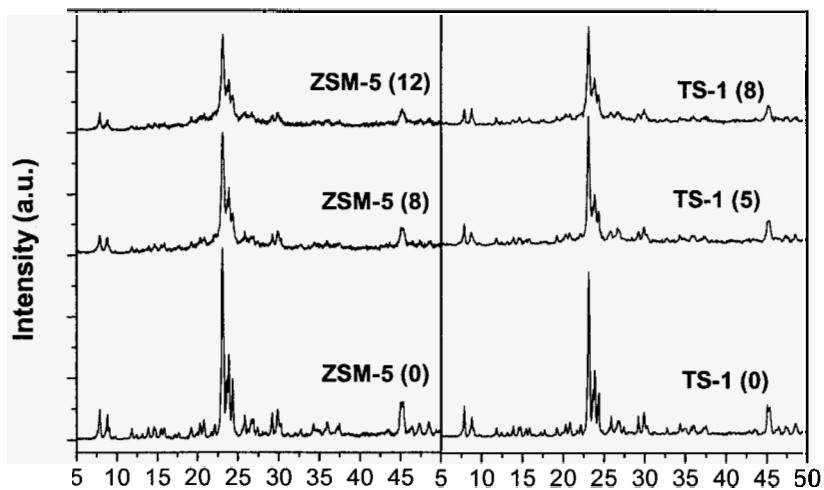
2.2. Characterization

X-Ray diffraction (XRD) patterns were collected with a Philips X'PERT MPD diffractometer using $\text{Cu K}\alpha$ radiation with a step size and counting time of 0.02° and 10 s, respectively. Aluminum and titanium contents of the synthesized samples were determined by means of atomic emission spectroscopy with induced coupled plasma (ICP-AES) analyses collected in a Varian Vista AX instrument. Nitrogen and argon isotherms at 77 K and 87.4 K, respectively, were measured using a volumetric adsorption apparatus equipped with a vacuum turbo-molecular pump for the determination of the surface area and the pore size distribution in the microporous range (Micromeritics, ASAP 2010). Thereby, the samples were previously outgassed at 300°C under vacuum for 5 h. The total surface area was estimated according to the BET method, whereas the external surface of the samples was calculated by the t-plot method. The pore size distribution was obtained by applying the NLDFT model with cylindrical pore geometry, using the software supplied by Quantachrome. TEM images were obtained in a PHILIPS TECHNAI 20 electron microscope operating at 200 kV. The organic content of the samples was determined by elemental analyses using an Elementar Vario EL III analyzer equipped with a thermal conductivity detector.

3. Results and discussion

Figure 1 illustrates the XRD diffractograms of a variety of as-made ZSM-5 and TS-1 zeolites, comparing the samples prepared from organofunctionalized seeds with those corresponding to conventional zeolite samples, which were obtained employing the same conditions but omitting the silanization step. All the samples

obtained after the final hydrothermal treatment are highly crystalline and show the typical pattern of the MFI zeolitic structure. The materials synthesized from silanized seeds possess lower intensity reflections than the reference samples, suggesting that a reduction in the crystalline domains has occurred. Moreover, this effect is more pronounced when increasing the amount of silanization agent.



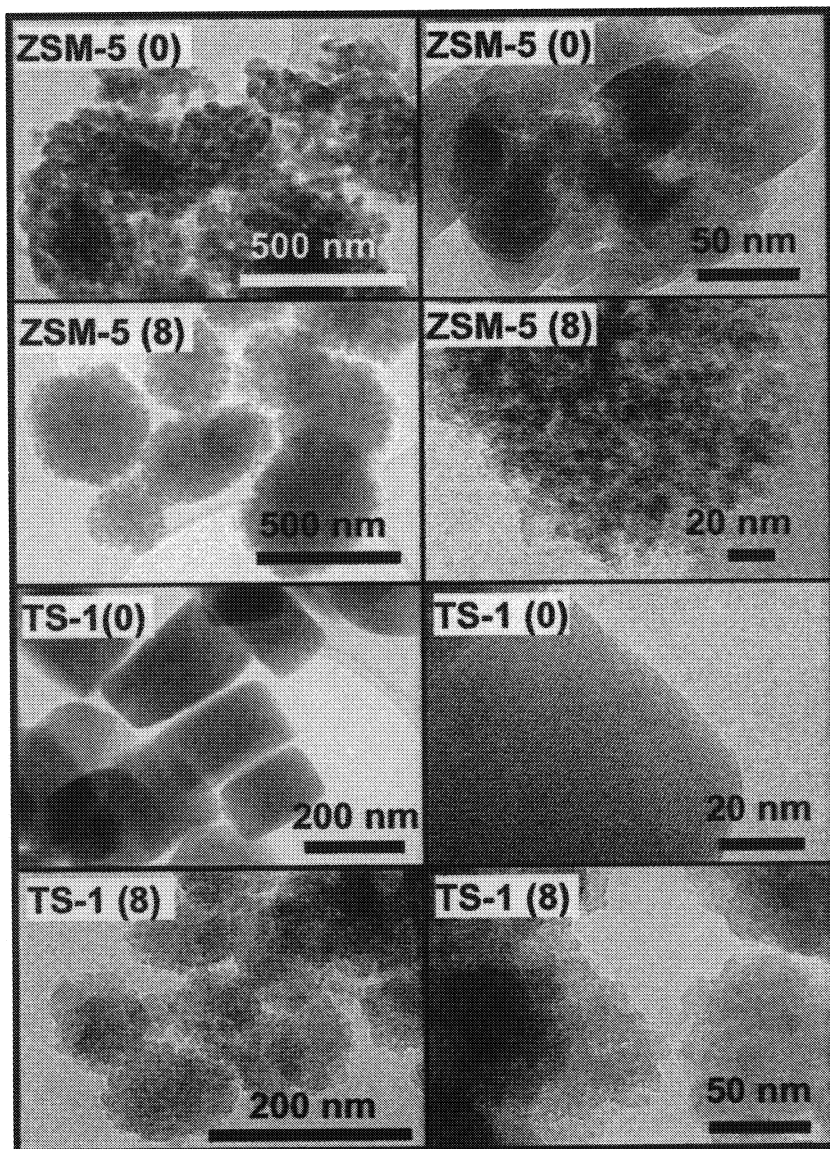


Figure 2. TEM micrographs of both reference samples (ZSM-5 (0) and TS-1 (0)) and materials prepared from silanized protozeolitic units (ZSM-5 (8) and TS-1 (8)).

The ZSM-5 reference sample, obtained omitting the silanization step (ZSM-5 (0)), is formed by aggregates of nanocrystals with sizes higher than 50 nm, hence this material can be considered as a standard nanocrystalline ZSM-5 zeolite. However, in the case of the sample synthesized from organofunctionalized seeds (ZSM-5 (8)), aggregates with diameters lower than 400 nm and sponge-like morphology are observed, which are formed by very small crystalline primary units with sizes around 10 nm. A similar effect occurs in the TS-1 materials. The reference zeolite is formed by highly perfect 200 nm crystals. In contrast, the material obtained from silanized seeds present particles with sizes in the range 100-150 nm, which are constituted by the tight packing of small crystalline primary units with sizes around 10-20 nm.

Figure 3 and Table 1 illustrates both N_2 adsorption isotherms and textural properties of the ZSM-5 and TS-1 samples.

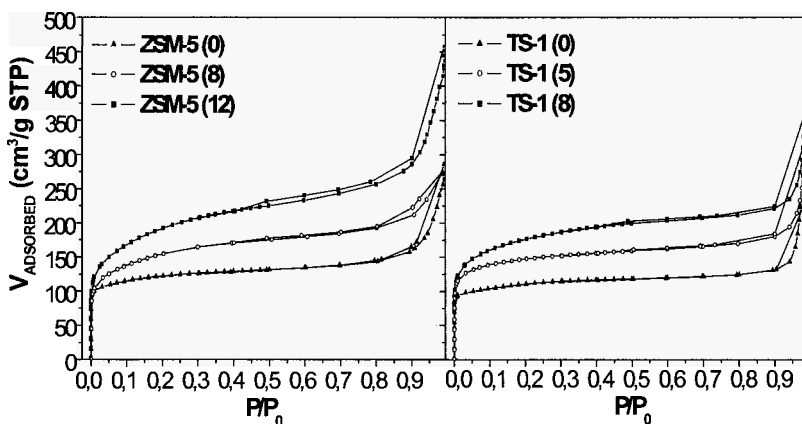


Figure 3. N_2 adsorption-desorption isotherms at 77 K of both reference samples (ZSM-5 (0) and TS-1 (0)) and materials prepared from protozeolitic units (ZSM-5 (8, 12) and TS-1 (5, 8)).

ZSM-5 and TS-1 reference materials present a type I isotherm, typical of microporous materials with high adsorption at low relative pressure (Figure 3). They exhibit also a significant adsorption at high relative pressure indicating the existence of interstitial porosity, which is characteristic of samples with low crystal sizes. Interestingly, the samples prepared from silanized seeds exhibit N_2 adsorptions clearly higher than those of the reference samples, denoting that these materials possess an enhanced porosity. Moreover, this effect is more pronounced when the amount of silanization agent is increased. At intermediate

relative pressures, the N₂ adsorption of two of the samples prepared by seed silanization is almost two fold higher than those of the reference materials. This result indicates that the *grafting* of the silanization agent causes a strong change in the zeolite porosity. The additional porosity arises from the void existing between the nanounits forming the aggregates observed in the TEM micrographs.

The MFI materials obtained from silanized seeds present enhanced BET and external surface areas (Table 1). The enhancement in the values of these properties is more pronounced when a larger amount of PHAPTMS is added during the silanization step. Thus, the BET surface areas of the ZSM-5 and TS-1 samples prepared using the highest amount of organosilane are exceptionally high for MFI zeolites: 698 and 634 m²/g, respectively. Likewise, the materials obtained by silanization of protozeolitic units present enhanced external surface areas.

Table 1. Composition and textural properties of the zeolite samples

Sample	Si / T ^a	PHAPTMS (wt%)	S _{BET} (m ² /g)	S _{MIC} (m ² /g)	S _{EXT} (m ² /g)	V _{MIC} (cm ³ /g)
ZSM-5 (0)	30	0	434	369	65	0.162
ZSM-5 (8)	34	7.3	555	410	145	0.182
ZSM-5 (12)	36	12.8	698	499	199	0.220
TS-1 (0)	81	0	390	340	50	0.152
TS-1 (5)	79	7.0	524	440	84	0.193
TS-1 (8)	72	13.2	634	472	162	0.207

^a T = Al or Ti for ZSM-5 and TS-1 samples, respectively.

For both ZSM-5 and TS-1 zeolites, Figure 4 compares the Ar adsorption-desorption isotherms at 87.4 K and the curves corresponding to the pore size distribution obtained by applying the NLDFT model. These results show that the ZSM-5 obtained from silanized seeds adsorbs larger Ar amounts at relative pressures above 5·10⁻² compared to the reference sample. However, at lower relative pressures the standard nanocrystalline ZSM-5 presents a higher adsorption than the modified ZSM-5. This fact means that in the material synthesized from organofunctionalized seeds the zeolitic microporosity is less significant although a higher overall pore volume is obtained.

The application of the NLDFT model to these isotherms allows a complete pore size distribution to be derived. The maximum observed for the reference zeolites (ZMS-5 (0) and TS-1 (0)) at around 0.52 nm agrees well with the size of

the MFI micropores. For ZSM-5 and TS-1 samples obtained from silanized seeds (ZSM-5 (12) and TS-1 (8)), the height of this first peak is significantly lowered. This fact could be related to the smaller crystalline primary units of the silanized zeolites in regards to the reference materials, and it is consistent with the trend observed in the XRD patterns and TEM micrographs. As it has been previously reported [18], a reduction in the crystal size within the nanometer range implies that a net transformation of internal into external surface occurs. These changes are accompanied by a decrease in the zeolitic microporosity. In contrast, a new and broader peak is observed between 1.5-5.0 nm, revealing the presence of an additional porosity in the supermicropore/low mesopore region. This additional porosity is related to the voids existing between the nanocrystalline units. Therefore, the presence of a hierarchical porosity is confirmed in the zeolites obtained employing the seed silanization step, which is expected to increase the accessibility to the internal surface area.

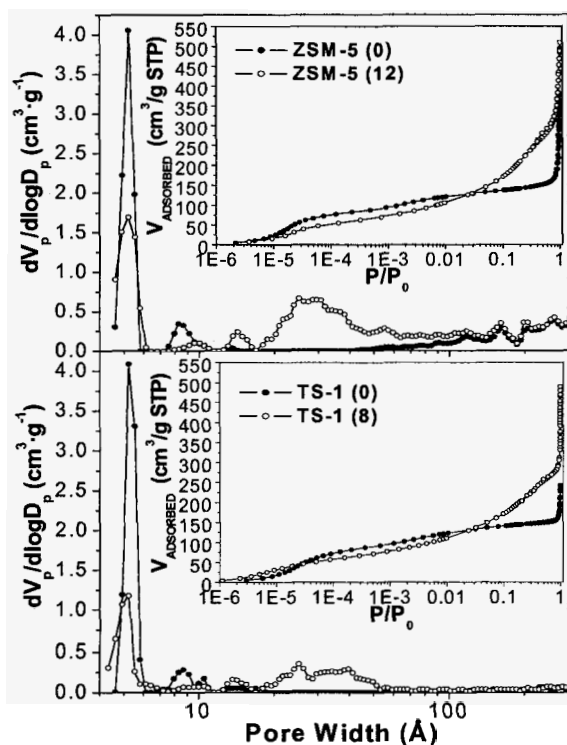


Figure 4. Ar adsorption-desorption isotherms at 87.4 K (inset) and NLDFT pore size distribution, calculated using a cylindrical pore model, of the calcined samples.

4. Conclusions

Perturbing the crystal growth of zeolites by organofunctionalization of protozeolitic units with organosilanes is an efficient method for the synthesis of MFI zeolites (ZSM-5 and TS-1) with enhanced textural properties. These materials exhibit a hierarchical pore network formed by an additional porosity in the range of the supermicropore/mesopore range in addition to the typical microporous zeolitic system. The generation of this secondary porosity is related to the silanization agent, which is anchored onto the zeolitic nuclei hindering both the crystal growth by aggregation of nanounits and the crystal densification. The degree of modification caused by the seed silanization treatment can be controlled by changing the amount of silanizing agent incorporated after the precrystallization step. The zeolitic materials prepared from silanized protozeolitic units present also enhanced BET surface area in regard to the conventional MFI zeolite samples, reaching values over 600 m²/g, which are quite higher than that typical of this type of zeolites (around 400 m²/g).

Acknowledgments

We want to thank “Ministerio de Educación y Ciencia” (Spain, project CICYT CTQ2005-097078) for its financial support to this research.

References

1. A. Corma, *J. Catal.* **216**, 298 (2003).
2. A. Dong, Y. Wang, Y. Tang, N. Ren, Y. Zhang, Y. Yue, G. Zi, *Adv. Mater.* **14(12)**, 926 (2002).
3. M. Müller, G. Harvey, R. Prins, *Micropor. Mesopor. Mat.* **34**, 135 (2000).
4. J. C. Groen, L. A. A. Peffer, J. A. Moulijn, J. Pérez-Ramirez, *Micropor. Mesopor. Mat.* **69**, 29 (2004).
5. C. Madsen, C. J. H. Jacobsen, *Chem. Commun.* **8**, 673 (1999).
6. S. Kim, J. Shah, T. J. Pinnavaia, *Chem. Mater.* **15**, 1664 (2003).
7. Z. Yang, Y. Xia, R. Mokaya, *Adv. Mater.* **16(8)**, 727 (2004).
8. L. Tosheva, V. P. Valchev, *Chem. Mater.* **17**, 2494 (2005).
9. A. Corma, V. Fornés, S. B. Pergher, Th. L. M. Maesen, J. G. Buglass, *Nature.* **396**, 353 (1998).
10. M. Choi, H. S. Cho, R. Srivastava, Ch. Venkatesan, D. H. Choi, R. Ryoo, *Nature Mater.* **5**, 718 (2006).
11. R. Srivastava, M. Choi, R. Ryoo, *Chem. Commun.* **43**, 4489 (2006).
12. Y. Liu, W. Zhang, T. J. Pinnavaia, *J. Am. Chem. Soc.* **122**, 8791 (2000).
13. Y. Han, S. Wu, Y. Sun, D. Li, F. S. Xiao, J. Liu, X. Zhang, *Chem. Mater.* **14**, 1144 (2002).

14. M. Hartmann, *Angew. Chem. Int. Ed.* **43**, 5880 (2004).
15. D. P. Serrano, J. Aguado, J. M. Escola, J. M. Rodríguez, A. Peral, *Chem. Mater.* **18**, 2462 (2006).
16. D. P. Serrano, J. Aguado, J. M. Rodríguez, A. Peral, *Stud. Surf. Sci. Catal.* **170**, 282 (2007).
17. M. Taramasso; G. Perego, B. Notari, USA Patent 4410501 (1983).
18. J. Aguado, D. P. Serrano, J. M. Escola, J. M. Rodríguez, *Micropor. Mesopor. Mat.* **75**, 41 (2004).

SYNTHESIS AND CHARACTERIZATION OF Y/ β COMPOSITE ZEOLITE AND ITS HYDROCRACKING PERFORMANCE

XIWEN ZHANG^{1,2} QUN GUO¹ ZHIZHI ZHANG² FENGXIANG LING² WANFU SUN² RUIFENG LI^{1*}

*1. Key Laboratory of Coal Science and Technology, MOE, Institute of Special Chemicals, Taiyuan University of Technology
Taiyuan, Shanxi, 030024, People's Republic of China*

*2. Fushun Research Institute of Petroleum and Petrochemicals, SINOPEC
Fushun, Liaoning, 113001, People's Republic of China*

A composite containing Y and β binary zeolite structures was synthesized through a one-pot procedure and characterized by PXRD, SEM, N₂ adsorption-desorption, FT-IR, ²⁹Si MAS NMR and the catalytic testing. The XRD pattern for this composite shows the presence of characteristic peaks of Y and β zeolites. The core-shell structure of this composite was shown by SEM analysis. The zeolite composite exhibited higher catalytic activity and selectivity in the VGO hydrocracking than a physical mixture of Y and β zeolites.

1. Introduction

To meet a strong continuing demand for the middle distillate products of improved quality, hydroprocessing (hydrotreating and hydrocracking) has emerged as the pivotal secondary refining process in modern petroleum refinery configuration, and the development of relative catalysts with high activity and selectivity is becoming exigent.

In recent years, scientific interest has been directed towards the synthesis of composite molecular sieves (microporous–microporous and microporous–mesoporous) and study of their catalytic synergism [1-8]. It has been demonstrated that composite molecular sieves combine the advantages of two type of molecular sieves and overcome the limitations of single materials, owing to the coexistence of both types of porosity and surface properties. This new type of materials has offered attractive features and exhibited obvious synergism in catalysis.

Microporous zeolites are widely used as acid catalysts due to the fact that they possess several catalytically desirable properties such as high surface area,

* Corresponding author. Tel.: +86 351 6010121 E-mail address: rfli@tyut.edu.cn

adjustable pore size, acidity, and high thermal and chemical stability. Zeolites have been known as the most active and selective heterogeneous catalysts. In particular, zeolites β and Y are two of the most unbeatable catalysts in catalytic cracking and hydrocracking. A composite zeolite with two-fold pore structure combines advantages of both materials and possibility of synergism in catalysis. In the present work, a composite of zeolites Y and β (denoted as Y/ β composite) was prepared and characterized, and its catalytic performance was tested in the VGO (Vacuum Gas Oil) hydrocracking reaction.

2. Experimental

The Y/ β composite was prepared in a Teflon-lined autoclave under static hydrothermal conditions by a two-step procedure. Firstly, NaY was prepared by a direct agent method. A direct agent with the molar ratio of $13\text{Na}_2\text{O}:15\text{SiO}_2:\text{Al}_2\text{O}_3:320\text{H}_2\text{O}$, was prepared by adding 11.13 g of sodium hydroxide, 32.55 ml of water glass (Na_2O 1.74 mol/L, SiO_2 8 mol/L, Qingdao Haiyang Chemical Company) and 5.82 ml of sodium aluminate (Na_2O 4.39 mol/L, Al_2O_3 2.98 mol/L) to 65 ml of deionized water, and aging at 35 °C for 24 h. Then NaY zeolite was prepared by adding 30 ml of water glass, 2.5 ml of H_2SO_4 (1 mol/L), 9.4 ml of sodium aluminate, and 3 ml of directing agent to 60 ml of deionized water under vigorous stirring, and being crystallized at 90 °C for 24 h. Then it was cooled to room temperature. Secondly, 18 g of tetraethylammonium bromide (TEABr, Beijing Xingbida Chemical Company), 6 ml of ammonia and 35 ml of deionized water were added to the mixture containing NaY made at the first step. pH value was adjusted to 13 by adding 1 mol/L H_2SO_4 . Finally, the mixture was heated at 140 °C for 4 days. The crystalline product was filtered, washed with distilled water, dried at 100 °C and calcined for 5 h at 500 °C.

Powder X-ray diffraction (PXRD) data were recorded using a Rigaku diffractometer with $\text{CuK}\alpha$ radiation. The nitrogen adsorption-desorption isotherms were determined by Micromeritics ASAP2400 at 77 K. All samples were outgassed at 573 K under a vacuum for 4 h prior to the analysis. Specific surface area was determined by BET equation, and the microporous structure was obtained by the t-plot analysis. IR spectra were obtained on a Bio-Rad spectrometer using KBr pellets. ^{29}Si MAS NMR was performed on a Bruker AV400 spectrometer equipped with a 4 mm double resonance MAS probe at a Si frequency of 79.457 MHz. SEM was carried out on a JEOL JSM-6301F scanning microscope. X-ray energy dispersive spectroscopy was carried out on Oxford-Link ISIS. Hydrocracking process was performed on a pilot test

installation with 100 ml fixed-bed. Iran VGO was employed as the feedstock for model catalyst testing. Experimental conditions were as follows: total pressure, 15.7 MPa; WHSV = 1.5 h⁻¹; and H₂/hydrocarbon molar ratio, 1500. Two temperatures were adopted, 385 °C and 382.5 °C. All data were collected during 0.75 h on stream.

4. Results and discussion

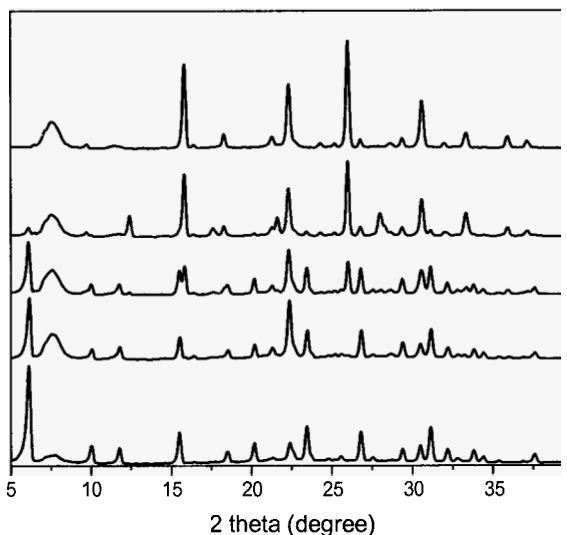


Figure 1. Powder XRD patterns for the samples obtained using different time during second-step crystallization process: (a) 48 h, (b) 72 h, (c) 96 h, (d) 120 h, (e) 144 h

Figure 1 shows XRD patterns for as-synthesized samples during the second-step crystallization process. Zeolite β phase appears in Figure 1 (a, b) and its relative amount in the composite increases with increasing crystallization time, which is shorter than 72 h. Hence the ratio of Y and β zeolites in the composite can be adjusted by controlling crystallization time. All characteristic peaks of Y and β zeolites are observed in the Y/ β composite zeolite, reflecting the coexistence of Y and β binary zeolites. However when crystallization time exceeds 72 h, the resulting materials are mainly Y, β and the other zeolites such as zeolite P and analcime. As crystallization of β is completed, zeolite Y would begin to transform partly into analcime and P zeolites. Finally only analcime, β and other stable inorganic phases are left. Unwanted zeolite phase could be

avoided by controlling crystallization time and pH value, just as reported in literature [3]. On the other hand, the unwanted zeolite P and analcime could be avoided by controlling the amount of silicon in the bulk liquid. The existence of a small amount of aluminum and alkali in as-prepared solution containing NaY is very beneficial to the crystallization of β zeolite, so as to shorten the crystallization time of β phase.

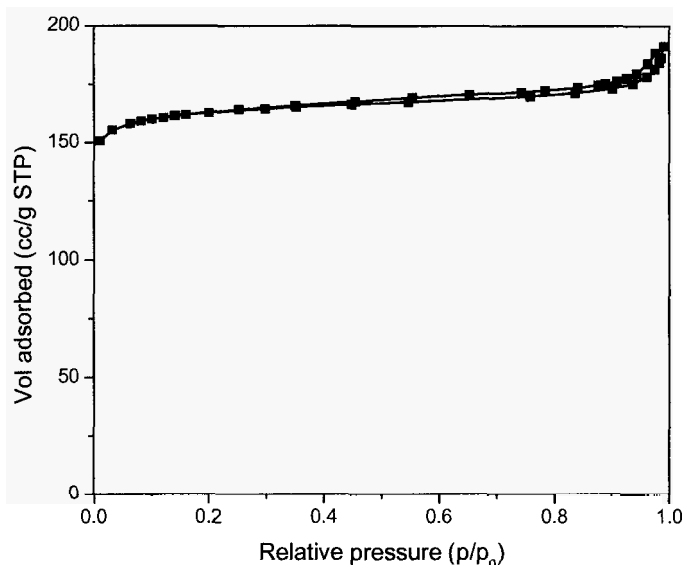


Figure 2. N_2 adsorption-desorption isotherm for Y/ β composite

Table 1. Properties of the Y/ β composite and Y zeolite.

Samples	S_{BET} (m^2/g) ^a	S_{micro} (m^2/g) ^b	S_{ext} (m^2/g) ^b	V_{microp} (m^3/g) ^b	V_{total} (m^3/g) ^c
Y	837	751	86	0.293	0.348
composite	625	518	107	0.198	0.285

a: multipoint BET surface area; b: t-plot method; c: $p/p_0 \sim 0.98$

N_2 adsorption-desorption isotherm for a typical Y/ β zeolite composite is shown in Figure 2. It is essentially type I isotherm, which is characteristic for microporous materials, with a small hysteresis loop indicating a small mesoporosity. The initial adsorption step at low relative pressure indicates complete filling of micropores. The resulting composite has a BET surface area as high as $625 \text{ m}^2/\text{g}$ and a micropore volume of $0.198 \text{ cm}^3/\text{g}$. In comparison to

single zeolite Y, the surface area and pore volume of the composite are smaller than the corresponding values of the former. However, the external surface area of composite increases, which may be due to the formation of nano zeolite β on the surface layer (see Table 1).

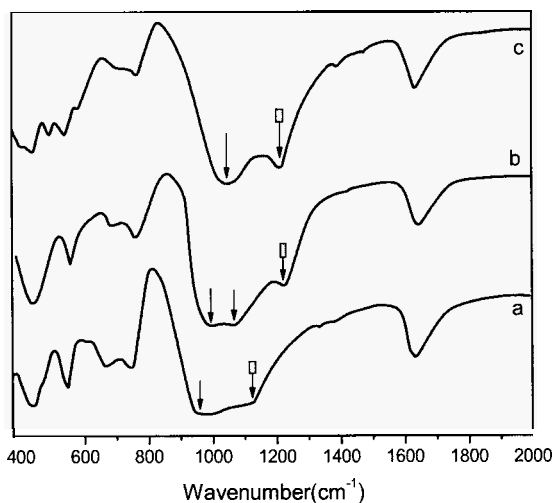


Figure 3. IR spectra for Y zeolite (a), composite (b) and β zeolite (c).

The FT-IR spectra for zeolites Y, β and the composite are shown in Figure 3. Apparently, all the major peaks of zeolites Y and β could be distinguished in the spectrum of the composite, although the peak position and height are not completely identical. The peaks at $440\text{ cm}^{-1} \sim 460\text{ cm}^{-1}$ are assigned to the structure insensitive internal TO_4 (T = Si or Al) tetrahedral bending vibrations; the peaks at $540\text{ cm}^{-1} \sim 560\text{ cm}^{-1}$ are attributed to the double ring external linkage vibrations [9,10]; The peaks at $660\text{ cm}^{-1} \sim 670\text{ cm}^{-1}$ are assigned to internal tetrahedral symmetrical stretching vibrations and the peaks at $740\text{ cm}^{-1} \sim 760\text{ cm}^{-1}$ are assigned to the external linkage symmetrical stretching vibrations. The peaks around 1639 cm^{-1} are assigned to the hydration of the sample and –OH vibrations. The peaks at 940 cm^{-1} and 1120 cm^{-1} (Figure 3a) are assigned to the internal tetrahedral asymmetrical stretching vibration and external linkage asymmetrical stretching vibration of Y zeolite, respectively [11]. In comparison to the Y zeolite, the peak assigned to the internal tetrahedral symmetrical stretching vibration, is divided into two peaks at 970 cm^{-1} and 1060 cm^{-1} (Figure

3b), which are assigned to the internal tetrahedral asymmetrical stretching vibrations of Y and β zeolites, respectively. The observed shift toward high wavenumber in the structure sensitive asymmetric stretching vibrations from 940 cm^{-1} to 970 cm^{-1} and from 1040 cm^{-1} to 1060 cm^{-1} indicates that β and Y zeolites in the composite have higher Si/Al ratio than pure Y and β zeolites [11].

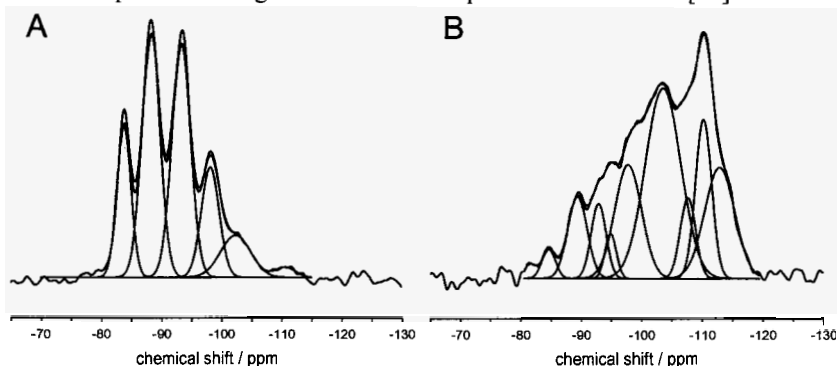


Figure 4. ^{29}Si MAS NMR spectra for Y zeolite (A) and composite (B).

^{29}Si MAS NMR spectra of the composite and zeolite Y are shown in Figure 4. The framework Si/Al ratio is calculated by deconvolving ^{29}Si MAS NMR spectra. Using Gaussian line shapes, five lines of Si(n Al) ($n=0, 1, 2, 3, 4$) sites are deconvolved from the spectra of Y zeolite. ^{29}Si MAS NMR peaks positioned at chemical shift values of δ -83.8, -88.25, -93.3, -98.14 and -102.4 are assigned to the Si coordination environments Si(4Al), Si(3Al), Si(2Al), Si(1Al) and Si(0Al), respectively [11]. For zeolite Y, the framework Si/Al ratio of 1.7 is determined according to NMR, the value is close to the result from chemical analysis. For the Y/ β composite, the complexity of Si coordination environment increases obviously; there exist many resonances of defect sites in this composite. Also, Si(4Si) environment is found to be dominant compared with Y zeolite (Figure 4a). The peaks at -84.66, -89.41, -94.87, -97.84 corresponding to the respective Si coordination environments Si(4Al), Si(3Al), Si(2Al) and Si(1Al) are observed; as well as peaks at -102.69, -107.63, -110.42, -112.79, corresponding to the equivalence sites of Si(4Si) [11,12-14] and peaks at -92.85 and -104.14 corresponding to Si(2Si, 2OH) and Si(3Si, 1OH) [14, 15] appear, respectively. The Si/Al ratio of the framework calculated from the spectra is 11.05, which is a little higher than that from chemical analysis (Si/Al = 10.09).

A core-shell type morphology for the Y/ β composite is shown on the SEM images (Figure 5). Y zeolite is wrapped by β zeolite. The core and the shell

are both confirmed by X-ray energy dispersive spectroscopy. The morphology of the Y/B composite varies as that of Y zeolite. They don't look like octahedral (as usually NaY), but like cylinder or spheroid particles. Different transects of the Y/6 composite are present in Figure 5, including the un-enwrapped (Y zeolite), the semi-enwrapped and fully-enwrapped. The B zeolite shell is composed of many nanoparticles, and the nanoparticles look like laminar hexagons. It is also observed that the hollow 6 zeolite shell is present, although it is very little. It indicates that Y zeolite has been consumed or separated from B zeolite shell by grinding and ultrasonic shake before SEM analysis is done. Many near-spheroid Y zeolite and some scattered zeolite B granules could be observed. Many researchers have mentioned that the shell of core-shell type composite zeolite is fragile [16]. The scattered zeolite B granules which could be found in the Y/B composite are probably separated from the composite zeolite by grinding and ultrasonic shake. Different procedures of reactants added in the second step have no impact on the morphology of the composite zeolite.

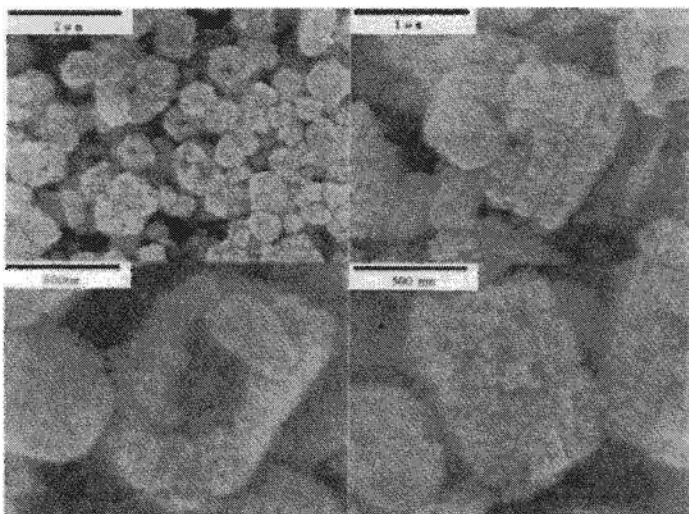


Figure 5. SEM images of the Y/B composite

Hydrocracking process is a refinery process for producing light fuels from heavy petroleum feedstock by cracking large hydrocarbon molecules in the presence of hydrogen. Here the catalytic performance of Y/B composite zeolite for hydrocracking of VGO is evaluated in the pilot test, and compared with that of the corresponding mixture of Y and B zeolites. The properties of feedstock

and reaction conditions are listed in Table 2 and Table 3. Composite shows an enhanced activity based on benchmark of mixture under the reaction temperature on the composite lower 2 °C than that on the mixture, provided that the conversion percentage is almost kept constant. Moreover, middle distillate selectivity of the composite is 2.69% higher than that of the mixture (see Figure 7). Hydrocracking product distribution is shown in Figure 6. More jet fuel and diesel oil are produced on the composite than that on the mixture. The properties of different distillates are listed in Table 4. Aromatization index of heavy naphtha obtained on the composite is 2.09 higher than that on the mixture. Arene content in jet fuel is 3.5% higher, solidifying point of diesel oil is 4 lower and cetane index is 7.05 higher. Obviously most of the properties of different distillates obtained on the composite are better than those on the mixture, except for the properties of tail oil.

Table 2. Properties of feed oil

Feed oil	Iran VGO
Density (20 °C), g/cm ³	0.9130
Distillation range, °C	336/542
CCR, m%	0.39
S, m%	1.59
N, µg·g ⁻¹	1700
Refractive, nD70	1.4835
BMCI index	45.9

Table 3. Reaction conditions

Catalysts	Mixture	Composite
Hydrogen pressure, MPa	15.7	
Ratio of hydrogen to oil	1500:1	
LHSV, h ⁻¹	1.5	
Temperature, °C	385	382.5

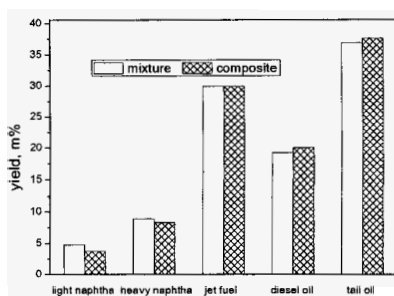


Figure 6. Hydrocracking product distribution

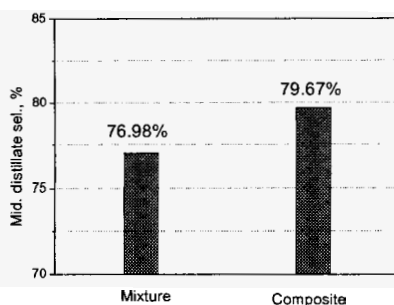


Figure 7. Middle distillate selectivity

Table 4. Properties of different distillates

Catalyst	Mixture	Composite
Heavy naphtha		
Density(20 °C), g/cm ³	0.7385	0.7403
Aromatization index, m%	60.10	62.19
Jet fuel		
Density(20 °C), g/cm ³	0.8046	0.8111
Freezing point, °C	<-60	<-60
Smoking point, mm	26	26
Arene content, v%	3.4	6.9
Diesel oil		
Density(20 °C), g/cm ³	0.8325	0.8385
Solidifying point, °C	-4	-8
Cetane number	64.0	71.05
Tail oil		
Density(20 °C), g/cm ³	0.8452	0.8439
CCR, m%	<0.01	<0.01
BMCI index	12.9	13.5

The above results have indicated that the composite zeolite is an advantage in the heavy oil catalytic cracking reaction. The core-shell structure of the composite zeolite might be benefit VGO transformation during the course of the cracking reaction. This suggests that Y and β zeolites in the composite exhibit a synergy effect due to the interfacial effect and the defect sites created by crystallization.

4. Conclusion

The Y/ β composite zeolite is synthesized by a one-pot procedure. Unwanted zeolites accompanying the transformation of Y zeolite to β zeolite could be avoided by adjusting the pH value and crystallization time and by controlling amount of silicon. Due to the presence of β zeolite, the surface area and pore volume of the composite zeolite are smaller than those of zeolite Y. The Si/Al ratio increased intensely in the composite zeolite, and consequently many defect sites were created in the Y/ β composite. As-synthesized sample exhibited a core-shell type morphology. In comparison to a physical mixture of Y and β zeolites, the composite zeolite showed higher activity and enhanced middle distillate selectivity when VGO is used as a feedstock for hydrocracking process due to the interfacial effect and defect sites present in the Y/ β composite.

References

1. P. Wang, B. J. Shen, J. S. Gao, *Catal. Commun.* 8, 1161 (2007).
2. S. I. Zones, Y. Nakagawa, U.S. Patent 5340563, 1994.

3. H. L. Chen, B. J. Shen, H. F. Pan, *Chem. Lett.* 32, 716 (2003).
4. Z. Zhang, B. N. Zong, *Chinese J. Catal.* 24, 856 (2003).
5. P. R. Joseph, C. P. Kevin, S. A. Raymond, et al. *Eur. Patent* 0293937 (1988); F. Fajula, F. Figueras, C. Gueguen, et al. *U.S. Patent* 4946580 (1990); T. C. Mark; D. P. Eugene, P. R. Hughes, *U.S. Patent* 5972205 (1999); M. Bourgoigne, G. L. Guth, R. Wey, *U.S. Patent* 4503024 (1985); Fajula Francois, Figueras Francois, Gueguen Claude, et al. *U.S. Patent* 4946580 (1990); Fajula Francois, Figueras Francois, Gueguen Claude, et al. *U.S. Patent* 4847224 (1989); Tsang Chih-Hao Mark, Dai Pei-Shing Eugene, Petty Randall Hughes, *U.S. Patent*, 5888921 (1999).
6. W. P. Guo, L. M. Huang, P. Deng, et al. *Micropor. Mesopor. Mater.* 44/45, 427 (2001).
7. L. M. Huang, W. P. Guo, P. Deng, et al. *J. Phys. Chem. B* 104, 2817 (2000).
8. Y. P. Li, X. L. Li, Y. Zhang, et al. *J. Fuel Chem. Tech.* 130, 162 (2002).
9. G. W. Skeels, D. W. Breck, in: D. H. Olson, A. Bisio (Eds.), *Proceedings of 6th International Zeolite Conference*, Butterworths, Guildford, 1984.
10. B. A. Holmberg, H. T. Wang, J. M. Norbeck, et al. *Micropor. Mesopor. Mater.* 59, 13 (2003).
11. B. A. Holmberg, H. T. Wang, Y. S. Yan, *Micropor. Mesopor. Mater.* 74, 189 (2004).
12. Perez-Pariente J., Sanz J., Fornes V., et al. *J. Catal.* 124, 217 (1990).
13. Chao K. J., Sheu S. P., Lin L. H., et al. *Zeolites*, 18, 18 (1987).
14. Fyfe C. A., Strobl H., Kokotail G. T., et al. *Zeolite*, 8, 132 (1988).
15. M. A. Camblor, A. Corma, S. Valencia, *Micropor. Mesopor. Mater.* 25, 59 (1998).
16. Younès Bouizi, Loïc Rouleau, Valentin P. Valtchev, *Micropor. Mesopor. Mater.* 91, 70 (2006).

PHOTORESPONSIVE MESOPOROUS ORGANOSILICA WITH MOLECULAR ORDER IN THE PORE WALLS

KRYSTYNA CZECHURA, ABDELHAMID SAYARI

*Centre for Catalysis Research and Innovation (CCRI), University Department,
University of Ottawa, Ontario K1N 6N5, Canada*

A bridged photoresponsive arylorganosilane 1,4'-bis(triethoxysilyl)azobenzene was used as a new precursor for the surfactant-assisted synthesis of PMO. For the first time, palladium catalyzed silylation using triethoxysilane was used for the preparation of PMO precursor from its iodo-derivative. The novel organosilica material with pore diameter of 39 Å and specific surface area of 384 m²/g also exhibits molecular scale periodicity within the pore walls. Reversible *trans*-to-*cis* isomerization of the azobenzene moieties integrated in the framework indicates that the organosilica remains flexible enough to undergo such contractions under UV irradiation. The photoisomerization is shown not to be limited to materials with chromophores diluted in silica.

1. Introduction

Periodic mesoporous organosilicas (PMOs) are prepared by condensation of organosiloxane precursors [(RO)₃Si-L-Si(OR)₃; L = organic spacer] in the presence of supramolecular structure-directing agents provided that L group is sufficiently rigid and the Si-L bond is stable under the synthesis and the template extraction conditions [1].

To expand the range of applications various organic functional groups have been incorporated into the silica framework by means of two or three terminal silyl groups; however, the organic spacers consisted mainly of simple species that serve primarily 'passive' roles such as reducing the dielectric constant of the framework or enhancing hydrophobicity [2].

Immobilization of novel intrinsic functionalities in the silica matrix gives possibility of providing new functional materials with unexpected properties [3]. Azobenzene is a well-known photosensitive chromophore that undergoes photoinduced and thermal geometric isomerization. Materials with azobenzene as the organic linker could be prepared with motivation of producing light-controlled functional materials.

Photoresponsive materials containing azobenzene functionality, including surface modified mesoporous silicas, are widely studied [4]. Self assembly of organosilicas derived from an azobenzene-bridged silsesquioxane was studied by

X-ray diffraction [4a]. Optical control of *d*-spacings corresponding to lamellar mesostructures of the *trans* and *cis* isomers was achieved through photoisomerization of the azobenzene moiety before or after assembly. The photo and thermal responsiveness was also evidenced by UV-vis spectroscopy for azobenzene derivatives grafted inside the channels of mesoporous silica films [4b]. Changing the length of the grafted moiety by photoisomerization enabled dynamic photocontrol of the pore size and hence regulated mass transport through the thin film [4c]. Immobilization of small amounts of azobenzene derivatives in a mesoporous silica matrix through co-condensation with TEOS was achieved while maintaining the photoswitchable property [4d].

2. Experimental

Coupling of 4-iodoaniline afforded 4,4'-diiodoazobenzene [5]. The corresponding arylsilane was then synthesized via palladium catalyzed silylation of alkenyliodide with triethoxysilane [6]. The use of hydrotriethoxysilane instead of tetraethoxysilane, led to higher yield [7]. The corresponding porous organosilica was prepared by self-assembly of the precursor in the presence of cetyltrimethylammonium bromide (CTAB) in basic aqueous medium.

2.1. Synthesis of bis(triethoxysilyl)azobenzene (B TSAZB)

A Schlenk flask was charged with Pd₂(dba)₃•CHCl₃ (80 mg, 0.08 mmol), P(*o*-tol)₃ (91 mg, 0.30 mmol), iodoazobenzene (1 g, 2.45 mmol) and NMP (20 mL; distilled from CaH₂ before use). The reaction vessel was purged with nitrogen, subsequently *i*-Pr₂NEt (2.6 mL, 15 mmol) and triethoxysilane (1.24 g, 7.5 mmol) were added via syringe. The mixture was stirred for 1 h at room temperature, then at 70 °C for 5 h. The reaction mixture was taken up in chloroform, extracted three times with water, dried and concentrated. Purification by column chromatography (hexanes:ethanol = 9:1) afforded 410 mg (32% yield) of pure product as orange oil. ¹H NMR (400 MHz, CDCl₃): *d* 1.27 (t, 18H, SiOCH₂CH₃), 2.15 (q, 18H, SiOCH₂CH₃), 7.4-8.0 (ArH); ¹³C NMR (100 MHz, CDCl₃): *d* 18.3 (SiOCH₂CH₃), 58.9 (SiOCH₂CH₃), 122.7, 129.1, 135.7 and 152.7 (ArC); ²⁹Si NMR (99.4 MHz, CDCl₃): *d* -58.3.

2.2. Synthesis of azobenzene-bridged organosilica

This material was prepared using B TSAZB as precursor and CTAB as template. The synthesis mixture had the following molar composition B TSAZB/CTAB/NH₄OH/H₂O/EtOH: 0.5/0.24/16/327/16. Initially the surfactant

was dissolved in water containing NaOH and after complete dissolution, the precursor dissolved in ethanol was added at room temperature. An orange precipitate appeared upon stirring. After 30 minutes of stirring, the temperature was raised to 80 °C and the mixture aged for another 4 days under static conditions. The solid product separated by filtration was dried at ambient conditions and the surfactant removed by two consecutive solvent extractions with acidified ethanol. Samples containing BTSAZB in mole fractions of 80%, 60%, 40%, 20% and 0% as a mixture with TEOS were also prepared.

2.3. Characterization

Powder X-ray diffraction (XRD) analysis was performed using a Philips PW3710 diffractometer operated at 45 kV, 40 mA, with CuK α radiation, 0.02° step size and 1.0 s accumulation time per step. Nitrogen sorption isotherms were determined with a Coulter Omnisorp 100 gas analyzer at 77 K. UV-visible spectra were recorded with a Varian Cary 300 spectrometer. The weight loss curves were recorded on a TGA thermogravimetric analyzer (model Q500-TGA, TA Instruments) coupled with a 1-300 amu mass spectrometer (Thermostar, Pfeiffer Vacuum). Samples were heated from ambient temperature to 1000 °C at a heating rate of 15 °C/min. The flowing gas was switched from nitrogen to air at the temperature of 900 °C. Raman spectra of materials were collected with a HORIBA Jobin Yvon LabRam-IR HR800 system. The powdered samples were irradiated with a Ar-ion laser ($\lambda = 785$ nm), and the backscattered radiation was collected through a 100x objective lens and detected by a CCD camera.

3. Results and discussion

The condensation of 1,4'-bis(triethoxysilyl)azobenzene in the presence of CTAB as a template resulted in mesoporous organosilica material with a low angle Bragg-diffraction peak at $2\theta \approx 2.7^\circ$ attributed to the occurrence of a mesophase. Assuming hexagonal symmetry ($a = 2d_{100}/\sqrt{3}$), this was found to correspond to a lattice constant (a) of 39 Å. The extracted product revealed a higher intensity, but broader low angle peak indicating that although the mesoporous order was retained within the sample, the pore size distribution widened. The XRD patterns lack the higher order reflections required to confirm the occurrence of hexagonal symmetry. In addition to the small angle diffraction a series of broad but distinct peaks appeared at higher angles (see arrows in Fig. 1), indicative of the occurrence of molecular order within the pore walls. Although, increasing the TEOS content from 0% to 20% gave rise to improved

periodic organization (Table 1), it understandably decreased the molecular order within the sample.

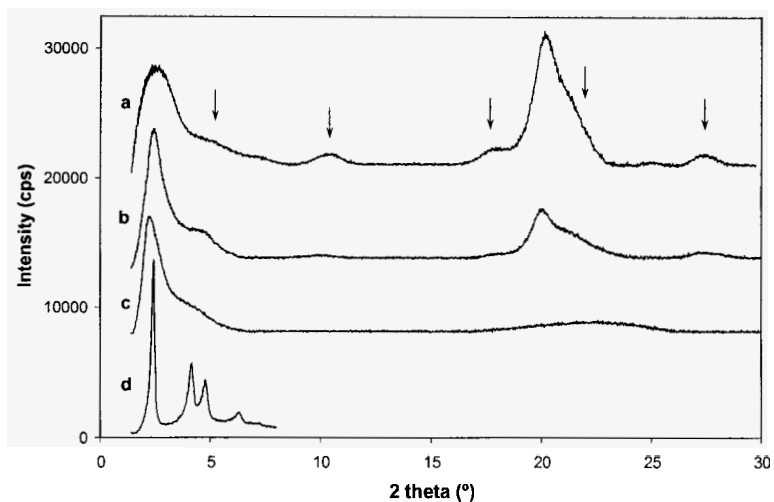


Figure 1. X-ray diffraction pattern of the extracted organosilica samples: a) 100%, b) 60%, c) 20% and d) 0% of BTSABZ.

Table 1. Structural properties of the mesoporous materials.

organosilica/TEOS molar ratio	% of organics		S_{BET} (m^2g^{-1})	V_{tot} (cm^3g^{-1})	d_{211} (nm)
	calculated	from TGA			
100	63.4	69.1	384	0.58	3.9
80	60.2	60.5	430	0.52	3.7
60	55.5	59.8	471	1.23	4.2
40	48.1	45.9	725	1.00	3.9
20	34.3	26.0	934	0.53	4.4
0	0	--	869	0.72	4.2

The nitrogen adsorption isotherm featured quite broad hysteresis loop confirming the occurrence of mesopores (Fig. 2). The BET surface area was $384 \text{ m}^2/\text{g}$ and the total pore volume was $0.58 \text{ cm}^3/\text{g}$.

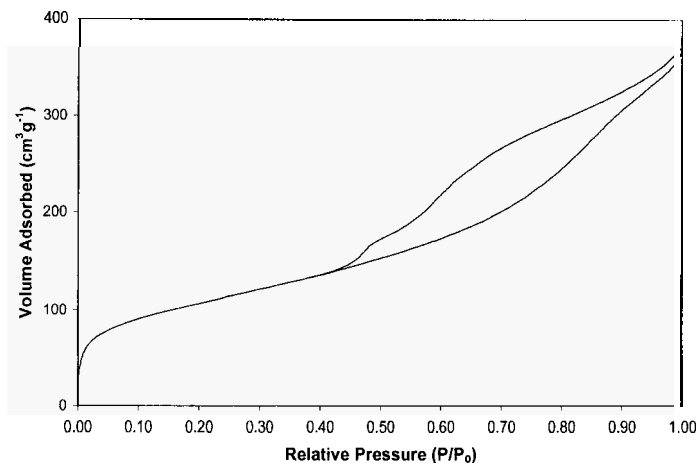


Figure 2. Adsorption isotherm of the azobenzene-bridged organosilica.

The structure of the obtained organosilica was confirmed by means of NMR data. The ^{29}Si NMR spectrum (Fig. 3) resembles a typical spectrum for bridged mesoporous organosilica [8]. It consists of a major T^3 (-79 ppm) resonance and a weak T^2 (-70 ppm) resonance representative of Si species covalently bonded to carbon atom. The presence of trace amount of the non functionalized Q species which occur between -90 and -120 ppm is interpreted as the sign of condensation of residual triethoxysilane in the monomer as a separate silica phase. The number of aromatic resonances in ^{13}C cross polarization MAS NMR spectrum is in accordance with the four distinct carbon atoms of the azobenzene moiety. This indicates that the azobenzene species and the Si-C bonds remained intact during the material synthesis.

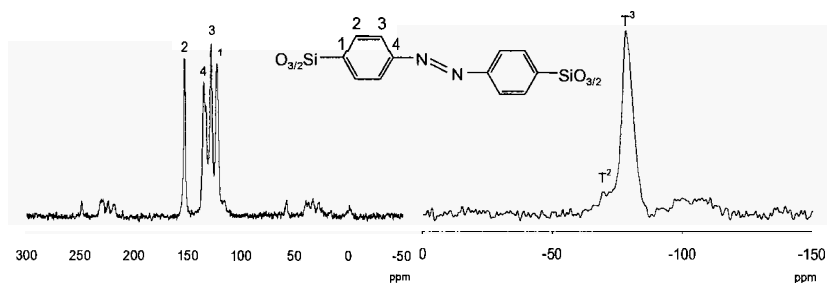


Figure 3. ^{29}Si and ^{13}C CP MAS NMR of the azobenzene-bridged PMO.

The thermal stability of the materials, as evaluated by TGA, was used for quantitative verification that the framework consists of the same relative amount of organo-bridged siloxane as predicted based on the composition of the synthesis mixture. High thermal stability of the material was observed as no substantial thermal degradation was detected under flowing nitrogen up to 320 °C. The total weight loss of 69.1 % found between 300 °C and 1000 °C is attributed to the decomposition of the bridging organic groups. This experimental value is in acceptable agreement with the calculated content (63.4 %) of azobenzene groups based on a framework composition of $O_{3/2}Si-C_4H_6-N=N-C_4H_6-SiO_{3/2}$. The percentages of the azobenzene incorporated in the samples with TEOS also agree with the calculated values based on the initial BTSABZ to TEOS ratios (Table 1). The decomposition temperature was higher than that of the materials prepared via surface modification which underwent decomposition of the organic moieties between 140 and 620 °C [4].

The Raman spectrum of the pure organosilica sample (Fig. 4) revealed distinctive features of motions related to azobenzene moiety. The Raman scattering features in the 1400 cm^{-1} has been unambiguously identified from its strong appearance as the $-N=N-$ stretching frequency [9]. Whereas, in-plane benzene ring vibrations and C-H out-of-plane bending bands appear at 1593 cm^{-1} and 999 cm^{-1} respectively.

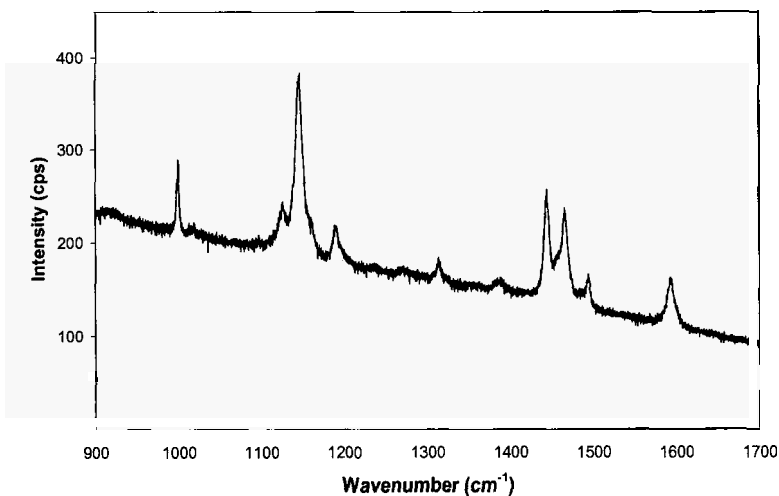


Figure 4. Resonance Raman spectrum of azobenzene-bridged PMO.

Once the photochemical behaviour of precursor in solution was confirmed by UV-vis spectroscopy, the photo-responsiveness of azobenzene moieties within the organosilica framework was characterized. The spectrum of the material exhibited an absorption band at 225 nm (λ_{max} of p-p* transition of the *trans* isomer) and a weaker band at 450 nm (due to n-p* transition of the *cis* form). UV-A lamps with overall power of 8 W were used as a light source and the absorption spectra of the irradiated sample were recorded 5 minutes after switching the light source off until the difference in absorbance was minimal.

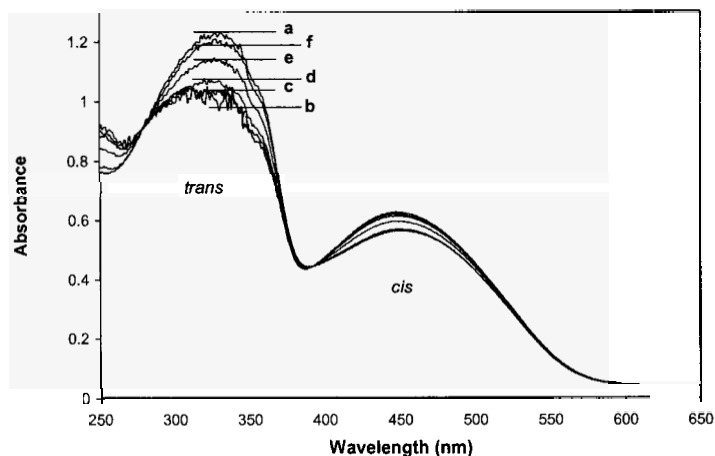


Figure 5. UV-vis absorption spectra of the organosilica sample (a) before exposure to UV-A for 30 min and (b) 5 min, (c) 30 min, (d) 1 h, (e) 3 h and (f) 1 day after the exposure.

The exposure time of 15 minutes was sufficient to trigger evident *trans*-to-*cis* isomerization. Figure 5 shows typical photoresponse of the azobenzene material irradiated for 30 minutes. Upon UV irradiation the intensity of the band at 225 nm was pronounced and that of the 450 nm band reduced signifying *trans* population decay. Gradual reversion of the *cis* isomer to the thermodynamically more stable *trans* isomer occurred after the exposure to the room light. The initial *trans* population was nearly restored after 1 day. Alternating exposure of the sample to UV and visible light showed repeatability and reversibility of the process. The photoresponsiveness of azobenzene functional groups supported on silica was found to be relatively smaller (not shown) suggesting that the pronounced isomerization of azobenzene-moieties within 100% PMO is perhaps induced by initial changes in *cis/trans* population and it is not affected by the possible restrictions in mobility of the molecules.

Acknowledgement

The generous financial support of the Natural Sciences and Engineering Council of Canada (NSERC) and the Ontario Research & Development Challenge Fund (ORDCF) is acknowledged. A. S. is a Canada Research Chair in Catalysis by Nanostructured Materials (2001-2008).

References

1. For review, see: (a) A. Sayari, S. Hamoudi, *Chem. Mater.* **13**, 3151 (2001). (b) F. Hoffmann, M. Cornelius, J. Morell, M. Froba, *Angew. Chem. Int. Ed.* **45**, 3216 (2006). (c) A. Stein, B. J. Melde, R. C. Schroden, *Adv. Mater.* **12**, 1403 (2000). (d) W. J. Hunks, G. A. Ozin, *J. Mater. Chem.* **15**, 3716 (2005).
2. (a) K. Okamoto, M. P. Kapoor, S. Inagaki, *Chem. Commun.* 1423 (2005), and references therein. (b) S. Inagaki, S. Guan, T. Ohsuna, O. Terasaki, *Nature* **416**, 304 (2002). (c) M. Kuroki, T. Asefa, W. Whitnal, M. Kruk, C. Yoshina-Ishii, M. Jaroniec, G. A. Ozin, *J. Am. Chem. Soc.* **124**, 13886 (2002). (d) A. Sayari, W. Wang, *J. Am. Chem. Soc.* **127**, 12194 (2005).
3. (a) O. Olkhoviyk, M. Jaroniec, *J. Am. Chem. Soc.* **127**, 60 (2005). (b) B. Lee, H.-J. Im, H. Luo, E. W. Hagaman, S. Dai, *Langmuir* **21**, 5372 (2005).
4. (a) N. Liu, K. Yu, B. Smarsly, D. R. Dunphy, Y.-B. Jiang, C. J. Brinker, *J. Am. Chem. Soc.* **124**, 14540 (2002). (b) N. G. Liu, Z. Chen, D. R. Dunphy, Y. B. Jiang, R. A. Assink, C. J. Brinker, *Angew. Chem. Int. Ed.* **42**, 1731 (2003). (c) N. G. Liu, D. R. Dunphy, P. Atanassov, S. D. Bunge, C. Chen, G. P. Lopez, T. J. Boyle, C. J. Brinker, *Nano. Lett.* **4**, 551 (2004). (d) E. Besson, A. Mehdi, D. A. Lerner, C. Reye, R. J. P. Corriu, *J. Mater. Chem.* **15**, 803 (2005). (e) M. Alvaro, M. Benitez, D. Das, H. Garcia, E. Peris, *Chem. Mater.* **17**, 4958 (2005).
5. (a) M. Z. Barakat, M. F. Abdel-Wahab, M. M. El-Sadr, *J. Chem. Soc.* 4685 (1956). (b) O. H. Wheeler, D. Gonzalez, *Tetrahedron* **20**, 189 (1964).
6. M. Murata, K. Suzuki, S. Watanabe, Y. Masuda, *J. Org. Chem.* **62**, 8569 (1997).
7. M. Murata, S. Watanabe, Y. Masuda, *Tetrahedron Lett.* **40**, 9255 (1999).
8. A. Sayari, S. Hamoudi, Y. Yang, I. L. Moudrakovski, J. R. Ripmeester, *Chem. Mater.* **12**, 3857 (2000).
9. A. Dupaix, J. J. Bechet, J. Yon, J. C. Merlin, M. Delhaye, M. Hill, *Proc. Nat. Acad. Sci. USA* **72**, 4223 (1975).

ULTRA-FAST HYDROTHERMAL SYNTHESIS OF DIASTEREOSELECTIVE PURE ETHYLENE-BRIDGED PERIODIC MESOPOROUS ORGANOSILICAS

CARL VERCAEMST*, MATTHIAS IDE, FRANCIS VERPOORT AND PASCAL VAN
DER VOORT

*Department of Inorganic and Physical Chemistry, Center for Ordered Materials,
Organometallics and Catalysis (COMOC), University of Ghent, Krijgslaan 281 (S-3)
Ghent, 9000, Belgium*

In this study, we present an ultra-fast hydrothermal synthesis of diastereoselective pure periodic mesoporous organosilicas (PMOs) with outstanding properties. This was realized by means of developing and applying the *E*-diastereoisomer of 1,2-bis(triethoxysilyl)ethene (~ 100 % *E*), by adapting a more efficient extraction procedure for the polymeric template pluronic P123 and by fine-tuning the reaction conditions. This hydrothermal synthesis procedure gives way to developing PMOs in a manner much faster than usually known, while maintaining high surface areas, large pore volumes and narrow pore size distributions.

1. Introduction

The field of ordered mesoporous materials, studied by scientists over the globe, only took form since, in 1992, researchers of the Mobil Oil company had the ingenious idea of performing sol-gel chemistry in the presence of a liquid crystal template [1,2]. Within the following decade, several thousands papers and several books appeared in the area of periodic mesoporous materials. An important part of these research efforts went into the development of new types of ordered mesoporous materials with organic functions.

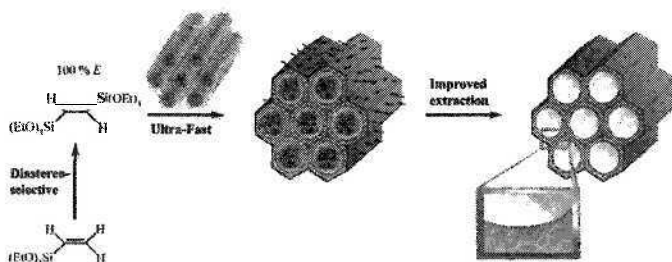
Recently, since 1999, these type of materials were expanded with the introduction of periodic mesoporous organosilicas [3-5]. These relatively novel materials are synthesized via the direct condensation of bridged organobissilanes, most commonly $(\text{RO})_3\text{Si-R}'\text{-Si}(\text{OR})_3$. PMOs are very unique and promising inorganic-organic hybrid materials that combine the structural features of ordered mesoporous silicas with the chemical functionality of organic groups [3-9]. The use of bridged organosilanes gives way to ordered mesostructures with very high organic content, while maintaining very narrow

* Corresponding author, e-mail: carl.vercaemst@ugent.be

pore size distributions, high surface areas and large pore volumes. Moreover, the organic functions are homogeneously distributed and are an intrinsic part of the pore walls. However, the required rigidity of the PMO pore walls implies that the organic functionality of the bridged organobissilane has to consist of a rigid structure, either as a short chain or as a small cyclic or aromatic system. For this reason, the range of suitable PMO-precursors is limited. The scope of PMOs can be expanded though, either by combining the use of rigid bridged organobissilanes and mono-organosilanes or by altering the PMO-functionality through post-synthesis modifications.

To date, the majority of literature reports on PMOs are concerned with ethylene-bridged PMOs, probably due to the wide commercial availability of bis(triethoxysilyl)ethane. However, the organic ethane function offers limited possibilities in terms of chemical modification. From this perspective, ethenylene-bridged PMOs offer much more possibilities by means of olefin chemistry. Only a handful of publications on ethenylene-bridged PMOs have been reported though [3,10-17].

In this contribution several aspects concerning the synthesis of diastereoselective pure ethenylene-bridged PMOs using Pluronic P123 as a template, are presented.



Herein the first synthesis procedure for the diastereoselective pure *E*-isomer of 1,2-bis(triethoxysilyl)ethene is introduced. A strategy to drastically reduce the synthesis time and an improved extraction procedure for polymeric templates is also covered.

2. Experimental

2.1. Chemicals

Vinyltriethoxysilane (VTES), $(\text{PCy}_3)_2\text{Cl}_2\text{Ru}=\text{CHPh}$, $\text{RuCl}_2(\text{PPh}_3)_3$, Pluronic P123 ($\text{EO}_{20}\text{PO}_{70}\text{EO}_{20}$), and TEOS were obtained from Aldrich.

2.2. *Classic synthesis of 1,2-bis(triethoxysilyl)ethene*

1,2-bis(triethoxysilyl)ethene (BTSE) was prepared via metathesis of VTES with $\text{RuCl}_2(\text{PPh}_3)_3$, according to a method described by Marciniak et al. In a typical synthesis, $\text{RuCl}_2(\text{PPh}_3)_3$ (0.051 g, 0.053 mmol) and VTES (10.086 g, 0.053 mol) were added to a Schlenk flask under argon. After stirring and refluxing for 24 h, unreacted VTES was distilled off. Subsequently, BTSE was vacuum distilled to give a clear colourless liquid. Yield: 6.25 g (67%). BTSE was identified by ^1H and ^{13}C NMR and GC-analysis as a diastereoisomeric mixture (~ 80 % *E*).

2.3. *Synthesis of the diastereoselective pure E-isomer of 1,2-bis(triethoxysilyl)ethene*

For the synthesis of the diastereoselective pure *E*-isomer of 1,2-bis(triethoxysilyl)ethene (*E*-BTSE), the Grubbs' first-generation catalyst was used. In a typical synthesis of *E*-BTSE, $(\text{PCy}_3)_2\text{Cl}_2\text{Ru}=\text{CHPh}$ (0.0535 g, 0.065 mmol) and VTES (42.95 ml, 0.2038 mol) were added to a Schlenk flask under argon. The mixture was left to stir for one hour and subsequently refluxed for an additional hour. Unreacted VTES was distilled off, after which *E*-BTSE was vacuum distilled to give a clear colourless liquid. Yield: 33.8 g (94 %). *E*-BTSE was identified by ^1H and ^{13}C NMR and GC-analysis as a diastereoisomeric pure product (~ 100 % *E*).

2.4. *Preparation of ethylene-bridged periodic mesoporous organosilicas*

In a typical synthesis procedure, 1.00 g of Pluronic P123 was diluted in an acidified solution containing 47.80 ml of H_2O , 3.42 ml of concentrated HCl and 2.45 ml of BuOH . The solution was stirred at room temperature for 1.5 h upon which 1.86 ml of the homemade *E*-BTSE was added. The final reactant molar composition was: $\text{P123}:\textit{E}\text{-BTSE}:\text{HCl}:\text{H}_2\text{O}:\text{BuOH} = 1:29.27:237.8:16098:155$. This solution was stirred for 4 h at 35 °C and successively aged for an additional 16 h at 90 °C under static conditions. The mixture was left to cool down to room temperature after which the precipitated PMO was filtrated and washed with distilled water. The surfactant was removed by means of soxhlet extraction using acetone over a period of 5 h.

To investigate the influence of several co-solvents (ethanol, propanol, and butanol) on the morphology, the co-solvent was varied while keeping the other reaction parameters constant. Besides the type of co-solvent, the influence of co-solvent concentration and acidity were investigated.

2.5. Preparation of SBA-15

SBA-15 was synthesized according to the following procedure: a mixture of 12.01 g of P123, 381.00 g of distilled H₂O and 69.62 g of concentrated HCl were mixed for 1.5 h at 45 °C after which, 25.50 g of TEOS was added and left to stir for an additional 6 h. The final reactant molar composition was: P123:TEOS:HCl:H₂O = 1:59.1:341.4:11389. This solution was subsequently aged at 80 °C for 15 h under static conditions. The mixture was left to cool down to room temperature after which the precipitated silica material was filtrated and washed with distilled water.

To investigate the efficiency of several organic solvents (dichloromethane, chloroform, acidified ethanol, ethyl acetate, isopropanol and acetone) for the extraction of the polymeric template, the surfactant-containing SBA-15 material was divided in portions. The surfactant was removed by means of soxhlet extraction using the respective solvents over a period of 5 h. One portion of the surfactant-containing SBA-15 material was calcined in a temperature controlled oven of which the temperature was razed from 25 °C to 550°C at 2 °C/min, followed by a 6 h treatment at 550 °C.

2.6. Bromination of ethenylene-bridged PMOs

The accessibility of the C=C double bonds in the ethene-PMOs was investigated by means of a bromine addition reaction. The PMOs were treated with bromine vapour under vacuum at 35 °C for 2 h. Physisorbed bromine was removed under vacuum at 90 °C, overnight.

2.7. Characterization

X-ray powder diffraction (XRD) patterns were collected on a Siemens D5000 Diffractometer with Cu Ka radiation with 0.15418 nm wavelength. Nitrogen adsorption experiments were performed at 77 K using a Belsorp-mini II gas analyzer. Samples were vacuum dried overnight at 90 °C prior to analysis. The specific surface area, S_{BET} , was determined from the linear part of the BET plot ($P/P_0 = 0.05-0.15$). The pore size distribution, PSD, was calculated from the desorption branch using the BJH (Barett, Joyner and Halenda) method. Scanning electron microscopy (SEM) images were collected on a Quanta 200 FEG instrument from FEI. FT-Raman and DRIFT spectra were acquired on an Equinox 55S hybrid FT-IR/FT-Raman spectrometer with a Raman module FRA 106 from Bruker. The spectrometer is fitted with a N₂-cooled germanium high sensitivity detector D418-T and a N₂-cooled MCT-B detector. The Raman

spectra were recorded from 0 to 3500 cm^{-1} . Everything below 50 cm^{-1} , including Rayleigh scattering was filtered away. The Raman laser wavelength used throughout this study was the 1064 nm line of an air cooled diode pumped neodymium yttrium aluminium garnet laser (Nd:YAG). The laser power was manually set to 300 mW. The FT-IR module was fitted with a temperature and pressure controlled DRIFT-cell. All DRIFT measurements were performed under vacuum. The spectra were recorded from 0 to 3500 cm^{-1} . The ^1H and ^{13}C liquid NMR spectra were collected on a Varian Unity-300 spectrometer. GC analysis was conducted on a Finnigan Trace GC ultra, equipped with a standard FID detector. A wall coated open tubular column with a length of 10 m, an internal diameter of 0.10 mm and a coating of 0.40 μm (5 % diphenyl and 95 % dimethyl polysiloxane) was used.

3. Results and discussion

3.1. Diastereoselective pure ethylene-bridged PMOs: role of catalyst

In our effort to catalytically obtain a pure isomer of 1,2-bis(triethoxysilyl)ethene, several catalysts were probed. Ultimately the best results were obtained with the commercially available Grubbs' first-generation catalyst $(\text{PCy}_3)_2\text{Cl}_2\text{Ru}=\text{CHPh}$. By employing merely 0.032 mol% of catalyst, *E*-BTSE was acquired in one step with a yield of 94 %, without further purification being necessary.

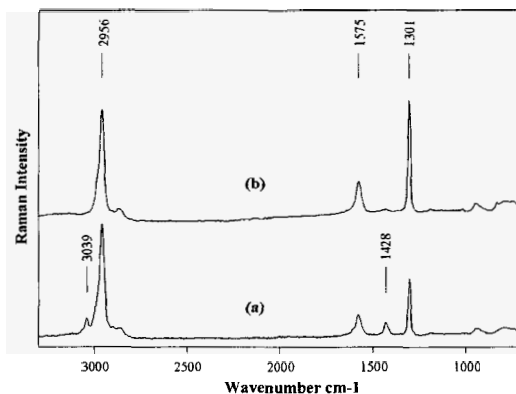


Figure 1. Raman spectra of ethylene-bridged PMOs synthesized with (a) BTSE (80 % *E*) and (b) *E*-BTSE (100 % *E*).

The resulting ethylene-bridged PMOs, synthesized using BTSE and *E*-BTSE were analyzed by means of FT-Raman spectroscopy. Figure 1 gives the Raman

spectra of (a) a diastereoselective pure PMO, and (b) a PMO consisting of a mixture of two diastereoisomers (80 % *E*).

As can be seen in figure 1, both Raman spectra exhibit intense peaks at 2956 cm^{-1} , 1575 cm^{-1} and 1301 cm^{-1} . These peaks can be assigned to the C-H stretch vibration, C=C stretch vibration and the in-plane C-H deformation of the *E*-isomer, respectively. The peaks at 3039 cm^{-1} and 1428 cm^{-1} , visible in spectrum (a), can be assigned to the *Z*-isomer of the diastereoisomeric mixture.

3.2. Optimization of the template extraction procedure

The extraction of pluronic P123 was investigated and evaluated by means of FT-Raman spectroscopy. To exemplify the efficiency, the solvent extraction was initially studied for SBA-15. This inorganic ordered mesoporous material, with similar morphological and structural features as our PMOs, has no active Raman vibrations. Therefore, the vibrations resulting in bands in the Raman spectra can be assigned exclusively to the surfactant template. Figure 2 gives the Raman spectra (C-H stretch region) of as-synthesized, solvent-extracted (5 h, soxhlet) and calcined SBA-15.

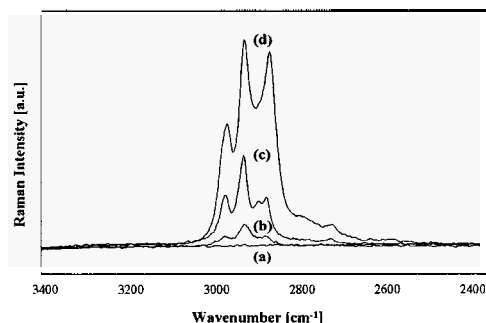


Figure 2. Raman spectra of SBA-15: (a) calcined, (b) acetone-extracted (5 hours), (c) ethanol-extracted (5 hours), (d) as-synthesized.

As can be seen from figure 2, acetone is more efficient for the extraction of P123 than acidified ethanol. In table 1, the efficiency of several solvents for the extraction of P123 is given. From this table can be seen that acetone is the most efficient solvent removing over 94 mol% of the template after a single soxhlet extraction of 5 hours.

The extraction of P123 was also studied for ethenylene-bridged PMOs, the results are given in table 2. As can be seen from this table, by applying the improved extraction procedure, the surface area, the total pore volume and the

pore diameter increase. Quantitative measurements via TGA-analysis were not reliable due to C=C decomposition of the PMO in the same temperature region as the surfactant decomposition.

Table 1. Extraction efficiency of several solvents for the removal of P123, after a single soxhlet extraction of 5 hours.

PMO samples	Surface area [m ² /g]	Total pore volume [cc/g]	Pore size [nm]
As-synthesized	263	0.451	5.0
Ethanol-extracted	970	0.978	5.4
Acetone-extracted	1018	1.034	5.9

3.3. Ultra-fast hydrothermal synthesis of ethenylene-bridged PMOs

According to literature data, the hydrothermal synthesis of PMOs typically takes about 48 hours [10-12,14]. To reduce the synthesis time, several parameters such as pH, temperature and the presence of additives play a key role. Lowering the pH increases both the silane-template interaction and the hydrolysis rate of the PMO-precursor. However, when the kinetics of the sol-gel reaction is too high, the surface area and the total pore volume decrease due to the increasing amount of disordered material. In order for the polycondensated organosilica particles to aggregate into an ordered mesoporous architecture, a strong template-precursor interfacial energy and a minimal repulsion force between the growing organosilica particles is required. Recent literature data indicate that additives such as salts and co-solvents can have dramatic effects on the morphology and structure of the obtained mesophases [14].

By combining the use of a diastereoselective pure precursor with an optimized synthesis route and an improved extraction method, an ultra-fast hydrothermal synthesis procedure for ethenylene-bridged PMOs with outstanding structural properties, was developed. In figure 3 the surface area is given as a function of the synthesis time. When compared with a typical literature procedure (48 hours), higher surface areas are obtained. Even with the

ultra-fast hydrothermal synthesis procedure (8 hours), a surface area of 795 m^2/g is attained. Figure 3 also illustrates the narrow pore size distribution of an ethene-PMO synthesized according to the improved synthesis method.

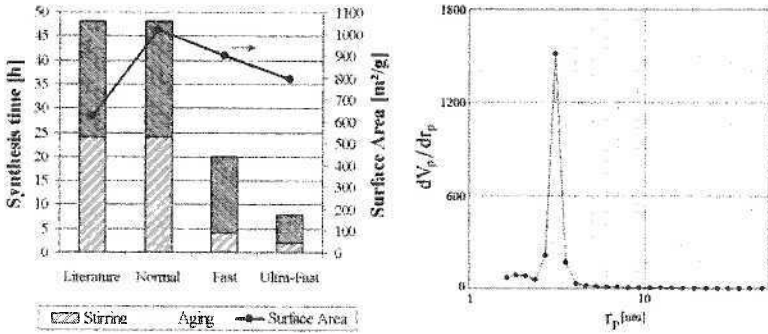


Figure 3. Left: Surface area as a function of synthesis time, compared with a typical literature procedure [14]. Right: Pore size distribution of an ethene-PMO synthesized according to the improved synthesis method.

The surface area of these PMOs is highly dependent on the pH (see figure 4) and on the concentration of co-solvent. However, changing the co-solvent has no significant effect on the surface area and the total pore volume. On the other hand, the latter strongly influences the ordering (see XRD-plot in figure 4) and the morphology of the PMOs (see figure 5).

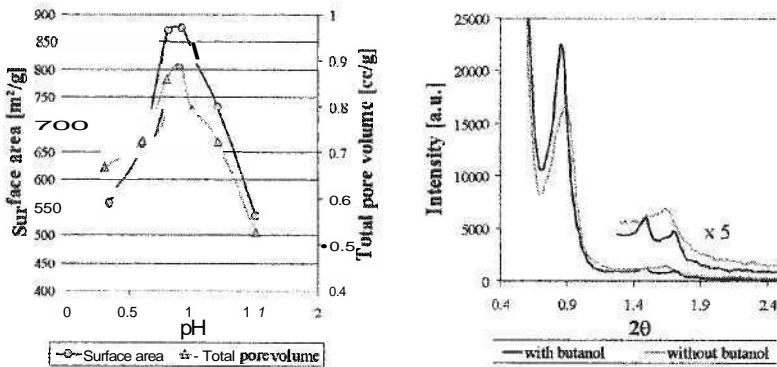


Figure 4. Left: Surface area and total pore volume as a function of pH (PMOs synthesized in the absence of cosolvents). Right: XRD-plot of ethene-PMOs synthesized with butanol and without butanol.

The XRD pattern shown in figure 4, reveals a strong peak at $2\theta = 0.86^\circ$, attributed to the (100) diffraction peak from the 2D hexagonal unit cells. Moreover, the PMO synthesized with butanol as co-solvent, exhibits two well-resolved peaks attributed to (110) and (200) reflections. These assignments are consistent with the occurrence of a mesophase with well-ordered hexagonal symmetry.

3.4. Control of morphology: Influence of co-solvent

In figures 5, SEM-images are given for ethylene-bridged PMOs, prepared in the presence of different co-solvents.

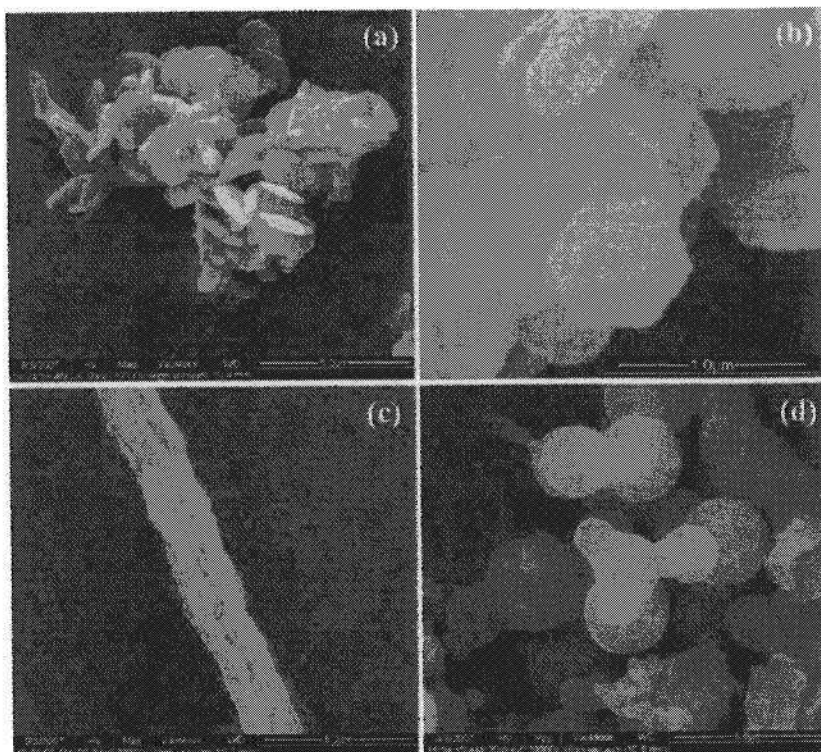


Figure 5. FE-SEM micrographs of ethylene-bridged PMOs prepared with different co-solvents: (a) ethanol, (b) propanol, (c) butanol (butanol:P123 = 94:1) and (d) butanol (butanol:P123 = 175:1). Micrographs (a), (c) and (d) are magnified 20000 times while (b) is magnified 80000 times.

As can be seen from figure 5, the type of co-solvent used in the synthesis of PMOs has a major influence on the morphology. For the PMOs synthesized with ethanol (a) and propanol (b), hexagonal plate-like disks are predominant. For the PMOs synthesized with butanol (c), ropelike macrostructures with lengths of over 150 μm and diameters of approximately 2 - 10 μm are predominant.

When the butanol:P123 ratio is increased from 94:1 (c) to 175:1 (d), spherical particles are obtained. However, the spheres are stuck together, forming small clusters. In figure 5 (d), some irregular chunks are also visible.

3.5. Chemical accessibility of the ethene-functions: Bromination

To demonstrate the chemical accessibility of the PMO ethene-functionalities, bromination of the ethylene-bridged PMOs was performed. Figure 6 gives the Raman spectrum of an ethylene-bridged PMO, before and after bromination. An intense peak at 639 cm^{-1} is visible in spectrum (b), which can be assigned to the C-Br stretch vibration. A reduction of the peak at 1573 cm^{-1} , which can be assigned to the C=C stretch vibration, is also visible. Via FT-Raman spectroscopy, the percentage of accessible C=C double bonds is estimated at approximately 30 %. By means of gravimetric analysis, the amount of brominated ethene-functions is estimated at 1.9 per nm^2 .

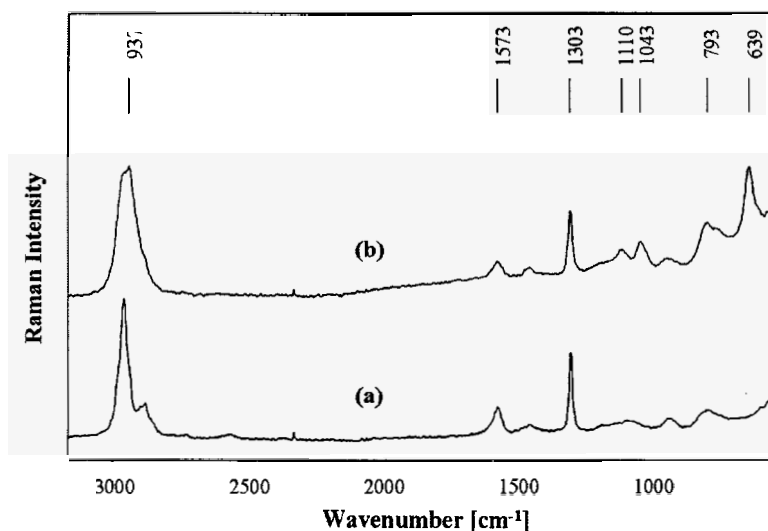


Figure 6. FT-Raman spectra of (a) an ethylene-bridged PMO and (b) a brominated ethylene-bridged PMO.

4. Conclusions

The present work demonstrates that diastereoselective pure ethenylene-bridged PMOs, with exceptional properties, can be prepared according to an ultra-fast synthesis procedure. This contribution further illustrates that acetone is a more efficient solvent for the extraction of polymeric templates than the commonly applied solvent, acidified ethanol. By means of using different cosolvents, the morphology of the ethenylene-bridged PMOs can be controlled.

Acknowledgments

The authors gratefully acknowledge the experimental aid of Mrs. Cindy Claes and Mr. Danny Vandeput. The authors are indebted to the FWO-Vlaanderen (Fund for Scientific Research Flanders) and the University of Ghent for a research grant and financial support.

References

1. C. T. Kresge, M. E. Leonowicz, W. J. Roth, J. C. Vartuli and J. S. Beck, *Nature* **359**, 710 (1992).
2. J. S. Beck, J. C. Vartuli, W. J. Roth, M. E. Leonowicz, C. T. Kresge, K. D. Schmitt, C. T. W. Chu, D. H. Olson, E. W. Sheppard, S. B. Mccullen, J. B. Higgins and J. L. Schlenker, *J. Am. Chem. Soc.* **114**, 10834 (1992).
3. T. Asefa, M. J. MacLachan, N. Coombs and G. A. Ozin, *Nature* **402**, 867 (1999).
4. S. Inagaki, S. Guan, Y. Fukushima, T. Ohsuna and O. Terasaki, *J. Am. Chem. Soc.* **121**, 9611 (1999).
5. B. J. Melde, B. T. Holland, C. F. Blanford and A. Stein, *Chem. Mater.* **11**, 3302 (1999).
6. S. Inagaki, S. Guan, T. Ohsuna and O. Terasaki, *Nature* **416**, 304 (2002).
7. K. Landskron, B. D. Hatton, D. D. Perovic and G. A. Ozin, *Science* **302**, 266 (2003).
8. K. Landskron and G. A. Ozin, *Science* **306**, 1529 (2004).
9. V. Rebbin, R. Schmidt and M. Froba, *Angew. Chem., Int. Ed.* **45**, 5210 (2006).
10. K. Nakai, Y. Oumi, H. Horie, T. Sano and H. Yoshitake, *Microporous Mesoporous Mater.* **100**, 328 (2007).
11. K. Nakajima, I. Tomita, M. Hara, S. Hayashi, K. Domen and J. N. Kondo, *J. Mater. Chem.* **15**, 2362 (2005).
12. K. Nakajima, I. Tomita, M. Hara, S. Hayashi, K. Domen and J. N. Kondo, *Catal. Today* **116**, 151 (2006).

13. C. Vercaemst, M. Ide, B. Allaert, N. Ledoux, F. Verpoort and P. Van der Voort, *Chem. Commun.* **2261** (2007).
14. W. H. Wang, S. H. Xie, W. Z. Zhou and A. Sayari, *Chem. Mater.* **16**, 1756 (2004).
15. Y. D. Xia and R. Mokaya, *J. Phys. Chem. B* **110**, 3889 (2006).
16. Y. D. Xia and R. Mokaya, *J. Mater. Chem.* **16**, 395 (2006).
17. Y. D. Xia, Z. X. Yang and R. Mokaya, *Chem. Mater.* **18**, 1141 (2006).

STRUCTURAL INVESTIGATION OF ORDERED MESOPOROUS SILICAS FUNCTIONALIZED BY DIRECT SYNTHESIS WITH CYCLAM DERIVATIVES

FABRICE GASLAIN, ANNE-CATHERINE FAUST, CLAIRE MARICHAL AND
BENEDICTE LEBEAU

*Laboratoire de Matériaux à Porosité Contrôlée, UMR 7016, CNRS-ENSCMu-UHA, 3
rue A. Werner, 68093 Mulhouse cedex, France*

YOANN ROUSSELIN, FRANCK DENAT

*Institut de Chimie Moléculaire de l'Université de Bourgogne, UMR5260, CNRS-UNIV.
BOURGOGNE, 9 Avenue Alain Savary, 21078 Dijon Cedex, France*

MATHIEU ETIENNE, ALAIN WALCARIUS

*Laboratoire de Chimie Physique et Microbiologie pour l'environnement, UMR 7564,
CNRS - Nancy Université, 405, rue de Vandoeuvre, 54600 Villers-lès-Nancy, France*

MCM-41- and MCM-48-type silicas functionalized by cyclam groups linked to the framework with one, two or four silanol arms, have been prepared by direct synthesis. Physicochemical characterization (X-Ray diffraction, N₂ adsorption - desorption and SEM) have revealed ordered materials with a bimodal porosity, similar morphology and particle size. Stability in aqueous medium and accessibility to the active sites have also been assessed.

1. Introduction

Environmental pollution as a result of technological development is a serious concern for ecology. Heavy metal ions contamination represents a significant threat to the ecosystem and especially to people. Hence, water purification is an important topic in many scientific disciplines [1]. Among existing solutions, silica based organic-inorganic ordered mesoporous materials have received an increasing interest since those materials take advantages of both the inorganic framework (non-swelling and stable under acidic conditions, which can be prepared with desired porosity and high surface area) and the complexation capacity of the organic functional groups anchored onto the silica surfaces [2]. In this context, we have developed a new series of ordered mesoporous silicas functionalized with cyclam derivatives adopting the MCM-41 and MCM-48

framework morphologies for the selective complexation of some heavy metals [3].

MCM-41- and MCM-48-type silicas functionalized by cyclam groups linked to the framework with one, two or four silanol arms, have been prepared by direct synthesis following in each case a very similar one-pot synthetic procedure previously developed in our laboratories [4]. Using this procedure, various comparable mesoporous hybrid materials (in terms of particle size, spherical morphology and framework types) with different kinds of cyclam precursors have been successfully obtained. Physicochemical characterization (X-Ray diffraction, N_2 adsorption - desorption and SEM) have revealed materials with a bimodal porosity.

For cleaning up applications, those materials will have to be left in water for long periods and the alkaline behaviour of the cyclam ligands could degrade the silica backbone. Therefore, the stability for these materials, which is a critical parameter has been checked. The accessibility to the active sites, i.e. chelating cyclam macrocycles, has also been characterized by protonation experiments.

2. Experimental section

2.1. Material preparation

Silylated cyclam precursors presented in Figure 1 were prepared according to the literature [5].

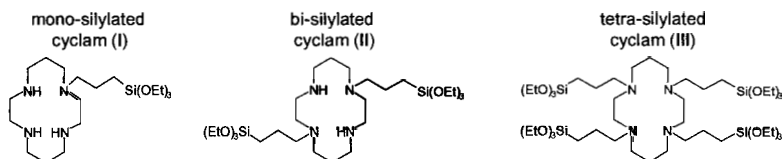


Figure 1. Representation of mono-, bi- and tetra-silylated cyclam precursors.

All silica materials were prepared by adapting procedures previously reported. The typical molar composition of reagents for MCM-41 materials was 1:0.4:14.5:53:180 SiO_2 precursor:CTAB:ammonia:methanol:water. For the preparation of MCM-48 materials, the amount of water was doubled and methanol was replaced by ethanol. Direct syntheses were made from a mixture of TEOS and mono, bi- or tetrasilylated cyclam derivatives in the molar ratio 0.95 TEOS:0.05 cyclam. In all cases, the surfactant was extracted under reflux with a mixture of HCl and ethanol.

2.2. Characterization methods

All hybrid materials were characterized by X-ray diffraction (XRD, PANanalytical X'PERT PRO diffractometer, equipped with a Cu anode), nitrogen adsorption-desorption measurements performed at 77K (Micromeritics Tristar), ^{29}Si and ^{13}C solid state nuclear magnetic resonance (NMR, Bruker Advance II, 300 MHz), scanning electron microscopy (SEM, FEI XL30 FEG operating at 5 KeV), and elemental chemical analysis (Thermo Electron CHNS analyzer).

2.3. Stability and accessibility experiments

Prior to those experiments, all hybrid materials were first deprotonated by using 2 eq. of triethylamine (per cyclam) in an equimolar EtOH/H₂O solution (15 min treatment). The solid samples were recovered after filtration, washing with water until neutrality, rinsing with EtOH and drying overnight at 70°C.

For stability experiments, a 10^{-2} mol.L⁻¹ KCl solution made from freshly distilled water was prepared. 60 mL of this solution were put in a vessel and the pH was adjusted to 7.00 by bubbling N₂ gas. Next, about 30 mg of cyclam material were added and the pH evolution was recorded throughout the 30 min experiment using an PC interfaced pH-meter.

For accessibility measurements, about 20 mg of material were dispersed in 5 mL of 10^{-2} mol.L⁻¹ HCl solution and were left to stir for 24 h. The solution was filtered off and the remaining filtrate was titrated with a freshly prepared 5×10^{-3} mol.L⁻¹ NaOH solution. Hence, we could estimate the number of protons consumed by the cyclam-functionalized material and therefore accessed the quantity of reactive cyclams considering that only two nitrogen atoms per cyclam would be neutralized by protons.

3. Results and discussion

3.1. Structural and textural characterization

SEM pictures show particles that are nearly spherical with an average diameter ranging from 0.25 to 0.5 μm (Figure 2). In the MCM-41 series, increasing the number of cyclam silylated arms increases the surface roughness. MCM-48 materials are not affected by this effect.

The amounts of nitrogen atoms determined by CHN analyses (%wt N_{exp}) are reported in table 1 and show that 75 to 100% of the initial cyclam groups were incorporated. Taking into account errors due to the calculation method for

theoretical %wt N_{th} , it can be considered that the organic groups incorporation is almost complete, which is not surprising since direct synthesis is a functionalization procedure that allows controlling the amount of functional group [6].

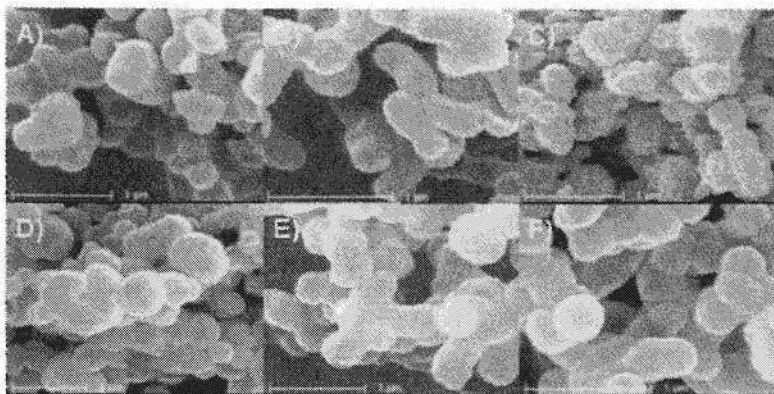


Figure 2. SEM images of MCM-41 solids functionalized with (a) mono-, (b) bi- and (c) tetrasilylated cyclam precursors and MCM-48 solids functionalized with (d) mono-, (e) bi- and (f) tetrasilylated cyclam precursor.

Table 1. N_2 adsorption-desorption and CHN analyses data of MCM-41 and MCM-48 samples functionalized with cyclam silylated precursors.

Material type	Surf. Area /m ² g ⁻¹	Pore vol. /cm ³ g ⁻¹	Pore $\bar{\phi}$ [§] / nm	%wt N_{th} [*]	%wt N_{exp}	
MCM-41	mono-	697	0.85	<2;5;7	3.66	2.72
	bi-	886	0.77	<2;4.8;7.5	3.47	3.10
	tetra-	773	1.07	<2;7	3.13	3.02
MCM-48	mono-	678	0.75	<2;4.3;7.8	3.66	2.90
	bi-	594	0.69	<2;3.8;7.5;18	3.47	3.02
	tetra-	542	0.77	<2;8;12	3.13	3.22

[§]average pore sizes determined by BJH method from adsorption branches

^{*} theoretical %wt N was calculated from the initial cyclam precursor/Si molar ratio under assumption that silylated cyclam precursors are fully condensed and silica network is constituted of 20% Q³/80%Q⁴ units.

XRD patterns of raw (not shown) and extracted materials are typical of A) MCM-41 and B) MCM-48 frameworks (Figure 3). In the MCM-41 series, the hexagonal framework was retained throughout all materials. However in the MCM-48 series, increasing the number of silylated arms in the cyclam derivative

tended to affect the cubic framework leading to more disordered materials. It is well known that most of the organic functions incorporated by direct synthesis tend to disorganize the spatial pore arrangement and consequently modifying the interaction at the multicharged hybrid siloxane/silica polymers/surfactant interfaces [7]. Disordering effects increase with increasing the amount of organic functions and affect more less stable micelles aggregates such as bicontinuous cubic mesophase compare to cylindrical micelles present in the hexagonal mesophase.

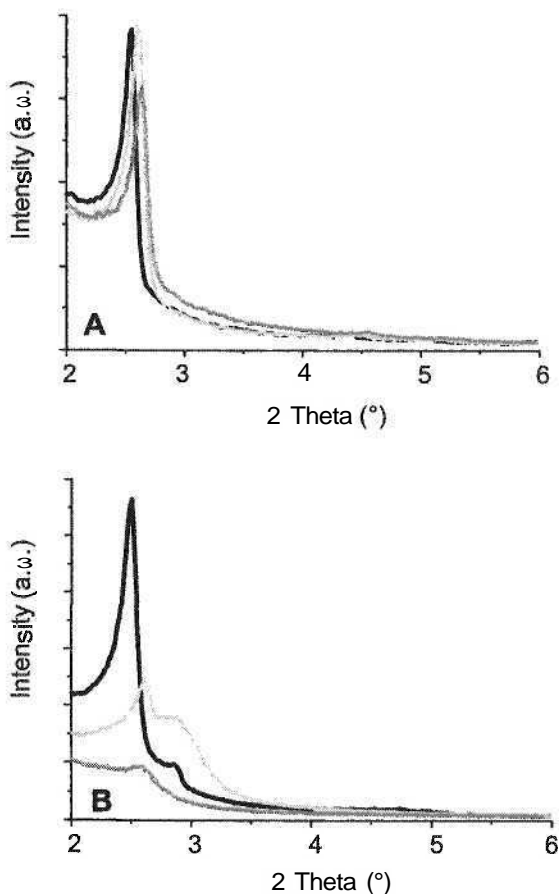


Figure 3. XRD patterns of (A) MCM-41 and (B) MCM-48 samples functionalized with mono-(—), bi-(---) and tetrasilylated (· · ·) cyclam precursors.

N_2 adsorption-desorption isotherms of all surfactant extracted solids were of type IV characteristic of mesoporous materials (Figure 4). Nevertheless, pore size distributions obtained by the BJH method from the adsorption/desorption branches showed the presence of mesopores in a broad range between 2 and 20 nm.

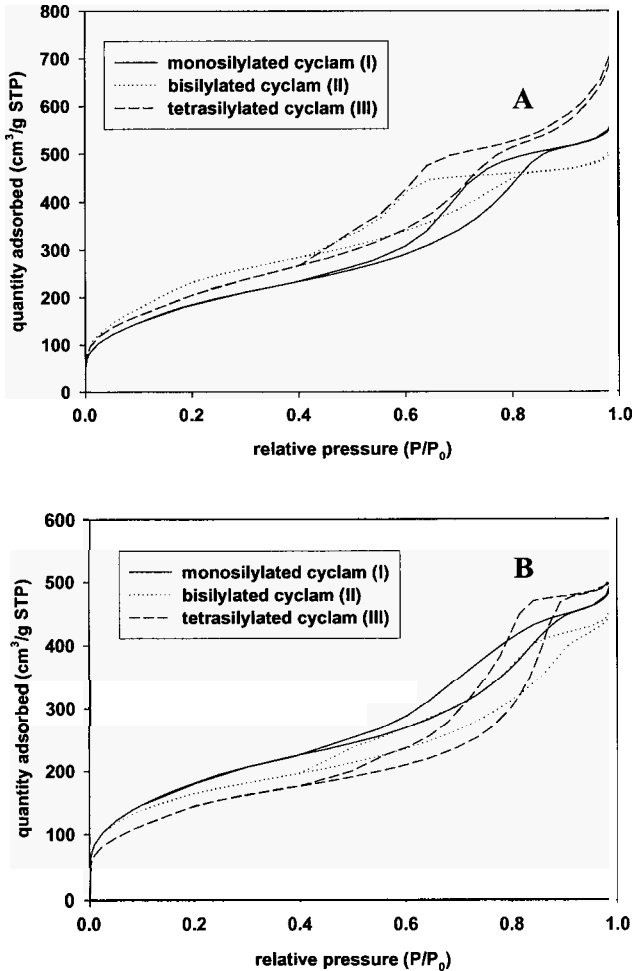


Figure 4. N_2 adsorption/desorption isotherms of (A) MCM-41 and (B) MCM-48 samples.

N_2 adsorption/desorption measurements were also performed on the as-synthesized cyclam I functionalized MCM-41 material (Figure 5). The resulting type IV isotherm indicates the exclusive presence of large mesopores which are the result of interparticles vacancies and are still observed after surfactant extraction. In this case, a surface area of $315 \text{ m}^2 \cdot \text{g}^{-1}$ and a pore volume of $0.59 \text{ cm}^3 \cdot \text{g}^{-1}$ were measured for the as-synthesized sample indicating that external porosity represents 70% of the mesoporosity. The presence of this hierarchical mesoporosity should be advantageous for diffusion of metallic species to the active complexing groups. It is also noteworthy that the presence of large mesopores which are out of the technique detection limit were also observed (N_2 adsorbed volumes rapidly increase when P/P_0 is close to 1).

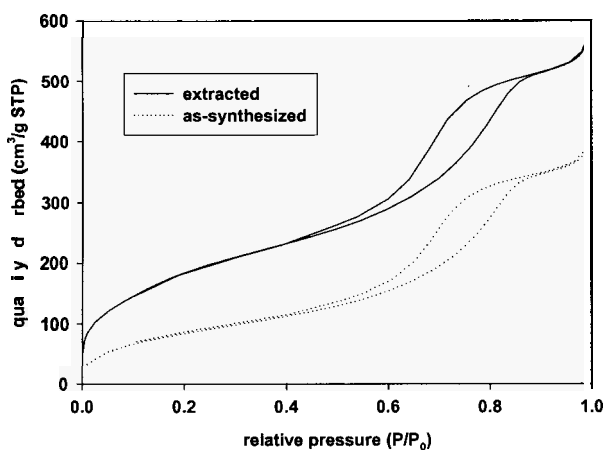


Figure 5. N_2 adsorption-desorption isotherms of extracted and as-synthesized MCM-41 sample functionalized by mono-silylated cyclam precursor.

Small mesopores seem to be incompatible with large pendant organic groups such as cyclam macrocycles within the mesopores. Cyclam macrocycles are probably located in the large mesopores and/or in the walls (in the case of cyclam groups anchored by two and four arms). These results would suggest a phase separation during the network formation leading to the internal surfactant-templated porosity and textural porosity. However, according to the low amount of organic functions, their presence is probably not sufficient to explain the textural porosity. Further characterization is under investigation to locate precisely cyclam macrocycles and explain the formation of the textural porosity.

The presence and the integrity of silylated-cyclam groups were checked for all samples by ^{13}C CP-MAS NMR experiments. ^{29}Si CP-MAS NMR experiments showed T_2 and T_3 (main component) units indicating that cyclam macrocycles were incorporated into the inorganic framework when using mono-, bi- and tetra-silylated precursors.

3.2. Stability in aqueous medium

The stability in water for a long period of time for these materials, which is a critical parameter, has also been assessed. The pH variation of neutral aqueous suspension of functionalized solids was constantly monitored as a function of time (Figure 6). An increase in the values of this parameter would reflect the degree of degradation of the material as a result of amine moieties leaching out of the solid in the external solution [8].

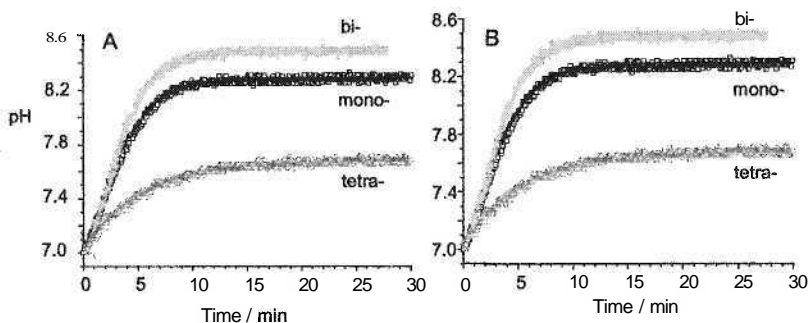


Figure 6. pH variation as function of time for silylated-cyclam functionalized (A) MCM-41 and (B) MCM-48 samples.

In both series of materials, the mesoporous silica functionalized with a mono-silylated cyclam derivative was degrading relatively fast. With material containing bi-silylated cyclam derivatives, this degradation was even more important whereas increasing the number of silylated cyclam arms to four drastically improved the overall material stability (tetra-silylated cyclam). These results were directly to be linked with the relative rigidity (i.e.: dependant to the number of silylated arms) of cyclam molecules. The very low stability observed for bi-silylated cyclam functionalized materials could be due to a closer proximity of basic groups to the silica backbone with enough mobility when macrocycles are only linked by two arms.

3.3. Accessibility experiments

For all the different materials, the proton accessibility to the cyclam sites of the different materials was estimated from the acid-base titrations and the total quantity of cyclam previously determined by elemental analyses [8].

Table 2. Quantities of cyclam determined by CHN elemental analyses and acid-base titration.

Material type		mmol/g cyclam	mmol/g reactive cyclam	% reactive cyclam
MCM-41	mono-	0.478	0.409	85.5
	bi-	0.569	0.556	97.7
	tetra-	0.542	0.343	63.2
MCM-48	mono-	0.518	0.230	44.3
	bi-	0.571	0.389	68.1
	tetra-	0.562	0.445	79.2

In the MCM-41 series, accessibility to cyclam macrocycles was improved when increasing the number of arms. This could be due to the fact that macrocycles were incorporated inside the framework and were not voluminous groups pendant to the mesopore surface. However, a lower accessibility could be observed for the tetrasilylated-cyclam functionalized materials resulting in a reduced mobility and a too close proximity of the macrocycles to the inorganic framework.

For the MCM-48 series, the results were different and showed a low accessibility for the mono-silylated cyclam functionalized material that may due to the pore network geometry. Increasing the number of arms lead to less ordered porous networks, which might have favoured the accessibility to the active sites.

4. Conclusion

Physicochemical characterizations of these cyclam derivatives functionalized M41S materials have revealed a bimodal porosity: the first one, ordered with a short diameter range resulting from the extracted surfactant arrangement and the second one, disordered with a large and broad diameter range probably resulting from inter particles vacancies. We have also evidenced structural and textural differences provoked by the number of silylated arms

depending on the starting cyclam precursors employed. Stability and accessibility experiments showed that the synthesis path for such materials has a great importance with respect to their potential use in heavy-metal remediation.

Acknowledgments

This work was funded by the ANR-05-3-41602 MESOPORELECT program and the CNRS.

References

1. P.K. Jal, S. Patel and B. K. Mishra, *Talanta* **62**, 1005 (2004)
2. (a) A. Walcarius, M. Etienne and J. Bessi re, *Chem. Mater.* **14**, 2757 (2002); (b) A. Walcarius, M. Etienne and B. Lebeau., *Chem. Mater.* **15**, 2161 (2003); (c) A. Walcarius and C. Delac te, *Chem. Mater.* **15**, 4181, (2003)
3. (a) L. Lindoy. *The Chemistry of Macrocyclic Ligand Complexes*, Cambridge University Press (1989); (b) P. Bernhardt G. A. Lawrance. *Coord. Chem. Rev.*, **104**, 297 (1990)
4. M. Etienne, B. Lebeau and A. Walcarius. *New J. Chem.* **26**, 384, (2002)
5. (a) G. Dubois, R. Corriu, C. Rey , S. Brand s, F. Denat and R. Guilard, *Chem. Commun.* 2283 (1999); (b) G. Dubois, C. Rey , R. Corriu, S. Brand s, F. Denat and R. Guilard, *Angew. Chem. Int. Ed.* **40**, 1087 (2001); (c) G. Dubois, R. Tripier, S. Brand s, F. Denat and R. Guilard, *J. Mater. Chem.* **12**, 2255 (2002)
6. S. L. Burkett, S. D. Sims and S. Mann, *Chem. Commun.* 1367 (1996)
7. M. H. Lim and A. Stein, *Chem. Mater.* **11**, 3285 (1999)
8. M. Etienne and A. Walcarius, *Talanta*, **59**, 1173 (2003)

FACILE SYNTHESIS OF FREE- STANDING PMO FILMS WITH AMORPHOUS AND CRYSTAL- LIKE WALL STRUCTURE

SUNG SOO PARK AND CHANG-SIK HA*

Department of Polymer Science and Engineering, Pusan National University, Busan 609-735, Korea

Free-standing and oriented periodic mesoporous organosilica (PMO) films with variable pore size have been synthesized at the air-water interface using cationic alkyltrimethylammonium surfactants (alkyl chain length from 12 to 18 carbon atoms; each designated as C₁₂TA, C₁₆TA, and C₁₈TA) as templates and 1,2-bis(triethoxysilyl)ethane as organosilica precursor. C₁₂TA-PMO, C₁₆TA-PMO, and C₁₈TA-PMO films have uniform thickness of ca. ~350 nm, ~670 nm, and ~400 nm, respectively. The films have highly ordered hexagonal mesostructure with amorphous pore walls. The pore diameter and the surface area of the films were 24.3 Å, 26.4 Å, and 32.8 Å and 890.3, 917.7, and 811.0 m²g⁻¹, respectively. On the other hand, the films with molecular-scale (*i.e.* 7.6 Å) periodical pore walls have been synthesized at the liquid-reaction bottle interface using cationic alkyltrimethylammonium surfactant as template and 1,2-bis(triethoxysilyl)benzene as organosilica precursor. The free-standing films have a highly ordered hexagonal mesostructure with benzene moieties inside the channel walls. The thickness of the films can be controlled 1.6 μm to 3.5 μm with the different reaction times. The pore diameter and surface area of the film were 37.6 Å and 863 m²g⁻¹, respectively.

1. Introduction

Surfactant-templated binuclear alkoxy silane precursors, (R'O)₃Si-R-Si(OR')₃, lead to a new class of nanocomposites with bridging organic groups (R) inside the channel walls, called periodic mesoporous organosilica (PMO) [1-4]. These PMO materials facilitate chemistry of the channels and provide new opportunities for controlling the chemical, physical, mechanical, and dielectric properties of the materials [5-8]. The morphology of PMO materials often controls their function and utility. Recently, mesoporous organosilica films were synthesized through a surfactant-templated self-assembly procedure using the hydrolysis and condensation of an alkoxy silane with a bridging organic group ((R'''O)₃-Si-R''-Si(OR''')₃) (R'''= -CH₃ or -C₂H₅, R''=ethane, ethylene, thiophene, and benzene) [9] or a cyclic siliquoxane precursor ([(EtO)₂SiCH₂]₃) [10]. However these mesoporous organosilica films were placed onto solid substrates such as silicon wafers or glass slides using spin- or dip-coating methods. In general, PMO samples have amorphous pore walls, which could

limit their utility. Recently, Inagaki and co-workers [3] reported a pioneering work in the PMO field, where an ordered benzene-silica hybrid PMO of a type of powder with a crystal-like wall structure was synthesized.

In this context, we synthesized the free-standing PMO films with a crystal-like wall and amorphous wall structure at the liquid-bottle interface and the air-water interface using 1,2-bis(triethoxysilyl)benzene and 1,2-bis(triethoxysilyl)ethane as organosilica precursors, respectively, and cationic alkyltrimethylammonium surfactants as templates.

2. Experimental

2.1. *Synthesis of Free-Standing PMO Films with Amorphous Pore Walls*

The synthesis of the free-standing PMO films with amorphous pore walls is achieved using the following reactant molar ratios and synthesis procedure [11]: BTSE : surfactant : NaOH : H₂O; 1.0 : 0.57 (C₁₂TABr) : 2.36 : 353 (C₁₂TA-PMO), 1.0 : 0.57 (C₁₆TABr) : 2.28 : 336 (C₁₆TA-PMO), 1.0 : 0.57 (C₁₈TABr) : 2.36 : 353 (C₁₈TA-PMO); where C₁₂TABr, C₁₆TABr, and C₁₈TABr are the cationic surfactants CH₃(CH₂)₁₁N(CH₃)₃Br, CH₃(CH₂)₁₅N(CH₃)₃Br, and CH₃(CH₂)₁₇N(CH₃)₃Br, respectively, and BTSE is the organosilica source reagent (C₂H₅O)₃SiCH₂CH₂Si(OC₂H₅)₃. Typically, we synthesized the PMO films in a 50 ml polyethylene (PE) bottle (diameter, 4.5 cm) with 1/353 scale of the reactant mole ratios. The surfactant solution is mixed with BTSE and stirred at 40 °C for 12 h and heated at 95 °C for 8 h. The free-standing PMO films grown at the air-liquid interface were rinsed with distilled water and dried at 80 °C in air. The surfactant in the PMO films was removed by a solvent extraction process with 150 ml EtOH including 3 ml of 35 wt % HCl at 60 °C for 12 h, and dried at 80 °C for 12 h.

2.2. *Synthesis of Free-Standing PMO Films with Crystal-Like Pore Walls*

The free-standing and benzene-bridged PMO (benzene-PMO) films with crystal-like pore walls were prepared with a procedure similar to that of PMO film grown at the air-water interface [12]. The synthesis of the films is achieved with 1.0:0.57:2.36:353 BTEB/C₁₈TABr/NaOH/H₂O, where C₁₈TABr is the cationic surfactant CH₃(CH₂)₁₇N(CH₃)₃Br and BTEB is the organosilica source (C₂H₅O)₃SiC₆H₄Si(OC₂H₅)₃. Films with a thickness of 1.6 μm to 3.5 μm and a width of ca. 2.5 cm have been grown at the liquid-polyethylene (PE) bottle interface, while the reactant solution is heated to 95 °C from 2 h to 24 h under static conditions.

3. Results and discussion

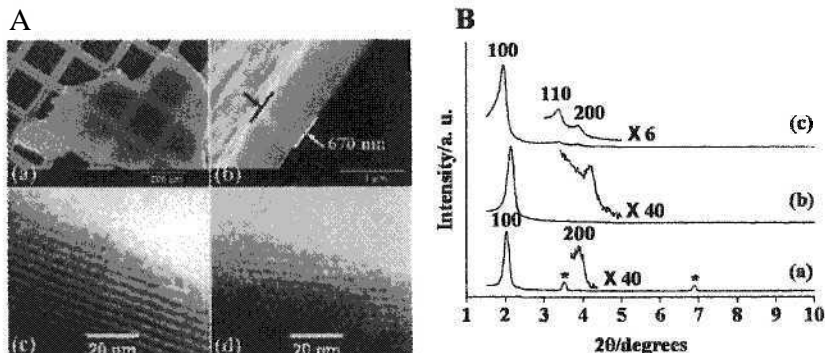


Figure 1. **A**, SEM images ((a) and (b)) and TEM images ((c) and (d)) of as-synthesized free-standing C₁₆TA-PMO film; SEM images of (a) C₁₆TA-PMO film transferred from the air-water interface onto a copper grid, (b) highly magnified edge of the film. TEM images showing (c) a highly ordered periodic structure consistent with a hexagonal close-packed arrangement of channels running parallel to the surface of the film and (d) hexagonal basal plane with a well-ordered hexagonal array. **B**, XRD patterns of (a) as-synthesized free-standing C₁₆TA-PMO film transferred from air-water interface onto a glass substrate, (b) calcined C₁₆TA-PMO film at 400 °C for 2 h in N₂, and (c) powdered and surfactant-extracted C₁₆TA-PMO film, respectively.

Scanning electron microscopy (SEM) (Philips XL30 S FEG (Netherlands) with an acceleration voltage of 15 kV) image of the C₁₆TA-PMO film that has been transferred onto a copper grid revealed that it is continuous, as shown in Figure 1A(a). The size of the PMO film that is formed at the air-water interface is dependent on the breadth of the reaction bottle. The C₁₆TA-PMO film has a uniform thickness of ca. ~670 nm, as shown in Figure 1A(b). The free-standing C₁₂TA- and C₁₈TA-PMO films can be also synthesized at the air-water interface with a procedure similar to that of the C₁₆TA-PMO film. The C₁₂TA- and C₁₈TA-PMO films have uniform thicknesses of ca. ~350 nm and ~400 nm, respectively.

The TEM (JEOL JEM-2010 microscope operating at 200 kV) images of C₁₆TA-PMO film showed that the film has a highly ordered periodic structure with a hexagonal close-packed arrangement of channels running parallel to the surface of the film, as shown in Figure 1A(c). This implies growth of the channels in an orientation parallel to the air-water interface. The periodicity with a hexagonal close-packed arrangement of one-dimensional channels viewed orthogonally to the film surface was observed with the microtomed section cut, as shown in Figure 1A(d). The C₁₂TA- and C₁₈TA-PMO films also have highly ordered hexagonal mesostructures with channels running parallel to the surface of the films.

Figure 1B(a) shows the X-ray diffraction (XRD) (Rigaku Miniflex diffractometer with Cu K_{α} radiation (40 kV, 30 mA)) patterns for the as-synthesized free-standing C_{16} TA-PMO film. The film reveals (100) and (200) reflections, consistent with the TEM observation that the channels run parallel to the surfactant overlayer at the air-water interface, as shown in Figure 1A(c) and (d), respectively. The d -spacing obtained from the (100) reflection of the as-synthesized C_{16} TA-PMO film is 43.7 Å. The d -spacing increases with longer alkyl chains in the structure-directing agent. The as-synthesized C_{12} TA-, C_{16} TA-, and C_{18} TA-PMO films have d -spacings of 40.1 Å, 43.7 Å, and 47.7 Å, as obtained from the (100) reflection, respectively. Two starred peaks in Figure 1B(a) are due to extra surfactants. These peaks nearly disappeared after calcination at 400 °C for 2 h in N_2 without cracking or loss of mesostructure, which is consistent with the XRD results in Figure 1B(b) and the TEM images of the calcined PMO film (not shown here). On calcination of the PMO films, the intensities of the (100) and (200) reflection peaks are increased and the anticipated contractions of the hexagonal ab -unit cell are observed, due to the removal of the surfactant template from the channels, which is concomitant with the condensation of the silanol (SiOH) groups in the channel walls [9(b), 13]. The calcined C_{12} TA-, C_{16} TA-, and C_{18} TA-PMO films have d -spacings of 39.1 Å, 41.3 Å, and 46.5 Å, as obtained from the (100) reflection, respectively. The XRD pattern of powdered and surfactant-extracted C_{16} TA-PMO film showed the expected (100, 110, 200) reflections typically observed in powder PMO materials [14] (Figure 1B(c)). The pore diameter and the surface area of the surfactant-extracted C_{16} TA-PMO film, obtained from the N_2 sorption isotherms (Micromeritics ASAP2010 instrument) were determined to be 26.4 Å and 917.7 m^2g^{-1} , respectively. The pore diameter and the surface area of the surfactant-extracted C_{12} TA- and C_{18} TA-PMO films were 24.3 Å, 32.8 Å and 890.3, 811.0 m^2g^{-1} , respectively, as shown in Table 1. The pore diameter and the surface area of the surfactant-extracted C_{16} TA-PMO film were 26.4 Å and 917.7 m^2g^{-1} , respectively. In Table 1, other textural data such as unit cell parameter, total pore volume, and wall thickness were also summarized for all the surfactant-extracted PMO films investigated in this work.

The Si-C bonding in the framework of the PMO film was confirmed by ^{29}Si and ^{13}C CP MAS NMR (Bruker DSX400 spectrometer) experiments (not shown here). The ^{29}Si MAS NMR spectrum of the as-synthesized PMO film shows two peaks at -61.2 ppm ($T^2 C(OH)Si(OSi)_2$) and -69.3 ppm ($T^3 CSi(OSi)_3$) [1(a), (b)]. The ^{13}C CP MAS NMR spectrum exhibits a peak at 6.3 ppm, which is attributed to carbons covalently linked to Si (Si- CH_2 - CH_2 -Si) [1(a), (b)]. After surfactant-extraction and calcination, it was confirmed by NMR experiments that

the organic-inorganic moiety (-Si-CH₂-CH₂-Si-) is the basic structural unit in the film.

Table 1. The unit cell parameter (a_0), surface area (S_{BET}), total pore volume (V_t), wall thickness (W) and pore diameter (D_{BJH}) of surfactant-extracted PMO films.

Sample name	a_0 (Å)	S_{BET} (m ² g ⁻¹)	V_t (cm ³ g ⁻¹)	W (Å)	D_{BJH} (Å)
C ₁₂ TA-PMO	48.0	890	0.62	23.7	24.3
C ₁₆ TA-PMO	52.2	918	0.77	25.8	26.4
C ₁₈ TA-PMO	56.9	811	0.78	24.1	32.8
Benzene-PMO	52.3	863	1.15	14.7	37.6

XRD unit cell parameter (a_0) is equal to $2d_{100}/\sqrt{3}$; S_{BET} is the apparent BET specific surface area obtained by analysis of N₂ adsorption isotherm; V_t is the total pore volume; W is the wall thickness ($W=a_0-D_{\text{BJH}}$); D_{BJH} is the pore diameter.

Yang *et al.* [13] reported that the formation of a mesoporous silica film involves collective interactions between silicate building-blocks, micellar solution species and a surfactant ‘hemi-micellar’ overstructure localized at the air-water interface. The PMO film growth is probably regulated by matching charge and geometry between micellar aggregates and organosilica precursors at a surfactant structured air-water interface, as suggested in case of silica films.

On the other hand, the films with molecular-scale (*i.e.* 7.6 Å) periodical pore walls have been synthesized at the liquid-reaction bottle interface using cationic alkyltrimethylammonium surfactant as template and 1,2-bis(triethoxysilyl)benzene as organosilica precursor. Films with a thickness of 1.6 μm to 3.5 μm and a width of ca. 2.5 cm have been grown at the liquid-polyethylene (PE) bottle interface, while the reactant solution is heated to 95 °C from 2 h to 24 h under static conditions.

As-synthesized and free-standing benzene-PMO film was lifted onto transmission electron microscopy (TEM) grids and directly viewed. The periodicity of the hexagonal closed-packed arrangement of one-dimensional channels viewed orthogonally to the flat surface of the film was observed from the microtomed section cut orthogonally to the film surface, as shown in Figure 2A(a). The TEM image of the film showed also that the films have a highly ordered periodic structure with a hexagonal closed-packed arrangement of channels running parallel to the flat external surface of the film, as shown in Figure 2A(b). A highly magnified TEM image reveals many lattice fringes-stacked along the channel axes, with a uniform spacing of 7.6 Å on the pore walls over the whole region [3], as shown in Figure 2A(b). After extraction of

surfactant, the pore diameter and surface area of the film obtained from an N_2 sorption isotherm were determined to be 37.6 Å and $863 \text{ m}^2\text{g}^{-1}$, respectively, as shown in Table 1.

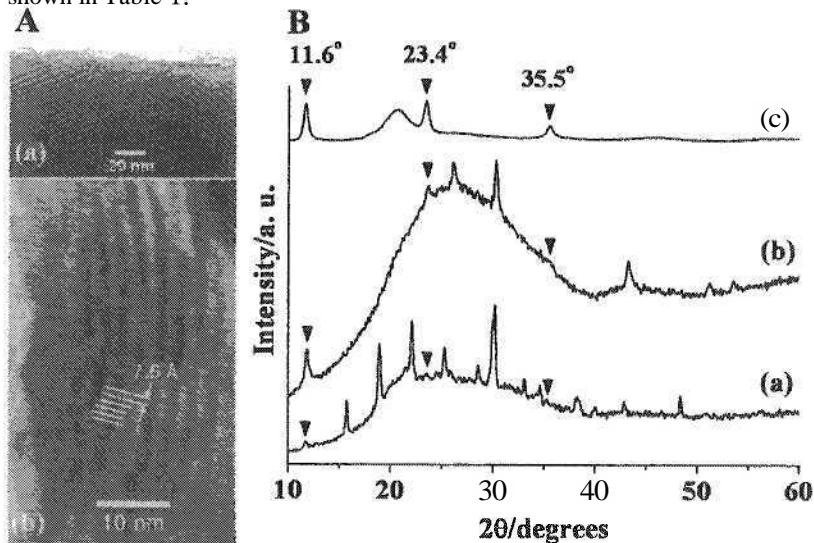


Figure 2. A, TEM images of as-synthesized and free-standing benzene-PMO film obtained with the microtomed section cut orthogonally to the film surface, showing (a) highly ordered mesoporous channels consistent with a hexagonal close-packed arrangement and (b) many lattice fringes with a spacing of 7.6 Å in the pore walls with [100] incidence perpendicular to the channels. B, XRD patterns of (a) as-synthesized and free-standing benzene-PMO film, (b) benzene-PMO film calcined at 400 °C for 2 h in N_2 , (c) powdered and surfactant-extracted benzene-PMO film.

The XRD patterns of the as-synthesized and calcined free-standing films lifted onto a glass slide substrate showed that they both reveal (100) and (200) reflections (not shown here), although the calcined free-standing film has a broad (200) reflection at $2\theta=4.5^\circ$, consistent with the TEM observation that the channels run parallel to the flat external surface of the film. The as-synthesized benzene-PMO film has a d -spacing of 44.8 Å from the (100) reflection. On calcination of the film, the anticipated contraction ($\Delta d_{100}=6.2$ Å) of the hexagonal ab -unit cell is observed due to the removal of the surfactant template from the channels and is concomitant with the condensation of silanol (SiOH) groups in the channel walls [9(b), 13]. The XRD patterns at $2\theta=10\text{--}60^\circ$ of as-synthesized and calcined benzene-PMO films display three peaks at $2\theta=11.6^\circ$, 23.4° , and 35.5° with the peaks due to extra surfactant, as shown in Figure 2B(a) and 2B(b). These diffraction peaks can be explained by a periodic structure with a spacing

of 7.6 Å [3]. This XRD result can not be expected from the wall of the benzene-bridged channel running parallel to the flat external surface of the film and the alternating arrangement of benzene layers and silicate layers along the direction of the channel. During the hydrothermal reaction for the formation of the benzene-PMO film, the precipitates were also formed on the bottom of the reaction bottle. Therefore, the appearance of these diffraction peaks (*i.e.* three peaks at $2\theta = 11.6^\circ$, 23.4° , and 35.5°) can be due to the small particles adhered to the surface of the film in a gradient. After extraction of surfactant, the XRD pattern of powdered PMO film showed the expected (100), (110), and (200) reflections in typical powder PMO material at $2\theta = 1.2\text{--}10^\circ$ (not shown here) with the three peaks to indicate molecular-scale periodicity in the pore walls as shown in Figure 2B(c) [3].

^{29}Si MAS NMR spectrum of the as-synthesized benzene-PMO film showed three peaks at -63.7 , -72.1 , and -80.6 ppm, which can be assigned to $\text{T}^1 \text{C}(\text{OH})_2\text{Si}(\text{OSi})$, $\text{T}^2 \text{C}(\text{OH})\text{Si}(\text{OSi})_2$, and $\text{T}^3 \text{CSi}(\text{OSi})_3$ (not shown here) [3]. The ^{13}C CP MAS NMR spectroscopy of the as-synthesized benzene-PMO film exhibits a peak at 134.0 ppm, which is attributed to carbons covalently linked to Si ($\text{Si-C}_6\text{H}_4\text{-Si}$) (not shown here) [3]. After surfactant-extraction and calcination, it was confirmed by NMR experiments that the organic-inorganic moiety ($\text{-Si-C}_6\text{H}_4\text{-Si-}$) is the basic structural unit in the film.

With the results described above, the mechanism for the formation of the free-standing and benzene-bridged PMO film with a crystal-like wall structure can be explained. Benzene groups are somewhat hydrophobic. Therefore, co-assembled surfactant/benzene-bridged organosilica species may interact with the hydrophobic surface of the polyethylene bottle when it is used as the reaction bottle to form a benzene-PMO film. Film growth is probably regulated by matching charge and geometry between micellar aggregates and benzene-bridged organosilica species. Finally, the free-standing and oriented benzene-bridged periodic mesoporous organosilica film has been grown at the liquid-reaction bottle interface, while mesoporous channels were formed parallel to the flat external surface of the film.

We performed thermogravimetric analysis (TGA) under nitrogen atmosphere to investigate the thermal stability of the PMO films after extraction of the surfactant (Figure 3). The TGA analysis of the ethane moieties containing PMO film exhibited its first weight loss below 100°C as a consequence of the desorption of physisorbed water [15].

The next decrease in the sample weight occurred at temperatures between $210\text{--}740^\circ\text{C}$; this weight loss corresponds to the loss of ethane fragments in the walls of the pores [15]. During this process, water molecules may also form

through the condensation of Si-OH groups in the pore walls. On the other hand, for the benzene-containing PMO film, decomposition of the benzene fragments in the pore wall gradually occurred over the temperature ranges from 510 to 900 °C [3]. The TGA analysis shows that the thermal stability of the benzene-containing PMO film was better than that of the ethane-containing PMO film.

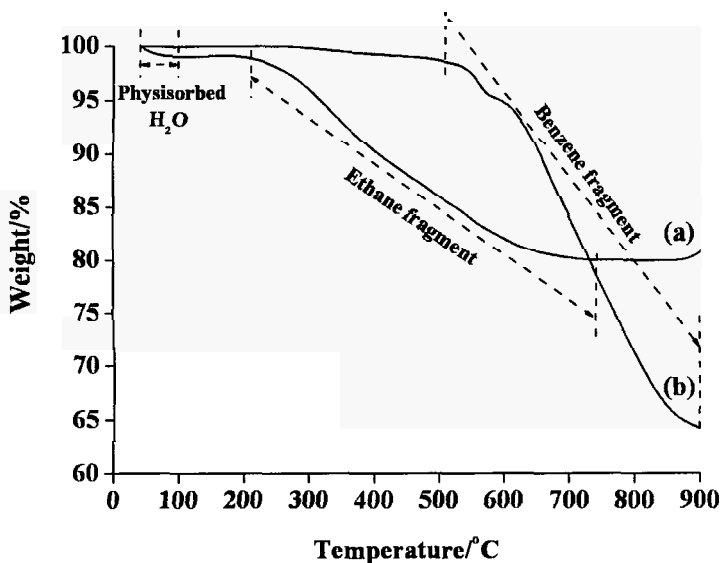


Figure 3. TGA curves of the surfactant-extracted (a) ethane and (b) benzene moieties containing PMO films in nitrogen atmosphere.

4. Conclusions

In conclusion, free-standing and oriented PMO films with amorphous and crystal-like wall structure were successfully synthesized at the air-water interface or the liquid-reaction bottle interface using cationic alkyltrimethylammonium surfactants (alkyl chain length from 12 to 18 carbon atoms) as the structure-directing agents and 1,2-bis(triethoxysilyl)ethane or 1,2-bis(triethoxysilyl)benzene as the organosilica precursors. The films have a hexagonal mesostructure, with the organic moieties inside the channel wall. Based on the thermogravimetric analysis, the thermal stability of the benzene-containing PMO film was better than that of the ethane-containing PMO film. The PMO films may have potential use in applications such as catalysis, sensing, separation, opto-electronics and so on.

Acknowledgments

This work was supported by Korea Science and Engineering Foundation (KOSEF) through the National Research Laboratory Program funded by the Ministry of Science and Technology (MOST; No.M10300000369-06J0000-36910), the SRC/ERC program of MOST/KOSEF (Grant #R11-2000-070-080020), and the Brain Korea 21 Project.

References

1. (a) S. Inagaki, S. Guan, Y. Fukushima, T. Ohsuna and O. Terasaki, *J. Am. Chem. Soc.* **121**, 9611 (1999). (b) B. J. Melde, B. T. Holland, C. F. Blanford and A. Stein, *Chem. Mater.* **11**, 3302 (1999). (c) T. Asefa, M. J. MacLachlan, N. Coombs and G. A. Ozin, *Nature* **402**, 867 (1999).
2. (a) A. Stein, B. J. Melde and R. C. Schrodin, *Adv. Mater.* **12**, 1403 (2000). (b) T. Asefa, G. A. Ozin, H. Grondey, M. Kruk and M. Jaromic, *Stud. Surf. Sci. Catal.* **141**, 1 (2002).
3. S. Inagaki, S. Guan, T. Ohsuna and O. Terasaki, *Nature* **416**, 304 (2002).
4. (a) W. Guo, J. Y. Park, M. O. Oh, H. W. Jeong, W. J. Cho, I. Kim and C. S. Ha, *Chem. Mater.* **15**, 2295 (2003). (b) W. Guo, I. Kim and C. S. Ha, *Chem. Commun.* 2692 (2003).
5. A. Fukuoka, Y. Sakamoto, S. Guan, S. Inagaki, N. Sugimoto, Y. Fukushima, K. Hirahara, S. Iijima and M. Ichikawa, *J. Am. Chem. Soc.* **123**, 3373 (2001).
6. M. C. Burleigh, S. Dai, E. W. Hagaman and J. S. Lin, *Chem. Mater.* **13**, 2537 (2001).
7. Q. Yang, M. P. Kapoor and S. Inagaki, *J. Am. Chem. Soc.* **124**, 9694 (2002).
8. (a) K. Yamamoto, Y. Nohara and T. Tatsumi, *Chem. Lett.* 648 (2001). (b) M. P. Kapoor, A. Bhaumik, S. Inagaki, K. Kuraoka and T. Yazawa, *J. Mater. Chem.* **12**, 3078 (2002). (c) A. Bhaumik, M. P. Kapoor and S. Inagaki, *Chem. Commun.* 470 (2003).
9. (a) Y. Lu, H. Fan, N. Doke, D. A. Loy, R. A. Assink, D. A. LaVan and C. J. Brinker, *J. Am. Chem. Soc.* **122**, 5258 (2000). (b) Ö. Dag, C. Yoshina-Ishii, T. Asefa, M. J. MacLachlan, H. Grondey, N. Coombs and G. A. Ozin, *Adv. Funct. Mater.* **11**, 213 (2001).
10. K. Landskron, B. D. Hatton, D. D. Perovic and G. A. Ozin, *Science* **302**, 266 (2003).
11. (a) S. S. Park and C.-S. Ha, *Chem. Commun.* 1986 (2004). (b) S. S. Park and C.-S. Ha, *Chem. Mater.* **17**, 3519 (2005).
12. S. S. Park, D. H. Park and C.-S. Ha, *Chem. Mater.* **19**, 2709 (2007).
13. H. Yang, N. Coombs, I. Sokolov and G. A. Ozine, *Nature* **381**, 589 (1996).

14. S. S. Park, C. H. Lee, J. H. Cheon and D. H. Park, *J. Mater. Chem.* **11**, 3397 (2001).
15. S. Guan, S. Inagaki, T. Ohsuna, O. Terasaki, *Micropor. Mesopor. Mater.* **44-45**, 165 (2001).

SYNTHESIS AND CHARACTERIZATION OF PERIODIC MESOPOROUS ORGANOSILICAS WITH DISULFIDE AND MERCAPTOPROPYL GROUPS

BOGNA E. GRABICKA, RAFAL M. GRUDZIEN, IAN P. BLITZ[†]
MIETEK JARONIEC*

Department of Chemistry, Kent State University, Kent, OH 44242, USA

Synthesis and characterization of channel-like bifunctional periodic mesoporous silicas (PMOs) with disulfide bridging groups and mercaptopropyl surface ligands is reported. These PMOs were prepared by co-condensation of bis(triethoxysilylpropyl)disulfide and (3-mercaptopropyl)trimethoxysilane in the presence of poly(ethylene oxide)-poly(propylene oxide)-poly(ethylene oxide) triblock copolymer Pluronic P123 (EO₂₀PO₇₀EO₂₀) as template. A series of PMOs with increasing amounts of incorporated disulfide bridging groups and mercaptopropyl surface ligands was studied by X-Ray powder diffraction, nitrogen adsorption, thermogravimetry and elemental analysis.

1. Introduction

Periodic mesoporous organosilicas (PMOs) [1-3] have attracted a lot of worldwide attention because of the easiness of altering their chemical and physical properties by introduction of various organic spacers into their frameworks. PMOs can be obtained in the presence of different organic templates including ionic surfactants [1-3], oligomeric surfactants [4] and nonionic block copolymers [5-7] by a self-assembly of bis-, tris- or tetra-(alkoxysilyl) bridged precursors. In contrast to pure mesoporous silicas [8,9], PMOs [1-3] are usually characterized by a homogeneous distribution of functional groups within the framework, a tunable ratio of hydrophobicity to hydrophilicity, and better hydrothermal stability [10]. From the adsorption point of view, PMOs also possess high BET surface area, high pore volume, and large pore diameters, which make them attractive materials for catalysis, bioseparations, chromatography, nanocasting, host-guest chemistry and so forth [11,12]. So far many PMOs with various morphologies and porous structures

* Corresponding author: Mietek Jaroniec - Tel: 1-330-672 3790, Fax: 1-330-672 3816, Email: jaroniec@kent.edu

[†] Undergraduate student from Beloit College, Beloit, WI 53511, USA; summer 2007.

have been synthesized using a variety of small aliphatic/aromatic organic groups such as ethane, ethylene, phenylene, thiophene, bipyridine, biphenylene, teraazacyclotetradecane, benzene ring linked to three silicon atoms and heterocyclic isocyanurate ring (see ref. [13-17], reviews [18-19] and references therein).

Recently, numerous attempts have been made to incorporate larger bridging groups such as thioether functionality into the silica framework [20-22] by co-condensation of (1,4)-bis(triethoxysilyl)propane)tetrasulfide and tetraethyl orthosilicate (TEOS) in the presence of cetyltrimethylammonium bromide ($C_{16}H_{33}N(CH_3)_3^+Br^-$) [20,21] and poly(ethylene oxide)-poly(propylene oxide)-poly(ethylene oxide) triblock copolymer Pluronic P123 ($EO_{20}PO_{70}EO_{20}$) [22] as templates under basic and acidic conditions, respectively. These attempts stimulated others [23] to fabricate bifunctional PMOs containing thioether and isocyanurate bridging groups. Introduction of such bulky bridging group may lead to small mesopores and may cause the deterioration of porous structure, which makes additional post-synthesis modifications more difficult.

Typically, bifunctionalization [16,17,23] of mesoporous silicas is performed to achieve desired surface properties of the resulting materials without significant changes in their adsorption characteristics and structural ordering. For instance, this strategy allows one to design bifunctional PMOs [16,17,23], which exhibit high affinity towards targeted species such as heavy metal ions, toxic volatile organic compounds, carbon dioxide, nitrogen and sulfur oxides, making them highly attractive adsorbents for removal of the aforementioned pollutants (see review [24]).

Recently, we synthesized PMOs using bis(triethoxysilylpropyl)disulfide instead of bis(triethoxysilylpropyl)tetrasulfide along with TEOS to design the organosiliceous frameworks analogous to the SBA-15, SBA-16 and FDU-1 mesostructures [25,26]. It is noteworthy that SBA-15 [9] exhibits (*P6mm*) hexagonally ordered cylindrical mesopores interconnected by complementary smaller pores.

Herein, we report the synthesis and characterization of bifunctional PMOs with disulfide bridging groups and mercaptopropyl surface ligands by co-condensation of bis(triethoxysilylpropyl)disulfide and 3-mercaptopropyl-trimethoxysilane and TEOS in the presence of poly(ethylene oxide)-poly(propylene oxide)-poly(ethylene oxide) triblock copolymer Pluronic P123 ($EO_{20}PO_{70}EO_{20}$) under acidic conditions. These PMOs were characterized by X-Ray powder diffraction, nitrogen adsorption, thermogravimetry and elemental analysis

may lead to pore blocking of the silica template due to accelerated carbon deposition, thus preventing further carbon deposition into the interior of the silica spheres. As a result, hollow spheres are obtained for the rapidly heated sample after HF treatment to remove the silica template. On the other hand, no pore blocking occurred under the slower heating ramp rate of 10 °C/min and therefore carbon deposition could proceed largely unhindered allowing deposition of carbon into the interior of the silica template and thus the formation of solid-core carbon spheres once the silica template was removed by HF treatment.

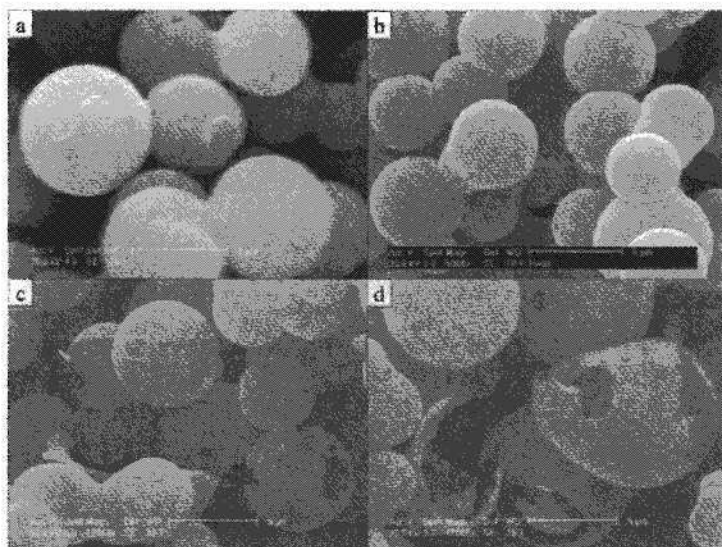


Figure 4. Representative SEM images of (a) SBA-15 solid spheres, and carbon materials prepared via CVD at 1000 °C at various heating ramp rates using the SBA-15 spheres as templates and acetonitrile as carbon precursor: (b) 10 °C/min (CSP-M) and (c, d) 20 °C/min (CSP-F).

The XRD patterns of carbon materials prepared via CVD at 1000 °C at a heating ramp rate of 10 or 20 °C/min are shown in Figure 5. The low angle region of the XRD patterns was featureless, so only the wide angle XRD region is shown. The absence of low angle XRD peaks indicates that the carbon materials have a low level of mesostructural ordering. The presence of the high angle peaks at 2θ of 26° and 43°, which are the (002) and (101) diffraction peaks from graphitic carbon, indicate that the carbon materials possess a significant

DS- x SH- y , where DS and SH stand for disulfide and mercaptopropyl groups, where x and y refer to their molar percentage, respectively.

Table 1. Molar composition and elemental analysis data for the PMOs studied.^a

Sample	Synthesis gel composition				Elemental analysis	
	n_{TEOS} mmol	n_{DS} mmol	n_{SH} mmol	S %	C* mmol/g	S %
DS10-SH10	30.72	1.92	3.84	8.73	2.05	5.77
DS10-SH20	26.88	1.92	7.68	12.00	3.12	9.24
DS20-SH10	26.88	3.84	3.84	12.02	2.51	9.57
DS20-SH20	23.04	3.84	7.68	14.78	3.47	10.19

^a n_{TEOS} , number of mmoles of TEOS; n_{DS} , number of mmoles of DS; n_{SH} , number of mmoles of SH; C*, total concentration of groups containing sulfur atoms evaluated from S% in the synthesis gel mixture; C, total concentration of groups containing sulfur atoms calculated on the basis of S% obtained by elemental analysis; S%, sulfur percentage.

2.3. Measurements

Nitrogen adsorption measurements were carried out using ASAP 2010 volumetric analyzers manufactured by Micromeritics, Inc. (Norcross, GA). Prior to each measurement all bifunctional organosilicas were outgassed under vacuum in the port of the adsorption instrument for at least 2 hours at 110 °C until the pressure dropped to less than 6 μmHg . Adsorption isotherms were measured at -196 °C over the interval of relative pressures from 10^{-6} to 0.995 using ultra high purity nitrogen from Praxair Distribution Company (Danbury, CT, USA). The Brunauer-Emmett-Teller (BET) surface area [27] was calculated using adsorption data at the 0.05-0.2 p/p_0 range. The single-point total pore volume was estimated at $p/p_0 = 0.99$ [28]. The pore size distribution was evaluated using the Kruk-Jaroniec-Sayari (KJS) method [29], which employs the Barrett-Joyner-Halenda (BJH) algorithm [30] but with the statistical film thickness curve and a Kelvin-type relation calibrated for a series of MCM-41 samples. The mesopore diameter, w_{KJS} , was obtained at the peak maximum of the PSD curve.

Quantitative estimation of total concentration of both disulfide and mercaptopropyl groups was performed using CHNS elemental analysis. Sulfur content for all organosilicas was determined using a LECO model CHNS-932 elemental analyzer from St. Joseph, MI.

Thermogravimetric measurements were performed under flowing nitrogen on a TA Instruments Inc. (New Castle, DE, USA) model TGA 2950 high-resolution thermogravimetric analyzer. The thermogravimetric weight change

(TG) curves were recorded over a temperature range from 35 to 800 °C. The instrument was equipped with an open platinum pan and an automatically programmed temperature controller. The high-resolution mode was used to record the TG data. The heating rate was adjusted automatically during measurements to achieve the best resolution; its maximum value was 10 °C min⁻¹.

3. Results and Discussion

Powder X-ray diffraction (XRD) was used to monitor the structural changes upon increasing concentrations of organic DS and SH groups in the bifunctional PMOs (see Panels A and B in Figure 1). As can be seen from these panels the XRD profiles recorded for the template-free DS10-SH10 and DS20-SH10 PMOs reveal low-angle peaks at $2\theta = 1.21$ and 1.45° that correspond to the d -spacing values of 7.36 and 6.11 nm, respectively. An additional introduction of 10% of mercaptopropyl ligands into the framework (adding up 20% of SH) resulted in poorly resolved broad peaks located at 1.45 and $1.44^\circ 2\theta$, which correspond to the d -spacing values of 6.11 and 6.12 nm for DS10-SH20 and DS20-SH20, respectively. Nevertheless, the appearance of one reflection on the XRD spectra for the PMOs studied indicates a deterioration of mesostructural ordering with increasing concentration of mercaptopropyl surface groups.

Nitrogen adsorption isotherms measured at -196 °C were used to further elucidate the mesostructural changes that occurred upon gradual introduction of both DS and SH groups. Adsorption parameters such as the BET specific surface area, the volume of complementary pores, the total pore volume and the KJS (Kruk-Jaroniec-Sayari) mesopore diameter for the PMOs under study are summarized in Table 2. As can be seen from Panel C of Figure 1, the adsorption isotherm for the DS10-SH10 sample (i.e., sample with 10% of disulfide and 10% of mercaptopropyl groups) exhibits a type IV isotherm with sharp capillary condensation/evaporation steps and a pronounced H1 hysteresis loop, which is characteristic for mesoporous materials such as SBA-15. The corresponding pore size distribution (PSD) shown in Panel E of Figure 1 has a maximum at 4.96 nm. However, an increase in the concentration of SH caused a dramatic change in the isotherm from type IV to type I with H4 hysteresis loop indicating a microporous character of the DS10-SH20 sample; this is confirmed by the lack of a distinct hysteresis loop, which is characteristic for mesopores, i.e., pores between 2 and 50 nm. Furthermore, in comparison to DS10-SH10, the PSD curve for DS10-SH20 (Panel E in Figure 1) consists of one peak located at 2.3 nm with a little shoulder originated from a small fraction of mesopores. It seems

that the ordering of mesopores in organosilicas with bulky bridging groups diminishes rapidly with increasing amount of surface ligands.

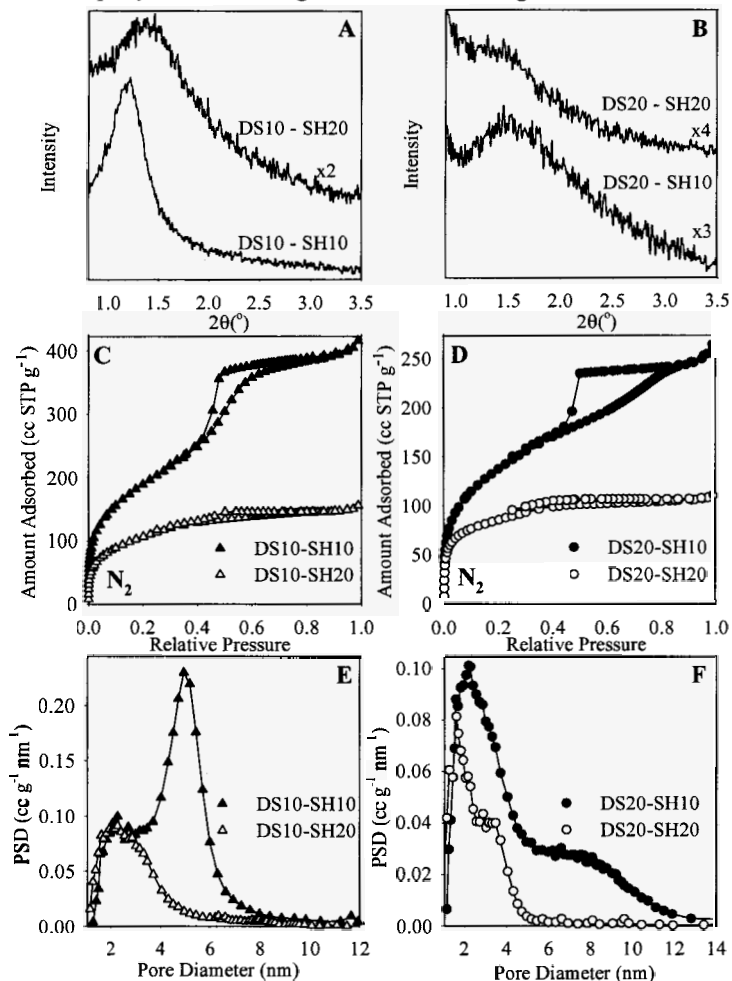


Figure 1. Powder X-ray diffraction (Panels A and B), nitrogen adsorption isotherms measured at -196 °C (Panels B and C) and the corresponding pore size distributions (PSDs) (Panels E and F) calculated according to the improved KJS method [30] for the extracted bifunctional PMOs with disulfide bridging and mercaptopropyl surface groups.

In the case of DS20-SH10 PMO (Panel D), having 20% of disulfide and 10% of mercaptopropyl groups, the adsorption branch exhibits a broad capillary

condensation step and the hysteresis loop resembling H2 type, which suggests the presence of pore constrictions. As can be seen from Panel F, the PSD curve for DS20-SH10 displays a narrow peak in the range from 1 to 5 nm and a wide shoulder between 6 and 12 nm. Contrary to DS10-SH10, the DS20-SH10 sample synthesized by doubling the concentration of disulfide bridging groups features a dramatic increase in the formation of micropores (see PSDs in Panels E and F), which is evidenced by an intensive peak in the micropore range. A further increase of the SH loading (DS20-SH20) leads to an isotherm that approaches type I characteristic for microporous materials. The PSD plot for DS20-SH20 shows a significant decrease in the mesopore diameter and the total pore volume.

Both samples DS10-SH10 and DS20-SH10, containing 10% of SH groups, possessed the BET surface areas equal to 700 and 506 m²/g, respectively, which after a further addition of 10% of SH groups decreased to 392 and 305 m²/g, respectively. In addition, the total pore volume was also reduced from 0.67 (DS10-SH10) to 0.26 (DS10-SH20) cc/g and from 0.42 (DS20-SH10) to 0.18 (DS20-SH20) cc/g, respectively (see Table 2).

Table 2. Adsorption, structural properties and TG weight loss data for the PMOs studied.^a

Sample	S _{BET} m ² /g	V _t cc/g	w _{KJS} nm	d nm	TG %
DS10-SH10	700	0.67	5.0	7.36	30.1
DS10-SH20	392	0.26	2.3	6.11	33.2
DS20-SH10	506	0.42	7.6	6.11	34.4
DS20-SH20	305	0.18	3.1	6.12	36.9

^aS_{BET}, BET specific surface area; V_t, single-point pore volume; w_{KJS}, mesopore diameter calculated by the improved KJS method [30] using BBJ algorithm [29]; d, interplanar spacing obtained on the basis of the XRD patterns; TG, thermogravimetric weight loss recorded in flowing nitrogen in the range between 100 and 800 °C.

The as-synthesized (template-containing) and extracted (template-free) PMOs were also analyzed by high-resolution thermogravimetry analysis conducted under flowing nitrogen from room temperature to 800 °C. Figure 2 shows the thermogravimetric weight change (TG) curves and the differential TG curves, known as the DTG curves. As can be seen from this figure, all TG curves (Panels A and B) for as-synthesized and extracted PMOs exhibit a small weight loss in the temperature range from 35 to 150 °C that reflects the thermodesorption of physisorbed water and ethanol. Moreover, all TG spectra for these PMOs show one major weight loss at 350 °C and a second one at around 480 °C indicating high thermal stability of these materials. For as-synthesized PMOs the first weight loss corresponds to the thermal decomposition of polymer template followed by the degradation of

mercaptopropyl and disulfide groups. Extraction caused a significant decrease in the weight loss from 65.08 to 30.15% and from 64.39 to 33.79 % for the DS10-SH10 and DS10-SH20 samples, respectively. Similarly, the weight losses for the DS20-SH10 and DS20-SH20 samples due to the solvent extraction changed from 65.65 to 34.33 and from 63.86 to 36.9 %, respectively. Thus, for the as-synthesized PMO samples over 30% of the total weight loss corresponds to the polymeric template.

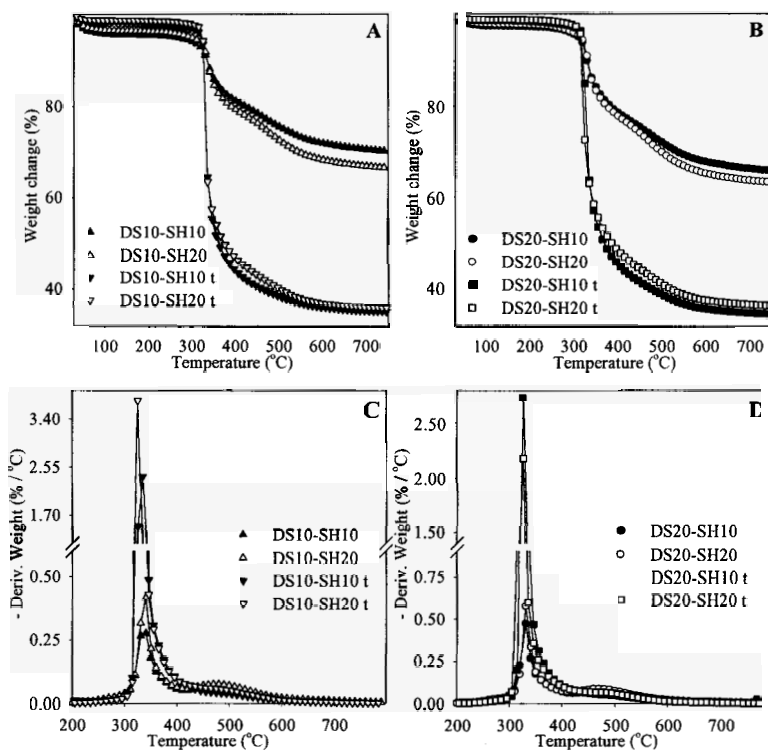


Figure 2. Thermogravimetric weight change (TG) curves (Panels A and B) and the corresponding differential TG (DTG) curves (Panels C and D) recorded in flowing nitrogen for the extracted and as-synthesized bifunctional PMOs with disulfide bridging groups and mercaptopropyl surface ligands; t in the sample codes refers to the as-synthesized PMOs.

4. Conclusions

A series of disulfide-bridged periodic mesoporous organosilicas with 10 % and 20% of mercaptopropyl surface groups were synthesized by co-condensation of

bis(triethoxysilylpropyl)disulfide and (3-mercaptopropyl)trimethoxysilane in the presence of Pluronic P123 as a structure directing agent. The resulting bifunctional PMOs with 10% of mercaptopropyl groups exhibited ordered porous structure with high surface area and large pore diameters; this ordering was dramatically reduced with increasing SH loading (see PMOs with 20% of SH). Also, the basic adsorption parameters such as the BET surface area, the pore volume and the pore size decreased with increasing SH loading. It is noteworthy that the disulfide-bridged PMOs with mercaptopropyl surface groups can be attractive adsorbents for mercury ions due to the high affinity of these ligands to mercury.

Acknowledgements

This material is based upon work supported by the National Science Foundation under Grants No. CTS-0553014 and REU CHE-0649017. The authors thank BASF Corporation for providing Pluronic P123 block copolymer.

References

1. S. Inagaki, S. Guan, Y. Fukushima, T. Ohsuna and O. Teresaki, *J. Am. Chem. Soc.* **121**, 9611 (1999).
2. B.J. Melde, B.T. Holland, C.F. Blandford and A. Stein, *Chem. Mater.* **11**, 3302 (1999).
3. T. Asefa, M. J. MacLachlan, N. Coombos and G.A. Ozin, *Nature* **402**, 867 (1999).
4. O. Dag and G.A. Ozin, *Adv. Mater.* **13**, 1182 (2001).
5. J.R. Matos, M. Kruk, L.P. Mercuri, M. Jaroniec, T. Asefa, N. Coombos, G. A. Ozin and O. Teresaki, *Chem. Mater.* **14**, 1903 (2002).
6. X. Y. Bao, X. S. Zhao, X. Li, P.A. Chia and J. Li, *J. Phys. Chem. B* **108**, 4684 (2004).
7. X. Y. Bao and X. S. Zhao, *J. Phys. Chem. B* **109**, 10727 (2005).
8. J.S. Beck, J.C. Vartuli, W.J. Roth, M.E. Leonowicz, C.T. Kresge, K.D. Schmitt, C.T.-W. Chu, D.H. Olson, E.W. Sheppard, S.B. McCullen, J.B. Higgins and J.L. Schlenker, *J. Am. Chem. Soc.* **114**, 10834 (1992).
9. D. Zhao, Q. Huo, J. Feng, B.F. Chmelka and G.D. Stucky, *J. Am. Chem. Soc.* **120**, 6024 (1998).
10. A. Stein, B.J. Melde and R.C. Schroden, *Adv. Mater.* **12**, 1403 (2000).
11. A. Sayari, and S. Hamoudi, *Chem. Mater.* **13**, 3151 (2001).
12. A.Taguchi, and F. Schuth, *Microporous Mesoporous Mater.* **77**, 1 (2005).
13. O. Olkhovik and M. Jaroniec, *J. Am. Chem. Soc.* **127**, 60 (2005).
14. O. Olkhovik, S. Pikus and M. Jaroniec, *J. Mater. Chem.* **15**, 1517 (2005).

15. R.M. Grudzien, S. Pikus and M. Jaroniec, *J. Phys. Chem. B* **110**, 2972 (2006).
16. R. M. Grudzien, B. E. Grabicka, S. Pikus and M. Jaroniec, *Chem. Mater.* **18**, 1722 (2006).
17. W.-H. Zhang, X. Zhang, Z. Hua, P. Harish, F. Schroeder, S. Hermes, T. Cadenbach, J. Shi and R.A. Fischer, *Chem. Mater.* **19**, 2663 (2007).
18. F. Hoffmann, M. Cornelius, J. Morell and M. Froba, *J. Nanosci. Nanotechnol.* **6**, 265 (2006).
19. B. Hatton, K. Landskron, W. Whitnall, D. Perovic and G.A. Ozin, *Acc. Chem. Res.* **38**, 305 (2005).
20. L. Zhang, W. Zhang, J. Shi, Z. Hua, Y. Li and J. Yan, *Chem. Commun.* 210 (2003).
21. J. Liu, J. Yang, Q. Yang, G. Wang and Y. Li, *Adv. Functional Mater.* **15**, 1297 (2005).
22. J. Liu, Q. Yang, L. Zhang, D. Jiang, X. Shi, J. Yang, H. Zhong and C. Li, *Adv. Functional Mater.* **17**, 569 (2007).
23. O. Olkhovyk and M. Jaroniec, *Ind. Eng. Chem. Res.* **46**, 1745 (2007).
24. O. Olkhovyk and M. Jaroniec, in: "Environmental Applications of Nanomaterials" (G. F. Fryxell and G. Cao, eds), Imperial College Press, London, 2007, pp. 179-212.
25. R.M. Grudzien, B. E. Grabicka, D. J. Knobloch and M. Jaroniec, *Adsorption* **12**, 293 (2006).
26. R.M. Grudzien, B.E. Grabicka, D.J. Knobloch and M. Jaroniec, *Stud. Surface Sci. Catal.* **165**, 443 (2007).
27. M. Jaroniec and L. A. Solovyov, *Langmuir* **22**, 6757 (2006)
28. E. P. Barrett, L. G. Joyner and P. P. Halenda, *J. Am. Chem. Soc.* **73**, 373 (1951).
29. S. Brunauer, P. H. Emmet and E. Teller, *J. Am. Chem. Soc.* **60**, 309 (1938).
30. K. S. W. Sing, D. H. Everett, R. A. W. Haul, L. Moscou, R. A. Pierotti, J. Rouquerol and T. Siemieniewska, *Pure. Appl. Chem.* **57**, 603 (1985).

TEXTURAL INVESTIGATIONS OF HIGHLY PROTON CONDUCTIVE FUNCTIONALIZED MESOPOROUS SiO_2

ROLAND MARSCHALL, MICHAEL WARK

Institute of Physical Chemistry and Electrochemistry, Gottfried Wilhelm Leibniz University Hannover, Callinstr. 3A, D-30167 Hannover, Germany

JIRÍ RATHOUSKÝ

J. Heyrovský Institute of Physical Chemistry of ASCR, v.v.i., Dolejškova 3, 18223 Prague 8, Czech Republic

MICHAELA WILHELM

Ceramic Materials und Components, University of Bremen, Am Biologischen Garten 2 / IW3, D-28359 Bremen, Germany

Mesoporous Si-MCM-41 materials modified with sulfonic acid groups were synthesized by fast co-condensation method with facile one-step template removal and thiol to sulfonic acid oxidation by microwave irradiation. Nitrogen and water vapor adsorption measurements were carried out to study the porous structure and the hydrophilic properties of the materials. The impedance spectroscopy measurements exhibited very high proton conductivities for the functionalized materials, which is highly promising for the application as solid state proton conductors. The proton conductivity increased continuously with temperature up to 0.2 S/cm.

1. Introduction

Since their discovery in 1992 [1], the ordered mesoporous materials (especially Si-MCM-41) have been in the center of attention in the research of porous materials and host guest chemistry. Their highly ordered structures, large surface areas and pore volumes make them highly promising for sensing, separation, catalysis and nanotechnology [2]. The easy and variable surface functionalization substantially enhances the attractiveness of these materials [3]. For example, by surface functionalization with sulfonic acid groups ($-\text{SO}_3\text{H}$), mesoporous silicas are becoming suitable in acid heterogeneous catalysis [4]. Recently, several publications dealing with reactions catalyzed with $-\text{SO}_3\text{H}$ functionalized mesoporous silica were published underlining the high topicality of the research topic [5-9]. However, these hybrid systems should also show excellent proton conductivities. Kaliaguine et al. showed already in 2002 that -

SO₃H functionalized non-specified mesoporous silicas have solid proton conductor properties [10]. As we recently demonstrated, Si-MCM-41 is more suitable than Si-SBA-15 and Si-SBA-16 for proton conduction in -SO₃H functionalized mesoporous materials, because in the narrower channels protons can hop more easily between SO₃⁻-groups located on opposite channels walls. For post-synthetically grafted samples the proton conductivity reaches 10⁻³ S/cm depending on temperature, relative humidity (RH) and pore geometry [11]. They show these high proton conductivities even at high temperatures up to 140 °C, what makes them suitable candidates as additives applied in membranes for high temperature polymer electrolyte membrane fuel cells (HT-PEMFC). Such HT-PEMFCs, operating at about 140 – 180 °C, are highly favorable as the cooling of the fuel cell system is simplified and the tolerance towards CO is increased, which leads to a more efficient fuel cell arrangement. The functionalized mesoporous additives are advantageous because, due to their hydrophilicity, they can provide additional water molecules, which facilitate the proton transport even at temperatures above 100 °C. However, due to the pore blocking effects by grafting reactions, the concentration of -SO₃H groups in Si-MCM-41 is limited to about 1 mmol/g Si-MCM-41[11].

Here we show that by simple co-condensation reaction of 3-mercaptopropyl trimethoxysilane (MPMS) with sodium metasilicate (NaSiO₃) and fast microwave oxidation of thiol (-SH) groups (with simultaneous template removal) -SO₃H loading of the mesoporous silica can be drastically increased and consequently the proton conductivity raises by two orders of magnitude up to 0.2 S/cm [12]. The pore filling with propyl chains bearing the -SO₃H groups is increased in such large extent (up to 2.3 mmol/g Si-MCM-41) that more than one -SO₃H group is present per nm² of the inner surface. Nitrogen and water adsorption isotherms of functionalized mesoporous silica with different organic moieties provide a deeper insight into the pore geometry and hydrophilicity of the system, because water has still a big influence on the proton conductivity in solid electrolyte systems [10,11].

2. Experimental

2.1. *Synthesis of functionalized mesoporous silicas*

Thiol-functionalized Si-MCM-41 was synthesized following the homogeneous precipitation procedure published in Ref. [13], however, a certain percentage (20, 30, 40 mol. %) of the silica source sodium metasilicate (NaSiO₃, Aldrich) was replaced by 3-mercaptopropyltrimethoxysilane (MPMS, Merck). In a typical

synthesis, 2.61 g of cetyltrimethylammonium bromide (CTAB, Aldrich) was dissolved in 400 mL of deionized water at 30 °C. After the complete dissolution of the surfactant, sodium metasilicate and MPMS were added under stirring. The molar ratio of the individual components of the reaction mixture was 1 (CTAB) : 3103 (H₂O) : 3.05-x (Na silicate) : x (MPMS) with x equaling either 0, 0.61, 0.92 or 1.22, respectively. Finally, 4 mL of ethyl acetate were added under vigorous stirring, whose hydrolysis to acetic acid ensures highly homogeneous acidification of the reaction mixture and consequently a uniform hydrolysis-condensation reaction of the metasilicate and MPMS. After 15 s, the stirring was stopped and the solution was kept still for 24 h at room temperature in a closed PE bottle. The final pH was around 10 for a typical synthesis. Hydrothermal treatment was carried out for additional 24 h at 100 °C. The white precipitate was recovered by filtration and washed with ethanol and water. Samples were dried at room temperature overnight. The same preparation route has also been used for chloro-functionalized silica using chloropropyl triethoxysilane as functionalization agent.

Microwave treatment for template removal and simultaneous thiol oxidation was carried out using an Ethos 1 microwave system (MLS) in Teflon reaction vessels, which are transparent for the microwave radiation. 0.1 g of the as-synthesized powder was suspended in a mixture of HNO₃ (65 %, Roth) and H₂O₂ (30 %, Roth). The mixture was treated by continuous microwave irradiation (max. 600 W) for up to 5 minutes at 200 °C, the maximum internal pressure being 20 bar.

The samples prepared using 20 and 40 mol. % of MPMS are designated as 20 and 40% SO₃H-MCM-41, respectively.

2.2. Characterization

Nitrogen adsorption-desorption experiments at the boiling point of nitrogen (ca -196 °C) were carried out with a Micromeritics ASAP 2010 apparatus. Prior to each adsorption measurement, samples were outgassed at 150 °C overnight. Water vapor adsorption-desorption isotherms were obtained by volumetric BELSORP 18-3 apparatus (Bel Japan, Inc.) at 22 °C with an equilibration time of 500 s.

Transmission electron microscopy (TEM) was performed at 200 kV using a field-emission Jeol JEM-2100F instrument with an ultra-high resolution pole piece (CS = 0.5 mm) that provides a point-resolution better than 0.19 nm. Moreover, the microscope was equipped with an Gatan GIF 2001 energy filter

with a 1k-CCD camera. Specimens were prepared by dispersing the samples in ethanol and fixating them on a carbon film, which is supported on a copper grid.

Proton conductivity was measured by impedance spectroscopy (IS) using a Zahner electrochemical workstation IM6e in a frequency range from 1 - 10⁶ Hz with an oscillating voltage of 100 mV. Prior to the measurement, the functionalized powders were pressed with 50 kN into small pellets 8 mm in diameter and 0.5-1 mm in thickness, which were inserted between two thin graphite slices (8 mm in diameter). Afterwards they were put into a PTFE specimen holder, which was located in a gas-tight stainless steel body with thermocouple access to the holder. This body was connected via a stainless steel tube to a stainless steel water reservoir. Relative humidity (RH) in the cell was controlled by adjusting the temperature of the water tank. The specific conductivity was calculated according to the formula $\sigma = (1/R)(L/A)$, where R is the resistance corresponding to the phase angle closest to zero in the Bode diagram, L the thickness of the sample between the electrodes, and A the cross-sectional contact area of the electrodes. This analysis procedure is typically used to interpret proton conductivities in powders or membranes¹⁰.

The ion exchange capacity was determined by titration. A small amount of functionalized powder was suspended in a 0.01 M sodium hydroxide solution for 48 hours, the remaining sodium hydroxide being titrated with hydrochloric acid.

3. Results and Discussion

In order to get a detailed information about both the porous structure and the chemical nature of the pore surface of the different as-synthesized and functionalized hybrid materials, two radically different adsorptives have been chosen, namely nitrogen and water vapor.

Figure 1 shows the adsorption isotherms of nitrogen at -196 °C on three different samples prepared by co-condensation as well as on the pristine Si-MCM-41. The Si-MCM-41 synthesized by the homogeneous precipitation route without adding MPMS exhibits the typical steep increase in the adsorption at the relative pressure P/P_0 of 0.27-0.34, which is due to the reversible capillary condensation within the Si-MCM-41 mesopores 2.7 nm in diameter. The broad hysteresis at P/P_0 from 0.5 to 1 is due to the presence of some imperfections and cracks within the particles of this material. The BET surface area, pore volume and pore size of the Si-MCM-41 achieve 1030 m²/g, 0.954 cm³/g and 2.7 nm, respectively.

Adding additional agents in the reaction mixture has a strong influence on the structure of the materials and their texture properties, because the micelles

formed by CTAB expand and incorporate the additional silanes. The BET surface area, pore volume and diameter of 20% Cl-MCM-41 and 20% SO₃H-MCM-41 equal 594 and 625 m²/g, 0.752 and 0.692 cm³/g and > 6 nm (for both), respectively. By increasing the amount of substitution, the change in the texture is becoming even more drastic. For the 40% SO₃H-MCM-41 sample the nitrogen isotherm is of type I, and the BET-equation is not applicable, which indicates a microporous nature of this sample. The loading of the materials with organic moieties is so much increased that the mesopores are narrowed and transformed to micropores and small mesopores of about 1.5 nm in size (the assessment based on the Langmuir surface area and the total pore volume). The successful functionalization is proven by IR measurement shown elsewhere [12].

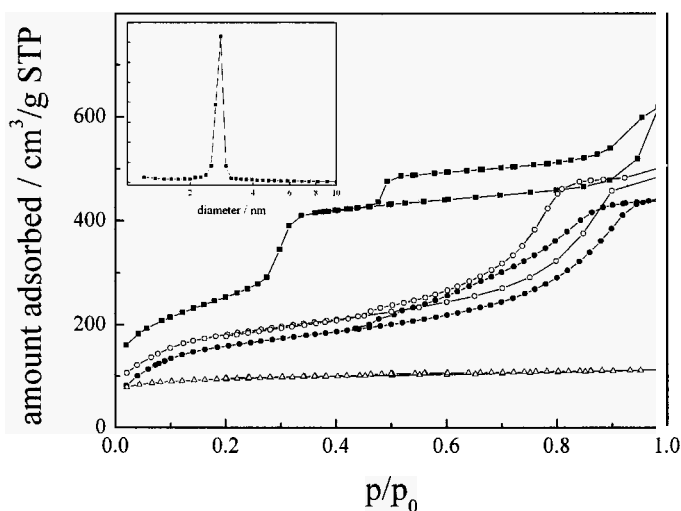


Figure 1. Nitrogen adsorption isotherms for pristine Si-MCM-41 (□), 20% SO₃H-MCM-41 (○), 20% Cl-MCM-41 (●) and 40% SO₃H-MCM-41 (Δ), after microwave template removal; inset: pore size distribution of pristine material.

However, as seen in Fig. 2, even the 40% sample exhibits the hexagonal pore arrangement characteristic for the pore structure of Si-MCM-41. This is also proved by XRD measurements after calcination, where the typical Si-MCM-41 pore geometry is recovered [12].

Figure 3 depicts schematically the situation inside a pore of the 40% SO₃H-MCM-41. The high loading of the pores leads to narrowed pore diameter. According to the ionic exchange capacity (IEC) of SO₃H-functionalized materials, the co-condensation results in a loading of 1.6 mmol/g for 20%

samples and 2.3 mmol/g for the 40% $\text{SO}_3\text{H-MCM-41}$, respectively [12], whereas the grafting route results only in loadings of about 1 mmol/g [11].

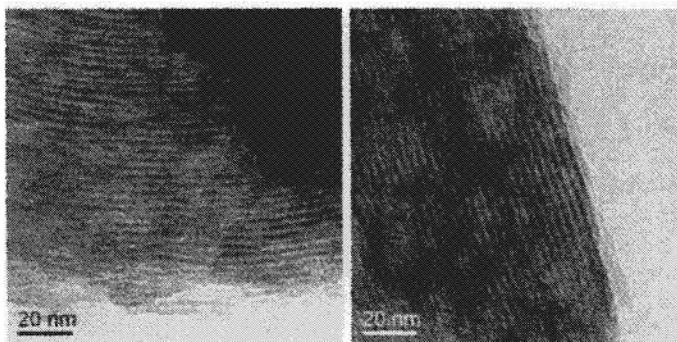


Figure 2. TEM images of 40% $\text{SO}_3\text{H-MCM-41}$ after microwave treatment.

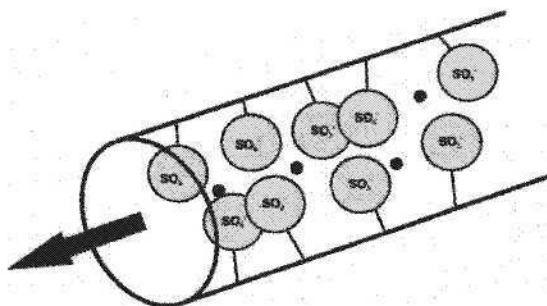


Figure 3. Situation inside the pores of Si-MCM-41 after functionalization. The arrow illustrates that the protons are transported predominantly along the channel axis.

For a better understanding of the chemical nature of the surface of the pore walls of functionalized Si-MCM-41, adsorption isotherms of water vapor have been measured. Fig. 4 shows the adsorption isotherms of water vapor on inorganic particles at 22°C in the relative pressure range of p/p_0 of 0.0 - 0.98.

The isotherms on the pristine Si-MCM-41 and grafted 20% $\text{SO}_3\text{H-MCM-41}$ are of type V [14], the pore filling and emptying occurring within a narrow range of relative pressure at ca 0.4 and 0.5, respectively. This values of relative pressure correspond to the pore diameters of about 2-3 nm as calculated from the Kelvin's equation [15]. The small shift in the location of sharp step in both

adsorption and desorption isotherms to towards lower relative pressures is due to a slight narrowing of the pore width caused by the grafting [16,17].

However, the isotherms of co-condensated materials are drastically changed. The isotherm on the 20% SO_3H -MCM-41 shows a higher adsorption at low relative pressures of 0-0.4, which indicates stronger interactions of water vapor molecules with the surface and corresponds to the hydrophilic nature of the surface of this sample. The broad and relative flat hysteresis loop is caused by the broad distribution of the pore width and some pore blocking effects, which may be due to the so called ink-bottle shaped pores.

In contrast, the 20% Cl-MCM-41 sample shows a very small water uptake, which somehow increases only at relative pressures above 0.6. While the surface of pristine Si-MCM-41 is typically quite hydrophilic due to the presence of a large number of surface silanol groups, these groups are removed by the functionalization and replaced by hydrophobic moieties, namely propyl chains

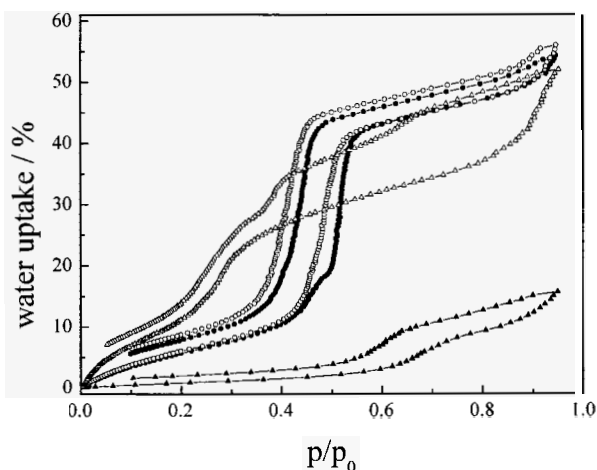


Figure 4. Water adsorption isotherms of Si-MCM-41 (\bullet), SO_3H -MCM-41 (20 mmol grafting¹¹, \circ), 20% Cl-MCM-41 (\blacktriangle), 20% SO_3H -MCM-41 (Δ).

with headgroups such as chlorine. This replacement of course renders surface hydrophobic [18,19]. Additionally, the pores are becoming narrower by surface functionalization leading to the same effect. Therefore, the Cl-MCM-41 sample has such a low water uptake compared to all other samples.

The comparison of water vapor isotherms on SO_3H - and Cl- functionalized samples clearly shows that the strong hydrophilicity of the sulfonic acid groups is able to overcome the hydrophobicity of the linking propyl chains and renders

the surface even more hydrophilic than that of the pristine Si-MCM-41. The water uptake for the SO_3H -functionalized Si-MCM-41 at the limiting relative pressure of 0.98 is about 55 wt.-%, which is 3.7 times more than on the Cl-MCM-41 functionalization with chloropropyl chains. Further it should be stressed that even at relative pressure as low as 0.1 the water vapor uptake achieves about 5 wt.-% for the 20% SO_3H -MCM-41. This is the special advantage of the co-condensation material.

Figure 5 shows proton conductivities for all samples measured under 100 % relative humidity (RH) are continuously increasing with temperature. Proton conductivity in the presence of water is due to the so-called Grotthus-mechanism [20]. In this mechanism, the proton transport is mainly caused by the hopping of the protons from one water molecule to another. To a smaller extent, also the diffusion of H_3O^+ ions enhances the proton transport.

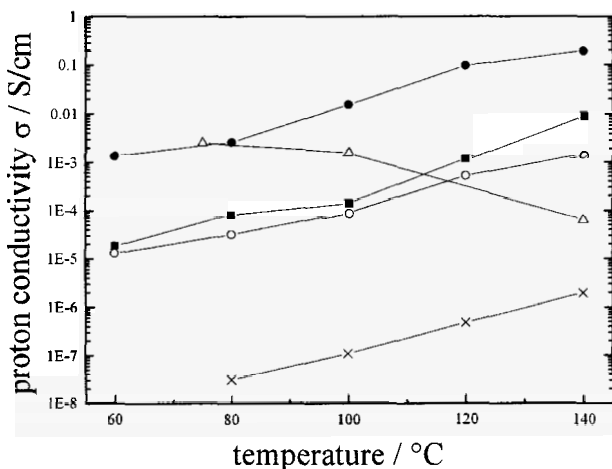


Figure 5. Proton conductivities under 100 % RH of Si-MCM-41 (x), 20 mmol SO_3H -MCM-41 (grafting, o), 20% SO_3H -MCM-41 (l), 40% SO_3H -MCM-41 (●) and Nafion® under the same conditions (Δ).

The increase in temperature strongly affects both mechanisms, hopping as well as diffusion become faster. Furthermore, because the anchoring propyl chains rotate and vibrate more easily, the $-\text{SO}_3\text{H}$ groups at the end of the chains can easier contact each other, which facilitates the direct proton transport. The pristine Si-MCM-41 alone shows only a negligible proton conductivity of about 10^{-6} S/cm, which results from a partial dissociation of water molecules in the

presence of silanol groups leading to an increased charge carrier concentration close to the inner surface [10].

Confirming the IEC results, the proton conductivities of co-condensed samples increase drastically with increased loading. The co-condensed powders have much higher values than the grafted ones: the 40% SO₃H-MCM-41 exhibits proton conductivity of even up to 0.2 S/cm. Although the IEC value of the grafted 20 mmol sample is significantly lower than that of the 20% co-condensed sample, the proton conductivities differ only slightly. This can be explained by the narrower pores in the grafted sample which facilitates proton hopping between SO₃⁻ groups bound on opposite pore walls. Such effect has also been found on SO₃H-grafted Si-MCM-41 and Si-SBA-15 samples [11]. It is remarkable that in contrast to Nafion[®] foils, for which the proton conductivity decreases drastically above 100 °C due to water loss [17,21], water seems to be kept inside the channels. This is in accordance with the water adsorption measurements. In addition, the channel geometry of the pores, in which the sulfonic acid groups are fixed, does not only help to keep water but also supports the guidance of the protons through the tested pellets (see Figures 2 and 3).

4. Conclusion

To sum up, a simple and fast method for the preparation of SO₃H functionalized Si-MCM-41 samples by the co-condensation synthesis and microwave treatment for an effective template removal with the simultaneous SH- to SO₃H-group oxidation has been presented. Pellets pressed from the synthesized powders showed very high proton conductivities of up to 0.2 S/cm at 100 % RH. Whereas for other kinds of proton conducting membranes, e.g. Nafion[®], the proton conductivity decreases drastically with temperature, the proton conductivity of these materials increases continuously with temperature. The high loading with SO₃H groups rendering the materials to be highly hydrophilic and being easily achieved by the co-condensation synthesis has turned out to be a crucial advantage.

Acknowledgments

This work was supported by the Deutsche Forschungsgemeinschaft (DFG) (CA 147/13-1, SPP1181). The authors thank Inga Bannat (Institute of Physical Chemistry, Leibniz University Hannover) for TEM measurements. Roland Marschall gratefully acknowledges a Georg-Christoph-Lichtenberg scholarship by the Ministry of Science and Culture of the German State of Lower Saxony.

References

1. C. T. Kresge, M. E. Leonowicz, W. J. Roth, J. C. Vartuli, J. S. Beck, *Nature* **359**, 710 (1992).
2. A. Vinu, K. Z. Hossain, K. Ariga, *J. Nanosci. Nanotech* **5**, 347 (2005).
3. F. Hoffmann, M. Cornelius, J. Morell, M. Fröba, *Angew. Chem. Int. Ed* **45**, 3216 (2006).
4. J. A. Melero, R. van Grieken, G. Morales, *Chem. Rev.* **106**, 3790 (2006).
5. I.K. Mbaraka, B.H. Shanks, *J. Catal.* **229**, 365(2005).
6. K.I. Shimizu, E. Hayashi, T. Hatamachi, T. Kodama, T. Higuchi, A. Satsuma, Y. Kitayama, *J. Catal.* **231**, 131 (2005) 131.
7. B. Sow, S. Hamoudi, M. H. Zahedi-Niaki, S. Kaliaguine, *Microporous Mesoporous Mater.* **79**, 129 (2005).
8. I. K. Mbaraka, K. J. McGuire, B. H. Shanks, *Ind. Eng. Chem. Res.* **45** 3022 (2006).
9. S. S. Reddy, B. D. Raju, V. S. Kumar, A.H. Padmasri, S. Narayanan, K.S. Rama Rao, *Catal. Commun.* **8**, 261 (2007).
10. S. Mikhailenko, D. Desplantier-Giscard, C. Danumah, S. Kaliaguine, *Microporous Mesoporous Mater.* **52**, 29 (2002).
11. R. Marschall, I. Bannat, J. Caro, M. Wark, *Microporous Mesoporous Mater.* **99**, 190 (2007).
12. R. Marschall, J. Rathousky, M. Wark, *Chem. Mater.* (2007), in press.
13. J. Rathousky, M. Zukalova, A. Zukal, J. Had, *Collect. Czech. Chem. Comm.* **63**, 1893 (1998).
14. K. S. W. Sing, D. H. Everett, R. A. W. Haul, L. Moscou, R. A. Pierotti, J. Rouquerol, T. Siemieniewska, *Pure Appl. Chem.*, **57**, 603 (1985).
15. S. Komarneni, R. Pidugu, V. C. Menon, *J. Porous Mater.*, **2**, 99 (1996).
16. S. J. Gregg and K. S. W. Sing, Adsorption, *Surface Area, and Porosity*, Academic Press, Inc., London, (1982)
17. R. Marschall, M. Wark, M. Jeske, M. Wilhelm, G. Grathwohl, J. Caro, *Stud. Surf. Sci. Catal.* **170, Part B**, 1540 (2007).
18. T. Kimura, S. Saeiki, Y. Sugahara, K. Kuroda, O. Langmuir, **15**, 2794(1999).
19. K. Kosuge, T. Murakami, N. Kikukawa, and M. Takemori, *Chem. Mater.*, **15**, 3184 (2003).
20. C.J.D. van Grothuis, *Ann. Chim.* **58**, 54 (1806).
21. M. Hogarth, X. Glipa, *ETSU Technical Report F/02/00189/REP* (2001).

MESOPOROUS CERIA BY STRUCTURE REPLICATION FROM VARIOUS POROUS MATRICES

JAN ROGGENBUCK, MICHAEL TIEMANN

*Institute of Inorganic and Analytical Chemistry, Justus Liebig University,
Heinrich-Buff-Ring 58, D-35392 Giessen, Germany*

Mesoporous ceria was synthesized by using both CMK-3 carbon and SBA-15 silica as structure matrices. All products exhibit uniform mesopores with diameters of 5-6 nm in a two-dimensional periodic arrangement in addition to varying amounts of interparticle porosity. The gas sensing properties (methane detection) of ordered mesoporous ceria was compared to a non-porous sample.

1. Introduction

Crystalline ceria-based materials are interesting due to their unique properties in a wide field of applications such as high temperature ceramics, catalysis [1,2], gas-sensing [3,4], or solid oxide fuel cells [5].

The conventional method of utilizing self-assembled, supramolecular aggregates of organic amphiphiles as structure directors in aqueous media are naturally limited to low synthesis temperatures, resulting in porous materials which are often amorphous on the atomic length scale. Thermal treatment, necessary for the generation of crystallinity, often causes a loss of structural order and reduces the surface area [6,7].

The structure replication concept which employs rigid, porous matrices is an efficient technique to overcome these problems [8,9]. An advantage of the replication method is the possibility of creation of novel nanostructures by using various mesoporous silicas and carbons as hard templates. Recently mesoporous silica [10-12] as well as carbon materials [13] have successfully been used for the synthesis of mesoporous ceria.

Here we present a comparative study of syntheses using both mesoporous CMK-3 carbon and mesoporous SBA-15 silica as structure matrices; both these templates are hexagonally ordered mesostructures (p6m symmetry group). CMK-3 is an inverse replica of SBA-15, which consists of hexagonally ordered channels interconnected with complimentary fine pores [14]. The products exhibit ordered mesopores with crystalline pore walls and show superior properties in methane gas sensing as compared to non-porous samples.

2. Experimental

2.1. *Synthesis of the Structure Matrices*

SBA-15 silica was synthesized in a modification of a literature procedure [15]. 12.0 g of P-123 block copolymer (Sigma) were dissolved in a mixture of 360 g deionized water and 43.0 g of HCl (32 %). After addition of 24.0 g of tetraethyl orthosilicate (TEOS; Merck) the mixture was stirred at 308 K for 24 h. The resulting gel was transferred to a Teflon-lined autoclave and kept at 353 K (for small mesopores and thick walls) and 413 K (for large mesopores and thin walls) respectively for 24 h. The resulting solid products were filtered off, washed with deionized water, and calcined under air atmosphere at 823 K for 6 h (heating rate 2 K min⁻¹). CMK-3 carbon was prepared according to a literature procedure [16].

2.2. *Synthesis of Mesoporous CeO₂ by Structure Replication*

Mesoporous ceria was prepared by incipient wetness impregnation of the respective mesoporous matrix, SBA-15 silica or CMK-3 carbon.

In case of SBA-15 silica 2 mL of a saturated aqueous solution of Ce(NO₃)₃ were added to 1 g SBA-15 and the resulting mixture was kneaded for three minutes. After drying at ambient temperature the sample was heated under air atmosphere to 573 K at a constant rate of 2.5 K min⁻¹ and kept at that temperature for 2 hours to convert cerium nitrate to cerium oxide. This procedure was repeated twice. The silica matrix was removed by repeated stirring in 50 mL aqueous NaOH solution (2 mol L⁻¹) at ambient temperature. A light yellow material was recovered by centrifugation and dried at 330 K.

Alternatively, mesoporous ceria was prepared using CMK-3 carbon as the structure matrix. 2 mL of a saturated aqueous solution of Ce(NO₃)₃ were added to 1 g CMK-3 and the resulting mixture was kneaded for three minutes. After drying at ambient temperature the sample was heated under air atmosphere to 473 K at a constant rate of 2.5 K min⁻¹ and kept at that temperature for 2 hours to decompose the nitrate. This procedure was repeated once. The carbon was removed by heating the sample under air atmosphere to 673 K at a constant rate of 2 K min⁻¹ and keeping the sample at that temperature for 2 hours.

2.3. *Characterization*

Powder X-ray diffraction (XRD) was carried out on a PANalytical X'Pert Pro system equipped with a high-speed X'Celerator detector (Cu K α radiation,

40 kV, 40 mA). N₂ physisorption was conducted at 77 K on a Quantachrome Autosorb 6; samples were degassed at 393 K for 24 hours prior to measurement. For data processing the Quantachrome Autosorb software comprising the NLDFT kernel "N₂ silica at 77 K, cylindrical pore model" was used. The specific surface area was calculated from the adsorption data in the relative pressure interval from 0.05 to 0.2 using the BET method. Transmission electron microscopy (TEM) and selected-area electron diffraction (SAED) was performed on a Philips CM30-ST microscope; for energy-dispersive X-ray (EDX) analysis an EDAX PV 9900 was used.

2.4. Gas Sensing

For the preparation of the sensors 50 mg of the mesoporous CeO₂ powders (synthesised by using CMK-3 carbon) were ground and dispersed in 1 mL deionized water. The dispersion was deposited onto commercial substrates (Umweltsensortechnik, UST) with integrated platinum electrodes and heating, dried at room temperature, and tempered for 60 hours at 623 K. The gas sensing properties were measured by means of a gas-mixing equipment using standard mass-flow controllers to provide a well-defined gas flow and a computer to control the experiment and record the resulting data.

3. Results and Discussion

3.1. CeO₂ Replicated from SBA-15 Silica

Figure 1 shows the powder X-ray diffraction patterns of two mesoporous SBA-15 silica samples used as a structure matrices. As a result of different synthesis temperatures (see experimental section), the two samples differ in their mesopore diameters (top: 11 nm, bottom: 7 nm) and pore wall thicknesses (top: 1 nm, bottom: 4 nm), as determined by physisorption (not shown). The low-angle reflections (100, 110, and 200) correspond to the hexagonal (*p6mm*) pore arrangement. The XRD patterns of the respective mesoporous ceria replicas are shown in the same graphs. In case of ceria replicated from large-pore SBA-15 the hexagonal symmetry is preserved, as evident from the fact that all three reflections are retained. On the other hand, the ceria sample replicated from small-pore SBA-15 shows significant broadening of the reflections, which indicates that the periodic structure is lost to a certain degree. The wide-angle regions of the XRD patterns (insets) indicate that both mesoporous ceria samples are crystalline; the reflections correspond to the fluorite-type structure of CeO₂.

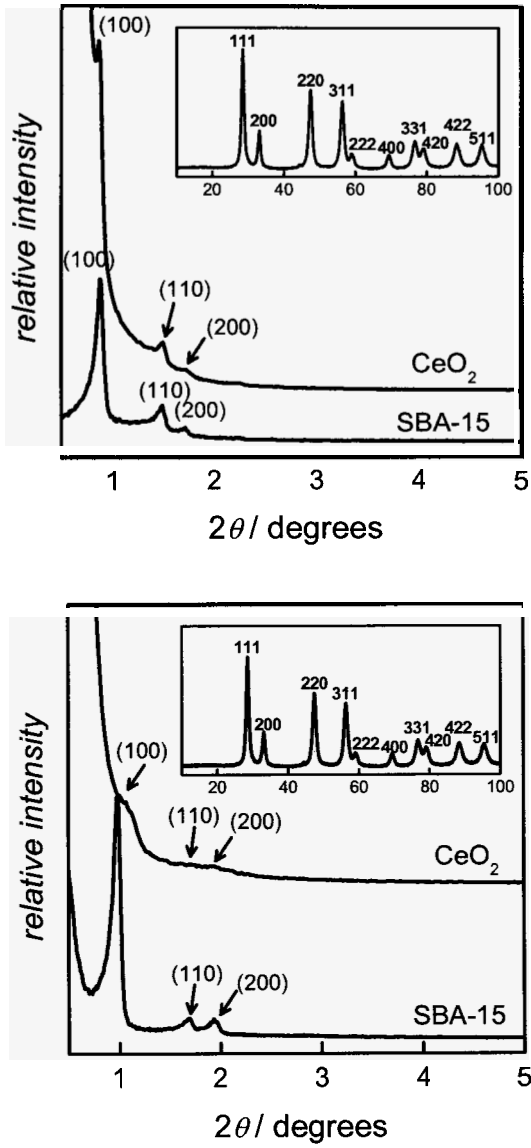


Figure 1. XRD patterns of mesoporous ceria and the corresponding structure SBA-15 silica matrices (top: SBA-15 with large mesopores; bottom: SBA-15 with small mesopores). The wide-angle reflections (insets) are assignable to crystalline CeO_2 .

N_2 physisorption data of both ceria samples (Figure 2) confirm that the ordered pore system is preserved to a different extent. For the sample prepared by using the large-pore SBA-15 silica the isotherm shape is close to type IV. Utilization of small-pore SBA-15, on the other hand, results in an isotherm which rather resembles a type II shape. Loss in structural order causes interparticle porosity to a greater extent, especially in case of ceria casted from small-pore SBA-15 silica. However, a sharp peak at ca. 5 nm in the pore diameter distribution is observed in both cases (Figure 2, insets), which confirms the presence of uniform pores. The specific BET surface areas and total pore volumes are $75 \text{ m}^2 \text{ g}^{-1}$ and $0.14 \text{ cm}^3 \text{ g}^{-1}$ (from large-pore SBA-15) and $70 \text{ m}^2 \text{ g}^{-1}$ and of $0.16 \text{ cm}^3 \text{ g}^{-1}$ (from small-pore SBA-15), respectively. The large-pore SBA-15 silica is apparently more suitable as a structure matrix than the small-pore SBA-15 sample. This is consistent with the fact that in the former case microporosity in the mesopore walls is much more pronounced [17], which leads to a better interconnectivity of the resulting ceria network.

Transmission electron micrographs of both ceria samples are shown in Figure 3. The left image is representative of ceria replicated from large-pore SBA-15 silica, showing long-range hexagonal periodicity. For ceria replicated from small-pore SBA-15 such well-ordered domains are rarer; instead, areas of loosely bundled wires without periodic arrangement are more frequent, which confirms the above mentioned lower interconnectivity of the ceria network.

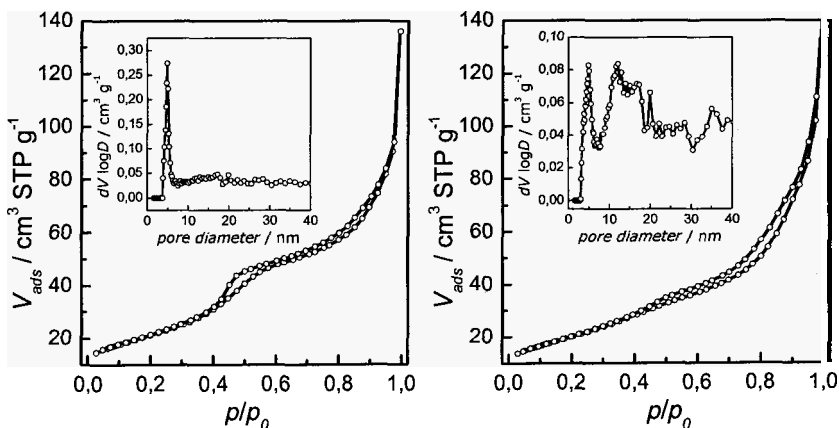


Figure 2. N_2 physisorption isotherms and DFT pore size distributions (insets) of mesoporous ceria casted from SBA-15 exhibiting large mesopores (left) and small mesopores (right).

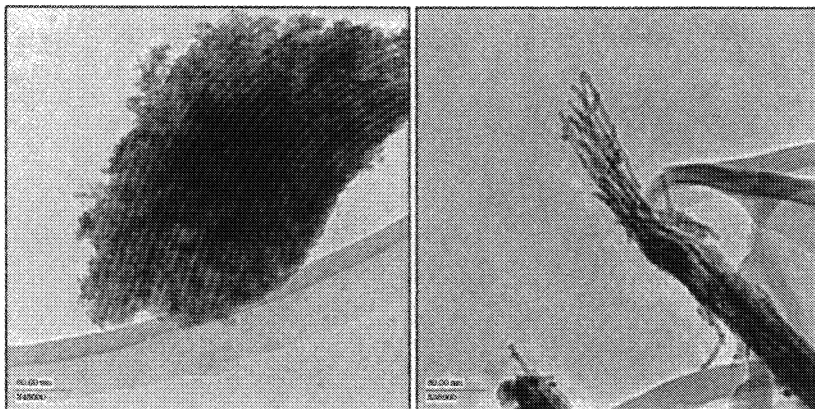


Figure 3. TEM images of mesoporous ceria replicated from SBA-15 exhibiting large mesopores (left) and small mesopores (right).

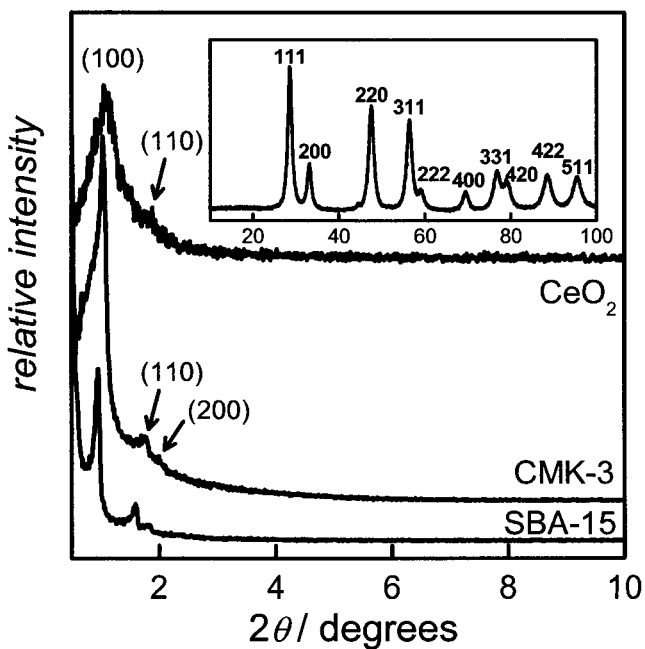


Figure 4. XRD patterns of mesoporous ceria and the corresponding structure matrices CMK-3 carbon and SBA-15 silica. The inset shows wide-angle reflections assignable to crystalline CeO_2 .

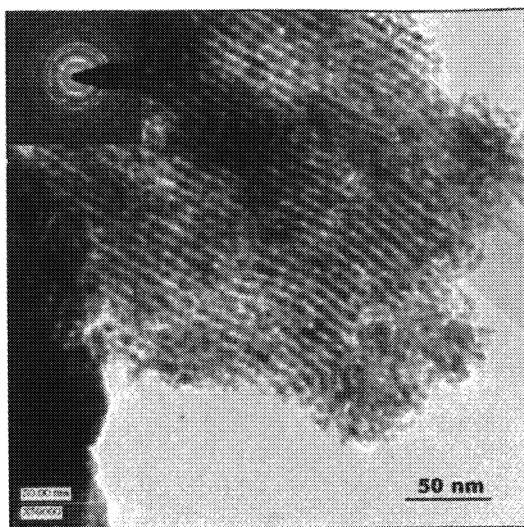


Figure 5. TEM image and SAED pattern (inset) of mesoporous ceria casted from CMK-3 carbon.

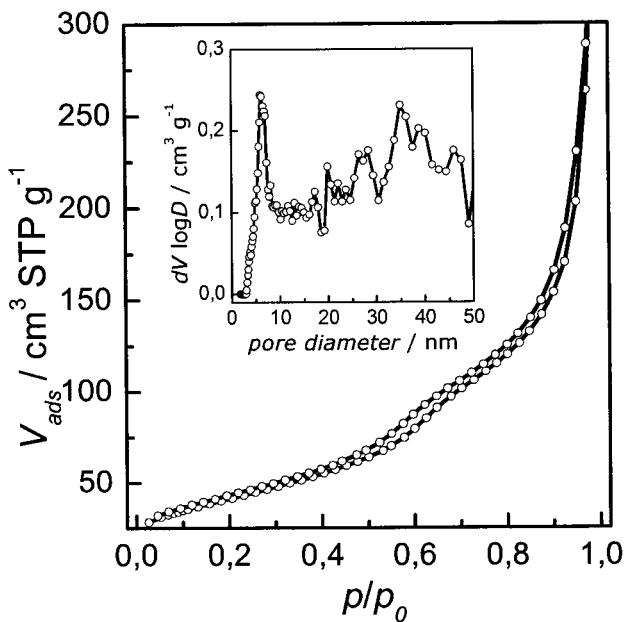


Figure 6. N₂ physisorption isotherms and DFT pore size distribution (inset) of mesoporous ceria casted from CMK-3 carbon.

3.2. *CeO₂ Replicated from CMK-3 Carbon*

Figure 4 shows the XRD patterns of mesoporous ceria as well as of the "parent" CMK-3 carbon and SBA-15 silica which have consecutively served as structure matrices. Again the low-angle reflections confirm the hexagonal periodicity of the pore system. For mesoporous ceria only the 100 and 110 reflection can be identified and a broadening of the peaks is observed indicating a certain degree of loss in structural order. The wide-angle region (Figure 4, inset) confirms the atomic-scale crystallinity of mesoporous ceria.

A representative TEM image (Figure 5) of mesoporous ceria shows predominantly areas of ordered pores, as well as from fractions exhibiting disordered, though still uniformly arranged pores. Selected area electron diffraction (SAED) pattern from the same part of the sample (Figure 5, inset) confirms that the pore walls are polycrystalline.

N₂ physisorption isotherms are shown in Figure 6. Again the isotherm shape is an intermediate between type II and type IV, indicating a contribution of interparticle porosity. This is also apparent from the broad DFT pore diameter distribution (Figure 6, inset) in the region of 20-50 nm. However, a sharp peak at ca. 6 nm confirms that the material also contains uniform pores. The specific BET surface area and the total pore volume are 148 m² g⁻¹ and 0.42 cm³ g⁻¹, respectively.

3.3. *Gas sensing properties*

Figure 7 shows the methane (CH₄) gas-sensing performance of mesoporous ceria synthesised by using CMK-3 carbon. The measurement was carried out at 573 K. The lower part of the figure shows the offered CH₄ concentration profile. The upper graph shows the relative change in conductance of the sensor. The sensor signal shows a fast and approximately linear response to CH₄. The response of a reference sensor prepared from non-porous ceria (specific BET surface area: 10 cm³ g⁻¹) for comparison was below the detection limit (signal to noise).

Conclusions

Mesoporous SBA-15 silica as well as CMK-3 carbon can be used as structure matrices for the synthesis of mesoporous ceria by the nanocasting process. The products exhibit periodically arranged uniform mesopores with polycrystalline pore walls. Depending on the applied matrix the products exhibit interparticle porosity to various extent. The mesoporous ceria shows fast and strong sensitivity to methane gas.

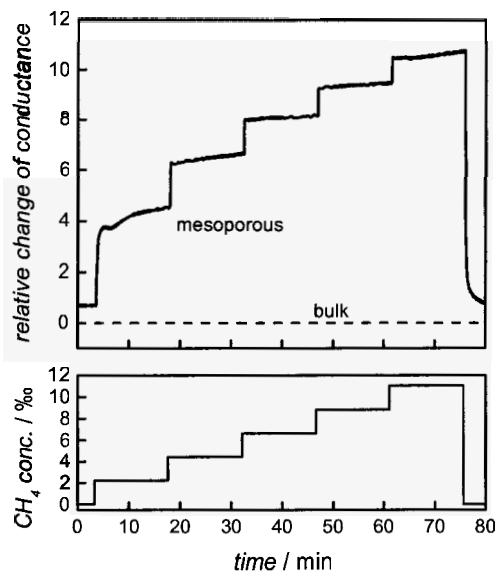


Figure 7. Gas sensor measurement showing the methane concentration (bottom) and the relative change of conductance of the sensor prepared with mesoporous ceria (top, solid line) and bulk ceria (top, dashed line).

Acknowledgments

We thank Prof. Michael Fröba for continuous support, Thorsten Wagner for gas sensing measurements, Günter Koch for recording the TEM images, and Marie-Luise Wolff for valuable help in the lab.

References

1. A. Trovarelli, *Catal. Rev. Sci. Eng.* **38**, 439 (1996).
2. J. Kašpar, P. Fornasiero, M. Graziani, *Catal. Today* **50**, 285 (1999)
3. H.-J. Beie, *Sens. Actuators B* **4**, 393 (1991).
4. P. Jasinski, Z. Suzuki, H. U. Anderson, *Sens. Actuators B* **95**, 73 (2003).
5. A. Tschöpe, *J. Electroceram.* **14**, 5 (2005).
6. D. M. Lyons, K. M. Ryan, M. A. Morris, *J. Mater. Chem.* **12**, 1207 (2002).
7. D. Terribile, A. Trovarelli, J. Llorca, C. de Leitenburg, G. Dolcetti, *J. Catal.* **178**, 299 (1998).
8. A.-H. Lu and F. Schüth, *Adv. Mater.* **18**, 1793 (2006).
9. H. Yang and D. Zhao *J. Mater. Chem.* **15**, 1217 (2005).

10. S. Laha and R. Ryoo, *Chem. Commun.*, 2138 (2003).
11. E. Rossinyol, J. Arbiol, F. Peiro, A. Cornet, J. R. Morante, B. Tian, T. Bo, D. Zhao, *Sens. Actuators B* **109**, 57 (2005).
12. W. Shen, X. Dong, Y. Zhu, H. Chen, J. Shi, *Microporous Mesoporous Mater.* **85**, 157 (2005).
13. J. Roggenbuck, H. Schäfer, T. Tsoncheva, C. Minchev, J. Hanss, M. Tiemann, *Microporous Mesoporous Mater.* **101**, 335 (2007).
14. M. Kruk, M. Jaroniec, C. H. Ko and R. Ryoo, *Chem. Mater.* **12**, 1961 (2000).
15. D. Zhao, Q. Huo, J. Feng, B. F. Chmelka, G. D. Stucky, *J. Am. Chem. Soc.* **120**, 6024 (1998).
16. S. Jun, S. H. Joo, R. Ryoo, M. Kruk, M. Jaroniec, Z. Liu, T. Ohsuna, O. Terasaki, *J. Am. Chem. Soc.* **122**, 10712 (2000).
17. A. Galarneau, H. Cambon, F. Di Renzo, R. Ryoo, M. Choib, F. Fajula, *New J. Chem.* **27** 73 (2003).

SYNTHESIS OF VANADIUM OXIDE NANOCCLUSERS IN CONFINED ENVIRONMENT VIA A TEMPLATE-EXCHANGE METHOD

PARASURAMAN SELVAM

*National Centre for Catalysis Research, Department of Chemistry,
Indian Institute of Technology-Madras, Chennai 600036, India; and
Solid State and Catalysis Laboratory, Department of Chemistry,
Indian Institute of Technology-Bombay, Mumbai 400076, India*

VIDYA KRISHNA

*National Centre for Catalysis Research, Department of Chemistry,
Indian Institute of Technology-Madras, Chennai 600036, India*

ARUNASISH LAYEK

*Solid State and Catalysis Laboratory, Department of Chemistry,
Indian Institute of Technology-Bombay, Mumbai 400076, India*

The paper discusses the preparation of vanadium oxides (V_2O_5) within the mesopores of MCM-41, via a template exchange method, which results in anchoring of VO^{2+} onto the defect sites of MCM-41, in addition to partial conversion of vanadyl ions to vanadium oxides. The samples were characterized by various spectroscopic and analytical techniques and the oxidation of toluene was studied over the vanadium incorporated catalyst.

1. Introduction

With the discovery of mesoporous molecular sieves (MCM-41, MCM-48, MCM-50) in 1992 by the Mobil Research Group [1], new opportunities have opened up to entrap catalytically active sites inside the uniform channels with controllable pore diameter (2-50 nm). Owing to these unique features, mesoporous molecular sieves have been found to be excellent hosts to anchor metal ions such as vanadyl (VO^{2+}) ions in the pores forming nanostructured heterogeneous catalysts [2]. However, the choice of vanadium as one of the most important transition metals for catalytic reactions stems from the fact that its oxidation states are variable and stable [3]. Further, the physicochemical properties of vanadium enable it to be a useful and versatile catalyst for selective oxidation reactions, e.g., o-xylene to phthalic anhydride [4] toluene to

benzaldehyde or benzoic acid [5] etc. However, most of these oxidation reactions are homogeneous in nature.

The utility of vanadium as an oxidation catalyst encouraged us to anchor them into the molecular matrix. The method involves a template ion-exchange route, where the surfactant cations, which act as a template in the formation of mesoporous materials, get exchanged by vanadyl ions from an aqueous solution [2]. What forms are anchored vanadyl species onto the defect sites of the molecular sieve. Calcination of such anchored samples results in the partial conversion of the anchored moieties to metal oxides. The template exchange method thus provides an advantage over impregnation methods, where in the former, the presence of residual surfactant molecules in the metal-exchanged samples aids in formation of metal oxides in the mesopores, owing to the exothermicity produced during combustion of the template. Further, the controllable pore-sizes of the matrix restrict the formation of metal oxides to a nanosize range. Thus, in the present investigation, an attempt has been made to synthesize nanoparticles of V_2O_5 in the mesoporous matrix by the template-exchange route and carry out liquid phase oxidation of toluene over VO^{2+} anchored MCM-41 catalyst.

2. Experimental

2.1. Synthesis of MCM-41

Mesoporous MCM-41 molecular sieves were synthesized hydrothermally as per the procedure described elsewhere [6] with a molar ratio: SiO_2 : 0.27 CTAB: 0.26 TMAOH: 0.13 Na_2O : 60 H_2O . The pH of the gel was adjusted to 11.5 either by adding dilute H_2SO_4 or aqueous NaOH and was placed in an air oven at 373 K for 24 h in Teflon-lined stainless steel autoclaves. The solid products obtained were washed, filtered and dried at 353 K. The as-synthesized MCM-41 was then calcined in a tubular furnace at 823 K in a flow of N_2 for 2 h followed by 8 h in air with a flow rate of 50 ml min^{-1} and a heating rate of 1 K min^{-1} [6].

2.2. Preparation of VO^{2+} /MCM-41 by template exchange method

The entrapment of VO^{2+} ions in the mesoporous matrix was carried out by direct template ion exchange method [2] by taking 1g of the as-synthesized sample with 80 ml of aqueous solution of vanadyl sulphate under constant stirring for 24h. Different loadings of vanadium were achieved by varying the Si/V ratio ($Si/V = 10, 15, \text{ and } 20$). The solid mass separated by filtration was followed by washing with distilled water several times and drying at 373 K overnight. These

VO^{2+} exchanged samples were calcined in a tubular furnace at 823 K in a flow of N_2 for 2 h followed by 8 h in air at a flow rate of 50 ml min^{-1} and a heating rate of 1 K min^{-1} and are designated as $\text{VO}^{2+}/\text{MCM-41}$. For a comparison, vanadyl-impregnated was prepared (VO^{2+} -MCM-41) with 15 wt % of vanadium in calcined MCM-41 sample.

3. Results and Discussion

Powder XRD of MCM-41 and vanadium incorporated MCM-41 was recorded on a Rigaku miniflex X-ray diffractometer. XRD of as-synthesized MCM-41 sample shows strong reflections corresponding to the (100) plane along with weak reflections from (110), (200), (210) planes, respectively, characteristic of hexagonal MCM-41 structure [1]. Vanadyl-exchanged MCM-41 samples exhibit reflections similar to parent MCM-41, indicating intactness of structure (see Fig. 1). It can be seen from Table 1 that the d-spacings and unit cell parameter (a_0) of the vanadium incorporated samples show an increase as compared to the parent MCM-41, which could be attributed to a partial isomorphous substitution of vanadium into the mesoporous matrix, in addition to anchoring (see Table 1) [7]. Calcined samples showed a decrease in unit-cell parameter compared to the as-synthesized/exchanged samples, owing to the removal of surfactant molecules and condensation of silanol groups, causing the unit cell to shrink.

Table 1. XRD data for vanadium incorporated samples.

Sample	d_{100} (Å)	a_0 (Å)	Vanadium content ⁸
As-synth MCM-41	40.67	43.78	-
Calcined MCM-41	36.78	40.48	-
VO^{2+} -exch MCM-41	42.43	45.99	3.64
$\text{VO}^{2+}/\text{MCM-41}$ (10)	40.48	43.76	3.64
VO^{2+} -exch. MCM-41	42.03	45.40	3.88
$\text{VO}^{2+}/\text{MCM-41}$ (15)	40.73	45.61	3.88
VO^{2+} -imp MCM-41	42.43	45.87	1.9
VO^{2+} -MCM-41 (15)	39.56	43.95	1.9

* ICP-analysis.

Figure 2 (a,b) represents typical TEM images and ED patterns of $\text{VO}^{2+}/\text{MCM-41}$ calcined at 550°C . TEM and ED analysis was carried out on JEOL 2000 FX and Phillips CM 200, operating at 160 and 200 kV, respectively. TEM micrograph shows the hexagonal ordered pore structure and a

representative ED pattern confirms the high periodicity of VO^{2+} -MCM-41 [1,8]. No formation of vanadium oxide moieties was observed in the TEM and ED patterns, indicating that vanadium is predominantly present in the form of VO^{2+} ions in the mesoporous matrix.

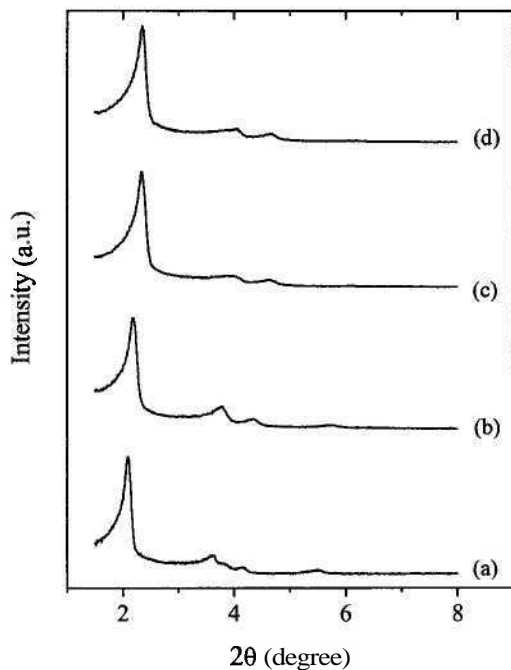


Figure 1. XRD patterns of: a) vanadyl-exchanged MCM-41, b) VO^{2+} /MCM-41, c) vanadyl-impregnated MCM-41, d) VO^{2+} -MCM-41.

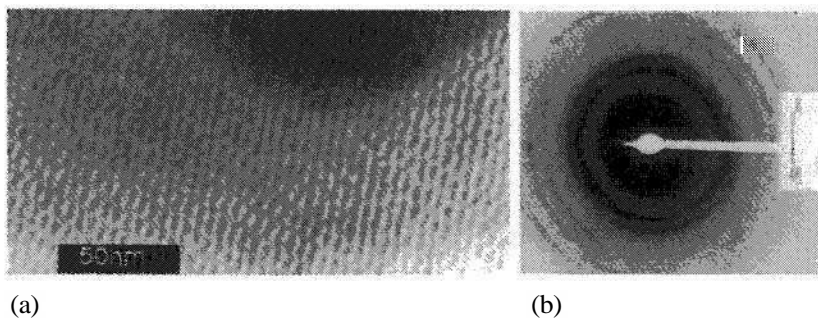


Figure 2. (a) TEM micrographs and (b) ED pattern of VO^{2+} /MCM-41.

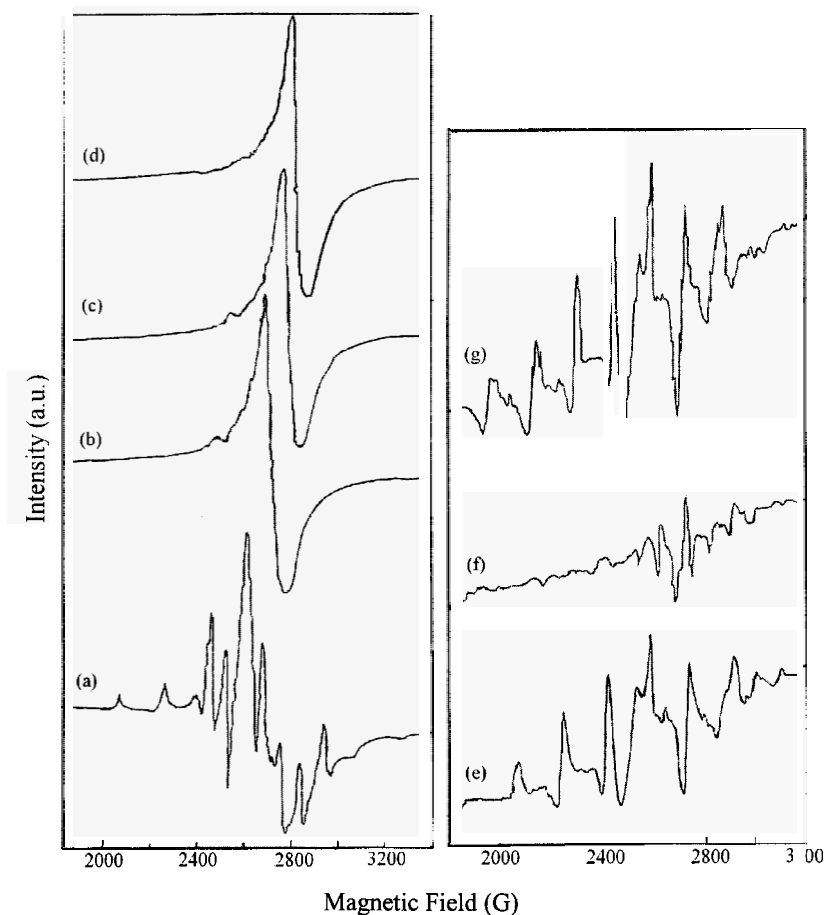


Figure 3. ESR spectra of (a) bulk vanadyl sulfate (b) calcined vanadyl sulfate (723 K) (c) V_2O_5 standard (d) V_2O_5 (at 77K) (e) vanadyl-exchanged MCM-41 (f) $VO^{2+}/MCM-41$ (g) $VO^{2+}/MCM-41(77K)$.

ESR spectra were recorded on Bruker ESP 300 X-band spectrometer. Figure 3 shows the ESR signal at room temperature of the vanadyl sulphate source and $VO^{2+}/MCM-41$ samples, which exhibit two axially symmetric sets of eight lines characteristic of VO^{2+} species (nuclear spin of vanadium = $7/2$ with unpaired electron) [8], indicating that vanadium retains its +4 oxidation state in the as-exchanged and calcined forms. However, the concentration of vanadium

(IV) is found to be very low due to partial conversion of some VO^{2+} species to V_2O_5 . Hence, in the calcined samples, we have observed the well resolved spectral line which is attributed to the decrease in the dipolar interaction among the V (IV) ions within the matrix. All the spectra were recorded at room

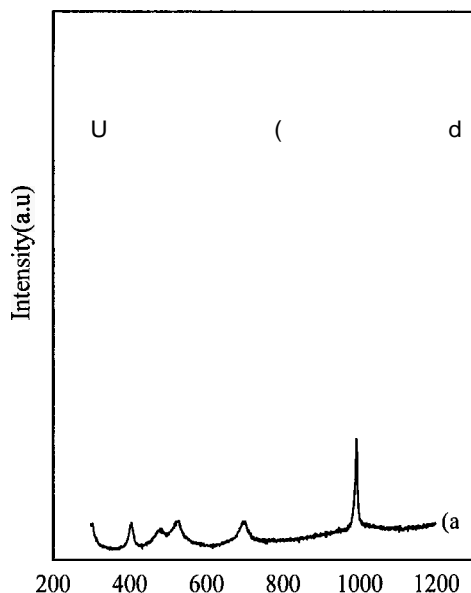


Figure 4. Raman spectra of: (a) V_2O_5 , (b) calcined VOSO_4 (550 °C), (c) VO^{2+} -exchanged MCM-41, (d) VO^{2+} /MCM-41.

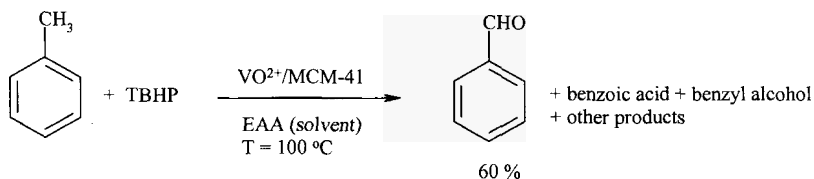
The Raman scattering measurements have been used to study the presence of microstructure of vanadium oxide in the mesoporous host. The vanadyl-exchanged MCM-41 and VO^{2+} /MCM-41 were analyzed on a Jobin Yvon HR 800 UV spectrometer in the range 300-1200 cm^{-1} . For a comparative study Raman scattering spectra of standard V_2O_5 and that of calcined VOSO_4 (550°C) were also recorded. The Raman scattering spectra are depicted in Fig. 4. From the spectrum it is very clear that when bulk vanadyl sulfate is calcined, it is converted into V_2O_5 . The strong band at $\sim 992 \text{ cm}^{-1}$ indicates terminal $\text{V}=\text{O}$ stretching mode [9,10] which is in good agreement with the standard V_2O_5 , whereas the band at $\sim 405 \text{ cm}^{-1}$ is assigned to bending vibration of $\text{V}=\text{O}$ [9]. The

Raman band at $\sim 703\text{ cm}^{-1}$ is assigned to the doubly coordinated oxygen ($V_2\text{—O}$) stretching mode, whereas that at $\sim 522\text{ cm}^{-1}$ corresponds to triply coordinated oxygen ($V_3\text{—O}$) stretching mode [9]. In vanadyl-exchanged MCM-41 and $\text{VO}^{2+}/\text{MCM-41}$, a band is observed at $\sim 954\text{ cm}^{-1}$ and $\sim 977\text{ cm}^{-1}$, respectively, which is assigned to (Si-O-V) stretching mode and also to the terminal V=O stretching of V_2O_5 ; the latter showing more sharpness and intensity as compared to the former, indicating partial conversion of VO^{2+} to V_2O_5 . Other band assignments of vanadium incorporated MCM-41 is presented in Table 2.

Table 2. Raman band assignments for vanadium incorporated MCM-41

Vanadyl-exchanged MCM-41	$\text{VO}^{2+}/\text{MCM-41}$	Band assignments
$\sim 954\text{ cm}^{-1}$	977 cm^{-1}	$\nu_s(\text{Si-O-V})$, $\nu(\text{V=O})$ of V_2O_5
$\sim 1079\text{ cm}^{-1}$	1036 cm^{-1}	$\nu_s(\text{Si-O-Si})$
$\sim 494\text{ cm}^{-1}$	492 cm^{-1}	$d(\text{V-O-V})$

Scheme 1. Liquid Phase Oxidation of Toluene



Toluene is one of the most important aromatic hydrocarbons, specially in the selective oxidation of toluene to benzaldehyde and benzyl alcohol, which are versatile intermediates in the chemical industry [11]. So far, the oxidation of toluene with air is mainly used to synthesize benzoic acid, and benzaldehyde and benzyl alcohol are synthesized by chlorination of toluene followed by hydrolysis, a seriously polluting process [12]. A new method of selective oxidation of toluene to benzaldehyde has been an attractive field as well as an important chemical challenge [13]. In this report, we have adopted liquid phase oxidation scheme (see Scheme 1) by using tertiary butyl hydroperoxide (TBHP) as oxidant and $\text{VO}^{2+}/\text{MCM-41}$ as catalyst. The reaction condition is as follows: TBHP (oxidant, 16 mmol), toluene (8 mmol) (oxidant to substrate ratio 2:1), 5.0 mg catalyst, ethyl acetoacetate solvent (5 ml). The reaction temperature was maintained at 100°C . The reaction mixture was analyzed by means of gas chromatographic technique. The conversion of toluene is found to be quite low

(<10 %) although benzaldehyde selectivity is good (~60 %). With increasing time benzaldehyde selectivity decreased and more benzoic acid was formed [8].

Acknowledgment

The authors thank SAIF, IIT-Bombay for TEM, ED, ESR, and Raman measurements.

References

1. J.S. Beck, J.C. Vartuli, W.J. Roth, M.E. Leonowicz, K.D. Schimdt, C.T.-W. Chu, D.H. Olson, E.W. Sheppard, S.B. McCullen, J.B. Higgins and J.L. Schlenker, *J. Am. Chem. Soc.* **114**, 10834 (1992).
2. K. Vidya, S.E. Dapurkar, P. Selvam, S.K. Badamali, D. Kumar and N.M. Gupta, *J. Mol. Catal. A.* **181**, 91 (2002); **191**, 149 (2003).
3. F. A. Cotton and G. Wilkinson, *Advanced Inorganic Chemistry*, Wiley, New York (1972).
4. G. C. Bond, *J. Catal.* **8**, 1949 (1989).
5. H.K. Matralis, Ch. Papadopoulou, Ch. Kordulis, A.A. Elguezabal and V.C. Corbean, *Appl. Catal. A.* **126**, 365 (1995).
6. S. E. Dapurker, S. K. Badamali and P. Selvam, *Catal.Today* **68**, 63 (2001).
7. K. Vidya, N.M. Gupta and P. Selvam, *Mater. Res. Bull.* **39**, 2035 (2004).
8. Z. Luan, J. Xu, H. He, J. Klinowski and L. Kevan, *J. Phys. Chem. B.* **100**, 19595 (1996).
9. W. Chen, L. Mai, J. Peng, Q. Xu and Q. Zhu, *J Solid State Chemistry* **177**, 377 (2004).
10. S. Shylesh, A. P. Sing, *J. Catal.* **233**, 359 (2005).
11. R.A. Sheldon, *Chemtech*, 556 (1991)
12. W. Partenheimer, *Catal.Today* **23**, 69 (1995)
13. B. Meunier, *Chem. Rev.* **92**, 1411 (1992).

SYNTHESIS OF Co_3O_4 , NiO NANOPARTICLES WITH MESOPOROUS STRUCTURE AND THEIR ELECTROCHEMICAL CAPACITIVE BEHAVIORS

MING-BO ZHENG, YU ZHAO, JIAN CAO, JIN-SONG LIU, HAI-JUN ZHAO,
JIE-MING CAO*, GUANG-BIN JI, HAI-YAN WANG, JIE TAO†

*Nanomaterials Research Institute, College of Materials Science and Technology,
Nanjing University of Aeronautics and Astronautics, Nanjing, 210016, P.R. China*

Mesoporous Co_3O_4 , NiO nanoparticles were prepared using KIT-6, SBA-15 as templates and $\text{Co}(\text{NO}_3)_2 \cdot 6\text{H}_2\text{O}$, $\text{Ni}(\text{NO}_3)_2 \cdot 6\text{H}_2\text{O}$ as precursors. X-ray diffraction and SEAD indicated that the samples had crystalline walls. N_2 adsorption-desorption analysis indicated that the samples had high BET surface areas and pore volume. Electrochemical capacitive properties of the mesoporous metal oxides were examined by cyclic voltammetry and galvanostatic charge-discharge measurements. The results showed that the mesoporous metal oxides had a higher specific capacitance and better capacitive behavior than the conventional metal oxide.

1. Introduction

Mesoporous metal oxides are of wide interest for applications in many fields, such as catalysts [1], gas sensors [2], and electrochemical electrode materials [3] because of their large specific surface areas, ordered pore structure, and shape-selective properties. These materials can be synthesized using organic soft templates, similar with the synthesis of mesoporous silica. However, soft templating method normally results in amorphous materials due to the low decomposition temperature of the template [4]. Recently, ordered mesoporous Fe_2O_3 , NiO, Co_3O_4 with crystalline walls have been synthesized using mesoporous silica as template [5-9].

Electrochemical capacitors (ECs) are becoming attractive energy storage systems because they have greater power density than common batteries and can be deeply discharged without any deleterious effect on lifetime. Energy storage mechanisms of electrochemical capacitors are classed into two areas: (1) double-layer capacitance arising from the charge separation at the electrode/electrolyte

* This work is supported by Doctor Innovation Funds of Jiangsu Province (BCXJ06-13), National Natural Science Foundation of China (50502020) and Natural Science Foundation of Jiangsu Province (BK2006195). Correspondence: jmcao@nuaa.edu.cn

interface and (2) pseudocapacitance arising from fast, reversible Faradaic reactions occurring at or near a solid electrode surface. Carbon materials with high surface areas are widely used for double-layer capacitors [10]. On the other hand, transition metal oxides like RuO_2 and IrO_2 exhibit Faradaic pseudocapacitance with capacitance reported to be as large as $760 \text{ F}\cdot\text{g}^{-1}$ [11]. But the high cost of these materials limits their commercialization. Then, other metal oxides such as nickel oxides [12-14], cobalt oxides [15] and manganese oxides [16] are studied because they are inexpensive and exhibit pseudocapacitance behavior similar to that of RuO_2 and IrO_2 .

Since electric double-layer capacitance and pseudocapacitance are interfacial phenomena, the materials for electrochemical capacitors should possess a high specific surface area with a suitable pore-size distribution to enhance the charge-storage capability. Thus, control of the surface morphology of electrode materials is one of the most important design parameters for making an electrochemical capacitor [17]. Recently, Y. Wang et al. synthesized mesoporous NiO using SBA-15 as the template [18]. However, the Brunauer-Emmett-Teller (BET) surface areas of the product is only $47 \text{ m}^2\cdot\text{g}^{-1}$ and therefore restrict its specific capacitance. In this work, mesoporous NiO, Co_3O_4 nanoparticles with high BET surface areas were synthesized using KIT-6 and SBA-15 as template and their electrochemical capacitive behaviors were evaluated in $2 \text{ mol}\cdot\text{L}^{-1}\text{KOH}$ electrolyte solution.

2. Experiment

2.1. Synthesis and Characterization of Mesoporous Metal Oxides

Mesoporous metal oxides were prepared using calcined 3D cubic KIT-6 or calcined 2D hexagonal SBA-15 as the template. Typically, 0.15 g of KIT-6 was dispersed in a 10 mL solution of 0.3 g of $\text{Co}(\text{NO}_3)_2\cdot 6\text{H}_2\text{O}$ in ethanol in a glass container. The solution was stirred at room temperature for 12 h. Ethanol was removed by evaporation by heating the container overnight at $40 \text{ }^\circ\text{C}$. Then, the dried compound was ground for 10 min in a mortar. Afterward, the resulting powder was calcined at $500 \text{ }^\circ\text{C}$ for 6 h in air atmosphere. The silica template was then removed at room temperature using a 5% HF aqueous solution. The etching of silica was repeated one more time. The black Co_3O_4 material was recovered by centrifugation and finally dried at $80 \text{ }^\circ\text{C}$. The product was nominated as $\text{Co}_3\text{O}_4\text{-KIT-6}$. The preparations of NiO-KIT-6, NiO-SBA-15, and $\text{Co}_3\text{O}_4\text{-SBA-15}$ are similar with that of the $\text{Co}_3\text{O}_4\text{-KIT-6}$. For NiO samples, $\text{Ni}(\text{NO}_3)_2\cdot 6\text{H}_2\text{O}$ was used as the precursor, and $2 \text{ mol}\cdot\text{L}^{-1}$ NaOH solution was used to remove the

silica template. Besides, conventional Co_3O_4 , NiO were prepared by direct calcining $\text{Co}(\text{NO}_3)_2 \cdot 6\text{H}_2\text{O}$, $\text{Ni}(\text{NO}_3)_2 \cdot 6\text{H}_2\text{O}$ at the same conditions.

The crystal structures of the samples were characterized by X-ray diffraction (XRD) (Bruker D8 advance). The size and morphology of the samples were examined by transmission electron microscopy (TEM) (FEI, TECNAI-20) and scanning electron microscopy (SEM) (LEO1530). The N_2 adsorption-desorption analysis was measured on a Micromeritics ASAP 2010 instrument.

2.2. Electrochemical tests

Electrodes for electrochemical capacitors were prepared by mixing the prepared powders with 10 wt.% acetylene black and 5 wt.% polyvinylidene fluoride (PVDF) binder of the total electrode mass. A small amount of N-methyl-2-pyrrolidinone (NMP) was then added to those composites to make more homogeneous mixtures, which were then pressed on nickel grid. Each electrode contained about 5 mg of active materials. The electrodes were dried at $90\text{ }^\circ\text{C}$ for 24 h. Before electrochemical tests, the electrodes were impregnated with $2\text{ mol}\cdot\text{L}^{-1}$ KOH solution to guarantee that the electrode material was thoroughly wetted by electrolyte. All electrochemical measurements were done in a three electrode experimental setup. The prepared electrode, platinum foil and SCE electrode were used as the working, counter and reference electrodes, respectively. All measurements were carried out in $2\text{ mol}\cdot\text{L}^{-1}$ KOH electrolyte. Cyclic voltammetry (CV) and galvanostatic charge/discharge was conducted using CHI660 electrochemical workstation.

3. Results and Discussion

The wide-angle XRD patterns (Figure 1A) of Co_3O_4 -KIT-6 and NiO-SBA-15 correspond to the face centered cubic Co_3O_4 and the cubic-phased NiO,

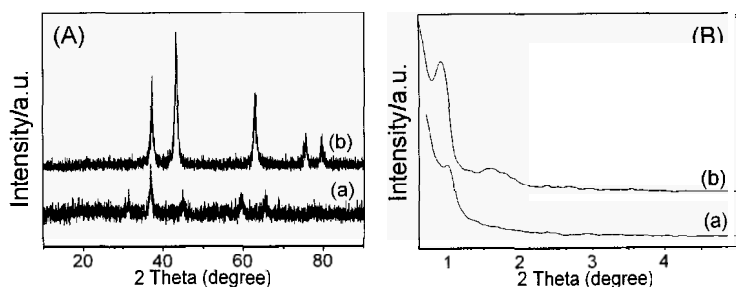


Figure 1. Wide-angle (A) and low-angle (B) X-ray diffraction patterns of the samples. (a) Co_3O_4 -KIT-6; (b) NiO-SBA-15.

respectively. No impurity phases were detected. Figure 1B shows the low-angle XRD patterns of $\text{Co}_3\text{O}_4\text{-KIT-6}$ and NiO-SBA-15 . The results prove the bulk structural order of the materials.

Figure 2 shows the SEM and TEM images of $\text{Co}_3\text{O}_4\text{-KIT-6}$. The SEM image indicates that $\text{Co}_3\text{O}_4\text{-KIT-6}$ sample is composed of nanoparticles. The typical diameter of the nanoparticles was estimated to be 20-150 nm, whereas the KIT-6 particle was several micrometers in size. The TEM images reveal the mesoporous structure of the nanoparticles. Besides, conventional cobalt oxide particles were not observed, which indicated that almost all nitrates had moved into the mesopores of KIT-6 during the calcination. Selected area electron diffraction (SAED) pattern reveals the crystalline walls of the mesoporous nanoparticles. The characterization results of NiO-KIT-6 are similar with that of the $\text{Co}_3\text{O}_4\text{-KIT-6}$. After the evaporation of ethanol, only a small quantity of the nitrates migrated into the mesopores of templates. Most of the nitrates dispersed on the outside surface of silica particles. The melting point of $\text{Co}(\text{NO}_3)_2 \cdot 6\text{H}_2\text{O}$ is about 55 °C, and the decomposition temperature of it is about 74 °C. With the increase of temperature, the nitrates turned into a liquid phase before decomposition and moved into the mesopores of KIT-6. The decomposition of the nitrates and crystallization of the corresponding oxides took place inside the mesopores at a higher temperature [9].

Figure 3 shows the SEM and TEM images of NiO-SBA-15 . The SEM image indicates that NiO-SBA-15 sample is also composed of nanoparticles. The TEM images reveal the hexagonal mesoporous structure of the nanoparticles. The SAED pattern also reveals the crystalline walls of the NiO-SBA-15 . The characterization results of the $\text{Co}_3\text{O}_4\text{-SBA-15}$ are similar with that of the NiO-SBA-15 .

Figure 4 shows the N_2 adsorption-desorption isotherms and BJH pore size distribution plots of the samples. All the samples have a sorption isotherm with a broad capillary condensation range starting at about $p/p_0 = 0.5$ and extending almost to $p/p_0 = 1$, indicative of a high fraction of textural porosity. The pore size distribution from the adsorption can be seen in the inset of image. The narrow pore size distribution at about 5 nm corresponds to the mesopore which was produced from the removal of pore wall of the SiO_2 template. Except the mesopore distribution, these samples also have broad distribution in the range of 10-100 nm. These nanoporous structures were mainly produced from the stack of the nanoparticles. The BET surface areas and the pore volumes for $\text{Co}_3\text{O}_4\text{-KIT-6}$, NiO-KIT-6 , $\text{Co}_3\text{O}_4\text{-SBA-15}$, and NiO-SBA-15 are estimated to be $133 \text{ m}^2 \cdot \text{g}^{-1}$, $0.76 \text{ cm}^3 \cdot \text{g}^{-1}$, $102 \text{ m}^2 \cdot \text{g}^{-1}$, $0.40 \text{ cm}^3 \cdot \text{g}^{-1}$, $128 \text{ m}^2 \cdot \text{g}^{-1}$, $0.46 \text{ cm}^3 \cdot \text{g}^{-1}$, $101 \text{ m}^2 \cdot \text{g}^{-1}$, $0.39 \text{ cm}^3 \cdot \text{g}^{-1}$, respectively. Besides, the BET surface areas and

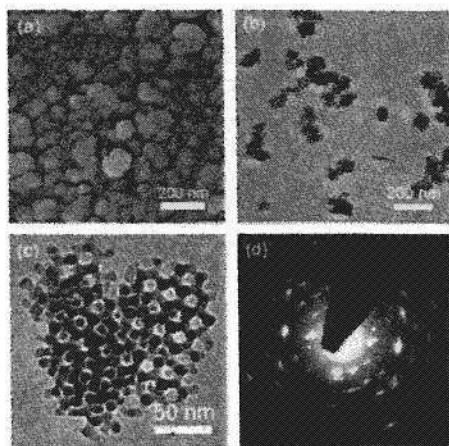


Figure 2. (a) SEM image of $\text{Co}_3\text{O}_4\text{-KIT-6}$; (b) (c) TEM images of $\text{Co}_3\text{O}_4\text{-KIT-6}$; (d) SAED image of $\text{Co}_3\text{O}_4\text{-KIT-6}$.

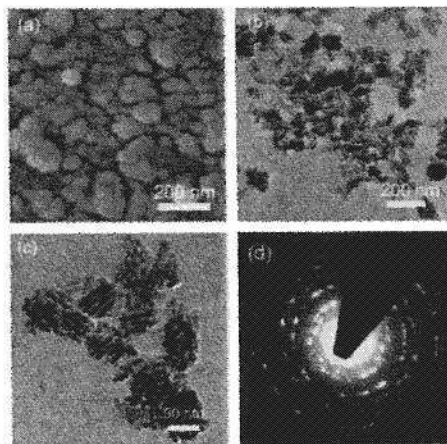


Figure 3. (a) SEM image of NiO-SBA-15 ; (b) (c) TEM images of NiO-SBA-15 ; (d) SAED image of NiO-SBA-15 .

the pore volumes for the conventional Co_3O_4 and NiO are $7.57 \text{ m}^2 \cdot \text{g}^{-1}$, $0.03 \text{ cm}^3 \cdot \text{g}^{-1}$, $7.66 \text{ m}^2 \cdot \text{g}^{-1}$, $0.05 \text{ cm}^3 \cdot \text{g}^{-1}$, respectively.

Cyclic voltammetry and galvanostatic charge-discharge techniques were used to determine the electrochemical properties of mesoporous oxide. Figure 5A shows the cyclic voltammetric behavior of the $\text{Co}_3\text{O}_4\text{-KIT-6}$ electrode at various scan rates. The curve shapes of the sample reveal that the capacitive

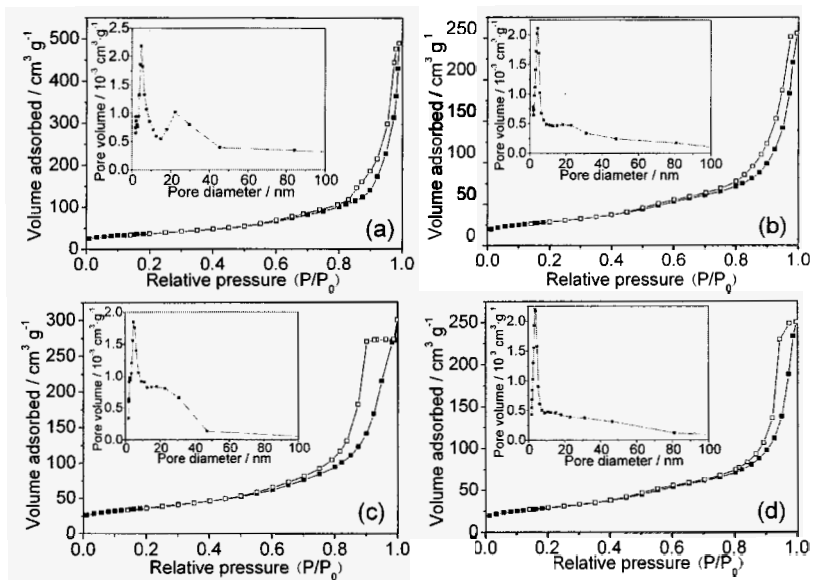


Figure 4. Nitrogen adsorption-desorption isotherms and BJH pore size distribution plots (inset) of the samples: (a) Co₃O₄-KIT-6; (b) NiO-KIT-6; (c) Co₃O₄-SBA-15; (d) NiO-SBA-15.

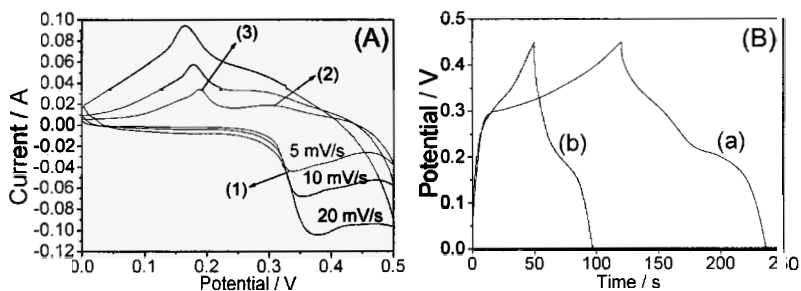
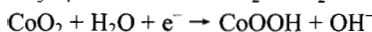
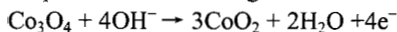


Figure 5. (A) CV curves of Co₃O₄-KIT-6 at different scan rates. (B) Charge-discharge curves of Co₃O₄-KIT-6 (a) and conventional Co₃O₄ (b). The working electrode contains 5 mg Co₃O₄.

characteristic is very distinguished from that of electric double-layer capacitance in which case it is normally close to an ideal rectangular shape. Since solution and electrode resistance can distort current response at the switching potential and this distortion is dependent upon the scan rate [19], the shape of the CV has changed with the scan rate increased. These results indicate that the measured

capacitance is mainly based on redox mechanism. The peak 1, peak 2, and peak 3 correspond to the following three electrochemical reactions:



The galvanostatic charge-discharge curves of Co_3O_4 -KIT-6 and conventional Co_3O_4 within potential range 0.45–0 V at the charge-discharge current of 10 mA after 150 cycles are shown in Figure 5B. The specific capacitance (C_m) can be calculated as follows: $C_m = I\Delta t/m\Delta v$, where I is the current of charge-discharge, Δt is the time of discharge, m is the mass of active materials in the work electrode, and Δv is 0.45 V. The evaluated specific capacitance of the Co_3O_4 -KIT-6 is about $516.3 \text{ F}\cdot\text{g}^{-1}$. However, the specific capacitance of the conventional Co_3O_4 is about $207.8 \text{ F}\cdot\text{g}^{-1}$.

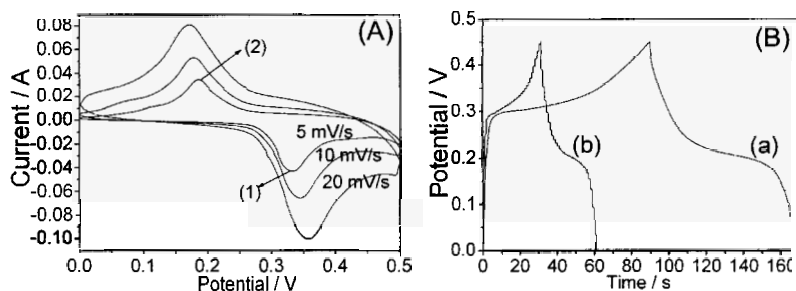


Figure 6. (A) CV curves of NiO-SBA-15 at different scan rates. (B) Charge-discharge curves of NiO-SBA-15 (a) and conventional NiO (b). The working electrode contains 5 mg NiO.

Figure 6A shows the cyclic voltammetric behavior of NiO-SBA-15 electrode at various sweep rates. A couple of redox peaks were observed within potential range 0.1–0.4 V (versus SCE), which can be considered to according to the following redox reaction:



The two strong redox reaction peaks are responsible for the pseudo capacitive capacitance. The anodic peak (peak 1) is due to the oxidation of NiO to NiOOH and the cathodic peak (peak 2) is for the reverse process.

The galvanostatic charge-discharge curves of NiO-SBA-15 and conventional NiO within potential range 0.45–0 V at the discharging current of 10 mA after 150 cycles are shown in Figure 6B. The evaluated specific capacitance of NiO-SBA-15 is about $345.3 \text{ F}\cdot\text{g}^{-1}$. However, the specific capacitance of the conventional NiO is about $130.8 \text{ F}\cdot\text{g}^{-1}$.

4. Conclusion

In summary, mesoporous Co_3O_4 , NiO nanoparticles with high BET surface areas have been synthesized using KIT-6, SBA-15 as the templates. Electrochemical measurements indicated that the mesoporous metal oxides had a higher specific capacitance and better capacitive behavior than the conventional metal oxides. Work in this direction is ongoing in our lab.

Acknowledgments

This work was supported by Doctor Innovation Funds of Jiangsu Province (BCXJ06-13), National Natural Science Foundation of China (50502020) and Natural Science Foundation of Jiangsu Province (BK2006195).

References

1. L. Yan, X. M. Zhang, H. P. Zhang, X. L. Wang and J. S. Suo, *Chem. Commun.* 860 (2002).
2. F. Jiao, K. M. Shaju and P. G. Bruce, *Angew. Chem. Int. Ed.* **44**, 6550 (2005).
3. W. Y. Li, L. N. Xu and J. Chen, *Adv. Funct. Mater.* **15**, 851 (2005).
4. F. Jiao and P. G. Bruce, *Angew. Chem. Int. Ed.* **43**, 5958 (2004).
5. B. Tian, X. Liu, H. Yang, S. Xie, C. Yu, B. Tu and D. Zhao, *Adv. Mater.* **15**, 1370 (2003).
6. F. Jiao, A. Harrison, J. Jumas, A. V. Chadwick, W. Kockelmann and P. G. Bruce, *J. Am. Chem. Soc.* **128**, 5468 (2006).
7. C. Dickinson, W. Zhou, R. P. Hodgkins, Y. Shi, D. Zhao and H. He, *Chem. Mater.* **18**, 3088 (2006).
8. Rumpelcker, F. Kleitz, E. Salabas and F. Schüth, *Chem. Mater.* **19**, 485 (2007).
9. W. Yue and W. Zhou, *Chem. Mater.* **19**, 2359 (2007).
10. J. M. Miller, B. Dunn, T. D. Tran and R. W. Pekala, *J. Electrochem. Soc.* **144**, L309 (1997).
11. J. P. Zheng, P. L. Cygan, T. R. Zow, *J. Electrochem. Soc.* **142**, 2699 (1995).
12. K. W. Nam and K. B. Kim, *J. Electrochem. Soc.* **149**, A306 (2002).
13. K. C. Liu, M. A. Anderson, *J. Electrochem. Soc.* **143**, 2699 (1995).
14. V. Srinivasan, J. W. Weinder, *J. Electrochem. Soc.* **144**, L210 (1997).
15. C. Lin, J. A. Ritter and B. N. Popov, *J. Electrochem. Soc.* **145**, 4097 (1998).
16. S. C. Pang, M. A. Anderson and T. W. Chapman, *J. Electrochem. Soc.* **147**, 444 (2000).
17. W. Xing, F. Li, Z. Yan and G. Q. Lu, *J. Power Sources* **134**, 324 (2004).
18. Y. Wang and Y. Xia, *J. Power Sources* **51**, 3223 (2006).
19. J. H. Jiang and A. Kucernak, *J. Electrochem. Soc.* **152**, A871 (2005).

SYNTHESIS AND CHARACTERIZATION OF NANOPOROUS Co₃O₄ VIA SOLVOTHERMAL-ANNEALING ROUTE*

HAI-JUN ZHAO[†], MING-BO ZHENG[†], DONG-MEI LIU, JING-SONG LIU,
XI-HUA JIANG, JIE TAO AND JIE-MING CAO[‡]

*Nanomaterials Research Institute, College of Materials Science and Technology,
Nanjing University of Aeronautics and Astronautics, Nanjing 210016, P. R. China*

An easy solvothermal-annealing route has been developed to synthesize nanoporous rhombohedral / microsphere Co₃O₄ with a specific surface area of 48.9 / 69.7 m²·g⁻¹. The method involves synthesizing the precursor through a simple solvothermal process and further annealing in a furnace. It can be described as easy-manipulated, and large scale in production. X-ray diffraction, scanning electron microscopy, N₂ adsorption-desorption measurements, and other techniques were used to characterize the rhombohedral/microsphere Co₃O₄ materials. The possible formation mechanism was discussed.

1. Introduction

Because of their unique properties, porous materials have been applied in many areas, such as heterogeneous catalysis [1], molecular separation [2,3], and nanocomposite preparation [4,5]. Porous materials with nanosized pore diameter have attracted considerable attention. A lot of methods have been developed to synthesize various nanoporous materials. Among them, the template method, which is usually categorized as a hard template (such as porous alumina [6], porous silicon [7]) method and a soft template (such as surfactants [8]) method, is based on first filling pre-prepared templates with desired materials and finally dissolving or burning them away. These fabrication techniques have the advantages of precise control over the size and structure of the final porous structure.

In recent years, Co₃O₄ has been extensively investigated in view of its application as solid-state sensors, ceramic pigments, rotatable magnets, heterogeneous catalysts and electrochromic devices [9-13].[†]

In this work, we successfully synthesized two kinds of cobalt carbonate with 3D architectures through an easy selected-control solvothermal process via the

* This work is supported by Doctor Innovation Funds of Jiangsu Province (BCXJ06-13) and the National Nature Science Fund of China. (50502020)

[†] These authors contributed equally to this work. [‡] Correspondence: jmcao@nuaa.edu.cn

direct reaction between cobalt salt ($\text{Co}(\text{CH}_3\text{COO})_2 \cdot 4\text{H}_2\text{O}$), urea and sodium dodecyl sulfate (SDS) under different solutions (ethanol and water). The corresponding nanoporous cobalt spinel Co_3O_4 were obtained by thermal conversion and oxidization of the cobalt carbonate, and the obtained nanoporous Co_3O_4 inherit the morphologies of their precursors to some extent. There are some significant features in this work: firstly, the synthesis process is simple and easy-manipulated; secondly, this is also the first report of 3D Co_3O_4 superstructure with rhombohedral morphology, which is further assembled by uniform nanosheets as observed from its microstructure; thirdly, it provides a new method for nanoporous materials.

2. Experimental section

2.1 Synthesis

All chemical reagents were of analytical grade and used as received without purification. In a typical procedure, $\text{Co}(\text{CH}_3\text{COO})_2 \cdot 4\text{H}_2\text{O}$ (5 mmol) and urea (50 mmol) were dissolved in ethanol-water or pure ethanol solvent (30 mL). Then 0.25 g SDS was added, under stirring to form homogeneous transparent solution. The solution was then transferred into a stainless steel autoclave with a Teflon liner of 50 mL capacity, and heated in an oven at 150 °C for 24 h. After the autoclave was air-cooled to room temperature, the resulting pink product was filtered, washed with distilled water and absolute ethanol for several times, then dried the precursor at 60 °C for 12 h. Porous Co_3O_4 nanostructures were prepared by calcining the precursor in a furnace at 400 °C for 5 h in air.

2.2 Characterization

The samples were characterized by X-ray powder diffraction (XRD) with a Bruker D8-ADVANCE X-ray powder diffractometer with Cu K α radiation ($\lambda = 1.54178 \text{ \AA}$). Infrared spectra were collected by using a Nicolet Impact 400 FTIR spectrometer on KBr pellets. The morphologies and sizes of the products were observed by scanning electron microscopy (SEM). The SEM images were obtained on a LEO1530VP field-emission (FE) scanning electron microscope. Thermal gravimetric analysis (TGA) of the as-synthesized samples was carried out on a Shimadzu TA-449C thermal analyzer at a heating rate of 5 $\text{K} \cdot \text{min}^{-1}$ from room temperature to 800 °C in air. Nitrogen adsorption-desorption isotherms were measured on a Micromeritics ASAP 2010 adsorption analyzer. These isotherms were used to calculate the BET specific surface area and pore size distributions.

3. Results and discussions

Figure 1 shows the XRD patterns of the precursors and their corresponding final products. It can be seen from Figure 1a and 1b that the diffraction data are in good agreement with the standard spectrum (JCPDS, No. 78-209), indicating that the precursors correspond to CoCO_3 . Figure 1c and 1d show XRD patterns of the samples after the precursor's calcination at 400°C , respectively. The broad reflection peaks corresponding to pure cubic Co_3O_4 appearing at $2\theta = 31.27, 36.85, 44.81, 59.36$ and 65.24 can be readily indexed as $(2\ 2\ 0), (3\ 1\ 1), (4\ 0\ 0), (5\ 1\ 1)$ and $(4\ 4\ 0)$ crystal planes. All these diffraction peaks, including not only the peak positions but also their lattice parameters, can be perfectly indexed into the cubic crystalline structure of Co_3O_4 . The results are in accordance with the standard spectrum (JCPDS, No. 42-1467).

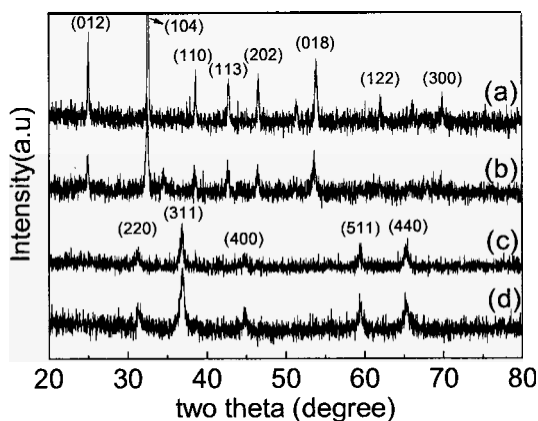


Figure 1. XRD patterns of the precursors prepared in different solutions: (A) $V_{\text{ethanol}} : V_{\text{water}} = 1:1$, (B) pure ethanol, and their corresponding final products: (c) and (d).

Figure 2 exhibits IR spectra for the precursors and the as-calcined nanoporous Co_3O_4 in different solutions. It can be seen from Figure 2a and 2b that the broad band centered at 3408 cm^{-1} and the peak at 1646 cm^{-1} are assigned to the O–H stretching and bending modes of water. C–H stretching vibrations of alkyl chains of the reagents is observed around $2850\text{--}2900\text{ cm}^{-1}$. The strong absorption band at 1425 cm^{-1} can be indexed to the ν_3 mode of CO_3^{2-} ions. The other bands at $1106, 867,$ and 746 cm^{-1} are characterized to the $\nu_1, \nu_2,$ and ν_4 modes of the carbonate ions, respectively [14]. The peaks of C–H and CO_3^{2-} ions vibrations almost disappear after calcination. In the case of Co_3O_4 nanoparticles

(Figure 2c, 2d), we observe sharp absorptions of Co(III)-O and Co(II)-O stretching vibrations at 575 and 669 cm^{-1} .

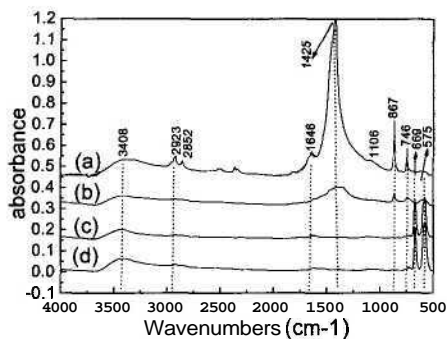


Figure 2. FT-IR spectra of the precursors prepared in different solutions: (a) $V_{\text{ethanol}} : V_{\text{water}} = 1:1$, (b) pure ethanol, and their corresponding final products: (c) and (d).

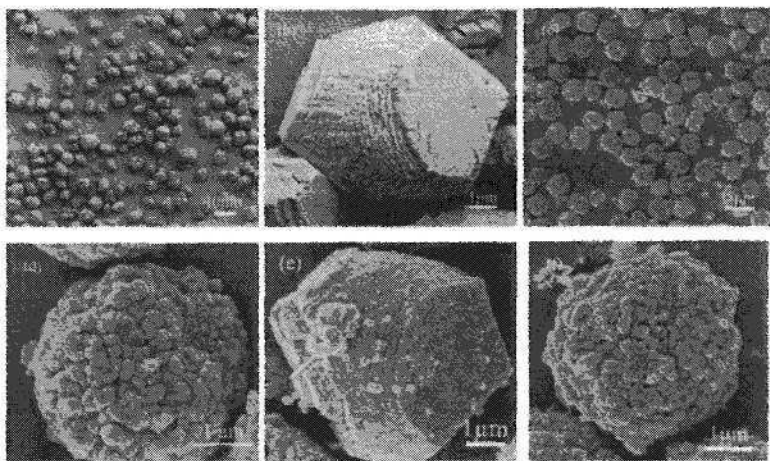


Figure 3. SEM images of the precursors prepared in different solutions: (a) and (b) $V_{\text{ethanol}} : V_{\text{water}} = 1:1$, (c) and (d) pure ethanol, and their corresponding final products: (e) and (f).

Typical SEM images of the as-prepared samples are shown in Figure 3. The images shown in Figure 3a and 3b reveal the overall morphology of the precursor obtained in ethanol-water solvent. As seen in Figure 1a, it was composed of a great deal of rhombohedral precursors with diameters from 2 to 8 μm , and the magnified image indicated these rhombohedral precursors were

assembled by uniform nanosheets (Figure 3b). In pure ethanol solvent, the morphology of the product obtained was quite different from samples obtained in ethanol-water solvent. The panoramic morphology of this sample (Figure 3c) indicates that the sample consists of uniform 3D microsphere architectures with average diameter of 3 μm . From the magnified image of a single microsphere (Figure 3d), one can find that this microsphere architecture is formed by many nanoparticles. Calcining the above precursors, the final products with similar morphology as illustrated in Figure 3e and 3f were obtained.

The thermal analysis result of the as-synthesized rhombohedral CoCO_3 is shown in Figure 4. One weight loss step at the temperature range 324–385 $^\circ\text{C}$ can be observed. The weight loss is mainly attributed to the decomposition of the cobalt carbonate. The weight loss is about 32%, which is close to the theoretical value (32.5%) calculated from the thermal decomposition of cobalt hydroxides: $3\text{CoCO}_3 + 1/2\text{O}_2 \rightarrow \text{Co}_3\text{O}_4 + 3\text{CO}_2$.

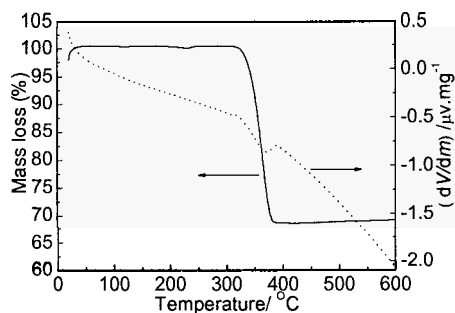


Figure 4. TG-DTA curves of the as-obtained rhombohedral cobalt carbonate.

The N_2 adsorption/desorption isotherms and the pore size distribution plots of the calcined Co_3O_4 samples are shown in Figure 5. It revealed that the isotherms belonged to type IV, which was the characteristic of most nanoporous materials. Figure 5A is the nitrogen adsorption/desorption isotherms of the rhombohedral Co_3O_4 . The rhombohedral nanoporous Co_3O_4 were obtained by calcining the precursors, which were obtained by the reaction of 7 h, 12 h and 24 h, respectively. With the extension of the reaction time, their Brunauer-Emmett-Teller (BET) surface areas are estimated to be 31.2 $\text{m}^2\cdot\text{g}^{-1}$, 35.0 $\text{m}^2\cdot\text{g}^{-1}$ and 48.9 $\text{m}^2\cdot\text{g}^{-1}$, respectively. And their pore volumes are estimated to be 0.19 $\text{cm}^3\cdot\text{g}^{-1}$, 0.18 $\text{cm}^3\cdot\text{g}^{-1}$ and 0.21 $\text{cm}^3\cdot\text{g}^{-1}$, respectively. According to the Figure 5B, the most probable pore size decreased under longer reaction time. The average pore sizes are estimated to be 24.6 nm, 21.5nm and 17.0nm, respectively.

Fig. 5C is the N_2 adsorption/desorption isotherms of the microsphere Co_3O_4 . Compared with the rhombohedral samples, the BET surface areas for the microsphere samples are larger. With the increase of the molar ratio of cobalt acetate and urea, their BET surface areas and average pore sizes are estimated to be $48.0 \text{ m}^2 \cdot \text{g}^{-1}$, 20.3 nm , $69.6 \text{ m}^2 \cdot \text{g}^{-1}$, 11.8 nm , $59.2 \text{ m}^2 \cdot \text{g}^{-1}$, 17.6 nm , $53.7 \text{ m}^2 \cdot \text{g}^{-1}$, 16.9 nm , respectively. And their pore volumes are estimated to be $0.24 \text{ cm}^3 \cdot \text{g}^{-1}$, $0.29 \text{ cm}^3 \cdot \text{g}^{-1}$, $0.26 \text{ cm}^3 \cdot \text{g}^{-1}$ and $0.23 \text{ cm}^3 \cdot \text{g}^{-1}$, respectively.

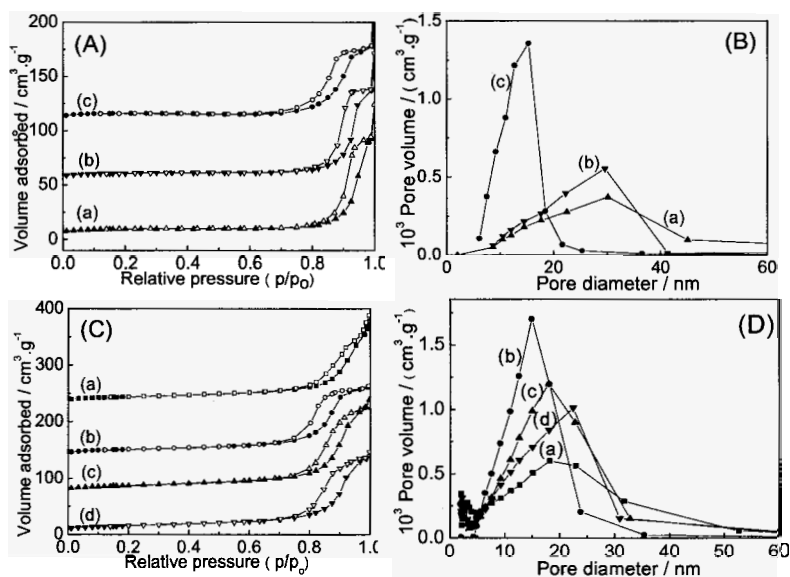


Figure 5. N_2 adsorption/desorption isotherms and the pore size distribution plots of the calcined Co_3O_4 samples: (A) and (B) rhombohedral samples obtained by calcining the precursors obtained at different reaction times: (a) 7 h, (b) 12 h, (c) 24 h; (C) and (D) microsphere samples obtained by calcining the precursors obtained in different molar ratios of cobalt acetate and urea at 24 h: (a) 1:7, (b) 1:10, (c) 1:12, (d) 1:15.

In order to investigate the effect of SDS on the framework and morphology of the product, we prepared the precursor in ethanol-water solution without SDS at 24 h. Its XRD pattern indicates that the precursor is $CoCO_3$. The morphology of the precursor obtained without SDS is different from that obtained with SDS. As seen in Figure 6, it was composed of a great deal of cubic precursors with diameter about $10 \mu\text{m}$, and the magnified image indicated these cubic precursors were assembled by nanosheets. The BET surface area for the cubic Co_3O_4 is estimated to be $32.3 \text{ m}^2 \cdot \text{g}^{-1}$. It is smaller than that of the rhombohedral Co_3O_4 ,

which is about $48.9 \text{ m}^2 \cdot \text{g}^{-1}$. The average pore size of the cubic sample is estimated to be 18.3 nm . The pore volume is estimated to be $0.15 \text{ cm}^3 \cdot \text{g}^{-1}$. We can see that SDS plays a crucial role on the framework and morphology of the product and can affect the final product's BET surface areas.

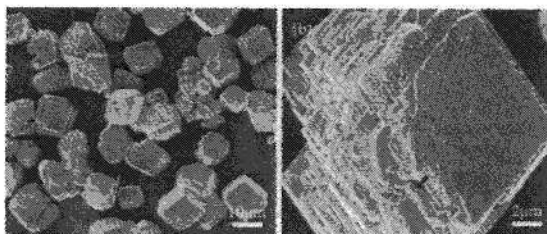
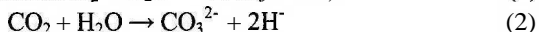


Figure 6. SEM images of the precursor prepared in ethanol-water ($V_{\text{ethanol}} : V_{\text{water}} = 1:1$) solution without SDS at 24 h. (a) low-magnification SEM image; (b) high-magnification SEM image.

The formation of cobalt carbonate involved a hydrolysis-precipitation process, in which urea afforded hydrolysis-precipitation to bivalent Co^{2+} ions. Urea, $(\text{NH}_2)_2\text{CO}$ is a non-ionic, non-toxic, cheap, stable, crystalline and water soluble compound. It decomposes and releases NH_3 and CO_2 at about 70°C , then CO_2 hydrolyzed to produce the precipitators CO_3^{2-} , which slowly deposits metal ion, and thus homogeneous precipitation of metal salt by urea hydrolysis can overcome the faults brought by directly adding precipitator into solution. The main reactions in the system can be expressed as follow:

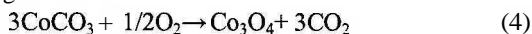


The formation of cobalt carbonate can formulate as:



These cobalt carbonate 3D assemblies formed spontaneously. The morphologies of cobalt carbonate 3D nanostructures obtained in different solvents have elucidated that reaction solvent plays a crucial role in the growth process of cobalt carbonate 3D assemblies. Besides, SDS can control the morphology of the product in the growth process of cobalt carbonate 3D assemblies. When SDS was added into the reaction system, SDS can adsorb on some crystal planes of the cobalt carbonate crystals. Through selective adsorption, surfactant can control the growth rate of different crystal planes in reaction kinetics, thus controlling the morphology of the product.

Annealing the precursor in a furnace at 400°C results in the formation of Co_3O_4 based on the following reaction:



When CoCO_3 is pyrolyzed into cubic Co_3O_4 , the three-dimensional framework remained and it released CO_2 to form the pores.

4. Conclusions

In conclusion, we successfully synthesized 3D architectures of cobalt carbonate through an easy selected-control solvothermal process via the direct reaction between cobalt salt ($\text{Co}(\text{CH}_3\text{COO})_2 \cdot 4\text{H}_2\text{O}$), urea and SDS under different solvents, in which the cobalt carbonate 3D nanostructures with morphologies of rhombohedral, and microsphere can be selectively prepared, respectively. The corresponding Co_3O_4 nanoporous materials were obtained by annealing the cobalt carbonate at $400\text{ }^\circ\text{C}$. Such nanoporous Co_3O_4 materials can be potentially utilized for catalysts and electrochromic devices.

Acknowledgements

This work was supported by Doctor Innovation Funds of Jiangsu Province (BCXJ06-13) and the National Nature Science Fund of China. (50502020)

References

1. X. He and D. Antoneili, *Angew. Chem. Int. Ed.* **41**, 214 (2001).
2. J. M. Kistler, A. Dahler, G. W. Stevens and J. O'Connor, *Microporous. Mesoporous. Mater.* **44**, 769 (2001).
3. B. A. Mccool, N. Hill, J. Dicarolo and W. J. Desisto, *J. Membr. Sci.* **218**, 55 (2003).
4. H. Parala, H. Winkler, M. Kolbe, A. Wohlfart, R. A. Fischer, R. Schmechel and H. Von-Seggern, *Adv. Mater.* **12**, 1050 (2000).
5. W. S. Chae, Y. R. Kim and J. S. Jung, *J. Phys. Chem. B.* **107**, 1585 (2003).
6. Q. Lu, F. Gao, S. Komarneni and T. E. Mallouk, *J. Am. Chem. Soc.* **126**, 8650 (2004).
7. R. L. Smith and S. D. Collins, *J. Appl. Phys.* **71**, R1 (1992).
8. C. T. Kresge, M. E. Leonowicz, W. J. Roth, J. C. Vartuli and J. S. Beck, *Nature*, **359**, 710 (1992).
9. G. A. Ei-Shobaky and A. M. Ghozza, *Mater. Lett.* **58**, 699 (2004).
10. D. Barreca, C. Massignan, S. Daolio, M. Fabrizio, C. Piccirillo, L. Armelao and E. Tondello, *Chem. Mater.* **13**, 588 (2001).
11. E. Matijevic, *Chem. Mater.* **5**, 412 (1993).
12. R. Xu and H. C. Zeng, *J. Phys. Chem. B.* **107**, 926 (2003).
13. J. Feng and H. C. Zeng, *Chem. Mater.* **15**, 2829 (2003).
14. Z. G. Zhao, F. X. Geng, J. B. Bai and H. M. Cheng, *J. Phys. Chem. C.* **111**, 3848 (2007).

SYNTHESIS OF NIOBIA NANOSTRUCTURES AND THEIR CATALYTIC AND PHOTOCATALYTIC ACTIVITY

IZABELA NOWAK, AGNIESZKA FELICZAK, KATARZYNA WALCZAK,
MONIKA DARUL

*Faculty of Chemistry, Adam Mickiewicz University
Grunwaldzka 6, Poznan, PL-60-780 Poznan, Poland*

MIETEK JARONIEC

*Chemistry Department, Kent State University
Kent, OH 44242, USA*

Nanoporous niobia with crystalline walls has been formed within the mesopores and on the outer surface of SBA-15 and FDU-1 by impregnation with niobium(V) chloride followed by calcination and silica template removal. The physicochemical properties of niobia particles was evaluated by powder X-ray diffraction, nitrogen adsorption, scanning and transmission electron microscopies, temperature programmed reduction and thermogravimetry. The resulting nanoniobia was tested in the liquid phase oxidation of cyclohexene with hydrogen peroxide and appeared to be catalytically active contrary to amorphous niobia. The nanoniobia was used in the photocatalytic removal of organic compounds from water.

1. Introduction

Nanoporous oxides can be synthesized by various methods: vapor-phase or solution-phase growth, microwave-assisted synthesis, sol-gel process, and templating synthesis and so on [1-4]. A rich variety of templates have already been employed for the preparation of nanoporous oxides including “soft” and “hard” templates, recently also called as “endo”- and “exotemplates” [5]. Typically, “hard” (“exo”) templates include channel-like alumina membranes [6], track-etched polycarbonates [7], zeolites [8], pristine [9, 10] or microwave-digested mesoporous silicas [11], carbon nanotubes [12, 13] or spheres [14] and surface-structured solid substrates [15]. Currently, nanocasting (hard-templating) involving three-dimensional (3D) mesostructured silicas as hard templates represents an attractive strategy for the synthesis of highly ordered transition metal oxides [16].

The extension of mesoporous structures into transition metal oxides represents a very important growth from the viewpoint of catalysis, adsorption,

electronics, etc. [17]. Nanocrystalline Nb_2O_5 exhibits optical and electronic properties that differ from those of bulk niobia and has also been shown to enhance catalysis. Particularly, niobia mesophases can be useful as photocatalysts. So far, mesoporous niobium oxides were prepared by ligand-assisted methods [18] or neutral templating [19].

To date, there is no report on the preparation of niobium oxide with crystalline pore walls using mesoporous silica templates and niobium(V) chloride as a metal source. In our previous study, we have employed ammonium tris(oxalate) complex of niobium(V) [20]. Bulk niobium oxides are extensively studied as heterogeneous catalysts in numerous reactions [17]. However, since the accessibility of active sites governs the reactivity, thus it is important to generate mesoporosity in such catalyst. Therefore, nanoporous niobia have been synthesized using hard- templating method.

2. Experimental

2.1. Catalyst Preparation

SBA-15 and FDU-1 templates for nanoniobia preparation were synthesized according to the previously reported procedures [21,22]. Niobium(V) precursors in the form of chloride – NbCl_5 (Aldrich; denoted later in the text as *Cl*) or ammonium tris(oxalate) complex – $(\text{NH}_4)[\text{NbO}(\text{C}_2\text{O}_4)_3]$ (CBMM – Brazil; *Co*) were introduced into the mesopores of the silica template by wetness impregnation method using aqueous or ethanol solutions, respectively. After stirring for 12 h, the mixture was filtered, washed with water three times to remove the remaining unanchored niobium species and to convert niobium precursors to hydroxide, and dried at 423 K for 5 h. The resulting sample was subjected to the programmed thermal decomposition of the niobium precursors up to 973 K in order to grow Nb_2O_5 single crystals in the silica templates. The product, niobia-silica composite, denoted later in the text as $\text{Nb-M/T-1}^{\text{st}}$ [Comp], where M is a niobium source and T denotes the silica template, was impregnated twice more with niobium precursor. The samples obtained after second and third successive impregnations are designated as $\text{Nb-M/T-2}^{\text{nd}}$ [Comp] and $\text{Nb-M/T-3}^{\text{rd}}$ [Comp], respectively. After each step of impregnation, the solid was recovered by filtration, washed, dried and calcined. The silica template was removed from the composite by treating it several times with dilute NaOH solution (2 M). The crystalline niobia is denoted as Nb-M/T , where as in the case of the niobia-silica composites M and T stand for the niobium source and silica template, respectively.

2.2. Characterization Methods

Quantitative chemical analysis was performed on Shimadzu EDX 700 equipment. X-ray diffraction (XRD) patterns were collected on a Philips PW1840 powder diffractometer using Ni-filtered CuK_α -radiation ($\lambda = 0.1542$ nm). Porosity and specific surface area were evaluated by analysis of nitrogen adsorption isotherms at 77 K measured on a Micromeritics 2010 instrument. The morphology of nanoniobia was analyzed on a Philips 515 scanning electron microscope (SEM). Thermogravimetric (TG) measurements were performed on a TA Instruments TGA 2950 thermogravimetric analyzer using a high-resolution mode. The weight change curves were recorded under nitrogen or air with a heating rate of 5 K min^{-1} up to 1273 K. Temperature-programmed reduction (TPR) was conducted using a conventional apparatus from Micromeritics (PulseChemiSorb 2705) equipped with a thermal conductivity detector. The reduction was performed by heating the sample from 298 up to 1373 K at a rate of 10 K min^{-1} using a 10 vol. % H_2/Ar mixture flow ($32 \text{ cm}^3 \text{ min}^{-1}$).

2.3. Cyclohexene Liquid Phase Catalytic Oxidation

Prior to the reaction, the catalysts were calcined at 673 K for 4 h in air to remove adsorbed water. Acetonitrile (10 cm^3) and catalyst (0.04 g) were added to a 25 cm^3 round-bottom flask that was fitted to a reflux condenser and a septum. The mixture was allowed to equilibrate at the reaction temperature of 318 K for 15 min. Then, cyclohexene (2 mmol) followed by aqueous H_2O_2 were added through the septum to the rapidly stirred solution under a flow of nitrogen. Aliquots were removed from the reaction mixture by syringe after each hour.

2.4. Photocatalysis

The photocatalytic activity experiments on the mesoporous Nb_2O_5 nanoparticles for the oxidation of toluene by hydrogen peroxide were performed at ambient temperature. The UV source was a 160 W Hg lamp with a maximum emission at approximately 365 nm. Typically, the aqueous Nb_2O_5 suspension was prepared by addition of catalyst (20 mg) to a 30 cm^3 aqueous solution containing toluene ($c_0 = 4.8 \times 10^{-5} \text{ M}$). All runs were conducted at ambient pressure and temperature. The distance between the Hg lamp and the reactor was 30 cm for each experiment. The suspension was magnetically stirred before and during illumination. The toluene solution was mixed with Nb_2O_5 for 10 min in the dark to adsorb substrates on the surface of photocatalysts, and then the reaction mixture was exposed to the UV-vis light. After irradiation and removal of the

Nb_2O_5 particles by microfiltration, the residual toluene was analyzed using a Varian Cary50 spectrophotometer.

3. Results and Discussion

3.1. Crystalline Niobia Formation

It is well known that both the silanol (Si-OH) and siloxane (Si-O-Si) groups are present on the surface of silica templates. At such conditions, niobium precursors are absorbed on the silica surface and during calcination of the impregnated silica templates there is possibility to incorporate niobium into silica framework and/or to form NbO_x species. The latter can coalesce and grow to form niobia nanoclusters. The formation of niobia-silica composites made of niobium(V) complex was characterized previously [20] and thus in this paper will be only used for comparison with new niobia precursor, i.e., niobium(V) chloride.

TGA analysis showed that the formation of hydroxide and further, oxide from niobium pentachloride was quite similar for both templates, i.e., FDU-1 and SBA-15. The template effect was more pronounced for FDU-1 probably due to the higher amount of niobium source incorporated; it seems that this incorporation was easier into 3D mesoporous structure of FDU-1 than into 2D structure of SBA-15. The crystallization temperature of the niobia-silica composites was lower in the case of niobium pentachloride than for the complex of niobium(V). There was only one peak (at ~ 400 -500 K) observed in the case of NbCl_5 used as a niobium source, which does not depend on the type of the silica template.

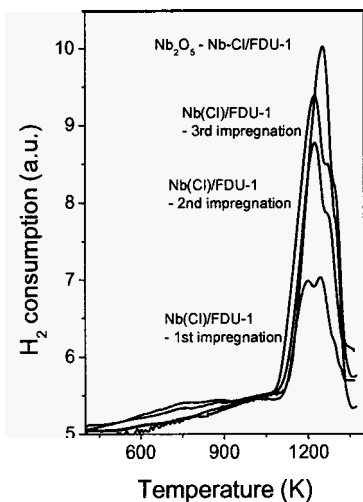


Figure 1. The H_2 -TPR profiles for the Nb-Cl/FDU-1 niobia-silica composites after 1st (a), 2nd (b) and 3rd (c) impregnation steps and for the nanoniobia material obtained after silica removal.

profiles of the $\text{Nb}_2\text{O}_5/\text{SiO}_2$ samples are shown in Figure 1. Depending on the

To further understand the chemical state of the active component, H_2 -TPR was used to characterize the chemical state of Nb species. The reduction

different factors (niobium source and silica template), the TPR profiles show one, two or three peaks over a wide temperature range (293-1273 K). It is well known that bulk Nb_2O_5 yields an intense maximum at 1100 K. For the samples prepared using niobium(V) chloride as a precursor, the one-, two- and three-time impregnated samples exhibited significant hydrogen consumption, giving the reduction profile different than that obtained for the bulk Nb_2O_5 . Taking into account the possibility of clusters formation [23] it can be postulated, that the peak at 1173 K would be assigned to the reduction of smaller niobium clusters, while that at 1223 K refers to the larger niobium clusters. It is likely that the niobia clusters become larger with increasing the niobium loading, which results in the merging of the low temperature peaks. With increasing the number of impregnations the positions of peaks shift to higher temperatures suggesting strong interaction with the silica support. The T_{max} values for the reduction of niobium species were found to increase with increasing Nb loading. The shift in T_{max} to higher temperatures with increasing Nb loading is due to the formation of crystalline Nb_2O_5 . This clearly shows that the reducibility increased with Nb loading. The area of the reduction peak, which corresponds to the amount of H_2 consumption during TPR, decreases in the following order: Nb-Cl/SBA-15-1st [Comp] < Nb-Cl/SBA-15-2nd [Comp] < Nb-Cl/SBA-15-3rd [Comp], indicating that the content of niobium oxide increases with the same order.

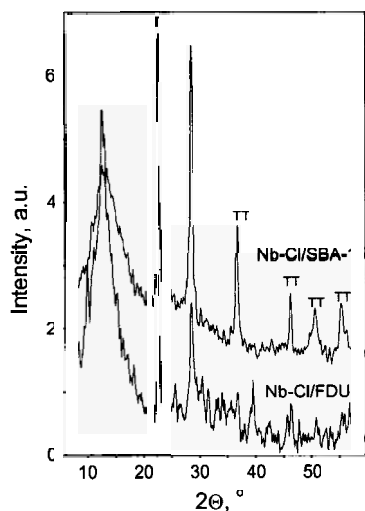


Figure 2. Wide-angle XRD patterns for the nanoniobia samples.

The low-angle powder XRD patterns for the templates, SBA-15 and FDU-1, were characteristic for the hexagonal and cubic structures, respectively. The XRD patterns of nanoniobia (not shown) were almost featureless in the range $1^\circ < 2\theta < 10^\circ$. The broadness of the main peak at the $2\theta < 4^\circ$ suggests that the mesopores in these materials were not well-aligned, indicating the formation of disordered mesopores.

Figure 2 shows the wide-angle XRD patterns for nanoniobia. As it can be seen from this figure, a very broad XRD peak at $2\theta = 13^\circ$ is originated from the diffraction of the holder used for recording diffractograms. The XRD patterns for the nanoniobia samples prepared from niobium pentachloride are

well-resolved. The sharp peaks that can be assigned to the niobia crystal phase, $\text{Ti-Nb}_2\text{O}_5$ (pseudo-hexagonal).

Energy dispersive X-ray analysis (EDAX) data showed Si, O, and Nb peaks on the profiles for mesoporous niobia/silicate composites. No Si was detected after silica etching (EDX detection limit was 0.001% w/w), confirming a complete removal of the silica template.

Nitrogen adsorption/desorption isotherms for the nanoniobia samples obtained after removal of the silica template are shown in Figure 3. Two regions of the adsorption isotherm are visible: (i) monolayer and multilayer adsorption and (ii) capillary condensation in mesopores. The shape of adsorption isotherms is typical for low surface area porous solids, which are analogous to those observed for porous transition metal oxides obtained by hard-templating method [24]. The BET surface area for the Nb-Cl/FDU-1 and Nb-Co/FDU-1 samples calculated from adsorption isotherms is in the range of $20\text{--}50\text{ m}^2\text{ g}^{-1}$. The surface area decreased from ~ 50 to $10\text{ m}^2\text{ g}^{-1}$ when SBA-15 was used instead of FDU-1. The observed loss in the surface area is attributable to the structure coalescence during crystallization of the walls separating mesopores. Subsequently, this tendency caused a significant decrease in the total pore volume.

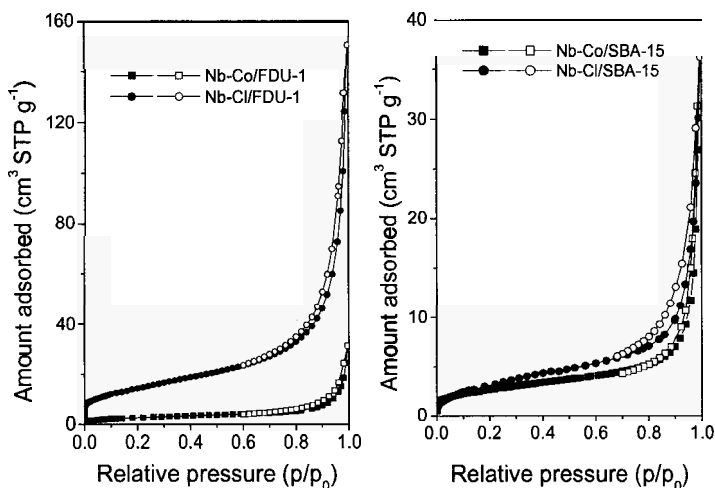


Figure 3. Nitrogen adsorption isotherms at 77 K for the nanoniobia samples

Table 1 summarizes the surface area, pore volume and particle size values for the samples studied. The particle size of nanoniobia crystals (D_{XRD}) was

estimated on the basis of peak broadening by using Scherrer's equation. The Nb-Cl/FDU-1 and Nb-Cl/SBA-15 crystals were estimated to be about 40 nm, while the sizes of Nb-Co/FDU-1 and Nb-Co/SBA-15 were smaller than 30 nm. The surface areas of the Nb-M/FDU-1 samples were larger than those of the Nb-M/SBA-15 samples.

Table 1. Textural and catalytic properties of the nanoniobia samples with crystalline walls

Sample	SBET ($\text{m}^2 \text{g}^{-1}$)	V_t ($\text{cm}^3 \text{g}^{-1}$)	D_{XRD} (nm)	Morphology	Cyclohexene conv., %	Selectivity, %	
						Epoxide	Diol
Nb-Cl/FDU-1	10	0.09	44	rope-like	45	48	52
Nb-Co/FDU-1	51	0.20	20	agglomerates	29	55	45
Nb-Cl/SBA-15	8	0.08	41	needles	8	41	37
Nb-Co/SBA-15	10	0.05	22	platelets & rods	3	23	40

The morphology of nanoniobia depended on the type of the silica template and niobium precursor. The SEM micrographs (Fig. 4A) of Nb-Cl/SBA-15 consist of fibers or needle-like particles with widths of $\sim 0.5 \mu\text{m}$. The lengths of the nanofibers (needles) vary from a few hundred nanometers up to $10 \mu\text{m}$ long. The SEM micrographs of Nb-Co/SBA-15 reveal agglomerates of very small globular particles (Fig. 4B). For Nb-Cl/FDU-1 macrostructures the rope-like agglomerates of a length about 15 nm and diameter less than $1 \mu\text{m}$ are predominant (Fig. 4C), which are bundles of necklace-shaped fibers. Analogous

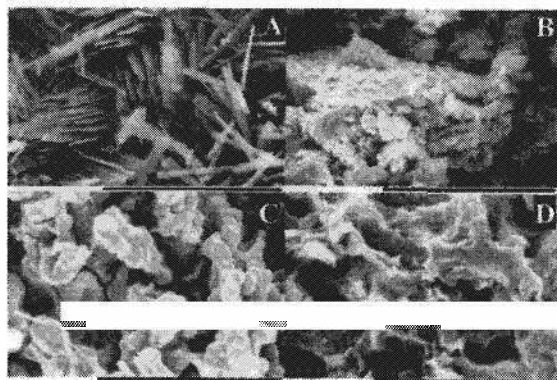


Figure 4. SEM images of nanoniobia samples: Nb-Cl/SBA-15 (A), Nb-Co/SBA-15 (B), Nb-Cl/FDU-1 (C) and Nb-Co/FDU-1 (D). The scale bars of images are $10 \mu\text{m}$.

morphology was observed for the FDU-1 template. Highly irregular morphologies, which are composed of randomly aggregated, nanosized platelets, rods and particulates, are observed in the case of Nb-Co/FDU-1 (see Fig. 4D). The SEM study of the nanoniobia particles indicates that they

may be formed in the mesopores of the silica templates as well as on their outer (external) surface. The mechanism of formation of niobium oxide particles of different morphologies is not yet clear. Nevertheless, SBA-15 and FDU-1 have

the ability to control the shape and size of the growing niobia particles. It seems that the structure of the mesoporous silica template plays a critical role in the formation of niobia because needles were not formed when the cage-like template (FDU-1) was used. Also, the niobium precursor seems to play an essential role too, as reflected by different morphologies of nanoniobia prepared from different precursors. It is likely that as in the case of formation of titania fibers [25], first NbCl_5 diffuses into the mesopores, and later, after its exposition to atmospheric moisture, the Nb species present at the pore openings and on the external surface hydrolyze and nucleate at the surface. Since niobium chloride is very reactive upon moisture exposure, niobia fibers start to grow immediately after diffusion of the salt into pores of the template.

3.2. *Catalytic and Photocatalytic Activity*

Cyclohexene oxide, cyclohexan-1,2-diol, cyclohex-2-en-1-one and cyclohex-2-en-1-ol were identified by FID gas chromatography (comparison with authentic standards) and by gas chromatography–mass spectrometry. The catalytic activity and selectivity in the oxidation of cyclohexene over various nanoniobia catalysts are shown in Table 1. Cyclohexene was oxidized to produce cyclohexene oxide as the main product, together with cyclohexan-1,2-diol and cyclohex-2-en-1-ol as by-products. In the case of oxidation reaction over the FDU-1 templated nanoporous niobia for 4 hours, the main product is cyclohexan-1,2-diol, whereas cyclohexene oxide was produced in a smaller amount. On the other hand, if this reaction was continued for 40 hours, cyclohexene oxide was formed with a yield higher than 20%. The efficiency of the oxidant (H_2O_2) was larger than 98% for all catalysts tested (not shown in Table 1). The cyclohexene conversion increased with time, while the epoxidation selectivity decreased. The reaction conversion reached a maximum level after ca. 1200 min. However, as the time proceeded, a slight decrease in the epoxidation selectivity was noticed, which was accompanied by a corresponding increase in the diol selectivity. The formation of the latter could be attributed to the secondary oxidation of epoxide.

For the SBA-15-templated nanoniobia the distribution of products was different. It seems that the hexagonal structure of SBA-15 did not provide a proper environment to produce an active catalyst (the activity did not exceed 10%). The selectivity towards cyclohex-2-en-1-ol was high (not shown in Table 1) at low conversion and rather decreased, while the selectivities towards epoxide and diol increased with time. The reduction of niobium in these samples (studied by H_2 -TPR) was rather small. Therefore, it is suggested that the suitable

oxidation/reduction properties of niobium-containing materials are necessary for achieving a good catalytic activity.

The niobia nanoparticles under study showed very high photocatalytic activity in the oxidation of toluene. The photoactivity of the calcined samples increased with increasing crystallinity and porosity of the particles. The samples prepared from niobium oxalate showed a slightly better performance (toluene was decomposed after 120 minutes) than those prepared from niobium pentachloride (135min).

4. Conclusions

It is shown that the crystalline nanoniobia prepared by using the SBA-15 and FDU-1 templates afforded particles of different morphologies. The DTG analysis indicates that the niobium precursor decomposes completely into niobium oxide above 973 K. Pure niobia was recovered by dissolution of the silica template with aqueous sodium hydroxide solution. The BET surface areas of the samples studied were in the range from a few to $60 \text{ m}^2 \text{ g}^{-1}$. The XRD patterns confirmed the crystalline nature of the calcined nanoniobia particles, which were quite active and selective in the epoxidation of cyclohexene and photodegradation of organic species in water.

Acknowledgments

I.N. thanks the Kosciuszko Foundation for supporting her research at Kent State University.

References

1. Z.R. Dai, Z.W. Pan and Z.L. Wang, *Adv. Funct. Mater.* **13**, 9 (2003).
2. L. Vayssieres, A. Hagfeldt and S.E. Lindquist, *Pure Appl. Chem.* **72**, 47 (2000).
3. G.J. de A.A. Soler-Illia, E. L. Crepaldi, D. Grosso and C. Sanchez, *Curr. Opin. Coll. Interface Sci.* **8**, 109 (2003).
4. G.J. de A.A. Soler-Illia, C. Sanchez, B. Lebeau and J.Patarin, *Chem. Rev.* **102**, 4093 (2002).
5. F. Schüth, *Angew. Chem. Int. Ed.* **42**, 3604 (2003).
6. Z.B. Zhang, D. Gekhtman, M.S. Dresselhaus and J.Y. Ying, *Chem. Mater.* **11**, 1659 (1999).
7. C.R. Martin and D.T. Mitchell, *Electroanal. Chem.* **21**, 1 (1999).
8. M.J. Edmondson, W. Zhou, S.A. Sieber, I.P. Jones, I. Gameson, P.A. Anderson and P.P. Edwards, *Adv. Mater.* **13** (2001) 1608.
9. Y.J. Han, J.M. Kim, G.D. Stucky, *Chem. Mater.* **12** (2000) 2068.

10. M.H. Huang, A. Choudrey, P. Yang, *Chem. Commun.* (2000) 1063.
11. B. Tian, X. Liu, H. Yang, S. Xie, Ch. Yu, B. Tu, D. Zhou, *Adv. Mater.* 15 (2003) 1370.
12. D. Ugarte, A. Chatelain, W.A. de Heer, *Science* 274 (1996) 1897.
13. C. Pham-Huu, N. Keller, C. Estourns, G. Ehret, J. M. Greneche, M. J. Ledoux, *Phys. Chem. Chem. Phys.* 5 (2003) 3716.
14. A. Dong, N. Ren, Y. Tang, Y. Wang, Y. Zhang, W. Hua, Z. Gao, *J. Amer. Chem. Soc.* 125 (2003) 4976.
15. M.P. Zach, K.H. Ng, R.M. Penner, *Science*, 290 (2000) 2120.
16. F. Schüth, *Chem. Mater.* 13 (2001) 3184.
17. I. Nowak, M. Ziolk, *Chem. Rev.* 99 (1999) 3603.
18. D.M. Antonelli, A. Nakahira, J.Y. Ying, *Inorg. Chem.* 35 (1996) 3126.
19. P. Yang, D. Zhao, D.I. Margolese, B.F. Chmelka, G.D. Stucky, *Chem. Mater.* 11 (1999) 2813; *Nature* 396 (1998) 152.
20. I. Nowak, M. Jaroniec, *Cat. Today*, accepted..
21. I. Nowak, M. Ziolk, M. Jaroniec, *J. Phys. Chem. B* 108 (2004) 3722.
22. I. Nowak, M. Jaroniec, *Langmuir* 21 (2005) 755.
23. M.M. Koranne, J.G. Goodwin Jr., G. Marcelin, *J. Catal.* 148 (1994) 369.
24. Y. Q. Wang, C. M. Yang, W. Schmidt, B. Spliethoff, E. Bill, F. Schuth, *Adv. Mater.* 17 (2005) 53.
25. Ch. Xiong, M. J. Kim, K. J. Balkus Jr., *Small* 2 (2006) 52.

SOFT MICROPOROUS FRAMEWORKS BASED ON OLIGOPEPTIDES

D.V. SOLDATOV

Department of Chemistry, University of Guelph, Guelph, ON, N1G 2W1, Canada

Recent studies indicate that many oligopeptides are predisposed to generating porous architectures in the solid state including the crystalline state. Certain cyclic oligomers form stacking H-bonded tubular structures with a channel inside the tube. Aliphatic oligomers form both tubular and layered porous architectures based on helix-type and β -sheet-type supermolecules. In particular, a series of hydrophobic dipeptides form microporous crystals built from H-bonded nanotubes with interstitial 1D chiral channels of 3-5 Å in diameter, the materials referred to as biozeolites. The peptide-based porous frameworks may be considered as alternatives to inorganic and metal-organic frameworks investigated to a much greater extent.

1. Introduction

A great diversity of chemical species that assemble in micro/nanoporous or inclusion architectures has been discovered or created to date [1,2]. At the same time, naturally occurring and biologically produced species are rarely used in the creation of materials with pores or other types of cavity space. The observation seems surprising as such biomaterials could create a set of evident advantages and would complement commonly used sorbents and host materials.

Peptide molecules provide an endless diversity of building elements used by the nature to create a very wide range of highly complex and self-organizing systems of life. Recent studies indicate that even the simplest peptide molecules may be used in the design of porous and inclusion frameworks. Porous materials, inclusion compounds and co-crystals based on such frameworks may be considered as alternatives to their inorganic and metal-organic prototypes in various future applications. The most evident advantages of peptide-based materials are their natural harmlessness, biocompatibility and chiral purity. Also, peptide frameworks possess bonding "softness" and can readily dissociate and reassemble under very mild conditions or change their structure and properties upon the action of external stimuli, the qualities of special interest in modern materials science [3,4].

This review is an introduction into porous frameworks formed by the very simplest peptide molecules, with two to twelve residues.

2. Cyclic Peptides

Ring-shape molecules are generally predisposed to create cavity space in solids [5-8]. Void space that is already available in the center of a cyclic molecule may combine into a channel as the molecules stack in a hollow tube (Figure 1, left). Three of the six possible stereoisomeric **cyclo- β -tetrapeptides** derived from 3-aminobutanoic acid (Figure 2, left) were found to form tube-like, H-bonded stacks in the solid state [9]. A similar structure was also observed earlier for another **cyclo-tetrapeptide** [10]. The external diameter of the **nanotubes** formed is about 8-9 Å, while the diameter of the inner channel does not exceed 2 Å and cannot host any guest molecules.



Figure 1. Formation of tubular cavity space by cyclic molecules (left) and a helical **supermolecule** (right).

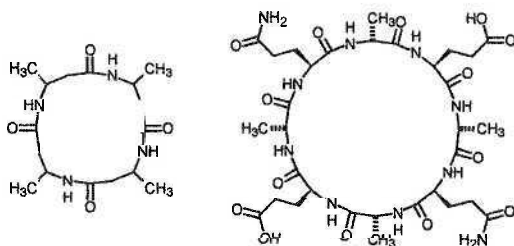


Figure 2. Examples of cyclic oligopeptides that form H-bonded nanotubes: **β -tetrapeptide** derived from 3-aminobutanoic acid (three of six possible **stereoisomers** were studied) [9] (left) and cyclo[**(D-A-E-D-A-Q)₂**] octapeptide [11] (right).

A series of **cyclo-octapeptides** (one is shown in Figure 2, right) was studied by Ghadiri and co-authors [11-14]. These molecules with alternating sequence of D and L residues adopt a ring-shaped flat conformation, with the external diameter from 12 Å and inner diameter of 6-7 Å. The rings form a rigid hollow tube fortified by eight H-bonds between every two neighbors. The tube exists both in solution and in crystal and may host the molecules of solvent. The strategy of using a sequence of alternating **chirally isomeric** residues seems to work on a **cyclo-hexapeptide** [15] and **cyclo-dodecapeptide** as well [16].

Other cyclic peptides were reported to form crystalline inclusion compounds, two cyclo-hexapeptides with alternating D and L residues, (D-V-L-V)₃ and (D-F-L-F)₃ [17], and a naturally occurring peptide ascidiacyclamide (containing four amino acid residues and four heterocyclic fragments) [18]. In both cases the peptide molecules keep a ring shape but they do not combine in tubes. Guest species reside either inside or outside the ring and the host-guest interactions vary from strong H-bonds [17] to weak H-bonds or van der Waals forces only [18].

Big cyclic peptides usually do not retain the ring shape and do not form nanotubes. A series of crystalline inclusion compounds was reported for cyclosporin A [19], a natural undecapeptide also used as a drug (Sandimmune[®], Cycloral[®]), and its derivatives [20-23]. The ring shape of the molecules is distorted to other conformations [24] due to intramolecular H-bonds and the topology of cavity space in the clathrates is different from that in a tubular architecture.

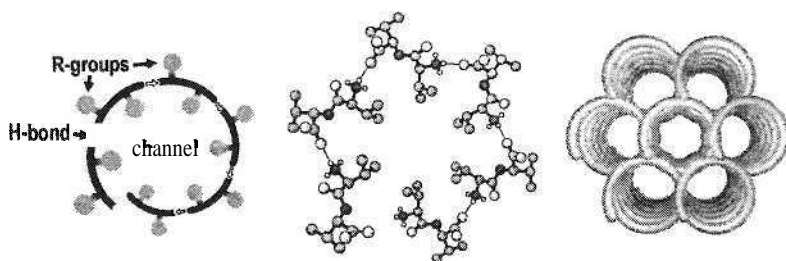


Figure 3. The formation of hydrophobic micropores in crystalline dipeptides: helical assembly of the molecules producing a hollow nanotube (left); VV, a fragment of the crystal structure (only amine H-atoms are shown) [25] (middle); the assembly of the peptide nanotubes in a crystal [25] (right).

3. Aliphatic Peptides

3.1. Dipeptides - Hydrophobic Channels. Biozeolites

The tubular cavity topology of stacking rings may be alternatively achieved through the assembly of small molecules into a giant helical supermolecule (Figure 1). The molecule forms a hollow nanotube with a channel that, in contrast to the channel formed by the stacking rings, always will be essentially chiral. A scheme illustrating such assembly is given in Figure 3.

Microporous crystals based on assembled helical nanotubes were obtained for the eight dipeptides listed in Figure 4. All crystals are hexagonal; the crystal

structures are very similar for all dipeptides except for LS. In order to build the helix, the dipeptide molecules adopt a *trans* conformation in which the two R-groups are on the opposite sides of the peptide backbone (Figure 3, middle). In the crystal, the tubes assembly as shown in Figure 3, right (except for LS); each nanotube H-bonds to and slightly overlaps with six neighboring nanotubes which also contribute to the walls of a channel running inside. As a result, the channel is essentially hydrophobic. The tubular structure appears to be surprisingly stable as the seven dipeptides (all except LS) crystallize in microporous form even in the absence of any guest template [25,26].

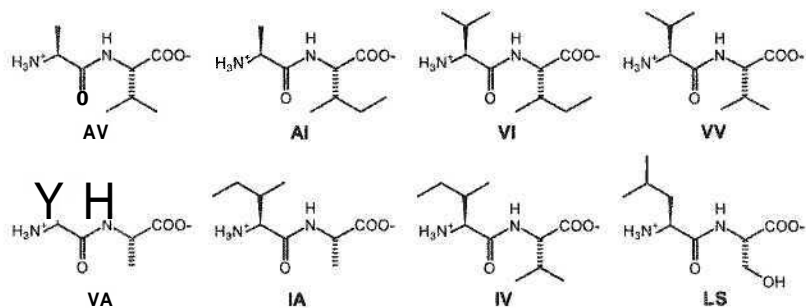


Figure 4. Dipeptides that form hexagonal crystals with hydrophobic micropores (biozeolites) [25].

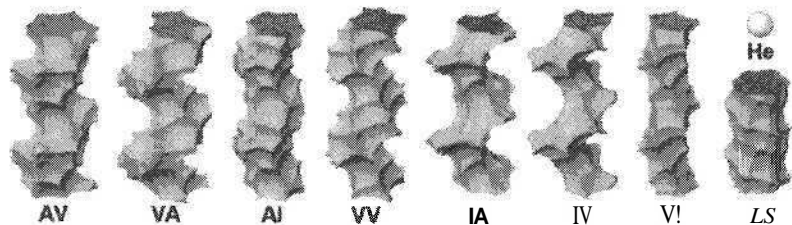


Figure 5. The shape and dimensions of the micropores in eight dipeptides (for formulas see Figure 4) compared with the helium atom (van der Waals radius of 1.4 Å) [25].

Direct sorption measurements conducted for the bulk materials indicated that from 4 to 13% of the materials' volume was reversibly accessible to He and Xe gases [25,26] and the materials were referred to as biozeolites, a bio-related group of organic zeolite mimics [25,27,28]. As illustrated in Figure 5, each biozeolite has a unique geometry of its microporous space and may be selective to a particular guest molecule. For example, the sorption of Xe gas in VA is four times more energetically favorable than in AV [26]. Ideally, for each given guest

species a highly selective biozeolite material could be designed with the objective of, for example, separating a component from a complex mixture, or trapping a pollutant from the environment. The geometric parameters of the micropore channels are compared in Table 1. The average diameter varies from ~ 3 to ~ 5 Å, while the helicity of the channels ranges from 0.1 to 1.1 Å.

Table 1. Parameters of micropores in crystalline dipeptides (see Figures 4 and 5) [25].

Dipeptide	AV	VA	AI	VV	IA	IV	VI	LS
Total porosity*, % from He pycnometry	12.5	11.2	8.3	6.9	5.7	4.8	3.7	5.1
Average diameter*, Å from He pycnometry	5.4	5.1	4.3	4.0	3.6	3.4	3.2	4.3
Average diameter, Å from XRD	5.0	4.7	4.7	4.4	3.7	3.9	3.7	4.9
Helicity**, Å from XRD	0.6	1.1	0.6	0.6	1.0	0.9	0.3	0.1

* Experimental error 2-5%.

** Average deviation of the channel center from a straight line (channel axis).

3.2. Dipeptides – Hydrophilic Channels

A third way of tubular topology organization is illustrated by a series of dipeptides listed in Figure 6. All these dipeptides form tubular supermolecules by wrapping a two-dimensional H-bonded sheet. The case of FF dipeptide [30] is illustrated in Figure 7. Each molecule is H-bonded to two neighbors on one side (using two H-atoms at N1) and to two neighbors on another side (using O2 and O3), the assembly being head-to-tail. In order to build such tube, the dipeptide molecules should adopt a cis-conformation in which the two R-groups are on the same side of the peptide backbone. As a result, the side hydrophobic fragments reside on outer surface of the tube, while inner surface is hydrophilic. In particular, a spare N-H bond of the terminal N-atom sticks inside the internal space of the channel.

Reportedly [31], FF dipeptide can also form self-assembled discrete nanotubular structures related to so-called amyloid fibrils [32], naturally occurring nanoobjects associated with Alzheimer's disease and other disorders. The structure of these discrete nanotubes was shown to be identical to that in the crystal structure of the dipeptide as illustrated in Figure 7 [33]. A modified version of FF dipeptide [34] and IF dipeptide [35] were found to assembly in similar discrete nanotubes as well.

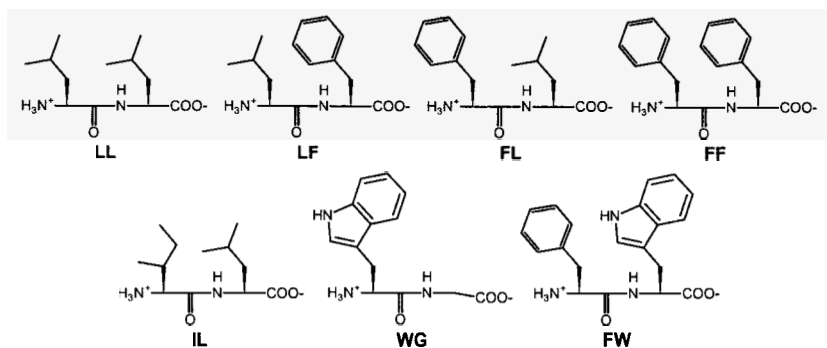


Figure 6. Dipeptides that form crystals with hydrophilic channels occupied by water [29]

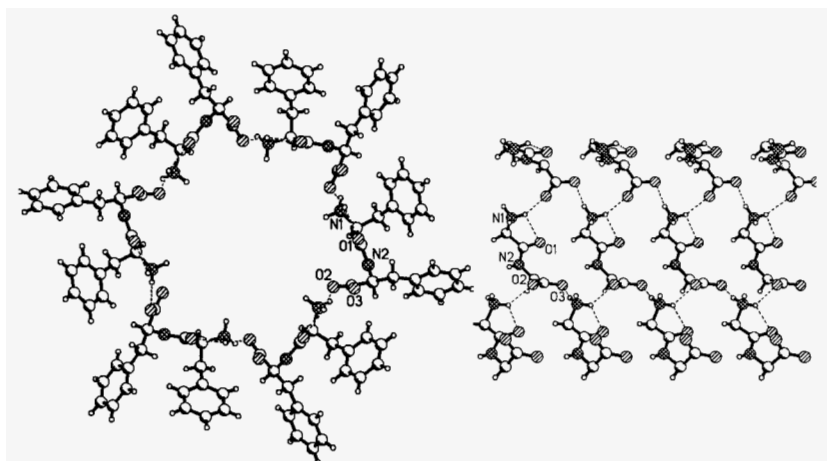


Figure 7. The formation of a hydrophilic channel in the hydrated crystal of FF dipeptide [30]: H-bonded nanotube along its axis (left) and a side view showing one half of the nanotube (side R-groups are omitted for clarity) (right).

In contrast to dipeptides forming biozeolites, the dipeptides with hydrophilic channels have bulkier hydrophobic R-groups (cf. Figures 4 and 6). Their crystals display a diversity of crystal structures, with crystal symmetry ranging from monoclinic (LF [30], IL [36]) and orthorhombic (LL [30], FL [30], FW [37]) to tetragonal (WG [38]) and hexagonal (FF [30]), and a variety of channel diameters (Table 2). As a rule, the dipeptides crystallize as hydrates with ~ 1 to

~2.5 moles of water per mole of dipeptide. The guest water molecules reside inside the channel and are attached through H-bonds to the walls.

Table 2. Approximate diameter (Å) of hydrophilic channels in hydrated dipeptide crystals as reported in [29] (for formulas see Figure 6).

Dipeptide	LL	LF	FL	FF	IL	WG	FW
Diameter	3.2	3.2	4.2	9.2	3.2	4.7	2.8

3.3. Layered Structures

The formation of H-bonded layers is very typical for peptide molecules. So-called pleated β -sheet is one of two most common structural patterns observed in higher peptides (another one is α -helix). The β -sheet is a very stable 2D supermolecule which makes it possible to realize all possible H-bonds at the backbone of a peptide molecule.

Similar layered structures are observed frequently in lower peptides. Two examples are illustrated in Figure 8. The H-bonded layer found in the clathrate of LL dipeptide with dimethylsulfoxide [39] (Figure 8, top) has a parallel arrangement of LL molecules. Each molecule forms six strong, charge-assisted H-bonds with four neighbors (using two H-atoms at N1 and oxygen atoms O2 and O3). In addition, the molecule forms two weaker H-bonds to two extra neighbors (using H-atom attached to N2 and atom O1). The third H-atom at N1 sticks out of the layer and contributes to H-bonding between the layer and guest molecules.

In contrast, the H-bonded layer found in the clathrate of LLL tripeptide with 2-methylpyridine [40] (Figure 8, bottom) has an antiparallel arrangement of LLL molecules. Head-to-tail bonded chains of the peptide molecules are further associated in distinctive bands consisted of two such chains. Each molecule forms eight H-bonds with three neighbors in the same band and two H-bonds with a fourth neighbor from an adjacent band. Again, one H-atom at N1 sticks out of the layer and contributes to H-bonding between the layer and guest molecules.

The 2D H-bonded layers form a packing of van der Waals type in the third dimension. The bulky R-groups of the leucyl residues prevent close packing and cavity space is formed between the layers. The mode of packing of the layers and the location of guests is shown schematically in Figure 9. The guest molecules are included in the residual voids and additionally attached to the host layer by H-bonds. In the LL inclusion the layer is symmetric, that is equivalent from both sides, while in the LLL inclusion the layer is asymmetric. Although other known

inclusion compounds of simple peptides vary in their structure, the basic structural motif illustrated in Figure 9 is usually preserved.

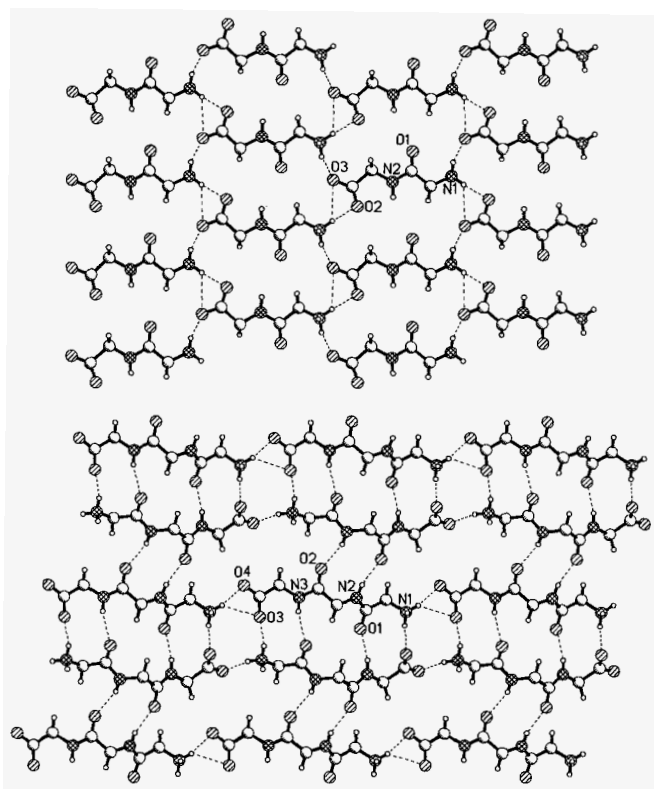


Figure 8. The structure of peptide H-bonded layer as found in inclusion compounds of LL with dimethylsulfoxide (top) and LLL with 2-methylpyridine (bottom). Side R-groups are omitted for clarity. Only strong H-bonds are shown (dashes).

A series of layered inclusion compounds was reported for LL dipeptide, with dimethylsulfoxide [39], ethanol, propanol, isopropanol [41] and isobutanol [42], and for LLL tripeptide, with methanol/water [43], pyridine and methylpyridines [40]. With LA dipeptide, inclusion compounds with dimethyl-, benzyl methyl- and isobutyl methyl-sulfoxides were obtained [44,45]. A number of inclusions with various guests was reported for arylglycyl-aryl-glycine dipeptides [46-49]. Reported examples of layered inclusion compounds of other

tripeptides include those of VVV [50], GLY [51-53] and KYS [54]. An inclusion with modified D-V-A-L-A tetrapeptide was also isolated [55]. Although even more inclusions have been reported so far, most of them were obtained by accident and almost no studies specifically aimed at the creation of cavity space in these materials have been conducted.

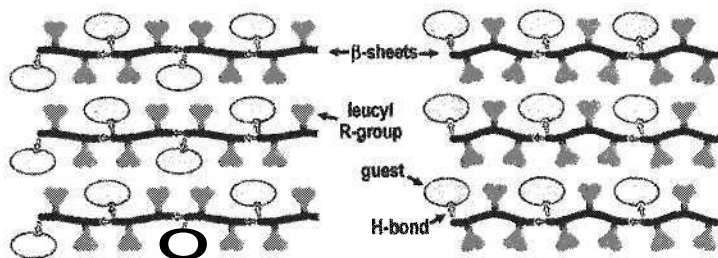


Figure 9. Typical host-guest arrangements in crystalline inclusion compounds of LL dipeptide (left) and LLL tripeptide (right).

4. Bonding Softness in Peptide Frameworks

Peptide frameworks are based on H-bonds which, in combination with van der Waals forces, endow peptide crystals with a remarkable property referred here as "softness". The crystals may undergo significant structural changes reversibly occurring both on micro- and macro-levels.

Changes on the micro-level are responsible for the diffusion of Xe atoms (van der Waals diameter 4.3 Å) inside very narrow channels (with diameter <4 Å) of some biozeolites (Table 1). Both the experimental observations [25] and calculations [56] indicate that the apparent "elasticity" of the pores is based on a complex dynamic process where the soft host framework is an active participant.

Changes on the macro-level can be directly observed, frequently as crystal-to-crystal transformations, for a single crystal subjected to either guest sorption or guest exchange. In particular, the distortion of the crystal symmetry for VA [57] and the formation of a superstructure for AV [58] caused by, correspondingly, the inclusion and replacement of a guest were reported.

The above observations put forward the flexibility of peptide frameworks as a major factor complicating the relation between the crystal structure and bulk properties of a porous peptide material. On the other hand, the softness of peptide crystals may create new opportunities for their applications. For example, the stacking of the H-bonded p-sheets in the layered structures is controlled in the third dimension by van der Waals forces only, giving the

flexibility for much larger guest molecules to be accommodated in the interlayer cavity space. Therefore, the incorporation in the peptide matrix of pharmaceuticals, flavors and odors becomes possible to facilitate the delivery, preservation or storage of these important bio-related substances.

References and Notes

1. J. L. Atwood, J. E. D. Davies and D. D. MacNicol (eds.), *Inclusion Compounds*, vols. 1-3, Academic Press, London, 1984; vols. 4-5, Oxford University Press, Oxford, 1991.
2. J. L. Atwood, J. E. D. Davies, D. D. MacNicol and F. Vögtle (eds.), *Comprehensive Supramolecular Chemistry*, vols. 1-11, Pergamon, Oxford, 1996.
3. D. V. Soldatov, "Soft and Smart Materials", in J. L. Atwood and J. W. Steed (eds.), *Encyclopedia of Supramolecular Chemistry*, Marcel Dekker, New York, 2004, pp. 1302-1306.
4. D. V. Soldatov, "Stimuli-Responsive Supramolecular Solids: Functional Porous and Inclusion Materials", in M. W. Urban (ed.), *Stimuli-Responsive Polymeric Films and Coatings*, ACS, Washington, 2005, pp. 214-231. [D. V. Soldatov, *ACS Symp. Ser.* **912**, 214 (2005).]
5. D. V. Soldatov, *J. Chem. Crystallogr.* **36**, 747 (2006).
6. T. Kawase, H. R. Darabi and M. Oda, *Angew. Chem. Int. Ed.* **35**, 2664 (1996), and refs. 4-7 therein.
7. H. Schwierz and F. Vögtle, *J. Inclusion Phenom.* **37**, 309 (2000), and refs. therein.
8. L. Dobrzanska, G. O. Lloyd and L. J. Barbour, *New J. Chem.* **31**, 669 (2007), and refs. 8b, 9 therein.
9. D. Seebach, J. L. Matthews, A. Meden, T. Wessels, C. Baerlocher and L. B. McCusker, *Helv. Chim. Acta* **80**, 173 (1997).
10. I. L. Karle, B. K. Handa and C. H. Hassall, *Acta Crystallogr.* **B31**, 555 (1975).
11. M. R. Ghadiri, J. R. Granja, R. A. Milligan, D. E. McRee and N. Khazanovich, *Nature* **366**, 324 (1993).
12. M. R. Ghadiri, K. Kobayashi, J. R. Granja, R. K. Chadha and D. E. McRee, *Angew. Chem. Int. Ed.* **34**, 93 (1995).
13. T. D. Clark, J. M. Buriak, K. Kobayashi, M. P. Isler, D. E. McRee and M. R. Ghadiri, *J. Am. Chem. Soc.* **120**, 8949 (1998).
14. D. T. Bong, T. D. Clark, J. R. Granja and M. R. Ghadiri, *Angew. Chem. Int. Ed.* **40**, 988 (2001).
15. X. Sun and G. P. Lorenzi, *Helv. Chim. Acta* **77**, 1520 (1994).
16. N. Khazanovich, J. R. Granja, D. E. McRee, R. A. Milligan and M. R. Ghadiri, *J. Am. Chem. Soc.* **116**, 6011 (1994).

17. V. Pavone, E. Benedetti, B. Di Blasio, A. Lombardi, C. Pedone, L. Tomasich and G. P. Lorenzi, *Biopolymers* **28**, 215 (1989).
18. T. Ishida, Y. In, M. Doi, M. Inoue, Y. Hamada and T. Shioiri, *Biopolymers* **32**, 131 (1992), and ref. 9 therein.
19. A. Jegorov, M. Hušák, B. Kratochvíl and I. Císarová, *Cryst. Growth Des.* **3**, 441 (2003), and refs. 9, 10, 14 therein.
20. D. Seebach, S. Y. Ko, H. Kessler, M. Köck, M. Reggelin, P. Schmieder, M. D. Walkinshaw, J. J. Bölsterli and D. Bevec, *Helv. Chim. Acta* **74**, 1953 (1991).
21. E. Pohl, R. Herbst-Irmer, G. M. Sheldrick, Z. Dauter, K. S. Wilson, J. J. Bölsterli, P. Bollinger, J. Kallen and M. D. Walkinshaw, *Helv. Chim. Acta* **78**, 355 (1995).
22. M. Hušák, B. Kratochvíl, M. Buchta, L. Cvak and A. Jegorov, *Collect. Czech. Chem. Commun.* **63**, 115 (1998).
23. A. Jegorov, L. Cvak, A. Husek, P. Šimek, A. Heydova, J. Ondráček, S. Pakhomova, M. Hušák, B. Kratochvíl, P. Sedmera and V. Havlíček, *Collect. Czech. Chem. Commun.* **65**, 1317 (2000).
24. B. Kratochvíl, M. Hušák, A. Jegorov, *Chem. Listy* **95**, 9 (2001).
25. D. V. Soldatov, I. L. Moudrakovski, E. V. Grachev and J. A. Ripmeester, *J. Am. Chem. Soc.* **128**, 6737 (2006).
26. D. V. Soldatov, I. L. Moudrakovski and J. A. Ripmeester, *Angew. Chem. Int. Ed.* **43**, 6308 (2004).
27. D. V. Soldatov and J. A. Ripmeester, "Organic Zeolites", in A. Sayari and M. Jaroniec (eds.), *Nanoporous Materials IV*, Elsevier, Amsterdam, 2005, pp. 37-54. [D. V. Soldatov and J. A. Ripmeester, *Stud. Surf. Sci. Catal.* **156**, 37 (2005).]
28. We use the term "biozeolites" to emphasize both zeolite-like sorption behavior of the dipeptides and their bio-related composition. Previously, some non-solids such as biological slimes and activated sludges also were referred to as "biozeolites" for their zeolite-like adsorbent properties. E. J. Theriault, *Ind. Eng. Chem.* **27**, 683 (1935).
29. C. H. Görbitz, *Chem. Eur. J.* **13**, 1022 (2007).
30. C. H. Görbitz, *Chem. Eur. J.* **7**, 5153 (2001).
31. S. Gilead and E. Gazit, *Supramol. Chem.* **17**, 87 (2005), and refs. therein.
32. D. Hamada, I. Yanagihara and K. Tsumoto, *Trends Biotechnol.* **22**, 93 (2004).
33. C. H. Görbitz, *Chem. Commun.*, 2332 (2006).
34. M. Gupta, A. Bagaria, A. Mishra, P. Mathur, A. Basu, S. Ramakumar and V. S. Chauhan, *Adv. Mater.* **19**, 858 (2007).
35. N. S. de Groot, T. Parella, F. X. Aviles, J. Vendrell and S. Ventura, *Biophys. J.* **92**, 1732 (2007).
36. C. H. Görbitz, *Acta Crystallogr.* **E60**, o626 (2004).

37. C. H. Görbitz, *Acta Crystallogr.* **C62**, o328 (2006).
38. H. Birkedal, D. Schwarzenbach and P. Pattison, *Angew. Chem. Int. Ed.* **41**, 754 (2002), and ref. 11 therein.
39. S. N. Mitra and E. Subramanian, *Biopolymers* **34**, 1139 (1994).
40. T. J. Burchell, D. V. Soldatov, G. D. Enright and J. A. Ripmeester, *CrystEngComm.* **9**, 922 (2007).
41. C. H. Görbitz, *Acta Chem. Scand.* **52**, 1343 (1998).
42. C. H. Görbitz, *Acta Crystallogr.* **C55**, 670 (1999).
43. K. Go and R. Parthasarathy, *Biopolymers* **36**, 607 (1995).
44. S. N. Mitra, L. Govindasamy and E. Subramanian, *Acta Crystallogr.* **C52**, 2871 (1996).
45. M. Akazome, A. Hirabayashi, K. Takaoka, S. Nomura and K. Ogura, *Tetrahedron* **61**, 1107 (2005).
46. M. Akazome, T. Takahashi, R. Sonobe and K. Ogura, *Tetrahedron* **58**, 8857 (2002).
47. M. Akazome, K. Senda and K. Ogura, *J. Org. Chem.* **67**, 8885 (2002).
48. M. Akazome and K. Ogura, *J. Synth. Org. Chem. Jpn.* **61**, 605 (2003).
49. M. Akazome, A. Hirabayashi and K. Ogura, *Tetrahedron* **60**, 12085 (2004), and refs. 5, 6, 8 therein.
50. B. Dittrich, T. Koritsánszky and P. Luger, *Angew. Chem. Int. Ed.* **43**, 2718 (2004).
51. R. Parthasarathy and E. Subramanian, *Curr. Sci.* **56**, 1210 (1987).
52. S. Wu, B. Tinant, J.-P. Declercq and M. Van Meerssche, *Bull. Soc. Chim. Belg.* **96**, 275 (1987).
53. B. Dalhus and C. H. Görbitz, *Acta Crystallogr.* **C52**, 2087 (1996).
54. N. Verdager, I. Fita and J. A. Subirana, *Int. J. Biol. Macromol.* **12**, 315 (1990).
55. V. Bobde, S. Durani, V. Pattashi and C. Sadasivan, *Int. J. Peptide Protein Res.* **45**, 332 (1995).
56. I. Moudrakovski, D. V. Soldatov, J. A. Ripmeester, D. N. Sears and C. J. Jameson, *Proc. Natl. Acad. Sci. USA* **101**, 17924 (2004).
57. C. H. Görbitz, *CrystEngComm.* **7**, 670 (2005).
58. C. H. Görbitz, *Acta Crystallogr.* **B58**, 849 (2002).

MESOPOROUS POLYMERS WITH CONTROLLED POROSITY AND FUNCTIONALITY DERIVED FROM SEMI-DEGRADABLE DIBLOCK COPOLYMERS

B. GORZOLNIK, J. PENELLE, AND D. GRANDE[†]

*Institut de Chimie et des Matériaux Paris-Est, UMR 7182 CNRS – Université Paris XII,
2, rue Henri Dunant, 94320 Thiais, France*

R. SEGUELA, V. MIRI,

*Laboratoire de Structure et Propriétés de l'Etat Solide, UMR 8008 CNRS – Université
Lille 1, 59655 Villeneuve-d'Ascq, France*

P. DAVIDSON

*Laboratoire de Physique des Solides, UMR 8502 CNRS – Université Paris-Sud, 91405
Orsay, France*

R. DENOYEL

*Laboratoire MADIREL, UMR 6121 CNRS – Université de Provence, 13331 Marseille,
France*

Polystyrene-*b*-poly(D,L-lactide) (PS-*b*-PLA) block copolymers with functional groups at the junction between both blocks were successfully synthesized, and subsequently used as precursors to functionalized mesoporous polystyrene membranes through the selective degradation of the PLA block. We used the combination of living anionic or Atom Transfer Radical Polymerization (ATRP) and Ring-Opening Polymerization (ROP) techniques in order to prepare well-defined diblock copolymers with carboxylic or amino functionalities at the junction between the PS and PLA blocks. By the proper design of the copolymer composition and a good control over the polymerization conditions, polymers with preferentially cylindrical morphology (PLA cylinders in PS matrix) were obtained. The PLA block could be removed by base hydrolysis, leaving behind porous PS membranes with functional groups located along the walls of the channels.

1. Introduction

Porous polymeric materials have recently attracted considerable attention due to their established and potential applications in many areas, including advanced

[†] Corresponding author: Ph +33 (0)1.49.78.11.77; Fax +33 (0)1.49.78.12.08; e-mail: grande@icmpe.cnrs.fr

filtration or separation techniques, heterogeneous catalysis and template-assisted synthesis of nanoobjects [1]. However, it is still a key challenge to prepare mesoporous organic materials with tunable morphology (pore size and pore size distribution) and functionality, while maintaining good mechanical properties and high chemical stability of the matrices. The synthesis of mesoporous polymeric structures can be accomplished by a variety of approaches such as template-oriented routes, *e.g.* supramolecular self-assembly, or selective degradation of one sub-network in Interpenetrating Polymer Networks (IPNs) [2]. A smart route relies on the synthesis of block copolymer precursors, which are known to self-organize into distinct well-ordered morphologies, followed by the selective removal of one of the blocks [3]. The block copolymer approach provides an excellent way to design mesoporous materials in a membrane form, with a high level of control over the porosity and the surface functionality of the pores [4].

In the present work, we report on the fabrication of functionalized (meso)porous polystyrene membranes obtained from diblock copolymers of polystyrene and poly(D,L-lactide) (PS-*b*-PLA) with a functional group (such as COOH or NH₂) at the junction between both blocks. A cylindrical morphology (PLA cylinders in PS matrix) is aimed for the polymeric precursors, which can be achieved by the proper selection of the copolymer composition and a good control over the polymerization conditions. The PLA block is then selectively removed either by base or acidic hydrolysis, leaving behind the porous PS membrane with functional groups located along the walls of the channels.

2. Experimental

2.1. Materials

All polymerizations were performed using standard Schlenk techniques under argon. Amine end-terminated polystyrene (PS-NH₂) ($M_n = 36.6 \text{ kg}\cdot\text{mol}^{-1}$, $M_w/M_n = 1.08$) was synthesized by anionic polymerization as described before [5]. 2-Hydroxyethyl-2-bromopropionate (HEBP) was synthesized as described previously [6]. CH₂Cl₂ (SDS, France) was dried over P₂O₅ and distilled directly into the reaction flask before use. Toluene (SDS, France) was dried over sodium and stored over freshly activated 4 Å molecular sieves until needed. CuBr (99% Aldrich) was stirred in glacial acetic acid, washed with acetone and dried under vacuum at room temperature. Styrene (Aldrich) was stirred over KOH and distilled over CaH₂ under vacuum just before use. D,L-lactide (Aldrich), 4-dimethylaminopyridine (DMAP, Aldrich), anisole (Aldrich), 1,1,4,7,7-

pentamethyldiethylenetriamine (PMDETA, 99%, Aldrich), tin (II) 2-ethylhexanoate ($\text{Sn}(\text{Oct})_2$, ~95%, Aldrich) and methanol (SDS) were used as received.

2.2. Synthesis of PS-b-PLA with NH_2 Functionality

0.825 g (0.023 mmol) of PS- NH_2 , 1.1 g (7.64 mmol) of D,L-lactide and 0.11 g (0.09 mmol) of DMAP were introduced into a dry and carefully purged with argon Schlenk flask, under an argon stream. The components were freeze-dried from toluene and dried overnight under vacuum. Afterwards, 5 mL of CH_2Cl_2 were directly distilled to the reaction flask and the solution was sealed via a Teflon[®] valve. The polymerization was carried out for 12 days at 40 °C. The polymerization mixture was diluted with CH_2Cl_2 , and the polymer was precipitated into methanol twice. The polymer was filtered and dried in vacuum at room temperature, up to constant weight. Yield: 0.99 g (51 %).

2.3. Synthesis of PS-b-PLA with COOH Functionality

In a typical experiment, 10 g (69.5 mmol) of D,L-lactide and 0.168 g (1.168 mmol) of CuBr were introduced into a dry and carefully purged with argon Schlenk flask. The components were freeze-dried from toluene and dried overnight under vacuum. 13.5 mL (117.7 mmol) of styrene, 20 mL of anisole, 0.21 mL (1.0 mmol) of PMDETA and 0.18 mL (0.76 mmol) of $\text{Sn}(\text{Oct})_2$ were added *via* oven-dried syringes. The flask was degassed under vacuum and back-filled with argon three times. 0.163 g (0.83 mmol) of HEBP was introduced and the flask was immersed in an oil bath at 110 °C. After polymerization, the solution was diluted with CH_2Cl_2 and precipitated into methanol, filtered, dissolved in CH_2Cl_2 and purified by fractional precipitation into methanol. Three fractions were isolated: the first and the last fractions were rich in homopolymers (PS and PLA, respectively), while the middle one contained the purified block copolymer. The obtained product was dried under vacuum up to constant weight. Yield of the middle fraction: 10.44 g (47 %).

2.4. Sample processing and alignment of block copolymers

An oscillatory shear flow procedure was used to orient nanodomains in block copolymer samples. First, 50 mg of polymer powder was warm-pressed (at a temperature of 160 °C and a pressure of 10 Psi) to form a 1 mm thick cylindrical tablet of 8 mm diameter. During the first 30 min, the sample was allowed to fill the mould at the mentioned temperature and was subsequently exposed to normal

atmosphere. Tablets of the block copolymer were then loaded in a 8 mm parallel plate geometry of an Ares Rheometer (Rheometric Scientific) equipped with a 2KFRT transducer. All tests were performed under stress controlled – dynamic mode. Typical conditions for the oscillatory shear flow alignment were 100-105 °C, 12-20 % strain amplitude, and a frequency of 1 Hz.

2.5. Selective Hydrolysis of PLA

The PS-*b*-PLA samples were placed in a water/ methanol mixture (MeOH/H₂O = 40/60 vol. %) containing 0.5 M NaOH at 65 °C. Alternatively, degradation was performed in a 6 M HCl solution at 80 °C. Typically, 1 to 5 days were needed to completely remove the PLA block.

2.6. Analytical Techniques

Size Exclusion Chromatography (SEC) was performed on a system equipped with a Spectra Physics P100 pump, two Polymer Laboratories polystyrene-divinylbenzene columns, and a Shodex RI71 refractive index (RI) detector. The eluent was tetrahydrofuran (THF) at a flow rate of 1 mL.min⁻¹. Calibration curves were obtained with polystyrene standards. ¹H NMR was performed on a Bruker Avance II 400 MHz spectrometer system in CDCl₃. Scanning Electron Microscopy (SEM) was performed with a LEO 1530 microscope at low operating voltage (3 kV) using InLens and Secondary Electron detectors. Prior to analyses, the samples were exposed to RuO₄ vapors or were coated with a palladium-platinum alloy in a Cressington 208 HR sputter-coater. The specific surface area values were quantified by nitrogen sorption porosimetry at 77 K using a Micromeritics ASAP 2000 gas adsorption instrument, and the data were exploited using the BET method.

3. Results and discussion

3.1. Synthesis of the block copolymer precursors

The PS-*b*-PLA copolymers with NH₂ and COOH functionalities as well as the PS-NH₂ precursor are listed in Table 1.

In order to synthesize PS-*b*-PLA with NH₂ functionality at the junction between both blocks, amine-terminated PS obtained from anionic polymerization was used as a macroinitiator in the ring-opening polymerization (ROP) of D,L-lactide with DMAP as a catalyst. The initiation from the terminal NH₂ group was completed rapidly compared with the propagation as evidenced by preserving a controlled character for the polymerization reaction (PDI ≈ 1.1). Although the

polymerization of lactide could be relatively well controlled under our experimental conditions, we found out that reactions catalyzed by DMAP proceeded somehow slowly and in consequence resulted in low conversions even after prolonged time (12 days).

Table 1. Composition and Molar Mass of Synthesized Polymers.

polymer	M_n PS ^a [kg/mol]	M_n PLA ^b [kg/mol]	PDI ^c	f_{PLA} ^d
PS-NH ₂	36.6	-	1.08	-
PS- <i>b</i> -PLA(NH ₂)	36.6	15.6	1.13	0.26
PS- <i>b</i> -PLA(COOH)	10.9	7.2	1.53	0.35

^a – calculated from SEC or ¹H NMR (in the case of PS-*b*-PLA(COOH)).

^b – calculated from ¹H NMR of block copolymer and SEC of macroinitiator for PS-*b*-PLA(NH₂) or ¹H NMR in the case of PS-*b*-PLA(COOH).

^c – polydispersity index (M_w/M_n) obtained from SEC.

^d – volume fraction of PLA calculated from ¹H NMR assuming that the densities of PS and PLA are 1.02 and 1.25 g cm⁻³, respectively.

Applying 2-hydroxyethyl-2-bromopropionate as a dual initiator in PS-*b*-PLA synthesis allowed us to introduce a carboxylic function at the junction between both blocks. This molecule containing two different functional groups (OH and bromopropionate) is capable of initiating two polymerization processes with distinct mechanisms: ROP and atom transfer radical polymerization (ATRP). Thus, block copolymers can be prepared by a sequential two-step procedure (without intermediate stages) or by a simultaneous one-step process. Following the one-step strategy, we synthesized a PS-*b*-PLA(COOH) that displayed broad molar mass distributions (PDI of 1.5 after fractionation), which was attributed to possible interferences of both polymerization mechanisms.

3.2. Morphology of the block copolymer precursors

In order to investigate the morphology of the block copolymer precursors, a PS-*b*-PLA(COOH) sample was spin-coated onto SiO₂ substrate from a 20 g L⁻¹ chlorobenzene solution. Figure 1 shows the SEM picture of a thin layer of PS-*b*-PLA(COOH) on the substrate after overnight annealing at 160 °C. To enhance the contrast, the layer was stained with RuO₄ that selectively reacted with styrene domains. The hexagonal structure of PLA cylinders perpendicular to the substrate (visible as dark dots) in PS matrix could be clearly recognized. The average diameter of PLA domains were determined to be equal to 10-14 nm.

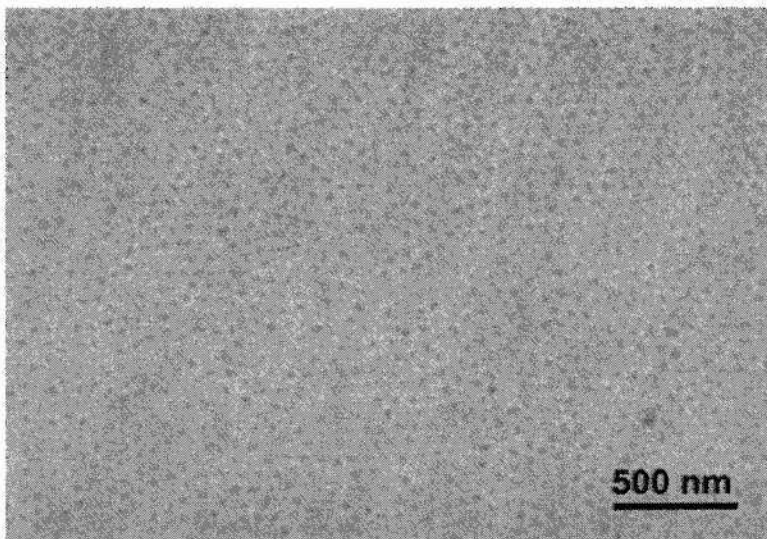


Figure 1. SEM picture of $\text{PS-}b\text{-PLA(COOH)}$ precursor spin-coated onto SiO_2 substrate.

3.3. Preparation of porous polymeric materials

Preliminary hydrolysis experiments were performed on the as-synthesized $\text{PS-}b\text{-PLA}$ samples containing an amino function. Our results show that the entire PLA block could be nearly removed by acidic or base hydrolysis after only 24 h. SEC analysis indicated that the polymers derived from degradation had molar mass and PDI nearly identical those of the PS-NH_2 macroinitiator, which was in good agreement with a gravimetric analysis (Figure 2). ^1H NMR suggests that base hydrolysis is slightly more efficient in the degradation process (Figure 3).

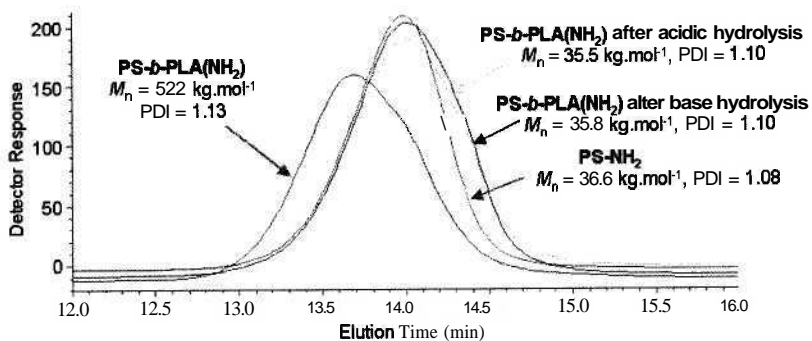


Figure 2. SEC traces showing PLA degradation with $\text{PS-}b\text{-PLA(NH}_2\text{)}$ precursor.

The PS-*b*-PLA(COOH) precursor appropriate for a cylindrical morphology was cast into a 0.5 mm-thick membrane from a 6 g L⁻¹ CH₂Cl₂ solution. Base hydrolysis was carried out for 5 days, and led to the complete removal of PLA. The morphology of the resulting porous material was examined by SEM (Figure 4). Randomly oriented nanochannels with an average diameter of 6-8 nm were observed. Such pore sizes were in reasonable agreement with the PLA domain sizes determined for the copolymer precursor. The big cracks were probably the consequence of the use of a low-boiling solvent during the film formation. The specific surface area as determined by nitrogen sorption porosimetry was equal to 102 m² g⁻¹.

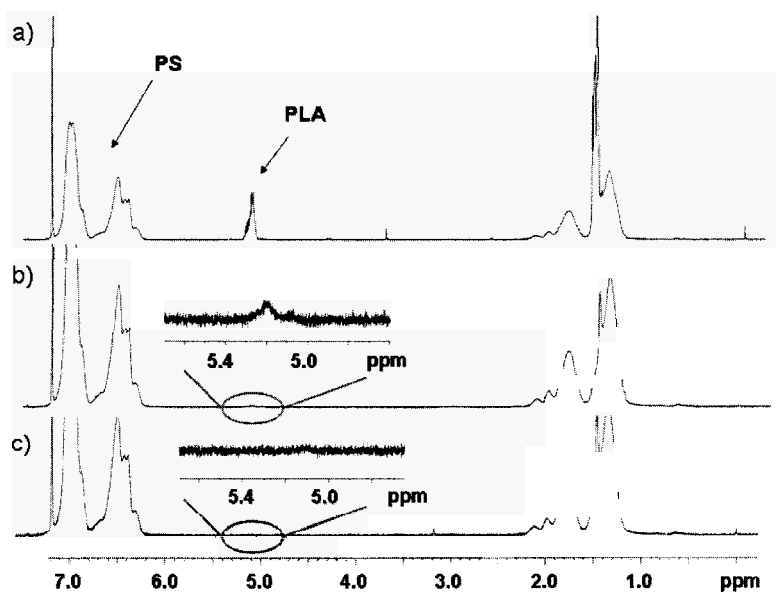


Figure 3. ¹H NMR of PS-*b*-PLA(NH₂) copolymer after synthesis (a), and acidic (b) as well as base (c) hydrolysis.

Alternatively, the PS-*b*-PLA(COOH) samples were pressed into tablets and were submitted to oscillatory shear flow experiments as described in the experimental section. Figure 5 shows optical microscopy images of a PS-*b*-PLA(COOH) precursor tablet after the alignment procedure. Upon turning the sample in polarized light, birefringence can be clearly seen, which indicates a global orientation of nanodomains. Subsequently, in order to completely remove the PLA block, base hydrolysis was carried out for 5 days. The morphology of

the resulting porous material was examined by SEM (Figure 6). Although cylinders were highly oriented locally, there was no long-range order in the sample. Two types of oriented pores could be observed: perpendicular ones (with an average diameter of 7-9 nm) and parallel ones with respect to the surface.

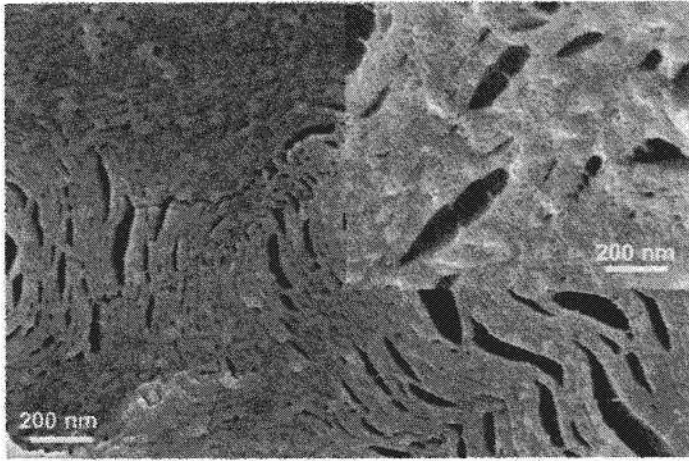


Figure 4. SEM pictures of porous material obtained from base hydrolysis of *PS-*b*-PLA(COOH)* precursor film cast from a CH_2Cl_2 solution.

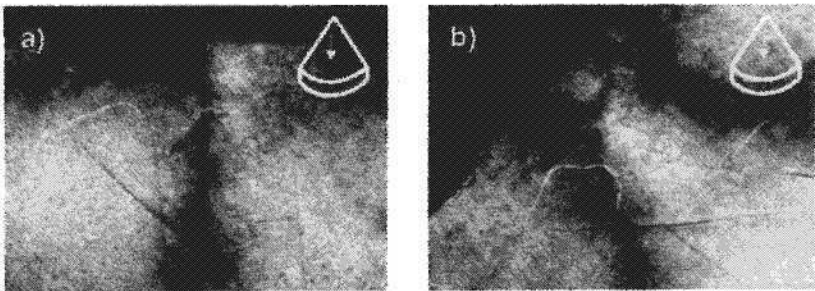


Figure 5. Optical microscopy images of aligned *PS-*b*-PLA(COOH)* precursor by oscillatory shear flow. Birefringence seen upon turning the sample in polarized light.

4. Conclusions

This communication illustrates a simple approach towards functionalized mesoporous polystyrene frameworks from semi-hydrolyzable nanostructured

diblock copolymers. Such frameworks are of potential interest for heterogeneous catalysis, advanced filtration, and selective transport applications. We are currently working on the macroscopic alignment of polymer domains and further characterization of the porous materials.

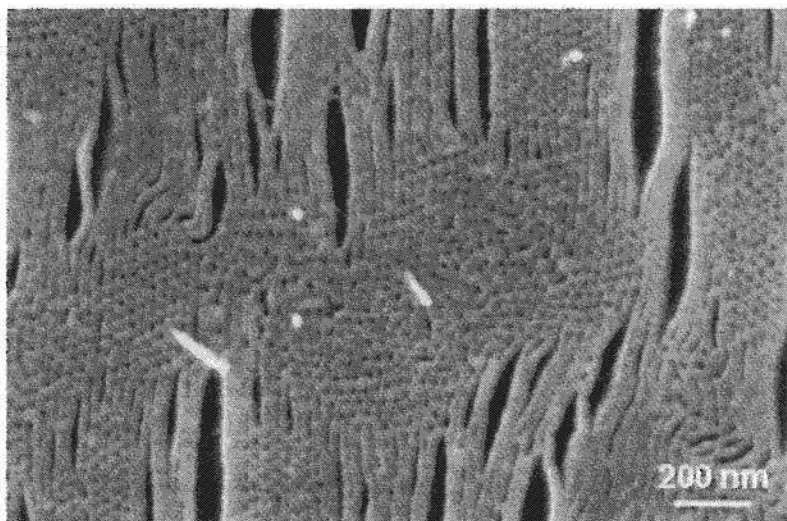


Figure 6. SEM pictures of porous material obtained from base hydrolysis of PS-*b*-PLA(COOH) precursor aligned by the oscillatory shear flow technique.

Acknowledgments

The authors thank Dr. A. Fahmi (University of Nottingham, UK) for the orientation experiments.

Financial support of the National Agency for Research (programme ANR/PNANO 2005, project POLYNANOCAT “ANR-05-NANO-025”) is gratefully acknowledged.

References

1. (a) H. Odani and T. Masuda, In *Design of Polymer Membranes for Gas Separation*; VCH: New York (1992). (b) C. R. Martin, *Science* 266, 1961 (1994). (c) C. F. Blanford, H. Yan, R. C. Schroden, M. Al-Daous and A. Stein, *Adv. Mater.* 13, 401 (2001).
2. (a) S. Valkama, A. Nykänen, H. Kosonen, R. Ramani, F. Tuomisto, P. Engelhardt, G. ten Brinke, O. Ikkala and J. Ruokolainen, *Adv. Funct. Mater.*

- 17, 183 (2007). (b) G. Rohman and D. Grande, *Polym. Mater. Sci. Eng.* **97**, 124 (2007).
3. T. Thurn-Albrecht, J. Schotter, G. A. Kastle, N. Emley, T. Shibauchi, L. Krusin-Elbaum, K. Guarini, C. T. Black, M. T. Tuominen and T. P Russell, *Science* **290**, 2126 (2000).
 4. (a) J. Lee, A. Hirao and S. Nakahama, *Macromolecules* **21**, 274 (1988). (b) A. S. Zalusky, R. Olayo-Valles, J. H. Wolf and M. A. Hillmyer, *J. Am. Chem. Soc.* **124**, 12761 (2002). (c) T. S. Bailey, J. Rzayev and M. A. Hillmyer, *Macromolecules* **39**, 8772 (2006).
 5. K. Ueda, A. Hirao and S. Nakahama, *Macromolecules*, **23**, 939 (1990).
 6. K. N. Jayachandran, A. Takacs-Cox and D. E. Brooks, *Macromolecules* **35**, 4247 (2002).

MESOSTRUCTURED POLYPYRROLE SYNTHESIZED BY ANIONIC SURFACTANT TEMPLATING ROUTE

MAHASWETA NANDI,¹ ASIM BHAUMIK^{*1}

Department of Materials Science and Centre for Advanced Materials, Indian Association for the Cultivation of Science, Jadavpur, Kolkata - 700 032, India

NAWAL KISHOR MAL,² MASAHIRO FUJIWARA²

Kansai Center, National Institute of Advanced Industrial Science and Technology, Ikeda, Osaka 563-8577, Japan

We report a new method to synthesize mesostructured polypyrrole by using the supramolecular assembly of an anionic surfactant sodium dodecylsulphate (SDS) as structure directing agent (SDA). Here the oxidative polymerization of pyrrole was carried out at room temperature in the presence of SDA micelles and dilute aqueous hydrochloric acid. Hydrogen peroxide was used as the oxidant. The effect of the addition of a co-surfactant in mesophase formation was also studied. Powder X-ray diffraction and transmission electron microscopic studies suggested wormhole-like disordered mesostructure and existence of mesopores in these mesostructured materials. Chemical bonding and electronic structure of the polypyrrole samples were studied by FT-IR and UV-Visible spectroscopy. These mesostructured polypyrrole samples showed very high resistivities at room temperature. These π -conjugated porous polymeric materials could find potential applications in variable resistors.

1. Introduction

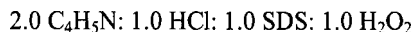
π -conjugated polymer composites with nanoscale dimension are in great demand [1] for last one decade. Template directed synthesis of the π -conjugated polymeric nanostructures is very attractive for the fabrication of macromolecular electronic devices having applications in electrooptics, microelectronics and photonics [1,2]. These polymers are usually synthesized in the presence of a surfactant, co-solvent and an inorganic acid. On the other hand, at low temperatures the liquid crystal-like arrays formed between the organic/inorganic-cluster and the self-assembly of organic surfactants readily undergo reversible lyotropic transformations leading to mesostructured materials [3]. Polypyrrole is a well-known conducting polymer [4] with many unique advantages, like easy to prepare, suitable for making composites with different types of binders, environmentally stable, special chemical and physical properties, excellent

mechanical strength [5,6], etc. Nanostructured polypyrrole has received special attention because of its potential in the fabrication of electronic devices [7,8], sensors [9] etc. Various synthetic routes for the preparation of π -conjugated polymeric nanostructures have been reported in the literature [10-13]. Usual aqueous phase polymerization of pyrrole involves the reaction between monomer pyrrole and an oxidant such as FeCl_3 in the presence of a strong mineral acid.

Nanostructured polypyrrole has shown enhanced electrical properties [14] due to high interfacial area between polypyrrole and its environment. The existence of nanopores in the organic materials [15] could further allow the fast diffusion of gas molecules into the framework. The most efficient way to enhance the surface area of nanostructured materials is to induce mesoporosity [3,16,17]. However, there are only few facile and reliable methods for making good quality porous organic nanostructures [18,19]. Anionic surfactants like SDS are ideal SDA for the synthesis of ordered mesoporous materials composed of framework protonated amines [20]. Thus these surfactant molecules can be efficiently used as SDA for the synthesis of various mesostructured composites, where positive charge resides on the framework moiety. Although there are reports for the preparation of mesoporous polyaniline in micelle solutions of SDS as polymerization medium [18], there is no report on the synthesis of nanoporous polypyrrole templated by the SDS micelles. Here the oxidation-polymerization synthetic route has been followed for the synthesis of mesostructured polypyrrole by using dilute aqueous H_2O_2 as the oxidizing agent. The in-situ oxidation-polymerization was conducted in the presence of the SDA molecules. Mesostructured polypyrrole sample thus prepared shows a very high resistivity compared to the mesoporous polyaniline synthesized by surfactant templating route [18].

2. Experimental

Sodium dodecyl sulphate, SDS (Loba Chemie) and Brij 35 (Loba Chemie) were used as SDA and hydrogen peroxide, H_2O_2 (30 wt % aqueous, E-Merck) was used as the oxidant for the polymerization of pyrrole in aqueous medium. In a typical synthesis, 2.88 g SDS was first dissolved in 20 ml of water. Then 1.34 g pyrrole (Fluka) was added to the above aqueous solution of SDS under stirring condition. After the reaction mixture becomes homogeneous, 1.36 g of H_2O_2 (30 wt% aqueous, Loba Chemie) taken in an aqueous solution of 1.22 g conc. HCl (E-Merck) was added dropwise to the above mixture and the whole mass was stirred overnight at room temperature. The mole ratio of the various constituents in the final reaction mixture was:



This sample has been designated as sample 1. In another batch (sample 2), identical synthesis procedure was followed except the addition of Brij 35 as a co-surfactant along with SDS. One non-templated pure polypyrrole sample was also synthesized without using any SDA, which has been designated as sample 3. All the samples are black in color. Except sample 3, other two samples were extracted three times with an aqueous solution containing ammonium acetate and the corresponding extracted samples have been designated as samples 1a and 2a, respectively. The batch compositions of the various samples have been given in Table 1.

Table 1. Synthesis of different mesostructured polypyrrole samples.

Sample	Pyrrrole (moles)	HCl (moles)	SDS (moles)	Brij-35 (g)	H ₂ O ₂ (moles)	Surface area [m ² g ⁻¹]	Resistance (MO)
1	0.02	0.01	0.01	-	0.01	-	10.0
1a	0.02	0.01	-	-	0.01	29.8	100.0
2	0.02	0.02	0.01	1.50	0.01	-	7.8
2a	0.02	0.01	-	-	0.01	23.5	28.0
3	0.02	0.02	-	-	0.01	-	0.01

For characterization, we have used all the samples listed in Table 1. X-ray diffraction patterns of the samples were recorded on a Seifert P 3000 diffractometer using Cu K_α ($\lambda = 0.15406$ nm) radiation. TEM images were recorded on a JEOL JEM 2010 transmission electron microscope. SEM images were recorded on a JEOL JEM 6700F field emission scanning electron microscope. N₂ adsorption / desorption isotherms of the samples were recorded on a Quantachrome Autosorb 1-C/TPD, at 77 K. Prior to the measurement, the samples were degassed at 343 K for 12 h under high vacuum. UV-Visible diffuse reflectance spectra were obtained by using a Shimadzu UV 2401PC spectrophotometer with an integrating sphere attachment. BaSO₄ pellet was used as background standard. FT-IR spectra of these samples were recorded on KBr pellets by using a Nicolet MAGNA-FT IR 750 spectrometer series II. Electrical conductivity of the mesostructured polypyrrole samples were measured by standard four-probe technique after making pellets out of the powder samples using Lake Shore 120 current source and Yokogawa 7562 digital multimeter.

3. Results and Discussion

In Fig. 1 low angle XRD patterns of different mesostructured polypyrrole samples are shown. A single low angle peak was observed for all the samples synthesized in the presence of SDAs. Sample 1 showed an intense low angle XRD peak and a narrow peak width, whereas sample 2 synthesized employing mixed surfactant system showed weak intensity with a broad peak-width. Sample 3 synthesized without any template showed no peak at all in the low angle region, as expected, since no mesostructure could be formed without the assista-

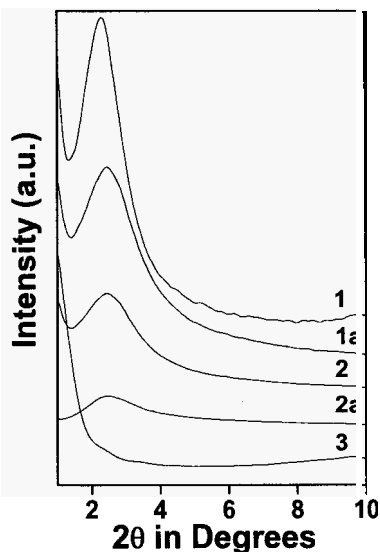


Figure 1. Low angle XRD pattern of samples 1, 1a, 2, 2a and 3.

nce of an SDA. Extracted sample 1a showed relatively weaker intensity and broader peak width over the as-synthesized sample 1, suggesting that although the mesophases have been retained after the removal of the surfactants (Fig. 1), however, the arrangement of the pores become more disordered. The extracted sample 2a showed a very poor XRD peak indicating that the structure is not as stable as that of 1a after the removal of template. In Fig. 2 the high angle diffraction pattern for samples 1, 1a and 3 are shown. Peak positions for polypyrrole sample 3 synthesized in the absence of any SDAs agree well with that for samples 1 and 1a, although there was little change in their respective intensities. This result suggested that the pore walls of our mesostructured polypyrrole samples are composed of polypyrrole framework moieties.

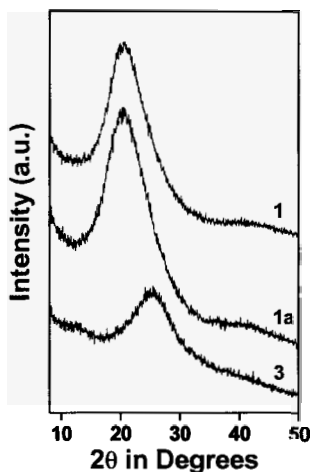


Figure 2. Wide angle XRD pattern of samples 1, 1a and 3.

The TEM image of a representative sample (sample 1) is shown in Fig. 3. The image confirms the formation of low electron density spherical white spots of *ca.* 2.0-3.0 nm size, corresponding to small to medium size mesopores for polypyrrole sample 1. The average pore size as depicted by the TEM observation (*ca.* 2.0-3.0 nm) agree well with the XRD diffraction patterns. The arrangements of the pores were found disordered in nature. Thus from the XRD patterns and the TEM image analysis we could conclude that these mesostructured polypyrrole samples have disordered wormhole-like structures. SEM image of sample 1 is shown in Fig. 4, exhibiting granular/spherical morphology. In these samples very tiny spheres of dimension 20-25 nm were found, which assembled together to form large spherical aggregates.

In Fig. 5 the N_2 adsorption/desorption isotherms for sample 1a at 77 K are shown. At P/P_0 between 0.05-0.8 the nature of the isotherm suggested the existence of large mesopores or macropores. No sharp capillary condensation was observed. Instead uptake of N_2 increases in this region gradually and this could be attributed to the multilayered adsorption in mesopores. In Table 1, Brunauer-Emmett-Teller (BET) surface areas of the samples are given. BET surface area for samples 1a and 2a were 29.8 and 23.5 m^2g^{-1} , respectively. It is pertinent to mention here that this is a preliminary report on mesoporous polypyrrole and further study to improve adsorption properties is in progress. The small hysteresis that is obtained at high relative pressure corresponds mainly to interparticle porosity.

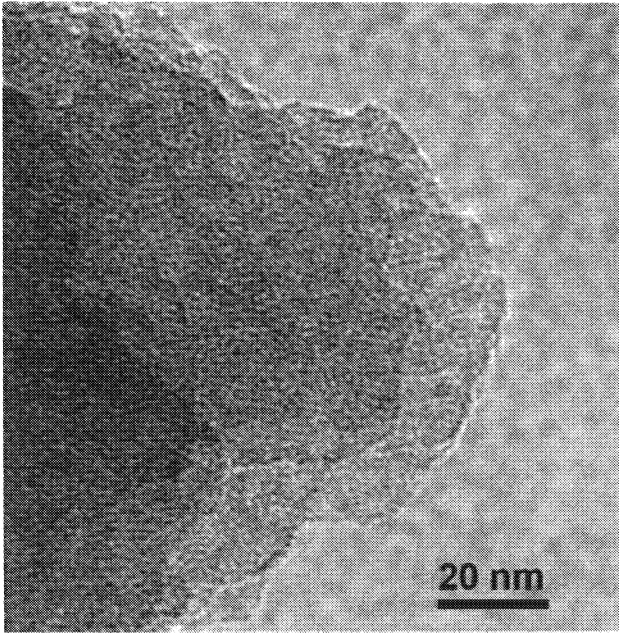


Figure 3. TEM image of as-synthesized mesostructured polypyrrole sample 1.

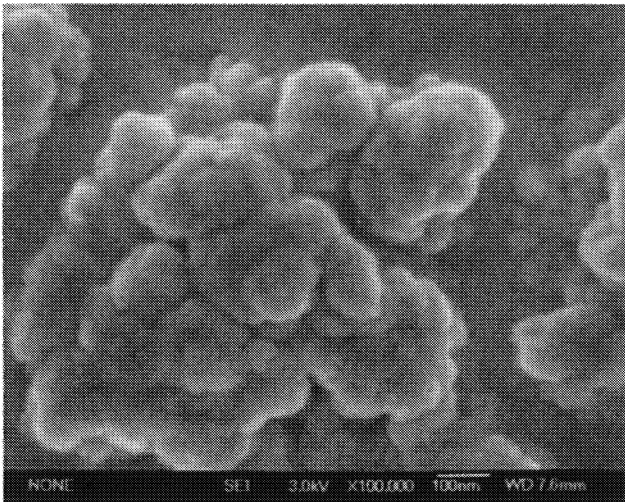


Figure 4. SEM image of as-synthesized polypyrrole sample 1.

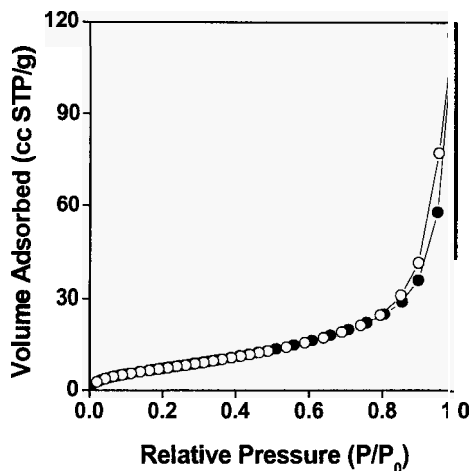


Figure 5. N_2 adsorption/desorption isotherm of polypyrrole sample 1a, at 77 K. Adsorption points are marked by filled circles and that of desorption by open circles.

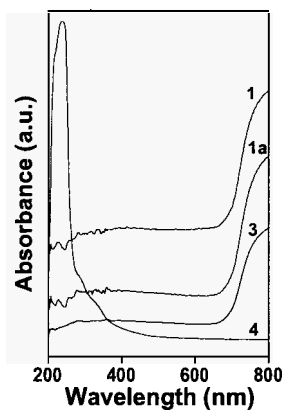


Figure 6. UV-visible diffuse reflectance spectra for samples 1, 1a, 3 and 4.

In the UV-visible spectra (Fig. 6) a strong absorption band at *ca.* 237 nm for pyrrole/HCl solution (sample 4) was observed. On the other hand the mesoporous polypyrrole samples, 1 and 1a showed no absorption in this region, rather broad bands for both at higher wavelength of 790 nm was observed, which was completely absent for 4. Absence of any absorption band at *ca.* 237 nm thus suggested that all the pyrrole units have been fully polymerized in our mesostructured polypyrrole. A close comparison between the UV-visible spectra

for samples 1 and 1a with pure polypyrrole sample 3 further suggested that the framework of our new mesoporous composite material is same as that of pure polypyrrole. Thus the UV-vis spectra suggested complete conversion of pyrrole into polypyrrole framework. Here the as-synthesized mesostructured polypyrrole is in its doped state with counter anion of SDS acting as SDA.

Electrical conductivity measurements were done on polypyrrole samples synthesized with or without surfactant. Unlike mesoporous polyaniline, which showed very high conductivity at room temperature [18], mesostructured polypyrrole samples were found to be highly resistive with respect to the sample synthesized in absence of template at room temperature. Comparing electrical conductivity of polypyrrole before and after extraction of surfactant, a noticeable change was observed. The as synthesized sample showed a lower value of resistivity of the order of kilo ohm, whereas the extracted sample gave a value in the mega ohm order. This could be attributed to the voids and pores present in these samples after the extraction of the SDA molecules.

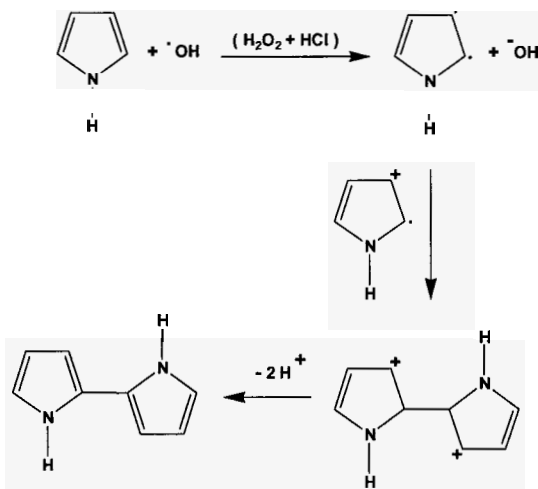


Figure 7. Scheme of the polymerization of pyrrole.

In Fig. 7 the reaction pathway for the polymerization of pyrrole in the presence of an oxidant under aqueous-acidic condition have been presented. The presence of the surfactant and/or co-surfactant in the reaction medium may help to organize this polypyrrole framework to grow around its periphery through ionic interaction of the $\text{C}_{12}\text{H}_{25}\text{SO}_3^-$ of SDA with the cationic moieties of the organic framework. From the above experimental observations we can propose a

model for the generation of mesopores in mesostructured polypyrrole samples as shown in Fig. 8. The image drawn is just a representative model of the expected structure. The sample is actually disordered but for the ease of representation a more specific and well-defined ring structure has been given. Eight pyrrole moieties giving rise to a mesopore is an arbitrary number and has no correlation with the rest of the data. Here the three dimensional network of polypyrrole could be grown around the surfactant micelles. Thus by using suitable surfactant molecules different mesostructured polypyrrole materials could be synthesized. Extraction of the surfactant molecules from these as-synthesized materials could generate mesoporosity.

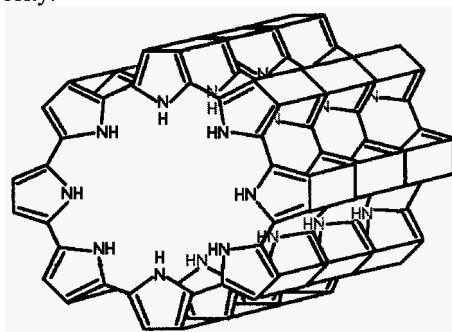


Figure 8. Structural model showing the mesopores in the nanostructured polypyrrole.

Conclusions

Mesostructured polypyrrole have been synthesized using supramolecular assembly of an anionic surfactant SDS through in-situ aqueous phase polymerization of pyrrole at room temperature, with hydrogen peroxide as the oxidant. Powder XRD and TEM results revealed wormhole-like disordered structure and existence of nanopores. FE SEM image analysis suggested very tiny spherical particles with sizes of 20-25 nm for these samples. UV-visible absorption data suggested the presence of polypyrrole network in these samples. These mesoporous polypyrrole samples showed a very high value of resistivity at room temperature, which could be utilized for the fabrication of resistors.

Acknowledgments

This work was partly funded by the Ramanna Fellowship and Nano Science and Technology Initiative grants of Department of Science & Technology, New Delhi. MN wishes to thank CSIR, New Delhi for a Senior Research Fellowship.

References

1. P. K. H. Ho, J. I. -S. Kim, J. H. Burroughes, H. Becker, S. F. Y. Li, T. M. Brown, F. Cacialli and R. H. Friend, *Nature* **404**, 481 (2000).
2. S. Holdcroft, *Adv. Mater.* **13**, 1753 (2001).
3. C. T. Kresge, M. E. Leonowicz, W. J. Roth, J. C. Vartuli and J. S. Beck, *Nature* **359**, 710 (1992).
4. B. A. Bolto, R. McNeill and D. E. Weiss, *Aus. J. Chem.* **16**, 1090 (1963).
5. N. Pini, M. Siegrist, S. Busato and P. Ermanni, *Poly. Eng. Sci.* **47**, 662 (2007).
6. M. Sasidharan, N. K. Mal and A. Bhaumik, *J. Mater. Chem.* **17**, 278 (2007).
7. T. R. Farhat and P. T. Hammond, *Chem. Mater.* **18**, 4149 (2006).
8. V. V. Rajasekharan and D. A. Buttry, *Chem. Mater.* **18**, 4541 (2006).
9. C. N. Aquino-Binag, N. Kumar and R. N. Lamb, *Chem. Mater.* **8**, 2579 (1996).
10. C. R. Martin, *Acc. Chem. Res.* **28**, 61 (1995).
11. L. Liang, J. Liu, C. F. Windisch, G. J. Exarhos and Y. H. Lin, *Angew. Chem. Int. Ed.* **41**, 3665 (2002).
12. K. De Moel, G. O. R. Alberda van Ekenstein, H. Nijland, E. and G. Ten Brinke, *Chem. Mater.* **13**, 4580 (2001).
13. R. Xiao, S. I. Cho, R. Liu and S. B. Lee, *J. Am. Chem. Soc.* **129**, 4483 (2007).
14. S. Virji, J. Huang, R. B. Kaner and B. H. Weiller, *Nano Lett.* **4**, 491 (2004).
15. J. Germain, J. Hradil, J. M. J. Fréchet and F. Svec, *Chem. Mater.* **18**, 4430 (2006).
16. M. Kruk, E. B. Celer and M. Jaroniec, *Chem. Mater.* **16**, 698 (2004).
17. A. Sayari and Y. Yang, *Chem. Mater.* **17**, 6108 (2005).
18. M. Nandi, R. Gangopadhyay and A. Bhaumik, *Microporous Mesoporous Mater.* DOI: 10.1016/j.micromeso.2007.04.049 (2007).
19. K. P. Gierszal and M. Jaroniec, *J. Am. Chem. Soc.* **128**, 10026 (2006).
20. S. Che, A. E. Garcia-Bennett, T. Yokoi, K. Sakamoto, H. Kunieda, O. Terasaki and T. Tatsumi, *Nature Mater.* **2**, 801 (2003).

SYNTHESIS AND CHARACTERIZATION OF THERMO-SENSITIVE NANOCOMPOSITE PNIPAAm / SBA-15

BOSHI TIAN AND CHUN YANG*

Jiangsu Key Laboratory of Biofunctional Materials, College of Chemistry and Environmental Science, Nanjing Normal University, Nanjing 210097, P. R. China

A nanocomposite consisting of occluded thermo-sensitive Poly(N-isopropylacrylamide) (PNIPAAm) and mesoporous silica SBA-15 has been synthesized by an in situ polymerization technique. The composite was characterized by IR, XRD, TEM, N₂ adsorption-desorption, TG and DSC. It is confirmed that the polymerization of monomer NIPAAm occurs in the composite, and most of the polymers are located within the channels of SBA-15 and form a coating clinging to the pore walls with a relatively uniform distribution. The polymerization and pore filling does not destroy the ordered hexagonal structure of SBA-15; but the surface area, the pore size and the pore volume of the composite are decreased due to the introduction of the polymer. Moreover, the thermo-sensitive property of PNIPAAm is retained in the nanocomposite, which has a lower critical solution temperature (LCST) similar to that of pure PNIPAAm.

1. Introduction

In recent years, the study and application of organic-inorganic nanocomposites based on mesoporous materials have received much attention. The larger pore size of mesoporous silicas compared with microporous zeolites provides us more opportunities to encapsulate large organic guest species in the ordered mesopore channels. Some groups have focused their studies on the encapsulation of polymer [1-3] into mesoporous silica hosts. The resultant composites show unique properties due to their regular mesoscopic structure and space restriction effect.

Poly(N-isopropylacrylamide) (PNIPAAm) is a well-known temperature-responsive polymer with lower critical solution temperature (LCST) of ~32°C [4] and exhibits a reversible volume phase transition at its LCST in aqueous solution. This property has been applied in many fields, such as bioseparations [5], immobilization of enzyme [6] and drug delivery systems [7]. In order to improve the thermal and mechanical stability of PNIPAAm, the composites of the organic polymers combined with rigid inorganic porous materials have been

* Corresponding author

developed. For instance, PNIPAAm was incorporated into clay [8], silica [9,10] or hydroxyapatite [11] to obtain thermo-sensitive organic-inorganic composite. However, few studies on composites of PNIPAAm /ordered mesoporous silica were reported [12,13].

In the present paper, we report a synthesis of hexagonal ordered mesoporous thermo-sensitive composite, PNIPAAm/SBA-15, in which PNIPAAm is occluded into the channels of SBA-15 host by impregnation with monomer and polymerization in situ. Because of the particular structure of SBA-15 and the control of synthesis condition, a nanocomposite with relatively homogeneous distribution of PNIPAAm in the mesopores is obtained. The thermo-sensitive property of PNIPAAm is also retained in the composite.

2. Experimental

2.1. Synthesis of Samples

Mesoporous silica SBA-15 was synthesized according to the method reported by Zhao *et al* [14]. The template surfactant P123 was removed by calcinations in air at 500°C for 6 h.

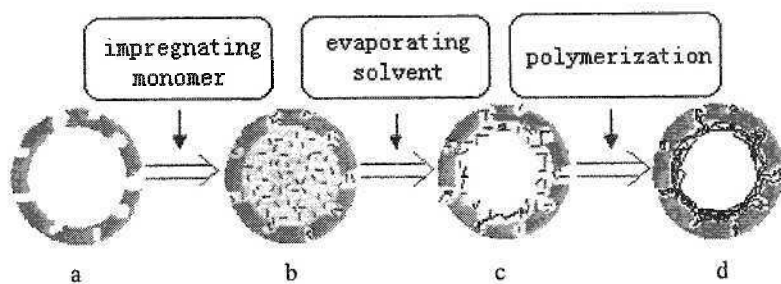
Composite PNIPAAm / SBA-15 was synthesized as follows: 0.15g of SBA-15 was activated at 250°C under vacuum for 6 h and cooled to room temperature. 0.14g of monomer N-isopropylacrylamide (NIPAAm), 0.0018g of crosslinker N, N'-methylenebisacrylamide (BIS) and 0.0029g of initiator azobisisobutyronitrile (AIBN) were dissolved in 3mL of acetone, and then the solution was injected into the activated SBA-15. After the slurry was sealed and subsequently stirred for 12 h at 0°C in the dark, the solvent was removed by volatilization at room temperature. The resultant powder was washed with deionized water (3mL) to remove the monomers adsorbed on the outside surface, followed by filtered and air-dried. The dried powder was wetted by a little deionized water in a flask under flowing N₂. N₂ flow was kept for 10 min to remove air, and then the flask was sealed and heated at 60°C for 12 h for polymerization. After that, the solid was soaked in acetone for 12 h to remove unreacted monomers and detachable polymer, followed by filtered, washed with acetone and dried under vacuum at 40°C for 10 h. The resultant PNIPAAm / SBA-15 composite was measured by TG analysis to determine the content of PNIPAAm. A ~24 wt% of PNIPAAm content in our composite sample was detected.

2.2. Characterization

Small-angle powder X-ray diffraction (XRD) patterns were recorded on an ARL X'TRA diffractometer using Cu K α radiation at 40 kV and 20mA. Infrared (IR) spectra were obtained on a Tensor-27 FT-IR spectrometer using KBr pellet technique. Transmission electron microscopy (TEM) micrographs were taken on a JEOL JEM-2100 microscope operating at 200 kV. Thermogravimetric (TG) analyses were carried out from 25°C to 700°C on a Perkin-Elmer Pyris 1 instrument under N₂ atmosphere at a ramp rate of 10°C min⁻¹. Differential scanning calorimetry (DSC) was performed from 25°C to 60°C on a Perkin-Elmer Diamond calorimeter with a heating rate of 2°C min⁻¹ in N₂ flow. N₂ adsorption-desorption isotherms were measured at -196°C on a Micromeritics ASAP 2020M instrument. The samples were outgassed at 100°C for 6 h. Total pore volume was taken at P/P₀=0.98 single point. Mesopore size and mesopore size distribution were calculated from the adsorption branch using the BJH model corrected by Kruk-Jaroniec-Sayari equation [15]. Micropore volume was evaluated using *t*-plot method in the *t* range from 0.4 to 0.7 nm. Statistical film thickness was calculated using Harkins-Jura equation with standard parameters.

3. Results and Discussion

In the synthesis of composite, the mixture of monomer NIPAAm, crosslinker BIS and initiator AIBN were dissolved in acetone and then introduced into the channels of SBA-15 by impregnation. After the solvent was volatilized, the monomer mixture was adsorbed and deposited on the pore wall, followed by wetted with water and heated for polymerization. This process is illustrated briefly in Scheme 1. The following characterization will further



Scheme 1 Preparation process of composite PNIPAAm/SBA-15. (a) mesoporous SBA-15; (b) the mixture of SBA-15, solvent and monomer mixture; (c) SBA-15 entrapped with monomer mixture wetted by deionized water; (d) the composite PNIPAAm/SBA-15.

elucidates the polymerization in the channels and the structure of composite.

Besides the thicker pore wall and higher stability, another reason for using SBA-15 as host is that there are some disordered micropores/small mesopores (complementary pores) within its pore wall [16,17]. Polymer can be entrapped into these complementary pores and interpenetrate with the silica framework through these pores to form the polymer network integrated with the silica framework, thus increasing significantly the immobility of PNIPAAm and the stability of the entire polymeric system [1].

The IR spectra of samples are shown in Fig.1. For pure PNIPAAm (Fig.1b), the bands at 1645 and 1458 cm^{-1} correspond to C=O stretching vibrations and N-H bending vibrations [18], respectively, the bands at 1367 and 1386 cm^{-1} arise from the methyl groups in $-\text{CH}(\text{CH}_3)_2$ [18,19], and the bands at 2978, 2930, 2876 and 1460 cm^{-1} are due to the stretching and the bending vibrations of C-H of methyl groups and methylene groups, respectively. These bands also appear in the spectrum of PNIPAAm / SBA-15 (Fig.1d), while the characteristic bands of NIPAAm monomer (1620 cm^{-1} for C=C and 1409 cm^{-1} for $\text{CH}_2=$ [20], see Fig.1a) are not present in Fig.1d, indicating that the polymerization has taken place in the channels of SBA-15 and the unreacted monomer has been removed by washed with acetone.

XRD patterns of SBA-15 and PNIPAAm / SBA-15 are shown in Fig.2. Both materials exhibit one very intense diffraction peak (100) and two weak

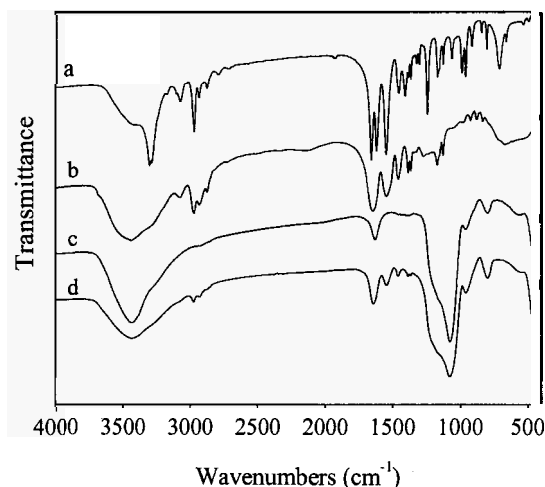


Fig.1 IR spectra of (a) NIPAAm, (b) PNIPAAm, (c) SBA-15 and (d) PNIPAAm / SBA-15

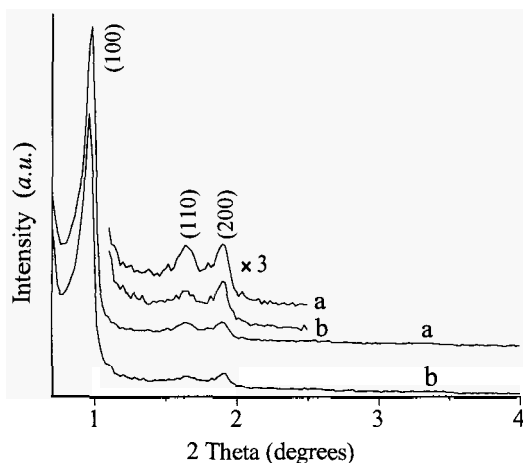


Fig.2 XRD patterns of (a) SBA-15 and (b) PNIPAAm / SBA-15

peaks (110) and (200) in the 2θ range of $0\sim 5^\circ$, characteristic of hexagonal structure of mesoporous materials [21]. The intensities of peaks of the composite is not obviously different from those of pure SBA-15, suggesting that the ordered hexagonal mesopore structure is retained perfectly after the incorporation of PNIPAAm and no notable change in scattering contrast between the pores and the walls occurs owing to a relatively homogeneous deposition of polymer on the pore walls, similar to the case reported by Choi *et al* [1], in which polychloromethylstyrene (PCMS) was entrapped uniformly in the channels of SBA-15. In addition, an increase in relative intensity of peak (200) to (110) after the introduction of PNIPAAm compared with that of pure SBA-15 is also observed in Fig.2, indicating the formation of a thicker pore wall in the former sample (it has been confirmed that the increase of wall thickness leads to an enhance of relative intensity of peak (200) to (110) for ordered mesoporous materials [22,23]), in agreement with the wall thickness data shown in Table 1. Apparently, the increase of pore wall thickness is a result of the formation of polymer coating clinging to the wall. The TEM images of PNIPAAm / SBA-15 are given in Fig 3. The hexagonal ordered mesostructure is shown and no deposition of bulk polymer on the external surface of SBA-15 particles is observed, suggesting that the most of polymers are formed inside the channels.

Table 1. Structural parameters of the SBA-15 and PNIPAAm / SBA-15 composite.

Sample	a_0 (nm)	D (nm)	L (nm)	S_{BET} ($m^2 g^{-1}$)	V_t ($cm^3 g^{-1}$)	V_{mi} ($cm^3 g^{-1}$)
SBA-15	10.4	8.0	2.4	813	0.84	0.16
PNIPAAm / SBA-15	10.6	7.0	3.6	344	0.42	0.02

a_0 : XRD unit cell parameter, D: pore size calculated by BJH method from the adsorption branch of N_2 isotherms, L: pore wall thickness, $L = a_0 - D$, SBET: surface area calculated by BET method, V_t : single point total pore volume, V_{mi} : micropore volume evaluated by t -plot.

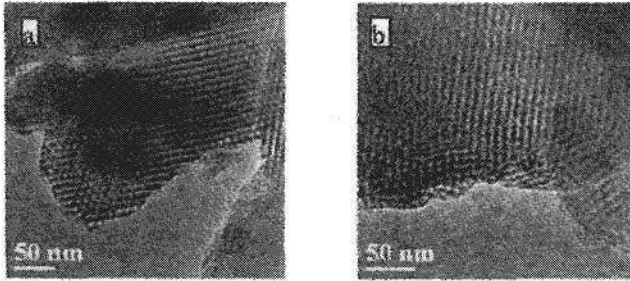


Fig.3 TEM images of PNIPAAm / SBA-15 viewed along the pore axis (a) and perpendicularly to the pore axis (b).

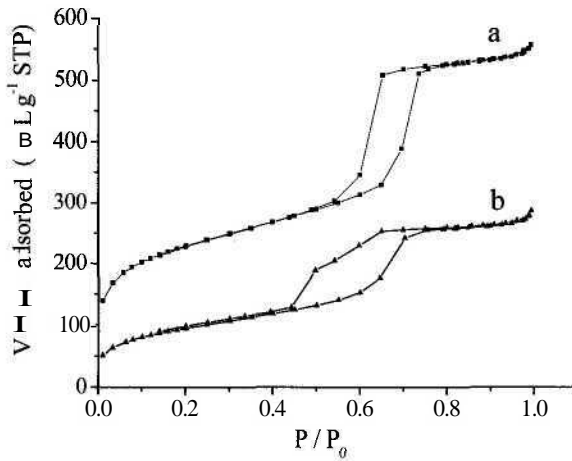


Fig.4 N_2 adsorption-desorption isotherms of (a) SBA-15 and (b) PNIPAAm / SBA-15

Fig.4 and Table 1 show the N₂ adsorption-desorption isotherms and the detailed texture parameters of samples, respectively. Type IV isotherms and type H1 hysteresis loop for SBA-15 (Fig.4a) are characteristic of mesoporous materials with cylindrical pore geometry [24]. After the inclusion of PNIPAAm into SBA-15, the amount of N₂ adsorbed decreases significantly (Fig.4b) and the pore size reduces from 8.0 to 7.0 nm (Table 1), directly evidencing the presence of PNIPAAm polymer in the channels. Moreover, the step of desorption branch is not so steep and the hysteresis loop deviates from type H1. This may be caused by partial pore blockage at such a high polymer loading. *t*-plots of the samples are shown in Fig.5. It is obvious that the curve of pure SBA-15 (Fig.5a) bends more severely at start section (lower *t* value region) than that of the composite (Fig.5b), implying that a considerable amount of micropores/small mesopores exists in SBA-15, but almost disappears after the inclusion of PNIPAAm. Table 1 shows the micropore volumes of samples evaluated by *t*-plots from the intercepts at ordinate. It can be seen that the micropore volume is about 19% of total pore volume for pure SBA-15, however, it decreases greatly after PNIPAAm was encapsulated, suggesting a penetration of polymer chains into the micropores/small mesopores within the wall. This indicates again that, in our synthesis, the NIPAAm monomers are introduced and polymerized as a relatively uniform coating on the surface of pore walls rather than polymerized randomly at the center of channels (if the polymerization occurs following the latter mode, the micropores/small mesopores of SBA-15 can not be occupied by polymer chains [1]).

It is well-known that the conformation and the solubility of PNIPAAm in water is related to the temperature. At the temperatures below the LCST, PNIPAAm is present in a water-swollen state because the intermolecular hydrogen bonds between water molecules and amide groups of the PNIPAAm chain are formed predominantly at such temperature, resulting in a coil-structure of polymer chains dissolved in water. At the temperatures above the LCST, however, PNIPAAm exhibits an insoluble state since the intramolecular hydrogen bonds between C=O and N-H groups in PNIPAAm chains are formed preferentially at such temperature, leading to a compact and collapsed conformation of the chains [25]. This volume phase transition of polymer is accompanied by an endothermic effect at the LCST, which can be measured by calorimetric technique. DSC curve of PNIPAAm included in SBA-15 is shown in Fig.6. A clear endothermic peak is observed at around 32°C due to the phase

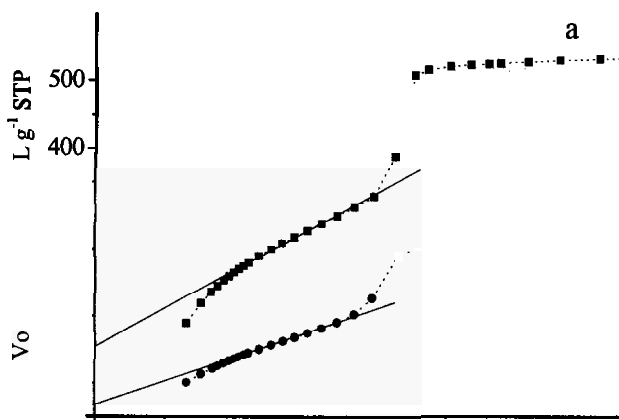


Fig.5 t -plots of (a) SBA-15 and (b) PNIPAAm / SBA-15

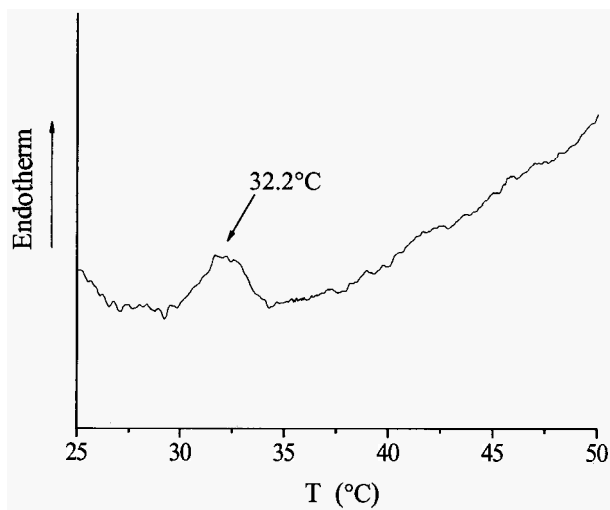


Fig.6 DSC curve of PNIPAAm / SBA-15 swollen in deionized water

transition happening in the composite. This temperature is consistent with the LCST of pure PNIPAAm, strongly suggesting that the thermo-sensitive property of PNIPAAm is retained in the composite PNIPAAm / SBA-15.

In conclusion, a thermo-sensitive nanocomposite, PNIPAAm / SBA-15, can be synthesized by impregnating monomers and polymerizing them in the channels of SBA-15. The distribution of polymer in the mesopores can be controlled and the temperature-responsive property of the polymer can be preserved. It is expected that this organic-inorganic composite material will be promising in smart control field.

Acknowledgments

We thank the Project of Advanced Technology of Jiangsu Province of China (BG-2005041) for financial support.

References

1. M. Choi, F. Kleitz, D. Liu, H. Y. Lee, W. S. Ahn, R. Ryoo, *J. Am. Chem. Soc.* **127**, 1924 (2005)
2. K. Moller; T. Bein, R. X. Fischer, *Chem. Mater.* **10**, 1841 (1998).
3. M. Sasidharan, N. K. Mal, A. Bhaumik, *J. Mater. Chem.* **17**, 278 (2007)
4. M. Heskings, J. E. Guillet, E. James, *J. Macromol. Sci. Chem.* **A2**, 1441 (1968).
5. A. Okamura, M. Itayagoshi, T. Hagiwara, M. Yamaguchi, T. Kanamori, T. Shinbo, *Biomaterials* **26**, 1287 (2005).
6. T. Nozaki, Y. Maeda, K. Ito, H. Kitano, *Macromolecules* **28**, 522 (1995).
7. X. Z. Zhang, D. Q. Wu, C. C. Chu, *Biomaterials* **25**, 3793 (2004).
8. L. Liang, J. Liu, X. Gong, *Langmuir* **16**, 9895 (2000).
9. T. Serizawa, K. Wakita, M. Akashi, *Macromolecules* **35**, 10 (2002).
10. K. Suzuki, T. Yumura, Y. Tanaka, M. Akashi, *J. Control. Release.* **75**, 183 (2001).
11. Y. Shin, J. Liu, J. H. Chang, G. L. Exarhos, *Chem. Commun.* 1718 (2002).
12. Q. Fu, G. V. R. Rao, L. K. Ista, Y. Wu, B. P. Anergiejewski, L. A. Sklar, T. L. Ward, G. P. López, *Adv. Mater.* **15**, 1262 (2003).
13. Q. Fu, G. V. R. Rao, T. L. Ward, Y. F. Lu, G. P. López, *Langmuir* **23**, 170 (2007).
14. D.Y. Zhao, Q. S. Huo, J. L. Feng, B. F. Chmelka, G. D. Stucky, *J. Am. Chem. Soc.* **120**, 6024 (1998).
15. M. Kruk, M. Jaroniec, A. Sayari, *Langmuir* **13**, 6267 (1997).
16. R. Ryoo, C. H. Ko, M. Kruk, V. Antochshuk, M. Jaroniec, *J. Phys. Chem. B.* **104**, 11465 (2000).

17. P. V. D. Voort, P. I. Ravikovitch, K.P. D. Jong, M. Benjelloun, E. V. Bavel, A. H. Janssen, A.V. Neimark, B. M. Weckhuysen, E. F. Vansant, *J. Phys. Chem. B* **106**, 5873 (2002).
18. C. Erbil, E. Kazancoiglu, N. Uyanik, *Eur. Polym. J.* **40**, 1145 (2004).
19. W. G. Liu, B. Q. Zhang, W. W. Lu, X. W. Li, D. W. Zhu, K. D. Yao, Q. Wang, C. R. Zhao, C. D. Wang, *Biomaterials* **25**, 3005 (2004).
20. H. K. Ju, S. Y. Kim, S. J. Kim, Y. M. Lee, *J. Appl. Polym. Sci.* **83**, 1128 (2002).
21. D. Y. Zhao, J. L. Feng, Q. S. Huo, N. Melosh, G. H. Fredrickson, B. F. Chmelka, G. D. Stucky, *Science* **279**, 548 (1998).
22. M. Kruk, M. Jaroniec, C. H. Ko, R. Ryoo, *Chem. Mater.* **12**, 1961 (2000).
23. B. P. Feuston and J. B. Higgins, *J. Phys. Chem.* **98**, 4459 (1994).
24. M. Kruk, and M. Jaroniec, *Chem. Mater.* **13**, 3169 (2001).
25. C. Y. Hong, Y. Z. You, C. Y. Pan, *Chem. Mater.* **17**, 2247(2005).

SYNTHESIS AND PREPARATION OF NOVEL POLYOXOMETALATE-FUNCTIONALIZED MESOPOROUS HYBRID MATERIALS

RONGFANG ZHANG AND CHUN YANG*

*College of Chemistry and Environmental Science, Nanjing Normal University, Nanjing
210097, P. R. China*

Novel polyoxometalate (POM)-functionalized mesoporous hybrid silicas were synthesized and prepared by the co-condensation using SiW_{11} as POM precursor and the post-synthesis grafting $\text{SiW}_{11}\text{Si}_2$ directly, respectively. The as-obtained hybrid samples were characterized by FT-IR, UV-vis/DRS, ^{29}Si CP MAS NMR, XRD, ICP-AES and N_2 adsorption-desorption measurements. The results show that these materials possess both hexagonal mesostructures with SBA-15 architecture and perfect Keggin units bound covalently with the silica wall. This covalent linkage results in a firm immobilization of POM on the mesoporous material.

1. Introduction

The study of functionalized ordered mesoporous silica materials has attracted much attention in the past decade due to their prospective application in adsorption, separation, catalysis, sensing, optics and other fields. Two approaches, grafting (post-synthesis) and co-condensation (one-step synthesis) have been developed as main functionalization strategies to introduce suitable functional moieties (catalytic active groups, reactive ligands *etc.*) onto the surface of mesoporous materials [1-4]. In both approaches, however, almost all of the introduction and immobilization of functionalities are based on the silanization reaction of surface with organosilanes containing functional moieties, or the anchoring of organosilanes at least at the first step as a bridge for the further introduction of functionalities. Few direct connections of functional groups, especially inorganic species, to silica surface were reported [5,6].

Polyoxometalates (POMs) with excellent catalytic performance (*e.g.*, heteropoly acids and their salts) have been supported on the periodic ordered mesoporous materials in order to acquire heterogeneous POM catalysts of high efficiency. However, the mesoporous silica-supported POMs are usually prepared by impregnation or inclusion, and the POMs are easily leached in

* Corresponding author

application using polar solvent as medium [7-9] since no a strong chemical linkage exists between the supports and the POMs. Therefore, it is an interesting challenge to anchor POMs onto the periodic ordered mesoporous silica by covalent bonding. Here, we report a novel POM-functionalized mesoporous hybrid material with SBA-15 architecture, which can be synthesized and prepared by both co-condensation and post-synthesis. In these syntheses, a Keggin-type monovacant polyoxometalate, $\text{SiW}_{11}\text{O}_{39}^{8-}$ (SiW_{11}), as well as its derivative $\text{SiW}_{11}\text{O}_{39}[\text{O}(\text{SiOH})_2]^{4-}$ ($\text{SiW}_{11}\text{Si}_2$) are used as precursors of POM.

2. Experimental

2.1. Materials and Syntheses of Samples

Potassium salt of $\text{SiW}_{11}\text{O}_{39}^{8-}$ (SiW_{11}) was synthesized using the procedure reported in Ref. [10]. $\text{SiW}_{11}\text{O}_{39}[\text{O}(\text{SiOH})_2]^{4-}$ ($\text{SiW}_{11}\text{Si}_2$) was synthesized referencing to the procedure in Ref. [11] by allowing the potassium salt of SiW_{11} to react with TEOS at room temperature under an acidic condition of pH=1. Tetrabutylammonium (TBA) salt was obtained by adding tetrabutylammonium bromide to the solution. Elemental analysis for the product was consistent with the formula, $[\text{Bu}_4\text{N}]_4\text{SiW}_{11}\text{O}_{39}[\text{O}(\text{SiOH})_2]$ (Found: C, 20.39; H, 3.96; N, 1.68; W, 53.79; Si, 2.29%; Calc: C, 20.49; H, 3.93; N, 1.49; W, 53.92 ; Si, 2.25%).

Co-condensation syntheses of the mesoporous hybrid silicas were carried out by reference to Ref. [12,13]. In a typical preparation, 1g of Pluronic P123 (Aldrich) were solved in 30 mL of 2 M HCl solution with stirring at 40°C. Then tetraethoxysilane (TEOS) was added into the solution. After a stirring at 40°C for 2 h for prehydrolysis of TEOS, the potassium salt of SiW_{11} and 7.5 mL of H_2O was added. The molar composition of the mixture for 1 g of copolymer was $(0.01-X)\text{TEOS} : X\text{SiW}_{11} : 0.06\text{HCl} : 1.96\text{H}_2\text{O}$, where $X = 0.00025$ (2.5%), 0.0005 (5%). The numbers in parentheses indicate the molar percentages of SiW_{11} in the initial mixture ($\text{SiW}_{11}+\text{TEOS}$). The resultant mixture was crystallized under stirring for an additional 24 h at 40°C, and subsequently aged at 80°C for 24 h under static condition. After cooled to room temperature, the solid product was recovered by filtration, washed thoroughly with water, and air-dried at room temperature overnight. The template was removed from the as-synthesized material by extraction with ethanol in a Soxhlet extractor for 36 h. The samples synthesized *via* this route are denoted as xx% SiW_{11} /MHS, where xx% refers to the molar percentages of SiW_{11} in the initial mixture.

Post-syntheses of the mesoporous hybrid silicas were made as follows: Hexagonal mesoporous silica SBA-15 was synthesized according to the method

reported [12,13]. After outgassed under vacuum at 120°C for 3 h, 0.25g of SBA-15 powder was introduced into 10 mL of acetonitrile solution of TBA salt of $\text{SiW}_{11}\text{Si}_2$. The mass ratio of SBA-15 to $\text{TBASiW}_{11}\text{Si}_2$ was kept to 1:x (x = 3 and 5, respectively) in the mixture. The slurry was stirred for 12 h at room temperature and then evaporated slowly at 50~60°C to remove the solvent. The resultant solid was calcined at 200°C for 2 h, followed by washed with 10 mL of acetonitrile under sonication for 10 min and then filtered to remove free $\text{TBASiW}_{11}\text{Si}_2$ molecules. After 10 repeated washings, the solid product was collected by filtration, and air-dried at room temperature. The samples synthesized *via* this route are denoted as 1:x $\text{SiW}_{11}\text{Si}_2/\text{MHS}$, where 1:x refers to the mass ratio of SBA-15 to $\text{TBASiW}_{11}\text{Si}_2$ (g/g) .

2.2. Characterization

Powder X-ray diffraction (XRD) patterns of the samples were recorded on an ARL X'TRA diffractometer using Cu K α radiation. Infrared (IR) spectra were collected on a Tensor-27 FTIR spectrometer, KBr pellets. UV-vis diffuse reflectance spectra (UV-vis/DRS) were recorded on a Varian Cary 5000 spectrophotometer. Elemental analyses were performed on a Leeman Lab Prodigy inductively coupled plasma-atomic emission spectroscopy (ICP-AES) instrument. Solid-state ^{29}Si CP MAS NMR measurements were performed on a Bruker AV-400 spectrometer operating at ^{29}Si frequency of 79.457 MHz and ^1H frequency of 399.952 MHz. N_2 adsorption-desorption isotherms at 77K were measured using a Micromeritics ASAP 2020M physisorption analyzer. The samples were outgassed under vacuum at 120°C for 6 h before the measurement.

3. Results and Discussion

In order to introduce POM into the mesophase by co-condensation or post-synthesis, a POM molecule with reactive sites on the surface, by which the POM can condense easily with the silica species, should be considered as POM precursor and employed in the synthesis. Keggin-type monovacant SiW_{11} is a suitable candidate, because it can react with organosiloxane, such as trialkoxysilane, under acidic condition to yield its saturated derivatives $\text{SiW}_{11}\text{O}_{39}[\text{O}(\text{SiR})_2]^{4-}$ [11]. Similar reaction of SiW_{11} with TEOS to yield $\text{SiW}_{11}\text{O}_{39}[\text{O}(\text{SiOH})_2]^{4-}$ ($\text{SiW}_{11}\text{Si}_2$) was also confirmed by us. In $\text{SiW}_{11}\text{Si}_2$ structure, Si-O-W bonds are formed, and there are two SiOH groups on the surface of the molecule, providing the reactive sites for the condensation with silica species. Consequently, the co-condensation syntheses of mesoporous hybrid silicas $\text{SiW}_{11}/\text{MHS}$ were carried out based on a sol-gel procedure

analogous to that for SBA-15 silica [12,13] and a direct employment of SiW_{11} as POM precursor; while the post-syntheses of mesoporous hybrid silicas $\text{SiW}_{11}\text{Si}_2/\text{MHS}$ were made by using a derivative of SiW_{11} , *i.e.*, $\text{SiW}_{11}\text{Si}_2$, as POM precursor to react with mesoporous silica SBA-15. The contents of SiW_{11} (calculated on $\text{SiW}_{11}\text{O}_{39}$ basis) in the hybrid samples were evaluated by elementary analysis (ICP-AES for W) and are given in Table 1 together with other property parameters.

Table 1. Property parameters of the samples

Sample	SiW_{11} wt%	d_{100} (nm)	S_{BET} (m^2/g)	V_t (mL/g)	D (nm)
SBA-15		10.04	887	1.06	7.9
1.25% $\text{SiW}_{11}/\text{MHS}$	18.2	9.60	589	0.70	6.9
5% $\text{SiW}_{11}/\text{MHS}$	26.4	9.82	429	0.52	6.1
1:3 $\text{SiW}_{11}\text{Si}_2/\text{MHS}$	16.3	9.93	513	0.59	7.5, 5.3
1:5 $\text{SiW}_{11}\text{Si}_2/\text{MHS}$	21.2	9.93	274	0.29	6.3, 4.6

d_{100} = (100) spacing, S_{BET} = surface area calculated by BET method, V_t = single point total pore volume, D = pore size calculated by BJH method from the adsorption branch of N_2 isotherm

The most important and concerned problem to us is whether the Si-O-W bond, *i.e.*, saturated $\text{SiW}_{11}\text{Si}_2$ structure is formed in the hybrid materials. This formation is a precondition of the establishment of covalent linkage between POM and mesoporous silica framework. Thus, the characteristic IR absorption data, which are almost the most effective means to identify the structures of $\text{SiW}_{11}\text{Si}_2$ in the hybrid samples, were investigated carefully. It is clearly seen from Fig.1 that the spectrum of $\text{SiW}_{11}\text{Si}_2$ (Fig.1b) is distinctly different from that of SiW_{11} (Fig.1a) owing to the saturation of Keggin structure. The features of the saturated $\text{SiW}_{11}\text{Si}_2$ are also observed in the spectra of hybrid samples $\text{SiW}_{11}/\text{MHS}$ (Fig.1d) and $\text{SiW}_{11}\text{Si}_2/\text{MHS}$ (Fig.1e), respectively. Although Si-O-Si band ($\sim 1050 \text{ cm}^{-1}$) and W=O band ($\sim 960 \text{ cm}^{-1}$) for $\text{SiW}_{11}\text{Si}_2$ structure are covered by Si-O-Si band and Si-O band of mesoporous silica itself, respectively, an additional band appears at $\sim 910 \text{ cm}^{-1}$ as compared to pure SBA-15 (Fig.1f), and the intensity increases with SiW_{11} loading. Clearly, this band results from Si-O vibration of the central SiO_4 unit of $\text{SiW}_{11}\text{Si}_2$ in $\text{SiW}_{11}/\text{MHS}$ and $\text{SiW}_{11}\text{Si}_2/\text{MHS}$, respectively. A more explicit exhibition of $\text{SiW}_{11}\text{Si}_2$ structure in hybrid materials is given in the subtraction spectrum for $\text{SiW}_{11}/\text{MHS}$ (Fig.1c). Almost all of characteristic bands of $\text{SiW}_{11}\text{Si}_2$ are shown clearly in Fig.1c, denoting that not only Keggin unit of the POM is retained perfectly, but also $\text{SiW}_{11}\text{Si}_2$ structure is formed, and thus SiW_{11} is covalently bound to the silica framework by co-condensation. Similar subtraction spectrum for $\text{SiW}_{11}\text{Si}_2/\text{MHS}$

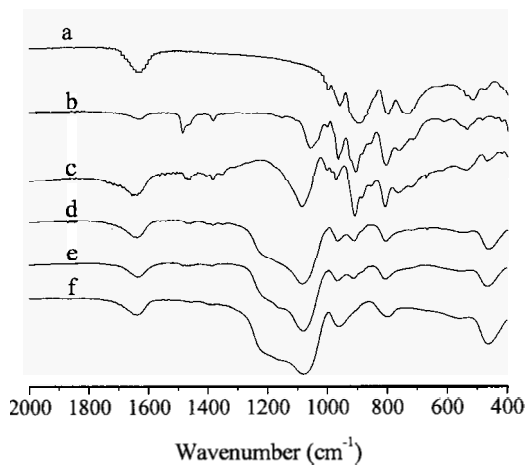


Fig.1. IR spectra of (a) SiW_{11} (K salt), (b) $\text{TBASiW}_{11}\text{Si}_2$, (c) subtracting (f) from (d), (d) 5% SiW_{11} /MHS, (e) 1:3 $\text{SiW}_{11}\text{Si}_2$ /MHS and (f) SBA-15

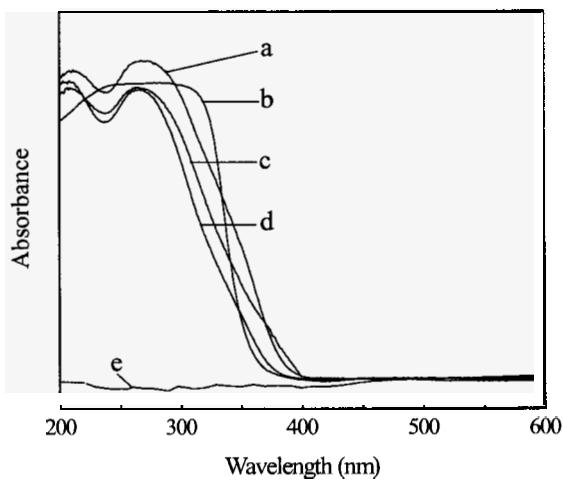


Fig.2. UV-vis/DRS spectra of (a) $\text{TBASiW}_{11}\text{Si}_2$, (b) SiW_{11} (K salt), (c) 5% SiW_{11} /MHS, (d) 1:3 $\text{SiW}_{11}\text{Si}_2$ /MHS and (e) SBA-15

(not shown here) is also obtained, indicating that $\text{SiW}_{11}\text{Si}_2$ molecules are successfully grafted on mesopore surface by post-synthesis.

UV-vis/DRS spectra of several samples are shown in Fig.2. Unlike pure SBA-15 (Fig.2e), all of the hybrid samples obtained by both routes exhibit UV absorption maxima at ~ 210 and ~ 265 nm (as shown in Fig.2c and 2d), which are attributed to oxygen-to-tungsten charge-transfer at $\text{W}=\text{O}$ and $\text{W}-\text{O}-\text{W}$ bonds of POM, respectively. It is noticed that the UV absorption peaks of the hybrid materials are different from those of monovacant SiW_{11} (Fig.2b) but similar to those of $\text{SiW}_{11}\text{Si}_2$ (Fig.2a), indicating again the presence of saturated Keggin unit in these materials.

Fig.3 exhibits ^{29}Si CP MAS NMR spectra before and after the introduction of POMs. Distinct resonance can be observed for various Si species in silica [$\text{Q}^n = \text{Si}(\text{OSi})_n(\text{OH})_{4-n}$, $n = 2\sim 4$; Q^4 at -111 ppm, Q^3 at -102 ppm and Q^2 at -93 ppm]. The change of relative integrated intensities of Q^n signals after the introduction of POMs reflects the interconversion between these Si species during the incorporation. It can be seen from Fig.3b and 3c that obvious increases in relative intensity of Q^4 and in Q^4/Q^n ($n = 2, 3$) integrated ratios occur when SiW_{11} or $\text{SiW}_{11}\text{Si}_2$ is incorporated, and the more the loading of POM is, the more the relative intensity of Q^4 increases, implying the transformation of Q^2 and Q^3 species into Q^4 species owing to the formation of Si-O-Si bonds, which results from the condensation reaction of terminal SiOH groups in silica with $\text{SiW}_{11}\text{Si}_2$ species. An additional signal at about -84.5 ppm attributed to central SiO_4 unit in $\text{SiW}_{11}\text{O}_{39}[\text{O}(\text{SiR})_2]^4$ [11] is also found in Fig.3b and 3c, further suggesting the introduction of $\text{SiW}_{11}\text{Si}_2$ moiety onto the silica wall of $\text{SiW}_{11}/\text{MHS}$ and $\text{SiW}_{11}\text{Si}_2/\text{MHS}$.

The small-angle powder XRD patterns of the hybrid materials (Fig.4) show intense diffraction peak (100) and weak peaks (110) and (200), characteristic of ordered hexagonal mesophase. For the samples obtained by the co-condensation (Fig.4c and 4d), however, the higher order (110) and (200) reflections diminish in intensities as the concentration of SiW_{11} in initial mixture increases, indicating the reduction of long-range order of mesophase with increasing initial SiW_{11} concentration. This is apparently caused by the perturbation of an elevated concentration of SiW_{11} on the formation and self-assembly of surfactant aggregates. For the samples obtained by post-synthesis (Fig.4a and 4b), not only peaks (110) and (200) but also peak (100) become weak as the loading of $\text{SiW}_{11}\text{Si}_2$ increases, as a result of the reduction in scattering contrast at higher pore filling. The broad-angle XRD patterns of the hybrid samples (not shown here) show no reflections of POM crystal, suggesting a high dispersion of POM in all of the materials. Moreover, as revealed by XRD measurement, a specified

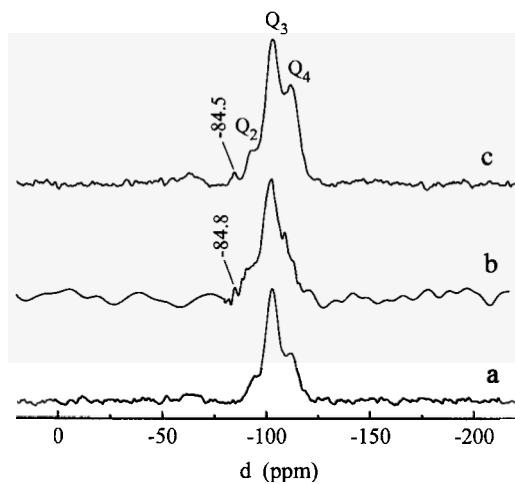


Fig.3. ^{29}Si CP MAS NMR spectra of (a) SBA-15, (b) 1:3 $\text{SiW}_{11}\text{Si}_2/\text{MHS}$ and (c) 5% $\text{SiW}_{11}/\text{MHS}$

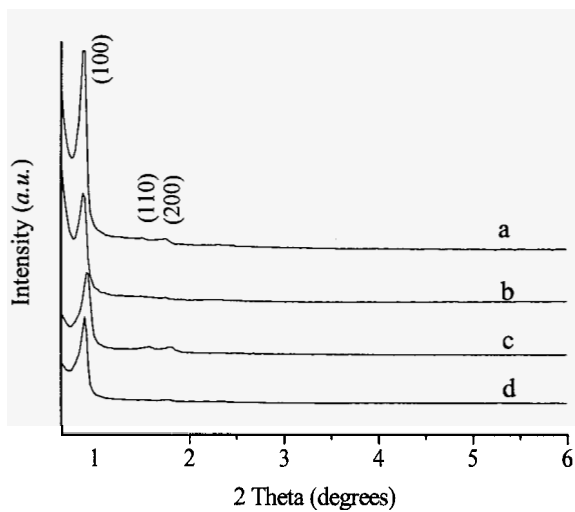


Fig.4. Small-angle XRD patterns of (a) 1:3 $\text{SiW}_{11}\text{Si}_2/\text{MHS}$, (b) 1:5 $\text{SiW}_{11}\text{Si}_2/\text{MHS}$, (c) 1.25% $\text{SiW}_{11}/\text{MHS}$ and (d) 5% $\text{SiW}_{11}/\text{MHS}$

TEOS prehydrolysis time is necessary to create ordered mesostructure in the co-condensation route, similar to the synthesis of organically functionalized SBA-15 [3]. An amorphous material was obtained at the higher initial SiW_{11} concentration and the shorter prehydrolysis time of TEOS in the co-condensation synthesis.

Nitrogen adsorption-desorption measurements show the type-IV isotherms and type-H1 hysteresis loops for the hybrid materials synthesized by the co-condensation (Fig.5a and 5b), characteristic of SBA-15 architecture [12]. A one-step capillary condensation occurring at $p/p_0 = 0.6\sim 0.8$ indicates the presence of regular mesopores with uniform size in these materials, as confirmed by narrow single peaks in the mesopore size distribution curves (Fig.6a and 6b). For those prepared by post-synthesis route, however, unsmooth isotherms and narrower hysteresis loops are observed (Fig.5c and 5d). Two-step isotherms, as well as dual maxima in the mesopore size distribution (Fig.6c and 6d) suggest that pore blocking occurs and two mesopores with different sizes are present in these materials. This phenomenon appears even at lower POM loading, and develops towards a severe blockage with increasing loading, leading to a great decline in both mesopore size and volume (see Fig.6c and 6d). Apparently, such pore blockage results from the bulky $\text{SiW}_{11}\text{Si}_2$ anions and TBA cations introduced,

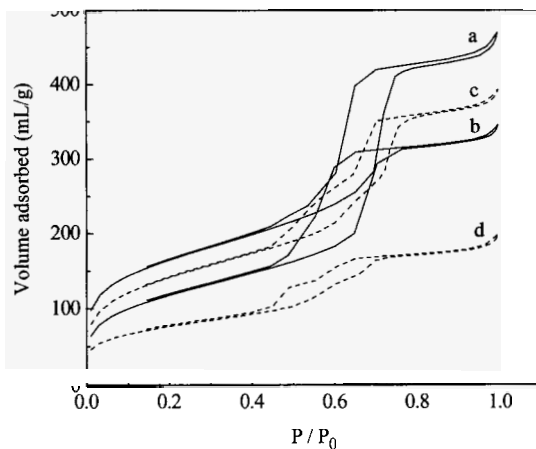


Fig.5. N_2 adsorption-desorption isotherms of (a) 1.25% SiW_{11} /MHS, (b) 5% SiW_{11} /MHS, (c) 1:3 $\text{SiW}_{11}\text{Si}_2$ /MHS and (d) 1:5 $\text{SiW}_{11}\text{Si}_2$ /MHS

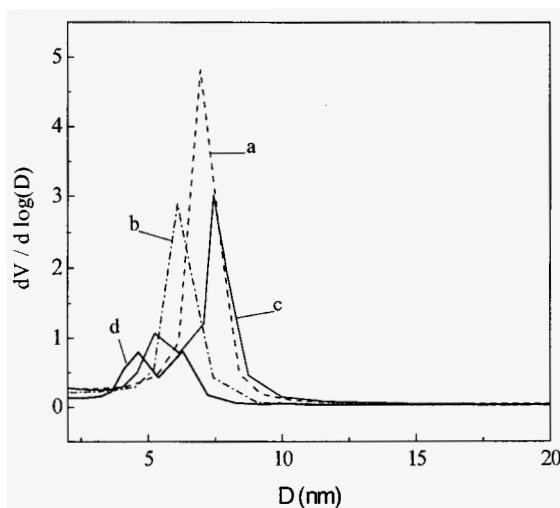


Fig.6. Mesopore size distribution of (a) 1.25% SiW₁₁/MHS, (b) 5% SiW₁₁/MHS, (c) 1:3 SiW₁₁Si₂/MHS and (d) 1:5 SiW₁₁Si₂/MHS

which occupy the interior pore void so severely that the secondary mesopores with smaller size are formed at some sites in channels where there is a higher density of POM filling.

The data from N₂ adsorption-desorption for several samples are listed in Table 1. In the case of co-condensation, despite no pore blockage, the reduction in specific surface areas and specific pore volumes is observed after the introduction of POM, and exacerbated as the POM loading increases. This may be attributed to the increase of specific weights of the samples containing POM of big molecular mass and the loss of a section of ordered mesostructure when the higher initial SiW₁₁ concentration is used.

In view of above characterization, we propose that SiW₁₁Si₂ is an important reactive species not only for the post-synthesis but also for the co-condensation synthesis. It is formed at first in the co-condensation mixture by the reaction of SiW₁₁ with TEOS, and then condenses with the preorganized silica framework (inorganic-organic composite) to connect the POM on to the framework. In the post-synthesis route, although reactive SiW₁₁Si₂ is incorporated directly by

impregnation, the calcination of sample at an elevated temperature is necessary, which offer a condition for the condensation between $\text{SiW}_{11}\text{Si}_2$ and silica wall.

In conclusion, a novel mesoporous hybrid material containing covalently linked POM can be synthesized and prepared by co-condensation and grafting technique, respectively. The key problem in these syntheses is choosing or creating a suitable POM precursor. Compared to the post-synthesis (grafting), the co-condensation method endows the materials with uniform pore size without pore blockage and homogeneous distribution of POM in the channels. However, whether an ordered mesoporous hybrid material can be obtained by the co-condensation is also restricted by synthesis conditions.

Acknowledgments

We thank the National Natural Science Foundation of China (20473037) for financial support.

References

1. I. Rodríguez, S. Iborra, A. Corma, F. Rey and J. L. Jordá, *Chem. Commun.* 593 (1999).
2. A. Vinu, K.-Z. Hossain and K. Ariga, *J. Nanosci. Nanotech.* **5**, 347 (2005).
3. D. Margolese, J. A. Melero, S. C. Christiansen, B. F. Chmelka and G. D. Stucky, *Chem. Mater.* **12**, 2448 (2000).
4. R. J. P. Corriu, A. Mehdi, C. Reyé and C. Thieuleux, *Chem. Mater.* **16**, 159 (2004).
5. M. Alvaro, A. Corma, D. Das, V. Fornés and H. García, *Chem. Commun.* 956 (2004).
6. Y. Inaki, Y. Kajita, H. Yoshida, K. Ito and T. Hattori, *Chem. Commun.* 2358 (2001).
7. K. Nowinska, R. Fórmaniak, W. Kaleta and A. Waclaw, *Appl. Catal. A* **256**, 115 (2003).
8. W. Chu, X. Yang, Y. Shan, X. Ye and Y. Wu, *Catal. Lett.* **42**, 201 (1996).
9. M. J. Verhoef, P. J. Kooyman, J. A. Peters and H. Bekkum, *Microporous Mesoporous Mater.* **27**, 365 (1999).
10. A. Tézé and G. Hervé, *J. Inorg. Nucl. Chem.* **39**, 999 (1977).
11. P. Judeinstein, C. Deprun and L. Nadjo, *J. Chem. Soc. Dalton Trans.* 1991 (1991).
12. D.-Y. Zhao, J.-L. Feng, Q.-S. Huo, N. Melosh, G. H. Fredrickson, B. F. Chmelka and G. D. Stucky, *Science* **279**, 548 (1998).
13. D.-Y. Zhao, Q.-S. Huo, J.-L. Feng, B. F. Chmelka and G. D. Stucky, *J. Am. Chem. Soc.* **120**, 6024 (1998).

SYNTHESIS OF A MICROPOROUS ORGANIC-INORGANIC HYBRID LAYERED NANOCOMPOSITE WITH BIS(METHYLDICHLOROSILYL)BIPHENYL AND SILICIC ACID OF ILERITE

RYO ISHII[†], TAKUJI IKEDA, TETSUJI ITOH, TOSHIROU YOKOYAMA,
TAKA-AKI HANAOKA, AND FUJIO MIZUKAMI

Research Center for Compact Chemical Process, National Institute of Advanced Industrial Science and Technology (AIST), Nigatake 4-2-1, Sendai, 983 8551, Japan

A microporous layered organic-inorganic nanocomposite has been prepared by interlayer silylation of a crystalline layered silicate, ilerite, with 4, 4'-bis(methyldichlorosilyl)-biphenyl. The nanocomposite has a gallery height of 2.11 nm, which is retained by bridging of the biphenylene units between the layers. The bridging yields microporous structure in the interlayer where the biphenylene units have a role in the framework of the micropore, leading to a higher adsorptivity for toluene than other porous silicas.

1. Introduction

Crystalline layered silicates such as magadiite, ilerite (octosilicate or RUB-18) and kanemite have been widely applied for synthesis of organic-inorganic nanocomposites. The nanocomposites are prepared by interlayer modification with organic cations or organosilanes. The modified interlayer provides hydrophobic nanospaces suitable for the entrapment for organic molecules, leading to the application as adsorbents or nanofillers. However, the entrapment capacity is limited because the nanocomposites have less porous structure due to the presence of bulky and flexible organic moieties in the interlayer, resulting from the interlayer modification. Thus, the construction of the porous structure in the nanocomposites would improve the entrapment ability of the nanocomposites.

We have developed microporous organic-inorganic hybrid nanocomposites by alkoxylation of 4, 4'-biphenylene-bridged alkoxy silane compounds [1]. The nanocomposites possess the porous structure resulting from the interlayer bridging of the biphenylene units. Furthermore, the biphenylene units show monolayer arrangement in the interlayer by using mono- or trifunctional

[†] Corresponding author

alkoxysilane, or double layer-like arrangement by using difunctional alkoxy silane. The present method is a new synthetic approach to produce the porous structure in the nanocomposites, which can be expected to contribute to the development of these organic-inorganic hybrid materials. On the other hand, the obtained nanocomposites are low crystalline layered compounds due to stacking faults caused by the incomplete silylation of the units with the silicic acid. These findings suggest that the reactivity of the organosilanes has an influence on the layered structure of the nanocomposites.

Here, we report a synthesis of the microporous nanocomposite using a biphenylene-bridged chlorosilane in order to improve the structural regularity of the nanocomposite. The approach focuses on the formation of the double layer arrangement in the interlayer using the biphenylene-bridged difunctional chlorosilane having methylchlorosilyl groups at each end of the unit because of the structural interest. In the present work, structural analyses of the resultant product were conducted. The porosity and adsorptivity of the products were then evaluated in order to determine the surface property. Finally, we proposed a model of the interlayer structure.

2. Experimental

2.1. Materials and synthesis

Ilerite was prepared from suspension containing 2 g of silica in 4 cm³ of 4 mol dm⁻³ NaOH aqueous solution at 378 K for 216 h, as described by Kosuge and Tsunashima [2]. Then, the silicic acid of ilerite (H-ilerite) was obtained by adding 70 cm³ of 0.1 mol dm⁻³ hydrochloric acid aqueous solution to the ilerite. The acid treatment was repeated twice. The white product was washed and then dried at 323 K overnight.

4, 4'-Bis(methylchlorosilyl)biphenyl (abbreviated as BCSB) was synthesized by chlorination of 4, 4'-bis(methyldiehoxy)silyl)biphenyl (BESB). The BESB compound was prepared according to the method reported by Shea *et al.* [3]. The BESB compound (6.0 g) was refluxed with acetyl chloride (10 ml) and tetrahydrofuran (10 ml) under argon at 353 K for 48 h. The volatile compounds were removed in vacuo. The procedure was repeated once. The resultant oil was distilled under *ca.* 0.3 mmHg at 457–476 K to give a clear oil (3.6 g, 60 %). The NMR data of the compound were as follows: BCSB: d_{H} (500 MHz; CDCl₃; Me₄Si), 7.84-7.56 (dd, 8 H, C₁₂H₈), 1.96 (s, 6 H, SiMe).

H-ilerite (0.2 g) was mixed with 1.2 cm³ of *n*-hexylamine and placed in a sealed Teflon tube for 48 h at room temperature. The H-ilerite and *n*-hexylamine

mixture was stirred with BCSB (0.3 cm^3) and *n*-hexane (10 cm^3) for 168 h at room temperature. A white compound was separated from the suspension by centrifugation. The compound was then air-dried for 120 h at room temperature and then dried for 8 h at 423 K. After drying, the compound was suspended in 20 cm^3 of 1 mol dm^{-3} HCl ethanol solution for 120 h at room temperature for the elution of *n*-hexylamine. The final product (BCSB-ilerite) was separated and dried at 423 K under reduced pressure for 8 h.

2-2. Characterization

Silicon contents of the solid were determined using an SPS7800 inductively coupled plasma (ICP) spectrometer (SEIKO Co., Japan) according to the method reported by Ishii *et al.* [4]. Total carbon (TC) and total nitrogen (TN) contents of the products were measured by gas chromatography with a SUMIGRAPH NCH-21 analyzer (Sumika Analysis Service Co., Ltd., Japan). Powder X-ray diffraction (XRD) data were measured using an M21X diffractometer (MAC Science Co., Ltd., Japan) with curved graphite monochromator (Cu K_α radiation) operated at 45 kV and 250 mA. ^{29}Si solid-state MAS-NMR experiments were performed on a Bruker AVANCE 400WB spectrometer operated at 79.495 MHz with a 7 kHz spinning frequency using a 7 mm MAS probe. ^{29}Si DDMAS NMR spectra were obtained with 30° pulse of $1.6 \mu\text{s}$ and 30 sec cycle delay time. A total of 1024 scans were accumulated for each sample. UV-vis diffuse reflectance spectra for the products were obtained on a UV-3100PC spectrometer (Shimadzu Co., Ltd., Japan) equipped with an integrating sphere unit (MPC-3100, Shimadzu Co., Ltd., Japan). Nitrogen adsorption and desorption measurements at 77 K were carried out on a Belsorp-MAX (Japan BEL Co., Ltd., Japan) for samples degassed at 423 K below 10^{-3} mmHg for 4 h. Water and toluene adsorption isotherms at 298 K were collected by a BELSORP-18 (Japan BEL Co., Ltd., for samples degassed at 423 K below 10^{-3} mmHg for 6 h.

3. Results and Discussion

Fig. 1 shows a SEM image for BCSB-ilerite. The crystal morphology of the original ilerite was a rectangular shape. BCSB-ilerite retains the similar morphology to that of H-ilerite, indicating no structural damage during the treatment.

XRD patterns for BCSB-ilerite before and after HCl/ethanol treatment as shown in Fig. 2. H-ilerite has the basal spacing of 0.74 nm. After the treatment with *n*-hexylamine and BCSB, the diffraction line corresponding to the basal

spacing shifted to a lower angle side at $2\theta = 3.14^\circ$ ($d = 2.81 \text{ nm}$) due to their intercalation between the silicate layers. The treatment also brought about some sharp peaks at $2\theta = 4.64, 18.28, 22.86^\circ$ and so on. These peaks are assigned to hexylamine hydrochloride that is formed by evolution of hydrochloric acid resulting from condensation of chlorosilyl groups in BCSB with silanol groups in the interlayer. They disappear after the following HCl/ethanol treatment due to

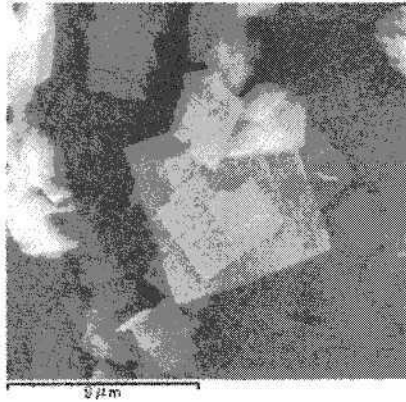


Fig. 1. A SEM image for BCSB-ilerite.

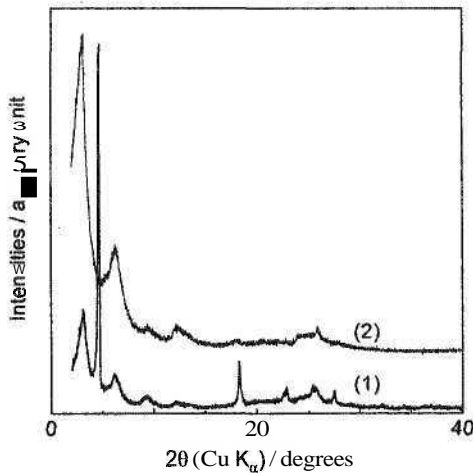


Fig. 2. XRD patterns for BCSB-ilerite: (1) before HCl/ethanol treatment, (2) after HCl/ethanol one.

the elution of the hexylamine hydrochloride from BCSB-ilerite. The final product has the basal spacing at $2\theta = 3.08^\circ$ ($d = 2.87$ nm). The product also has clear (001) reflections at $2\theta = 6.30$ and 9.38° , indicating that BCSB-ilerite has a layered structure with the good order of the stacking.

A diffuse reflective UV-vis spectrum for BCSB-ilerite showed a peak around 280 nm due to the UV absorption of the biphenylene unit. Chemical analysis for BCSB-ilerite revealed that Si, TC and TN contents were 30.0, 30.8 and 0.05 wt%. The TN content is almost negligible due to the elution of *n*-hexylamine. The TC contents originate from the BCSB molecules. These results indicate that the BCSB molecules are intercalated in the interlayer of H-ilerite and that have a role as a pillar to retain the large gallery space. We calculated the number of the BCSB molecules based on the crystalline structure of the original ilerite. The number, which is derived from these contents and the structure of the ilerite, was estimated as 7.9 molecules in the unit cell of the ilerite. The number is higher than the number (= 5.8) for BESB-ilerite that was obtained by a similar manner using 4, 4'-bis(methyldiethoxysilyl)biphenyl. The higher number suggests that the immobilization of the biphenylene units was promoted by the exchange from ethoxysilyl group to chlorosilyl one.

^{29}Si MAS NMR spectra for H-ilerite and BCSB-ilerite are presented in Fig. 3. Two peaks at -103 and -111 ppm are observed in the spectra. They are assigned to Q^3 ($\text{Si}(\text{OSi})_3(\text{OR})$) and Q^4 ($\text{Si}(\text{OSi})_4$) structural units that originate from the framework of the silicate sheets of H-ilerite. While the Q^3/Q^4 integral ratio is 1

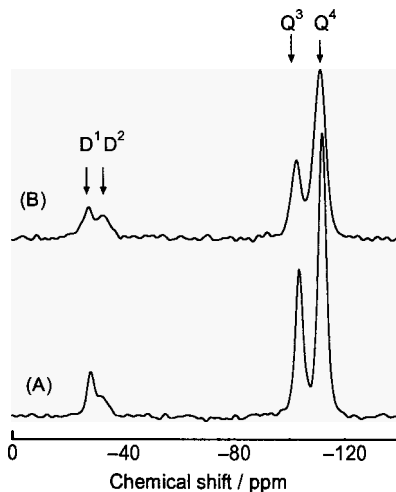


Fig. 3. ^{29}Si MAS NMR spectra for BCSB-ilerite (A) before and (B) after HCl/ethanol treatment.

for H-ilerite, the ratio is estimated as 0.43 for BCSB-ilerite, being less than that for H-ilerite due to the decrease in the Q^3 intensity. This finding indicates that the Q^3 units, corresponding to the silanol groups, are converted to the Q^4 ones after the treatments. In addition, two peaks at -27.8 and -32.8 appear in the spectrum for BCSB-ilerite. They are assigned to D^1 ($R_2Si(OSi)OR$) and D^2 ($R_2Si(OSi)_2$) structural units that originate from the Si atoms at each end of the condensed BCSB molecule. Therefore, the decrease in the Q^3 intensity and the appearance of D^1 and D^2 units indicate that the BCSB molecules are connected with the silanols in the interlayer of H-ilerite. In order to quantitatively evaluate the bonding between BCSB molecule and H-ilerite, the number of the generated siloxane bonding per one BCSB molecule with H-ilerite is calculated as follows:

$$N = ((1 - (Q^3/Q^4)) / (1 + (Q^3/Q^4))) \times N_s / N_{BCSB} \quad (1)$$

where N represents the number of the generated siloxane bonding per one BCSB molecule with H-ilerite and (Q^3/Q^4) represents the integral ratio of the Q^3 intensity to the Q^4 one in the spectrum. N_s means the number of the silanol groups in the unit cell of the original ilerite. The N_s is 16 from the cell content of the ilerite after the protonation. N_{BCSB} represents the number of the BCSB molecules containing in the unit cell. The chemical analysis revealed that the N_{BCSB} is 7.9. The $(1 - (Q^3/Q^4)) / (1 + (Q^3/Q^4))$ represents the conversion ratio of the silanol group to the siloxane bonding in H-ilerite, being calculated as 0.40 for BCSB-ilerite. Therefore, N is estimated as 0.8. The number ($= 0.8$) revealed that a BCSB molecule is almost bound to H-ilerite through either side of the biphenylene unit because the molecule has two silyl groups at each end of the unit. The number, however, is inconsistent with the presence of the D^1 and D^2 units in the spectrum because these units mean that the BCSB molecule has more than one siloxane bonding at each end of the unit. The inconsistency suggests that the BCSB molecules are condensed with the neighboring BCSB molecules. In addition, the quantitative comparison of the D^1 and D^2 units showed the difference in the degree of their condensation between BCSB- and BESB-ilerite. The $D^2/(D^1+D^2)$ integral ratio is estimated as 0.43 for BCSB-ilerite although the ratio was 0.27 for BESB-ilerite. The ratio indicates that the BCSB molecules are condensed well with each other, probably due to their high reactivity.

Nitrogen adsorption isotherm for BCSB-ilerite is presented in Fig. 4(a). The N_2 isotherm has a steep rise up to $p/p_0 = 0.1$ as compared with that for H-ilerite, indicating that BCSB-ilerite is a microporous material. The BET surface area, which is derived from the N_2 uptakes between $p/p_0 = 0.05$ and 0.1 , is estimated as $642 \text{ m}^2/\text{g}$. Based on a slit-pore model, the pore width is estimated as 0.991 nm

in size, resulting from the division of the total pore volume (the N_2 uptake at $p/p_0 = 0.906$, $206 \text{ cm}^3 \text{ (STP)/g}$) by the BET surface area. The width is smaller than the basal spacing (2.87 nm) for BCSB-illerite, indicating that the width reflects not the gallery height but the interval between the intercalated biphenylene units. A water adsorption isotherm for BCSB-illerite is presented in Fig. 4(b). The isotherm shows a type-V of the BDDT classification [5]. The isotherm shows very low uptakes at the relative pressure up to $p/p_0 = 0.1$, although the N_2 isotherm shows the steep rise at the corresponding region. This indicates that BCSB-illerite has a hydrophobic micropore. On the other hand, toluene adsorption isotherm has the type-I similar to the N_2 adsorption isotherm as shown in Fig. 4(b). The affinity is due to the interaction between toluene and the biphenylene units that

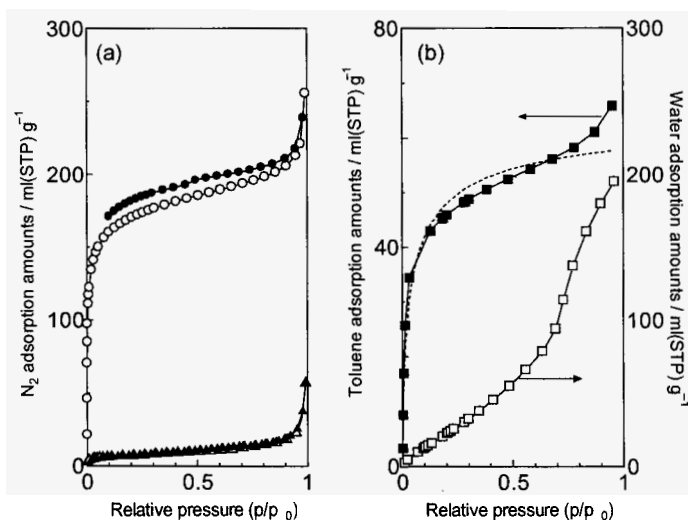


Fig. 4. (a) Nitrogen adsorption and desorption isotherms for BCSB-illerite and H-illerite: (○); adsorption and (●) desorption lines for BCSB-illerite, (△) adsorption and (▲) desorption lines for H-illerite. (b) Water and toluene adsorption isotherms for BCSB-illerite: (□) water, (■) toluene. The broken line represents the fitting curve obtained by Langmuir-Freundlich analysis.

constitute the framework of the micropore. In order to evaluate the interaction, we carried out Langmuir-Freundlich analysis [6, 7]. The Langmuir-Freundlich equation expresses as follows:

$$q = q_m(bp)^{1/n} / (1 + (bp)^{1/n}) \quad (2)$$

where q and q_m are the adsorbed amount at equilibrium pressure p , and monolayer adsorption capacity, respectively. Parameters b and n represent the sorbate-sorbent interaction and system heterogeneity, respectively. The equation fits the isotherm for BCSB-ilerite as shown in Fig. 4(b). The fitting parameters for the product and other porous silica materials are presented in Table. 1. The b value for BCSB-ilerite is higher than those for other porous silicas such as silicalite, BEA-type zeolites and FSM-type mesoporous silica (FSM-22). This would be due to the specific interaction such as p-p interaction, while the other porous silica materials have no specific interaction with toluene molecule.

Table. 1 The fitting parameters derived from Langmuir-Freundlich analysis.

Sample	$qm / \text{mmol/g}$	$b / 10^{-3} \text{ Pa}^{-1}$	n
BSCB-ilerite	2.93	24.2	1.57
Silicalite ^a	1.35	10.7	1.00
BEA-type zeolite ^a	2.89	5.25	0.67
FSM-22 ^a	3.63	2.95	0.70

^a The data were referred from R. Ishii *et al.* [8].

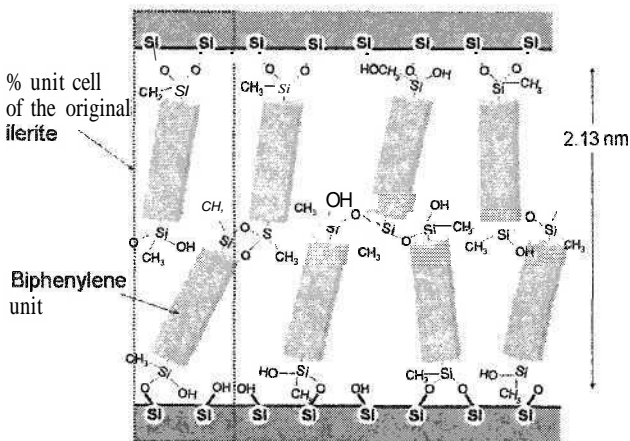


Fig. 5. A structural model for BCSB-ilerite.

Finally, a structural model for BCSB-ilerite is presented in Fig. 5. The basal spacing of BCSB-ilerite is 2.87 nm, indicating the gallery height of 2.13 nm by subtracting of a layer thickness (0.74 nm). Since the molecular length of the organic spacer (Si-C₁₂H₄-Si) in BCSB molecule is estimated as 1.2 nm, the basal spacing is almost twice larger than the dimension of one BCSB molecule, suggesting that two BCSB molecules connect one side of the interlayer gallery with the other side. The chemical analysis supports the geometric relation, because the analysis reveals that there are 7.9 BCSB molecules in the unit cell based on the crystalline structure of the original ilerite, corresponding to about two molecules in the 1/4 unit cell of the original ilerite as shown in Fig. 5. The BCSB molecule is bound to the surface of H-ilerite via one silyl group at either side of the unit. The ²⁹Si MAS NMR and chemical analysis indicate that the use of the BCSB molecule rather than the BESB molecule enhances the connectivity between the biphenylene units owing to its high reactivity, leading to the stable bridging between the silicate layers. From these results, we deduce that the resultant interlayer structure has the double-layer arrangement of the biphenylene units similar to that of conventional organo-clays. The arrangement, however, does not form the dense packing of the biphenylene units. There are vacant spaces at a molecular level between the units. The spaces form the micropores whose framework consists of the biphenylene units, having the strong affinity with the toluene molecules. The microporous interlayer structure having the double-layer arrangement would provide characteristic features for the entrapment of the organic molecules, giving a high possibility for the separation and catalytic application.

4. Conclusion

We have synthesized the microporous layered organic-inorganic nanocomposite (BCSB-ilerite) by the interlayer silylation of the BCSB molecule. The BCSB-ilerite has the layered structure whose basal spacing is 2.87 nm with the higher (001) reflections. The chemical analysis and ²⁹Si MAS NMR reveal that the use of the BCSB molecule improves the structural regularity of the stacking due to the sufficient silylation to retain the gallery space owing to its high reactivity. The gallery height and the silylation behavior suggest that the biphenylene units form the double-layer arrangement in the interlayer. The arrangement yields a high microporosity in the interlayer where the biphenylene units form the framework of the micropores. This is very interesting because conventional nanocomposites such as organo-clays yield no porosity in the interlayer due to the dense aggregation. The BCSB-ilerite shows the higher

adsorptivity for toluene than other porous silicas due to the strong interaction between the biphenylene units and the toluene molecules. Consequently, we have successfully developed the microporous nanocomposite characteristic to the large interlayer space with the hydrophobic microporosity.

References

1. R. Ishii, T. Ikeda, T. Itoh, T. Ebina, T. Yokoyama, T. Hanaoka and F. Mizukami, *J. Mater. Chem.* **16**, 4035 (2006).
2. K. Kosuge and A. Tsunashima, *J. Chem. Soc., Chem. Commun.*, 2427 (1995).
3. K. J. Shea, D. A. Loy and O. Webster, *J. Am. Chem. Soc.* **114**, 6700 (1992).
4. M. Nakatsuji, R. Ishii, Z-M. Wang and K Ooi, *J. Colloid and Interface Sci.* **272**, 158 (2004).
5. S. J. Gregg and K. S. W. Sing, *Adsorption, Surface Area and Porosity 2nd Ed.*, Academic Press, London, 1982, p3.
6. B. L. Newalkar, N. V. Choudary, P. Kumar, S. Komarneni and T. S. G. Bhat, *Chem. Mater.* **14**, 304 (2002).
7. B. L. Newalkar, N. V. Choudary, U. T. Turaga, R. P. Vijayalakshmi, P. Kumar, S. Komarneni and T. S. G. Bhat, *Chem. Mater.* **15**, 1475 (2003).
8. R. Ishii, Y. Kiyozumi and F. Mizukami, *Clay Sci.*, **13**, 81(2006).

PREPARATION OF THREE-DimensionALLY INTERCONNECTED ORDERED MESOPOROUS CARBONS BY USING NOVEL SILICA NANOSPHERES AS TEMPLATE

TOSHIYUKI YOKOI, RYOTA WATANABE, SEIGO OHTA, JUNKO. N. KONDO,
TAKASHI TATSUMI*

*Chemical Resources Laboratory, Tokyo Institute of Technology, 4259 Nagatsuta,
Midori-ku, Yokohama 226-8503, Japan*

TATSUYA OKUBO

*Department of Chemical System Engineering, The University of Tokyo, 7-3-1 Hongo,
Bunkyo-ku, Tokyo 113-8656, Japan*

Recently, we reported a novel and simple liquid-phase method for the preparation of three-dimensionally ordered and uniformly-sized silica nanospheres, forming a cubic closed pack (ccp) structure, by using tetraethyl orthosilicate (TEOS) and basic amino acids. Here we report that the successful control of the sphere sizes in the range from 10 to 120 nm was accomplished by the seed regrowth method and/or by using mixed solvents of water and ethanol. The preparation of three-dimensionally interconnected ordered porous carbons by using the silica nanospheres as a template is also reported. The pore sizes of the carbon structure can be easily controlled by varying the size of silica spheres.

1. Introduction

Porous carbon materials with tailored and well-ordered pores have received much attention because of their potential applications to gas separation, water purification, catalyst supports, electrodes for electrochemical double layer capacitors and fuel cells [1-4]. Since the discovery of templated synthesis of porous carbon [5], a variety of porous carbon materials with uniform-sized pores possessing micropores, mesopores and macropores have been prepared by using various inorganic templates, including silica nanoparticles, zeolites, anodic alumina membranes and mesoporous silica materials. Although many porous carbon materials have been developed by using the above-mentioned methods, the synthesis of carbon materials, which are three-dimensionally interconnected ordered pores with the sizes ranging from 10 to 80 nm, has been very challenging. For this purpose, the well-ordered spherical silica particles with

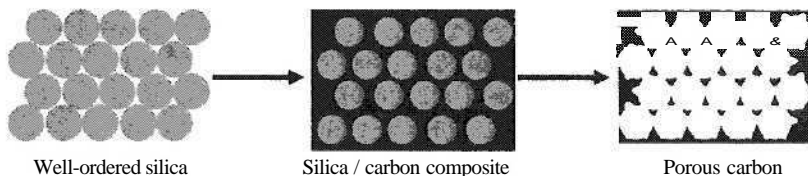
such sizes should be used as a template. Meanwhile, the preparation of such uniform-sized silica spheres with three-dimensional array is also challenging.

Stober and his co-workers pioneered the preparation of uniformly-sized silica spheres [6]. This innovative method is based on the ammonia-catalyzed hydrolysis of silicon alkoxides in water-ethanol solutions, producing spherical particles in a size range of several hundreds nanometers. Since the emergence of the "Stober method", the improvements and modifications of this method have been extensively conducted [7-10]. Nevertheless, the preparation of such uniform-sized silica spheres with three-dimensional array has not been successfully achieved.

We have developed a simple liquid-phase method for forming uniform-sized silica nanospheres with a size range of 10 nm by using tetraethyl orthosilicate (TEOS) and basic amino acids such as lysine and arginine [11]. Furthermore, the arrangement of such silica nanospheres with a cubic closed packed (ccp) assembly has been successfully achieved upon solvent evaporation and calcination. Note that the arrangement of uniform hard-nanospheres simultaneously created intraparticle uniform voids of about 3 nm. Meanwhile, the process for formation of mesoporous materials by means of assembling nanospheres with regularity has been named "hard-sphere packing (HSP)" mechanism [12]. The obtained well-ordered silica nanospheres having three-dimensional mesopores can serve as a template for fabricating the porous carbon replica.

While this technique using the combination of TEOS and basic amino acids is attracting much attention, the size variation has been limited; the size of the silica nanospheres can be finely tuned to between 8 and 25 nm by varying the amount of the amino acid [13]. Furthermore, diversification of the uniform intraparticle voids in size would be desirable for expanding a range of applications.

Here we report that the successful control of the sphere sizes ranging from 10 to 120 nm was accomplished by the seed regrowth method (mentioned below)



Scheme 1. Synthetic procedure for three-dimensionally interconnected ordered porous carbons by using the silica nanospheres as a template

and/or by using mixed solvents of water and ethanol. The preparation of three-dimensionally interconnected ordered porous carbons by using the silica nanospheres as a template is also reported.

2. Experimental

2.1. Preparation of Silica spheres

The seed regrowth method, which was originally adopted to improve the monodispersity and size control of the Stöber silicas, was adopted to control the size of our silica nanospheres.

Parent silica nanospheres which are employed as seed with a size of 15 nm were synthesized by using tetraethyl orthosilicate (TEOS) as a silica source in the presence of basic amino acids according to the original method [11] with slight modifications. Arginine was dissolved in deionized water with stirring. TEOS was added to this solution, and the mixture was stirred at 343 K for 20 h followed by being kept statically at 373 K for 20 h. The molar composition of the mother gel was 1 TEOS: 0.02 arginine: 154.4 H₂O. Although the resulting solution was clear with no precipitate in the resulting solution, TEM observations revealed that silica nanospheres with a size of 15 nm were highly dispersed in the resulting solution. Thus, the prepared solution was used as the seed-solution.

For the regrowth of seeds, an appropriate amount of the seed-solution containing silica nanospheres was added to the solution containing water, ethanol and arginine. Subsequently, TEOS was added to the resulting solution, and the mixture was stirred at 343 K for 20 h followed by being kept statically at 373 K for 20 h. Finally, the solution was transferred to an evaporating dish, and then directly evaporated in an oven at 373 K, resulting in the formation of the silica nanospheres. The obtained silica was calcined in an oven at 873 K. The proportion of the amounts of the seed-solution to the additional TEOS and the ethanol / water ratio at the regrowth of the seeds were investigated.

2.2. Preparation of carbon replica

The carbon replica with well-ordered mesopores was synthesized according to a slightly modified method reported in [11]. The silica nanospheres, furfuryl alcohol (C₅H₆O₂) and oxalic acid were used as a template, a carbon source and an acid catalyst, respectively. The voids between nanoparticles were filled with furfuryl alcohol and oxalic acid by the incipient-wetness technique. The silica template containing furfuryl alcohol was heated to 353 K under vacuum for 24 h

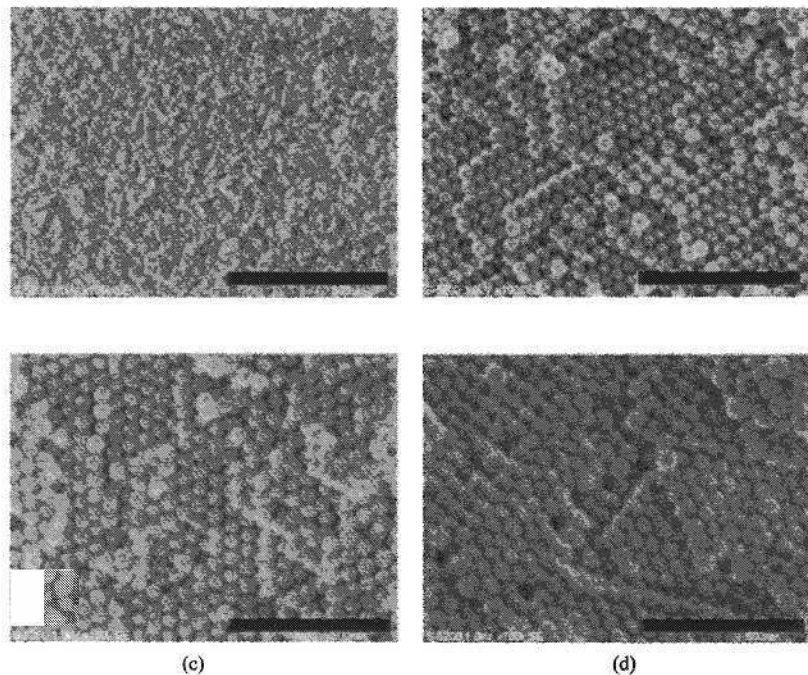


Figure 1. FE-SEM images of the silica nanospheres with diverse sizes of (a) 15, (b) 45, (c) 63 and (d) 75 nm. The scale bar corresponds to 500 nm.

and then to 423 K for 8h for polymerization of furfuryl alcohol. Subsequently, the polymerized furfuryl alcohol was converted to carbon inside the silica template by carbonization at 1173 K for 6 h under flowing argon. The above treatments produced black powder, which was treated with 5 % HF aqueous solution at room temperature to remove the silica.

2.3. Characterizations

Size and morphology of the samples were observed on a field emission scanning electron microscopy (FE-SEM, Hitachi S-5200) without any metal coating. Nitrogen adsorption-desorption measurements were conducted at 77 K on a Quantachrome Autosorb 1-MP/TT. The pore size distributions were calculated by the BJH method using the adsorption branch.

3. Results and Discussion

3.1. Preparation of Silica spheres

It is noted that all the products are monodispersed silica spheres irrespective of the proportion of the seed-solution, and different-sized spheres are hardly observed. These facts directly indicate that an additional TEOS was consumed not for the additional nucleation but for the regrowth of seeds. The solubility of silica was low under synthesis conditions because of a relative low pH derived from **arginine** (ca. 9.2) [14], restraining the additional nucleation.

The proportion of the seed-solution to the additional TEOS strongly affected the size of the final silica spheres; the size of the final silica spheres was decreased with increasing proportion of the seed-solution. The increase in the proportion of the seed-solution would lead to the increase in the number of seeds. The relative amount of additional TEOS for the regrowth of one seed must be

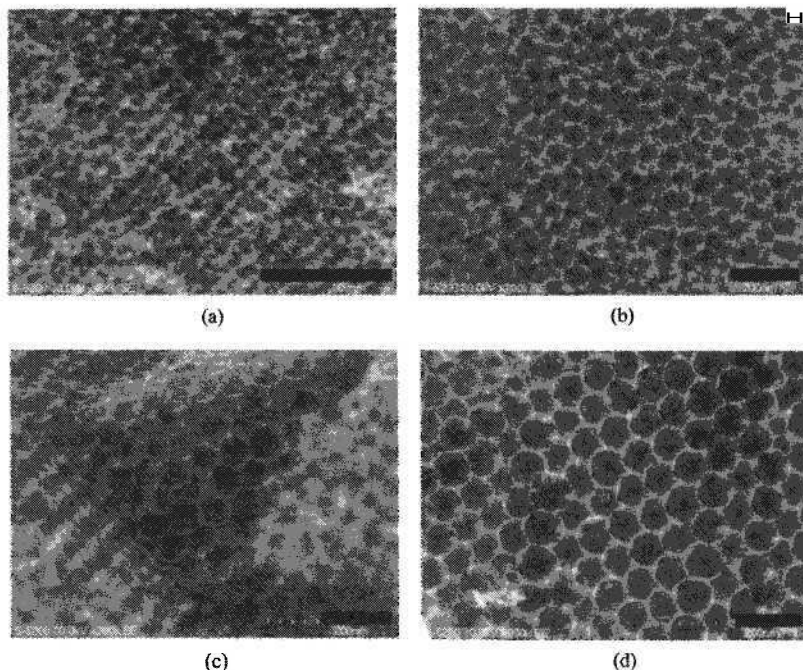


Figure 2. FE-SEM images of the carbon replica synthesized using the corresponding silica nanospheres with diverse sizes of (a) 15, (b) 40, (c) 60 and (d) 80 nm as a template. The scale bar corresponds to 100 nm.

decreased, resulting in the formation of the smaller sizes of silica spheres.

The ethanol / water ratio of the solvent was also important for the regrowth of the seeds; the size of the final silica spheres was increased with an increase in the ethanol / water ratio. This phenomenon was already observed in the Stöber method [10].

The uniform-sized silica nanospheres with the sizes ranging from 8 to 120 nm were successfully obtained by integrating two factors, the proportion of the seed-solution and the ethanol / water ratio of the solvent. Figure 1 shows representative FE-SEM images of the silica nanospheres of diverse sizes of (a) 15, (b) 45, (c) 63 and (d) 75 nm, indicating that the silica nanospheres were well-ordered to form a cubic closed pack (ccp) structure.

The mechanism of control of the sphere sizes depending on the synthesis conditions is currently being studied and will be reported elsewhere [15].

3.2. Preparation of carbon replica

The carbon replica with well-ordered pores was synthesized by using the silica nanospheres of diverse sizes as a template (Figure1). Figure 2 shows

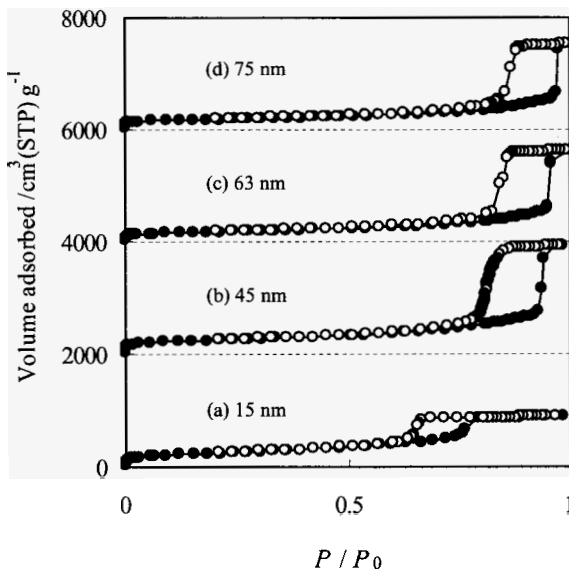


Figure 3. N_2 adsorption-desorption isotherms of the carbon replica synthesized using the corresponding silica nanospheres with diverse sizes of (a) 15, (b) 45, (c) 63 and (d) 75 nm as templates.

representative FE-SEM images of the carbon replica samples, exhibiting the inverse contrast to the silica template. The pores are uniform, close-packed and spherical, resulting in the formation of a highly ordered porous carbon framework. Each of the spherical pores is also three-dimensionally interconnected to neighboring pores through small holes, which were attributed to the contact points between silica spheres closely-packed.

N₂ adsorption-desorption isotherms of the carbon replica samples are shown in Figure 3. The isotherms of the all samples exhibit a sharp capillary condensation step and its position is shifted to higher relative pressure ($P / P_0 = 0.9 - 1.0$) with an increase in the pore size. The BET specific surface area, the average pore size and the total pore volume are summarized in Table 1. The pore sizes of the carbon structure can be easily controlled by varying the size of silica spheres.

Table 1 Structural properties of the carbon replica synthesized using the corresponding silica nanospheres with diverse sizes.

Template		Carbon replica		
Sphere size [*]	BET surface area	Total pore volume	Pore size ^{**}	
[nm]	[m ² /g]	[cm ³ /g]	[nm]	
15	872	1.39	9	
45	892	3.00	33	
63	622	2.36	44	
75	638	2.28	68	

*Estimated by FE-EM image, ** calculated by the BJH method using adsorption branch

4. Conclusions

The successful control of the sphere sizes in the range from 8 to 120 nm was accomplished by the seed regrowth method and/or by using mixed solvents of water and ethanol. Three-dimensionally interconnected ordered porous carbons were also prepared by using the synthesized silica nanospheres as a template. The pore size of the carbon structure can be easily controlled by varying the size of silica spheres. Thus, the prepared carbon replica would offer the prospects for a wide diversity of applications.

Acknowledgments

This work was partly supported by Core Research for Evolutional Science and Technology (CREST) of JST Corporation to T.T.

References

1. A. A. Zakhidov, R. H. Baughman, Z. Iqbal, C. Cui, I. Khayrullin, S. O. Dantans, J. Marti, V. G. Ralchenko, *Science*, **282**, 897 (1998).
2. T. Kyotani, *Carbon*, **38**, 269 (2000).
3. G. S. Chai, S. B. Yoon, J.-S. Yu, J.-H. Choi, Y.-E. Sung, *J. Phys. Chem. B*, **108**, 7074 (2004).
4. J. Lee, J. Kim, T. Hyeon, *Adv. Mater.*, **18**, 2073 (2006).
5. J. H. Knox, B. Kaur, G. R. Millward, *J. Chromatogr.*, **352**, 3 (1996).
6. W. Stöber, A. Fink, *J. Colloid Interface Sci.* **26**, 62 (1968).
7. S. Sakka, K. Kamiya, *J. Non-Cryst. Solids*, **48**, 31 (1982).
8. A. Van Blaaderen, A. Van Geest, A. Vrij, *J. Colloid Inter. Sci.*, **154**, 481 (1992).
9. H. Giesche, *J. Eur. Ceram. Soc.* **125**, 15589 (1994).
10. K. S. Rao, K. El-Hami, T. Kodaki, K. Matsushige, K. Makino, *J. Colloid Inter. Sci.*, 289, 125 (2005).
11. T. Yokoi, Y. Sakamoto, O. Terasaki, Y. Kubota, T. Okubo, T. Tatsumi, *J. Am. Chem. Soc.*, **128**, 13664-13665 (2006).
12. J. Tang, X. Zhou, D. Zhao, G. Q. Lu, J. Zou, C. Yu, *J. Am. Chem. Soc.*, 129, 9044 (2007).
13. T. Yokoi, M. Iwama, R. Watanabe, Y. Sakamoto, O. Terasaki, Y. Kubota, J. N. Kondo, T. Okubo, T. Tatsumi, *Stud. Surf. Sci. Catal.*, **170B**, 1774 (2007).
14. R. K. Iler, *The Chemistry of Silica*, Wiley: New York (1979).
15. R. Watanabe, S. Ohta, J. N. Kondo, T. Yokoi, T. Tatusmi, unpublished results.

POROUS CARBON MATERIALS VIA CHEMICAL VAPOUR DEPOSITION USING AS-SYNTHESISED ZEOLITES AS TEMPLATE: SYNTHESIS AND HYDROGEN STORAGE PROPERTIES

ALEXANDRA PACULA

*School of Chemistry, University of Nottingham, University Park Nottingham NG7 2RD,
United Kingdom*

*Institute of Catalysis and Surface Chemistry, Polish Academy of Sciences, ul.
Niezapominajek 8, 30-239 Kraków, Poland*

ROBERT MOKAYA

*School of Chemistry, University of Nottingham, University Park Nottingham NG7 2RD,
United Kingdom*

As-synthesised zeolite β has been successfully used as a template for the preparation, via chemical vapour deposition, of well ordered zeolite-like carbon materials that exhibit high surface area (up to 2535 m²/g) and high hydrogen storage capacity (5.3 wt% and 2.3 wt% at 20 bar and 1 bar respectively). Carbon materials prepared at 800 and 850 °C are non-graphitic and retain the particle morphology of the zeolite templates. Carbon prepared at 900 °C contains some graphitic domains (as evidenced by XRD patterns) and irregular particles that are dissimilar to the zeolite template particles. The use of as-synthesized (rather than calcined) zeolite β significantly improves the carbon yield and reduces the number of steps in the preparation of the templated carbons.

1. Introduction

Porous carbon materials have been intensively studied as hydrogen storage media because of their high surface area [1]. Porous carbons may be obtained via carbonisation of suitable precursors followed by activation [1]. The ability to control pore size and structural ordering is a desirable feature of any synthesis process for porous carbons. Several methods have been explored for the preparation of porous carbons with controlled microporosity and/or mesoporosity [2,3]. In particular, the template carbonisation route, in which microporous zeolites and mesoporous silicas and aluminosilicas are used as hard template, has attracted much attention for the preparation of well ordered porous carbon materials with controlled pore size and particle morphology [2,3]. In general, the structural ordering of mesoporous hard templates is readily

replicated in mesoporous carbons [3], while for zeolite hard templates, the replication of zeolite structural ordering in carbons is much more difficult.

Recent work has however shown that the structural regularity of zeolite templates may be replicated in carbons. Kyotani and co-workers prepared microporous carbon with high surface area, which retained the structural regularity of zeolite Y, via a two-step method [4]. Garsuch and Klepel have also reported on carbons that preserve the structural regularity of zeolite Y templates [5], while Gaslain and co-workers have prepared a carbon replica with a well resolved X-ray diffraction pattern using zeolite EMC-2 as template [6]. Most recently, we have prepared zeolite-like carbon materials that exhibit well resolved powder XRD patterns and high surface area via a chemical vapour deposition (CVD) route using zeolite β as hard template [7]. The zeolite-like carbons were found to possess high hydrogen uptake capacity [7]. In an effort to simplify the hard templating process for carbon materials with potentially high hydrogen storage capacity, we have now explored the use of as-synthesised zeolites as hard templates. Here we report on the synthesis and hydrogen storage properties of porous carbon materials obtained by using as-synthesized zeolite β as template via CVD at 800 – 900 °C, with acetonitrile as carbon precursor. The use of as-synthesized (rather than calcined) zeolite β reduces the number of steps in the preparation of the templated carbons.

2. Experimental section

2.1. Material Synthesis

The as-synthesised zeolite β templates were obtained as follows; 8.33 g TEOS was added to a mixture of 0.066 g NaAlO_2 , 5.22 g H_2O and 4.07 g tetraethylammonium fluoride, and 0.048 g zeolite β was added as seed. This mixture was stirred overnight in a sealed beaker, and then transferred into an autoclave for hydrothermal treatment 160 °C for 4 days. The resulting product was obtained by filtration, washed repeatedly with a large amount of water and air dried at room temperature. The porous carbon materials were prepared as follows: an alumina boat with 0.5 g of dry as-synthesised zeolite β was placed in a flow through tube furnace. The furnace was heated to the required temperature (800 – 900 °C) under a flow of nitrogen saturated with acetonitrile and then maintained at the target temperature for 3 hours, followed by cooling under a flow of nitrogen only. The resulting zeolite/carbon composites were recovered and washed with 10% hydrofluoric (HF) acid several times to remove the zeolite framework. Finally the resulting carbon materials were dried in an oven at 50 °C.

2.2. Material Characterization

Powder XRD analysis was performed using a Philips 1830 powder diffractometer with Cu K α radiation (40 kV, 40 mA), 0.02° step size and 2 s step time. Textural properties were determined via nitrogen sorption at -196 °C using a conventional volumetric technique on an ASAP 2020 sorptometer. Before analysis the samples were oven dried at 150 °C and evacuated for 12 hours at 200 °C under vacuum. The surface area was calculated using the Brunauer-Emmett-Teller (BET) method based on adsorption data in the partial pressure (P/P_0) range 0.02 to 0.25 and total pore volume was determined from the amount of nitrogen adsorbed at $P/P_0 = \text{ca. } 0.99$. Micropore surface area and micropore volume were obtained via t -plot analysis. Thermogravimetric analysis (TGA) was performed using a Perkin Elmer TGA 6 analyser with a heating ramp rate of 2 °C/min under static air conditions. Scanning electron microscopy (SEM) images were recorded using a JEOL JSM-820 scanning electron microscope. Samples were mounted using a conductive carbon double-sided sticky tape. A thin (*ca.* 10 nm) coating of gold sputter was deposited onto the samples to reduce the effects of charging.

2.3. Hydrogen Uptake Measurements.

Hydrogen uptake measurements were performed using high purity hydrogen (99.9999%), additionally purified by a molecular sieve filter, over the pressure range 0 to 20 bar with an Intelligent Gravimetric Analyzer (IGA-003, Hiden) that incorporates a microbalance capable of measuring weights with a resolution of $\pm 0.2 \mu\text{g}$. The samples in the analysis chamber of the IGA-003 were vacuumed up to 10^{-10} bar under heating at 200 °C overnight before measurement. The hydrogen uptake measurements were carried out at -196 °C in a liquid nitrogen bath.

3. Results and discussion

Figure 1A shows the powder X-ray diffraction (XRD) patterns of the carbon materials. For comparison the XRD pattern for the zeolite β is also shown. The XRD patterns of the carbons show a peak, similar to the (100), (101) diffraction of the as-synthesised zeolite β template, at $2\theta = 8^\circ$. The XRD patterns of the carbons exhibit a further low intensity peak at $2\theta = 15^\circ$, which is at a position similar to the (201), (202) diffraction of the as-synthesised zeolite β template. The presence of these two peaks indicates that the carbon materials exhibit zeolite-like structural pore ordering replicated from the zeolite β template [4-9].

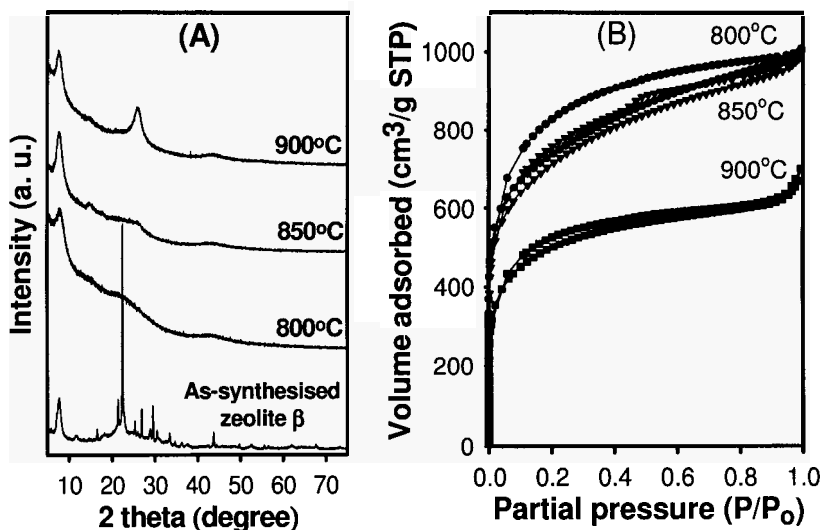


Figure 1. Powder XRD patterns (A) and nitrogen sorption isotherms (B) of carbons prepared via CVD using as-synthesised zeolite β as template.

The XRD patterns of carbons prepared at 800 and 850 °C exhibit a broad and very low intensity peak at 2θ of ca. 26°, which is the (002) diffraction from turbostratic carbon. The low intensity of this peak suggests that carbon materials prepared at 800 or 850 °C are essentially amorphous (i.e., non-graphitic). We have previously found that a combination of zeolite-like structural ordering and the absence of graphitisation in zeolite templated carbons imply that most of the carbon precursor is deposited within the zeolite pores (rather than on the external surface of the zeolite particles) [7]. This assumption is based on the fact that it is only carbon that is deposited on the external surface of the zeolite particles (and which has no spatial limitations) that can undergo graphitization [10]. The carbon sample prepared at CVD temperature of 900 °C contains some turbostratic/graphitic domains as indicated by the peak observed at 2θ of ca. 26°. Overall, the XRD patterns indicate that as-synthesised zeolites may be successfully used as templates to nanocast structurally well ordered carbons.

The nature and thermal stability of the carbon materials were probed by thermogravimetric analysis (TGA). Thermal analysis indicated that the carbon materials are template free as no zeolite residue was observed. The carbons are therefore efficiently generated from the carbon/zeolite composites during the

zeolite removal step (washing in HF acid). Data on the thermal behavior of the samples may yield information on the nature of the carbon framework. The mass loss events during thermal analysis are shown in the DTG profiles in Figure 2. The sample prepared at 800 °C exhibits one mass loss event in the temperature range 300 – 700 °C whereas the samples obtained at 850 and 900 °C have two mass loss events (Figure 2). We ascribe the mass loss centered at 518 – 535 °C to combustion of amorphous (non-graphitic) carbon, while for the sample prepared at 900 °C, the mass loss event at 630 °C is due to the combustion of turbostratic/graphitic carbon. The sample prepared at 850 °C exhibits a limited mass loss at 602 °C due to combustion of small amounts of turbostratic carbon. The thermal analysis data therefore confirms that the carbon in samples prepared at 800 and 850 °C is largely amorphous (i.e., non-graphitic). Significant amounts of turbostratic/graphitic carbon are only present for the sample prepared at 900 °C. This findings are consistent with the XRD patterns in Figure 1.

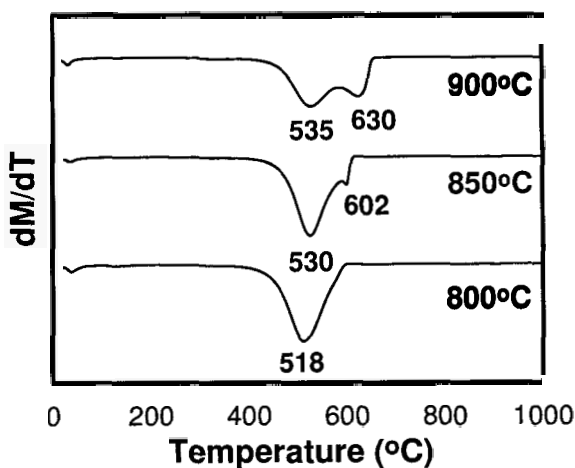


Figure 2. Differential thermogravimetric (DTG) profiles of carbon materials prepared via CVD using as-synthesised zeolite β as template.

As stated above, turbostratic/graphitic carbon can only form on the surface of the zeolite templates, and therefore the presence of such carbon may be probed using scanning electron microscopy (SEM) [7]. SEM images of the carbon materials shown in Figure 3 indicate that the sample prepared at 800 °C has well formed particles similar to those of zeolite β template and there are no other irregular particles. The particle morphology is consistent with carbon deposition within the pores of the zeolite template, which forms amorphous

carbon within the zeolite pores and eventually generates zeolite-like structural ordering after removal of the zeolite framework; this scenario allows the retention of the particle morphology of the zeolite in the replicated carbon. The SEM images indicate that the 850 °C sample contains a small amount of irregular particles, while the 900 °C sample has a significant amount of irregular particles. We ascribe the irregular particles to **turbostratic/graphitic** carbon that grows outside the zeolite pore system free of spatial constraints. The SEM images are consistent with the XRD and TGA data described above with respect to the nature (graphitic or amorphous) of the carbon framework.

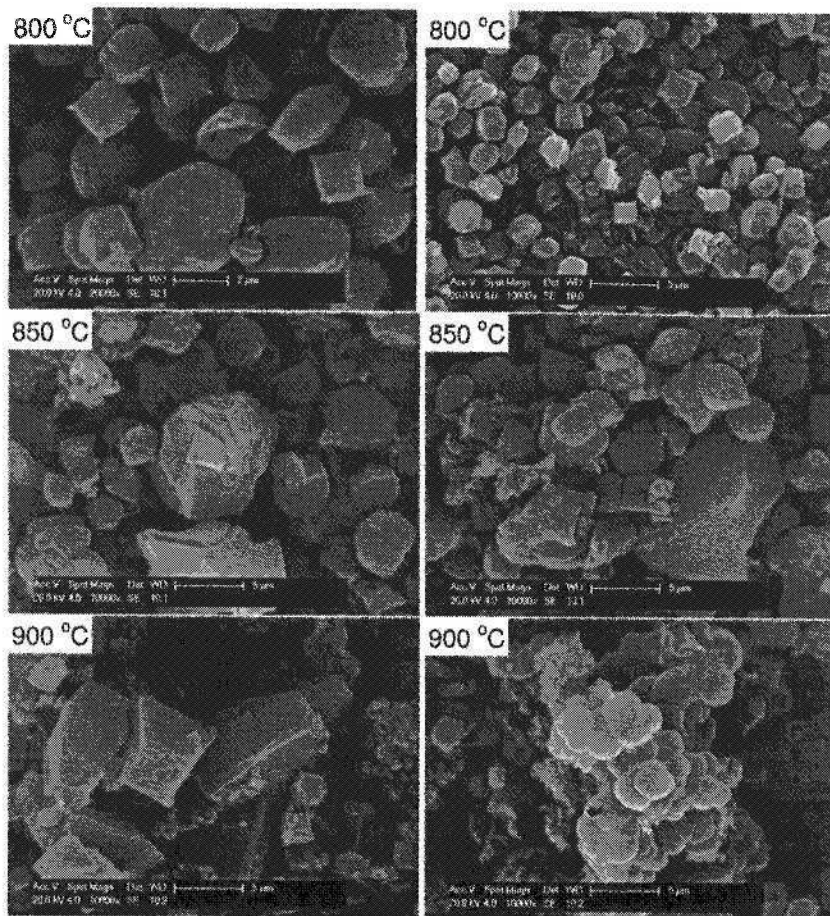


Figure 3. SEM images of carbon materials prepared using as-synthesised zeolite P as template via CVD at various temperatures.

A key difference between the use of calcined or as-synthesised zeolite as template is that the later contains some organic matter prior to the CVD process. Preliminary data shows that at least some of the organic matter in the as-synthesised template is incorporated into the carbon. Indeed, for carbon materials prepared similarly and in the absence of externally deposited carbon, we generally observed a higher carbon yield from as-synthesised templates. For example, at CVD temperature of 800 °C, the yield of carbon was ca. 20% higher from as-synthesised templates. The higher yield may also be related to a more hydrophobic surface in the as-synthesised templates, which favours greater carbon deposition.

The nitrogen sorption isotherms of the carbon materials are shown in Figure 1B. The isotherms of all the samples exhibit significant adsorption below $P/P_0 = 0.02$, due to micropore filling. The carbon materials are therefore predominantly microporous. The isotherms also exhibit some limited nitrogen uptake at $P/P_0 > 0.2$, which may be attributed to adsorption into mesopores. The isotherms are typical for zeolite-templated carbons that possess a high proportion of microporosity [4-9]. The textural properties of the carbons are summarized in Table 1. All the carbons have high surface area (1700 – 2500 m²/g) and pore volume (1.1 – 1.6 cm³/g). The surface area is high for carbon materials prepared at 800 °C (2535 m²/g) and 850 °C (2470 m²/g). The sample prepared at 900 °C has a lower surface area (1720 m²/g), which is consistent with the fact that it contains significant amounts of turbostratic/graphitic carbon. A large proportion of the surface area of the carbons is due to micropores; 65% for 800 and 850 °C samples and 76% for the 900 °C sample. The high surface area and microporosity of the carbon samples is related to their zeolite-like structural ordering [4-7].

Table 1. Textural properties and hydrogen uptake of carbons prepared via CVD at various temperatures using as-synthesised zeolite β as template.

CVD temperature (°C)	Surface area (m ² g ⁻¹) ^[a]	Pore volume (cm ³ /g) ^[a]	H ₂ uptake (wt%) ^{[b][c]}
800	2535 (1631)	1.56 (0.77)	5.3 (2.3)
850	2470 (1611)	1.54 (0.76)	5.2 (2.0)
900	1721 (1310)	1.09 (0.61)	3.3 (1.2)

^[a]Values in parentheses are micropore surface area and pore volume;

^[b]Hydrogen uptake capacity at -196 °C and 20 bar; ^[c]Values in parentheses are hydrogen uptake capacity at -196 °C and 1 bar.

Figure 4 shows hydrogen uptake isotherms of the carbon materials, measured gravimetrically with an IGA [7,8]. The sorption isotherms show that the uptake of hydrogen by the carbon materials is reversible with no hysteresis, and that the adsorption branch closely matches the desorption branch. It is also clear that hydrogen uptake does not approach saturation even at 20 bar implying that even greater uptake capacity is possible at elevated pressure. The hydrogen uptake capacity of the carbon materials, at 1 and 20 bar, is given in Table 1. The hydrogen uptake capacity of the sample prepared at 900 °C is 3.3 wt% and 1.2 wt% at 20 and 1 bar respectively. Samples prepared at 800 and 850 °C, have a much higher hydrogen uptake capacity that reaches 5.3 wt% and 2.3 wt% at 20 and 1 bar respectively. The trend in hydrogen uptake capacity is clearly related to the textural properties of the carbon materials, and in particular the surface area.

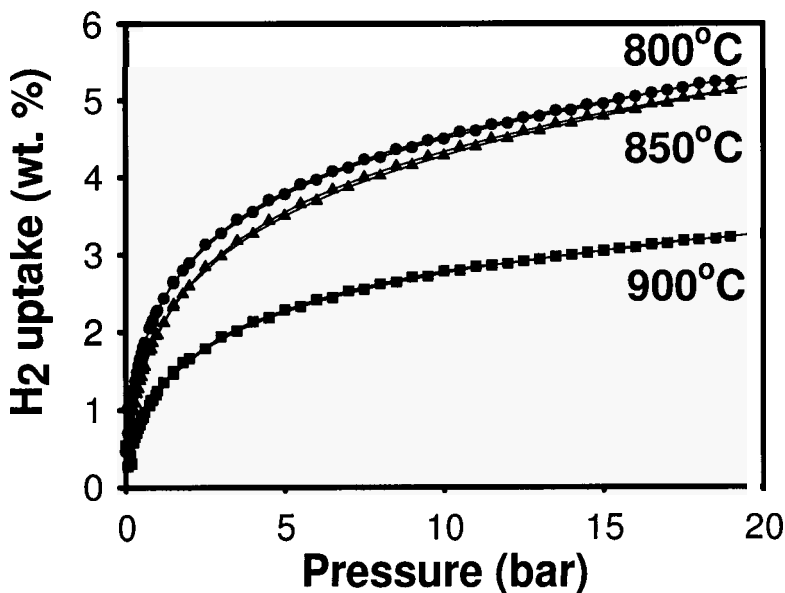


Figure 4. Hydrogen sorption isotherms at -196 °C of carbons obtained via CVD at various temperatures using as-synthesised zeolite β as template. (Carbon density of 1.5 g/cm³ was used and hydrogen density of 0.04 g/cm³ was used for buoyancy correction of adsorbed H₂).

The hydrogen uptake capacity (3.3 – 5.3 wt% at -196 °C and 20 bar) is comparable to that of carbons prepared using calcined zeolites as template, and greater than that of most other porous carbon materials [8,11-15]. Indeed, a recent evaluation of the hydrogen storage capacity of a wide range of high surface area carbon materials found a maximum capacity of ca. 4.5 wt% at a much higher pressure of 70 bar [11]. We have recently observed uptake of up to 4.5 wt% at 20 bar for zeolite-templated carbons with low levels of zeolite type structural ordering [8], and up to 6.9 wt% for zeolite-like carbons [7]. The use of as-synthesised zeolites as template therefore presents no disadvantages with respect to hydrogen storage capacity.

In summary, carbon materials have been prepared using as-synthesised zeolite β as template via CVD at 800 – 900 °C. The carbon materials have high surface area (1720 – 2535 m²/g), high pore volume (1.09 – 1.56 cm³g⁻¹) and exhibit some zeolite-like structural ordering replicated from the zeolite template. Carbon materials prepared at 800 and 850 °C are essentially amorphous (non-graphitic) and retain the particle morphology of the zeolite templates. Carbon prepared at 900 °C contains some turbostratic/graphitic domains and irregular particles that are dissimilar to the zeolite template particles. We observed hydrogen uptake of up to 5.3 wt% at -196 °C and 20 bar, and 2.3 wt% at 1 bar for the carbon materials. The hydrogen uptake is dependent on the surface area of the carbons. The use of as-synthesized (rather than calcined) zeolite β offers the attractive advantages of higher carbon yield and fewer steps in the preparation of the templated carbons, but without any compromise on the textural properties and hydrogen sorption capacity.

Acknowledgements

This research was funded by the European Commission within Marie Curie Host Fellowships for the Transfer of Knowledge, No MTKD-CT-2004-509832.

References

1. C. R. Bansal, J. B. Donnet and F. Stoeckli, 'Active carbon', Marcel Dekker, (1988).
2. (a) T. Kyotani, *Carbon* **38**, 269 (2000). (b) T. Kyotani, Z. X. Ma and A. Tomita, *Carbon* **41**, 1451 (2003).
3. (a) R. Ryoo, S. H. Joo, M. Kruk and M. Jaroniec, *Adv. Mater.* **13**, 677 (2001). (b) H. F. Yang and D. Y. Zhao, *J. Mater. Chem.* **15**, 1217 (2005). (c) R. Ryoo, S. H. Joo and S. Jun, *J. Phys. Chem. B* **103**, 7743 (1999). (d) J. Lee, J. Kim and T. Hyeon, *Adv. Mater.* **18**, 2073 (2006).

4. (a) Z. Ma, T. Kyotani, Z. Liu, O. Terasaki, and A. Tomita, *Chem. Mater.* **13**, 4413 (2001). (b) Z. X. Ma, T. Kyotani, and A. Tomita, *Chem. Commun.* 2365 (2000). (c) P. Hou, H. Orikasa, T. Yamazaki, K. Matsuoka, A. Tomita, N. Setoyama, Y. Fukushima, and T. Kyotani, *Chem. Mater.* **17**, 5187 (2005).
5. (a) A. Garsuch, O. Klepel, R. R. Sattler, C. Berger, R. Glaeser, and J. Weitkamp, *Carbon* **44**, 593 (2006). (b) A. Garsuch and O. Klepel, *Carbon* **43**, 2330 (2005).
6. F. O. M. Gaslain, J. Parmentier, V. P. Valtchev, and J. Patarin, *Chem. Commun.* 991 (2006).
7. Z. Yang, Y. Xia and R. Mokaya, *J. Am. Chem. Soc.* **129**, 1673 (2007).
8. Z. Yang, Y. Xia, X. Sun and R. Mokaya, *J. Phys. Chem. B* **110**, 18424 (2006).
9. (a) Z. Yang, Y. Xia and R. Mokaya, *Micropor. Mesopor. Mater.* **86**, 69 (2005). (b) Z. Yang, Y. Xia and R. Mokaya, *Stud. Surf. Sci. Catal.* **156**, 573 (2005).
10. S. A. Johnson, E. S. Brigham, P. J. Ollivier, and T. E. Mallouk, *Chem. Mater.* **9**, 2448 (1997).
11. M. Hirscher and B. Panella, *J. Alloys Compd* **404**, 399 (2005).
12. X. B. Zhao, B. Xiao, A. J. Fletcher and K. M. Thomas, *J. Phys. Chem. B* **109**, 8880 (2005)
13. J. Pang, J. E. Hampsey, Z. Wu, Q. Hu and Y. Lu, *Appl. Phys. Lett.* **85**, 4887 (2004).
14. E. Terres, B. Panella, T. Hayashi, Y. A. Kim, M. Endo, J. M. Dominguez, M. Hirscher, H. Terrones and M. Terrones, *Chem. Phys. Lett.* **403**, 363 (2005).
15. L. Chen, R. K. Singh and P. Webley, *Micropor. Mesopor. Mater.* **102**, 159 (2007).

EFFECT OF CARBONISATION HEATING RAMP RATE ON THE PROPERTIES OF ORDERED MESOPOROUS CARBONS

ZHUXIAN YANG

*School of Chemistry, University of Nottingham, University Park Nottingham NG7 2RD,
United Kingdom.*

ROBERT MOKAYA

*School of Chemistry, University of Nottingham, University Park Nottingham NG7 2RD,
United Kingdom.*

The heating ramp rate plays an important role in determining the properties of mesoporous carbon materials prepared via either liquid impregnation (LI) or chemical vapor deposition (CVD). For LI (at final carbonization temperature of 900 °C), fast heating ramp rate (20 °C/min) results in poorly ordered mesoporous carbons while slower heating ramp rates (5 or 1 °C/min) generate well ordered mesoporous carbons. The surface area is highest (ca. 1360 m²/g) for carbons prepared at a ramp rate of 1 °C/min. Mesoporous carbons prepared at low heating ramp rate (1 °C/min) are micropore free and exhibit only framework-confined mesoporosity. On the other hand fast heating ramp rate generates carbons with significant microporosity (15% of surface area is associated with micropores) and some non-framework porosity (i.e., large mesopores). For CVD derived mesoporous carbons (prepared at 1000 °C), the particle morphology changed from solid core spheres (10 °C/min) to hollow spheres (20 °C/min) depending on the heating ramp rate. Although textural properties were comparable for CVD derived carbons, higher levels of graphitisation were observed for fast heating ramp rates.

1. Introduction

Ordered mesoporous carbons with uniform pores have drawn much attention due to their potential application in a variety of applications. The template carbonisation method whereby mesoporous silicas are used as solid templates for nanocasting mesoporous carbons, has been extensively studied [1-3]. Infiltration of suitable carbon precursor into the internal space of the solid templates is usually achieved via liquid impregnation (LI) or chemical vapour deposition (CVD), and carbonisation is an essential part of the nanocasting process. Here we report on the effect of the carbonisation heating ramp rate on the properties of mesoporous carbon materials prepared via (1) LI with sucrose as carbon precursor, or (2) CVD with acetonitrile as carbon precursor. We show that fast heating ramp rates generate poorly ordered sucrose-derived carbons while slower

heating rates generate well ordered mesoporous carbons. For the CVD process, the heating ramp rate can be used to tailor the morphology between hollow or solid-core particles.

2. Experimental section

2.1. Material Synthesis

Conventional mesoporous SBA-15 was synthesised using a triblock polymer, poly(ethylene glycol)-*block*-poly(propylene glycol)-*block*-poly(ethylene glycol) (Pluronic P123, $\text{EO}_{20}\text{PO}_{70}\text{EO}_{20}$, $M_{\text{av}} = 5800$, Aldrich) as the structure-directing agent and tetraethylorthosilicate (TEOS) as the silica source [4]. In brief, 4.0 g P123 was dissolved in a solution of 125 g H_2O and 25 g HCl (35%) followed by the addition of 8.59 g TEOS. The mixture was stirred at 35 °C for 20 h followed by hydrothermal reaction at 80 or 100 °C for 24 h. The product (SBA-15) was recovered by filtration and calcined in air at 550 °C for 6 h. The final SBA-15 samples had surface area of ca. 920 m^2/g , pore volume of ca. 1.1 cm^3/g and pore size of 8 nm [4,5]. The SBA-15 was used as template for the preparation of mesoporous CMK-3 carbons via liquid impregnation as follows [5]. 1 g SBA-15 was added to a solution of 0.14 g H_2SO_4 , 5 g H_2O and 1.25 g sucrose. The mixture was stirred for 1 h, followed by aging at 100 °C for 6 h first, then 160 °C for 6 h. The aged mixture was ground into powder and added to a solution of 0.09 g H_2SO_4 , 5 g H_2O and 0.8 g sucrose, which was stirred for 1 h followed by further aging as described above. The resulting composite was carbonised at a heating ramp rate of 20, 5 or 1 °C/min under nitrogen flow and held at 900 °C for 7 h. The silica was then removed using 10% hydrofluoric acid (HF) and the resulting carbons dried at 150 °C. The resulting CMK-3 carbons were designated as CMK-3F-X, CMK-3M-X and CMK-3S-X where F, M and S indicates a fast, medium or slow heating ramp rate of 20, 5 and 1 °C/min respectively, and X is the temperature at which the SBA-15 template is prepared (i.e, 80 or 100 °C).

Mesoporous silica SBA-15 solid core spheres were synthesized according to reported procedure [6]: Triblock copolymer P123 (3.0 g) and 0.5 g of cetyltrimethylammonium bromide were dissolved in a mixture containing 25 mL of ethanol, 30 mL of H_2O , and 60 mL of 2 M HCl, followed by addition of 10 mL of tetraethylorthosilicate (TEOS) under stirring. After continuous stirring for 1 h at room temperature, the resulting gel was transferred to a Teflon-lined autoclave, which was first heated at 80 °C for 6 h, followed by further heating at 110 °C for 12 h. The autoclave was cooled to room temperature, and the solid product was obtained via filtration, air-dried, and calcined at 500 °C for 6 h

under static air conditions to yield calcined SBA-15 spheres. The final SBA-15 spheres had surface area of $980 \text{ m}^2/\text{g}$, pore volume of $0.85 \text{ cm}^3/\text{g}$ and pore size of 3.7 nm . The SBA-15 spheres were used as template for the preparation of mesoporous CMK-3 carbons via chemical vapour deposition route as follows. An alumina boat with 0.5 g of SBA-15 spheres was placed in a flow-through tube furnace. The furnace was heated to $1000 \text{ }^\circ\text{C}$ under a nitrogen flow with a heating ramp rate of 10 or $20 \text{ }^\circ\text{C}/\text{min}$ and maintained for 3 h under a flow of nitrogen saturated with acetonitrile, followed by cooling under nitrogen. The resulting silica/carbon composites were recovered and washed with 10% HF acid several times to remove the silica template. Finally, the resulting carbon materials were dried in an oven at $120 \text{ }^\circ\text{C}$. Carbon materials were designated as CSP-M and CSP-F for heating ramp rate of 10 and $20 \text{ }^\circ\text{C}/\text{min}$ respectively.

2.2. Material Characterization

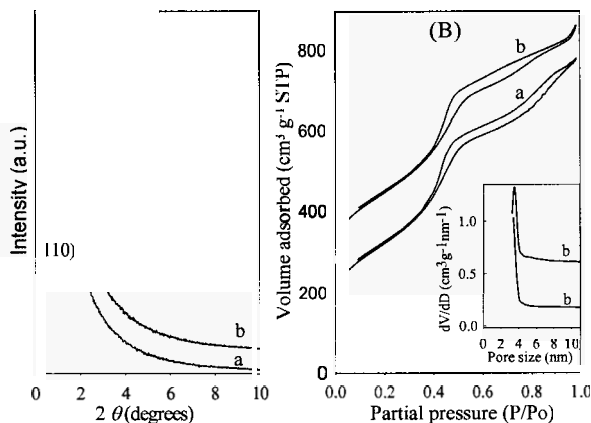
Powder XRD patterns were obtained using a Philips 1830 powder diffractometer with $\text{Cu K}\alpha$ radiation (40 kV , 40 mA), 0.02° step size and 2 s step time. Textural properties were determined via nitrogen sorption at $-196 \text{ }^\circ\text{C}$ using a volumetric technique on an ASAP 2020 sorptometer. Before analysis the samples were oven dried at $150 \text{ }^\circ\text{C}$ and evacuated for 12 hours at $200 \text{ }^\circ\text{C}$. The surface area was calculated using the Brunauer-Emmett-Teller (BET) method based on adsorption data in the partial pressure (P/P_0) range 0.02 to 0.25 and total pore volume was determined from the amount of nitrogen adsorbed at $P/P_0 = \text{ca. } 0.99$. The pore size distribution was determined using the BJH method applied to adsorption data. Micropore surface area and micropore volume were obtained via t -plot analysis. Scanning electron microscopy (SEM) images were recorded using a JEOL JSM-820 scanning electron microscope. A thin (*ca.* 10 nm) coating of gold sputter was deposited on the samples to reduce the effects of charging.

3. Results and discussion

3.1. Mesoporous carbons prepared via liquid impregnation

The XRD patterns, nitrogen sorption isotherms and PSD curves of CMK-3F samples prepared at $900 \text{ }^\circ\text{C}$ at heating ramp rate of $20 \text{ }^\circ\text{C}/\text{min}$ using conventional mesoporous SBA-15 as template are shown in Figure 1. The textural properties of the CMK-3F samples are summarised in Table 1. Only a very weak XRD peak is observed for the CMK-3F samples, which we tentatively assign to the (100) or (110) diffraction of $p6mm$ hexagonal symmetry [4]. The XRD patterns suggest that the CMK-3F samples are not mesostructurally well ordered. The

isotherms in Figure 1B show that the CMK-3F carbons are mesoporous, possessing both framework-confined mesopores (represented by the pore filling step at partial pressure, P/P_0 0.4 to 0.6) and larger mesopores (adsorption at $P/P_0 > 0.8$). The pore size of the CMK-3F samples shown in the inset of Figure 1B is ca. 3.7 nm (Table 1). As shown in Table 1, the surface area (ca. 1140 m^2/g) and pore volume (ca. 1.1 cm^3/g) of the CMK-3F carbons is high despite the rather poor mesostructural ordering. The nature of the silica template (i.e., prepared at 80 or 100 °C) has no affect on the textural properties. Overall, it is



clear that a fast heating ramp rate (20 °C/min) generates poorly ordered carbons. Figure 1. XRD patterns (A) and nitrogen sorption isotherms (B) of CMK-3F carbons: (a) CMK-3F-80 and (b) CMK-3F-100. Isotherm b is offset (y-axis) by 130. The inset in (B) shows PSD curves.

Table 1. Textural properties of mesoporous carbon materials prepared via liquid impregnation or CVD, at various heating ramp rates using SBA-15 as template.

Sample	Surface area ^a (m^2/g)	Pore volume (cm^3/g)	Pore diameter (nm)
CMK-3F-80	1145 (172)	1.2	3.6
CMK-3F-100	1131 (174)	1.1	3.7
CMK-3M-80	973 (57)	1.0	3.7
CMK-3M-100	1153 (41)	1.2	3.4
CMK-3S-100	1358 (7)	1.1	< 3.2
CSP-M	731	0.8	3.7
CSP-F	819	0.8	3.7

^a Values in parentheses are contributed by micropores.

Figure 2 shows the XRD patterns, nitrogen sorption isotherms and PSD curves of CMK-3M samples prepared at 900 °C at a ramp rate of 5 °C/min. The textural properties are summarised in Table 1. A basal peak corresponding to the (100) diffraction of 2-d hexagonal $p6mm$ array of pores [4] is observed for the CMK-3M carbons. The presence of the basal (100) peak indicates that the CMK-3M carbons are relatively well ordered [4]. The XRD patterns in Figure 2A therefore indicate that the mesostructural ordering of the SBA-15 template is better replicated in the CMK-3 carbons materials when a heating ramp rate of 5 °C/min (rather than 20 °C/min) is used.

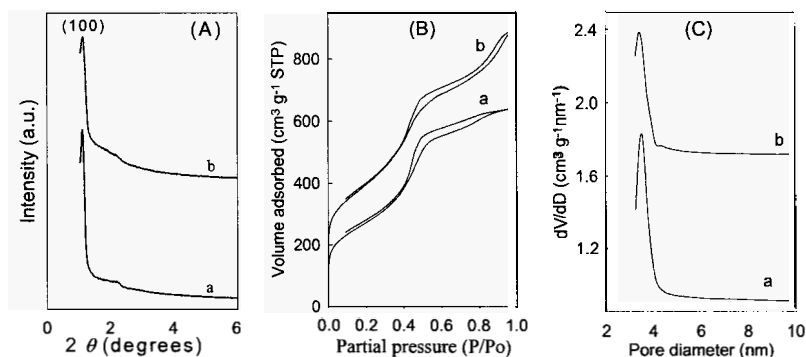


Figure 2. XRD patterns (A), nitrogen sorption isotherms (B) and pore size distribution (PSD) curves (C) of CMK-3M carbons: (a) CMK-3M-80, (b) CMK-3M-100. Isotherm b is offset (y-axis) by 50.

The nitrogen sorption isotherms of the CMK-3M carbon samples in Figure 2B are typical for mesoporous materials. All the isotherms exhibit a pore filling step in the partial pressure range (P/P_0) between 0.4 and 0.6, which is due to adsorption into framework-confined mesopores. In addition, sample CMK-3M-100 shows further sorption at partial pressure (P/P_0) above 0.8, which is contributed by non-framework mesopores (or interparticle voids). The PSD curves in Figure 2C show that the samples have a narrow distribution of framework-confined mesopores. The surface area and pore volume is generally higher for sample CMK-3M-100 (Table 1). The differences between the two CMK-3M samples suggest that the nature of the silica template (i.e., prepared at 80 or 100 °C) has an influence on textural properties when a heating ramp rate of 5 °C/min is used. The CMK-3M samples possess low amounts of micropores (3.5 – 6% of surface area is due to micropores). Overall, the data in Figure 2 indicates that slower heating ramp rate (5 °C/min) generates better (c.f. 20 °C/min) ordered mesoporous carbons.

To further probe the effect of heating ramp rate, synthesis was performed at 1 °C/min. Figure 3 compares the XRD patterns and nitrogen sorption isotherms of CMK-3 samples carbonised at 900 °C at various heating ramp rates (20, 5 and 1 °C/min), using SBA-15 synthesized at 100 °C as template. The textural properties of all the carbons are summarised in Table 1. The low angle (100) peak, which is an indication of well ordered CMK-3 was only observed for samples obtained at a heating ramp rate of 5 and 1 °C/min. All the isotherms in Figure 3B are typical for mesoporous materials, with a steep sorption step at partial pressure P/P_0 ca. 0.3 – 0.4. In particular, the isotherm for the carbon sample obtained at heating ramp rate of 1 °C/min indicates the presence of framework-confined mesopores only as there is no adsorption at P/P_0 higher than 0.8. The isotherms of carbon samples obtained at 5 and 20 °C/min show both framework mesopores (at P/P_0 of 0.3 – 0.6) and larger pores (at $P/P_0 > 0.8$). The larger pores may arise from non-homogeneous carbonization of the sucrose precursor within the pores of the SBA-15 template due to the faster heating ramp rate. The PSD curves (inset Figure 3B) show that the pore diameters decrease from 3.6 to less than 3.2 nm (Table 1) at lower heating ramp rate.

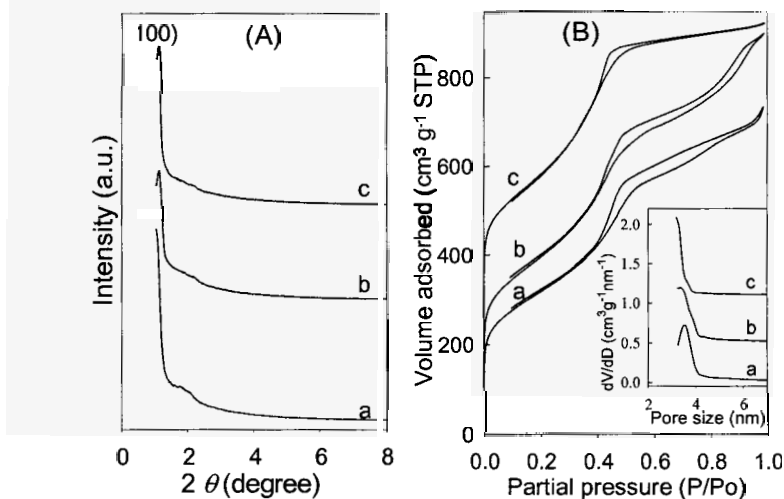


Figure 3. XRD patterns (A) and nitrogen sorption isotherms (B) of CMK-3 samples carbonised at 900 °C at various heating ramp rates: (a) CMK-3F-100, (b) CMK-3M-100 and (c) CMK-3S-100. The isotherms are offset by: (b) 50 and (c) 200. The inset in (B) shows the corresponding PSD curves, and the PSD curves are offset by: (b) 0.5 and (c) 1.1.

The surface area of the carbon CMK-3X-100 samples (Table 1) increases at lower heating ramp rate. On the other hand, the micropore surface area decreases at lower heating ramp rate, and a ramp rate of 1 °C/min generates mesoporous carbon that is virtually free of micropores. The above results imply that heating ramp rate plays an important role in determining the properties of templated CMK-3 mesoporous carbons. Fast heating ramp rate of 20 °C/min results in poorly ordered mesoporous carbons, that exhibit some microporosity and larger (non-framework) pores in addition to framework-confined mesopores. Lower heating ramp rates (5 or 1 °C/min) generate well ordered mesoporous carbons. A ramp rate of 1 °C/min leads to mesoporous carbon with the best ordering, highest surface area and virtually no microporosity or non-framework porosity. The effect of heating ramp rate may be explained by considering that the carbonisation of the sucrose precursor starts as soon as the temperature is high enough (not necessarily at 900 °C). A slower heating ramp rate offers a more homogenous environment for the carbonisation process, which results in better replication of the mesostructural ordering of the SBA-15 template in the carbon.

3.2. Mesoporous carbons prepared via chemical vapor deposition

The preparation of hollow particle morphologies (e.g. spheres) of structurally well ordered and graphitic mesoporous carbon nanocast via CVD using mesoporous silica SBA-15 as a template has been reported [7]. A CVD temperature of 1000 °C was found to be essential for the successful formation of carbon hollow spheres [7]. It has also been demonstrated that the carbons exhibit significant graphitisation especially for materials prepared at a CVD temperature of 1000 °C [8]. Based on these previous results, the intention in this study was to investigate the effect of other factors on the formation of hollow spheres and graphitisation. We accordingly investigated the effect of heating ramp rate by performing CVD at 1000 °C with a heating ramp rate of 10 or 20 °C/min.

Representative SEM images of the mesoporous silica SBA-15 solid-core spheres used as template and the resulting carbon materials are shown in Figure 4. The SBA-15 template consists of solid-core spheres with diameter of ca. 5 µm. The carbon sample (CSP-M), obtained at a heating ramp rate of 10 °C/min, also exhibits solid-core spheres with diameter of ca. 5 µm. The solid core sphere morphology of the SBA-15 template is therefore retained in the CSP-M carbon sample despite the high (1000 °C) CVD temperature [7,8]. However, hollow spheres of diameter ca. 5 µm were observed for the carbon sample (CSP-F) obtained at a faster heating ramp rate of 20 °C/min. The formation of solid and hollow spheres of carbon can be explained as follows: rapid heating (20 °C/min)

may lead to pore blocking of the silica template due to accelerated carbon deposition, thus preventing further carbon deposition into the interior of the silica spheres. As a result, hollow spheres are obtained for the rapidly heated sample after HF treatment to remove the silica template. On the other hand, no pore blocking occurred under the slower heating ramp rate of 10 °C/min and therefore carbon deposition could proceed largely unhindered allowing deposition of carbon into the interior of the silica template and thus the formation of solid-core carbon spheres once the silica template was removed by HF treatment.

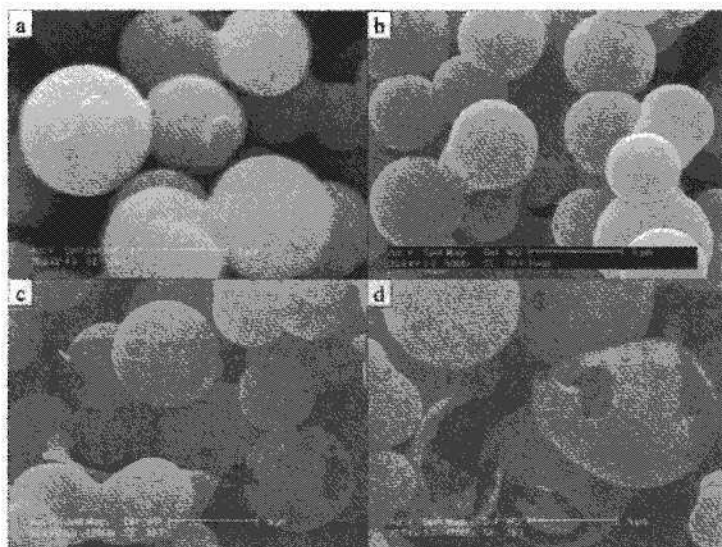


Figure 4. Representative SEM images of (a) SBA-15 solid spheres, and carbon materials prepared via CVD at 1000 °C at various heating ramp rates using the SBA-15 spheres as templates and acetonitrile as carbon precursor: (b) 10 °C/min (CSP-M) and (c, d) 20 °C/min (CSP-F).

The XRD patterns of carbon materials prepared via CVD at 1000 °C at a heating ramp rate of 10 or 20 °C/min are shown in Figure 5. The low angle region of the XRD patterns was featureless, so only the wide angle XRD region is shown. The absence of low angle XRD peaks indicates that the carbon materials have a low level of mesostructural ordering. The presence of the high angle peaks at 2θ of 26° and 43°, which are the (002) and (101) diffraction peaks from graphitic carbon, indicate that the carbon materials possess a significant

level of graphitic character. The rapidly heated sample (CSP-F) appears to have a slightly higher level of graphitisation. This is consistent with greater deposition of carbon on the surface of the SBA-15 template particles [9,10]. Figure 5B shows nitrogen sorption isotherms of the SBA-15 silica spheres and the carbon materials. The SBA-15 silica template and both carbon materials exhibit type IV isotherms. All the isotherms exhibit H2 type hysteresis loop indicating the presence of pores with narrow mouth [11]. The textural properties of the SBA-15 template and carbon materials are shown in Table 1. There are no significant differences in the textural properties of the two CSP carbon samples.

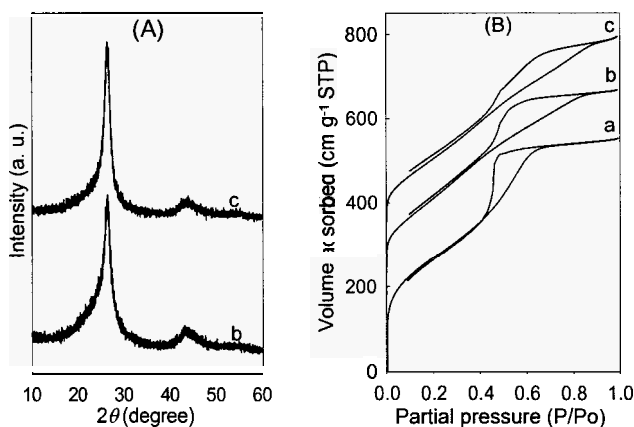


Figure 5. XRD patterns (A) and nitrogen sorption isotherms (B) of (a) mesoporous silica SBA-15 spheres, and carbon materials prepared via CVD at 1000°C and a heating ramp rate of (b) $10^\circ\text{C}/\text{min}$ (CSP-M) and (c) $20^\circ\text{C}/\text{min}$ (CSP-F). Isotherms b and c are offset (y-axis) by 180 and 280 respectively.

In summary, The carbonisation heating ramp rate used for the synthesis of CMK-3 mesoporous carbons plays an important role in determining the textural properties of the resulting materials. Fast heating ramp rate of $20^\circ\text{C}/\text{min}$ results in poorly ordered mesoporous carbon materials. However, with a slow carbonisation heating ramp rate of $5^\circ\text{C}/\text{min}$, well ordered mesoporous carbons can be obtained. A slower heating rate of $1^\circ\text{C}/\text{min}$ does not significantly alter the pore ordering but generates high surface area mesoporous carbons that exhibit no microporosity or non-framework porosity. The effect of heating ramp rate for liquid-impregnation derived carbons may be explained by considering that the carbonisation of the sucrose precursor starts as soon as the temperature is high

enough (i.e., not necessarily at the final 900 °C). A slower heating ramp rate offers a more homogenous environment for the carbonisation process, which results in better replication of the mesostructural ordering of the SBA-15 template in the carbon. For CVD derived mesoporous carbons, the particle morphology may be varied from solid core particles (at a heating ramp rate of 10 °C/min) to hollow particles (at a ramp rate of 20 °C/min). Higher levels of graphitisation are achieved for fast heating ramp rates due to greater deposition of carbon on the external surface of the SBA-15 template particles.

Acknowledgements

This research was funded by the EPSRC.

References

1. (a) R. Ryoo, S. H. Joo, M. Kruk and M. Jaroniec, *Adv. Mater.* **13**, 677 (2001). (b) R. Ryoo, S. H. Joo and S. Jun, *J. Phys. Chem. B* **103**, 7743 (1999).
2. H. F. Yang and D. Y. Zhao, *J. Mater. Chem.* **15**, 1217 (2005).
3. J. Lee, J. Kim and T. Hyeon, *Adv. Mater.* **18**, 2073 (2006).
4. D. Y. Zhao, J. Feng, Q. Huo, N. Melosh, G. H. Frederickson, B. F. Chmelka, and G. D. Stucky, *Science* **279**, 548 (1998).
5. S. Jun, S. H. Joo, R. Ryoo, M. Kruk, M. Jaroniec, Z. Liu, T. Ohsuna, and O. Terasaki, *J. Am. Chem. Soc.* **122**, 10712 (2000).
6. D. Zhao, J. Sun, Q. Li, and G. D. Stucky, *Chem. Mater.* **12**, 275 (2000).
7. (a) Y. Xia and R. Mokaya, *Adv. Mater.* **16**, 886 (2004). (b) Y. Xia, Z. Yang and R. Mokaya, *J. Phys. Chem. B* **108**, 19293 (2004). (c) Y. Xia, Z. Yang and R. Mokaya, *Stud. Surf. Sci. Catal.*, **156**, 565 (2005).
8. (a) Y. Xia and R. Mokaya, *Adv. Mater.* **16**, 1553 (2004). (b) Y. Xia and R. Mokaya, *Chem. Mater.* **17**, 1553 (2005). (c) Y. Xia, Z. Yang and R. Mokaya, *Chem. Mater.* **18**, 140 (2006).
9. (a) Z. Yang, Y. Xia and R. Mokaya, *Micropor. Mesopor. Mater.* **86**, 69 (2005). (b) Z. Yang, Y. Xia and R. Mokaya, *Stud. Surf. Sci. Catal.* **156**, 573 (2005).
10. (a) Z. Yang, Y. Xia and R. Mokaya, *J. Am. Chem. Soc.* **129**, 1673 (2007). (b) Z. Yang, Y. Xia, X. Sun and R. Mokaya, *J. Phys. Chem. B* **110**, 18424 (2006).
11. M. Kruk and M. Jaroniec, *Chem. Mater.* **13**, 3169 (2001).

NOVEL MESOPOROUS NITRIDES AND NITROGEN DOPED CARBON MATERIALS WITH DIFFERENT STRUCTURE, PORE DIAMETERS, AND NITROGEN CONTENTS

AJAYAN VINU*

Nano-ionics Materials Group, National Institute for Materials Science, 1-1 Namiki, Tsukuba, Ibaraki 305-0044, Japan, Email: vinu.ajayan@nims.go.jp

Here we report on the synthesis of novel highly ordered one and three dimensional cage type mesoporous carbon nitride (MCN-1 and MCN-2) with very high surface area and pore volume using SBA-15 and three dimensional cage type mesoporous silica, SBA-16, respectively, as template through a simple polymerization reaction between ethylenediamine (EDA) and carbon tetrachloride (CTC). The materials have been unambiguously characterized by various sophisticated techniques such as XRD, nitrogen adsorption, HRTEM, and FT-IR spectroscopy. The XRD results reveal that MCN-1 possesses two dimensional structure with $p6mm$ space group, which is quite consistent with the data from HRTEM while MCN-2 exhibits three dimensional structure with a $Im3m$ space group. We also demonstrate here the pore diameter of the MCN-1 materials can be controlled by tuning the pore diameter of the silica template while the textural parameters and the nitrogen content of the materials can also be controlled by varying the weight ratio of the EDA to CTC in the synthesis gel.

1. Introduction

Porous carbon materials have attracted much attention due to their remarkable performance in the fields of science and technology, including adsorption, separation, catalysis, energy devices, and chromatography [1-13]. Especially, porous carbon materials with well ordered mesoporous structure are of great interest mainly due to their excellent textural characteristics which offer them many distinct advantages not only for the adsorption of large biomolecules or bulky molecule transformation, but also for several other applications such as support for catalysis, energy storage and, fuel cells [1-13]. These mesoporous carbon materials have been first fabricated by Ryoo and his coworkers using two (2D) or three dimensional (3D) mesoporous silica materials as inorganic templates and sucrose as the carbon source [3,4]. Similar synthetic strategies have been also employed by several other researchers for the preparation of various kinds of mesoporous carbon materials with templating various types of mesoporous materials such as SBA-15, MCM-48, HMS, and MSU-H [9,10,14,15]. Recently, Vinu et al. have also synthesized mesoporous carbon

materials with different pore diameters using SBA-15 materials synthesized at different temperatures [5,11]. These materials have been utilized for the immobilization of biomolecules from aqueous solutions. We also introduced several strategies to prepare mesoporous carbon materials with high surface area, pore volume, and different structures, especially, the controlled pore filling technique has been employed to tune the textural characteristics of two dimensional hexagonally ordered mesoporous carbon materials [16,17].

Incorporation of heteroatoms such as nitrogen and boron in the carbon nanostructures including carbon nanotubes and porous carbon materials has attracted much attention because the dopant atoms can enhance the mechanical, semiconducting, field emission, optical, electrical, electronic, and surface properties [18-22]. Hitherto, considerable efforts have been made to dope the boron or nitrogen atoms in the carbon nanotubes whereas only little attention has been given to the doping of carbon materials with porous structure. Carbon nitride (CN) is a well known and fascinating material that has attracted worldwide attention because the incorporation of nitrogen atoms in the carbon nanostructure can enhance the mechanical, conducting, field emission, and energy storage properties [23-30]. CN materials with five different structures have been predicted so far: one is two dimensional graphitic C_3N_4 and four are three-dimensional carbon nitrides, namely α - C_3N_4 , β - C_3N_4 , cubic- C_3N_4 , and pseudocubic- C_3N_4 . Among the CN materials, β - C_3N_4 and its allotropic cubic and pseudo-cubic phases are superhard materials whose structure and properties are expected to be similar to those of diamond and β - Si_3N_4 [23]. Owing to its unique properties such as semi-conductivity, intercalation ability, hardness, CN is regarded as a promising material which could find potential applications in many fields. CN materials with no porous structure can be prepared either from molecular or chemical precursors at very high temperatures. Very recently, Gao and Giu have reported the chemical synthesis of nonporous turbostratic carbon nitride crystallites from polymerized ethylenediamine and carbon tetrachloride [25]. By constructing CN materials with porous structure, many novel applications could emerge: from catalysis, to separation and adsorption of very bulky molecules, and to the fabrication of low dielectric devices. However, only a little attention has been given to the synthesis of porous CN materials. Very recently, Vinu et al. have successfully reported the preparation of mesoporous carbon nitride with uniform pore size distribution (MCN-1) using SBA-15 as a template [31]. Groenewolt and Antonietti reported that the nanoparticles of graphitic C_3N_4 with different diameters and morphology could be immobilized inside the channels of mesoporous of silica host matrices [32]. It has been also

shown that the graphitic C_3N_4 nanoparticles immobilized mesoporous silica exhibits excellent photoluminescence properties.

Here we report on the synthesis of novel highly ordered one and three dimensional cage type mesoporous carbon nitride (MCN-1 and MCN-2) with very high surface area and pore volume using SBA-15 and three dimensional cage type mesoporous silica, SBA-16, respectively, as templates through a simple polymerization reaction between ethylenediamine (EDA) and carbon tetrachloride (CTC). The materials have been unambiguously characterized by various sophisticated techniques such as XRD, nitrogen adsorption, HRTEM, and FT-IR spectroscopy. We also demonstrate here the pore diameter of the MCN-1 materials can be controlled by tuning the pore diameter of the silica template while the textural parameters and the nitrogen content of the materials can also be controlled by varying the weight ratio of the EDA to CTC in the synthesis gel. The nature and the coordination of nitrogen atom in the carbon nitrides have been confirmed by FT-IR while the amount of nitrogen in the materials was obtained by CHN analysis.

2. Experimental Section

SBA-15 and SBA-16 were synthesized using non-ionic surfactant in a highly acidic medium. The detailed procedure for the preparation of the template materials can be found elsewhere [2,5]. MCN-1 was prepared by using SBA-15 as the template. In a typical synthesis, 0.5 g of calcined SBA-15 was added to a mixture of EDA (1.35 g) and CTC (3 g). The resultant mixture was refluxed and stirred at 90 °C for 6 hours. Then, the obtained dark brown colored solid mixture was placed in a drying oven for 12 hours, and ground into fine powder. Two sets of samples were prepared. A first set of the samples was prepared using SBA-15 materials with various pore diameters, which were synthesized at different temperature, and the samples were labeled as MCN-1-T where T indicates the synthesis temperature of mesoporous silica template. Another set of the samples was prepared using different weight ratio of EDA to CTC and the samples were labeled as MCN-1-130-x where x represents the weight ratio of EDA to CTC. The template-carbon nitride polymer composites were then heat treated in a nitrogen flow of 50 ml per minute at 600 °C with the heating rate of 3.0 °C min⁻¹ and kept under these conditions for 5 h to carbonize the polymer. The mesoporous carbon nitrides were recovered after dissolution of the silica framework in 5 wt % hydrofluoric acid, by filtration, washed several times with ethanol and dried at 100 °C. MCN-2 was prepared with the SBA-16 as the

template using the above procedure except the addition of 2.31 g of CTC instead of 3.

The powder X-ray diffraction (XRD) patterns of mesoporous carbon nitride materials were collected on a Rigaku diffractometer using $\text{CuK}\alpha$ ($\lambda = 0.154$ nm) radiation. The diffractograms were recorded in the 2θ range of 0.8 to 10° with a 2θ step size of 0.01 and a step time of 1 s. Nitrogen adsorption and desorption isotherms were measured at -196°C on a Quantachrome Autosorb 1 sorption analyzer. All samples were outgassed at 250°C for 3 h prior to the nitrogen adsorption measurements. The specific surface area was calculated using the Brunauer-Emmett-Teller (BET) method. The pore size was obtained from the adsorption branch of the nitrogen isotherms by Barrett-Joyner-Halenda method. Elementary analysis was done using Yanaco MT-5 CHN analyzer. FT-IR spectra of MCN were recorded on a Nicolet Nexus 670 instrument by averaging 200 scans with a resolution of 2 cm^{-1} measuring in transmission mode using the KBr self-supported pellet technique. The spectrometer chamber was continuously purged with dry air to remove water vapor. HRTEM image was obtained by using JEOL-3000F and JEOL-3100FEF.

3. Results and Discussion

Figure 1A shows the powder XRD diffraction patterns of MCN-1 materials. The materials presented are synthesized using SBA-15 with various pore diameters as template. Remarkably, the quality of the XRD pattern and the position of the main peak vary significantly with the pore diameter of the SBA-15 template used. MCN-1-100 and MCN-1-130 exhibit three clear peaks, which can be indexed to the 100, 110, and 200 reflections of highly ordered two dimensional hexagonal mesostructure with the space group of $p6mm$, similar to the XRD pattern of parent mesoporous silica template SBA-15 which consists of the hexagonal arrangement of cylindrical pores and the pores are interlinked by the micropores present in the walls. Such materials with one dimensional mesopores are arranged in a hexagonal net are defined as two dimensional because the diffraction peaks pattern shows two dimensional $p6mm$ symmetry. MCN-1-150 shows a sharp (100) peak together with only a weak (110) peak, indicating that the increase of pore diameter of the template leads to some loss of higher order reflections in the diffraction pattern. The intensity of (110) peak of MCN-1-150 is much lower as compared to that of MCN-1-100 and MCN-1-130. This could be attributed to empty carbon nitride mesopores, which are created by the incomplete filling of the ultra large hexagonal mesoporous SBA-15 and weaken the peak intensity by interference of X-ray diffraction between inner and

outer carbon walls. However, the presence of a sharp and a high intense (100) reflection in MCN-1-150 reveals that the structural order of the template is almost retained in the sample even after removal of the template.

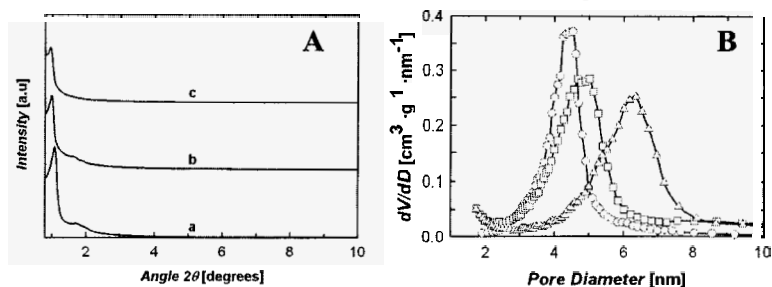


Figure 1: Powder XRD patterns of mesoporous carbon nitride with various pore diameters prepared from SBA-15-X templates: (a) MCN-1-100, (b) MCN-1-130, and (c) MCN-1-150, and (B) BJH pore size distributions of mesoporous carbon nitride with various pore diameters (●) MCN-1-100, (□) MCN-1-130, and (▲) MCN-1-150.

The specific surface area and the pore volume of MCN-1-130 are much higher as compared to those for the MCN-1-100 and the MCN-1-150. The specific surface area and the specific pore volume of MCN-1-130 are 830 m²/g and 1.25 cm³/g, respectively, whereas MCN-1-100 and MCN-1-150 possess the specific surface areas of 505 and 650 m²/g, respectively, and the specific pore volumes of 0.89 and 0.55 cm³/g, respectively. The high surface area in MCN-1-130 may be due to the difference in the defect sites which creates microporosity in the material. Figure 1B shows the BJH adsorption pore size distribution of MCN-1-100, -130 and -150. All the samples show a main peak, which mainly comes from the mesopores formed after dissolution of the silica matrix from the template. The pore diameter of the MCN materials increases with increasing the pore diameter of the silica templates used. It should also be mentioned that the full width half maximum of the BJH adsorption pore size distribution of the MCN-1-150 is much larger than that of the MCN-1-100 and MCN-1-130. Among the MCN samples prepared by using SBA-15-X as template, MCN-1-150 exhibits a very large pore diameter, which is around 6.4 nm. This could be mainly due to the incomplete filling of CN polymer matrix in the ultra large mesopores of SBA-15-150 as the same weight ratio of the EDA to CTC is used for filling the mesopores of the templates with different pore diameter.

Figure 2A shows the FT-IR spectra of MCN samples with different pore diameters. All the samples show three major broad bands centred around 1257, 1571 and 3412 cm⁻¹, which are attributed to aromatic C-N stretching bonds, aromatic ring modes, and the stretching mode of N-H groups in the aromatic

ring, respectively. A similar result has also been observed in the non-porous carbon nitride samples [25-30]. Further, UV-Vis absorbance study was also conducted to confirm the presence of *s*-triazine ring in the MCN-1-100. The amount of carbon and nitrogen source in the mesoporous silica template has a great impact on the textural parameters such as specific surface area, specific pore volume, and pore size distribution of the mesoporous carbon nitride replica materials. The MCN-1-130 material has been chosen for studying the effect of the composition of carbon and nitrogen source in the synthesis mixture as the material shows an excellent structural order and interesting textural parameters. The specific pore volume of the MCN materials systematically decreases with increasing the weight ratio of EDA to CTC while the specific surface area of the materials increases from 731 to 818 cm^2/g with increasing the weight ratio of EDA to CTC from 0.3 to 0.45 and then decreases to 552 cm^2/g for MCN-1-130-0.9 (Figure 2B). Surprisingly, the nitrogen content of the material significantly increases when the weight ratio of EDA to CTC is increased. The carbon to nitrogen ratio calculated from the CHN analysis decreases from 4.5 to 3.3 with increasing the weight ratio of EDA to CTC from 0.3 to 0.9. This is also further confirmed by the EEL spectra of the samples prepared at the weight ratio of EDA to CTC of 0.45 and 0.90.

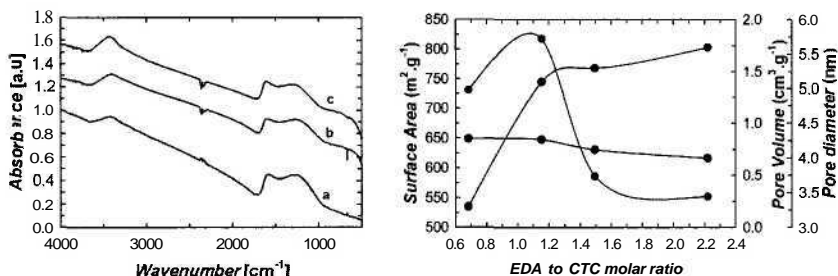


Figure 2: (A) FT-IR spectra of mesoporous carbon nitride with various pore diameters prepared from SBA-15-X templates: (a) MCN-1-100, (b) MCN-1-130, and (c) MCN-1-150 and (B) Effect of EDA and CTC weight ratio on the textural parameters of MCN-1-130; the curve with maximum refers to the surface area, the decreasing curve refers to the pore volume and the increasing curve refers to the pore diameter.

Figure 3A shows the powder XRD pattern of MCN-2 along with the parent mesoporous silica, SBA-16. It can be seen that SBA-16 mesoporous silica template exhibits well resolved (110), (200) and (211) reflections, characteristics of the body centered three dimensional cubic space group $Im\bar{3}m$. The powder XRD pattern of MCN-2 also shows a sharp low angle peak and a broad higher order peak and is almost similar to that obtained for the SBA-16 mesoporous

silica template (Figure 1). The results indicate that the material possesses a possible a three dimensional mesoporous cage structure replicated from the template SBA-16. It is interesting to note that the intensity of the (110) peak of MCN-2 is much higher than that of the silica template. The unit cell parameter of the MCN-2 is calculated using the formula $2^{1/2}d_{110}$ to be 13.4 nm. The higher angle powder diffraction pattern of MCN-2 is also shown in Figure 1B. The samples exhibits a single broad diffraction peak (inset) near 25.47° ($d = 3.42 \text{ \AA}$). This peak is almost similar to the characteristic 002 basal plan diffraction peak in the nonporous carbon nitride spheres. This reveals the presence of turbostratic ordering of the carbon and nitrogen atoms in the graphene layers of MCN-2.

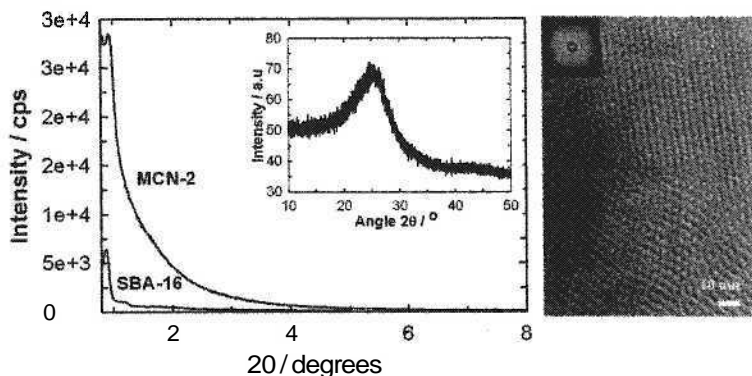


Figure 3: (A) Powder XRD patterns of SBA-16 and MCN-2 (inset: higher angle powder XRD pattern of MCN-2) and (B) HRTEM image of MCN-2 and its corresponding fast Fourier transform (FFT) image.

Figure 3B shows the HRTEM image of MCN-2 in which the bright contrast strips on the image represent the pore wall images, whereas dark contrast cores display empty channels, shows well ordered mesoporous structure with a regular intervals of linear array of mesopores throughout the samples which is characteristics of well ordered SBA-16 mesoporous silica. Figure 3B also clearly shows the presence of well ordered domains of three dimensional cubic mesoporous structure of MCN-2 sample which is almost similar to the structure of SBA-16. The corresponding fast Fourier transform pattern is shown in Figure 3B (inset), which can be attributed to the [110] axis of the cubic MCN-2 material. Based on the HRTEM image and the FFT pattern, it is suggested here the occurrence of well ordered mesopores with a possible three dimensional cubic mesoporous structure in MCN-2, which is consistent with the XRD results and suggests the possible replicated synthesis of the three dimensional carbon nitride from SBA-16.

The elemental mapping of MCN-2 (not shown) reveals that the carbon (C) and nitrogen (N) are uniformly distributed throughout the sample. No other elements were found in the elemental mapping, indicating that the material is mainly composed of C and N. The C to N ratio of MCN-2 calculated from the EELS is ca. 4 which is in close agreement with the value obtained from CHN analysis, i.e. 4.1. The FT-IR spectrum of MCN-2 also reveals the existence of the CN matrix and shows four well resolved bands centered at 742, 1209, 1560 and 3431 cm^{-1} (Figure 4). The bands at 742, 1209, 1560 cm^{-1} are attributed to the sp^2 graphitic sites, C-N stretching and C=N stretching, respectively, while the band at 3431 is assigned to the residual NH or NH_2 components [24-30]. On the whole, the major IR characteristics bands are consistent with the general characteristics of other amorphous non porous carbon nitride materials and MCN-1.

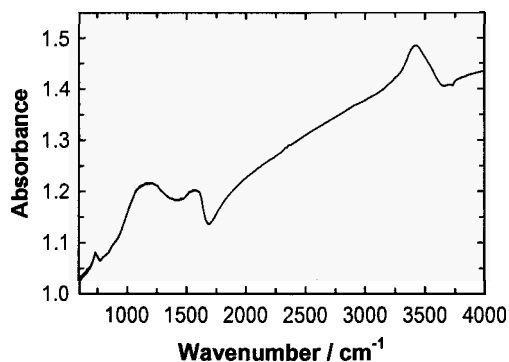


Figure 4: FT-IR spectrum of MCN-2 material.

4. Conclusions

In summary, we have demonstrated the fabrication of mesoporous carbon nitride materials (MCN) with tunable pore diameters and different structures from SBA-15 materials with different pore diameters and SBA-16 as hard templates through a simple polymerization reaction between EDA and CTC. The materials have been unambiguously characterized by various sophisticated techniques such as XRD, nitrogen adsorption, HRTEM, FT-IR, and CHN analysis. It has been found that the pore diameter of the MCN materials can be tuned from 4.2 to 6.4 nm by the simple adjustment of the pore diameter of the mesoporous silica templates. We also demonstrated that the textural parameters and the nitrogen content of MCN materials can be easily tuned by the simple adjustment of the weight ratio of EDA to CTC in the synthesis mixture. Thus, we

believe that the methods described here of tuning the pore diameter of the mesoporous silica template and the composition of the synthesis mixture to control the textural parameters, especially the pore diameter, and the nitrogen content of the mesoporous carbon nitride materials offer the novel path way for fabricating new porous nitrides with very high nitrogen contents and tunable textural parameters and for the development of novel nanostructured nitrides. The porous carbon nitrides materials with tunable textural parameters and the chemical composition could also offer many opportunities for the applications including catalysis, energy storage, capacitors, separation and adsorption of small and large organic toxic and biomolecules, vitamins and amino acids, and fuel cells.

References

1. T. Kyotani, Z.X. Ma and A. Tomita, *Carbon* **41**, 1451 (2003).
2. J.M. Kim, Y. Sakamoto, Y.K. Hwang, Y.U. Kwon, O. Terasaki, S.-E. Park, G.D. Stucky, *J. Phys. Chem. B* **106**, 2552 (2002).
3. S.H. Joo, S.J. Choi, I. Oh, J. Kwak, Z. Liu, O. Terasaki and R. Ryoo, *Nature* **412**, 169 (2001).
4. R. Ryoo, S.H. Joo and S. Jun, *J. Phys. Chem. B* **103**, 743 (1999).
5. A. Vinu, C. Streb, V. Murugesan and M. Hartmann, *J. Phys. Chem. B* **107**, 8297 (2003).
6. J.Y. Kim, S.B. Yoon and J.-S. Yu, *Chem. Mater.* **15**, 1932 (2003).
7. A. Vinu and M. Hartmann, *Catal. Today* **102**, 189 (2005).
8. A. Vinu and K. Ariga, *Chem. Lett.* **34**, 674 (2005).
9. S.B. Yoon, J.Y. Kim and J.-S. Yu, *Chem. Commun.* 1536 (2002).
10. S.B. Yoon, J.Y. Kim and J.-S. Yu, *Chem. Commun.* 559 (2001).
11. A. Vinu, M. Miyahara and K. Ariga, *J. Phys. Chem. B* **109**, 6436 (2005).
12. A. Vinu, K. Z. Hossain and K. Ariga, *J. Nanosci. Nanotechnol.* **5**, 347 (2005).
13. A. Vinu, M. Miyahara and K. Ariga, *J. Nanosci. Nanotechnol.* **6**, 1510 (2006).
14. J. Lee, S. Yoon, S.M. Oh, S. Shin and T. Hyeon, *Adv. Mater.* **12** 359 (2000).
15. S.S. Kim and T.J. Pinnavaia, *Chem. Commun.* 2418 (2001).
16. A. Vinu, P. Srinivasu, M. Takahashi, T. Mori, V.V. Balasubramanian and K. Ariga, *Micropor. Mesopor. Mater.* **100**, 20 (2007).
17. A. Vinu, K.Z. Hossain, P. Srinivasu, M. Miyahara, S. Anandan, N. Gokulakrishnan, T. Mori, K. Ariga, *J. Mater. Chem.* **17**, 1819 (2007).
18. R.B. Sharma, D.J. Late, D.S. Joag, A. Govindaraj and C.N.R. Rao, *Chem. Phys. Lett.* **428**, 102 (2006).

19. M. Koh and T. Nakajima, *Carbon* **38**, 1947 (2000).
20. F.V. Paez, A. Zamudio, A. L. Elias, H. Son, E. B. Barros, S. G. Chou, Y.A. Kim, H. Muramatsu, T. Kayashi, J. Kong, H. Terrones, G. Dresselhaus, M. Endo, M. Terrones and M. S. Dresselhaus, *Chem. Phys. Lett.* **424**, 345 (2006).
21. C-M. Yang, C. Weidenthaler, B. Spliethof, M. Mayanna and F. Schüth, *Chem. Mater.* **17**, 355 (2005).
22. P-X. Hou, H. Orikasa, T. Yamazaki, K. Matsuoka, A. Tomita, N. Setoyama, Y. Fukushima and T. Kyotani, *Chem. Mater.* **17**, 5187 (2005).
23. A.Y. Liu and M.L. Cohen, *Science* **245**, (1989) 841.
24. M. Kawaguchi, S. Yagi and H. Enomoto, *Carbon* **42**, 345 (2004).
25. a) Y. Qiu and L. Gao, *Chem. Commun.* 2378 (2003). b) Q. Guo, Q. Yang, L. Zhu, C. Yi, S. Zhang and Y. Xie, *Solid State Commun.* **132**, 369 (2004).
26. E. Kroke and M. Schwarz, *Coordin. Chem. Rev.* **248**, 493 (2004).
27. Y-J. Bai, B. Lu, Z-G. Liu, L. Li, D-L. Cui, X-G. Xu and Q-L. Wang, *J. Crystal Growth* **247**, 505 (2003).
28. a) J. L. Zimmerman, R. Williams, V. N. Khabashesku and Margrave, *Nano. Lett.* **12**, 731 (2001); b) V. N. Khabashesku, J. L. Zimmerman, J. L. Margrave, *Chem. Mater.* **12**, 3264 (2000); c) J. Wang, D. R. Miller and E. G. Gillan, *Carbon* **41**, 2031 (2003); d) E. G. Gillan, *Chem. Mater.* **12**, 3906 (2000); e) D. R. Miller, J. Wang and E. G. Gillan, *J. Mater. Chem.* **12**, 2463 (2002).
29. J. Kouvetakis, A. Bandari, M. Todd and B. Wilkens, N. Cave, *Chem. Mater.* **6**, 811 (1994).
30. J. Wang, D. R. Miller and E. G. Gillan, *Carbon* **41**, 2031 (2003).
31. A. Vinu, K. Ariga, T. Mori, T. Nakanishi, S. Hishita, D. Golberg and Y. Bando, *Adv. Mater.* **17**, 1648 (2005).
32. a) F. Goettmann, A. Fischer, M. Antonietti and A. Thomas, *Angew. Chem. Int. Ed.* **45**, 4467 (2006); b) M. Groenewolt and M. Antonietti, *Adv. Mater.* **17**, 1789 (2005).

CARBOXYL, AMINE AND THIOL FUNCTIONALIZED MESOPOROUS CARBON MATERIALS

DHANASHRI P. SAWANT, JOSENA JUSTUS, AND AJAYAN VINU*
*WPI Center for Materials Nanoarchitectonics, National Institute for Materials Science,
1-1, Namiki, Tsukuba, 305-0044, Japan, Email: vinu.ajayan@nims.go.jp*

The covalent functionalization of ethylene diamine (EN) and methionine (MET) on the surface of the mesoporous carbon materials treated with ammonium persulphate (APS) followed by SOCl_2 has been demonstrated. The functionalized materials have been unambiguously characterized by XRD, nitrogen adsorption, HRSEM-EDX, and FT-IR measurements. The XRD results reveal that the structure of the mesoporous carbon materials is retained even after the functionalization. FT-IR results confirm that EN and MET molecules are indeed covalently attached with the COCl groups on the surface of the mesoporous carbons. We strongly believe that the functionalized materials may be utilized as the supports for catalysis, drug delivery, separation and adsorption technology and the demonstrated method could be applied for functionalization of various kinds of mesoporous carbon materials with different structure and textural parameters.

1. Introduction

Significant efforts have been devoted to the synthesis of mesoporous carbons with ordered porous structure, due to their potential applications in separation, adsorption, and electronic devices [1]. Ryoo et al. first reported the highly ordered mesoporous carbon, by using MCM-48 as template and sucrose as carbon precursor which leads to the formation of CMK-1 carbon with 3-D ordered pores and large surface area [2-4]. Till now mesoporous carbons with different structures have been synthesized using a variety of templates and carbon precursors [5-12]. But chemical modification of carbon is difficult because of its low reactivity. The conventional modification of carbon involves oxidation with acids or ozone and the subsequent reaction with thionyl chloride with the carboxylic groups makes it possible to graft and further elaborate the surface properties [13]. Covalent functionalization of ordered mesoporous carbon is done by using diazonium compounds [14,15]. Here we demonstrate the covalent functionalization of carboxyl, amine, and thiol groups on the surface of the hexagonally ordered mesoporous carbon materials through a simple oxidation using ammonium persulfate solution (APS) followed by SOCl_2 treatment and the reaction with the organic diamines and amino-thiol molecules. The functionalized materials have been characterized by XRD, nitrogen

adsorption, HRSEM-EDX and FT-IR. A relatively high degree of grafting density was achieved by using this efficient modification method. We strongly believe that the combination of the modified surface functionalities with ordered pore channels allows advanced applications of porous carbons in drug delivery, separation, catalysis, and biotechnologies [16-20].

2. Experimental Section

2.1 Materials

Tetraethylorthosilicate, sucrose, and tri-block copolymer Pluronic P123 were obtained from Aldrich. APS, thionyl chloride, dimethyl formamide, tetrahydrofuran, dichloromethane were purchased from Wako chemicals, Japan. Ethylenediamine and methionine (99%) were obtained from Aldrich. All chemicals were used without further purification.

2.2 Synthesis of Mesoporous Carbon

Mesoporous carbon was prepared by using SBA-15-100 as a template and sucrose as a carbon source. In a typical synthesis of mesoporous carbon, 1 g of the mesoporous silica template was added to a solution obtained by dissolving 1.25 g of sucrose and 0.14 g of sulphuric acid in 5 g of water. The obtained mixture was kept in an oven for 6 h at 100 °C. Subsequently, the oven temperature was raised to 160 °C and keeping the brown coloured solid mixture at the final temperature for 6 h. In order to obtain fully polymerized and carbonized sucrose inside the pores of the silica template, 0.8 g of sucrose, 0.09 g of sulphuric acid and 5 g of water were again added to the pretreated sample and the mixture was again subjected to the thermal treatment described above. The template-polymer composite was then pyrolyzed in a nitrogen flow at 900 °C and kept under these conditions for 6 h to carbonize the polymer. Then, the mesoporous carbon was recovered after dissolution of the silica framework in 5 wt. % solution of hydrofluoric acid, by filtration, washed several times with ethanol, and dried at 100 °C.

2.3 Oxidation Treatment with APS

The oxidation treatment of mesoporous carbon material was done through the reaction with a solution of 1.0 M APS in 2M H₂SO₄ for obtaining carboxyl groups on the porous surface. In a typical oxidation experiment, 200 mg of the mesoporous carbon was added to 12 g of APS solution. The mixture was stirred at room temperature for 9 h. All the oxidized sample was filtered, washed

several times with distilled water until there was an absence of sulfates in the washing water, and dried it in a vacuum oven at 50 °C overnight. However, a trace amount of sulfur was detected in the oxidized sample when the sample was analyzed using EDX analysis.

2.4 *SOCl₂ Treatment*

In a typical experiment 150 mg of carboxyl functionalized mesoporous carbon (CMK-3-COOH) was added to 30 ml thionyl chloride and 1.5 ml of N,N' dimethyl formamide (DMF). The mixture was stirred at 70°C for 24 h. After complete evaluation of HCl and SO₃ gas, the yellow solution was decanted from the mixture. The mixture was added to 20 ml of anhydrous tetrahydrofuran (THF) and centrifuged with a speed of 3400 rpm for 5 min. The supernatant solution was removed after the material settle down completely and the above centrifugation process was repeated several times until the colour of the solution changes from yellow to colourless solution. Finally, the material was filtered, washed with anhydrous THF, and dried in a vacuum oven at 50 °C over night. The final material was denoted as CMK-3-COCl.

2.5 *Covalent Functionalization of Ethylene diamine (EN)*

The covalent attachment of EN was done by adding 100 mg of CMK-3-COCl to 1 g of EN and 3 g of DMF. The mixture was stirred at 100 °C for 24 h under N₂ atmosphere. Then the mixture was centrifuged four times with anhydrous dichloromethane until the complete removal of unreacted amine from the material. Finally, the reaction mixture was filtered using membrane filter paper, washed with anhydrous dichloromethane (DCM), and dried in a vacuum oven at 50 °C overnight. The final material was denoted as CMK-3-COEN.

2.6 *Covalent Functionalization of Methionine (MET)*

To increase the solubility of amino thiol, 1 g of MET was added to 5 g of DMF and the resulting mixture was ultra-sonicated at room temperature for 90 min. Subsequently, 1 g of CMK-3-COCl was added to the above mixture with vigorous stirring at 70 °C and the stirring was continued under nitrogen atmosphere for 24 h. Then the resultant mixture was centrifuged several times with anhydrous dichloromethane to make sure the complete removal of the unreacted MET molecules from the surface of the material. Finally, the reactant mixture was filtered using membrane filter paper, washed with DCM, and dried in a vacuum oven at 50 °C overnight. The final material was denoted as CMK-3-COMET.

2.7 Characterization

The powder X-ray diffraction (XRD) patterns of the functionalized mesoporous carbon materials were collected on a Rigaku diffractometer using $\text{CuK}\alpha$ ($\lambda = 0.154 \text{ nm}$) radiation. The diffractograms were recorded in the 2θ range of 0.8 to 10° with a 2θ step size of 0.01° and a step time of 6 sec . Nitrogen adsorption and desorption isotherms were measured at -196°C on a Quantachrome Autosorb-1C instrument. All samples were outgassed at 80°C for 24 h prior to the nitrogen adsorption measurements. The specific surface area was calculated using the Brunauer-Emmett-Teller (BET) method. The morphology and the elemental composition of the materials after the functionalization were observed on a Hitachi S-4800 field emission scanning electron microscope (HR-FESEM) with EDX using an accelerating voltage of 5.0 kV . The nature and the amount of surface functional groups on the surface of the mesoporous carbon were determined using FT-IR spectroscopy.

3. Results and Discussion

In order to check the effect of covalent functionalization on the structure and the textural parameters, the materials after each treatment were characterized by powder XRD, nitrogen adsorption and HRSEM measurements. Figure 1 shows the powder XRD patterns of the mesoporous carbons after treatment with APS, SOCl_2 and EN. All the samples except CMK-3-COEN exhibit a sharp lower angle peak with several higher order weak peaks, which is indicative of the retention of the hexagonally ordered mesoporous structure even after the functionalization. It can also be seen from the Figure 1 that the intensity of the (100) peak significantly decreases, which shifted toward higher angle, after the functionalization, which indicates that the pores are filled with the organic molecules which are covalently attached with the COOH groups present on the surface of the mesoporous carbons. The large difference in the intensity of the (100) peaks of the mesoporous carbon before and after the functionalization may not be interpreted as complete damage to the structural order, but it is likely that larger contrast in density between the silica walls and the open pores relative to that between the silica walls and covalently bonded organic molecules is responsible for the observed decrease the intensity.

Figure 2 shows the effect of functionalization on the specific surface area of the CMK-3 materials after functionalization. It is clearly seen that the specific surface area of the materials calculated from the nitrogen adsorption isotherms drastically decreases upon the functionalization. The specific surface area amounts to $1250 \text{ m}^2/\text{g}$ for pure CMK-3, which decreases to 590 and $515 \text{ m}^2/\text{g}$ for

CMK-3-COEN and CMK-3-CO-MET, respectively. While the pore volume for pure CMK-3 ($1.10 \text{ cm}^3/\text{g}$) also decreases to $0.39 \text{ cm}^3/\text{g}$ and $0.52 \text{ cm}^3/\text{g}$ in case of CMK-3-COEN and CMK-3-CO-MET, respectively. So this significant decrease in pore volume of the CMK-3 after functionalization evidenced that the organic molecules are certainly covalently attached on the mesoporous surface.

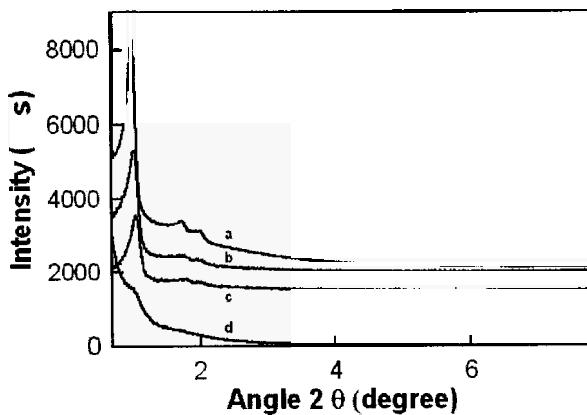


Figure 1: Low-angle XRD patterns of (a) Pure CMK3, (b) CMK3-COOH, (c) CMK3-COCl, and CMK3-COEN.

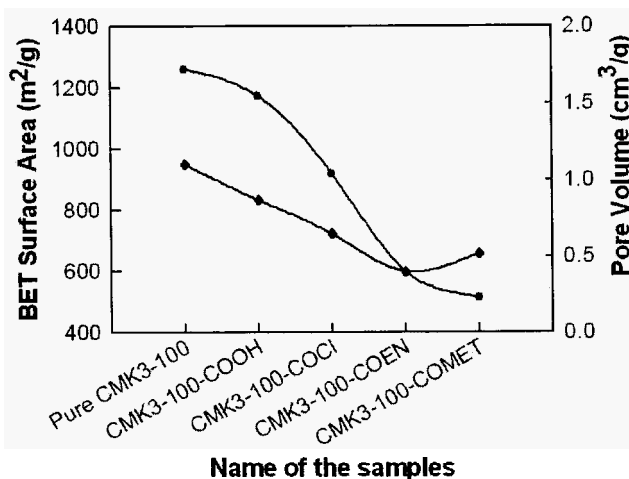


Figure 2: Effect of the functionalization on the (●) BET surface area and (◆) pore volume of mesoporous carbon material.

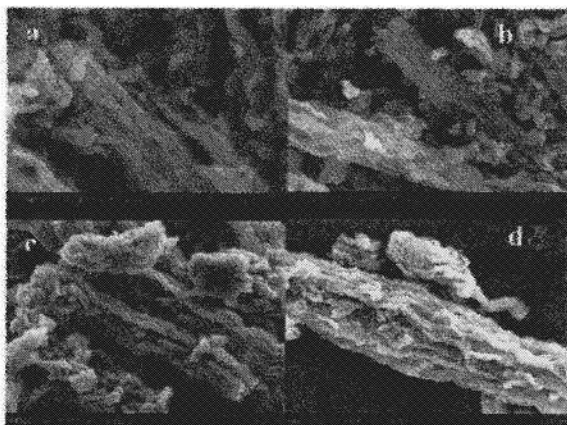


Figure 3a: HRSEM of a) CMK3-COOH, b) CMK3-COCl, c) CMK3-COEN, and d) CMK3-COMET.

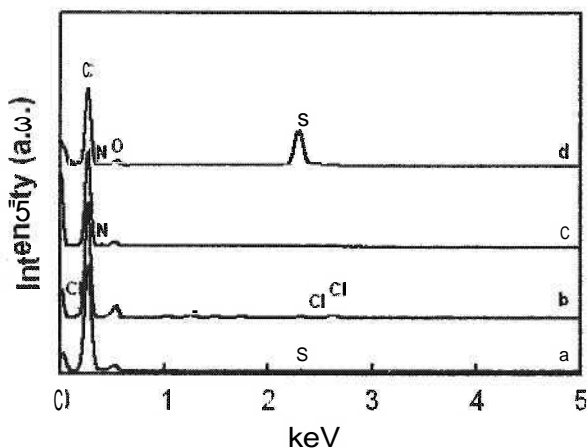


Figure 3b. EDX pattern of a) CMK3-COOH, b) CMK3-COCl, and c) CMK3-COEN; (C:69.57%,N:16.97%,O:13.46%) and d) CMK3-COMET (C:79.01%,N:10.22%,O:8.09%,S:2.68%).

To gain the understanding about the morphology of the materials after the covalent functionalization of organic molecules, the materials were characterized by HRSEM and EDX analysis. Figure 3a shows the HRSEM images of CMK-3 materials after functionalization. All the samples show a rod like morphology and the rods are aggregated together and form nanorod bundles. It is interesting to note that the morphology of the materials is completely retained even after the

functionalization. Moreover, the aggregation of the nanorods is more pronounced for the CMK-3-COEN and CMK-3-COMET. This could be mainly due to the strong interaction between functionalized nanorods through Van der Waals forces.

Figure 3b shows the EDX patterns of the functionalized CMK-3 materials along with the pure CMK-3. The sample CMK-3-COEN exhibits the peaks corresponding to C, O and N, which indicates that the EN molecules are bonded with the carboxyl groups on the surface of the CMK-3-COCl, where as CMK-3-COMET displays the peak for C, O and S, confirming that the aminothiols groups are attached on the porous surface.

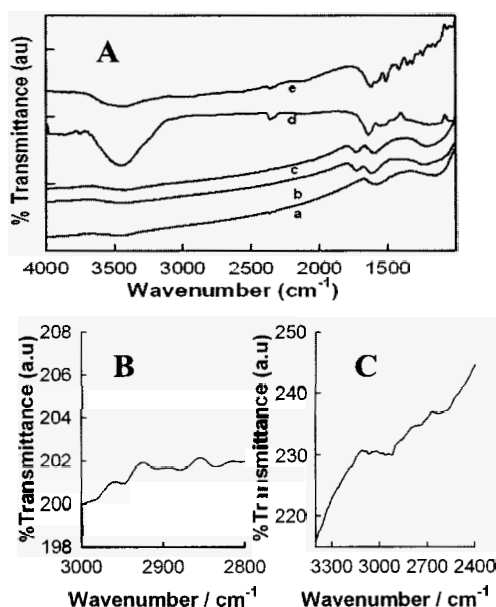


Figure 4: FT-IR spectra of (A): a) pure CMK-3, b) CMK3-COOH, c) CMK3-COCl, d) CMK3-COEN, and e) CMK3-COMET; and enlarged spectrum of (B) CMK3-COEN, and (C) CMK3-COMET.

FT-IR is a powerful tool for getting the information about the type, nature and the amount of functionality introduced on the surface of carbon materials. FT-IR spectra of mesoporous carbon treated with APS, SOCl_2 and then further with amine and amino thiol functionalized materials are shown in Figure 4. Sample after oxidation treatment show two sharp bands centered around 1723 and 1587 cm^{-1} and those are assigned to $\text{C}=\text{O}$ stretching vibration of non-

aromatic carboxyl groups and aromatic ring stretching coupled to highly conjugated keto groups, respectively [21-23]. The band at 1400 cm^{-1} could be assigned either to carboxyl-carbonate structures or to aromatic C=C bond where as the band at 1250 cm^{-1} might be attributed to C-O-C vibrations [24,25]. The broad band appeared at $3300\text{-}3600\text{ cm}^{-1}$ is attributed to the formation of carboxylic structure. Both -COOH and -COO^- were transformed into acyl chloride functionalities upon reacting with thionyl chloride, and the distinctive stretching vibration of -COCl should have been observed. However, the high hydrolytic reactivity of -COCl in air tended to convert them back into carboxylate ions, and this made FTIR (operated in air) detection of the stretching vibration of -COCl extremely difficult.

After amine functionalization, the appearance of new peaks in the region $3400\text{-}3100$, $3000\text{-}2800$, and $1250\text{-}1000\text{ cm}^{-1}$ regions (Figure 4B) attributed to the N-H, C-H, and C-N stretches, respectively, give a strong indication of the amino group attachment to the -CO functionality of mesoporous carbon. While MET functionalized sample (Figure 4C) showed an S-H stretching band at 2564 cm^{-1} where as four stretching bands at 2878 , 2921 , 3157 , and 3315 cm^{-1} were also observed. The bands at 2878 and 2921 cm^{-1} are assigned for C-H stretching where as the bands at 3157 and 3315 cm^{-1} are associated with the N-H stretching. The bands at $1625\text{-}1680\text{ cm}^{-1}$, which are attributed to the C=O stretching in -CONH- , are clearly observed for both the CMK-3-COEN and CMK-3-COMET samples. However, the disappearance of C=O stretching vibration of non-aromatic carboxyl groups ($\sim 1723\text{ cm}^{-1}$) and shifting of above peak of C=O stretching indicate that there is complete conversion of COCl into CO-amino and CO-amino thiol attachment.

4. Conclusions

The mesoporous carbon material has been successfully functionalized with the amine and aminothiols groups. Before introducing the amine and the aminothiols groups, the mesoporous carbon materials were treated with ammonium persulphate solution (APS) followed by SOCl_2 treatment to form the COCl groups on the surface of the mesoporous carbons. We demonstrate that the amine and aminothiols groups can be introduced on the surface of the mesoporous carbons. The obtained materials have been unambiguously characterized by several sophisticated techniques such as XRD, N_2 adsorption, HRSEM-EDX, and FT-IR. The FT-IR results revealed that the amine and aminothiols groups have been covalently attached with the CO groups on the surface of mesoporous carbon. We strongly believe that these functionalized

mesoporous carbon materials may be utilized as a solid and stable support for immobilizing chiral amine complexes and salen complexes and could also find applications in drug delivery, separation and adsorption technology.

References

1. R. Ryoo, S. H. Joo and S. Jun, *J. Phys. Chem. B* **103**, 7743 (1999).
2. R. Ryoo, S. H. Joo, M. Kruk and M. Jaroniec, *Adv. Mater.* **13**, 677 (2001).
3. S. Jun, S. H. Joo, R. Ryoo, M. Kruk, M. Jaroniec, Z. Liu, T. Ohsuna and T. Terasaki, *J. Am. Chem. Soc.* **122**, 10712 (2000).
4. R. Ryoo, I. S. Park, S. Jun, C. W. Lee, M. Kruk and M. Jaroniec, *J. Am. Chem. Soc.* **123**, 1650 (2001).
5. A. Vinu, M. Miyahara, V. Sivamurugan, T. Mori and K. Ariga, *J. Mater. Chem.* **15**, 5122 (2005).
6. T.-W. Kim, R. Ryoo, K. P. Gierszal, M. Jaroniec, L. A. Solovyov, Y. Sakamoto and O. Terasaki, *J. Mater. Chem.* **15**, 1560 (2005).
7. A. Vinu, M. Miyahara and K. Ariga, *Studies in Surface Science and Catalysis*, **58** (2), 971 (2005).
8. A. Vinu, T. Mori and K. Ariga, *Science and Technology of Adv. Mater.* **7**, 753 (2006).
9. A. Vinu, P. Srinivasu, M. Takahashi, T. Mori, V. V. Balasubramanian and K. Ariga, *Microporous and Mesoporous Materials*, **100**, 20 (2007).
10. C. Vix-Guterl, S. Saadallah, L. Vidal, M. Reda, J. Parmentier and J. J. Patarin, *Mater. Chem.* **13**, 2535 (2003).
11. Z. J. Li and M. J. Jaroniec, *Phys. Chem. B*, **108**, 824 (2004).
12. B. Z. Tian, S. N. Che, Z. Liu, X. Y. Liu, W. B. Fan, T. Tatsumi, O. Terasaki and D. Y. Zhao, *Chem. Commun.* 2726 (2003).
13. K. Kinoshita, *Carbon Electrochemical and Physicochemical Properties*; Wiley: New York, (1988).
14. J. L. Bahr and J. M. Tour, *J. Mater. Chem.* **12**, 1952 (2002).
15. M. B. Martinhopkins, R. K. Gilpin and M. J. Jaroniec, *Chromatogr. Sci.* **29**, 147 (1991).
16. Z. J. Li, G. D. Del Cul, W. F. Yan, C. D. Liang and S. Dai, *J. Am. Chem. Soc.* **126**, 2782 (2004).
17. S. Jun, M. Choi, S. Ryu, H. Y. Lee and R. Ryoo, *Nanotechnol. Mesostruc. Mater.* **146**, 37 (2003).
18. Z. J. Li and M. Jaroniec, *Anal. Chem.* **76**, 5479 (2004).
19. C. D. Liang, S. Dai and G. Guiochon, *Anal. Chem.* **75**, 4904 (2003).
20. C. D. Liang, K. L. Hong, G. Guiochon, J. W. Mays and S. Dai, *Angew. Chem., Int. Ed.* **43**, 5785 (2004).
21. J.-W. Shim, S.-J. Park and S. K. Ryu, *Carbon*, 2001, 39, 1635.

22. J. Zawadzki, Infrared Spectroscopy in Surface Chemistry of Carbons. In: Thrower, P.A., Editor, Chemistry and Physics of Carbon, New York, Dekker, 147 (1989).
23. P. Painter, M. Starsinic and M. Coleman, Determination of Functional Groups in Coal by Fourier Transform Interferometry. In: Fourier Transform Infrared Spectroscopy, New York, Academic Press, 169 (1985).
24. P.E. Fanning and M.A. Vannice, *Carbon*, **31**, 721 (1993).
25. J. Kazmierczak, S. Biniak, A. Swiatkowski and K.H. Radeke, *J. Chem. Soc. Faraday Trans.*, **87**, 3357 (1991).

CONTROL OF PORE SIZE DISTRIBUTION AND CONDUCTIVITY OF ORDERED MESOPOROUS CARBON

CHANHO PAK*, SANG HOON JOO, DAE JONG YOU AND HYUK CHANG
Energy and Environment Lab, Samsung Advanced Institute of Technology, P.O. Box 111, Suwon 440-600, Korea, Email: Chanho.Pak@samsung.com

HYUNG IK LEE, JIN HOE KIM AND JI MAN KIM*
Functional Materials Lab, Dept. of Chemistry, BK21 School of Chemical Materials Science and SKKU Advanced Institute of Nanotechnology, Sungkyunkwan University, Suwon 440-746, Korea, Email: Jimankim@skku.edu

A facile method of controlling the mesopore size in ordered mesoporous carbon (OMC) samples is presented. By adding boric acid to the carbon precursor solution, the mesopore size of OMC was easily increased from 3.8 nm to 8.5 nm as the amount of boric acid was increased from 0% to 12%. The TEM images showed that there was an increase in the space between the carbon nano rods, which confirmed the increase of the pore diameter. Also, the electrical resistance of the OMC materials was reduced simultaneously. In order to use them as carbon supports, Pt nanoparticles were supported on the OMC materials by the incipient wetness impregnation method and the size of the Pt was found to be around 3.5 nm at a 60wt% loading. The electrochemical surface area and the activity of the Pt supported catalyst on OMC in the oxygen reduction reaction show that the OMC materials can be used as supports for electrocatalysts.

1. Introduction

Recently, various new types of nanocarbons have been used as supports for direct methanol fuel cell (DMFC) catalysts in order to exploit advantageous structural properties of these nanomaterials [1,2] and to enhance the performance of electrocatalysts. Among these nanocarbons, ordered mesoporous carbon (OMC) is a very promising support for increasing the performance of DMFCs [3] due to its large surface area and mesoporous structure. However, to further improve the OMC material as a carbon support, the control of the electrical conductivity, pore size and structure needs to be achieved as suggested in a recent review [3]. Since the first report [4] on the preparation of OMC using a mesoporous silica template, many attempts have been made to control or expand the pore size in the OMC materials. For example, in previous studies, the mesopore size in OMC was changed by varying the thickness of the framework

and lattice constant of the mesoporous silica [5,6] used as the template. However, this approach is limited by the difficulty of synthesizing the template materials.

In this study, a facile method of controlling the mesopore size in OMC is presented, which involves the addition of boric acid to the precursor solution used to modify the carbon surface [7,8]. Also, the physical properties of OMC such as its pore size and electronic resistance were investigated by various methods. In addition, Pt nanoparticles were supported by incipient wetness impregnation with a 60wt% loading to demonstrate the possibility of using the OMC studied as a new support for electrocatalysts.

2. Experimental Section

2.1. *Synthesis of template and OMC materials*

A mesoporous silica template (MSU-H type) with two-dimensional hexagonal symmetry was prepared by a previously reported method with a slight modification [9], using Pluronic P123 triblock copolymer and sodium silicate as a silica source under near neutral conditions. The silica source, sodium silicate solution with a ratio of Na/Si = 2.5 (10wt% SiO₂), was prepared from colloidal silica Ludox HS-40 purchased from Aldrich, NaOH and deionized water. Briefly, P123 copolymer and sodium silicate solution were mixed in deionized water with mechanical stirring in a water-jacketed flask, and then acetic acid solution was added to neutralize the total mixture. The molar ratio in the mixture was 1 SiO₂: 0.017 P123: 2.595 Acetic acid: 255 H₂O. The reaction mixture was stirred at 40 °C for 20 h and heated in an oven at 100 °C for 24 h under static conditions. The white sample was finally calcined in static air at 550 °C for 3 h.

The procedure used for the synthesis of OMC is the same as the previously reported nano-replication method [4] with a mesoporous silica template (MSU-H) except for the use the precursor solution consisting of a mixture of sucrose and boric acid with different molar ratios. The samples are designated as OMC-B-*n*, where *n* is the molar percentage of boron in the precursor solution. In the typical preparation of OMC-B-4, 1 g of mesoporous silica was impregnated with a carbon precursor solution which consisted of 1.25 g of sucrose, 0.141 g of sulfuric acid, 0.109 g of boric acid and 4 g of deionized water. The mixed samples were placed in an oven at 100 °C and 160 °C oven for 6 hrs, sequentially. After drying, the impregnation step was repeated one more time with two thirds of the amount of the solution used in the first step. The carbonization of the sample was conducted at 900 °C for 3 hrs under nitrogen flow. The OMC-B-4

sample was obtained by the selective removal of silica by means of an HF solution.

2.2. Preparation of Pt supported catalysts

Half a gram of the OMC-B-*n* samples was placed in a vinyl bag and mixed with 1.5 ml acetone solution containing 1.4615 g of $\text{H}_2\text{PtCl}_6 \cdot x\text{H}_2\text{O}$ (Umicore) by the incipient wetness method. The amount of $\text{H}_2\text{PtCl}_6 \cdot x\text{H}_2\text{O}$ in the solution corresponded to a metal loading of 60 wt%. After drying at 60 °C overnight, the impregnated OMC material was heated in H_2 flow to 200 °C and kept at this temperature for 2 h. The adsorbed hydrogen was removed by heating to 350 °C and the sample was kept at this temperature for 2 h under nitrogen flow. The samples thus prepared were denoted as Pt/OMC-B-*n*.

2.3. Characterization

Nitrogen adsorption experiments were performed at 77K using a Micromeritics ASAP 2010 system. The surface areas of the samples were calculated using the BET equation, while their pore size distributions were estimated by the BJH method from the adsorption branches of the isotherms. Transmission electron microscopy (TEM) images were taken with a G2 FE-TEM Tecnai microscope at an accelerating voltage of 200 kV. The electrical sheet resistances were measured by the four-point probe method using a Changmin Tech. CMT series at room temperature. Sample powders were compressed at 150 kg_f/cm^2 for the measurements without any binders. The X-ray diffraction (XRD) patterns were obtained using a Philips X'pert Pro X-ray diffractometer equipped with a Cu K_α source at 40 kV and 40 mA. X-ray photoelectron spectroscopy (XPS) was used to investigate the species of boron and its amount.

The electrochemical properties of the catalyst were evaluated with a rotating disk electrode (RDE) system. Glassy carbon was used as substrate for the working electrode and the catalyst slurry was made using a similar method to that of Schmidt et al. [8]. The RDE experiment was performed with a half cell configuration in which the reference electrode was Ag/AgCl and the counter electrode was Pt foil. HClO_4 aqueous solution (0.1M) was used as the electrolyte. Cyclic voltammetry measurements were conducted with a nitrogen-saturated electrolyte at a scan rate of 10mV/s and linear scan voltammetry was used to evaluate the oxygen reduction reaction (ORR) with an oxygen-saturated electrolyte at a scan rate of 1 mV/s [9]. The potentials in this study are presented on the basis of the reversible hydrogen potential (RHE).

3. Results and Discussion

The structural order of the OMC-B-*n* samples was investigated by XRD and nitrogen adsorption. The XRD patterns (not shown here) displayed a weak shoulder peak at around 0.9° for all of the samples, which suggests that the long range order of the OMC-B-*n* samples is not good. However, their mesopore structure was revealed by nitrogen adsorption and TEM images, as described later in this section and shown in Figures 1 and 2. In addition, the boron species in the samples were determined by XPS to be boron oxide and its amount was less than 1%, which suggests that it can be removed by the HF treatment.

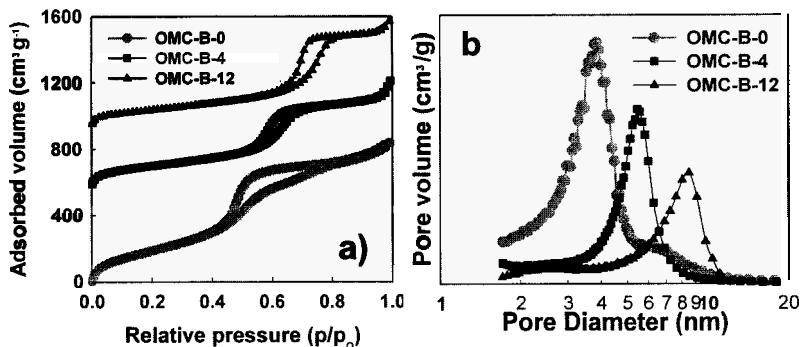


Figure 1. (a) Nitrogen adsorption and desorption isotherms for the OMC-B-*n* samples and (b) the corresponding pore size distributions.

All of the isotherms in Fig. 1a display a sharp step in the range of relative pressure of 0.4 to 0.9 due to the capillary condensation of nitrogen inside the mesopores in the OMC samples, which coincide with the previous reported data [3-6, 12]. The position of this step gradually moved to a higher value as the amount of boric acid increased, indicating that the mesopore size was increased. The sizes of mesopores in the OMC-B-*n* samples, where *n* is 0, 4 and 12, were determined to be 8, 5.5 and 8.5 nm, respectively (Figure 1b). The pore size distribution did not expand in any of the samples, which suggest that the structure of the OMC-B-*n* samples did not change very much. This was confirmed by the TEM images of the samples. The carbon nanorods in all of the OMC-B-*n* samples showed a good hexagonal ordering inside particles which agreed with the nitrogen adsorption data. The pores in the OMC materials can be more clearly observed in the form of the space between the carbon rods, which is generated from the framework of the silica template. The space (white areas in the TEM image) between the carbon nanorods gradually widened from

the OMC-B-0 (Fig. 2a) to OMC-B-12 (Fig. 2c) samples, indicating that the pore size increased with increasing amount of boric acid in the precursor mixture. At a larger magnification, the pore size was easily estimated to be around 8 nm in the case of OMC-B-12 by comparing the space and the scale bar in Fig. 2d.

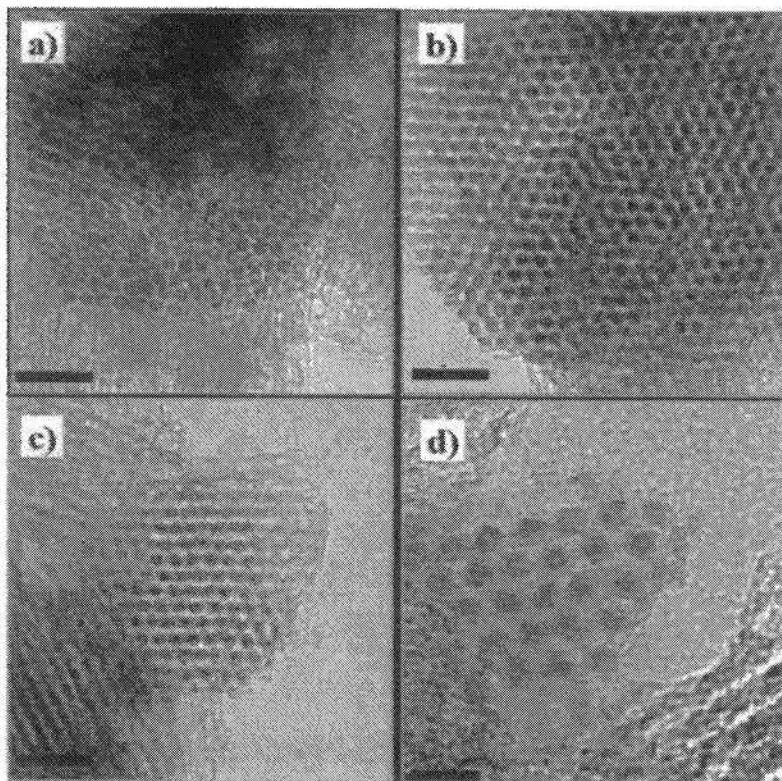


Figure 2. TEM images of (a) OMC-B-0, (b) OMC-B-4 and (c) OMC-B-12 and high magnification TEM image of (d) OMC-B-12. Scale bar, which reproduced from the scale that inserted automatically by TEM device, for (a), (b) and (c) is 50 nm and for (e) is 20 nm.

As the pore size was increased, the diameter of the carbon nanorods was decreased, as shown in Fig. 2. It was suggested that the packing of the carbon materials in the nanorods of OMC-B-12 is denser than that of OMC-B-0, because the amount of carbon precursor used for the various OMC-B-*n* samples was the same. That is, the packing of the same amount of carbon in the smaller carbon nanorods results in a higher density of carbon atoms within the same

volume. Also, the boric acid could catalyze the carbonization of sucrose during the thermal carbonization up to 900 °C, resulting in a denser carbon framework. Thus, it was expected that some of the physical properties would be changed by this increase in packing density and we therefore measured the electrical resistance of the OMC-B-n samples under high pressure compression.

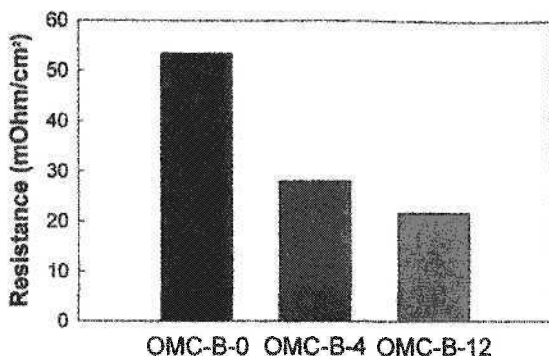


Figure 3. Sheet resistance of OMC-B-n samples

The resistance of the samples obtained from the compacted powder was drastically decreased from 53.4 $\text{m}\Omega/\text{cm}^2$ for OMC-B-0 to 21.4 $\text{m}\Omega/\text{cm}^2$ for OMC-B-12 containing the highest amount of boric acid, as shown in Fig. 3, which means that the electrical conductivity of the carbon support was increased. As suggested in the above discussion, this maybe attributed to the compact carbon **nanorods** present in the samples resulting from the decrease their diameter. In a previous study of OMC supports [12], it was suggested that decreasing the resistance of the OMC support is very important to improve the performance of the MEA for DMFCs. Also, the enlargement of the pore size inside the OMC particles could enhance the diffusion rate of fuel and byproduct in the reaction. Therefore, it was suggested that the OMC-B-4 and 12 samples can be used as novel supports for the **electrocatalysts** due to their larger pore size and higher electrical conductivity, as described above.

To explore the possibility using them as new catalyst supports, as attempted in recent previous studies [12-14], Pt **nanoparticles** were supported on the OMC-B-n samples by the incipient wetness method previously reported in the literature [12] and the supported catalysts were characterized by XRD and electrical measurements such as cyclic voltammetry in a liquid electrolyte to estimate the **electrochemically** active surface area and linear scan voltammetry to measure the mass activities of the catalysts for the oxygen reduction reaction.

A high total loading of Pt of 60 wt% was used, because the electrode catalyst for DMFC applications requires such a very high metal loading [3,12]. Figure 4 shows the XRD patterns for the 60 wt% Pt loaded OMC-B-*n* catalysts. All of the XRD patterns for the Pt/OMC-B-*n* catalysts exhibited distinct peaks at around $2\theta = 39.8^\circ$, 46.3° , 67.5° , and 81.3° , which correspond to the (111), (200), (220), and (311) planes of the face centered cubic (FCC) Pt structure, respectively. There is no evidence of peaks related to the oxide of Pt, indicating that the Pt precursor was completely reduced by the H_2 treatment at 473 K. The average particle sizes of the catalysts estimated by the Debye–Scherrer equation were 3.2, 3.6 and 3.6 nm for Pt/OMC-B-0, Pt/OMC-B-4 and Pt/OMC-B-12, respectively. Such sizes of Pt particles supported on OMCs are very small, considering that the metal content was as high as 60 wt%, although they are somewhat larger than those of the OMC-supported Pt catalyst previously reported in the literature [12].

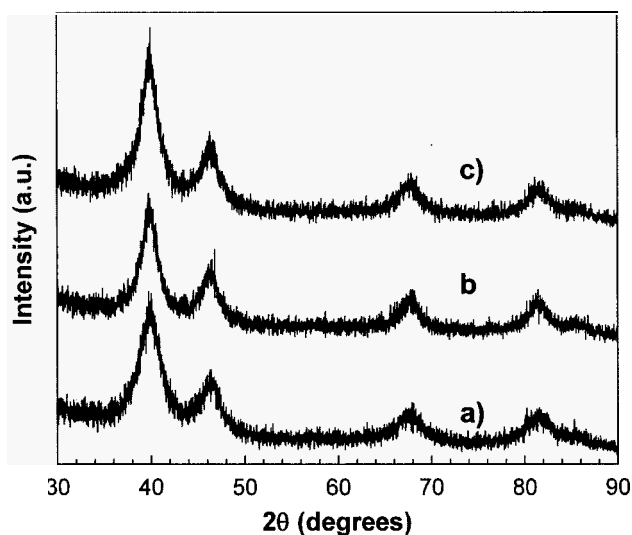


Figure 4. XRD of (a) Pt/OMC-B-0, (b) Pt/OMC-B-4 and (c) Pt/OMC-B-12.

The cyclic voltammograms (CVs) of the Pt/OMC-B-*n* catalysts were obtained in N_2 -purged 0.1 M $HClO_4$ solution (Fig. 5). The electrochemically active surface area of the Pt/OMC-B-*n* catalysts was obtained by integrating the total charge corresponding to the desorption peak of hydrogen, and normalizing it with respect to the scan rate, Pt loading, and the charge value of $210 \mu C/cm^2$ for the Pt surface [15]. The active surface areas of the supported catalysts obtained

in this manner were $70.3 \text{ m}^2/\text{g}$ for Pt/OMC-B-0, $67.7 \text{ m}^2/\text{g}$ for Pt/OMC-B-4 and $57.2 \text{ m}^2/\text{g}$ for Pt/OMC-B-12. These values are very similar to those previously reported in the literature for OMC-supported Pt catalysts [12] and also larger than that of commercial Pt catalyst supported on activated carbon with similar loading (HiSpec 9100 catalyst; average Pt particle size maximum 2.8 nm [16]). The electrocatalytic activities of the OMC-supported Pt catalysts toward the oxygen reduction reaction were measured by linear scan voltammetry using the RDE (not shown). The mass activities based on the amount of Pt used at 0.75V versus RHE are -18.6, -16.7 and -18.5 $\text{A}/\text{g}_{\text{Pt}}$ for Pt/OMC-B-0, Pt/OMC-B-4, and Pt/OMC-B-12, respectively. These results indicate that the Pt/OMC-B-*n* catalysts exhibit some ORR activity and that the OMC-B-*n* samples can be used as carbon supports for electrocatalysts. The beneficial effect expected from the large pore size and enhanced conductivity of the OMC-B-4 and 12 samples was not reflected in the ORR measurements. Based on our previous study of the electrical conductivity of OMCs [12], the effect of the conductivity of OMC support on the mass activity was known to be very small in the case where half cell measurements are conducted in a liquid electrolyte using a glassy carbon electrode. Thus, further measurements of the OMC-B-*n* samples using a single cell configuration [12] are required.

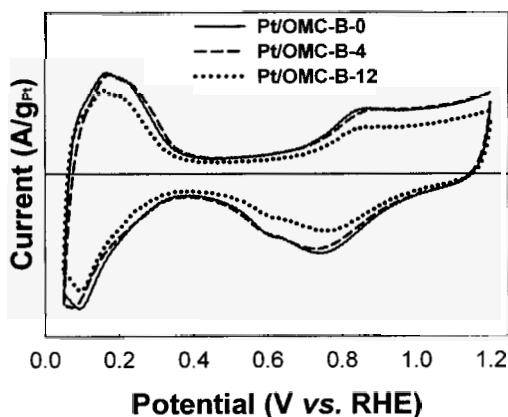


Figure 5. Cyclic voltammogram for Pt/OMC-B-*n* catalysts

4. Conclusion

Ordered mesoporous carbon materials with expanded pore size and increased conductivity were prepared by a facile method involving the addition

of boric acid to the initial carbon precursor mixture. The nitrogen adsorption measurements and TEM images indicated that the OMC-B-*n* samples have the inverse structure of the template. The pore size increased from 3.8 nm to 8.5 nm as the amount of boric acid was increased from 0% to 12%, and this was accompanied by a decrease of the electrical resistance from 53.4 to 21.3 m Ω /cm². 60wt% Pt nanoparticles approximately 3.5 nm in size were supported on the OMC-B-*n* supports by the incipient wetness method. This catalyst showed comparable electrochemical surface area obtained from the cyclic voltammogram with half cell configuration. In addition, these Pt supported catalysts exhibited electrocatalytic activity toward the oxygen reduction reaction, which suggested that the OMC-B-*n* can be used as novel supports for electrocatalysts.

Acknowledgments

C. Pak would like to acknowledge the contributions of Dr. Kyungjung Kwon for the ORR measurements and Ms. Hyeran Choi for the TEM measurement.

References

1. Y. Lin, X. Cui, C. Yen, C. M. Wai, *J. Phys. Chem. B* **109**, 14410 (2005).
2. J. N. Wang, L. Zhang, J. J. Niu, F. Yu, Z. M. Sheng, Y. Z. Zhao, H. Chang, C. Pak, *Chem. Mater.* **19**, 453 (2007).
3. H. Chang, S. H. Joo, C. Pak, *J. Mater. Chem.* **17**, 3078 (2007).
4. R. Ryoo, S. H. Joo, S. Jun, *J. Phys. Chem. B* **103**, 7743 (1999).
5. J. S. Lee, S. H. Joo, R. Ryoo, *J. Am. Chem. Soc.* **124**, 1156 (2002).
6. C. Yu, J. Fan, B. Tian, D. Zhao, G. D. Stucky, *Adv. Mater.* **14**, 1742 (2002).
7. M. Endo, C. Kim, T. Karaki, Y. Nishimura, M. J. Matthews, S. D. M. Brown, M. S. Dresselhaus, *Carbon* **37**, 561 (1999).
8. C. Kim, T. Fujino, T. Hayashi, M. Endo, M. S. Dresselhaus, *J. Electrochem. Soc.* **147**, 1265 (2000).
9. S.-S. Kim, T. R. Pauly, T. J. Pinnavaia, *Chem. Commun.* 1661 (2000).
10. T. J. Schmidt, H. A. Gasteiger, G. D. Stab, P. M. Urban, D. M. Kolb, R. J. Behm, *J. Electrochem. Soc.* **145**, 2354 (1998).
11. H. R. Colon-Mercado, B. N. Popov, *J. Power Sources* **155**, 253 (2006).
12. S. H. Joo, C. Pak, D. J. You, S.-A. Lee, H. I. Lee, J. M. Kim, H. Chang, D. Seung, *Electrochim. Acta* **52**, 1618 (2006).
13. K. Wikander, A. B. Hungria, P. A. Midgley, A. E. C. Pamqvist, K. Holmberg, J. M. Thomas, *J. Colloid Inter. Sci.* **305**, 204 (2007).
14. L. Calvillo, M. J. Lazaro, E. Garcia-Dordeje, R. Moliner, P. L. Cabot, I. Esparbe, E. Pastor, J. J. Quintana, *J. Power Sources* **169**, 59 (2007).

15. Z. Hou, B. Yi, H. Zhang, *Electrochem. Solid-State Lett.* **6**, A232 (2003).
16. HiSpec Catalyst Customer Chart ([http://www.jmfuelcells.com/HiSPEC Customer Chart.pdf](http://www.jmfuelcells.com/HiSPEC%20Customer%20Chart.pdf)).

SBA-15 TEMPLATING SYNTHESIS AND PROPERTIES OF PYRROLE-BASED ORDERED MESOPOROUS CARBONS[†]

JOANNA GORKA, MIETEK JARONIEC*
Chemistry Department, Kent State University
Kent, OH 44242, USA

Nitrogen-doped ordered mesoporous carbons (OMCs) with the *p6mm* symmetry (CMK-3) were successfully synthesized via chemical vapour infiltration of pyrrole into the pores of Fe(III)-containing SBA-15 silica templates followed by low-temperature carbonization. The adsorption and structural properties of the silica templates and the corresponding OMCs obtained via inverse replication of SBA-15 were investigated by nitrogen adsorption at -196°C, thermogravimetric analysis and small angle X-ray diffraction (XRD). These properties were shown to be strongly affected by properties of the SBA-15 host material and by the final carbonization temperature. Three SBA-15 samples were prepared from tetraethyl orthosilicate (TEOS) at different hydrothermal synthesis temperatures: 60, 100 and 140°C in order to obtain materials of different complementary porosity, mesopore widths and pore volumes. In general, by tuning the pore size of the silica templates, the diameter of the interconnected carbon rods as well as the accessible mesopores (spaces between rods) can be tailored. The degree of graphitization of the resulting carbons increases with increasing carbonization temperature from 700 to 1000°C. Also, the diameter of the carbon rods increased, whereas the pore width and the pore volume of the CMK-3 carbons decreased with increasing carbonization temperature.

1. Introduction

The discovery of ordered mesoporous silicas (OMSs) such as MCM-41 and MCM-48 is considered as a major breakthrough in materials science. The presence of ordered and uniform pores in OMSs make them attractive hard templates for replication synthesis (nanocasting) of novel non-silica materials such as carbons, polymers, metal oxides and so on.

The first report by Ryoo et al. [1] on the preparation of carbon inverse replicas of OMSs is another example of a major discovery in the area of porous materials; specifically, in the area of porous carbons. The idea of employing the MCM-48 silica (OMS with *Ia3d* structure) as a hard template and sucrose as a

[†] Work supported through subcontract under the NIRT DMR-0304508 grant from the National Science Foundation (USA) awarded to the Carnegie Mellon University

* Corresponding author: Mietek Jaroniec, e-mail: jaroniec@kent.edu

carbon precursor followed by carbonization of the carbon-silica composite and by etching the silica template, opened a new way for the preparation of nanomaterials, so-called hard-templating synthesis. A wide range of novel OMCs was synthesized by using not only a variety of carbon precursors, but also different silica templates such as MCM-41, SBA-15, SBA-16, FDU-1, KIT-6 and others [2-4].

While carbons templated by MCM-48 often undergo a symmetry change [5] and those prepared with help of MCM-41 lose the structural ordering after template removal [6], the ones obtained by replication of SBA-15 retain the template symmetry [7]. The SBA-15-templated carbons consist of interconnected rods [8,9], which are created by filling the ordered mesopores of SBA-15 with a carbon precursor followed by carbonization and the template removal. The stability of carbon replicas of SBA-15 depends on the amount of complementary pores (i.e., pores that interconnect hexagonally ordered mesopores of SBA-15) because they are templates for carbonaceous interconnections between ordered carbon rods.

Porous carbons are most often amorphous solids. To improve their electric properties a high temperature treatment in argon (over 2000°C; graphitization) is frequently performed in order to form graphitic domains. Usually, this treatment is accompanied by a significant shrinkage of the structure and a substantial reduction of the specific surface area and pore volume [10]; in many cases carbonization leads to a complete collapse of the porous network. Also, the final yield after carbonization and graphitization is very low. A promising alternative to the high temperature treatment is a low temperature graphitization in the presence of a catalyst, which eliminates the aforementioned drawbacks of carbonization and leads to the enhancement of electric properties of the resulting carbons. Several carbon precursors such as mesophase pitch [11,12], polyacrylonitrile [12,13] and polypyrrole [14-19] have been explored because their catalytic carbonization gives carbons with relatively high degree of graphitization. Furthermore, polyacrylonitrile and polypyrrole afford nitrogen-doped carbons with relatively large graphitic domains. Especially polypyrrole is an attractive precursor due to its high electrical conductivity, environmental stability and easiness of polymerization and carbonization. The electron conductivity of polypyrrole arises from a highly aromatic five-member ring composed of four carbon atoms and one nitrogen in each monomer, pyrrole. After polymerization of pyrrole, the conformation of the resulting polymer chains depends on the reaction conditions. Polymerization of pyrrole can be performed either by electrochemical methods [20], or by oxidative polymerization in the presence of a catalyst (Fe^{3+} , Cu^{2+} , I_2 , Br_2 , Ag^+ or AsF_5)

[21-24]. According to Dias et al. [25], among all of these oxidants, Fe^{3+} affords the polymer with the best conductivity properties. Furthermore, an arrangement of polymeric pyrrole chains in a planar conformation facilitates that the formation of a p-conjugated system similar to the graphene sheets present in the graphite structure. Besides acting as a polymerization catalyst [26], Fe^{3+} also acts as a catalyst for the formation of graphitic domains during carbonization at temperatures far below those used in the synthesis of graphitic carbons. For these reasons Fe^{3+} has been most often used as a catalyst for the preparation of carbon inverse replicas of OMSs.

The polypyrrole-based carbons have been prepared *via* vapour deposition of pyrrole, incipient wetness impregnation and aqueous solution routes using SBA-15 as a hard template. The incipient wetness impregnation of an alcoholic solution containing Fe^{3+} onto the silica template containing the adsorbed pyrrole [15, 17, 18] presents some drawbacks because pyrrole is volatile and toxic. Also, it is very difficult to determine accurately the wetness point in this process because pyrrole may quickly polymerize on the external surface of the silica template and consequently, may block the ordered mesopores and prevent the penetration of catalyst into the interior of these pores. Thus, the resulting carbons may have large structural defects after template removal. The gas phase infiltration of pyrrole into pores of the silica template [19, 27-29] not only eliminates the use of solvents but also allows one to control the pyrrole uptake by adjusting the adsorption properties of the template and the catalyst loading.

So far, there are a few reports on the polypyrrole-based carbons obtained by using the SBA-15 template; these reports are focused on the effect of the catalyst loading [19], on the amount of doped nitrogen [13-15] and on the possibility of obtaining OMCs with magnetic nanoparticles [30]. Other parameters such as the effect of the template used (SBA-15) on the chemical vapour infiltration and the effect of carbonization temperature have not been investigated yet. In the present work the polypyrrole-based carbon inverse replicas of various iron supported-SBA-15 templates were successfully prepared *via* chemical vapour infiltration method. Furthermore, the effect of the carbonization temperature on the final adsorption and structural properties of the resulting OMC replicas was studied by nitrogen adsorption at -196°C , small angle powder X-ray diffraction (XRD), thermogravimetry and CHNS elemental analysis.

A series of the SBA-15 templates having different porous structures were obtained by varying the time and temperature of hydrothermal synthesis. This series was used to study the effect of pore width, mesopore volume and pore connectivity on the properties of the resulting carbon inverse replicas.

Furthermore, the width of carbon rods, the specific surface area and porosity of these replicas were tailored by adjusting the carbonization temperature. Although the percentage of nitrogen decreased with increasing carbonization temperature, the resulting OMCs do not lose completely of nitrogen even at 1000°C. Importantly, thermogravimetric analysis showed an increase in the degree of graphitization with increasing carbonization temperature.

2. Experimental

2.1. Synthesis of SBA-15 and Carbon Materials

SBA-15 was synthesized according to the method reported by Zhao [31], in which 2.00g of poly(ethylene oxide)-poly(propylene oxide)-poly(ethylene oxide) triblock copolymer ($\text{EO}_{20}\text{PO}_{70}\text{EO}_{20}$; Pluronic 123 from BASF) was added to 74 mL of 1.7 M aqueous solution of hydrochloric acid and stirred for 4 hours at 40°C. Next, tetraethyl orthosilicate (TEOS from Acros Organics) was added dropwise at the mass ratio of TEOS/P123 = 2 and the mixture was vigorously stirred for 2 to 6h. Finally, the gel was transferred to Teflon-lined sealed containers and kept at 60, 100 and 140°C for 72, 48 and 24h, respectively, under static conditions; the resulting samples were labelled as SBA15-60, SBA15-100 and SBA15-140, respectively. The final products were filtered, washed with water and dried for 24 hours at 80°C. The as-synthesized samples were calcined at 540°C for 3 hours under N_2 atmosphere and for 2 hours under flowing air.

Carbon inverse replicas were prepared by using about 0.50g of the template-free SBA-15, which was stirred for ~2h in an iron chloride solution containing 0.80g of anhydrous FeCl_3 (Acros Organics) in 50mL of ethanol (Sigma-Aldrich). Next, the solvent was allowed to evaporate at 60°C for at least 12h under air atmosphere; this process was continued for at least two additional hours at 80°C under vacuum. The iron-supported silica was exposed to pyrrole vapour for ~24h in a sealed chamber at reduced air pressure to facilitate the evaporation of the monomer. The resulting Fe-containing pyrrole-SBA-15 composite was divided to four equal parts, which were respectively carbonized in flowing nitrogen at 700, 800, 900 and 1000°C using a heating rate of $5^\circ\text{C}\cdot\text{min}^{-1}$; each sample was kept in flowing nitrogen for additional 3h at the final carbonization temperature. The resulting nanocomposites were treated with HF (48% w/w) for 24h at room temperature to remove the silica templates. Finally, the carbon samples were washed with water and dried at 80°C under vacuum. These carbon samples were labelled as CPPy- x - y where x indicates the hydrothermal treatment temperature of SBA-15 and y denotes the carbonization

temperature.

2.2. Characterization

The silica templates, carbon-silica nanocomposites and final carbon replicas were studied by nitrogen adsorption, small angle powder XRD, thermogravimetry (TG) and CHNS elemental analysis.

Nitrogen adsorption isotherms were measured at -196°C using ASAP 2010 and ASAP 2020 volumetric adsorption analyzers from Micromeritics, Inc. (Norcross, GA). Prior to each measurement all samples were degassed under vacuum at 200°C for 2 h. The specific surface area was determined by the standard BET method in the relative pressure range of 0.05-0.2. The pores size distribution (PSD) curves were calculated using the BJH method for cylindrical pores improved by Kruk, Jaroniec and Sayari (KJS) [32].

The small angle powder XRD measurements were conducted in the range of $0.04^{\circ} < 2\theta < 3.50^{\circ}$ on a PANalytical, Inc. X'Pert Pro Multi Purpose Diffractometer with $\text{Cu K}\alpha$ radiation, using 40mA and an operating voltage of 40kV, 0.01° step size and 20s step time.

The TG measurements were performed on a TA Instruments TGA 2950 thermogravimetric analyzer using a high-resolution mode. The curves were recorded under flowing air with a heating rate of $10^{\circ}\text{C}\cdot\text{min}^{-1}$ and final temperature of 800°C .

Quantitative analysis of carbon and nitrogen was made using a LECO CHNS-932 elemental analyzer (St. Joseph, MI).

3. Results and Discussion

3.1. XRD Studies

As shown in Figure 1A, the XRD patterns for three SBA-15 samples are characteristic for 2-D hexagonally ordered cylindrical mesopores ($p6mm$ symmetry group). At least three peaks are present in the small angle range indicating a good ordering of mesopores in these samples. The most intense reflection is assigned as 100; it shifts towards higher angles with decreasing temperature of the hydrothermal synthesis from 140 to 60°C . These results show a decrease in the unit cell of these materials from 11.3 to 9.8 nm with decreasing temperature, which agrees with previous findings (e.g., see ref. [33]).

Figures 1B, C and D show the XRD patterns for the carbon inverse replicas, having an intense 100 reflection; other weak reflections, characteristic for $p6mm$ symmetry group, are visible for the carbon samples templated by using SBA15-

100 and SBA15-140 samples. The unit cell parameters calculated from the 100 reflections vary from 9.0 nm for the SBA15-60-templated carbon to 9.9 nm for the carbon obtained with help of SBA15-140 at the same carbonization temperature of 700°C. Within each set of the carbon samples prepared by using the same silica template the unit cell parameter decreased with increasing carbonization temperature from 700 to 1000°C (see Table 1), which is attributed to a larger shrinkage of these nanostructures at higher carbonization temperatures.

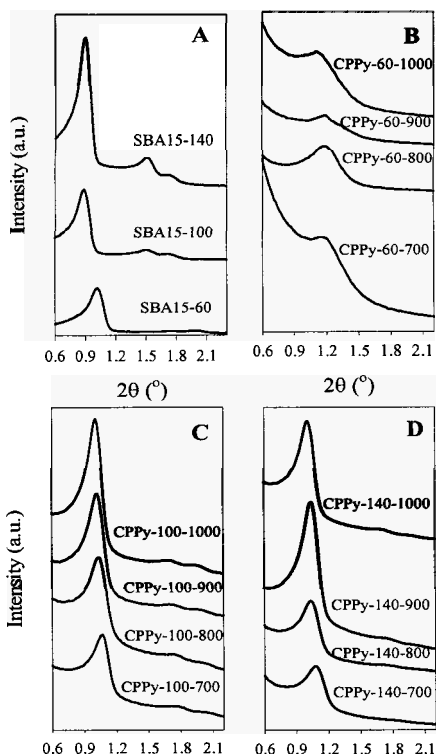


Figure 1. Small angle XRD patterns for the SBA-15 samples studied (A) and the corresponding inverse carbon replicas (B-D).

increasing temperature of hydrothermal synthesis, which is associated with an enlargement of ordered mesopores as well as interconnecting smaller pores. These observations are confirmed by the PSD curves calculated by using the improved KJS method [32] (Figure 3A). As can be seen from Figure 3A, the SBA-15 samples obtained at 60 and 100°C clearly possess larger fractions of complementary pores (below 3nm) than SBA-15 prepared at 140°C, PSD of which shows a narrow peak reflecting mainly large primary mesopores. The single-point pore volume for SBA15-60 is smaller than those for SBA15-100

3.2. Nitrogen Adsorption

Nitrogen adsorption isotherms for both SBA-15 template materials and the corresponding carbon replicas are shown in Figure 2; the corresponding adsorption parameters are listed in Table 1. The isotherms for the silica template materials possess steep

steps, which suggest highly uniform pores. The high BET surface area, in the range from 600 to 1000 m²/g, decrease with

and SBA15-140, whereas the volumes for two latter samples are similar. However, the volume of complementary pores gradually decreases with increasing temperature of hydrothermal synthesis. The contribution of these pores to the total pore volume diminishes from about 30% for SBA15-60 to ~3% for SBA15-140. Furthermore, the PSD curves are narrow for all silica templates and possess maxima at 7.4, 9.5 and 9.9 nm for the SBA-15 samples prepared at 60, 100 and 140°C, respectively.

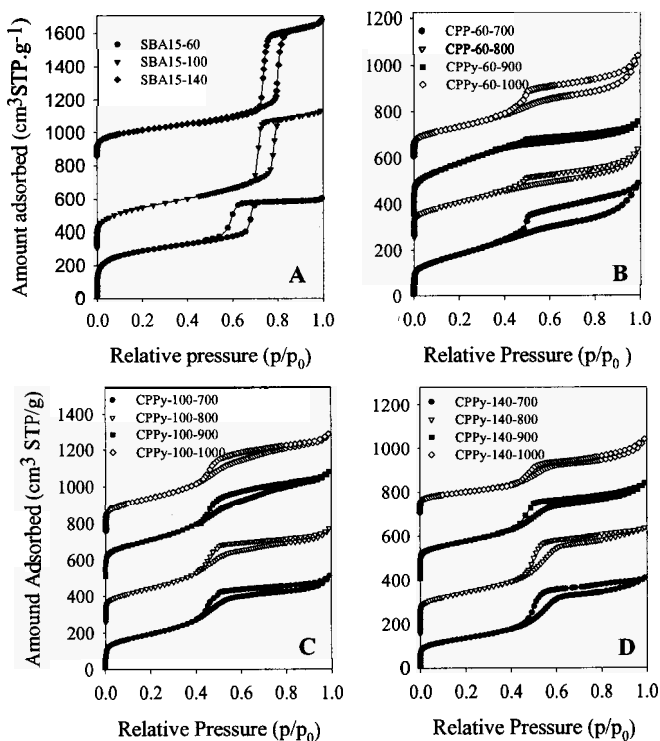


Figure 2. Nitrogen adsorption isotherms measured at -196°C for the SBA-15 samples studied (A) and the corresponding inverse carbon replicas (B-D). Adsorption isotherms were offset by 300 and 850 cc STP/g for SBA15-100 and SBA15-140, respectively (Panel A), by 250, 350 and 600 cc STP/g for CPPy-60-800, CPPy-60-900 and CPPy-60-1000, respectively (Panel B), by 250, 500 and 750 cc STP/g for CPPy-100-800, CPPy-100-900 and CPPy-100-1000, respectively (Panel C), and by 150, 400 and 700 cc STP/g for CPPy-140-800, CPPy-140-900 and CPPy-140-1000, respectively (Panel D).

Figure 4 shows nitrogen adsorption isotherms and the corresponding PSDs for selected silica-carbon composites. For these samples much smaller pore

volumes and condensation steps are observed, which shows that only a small fraction of mesopores remained partially unfilled. The PSD curves obtained for these nanocomposites were used to estimate the carbon film thickness in the interior of siliceous mesopores [34]. The difference between the mesopore widths of the silica templates and those of the carbon-silica nanocomposites should be approximately equal to the carbon film thickness. This thickness was estimated to be about ~ 2.7 nm for the aforementioned composites. Also, the broader PSD curves for these composites in the range of larger mesopores suggest a non-uniform carbon layer.

Table 1. Structural properties of ordered mesoporous silica and carbon samples.

Sample	S_{BET} (m^2/g)	V_{sp} (cm^3/g)	V_c (cm^3/g)	w_{KJS} (nm)	w_d (nm)	$w_{c\text{rod}}$ (nm)	w_{CMK} (nm)	d (nm)	a (nm)
SBA15-60	1027	0.93	0.29	7.4	7.0			8.5	9.8
CPPy-60-700	657	0.75	0.40	-		8.06	2.34	7.8	9.0
CPPy-60-800	578	0.58	0.35	-		8.53	2.00	7.9	9.1
CPPy-60-900	823	0.62	0.46	-		8.21	1.52	7.3	8.4
CPPy-60-1000	485	0.68	0.38	-		7.67	2.06	7.3	8.4
SBA15-100	898	1.27	0.14	9.5	9.6			9.8	11.3
CPPy-100-700	696	0.79	0.04	4.7		6.92	4.68	8.7	10.0
CPPy-100-800	700	0.79	0.05	4.7		6.82	4.51	8.5	9.8
CPPy-100-900	756	0.88	0.04	4.7		6.46	4.74	8.4	9.7
CPPy-100-1000	678	0.81	0.04	4.7		6.47	4.46	8.2	9.4
SBA15-140	592	1.26	0.04	9.9	9.9			9.7	11.1
CPPy-140-700	486	0.63	0.02	5.5		7.17	4.30	8.6	9.9
CPPy-140-800	690	0.74	0.04	5.5		6.73	4.34	8.3	9.5
CPPy-140-900	627	0.66	0.04	5.1		7.04	4.16	8.4	9.7
CPPy-140-1000	356	0.53	0.02	5.2		6.98	3.69	8.0	9.2

S_{BET} , the BET specific surface area; V_{sp} , the total pore volume calculated at 0.99 p/p₀; w_{KJS} , the pore diameter calculated using the improved KJS method; w_d , $w_{c\text{rod}}$, w_{CMK} , the parameters calculated from geometrical equations; d , the d-spacing; a , the unit cell parameter.

Nitrogen adsorption isotherms for the carbon inverse replicas (Figure 2 B-D) are type IV. The capillary condensation steps visible on these isotherms are located at lower relative pressures than those for the silica templates, reflecting smaller sizes of mesopores present in the carbon replicas in comparison to those in the SBA-15 templates. The capillary condensation steps visible on the adsorption isotherms for the carbons prepared by using the SBA-15-140 and SBA-15-100 templates are steeper than those for the remaining carbons, indicating the presence of more uniform pores in the former samples. Note that all the carbon replicas listed in Table 1 possess quite high BET surface areas, up to $800 \text{ cm}^2/\text{g}$. For the carbon replicas templated by SBA15-60 and SBA15-100 the surface area values are always lower than those for the corresponding silica templates;

however, this is not the case for the SBA15-140-templated carbons. The largest differences between the surface areas of the carbon replicas and the corresponding silica templates are observed for the series of CPPy-60 carbons. For the latter series, this reduction in the BET surface area was about 50% for the carbon treated at 1000°C. A relatively large nitrogen uptake for the CPPy-60 carbons is caused by the presence of fine pores (mostly micropores), which represent about 50% of the total pore volume. In contrast, both series CPPy-100 and CPPy-140 exhibit reduced nitrogen adsorption at low relative pressures, suggesting a smaller microporosity of these carbons in comparison to the CPPy-60 carbons (see Table 1).

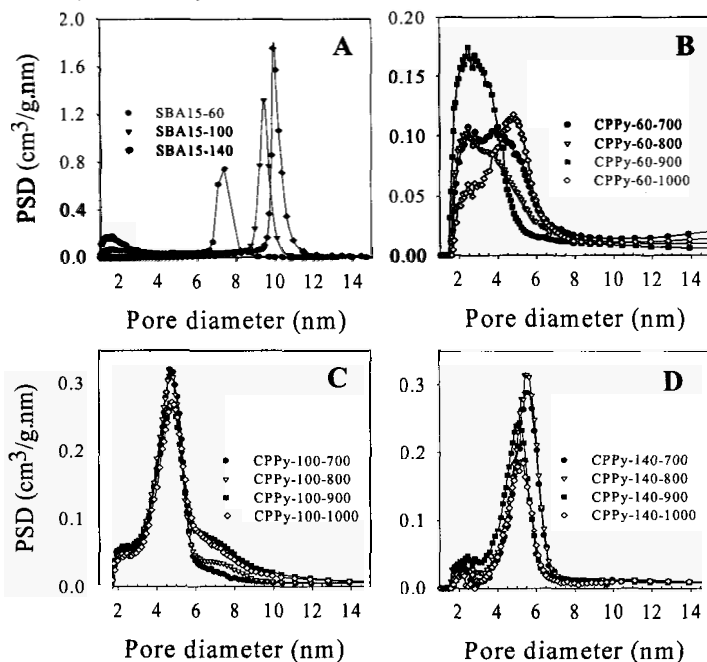


Figure 3. Pore size distributions calculated from nitrogen adsorption isotherms for the SBA-15 samples studied (A) and the corresponding inverse carbon replicas (B-D).

The single-point pore volumes of the carbons studied are in the range of 0.6 to 0.8 cm^3/g , which are lower than the corresponding pore volume of the silica templates. For CPPy-60 carbons the fraction of micropores is about 50-70% of the single-point pore volume; it is much larger than the corresponding value (about 30%) for the silica template. However, the CPPy-100 and CPPy-140

carbons are mostly mesoporous with a small percentage of micropores (about 5%).

Shown in Figure 3 B-D are the PSD curves for the carbon inverse replicas calculated by using the improved KJS method. The pore widths at the maximum of PSDs listed in Table 1 are about 4.7 and 5.3 nm for the CPPy-100 and CPPy-140 carbons, respectively. Each of these PSD curves shows one main peak located at the aforementioned values of the pore width and a distinct shoulder or peak in the micropore range (about 2 nm). In the case of CPPy-100 there is an additional shoulder (6-8 nm) at larger pores, which may be originated from incomplete filling of the mesopores of the silica template (carbon pipes) (see Figure 4 showing PSDs for two composites). In the case of the CPPy-60 carbons the PSD curves shift to the micropore range and it is difficult to distinguish fine pores in the carbon matrix from those between carbon rods due to the peak overlapping; mainly larger mesopores are observed for the carbon prepared at 1000°C.

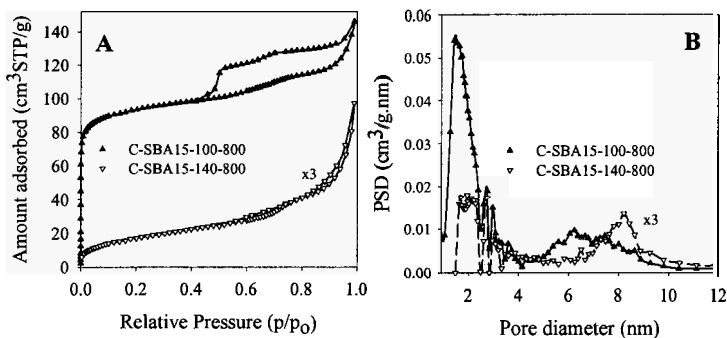
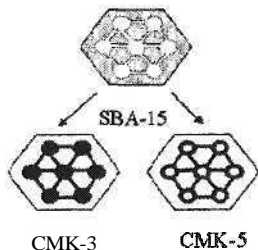


Figure 4. Nitrogen adsorption isotherms and corresponding pore size distributions for two different silica-carbon composites carbonized at 800°C.

In addition, the pore widths for the carbon inverse replicas of SBA-15 were calculated using the geometrical relation between the pore volumes obtained by integration of PSDs and the d-spacing from the small angle XRD data [34]. The resulting values of the pore width are listed in Table 1; they are in the range of 4.46-4.74 nm and 3.69-4.34 nm for the CPPy-100 and CPPy-140 carbons, respectively. These values are comparable with those obtained by the KJS method; the observed difference between both calculation methods is expected because the KJS method is applicable for cylindrical mesopores, whereas mesopores in the carbon replicas represent the space between hexagonally

ordered carbon rods. An appropriate geometrical equation was also used to estimate the thickness of the carbon rods for the CPPy-100 and CPPy-140 samples (Table 1). This estimation shows that slightly thicker carbon rods were obtained for the template with larger pore widths; the resulting values are in the range of 6.5-6.9 nm and 6.7-7.2 nm for the CPPy-100 and CPPy-140 carbons, respectively.



Scheme 1. Illustration of the CMK-3 and CMK-5 structures.

Polymerization of pyrrole inside pores of SBA-15 followed by carbonization gives the carbon-silica composites in Scheme 1, illustrating two types of possible carbon nanostructures, CMK-3 and CMK-5. The formation of these nanostructures can be controlled by the amount of the carbon precursor introduced into mesopores of the SBA-15 templates. The nanostructure composed of

hexagonally ordered carbon rods is denoted CMK-3. This structure is obtained by a complete filling of the ordered mesopores of the silica template [34]; however, an incomplete filling of these mesopores results in hexagonal arrangement of carbon pipes, known as CMK-5 [35,36]. Note that both CMK-3 and CMK-5 are extreme models and in practice some hybrid carbon nanostructures can be formed.

On the basis of nitrogen adsorption isotherms for the selected carbon-silica composites (Figure 4) it was possible to predict the predominant scenario. The composites studied exhibited a small nitrogen adsorption, which suggests an incomplete filling of the mesopores of SBA-15; this is especially true for SBA15-100. During the chemical vapor infiltration, the degree of filling of the template pores with polymeric carbon precursor depends on the ability of the monomer, pyrrole, to diffuse and reach the catalyst within these pores. To enhance the diffusion of monomer molecules in the siliceous mesochannels and to facilitate the filling of these channels with carbon precursor, the presence of larger interconnecting pores in the template is essential. Since a better connectivity between ordered mesopores was achieved for SBA15-140, the quality of the carbon inverse replicas of SBA15-140 is better in comparison to the remaining carbons.

3.3. Thermogravimetric and CHNSElemental Analysis

The TG curves for the CPPy-60 and CPPy-140 carbons are presented in Figure 5. These curves recorded under air show 2-3 major TG events. The first

major weight loss occurs in the range of 400-450°C; it can be attributed to the oxidation of amorphous carbon. The second, or even the third, events at ~550-700°C are usually attributed to the carbons having graphitic domains; the corresponding weight loss in this range depends on the amount of graphitic carbon [15]. The percentage of the latter weight loss increased for the carbons with increasing carbonization temperature. For instance, the values of the weight loss at ~550°C for the carbons templated by SBA15-60 are higher than those for the corresponding carbons templated by SBA15-140, which suggests higher percentage of graphitic carbon in the former samples. Also, within each set of carbons a noticeable increase in the percentage of graphitic carbon is observed with increasing carbonization temperature from 700 to 1000°C.

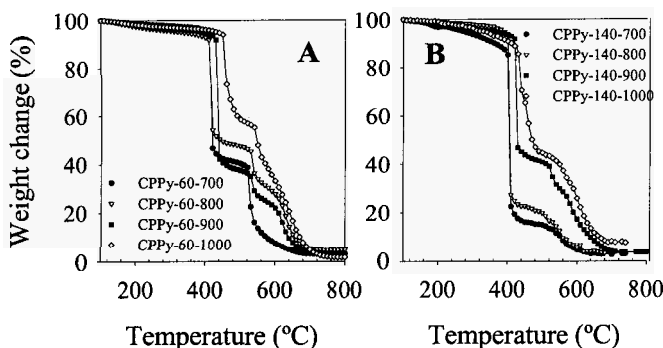


Figure 5. Weight change patterns for the CPPy-60 and CPPy-140 carbons.

Table 2. Carbon and nitrogen elemental analysis data for ordered mesoporous carbons studied.

Name of sample	C%	N%	C/N ratio
CPPy-60-700	63.43	4.70	13.5
CPPy-60-800	75.26	3.64	20.7
PPy-60-900	83.18	3.54	23.5
CPPy-60-1000	77.97	2.93	26.6
CPPy-100-700	76.01	7.47	10.2
CPPy-100-800	68.95	5.11	13.5
CPPy-100-900	70.53	3.81	18.5
CPPy-100-1000	64.62	2.45	26.4
CPPy-140-700	61.76	7.98	7.7
CPPy-140-800	71.42	5.08	14.1
CPPy-140-900	67.27	3.23	20.8
CPPy-140-1000	74.38	2.73	27.2

contents are in the range of 3-7 wt %. For all samples studied the carbon-

Another important property of the carbons studied was revealed by the CHNS elemental analysis, which showed the presence of nitrogen in all samples, even after carbonization at 1000°C. The CHNS analysis shows higher %N values than those reported previously for mesoporous carbons synthesized from nitrogen-containing precursors [13, 15]. As can be seen in Table 2, the nitrogen

nitrogen (C/N) ratio shows almost linear dependence on the carbonization temperature; this ratio increases with increasing carbonization temperature, indicating a gradual reduction in the nitrogen content for the carbons studied.

4. Conclusions

Ordered mesoporous carbons were successfully synthesized via hard-templating route. This study shows the effect of the silica template properties on the adsorption and structural properties of the resulting carbon replicas. Not only the SBA-15 templates with larger mesopores were studied, but also those with better interconnectivity were examined in order to enhance the diffusion of pyrrole vapor within channels of the template. Furthermore, this work shows that the carbonization temperature plays an important role in the formation of carbon replicas. This temperature was also essential for tailoring the nitrogen content in the carbon replicas as well as for promoting the formation of graphitic domains in the presence of an iron-containing catalyst.

Acknowledgments

The financial support for this research was provided by subcontract under the NIRT DMR-0304508 grant from the National Science Foundation (USA) awarded to the Carnegie Mellon University.

References

1. R. Ryoo, S. H. Joo and S. Jun, *J. Phys. Chem B.* **103**, 7743 (1999).
2. J. Lee, S. Han and T. Hyeon, *J. Mater. Chem.* **14**, 478 (2004).
3. J. Lee, J. Kim and T. Hyeon, *Adv. Mater.* **18**, 2073 (2006).
4. R. Ryoo, S. H. Joo, M. Kruk and M. Jaroniec, *Adv. Mater.* **13**, 677 (2001).
5. M. Kaneda, T. Tsubakiyama, A. Carlsson, Y. Sakamoto, T. Oshuna and O. Tarasaki, *J. Phys. Chem. B.* **106**, 1256 (2002).
6. J. Lee, S. Yoon, M. Oh, C. H. Shin and T. Hyeon, *Adv. Mater.* **12**, 359 (2000).
7. S. Jun, S. H. Joo, R. Ryoo, M. Kruk, M. Jaroniec, Z. Liu, T. Ohsuna and O. Tarasaki, *J. Am. Chem. Soc.* **122**, 10712 (2000).
8. M. Kruk, M. Jaroniec, C. H. Ko and R. Ryoo, *Chem. Mater.* **12**, 1961 (2000).
9. M. Imperor-Clerc, P. Davidson and A. Davidson, *J. Am. Chem. Soc.* **122**, 11925 (2000).
10. Y. Hanzawa, H. Hatori, N. Yoshizawa and Y. Yamada, *Carbon* **40**, 575 (2002).
11. Z. Li and M. Jaroniec, *J. Am. Chem. Soc.* **123**, 9208 (2001).

12. Z. Li and M. Jaroniec, *Carbon* **39**, 2077 (2001).
13. A. Lu, A. Kiefer, W. Schmidt and F. Schuth, *Chem. Mater.* **16**, 100 (2004).
14. C. H. Kim, S. S. Kim, F. Guo, T. P. Hogan and T. J. Pinnavaia, *Adv. Mater.* **16**, 736 (2004).
15. A. B. Fuertes and T. A. Centeno, *J. Mater. Chem.* **15**, 1079 (2005).
16. Q. Cheng, V. Pavlinek, A. Lengalova, C. Li, Y. He and P. Saha, *Microporous Mesoporous Mater.* **93**, 263 (2006).
17. Y. S. Choi, S. H. Joo, S. A. Lee, D. J. You, H. Kim, H. Pak, H. Chang and D. Seung, *Macromolecules* **39**, 3275 (2006).
18. A. B. Fuertes, *Macromol. Rapid Commun.* **26**, 1055 (2005).
19. C. M. Yang, C. Weidenthaler, B. Spliethoff, M. Mayanna and F. Schuth, *Chem. Mater.* **17**, 355 (2005).
20. L. Xu, W. Vhen, A. Mulchandani and Y. Yan, *Angew. Chem. Int. Ed.* **44**, 6009 (2005).
21. V. Bocchi and G. P. Gardini, *Chem. Commun.* 148 (1986).
22. M. M. Castillo-Ortega, M. B. Inoue and M. Inoue, *Synth. Met.* **28**, C65 (1989).
23. T. H. Chao and J. March, *J. Polym. Sci. A* **26**, 743 (1988).
24. S. Rapi, V. Bocchi and G. P. Gardini, *Synth. Met.* **24**, 217 (1988).
25. H. V. R. Dias, M. Fianchini and R. M. G. Rajapakse, *Polymer* **47**, 7349 (2006).
26. R. B. Bjorklund, *J. Chem. Soc., Faraday Trans.* **83**, 1507 (1987).
27. H. Wang, L. Zhang and G. R. Gavalas, *J. Membrane Sci.* **177**, 25 (2000).
28. A. B. Fuertes, *Carbon* **40**, 1597 (2002).
29. A. B. Fuertes and D. M. Nevskaja, *J. Mater. Chem.* **13**, 1843 (2003).
30. J. Lee, J. Sunmi, J. Hwang, J. G. Park, H. M. Park and T. Hyeon, *Carbon* **43**, 2536 (2005).
31. D. Zhao, J. Feng, Q. Huo, N. Melosh, G. H. Fredrickson, B. F. Chmelka and D. G. Stucky, *J. Am. Chem. Soc.* **120**, 6024 (1998).
32. M. Jaroniec and L. A. Solovyov, *Langmuir* **22**, 6757 (2006).
33. P. F. Fulvio, S. Pikus and M. Jaroniec, *J. Mater. Chem.* **15**, 5049 (2005).
34. S. H. Joo, R. Ryoo, M. Kruk and M. Jaroniec, *J. Phys. Chem. B* **106**, 4640 (2002).
35. M. Kruk, M. Jaroniec, T. W. Kim and R. Ryoo, *Chem. Mater.* **15**, 2815 (2003).
36. A. B. Fuertes, *Microporous Mesoporous Mater.* **67**, 273 (2004).

MONO AND BIMODAL POROSITY BY PYROLYSIS OF BLOCK COPOLYMER-PHENOLIC RESIN COMPLEXES

ANTTI SOININEN, SAMI VALKAMA, HARRI KOSONEN, ANTTI NYKÄNEN,
RAMASUBBU RAMANI, OLLI IKKALA, JANNE RUOKOLAINEN*

*Optics and Molecular Materials, Helsinki University of Technology, P.O. Box 2200
02015 TKK, Finland*

FILIP TUOMISTO

*Laboratory of Physics, Helsinki University of Technology, P.O. Box 1100, 02015 TKK,
Finland*

PETER ENGELHARDT

*Laboratory of Computational Engineering, Helsinki University of Technology, P.O. Box
9203, 02015 TKK, Finland and Department of Pathology and Virology, Haartman
Institute, Helsinki University, P.O. Box 21, Helsinki, 00014, Finland*

GERRIT TEN BRINKE

*Materials Science Center, University of Groningen, Nijenborgh 4, Groningen, 9747 AG,
The Netherlands*

The porosity of block copolymer poly(styrene)-*block*-poly(4-vinyl pyridine) templated phenolic resin can be controlled by pyrolysis conditions. At approximate 40 wt.-% poly(styrene) content the complex consists of poly(styrene) cylinders in poly(4-vinyl pyridine)-phenolic resin matrix. Slow heating to 420 °C results in the degradation of poly(styrene) while keeping the structure intact. At this point the material is mesoporous with total surface area of 40 m²/g as indicated by Brunauer-Emmet-Teller method. Subsequent isothermal treatment at this temperature leads to further degradation of poly(styrene) and also poly(4-vinyl pyridine), the latter resulting in well-defined microporous structure in addition to the mesopores.

1. Introduction

Well-defined narrow pore size distribution hierarchical porous systems can lead to enhanced transport properties over large distances compared to wide pore size distribution materials. In these materials macropores and/or mesopores form

* To whom correspondence should be addressed. Janne.Ruokolainen@tkk.fi

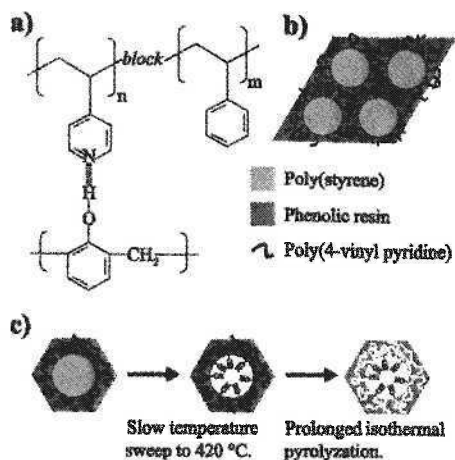


Figure 1. a) A schematic presentation of P4VP-*b*-PS hydrogen bonded with phenolic resin. b) Due to the hydrogen bonding, the phenolic resin remains in the P4VP domains when the block copolymer microphase separates. After crosslinking of the resin, the structure is frozen. c) Slow heating at a rate of 1 °C/min to 420 °C leads to mesopores when PS cylinders degrade. The P4VP chains degrade in prolonged isothermal treatment at the same temperature and microporosity is obtained. Note the OH groups which are left at the pore walls when PS is pyrolyzed.

channels which promote the transportation and micropores act as sites of selectivity and activity. Such hierarchically porous materials have been investigated for example for biomaterials engineering, electrode materials, catalysis, filters and separation [1,2].

Block copolymers which readily self-assemble into various structures are feasible templates for mesoscopically structured materials [3]. The interplay between entropy and surface energy between the different polymer blocks leads to microphase separation and results in periodic phases such as spherical, cylindrical and lamellar [4]. The phase and characteristic length can be tailored by choosing the volume fractions of different constituents and the molecular weight of the block copolymer accordingly.

The idea behind this work is schematically illustrated in Figure 1. If one of block copolymer's blocks forms strong enough hydrogen bond between phenolic hydroxyls of uncured phenolic resin, the resulting microphase separated structure is preserved even after curing [5-8]. In this work poly(styrene)-*block*-poly(4-vinyl pyridine) (see Figure 1a) (PS-*b*-P4VP) was used as the template. The block copolymer template can then be removed by pyrolysis while preserving the original structure (see Figure 1c) [5, 9]. As has been shown, PS weight fraction of 40 % leads to cylindrical PS domains in P4VP-phenolic resin matrix [9].

Here, we present a method to control the final porosity by the pyrolysis conditions.

2. Experimental

2.1. Materials

PS-*b*-P4VP diblock copolymer (number average molecular weight $M_{n,PS} = 40\,000$ g/mol, $M_{n,P4VP} = 5600$ g/mol) by Polymer Source Inc. was used as received. Phenolic resin (Novolac) was received from Bayer (Vulcadur RB). Hexamethylenetetramine (HMTA) by Aldrich was used as crosslinking agent. Tetrahydrofuran (THF) was acquired from Riedel-de Haën.

2.2. Sample Preparation

In order to obtain cylindrical structure, the weight fraction of PS was chosen to be 40 % of the whole complex. The ratio of weights between Novolac and HMTA was 88:12. All three materials were dissolved in THF separately and the solutions were combined, stirred and finally the solvent was evaporated in room temperature. The samples were dried at 30 °C in a vacuum oven for one day prior to curing which was accomplished as follows: 100 °C for 2 h, 150 °C for 2 h and 190 °C for 2 h. The rate of heating between the isothermal plateaus was 1 °C/min. Pyrolysis was done without protective gas atmosphere from room temperature to 330-420 °C by slowly heating at 1 °C/min. At the final temperature of 420 °C, heating was ceased and an isothermal treatment of 0, 15, 30, 60 and 120 minutes was performed.

2.3. TEM

The TEM was performed by Tecnai 12 using a 120 kV accelerating voltage and 40-70 nm thick microtomed samples.

2.4. PALS

PALS measurements were performed with a fast-fast coincidence timing spectrometer with a time resolution of 0.270 ns (FWHM) determined from a ^{60}Co prompt spectrum. A ^{22}Na positron source with an activity of 8 μCi was deposited and sealed between two thin aluminium foils. Two films (thickness ca. 400 μm) of sample material was stacked on the both sides of the source. This "sandwich" was placed between two scintillation detectors. A positron lifetime spectrum of more than million counts was accumulated from every sample and

averaged over ten measurements. The results were analyzed by PATFIT-88 program. The results were interpreted in terms of three component lifetime.

2.5. BET

The surface area measurements were performed with a Coulter Omnisorp 100CX gas adsorption instrument using static volumetric adsorption and desorption method. After loading the sample it was first evacuated at room temperature to a pressure of $1 \cdot 10^{-4}$ Torr or lower. Then the evacuating temperature was raised first to 90 °C and evacuated for at least 30 minutes prior to raising the temperature to final evacuation temperature of 200 °C until the pressure went below $1 \cdot 10^{-5}$ Torr, which typically took between 3 and 4 h. Nitrogen was used as an adsorptive gas and measurements were done in a liquid-nitrogen bath at 77 K. Adsorption isotherms were measured by dosing nitrogen to the sample and measuring the adsorbed amount as a function of nitrogen pressure.

2.6. UV-vis Spectroscopy

The spectra were measured with as Perkin-Elmer Lambda 950 spectrophotometer in the wavelength range 250-900 nm. MB was received from Fluka (97 %) and it was dissolved in Milli-Q water at a weight fraction of less than 0.013. The samples were grounded by mortar and immersed into the solutions in such amounts that the number of MB molecules was 6.25 % of the nominal moles of the hydroxyl groups of the phenolic resin.

3. Results and Discussion

The materials were prepared as explained in the Experimental section. The TEM image in Figure 2b shows the cylindrical structure of the starting material. Previous experiments suggested that the pyrolysis temperature should not exceed ca. 420 °C because the cured phenolic resin would be removed in higher temperatures [9]. Also, heating rate was fixed at 1 °C/min to minimize the deformation of the material. Thus, pyrolysis conditions as shown in Table 1 were used. The pyrolysis of three samples was stopped when a certain temperature was reached while rest of the samples received isothermal pyrolysis at 420 °C after the heating phase. Additionally, the table shows results of Brunauer-Emmett-Teller method (BET) for evaluation of porosity of the samples. Phenolic resin only reference samples are not porous even after 120 minutes of isothermal treatment at 420 °C while the porosity of the PS-*b*-P4VP templated samples

Table 1. The pyrolysis conditions, resulting surface areas and pore diameters of cured PS-*b*-P4VP-phenolic resin complexes with PS weight fraction of 40%. The diameters of mesopores are obtained from TEM images and the diameters of micropores from PALS by means of a simple quantum mechanical model.

Sample	Pyrolysis conditions		Total surface area [m ² g ⁻¹]	Mesoporous surface area [m ² g ⁻¹] (mesopore diam. [nm])	Microporous surface area [m ² g ⁻¹] (micropore diam. [nm])
	Final temperature [°C]	Isothermal treatment			
phenolic resin			<5	-	-
		120 min at 420°C	<5	-	-
PS- <i>b</i> -P4VP-phenolic resin	330		<5	-	-
	360	-	<5	-	-
	390		24	22 (30)	2 (0.295)
"	420	0 min at 420°C	40	25 (30)	15 (0.282)
"	420	15 min at 420°C	260	95 (30)	165 (0.282)
"	420	30 min at 420°C	361	105 (30)	256 (0.282)
"	420	60 min at 420°C	456	101 (30)	356 (0.282)
"	420	120 min at 420°C	557	66 (20)	491 (0.282)

increases during the last steps of the heating and subsequent isothermal treatment.

The start of the development of the mesopores in the material, as indicated by BET in Table 1 (some adsorption isotherms shown on Figure 3), is clearly seen in transmission electron microscope (TEM) micrograph shown in Figure 2c. The PS cylinders start to degrade at a temperature a couple of dozens of centigrades below the final isothermal pyrolysis temperature at 420 °C. The maximal surface area of mesopores is reached after 30 minutes at 420 °C. Figure 2a shows a three dimensional (3D) tomography of the material after 60 minutes. Prolonged pyrolysis at the same temperature leads to the deformation of the matrix and the hollow cylinders collapse. The BET measurements reveal the development of micropores during the isothermal treatment. This is seen in the adsorption isotherms in Figure 3. The micropores are attributed to the removal of P4VP chains from the material. Their development has been further investigated by positron annihilation lifetime spectroscopy (PALS). Ortho-positronium (o-Ps) pick-up annihilation lifetime is directly related to the mean

free-volume (microporosity) size. The intensity of the o-PS lifetime is often attributed to the micropore volume density. The pick-up annihilation lifetime was found to be constant until a temperature of 390 °C is reached, whereas the intensity drops upon the heating. The phenomenon can be explained by the preferential localization of o-PS in the mesopores formed by degraded PS. When the final temperature is reached, the lifetime falls by 0.175 ns to a value where it stays constant during the isothermal treatment. The intensity, on the other hand, increases after long enough isothermal treatment time. The drastic change in the lifetime can be interpreted as a result of the formation of micropores as P4VP chains are degraded from the cured P4VP-phenolic resin matrix. This is in agreement with the BET results shown in Table 1, even though no correlation was obtained between the pore number derived from the intensity value and the BET results.

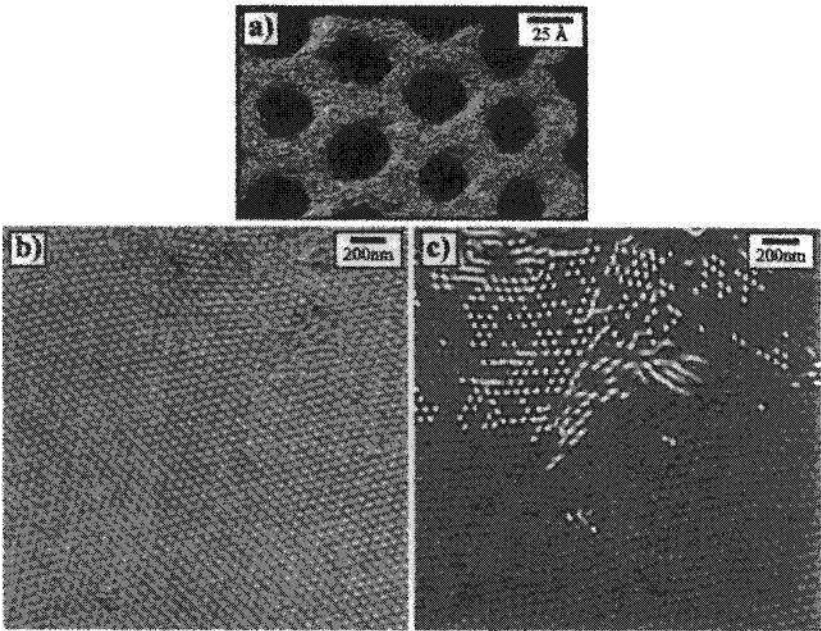


Figure 2. a) 3D TEM tomograph of microtomed thin section of cured PS-P4VP-phenolic resin complex isothermally pyrolyzed at 420 °C for 60 min. Rendered in isosurface mode. b) TEM image of the cured complex. PS (light domains) forms hexagonal cylindrical structures. c) Complex heated to 360 °C at a rate of 1 °C/min which results in PS is partially removed from the material.

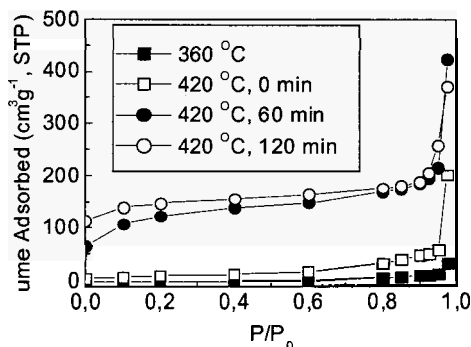


Figure 3. Adsorption isotherms of cured block copolymer-phenolic resin samples after pyrolysis in different conditions. P and P₀ are the pressure of nitrogen and saturated nitrogen at 77K, respectively.

The size of the micropores can be roughly estimated by means of a simple quantum-mechanical model, where the *o*-Ps is approximated to be localized in an infinite spherical potential well. This estimation results in an average micropore radius of 0.27 nm.

The OH groups on the mesopore walls were probed by methylene blue (MB) absorption rate experiment. There is a strong hydrogen bonding between the nitrogen containing aromatic ring of MB and the hydroxyl groups. The unpyrolyzed sample does not absorb MB at all while the samples heated to 330, 360, 390 and 420 °C absorb only a small amount of dye. In contrast, the samples which received isothermal treatment subsequent to heating to 420°C absorb MB more rapidly and the absorption does not level off even after six months.

4. Conclusions

Our work has shown that it is possible to achieve hierarchical porosity by using self-assembled block copolymers as templates. Degradation of the PS block in the PS-*b*-P4VP-phenolic resin complex results in mesoporous material with hydroxyl groups on the pore walls. These can be readily utilized as absorption sites as our MB experiments show. Also, the OH groups are chemically active and are thus potential sites for further functionalization. Microporosity is achieved by isothermal treatment after heating. This is due to the degradation of the P4VP chains within the cured phenolic resin matrix. The formation of both meso and micropores can be controlled by the degradation conditions. With the fact that the size of the mesopores can be changed by varying the molecular weight of the block copolymer, this results in highly customizable hierarchically

porous material. With the molecular weight of PS-*b*-P4VP used in this study, mesopores with a diameter of ca. 30 nm were obtained. Currently we are investigating the possibility to infiltrate colloidal crystals with PS-*b*-P4VP-phenolic resin complex. These systems are expected to be hierarchically porous in three levels: The degradation of the colloidal crystal results in well-defined macropores whereas the degradation of the block copolymer-phenolic resin complex results in the meso and microporous system presented here. We believe that such materials could be useful for sensors, separation materials, filters and templates for catalysis as they have high density of pores and the pore walls are covered by hydroxyl groups. The fact that the shape of these materials is not restricted (also they can be molded furthermore) broadens the plethora of possible applications.

Acknowledgments

The work was carried out in the Centre of Excellence of Finnish Academy ("Bio- and Nanopolymers Research Group", 77317) and supported by the European Commission-project COMPOSE no. NMP3-CT-2003-505633.

References

1. Z.-Y. Yuan and B.-L. Su, *J. Mater. Chem* **16**, 663 (2006)
2. J. Jones, P. Lee and L. Hench, *Philos. Trans. R. Soc. London, Ser. A* **364**, 263 (2006)
3. M. Lazzari and M. Lopez-Quintela, *Adv. Mater.* **15**, 1583 (2003)
4. I. W. Hamley, *The Physics of Block Copolymers*, Oxford University Press, 1998
5. C. Liang and S. Dai, *J. Am. Chem. Soc.* **128**, 5316 (2006)
6. C. Liang, K. Hong, G. A. Guiochon, J. W. Mays and S. Dai, *Angew. Chem. Int. Ed.* **43**, 5785 (2004)
7. H. Kosonen, J. Ruokolainen, P. Nyholm and O. Ikkala, *Macromolecules*, **34**, 3046 (2001)
8. H. Kosonen, J. Ruokolainen, M. Torkkeli, R. Serimaa, P. Nyholm and O. Ikkala, *Macromol. Chem. Phys.*, **293**, 288 (2002)
9. H. Kosonen, S. Valkama, A. Nykänen, M. Toivanen, G. ten Brinke, J. Ruokolainen and O. Ikkala, *Adv. Mater.*, **18**, 201 (2006)
10. S. Valkama, A. Nykänen, H. Kosonen, R. Ramani, F. Tuomisto, P. Engelhardt, G. ten Brinke, O. Ikkala and J. Ruokolainen, *Adv. Funct. Mat.* **17**, 183 (2007)

UNIFORM POROSITY IN MODIFIED CARBON CRYOGELS

SAGHAR SEPEHRI, BETZAIDA BATALLA GARCÍA, QIFENG ZHANG, AND
GUOZHONG CAO

*Materials Science & Engineering, University of Washington, 302 Roberts Hall, Box
352120, Seattle, Washington, 98195*

Resorcinol formaldehyde derived carbon cryogels with narrow pore size distribution were obtained via chemical modification using ammonia borane. This chemical modification was achieved by adding ammonia borane (AB) to the hydrogels during the solvent exchange stage. Nitrogen sorption analysis, scanning electron microscopy, X-ray photoelectron spectroscopy, and electrochemical impedance spectroscopy are used to investigate the pore structure, morphology, and electrochemical properties of the modified carbon cryogel. After pyrolysis, the AB modified carbon cryogels have a uniform porous structure, increased surface area, larger mesopore volume, and a narrow pore size distribution in comparison to the untreated precursor. Moreover, electric double-layer supercapacitors made from the AB modified samples show pseudocapacitive behavior, higher current density and capacitance.

1. Introduction

Among the porous carbon materials, carbon aerogels (CAs), possessing a range of desirable properties, including tunable mass densities, continuous porosities, and high surface areas, have been the subject of considerable attention for numerous applications [1-6]. The physical, chemical, and electrochemical characteristics of CAs depend strongly on the fabrication method; therefore, different synthesis and processing methods can be used to produce tailored gels for specific applications. CAs can be made from organic hydrogels generated by the sol-gel polycondensation of organic monomers such as resorcinol (R) and formaldehyde (F) in aqueous solution in the presence of a polymerization catalyst [7]. The aerogel is produced by drying the resorcinol-formaldehyde (RF) hydrogel supercritically. Hydrogels may be alternatively subjected to freeze-drying to produce cryogels or be converted into xerogels by vacuum or air drying. Freeze-drying is as an appealing alternative to the expensive supercritical drying employed to produce CAs, while still producing similar porous structures [8]. Pyrolysis of hydrogels usually decreases the pore volume, pore size and increases microporosity (by IUPAC classification regarding pore widths [9]: micropores <2nm, mesopores 2-50 nm, and macropores > 50nm) [10]. For many

applications, a mesoporous structure with sharp pore size distribution and minimum microporosity is preferred [11]. In addition to tailoring the pore structure, doping carbon gels can provide them with altered or novel properties that expand their applications. An example is that doping carbon with nitrogen and boron has been shown to change the surface chemistry and improve its electrochemical properties [12, 13].

In a previous study, we investigated the hydrogen storage properties of a carbon cryogel – ammonia borane nanocomposites [14]. It was shown that ammonia borane (AB), NH_3BH_3 , could be successfully dispersed throughout a carbon cryogel (CC) matrix by soaking CC in AB/THF solution. In this study, we used the same strategy to produce modified RF hydrogels that are doped with AB, followed by freeze-drying and pyrolysis to generate modified CCs. These materials contain nitrogen and boron, while their porous structure is still maintained. Our investigations confirm that this method homogeneously disperses the dopants throughout the carbon cryogel structure and uniformly changes the CC morphology and structure. The modified CCs in this study, exhibit higher surface area and larger pore volume with a narrow mesopore size distribution. Also, the improvement in the current density and capacitance of the electric double-layer supercapacitors (EDLS) electrodes made from modified carbon cryogels indicates the doping elements are active in pseudocapacitive reactions. The nitrogen-boron co-doped mesoporous carbon cryogels here reported have the potential to be implemented in a variety of applications, including supercapacitors and hydrogen storage materials.

2. Experimental Section

2.1. Sample preparation

AB-doped organic cryogels were prepared as previously reported [15]. In general, resorcinol (R) was mixed with formaldehyde (F) solubilized in distilled water (W), using sodium carbonate as a catalyst (C). The R/W ratio was 0.035 g/ml, the R/C ratio was 200:1, and the R/F ratio was 0.5. The clear solutions were then poured into glass vials (inner diameter=10 mm) that were then sealed and cured at 90°C for 7 days to complete the gelation process. The precursor dark red and transparent RF hydrogels were placed in ten times their volume of trifluoroacetic acid solution (pH: 1.9) at 45°C for three days to stop the condensation reaction. Solvent exchange stage, which is necessary for freeze drying, was carried out by placing the gels in fresh t-butanol ten times their volume at room temperature for 24 hours and then repeated twice more with

fresh solution. For the modified samples, 2 wt% of ammonia borane (AB) was dissolved in t-butanol during the first solvent exchange step. The gels, initially dark red in color, changed to light red during this step. The rest of the solvent exchange process was done using fresh t-butanol to avoid the precipitation of residual ammonia borane in the pores of the gels. All the samples were freeze dried for a week under vacuum (at -50°C) to obtain the RF and ABRF (modified) cryogels. These cryogels were pyrolyzed for 4 hours at 1050°C (heating rate $5^{\circ}\text{C}/\text{min}$ and, nitrogen flow $25\text{ ml}/\text{min}$), to produce carbon cryogels (CC) and ammonia borane modified carbon cryogels (referred hereinafter to as ABCC), respectively. However, it should be noted that after pyrolysis, ABCC is carbon cryogel codoped with boron and nitrogen.

2.2. Characterization

The pore structure of carbon cryogels was analyzed by means of nitrogen sorption at -196°C using a Quantachrome NOVA 4200e instrument. Specific surface area, micropore and mesopore volumes were determined using multi point BET, t-method and BJH analyses, respectively.

Surface morphology of the cross sections of the samples was studied by a JEOL JSM 7000F scanning electron microscope (SEM). RF samples for SEM were Pt coated in order to prevent charging. All X-ray photoelectron spectroscopy (XPS) were done on a thin slice of the samples, using a Surface Science Instruments S-probe spectrometer (sampling depth about 50 \AA , X-ray spot size $800\mu\text{m}$).

The electrochemical measurements, galvanic cycles (GC), cyclic voltammograms (CV) and electrochemical impedance spectroscopy were performed in a Solartron 1287A in a voltage range between 0 to 2V. The cyclic voltammograms were scanned at 10, 50 and $100\text{mV}/\text{s}$ and the galvanic cycles measured at 0.5, 1, 5, 10, 50 and 100mA . Electrochemical impedance spectroscopy was done using the Solartron 1287A in conjunction to the Solartron 1260 FRA/impedance analyzer, the samples were cycled and pretreated at +2V. The electrodes (thickness $\sim 0.08\text{mm}$, diameter $\sim 9\text{mm}$) were prepared by grinding monoliths into a fine powder then mix with 3% wt of polytetrafluoroethylene (PTFE). Assembly and test of the 2-electrode electrochemical test cell took place under Argon. Tetraethylammonium tetrafluoroborate (TEATFB) in saturated 50/50 propylene carbonate (PC)/dimethylcarbonate (DMC) was used as the electrolyte.

3. Results and discussion

3.1. Scanning electron microscopy

The SEM images of RF and CC samples are shown in figures 1 through 3. One can see that the modified cryogel samples (ABRF), (Fig. 1b), has a similar morphology to RF samples (Fig. 1a).

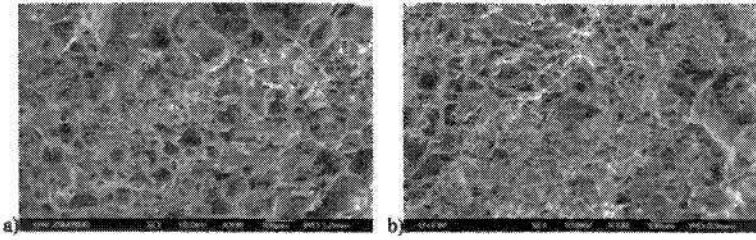


Fig. 1 - SEM images of RF (a) and ABRF (b) samples (scale bar= 100 μ m)

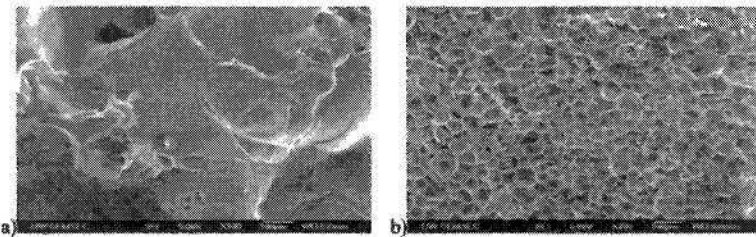


Fig. 2 - SEM images of CC (a) sample and ABCC (b) sample (scale bar= 100 μ m)

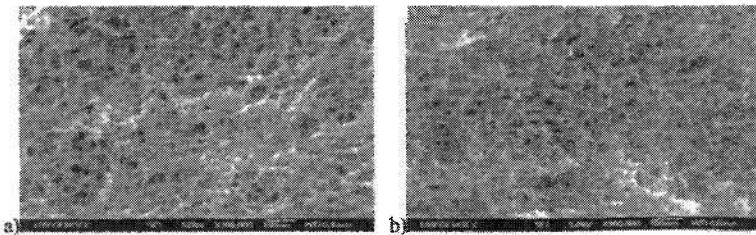


Fig. 3 -SEM images of CC (a) sample and ABCC (b) samples (scale bar= 100nm)

However, after pyrolysis CC and ABCC morphology is very different (Fig. 2 and 3). A more ordered porous structure consisting of smaller particles is observed in the modified sample (Fig. 2b and 3b).

3.2. X-ray photoelectron spectroscopy (XPS)

XPS measurements on the cross section of carbon cryogel samples reveal the elemental changes in the modified sample due to incorporation of AB throughout the carbon structure. The result is shown in Table 1. It is known that substitution of boron in carbon can change the surface characteristics possibly by formation of B_2O_3 [16]. In our study a different surface chemistry is observed for the ABCC sample, where 2.2 wt% boron is observed and oxygen content tripled compared to the CC sample. Also notice the reduction in sodium levels in the ABCC sample. In addition, a very small N1s peak (about 0.1 atomic %) was observed for the ABCC sample. Nevertheless, this nitrogen content may be also responsible for the electrochemical observation that is discussed later.

Table1 – Elemental distribution at the surface of cryogel samples

Sample		C	O	Na	B
CC	atomic content %	96.8	2.9	0.3	0
	mass content %	95.6	3.8	0.6	0
ABCC	atomic content %	88.7	8.8	0	2.5
	mass content %	86.4	11.4	0	2.2

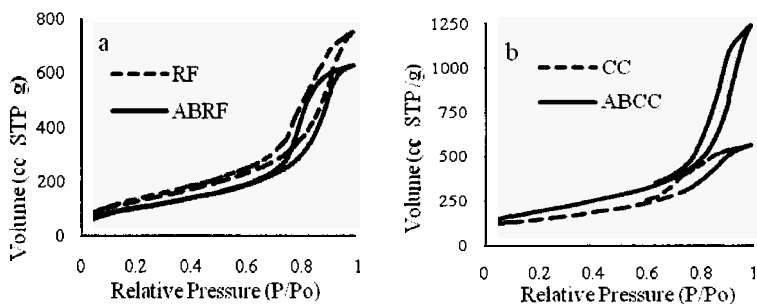


Fig.4– Nitrogen sorption isotherms of RF, ABRF (a) and CC, ABCC (b) samples (-196 °C).

3.3. Nitrogen physisorption

The nitrogen sorption isotherms for both CC and ABCC samples (Fig. 4) exhibit a type IV isotherm [9], with hysteresis associated with the dominance of mesoporosity. Before pyrolysis the RF samples exhibit larger pore volume and greater diameter compared to ABRF (Fig. 4a). After pyrolysis the amount of nitrogen adsorbed on CC is smaller than that on RF sample, which indicates reduced pore volume and smaller pores (possibly due to shrinkage) [10]. For the

ABCC samples, on the other hand, the isotherm shifts toward higher nitrogen adsorption which means an increase in pore volume for ABCC samples compared to ABRF (Fig. 4b).

The pore size distribution of the RF and ABRF samples shows a major concentration of pores of radii of about 6 and 11 nm, while higher volume of the latter size are observed in RF sample (Fig. 5a). However, after pyrolysis, the concentration of 11nm radius pores disappears, due to collapse of the pores, and a broad distribution of pore sizes is observed for CC sample. Conversely no such collapse is detected in the ABCC sample and a dominant concentration of pores with a radius of 11nm appears (Fig. 5b).

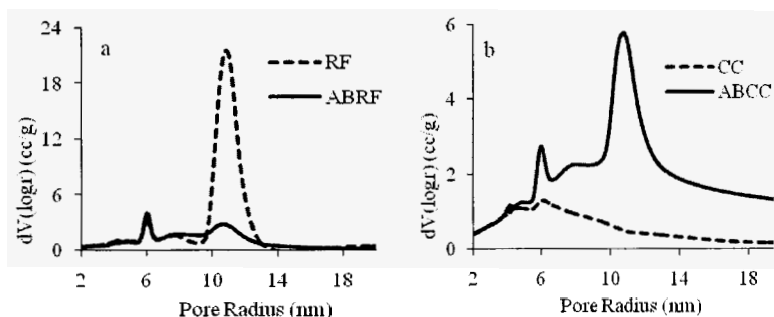


Fig. 5 – Pore size distribution of RF, ABRF (a) and CC, ABCC (b) samples (BJH adsorption)

The highly mesoporous structure of the samples is detailed in Table 2. Upon pyrolysis, the specific total surface area, (BET), slightly increases for CC sample while the mesopore (BJH) surface area decreases. This increase is attributed to the formation of micropores in the CC sample during the pyrolysis [17]. Micropore volume is halved in modified samples, compared to CC samples. While, about 80% and 55% enhancement in the total and mesoporous surface areas, respectively, is observed for ABCC samples indicating that the porous network in the ABCC is expanded by pyrolysis.

Table2 - Porosimetry data for original samples and modified samples before and after pyrolysis

Sample	BET Surface Area (m ² /g)	Mesopore Surface Area (m ² /g)	Micropore Surface Area (m ² /g)	Mesopore Volume (cc/g)	Micropore Volume (cc/g)	BJH ads. Pore Radius (nm)
RF	464	359	-	1.08	-	10.9
ABRF	377	312	-	0.92	-	6
CC	494	307	44	0.75	0.028	4
ABCC	673	484	17	1.78	0.012	10.8

3.4. Electrochemistry

The cyclic voltammogram measurements for the ABCC sample had an increased current density over the ones made from CC (Fig.6a). In addition the capacitance of the ABCC device was 30% higher than that of the CC (Fig. 6b). This may be the result of two factors: altered pore structure and surface chemistry of the sample. Improved capacitive behavior has been observed in carbon materials due to the presence of active species that contribute to the total specific capacitance by the pseudocapacitive effect, while large specific surface area and porosity are essential for high current density and charge storage [18].

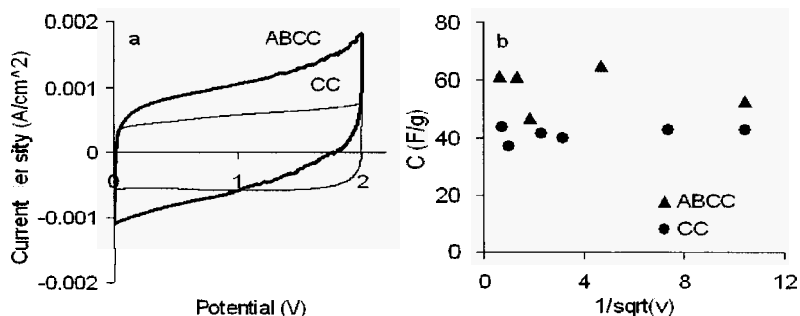


Figure 6- a) Cyclic voltammogram of AB and CC samples, b) Capacitance of samples vs. $1/\sqrt{v}$. The constant behavior is characteristic of mesoporous or larger structures that are not affected by the electrolyte penetration [19].

The pseudocapacitive behavior of the ABCC sample is presented in Figure 7. For the ABCC sample measured at a scan rate of 100mV/s, two distinct current peaks were observed during the first two cycles (Fig.7a), but were absent in a similar measurement for the CC sample. Such pseudocapacitive behavior may only be attributed to the sample's chemical composition as the aprotic (organic) electrolyte used does not exhibit pseudocapacitance nor does it decompose in the applied voltage range. Introducing nitrogen atoms in carbon structures has been shown to create a pseudocapacitive effect and, thereby, improve their physiochemical properties of double-layer capacitors [20, 21]. The galvanic cycles similarly exhibit a difference between ABCC and CC samples. While the CC has the symmetric triangular charge-discharge behavior typical of electric double-layer capacitors, this symmetry is lost in the ABCC samples (Fig. 7b). This asymmetry is likely due to the reaction involved in the diffusion of new chemical species during or after the reaction.

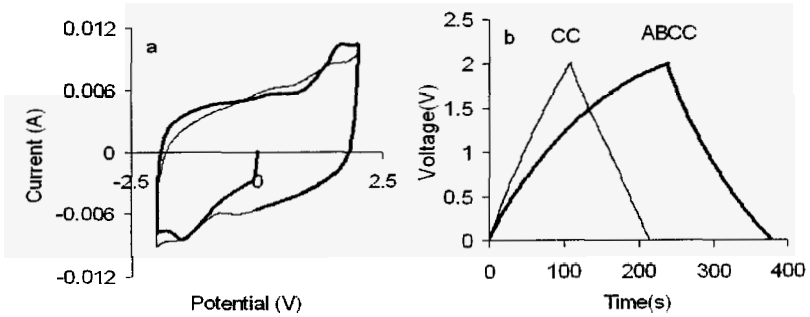


Figure 7- a) First cyclic voltammograms for ABCC, b) Galvanic Cycles for CC and ABCC samples.

The Nyquist plot of the two samples (Fig. 8) indicates contrasting effects in their bulk electrolyte properties [22]. The CC sample has a wide arch and an ESR of 22 ohms, while the ABCC samples had only a small contribution from the bulk electrolyte properties and its ESR was only 6.3 ohms. The reduced bulk effect in the ABCC samples is possibly related to the small amount of large macropores, $> 100\mu\text{m}$, present in this sample (Fig. 5b and Fig. 2a & 2b). At the low frequency range, the CC electrodes show signs of pore exhaustion and ideal capacitor behavior, while the ABCC samples deviate from ideality (Fig. 8b). This deviation is likely a result of the pseudocapacitance in the ABCC electrodes.

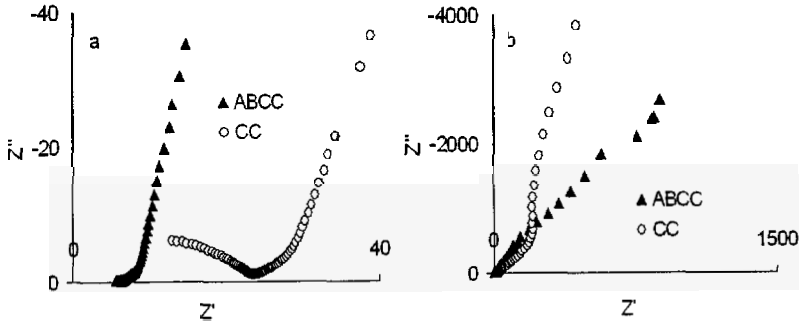


Figure 8- a) Nyquist Plot at the high frequency (bulk impedance), b) Low frequency data

The electrochemistry results for carbon cryogel samples confirm that the dopant in ABCC samples is electrochemically active and has introduced other charged species during potential cycling, while the CC sample relies completely on the electrolyte for active species in forming the electric double-layers.

4. Conclusions

Nitrogen-boron codoped carbon cryogels (ABCC) can be readily synthesized by homogenous dispersion of ammonia borane (AB) in RF hydrogel during solvent exchange and followed by freeze-drying and pyrolysis at elevated temperatures in nitrogen, and such co-doping results in significant porous structure change and improved electrochemical properties. Higher mesoporosity, increased pore volume, larger specific surface area, more uniform mesopore size distribution, increased current density and specific capacitance were observed in ABCC samples as compared to CC samples. A further investigation on the effects of incorporating nitrogen and boron in CCs with different pore sizes can be expected to provide additional information for these modified carbon cryogels. High pore volume and surface area should improve the hydrogen storage properties of the ABCC when used as a nanoscaffold with these studies to be the subject of a future report.

Acknowledgements

Support for this work is provided by NSF (DMR-0605159), WTC, and EnerG2 LLC as well as the DoE Center of Excellence in Chemical Hydrogen Storage funded by the DOE H₂ Program. XPS measurements were made at the University of Washington NESAC/BIO Surface Analysis Facility.

References

1. R. W. Pekala, C. T. Alviso, F. M. Kong and S. S. Hulsey, *J. Non-Cryst. Solids* **145**, 90 (1992).
2. Y. Yamamoto, T. Sugimoto, T. Suzuki, S. R. Mukai and H. Tamon, *Carbon* **40**, 1345 (2002).
3. J. C. Farmer, D. V. Fix, G. V. Mack, R. W. Pekala and J. F. Poco, *J. Appl. Electrochem.* **26**, 1007 (1996).
4. M. V. Ernest, J. P. Bibler, R. D. Whitley and N.H. L. Wang, *Ind. Eng. Chem. Res.* **36**, 2775 (1997).
5. R. Petricevic, M. Glora and J. Frick, *J. Power Sources* **271**, 167 (2002).
6. E. Frackowiak and F. Beguin, *Carbon* **39**, 937 (2001).
7. R.W. Pekala, *J. Mater. Sci.* **24**, 3221 (1989).
8. H. Tamon, H. Ishizaka, T. Yamamoto and T. Suzuki, *Carbon* **37**, 2049 (1999).
9. K. S. W. Sing, D. H. Everett, R. A. W. Haul, L. Moscou, R. A. Pierotti, J. Rouquerol and T. Siemieniewska, *Pure Appl. Chem.* **57**, 603 (1985).
10. S. A. Al-Muhtaseb and J. A. Ritter, *Adv. Mater.* **15**,101 (2003).

11. R. Ryoo, S. H. Joo, M. Kurk and M. Jaroniec, *Adv. Mater.* **13**, 677 (2001).
12. T. Matsuoka, H. Hatori, M. Kodama, J. Yamashita, and N. Miyajima, *Carbon* **42**, 2346 (2004).
13. E. Frackowiak, *Phys. Chem. Chem. Phys.* **9**, 1774 (2007).
14. A. Feaver, S. Sepehri, P. Shamberger, A. Stowe, T. Autrey and G. Z. Cao, *J. Phys. Chem.* **B111**, 7469 (2007).
15. A. Feaver and G. Z. Cao, *Carbon* **44**, 590 (2006).
16. L. R. Radovic, M. Karra, K. Skokova and P. A. Thrower, *Carbon* **36**, 1841 (1998).
17. T. Yamamoto, T. Nishimura, T. Suzuki and H. Tamon, *J. Non-Cryst. Solids* **288**, 46 (2001).
18. B. E. Conway, *Electrochemical supercapacitors: Scientific Fundamentals and Technological application*; Kluwer-Plenum Press: New York, (1999).
19. J. G. Lee, J. Y. Kim and S. H. Kim, *J. Power Sources* **160**, 1495 (2006).
20. M. Kodama, J. Yamashita, Y. Soneda, H. Hatori, S. Nishimura and K. Kamegawa, *Mater. Sci. Eng.* **B108**, 156 (2004).
21. D. Hulicova, J. Yamashita, Y. Soneda, H. Hatori and M. Kodama, *Chem. Mater.* **17**, 1241 (2005).
22. E. Barsoukov and J. R. Macdonald, *Impedance Spectroscopy*, John Wiley and Sons, Inc (2005).

EFFECT OF PORE MORPHOLOGY ON THE ELECTROCHEMICAL PROPERTIES OF ELECTRIC DOUBLE LAYER CARBON CRYOGEL SUPERCAPACITORS

BETZAIDA BATALLA GARCÍA, AARON M. FEAVER, GUOZHONG CAO
*Materials Science and Engineering, University of Washington, 302 Roberts Hall
Seattle, WA 98195-2120*

GERALD T. SEIDLER, TIM T. FISTER, KEN P. NAGLE
*Department of Physics, University of Washington, 3910 15th Ave. NE
Seattle, WA 98195-1560*

In this study a group of resorcinol-formaldehyde carbon cryogels (CC) have been processed chemically, via catalysis and activation, to obtain various nanostructures and pore size distributions. To understand the relation between structure and electrochemical properties an alternate approach to the transmission line's cylindrical pore method is used. Using electrochemical impedance spectroscopy (EIS), the capacitor can be studied as a dielectric system composed of the porous electrode and the electrolyte (PC/TEATFB). The complex capacitance and power are used to study the behavior of the system below the relaxation frequency f_o ($f = -45^\circ$). Therefore, the relaxation of the capacitor system at the low frequency range, $f < f_o$, can be used as a measure of pore/electrolyte interaction. The approach here proposed also allows for a direct experimental characterization of the capacitance and power at low frequencies where small pores are likely to affect the diffusion dynamics of the electrolyte molecules. The results suggest a correlation between the occurrence of small micropores and that of high power losses that are related to the resistive element produced at the low frequency range. The measurements show that the dissipative power of the samples increased with decreasing micropore diameter (1.6 – 1.2 nm), from 8% to 36% when measured at a frequency of 0.004Hz (below f_o). Moreover, the impact that the micropore structure has in the supercapacitor's performance can be seen in its capacitance and energy as well. In addition to the complex power and capacitance; other measurements like BET Nitrogen sorption, cyclic voltammetry, galvanic cycling and X-Ray Raman Scattering were used to characterize the samples and support these results.

1. Introduction

Carbon cryogels (CC) from the resorcinol formaldehyde polycondensation are excellent precursor materials to use as electrodes in electric double layer supercapacitor (EDLS). Their tunable nanostructure, high surface area and good conductivity make them suitable for such application. The ability to tune the

pore sizes is a very important feature to support the ionic double layer. Although the tunable structure of these cryogels is highly desirable, unwanted structures are often produced. Recent studies have addressed the structure/ charge problem by measuring the total surface area and capacitance [1]. Unfortunately, the use of absolute quantities does not provide a clear boundary of the role that specific structures have in charge storage. Understanding this role is necessary to design better CC supercapacitors.

Electrochemical impedance spectroscopy (EIS) has been used to characterize the mechanisms of electrolyte diffusion in porous media. De Levý and his successors have demonstrated the relation between pore size and the electrochemical properties of the electrode [2-5]. Moreover porosimetry models based on this technique have been developed as well [2]. Unfortunately, this technique is only useful to determine the frequency response of well-behaved systems (cylindrical pores, single pore size distributions) but does not address the problem of amorphous porous electrodes in its entirety (i.e. bimodal distributions of charges and pores of various lengths, diameters and shapes). The many models developed to address the amorphous electrode problem and ambivalence of the circuit models are an example of the challenges presented to link the structure to the electrochemical properties [5].

Another way to study the supercapacitor's electrochemical properties using EIS is to treat it as a dielectric fluid. The molecular relaxation of the electrode/ electrolyte system can be probed in a wide frequency range and ultimately related to its structure. Structural differences can alter the relaxation of the fluid's molecules, especially in the presence of a voltage bias. Also Debye, Cole-Cole and Havriliak-Negami have described dielectric relaxation of bulk fluids through EIS models [5,6]. Most recently the effect of molecular relaxation has been studied in porous media for various systems like planar electrodes, cylindrical pores or colloidal particles to mention a few [7,8]. These studies support the fact that confinement affects the molecular relaxation especially at the solid/ liquid interface regardless of external stimuli like voltage bias, temperature, etc. Therefore, the molecular relaxation can be used to study the effect of surface morphology in the electrolyte's molecules. Moreover the impact is expected to be particularly strong when the pores or features approach the size of the electrolyte's molecules.

To study the capacitor as a dielectric system, the complex capacitance and power are used [9]. By separating the complex capacitance into its active (real) and reactive (imaginary) parts the appearance of capacitive peaks in the frequency spectrum can be associated with the effect that some pore sizes have in the electrolyte. Since the energy is proportional to the capacitance, the

imaginary capacitance can be used to study the energy loss produced by the molecular relaxation [9]. The complex power is calculated in a similar fashion and can be separated into its reactive and active power. Therefore allowing the measure of dissipative and capacitive power associated with the molecular relaxation. Recently, this method has been used to study other characteristics of the capacitor system like leakage current [10,11]. In this study, various CC supercapacitors were chemically tuned via catalyst and activation to obtain various structures. EIS is used to evaluate the relaxation of the CC supercapacitors and compare it to their morphology and other electrochemical properties.

2. Experimental

2.1. Carbon cryogel electrodes

The carbon cryogels were prepared using the resorcinol formaldehyde polycondensation process published by Pekala [12], the samples used in this study were synthesized by A. Feaver and the preparation is fully described in his letter [13]. In summary, to produce the various levels of pore structures, the samples were chemically altered using two different amounts of catalyst and CO₂ activation. The amounts of resorcinol to catalyst ratio used in the experiment were 25 and 75 and the samples were activated to 36 and 70% burn-off, all the samples had a resorcinol to water ratio of 0.25. The CCs were then ground into a fine powder and mixed with 3% wt of polytetrafluoro-ethylene (PTFE). The resulting mixture was then kneaded several times to produce the electrodes. Table 1 summarizes the samples' chemical modification.

Table 1 Catalyst amount and activation percentage used to process the cryogels
(Resorcinol to water ratio for all samples is 0.25)

Sample ID	Resorcinol to Catalyst ratio (RC)	CO ₂ Activation (%)
A-70	25	70
C-70	75	70
C-36		

2.2. Electrochemistry

The electrochemical measurements, galvanic cycles (GC), cyclic voltammograms (CV) and electrochemical impedance spectroscopy were done using a symmetric 2-electrode test cell (the CC electrodes were used as working and counter electrodes). The electrolyte was tetraethylammonium tetrafluoroborate (TEATFB) in saturated 50/50 propylene carbonate (PC)/

dimethylcarbonate (DMC). The working and counter electrodes were sandwiched between two, specially coated, aluminum contacts and separated by a Celgard porous membrane. The coating of the Al contacts reduces the impact of the bulk electrolyte effect. The CC electrode discs had a diameter of 8.72 mm and a thickness of 0.08 mm. The assembly, wetting, and sealing of the capacitors were carried out in an Argon glove box. All potentiostatic and galvanostatic measurements were performed using a Solartron 1287A potentiostat/galvanostat. The cyclic voltammograms were executed at scan rates of 10, 50, and 100 mV/s, while the galvanic cycles were measured at 0.5, 1, 5, 10, 50, and 100 mA. Electrochemical impedance spectroscopy was performed using the Solartron 1287A in conjunction with a Solartron1260 FRA/ impedance analyzer. The samples were cycled 30 times between 0 to 2 V, during both CV and GC measurements, and then were treated at +2 V for 10 minutes prior to EIS testing. The applied AC voltage amplitude was of 10 mV.

Data reduction for the potentiostatic and complex impedance measurements was done according to [23] and [9] respectively. The volumetric capacitance is used since it only takes into account the device geometry. The equivalent circuit in Figure 1 was used to calculate the effect of bulk electrolyte using the Warburg open-end impedance to fit the arch data and reduce the fit error to less than 5%. In the circuit R_s , R_p , W_o and CPE are the contact series resistance, the parallel bulk resistance, the Warburg open-end impedance and the constant phase element respectively. The CPE is also composed of two parameters $CPE-T$ and $CPE-P$. That measures the CPE capacitance and its deviation from ideality. The equivalent series resistance is measured using the real part of the impedance Z' at $f=1000$ Hz and corresponds to the resistance produced by $R_s + R_p$.

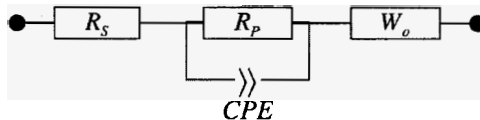


Figure 1 Equivalent circuit used to measure bulk effect of electrolyte.

2.3. Surface Area and Nitrogen Sorption Analysis

The nitrogen sorption was done using a NOVA 4200e. The total surface area (SA) was determined using the multi point BET method. The t-method was used to measure the micropore area and volume. Also the t-method was used to obtain the surface area of macropores (difference of external SA minus mesopore SA). The micropore size distribution was measured using the DA method [14]. For the mesopore volume and area the BJH method was used. The adsorption

isotherm was used in calculations due to the microporous nature of the samples and to avoid artifacts from the isotherm's hysteresis [15]. The surface area was modified from gravimetric to volumetric by multiplying the density of the electrodes. This allows for a direct comparison with the volumetric capacitance used in this study.

2.4. X-Ray Raman Scattering

To characterize the short-range order of the CC samples, non-resonant x-ray Raman scattering (XRS) measurements were performed with the LERIX facility [16] at sector 20-ID of the Advanced Photon Source at Argonne National Labs. Due to the use of high-energy (~10 keV) incident photons, XRS provides a bulk-sensitive alternative [17] to x-ray absorption spectroscopy and electron energy loss measurements for low-Z elements. All samples were measured in a transmission geometry while in hermetically-sealed containers with 25 mm thick kapton windows. The contamination of the C *K*-edge signal from the kapton windows was typically of order a few percent.

3. Results and Discussion

3.1. Morphology, feature production & measurements

The CC in this study forms glassy carbons that when pyrolyzed are known to have graphite like structure, or graphene ribbons, that have short range order but lack a long-range crystalline structure [18]. X-ray Raman scattering data supports this characteristic of the cryogels. The samples in this study all had the same X-ray spectrum as shown in Figure 2. The same was true of other samples included in the X-ray study that came from various sources (i.e. were pyrolyzed at various temperatures from 700 °C to 1200 °C and various activations). The samples are highly defective or have large amount of dangling bonds and have long C–C bond length. All carbons are sp^2 hybridized, which accounts for their conductivity [19] (see Figure 2). From the structural point of view the most important features are their short-range order, amorphous structure and the large amount of dangling bonds. During activation these features are responsible of producing selective areas in which new microporosity can form [20]. This effect can be seen in samples with the same chemical composition but different activations.

The activation as well as the chemical composition produces different structural properties that can be later related to their structure. The two most important structural parameters are the surface area, related to the charge

storage, and the pore size that limits the diffusion of the electrolyte. Samples with the same composition, C-36 and C-70, that have different levels of activation exhibit similar pore size while having varying pore volume and area [22]. This is seen in the isotherms of the two samples that have same shape but differ in the adsorbed volume see Figure 3. This is also the case in both the gravimetric and volumetric surface areas see Table 2 and 3. The pore size distributions of C-36 and 70 extend from 1.2 nm in the DA distribution until it vanishes at around 10 nm in the BJH distribution. Unfortunately, there is a gap between the micropore-mesopore regions of the pore size distributions. This gap is produced by the difference between the relative pressures used by the two methods ($DA < 0.1$ micropore filling and $BJH > 3.5$ capillary condensation). Figure 4 shows a portion of the BJH below the relative pressure of 3.5. Although this data is not accurate for pore size calculation provides an idea of how the method diverge into the micropore region < 2 nm. Moreover other micropore methods like the DR method that covers the remaining pressure range are not suitable for activated carbons [22]. This gap will prove to have distinct effects in the electrochemical properties of the material.

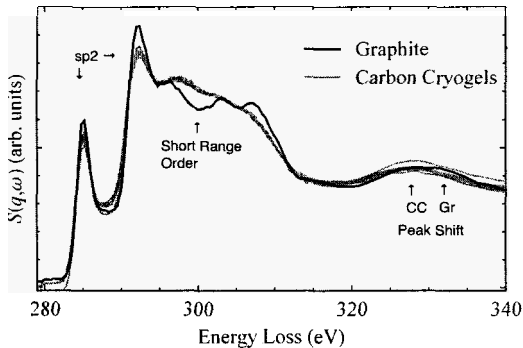


Figure 2 X-ray Raman scattering of carbon cryogels compared to graphite

On the other hand, the two samples with different chemical composition and same activation A-70 and C-70 had different pore size distributions in addition to surface area and volume. A-70 has mostly pores in the micropore region 80% in contrast to only 57% micropores in C-70. In addition the range of pore sizes has a narrower distribution, from 1.62 nm and covering a similar extent to C-36 and C-70 in the mesopore region as seen in Figure 4 B.

Macropores produced by the fine ground CC particles are also part of the electrode's pore structure. Tables 2 and 3 show the surface area produce by these particles that in most cases can exceed the surface area produced by the

mesopores themselves. These macropores have an influence the electrochemical properties of the bulk electrolyte.

Table 2 Gravimetric N_2 sorption characterization of micropores, mesopores and macropores in terms of their surface S , volume V , and pore diameter D

Sample ID	S_{BET} (m^2/g)	S_{Micro} (m^2/g)	V_{Micro} (cc/g)	D_{DA} (nm)	S_{Meso} (m^2/g)	V_{Meso} (cc/g)	S_{Macro} (m^2/g)
A-70	1814	1460	0.765	1.62	96	0.165	258
C-70	571	329	0.179	1.30	80	0.111	163
C-36	777	459	0.252	1.26	108	0.165	210

Table 3 Volumetric surface area and percent of micro, meso and macropores to the total area S_{BET}

Sample ID	S_{BET} (m^2/cc)	S_{Micro} (m^2/cc)	S_{Micro} (%)	S_{Meso} (m^2/cc)	S_{Meso} (%)	S_{Macro} (m^2/cc)	S_{Macro} (%)
A-70	653	526	80	34	5	93	14
C-70	553	319	58	77	14	157	28
C-36	754	445	59	105	14	204	27

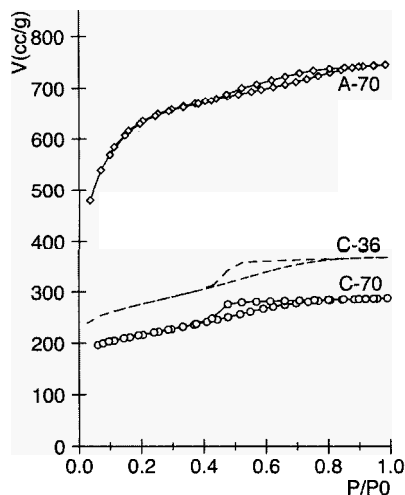


Figure 3 Isotherms of samples with various RC and activations.

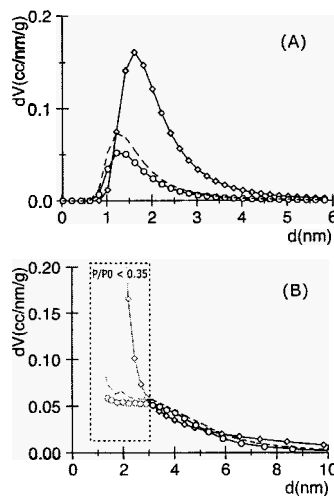


Figure 4 DA (A) and BJH adsorption (B) distributions.

3.2. Electrochemical analysis using potentiostatic and galvanostatic measurements

The effect of ion electrosorption at the interface of the CC porous network was measured using cyclic voltammograms and galvanic cycles at various rates and currents. Cyclic voltammetry has been used in the past to measure the influence of pore size in porous electrodes [23]. This is possible since the kinetics of

charge transfer and diffusion of the electrolyte are affected by confinement and are dependent of the voltage rate [23]. Three samples with distinct pore size distributions were tested at 100, 50 and 10mV/s. With each sample the capacitance increased with lowering voltage rate, Figure 5. A-70, a sample with mostly micropores and a pore diameter mode of 1.62 nm had almost constant capacitance regardless the rate (ca. 45F/cc). The samples C-70 and C-36 with pores between the meso and micropore regions had the largest increases in specific capacitance with decreasing voltage rate (26 - 34 F/cc and 53-71 F/cc respectively). In porous electrodes the capacitance is linearly dependent to $1/\sqrt{v}$ [23]. But, samples, C-70 and C-36, have non-linear behavior with multiple slopes, an indication that more than one type of charge diffusion mechanism is present (Figure 5 A). This effect is particularly strong in C-36, which has similar initial capacitance to C-70 (20 F/cc) at high voltage rate but increases to 71 F/cc at lower rates. This change in capacitance can be directly related to the morphology of these samples that have a higher percentage of mesopores compared to A-70 see Table 2 and 3. The pore size differences in these three samples limit the ability to transfer the charges. Therefore for samples with small micropores the charge can be harvested only at the low voltage rate. Conversely A-70 which have mainly SA derived from large micropores has a steady capacitance rate throughout the voltage rate provided. The galvanic cycles also supports the porous nature of the electrodes in their linear charge and discharge characteristic of transmission line systems, see Figure 5 B.

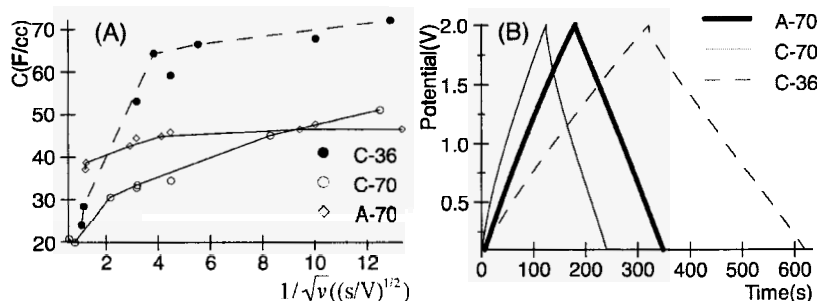


Figure 5 Volumetric capacitance as a function of $1/\sqrt{v}$; (A), data was measured using the galvanic cycle (connected points) and by cyclic voltammetry, (free points). Galvanic discharge of samples at 1mA, (B)

3.3. Electrochemical analysis using impedance measurements, complex capacitance and complex power

The bulk electrolyte properties were used as a measure of pore and particle morphology. Large voids in the electrode, from its porous structure or from the

particle constituents, can allow regions where the electrolyte molecules reorient with the AC signal producing a dielectric loss (energy absorption) at the high frequency range [5, 9]. Since the contacts are treated to reduce the bulk effect between the carbon electrode and the aluminum contact, it is assumed the bulk effect must come from the electrode's structure. The macropore surface area reported in Table 2 suggests significant amounts of such pores in the electrodes and its effect is seen in the response of the bulk electrolyte. All these samples have depressed Cole-Cole distributive elements. This is evident from the measurements of the constant phase element parameter $CPE-P$ that all have values below 1. In the case of a Cole-Cole CPE this indicate a distribution of relaxations [5], for the samples in this study is due to the effect that the pore size distribution has on the electrolyte's relaxation as seen in Table 4. The decrease in the $CPE-P$ value is also a sign of the widening of the distribution of relaxations and can be used to characterize the pore size. More data is needed to study macropore distribution.

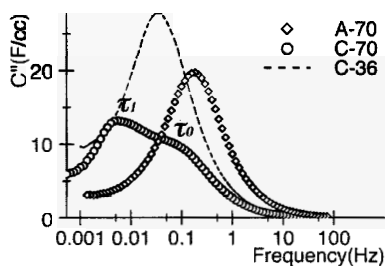


Figure 6 The imaginary part of the capacitance of samples A-70, C-70 and C-36

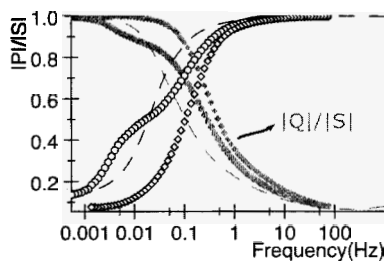


Figure 7 Reactive, $|Q|/|S|$, and active, $|P|/|S|$, power curves

Table 4 Relation between pore size, relaxation time, power dissipation and bulk properties

Sample ID	D_{DA} (nm)	f_0 (Hz)	τ_0 (s)	$ P / S $ @ 0.004Hz	ESR @ 1kHz (Ohms)	R_S (Ohms)	R_P (Ohms)	CPE-T (mF)	CPE-P
C-36	1.26	0.040	25.1	20%	11.53	1.8	11.40	1.18	0.31
C-70	1.30	0.100	10.0	36%	23.12	1.8	23.27	0.10	0.46
A-70	1.62	0.215	4.6	8%	5.00	3.6	1.58	1.46	0.56

The frequency response of the capacitors was studied using the complex volumetric capacitance separated into its real and imaginary components. Figure 6A is the imaginary capacitance and shows various peaks across the frequency spectrum. These capacitive peaks are related to the relaxation of the molecules adsorbed in the pores and are related to the energy loss of the capacitor at the low frequency range (linear elements in the Nyquist plot) [2, 9]. The sample A-

70 has a single distribution and show signs of pore exhaustion at the low frequency range as $\omega \rightarrow 0$ in Figure 6. Also, A-70's relaxation time, $\tau_o = 4.6$ s, correspond to its peak frequency. This is expected since this sample has mostly micropores in the 2 nm range as seen in Figure 4. In the cases of C-36 and C-70 a different behavior is observed. In C-36 the capacitance peak shows signs of additional processes (characterized by the leakage current [10, 11]) at lower frequencies and a single relaxation peak at $\tau_o = 25.1$ s. But in C-70, a bimodal capacitance distribution is seen and the relaxation peak at $\tau_o = 10$ s corresponds to the fastest relaxation peak in Figure 6. In addition a second slower relaxation peak is produced as well at $\tau_1 = 166$ s. According to the BET data these two samples have almost identical isotherms and distributions with the exception of the amount in micropores. It is possible that during the activation process of C-36 additional pores between the sizes reported by the DA and BJH were created. In C-70 the higher activation level likely widen some of the micropores in addition to remove the ones produced in the surface [22] of the CC particles at the C-36 activation leaving a bimodal distribution of pores and the peak separation in the imaginary capacitance. A more accurate measurement of the pore distribution will be required to determine their impact.

While the imaginary capacitance shows how the relaxation is affected by the various structures. The results from the complex power determine the impact of the pore size in the EDL capacitor's power performance. Figure 7 shows the normalized complex power in terms of Q (reactive) and P (active). Notice that all samples reach 1 (or 100%) reactive power indicating that have capacitor behavior but the active power P shows various degrees of dissipation indicating that the samples have a resistive element. This resistive element is also linked to the effect of small pore size in the dielectric losses of the CC electrode system. This resistive behavior is strongest in samples C-36 and C-70. Table 4 shows the evolution of this power dissipation at the frequency in which A-70 (sample with lowest relaxation time) reaches the pore exhaustion region. The power dissipation as well as the ESR rises with the decrease of micropore size. In general small pores contribute to the total capacitance, but the smaller pores in C-36 can be detrimental to the power production (see Table 5).

Table 5. Maximum capacitance C , energy E , and power P , using galvanic cycling at 2V and 1mA

Sample	C_V (F/cc)	C_G (F/g)	P_V Max (kW/cc)	P_G Max (kW/kg)	E_V Max (kWh/cc)	E_G Max (kWh/kg)
C-36	72	73	1060	1000	10.02	10
C-70	45	42	663	620	6.46	5.9
A-70	46	127	2660	22800	6.26	17

3.4. Dielectric constant and electrode characterization

Although, the capacitance, power, ESR and CPE can characterize the overall performance of EDL supercapacitors, these are not material properties of the system. Moreover what determines the frequency dependence of such elements in a capacitor is the dielectric constant $k = \epsilon/\epsilon_0$, an intensive physical property of the system dependent on the molecular relaxation τ_m and the applied signal frequency ω . The total capacitance $C = kC_0$ differs from the dielectric constant by C_0 the capacitance of the capacitor in vacuum a measurable quantity. Therefore, to better understand the role of morphology in the capacitor performance, the dielectric relaxation of the system should be studied in more detail. The Havriliak-Negami equation [6] a generalization of systems with multiple relaxations can be used as a starting point for future studies.

4. Conclusions

A relation between the CC supercapacitors morphology and its electrochemical properties has been demonstrated using various methods. The potentiostatic/galvanostatic measurements show that the structure of the samples is directly related to the charge storage. Also, the frequency response of the complex capacitance and power demonstrate the impact the pore size distribution in the capacitance and power of the device. Moreover, from the results it is evident that the micropore production has a sensitive region in which the capacitor's performance can be affected by the effect of dielectric losses in the CC/TEATFB electrolyte system. Most important the relevance of the structural properties in the performance is represented in the capacitance and figures of merit of the systems. The samples can achieve high specific capacitance per unit gram ca. 127 F/g and the sample C-36 had both high specific capacitance per unit gram and volume 73F/g and 72F/cc. The capacitance and power can be increased with the increase in surface area produced by small micropores but the size of such micropores can be also detrimental to achieve high power.

Although this study relies in an empirical description of the capacitance and power as it relates to the morphology of the CC electrodes, it can be a starting point for other studies. First, direct diagnostic method of supercapacitor performance. Second, provide an alternate method to electrochemical porosimetry. The latter can instead use dielectric relaxation methods, similar to Havriliak-Negami's equation for multiple dielectric relaxations, to study the effect of surface/ electrolyte interaction.

5. Acknowledgements

This work is supported in part by National Science Foundation (DMI-0455994 and DMR-0605159), Air Force Office of Scientific Research (AFOSR-MURI, FA9550-06-1-032), Washington Technology Center (WTC), and EnerG2 LLC.

References

1. J. G. Lee, J. Y. Kim and S. H. Kim, *J. Power Sources*, **160**, 1495 (2006).
2. H. K. Song, J. H. Jang, J. J. Kim and S. M. Oh, *Electrochem. Commun.*, **8**, 1191 (2006).
3. G. J. Lee, S. I. Pyun and C. H. Kim, *J. Solid State Electr.*, **8**, 110 (2004).
4. M. Itagaki, S. Suzuki, I. Shitanda, K. Watanabe and H. Nakazawa, *J. Power Sources*, **164**, 415 (2007).
5. E. Barsoukov and J. R. Macdonald, *Impedance Spectroscopy*, John Wiley and Sons, Inc (2005).
6. S. Havriliak and S. J. Havriliak, *Polymer*, **37**, 4107 (1996).
7. H. Sanabria and J. H. Miller, *Phys. Rev. E*, **74**, 9 (2006).
8. B. Batalla, G. Sinha and F. Aliev, *Mol. Cryst. Liq. Cryst. A*, **331**, 1981 (1999).
9. P. L. Taberna, P. Simon and J. F. Fauvarque, *J. Electrochem Soc.*, **150**, A292 (2003).
10. J. H. Jang, S. Yoon, B. H. Ka, Y. H. Jung and S. M. Oh, *J. Electrochem Soc.*, **152**, A1418 (2005).
11. J. H. Jang and S. M. Oh, *J. Electrochem Soc.*, **151**, A571 (2004).
12. R. W. Pekala, *J. Mater. Sci.*, **24**, 3221 (1989).
13. A. Feaver and G. Z. Cao, *Carbon*, **44**, 590 (2006).
14. H. F. Stoeckli, *Carbon*, **28**, 1 (1990).
15. G. Q. Lu and X. S. Zhao, *Nanoporous Materials – Science and Engineering*, Imperial College Press, London (2004).
16. T. T. Fister, G. T. Seidler, L. Wharton, A. R. Battle, T. B. Ellis, J. O. Cross, A. T. Macrander, W. T. Elam, T. A. Tyson and Q. Qian, *Rev. Sci. Instrum.*, **77**, 7 (2006).
17. U. Bergmann, P. Glatzel and S. P. Cramer, *Microch. J.*, **71**, 221 (2002).
18. S. R. P. Silva, *Properties of Amorphous Carbon*, INSPEC, London (2003).
19. J. Stöhr, *NEXAFS spectroscopy*, Springer-Verlag, Berlin (1992).
20. W. Daud, W. S. W. Ali and M. Z. Sulaiman, *J. Chem. Technol. Biot.*, **78**, 1 (2003).
21. A. Braun, M. Bartsch, B. Schnyder, R. Kotz, O. Haas and A. Wokaun, *Carbon*, **40**, 375 (2002).
22. S. Blazewicz, A. Swiatkowski and B. J. Trznadel, *Carbon*, **37**, 693 (1999).
23. B. Babic, B. Kaluderovic, L. Vracar and N. Krstajic *Carbon*, **42**, 2617 (2004).

SHAPED METAL OXIDE-PHOSPHATE COMPOSITE NANOPARTICLES SYNTHESIZED BY TEMPLATED DISASSEMBLY*

FAN LI, SARAH A. DELO, ANDREAS STEIN†

*Department of Chemistry, University of Minnesota, 207 Pleasant St. S.E.
Minneapolis, MN 55455, U.S.A.*

$\text{Al}_2\text{O}_3\text{-P}_2\text{O}_5$, $\text{ZrO}_2\text{-P}_2\text{O}_5$ and Au-doped $\text{TiO}_2\text{-P}_2\text{O}_5$ nanoparticles with cubic or rounded-cube shapes and uniform sizes were synthesized by combining templating and disassembly of sol-gel/surfactant precursors within the confinement of a well-ordered colloidal crystal template. The nanoparticles were not highly agglomerated. The undoped, as-synthesized materials were amorphous. Doping of the $\text{TiO}_2\text{-P}_2\text{O}_5$ system with Au clusters induced the formation of a crystalline anatase phase within the nanoparticles.

1. Introduction

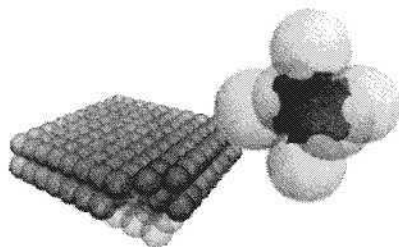
Interest in nanoparticles has escalated during the last few years, in part due to the unique optical, electronic, magnetic, reactive and structural properties at the nanometer size level. Although nanoparticle syntheses have been relatively well developed [1], sometimes researchers encounter a dilemma between simultaneous control over morphology and composition. Except for trivial spherical shapes, particle morphologies normally relate to the nature of the materials so that methods of shaping particles that have been developed for one composition may not be easily extendable to different compositions. As the compositional complexity increases, the functionality of nanoparticles may be enriched, but particle shape becomes even more difficult to predict and control. Therefore, methods for facile manipulation of both nanoparticle morphology and composition are highly desired for advanced applications of nanoparticles such as the fabrication of functional nanodevices.

Recently, we developed a templating approach, which promises to become a general way for preparing monodisperse, shaped nanoparticles [2]. In this

* This work is supported by the Petroleum Research Foundation administered by the American Chemical Society (ACS-PRF grant number 42751-AC10), the National Science Foundation (DMR-0704312), and in part by the MRSEC program of the NSF (DMR-0212302) which supports the University of Minnesota Characterization Facility.

† Corresponding author. Tel.: +1-612-624-1802, e-mail: stein@chem.umn.edu.

method, we use colloidal crystals as hard templates to sculpt particles. These colloidal crystals consist of uniform, close-packed spheres of sub-micrometer size. When prepared in highly ordered form, they are **polycrystalline** with face-centered cubic (**fcc**) symmetry [3]. After infiltration of these templates with appropriate precursors and removal of the template, features of the colloidal crystal are translated into an inverse replica, which consists of a solid network embedding interconnected air balls where the spheres existed originally. This structure is termed a "three dimensionally ordered **macroporous**" (3DOM) structure. The order and symmetry of the 3DOM structure are inherited from the original colloidal crystal, so that the 3DOM structure can be considered as built up from certain basic units. One of the building blocks derives from the octahedral voids surrounded by six spheres in the fcc colloidal crystals (Scheme 1), the other from smaller **tetrahedral** holes [2]. The truncated octahedral spaces have **cubic-like** shape. Therefore, once the 3DOM structure is disassembled, monodisperse nanocubes are obtained, together with smaller monodisperse spheres in a number ratio of 1:2. Such a disassembly process from the **kinetically stabilized** 3DOM structure to **thermodynamically favorable** particles can proceed spontaneously after being triggered by calcination.



Scheme 1. Schematic of **nanocube** formation within octahedral voids of a colloidal crystal.

Since the particle shape is dictated by the colloidal crystals in this templating process, the composition may be flexible. Herein, we report the preparation and characterization of Au cluster-doped $\text{TiO}_2\text{-P}_2\text{O}_5$ nanocubes in which the Au is evenly distributed within the oxide and influences the anatase crystallinity. We also show syntheses of $\text{ZrO}_2\text{-P}_2\text{O}_5$ and $\text{Al}_2\text{O}_3\text{-P}_2\text{O}_5$ nanoparticles following the same disassembly method.

2. Experimental

Monodisperse poly(methyl methacrylate) (PMMA) spheres were prepared by **emulsifier-free** emulsion polymerization of MMA (99%, Aldrich) [4]. A

colloidal crystal was formed through gravitational sedimentation of the spheres in a capped crystallization dish. Water was then removed via evaporation under ambient conditions. Afterwards the sample was cut into millimeter-size pieces for use as templates.

Metal alkoxide precursors were prepared as follows: in a vial, 0.50 g acetylacetone (*acac*) (>99%, Aldrich) was mixed with an appropriate amount of metal alkoxide (see Table 1), followed by the addition of 0.91 g triethyl phosphate (>99.8%, Aldrich). For the Ti sample, 0.20 g Au dispersion (prepared following a literature procedure that produces Au particles with average diameters of 12 nm [5]) was also added. This mixture (A) was stirred for 30 min with a magnetic bar. Meanwhile another mixture (B) of 1.37 g Brij 56 surfactant (C₁₆EO_n, $n \sim 10$) (Aldrich), 1.0 g *n*-propanol (Fisher), 0.20 g H₂O and 0.2 g HCl (37%, Mallinckrodt) was prepared. After homogenization, mixture B was added to mixture A dropwise under vigorous stirring. Depending on the nature of the alkoxide, some precipitation or gelation was initially observed, but the precursor mixture cleared partially after several hours of stirring. The clear supernatant was used for subsequent infiltration of the template.

Table 1. Information about the three metal alkoxides used in the nanocube syntheses.

Chemicals	Quantity (g)	Purity	Supplier
Titanium isopropoxide	2.930	97%	Aldrich
Zirconium butoxide	4.812	80% in BuOH	Aldrich
Aluminum <i>sec</i> -butoxide	2.462	98+%	Gelest

Infiltration of the precursor into colloidal crystals was performed in 12 mL glass vials, each containing several pieces of PMMA templates. The above mixture was added to the vials to allow the PMMA templates to be half-immersed in the solution. The precursor entered the voids in the template by capillary forces and infiltrated them thoroughly within hours, indicated by a color change of the non-immersed portions of the template. The template pieces were retrieved from the vials and extra precursor on the surface was wiped off with tissue paper. Then the template composites were sealed in a glass container, stored at 50 °C overnight and subsequently heated in flowing air (0.5 L/min) at 400 °C for 12 h to process the structure and to remove the polymer spheres and other organic components.

The sample morphologies (sizes and shapes) were characterized by electron microscopy. Scanning electron microscopy (SEM) images were taken using a JEOL 6700 field emission microscope (5 kV). A 5 nm-thick Pt coating was

applied to avoid charging effects. Low-magnification transmission electron microscopy (TEM) and selected-area electron diffraction (SAED) were performed on an FEI Tecnai T12 microscope (120 kV). Samples were sonicated for 20 min in ethanol and deposited onto a carbon-film-coated copper grid. High-resolution TEM (HRTEM) images were recorded on an FEI Tecnai G2 F30 TEM system (300 kV). The Au content was determined with a ThermoElemental PQ-ExCell quadrupole ICP-MS. X-ray diffraction (XRD) patterns were acquired using a Bruker AXS diffractometer.

3. Results and Discussion

To obtain the desired cubic nanoparticles, highly ordered colloidal crystals must be used as templates. A variety of methods deal with improving the order of colloidal crystals [6]. Here, highly ordered structures were obtained by very slow sedimentation of monodisperse PMMA spheres (ca. 378 nm) in a closed system with minimal perturbation. After one to several months, the sediment showed vivid opalescence in cross section as well as on the surface, indicating structural ordering on a bulk scale. Then the cap was removed partially and water was allowed to evaporate. This process is contrasted to sedimentation in an open system, where self-assembly occurs primarily at the water-air interface. In that case, only the near-surface areas are highly ordered whereas the bulky interior remains largely disordered.

The order in the colloidal crystal template was verified by SEM. Ordered packing is observed throughout the sample, as exemplified in Figure 1. It has been demonstrated that these types of colloidal crystal have mainly fcc symmetry mixed with some hexagonal close packing (hcp) [3]. Here, we did not attempt to differentiate between these two symmetries, as the product of cubic nanoparticles can be formed from templates with both hcp and fcc packing.

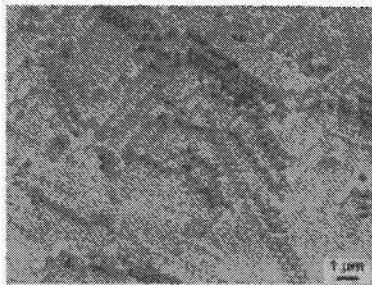


Figure 1. SEM image of the PMMA template.

Through the templated-disassembly process, Au cluster-doped $\text{TiO}_2\text{-P}_2\text{O}_5$ nanoparticles were formed. This process required the presence of phosphorus oxide within a limited ratio of metal:P. The ratio provided in the experimental section produced the well-shaped particles. Figure 2a is a TEM image of several nanocubes. These particles still possess slightly protruding corners, remains from connecting bridges in the original extended 3DOM framework. The average edge length of the cubes is ca. 100 nm, when PMMA spheres with 378 nm diameters are used in the template. The geometrical relationship between the initial colloidal crystal template and the isolated particles has been discussed previously [2]. A cube originates from an octahedral void surrounded by six spheres in octahedral coordination, so the theoretical ratio between the diameter of the PMMA sphere and the edge length of the cube is calculated to be 1:0.51. However, the actual cube size is usually much smaller, indicating that shrinkage occurred during processing. Such shrinkage is believed to be the driving force for this disassembly process.

The extent of Au doping in the particles was evaluated by TEM (Figure 2b). The Au clusters are evenly dispersed inside the cubes without any observable agglomeration. This pattern results from the fact that Au particles, once dispersed in the titania sol, are trapped in their positions by gelation, and eventually distributed throughout the $\text{TiO}_2\text{-P}_2\text{O}_5$ cubes. Elemental analysis revealed an Au content of 1.95×10^{-3} wt% in the sample. Although the doping level is quite low, it significantly enhances the crystallinity of the TiO_2 phase in the material compared to undoped samples [7]. Highly ordered, poly-crystalline regions can be clearly observed inside Au- $\text{TiO}_2\text{-P}_2\text{O}_5$ particles under HRTEM (Figure 2c), and the SAED image (Figure 1c inset) shows strong diffraction rings indexed to the anatase phase of TiO_2 , indicating that phosphorus oxide is present as a separate phase. Previously we found that the crystallinity of TiO_2 in $\text{TiO}_2\text{-P}_2\text{O}_5$ cubes can be adjusted by the amount of H_2O [7]. Here, although a small amount of H_2O was also introduced with the Au dispersion, the crystallinity enhancement can be unambiguously attributed to the effect of Au nanoparticles. A comparison of XRD patterns (Figure 2d) of Au- $\text{TiO}_2\text{-P}_2\text{O}_5$ and $\text{TiO}_2\text{-P}_2\text{O}_5$ made with a similar amount of H_2O clearly shows the difference: much stronger diffraction peaks were present in the pattern of the Au-doped sample. Similar enhancement of TiO_2 crystallinity by Au-doping has been observed before, but the mechanism is still under discussion [8]. Therefore, it is not clear whether this crystallinity induction can be applied to other systems. Nevertheless, the Au/anatase nanocomposite system is a promising candidate for

applications in photocatalytic processes that rely on collaborative effects between Au clusters and anatase TiO_2 [9].

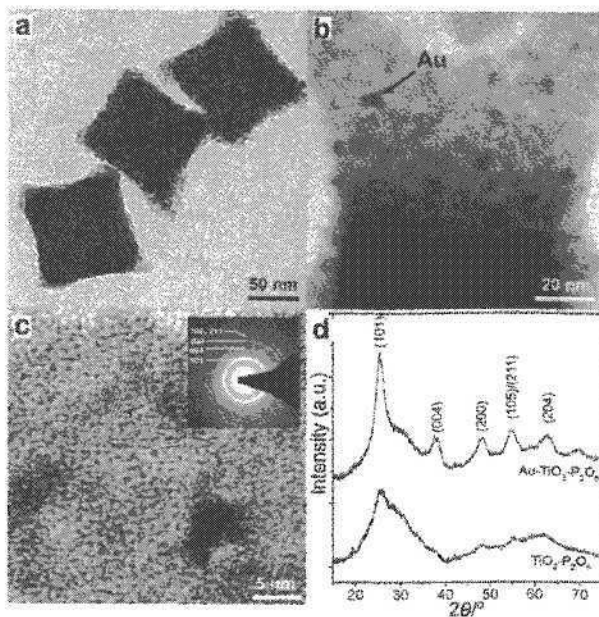


Figure 2. Electron micrographs and diffraction patterns of Au-doped $\text{TiO}_2\text{-P}_2\text{O}_5$ nanoparticles: (a) TEM image of cubic nanoparticles. (b) TEM image showing Au clusters embedded in the $\text{TiO}_2\text{-P}_2\text{O}_5$ matrix. (c) HRTEM image of crystalline TiO_2 regions (inset: SAED pattern). (d) A comparison of XRD patterns between Au-induced crystallinity and the effect by a similar amount of H_2O present in the synthesis. The top trace corresponds to the sample containing Au clusters, the bottom trace to the sample without Au. Indexed lines correspond to the anatase phase.

We further extended the alkoxide-based sol-gel disassembly method to preparations of $\text{ZrO}_2\text{-P}_2\text{O}_5$ and $\text{Al}_2\text{O}_3\text{-P}_2\text{O}_5$ nanoparticles. Zirconium butoxide and aluminum *sec*-butoxide were used in the precursor mixtures. Although these reagents were more reactive than titanium isopropoxide, the procedures were largely similar to those used for the $\text{TiO}_2\text{-P}_2\text{O}_5$ system, except that more extensive precipitation occurred during mixing and longer stirring times were needed to re-dissolve most of the precipitate.

SEM and TEM images of the $\text{ZrO}_2\text{-P}_2\text{O}_5$ product show discrete nanoparticles after calcination (Figure 3). Although most of the particles derived from octahedral holes have cubic shapes, their corners are more rounded than those of the titania-based products. The same observations apply to $\text{Al}_2\text{O}_3\text{-P}_2\text{O}_5$

nanoparticles, whose morphologies are shown in the SEM and TEM images in Figure 4. In this case the rounding effect is so acute that some particles almost appear spherical, in particular in the TEM image. The rounding effect is attributed to minimization of surface energies during sample processing. It is composition-dependent and tends to be more pronounced for small particles [7]. Due to a relatively small atomic number of Al, the $\text{Al}_2\text{O}_3\text{-P}_2\text{O}_5$ nanoparticles show less contrast in the TEM image (Figure 4b). Overlapping regions between adjacent particles can be clearly seen, but particles remain disconnected from each other, indicating that the degree of agglomeration among these particles is low as in the other two samples.

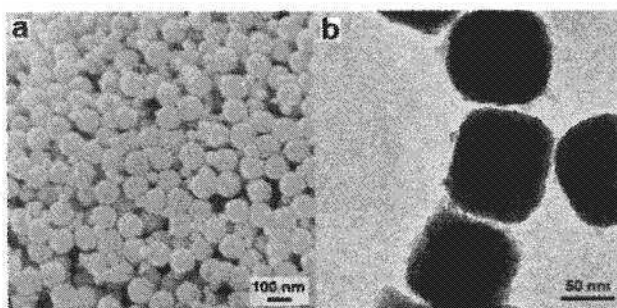


Figure 3. SEM (a) and TEM (b) micrographs of $\text{ZrO}_2\text{-P}_2\text{O}_5$ nanoparticles. The larger cubes arise from octahedral holes in the template, the smaller spheres from tetrahedral voids after some sintering.

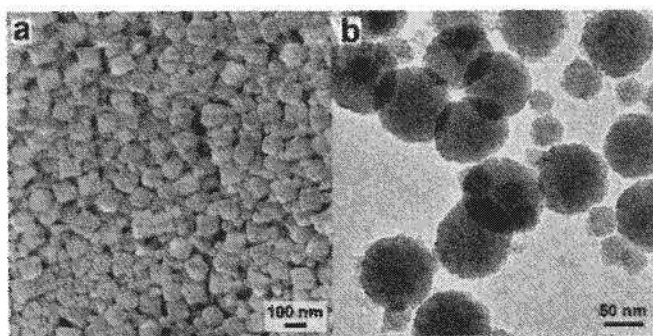


Figure 4. SEM (a) and TEM (b) micrographs of $\text{Al}_2\text{O}_3\text{-P}_2\text{O}_5$ nanoparticles.

The $\text{ZrO}_2\text{-P}_2\text{O}_5$ and $\text{Al}_2\text{O}_3\text{-P}_2\text{O}_5$ samples are mainly amorphous, based on both HRTEM and power XRD data. This is consistent with the amorphous nature of a $\text{TiO}_2\text{-P}_2\text{O}_5$ sample prepared under similar conditions [7].

4. Conclusions

In conclusion, we described herein syntheses of monodisperse Au-doped $\text{TiO}_2\text{-P}_2\text{O}_5$, $\text{ZrO}_2\text{-P}_2\text{O}_5$ and $\text{Al}_2\text{O}_3\text{-P}_2\text{O}_5$ nanocubes and rounded cubes following a templated disassembly strategy. The Au nanoclusters in the $\text{TiO}_2\text{-P}_2\text{O}_5$ matrix are evenly distributed and significantly enhance the crystallinity of anatase TiO_2 . These nanoparticles may have applications in the fields of sensing, nanoelectronics, catalysis, photonics and other uses. Through this study we have demonstrated the flexibility of the disassembly method for the preparation of nanoparticles with cubic shapes. We believe that in the future, more compositions and complex structures can be realized through disassembly, and this may benefit the design of functional materials in the nanosize regime.

Acknowledgments

The authors thank Rick A. Knurr for elemental analysis.

References

1. C. Burda, X. Chen, R. Narayanan, and M. A. El-Sayed, *Chem. Rev.* **105**, 1025 (2005).
2. F. Li, Z. Wang, and A. Stein, *Angew. Chem., Int. Ed.* **46**, 1885 (2007).
3. H. Miguez, F. Meseguer, C. Lopez, A. Mifsud, J. S. Moya, and L. Vazquez, *Langmuir* **13**, 6009 (1997).
4. R. C. Schrodien, M. Al-Daous, S. Sokolov, B. J. Melde, J. C. Lytle, A. Stein, M. C. Carbajo, J. T. Fernandez, and E. E. Rodriguez, *J. Mater. Chem.* **12**, 3261 (2002).
5. Y. Kang, T. A. Taton, *Angew. Chem., Int. Ed.* **44**, 409 (2005).
6. Y. Yin and Y. Xia, *Adv. Mater.* **13**, 267 (2001).
7. F. Li, S. A. Delo, and A. Stein, *Angew. Chem., Int. Ed.* **46**, 6666 (2007).
8. N. Perkas, V. G. Pol, S. V. Pol, and A. Gedanken, *Cryst. Growth Des.* **6**, 293 (2006).
9. N. Weiher, A. M. Beesley, N. Tsapatsaris, L. Delannoy, C. Louis, J. A. van Bokhoven, and S. L. M. Schroeder, *J. Am. Chem. Soc.* **129**, 2240 (2007).

METAL OXIDE NANOPARTICLES AS BUILDING BLOCKS FOR PERIODIC MESOPOROUS MATERIALS: APPLICATION IN NANOTECHNOLOGY

CARMELA APRILE, MERCEDES ALVARO AND HERMENEGILDO GARCIA

Departamento de Química and Instituto Universitario Mixto de Tecnología Química Csic-Upv, Camino De Vera S/N 46022, Valencia, Spain. Fax: 0034-963877809. Tel: 0034-963877807. Hgarcia@gim.upv.es

Starting from colloidal suspension of metal oxide nanoparticles (3-5 nm), such as TiO₂, Fe₃O₄, CeO₂ and SnO₂, different periodic mesoporous solids have been prepared. The structure was confirmed by transmission electron microscopy and X ray diffraction, pore volume and BET surface area going from 99 to 429 m²/g. All the synthesized materials have been applied in photochemistry and nanotechnology exhibiting in some cases unique properties compared to the unstructured nanoparticles, these specific properties arising from the large surface area and accessibility of the sites.

1. Introduction

Since the first report from Mobil [1,2] describing the synthesis of mesoporous materials, a large number of publications has focused on developing different synthetic strategies in order to prepare new generations of structured silicates including metallo- and organosilicas [3-5]. In the case of mesoporous metal oxides, the interest arises from the possibility of combining the intrinsic properties of the unstructured metal oxide with the additional features of a periodic mesoporous solid. It is known that most of the potential applications of the resulting materials (photocatalysis, solar cells, photochromism, sensing, and other applications in nanotechnology) are largely dependent on porosity, total surface area, structural uniformity and particle size [6].

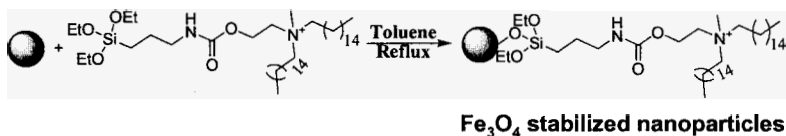
A general strategy to obtain periodic mesoporous metal oxides consists of a template-mediated synthesis starting from a molecular precursor containing a single metal atom. The main problem of this strategy is the poor thermal and hydrothermal stability of the resulting porous metal oxide [3,7]. This unsatisfactory structural stability is assumed to arise from the thin wall thickness, a cross section of the wall being constituted by only a few metal atoms. An alternative to overcome this instability could be by the direct structuring of small metal oxide nanoparticles forming the channels of the mesopores. In this case the nanoparticles constitute the real building blocks and can be used in combination

with, or as an alternative to, molecular precursors containing a single metal atom.

In this work we report the synthesis of a series of mesoporous materials partially or totally constituted by metal oxide nanoparticles such as CeO_2 [8], Fe_3O_4 [9], TiO_2 [10] and SnO_2 and their potential in different fields going from catalysis to nanotechnology.

2. Results and Discussion

Metal oxide nanoparticles with a size distribution between 3 and 5 nm, were prepared following the methods described in the literature for each metal oxide [11-13]. In the case of iron oxide, before proceeding to the synthesis of the mesoporous material, we anchored covalently, through the terminal OH groups, a triethoxysilane having a quaternary ammonium ion in its structure. The idea behind the design of this molecule was to obtain a compound that on one hand can stabilize the iron nanoparticles and co-condense with the triethylorthosilicate (TEOS) during the following step and on the other hand it should favor, through the presence of the alkyl ammonium salt, the hydrophobic interaction with the cetyltrimethylammonium bromide (CTABr) used as structure directing agent. In this way we were able to arrange spatially the metal nanoparticles forming a mesoporous material. The synthesis of the functionalized iron nanoparticles is presented in Scheme 1.



Scheme 1. Preparation of functionalized Fe_3O_4 nanoparticles.

In the other cases (TiO_2 , CeO_2 and SnO_2) we have used directly unfunctionalized metal oxide nanoparticles as building block for the structured solid. All the materials have in common that the particles constitute the walls of the mesoporous structured material.

Figure 1 shows two transmission electron microscopy (TEM) images recorded in dark and bright field for SnO_2 in which the nanometric size of the particles used to form mesoporous tin oxide can be seen.

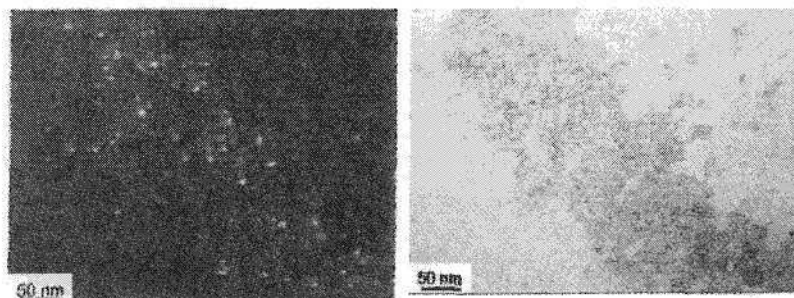
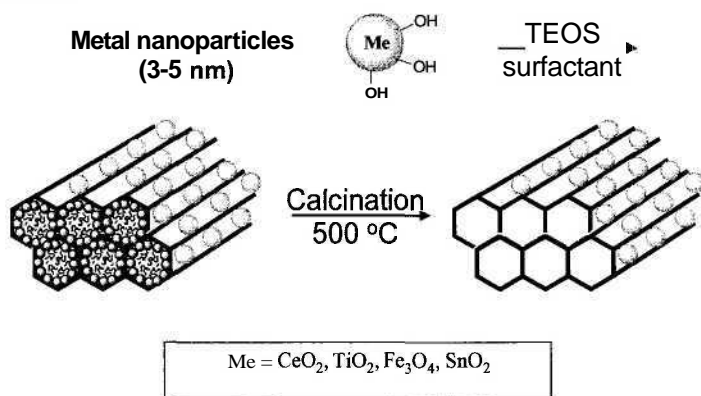


Figure 1. Dark and bright field TEM images of the SnO_2 nanoparticles used as building blocks in this work.

Metal nanoparticles were used in combination with TEOS and different structure directing agents (cetyltrimethylammonium bromide or Pluronic triblock copolymer) to obtain the structured material. Scheme 2 illustrates the general strategy followed for the preparation of the mesoporous solids. The synthesis conditions are analogous to those commonly used for mesoporous MCM-41 and SBA-15 silicas. The structure of the mesoporous materials was confirmed by isothermal gas adsorption, transmission electron microscopy, and X-ray diffraction.



Scheme 2. General strategy to synthesize structured mesoporous metal oxides from metal oxide nanoparticles.

The list of some of mesoporous metal oxides materials studied and the most relevant analytical and porosity data are given in Table 1.

Table 1. Mesoporous metal oxides prepared with the concept of scheme 2 with indication of the structure directing agent employed in the synthesis and their analytical and porosity data. For the detailed synthetic conditions see references 8, 9 and 10.

	Template	MeO ₂ /TEOS content (wt%)	Pore Size (Å)	BET Surface area (m ² /g)
mpTiO ₂ -50	CTABr	50/50	31	238
mpTiO₂-100	CTABr	99/1	86	99
mpSnO ₂ -50	CTABr	50/50	33	317
mpSnO ₂ -100	CTABr	99/1	47	70
mpCeO ₂ -100	Pluronic P123	100/0	75	160
mpFe ₃ O ₄ -20	CTABr	20/80	36	429

Powder X-ray diffraction (XRD) of all the samples before and after calcination at 500 °C exhibit peaks at 2θ value corresponding to the d_{100} , d_{200} and d_{110} of MCM-41 or SBA-15 like materials with a hexagonal arrangement. Two examples corresponding to mpFe₃O₄-20 and mpSnO₂-50 are shown in Figure 2. As it can be seen there and as a general rule of thumb, even though the most intense d_{100} peak was always observed in all the XRD patterns, increasing the ratio of metal oxide nanoparticles vs. TEOS in the synthesis gel reduces the intensity and resolution of the XRD pattern.

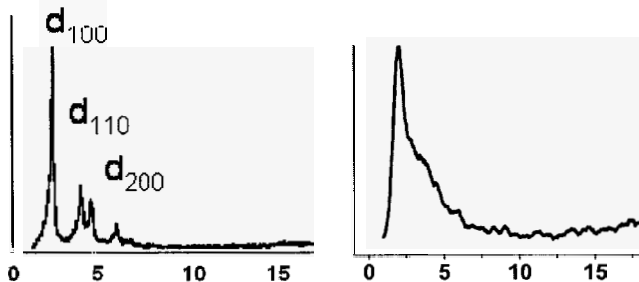


Figure 2. XRD patterns of mpFe₃O₄-20 (left) and mpSnO₂-50 (right)

In the case of CeO₂, the nanoparticles were self-assembled in the presence of Pluronic P123 as structure directing agent. For the mesoporous titanium dioxide solids (mpTiO₂), Raman spectroscopy was used to determine the anatase/rutile percentage because it is known that the photocatalytic activity is largely dependent on the anatase content. As anticipated in view of the phase

composition of the starting TiO_2 nanoparticles, Raman spectroscopy of the calcined mpTiO_2 solids confirmed the exclusive presence of anatase phase. As shown in Figure 3, the spectrum of mpTiO_2 -100 (shown as a representative example of the titanium series), matches very well with the characteristic peaks of anatase crystal phase (139, 389, 508, 634 cm^{-1}). In general, the pore diameter of mpTiO_2 ranged between 31 and 86 nm, and the BET surface area varied between 99 and 429 $\text{m}^2 \text{g}^{-1}$.

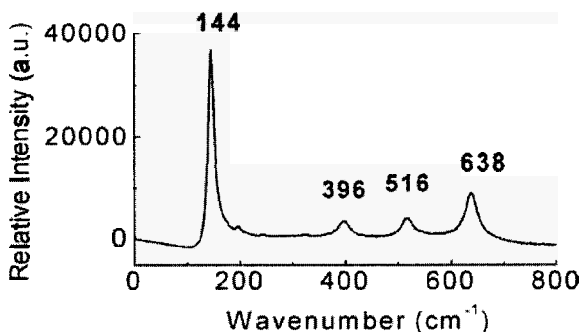


Figure 3. Raman spectra recorded for mpTiO_2 -100.

3. Applications

The photochemical behaviour of mpTiO_2 materials [10] was tested for the photodegradation of phenol in aqueous solutions. The disappearance of the organic compound in the reaction mixture was followed at different irradiation times and in presence of various titania samples. The main parameters used to characterize the photocatalytic performance of the materials were the initial degradation rate (r_0 , slope of the phenol disappearance vs. time plot at zero time) and the phenol degradation percentage after 3 h irradiation (initial phenol concentration minus the concentration at 3 h divided by the initial concentration, Table 2). We also calculate the turnover frequency (TOF, $\text{mol of degraded phenol} \times \text{mol of titania}^{-1} \times \text{h}^{-1}$). Initial reaction rate (r_0) and TOF are the parameters normally used in catalysis to determine the average intrinsic activity per site. The phenol solution in absence of photocatalyst and the same water mixture in the presence of MCM-41 silica were used as blank controls. The results were compared with the activity of P25 taken as a photocatalyst standard.

Table 2. Comparison of the photocatalytic activity of different mpTiO₂ materials and P25 measured as initial reaction rate (r_0) and final degradation at 3 h.

	r_0 (% min ⁻¹)	Final Degradation (%)	TOF r_0 /ti content
mpTiO ₂ -5	0.47	42	24.74
mpTiO ₂ -50	0.65	62	3.47
mpTiO ₂ -100	1.05	83	2.84
P25	4.01	100	10.69
MCM-41	0.1	9	--

We found that mesoporous materials with low titania content have the highest TOF value, about two and four times higher than that of P25 for structured MCM-41-like and SBA-15-like materials, respectively [10]. However, increasing the titania content of the mpTiO₂ solid reduces the TOF for phenol degradation. Thus, mpTiO₂ materials with low Si content have a final degradation percentage comparable with commercial P25 TiO₂, but the photocatalytic activity is about four times lower than P25. Since the TOF value represents the activity per site (titanium atom), we attribute this behavior to the better accessibility of all titanium atoms and isolation of the titania domains in the mpTiO₂ materials with low titanium content.

In the case of mpFe₃O₄ materials [9], we studied their magnetic response by measuring the magnetic susceptibility in continuous and alternating field. To confirm the ferromagnetic response, we also performed hysteresis measurements at about ambient temperature. We found that even at 20 wt % of iron oxide nanoparticles dispersed in structured silica domains the mpFe₃O₄ exhibits a ferromagnetic response and a long-range ordering confirmed by the fast increasing of the magnetization and by the fact that it reaches the saturation very rapidly even with very low applied magnetic fields. The hysteresis cycles show that mpFe₃O₄ is a soft magnet with a very low coercive field of ca. 1.5 mT in the temperature range between 300 and 400 K. Moreover, the magnetic nature of this material is also visually demonstrated by the strong attraction of the powder to magnetic bars.

An important application of the magnetic properties of the iron nanoparticles used as building blocks for the preparation of mpFe₃O₄ materials is the preparation of oriented films with the axes of the channels perpendicular to the surface. Preparation of these oriented films was accomplished by performing the

synthesis of the **mesoporous** solid in the presence of a magnetic field. The ordering was confirmed by transmission electron microscopy (TEM) and atomic force microscopy (AFM) experiments (Figure 4). From the examination of both kinds of images we conclude that the prepared films, even presenting terraces and a non-flat texture, show the entire pore opening perpendicularly to the surface. Figure 4 right shows that the pore openings of an oriented film of Fe_3O_4 are perpendicular to the surface.

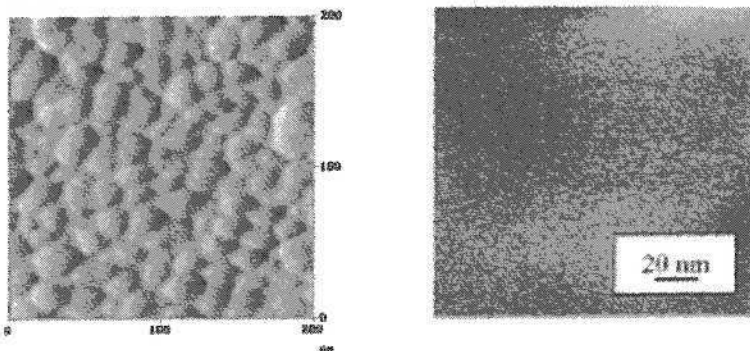


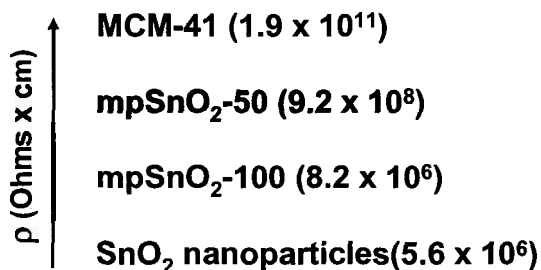
Figure 4. AFM (right) and TEM (left) of a mpFe_3O_4 film showing that all the pore opening are oriented perpendicularly to the surface.

Structured mesoporous cerium dioxide [8] was used with the objective of increasing the efficiency of the semiconductor solar cells normally based on TiO_2 . It is known that micrometric CeO_2 particles behave as insulator, but upon decrease of the particle size to the **nanometric** range, CeO_2 becomes semiconductor due to the creation of a large percentage of oxygen lattice defects. In addition, for solar cell applications it is necessary that the absorption spectrum of the photoactive component coincides as much as possible with the solar emission spectrum. Titanium dioxide can only absorb light of wavelength shorter than 350 nm and for this reason it is doped with organic or metallic compounds to red-shift the absorption spectrum. However, the presence of a dopant in a solar cell may limit the efficiency of charge separation due to the creation of hole and electron recombination centers. Also the long term stability of the device can increase if the semiconductor absorption spectrum absorbs in the solar emission spectrum since otherwise the presence of organic dyes is necessary and most of them tend to become degraded upon continuous operation of the cell.

In the case of CeO_2 **nanoparticles**, the absorption spectrum is **redshifted** about 80 nm as compared to TiO_2 , which gives a considerably better response in the visible region of the solar spectrum without the addition of an external dye. The bandgap of

the CeO₂ nanoparticles estimated from the onset of the absorption spectrum was 3.0 eV. The efficiency of a series of solar cells constructed with mpCeO₂ using I⁻/I₃⁻ as electrolyte and ITO and platinumized Al electrodes was tested under standard conditions [8]. The behavior of the nanostructured ceria oxide was compared with unstructured CeO₂ nanoparticles and with P25 under the same experimental conditions. We note that the photovoltaic behaviour of nanocrystalline CeO₂ is different from that of bulk CeO₂. A possible explanation is that the high surface/grain-boundary area characteristic of nanocrystals increases considerably the presence of defects that enhance the electronic transport properties of sintered nanocrystalline CeO₂ with respect to that of bulk ceria.

It is well known that, for its unique characteristic, tin oxide is a material with application in gas sensing [14], catalysis [15], electrochemistry [16], and optoelectronic devices [17]. Most of the important properties of SnO₂ derive from its behaviour as wide-band gap semiconductor. Therefore, both size and morphology of SnO₂ grains play a determinant role on the performance of SnO₂. For this reason we synthesized mesoporous mpSnO₂ materials constituted by tin oxide nanoparticles and test their conductive response [18]. The performance of mpSnO₂ was compared with that of commercial tin oxide nanoparticles and plain MCM-41 silica. The resistivity of the materials as function of the applied voltage



Scheme 3. Ordering of a series of materials according to their resistivity in measured in micrometric films under 785 N pressure.

was measured and the mean value between 1 and 3 V was calculated for all the samples (Scheme 3). It was observed, as expected, that the resistivity of mpSnO₂-100 is lower than mpSnO₂-50, reaching a conductivity that makes this mesoporous solid a promising conducting material

Figure 5 shows a comparison of the electrical properties between commercial tin oxide nanoparticles and the nanostructured solid mpSnO₂-100.

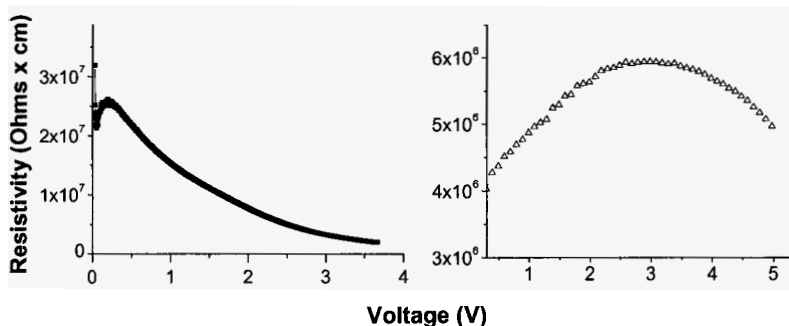


Figure 5. Resistivity vs applied voltage for the mpSnO₂-100 (on the left) and commercial SnO₂ nanoparticles (on the right).

These measurements show that the ordered mpSnO₂-100 has a conductivity comparable with the commercial nanoparticles, but a higher surface area and pore volume due to the special ordering than can be used to include in the internal void conductive polymers (such as PPV) favoring the current flow from external electrodes to the incorporated guests. Further studies are focused on the optimization of the synthesis of these hybrid semiconductive materials and also on the preparation of oriented films.

In conclusion, herein we have illustrated the importance of having metal oxide nanoparticles ordered in a mesoporous solid. The increase of the surface area and of the stability of the materials are determinant factors that contribute to the observed performance. As shown, the range of application of these materials is very large and covers many different fields.

Acknowledgements

Financial support by the Spanish DGI is gratefully acknowledged. CA also thanks the Spanish Ministry of Science and Education for a Juan de la Cierva research associate contract.

References

1. C. T. Kresge, M. E. Leonowicz, W. J. Roth, J. C. Vartuli and J. S. Beck, *Nature* **359**, 710 (1992).
2. J. S. Beck, *J. Am. Chem. Soc.* **114**, 10834 (1992).
3. S. Biz and M. L. Occelli, *Catal. Rev. - Sci. and Eng.* **40**, 329 (1998).

4. R. Ryoo, J. M. Kim and C. H. Ko, *Stud. Surf. Sci. Catal.* **117**, 151 (1998).
5. F. Hoffmann, M. Cornelius, J. Morell and M. Froeba, *J. Nanosci. Nanotech.* **6**, 265 (2006).
6. S. Foerster and M. Antonietti, *Adv. Mater.* **10**, 195 (1998).
7. M. Hartmann, *Angew. Chem., Int. Ed.* **43**, 5880 (2004).
8. A. Corma, P. Atienzar, H. Garcia, and J.-Y. Chane-Ching, *Nature Mater.* **3**, 394 (2004).
9. M. Alvaro, C. Aprile, H. Garcia and C. J. Gomez-Garcia, *Adv. Funct. Mater.* **16**, 1543 (2006).
10. M. Alvaro, C. Aprile, M. Benitez, E. Carbonell and H. Garcia, *J. Phys. Chem. B* **110**, 6661 (2006).
11. E. Katz, L. Sheeney-Haj-Ichia and I. Willner, *Chem.-A Euro. J.* **8**, 4138 (2002).
12. M. Addamo et al. *J. Phys. Chem. B* **108**, 3303-3310 (2004).
13. J. Ba, J. Polleux, M. Antonietti and M. Niederberger, *Adv. Mater.* **17**, 2509 (2005).
14. G. Gaggiotti, A. Galdikas, S. Kaciulis, G. Mattogno and A. Setkus, *J. Appl. Phys.* **76**, 4467 (1994).
15. Y. Zhang, A. Kolmakov, Y. Lilach and M. Moskovits, *J. Phys. Chem. B* **109**, 1923 (2005).
16. Y. Idota, T. Kubota, A. Matsufuji, Y. Maekawa and T. Miyasaka, *Science* **276**, 1395 (1997).
17. A. Andersson et al. *Adv. Mater.* **10**, 859 (1998).
18. M. Alvaro, C. Aprile, D. Fabuel and H. Garcia, *Unpublished Results*.

RESPONSIVE NANOPOROUS ORGANIC-INORGANIC COLLOIDAL FILMS*

ANDREW K. BOHATY, JULIE CICHELLI, OLGA SCHEPELINA,
AND ILYA ZHAROV

*Department of Chemistry, University of Utah, 315 South 1400 East
Salt Lake City, UT 84112, USA*

Nanoporous colloidal films form via self-assembly of nanoscale-sized silica spheres into a close-packed face-centered cubic lattice and contain highly ordered arrays of three-dimensional interconnected pores 5-100 nm in size. We modified the surface of colloidal nanopores with organic moieties whose charge and shape respond to external stimuli, such as pH, light or temperature. As a result of the surface modification, we were able to control the molecular transport through the colloidal nanopores by changing the environmental conditions.

1. Introduction

Nanoporous membranes have attracted attention in fundamental research and technology [1-3]. Single synthetic nanopore structures [4] have been synthesized at the nanometer scale using carbon nanotubes [5], by top-down techniques [6-8] using protein channels (both natural and engineered) in lipid bilayers [9-11], and have been used in DNA studies and stochastic sensors. Films and membranes with multiple nanopores have been made in polycarbonate by track-etching and were further modified by wall-activating glow discharge [12] or gold-plating [13]. Nanoporous membranes have been also prepared using polymeric [14], zeolites [15], silicon nitride [16,17], silica [18], alumina [19,20], and using nanotubes [21,22].

Responsive and selective nanoporous membranes have been prepared by surface modification of Au-plated track-etched polycarbonate membranes [23-25] and by placing ultrathin organic films over the openings of inorganic nanopores [26,27]. Transport selectivity has been built into micron-sized pores using grafted molecules that respond to environmental stimuli [28-30].

The focus of our work is on silica colloidal films and membranes whose surface is modified with organic moieties to render them responsive in a way similar to that described for polymeric materials [31]. Silica colloidal crystals

* This work is supported by an NSF CAREER Award and Dreyfus Foundation New Faculty Award.

comprise a close-packed face-centered cubic (fcc) lattice of silica spheres of a sub-micrometer diameter (Figure 1) with ordered arrays of nanopores [32]. The preparation of silica spheres (1, Scheme 1) is straightforward [33], self-assembly of the spheres is well developed [34], and pore size in the crystals can be readily controlled by selecting the sphere size (the distance from the center of the nanopore to the nearest silica sphere surface is ca. 15% of the sphere radius). Surface silanol groups can be directly modified by nucleophilic silylation to introduce a variety of functional groups [35]. Alternatively, silica surface can be first modified with 3-aminopropyl-triethoxysilane (2, Scheme 1), followed by treatment with organic molecules carrying electrophilic moieties such as acyl chloride, isocyanate, isothiocyanate, carboxylic acid, sulfonyl chloride [36], or succinimidyl ester [37].

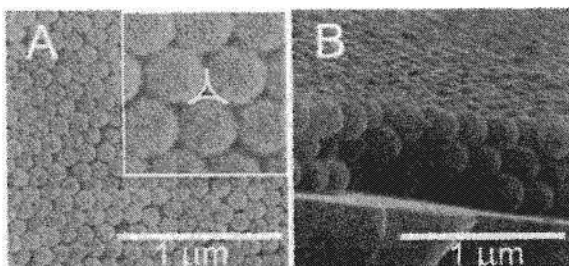
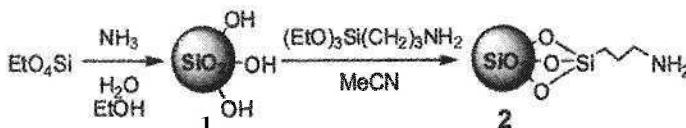


Figure 1. SEM images of the chemically-modified opal prepared from 440 nm diameter silica spheres (A) top view, the geometric projection of a pore observed from the (111) plane is outlined in the inset. (B) Side view. (C) Scheme of a permselective colloidal membrane.



Scheme I. Preparation and surface amination of silica spheres.

An important advantage of using colloidal crystals as nanoporous membranes is their highly ordered nature, which allows creating accurate mathematical descriptions of transport rates [38-42]. The effective diffusivity of molecules in the fcc lattice D_{fcc} , can be expressed as $(\epsilon/\tau)D_{sol}$, where D_{sol} is the diffusivity of molecules in free solution, the void fraction ϵ (0.26) and the tortuosity τ (~ 3.0) are intrinsic geometrical parameters independent of the size of the silica spheres used to prepare the colloidal crystal. An estimate of the molecular flux J_{fcc} can be obtained using equation (1) [38], where AC is the

concentration gradient and L is the thickness of the membrane [38]. For a typical D_{sol} of $10^{-5} \text{ cm}^2\cdot\text{s}^{-1}$, L of $10 \text{ }\mu\text{m}$, and ΔC of 10 mM , J_{fcc} is $\sim 10^{-8} \text{ mol/cm}^2\cdot\text{s}$. This is several orders of magnitude higher than the molecular fluxes reported for polycarbonate membranes with cylindrical pores ($\sim 10^{-11} \text{ mol/cm}^2\cdot\text{s}$).

$$J_{\text{coll}} = (\Delta C/L) \times (\varepsilon/\tau)D_{\text{sol}} \quad (1)$$

Importantly, the diffusive flux of small molecules normal to the (111) plane of a semi-infinite colloidal crystal is only ca. 10 times smaller relative to the free solution value, independent of the size of the spheres used to assemble the crystal [40]. Thus, the rate of molecular transport remains significant, even when the pore size is reduced to the nanoscale to impart molecular transport selectivity.

All of the above features make silica colloidal crystals ideal candidates for highly-selective nanoporous membranes. However, until 2005, there were no publications describing transport through surface-modified colloidal membranes or their use for separations. In 2005 we introduced, for the first time, the concept of permselective colloidal nanoporous membranes by describing amine-modified colloidal membranes with controlled transport of positively charged species [43]. Last year, we reported a detailed study of transport through amine-modified colloidal membranes [44] as well as membranes modified with chiral selector molecules [45] and polymer brushes [46], and suspended colloidal membranes [42]. Most recently, we reported a detailed study of the molecular transport in chiral colloidal membranes [47].

2. Amine-Modified Nanoporous Colloidal Films

To demonstrate that a colloidal membrane can be functionalized to acquire permselectivity, we modified the surface of silica spheres with amino groups, with the goal of imparting pH-dependent permselectivity based on electrostatic interactions between the protonated amino groups and the charged permeants.

To prepare surface-modified colloidal membranes, we first assembled a thin colloidal film from $440 \pm 11 \text{ nm}$ silica spheres [43] on the surface of $25\text{-}\mu\text{m}$ -radius disk-shaped Pt microelectrodes shrouded in glass [43]. These electrodes will be called *opal electrodes* throughout the text. Chemical modification of the colloidal films was achieved by treatment with 3-aminopropyl-triethoxysilane [43]. A representative SEM image of a three-layer modified film deposited on the Pt electrode is shown in Figure 1. The permselectivity of the surface-modified films was determined by measuring the flux of redox-active molecules across the films in quasi-steady-state voltammetric experiments [48].

Figure 2 shows the voltammetric responses of a Pt electrode in aqueous solutions of either 5.1 mM $\text{Ru}(\text{NH}_3)_6^{3+}$, 5.2 mM $\text{Fe}(\text{CN})_6^{4-}$, or 1.6 mM hydroxymethylferrocene ($\text{Fc}(\text{CH}_2\text{OH})_2$) and 0.1M KCl as supporting electrolyte. To separate the effects of the lattice tortuosity and surface chemistry on the molecular flux, voltammograms were recorded for: (i) the bare electrodes, (ii) the electrodes after the film self-assembly, and (iii) the electrodes after chemical modification of the film with 3-aminopropyltriethoxysilane.

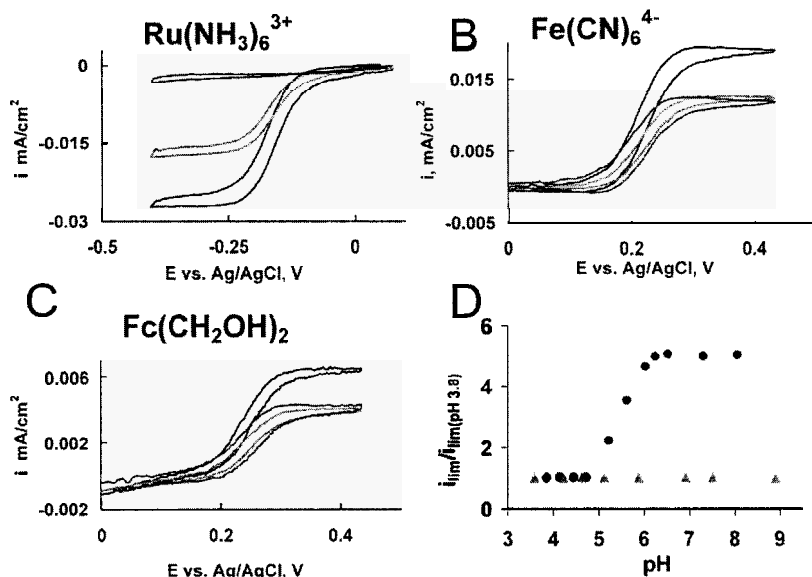


Figure 2. Voltammetric responses of a Pt electrode: (A) bare (bottom), after opal assembly (middle), and after chemical modification of the thin colloidal film with 3-aminopropyl-triethoxysilane (top). (B)-(C) bare (top), after opal assembly and after chemical modification of the thin colloidal film with 3-aminopropyl-triethoxysilane (middle). (D) Voltammetric responses of a Pt electrode as a function of pH for unmodified (triangles) and modified (circles) opal electrode.

The voltammetric response of the bare electrode for each redox species, Figure 2, displays a sigmoidal shape characteristic of radial transport to a microelectrode [49]. Following deposition of the colloidal thin film, similar sigmoidally shaped voltammetric responses were obtained, but with a $\sim 30\%$ reduction in i_{lim} for all molecular species (Figure 2A-C). The reduction in current for the electrode, *prior to chemical modification*, is due solely to

geometrical effects associated with the tortuous path that the redox molecules take when diffusing through the colloidal lattice.

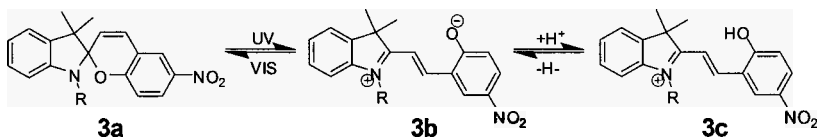
Permselective behavior is readily apparent in the voltammetric response of the electrode after covalent attachment of amino groups to the silica spheres. At pH ~4, the voltammetric limiting current, i_{lim} , corresponding to the one-electron reduction of $Ru(NH_3)_6^{3+}$ is greatly diminished (Figure 2A) while i_{lim} for the one-electron oxidations of $Fe(CN)_6^{4-}$ and $Fc(CH_2OH)_2$ remains approximately the same as before surface modification (Figure 2B and 2C). This result is consistent with electrostatic repulsion of the cationic species, $Ru(NH_3)_6^{3+}$, by protonated surface amines. To demonstrate that the permselectivity arises from electrostatic interactions involving the surface amine functionality, we recorded the voltammetric limiting current for $Ru(NH_3)_6^{3+}$ reduction as a function of the pH. Figure 2D shows a plot of the voltammetric limiting current recorded at different pH's. The flux of $Ru(NH_3)_6^{3+}$ increases sharply beginning at pH 5 and rises by a factor of 3-5 as the pH is raised to a value of 7. Above this pH, i_{lim} remains constant. The sigmoidal shape of the normalized plot of $i_{lim}/i_{lim(pH\ 3.8)}$ vs. pH is consistent with RNH_2/RNH_3^+ equilibrium with a pK_a of 5.7 ± 0.2 [43,50].

Furthermore, we studied the dependence of the permselectivity upon supporting electrolyte concentration [44]. For the modified colloidal membranes at neutral pH, increasing the electrolyte concentration led to a small decrease in the $Ru(NH_3)_6^{3+}$ limiting current, a consequence of the electrolyte reducing the electrical field (and resulting ion migration) created by the reduction of $Ru(NH_3)_6^{3+}$ [49]. Conversely, at low pH, increasing the electrolyte concentration led to a large *increase* in the limiting current. We interpret the latter dependence as being due to screening of the positively charged surface ammonium groups by the electrolyte ions that "opens" the pores for the diffusion of $Ru(NH_3)_6^{3+}$.

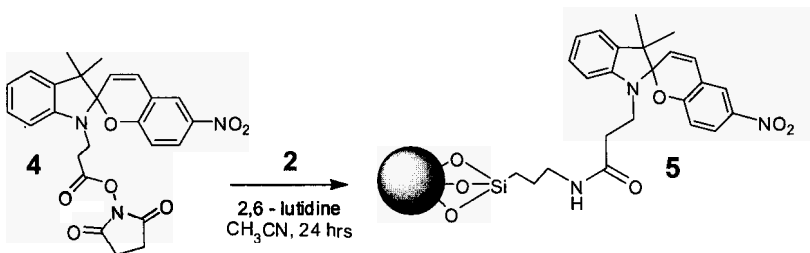
3. Light Responsive Nanoporous Colloidal Films

A spiropyran moiety that undergoes a reversible transformation from the neutral form **3a** to the charged merocyanine forms **3b/3c** and back upon irradiation with UV and visible light, respectively (Scheme 2) [51] appeared to be suitable for controlling ionic permselectivity of a colloidal membrane by light.

We prepared the succinimidyl ester derivative (**4**) [52] of the spiropyran and treated the amine modified colloidal films **2**, assembled on a Pt electrode, with **4** (Scheme 3) and confirmed the successful silica surface modification with spiropyran moieties using UV spectroscopy.



Scheme 2. Interconversions of neutral, zwitterionic and charged spiroopyran forms



Scheme 3. Attachment of spiroopyran moiety to the silica sphere surface

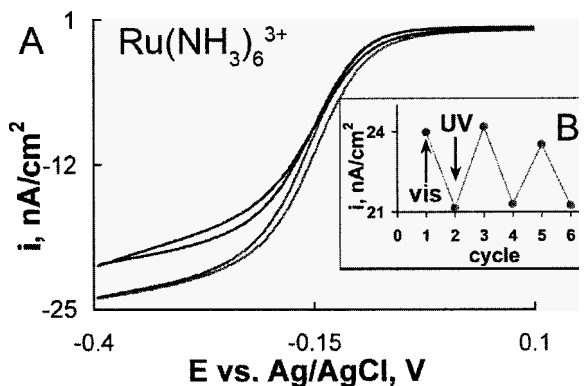


Figure 3. (A) Voltammetric response of a spiroopyran-modified opal Pt electrode after irradiation with UV (top curve) and visible light (bottom curve). (B) Time profile of the response.

Next, we measured the flux of charged molecules through the spiroopyran-modified nanoporous films **5** using cyclic voltammetry, in the same way as for the amine-modified films. We found that upon irradiation with UV light the transport of positively charged species decreased, and that it can be restored to its original value upon irradiating the film with visible light (Figure 3).

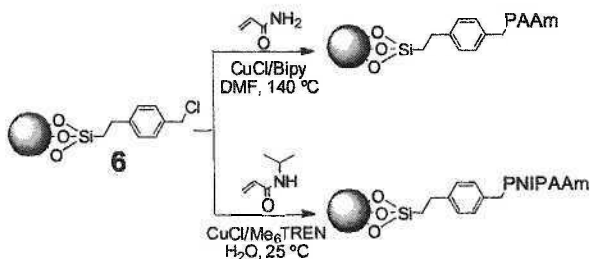
The permselectivity for the molecular transport of cations is only about 15% for the spiropyran-modified films, compared to nearly 100% in the case of amine modified films. This may result from having fewer spiropyran molecules on the surface, or from incomplete conversion of the spiropyran molecules to the merocyanine form, factors presently under investigation.

4. Polymer Modified Colloidal Films

To introduce polymers onto the nanopore walls radical polymerization initiator molecules [53] can be attached to the surface followed by the growth of dense polymer brushes [54]. This approach has been used to introduce amphiphilic block-copolymer [54], two-component [55], polysulfonate [56] and polycarboxylic acid [57] brushes onto silicon surfaces, which indeed undergo a change in morphology in response to solvent polarity [54,55], ionic strength [55] and pH [56]. Importantly, Wirth *et al.* prepared polyacrylamide on a porous silica surface and demonstrated that a uniform film is formed without blocking the pores [58]. Thus, we decided to use atom transfer radical polymerization (ATRP) [59] to form polymer brushes inside the nanopores.

In order to determine if the colloidal crystal lattice would remain unperturbed by surface polymerization, we performed ATRP of acrylamide (Scheme 4) on 7- μm -thin colloidal films assembled on glass slides using a 1.5 wt% solution of 205 nm silica spheres. The surface of the silica spheres was modified with the initiator moieties (6, Scheme 4) and polymerization of acrylamide was performed for 43 hours. The SEM image of the resulting hybrid film is shown in Figure 4. It is clear that the colloidal lattice remained intact (although some silica spheres are missing from the top colloidal film layer), and it appears that spheres are “sintered” together (Figure 4 inset) as a result of the polymer brush formation. It is also apparent from Figure 5 that a thick polymeric film does not cover the colloidal film, and that the nanopores are still present.

Next, we assembled the colloidal films on the surface of eight Pt microelectrodes shrouded in glass, modified their surfaces with initiator moieties, and performed polymerization of acrylamide on the opal electrodes for different periods of time. We then measured the limiting current of $\text{Ru}(\text{NH}_3)_6^{3+}$ using these polymer-modified opal electrodes, and compared the current to that measured before the polymerization.



Scheme 4. Preparation of PAAm and PNIPAAm brushes on silica sphere surface.

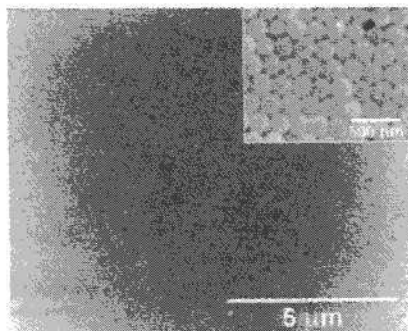


Figure 4. SEM image of the opal film assembled from 205 nm silica spheres, after surface modification with initiator moieties and ATRP polymerization of acrylamide for 43 hours.

The relative limiting current measured for the electrodes decreased logarithmically as a function of polymerization time. The smooth change in i_{lim} suggests that a uniform polymer brush is being formed inside the nanopores. Using expressions for the limiting current [49], the molecular flux through the colloidal crystal [38], and straightforward geometrical considerations, we were able to calculate the polyacrylamide brush thickness inside the nanopores. It increases logarithmically with polymerization time and reaches 8.5 nm after 26 hours. The nanopore size (the distance from the center of the pore to the nearest silica sphere surface) decreases from its initial value of 16 nm for unmodified colloidal crystal to 7.5 nm for the polymer-modified nanopores after 26 hours of polymerization.

Poly(*N*-isopropylacrylamide), PNIPAAm, is a well-known temperature responsive polymer [60] that has been used in the preparation of thermoresponsive membranes [61,62]. We modified colloidal film nanopores with PNIPAAm brushes (Scheme 4) [63] and measured the temperature

response for nanoporous films modified at different polymerization times. As can be clearly seen in Figure 5, two types of response are observed. For nanoporous films modified with a thin polymer brush, the limiting current increases with temperature, with an gradual change at ca. 29 °C (Figure 5A). For colloidal films modified with thick polymer brush a reverse change is observed, where the limiting current decreases with increasing temperature, with an abrupt change at ca. 29 °C (Figure 5B).

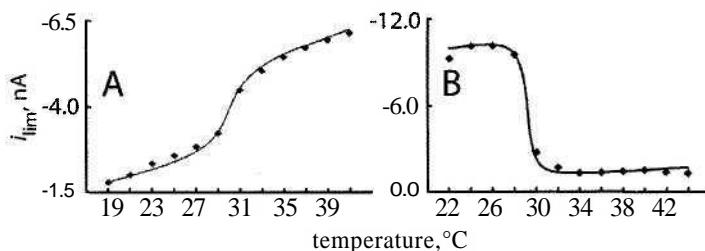


Figure 5. Limiting current ($\text{Ru}(\text{NH}_3)_6^{3+}$) as a function of increasing temperature for PNIPAAm-opal film Pt electrodes after polymerization for (A) 15 min, and (B) 90 min.

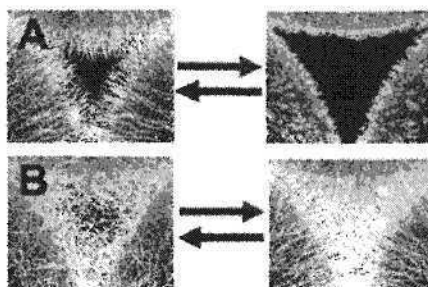


Figure 6. Schematic representation of the processes that occur upon heating and cooling of (A) PNIPAAm brush (15 min polymerization) and (B) PNIPAAm gel (90 min polymerization) inside a colloidal nanopore.

These results are consistent with two types of PNIPAAm morphologies [62,64] inside the nanopores, which lead to two types of molecular transport mechanisms through these nanopores. We believe that when *N*-isopropylacrylamide is polymerized for a short period of time, it forms a dense brush (Figure 6A). Transport through such nanopores mainly happens in the polymer-free volume of the nanopores. With rising temperature the conformation of the polymer chains inside the brush changes in such a way that the brush shrinks, providing a larger volume for diffusion (Figure 6A), which

results in the observed increase in molecular transport. When polymerization is conducted for a sufficiently long time (over 30 min) polymer chains in the brushes growing from the opposite nanopore wall become long enough to meet and interpenetrate. We speculate that this leads to a highly porous and permeable hydrogel structure (Figure 6B). When the temperature is increased, the hydrogel becomes dehydrated and impermeable to aqueous permeants (Figure 6B), but it does not shrink to open the nanopores [61,62].

5. Summary

The above results from our lab demonstrate that transport through surface modified nanoporous colloidal membranes can be controlled by (i) pH and ionic strength, (ii) light, and (iii) polymer brush conformation. Two properties of colloidal membranes are particularly important: (i) selectivity and (ii) high molecular throughput. Our results suggest that the tortuous pathway through the colloidal lattice and the high surface area of the chemically modified spheres enhance the interactions with the diffusing ions and molecules. These results provide critical evidence that surface-modified nanoporous colloidal membranes offer an entirely new and successful approach to nanoporous membranes and may lead to the paradigmatic shift from fabricating nanopores in solid materials.

References

1. P. T. Tanev and J.-R. Butruille, In *Chem. Adv. Mater.*, L. V. Interrante and M. J. Hampden-Smith, Eds., Wiley-VCH: New York, 1998.
2. M. E. Davis, *Nature* **417**, 813 (2002)
3. H. Bayley and C. R. Martin, *Chem. Rev.* **100**, 2575 (2000).
4. Siwy, *Z. Adv. Funct. Mater.* **16**, 735 (2006).
5. L. Sun and R. M. Crooks, *J. Am. Chem. Soc.* **122**, 12340 (2002).
6. J. Li, D. Stein, C. McMullan, D. Branton, M. J. Aziz and J. A. Golovchenko, *Nature* **412**, 166 (2001).
7. A. J. Storm, J. H. Chen, X. S. Ling, H. W. Zandbergen and C. Dekker, *Nature Mat.* **2**, 537 (2003).
8. O. A. Saleh and L. L. Sohn, *Nano Lett.* **3**, 37 (2003).
9. S. Howorka, S. Cheley and H. Bayley, *Nature Biotech.* **19**, 636 (2001).
10. J. J. Kasianowicz, *Nature Mat.* **3**, 355 (2004).
11. D. W. Deamer and D. Branton, *Acc. Chem. Res.* **35**, 817 (2002).
12. Y. Ito, Y. S. Park and Y. Imanishi, *J. Am. Chem. Soc.* **119**, 2739 (1997).
13. M. Nishizawa, V. P. Menon and C. R. Martin, *Science* **268**, 700 (1995).
14. M. Ulbricht, *Polymer* **47**, 2217 (2006).
15. S. Kallus, J.-M. Condre, A. Hahn, G. Golemme, C. Algieri, P. Dieudonne, P. Timmins and J. D. F. Ramsay, *J. Mat. Chem.* **12**, 3343 (2002).

16. B. K. Yen, R. L. White, R. J. Waltman, Q. Dai, D. C. Miller, A. J. Kellock, B. Marchon, P. H. Kasai, M. F. Toney, B. R. York, H. Deng, Q.-F. Xiao and V. Raman, *J. Vac. Sci. Tech.* **A21**, 1895 (2003).
17. H. D. Tong, H. V. Jansen, V. J. Gadgil, C. G. Bostan, C. G. E. Berenschot, C. J. M. van Rijn and M. Elwenspoek, *Nano Lett.* **4**, 283 (2004).
18. L. Nicole, C. Boissiere, D. Grosso, A. Quach and C. Sanchez, *J. Mater. Chem.* **15**, 3598 (2005).
19. C.-S. Toh, B. M. Kayes, E. J. Nemanick and N. S. Lewis, *Nano Lett.* **4**, 767 (2004).
20. A. Yamaguchi, F. Uejo, T. Yoda, T. Uchida, Y. Tanamura, T. Yamashita and N. Teramae, *Nature Mat.* **3**, 337 (2004).
21. B. J. Hinds, N. Chopra, T. Rantell, R. Andrews, V. Gavalas and L. G. Bachas, *Science* **303**, 62 (2004).
22. S. A. Miller and C. R. Martin, *J. Am. Chem. Soc.* **126**, 6226 (2004).
23. P. Kohli, C. C. Harrell, Z. Cao, R. Gasparac, W. Tan and C. R. Martin, *Science* **305**, 984 (2004).
24. S. B. Lee, D. T. Mitchell, L. Trofin, T. K. Nevanen, H. Söderlund and C. R. Martin, *Science* **296**, 2198 (2002).
25. J.-R. Ku and P. Stroeve, *Langmuir* **20**, 2030 (2004).
26. B. W. Stanton, J. J. Harris, M. D. Miller and M. L. Bruening, *Langmuir* **19**, 7038 (2003).
27. N. G. Liu, D. R. Dunphy, P. Atanassov, S. D. Bunge, Z. Chen, G. P. Lopez, T. J. Boyle and C. J. Brinker, *Nano Lett.* **4**, 551 (2004).
28. V. Smuleac, D. A. Butterfield and D. Bhattacharyya, *Chem. Mater.* **16**, 2762 (2004).
29. T. Ito, Y. Sato, T. Yamaguchi and S. Nakao, *Macromolecules* **37**, 3407 (2004).
30. T. Ito and T. Yamaguchi, *J. Am. Chem. Soc.* **126**, 6202 (2004).
31. Stimuli-Responsive Polymeric Films and Coatings, M. W. Urban, Ed., ACS: Washington, 2005 (ACS Symposium Series, Vol. 912).
32. S. Wong, S.; V. Kitaev and G. A. Ozin, *J. Am. Chem. Soc.* **125**, 15589 (2003).
33. W. Stoeber, A. Fink and E. Bohn, *J. Colloid. Interface Sci.* **26**, 62 (1968).
34. P. Jiang, J. F. Bertone, K. S. Hwang and V. L. Colvin, *Chem. Mater.* **111**, 2132 (1999).
35. T. Hanai, *Adv. Chrom.* **40**, 315 (2000).
36. S. Flink, F. C. J. M. van Veggel and D. N. Reinhoudt, *J. Phys. Org. Chem.* **14**, 407 (2001).
37. N. Kanoh, S. Kumashiro, S. Simizu, Y. Kandoh, S. Hatakeyama, H. Tashiro and H. Osada, *Angew. Chem. Int. Ed.* **42**, 5584 (2003).
38. E. L. Cussler, *Diffusion. Mass Transfer in Fluid Systems*. 2nd Ed., University Press: Cambridge, 1997.

39. J. Crank, *The Mathematics of Diffusion*, 2nd Ed., Oxford University Press: New York, 1975.
40. H. Brenner and D. A. Edwards, *Macrotransport Processes*; Butterworth-Heinemann: Boston, 1993.
41. M. R. Newton, K. A. Morey, Y. Zhang, R. J. Snow, M. Diwekar, J. Shi and H. S. White, *Nano Lett.* **4**, 875 (2004).
42. A. K. Bohaty and I. Zharov, *Langmuir* **22**, 5533 (2006).
43. M. R. Newton, A. K. Bohaty, H. S. White and I. Zharov, *J. Am. Chem. Soc.* **127**, 7268 (2005).
44. M. R. Newton, A. K. Bohaty, H. S. White and I. Zharov, *Langmuir* **22**, 4429 (2006).
45. J. Cichelli and I. Zharov *J. Am. Chem. Soc.* **128**, 8130 (2006).
46. O. Schepelina and I. Zharov, *Langmuir* **22**, 10523 (2006).
47. J. Cichelli and I. Zharov *J. Mater. Chem.*, **17**, 1870 (2007).
48. R. Naegeli, J. Redepenning and F. C. Anson, *J. Phys. Chem.* **90**, 6227 (1986).
49. A. J. Bard and L. R. Faulkner, *Electrochemical Methods: Fundamentals and Applications*, 2nd Ed.; Wiley: New York, 2001.
50. J.-J. Shyue, M. R. De Guire, T. Nakanishi, Y. Masuda, K. Koumoto and C. N. Sukenik, *Langmuir* **20**, 8693 (2004).
51. R. C. Bertelson, Spiropyrans. In *Organic Photochromic and Thermochromic Compounds*. J. C. Crano and R. J. Guglielmetti, Eds., Plenum Publishing Corp.: New York, 1999.
52. A. Fissi, O. Pieroni, G. Ruggeri and F. Ciardelli, *Macromolecules* **28**, 302 (1995).
53. K. Matyjaszewski, *Polym. Mat. Sci. Eng.* **84**, 363 (2001).
54. X. Kong, T. Kawai, J. Abe and T. Iyoda, *Macromolecules* **34**, 1837 (2001).
55. S. Minko, D. Usov, E. Goreschnik and M. Stamm, *Macromol. Rapid. Commun.* **22**, 206 (2001).
56. Y. T. Auroy and L.-T. Lee, *Macromolecules* **32**, 8952 (1999).
57. M. Biesalski, D. Johannsmann and J. Ruhe, *J. Chem. Phys.* **117**, 4988 (2002).
58. X. Huang and M. J. Wirth, *Anal. Chem.* **69**, 4577 (1997).
59. J. Wang and K. Matyjaszewski, *Macromolecules* **28**, 7901 (1995).
60. M. Heskins and J. E. Guillet, *J. Macromol. Sci., Chem.* **A2**, 1441 (1968).
61. T. Peng and Y.-L. Cheng, *J. Appl. Polym. Sci.* **70**, 2133 (1998).
62. Y. Li, L.-Y. Chu, J.-H. Zhu, H.-D. Wang, S.-L. Xia and W.-M. Chen, *Ind. Eng. Chem. Res.* **43**, 2643 (2004).
63. N. Idota, A. Kikuchi, J. Kobayashi, Y. Akiyama, K. Sakai and T. Okano, *Langmuir* **22**, 425 (2006).
64. T. Peng and Y.-L. Cheng, *J. Appl. Polym. Sci.* **70**, 2133 (1998).

COMPUTER SIMULATION STUDY IN ADSORPTION OF WATER IN CARBON NANOTUBES*

ATICHAT WONGKOBLAP,[†] DUONG D. DO^a

*Department of Chemical Engineering, University of Queensland, St Lucia
Brisbane, Queensland 4072, Australia*

Water adsorption in carbon nanotubes is an important topic under continuing intensive investigation to understand its mechanism. Therefore in this study water adsorption isotherms are obtained by using a Grand Canonical Monte Carlo (GCMC) simulation for the water potential model proposed by Muller *et al.* [1] in carbon nanotubes at 298 K. The simulated single walled carbon nanotubes (SWCNs) have a cylinder geometry and diameters of 10.8, 13.6, and 16.3 Å. The nanotubes in the presence and absence of hydroxyl groups as well as the location and concentration of hydroxyl groups on carbon surfaces are used to study the effects of surface heterogeneity on the adsorption isotherms. In homogeneous nanotubes, the pore filling pressure is lower than the saturation pressure of water model which is different from that in homogeneous slit pores, and it increase with pore diameter. The size of hysteresis loop changes significantly with pore length and it decreases with an increase in length. The adsorption of water in carbon nanotubes is strongly affected by the location and the concentration of functional group. The pore filling pressure is lower with an increase of functional groups or with the functional groups located at the middle of the carbon nanotube. Study of snapshots of water molecules shows that water molecules are nucleated at the functional groups and this cluster grows in all directions until the pore is completely filled.

1. Introduction

Carbon nanotubes have been increasingly used in many applications, for example the energy storage for hydrogen [2-4], methane [5], sensor technology and medical technology [6] since their discovery by Iijima [7]. A structure of single walled carbon nanotubes (SWCNs) is well defined tubular shaped with very narrow tube size distribution [8-9]. It is reported in the literature [4] that SWCNs could act as metals or as semiconductors [10-11], and as such chemical reaction could occur inside the nanotubes [12] and the adsorption of NO₂, O₂ and NH₃ [13-14] in carbon nanotubes is also affected by their electronic properties which depend on the carbon atoms arrangement. In the adsorption of

* This work is supported by the Australian Research Council.

[†] Financial supported by the Royal Thai Government and Suranaree University of Technology, Thailand.

^a Corresponding author: E-mail: duongd@cheque.uq.edu.au

gases, water vapor may involve and could affect the performance of nanotubes. Therefore, it is important to understand the behavior of water molecules adsorbed in carbon nanotubes which can be applied further in adsorption science to study adsorption of mixture involving water.

Molecular simulation has been applied to elucidate the adsorption mechanism of water in SWCNs with infinite length in axial direction [4, 15-18], and the experimental data of water adsorption inside 10:10 SWCNs at 289 K using ^1H nuclear magnetic resonance (NMR) has been reported [8]. Experimental data show that water uptake slightly increases at low relative pressure, and then it rises sharply above the relative pressure of 0.4 ($P/P_0 = 0.4$) to $P/P_0 = 0.55$, after that region it gradually increases to the completion of pore filling [8]. While the simulation results of water inside the infinite SWCNs show a negligible adsorption at low relative pressure and a sudden change of isotherm and a completion of pore filling once a certain relative pressure threshold is reached [4, 15-18]. Therefore there is a need to reconcile simulation results and experimental data.

In simulation studies, two popular molecular simulation methods applied to study water adsorption are Molecular Dynamics (MD) and Monte Carlo simulation (MC), and two types of water potential models have been used. One is the point charge models such as SPC/E model [19], while the other is the square well site models such as the Primitive model (PM) [20-23] and the Muller *et al.* [1, 24] models. The point charge model involves long-range Coulombic forces which require a large simulation system size in order to minimize the cut-off errors induced due to the effect of simulating a finite system [1] and the greatly increased computation time [25], while the Muller *et al.* model can mimic the association without the need for large simulation system and computation time [26].

The more accurate molecular potential model for water should account for not only the usual dispersion and repulsive forces and hydrogen bonding, but also the long range electrostatic force, polarizability, quantum effects, bond flexibility and multibody effects. The Muller *et al.* water potential model, however, uses the off-centre square well interactions to describe bonding sites [27] and increases the energy well depth for unlike sites to form the hydrogen bonding which accounts for the electrostatic and attractive forces [1]. The quantum and bond flexibility effects are not taken into account; this is due to the fact that the influence of these effects is small enough to be neglected [27]. The molecular parameters are evaluated by using Wertheim's TPT1 theory and fitted to thermodynamic properties such as the gas-liquid coexistence properties of bulk water at 298 K and vaporization energy [1, 24]. Although the Muller *et al.*

model does not carry any partial charges, its square well interaction to describe hydrogen bonding is adequate to capture correctly the interaction between water molecules. Furthermore, this model can describe adsorption behavior of water in slit pore equally well, when compared with the behaviors described by models with partial charges such as SPC/E [25, 26]. The comparison between the Muller *et al.* water model adsorption on a functional graphite pore against the experimental data of commercial activated carbon has been reported in the literature [24, 28-29], and agreement is found to be satisfactory.

This study focuses on using homogeneous and heterogeneous finite pores together with the Muller *et al.* potential model to investigate the adsorption of water in carbon nanotubes. The adsorption isotherms of water in cylindrical pores at 298.15 K are obtained by using the Grand Canonical Monte Carlo (GCMC) simulation. The functional group used in this study is taken to be the hydroxyl (OH) group. We will study the effects of the position and the concentration of functional groups on the adsorption isotherm. The results have been obtained for two different configurations of the functional group located on the carbon surface. The detail of solid surface and functional group will be described in Section 2.2.

2. Methodology

2.1. Water model

The Muller *et al.* water model is used in this study and it is treated as a spherical LJ molecule with one dispersive site (oxygen atom) at the centre of a tetrahedral and four square well (SW) associating sites placed at the vertices of the tetrahedral. These four sites represent two hydrogen atoms and two lone pairs of electrons. The molecular parameters used in this study are listed in Table 1.

Fluid	$s_{OO}, \text{\AA}$	$\epsilon_{OO}/k, \text{K}$	$r_{OH}, \text{\AA}$	$s_{HB}, \text{\AA}$	$\epsilon_{HB}/k, \text{K}$
H ₂ O	3.06	90.0	1.2852	0.612	3800

where ϵ_{OO} and s_{OO} are the energy well depth and the collision diameter of the dispersive site, respectively, k is the Boltzmann's constant, and r_{OH} is the distance between a SW site and the oxygen atom. The energy well depth for unlike sites (a hydrogen atom of one water molecule and a lone pair of electrons

of another water molecule) to form a hydrogen bond is ϵ_{HB} while that for the like sites interaction is zero, and s_{HB} is the diameter of the associating site. A cut-off radius in the calculation of interaction energy of five times the collision diameter ($5s_{OO}$) is used in this study. The interaction energy between two dispersive sites is calculated using the Lennard-Jones 12-6 equation. If A represents a hydrogen atom on one water molecule and B is a lone pair of electrons on another water molecule, the interaction potential energy between A and B to form a hydrogen bond can be calculated by using equation 1 [1].

$$\varphi_{HB}(r_{AB}) = \begin{cases} & r_{AB} < \sigma_{HB} \\ & otherwise \end{cases}$$

where r_{AB} is the distance between A and B. In this study, the long-range interactions are not taken into account.

2.2. Solid model and functional group

The solid model used in this study is the carbon-based adsorbents whose pores are cylindrical in shape. A cylindrical pore consists of only one graphene wall and its diameter is that of a ring passing through the centre of the carbon layer. The carbon-carbon bond length in the graphene layer is 1.42 Å [30]. The LJ parameters for carbon atom, σ_{ss} and ϵ_{ss}/k , are 3.4 Å and 28 K, respectively. The interaction energy between the oxygen atom of a water molecule and a carbon atom is calculated by the Lennard-Jones 12-6 equation, and the cross molecular parameters, s_{sf} and ϵ_{sf} are calculated from the Lorentz-Berthelot rule. The homogeneous single walled carbon nanotubes (SWCNs) used in this study are 8:8, 10:10, and 12:12 SWCNs, which correspond to the diameter of 10.8, 13.6, and 16.3 Å, respectively, while the heterogeneous SWCN with diameter of 13.6 Å is only used in this study.

The functional groups on carbon surfaces have been identified as hydroxyl, carbonyl, carboxylic, phenolic, lactonic, and pyrone [24], however to simplify the model only the hydroxyl (OH) group is assumed in this study. The hydroxyl group is modeled as a LJ dispersive site at the centre of oxygen atom and a single square well (SW) site at the hydrogen atom, and their molecular parameters are the same as those of water model except the hydrogen bond strength. The energy well depth to form hydrogen bond between the SW site on the hydroxyl group and the lone pair of electrons on a water molecule is 5000 K [24]. The LJ dispersive site of the hydroxyl group is located at a distance of 1.364 Å along the radial direction from the centre of carbon layer to the centre of cylindrical tube while the SW site is placed at 1.2852 Å from the LJ centre of

hydroxyl group along the tube radius. It is reported in the literature [31] that heteroatoms chemically combined with the carbon skeleton, i.e. hydrogen as a residue of incomplete carbonization, can be distributed within the whole volume of the activated carbon and they need not be bonded directly to the carbon skeleton. Thus hydrogen may be bonded via a C-OH residue (hydroxyl group) and heteroatoms can be decreased by burn-off of coal at temperatures over 1000°C . They can be combined both with carbon atoms at the corners and edges of the graphene layers, and in intercrystalline spaces and even in defect zones of particular graphene layers, mostly they are located at the surface of porous carbons [31]. In this study, two different configurations to investigate the effects of functional group location on the adsorption isotherm of water in a cylindrical pore are used. The first configuration assumes that the hydroxyl groups are positioned at one tube end (Figure 1a); while the other configuration assumes that the functional groups are placed at the middle of the carbon nanotube along the axial direction (Figure 1b). Hereafter, we will use the terms *edge* and *centre* topologies to describe these configurations. In this figure, grey spheres represent carbon atoms while big black spheres and small black spheres represent oxygen atom and hydrogen atom of the OH groups, respectively.



(a) Edge topology

(b) Centre topology

Figure 1. The solid configuration for the edge (a) and centre (b) topology models.

The effects of the concentration of functional group on the adsorption isotherm are investigated by varying a number of hydroxyl groups on the pore wall. The following concentrations used in this study are 1, 2 and 3 hydroxyls groups in the carbon nanotube of length 50 \AA . The distance between functional groups is 4.26 \AA along a circumference of carbon nanotube.

2.3. Simulation method

In this paper we adopt the Metropolis algorithm in the simulations [32]. The GCMC is used to obtain adsorption isotherm of water in a finite-length nanotubes. In this ensemble, we specify the volume of the box (i.e. pore

volume), the chemical potential and the temperature of the system to obtain the adsorption equilibrium. Each simulation cycle consists of displacement of a randomly selected particle, and either deletion of a randomly selected particle or insertion of a particle at a random position.

In our study, one GCMC cycle consists of one thousand displacement moves and attempts of either insertion or deletion with equal probability. In each displacement move, the molecule is also rotated around x, y or z axis with equal probability. For each point on the adsorption branch, we use an empty box as the initial configuration, and the simulation is carried out until the number of particles in the box does not change (in statistical sense). Once this is achieved, the chemical potential is increased to a new value, and the final configuration of the previous chemical potential is used as the initial configuration for the MC simulation. For low relative pressures which are low density states, there are a few molecules adsorbed in the pore however to obtain good statistics, we used run lengths for each point on the adsorption branch of 700 million configurations to reach equilibrium and to obtain ensemble averages. For denser states, the run lengths of 700 to 1000 million configurations are used. Although the Muller *et al.* potential model takes much less computation time to evaluate than the point charge potential models, the singular nature and strength of the square well association interaction makes it more difficult to sample configuration space efficiently so that longer run lengths are required [26].

On the other hand, desorption branch of the isotherm is started with the highest chemical potential, and then the chemical potential is decreased to a new value. The equilibrium configuration of the previous chemical potential is used as the starting point for the new chemical potential, and the process is repeated until the simulation box is empty. The virial equation [33] is used to determine the relative pressure of the bulk gaseous phase for a given chemical potential. In the case of infinite cylindrical pore, periodic boundary condition are applied in z direction [32, 34] while in the case of finite pore, the particle move is rejected if it places the particle outside the simulation box.

Pore Density

The cylindrical pore volume is $\pi R^2 L$, where R is the subtraction of half a collision diameter of carbon atom from the pore radius and L is the pore length. The average adsorption density is calculated as $\rho_{av} = \langle N \rangle / \pi R^2 L$, where N is the number of particle.

Isosteric Heat

A thermodynamic quantity in adsorption studies is the isosteric heat (q_{st}). Using the fluctuation theory, the isosteric heat is evaluated using the equation,

$q_{st} = \frac{[\langle U \rangle \langle N \rangle - \langle UN \rangle]}{[\langle N^2 \rangle - \langle N \rangle \langle N \rangle]} + kT$, where U is the configuration energy of the system [35].

3. Results and discussions

We start our discussion by first presenting the adsorption isotherms of water using Muller et al. model for homogeneous cylindrical pores with different lengths to show the effects of pore length on the adsorption behaviors. Next, the adsorption isotherms obtained for heterogeneous cylindrical pores of edge and centre topologies will be presented to show the effects of functional group and its location on the adsorption isotherms. Final, the effects of concentration of functional groups on adsorption isotherms are investigated.

3.1. *The effects of pore length on the adsorption isotherm*

The simulated isotherms versus relative pressure of water in homogeneous cylindrical pores at 298.15 K are shown in Figures 2. The dashed lines are for an infinite pore, while results for a finite pore are shown as solid lines. In general, the adsorption behavior for the infinite pores is similar to that for finite pores; they show the type V isotherm and a distinct hysteresis loop. The onset of the pore filling occurs at a pressure lower than the saturation pressure of the water potential model and it increases with pore diameter. While in the case of homogeneous slit pores, the onset pressure is higher than the saturation pressure for both infinite and finite pores [36] and the relative pore filling pressure for the cylindrical pore is lower than that for the slit pore of similar size. This is due to the effects of curvature on the adsorption behavior of water in carbon nanopores (enhancement in adsorption potential). The similar behavior is also observed in the case of adsorption of the SPC/E water potential model in the infinite cylindrical and slit pores [18]. It is noted that the adsorbed amount of water at saturation in slit pore is greater than that in cylindrical pores of similar size [18, 36] and the adsorption capacity of cylindrical pores at saturation is lower than water density which correspond to the experimental data of activated carbon and SWCN in the literature [8]. This is due to the effects of curvature and water molecules do not fill all the available pore volume [18].

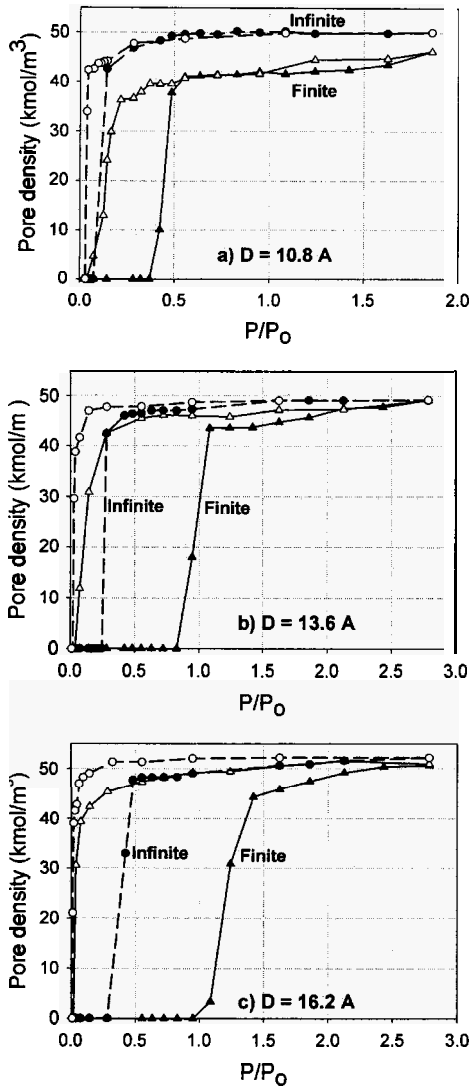


Figure 2. Adsorption isotherms of water at 298.15 K for homogeneous infinite cylindrical pore (dashed line with circle symbols; filled symbols for adsorption and unfilled symbols for desorption) and finite length cylindrical pore (solid line with triangle symbols) of various diameters: D = 10.8 (a), 13.6 (b) and 16.2 Å (c).

However the following differences between infinite and finite nanotubes are observed (i) a less sharp adsorption branch of isotherm, (ii) the greater condensation and evaporation pressures and (iii) a greater hysteresis loop in finite pore. The sensitivity of the loop size is manifested in cylindrical pore; such behavior is not observed in slit pore [36]. For a given pressure, the adsorption capacity is greater in the case of infinite cylindrical pores, and this is due to the greater interaction potential between water molecules and carbon atoms. Take a nanotube of 10.8 Å diameter as an example, the interaction between water and carbon at the saturation condition for infinite pore is -14.62 kJ/mol and it contributes to the total interaction potential of -59.97 kJ/mol (around 24.4% of total potential) while that for the corresponding finite pore of 50 Å length ($f_{sf} = -9.33$ kJ/mol) contributes 16.7 % to the total potential of -55.94 kJ/mol.

The adsorption data of water in 10:10 SWCN (13.6 Å diameter) at 289 K obtained by using ^1H nuclear magnetic resonance (NMR) show a less steep increase of adsorption branch of isotherm above $P/P_0 = 0.55$ [8], the similar less steep rise in adsorption isotherm is also observed in the case of finite length nanotubes. However the pore filling pressures for the experimental data is lower than that for the corresponding simulation result. This is due to the heterogeneity of solid surface. We will investigate the heterogeneity in the form of functional groups and see whether we could reconcile the simulation results and the experimental data.

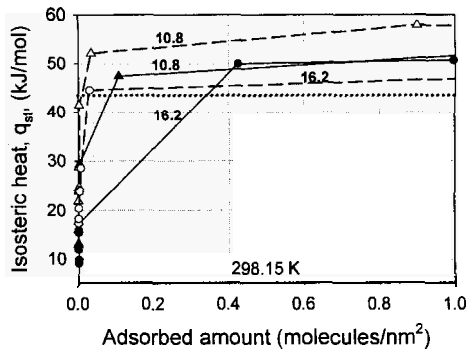


Figure 3. Isosteric heats of adsorption for water at 298.15 K for finite pores (solid line with filled symbols) and those for infinite pores (dashed line with unfilled symbols) having diameters of 10.8 Å (triangle symbols) and 16.2 Å (circle symbols).

Figure 3 shows the isosteric heats of water adsorption in homogeneous nanotubes as dashed lines for infinite pores and solid lines for finite pores of 50 Å. The heat of liquefaction of water at 298.15 K ($H_{liq} = 43.99$ kJ/mol) is also

presented as horizontal dotted line in the same figure. The heat curves start from a minimum value, which is below the heat of liquefaction and then increase with increasing surface coverage, crossing the heat of liquefaction at the pore filling pressures. At low coverages, the isosteric heat for the finite pore is less than that for the infinite pore of the same diameter; this is contributed by the less water-carbon interaction and it leads to the less adsorption capacity and higher pore filling pressure as shown in Figure 2.

3.2. *The effects of functional group on the adsorption isotherm*

Next we study the effects of functional groups and their location on the adsorption of water in nanotube of 13.6 Å diameter (10:10 SWCN) which is the same diameter as the SWCN used experimentally [8]. The GCMC simulations for heterogeneous pores with edge topology (triangle symbols) and centre topology (circle symbols) are presented in Figure 4. The isotherm of a corresponding homogeneous pore (dashed line) is also plotted in the same figure. Three hydroxyl groups are placed on the pore wall with a separation distance of 4.26 Å along the circular direction. The isosteric heats of water adsorption in these homogeneous and heterogeneous nanotubes are presented in Figure 5. Snapshots of water molecules in heterogeneous nanotubes at low relative pressures are presented in Figure 6 to investigate the onset of adsorption of water in SWCNs.

Due to the presence of functional group, the following features are observed for the adsorption of water in carbon nanotubes:

1. An early onset of adsorption for heterogeneous nanotubes is observed, and the isotherms obtained for heterogeneous pores are greater than that for the homogeneous pore. This is due to the favorable adsorption of water molecules around functional groups via hydrogen bonding.
2. The pore filling pressure and the evaporation pressure for heterogeneous pores are lower than those for homogeneous pore.
3. The hysteresis loop in the case of heterogeneous pores is smaller than that of homogeneous pore.
4. The isotherm for the centre topology is greater than that for the edge topology at low relative pressures; this behavior is similar to that observed in the case of slit pores [25, 36]. This is due to the fact that water molecules which directly formed the hydrogen bond to the functional group and become nucleation centre for other water molecules to form aggregates are close to more number of carbon atoms on the pore wall in the case of centre topology.
5. The heats of adsorption start from a minimum value, however the isosteric heats for heterogeneous pores start at a higher value than that for the

homogeneous pore and they reach the maximum when a nucleation of water molecules is formed at the functional groups. This is due to the greater interaction between water molecule and functional group via hydrogen bond than that between water and carbon atom.

- The heat curve for the centre topology is greater than that for the edge topology at zero coverage; this is due to the same reason mentioned in part (4) above.

We note that the smaller evaporation pressure and the smaller hysteresis loop are similar to those of the homogeneous infinite pores; however the hysteresis loop for heterogeneous pores is smaller.

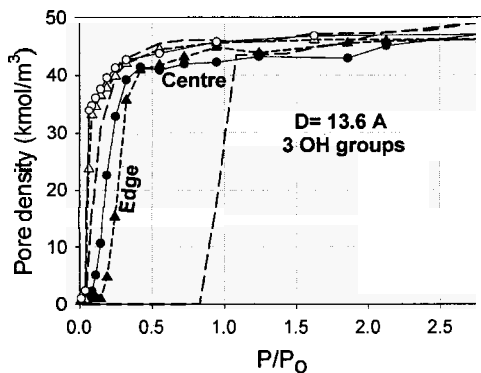


Figure 4. Adsorption isotherms at 298.15 K for the Muller *et al.* water model in cylindrical pore having diameter of 13.6 Å for the edge (triangle symbols; filled symbols for adsorption and unfilled symbols for desorption), centre topologies (circle symbols) and homogeneous pore (dashed line).

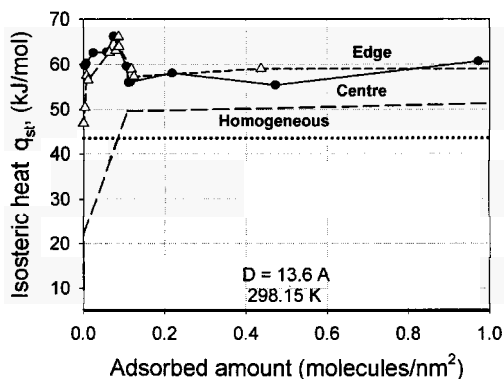


Figure 5. Isothermic heats of adsorption for water at 298.15 K for the Muller *et al.* water model in cylindrical pore having diameter of 13.6 Å for the edge (triangle symbols), centre topologies (circle symbols), homogeneous pore (dashed line) and heat of liquefaction (dotted line).

Figure 6 shows the configurations of water molecules in the heterogeneous pore at various pressures. We observe that a few water molecules are nucleated around the functional groups at low relative pressures, and then this water cluster grows in all directions until the pore is completely filled with water molecules. The pore filling mechanism of the Muller *et al.* water potential model in cylindrical pores is similar to that of SPC/E water potential model in infinite cylindrical pores [4].

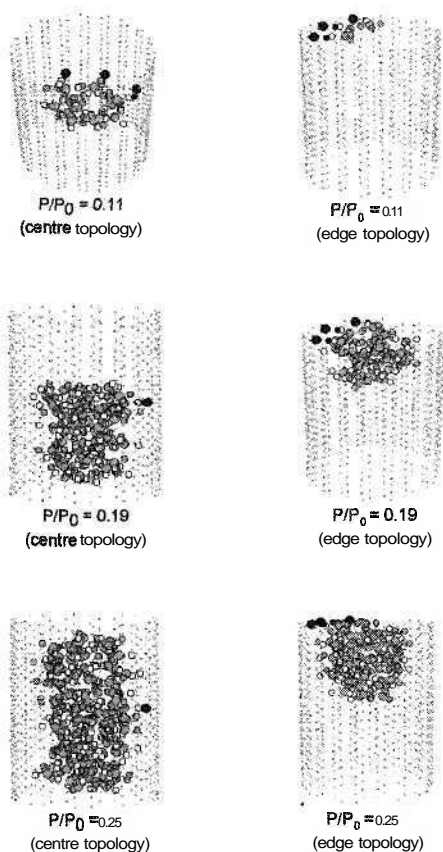


Figure 6. Snapshots of water molecules in heterogeneous cylindrical pore of 13.6 Å diameter. In these figures, gray dots represent carbon atoms, big and small black spheres represent oxygen and hydrogen atoms of hydroxyl group, respectively, and big dark gray spheres represent oxygen atoms of water while small gray spheres and small white spheres represent hydrogen atoms and lone pairs of electrons of water molecules, respectively.

3.3. The effects of concentration of functional group on the isotherm

We now turn to the effects of concentration of functional groups on the adsorption isotherm of water in 10:10 SWCN. The concentration used in this study is varied from 1 to 3 molecules of hydroxyl groups on the wall of 50 Å lengths, and the separation distance between two functional groups is 4.26 Å. The GCMC simulated isotherms for the edge and centre topologies are shown in Figures 7a and 7b, respectively.

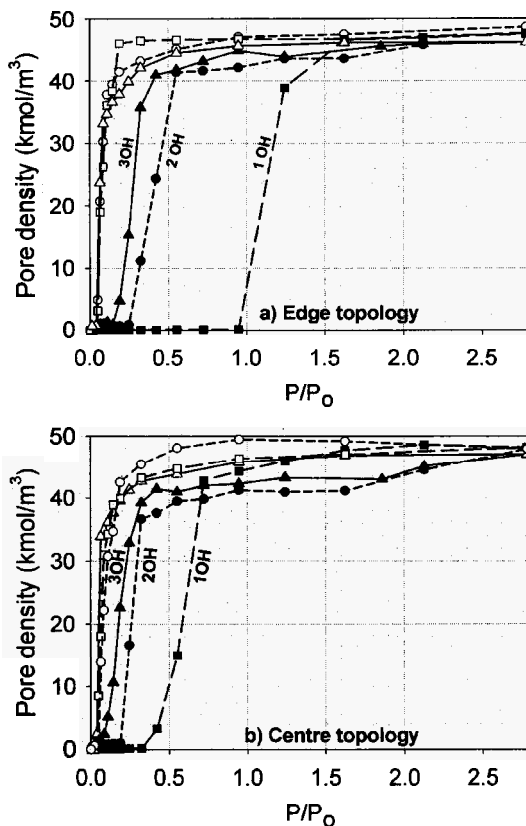


Figure 7. The adsorption isotherms of water in heterogeneous cylindrical pore of 13.6 Å diameter with 1 hydroxyl group (square symbols; filled symbols for adsorption and unfilled symbols for desorption), 2 hydroxyl groups (circle symbols) and 3 hydroxyl groups (triangle symbols) for (a) edge topology and (b) centre topology.

The common characteristics of these isotherms are observed with different concentrations of functional group;

1. In the low relative pressure region, the adsorption isotherm decreases by decreasing the concentration of functional groups. This is due to the less available strong energy sites for water molecules to interact with. The simulation result agrees with the experimental observations of Morimoto and Miura [37] which show that the reduced amount of surface groups leads to a significant decrease of the water adsorbed amount.
2. An increase in the concentration leads to an early onset of pore filling pressure; this is due to the greater water-water interaction.
3. The size of the hysteresis loop decreases with an increase in the concentration of functional groups, resulting from the early onset of adsorption isotherm as mentioned above.

The adsorption isotherm obtained for the finite-length of 10:10 SWCN agrees well with the experimental data for 10:10 cut-SWCN [8] when one functional group is located in the middle of the nanotube (centre topology). It shows a steep increasing (but not vertical) of adsorption isotherm above the relative pressure of 0.4 but it does not reach the completion of pore filling until the relative pressure is about 0.95.

4. Conclusions

In this paper, we have presented the adsorption of water in carbon nanotubes and considered the effects of functional groups on the adsorption isotherm using a Grand Canonical Monte Carlo (GCMC) simulation. The isotherm of type V and the obvious hysteresis for both homogeneous and heterogeneous pores can be observed. The size of hysteresis loop for the cylindrical pore is more sensitive to the pore length than that for the slit pore. The functional group shows significant effects on the adsorption isotherm. We observe an early onset of adsorption isotherm, a lower pore filling pressure and a smaller hysteresis loop.

Acknowledgments

This project is supported by the Australian Research Council. We acknowledge the Royal Thai Government and Suranaree University of Technology in Thailand for financial support to AW.

References

1. E.A. Muller, L.F. Rull, L.F. Vega and K.E. Gubbins, *J. Phys. Chem.* **100**, 1189 (1996).
2. Y. Zhou, K. Feng, Y. Sun and L. Zhou, *Chem. Phys. Lett.* **380**, 526 (2003).

3. P.X. Hou, S.T. Xu, Z. Ying, Q.H. Yang, C. Liu and H.M. Cheng, *Carbon* **41**, 2471 (2003).
4. A. Striolo, A.A. Chialvo, P.T. Cummings and K.E. Gubbins, *J. of Chem. Phys.* **124**, 074710 (2006).
5. L. Zhou, Y. Sun, Z. Yang and Y. Zhou, *J. of Colloid and Interface Sci.* **289**, 347 (2005).
6. T. Kimura, H. Kanoh, T. Kanda, T. Ohkubo, Y. Hattori, Y. Higaonna, R. Denoyel and K. Kaneko, *J. Phys. Chem. B* **108**, 14043 (2004).
7. S. Iijima, *Nature* (London) **354**, 56 (1991).
8. S. Mao, A. Kleinhammes and Y. Wu, *Chem. Phys. Lett.* **421**, 513 (2006).
9. A. Thess et al., *Science* **273**, 483 (1996).
10. J.W. Mintmire, B.I. Dunlap and C.T. White, *Phys. Rev. Lett.* **68**, 631 (1992).
11. N. Hamada, S.-i. Sawada, and A. Oshiyama, *Phys. Rev. Lett.* **68**, 1579 (1992).
12. M.D. Halls and H.B. Schlegel, *J. Phys. Chem. B* **106**, 1921 (2002).
13. J. Kong, N.R. Franklin, C. Zhou, M.G. Chapline, S. Peng, K. Cho and H. Dai, *Science* **287**, 622 (2000).
14. P.G. Collins, K. Bradley, M. Ishigami and A. Zettl, *Science* **287**, 1801 (2000).
15. A. Striolo, A.A. Chialvo, K.E. Gubbins and P.T. Cummings, *J. of Chem. Phys.* **122**, 234712 (2005).
16. K. Koga, G.T. Gao, H. Tanaka and X.C. Zeng, *Nature* **412**, 802 (2001).
17. J.H. Walther, R. Jaffe, T. Halicioglu and P. Koumoutsakos, *J. Phys. Chem. B* **105**, 9980 (2001).
18. A. Striolo, K.E. Gubbins, A.A. Chialvo and P.T. Cummings, *Molecular Physics* **102**, 243 (2004).
19. H.J.C. Berendsen, J.P.M. Postma, W.F. van Gunsteren, and J. Hermans, in B. Pullman (Ed.), *Intermolecular Forces*, Reidel, Dordrecht, the Netherlands, 331 (1981).
20. I. Nezbeda and J. Slovak, *Molecular Physics* **90**, 353 (1997).
21. I. Nezbeda, *J. of Molecular Liquids* **73, 74**, 317 (1997).
22. M. Predota and I. Nezbeda, *Molecular Physics* **96**, 1237 (1999).
23. M. Predota, I. Nezbeda and P.T. Cummings, *Molecular Physics* **100**, 2189 (2002).
24. C.L. McCallum, T.J. Bandosz, S.C. McGrother, E.A. Muller and K.E. Gubbins, *Langmuir* **15**, 533 (1999).
25. G. R. Birkett and D.D. Do, *Molecular Physics* **104**, 623 (2006).
26. J.C. Liu and P.A. Monson, *Langmuir* **21**, 10219 (2005).
27. E.A. Muller and K.E. Gubbins, *Ind. Eng. Chem. Res.* **34**, 3662 (1995).
28. J.C. Liu and P.A. Monson, *Ind. Eng. Chem. Res.* **45**, 5649 (2006).

29. A. Wongkoblap and D.D. Do, *Chemeca 2007 Conference*, Melbourne, Australia, (2007).
30. D. D. Do, *Adsorption Analysis: Equilibria and Kinetics*, Imperial College Press, New Jersey, (1998).
31. H. Jankowska, A. Swiatkowski and J. Choma, *Active Carbon*, Ellis Horwood, Poland, (1991).
32. D. Frenkel, and B. Smit, *Understanding Molecular Simulation*, Academic Press, New York, (2002).
33. E.A. Muller, F.R. Hung and K.E. Gubbins, *Langmuir* **16**, 5418 (2000).
34. M.P. Allen and D.J. Tildesley, *Computer Simulation of Liquids*, Oxford Science Publications, New York, (1987).
35. D. Nicholson and N.G. Parsonage, *Computer Simulation and the Statistical Mechanics of Adsorption*, Academic Press, London, (1982).
36. A. Wongkoblap and D.D. Do, *J. Phys. Chem. B*, (2007).
37. K. Miura and T. Morimoto, *Langmuir* **10**, 807 (1994).

ADSORPTIONS OF CH₄ AND C₂H₄ ON MOP-28 BASED CLUSTERS: A COMBINED QM AND QM/MM STUDY

SAOWAPAK CHOOMWATTANA^{1,2}, PIPAT KHONGPRACHA^{1,2,3},
JUMRAS LIMTRAKUL^{1,2,3*}

⁽¹⁾ *Physical Chemistry Division, Department of Chemistry, Faculty of Science,
Kasetsart University, Bangkok 10900, Thailand*

⁽²⁾ *Center of Nanotechnology, Kasetsart University Research and Development Institute,
Bangkok 10900, Thailand*

⁽³⁾ *NANOTEC Center of Excellence, National Nanotechnology Center,
Kasetsart University, Thailand*

The adsorption properties of CH₄ and C₂H₄ on MOP-28 based clusters have been investigated by quantum mechanics (QM) and QM/MM approaches. The quantum clusters of the reaction center termed “paddlewheel” and “paddlewheel-ligand” are studied at the B3LYP/6-31G(d, p) level of theory. The environmental framework of the MOP-28 is included via a QM/MM model, where the QM has been represented by using the B3LYP while the MM is well represented by a well-calibrated universal force field, UFF. Thiophene as a ligand was found to polarize the paddlewheel. From the population charge analysis, thiophenes induced the electron transfer in the “paddlewheel” from its C atoms to O atoms, and passing over to Cu atoms. Their adsorption energies in both QM and QM/MM approaches are in the order of CH₄ (-1 kcal/mol) < C₂H₄ (-6 kcal/mol). The van der Waals contribution due to the environmental framework of the MOP-28 for all complexes can be accounted for up to, at most, 20% of their interactions. The combined interactions of the p-bond of the alkene molecule with Cu and backbonding of the metal to alkene have been nicely demonstrated by the natural bond orbital (NBO) analysis.

1. Introduction

Since the discovery of solids that have outstanding properties [1], such as high porosity, a new family of the porous materials, metal organic materials, has been investigated on its adsorption property, catalytic activity, and molecular storage capacity. The porous metal-organic polyhedra (MOP) is comprised of several metal clusters, each of which has two or more metal ions, and a sufficient number of capping ligands to inhibit polymerization of the metal organic polyhedra. The porous metal-organic polyhedra further includes multidentate linking ligands that connect adjacent metal clusters into a geometrical shape, describable as a polyhedral, with metal clusters positioned at one or more vertices of the polyhedron [2].

* Corresponding authors: J. Limtrakul, email: fscjrl@ku.ac.th, Fax: (+66)2-562-5555 ext 2119

MOP-28 [3] is a metal-organic truncated octahedron composed of six rigid square-shaped $\text{Cu}_2(\text{CO}_2)_4$ paddlewheel building units and twelve 2,2':5',2"-terthiophene-5,5"-dicarboxylate (TTDC) linkers. These linkers in the *cis,cis* conformation provide the critical 90° linkage for this unique construction. Previous studies showed that the MOP can trap and separate organics and small gas molecules. Till now, MOP-28 is the most porous molecular structure and stands among the first MOP to be characterized by gas sorption.

As observed in the zeolite framework, the interactions between the framework and any adsorbate molecule contribute remarkably to the sorption properties. These interactions, described by the term "confinement effect" [4, 5], consist dominantly of dispersive van der Waals interactions. For the adsorbed molecule with comparable in size to the pore dimension, the confinement effect should be considered [6].

Similar to zeolites, the MOP structure possesses a large number of atoms. To achieve the *ab initio* calculation for the paddlewheel active site with the effect from the framework taken into account, the recent development of hybrid methods, such as the embedded cluster or combined quantum mechanics/molecular mechanics (QM/MM) [7-12] methods. For very large systems, the ONIOM (our-Own-N-layered Integrated molecular Orbital + molecular Mechanics) method [13, 14], has been applied in order to reach a satisfactorily accurate result and, at the same time, with a sensible computational expense.

In this work, the adsorptions of CH_4 and C_2H_4 on MOP-28 models (QM and QM/MM) are examined to clarify the adsorption process and to address the confinement effect in the mesoporous materials. The ONIOM method enables us to use the density functional theory, for the precise treatment of the interaction between the adsorbed molecule and the active site, and the universal force field (UFF) to account for the van der Waals interaction, which is found to be significant for the adsorption [15-20]. Since there is no experimental measurement for the adsorption of our chosen adsorbed molecules available now, this scheme should be only treated as a promising trend for the adsorption.

2. Methodology

The MOP-28 structure [4] is rhombohedral space group with unit cell parameters $a=b=29.457(5)\text{\AA}$, $c=54.236(20)\text{\AA}$. The framework consists of 6 $\text{Cu}_2(\text{CO}_2)_4$ paddlewheel building blocks and 12 *cis,cis*-terthiophene linking units (see Figure 1). Two different strategies have been employed to model the alkane- and alkenes-adsorbed metal-organic framework. First, the paddlewheel-ligand cluster model cut from the MOP-28 structure was used to represent the local active site of the MOP-28 framework. The quantum mechanical (QM) model with fixed terminating

hydrogen atoms and probe molecules are fully geometrically optimized by employing the hybrid density functional theory (DFT) and B3LYP functional. The polarized double- ζ 6-31G(d,p) basis set was used for all light elements, while for Cu metal atoms, nonrelativistic effective core potential (ECP) was employed. The valence basis set used in connection with the ECP is essentially of double- ζ quality (the Stuttgart basis set). The QM/MM method with two-layer ONIOM (ONIOM2) scheme at B3LYP/6-31G(d,p):UFF was employed to study the adsorption. That is, for computational efficiency, only the small active region is treated quantum mechanically with the density functional theory method, while the contribution of interactions from the rest of the model is approximated by a less computationally expensive method. The B3LYP/6-31G(d,p) level of theory was applied for the paddlewheel-ligand cluster, which is considered to represent the active site. The rest of the framework was treated with the universal force field (UFF) [21]. This force field has been found to provide a good description of the short-range van der Waals interactions. All the calculations were accomplished by Gaussian 03 program package [22].

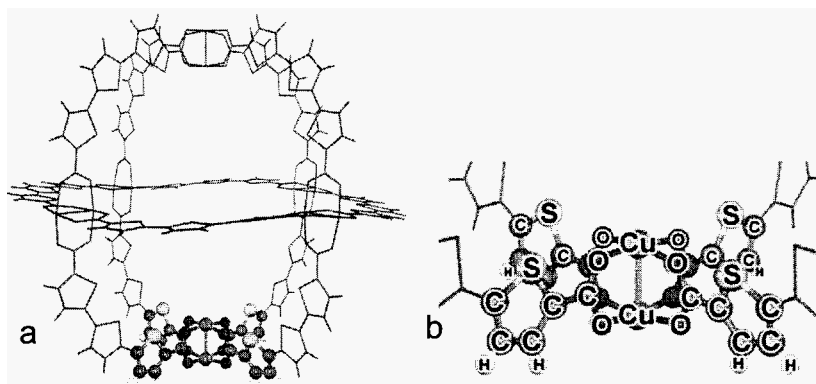


Figure 1. MOP-28 structure – (a) the framework system consists of 6 $\text{Cu}_2\text{-(CO}_2\text{)}_4$ paddlewheel building blocks and 12 *cis,cis*-terthiophene linking units (b) the closer view of paddlewheel block

3. Results and Discussion

For the purpose of clarity, the discussion is divided into three sections. First, the bare quantum mechanical (QM) model is compared to the bare quantum mechanical / molecular mechanical (QM/MM) model. Then, the adsorption of ethylene to the clusters is discussed. In the last part, we also compare the adsorption of ethylene to those of methane with the clusters.

3.1 Comparison of the QM model to the QM/MM model

The XRD data are used to construct the paddlewheel cluster with four ligands of thiophene and the whole unit of MOP-28 which is used in the QM and QM/MM calculations, respectively (Fig.2).

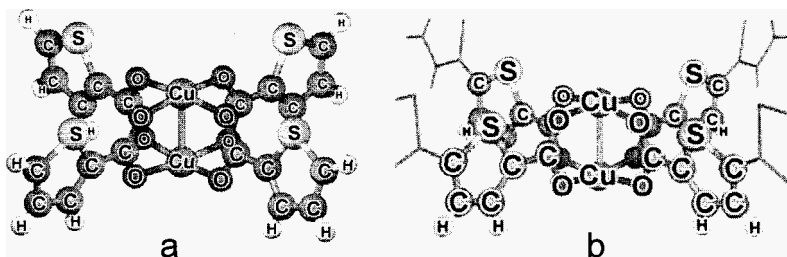


Figure 2. MOP-28 model used in the calculations. (a) For the model chosen for QM calculation, the region represented in ball-and-stick style is the active site. (b) For ONIOM approach, the active site and four linkers, calculated with B3LYP/6-31G(d,p) level of theory, is shown in ball-and-stick style. The rest of the structure is omitted for clarity.

To assess the sensitivity of the active site structure with varying environments, we optimized the active site, $[\text{Cu}_2(\text{CO}_2)_4]$ with four 2,2':5',2''-terthiophene-5,5''-dicarboxylate (TTDC) groups, known as the paddlewheel with four ligands], for all the clusters, while the remaining atoms were kept fixed at the crystallographic positions.

For the investigation on the spin state of the MOP-28 models, since the d-metal active site has a possibility not to be singlet, we investigated the spin state of the paddlewheel with four ligands quantum cluster and MOP-28 ONIOM scheme. It is found that both the quantum cluster and the ONIOM scheme are likely to be in a triplet state because the calculated energy for the triplet is lower than that for the singlet state (31.65 kcal/mol for both the quantum and ONIOM calculations). Therefore, the following discussion will be related to the bare optimized structures in the triplet state.

Regarding the geometries of the MOP-28 models, we compared the structure between the full quantum cluster of the active site and ONIOM scheme. The extended framework has the effect of insignificantly lengthening the Cu-Cu distance, as the distances are 2.512 Å and 2.519 Å for the quantum cluster and MOP-28 ONIOM scheme, respectively, thus they have no effect on the activity of the paddlewheel active site.

3.2 The adsorption of ethylenewith the clusters

The optimized structures of the adsorption complexes of C_2H_4 in both QM and ONIOM calculations are illustrated. There are two possible orientation of ethylene over the active site. It is found that the staggered orientation (Fig.3) is more stable. Then, the orientation is chosen to be studied in this work. Key geometrical parameters of the complexes and their analogous adsorption energies are shown in Table 1 and 2, respectively.

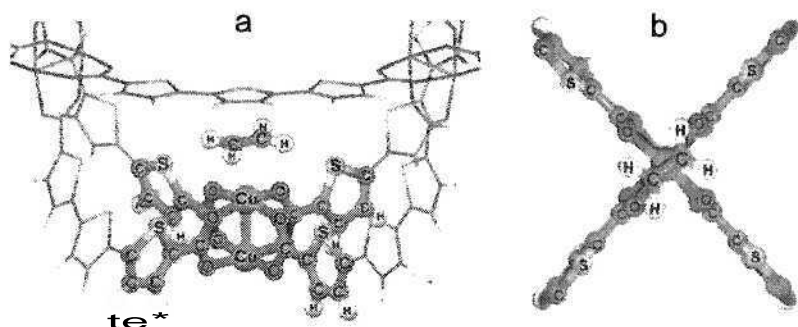


Figure 3. C_2H_4 adsorption in staggered orientation on MOP-28 in perspective (a) and top (b) view

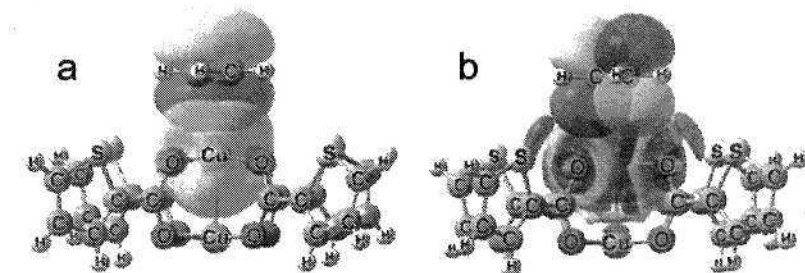


Figure 4. From NBO analysis, the C_2H_4 adsorption on MOP-28 model consists of (a) σ -donation from C_2H_4 to Cu atom (b) π -backbonding from Cu atom to C_2H_4

We have observed C_2H_4 adsorption in different orientation. It is found to be adsorbed on the Cu atom in staggered orientation inside the cavity of MOP-28 via the p -complexation. The changes of the structural parameters that occurred in the adsorption are small. For both QM and ONIOM calculations, the Cu-Cu distance is elongated from 2.51 Å to 2.57 Å. It can be assumed that the inner Cu atom moved toward the ethylene to form an interaction. This assumption is supported by the lengthened C=C bond in the ethylene. In a detailed investigation, the combined interactions of the p -bond of C_2H_4 with Cu and backbonding of the metal to C_2H_4 is

found and illustrated by natural bond orbital (NBO) analysis. It showed that p-bonding molecular orbital of C_2H_4 transfers electron to the unoccupied s orbital of the Cu atom, while the electron from d orbital of the Cu transfers back to the vacant p orbital in the C atom.

Analyzing the energetics, it is noted that the adsorption energy of C_2H_4 is -6.89 kcal/mol, while in the ONIOM calculation the energy is found to be -7.18 kcal/mol.

3.3 Comparison between the adsorptions of ethylene and methane with the clusters

Methane and ethylene adsorptions to the model and ONIOM scheme are performed by QM and QM/MM calculations, respectively.

Table 1. The key optimized geometrical parameters of the adsorption of CH_4 and C_2H_4 on MOP-28 models

Distance (Å)	QM		ONIOM2	
	CH_4	C_2H_4	CH_4	C_2H_4
Cu...Cu	2.520	2.571	2.518	2.572
Cu...C _{ads}	3.230	2.687	3.222	2.683
	2.752	2.687	2.750	2.694
Cu...H _{ads}	2.779		2.768	
C _{ads} -H _{ads}	1.094	-	1.094	-
C _{ads} =C _{ads}	-	1.339	-	1.339

In the bare cluster: For QM calculations, Cu...Cu = 2.512 Å

For ONIOM2 calculations, Cu...Cu = 2.519 Å

For isolated CH_4 , C-H distance = 1.092 Å. For isolated C_2H_4 , C=C distance = 1.330 Å

We compare the geometrical parameters in order to evaluate the interaction of adsorbents with MOP-28. As predicted, the Cu...Cu distance in the CH_4 adsorbed system is insignificantly different from the distance in the bare MOP-28, because of the molecular nonpolarity of the adsorbate. It is in the same trend with Cu...C_{ads} distances that the value in CH_4 adsorbed system is noticeably different from the distances in the C_2H_4 adsorbed system. Thus, it can be implied that the interaction of C_2H_4 is unlike the interaction of CH_4 .

Since any distinction between the geometrical parameters from the QM and ONIOM calculations cannot be observed, it can hardly to be concluded that there is a confinement effect for the adsorptions of CH_4 and C_2H_4 on MOP-28 models. In the case of CH_4 , the adsorption energy reveals the importance of the extended

structure. Moreover, the effect would become essential if the loading is increased or size of absorbing molecules is comparable in size to the MOP nanocavity.

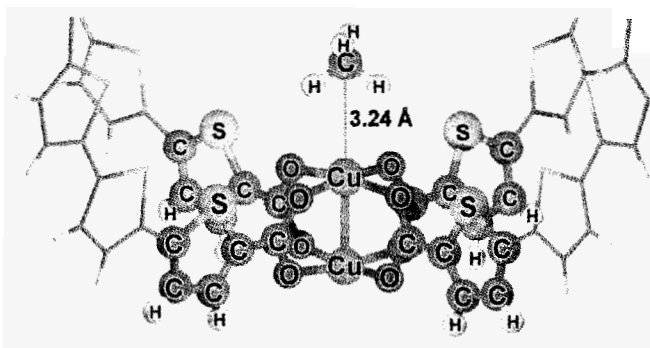


Figure 5. The adsorption of CH_4 on MOP-28 model in ONIOM calculation

Table 2. The adsorption of CH_4 and C_2H_4 on MOP-28 models at QM (B3LYP/6-31G(d,p)) and QM/MM at B3LYP/6-31G(d,p): UFF

Calculation	Adsorption Energy (kcal/mol)	
	CH_4	C_2H_4
QM	-1.05	-6.89
ONIOM2	-1.32	-7.18

4. Conclusions

The adsorptions of CH_4 and C_2H_4 on MOP-28 were studied by using combined QM and QM/MM approaches. For the adsorption of CH_4 and C_2H_4 on MOP-28, the adsorption energies were predicted by ONIOM2 calculations to be -1.32 and -7.18 kcal/mol, respectively. The ONIOM model applied in this study can express the confinement effect of the MOP cavity. The van der Waals contribution due to the environmental framework of the MOP-28 for CH_4 adsorption and C_2H_4 adsorption complexes can be accounted for 0.27 kcal/mol (20%) and 0.29 kcal/mol (4%) respectively. The extended MOP framework that was represented by the UFF was found to be necessary for illustrating the confinement effect of the MOP and led to the further investigations on larger adsorbates.

Acknowledgements

This work was supported in part by grants from the Thailand Research Fund (to JL) and the Kasetsart University Research and Development Institute (KURDI), the

National Nanotechnology Center (NANOTEC Center of Excellence and Computational Nanotechnology Consortium) and the Commission on Higher Education, Ministry of Education under Postgraduate Education and Research Programs in Petroleum and Petrochemicals, and Advanced Materials.

References

1. J.L.C. Rowsell and O.M. Yaghi *Micropor. Mesopor. Mater.* **73**, 3-14 (2004).
2. O.M. Yaghi, A.C. Sudik, Patent, WO 028479, 2006.
3. Z. Ni, A. Yassar, T. Antoun, O.M. Yaghi *J. Am. Chem. Soc.*, **127**, 12752 (2005).
4. E.G. Derouane, J.M. Andre, A.A. Lucus *J. Catal.* **110**, 58 (1988).
5. C.M. Zicovich-Wilson, A. Corma, P. Viruela *J. Phys. Chem.* **98**, 10863 (1994).
6. P. Pantu, B. Boekfa, J. Limtrakul *J. Mol. Catal. A* In Press, Accepted Manuscript, Available online 26 July 2007,
7. M. Brändle, J. Sauer *J. Am. Chem. Soc.* **120**, 1556 (1998).
8. S.P. Greatbanks, I.H. Hillier, N.A. Burton, P. Sherwood *J. Chem. Phys.* **105**, 3770 (1996).
9. J. Limtrakul, S. Jungsuttiwong, P. Khongpracha *J. Mol. Struct.* **525**, 153 (2000).
10. P. Treesukol, J.P. Lewis, J. Limtrakul, T.N. Truong *Chem. Phys. Lett.* **350**, 128 (2001).
11. R.Z. Khaliullin, A.T. Bell, V.B. Kazansky *J. Phys. Chem. A* **105**, 10454 (2001).
12. I.H. Hillier, *Theochem* **463**, 45 (1999).
13. S. Dapprich, I. Komiro, K.S. Byun, K. Morokuma, M. J. Frisch *Theochem* **461-462**, 1 (1999).
14. M. Svensson, S. Humbel, R.D.J. Froese, T. Matsubara, S. Sieber, K. Morokuma *J. Phys. Chem.* **100**, 19357 (1996).
15. P.E. Sinclair, A. de Vries, P. Sherwood, C.R.A. Catlow, R.A. van Santen *J. Chem. Soc., Faraday T* **94**, 3401 (1998).
16. K. Sillar, P. Burk *Theochem* **589**, 281 (2002).
17. X. Solans-Monfort, M. Sodupe, V. Branchadell, J. Sauer, R. Orlando, P. Ugliengo *J. Phys. Chem. B* **109**, 3539 (2005).
18. S. Kasuriya, S. Namuangruk, P. Treesukol, M. Tirtowidjojo, J. Limtrakul *J. Catal.* **219**, 320 (2003).
19. S. Namuangruk, P. Pantu, J. Limtrakul *ChemPhysChem* **6**, 1333 (2005).
20. S. Namuangruk, P. Khongpracha, P. Pantu, J. Limtrakul *J. Phys. Chem. B* **110**, 25950 (2006).
21. A.K. Rappe, C.J. Casewit, K.S. Colwell, W.A. Goddard, W.M. Skiff *J. Am. Chem. Soc.* **114**, 10024 (1992).
22. M.J. Frisch et al *Gaussian 03, revision B.05*; Gaussian, Inc.: Wallingford, CT, (2004).

EFFECTS OF THE FRAMEWORK ON ADSORPTION OF METHANE ON IRMOF-1, IRMOF-2 AND IRMOF-6 METAL-ORGANIC FRAMEWORKS: A COMBINED QM AND MM STUDY

BUNDET BOEKFA^{1,2}, SAOWAPAK CHOOMWATTANA^{1,2},
CHULARAT WATTANAKIT^{1,2}, PAILIN LIMTRAKUL^{1,2}, PIBOON PANTU^{1,2,3},
PIPAT KHONGPRACHA^{1,2,3}, JUMRAS LIMTRAKUL^{1,2,3*}

⁽¹⁾ *Physical Chemistry Division, Department of Chemistry, Faculty of Science, Kasetsart University, Bangkok 10900, Thailand*

⁽²⁾ *Center of Nanotechnology, Kasetsart University Research and Development Institute, Bangkok 10900, Thailand*

⁽³⁾ *Center of Excellence, National Nanotechnology Center, Kasetsart University, Bangkok 10900, Thailand*

The adsorption and interaction of methane on three different isorecticular metal-organic frameworks (IRMOFs) have been theoretically investigated at the ONIOM (MP2/6-31G(d,p):PM3) level of theory. Adsorption sites and various adsorbed structures were determined. Methane preferentially adsorbs at the corner region of the cubic structure of IRMOF by interacting with the three carboxylate groups of the 1,4-benzenedicarboxylate (BDC) linkers. The adsorption energy of methane on the IRMOF-1 is calculated to be -4.54 kcal/mol. The addition of a substituent on the linker molecule increases the adsorption energy to -6.75 and -5.00 kcal/mol for IRMOF-2 (BDC-Br) and IRMOF-6 (BDC-C₂H₄), respectively. The higher adsorption energy of methane in IRMOF-2 may be due to both the inductive and steric effects of the substituted Br atom.

1. Introduction

Metal-organic frameworks (MOFs) are new, important porous materials with potential applications in separation, catalysis, and gas storage [1-12]. These crystalline porous materials are composed of three-dimensional clusters of metal oxide held together by organic linkers forming into a systematic network with periodic channels and cavities in the nanoscale. The pore structure can be tailored to suit various applications by using suitable linkers.

The MOF-5 structure is composed of octahedral clusters of the Zn₄O tetrahedral cores each attached to six edge-bridged 1,4-benzenedicarboxylate (BDC) linkers that assemble into a network of the three-dimensional cubic

* Corresponding authors: J. Limtrakul, email: fscijrl@ku.ac.th, Fax: (+66)2-562-5555 ext 2119

structure [1,2]. By changing the organic linkers, various isoreticular metal-organic frameworks (IRMOFs) were designed and synthesized without changing the prototype structure of MOF-5. Yaghi and coworkers [3] synthesized 16 IRMOF materials with pore sizes ranging from 3.8-28.8 Å. These materials have the advantages of low density (1.0 to 0.20 g/cm³) and large surface areas (500 to 4,500 m²/g) and high free volume in crystals (55.8-91.1%). Therefore, IRMOFs are excellent materials for molecular storage [3-7] and separation [8-12]. The IRMOF-6 was reported to have the highest methane storage capacity [3].

The methane storage on IRMOF-6 has been studied and compared with other materials such as FAU zeolite, silicalite zeolite, MCM-41 and carbon nanotubes [5,6]. The IRMOF-6 is one of the best materials for methane storage due to its high free volume, low framework density, and strong energetic interaction between the framework and methane molecules. In addition to this, the simulations predicted that the linkers change to 1,4-tetrabromobenzene-dicarboxylate and 9,10-anthracenedicarboxylate, the amount adsorbed per volume can be increased [5].

One of the main targets in the development of metal-organic frameworks is the focus on applying them to trap and separate organics and small gas molecules, especially for hydrogen storage and methane storage. Understanding the properties of the high porosity surface materials is a very important aspect of achieving the goals for being suitable for gas storage. The knowledge of adsorption sites and interactions with the adsorbed molecule would be of great benefit for the design of better metal-organic frameworks. In this study, the interactions of methane on IRMOF-1 (BDC-H), IRMOF-2 (BDC-Br) and IRMOF-6 (BDC-C₂H₄), are investigated with the ONIOM calculation. The aims of this paper are: 1) to investigate the adsorption behavior of methane on IRMOF; 2) to discuss the effect of the framework from the ONIOM calculation; and 3) to study the effect of the linker-BDC to the adsorption properties of methane via IRMOF-1, 2 and 6.

2. Methodology

The structures of IRMOF were generated from the crystallographic X-Ray pattern [2]. The smallest model consisted of Zn₄O(CO₂)₆ and one BDC linker (total of 39 atoms). The next model had the metal cluster and three BDC linkers to represent a corner of the cubic structure of MOF-5 (total of 59 atoms). Full quantum calculations were used for these two models. To include the extended framework of the MOF-5 structure, the ONIOM2 method was employed to take advantage of the computational efficiency with a satisfactory degree of accuracy.

The IRMOF-1 cluster was divided into two layers of calculation methods. The inner layer was the cluster of 59 atoms of one $Zn_4O(CO_2)_6$ unit and three BDC linkers modeled with density functional theory B3LYP/3-21G. The extended structures up to 1215 were modeled with semi-empirical methods. The extended 251-atom model covered the six $Zn_4O(CO_2)_6$ clusters around the quantum cluster. The extended 439-atom model covered one complete unit cell (see Fig. 1). The largest model of 1215 atoms covered the 8 unit cells. The structures of IRMOF-2 and IRMOF-6 were similar to the IRMOF-1 but with different linker molecules (see Fig. 2).

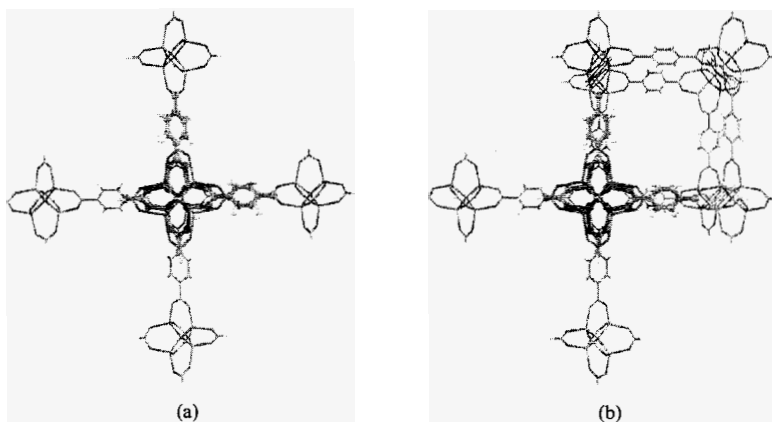


Figure 1. The IRMOF-1 structure represented with (a) 251 atoms and (b) 439 atoms. The high level region of one $Zn_4O(CO_2)_6$ unit and three BDC linkers (total of 59 atoms) at the center is illustrated by ball-and-stick and the extended framework is illustrated by wire frame.

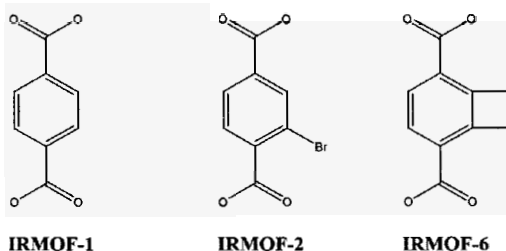


Figure 2. Linker structure of various isoreticular metal-organic frameworks (MOFs).

The $Zn_4O(CO_2)_6$ cluster and the probe molecule were allowed to relax while the linkers were kept fixed along the crystalline coordinates. The single point energy calculations at MP2/6-31G(d,p) level of theory were performed to refine

the adsorption energies since it is known that DFT does not take into account the dispersion force of the interactions. The extended frameworks are treated with 3 approaches: AM1; PM3; and UFF levels of calculation via ONIOM methodology [13]. All calculations were performed with the Gaussian 03 program [14].

3. Results and Discussion

3.1. *The effect of the cluster size on the adsorption of methane*

Adsorption of methane on IRMOF-1 was investigated on various sizes of fragment clusters. The smallest model consisted of $Zn_4O(CO_2)_6$ and one BDC linker (total of 39 atoms). The next model added two more BDC linkers to complete one corner of the cubic structure of MOF-5 (total of 59 atoms). Extended structures of the IRMOF-1 were included by using the ONIOM2 method. Semi-empirical methods were used to model extended structures up to 251 and 439 atoms. The calculated structures for Zn-O and O-C distances were close to experimental measurements of 1.91 and 1.30 Å, respectively. The O-C-O and Zn-O-C angles were also close to experimental measured values of 125.0 and 130.4 degrees, respectively [1,10]. Methane adsorbed on the corner region having its three hydrogen atoms placed in the middle of each pair of carboxylate groups of the linkers (see Fig. 3). For example, the distances between the H1 atom of the adsorbed methane to O1 and O6 of the carboxylate groups are almost equal at 2.85, and 2.90 Å, respectively.

The calculated adsorption energies were tabulated in Table 1. The adsorption energy was -3.97 kcal/mol for the smallest cluster. Increasing the cluster size to 59 atoms increased the adsorption energy to -4.27 kcal/mol. Addition of the extended framework by semi-empirical methods slightly increased the overall adsorption energy by 0.2-0.4 kcal/mol. Although the effect of the extended framework is very little at this low loading condition, it may be important for the adsorption at high loading. All the semi-empirical methods used in this study showed similar results. The PM3 method was selected for further study because this approach always provides more reliable results for structure and adsorption properties of the complexes involving metal-ligand as well as hydrogen bonding interactions as compared to the AM1 approach.

Other adsorption structures were also studied. Methane can also adsorb on one of the carboxylate oxygen atoms, but with a smaller adsorption energy. Methane was found to have little interaction with the benzene ring, and an adsorption structure near the benzene ring was not found.

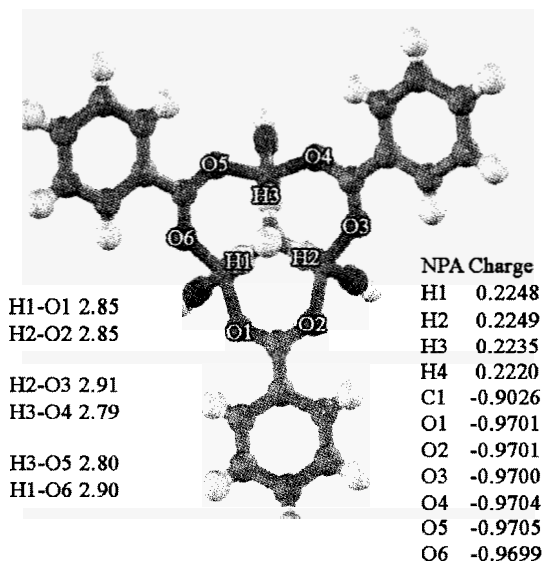


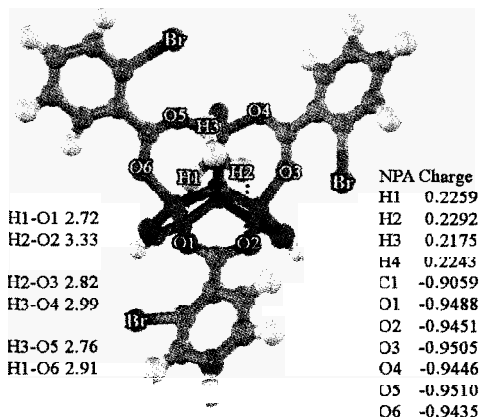
Figure 3. The optimized structure of the methane adsorption on IRMOF-1. Atoms near the adsorption site are labeled atomically and numerically and the extended framework is omitted for clarity. Selected distances (in Å) and NPA charge parameters are shown.

Table 1. Adsorption energies (kcal/mol) of methane on IRMOF-1 with MP2/6-31G(d,p)//B3LYP/3-21G.

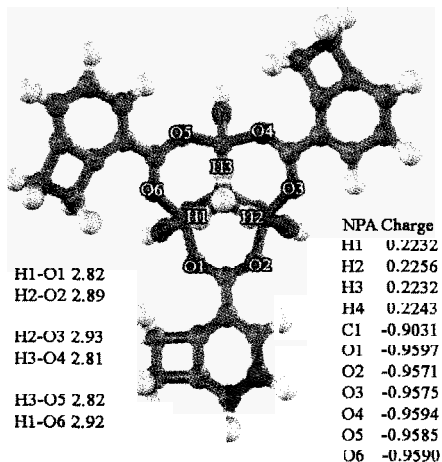
Methods	Size of framework (atoms)				
	39	59	59/251	59/439	59/1215
MP2	-3.97	-4.27			
MP2:AM1			-4.55	-4.60	
MP2:PM3			-4.52	-4.54	
MP2:UFF			-4.67	-4.69	-4.68

3.2. Methane adsorption on IRMOF-2 and IRMOF-6

The methane adsorptions on IRMOF- 1, 2 and 6 have been studied with ONIOM MP2/6-31G(d,p):PM3//B3LYP/3-21G:PM3. The optimized structures are shown in Fig. 4. and geometrical parameters are tabulated in Table 2. The adsorption energies of methane are -4.54, -6.75 and -5.00 kcal/mol for IRMOF-1, 2 and 6, respectively.



(a)



(b)

Figure 4. The optimized structure of the methane adsorption on (a) IRMOF-2 and (b) IRMOF-6. Atoms near the adsorption site are labeled atomically and numerically and the extended framework is omitted for clarity. Selected distances (in Å) and NPA charge parameters are shown.

The substitute groups on IRMOF-2 and IRMOF-6 caused unsymmetrical adsorption. The interaction between the hydrogen atom (H1) of methane to the O1 oxygen atom, that sits closer to the Br atom, appeared to be stronger than the interaction between the H2 and O2 atoms as indicated by the shorter distance of O1--H1 (2.72 Å) than the O2--H2 distance (3.33 Å). Due to the electron withdrawing property of the Br atom, the atomic charges of oxygen atoms of the carboxylate groups of IRMOF-2 (average of -0.95 e) are slightly less negative

than on the other (average of -0.97 and -0.96 e for IRMOF-1 and IRMOF-6, respectively). The stronger adsorption energy for IRMOF-2 and IRMOF-6 as compared to the unsubstituted IRMOF-1 is due to the reduction in pore size that is well known to enhance the interaction energy and in the case of the IRMOF-2, to some extent, may be due to the inductive effect of the Br atom. The higher adsorption energy on IRMOF-6 compared to IRMOF-1 is in agreement with its better methane uptake [3]. Düren [5] also reported that the isosteric heat of adsorption at low loading of methane on IRMOF-6 was higher than that on IRMOF-1 and predicted that a higher adsorption heat for IRMOF-992 (than that of IRMOF-6), which used 1,4-tetrabromobenzenedicarboxylate as the linker molecule. In this study, we also observed the same trend of adsorption energies, IRMOF-1 < IRMOF-6 < IRMOF-2.

Table 2. The geometrical parameters of methane on IRMOF-1, 2 and 6 with MP2/6-31G(d,p):PM3//B3LYP/3-21G:PM3 (distances in Å and angles in radius).

	IRMOF-1		IRMOF-2		IRMOF-6	
	59/439		59/439		71/499	
	Bare	Complex	Bare	Complex	Bare	Complex
distances						
Zn-O1	1.88	1.88	1.86	1.86	1.86	1.86
Zn-O2	1.88	1.88	1.87	1.87	1.86	1.86
O1-C1	1.29	1.29	1.28	1.28	1.28	1.28
O2-C1	1.29	1.29	1.29	1.28	1.28	1.28
O1 - - H1		2.85		2.72		2.82
O2 - - H2		2.85		3.33		2.89
H1-C	1.09	1.09	1.09	1.09	1.09	1.09
H2-C	1.09	1.09	1.09	1.09	1.09	1.09
O1 - - C		3.63		3.64		3.61
O2 - - C		3.63		3.89		3.74
angles						
O2-C1-O2	121.8	121.8	122.8	122.9	123.5	123.6
C1-O1-Zn1	132.8	132.6	138.1	138.3	131.7	132.1
C1-O2-Zn2	132.8	132.9	125.7	125.6	131.6	131.2
O1-H1-C		127.2		141.7		133.1
O2-H2-C		126.9		113.0		125.8

4. Conclusions

The influence of the extended metal-organic framework (MOF) on adsorption properties of methane interacted with various isoreticular MOFs, namely IRMOF-1, IRMOF-2, IRMOF-6 were carried out at the well-calibrated MP2/6-31G(d,p):PM3 theoretical level. Although the effect of the extended structure at low loading amounts to only about 10%, it may, however, be essential if the loading is increased. The interactions of methane with three different MOF

derivatives: IRMOF-1; IRMOF-2; and IRMOF-6 are predicted to be -4.54, -6.75 and -5.00 kcal/mol, respectively. The substituent groups on IRMOFs (X = H, Br, and C₂H₄) play a prominent role in the structure and adsorption properties of the complexes, which is due to their inductive and steric effects being in good agreement with experimental observations. This information is useful for diffusion properties, adsorption capacity, and reaction mechanisms, which is important for material development.

Acknowledgments

This work was supported in part by grants from the Thailand Research Fund (to JL) and the Kasetsart University Research and Development Institute (KURDI), the National Nanotechnology Center (NANOTEC Center of Excellence and CNC Consortium) and the Commission on Higher Education, Ministry of Education under Postgraduate Education and Research Programs in Petroleum and Petrochemicals, and Advanced Materials.

References

1. H. Li, M. Eddaoudi, M. O'Keeffe and O. M. Yaghi, *Nature* **402**, 276 (1999).
2. M. Eddaoudi, D. B. Moler, H. Li, B. Chen, T. M. Reineke, M. O'Keeffe and O. M. Yaghi, *Acc. Chem. Res.* **34**, 319 (2001).
3. M. Eddaoudi, J. Kim, N. Rosi, D. Vodak, J. Wachter, M. O'Keeffe and O. M. Yaghi, *Science* **295**, 469 (2002).
4. N. L. Rosi, J. Eckert, M. Eddaoudi, D. T. Vodak, J. Kim, M. O'Keeffe and O. M. Yaghi, *Science* **300**, 1127 (2003).
5. T. Düren, L. Sarkisov, O. M. Yaghi and R. Q. Snurr, *Langmuir* **20**, 2683 (2004).
6. M. J. Rosseinsky, *Microporous Mesoporous Mater.* **73**, 15 (2004).
7. H. Frost, T. Düren, R. Q. Snurr, *J. Phys. Chem. B* **110**, 9565 (2006).
8. T. Düren, R. Q. Snurr, *J. Phys. Chem. B* **108**, 15703 (2004).
9. J. L. C. Rowsell, E. C. Spencer, J. Eckert, J. A. K. Howard and O. M. Yaghi, *Science* **309**, 1350 (2005).
10. T. Sagara, J. Klassen, J. Ortony and E. Ganz, *J. Chem. Phys.* **123**, 014701 (2005).
11. A. Samanta, T. Furuta and J. Li, *J. Chem. Phys.* **125**, 084714 (2006).
12. J. Jiang, S. I. Sandler, *Langmuir* **22**, 5702 (2006).
13. S. Dapprich, I. Komirovi, K. S. Byun, K. Morokuma and M. J. Frisch, *Theochem* **461-462**, 1 (1999).
14. M.J. Frisch et al *Gaussian 03, revision B.05*; Gaussian, Inc.: Wallingford, CT, (2004).

ADSORPTIONS OF CO AND NO MOLECULES ON MOF-11: A QM/MM STUDY

PIPAT KHONGPRACHA^{1,2,3}, SUPAWADEE NAMUANGRUK⁴
JUMRAS LIMTRAKUL^{1,2,3,*}

⁽¹⁾Physical Chemistry Division, Department of Chemistry, Faculty of Science,
Kasetsart University, Bangkok 10900, Thailand

⁽²⁾Center of Nanotechnology, Kasetsart University Research and Development Institute,
Kasetsart University, Bangkok 10900, Thailand

⁽³⁾NANOTEC Center of Excellence, National Nanotechnology Center,
Kasetsart University, Bangkok 10900, Thailand

⁽⁴⁾National Nanotechnology Center (NANOTEC), The National Science and
Technology Development Agency, 130 Phaholyothin Rd., Klong Luang,
Pathumthani 12120, Thailand

The chemistry of metal-organic frameworks (MOFs) has been extensively studied, with particular attention being paid to these porous compounds due to their many potential applications: such as gas storage; molecular sieves; and catalysis. In this work we studied the adsorptions of a molecule of the CO and NO gases on the open form of a copper dimer cluster, called the “paddlewheel” configuration, taken from the framework of the MOF-11 compound. The quantum cluster consisting of the paddlewheel and adamantane ligands was treated at the UB3LYP/6-31G(d) level of theory. In order to represent the environmental effect of the MOF framework, we applied the universal force field (UFF) to the system via our Own N-layered Integrated molecular Orbital + molecular Mechanics (ONIOM) scheme. The interaction energies in the ONIOM calculation are -8.39 and -31.24 kcal/mol for the adsorptions of CO and NO molecules, respectively. The van der Waals contributions from the framework of the MOF-11 in both systems are found to be, at most, 7% and insensitive to their interactions. These results indicate that the MOF-11 is very selective to NO gas and can be applied to separate a mixture of gases.

1. Introduction

The design and assembly of metal-organic framework networks have gained ever increasing attention in recent years due to their many potential applications: such as gas storage; molecular sieves; and catalysis [1,2]. The porous metal-organic framework (MOF) consists of metal ion units and organic ligand linkages. There are numerous transition metal (Zn^{II} , Cu^I , Ag^I or Cd^{II}) ions that have been extensively selected for being a part of secondary building units (SBUs). The

* To whom correspondence should be addressed. E-mail: jumras.l@ku.ac.th

SBUs possess many coordination patterns, such as the copper-carboxylate paddlewheel, $\text{Cu}_2(\text{O}_2\text{C})_4$, and the octahedral basic zinc carboxylate, $\text{Zn}_4\text{O}(\text{O}_2\text{C})_6$, which act as square and octahedral joints. In addition, a number of three-dimensional coordination polymers have been characterized and prepared for connecting each of the SBUs to form a three dimensional network.

Among a large number of porous metal-organic framework compounds, $\text{Cu}_2(\text{ATC})$ or MOF-11 is one of the more interesting structures [3]. The formation of $\text{Cu}_2(\text{ATC})\cdot 6\text{H}_2\text{O}$ crystal can be assembled from a copolymerization of 1,3,5,7-adamantane tetracarboxylate (ATC) with Cu(II) metal ions, giving the paddle-wheel Cu-C-O shape with the adamantane network. The paddle-wheel metal cluster motif is considered to be very active for the adsorption process as there is more open area near the metal center. This accessible space is available for capturing molecules of incoming gas.

One of the main targets in the development of metal-organic frameworks is the focus on applying them to trap and separate organics and small gas molecules. To date, many of the works on these compounds have concentrated mainly on applying them for hydrogen storage. Understanding the properties of the high porosity surface materials is a very important aspect of achieving the goal to use them for gas storage. Previous *ab initio* as well as force field calculations were also utilized to investigate the adsorption properties of the compounds at the metal and polymeric linkage sites. Among many types of small gases, carbon monoxide and nitrous oxide molecules are known as common choices for probe molecules. Here, we describe the adsorption of CO and NO molecules on an MOF-11 material by taking advantage of the density functional theory. The environmental influence due to the interactions of atoms in the framework pore with a probe molecule, named the 'confinement effect' was taken into consideration via the two-layer our Own N-layered Integrated molecular Orbital + molecular Mechanics (ONIOM) technique [4].

2. Computational Details

The MOF-11 framework was modeled by the $\text{Cu}_{36}\text{O}_{144}\text{C}_{152}\text{H}_{136}$ cluster taken from its lattice structure. This cluster holds a region of eighteen copper oxide paddlewheel units connected to each other through eight adamantane organic linkages. The dangling bonds resulted from cutting the C-C bonds that were terminated by the H atoms. In order to take advantage of the computational efficiency with a satisfactory degree of accuracy, the MOF-11 cluster was divided into two layers of calculation methods as in the Quantum mechanical/Molecular mechanical (QM/MM) concept via the two-layer our Own

N-layered Integrated molecular Orbital + molecular Mechanics (ONIOM2) scheme (Figure 1). The inner layer or the quantum mechanical (QM) cluster, including one copper oxide paddlewheel and four adamantane organic linkages, was treated by the hybrid density functional theory approach (UB3LYP) combined with the 6-31G(d) basis set to represent the active site of MOF-11. The remaining extended framework that surrounds the inner layer was treated as the molecular mechanical (MM) layer via the universal force field (UFF) [5]. The force field has been found to provide a good description of the short-range van der Waals (vdW) interactions in many systems [6]. All calculations were performed using the Gaussian 03 code [7]. During optimization, only atoms in the inner layer were allowed to relax while the remainders were fixed along the position of the crystallographic lattice. A probe molecule (CO or NO) was placed nearby the active paddlewheel unit and optimized to reach the minimum energy configuration. The QM/MM adsorption energy (ΔE_{ads}) for such a probe molecule was obtained from Equation (1) while the QM adsorption energy ($\Delta E_{\text{ads}}(\text{QM})$) was calculated from Equation (2). Thus, the MM adsorption energy ($\Delta E_{\text{ads}}(\text{MM})$) can be derived from the difference between ΔE_{ads} and $\Delta E_{\text{ads}}(\text{QM})$.

$$\Delta E_{\text{ads}} = E_{\text{MOF-11/CO}}^{(\text{QM/MM})} - E_{\text{MOF-11}}^{(\text{QM/MM})} - E_{\text{CO}}^{(\text{QM})} \quad (1)$$

$$\Delta E_{\text{ads}}(\text{QM}) = E_{\text{MOF-11/CO}}^{(\text{QM})} - E_{\text{MOF-11}}^{(\text{QM})} - E_{\text{CO}}^{(\text{QM})} \quad (2)$$

3. Results and Discussion

The optimized structures of the MOF-11 and their complexation with CO and NO molecules are illustrated in Figure 1. Selected geometrical parameters of the complexes and their corresponding adsorption energies are tabulated in Table 1. The CO molecule adsorbs linearly on the Cu atom inside the MOF-11 nanopore with a C-bound direction. The adsorption energy for the CO molecule is -8.39 kcal/mol. The NO molecule also interacts linearly with Cu atom with the Cu₁-N distance of 1.926 Å. On the adsorption of the CO molecule, the Cu₁ atom moves away from the cluster toward the CO molecule. The Cu₁-Cu₂ bond is lengthened from 2.525 Å to 2.771 Å while those Cu₁-O bonds are lengthened from 1.958 Å to 2.063 Å in the CO adsorption adduct. As for the MOF-11/NO complex, its adsorption energy is -31.24 kcal/mol, which comes mostly from the QM calculation for -30.88 kcal/mol (see Table 1). The effect of the extended MOF-11s framework on the probe molecules is very weak, which is due mainly to the small sizes of the molecules. The distance between the NO molecule and the Cu₁ atom is 2.372 Å. Despite the high adsorption of the NO molecule, the bonds in

the metal oxide cluster are contracted. On the adsorption of the NO molecule, the $\text{Cu}_1\text{-Cu}_2$ bond is contracted from 2.525 Å to 2.503 Å and those $\text{Cu}_1\text{-O}$ bonds are shortened slightly from 1.958 Å to 1.952 Å.

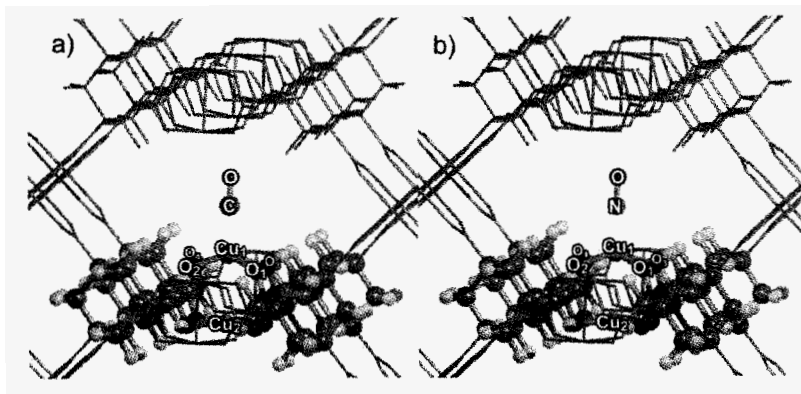


Figure 1. Models for the adsorptions of a) CO and b) NO molecules on MOF-11: the inner cluster (balls and sticks) was computed at the UB3LYP/ 6-31G(d) and the surrounding framework (lines) was treated with the universal force field (UFF).

The MOF-11/CO and MOF-11/NO adducts have been analyzed by calculating the differences of their electron densities compared to the noninteracting systems as shown in Figure 2. The results were compared to the Mulliken analysis. It is found that the electron density redistribution due to the interaction of the CO molecule with the paddlewheel cluster occurs mostly in the Cu_1 atom and CO molecule region. There is a small change of the electron density in the carboxylate groups and the Cu_2 atom. These findings are confirmed by the changes in the Mulliken charges. On the adsorption of the CO molecule, the positive charge of the Cu_1 atom decreases from 0.461 to 0.313 and the CO molecule gains a more positive charge by 0.110 while only few changes are found in the Cu_2 (+0.027) and those $\text{O}_1\text{-O}_4$ (+0.016) atoms. In the case of the interaction of the NO molecule, it adsorbs on the MOF-11 framework at the same site as the CO molecule, the rearrangements of electron density are entirely different. There are much more electron density changes in both the paddlewheel and the NO molecule (Figure 2b). There are noticeable electron density reductions on both copper atoms along with electron density gatherings on those carboxylate oxygen atoms. Interestingly, there is no electron accumulation found in the intermolecular space between the paddlewheel cluster and the NO molecule. From the Mulliken population analysis, there is a very small net charge transfer (0.014 e) from the paddlewheel cluster to the NO molecule. The

positive charges of copper atoms are increased from 0.461 to 0.635 and 0.553 for Cu₁ and Cu₂, respectively, while the negative charges of carboxylate oxygen atoms are also changed from -0.520 to -0.550 as well. These changes cause a higher ionicity in the metal oxide paddlewheel cluster and contract those Cu-Cu and Cu-O bonds in the cluster.

Table 1. Optimized bond parameters (angstroms) of all isolated and adsorption complexes, adsorption energies (kcal/mol) and Mulliken populations (e). Values in parenthesis belong to isolated gas molecules.

	MOF-11	MOF-11/CO	MOF-11/NO
Cu ₁ -Cu ₂	2.525	2.771	2.503
Cu ₁ -O _{1,2,3,4}	1.958	2.063	1.952
Cu ₁ -C/-N	-	1.926	2.372
C-O/N-O	(1.137/1.159)	1.137	1.152
qCu ₁	0.461	0.313	0.635
qCu ₂	0.461	0.488	0.553
qO _{1,2,3,4}	-0.520	-0.504	-0.550
qC/qN	(0.174/0.112)	0.387	0.155
qO _{gas}	(-0.174/-0.112)	-0.277	-0.169
qCO/NO	0.000	0.110	-0.014
AE _{ads}	-	-8.39	-31.24
AE _{ads} (QM)	-	-7.82	-30.88
AE _{ads} (MM)	-	-0.57	-0.36

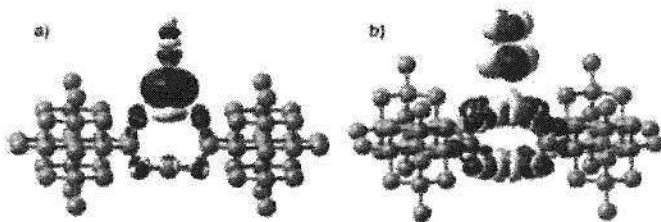


Figure 2. Electron density differences for the interactions of a) CO and b) NO molecules on the *model of the MOF-11 surface. Dark blue and light yellow surfaces refer to electron accumulating and electron depleting areas, respectively. Hydrogen atoms and the framework were excluded for clarification.

4. Conclusions

The density functional theory was used to study the adsorptions of CO and NO molecules on the open metal paddle-wheel cluster. To represent the influence of

the MOF framework on a guest molecule, we treated this issue by performing B3LYP/6-31G(d):UFF calculations through the ONIOM scheme. The adsorption energies for CO and NO molecules on MOF-11 are -8.39 and -31.24 kcal/mol, respectively. Although there is a very small amount of net electron density transfer (0.014 e) between the paddlewheel cluster and the NO molecule, the metal oxide cluster is polarized to hold a higher ionicity characteristic. Through the interaction of the NO molecule, copper atoms gain higher positive charges while those carboxylate oxygens have more negative charges, and the contractions of Cu-Cu and Cu-O bonds in the metal oxide cluster are noticeably observed. This induced ionicity causes the MOF-11/NO complex to have a much higher stability and a larger binding energy compared to the MOF-11/CO adduct. These results reveal that this type of nanoporous material is very selective to incoming guest molecules. Therefore, it can be used as a molecular sieve for separating a mixture of gases.

Acknowledgments

This work was supported in part by grants from the Thailand Research Fund and the Kasetsart University Research and Development Institute (KURDI), the National Nanotechnology Center (NANOTEC Center of Excellence and CNC Consortium) and the Commission on Higher Education, Ministry of Education under Postgraduate Education and Research Programs in Petroleum and Petrochemicals, and Advanced Materials.

References

1. H. Li, M. Eddaoudi, M. O'Keeffe and O. M. Yaghi, *Nature* **402**, 276 (1999).
2. M. Eddaoudi, D. B. Moler, H. Li, B. Chen, T. M. Reineke, M. O'Keeffe and O. M. Yaghi, *Acc. Chem. Res.* **34**, 319 (2001).
3. B. Chen, M. Eddaoudi, T.M. Reineke, J.W. Kampf, M. O'Keeffe, O.M. Yaghi, *J. Am. Chem. Soc.* **122**, 11559 (2000).
4. S. Dapprich, I. Komirovi, K. S. Byun, K. Morokuma and M. J. Frisch, *Theochem* **461-462**, 1 (1999).
5. A.K. Rappe, C.J. Casewit, K.S. Colwell, W.A. Goddard, W.M. Skiff *J. Am. Chem. Soc.* **114**, 10024 (1992).
6. S. Namuangruk, P. Khongpracha, P. Pantu, J. Limtrakul, *J. Phys.Chem. B.* **110**, 25950 (2006).
7. M.J. Frisch et al *Gaussian 03, revision B.05*; Gaussian, Inc.: Wallingford, CT, (2004).

THERMAL ANOMALY AND MOLECULAR MOTION OF ORGANIC MOLECULES CONFINED IN THE NANOCAVITY OF METAL-ORGANIC FRAMEWORKS IRMOF-1

TAKAHIRO UEDA^{1,2*}, KENJI KUROKAWA¹, YOSHIKI KAWAMURA¹, KEISUKE MIYAKUBO¹, TARO EGUCHI^{1,2}

¹*Department of Chemistry, Graduate School of Science, Osaka University, Toyonaka, Osaka 560-0043, Japan*

²*The Museum of Osaka University, Osaka University, Toyonaka, Osaka 560-0043, Japan*

The first observation of thermal anomaly in IRMOF-1 accommodating various organic molecules as a guest has been reported. Endothermic and exothermic peaks were observed in DTA measurements of heating and cooling, respectively, for IRMOF-1, including various guests. In each guest, the thermal anomaly was observed at a temperature lower than the melting point of bulk. In addition, molecular motion of cyclohexane in the nanocavity was examined using solid-state ¹H wide-line NMR. The abrupt narrowing of the resonance line occurred at 210 K, which was coincident with appearance of the endothermic peak in this specimen. The second moment analysis indicates liquid-like behaviour of cyclohexane at temperatures greater than 210 K, rendering it possible to assign the thermal anomaly observed in DTA to melting of cyclohexane.

1. Introduction

Isorecticular metal-organic framework (IRMOF) is the general term representing a series of porous compounds that consist of tetrahedron of Zn₄O and the derivatives of terephthalic acid. In fact, [Zn₄O(O₂CC₆H₄CO₂)₃]_n (IRMOF-1) is a prototype of these compounds, in which terephthalic acid is included as a cross-linker. This compound crystallises in the cubic lattice with a space group $Fm\bar{3}m$ and the unit cell with the lattice constant of 2.58849 nm contains eight empirical [Zn₄O(O₂CC₆H₄CO₂)₃] formula units [1]. Depending on the orientation of phenyl ring in the terephthalic acid moiety, two spherical void types are formed: the larger one has 1.51 nm diameter; the smaller one has 1.10 nm diameter. These cavities are arranged alternately and are mutually linked with a window of 0.80 nm opening. The high crystallinity of IRMOF-1 gives a uniform and homogeneous pore structure with narrow pore distribution. The fundamental

* Corresponding author. Fax: +81 6 6850 5785, E-mail address: ueda@museum.osaka-u.ac.jp

properties of adsorbency in IRMOF-1 have been studied extensively and in detail. Actually, IRMOF-1 exhibits I-type adsorption isotherms for various gases and organic solvents such as Ar, N₂, CCl₄, CHCl₃, benzene, and cyclohexane [2]: it can accommodate 6.38 molecules of cyclohexane in a cage at the saturated amount of adsorption. Furthermore, ¹²⁹Xe NMR studies have been carried out to characterise both the porosity and intermolecular interaction of xenon adsorbed in IRMOFs. Those studies have also investigated the xenon adsorption enthalpies, the exchange behaviour of xenon between adsorption sites as well as those between inner space of the lattice and outer gases, and the xenon adsorption sites in the cavity [3, 4].

Recently, physicochemical properties, especially the dynamic behaviour, of adsorbed gases in the highly ordered metal-organic cavity have attracted much attention. Results of solid-state NMR studies have underscored the mobility of benzene guest in the IRMOF-1 nanocavity as well as of the terephthalic acid moiety [5]. The diffusion behaviour of various guests in IRMOF-1 has also been investigated using PFG-NMR diffusion measurement [6]. In addition, confinement of the guest molecules is expected to show different properties from those of bulk. Just recently, we have reported the dynamic behaviour of cyclohexane in the IRMOF-1 nanocavity using solid-state ²H NMR spectroscopy as well as the finding of thermal anomaly caused by the dynamic behaviour of guests [7].

In this study, we report the first observation of thermal anomaly in IRMOF-1, including various organic molecules as a guest. Molecular motion of cyclohexane in the nanocavity has also been examined using solid-state ¹H wide-line NMR. Results showed that the thermal anomaly took place simultaneously with excitation of isotropic molecular motion of the guests.

2. Experimental

The IRMOF-1 was prepared according to a description given in Ref. 5. 2.0 g of Zn(NO₃)₂·6H₂O and 0.80 g of terephthalic acid were dissolved in each of 100 ml diethylformamide, and two solutions were mixed in a pressure-resistant Teflon-jaw with a sealing cap. White precipitates were obtained by heating at 373 K for 24 h, filtered and washed with DMF. Guest-free IRMOF-1 powders were obtained by evacuation at 573 K for 24 h. Details of characterisation have been described elsewhere [7].

We used the following solvents as guest molecules: benzene, toluene, *m*-xylene, *p*-xylene, cyclohexane, *n*-hexane, *n*-octane, *n*-decane, chloroform, and carbon tetrachloride. Adsorption of the various guest molecules was carried out

according to the following procedure. An appropriate volume of organic solvent, which was measured using a microsyringe, was added to a constant amount of guest-free IRMOF-1 powdered specimen in a DTA sample tube with Schlenk tube under a N_2 atmosphere. The sample tube containing IRMOF-1 and guest was connected to a vacuum line; it was then sealed by flame after loading He gas (ca. 150 Torr) under immersion in liquid nitrogen. No endothermic peaks corresponding to bulk solvent were observed in the DTA diagram of IRMOF-1 with various guests (*vide infra*), supporting that the IRMOF-1 framework virtually accommodates adsorbate. The amount of guest in the sealed sample tube was estimated using the weight increment after sealing. The resultant sample tube was maintained at ambient temperature for 2–3 days to achieve the adsorption equilibrium. The adsorption amount of guest was represented by the percentage of added volume of solvent to the pore volume ($V_{\text{pore}} = 1.16 \text{ cm}^3 \cdot \text{g}^{-1}$), as determined using the N_2 adsorption isotherm. For NMR measurement, cyclohexane was used as a guest solvent.

Differential thermal analysis (DTA) was carried out using a homebuilt apparatus at temperatures of 97–370 K. The DTA diagrams were recorded in both directions during heating and cooling. Furthermore, the measurements were repeated a few times to check the thermal hysteresis.

The NMR measurements were carried out using a spectrometer (DSX-200; Bruker Analytik GmbH) operating at the Larmor frequency of 200.13 MHz for the ^1H nucleus. The free induction decay (FID) signals were recorded using a single pulse sequence in the temperatures of 118–298 K.

3. Results and discussion

3.1. Differential thermal analysis (DTA)

Figure 1 presents DTA diagrams of guest-free IRMOF-1 and IRMOF-1 with various organic solvents. In guest-free IRMOF-1, any exothermic and endothermic peaks were invisible at temperatures of 97–300 K. On the other hand, thermal anomalies were observed reversibly in the IRMOF-1 samples accommodating the guest molecules on both heating and cooling processes, although the transition points depend on the kinds of the guest molecules. The transition points determined from the heating process are summarised in Table 1. Hysteresis of the thermal anomalies is apparently small in each specimen. Moreover, no peaks from bulk crystal of any guest were observed in the DTA diagrams (Figs. 1(b) – 1(k)), strongly suggesting that IRMOF-1 quite accommodates the loaded organic solvents into the nanocavity. These aspects

indicate that the thermal anomalies are originated from the thermal behaviour of the guest molecules. In other words, the observation of reversible phase transition implies the existence of the long-range order between the guest molecules confined in the IRMOF-1 nanocavity.

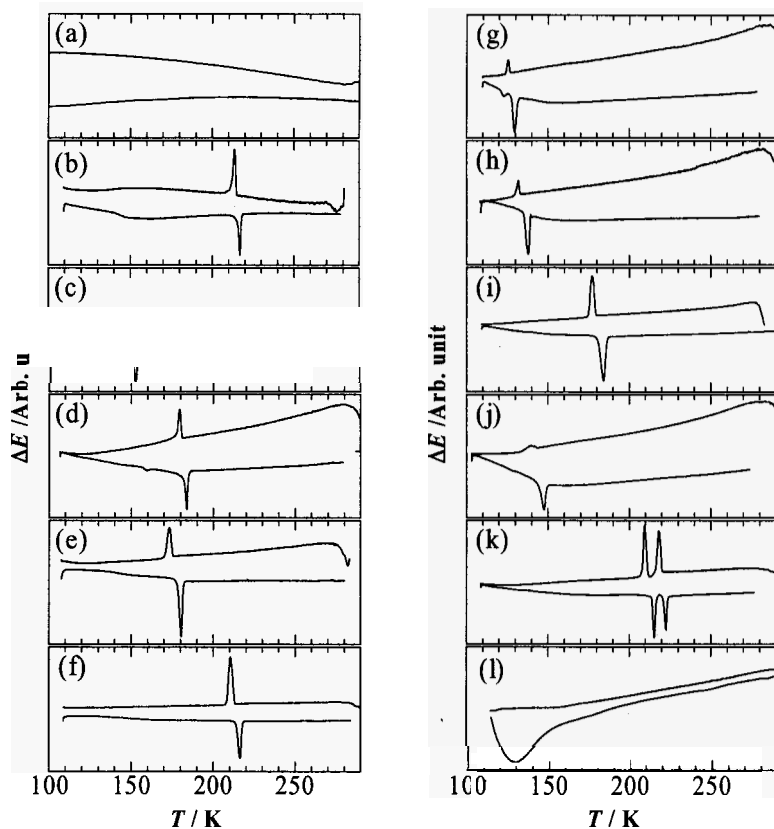


Figure 1. Differential thermal analysis diagrams of guest-free IRMOF-1 (a). IRMOF-1 accommodating various solvents: benzene (b), toluene (c), *m*-xylene (d), *p*-xylene (e), cyclohexane (f), *n*-hexane (g), *n*-octane (h), *n*-decane (i), chloroform (j), carbon tetrachloride (k), and molecular sieves 13X accommodating cyclohexane (l). The upper curves show data obtained during cooling; the lower ones show data obtained during heating. The upward and downward peaks respectively signify exothermic and endothermic phenomena.

Interestingly, the thermal anomalies were also observed in IRMOF-1 with different amounts of guest organic solvent. For example, IRMOF-1 with

cyclohexane of 36% saturation (2.3 molecules per cavity) gave an endothermic peak at 213 K [7]. This aspect implies that the guest molecules behave collectively each other in IRMOF-1 even with partial loading. It is feasible that the guest molecules were mutually assembled in the IRMOF-1 framework to form the domain structure of fully occupied cavities. Remarkably, two sharp endothermic peaks appear on DTA diagram of carbon tetrachloride in IRMOF-1. This behaviour is likely to the thermal behaviour of bulk solid, in which monoclinic phase of CCl_4 changes into fcc plastic phase at 225.7 K and it melts at 246.0 K [8]. In general, the transition of low temperature phase into plastic phase accompanies large endothermic peak because of the orientational disorder of the molecule. The clear and sharp peaks for CCl_4 in IRMOF-1 imply appearance of successive phase transition of guest CCl_4 in IRMOF-1 like those in bulk.

Table 1. Phase transition point determined from DTA measurements in various guests confined in IRMOF-1.

Guest	Filling (%)	$T_m(\text{bulk}) / \text{K}$	$T_m(\text{confined}) / \text{K}$
benzene	63	279	216
toluene	79	178	149
<i>m</i> -xylene	100	225	158, 182
<i>p</i> -xylene	63	286	178
cyclohexane	100	280	(121) ^a , 213
<i>n</i> -hexane	61	173	121, 127
<i>n</i> -octane	64	216	135
<i>n</i> -decane	82	243	181
chloroform	69	210	144
carbon tetrachloride	73	250	214, 221

a) This peak was not observed in this study, but was observed clearly in our previous work [7].

Co-operative and collective phenomena such as solid-solid phase transition and melting for the confined molecules have been commonly observed in mesopores with diameter greater than 2 nm [9–12], but rarely reported in the micropore of aluminosilicates. Figure 1(l) shows the DTA diagram of molecular sieves 13X accommodating cyclohexane. No exothermic or endothermic peaks were observed. The opening (0.80 nm) of the window between the cavities in IRMOF-1 resembles that in molecular sieves 13X (ca. 0.74 nm) [13]. Therefore, the appearance of the phase transition might be more strongly affected by the structural regularity rather than direct molecular contact between guests occupying the neighbouring cavities. Structural irregularities such as inhomogeneous distribution of exchanged cations, aluminium atoms, and

hydroxyl group on the pore wall in the aluminosilicates will create incoherent potential fields for the guest-wall interactions, engendering disordered and inhomogeneous distributions of adsorbates in the cavities. In fact, Halasz et al. reported that highly aluminium-deficient Y zeolites with low hydroxyl content accommodate adsorbates with ordered structure in the microporous framework [14]. In IRMOF-1, high crystallinity produces a regularly ordered structure of the pore wall and high periodicity in the cavities. These situations probably give rise to coherent potential fields over the IRMOF-1 cavities and to collective phenomenon concerning with guest molecules which occupy some continuous cavities of IRMOF-1.

3.2. Temperature dependence of solid-state ^1H wide-line NMR spectrum

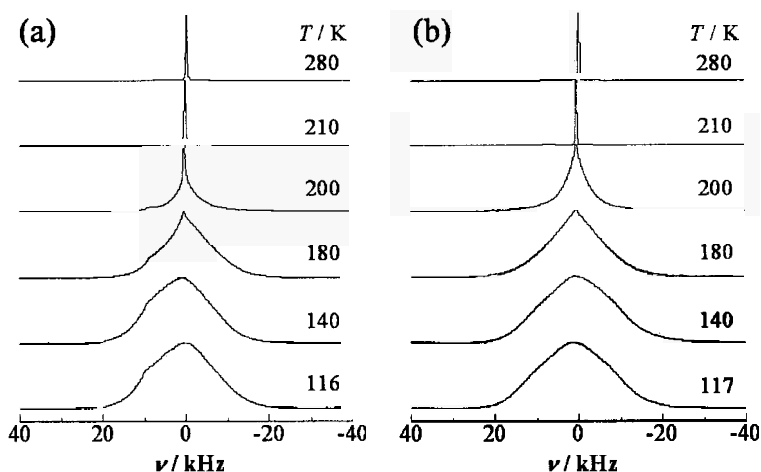


Figure 2. Temperature dependence of ^1H wide-line NMR spectrum of cyclohexane confined in the IRMOF-1 nanocavity with adsorption amount of 45% (a) and 95% (b) saturation.

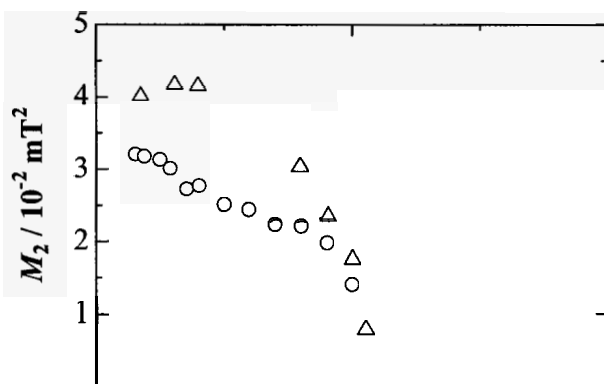
Figure 2 shows the temperature dependence of ^1H wide-line NMR spectrum of cyclohexane confined in the IRMOF-1 nanocavity. Although the spectrum consisted of ^1H nuclei in both of cyclohexane and terephthalic cross-linker, cyclohexane gave a main peak and the cross-linker was observed as a minor shoulder on the higher frequency side of the main peak. The spectrum depends effectively on the temperature, indicating the motional narrowing processes of cyclohexane. For that reason, we examine the molecular motion of cyclohexane in terms of the second moment (M_2) of the ^1H NMR resonance line. As is well known, M_2 is calculable from the well defined ^1H - ^1H distances in the molecules

and/or crystals under the rigid lattice [15]. The M_2 value was reduced by a factor based on the assumed motional mode when molecular motion was excited.

The second moment of the resonance line is defined as

$$M_2 = \frac{\int_{-\infty}^{\infty} (\omega - \omega_0)^2 f(\omega) d\omega}{\int_{-\infty}^{\infty} f(\omega) d\omega} \quad (1)$$

where $f(\omega)$ is the spectral shape function. Figure 3 portrays the evaluated second moment values (M_2) plotted against temperature. The M_2 values are in $3\text{--}4 \times 10^{-2} \text{ mT}^2$ below 130 K in both specimens. In IRMOF-1 accommodating cyclohexane with 95% saturation, the M_2 value was somewhat larger than that in the case of 45% saturation because of the large contribution of the intermolecular $^1\text{H}\text{--}^1\text{H}$ dipolar interaction to the M_2 value in the high-loading specimen. By Andrew [16], the M_2 value was reported as $2.73 \times 10^{-1} \text{ mT}^2$ for cyclohexane with chair-conformation in bulk rigid lattice. In this value, the intramolecular contribution of the $^1\text{H}\text{--}^1\text{H}$ dipolar interaction was $1.73 \times 10^{-1} \text{ mT}^2$, and reduced to $3.6 \times 10^{-2} \text{ mT}^2$ by partial averaging of the $^1\text{H}\text{--}^1\text{H}$ dipolar interactions because of the molecular reorientation around the C_3 symmetry axis. This value shows good agreement with our M_2 values below 130 K, indicating that cyclohexane confined in the IRMOF-1 nanocavity undergoes uni-axial molecular reorientation around a C_3 -axis below 130 K.



With increasing temperature, the observed M_2 values gradually decreases to $2.5 \times 10^{-2} \text{ mT}^2$ up to 200 K, implying the further motional narrowing process. The principal axis of the averaged dipolar coupling tensor by the C_3 reorientation is coincident with the C_3 symmetry axis. Therefore, the reorientation of the C_3 axis is most feasible to interpret the temperature dependence of the M_2 value at temperatures of 130–200 K. In fact, in our previous work, the precession of the C_3 axis was interpreted as the line shape of ^2H NMR spectrum of cyclohexane- d_{12} confined in the IRMOF-1 nanocavity [7]. Applying the same model as the motional mode, the M_2 value will be reduced by a factor of $(1/4)(3\cos^2\theta-1)^2$, where θ is the angle between C_3 and precession axis [15]. Assuming $3.6 \times 10^{-2} \text{ mT}^2$ as the residual intramolecular dipolar interaction by rapid C_3 rotation and $2.5 \times 10^{-2} \text{ mT}^2$ as a resultant M_2 value attributable to the further averaging process, the reduction factor showed 20° for θ , which shows good agreement with our previous results in ^2H NMR line shape analysis ($\theta = 23^\circ$).

At temperatures greater than 200 K, the M_2 values abruptly decrease to less than $5 \times 10^{-4} \text{ mT}^2$. The observed M_2 values were more comparable to a liquid state rather than a solid state. In a plastic phase of bulk cyclohexane, the intermolecular ^1H - ^1H dipolar interaction commonly gives $1.1 \times 10^{-2} \text{ mT}^2$, and the translational diffusion reduces to M_2 of less than $1 \times 10^{-4} \text{ mT}^2$ [16]. The observed M_2 value strongly suggests that the intermolecular ^1H - ^1H dipolar interaction rarely contributes to the M_2 value and that the confined guest molecules will undergo rapid diffusion through the cavities. That is, the guest molecules are in melt above the highest phase transition points observed in the DTA diagrams (Fig. 1(f)). Consequently, we conclude that the main endothermic peaks observed in DTA correspond to melting of guests in IRMOF-1.

3.3. Intermolecular interaction of guests in IRMOF-1

The melting of guests in IRMOF-1 was depressed in comparison to the bulk ones, as presented in Table 1. Depression of melting in the restricted space was well-analyzed using the Gibbs-Thomson equation [17]:

$$\frac{T_f - T_{fb}}{T_{fb}} = -2 \frac{(\gamma_{ws} - \gamma_{wl})V_{ml}}{R\Delta H_{fb}}, \quad (2)$$

where T_f and T_{fb} are the respective melting points of the confined and bulk liquid, γ_{ws} and γ_{wl} respectively denote the corresponding wall-solid and wall-liquid surface tensions, V_{ml} is the molar volume of the liquid, ΔH_{fb} is the enthalpy of fusion in the bulk, and R is size of domain contributing to melting.

The sign of $T_f - T_{fb}$ depends on whether γ_{ws} is greater or less than γ_{wl} . Commonly, depression of the freezing point engenders the relation $T_f - T_{fb} < 0$; thereby the condition $\gamma_{ws} > \gamma_{wl}$ is satisfied. From a microscopic viewpoint, surface tension is related closely to intermolecular interaction to form an interface and/or surface close to a relevant molecule. The difference in the surface tension between wall-solid and wall-liquid interfaces ($\gamma_{ws} - \gamma_{wl} = \Delta\gamma$) reflects the difference of the intermolecular interaction of guests between solid and liquid states. When R is well-defined, equation (2) would lead to $\Delta\gamma$. However, it is difficult to evaluate R in our case, because the guest molecules occupying some continuous cavities in IRMOF-1 will contribute collectively to melting. Thus, we conveniently consider the expedient quantity, $\Delta\gamma/R$, with a dimension of energy per unit volume, and will be proportional to $\Delta\gamma$. Therefore, $\Delta\gamma/R$ may be a tentative index to measure the relative difference of the intermolecular interaction of each guest between solid and liquid states in IRMOF-1, and will be compared with $\Delta H_{fb}/V_{ml}$ to discuss the effect of confinement on the intermolecular interaction. Applying of Eq. (2) to our results, we evaluate $\Delta\gamma/R$ as listed in Table 2.

Table 2. Depression of melting points, enthalpy of fusion in bulk, molar volume of bulk liquid and difference in surface tension between solid and liquid phases divided by size of domain contributing to melting for various organic solvents in IRMOF-1.

Guest	$\Delta T/K$	$\Delta T/T_{fb}$	$\Delta H_{fb}^a/kJ\cdot mol^{-1}$	$V_{ml}^b/10^{-4}m^3\cdot mol^{-1}$	$\Delta\gamma/R\ 10^3kJ\cdot m^{-3}$
benzene	-63	-0.226	9.837	0.888	12.5
toluene	-29	-0.163	6.62	1.06	5.07
<i>m</i> -xylene	-43	-0.191	11.6	2.22	4.99
<i>p</i> -xylene	-108	-0.378	17.1	2.23	14.5
cyclohexane	-66	-0.236	6.69	1.08	7.31
<i>n</i> -hexane	-46	-0.266	13.03	1.27	13.6
<i>n</i> -octane	-81	-0.375	20.8	1.62	24.1
<i>n</i> -decane	-62	-0.255	28.8	1.95	18.9
chloroform	-66	-0.314	9.2	0.782	18.5
carbon tetrachloride	-29	-0.116	2.56	0.965	1.54

a) Referred from the literature [18, 19].

b) These are evaluated by dividing the molecular weight by the bulk liquid density.

Figure 4 shows the correlation between the evaluated $\Delta\gamma/R$ values and $\Delta H_{fb}/V_{ml}$. It seems that the linear relation is satisfied approximately between both quantities. This aspect implies that the relative difference of intermolecular interactions of guests between the solid and liquid states at melting point is likely

to those in bulk ones. That is, the depression of melting in IRMOF-1 will be caused mainly by the effect of surface energy enhanced by the small particles or space, although, of course, the other factors such as molecular packing or the guest-wall interactions may also affect depression of melting. We are now planning quantitative thermal analyses as well as diffraction experiments to obtain more detailed information related to the microscopic behaviour of guests.

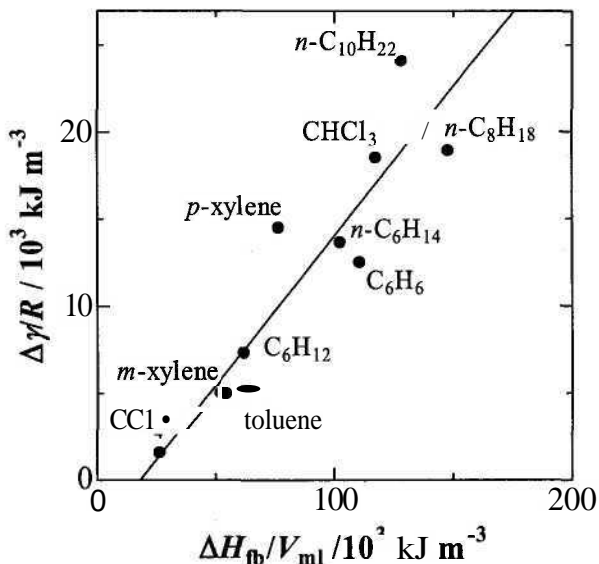


Figure 4. Comparison of $\Delta\gamma/R$ with $\Delta H_{fb}/V_m$ in various guests. The solid line represents the least squared fitting by assuming a linear relation between these quantities.

4. Conclusion

We found phase transitions of various guests confined in IRMOF-1 by DTA measurements. In addition, temperature dependence of ^1H wide-line NMR spectrum and their second moment analysis in cyclohexane suggested isotropic rotation as well as translational diffusion at temperatures greater than 210 K, leading to melting of guests in IRMOF-1. Results of this study strongly suggest the co-operative interaction between the guests in the different cavities. The Gibbs-Thomson formula gives a tentative index to measure the relative difference of the intermolecular interaction of each guest between solid and liquid states in IRMOF-1. These features might result from highly regular and homogeneous porous structure in IRMOF-1. Further investigation into

periodicity and long-range ordering of guests will reveal new insights into the phase transition of adsorbates in microporous materials.

Acknowledgments

The authors acknowledge Grants-in-Aid for Scientific Research (No. 11440176 and No. 16550013) from the Japanese Ministry of Education, Culture, Sports, Science, and Technology.

References

1. H. Li, M. Eddaoudi, M. O'Keeffe and O. M. Yaghi, *Nature* **402**, 276 (1999).
2. M. Eddaoudi, H. Li and O. M. Yaghi, *J. Am. Chem. Soc.* **122**, 1391 (2000).
3. S. Pawsey, I. Moudrakovski, J. Ripmeester, L.-Q. Wang, G. J. Exarhos, J. L. C. Rowsell and O. M. Yaghi, *J. Phys. Chem. C* **111**, 6060 (2007).
4. K. J. Ooms and R. E. Wasylshen, *Micropor. Mesopor. Mater.* **103**, 341 (2007).
5. J. Gonzalez, R. N. Devi, D. P. Tunstall, P. A. Cox and P. A. Wright, *Micropor. Mesopor. Mater.* **84**, 97 (2005).
6. F. Stallmach, S. Gröger, V. Künzel, J. Kärger, O. M. Yaghi, M. Hesse and U. Müller, *Angew. Chem. Int. Ed.* **45**, 2123 (2006).
7. T. Ueda, K. Kurokawa, H. Omichi, K. Miyakubo and T. Eguchi, *Chem. Phys. Lett.* **443**, 293 (2007).
8. J. A. Morrison and E. L. Richards, *J. Chem. Thermodyn.*, **8**, 1033 (1976).
9. J. Dore, B. Webber, J. Strange, H. Farman, M. Descamps and L. Carpentier, *Physica A* **333**, 10 (2004).
10. O. Petrov and I. Furó, *Phys. Rev. E* **73**, 011608 (2006).
11. D. W. Aksnes, K. Førland and L. Kintys, *J. Mol. Struct.* **708**, 23 (2004).
12. D. W. Aksnes, K. Førland and M. Stöcker, *Micropor. Mesopor. Mater.* **77**, 79 (2005).
13. L. Broussard and D. P. Shoemaker, *J. Am. Chem. Soc.* **85**, 1041 (1960).
14. I. Halasz, S. Kim, B. Marcus, *Mol. Phys.* **100**, 3123 (2002).
15. C. P. Slichter, *Principles of Magnetic Resonance*, 3rd Enlarged and Updated Ed., Chapter 3, Springer-Verlag, Berlin, 1989.
16. E. R. Andrew and R. G. Eades, *Proc. Roy. Soc.* **A216**, 398 (1953).
17. R. Evans and U. Mariri Betello Marconi, *J. Chem. Phys.* **86**, 7138 (1987).
18. D. R. Stull, E. F. Westrum, Jr. and G. C. Sinke, *The Chemical Thermodynamics of Organic Compounds*, John Wiley & Sons, New York, 1967.
19. K. Kaneko, A. Watanabe, T. Iiyama, R. Radhakrishnan and K. E. Gubbins, *J. Phys. Chem. B* **103**, 7061 (1999).

This page intentionally left blank

SPRAY DRYING: A VERSATILE ROUTE FOR THE PREPARATION OF NEW ACIDIC MESOSTRUCTURED POWDERS

S. PEGA, A. COUPE, C. BOISSIERE, T. AZAIS, D. GROSSO, C. SANCHEZ*

Université Pierre et Marie Curie, CNRS, Laboratoire Chimie de la Matière Condensée de Paris, 4 place Jussieu, 75252 PARIS Cedex, FRANCE

J. BLANCHARD

Université Pierre et Marie Curie, CNRS, Laboratoire de Réactivité de Surface, 4 place Jussieu, 75252 PARIS Cedex, FRANCE

D. MASSIOT

CNRS, CRMHT, 1D avenue de la Recherche Scientifique, 45071 Orléans cedex 2, France

A. CHAUMONNOT

IFP-LYON, Rd point de l'échangeur de Solaize -BP3- 69360 Solaize, France

This work describes the preparation by spray drying and the characterization of acidic mesostructured powders. Two ways of promoting acidity were explored. In the first one, hybrid sulfonic acid functionalized silica particles were prepared by one pot grafting of organosilanes and, when required, chemical modification of the grafted molecules. Depending on the organosilane, materials could be obtained with varying degrees of mesostructuration and proton exchange capacity. Some samples exhibited exchange capacities higher than 2 mmol.g⁻¹ of silica. In a second approach, pure inorganic mesostructured aluminosilicate powders were synthesized with different [Si]/[Al] ratios using either ionic or non ionic surfactants. Both chemical and processing parameters were found having a tremendous effect on the homogeneity of incorporation of aluminum centers and the final textural properties. A detailed study of acidic properties performed by ²⁷Al, ¹H NMR and CO adsorption is presented.

1. Introduction

Since the first synthesis in late sixties [1] and later the first report of surfactant templated mesostructures in 1992 [2], lots of work have been dedicated to the preparation of high surface area acidic mesostructured materials shaped as films,

* Clems@ccr.jussieu.fr

powders or monoliths [3-6]. In the last fifteen years, the major part of the research effort in this field has focused on the preparation of precipitated silica and aluminosilicate powders, either in basic, neutral or acidic media [7-11]. Two strategies were mainly used for designing acidic mesoporous materials: the introduction of aluminum centers in the silica framework and the grafting of organosilane molecules (mainly sulfonates) to the silica walls [12-16]. Both methods have proved to be efficient for obtaining highly acidic mesoporous powders. However, the usual preparation mode employed (that is, precipitation) produces large amounts of waste solution, the recycling of which hinders mass production. In the late nineties, the evaporation induced self assembly of mesostructured silica powders by spray drying was reported as a very attractive alternative to the precipitation method [17,18]. Indeed, this process is already well implanted into the industrial network, produces no liquid waste and is a continuous and very rapid preparation process. For these reasons, the interest for spray drying preparation of mesostructured powders is growing very quickly [19-23]. So far, very little work has been dedicated to the spray drying preparation of mesostructured acidic powders [23-26].

This work focuses onto the preparation and the characterization of spray-dried acidic mesostructured powders. Two strategies have been investigated. The first, never adapted so far to the spray drying process, is the one pot grafting of organosilanes followed by the transformation of thiol or phenylethyl functions into grafted sulfonic acid functions. The direct grafting of sulfonic acid is given as a reference [26]. The second strategy is the direct incorporation of aluminum centers in the silica network, as already described in several patents [24,25] and one publication [23]. The first detailed study of acidic properties performed by ^{27}Al , ^1H NMR and CO adsorption is given. In both cases, spray drying was found to be a very versatile preparation route in which processing conditions are as important as the chemical parameters for the preparation of homogeneous powders.

2. Experimental

2.1. *Sulfonic acid functionalized powders*

Tetraethylorthosilicate (TEOS) and cetyltrimethylammonium bromide (CTAB) were used respectively as silica precursor and structure directing agent (SDA) for these experiments. The organosilanes used for one-pot functionalization were either mercaptopropyltriethoxysilane (MPTS), phenylethyltriethoxysilane (PETMS) or chlorosulfonicphenylethyltrimethoxysilane (Cl-SPETMS). The

atomized precursor solutions had molar compositions in TEOS : organosilane : CTAB : H₂O : EtOH : HCl of (1-x) : x : 0.18 : 40 : 30 : 0.02 with x=0.1 to 0.2. The transparent solutions were atomized with a 6-Jet 9306A atomizer from TSI after stirring 2h30 at ambient temperature. Obtained powders were further dried one night at 130°C. CTAB extraction was performed by a 2 h reflux in ethanol for mercaptopropyl (MP) and phenylethyl (PE) functionalized products, and by a 18 h reflux in an hydro-ethanolic solution containing HCl (1M) for ethylphenylsulfonic (EPS) functionalized materials. CTAB-free PE functionalized products were sulfonated in anhydrous conditions using an excess of chlorosulfonic acid in CHCl₃ [27]. CTAB-free MP functionalized products were oxidized 24 h under stirring either by H₂O₂ [14] or by nitric acid [28]. Oxidized powders as well as CTAB-free EPS functionalized materials were acidified with 0.05 M sulfuric acid and washed with water until neutral pH. All the products were finally dried overnight at 60°C. The materials obtained were noted X-FUNC-POST where X is the [R-Si]/[Si] molar ratio, FUNC is the initial organic moiety introduced during the synthesis and POST the post-treatment undergone by the material (cf. Table 1). The solids were characterized by FTIR spectroscopy in KBr using a Nicolet 550 spectrometer; low angle XRD using a D8 diffractometer from Bruker instruments (wavelength 0.154 nm), ¹H}-¹³C CP MAS NMR (t_{CP} = 1 ms; ν_{MAS} = 5 kHz) on a Bruker Avance 300, and thermogravimetric analysis (TGA) on a SDT2960 TA apparatus (5°C/min until 1000°C under air flow). Nitrogen adsorption-desorption volumetry was performed on a Micromeritics ASAP 2010 (130°C vacuum out gassing). TEM imaging was done on microtome thin layers with a CM-12 Philips (120 kV acceleration). Proton exchange capacities were evaluation by acide-base titration using a 0.01M NaOH solution (powder dispersed in 50 mL NaCl (100g/L) solution and stirred one day at room temperature previous to titration).

2.2. Aluminosilicate powders

CTAB (or P123 block copolymer) was mixed with ethanol, water and hydrochloric acid to obtain a transparent solution. After dissolution of aluminum chloride (AlCl₃.6H₂O), TEOS was added. Molar ratio of (Si +Al) : EtOH : H₂O : HCl : CTAB (P123) used was 1 : 30 : 40 : 0.02 : 0.18 (0.01). Two hydrolysis times were tested, 10 or 1000 minutes (almost 18 hours) before atomization. The samples were referred as C(P)-X-Y, where X and Y denote the (Si/Al) molar ratio (particularly, X = Si for the pure silica reference) and the stirring time (Y = 10 or 1000 minutes); C and P refer to CTAB and P123 respectively. EDX

analyses were performed onto 50 nm thick slice of microtomed particles with a probe resolution of 15 nm.

The probing of CO adsorption was performed at 100 K on a powder pellet previously outgassed at 450°C for one hour. FTIR spectra of the pellet were registered upon successive introduction of CO (from 0.098 to 8.883 μmol). Experimental results are plotted as of the difference between the registered spectra and the reference spectrum as a function of wave number.

3. Results and Discussions

3.1. Sulfonic acid functionalized mesoporous silica nanospheres

In literature, two different strategies implying the co-condensation of an organosilane with a silica precursor have been reported for the preparation of acidic hybrid organic/inorganic mesostructured silica: i) a one-pot mercaptopropyl functionalization followed by an oxidation post-treatment

Table 1: synthesized materials, their chemical properties and specific surface area (a: MP for mercaptopropyl, PE for phenylethyl, EPS for ethylphenyl sulfonic initial functionalization; b: S for sulfonation, H₂O₂ and HNO₃ for oxidations, '-' for CTAB extracted; c: by ICP; d: by acid-base titration, SiO₂ content evaluated by TGA at 990°C, theoretical capacities are 1.66 and 3,33 mmol H⁺/g respectively for S/Si = 10% and 20%; e: non measurable).

R-Si/Si (% mol.)	Initial funct. ^a	Post- treatment ^b	S/Si ^c (% mol.)	H ⁺ (mmol/g SiO ₂) ^d	S _{BET} (m ² /g)
10	MP	-	10	0.40	1200
10	MP	H ₂ O ₂	7	1.28	1010
10	MP	HNO ₃	10	1.42	800
10	PE	-	-	-	1220
10	PE	S	10	1.11	952
10	EPS	-	9	1.1	810
20	MP	-	20	-	1140
20	MP	H ₂ O ₂	16	2.03	590
20	MP	HNO ₃	19	1.75	460
20	PE	-	-	-	830
20	PE	S	20	2.44	260
20	EPS	-	16	1.70	n. m. ^e

[13-15]; ii) and a direct one-pot functionalization with ethylphenylsulfonic acid moieties [16]. A third route, inspired from works on grafted silicas [29] or zirconium oxide [27] can be imagined by one-pot ethylphenyl functionalization followed by a sulfonation post treatment. At the moment, only methyl, fluoroalkane, vinyl or methacrylate groups were reported to be introduced in silica matrices by co-condensation using the spray-drying synthesis [30,31].

The present work was focused on the synthesis of sulfonic acid functionalized silicas by spray-drying following the three functionalization routes already explored with conventional precipitation methods.

3.1.1. *Synthesis with post-sulfonation or post-oxidation*

Between 90 to 95% of CTAB initially contained in MP and PE functionalized materials have been successfully removed by the ethanolic reflux according to C, Si and N elemental analysis and FTIR studies (not shown here).

The initial materials' functionalization and the efficiency of post-oxidation (or post-sulfonation) of the organic moieties have been confirmed by ^{13}C CP-MAS NMR experiments. As shown in Figure 1 (for R-Si/Si = 10%), MP functionalized materials exhibit in particular the 27 ppm resonance due to

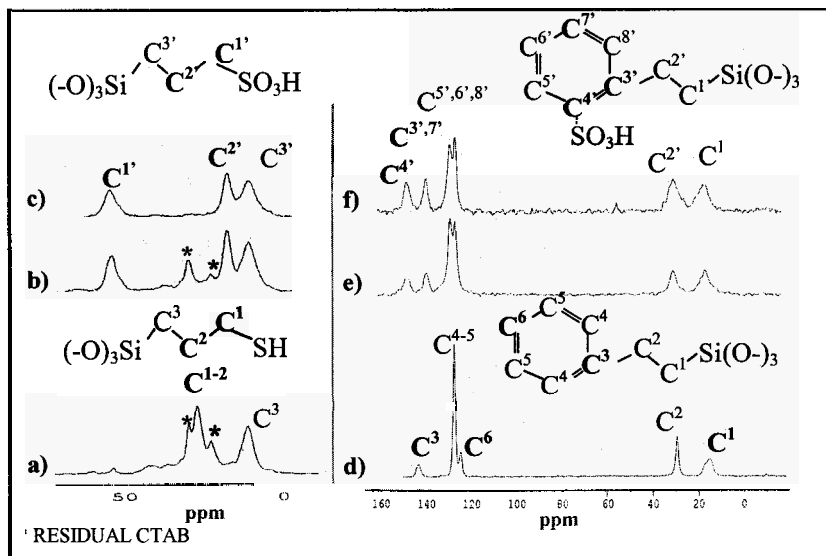


Figure 1: ^{13}C CP-MAS NMR spectra of a) 10-MP, b) 10-MP-HNO₃, c) 10-MP-H₂O₂, d) 10-PE, e) 10-PE-S and f) 10-PES materials. (Performed on a Bruker AV300 $t_{\text{CO}}=1\text{ms}$, $\nu_{\text{MAS}} = 5\text{ kHz}$)

C¹ and C² in (-O)₃Si-C³H₂-C²H₂-C¹H₂-SH (Fig. 1.a). After oxidation, either by HNO₃ (Fig. 1.b) or by H₂O₂ (Fig. 1.c), this 27 ppm signal is no longer detectable while two new resonances appear at 18.5 and 54 ppm. These are attributed respectively to C^{2'} and C^{1'} in the oxidized moiety (-O)₃Si-C³H₂-C²H₂-C¹H₂-SO₃H. The PE functionalization is also confirmed by ¹³C CP-MAS NMR (Fig. 1.d). Modifications in the aromatic frequencies (120-150 ppm) can be observed in the post-sulfonation spectrum (Fig. 1.e), which is similar to 10-EPS spectrum, the ethylphenylsulfonic material that was directly synthesized by use of the Cl-SPETMS precursor (Fig. 1.f). All of these spectroscopic features are characteristic of the sulfonation on the aromatic moieties. Similar NMR observations were found for R-Si/Si = 20% materials.

In both MP and PE-S materials, [S]/[Si] ratios evaluated by ICP elemental analysis are consistent with the [R-Si]/[Si] organosilane ratio of 10 % or 20 % introduced in the initial precursor solutions (Tab.1). This demonstrates i) that the aerosol synthesis allows a very good control of the functionalization ratio and ii) that sulfonation of PE groups was quantitative, leading to highly acidic powders, up to 2.44 mmol H⁺/g of silica (Tab.1 sample 20-PE-S). The oxidation of MP moieties can be optimized depending on the nature of the oxidant. Indeed, the [S]/[Si] ratio is preserved after the HNO₃ treatment whereas its decrease during H₂O₂ treatment indicates that some thiols groups are lost during the H₂O₂ treatment (Tab.1). However, it is not possible to conclude on which treatment should be preferred if only considering the proton exchange capacities (Tab. 1). It is noteworthy that our spray dried powders present, after oxidation of MP material proton exchange capacities (Tab. 1) higher than those previously reported for materials with comparable functionalization ratios but prepared by co-precipitation (and post-oxidation) [13-15]. This result may be explained by an enhanced accessibility of the organic functions, during post-treatments and/or titration steps, provided by the nanometer size of spherical particles generated by spray-drying.

XRD patterns of 10% MP and PE functionalized materials (respectively Fig. 2.a and 3.a) show a long range 2D-hex organization of the porosity since (10), (11) and (20) diffraction peaks are exhibited. The corresponding N₂ adsorption-desorption isotherms are typical of materials with a narrow pore size distribution centered between 20 and 30 Å (Fig. 2.c and 3.b) and very high specific surface areas around 1200 m²/g (Tab.1). These 10% functionalized materials retain good mesostructure after oxidation or sulfonation post-treatment as demonstrated by XRD patterns (Fig. 2.a and 3.a respectively) and high specific surface areas from 800 to 1000 m²/g (Tab. 1). On the contrary, 20% MP and PE functionalized materials exhibit broader XRD peaks, characteristic of a short

range meso-organization (Fig. 2.b). Their pore size distribution remains, however, narrow and centered around 2 nm (Fig. 2.d). As previously reported for materials processed either by EISA [32,33] or by precipitation [13], increasing the organosilane to silica ratio influences the mesostructure. In the case of

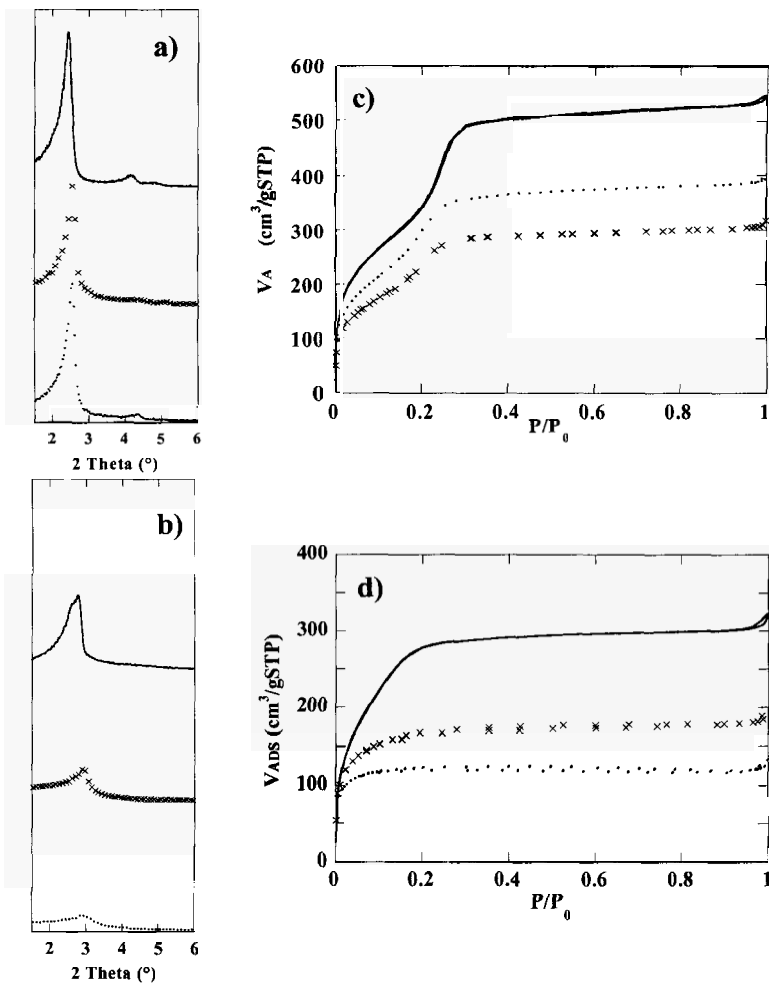


Figure 2: XRD diffraction patterns and N₂ adsorption isotherms (respectively a and c) of 10% functionalized and (respectively b and d) of 20% functionalized materials, plain lines for MP, crosses for MP-HNO₃ and dots for MP-H₂O₂ materials. capacities (up to 2 mmol H⁺/g of silica).

our materials, it yields a lower degree of organization. Moreover, the structuration of 20% functionalized materials is hardly maintained upon post-treatments as evidenced by broad diffraction peaks (Fig. 2.a and 3.a) and the reduction of the specific surface area (Tab.1). This effect is especially dramatic for the 20-PE-S compound whereas 20-MP-H₂O₂ and 20-MP-HNO₃ materials still exhibit specific surface areas higher than 450 m²/g coupled with high proton exchange capacities (up to 2 mmol H⁺/g of silica).

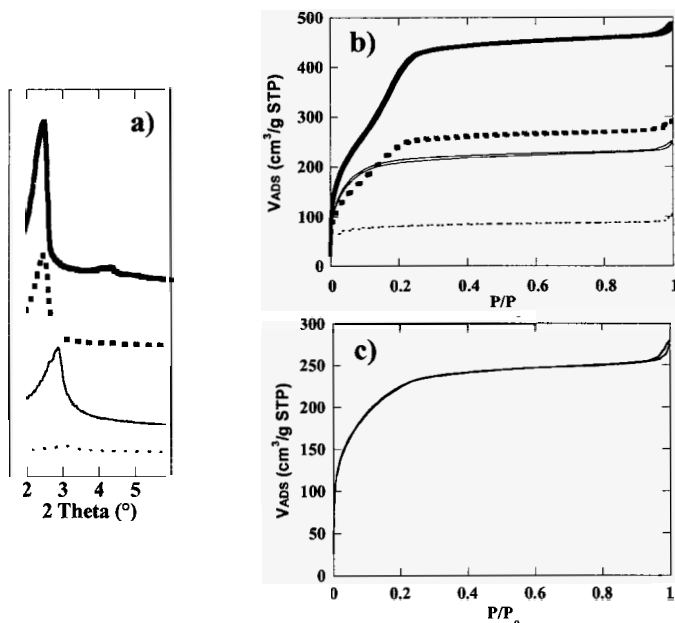


Figure 3: (a) XRD diffraction patterns and (b) N₂ adsorption isotherms of: PE materials (plain lines) and PE-S materials (dashed lines) with thick lines for 10% and thin lines for 20% functionalization; (c) N₂ adsorption isotherm and XRD diffraction pattern of 10-EPS sample.

3.1.2. Direct synthesis

The direct co-condensation of a sulfonic organosilane (Cl-SPETMS) by aerosol synthesis was used here to avoid the oxidation or sulfonation post-treatments which were proved in this work to affect the structure of the materials, especially at high functionalization ratios (cf. 3.1.1.). However, contrary to MP and PE functionalized materials, ethanolic reflux was not sufficient. Only a strongly acidified media allowed the extraction of CTAB in EPS materials, as verified by the absence of CTAB signals on ¹³C MAS-NMR spectra (Fig. 2.f). Ionic

interactions between the $(-O)_3Si-(CH_2)_2-PhSO_3^-$ groups and the polar head of the CTA^+ are assumed to be responsible for the difficulty of CTAB extraction: a cationic exchange with a large excess of proton is needed to remove the CTA^+ . EPS materials demonstrate a dramatic loss of structuration during acidic extraction. Indeed, 10-EPS exhibited XRD peaks of poor quality (Fig. 3.c) but conserved the high surface area of $810\text{ m}^2\cdot\text{g}^{-1}$ (Tab. 1). With twice this functionalization ratio, 20-EPS was found nearly non-porous ($80\text{ m}^2/\text{g}$) and gave no diffraction peaks (data not shown here). 10% and 20% EPS materials also exhibit quite poor proton exchange capacities compared to the other two sulfonic acid functionalization routes (Tab.1). This is partly explained by the loss of sulfonic moieties during reflux as ICP analysis show lower $[S]/[Si]$ molar ratios than the starting solutions (Tab. 1). Thus, even if this synthesis pathway is promising because no post-treatment is needed to generate sulfonic moieties, drawbacks arise concerning the extraction of CTA^+ . A non ionic surfactant will be likely better adapted for successful one-pot direct synthesis of hybrid silica-sulfonic mesostructured materials [16].

3.2. *Aluminosilicate mesoporous nanospheres*

Among the different synthesis processes leading to mesostructured aluminosilicate powders, spray drying is increasingly attractive because it is the only one that forces the stoichiometry of the final product above conventional limits. Indeed, by using the usual precipitation route, aluminum centers introduced in the reactive medium are only partially incorporated to the silica matrix. Experimentally, the result of this partition is a limitation of the powders $[Si]/[Al]$ ratio to values higher than 10 (some rare publications report ratios of 5). On the other hand, spray dried powders exhibit the exact composition of non-volatile compounds as in precursor solution, overcoming the thermodynamic limit of incorporation of aluminum usually met in precipitation. However, along to this compositional freedom, difficulties in controlling the homogeneous distribution of aluminum atoms in the material may arise [23]. Here we analyse the chemical and processing parameters influencing the incorporation of aluminum centers of spray dried mesostructured nanoparticles with low $[Si]/[Al]$ ratios (< 10).

We investigated the aluminum loading capacity of the powders by varying the structuring agents (CTAB or P123), the $[Si]/[Al]$ ratio and the silica hydrolysis time which influences the size of silica oligomers in the solution before the spray. TEM analysis showed that all prepared powders (Fig. 4) are mesostructured materials with periodically arranged pores. The pure silica

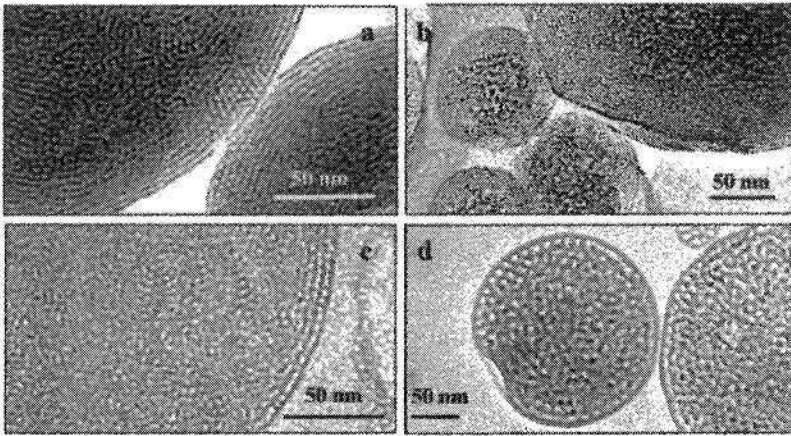


Figure 4: TEM pictures of microtomed aerosols prepared with a) CTAB, $[\text{Si}]/[\text{Al}] = 9.3$ and hydrolysis time of 10 min, b) CTAB, $[\text{Si}]/[\text{Al}] = 4$ and hydrolysis time of 1000 min, c) CTAB, $[\text{Si}]/[\text{Al}] = 4$ and hydrolysis time of 10 min, d) P123, $[\text{Si}]/[\text{Al}] = 4$ and hydrolysis time of 1000 min.

Table 2: Summary of porous structure parameters of aerosol powders.

* From BJH model. ** From Broekhoff and DeBoer model

SAMPLE	$[\text{Si}]/[\text{Al}]$	Hydrolysis time (min)	Phase separation	S_{BET} ($\text{m}^2 \cdot \text{g}^{-1}$)	V_p ($\text{cm}^3 \cdot \text{g}^{-1}$)	Pore Size (nm)
C-Si-10	8	10	NO	791	0.72	3.1 *
C-9.3-10	9.3	10	NO	741	0.58	3.1 *
C-4-10	4.0	10	NO	646	0.50	3.1 *
C-2.3-10	2.3	10	YES	514	0.38	2.9 *
C-1-10	1.0	10	YES	556	0.44	2.3 *
C-Si-1000	8	1000	NO	995	0.82	3.2 *
C-9.3-1000	9.3	1000	NO	832	0.51	2.4 *
C-4-1000	4.0	1000	YES	839	0.57	<2.0 *
C-2.3-1000	2.3	1000	YES	664	0.44	<2.0 *
C-1-1000	1.0	1000	YES	482	0.39	<2.0 *
P-4-10	4.0	10	NO	207	0.32	10.3 **
P-4-1000	4.0	1000	NO	238	0.38	7.2 **
P-2.3-1000	2.3	1000	NO	190	0.30	7.8 **
P-1-1000	1.0	1000	NO	156	0.26	7.8 **

references prepared with CTAB (C-Si-10 and C-Si-1000) exhibited porous structures that appear homogeneous all over the particles, regardless of their size (from 50 nm to 1500 nm). As a general trend, when more and more silica centers were substituted by aluminum centers, the average ordered domain size decreased (as attested by the progressive broadening of X-Ray diffraction peaks not shown here). Above a certain substitution ratio, some powders exhibited a composite structure made of what appears to be an amorphous worm like core and a mesostructured shell. The critical aluminum content was found to be related to the type of structuring agent used (CTAB powders exhibited this phase separation -Fig.4b-, but not P123 powders-Fig.4d), and also to the hydrolysis time of the solution before spraying (for 1000 min hydrolysis, separation happened for $[\text{Si}]/[\text{Al}] = 4$, whether for 10 min hydrolysis, separation happened

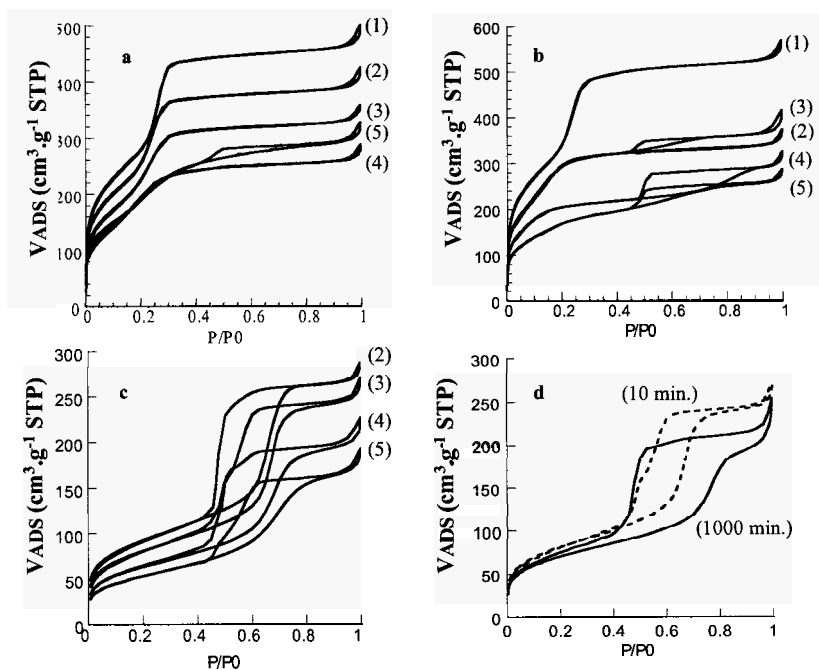


Figure 5: Nitrogen adsorption-desorption isotherms of mesostructured aerosol powders prepared with: a) CTAB surfactant and hydrolysis time of 10 minutes, b) CTAB surfactant and hydrolysis time of 1000 minutes, c) P123 surfactant and hydrolysis time of 1000 minutes. (1), (2), (3), (4), and (5) account for $[\text{Si}]/[\text{Al}]$ ratio equal to 8, 9.3, 4, 2.3 and 1. The d) diagram gives a comparison of 2 aerosols prepared with P123 and hydrolysis times of 10 and 1000 minutes.

for $[\text{Si}]/[\text{Al}] = 2.3$). The porous structure characterization, made by N_2 adsorption-desorption (Fig. 5), showed that samples looking homogeneous in TEM present a monomodal mesopore size distribution similar to those obtained by precipitation (cf. Table 2). For samples exhibiting the phase separation, an additional second adsorption step, characteristic of a very broad pore size distribution, appeared at high relative pressure (Fig. 5). Consistent with previous reports, the surface area of the powders decreases with increasing aluminum content [23]. A more local probing of the particles composition was made by localized EDX analysis of microtomed particles. With a spatial resolution of 15 nm, we measured the dispersion of Al atoms from the edge to the center of the particles. As shown in the figure 6 for C-4-10 and C-4-1000 examples, homogeneously textured particles are also homogeneous in composition. In contrast, phase separated particles exhibit cores heavily enriched in aluminum when compared to their edges. The phase separation phenomenon observed in aluminum-rich particles is thus linked to a migration of aluminum during the drying of the CTAB structured particles. This inhomogeneity can be rationalized by several arguments. In the acidic precursor solution ($\text{pH} = 2$), aluminum species are stable as very mobile hexaaquo cations $[\text{Al}(\text{H}_2\text{O})_6]^{3+}$. The hydrolysis of TEOS in similar medium leads to the slow homo-condensation of $\text{Si}(\text{OH})_4$ tetrahedra. ^{29}Si NMR (not shown here) showed that after 10 minutes of hydrolysis, silica species form monomers and dimers. Extending hydrolysis to 1000 minutes leads to larger silica oligomers, mainly composed of Q^2 and Q^3 silicon centers.

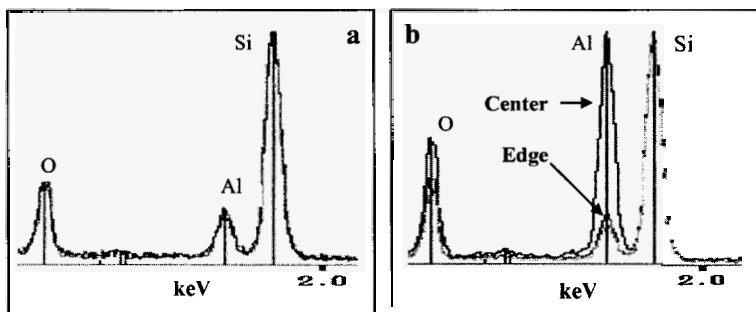


Figure 6: EDX spectra of the center and the edge of microtomed C-4-10 aerosol particles with a) hydrolysis time of 10 min and b) hydrolysis time of 1000 min.

An estimation of the hydrodynamic radius of silica oligomers by a Flory approach and the Stoke-Einstein equation gives a first order approximation of

the diffusion coefficients of linear silica oligomers with different molecular weights M_w (equation 1).

$$\frac{D_{OLIGOMER}}{D_{MONOMER}} = \frac{1}{(M_w)^{0.6}} \quad (1)$$

From this, one can qualitatively see that as hydrolysis time increases, silica oligomers diffuse more slowly. For example, a linear oligomer of only 14 tetrahedra diffuses about 5 times slower than the monomer. During spray drying, the progressive evaporation of solvent creates a radial concentration gradient within droplets that leads to a migration of non-volatile species from the edge to the center. At long hydrolysis times, it is likely that silica oligomers diffuse much more slowly than monomeric $[\text{Al}(\text{H}_2\text{O})_6]^{3+}$ ions, thus promoting the observed Al enrichment of the center of the particles. According to Fick's law, the flux of $[\text{Al}(\text{H}_2\text{O})_6]^{3+}$ is proportional to its original concentration. As a consequence, below a certain $[\text{Si}]/[\text{Al}]$ ratio, the particle center can attain a critical alumina concentration that hinders the mesostructuration, promoting the appearance of a second type of phase. However, with P123 block copolymer, no phase separation was observed. We assume that both the higher viscosity of these solutions (about seven times that of CTAB solutions) and the complexing ability of PEO chains for Al cations strongly limited the phase separation by limiting the mobility of aluminum species.

The acidic properties of the homogeneous powders were probed using the FTIR analysis of CO adsorption. The progressive adsorption of CO molecules (example of C-4-10 powder is given in Figure 7) demonstrated that these

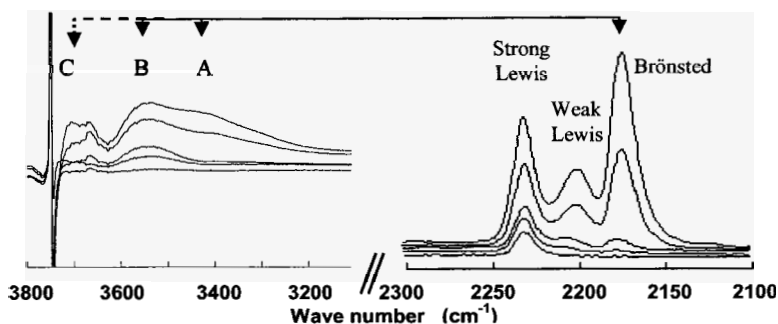


Figure 7: FTIR followed adsorption of CO on C-4-10 particles previously out gazed at 450°C.

powders exhibit strong and weak Lewis acidity ($\nu_{\text{CO}} = 2210$ and 2228 cm^{-1} respectively), as well as strong, medium and weak Brønsted acidity ($\nu_{\text{CO}} = 2171$

$\text{cm}^{-1} + \nu_{\text{OH}} = 3400, 3530 \text{ and } 3660 \text{ cm}^{-1}$ respectively). These acidic properties are similar to those of precipitated aluminosilicate powders [34].

Further characterizations of dehydrated samples by solid state NMR were performed in conditions as close as possible to those used for the CO adsorption measurements. Thus, calcined sample where first studied (^1H and ^{27}Al NMR) through MAS conditions. Then, the powder was kept in open rotor and dehydrated one night at 75°C and 3h30 at 200°C before sealing under argon. Figure 8 shows the ^1H MAS spectrum of dehydrated C-4-10 and the corresponding deconvolution. The spectrum reveals three components at 1.7, 2.5 and 3.8 ppm. The absence of any signal around 5 ppm characteristic of adsorbed water confirms the efficiency of dehydration process. The intense signal at 1.7

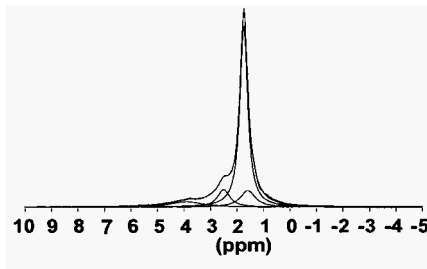


Figure 8: ^1H ECHO MAS spectrum of dehydrated C-4-10 ($\gamma^1\text{H} = 750 \text{ MHz}$, $\nu_{\text{MAS}} = 14 \text{ kHz}$ on a Bruker AV750; $\text{D1} = 30\text{s}$, $t = 0,13 \text{ ms}$).

ppm can be safely assigned to isolated Si-OH [35]. The signal at 2.5 ppm can be assigned to Al-OH by analogous results obtained on zeolites [36]. The signal at 3.8 ppm could be assigned to bridging hydroxyl groups Si-OH-Al corresponding to the Brönsted acidic sites in zeolites according to previous studies [37-41]. The latter signal is usually intense for zeolites, which is not the case with our material. However, the amorphous nature of our materials leads to a distribution in bonds and angles within Si-OH-Al groups. This induces a chemical shift distribution that can explain the broadness of the peak at 3.8 ppm. Three different hydroxyl groups in our dehydrated material are evidenced by solid state NMR. Interestingly, a similarity between these results and those concerning the CO adsorption measurements is observed. Thus, the following comparison can be done: isolated silanols Si-OH have been identified by both solid state NMR and CO adsorption measurements as weak Brönsted sites. Brönsted sites (A), that are the most acidic, could be assigned to the 3.8 ppm signal. Thus, Brönsted sites (B) could be assigned to the 2.5 ppm signal. Weakly acidic groups at 1.7 ppm were labeled (C) in the Figure 7.

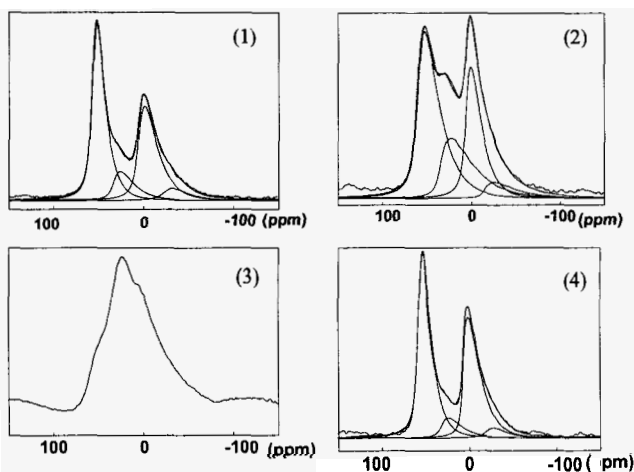


Figure 9: ^{27}Al echo MAS spectra of (1) as-synthesized, (2) calcined, (3) dehydrated and (4) rehydrated C-4-10 ($B_0 = 9.4 \text{ T}$; $\nu_{\text{MAS}} = 14 \text{ kHz}$).

The figure 9 displays the ^{27}Al echo MAS spectra of as-made, calcined, dehydrated and rehydrated C-4-10 ($B_0 = 9.4 \text{ T}$; $\nu_{\text{MAS}} = 14 \text{ kHz}$) with their respective deconvolutions. The deconvolution was obtained with the GIM model (Gaussian Isotropic Model) [40] implemented in the DmFit software [41] where the lineshapes correspond to a Gaussian distribution of quadrupolar parameters $P(\nu_Q, \eta_Q)$ associated to Gaussian distribution of chemical shifts that allows to extract the ratios of 4, 5, 6-fold coordinated aluminum sites (Table 3). For the calcined sample, besides 4-fold coordinated aluminum sites, a large amount of 5 (22 %) and 6-fold (38 %) coordinated sites is observed with quadrupolar constants C_Q around 2-3 MHz.

Table 3: Coordination of aluminum centers in C-4-10

Coord	As made "Hydrated"	Calcined "Hydrated"	Calcined "Dehydrated"		Calcined "Dehydrated" "Rehydrated"
	$B_0 = 9.4 \text{ T}$ (%)	$B_0 = 9.4 \text{ T}$ (%)	$B_0 = 17.6 \text{ T}$ (%)	C_Q (MHz)	$B_0 = 9.4 \text{ T}$ (%)
AlO_4	47	42	64	14.2	42
AlO_5	11	22	37	11.4	13
AlO_6	42	38	2	0.5	45

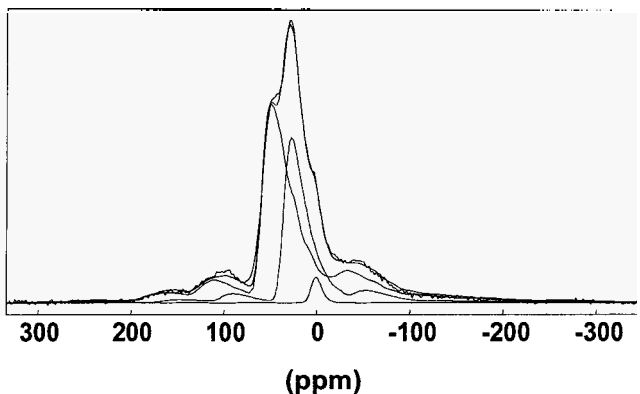


Figure 10: ^{27}Al echo MAS spectrum of dehydrated C-4-10 recorded at high magnetic field (17.6 T ; $\nu_{\text{MAS}} = 14$ kHz)

The profile of the dehydrated sample (the catalytically active form) is radically different from the others in the sense that the lineshapes are much broader. Furthermore, the spinning side bands of the central transition are clearly observable. These observations are evidence of an increased quadrupolar interaction. To improve the spectral resolution, a ^{27}Al echo MAS experiment of dehydrated C-4-10 was recorded at higher magnetic field (17.6 T ; $\nu_{\text{MAS}} = 14$ kHz) (Fig. 10). Indeed, after dehydration, the proportion of 4-fold and 5-fold aluminum is increasing but 6-fold aluminum with small CQ (0.5 MHz) is still present as it is evidenced by MQ MAS experiment (not shown). The dramatic increase of the quadrupolar interaction ($C_Q = 14$ and 11.4 MHz for 4-fold and 5-fold aluminum, respectively) indicates a distortion of the coordination polyhedra of 4-fold and 5-fold aluminum during the dehydration process. This phenomenon is complex and concerns the environment modifications of all the aluminum sites. It does not correspond to a simple desorption of the physisorbed water onto the surface. This conclusion is of paramount importance for the study of acid catalysts since it proves that, to be relevant (that is to help at the prediction of catalytic properties), an ^{27}Al NMR study has to be performed with carefully dehydrated aluminosilicate samples.

Finally, cross polarization $\{^1\text{H}\}$ - ^{27}Al CP MAS experiments were done to investigate spatial proximities. Figure 11 displays the $\{^1\text{H}\}$ - ^{27}Al CP MAS spectrum of dehydrated C-4-10 recorded with a contact time $t_{\text{CP}} = 500$ μs . The CP MAS signal is very broad and could correspond to 5-fold aluminum close to a proton source in the sample.

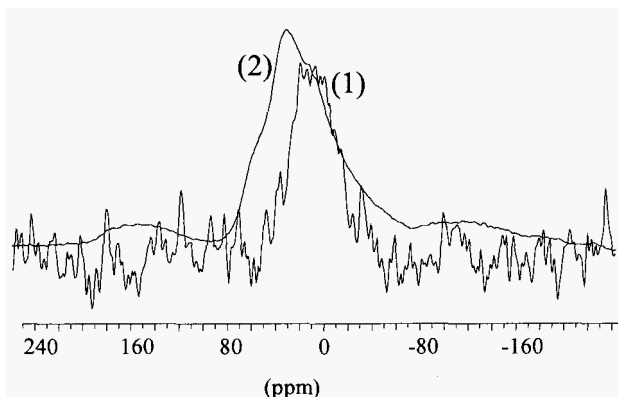


Figure 11: (1) $\{^1\text{H}\}$ - ^{27}Al CP MAS spectrum recorded with a contact time $t_{\text{CP}}=500 \mu\text{s}$ and (2) ^{27}Al echo MAS spectrum of dehydrated C-4-10 ($B_0 = 9.4 \text{ T}$; $\nu_{\text{MAS}} = 14 \text{ kHz}$).

4. Conclusions

The successful coupling of sol-gel chemistry and spray drying process allows the fast and continuous preparation of acidic silica-based mesostructured powders under a variety of synthesis approaches.

Hybrid sulfonic acid functionalized mesostructured silica nanoparticles were successfully prepared. Very good structuration with high organization and specific surface areas could be obtained for 10% functionalized materials. 20% functionalized materials were initially less organized and underwent dramatic losses in structuration during post-treatments. However materials with surface areas larger than $450 \text{ m}^2/\text{g}$ coupled with proton exchange capacities of $1.75\text{-}2.03 \text{ mmol H}^+/\text{g}$ of silica could still be obtained by the thiol/oxidation route with 20% functionalization. Aside from the rapidity and the simplicity of the process, it could be emphasized that the nanospheres exhibited proton exchange capacities globally higher than those reported for precipitated materials with similar functionalization ratios.

On the other hand, pure homogeneous inorganic aluminosilicate nanoparticles with $[\text{Si}]/[\text{Al}]$ as low as 1 were successfully prepared. Both the hydrolysis time and the nature of the structuring agent were found having an important impact on the composition homogeneity of the final particles. The powders, dehydrated for the realistic simulation of catalytic conditions, exhibited acidic properties similar with those of precipitated aluminosilicate powders. A correlation between vibrational ν_{CO} and ν_{OH} bands, and local environment of OH acidic groups could be given by crossing FTIR and solid NMR data.

Acknowledgments

The authors would like to thank very much Jean Marc Krafft from LRS for CO adsorption measurements, Guillaume Laurent and Jocelyne Maquet for NMR analyses, Patricia Beaunier for EDX measurements and the French Institute of Petroleum for funding.

References

1. F. Di Renzo, H. Cambon, R. Dutartre, *Microporous Materials* **10**, 283, (1997).
2. C. T. Kresge, M. E. Leonowicz, W. J. Roth, J. C. Vartuli, J. S. Beck, *Nature* **359**, 710, (1992).
3. C. Sanchez, C. Boissiere, D. Grosso, C. Laberty, L. Nicole, *Chemistry of Materials (special Issue on templated materials)* (**in press**), (january 2008).
4. A. Sayari, S. Hamoudi, *Chem. Mater.* **13** (10), 3151, (2001).
5. A. Tagushi, F. Schuth, *Microporous and Mesoporous Materials* **77** (1), 1, (2005).*
6. G. J. d. A. A. Soler-Illia, C. Sanchez, B. Lebeau, J. Patarin, *Chemical Reviews* **102**, 4093, (2002).
7. S. A. Bagshaw, E. Prouzet, T. Pinnavaia, *Science* **269**, 1242, (1995).
8. P. Yang, D. Zhao, D. I. Margolese, B. F. Chmelka, G. D. Stucky, *Nature* **396**, 152, (1998).
9. C. Boissière, A. van der Lee, A. E. Mansouri, A. Larbot, E. Prouzet, *Chemical Communications*, 2047, (1999).
10. E. Prouzet, F. Cot, G. Nabias, A. Larbot, P. Kooyman, T. J. Pinnavaia, *Chemistry of Materials* **11** (6), 1498, (1999).
11. H. Wang, Y. Liu, T. Pinnavaia, *Journal of physical chemistry B* **110** (10), 4524, (2006).
12. J. A. Melero, R. vanGrieken, G. Morales, *Chem. Rev.*, (2006).
13. D. Margolese, J. A. Melero, S. C. Christiansen, B. F. Chmelka, G. D. Stucky, *Chem. Mater.* **12** (8), 2448, (2000).
14. M. H. Lim, C. F. Blanford, A. Stein, *Chem. Mater* **10**, 467, (1998).
15. S. Mikhailenko, D. Desplandier-Giscard, C. Danumah, S. Kaliaguine, *Microporous and Mesoporous Materials* **52**, 29, (2002).
16. J. A. Melero, G. D. Stucky, R. Van Grieken, G. Morales, *J. Mater. Chem.* **12**, 1664, (2002).
17. C. J. Brinker, Y. Lu, A. Sellinger, H. Fan, *Advanced Materials* **11** (7), 579, (1999).

18. C. Boissière, D. Grosso, H. Amenitsch, A. Gibaud, A. Coupé, N. Baccile, C. Sanchez, *Chemical Communications*, 2798–2799, (2003).
19. Y. Lu, H. Fan, A. Stump, T. L. Ward, T. Rieker, C. J. Brinker, *Nature* **398**, 223, (1999).
20. D. Grosso, G. Illia, E. L. Crepaldi, B. Charleux, C. Sanchez, *Advanced Functional Materials* **13** (1), 37, (2003).
21. S. Areva, C. Boissiere, D. Grosso, T. Asakawa, C. Sanchez, M. Linden, *Chemical Communications* (14), 1630, (2004).
22. C. Boissiere, L. Nicole, C. Gervais, F. Babonneau, M. Antonietti, H. Amenitsch, C. Sanchez, D. Grosso, *Chemistry of Materials* **18** (22), 5238, (2006).
23. M. T. Bore, R. F. Marzke, T. L. Ward, A. K. Datye, *Journal of Materials Chemistry* **15**, 5022, (2005).
24. A. Chaumonnot, A. Coupé, C. Sanchez, P. Euzen, C. Boissiere, D. Grosso, N° FR 2872151, **2005**.
25. A. Chaumonnot, A. Coupé, C. Sanchez, P. Euzen, C. Boissiere, D. Grosso, N° WO 2006128989, **2006**.
26. A. Chaumonnot, S. Pega, C. Sanchez, C. Boissiere, D. Grosso, N° WO 2007065982, **2007**.
27. S. Parambadath, M. Chidambaram, A. P. Singh, *Catalysis Today* **97** (4), 233, (2004).
28. Q. Yang, M. P. Kapoor, N. Shirokura, M. Ohashi, S. Inagaki, J. N. Kondo, K. Domen, *J. Mater. Chem.* **15**, 666, (2005).
29. R. Badley, W. T. Ford, *J. Org. Chem.* **54**, 5437, (1989).
30. B. Alonso, C. Clinard, D. Durand, E. Véron, D. Massiot, *Chem. Commun.*, 1746, (2005).
31. X. Ji, Q. Hu, J. E. Hampsey, X. Qiu, L. Gao, J. He, Y. Lu, *Chem. Mater.* **18** (9), 2265, (2006).
32. F. Cagnol, D. Grosso, C. Sanchez, *Chem. Commun.*, 1742, (2004).
33. L. Nicole, C. Boissiere, D. Grosso, A. Quach, C. Sanchez, *J. Mater. Chem.* **15**, 3598, (2005).
34. C. Morterra, G. Cerrato, G. Meligrana, *Langmuir* **17**, 7053, (2001).
35. E. Brunner, *Catalysis Today* **38**, 361, (1997).
36. C. Crépeau, V. Montouillout, A. Vimont, L. Marley, T. Cseri, F. J. Maugé, *Journal of Physical Chemistry B* **110**, 15172, (2006).
37. L. W. Beck, J. L. White, J. F. Haw, *J. Am. Chem. Soc* **116** (9657), (1994).
38. D. Freude, *Chem. Phys. Lett.* **235**, 69, (1995).
39. P. Sarv, C. Fernandez, J. P. Amoureux, K. Keskinen, *J. Phys. Chem* **100**, 19223, (1996).
40. D. R. Neuville, R. Cormier, D. Massiot, *Geochemica et Cosmochimica Acta* **68**, 5071, (2004).

41. D. Massiot, F. Fayon, M. Capron, I. King, S. Le Calvé, B. Alonso, J. O. Durand, B. Bujoli, Z. Gan, G. Hoaston, *Magnetic Res. Chem.* **40**, 70, (2002).

LEWIS ACIDITY OF MESOPOROUS MOLECULAR SIEVES FOR ACYLATION REACTIONS*

MARTINA BEJBLOVÁ, JOSEF VLK, DANA PROCHÁZKOVÁ, HELENA ŠIKLOVÁ
AND JIRÍ CEJKA

*J. Heyrovský Institute of Physical Chemistry, Academy of Sciences of the Czech Republic,
v.v.i., Dolejškova3, Prague, CZ-182 23, Czech Republic*

The effect of the concentration of Lewis acid sites on the activity and selectivity of different molecular sieve catalysts was investigated in the Friedel-Crafts acylation of ferrocene with acetic anhydride, toluene with isobutyryl chloride, and cyclohexene and 1-methylcyclohexene with propionic anhydride. H-, Zn-, Fe-, Al- and La-forms of mesoporous molecular sieves (Al)MCM-41 and (Al)SBA-15 were studied and compared with large-pore zeolites. No general relationship between the type of cation and conversion of substrate was found. In acylation of ferrocene the highest ferrocene conversions were reached over Zn- and H-forms while in toluene acylation Al-forms were the most active. The selectivities over mesoporous molecular sieves were lower (61 – 89 %) compared with zeolites (82 – 98 %).

1. Introduction

Friedel-Crafts acylation of aromatic hydrocarbons is one of the most important reactions to produce aryl-alkyl or aryl-aryl ketones, which are very important products or intermediates for fine chemicals synthesis [1,2] such as pharmaceuticals (Naproxen, Ibuprofen, Warfarin), fragrances (acetylanisole [3], acetoveratrole [4], 2-acetylnaphthalene [5]), dyes or agrochemicals. Conventionally, acylation reactions are carried out in homogenous phase with acid anhydrides or acyl halides as acylating agents by using Lewis and Brønsted acids like AlCl_3 , FeCl_3 , BF_3 , TiCl_4 , ZnCl_2 or HF and H_3PO_4 . The major drawback of these catalysts is that they are not-regenerable, corrosive and must be used in more than stoichiometric amount. From these reasons, the development of new type of acid catalysts, especially heterogeneous ones, is rather challenging. Many solid acid catalysts (heteropolyacids, metal oxides, clays, sulfated zirconia, Nafion, triflates, molecular sieves) have been investigated for acylation reactions.

Mesoporous molecular sieves, MCM-41 and SBA-15, duo to the narrow pore size distribution, high surface area, hydrothermal stability and large pore

* This work is supported by the Grant Agency of the Czech Republic (104/07/0383).

volume have wide applications as heterogeneous catalysts in organic synthesis and they are also used for adsorption purposes. Although these materials are valuable for many organic reactions, enhancement of their acidity is desirable for their broader applications. Incorporation of various metal ions such as Al [6,7], Ce [7], Fe [8], Ga [9-11] or impregnation of these materials with InCl_3 [6] enabled their use in acid catalyzed reactions. Ga doped SBA-15 was active catalyst for liquid phase acylation of anisole with benzoyl chloride [9-11], FeSBA-15 was successfully used for toluene acylation with acetic anhydride [8], sulfated zirconia supported on MCM-41 was investigated in veratrole acylation with acetic anhydride [12]. Selvaraj [6] studied catalytic activity of Al-MCM-41 and $\text{SO}_4^{2-}/\text{Al-MCM-41}$ in acylation of 2-methoxynaphthalene.

The objective of this contribution was to study the effect of the type of acid sites of mesoporous molecular sieves (Al)MCM-41 and (Al)SBA-15 and their ion-exchanged forms on the activity and selectivity in acylation of ferrocene, toluene and cyclohexene.

2. Experimental

2.1. Catalysts

Mesoporous molecular sieves (Al)MCM-41 and (Al)SBA-15, and their ion-exchanged forms were tested in acylation reactions of ferrocene, toluene, cyclohexene and 1-methylcyclohexene. The list of catalysts used with their structure characterization, pore dimensions and Si/Al ratios is given in Table 1.

Table 1. Structural and chemical characteristics of used catalysts.

Catalyst	Channel structure	Channel diameter (nm)	Si/Al ratio
MCM-41	1D	~ 3.4	8.5
SBA-15	1D	~ 6.5	14

All the catalysts were used in acylation reactions in protonated (H^+) and ion-exchanged forms (Zn^{2+} , Fe^{3+} , La^{3+} and Al^{3+}). Ion-exchanged forms were prepared by the following procedure. Molecular sieves were converted to sodium form by four-time repeated ion-exchange with 0.5 M sodium nitrate for 4 h at room temperature. Then the Na-forms were transformed to corresponding cation forms via four-fold repeated ion-exchange with 0.25 M nitrate of the respective element for 4 h at room temperature. Finally, molecular sieves were recovered by filtration, washed out with distilled water, dried and calcined at 550 °C for 6 h of a heating rate of 1 °C/min.

2.2. Synthesis of (Al)MCM-41 and (Al)SBA-15

For the synthesis of (Al)MCM-41, sodium silicate, aluminum isopropoxide and trimethyltetradecylammonium bromide as template was used. In a typical synthesis, 9.81 g of trimethyltetradecylammonium bromide was dissolved in 500 ml of water in an autoclavable polypropylene bottle, then 1.12 g of aluminum isopropoxide was added and this mixture was stirred for ca. 1 h. Later on, 450 ml of water was added, followed by 10 g of sodium silicate and it was stirred for 30 min. Finally, 15 ml of ethyl acetate was added, the mixture was aged for 5 h at room temperature and then for 2 days at 90 °C.

Mesoporous molecular sieve SBA-15 was prepared according to the following procedure. 20 g of copolymer poly(ethylene oxide)-poly(propylene oxide)-poly(ethylene oxide), Pluronic 123 was dissolved in 645 ml of water and 106 ml of 35 % HCl and stirred at 35 °C. Then 45.5 ml of tetraethoxysilane was added to the clear solution and the mixture was stirred until became homogeneous. The mixture was allowed to stand at 35 °C for 24 h and subsequently at 95 °C for 48 h. The resulting solid phase was recovered by filtration, washed with distilled water and ethanol, and dried at room temperature. Calcination was carried out at 540 °C for 8 h with temperature ramp of 1 °C/min.

Aluminum was added to the SBA-15 samples by post-synthesis alumination. The reaction mixture of 5 g of SBA-15 and 1 g of aluminum chlorohydrate in 125 ml of distilled water was heated at 80 °C for 2 h. The solid was recovered by filtration, washed out with water and dried at ambient temperature. Calcination was carried out at 550 °C for 4 h with temperature ramp of 1 °C/min.

2.3. Characterization of catalysts

The phase purity of synthesized materials was determined by X-ray powder diffraction (Bruker D8 X-ray powder diffractometer). The nitrogen adsorption-desorption isotherms were recorded on a Micromeritics ASAP 2020 volumetric instrument at -196 °C. Chemical analysis was carried out by X-ray fluorescence analysis (spectrometer Philips PW 1404 with an analytical program UniQuant). The concentration and the type of acid sites were determined by adsorption of pyridine as probe molecule followed by FTIR spectroscopy (Nicolet Protégé 460). The concentrations of Brønsted and Lewis acid sites were calculated from integral intensities of individual adsorption bands characteristic of pyridine on Brønsted acid sites at 1545 cm^{-1} and band of pyridine on Lewis acid site at 1455 cm^{-1} and molar absorption coefficients [13] of $\epsilon(\text{B})=1.67\pm 0.1 \text{ cm}\cdot\mu\text{mol}^{-1}$ and $\epsilon(\text{L})=2.22\pm 0.1 \text{ cm}\cdot\mu\text{mol}^{-1}$, respectively.

2.4. Catalytic experiments

2.4.1. Acylation of ferrocene

In a typical experiment, 0.6 g of ferrocene, 8 ml of decahydronaphthalene (solvent), dodecane (internal standard) and 0.6 g of an activated catalyst were heated to the preset reaction temperature. Then 1.9 ml of acetic anhydride was added to the reaction mixture and the reaction started. The reaction temperature was 140 °C.

2.4.2. Acylation of toluene

In a typical experiment, 8.0 ml of toluene, dodecane (internal standard) and 1.2 g of an activated catalyst were heated to the preset reaction temperature. Then 1.9 ml of isobutyryl chloride was added to the mixture and the reaction started. The reaction temperature was 110 °C.

2.4.3. Acylation of cyclohexene and 1-methylcyclohexene

In a typical experiment, 10 ml of propionic anhydride, 0.5 g of tetradecane (internal standard) and 1 g of an activated catalyst were heated to the preset reaction temperature. Then 2.5 ml of cyclohexene or 1-methylcyclohexene was added to the mixture and the reaction started. The reaction temperature was 80 °C.

3. Results and Discussion

3.1. Characterization

The concentration of cations in molecular sieves used was determined by X-ray fluorescence analysis. The Me^{nt}/Al ratios are given in Table 2.

Acidic properties of molecular sieves were investigated using FTIR spectroscopy. The type and concentrations of Brønsted and Lewis acid sites were determined by pyridine adsorption (see Table 2). The intensity of the absorption band corresponding to the interaction between pyridine and Lewis acid site at 1445 cm⁻¹ decreased in the order: Zn > Al > H > La > Fe for (Al)MCM-41 and Zn > Al > H > Fe > La for (Al)SBA-15. Only a negligible band corresponding to pyridinium ion was found in the samples. This indicates that practically no acid OH groups are present in the mesoporous materials.

Zeolite	Me ⁿ⁺	Me ⁿ⁺ (wt %)	Me ⁿ⁺ /Al ratio	c _{LC} (mmol/g)	c _{BC} (mmol/g)
(Al)MCM-41	H ⁺			0.21	0.04
	Zn ²⁺	3.5	0.34	0.40	0.04
	Fe ³⁺	2.7	0.35	0.10	0.01
	Al ³⁺	1.9*	0.32	0.27	0.04
	La ³⁺	2.3	0.11	0.16	0.04
(Al)SBA-15	H ⁺			0.15	0.01
	Zn ²⁺	1.7	0.29	0.28	0.02
	Fe ³⁺	0.89	0.19	0.16	0.02
	Al ³⁺	0.7*	0.22	0.17	0.03
	La ³⁺	5.8	0.45	0.11	0.01

3.2. Catalytic activity

3.2.1. Acylation of ferrocene

The liquid phase acylation of ferrocene with acetic anhydride was investigated over mesoporous molecular sieves (Al)MCM-41, (Al)SBA-15 and their ion-exchanged forms with Zn²⁺, Fe³⁺, La³⁺, Al³⁺ to study the effect of type of acid sites. In some case the results were compared with large-pore zeolites Beta (Si/Al=12.5) and USY (Si/Al=15).

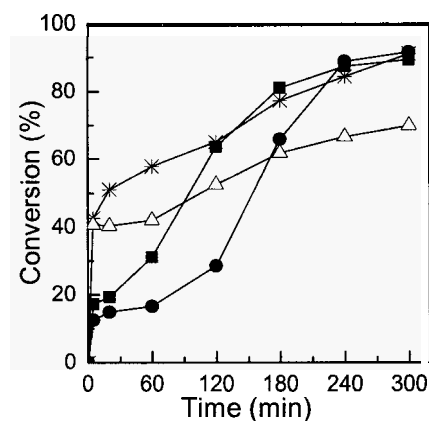


Fig. 1. The effect of structure of molecular sieve on the conversion of ferrocene in ferrocene acylation with acetic anhydride over molecular sieves: Beta *, USY Δ, (Al)MCM-41 ■, (Al)SBA-15 ●. Ferrocene/acetic anhydride ratio 1:6.

The comparison of catalytic activity in ferrocene acylation over mesoporous molecular sieves and large-pore zeolites is presented in Fig. 1. The lowest ferrocene conversion was achieved over zeolite USY (about 70 % after 300 min of TOS). The ferrocene conversions over zeolite Beta and (Al)MCM-41 and (Al)SBA-15 after 300 min of TOS were almost the same (about 90 %), however, the initial reaction rates were different. While zeolite Beta was very active from the beginning of the reaction (the ferrocene conversion reached about 60 % after 60 min of the reaction), the initial reaction rates of mesoporous molecular sieves were significantly lower (ferrocene conversions after 60 min of the reaction were 31 % and 17 %, respectively).

Fig. 2 shows the effect of the type of Lewis acid sites on the ferrocene conversion in ferrocene acylation with acetic anhydride over (Al)MCM-41 and (Al)SBA-15 and their ion-exchanged forms. With mesoporous molecular sieve (Al)MCM-41, the highest conversion of ferrocene was reached with H-form (about 90 %). Some decrease in the conversion was observed over Zn-(Al)MCM-41 (71 %) and the lowest conversion was obtained with Fe-(Al)MCM-41.

Very similar results were obtained with (Al)SBA-15; however, the activity of Zn- and H-(Al)SBA-15 were comparable. The lowest ferrocene conversion was again obtained with Fe-form.

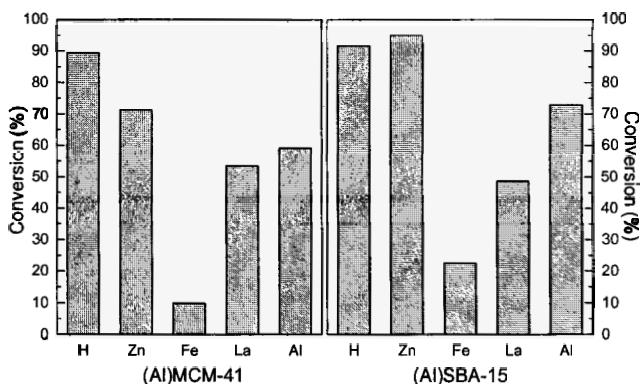


Fig. 2. The effect of type active site on the conversion of ferrocene in ferrocene acylation with acetic anhydride over ion-exchanged forms of (Al)MCM-41 and (Al)SBA-15, conversions at 300 min. Ferrocene/acetic anhydride ratio 1:6.

No relationship between the concentration of Lewis acid sites and ferrocene conversion in the case of mesoporous catalysts was found, while in the case of acylation of ferrocene over ion-exchanged forms of zeolites (Beta, USY) the correlation between the concentration of Lewis acid sites and ferrocene conversion was found (the higher the concentration of Lewis acid sites the higher ferrocene conversion).

3.2.2. Acylation of toluene

The liquid phase acylation of toluene with isobutyryl chloride produces all three isomers of isopropyl tolyl ketone with preference to *para*-isomer. Mesoporous molecular sieves (Al)MCM-41 and (Al)SBA-15 and their ion-exchanged forms (Zn^{2+} , Fe^{3+} , La^{3+} , Al^{3+}) were investigated in this reaction. The effect of the presence of added Lewis acid sites on the isobutyryl chloride conversion and selectivity to isopropyl *p*-tolyl ketone is clearly seen in Table 3.

Al^{3+} ion-exchanged forms of mesoporous molecular sieves (Al)MCM-41 and (Al)SBA-15 were highly active catalysts in toluene acylation. The conversions of isobutyryl chloride obtained over these catalysts after 240 min of T-O-S were 60.5 % and 62.7 %, respectively. The lowest isobutyryl chloride conversion (ca 37 %) was reached with the H-(Al)MCM-41. Surprisingly, the conversion of isobutyryl chloride over Fe-(Al)MCM-41 was about 62 % while in ferrocene acylation Fe-(Al)MCM-41 showed a very low conversion. This indicates that Fe-Lewis-acid sites easily activate toluene in contrast to ferrocene. H-forms of both mesoporous molecular sieves were not so active in toluene acylation as in the acylation of ferrocene.

Table 3. The effect of the type of active sites on the conversion of isobutyryl chloride and selectivity to isopropyl *p*-tolyl ketone in toluene acylation over ion-exchanged forms of (Al)MCM-41 and (Al)SBA-15.

catalyst	Me ^{nt+}	conversion ^a	selectivity ^b	selectivity ^c
(Al)MCM-41	H ⁺	37.1	86.3	83.3
	Zn ²⁺	43.7	83.2	75.8
	Fe ³⁺	62.7	78.0	63.4
	La ³⁺	56.2	86.1	71.2
	Al ³⁺	60.5	80.5	71.2
(Al)SBA-15	H ⁺	43.2	88.8	77.0
	Zn ²⁺	55.6	76.4	69.9
	Fe ³⁺	45.4	56.1	54.3
	La ³⁺	54.1	76.3	66.2
	Al ³⁺	62.7	61.0	55.3

^a conversion of isobutyryl chloride at 240 min

^b selectivity to isopropyl *p*-tolyl ketone at isobutyryl chloride conversion 20 %

^c selectivity to isopropyl *p*-tolyl ketone at 240 min

The selectivities to isopropyl p-tolyl ketone at the conversion of isobutyryl chloride of 20 % over mesoporous molecular sieves (Al)MCM-41 and (Al)SBA-15 and their ion-exchanged forms were a little lower (see Table 3) compared with the zeolites used (selectivities over zeolites Beta and USY were more than 90 % with the exception of Fe-forms). This is due to larger channel diameters of mesoporous molecular sieves, which enable the formation of the bulkier ortho-isomer and also consecutive acylation of toluene to di-isobutyryltoluenes. The selectivity to para-isomer over (Al)MCM-41 ranged from 78 to 86 %. After 240 min of the reaction the selectivities to isopropyl p-tolyl ketone were about 10 % lower due to the higher extent of consecutive reactions.

3.2.3. *Acylation of cyclohexene and 1-methylcyclohexene*

The liquid phase acylation of cyclohexene with propionic anhydride over molecular sieves is complicated by the formation of a number of side-products. Except desired α,β -unsaturated ketone, β,γ -unsaturated ketone, cyclohexylester of propionic acid, dipropionylcyclohexene and propionylcyclohexylester of propionic acid were observed in the reaction mixture. However, while over zeolite Beta and USY the conversions of cyclohexene were about 60 %, mesoporous molecular sieves (Al)MCM-41 and (Al)SBA-15 and their ion-exchange forms did not show any activity in cyclohexene acylation.

In the case of acylation of 1-methylcyclohexene (Fig. 3) over (Al)MCM-41 the highest conversion of 1-methylcyclohexene was achieved with La- (61 %) and H-forms (53 %) and over (Al)SBA-15 with Zn- (50 %) and H-forms (40 %). The lowest conversion was found for Al-forms of both molecular sieves. As for the selectivity to 1-(2-methylcyclohexenyl)propan-1-on (Fig. 3) over (Al)SBA-15 the selectivities were very similar (about 85 %) with all ion-exchanged forms studied. Over (Al)MCM-41 the highest selectivities to 1-(2-methylcyclohexenyl)propan-1-on were achieved with Fe- nad H-forms (about 95 %).

4. Conclusions

Friedel-Crafts liquid phase acylation of ferrocene, toluene, cyclohexene and 1-methylcyclohexene was investigated over mesoporous molecular sieves (Al)MCM-41 and (Al)SBA-15. Exchanged forms of the molecular sieves with Zn^{2+} , Fe^{3+} , La^{3+} , Al^{3+} were prepared and the effect of the type of Lewis acid sites on the activity and selectivity was studied. The concentration of Lewis and Brönsted acid sites was determined by adsorption of pyridine followed by FTIR

spectroscopy. The highest concentrations of Lewis acid sites were found for Zn- and Al-forms of (Al)MCM-41 and (Al)SBA-15 and the lowest for Fe- and La-forms.

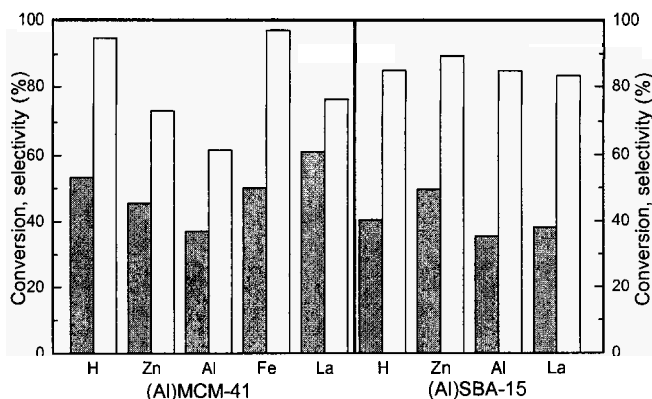


Fig. 3. The effect of type of active site on the conversion of 1-methylcyclohexene and selectivity to 1-(2-methylcyclohexenyl)propan-1-ol in acylation of 1-methylcyclohexene with propionic anhydride over ion-exchanged forms of (Al)MCM-41 and (Al)SBA-15. ■ Conversion (at 300 min), □ selectivity (at 1-methylcyclohexene conversion 40 %).

No general relationship between the type of cation and substrate conversion was found. In acylation of ferrocene over mesoporous molecular sieves (Al)MCM-41 and (Al)SBA-15, the highest conversions of ferrocene were reached over Zn- and H-forms. In acylation of toluene, Al-forms of mesoporous catalysts were the most active. The selectivities to *para*-isomer in toluene acylation over (Al)MCM-41 and (Al)SBA-15 and their ion-exchanged forms were lower (61 - 89 %) compared with zeolites (82 - 98 %). This was due to larger channel diameters of these materials, which enables the formation of sterically more demanding *ortho*-isomer and also consecutive acylation of toluene to diisobutyltoluenes. (Al)MCM-41 and (Al)SBA-15 and their ion-exchanged forms were not active in acylation of cyclohexene. In the acylation of 1-methylcyclohexene the highest conversions were obtained with La- and H-(Al)MCM-41 and with Zn- and H-(Al)SBA-15.

Acknowledgments

The authors thank the Grant Agency of the Czech Republic (104/07/0383) for financial support.

References

1. H. van Bekkum, A. J. Hoefnagel, M. A. van Koten, E. A. Gunnewegh, A. H. G. Vogt and H. W. Kouwenhoven, *Stud. Surf. Sci. Catal.* **83**, 379 (1994).
2. S. K. Jana, *Catal. Surv. Asia* **10**, 98 (2006).
3. S. G. Wagholikar, P. S. Niphadkar, S. Mayadevi and S. Sivasanker, *Appl. Catal. A* **317**, 250 (2007).
4. P. Moreau, A. Finiels and P. Meric, *J. Mol. Catal. A* **154**, 185 (2000).
5. L. Cervený, K. Mikulcová and J. Cejka, *Appl. Catal. A* **223**, 65 (2002).
6. M. Selvaraj, K. Lee, K. S. Yoo and T. G. Lee, *Microporous Mesoporous Mater.* **81**, 343 (2005).
7. M. D. Kadgaonkar, S. C. Laha, R. K. Pandey, P. Kumar, S. P. Mirajkar and R. Kumar, *Catal. Today* **97**, 225 (2004).
8. A. Vinu, T. Krithiga, N. Gokulakrishnan, P. Srinivasu, S. Anandan, K. Ariga, V. Murugesan, V. V. Balasubramanian and T. Mori, *Microporous Mesoporous Mater.* **100**, 87 (2007).
9. Z. El Berrichi, L. Cherif, O. Orsen, J. Fraissard, J. P. Tessonnier, E. Vanhaecke, B. Louis, M. J. Ledoux and C. Pham-Huu, *Appl. Catal. A* **298**, 194 (2006).
10. Z. El Berrichi, L. Cherif, J. P. Tessonnier, B. Louis, J. Fraissard, M. J. Ledoux and C. Pham-Huu In *Molecular Sieves: from Basic Research to Industrial Applications, Pts a and B*; Elsevier Science Bv: Amsterdam, 2005; Vol. 158, p 1413.
11. Z. El Berrichi, B. Louis, J. P. Tessonnier, O. Ersen, L. Cherif, M. J. Ledoux and C. Pham-Huu, *Appl. Catal. A* **316**, 219 (2007).
12. A. Breda, M. Signoretto, E. Ghedini, F. Pinna and G. Cruciani, *Appl. Catal. A* **308**, 216 (2006).
13. B. Wichterlová, Z. Tvarůžková, Z. Sobalík and P. Sarv, *Microporous Mesoporous Mater.* **24**, 223 (1998).

FORMATION OF SUPERBASIC SITES UNDER MILD CONDITIONS THROUGH DISPERSION AND REDOX OF NEUTRAL POTASSIUM NITRATE SALT ON ALUMINA

LIN BING SUN¹, FANG NA GU¹, LING GAO¹, JING YANG¹, JIA HUI KOU², YUAN CHUN¹, YING WANG², JIAN HUA ZHU^{1,*}, ZHI GANG ZOU²

¹ Key Laboratory of Mesoscopic Chemistry of MOE, School of Chemistry and Chemical Engineering, Nanjing University, Nanjing 210093, China. E-mail: jhzh@nju.edu.cn,

² Ecomaterials and Renewable Energy Research Center, Nanjing University, Nanjing 210093, China

A new redox strategy is adopted to convert neutral salt KNO_3 and to generate the superbasicity with strength (H_c) of 27.0 on alumina. Different from the conventional thermal decomposition, the redox approach can convert the KNO_3 supported at mild condition and suppress the release of nitrogen oxides, being energy-saving and environmentally benign.

1. Introduction

Solid superbases are extremely desirable for developing environmentally benign and economical catalytic processes, since they can catalyze various reactions under mild conditions and reduce the production of pollutants. Many attempts have been made to prepare solid superbases [1]. Among them doping sodium hydroxide and sodium [2] or impregnating an ammoniacal solution of potassium [3] on alumina can produce solid superbases. Besides, loading the hydroxides of potassium, rubidium, and cesium on alumina also exhibit superbasicity if activated properly [4]. However, most of these bases are oxygen-sensitive and/or easy to be contaminated by CO_2 in atmosphere [5]. To overcome the disadvantages, neutral salt KNO_3 has been introduced as base precursor and thus many solid bases are derived from the KNO_3 supported on porous materials [5-10]. Since the strong basicity is only generated from KNO_3 decomposition in the activation of the composites prior to reaction, the contamination of CO_2 can be avoided and the samples show high activity in catalytic processes [5, 6]. However, two factors hinder the applications of KNO_3 -derived bases. One is the high temperature ($\approx 600\text{ }^\circ\text{C}$) needed to decompose the KNO_3 , which certainly cause the shrinkage of support and be energy-consuming; another is the liberation of harmful gases nitrogen oxides (NO_x) during the decomposition [11].

Therefore, it is desirable to develop an environmentally benign approach to convert supported KNO_3 under relatively mild condition. In the present study, we adopted a new strategy to convert KNO_3 and to generate superbasicity on Al_2O_3 by use of redox, which can be conducted at $450\text{ }^\circ\text{C}$ and suppress the majority of the NO_x liberation.

2. Experimental

γ -alumina (Al_2O_3) with BET surface area of $208\text{ m}^2\cdot\text{g}^{-1}$ and pore volume of $0.393\text{ cm}^3\cdot\text{g}^{-1}$, and KNO_3 with AR grade were provided by Nanjing Inorganic Chemical and Shanghai Chemical, respectively. Methanol, ethanol, 2-propanol, *tert*-butanol, and 1-hexene were commercially available reagents with AR grade. KNO_3 was loaded on Al_2O_3 through impregnation. The given amount of KNO_3 was dissolved in 10 mL of water, and then 1.0 g of Al_2O_3 support was added. After stirring for 2 h, the mixture was evaporated at $80\text{ }^\circ\text{C}$ followed by drying at $100\text{ }^\circ\text{C}$ overnight. The obtained samples were denoted as *n*KNA, where *n* represents the mass percentage of KNO_3 .

XRD patterns of the samples were recorded with a Rigaku D/max-rA system using CuK_α radiation in the 2θ range from 5° to 70° at 40 kV and 40 mA. The XRD peak of KNO_3 , the sum of the line at 23.5° and 27.2° for orthorhombic and hexagonal phase, respectively, was compared with that of Al_2O_3 , the line at 66.8° , and the intensity ratio was denoted as factor R to characterize the dispersion of KNO_3 on alumina. FTIR measurements were performed on a Bruker 22 FTIR spectrometer by means of KBr pellet technique. The N_2 adsorption-desorption isotherms were measured using a Micromeritics ASAP 2020 system at $-196\text{ }^\circ\text{C}$. Temperature programmed decomposition (TPDE) of KNO_3 supported on Al_2O_3 was carried out in a flow reactor. The sample was kept contacting with methanol during the TPDE process, for which methanol was introduced with a syringe pump. The sample was heated in a flow of N_2 ($30\text{ mL}\cdot\text{min}^{-1}$) from 25 to $450\text{ }^\circ\text{C}$ at the rate of $8\text{ }^\circ\text{C}\cdot\text{min}^{-1}$ and kept at that temperature until KNO_3 was decomposed completely. The NO_x liberated in the process was detected by the colorimetric method [5].

The KNO_3 -modified samples were treated with reducing agent in a conventional flow reactor at atmospheric pressure, in which the reducing agent was introduced with a syringe pump at a rate of $1.2\text{ mL}\cdot\text{g}^{-1}\cdot\text{h}^{-1}$. In a typical procedure, 100 mg of KNA sample was treated with $1.2\text{ mL}\cdot\text{g}^{-1}$ methanol at $450\text{ }^\circ\text{C}$. Based on these conditions, the effects of methanol amount, KNO_3 loading, treatment temperature, and reducing agent type including methanol, ethanol, 2-propanol, and *tert*-butanol were investigated. The base strength and basicity of

the samples were measured by titration methods using Hammett indicator as reported elsewhere [6]. The catalytic decomposition of 2-propanol was conducted in a conventional flow reactor. The sample pellet with 20–40 mesh was treated with methanol ($1.5 \text{ mL} \cdot \text{g}^{-1}$) at $450 \text{ }^\circ\text{C}$ and then cooled to the reaction temperature ($400 \text{ }^\circ\text{C}$). The reactant 2-propanol was introduced using a syringe pump with the space velocity of 1.9 h^{-1} . The reaction mixture was analyzed by on-line GC (Varian 3700). In similar process, the isomerization of 1-hexene was conducted at the reaction temperature of $40 \text{ }^\circ\text{C}$; the conversion represented the activity of the sample while the cis/trans ratio of products reflected the basicity of the catalyst [12].

3. Results

3.1. Dispersion and Redox Conversion of KNO_3 Supported on Al_2O_3

Figure 1A depicts the dispersion of KNO_3 on Al_2O_3 , in which the straight line gives an intercept to indicate the monolayer dispersion threshold of ca. 14 wt%. Crystalline KNO_3 is detected in the XRD patterns of KNA samples loaded with KNO_3 exceeded the dispersion threshold.

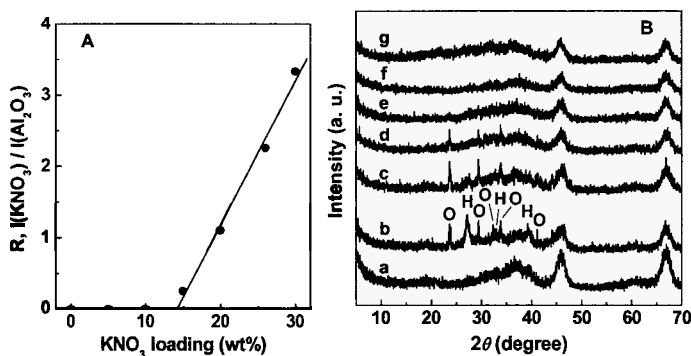


Figure 1. (A) The dispersion of KNO_3 on Al_2O_3 . (B) XRD patterns of (a) Al_2O_3 as well as 26KNA (b) as-prepared, (c) thermal activation at $450 \text{ }^\circ\text{C}$ and treated with (d) 0.1, (e) 0.3, (f) 0.6, and (g) $1.5 \text{ mL} \cdot \text{g}^{-1}$ of methanol at $450 \text{ }^\circ\text{C}$. O and H denote orthorhombic and hexagonal KNO_3 , respectively.

Figure 1B shows the XRD patterns of parent Al_2O_3 and KNA samples. KNO_3 supported on Al_2O_3 exists in two crystalline phases, i. e. orthorhombic (JCPDS No. 74-2055) and hexagonal (JCPDS No. 76-1693) phase. Since KNO_3 itself is in the crystalline form of orthorhombic even after it is treated with the same process as the preparation of KNA samples, the interaction between KNO_3

and support is believed to be crucial to the formation of hexagonal phase. After thermal activation at 450 °C, the hexagonal phase decreases apparently while the orthorhombic phase increases slightly. However, the phase of hexagonal vanishes meanwhile the orthorhombic phase declines evidently once the sample is contacted with 0.1 mL·g⁻¹ of methanol. Furthermore, the diffraction lines of KNO₃ disappear in the XRD pattern when the sample is treated with methanol more than 0.6 mL·g⁻¹.

Figure 2 displays the IR spectra of samples. The bands at 2406, 1766, and 1385 cm⁻¹ assigned to the vibration of nitrate [13] are obvious on the as-prepared sample. No apparent decrease of these bands is observed after the sample is thermally activated at 450 °C. However, introducing 0.3 mL·g⁻¹ of methanol at 450 °C makes these bands decrease obviously. As the amount of methanol rises, the bands of nitrate decline meanwhile the bands at 1547 and 1413 cm⁻¹ originated from CO₂ adsorbed on basic sites [14] are gradually stronger. The emergence of 1269 cm⁻¹ band on some samples indicates the formation of a quantity of KNO₂ as an intermediate. After treated with methanol, the broad band around 3486 cm⁻¹ assigned to the vibration of Al-OH group shifts to 3438 cm⁻¹, implying the formation of Al-OK groups [15]. Together with the XRD results, it is clear that the KNO₃ on alumina is converted by redox.

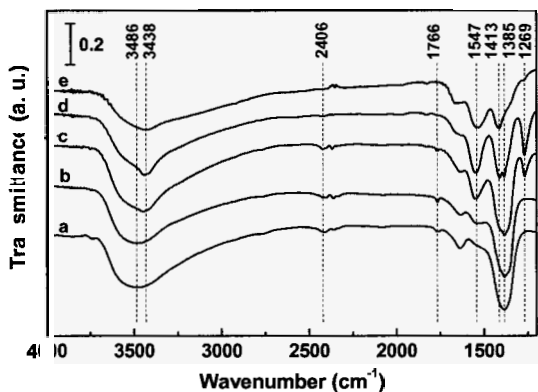


Figure 2. IR spectra of 26KNA (a) as-prepared, (b) activated at 450 °C for 1 h and treated with (c) 0.1, (d) 0.3, and (e) 1.5 mL·g⁻¹ of methanol at 450 °C.

3.2. Basicity Generated through Redox Approach on KNA Composites

The effect of methanol amount on the generation of basic sites in KNA samples is examined. As shown in Figure 3A, the base strength (H_{L}) of 7.2 is detected on the untreated sample whereas employing only 0.1 mL·g⁻¹ of methanol causes the

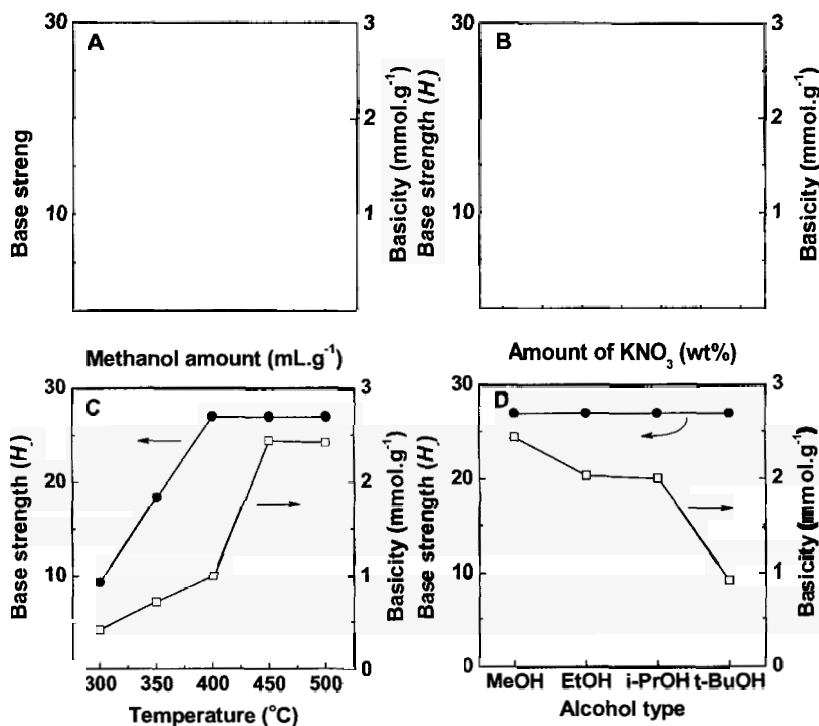


Figure 3. Effects of (A) methanol amount, (B) KNO_3 loading, (C) treatment temperature, and (D) reducing agent type on the basicity formed on KNA samples. General conditions: methanol, $1.5 \text{ mL}\cdot\text{g}^{-1}$, loading amount of $\text{KNO}_3 = 26 \text{ wt}\%$, temperature = $450 \text{ }^{\circ}\text{C}$.

appearance of base strength (H_{L}) of 27.0. The basicity enhances gradually as the methanol amount rises to $1.5 \text{ mL}\cdot\text{g}^{-1}$. Figure 3B depicts the influence of KNO_3 loading on basic properties of KNA samples. The basic sites with strength (H_{L}) of 27.0 emerge when KNO_3 loading arrives at 15 wt%. Additionally, the resulting basicity rises on the composite with the increased KNO_3 loading. As for the treatment temperature (Figure 3C), $450 \text{ }^{\circ}\text{C}$ seems optimal since both the base strength (H_{L}) of 27.0 and the largest amount of basicity can be obtained at this temperature. Figure 3D presents the impact of reducing agents on the basic properties of KNA samples. Although the base strength (H_{L}) of 27.0 is observed on the samples treated with all of the reducing agents employed, i. e. methanol, ethanol, 2-propanol, and *tert*-butanol, the obtained basicity decreases with the

increase of the molecular size of the agent. For 26KNA sample the optimum temperature and methanol dosage are 450 °C and 1.5 mL·g⁻¹, respectively.

The reaction of 2-propanol is employed to probe the surface acidity-basicity of solid samples, since 2-propanol undergoes dehydrogenation to form acetone over basic sites whereas acidic sites favor the dehydration of 2-propanol to propene. As shown in Figure 4A, 2-propanol is completely converted to propene on bare Al₂O₃. With the increased loading amount of KNO₃, the yield of propene decreases apparently while a large amount of acetone is produced, mirroring the generation of basic active sites and the suppression of acidic sites on the samples after KNO₃ modification and methanol treatment.

The isomerization of 1-hexene was conducted to probe the strong basicity of the samples. As shown in Figure 4B, the conversion of 1-hexene is low (1.5%) on bare Al₂O₃, and the cis/trans ratio is equal to unity indicative of the acid-catalyzed isomerization [12]. Loading KNO₃ on Al₂O₃ increases the conversion of 1-hexene and the cis/trans ratio, and the increase is especially obvious for the samples with KNO₃ loading exceeds 15 wt%. For example, a high cis/trans ratio of 3.5 is achieved over 26KNA sample, implying the existence of strong basic sites [12]. These results are consistent with the results of base strength (Figure 3), showing the superbasicity generated on KNA samples by redox.

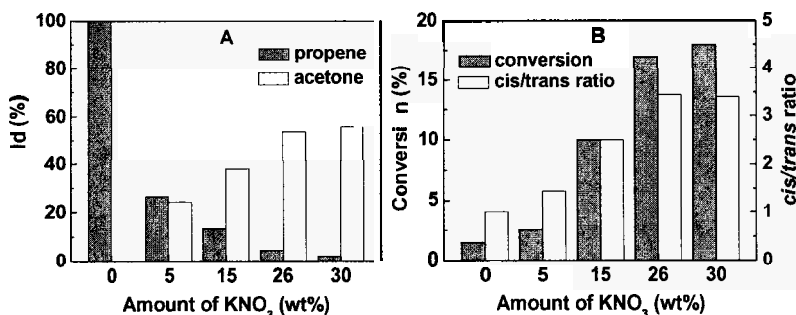


Figure 4. (A) The decomposition of 2-propanol over Al₂O₃ and KNA at 400 °C. (B) The isomerization of 1-hexene over Al₂O₃ and KNA at 40 °C. The samples of KNA were treated with methanol (1.5 mL·g⁻¹) at 450 °C before reaction.

3.3. Retain of Pore Size and Suppression of NO_x

The isotherms of KNA samples treated with methanol at 450 °C keep the similar shape as that of bare Al₂O₃ (Figure 5A), indicative of retaining of the original pore structure. For the sample to be thermally activated at 600 °C, however, the shape of hysteresis loop obviously changes and the inflection point value of

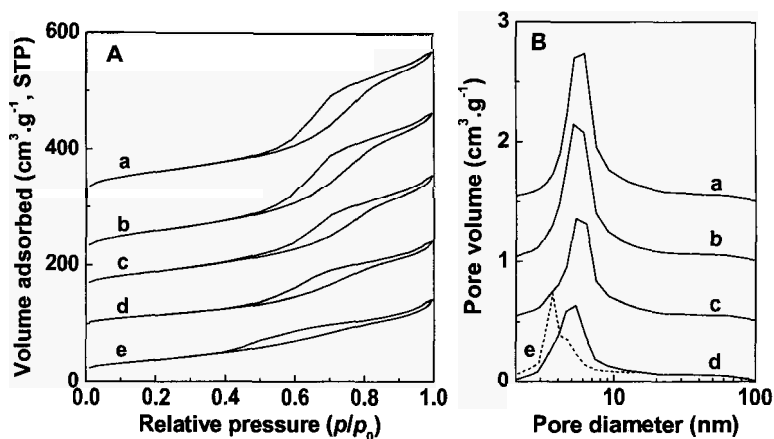


Figure 5. (A) N_2 adsorption-desorption isotherms and (B) BJH pore size distributions determined from the desorption branch of different samples. (a) Al_2O_3 , (b), (c), and (d) denote 5KNA, 15KNA, and 26KNA treated with methanol at 450 °C, respectively, (e) 26KNA activated at 600 °C. The ordinates of a-d in Figure A are offset by 300, 200, 140, and 80 $cm^3 \cdot g^{-1}$, respectively; while the ordinates of a-c in Figure B are offset by 1.5, 1.0, and 0.5 $cm^3 \cdot g^{-1}$, respectively.

relative pressure decreases from about 0.5 to around 0.4 (Figure 5A), implying the formation of smaller pores, which is confirmed by the pore size distributions shown in Figure 5B. Furthermore, the BJH average pore diameter calculated from the desorption branches of the isotherms of Al_2O_3 and two modified analogues, 26KNA treated with methanol at 450 °C or thermally activated at 600 °C, is 6.2, 6.0 or 5.1 nm, respectively. That is to say, the change of pore diameter is slight after methanol treatment, while the pore diameter declines obviously after thermal activation. Thus, it is clear that the thermal activation at 600 °C leads to the shrinkage of alumina support, whereas the pore structure of alumina is well preserved by using redox method at 450 °C.

Thermal decomposition of KNO_3 on porous supports unavoidably produces NO_x [8], which is harmful for environment. For example, 2.57 $mmol \cdot g^{-1}$ of NO_x will be released from 26KNA sample if the supported KNO_3 is thermally decomposed (Figure 6). In case that the composite is treated with our new strategy, however, only 0.28 $mmol \cdot g^{-1}$ of NO_x is detected when the guest KNO_3 is converted by redox approach. Thus, 89% of NO_x is suppressed in the process of redox. The effective suppression of NO_x is also observed on other KNA samples as demonstrated in Figure 6, indicating the redox approach is environmentally benign.

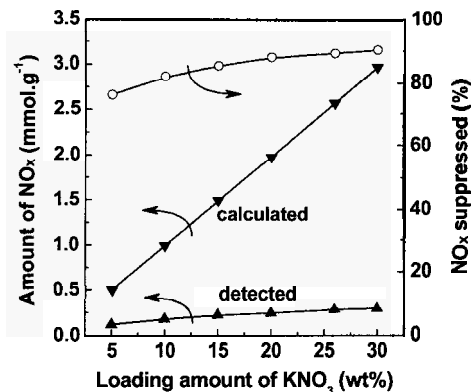


Figure 6. Suppression of NO_x from KNO₃ decomposition on Al₂O₃ by use of methanol.

4. Discussion

To gain a deep insight into the conversion of KNO₃ on Al₂O₃, the interaction of host-guest should be taken into consideration. The surface of Al₂O₃ comprises (110) and (100) planes, and the (110) plane is preferentially exposed so that Al₂O₃ can be supposed to consist of particles formed by one-dimensional stacking of C- and D-layers with the equal exposure possibility [16]. There are vacant sites with a density of 18.80 nm⁻² in the C-layer and 20.57 nm⁻² in the D-layer of Al₂O₃, and the ratio of the usable octahedral sites to the tetrahedral vacant sites is 1:3 and 1:4 in the C- and D-layer, respectively. However, potassium cation with a radius of 0.13 nm can only insert in the octahedral vacant sites in the surface lattice of Al₂O₃ [17], therefore the dispersion capacity of KNO₃ can be estimated to be about 4.4 K⁺·nm⁻² theoretically. The Al₂O₃ employed here has a surface area of 208 m²·g⁻¹, so about 13 wt% of KNO₃ can be dispersed, being consistent with the measured value (14 wt%). Hence, the dispersion of guest KNO₃ on Al₂O₃ is proposed to proceed via the insertion of K⁺ to surface vacant sites, which leads to a strong host-guest interaction [18]. Consequently, KNO₃ tends to disperse separately and the bound between K⁺ and NO₃⁻ is weakened [6, 19]. However, only dispersion and anchor of guest on host cannot cause the stress strong enough to decompose or dissociate KNO₃ itself and thus the external assistance is needed. Conventionally, thermal method is employed to assist the decomposition of supported KNO₃, and the sample has to be heated to 600 °C [6] in order to rupture the bound between potassium cation and nitrate anion. Here, we provide another assistance to decompose the KNO₃

dispersed in porous host. With the aid of redox the supported KNO_3 can be converted at $450\text{ }^\circ\text{C}$. It should be pointed out that the bulk KNO_3 alone cannot be converted at all when it is treated with methanol under the same conditions. Thus, the dispersion and anchor of guest KNO_3 on Al_2O_3 is proven to be crucial for the redox conversion of KNO_3 , the guest-host interaction limits the movement of KNO_3 and enables more KNO_3 molecules to be dispersed and contacted with the reducing agent. In other words, the effective redox conversion of KNO_3 on Al_2O_3 at relatively low temperature depends on the synergic effect of two factors, the host-guest interaction and the chemical reaction. The strong interaction between KNO_3 and alumina is crucial to disperse/anchor the supported KNO_3 , which is essential to the subsequent conversion of KNO_3 whatever method is used; while the redox method provides an approach to convert the KNO_3 to basic sites at low temperature. In fact, the present study may give a clue how to combine the chemical reaction and the host-guest interaction for design and synthesis of new functional materials.

For the first time, the KNO_3 supported on Al_2O_3 is converted to generate the superbasic sites with strength (H_-) of 27.0 at $450\text{ }^\circ\text{C}$. In contrary, the temperature of $600\text{ }^\circ\text{C}$ is needed to thermally decompose the KNO_3 supported on Al_2O_3 or ZrO_2 to generate superbasicity and even higher temperature is desirable ($700\text{--}900\text{ }^\circ\text{C}$) for the superbases derived from CaO and SrO [5, 6, 12]. As mentioned above, such high temperature will lead the shrinkage of host and it is unavoidably energy-consuming. Here, the redox approach provides a new strategy to spread the industrial application of KNO_3 -derived solid bases because it can be conducted at relatively mild condition, not only to retain the porous structure of support, but also to save energy. Further, most of the NO_x production, that is unavoidable in thermal decomposition of KNO_3 , is suppressed in this new process due to the special decomposition of nitrate anion in the redox procedure [8]. On the basis of these results, it is conclusive that, even tentatively, the redox approach for the preparation of solid strong base derived from KNO_3 modified materials is the environmentally benign and economical one, which may open a green way to convert the KNO_3 supported to form the strong basic sites on porous host.

5. Conclusions

Neutral salt KNO_3 is used as base precursor to modify Al_2O_3 and the dispersion threshold is about 14 wt%. Unlike that a high temperature of $600\text{ }^\circ\text{C}$ is needed to thermally decompose the KNO_3 supported, the guest KNO_3 can be converted on alumina at $450\text{ }^\circ\text{C}$ by use of redox strategy. The superbasicity ($H_- = 27.0$) can be

generated on Al_2O_3 provided the loading of KNO_3 exceeds the dispersion capacity (> 14 wt %). Rather, about 80% of NO_x is suppressed meanwhile the pore structure of Al_2O_3 is retained through the redox approach.

Acknowledgments

The National Natural Sciences Foundation of China (20773061, 20673053 and 20373024), National Basic Research Program of China (2007CB613301) and the Analysis Center of Nanjing University financially support this research.

References

1. Y. Ono, *J. Catal.* **216**, 406 (2003).
2. G. Suzukamo, M. Fukao and M. Minobe, *Chem. Lett.* 585 (1980).
3. T. Baba, H. Handa and Y. Ono, *J. Chem. Soc., Faraday Trans.* **90**, 187 (1994).
4. B. Sels, D. E. De Vos and P. A. Jacobs, *Catal. Rev.* **43**, 443 (2001).
5. Y. Wang, W. Y. Huang, Y. Chun, J. R. Xia and J. H. Zhu, *Chem. Mater.* **13**, 670 (2001).
6. J. H. Zhu, Y. Wang, Y. Chun and X. S. Wang, *J. Chem. Soc., Faraday Trans.* **94**, 1163 (1998).
7. Z. Y. Wu, Q. Jiang, Y. M. Wang, H. J. Wang, L. B. Sun, L. Y. Shi, J. H. Xu, Y. Wang, Y. Chun and J. H. Zhu, *Chem. Mater.* **18**, 4600 (2006).
8. L. B. Sun, Y. Chun, F. N. Gu, M. B. Yue, Q. Yu, Y. Wang and J. H. Zhu, *Mater. Lett.* **61**, 2130 (2007).
9. Y. Wang, W. Y. Huang, Z. Wu, Y. Chun and J. H. Zhu, *Mater. Lett.* **46**, 198 (2000).
10. J. H. Zhu, Y. Chun, Y. Wang and Q. H. Xu, *Catal. Today* **51**, 103 (1999).
11. Y. Wang, J. H. Zhu and W. Y. Huang, *Phys. Chem. Chem. Phys.* **3**, 2537 (2001).
12. H. Hattori, *Chem. Rev.* **95**, 537 (1995).
13. K. Nakamoto, *Infrared Spectra of Inorganic and Coordination Compounds*, John Wiley, New York, p. 98 (1970).
14. V. K. Diez, C. R. Apesteguia and J. I. Di Cosimo, *J. Catal.* **240**, 235 (2006).
15. M. I. Zaki, T. H. Ballinger and J. T. Yates, *J. Phys. Chem.* **95**, 4028 (1991).
16. Y. Chen and L. F. Zhang, *Catal. Lett.* **12**, 51 (1992).
17. A. R. West, *Solid State Chemistry and Its Application*, John Wiley & Sons Inc., New York, p. 271 (1984).
18. Z. Liu, L. Dong, W. J. Ji and Y. Chen, *J. Chem. Soc., Faraday Trans.* **94**, 1137 (1998).
19. T. Yamaguchi, J. H. Zhu, Y. Wang, M. Komatsu and M. Ookawa. *Chem. Lett.* 989 (1997).

EFFICIENT AND SELECTIVE NANOPOROUS CATALYSTS BY PLACING MULTIPLE SITE-ISOLATED FUNCTIONAL GROUPS ON MESOPOROUS MATERIALS*

TEWODROS ASEFA[†], KRISHNA K. SHARMA, ABHISHEK ANAN, RAJYALAKSHMI VATHYAM, ROBERT P. BUCKLEY, HIEU MINH DAM, YOUWEI XIE, SEAN QUINLIVAN, GANG WANG, AND COLE DUNCAN

*Department of Chemistry, Syracuse University, 111 College Place
Syracuse, New York 13244, USA, tasefa@syr.edu*

The design, synthesis and self-assembly of inorganic, organic and organometallic molecules into solid-state nanoscale structures is important for the development of nanostructured and mesostructured materials for various electronics, catalytic, sensing, separation, biological and medical applications. We describe a synthetic strategy involving self-assembly of mesoporous materials and a solvent-assisted grafting of site-isolated organic functional groups on the mesoporous materials in *polar* solvents for the synthesis of various efficient multifunctional mesoporous materials with high surface areas and efficient catalytic properties. By judicious choice of multiple functional groups, the catalytic selectivity of the materials for specific reactant in a mixture of reactants or for the generation of specific products, where two or more products are possible such as Henry reaction, was also demonstrated. The materials structures were characterized by a combination of small angle X-ray scattering, power X-ray diffraction, TEM and gas adsorption. The degree of site-isolation of the functional groups was probed by a simple colorimetric technique. The relationships between the structures and compositions and the catalytic properties of the materials towards reactions such as Henry and Michael reactions were investigated.

1. Functional Nanostructured and Mesostructured Materials

The development of synthetic methods to ordered nanostructured materials has captured researchers' attention for the last several years now [1]. This is evidenced by numerous reports of successful synthesis and characterization of various types of nanoporous materials, nanoparticles and nanowires and demonstration of the potential applications of many of these materials. In particular, "bottom-up" synthetic methods involving self-assembly of molecular building blocks into well-ordered supramolecular templates and the use of the

*This work is supported by the U.S. National Science Foundation, CAREER Grant, CHE-0645348, by the Syracuse Center of Excellence in Environmental and Energy Systems (Syracuse CoE) through a CARTI grant, and by Syracuse University Start-Up Fund.

resulting self-aggregates as templates to create other well-ordered nanostructures have become a method of choice among materials chemists in their efforts to make novel nanoporous materials [2]. The materials resulting from these procedures often have interesting properties such as high surface area, highly ordered mesostructures, uniform nanometer pore sizes, high pore volumes and intrinsically unique properties that are required for catalysis, drug-delivery, adsorption, and separations applications [3]. Furthermore, they have nanopores that can be used as “hard-templates” for creating metallic and semiconductor nanostructures [4].

Mesoporous materials, which are a class of nanostructured materials, are synthesized by supramolecular templating and self-assembly of surfactants in the presence of various organometallic precursors [5]. While many of these materials have inorganic metal oxide composition, the most ordered ones often resulted with silica. Although the latter have highly ordered structures, they do not have a range of functional groups in their structures to allow them to be useful for many applications. Consequently, the functionalization of mesoporous silica materials with organic and organometallic groups had been an active area of research for over a decade now [6]. This allows the materials to have properties important for numerous applications [7]. For instance, the surface properties and adsorption capacity of mesoporous silica materials for soft heavy metal ions was increased by incorporating alkane thiol moieties on the surface of the mesoporous silica [8]. Various solid acid catalysts have also been synthesized by anchoring cyanopropyl and alkane thiols into the mesoporous silica and oxidizing them into alkanecarboxylic acid and alkanesulfonic acid groups, respectively [9].

In our effort to synthesize organic functionalized nanoporous materials, our research group has recently developed synthetic methods to various efficient multifunctional mesoporous materials containing multiple site-isolated functional groups including organoamine catalytic sites [10]. We also investigated the catalytic properties of the materials and their structure-catalytic property relationships. Our synthesis involved combinations of self-assembly of mesoporous silica with previously reported procedures followed by a unique and hitherto unexplored functionalization procedure involving grafting of organosilanes in *polar* solvents. The grafting in polar solvents allowed quantitative control over the degree of organic loading. The method leads to immobilization of lesser populated and hence site-isolated organic groups leaving large numbers of ungrafted silanol groups shown to be playing pivotal role in number of catalytic processes. The grafted functional groups included various types of aminopropyl groups, organodiamine, mercaptopropyl,

cyanopropyl, ureidopropyl, and methyl groups. Interestingly, smaller organic loading in site-isolation resulted in high surface area and enhanced solid-base catalytic property compared to the corresponding materials grafted with toluene, which was a more commonly used solvent up till now for grafting organic groups on mesoporous materials. Further control over the concentration of the site-isolated groups was enabled with the duration of grafting. Manipulation in the grafting techniques such as use of an appropriate solvent according to the type of organosilane to be grafted and varying grafting duration allowed optimization and enhancing the catalytic properties of the materials. The residual silanol groups were proved to enhance the catalytic properties of the materials, often by behaving as weak general-acids. The surface silanols were shown not only to dictate the selectivity in terms of reactants but also the type of products formed. By further using these silanol groups, we introduced secondary functional groups such as 3-cyanopropyl, 3-mercaptopropyl and methyl groups to change the surface properties of the mesopores and its selective catalytic properties. These secondary functional groups enabled preferential diffusion and mass transport of specific reagents in a mixture of reactants, which in turn, resulted in selective catalysis of specific reactants in the Henry reaction [11]. By systematically changing the types of the secondary groups, the material was made to be selective for either hydrophilic or hydrophobic aldehydes in the Henry reaction while the site isolated catalytic groups and silanols offered its efficient catalysis. This synthetic strategy of judiciously choosing two or more judiciously chosen functional groups in polar solvents is important for the development of other nanocatalysts.

2. Experimental

2.1. *Synthesis of the Functionalized Mesoporous Materials with Site-Isolated Groups*

The synthesis of the multifunctional mesoporous materials was carried out by grafting parent mesoporous silica materials under various conditions in *polar* solvents. The parent MCM-41 type and SBA-15 type mesoporous silica materials were synthesized under base and acid catalyzed conditions, respectively, as reported before [12,13].

The MCM-41 was synthesized as follows. A solution of 5.5 mmol cetyltrimethylammonium bromide (CTAB), 26.7 mmol of millipore water and 7 mL, 2.0 M NaOH was prepared under stirring for 30 min at 80 °C. Then, 50.6 mmol tetraethoxysilane (TEOS) was added into it. The mixture was stirred moderately for 2 h at 80 °C. The solution was filtered and the precipitate was

washed with 40 mL millipore water, followed by ethanol and dried under air for 4 h. The CTAB was extracted by stirring 1 g of the sample in a solution of 0.5 mL of HCl / 150 mL of EtOH at 50 °C for 5 h. The solution was filtered and the precipitate was washed with ethanol resulting in MCM-41. The SBA-15 sample was prepared by following the procedure in Stucky *et al.* [13].

The functionalization of the mesoporous silica materials with site-isolated organoamine catalytic sites in polar and non-polar solvents were carried out by grafting various concentrations of 3-aminopropyltrimethoxysilane (APTS) and *N*-(2-aminoethyl)-3-aminopropyltrimethoxysilane (AAPTS) in ethanol on a well-dried MCM-41 or SBA-15 samples. Typically, 500 mg of MCM-41 was stirred under reflux in 3.68 mmol of APTS, in ethanol at 80 °C for 6 h. The precipitate was separated by filtration, washed with ethanol and dried in air resulting in aminopropyl functionalized mesoporous silica sample (APE). For comparison purposes, grafting was carried out in toluene under the same procedure as above resulting in sample APT. The grafting of AAPTS in ethanol and toluene resulted in samples AAPE and AAPT, respectively. Further, grafting of the mesoporous silica samples in ethanol and toluene with various concentrations of APTS and AAPTS for different grafting times (3 min - 6 h) were also carried out (Table 1).

2.2. Synthesis of Selective Efficient Catalysts

A 1:1 mixture of two organosilanes such as APTS and 3-mercaptopropyltrimethoxysilane (MPTS) was grafted on MCM-41 or SBA-15 samples following the same procedure as above. Additionally, grafting of one organosilane in ethanol followed by a second organosilane in ethanol (or toluene) was carried out. For instance, the grafting of APTS at 80 °C for 6 h followed by grafting of MPTS at 80 °C for 6 h was carried out. This was done for various combinations of organosilanes such as APTS:MPTS and APTS:methyltriethoxysilane (MTS).

2.3. Henry (Nitroaldol Condensation) Reaction

The materials synthesized above were used as catalysts in the Henry reaction. The reaction was performed between 1 mmol *p*-hydroxybenzaldehyde and 10 mL of nitromethane in the presence of 20 mg of the aminofunctionalized mesoporous sample at 90 °C under nitrogen. The reaction mixture in the course of the reaction time was characterized by solution ¹H NMR spectroscopy in deuterated acetone and GC-MS.

2.4. Characterizations of the Mesoporous Materials and Reaction

The powder X-ray diffraction of the mesoporous materials was measured by using a Scintag powder diffractometer. The thermogravimetric analysis was carried out with a Q-500 Quantachrome instrument (TA-Instruments). The solid-state NMR spectra were measured with a 300 MHz Bruker Avance NMR spectrometer. The solution ^1H NMR spectra were measured using a Bruker DPX-300 NMR spectrometer while the GC-MS was measured with HP-5971 GC-MS spectrometer. The BET gas adsorptions were measured with Micromeritics ASAP 2020 and Tristar 3000 volumetric analyzers at 77 K. The TEM was obtained on FEI Tecnai instrument working at 120 KeV.

Table 1. Synthesis of various aminofunctionalized samples.

Sample	Organosilane	Amount	Solvent	Grafting Temperature °C	Grafting Time (h)
APE-1	APTS	Excess (3.68 mmol)	Ethanol	80	6
API-1	APTS	Excess (3.68 mmol)	Toluene	80	6
APE-2	APTS	1.21 mmol	Ethanol	80	1
APE-3	APTS	0.92 mmol	Ethanol	80	6
APT-2	APTS	Excess (3.68 mmol)	Toluene	80	1
APT-3	APTS	1.21 mmol	Toluene	80	6
APT-4	APTS	1.21 mmol	Toluene	80	1
APT-5	APTS	0.92 mmol	Toluene	80	6
APT-6	APTS	0.92 mmol	Toluene	80	1
APT-7	APTS	0.92 mmol	Toluene	80	1
AAPE-1	AAPTS	Excess (3.68 mmol)	Ethanol	80	6
AAPE-1	AAPTS	Excess (3.68 mmol)	Toluene	80	6
AAPT-1	AAPTS	Excess (3.68 mmol)	Toluene	80	2

3. Discussion

3.1. Synthesis and Characterization of the Materials

We have recently demonstrated that by grafting of aminopropyl groups on the surfaces of mesoporous silica (MCM-41 and SBA-15) materials in polar solvents such as ethanol [10], functionalized materials with high surface area and pore volume and enhanced catalytic properties will be obtained. The parent MCM-41 was synthesized by following the procedure reported by Lin *et al.* [1] while the SBA-15 was synthesized by following the procedure in Stucky *et al.* By grafting

a mixture of organosilanes in ethanol, materials with multiple site-isolated groups were also obtained.

The structures of the functionalized and multifunctional mesoporous materials were characterized by powder X-ray diffraction (XRD). Figure 1 shows representative XRD patterns of some of the materials. The materials resulted from MCM-41 showed unit cell dimensions between 4.3 – 4.6 nm after indexing based on their (100) peak on hexagonal lattice P_{6mm} . The SBA-15 materials showed unit cell of 10.7 – 10.9 nm.

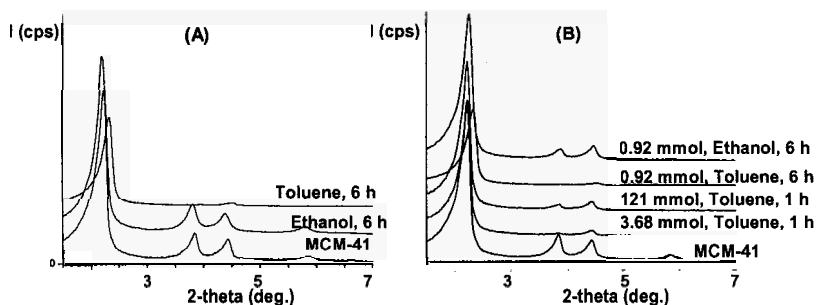


Fig. 1. Powder X-ray diffraction (XRD) patterns of various monoamine and diamine grafted mesoporous samples in ethanol and toluene.

The TEM images of all the grafted samples showed well-ordered mesoporous structures corresponding to MCM-41 and SBA-15 types. Figure 2 shows representative examples of TEM images of functionalized mesoporous samples with site isolated multiple functional groups.

N_2 gas adsorption measurements of all the mesoporous materials with the site-isolated groups exhibited Type-IV isotherms with sharp capillary condensation steps at P/P^0 of ~ 0.3 (Figure 3). This is a further indication of the presence of highly ordered mesostructures. The BJH pore size distribution of the materials also showed a well monodispersed pore distribution centered at ~ 3.0 nm for the MCM-41 type materials and ~ 6.0 for the SBA-15 type materials. The wall thickness, calculated from the difference between the pore widths and unit cell dimensions, was obtained to ~ 1.5 nm for the former and 5.0 nm for the latter. The BET surface areas of the materials grafted in ethanol ranged between 800 - 1,000 m^2/g . Interestingly, the materials grafted with toluene by us and previously by others exhibited lower surface areas ranging between ~ 50 - 300

m^2/g . This is consistent with the fact that grafting in toluene results in much higher concentration of organic groups compared to the latter (See below).

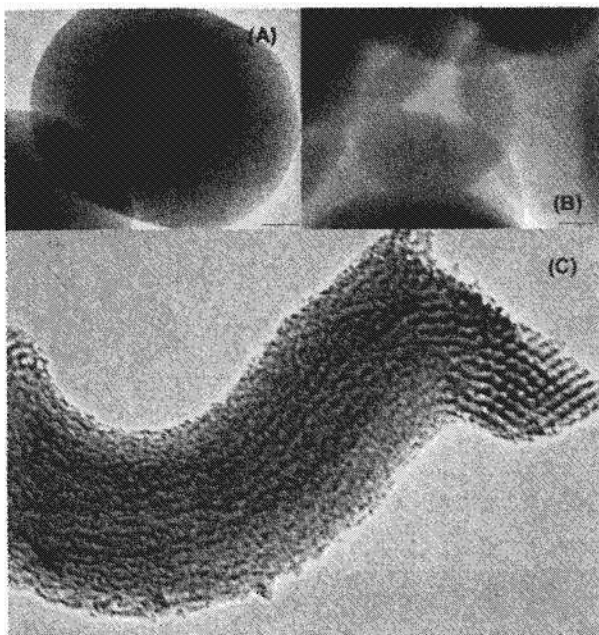


Fig. 2. Representative TEM image of (A,B) MCM-41 type and (C) SBA-15 type samples. Scale bar = 50, 50 and 100 nm, for A, B and C, respectively.

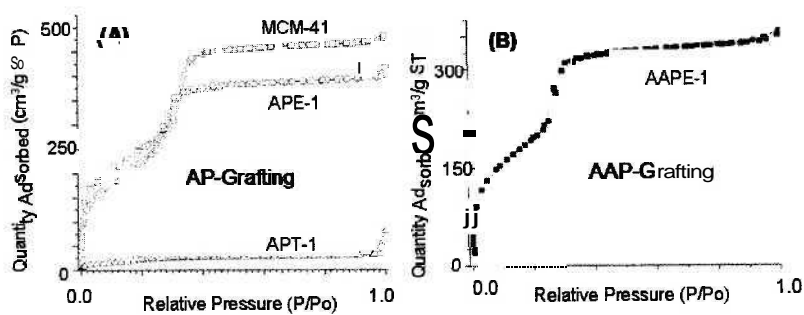


Fig. 3. N_2 gas adsorption isotherms and pore-size distribution of representative mesoporous materials with site-isolated organic functional groups.

By using the weight losses between 100 - 600 °C on thermogravimetric traces, the relative percentage of organic groups in the samples was estimated. While the monoamine groups grafted in ethanol, APE showed the lowest weight loss (10.7%), the monoamine grafted samples in toluene showed higher percentage (14.8 %). Furthermore, the samples grafted with organodiamine groups showed higher weight losses than the corresponding monoamine grafted samples. The latter is consistent with the molecular weight of the grafted groups. Interestingly, the grafting in ethanol gave lower grafting concentration for both types of organoamines compared to those in toluene.

These composition and relative concentrations of the materials were further analyzed by solid-state NMR spectroscopy (Fig. 4). The ^{13}C CP-MAS NMR spectra showed peaks corresponding to aminopropyl groups at 43.1, 24.7, and 8.4 ppm while the ^{29}Si MAS NMR also showed T peaks corresponding to the presence of grafted organosilicon groups. The ^{29}Si MAS NMR spectra also indicated that samples grafted in ethanol to have lower percentage of T groups compared to those grafted in toluene. Our analysis of the composition of the materials based on the solid-state ^{29}Si MAS NMR spectra, we obtained that sample APE and APT to have 1.3 and 4.1 mmol/g, respectively. These results were further corroborated by elemental analysis, which indicated that the samples grafted in polar solvents gave wt.% of nitrogen of 1-2 % while samples grafted in toluene gave wt.% of nitrogen of 3-4 % per unit gram of sample.

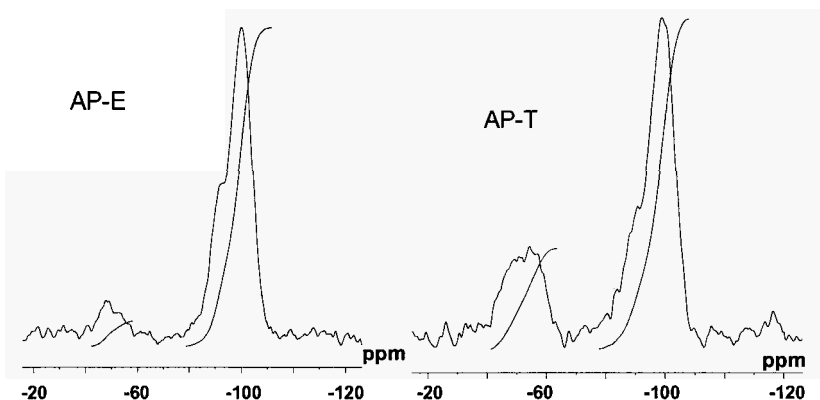


Fig. 4. ^{29}Si MAS NMR spectra of mesoporous materials with site-isolated of 3-aminopropyl and (2-amino ethyl) 3-aminopropyl-grafted in ethanol and toluene.

By taking into account the above characterization results and by using electronic spectrum of Cu^{2+} complexed with the amine groups in the materials,

the composition, site-isolation of functional groups and possible structures of the materials were proved to be as in Fig. 5 [14]. The samples grafted in ethanol have about three times less number of moles of organic groups compared to the samples grafted in toluene. Furthermore, Hicks *et al.* [15] has proved that samples grafted in toluene often result in aggregation of the aminopropyl groups.

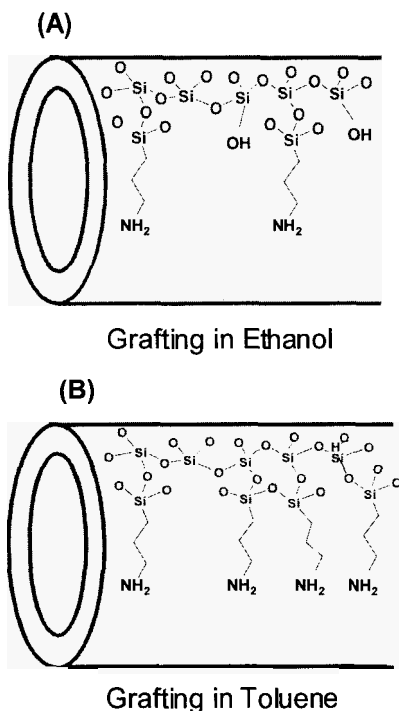


Fig. 5. Proposed structure of (A) functionalized mesoporous materials grafted in ethanol and which contained site-isolated of 3-aminopropyl groups compared with (b) samples grafted in toluene and which contained aggregated 3-aminopropyl groups.

Interestingly, the materials we synthesized in a polar solvent, ethanol, catalyzed the Henry reaction with much superior efficiency compared to those grafted in toluene and many of previously reported materials in the literature [12] (Figure 6A). Furthermore, this trend is true for both the monoamine and diamine grafted samples. We typically obtained % conversions as high as > 99 % within 15 minutes of reaction time with samples grafted with 3-aminopropyl groups in polar solvents such as ethanol and for 50 mg of catalyst and 2.5 mmol of reactant (See for sample AP-E1, Fig. 6A). The grafting of secondary

functional group on the mesoporous materials has slightly reduced the catalytic efficiency. This might be due to the fact that additional grafting reduced the number of silanol groups, added more organic groups and/or decreased the surface area of the materials resulting in decreased catalytic activity. The catalysts were also proved to be recyclable and they maintained their structures.

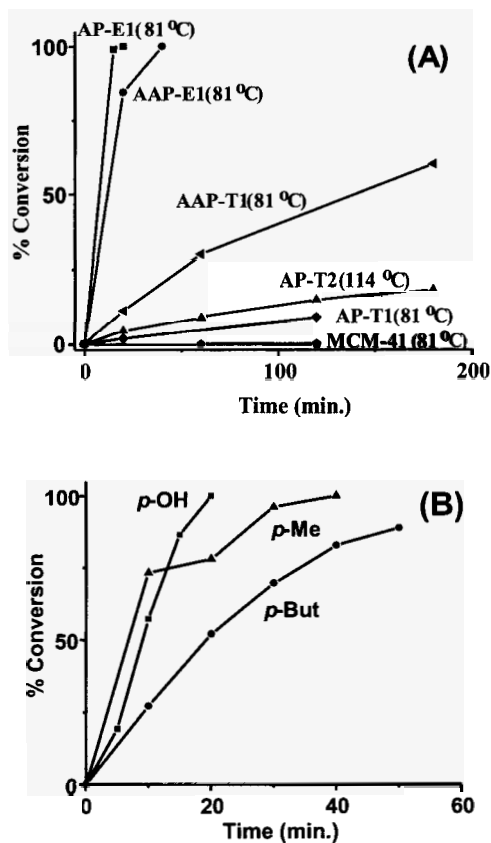


Fig. 6. (A) Percent conversion versus reaction time for the Henry reaction catalyzed by various samples containing site-isolated 3-aminopropyl groups and 2-aminoethyl(3-aminoaminopropyl) groups. (B) Comparisons of percent conversion versus reaction time in the Henry reaction for *p*-hydroxybenzaldehyde, *p*-hydroxybenzaldehyde, and *p*-methylbenzaldehyde catalyzed by sample containing methyl and aminopropyl groups.

Selective catalysts for a 1:1 mol mixture of different pair of *p*-substituted benzaldehydes including *p*-hydroxybenzaldehyde (*p*-OH), *p*-butoxybenzaldehyde (*p*-But), and *p*-methylbenzaldehyde (*p*-Me) was performed by various samples containing site-isolated multiple organic groups and silanols. The catalysts containing aminopropyl and secondary organic groups such as mercaptopropyl and methyl groups showed a selectivity of ~ 2 for *p*-OH over *p*-But. This selectivity was obtained in ~ 10 -15 min of reaction time. Typical yield was found to be 70% in 10 min for more selectively reacted reactant, *p*-OH, with the highest being 90% and 60% at 30 min for *p*-OH and *p*-But, respectively. As expected, hydrophobic catalysts, which contained methyl or mercaptopropyl groups showed a decreased selectivity of 1.6 for *p*-OH compared to *p*-But (Fig. 6B). The samples grafted with 1:1 mole ratio of AP and the secondary functional groups showed little selectivity for *p*-Me compared to *p*-OH with values of ~ 1.0 being obtained in all cases. However, the highly hydrophobic catalysts containing higher percentages of methyl groups showed a selectivity of 2.2 for *p*-Me over *p*-OH. Since these two reactants have similar sizes, this confirms to the fact that the catalyst does not discriminate between *p*-Me and *p*-OH on the basis of size but hydrophobicity. However, comparing *p*-Me with *p*-But, all the samples showed higher selectivity for *p*-Me than *p*-But. The selectivity was a result of differences in reactivity, hydrophobicity and the size of the reactants.

Acknowledgments

We thank the financial support by the U.S. National Science Foundation, CAREER Award, CHE-0645348, by the Syracuse Center of Excellence in Environmental and Energy Systems, and by Syracuse University for this work.

References

1. S. Huh, H.-T. Chen, J. W. Wiench, M. Pruski, V. S.-Y. Lin, *Angew. Chem., Int. Ed.* **44**, 1826 (2005).
2. A. Corma, *Chem. Rev.* **97**, 2373 (1997).
3. T. Asefa, M. J. MacLachlan, N. Coombs, G. A. Ozin, *Nature* **402**, 867 (1999).
4. T. Asefa, R. B. Lennox, *Chem. Mater.* **17**, 2481 (2005).
5. C. T. Kresge, M. E. Leonowicz, W. J. Roth, J. C. Vartuli, J. S. Beck, *Nature* **359**, 710 (1992).
6. A. Stein, B. J. Melde, R. C. Schrodin, *Adv. Mater.* **12**, 1403 (2000).
7. A. Sayari, S. Hamoudi, *Chem. Mater.* **13**, 3151 (2001).
8. X. Feng, G.-E. Fryxell, L.-Q. Wang, A.-Y. Kim, J. Liu, K.-M. Kemner, *Science* **276**, 923 (1997).

9. W. M. van Rhijn, D. E. De Vos, B. F. Sels, W. D. Bossaert, P. A. Jacobs, *Chem. Commun.* 317 (1998).
10. K. K. Sharma, T. Asefa, T. *Angew. Chem. Int. Ed.* **46**, 2879 (2007).
11. A. Anan, K. K. Sharma, T. Asefa. Submitted.
12. S. Huh, H.-T. Chen, J. W. Wiench, M. Pruski, V. S.-Y. Lin, *J. Am. Chem. Soc.* **126**, 1010 (2004).
13. P. Yang, D. Zhao, D. I. Margolese, B. F. Chmelka, G. D. Stucky, *Nature*, **396**, 152 (1998).
14. K. K. Sharma, A. Anan, R. P. Buckley, W. Ouellette, T. Asefa, T. *J. Am. Chem. Soc.* (2007) In Press.
15. J. C. Hicks, R. Dabestani, A. C. Buchanan, C. W. Jones, *Chem. Mater.* **18**, 5022 (2006).

POLYMERIC ACTIVATED CARBON-SUPPORTED COPPER AND MAGNESIUM FOR ETHYLBENZENE DEHYDROGENATION WITH CARBON DIOXIDE

SÉRGIO BOTELHO DE OLIVEIRA, DANNS PEREIRA BARBOSA, MARIA DO CARMO RANGEL[†]

GECCAT Grupo de Estudos em Cinética e Catálise, Instituto de Química, Universidade Federal da Bahia, Campus Universitário de Ondina, Federação, 40170-280 Salvador, Bahia, Brazil. E-mail: mcarmov@ufba.br

DENILSON RABELO

Instituto de Química, Universidade Federal de Goiás, Campus Samambaia Goiânia, Goiás, Brazil

Polymeric activated carbons find several applications, including catalytic supports for ethylbenzene dehydrogenation with carbon dioxide to produce styrene. Aiming to get efficient catalysts for this reaction, the preparation and characterization of polymeric activated-supported copper and magnesium were studied in this work. It was observed that copper increases the ethylbenzene conversion but decreases the selectivity to styrene, while its combination with magnesium results in an increase of both activity and selectivity. The treatment of the catalyst containing both metals with a sodium hydroxide solution improved even more its performance. These findings were attributed to the ability of copper in catalyzing the reaction as well as to the ability of magnesium in neutralizing the acid sites, favoring the mesoisomerization and the rearrangement of the surface groups in lactones and anhydrides that are more selective to styrene.

1. Introduction

The most used commercial route for styrene production is the ethylbenzene dehydrogenation in the presence of steam. The reaction (Equation 1) is endothermic and equilibrium limited and is often performed over an iron oxide-based catalyst (hematite, $\gamma\text{-Fe}_2\text{O}_3$), promoted with chromium, cerium and potassium oxides [1,2].



[†] To whom the correspondence should be addressed

Steam has been used for several purposes, such as to oxidize the coke produced on the catalyst, which causes its deactivation. However, it increases the operational cost of the commercial operations and thus catalysts that can work without steam are much needed. Potassium also reduces the coke formation and increases the activity of iron oxide [3]. The commercial catalyst has low cost and high resistance against poisoning but deactivates with time, in industrial operations, mainly due to the loss of potassium [4]. The toxicity of chromium is another disadvantage of this catalyst.

In order to diminish the costs of styrene production, several changes have been performed regarding the process and the catalysts [1, 3]. In recent years, for example, the use of carbon dioxide replacing steam has been proposed as a promising option for reducing energy reduction in the process and also for increasing the selectivity to styrene [5]. On the other hand, activated carbon has been pointed out as a promising catalyst for oxidative dehydrogenation of ethylbenzene, due to the functional groups on the surface, which are able to catalyze the reaction [6].

The preparation of activated carbons from polymeric precursors seems to be a promising route for preparing supports and catalysts, since it provides the pureness, thermal stability and high specific surface area required for catalytic purposes [7-9]. The carbonization and activation of the sulfonated styrene-divinylbenzene resin, for instance, result in activated carbon with higher thermal stability, as compared to other polymeric precursors, due to its reduced depolymerization [10-12]. Moreover, it is able to interact with several metals, making them suitable catalytic supports. They can also be changed by several treatments [13], such as oxidation, for the introduction of oxygenates groups, which diminish the carbon hydrophobicity, favoring the metal adsorption [14].

Previous studies [15] showed that copper increases the ethylbenzene conversion but decreases the selectivity to styrene. On the other hand, magnesium is able to neutralize the acidic sites, increasing the selectivity to styrene. In the present work, the preparation and characterization of activated carbon-supported copper and magnesium were described, aiming to get more selective catalysts for styrene production by ethylbenzene dehydrogenation with carbon dioxide.

2. Experimental

The copolymer based on styrene and divinylbenzene was synthesized through polymerization in suspension. It was rinsed with ethanol and dried. Only spheres with diameters in the range of 125-250 μm were used in this work.

The copolymer was sulfonated at 70 °C, dispersing the copolymer in a sulfuric acid solution (15/3 mL.g⁻¹) and keeping the system under stirring, for 4 h. The copolymer was filtered, rinsed with water and dried at 110 °C. It was then heated at 300 °C for 2 h in air, carbonized at 900 °C, in nitrogen, for 3 h and activated at 800 °C, for 2 h, under nitrogen flow saturated with steam (PAC sample). After this, it was oxidized at 600 °C in 5%O₂/N₂ (v/v) mixture for 1 h (CON sample). This step is needed because sulfonation leads to a high thermal stability, and then to a low weight loss, since sulfur acts as a crosslinker [15].

The co-adsorption of Cu²⁺ and Mg²⁺ ions were carried by dispersing the CON sample in an ethanol solution (15%). For each 1 g of sample, 20 mL of copper nitrate (0.20 mol.L⁻¹) and 17 mL of magnesium nitrate (0.04 mol. L⁻¹) were used. The system was kept for 24 h, at room temperature under stirring and then was filtered, rinsed with distilled water and dried at 110 °C (CON-CM sample). This procedure was repeated using a solution with only copper to get the CON-C sample. An amount of the CON-CM sample was further treated with 25 mL of sodium hydroxide solution (0.1 mol. L⁻¹), for 1h and then filtered, rinsed and dry at 110 °C, to produce the CON-CMN sample.

The copper and magnesium in the catalysts were determined by atomic absorption spectrometry, in Perkin-Elmer 306 equipment. The analysis of sulfur was performed in LECO CS-200 equipment and the morphological analysis was carried out in a scanning electron microscope SEM/EDS Jeol JSM 6360LV. The textural properties were measured by adsorption of nitrogen at -196 °C, in Micromeritics ASAP 2010 apparatus.

The thermal stability of the materials was evaluated by thermogravimetry, in a TGA/SDTA 851E of Mettler Toledo equipment, under nitrogen flow. The samples were heated at 5 °C.min⁻¹ up to 500 °C, kept for 1 h at this temperature and then heated at 20 °C.min⁻¹ up to 800 °C. The thermoprogrammed decomposition (TPD) was carried out using a home-made equipment.

The evaluation of catalysts (CON-C, CON-CM and CON-CMN samples) was performed in a microreactor, using 0.300 g of the samples and working at 500 °C and atmospheric pressure, with an ethylbenzene to carbon dioxide molar ratio of 10. The reactor effluent was continuously monitored by a Varian chromatograph 3600-X, in 30 min injection intervals.

3. Results and Discussion

Table 1 shows the copper concentration in the samples, before and after reaction. It can be seen that the adsorbed amounts of the two metals were close, despite of the fact that a more concentrated copper solution was used. This fact

Table 1. Copper and magnesium concentration in the catalysts, before and after reaction.

Samples	Cu (mg.g ⁻¹)	Mg (mg.g ⁻¹)
CON-C	2.45	0
CON-CM (before)	2.16	1.70
CON-CM (after)	1.89	1.44
CON-CMN (before)	1.83	1.73
CON-CMN (after)	1.81	1.16

is probably related to kinetic (hydrated radio, ionic mobility and size of the support pore, among others) and thermodynamic factors (free energy of the ions), as well as to the support affinity for the adsorbed ion, that determine the adsorption. The treatment of the copper and magnesium containing sample with sodium hydroxide caused a decrease of copper concentration, as we can inferred by comparing the CON-CM and CON-CMN samples. This is probably due to copper removal by the neutralization of residual acidic sites acid, during this treatment. On the other hand, the concentration of Mg²⁺ adsorbed species was not influenced by the neutralization, due to low solubility of earth alkaline metals in alkaline solutions. During reaction, copper and magnesium were lost and this effect was more intense for magnesium, suggesting that the copper was stronger adsorbed on the support. The catalysts treated with sodium hydroxide lost a higher amount of magnesium than the untreated solid (CON-CM).

The metal incorporation on the activated carbon and the rinsing with the sodium hydroxide solution did not affect significantly the specific surface area, as shown in Table 2. However, during reaction it strongly decreased as well as the micropores areas and pore volume. It means that most of micropores had been collapsed or were blocked by coke depositions during reaction.

Table 2. Catalysts textures properties, before and after reaction.

Samples	S _{BET} (m ² .g ⁻¹)	S _{MIC} (m ² .g ⁻¹)	V _p (cm ³ .g ⁻¹)
CON	595	362	0.803
CON-CM (before)	558	333	0.729
CON-CM (after)	180	22	0.690
CON-CMN (before)	587	356	0.795
CON-CMN (after)	166	23	0.573

The nitrogen sorption curves of the catalysts CON-CM and CON-CMN, before and after reaction, presented typical profiles of II or IV type, characteristic of associated micropores to mesopores Fig. 1 (a) e (b). The curves

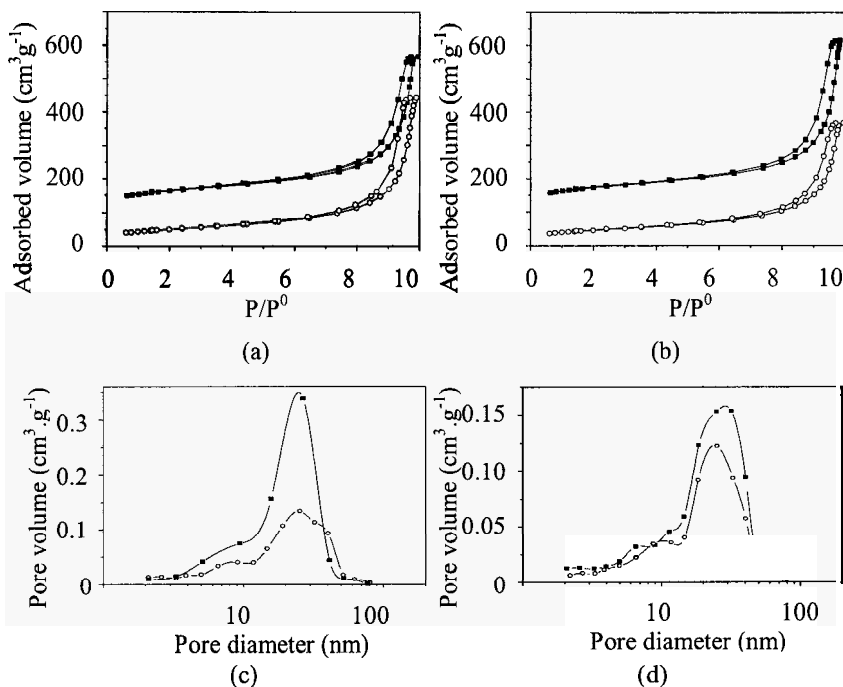


Figure 1. N_2 adsorption isotherms and the corresponding pore size distribution curves for (a) and (c) CON-CM and (b) and (d) CON-CMN samples before (■) and after (○) reaction.

of the pore size distribution, before and after reaction, are shown in Fig. 1. The solid treated with sodium hydroxide (CON-CMN), before and after the reaction, presented a polymodal distribution with mesopores between 10 and 55 nm, while the untreated one (CON-CM) showed a narrower distribution curve (10-40 nm), with the pore diameter kept in a value of 25 nm.

Fig. 2 shows the thermograms of the catalysts (CON-CM and CON-CMN). They showed a weight loss of 7 and 2%, in the range of 25 to 460 $^{\circ}\text{C}$, respectively, due to water loss and to decomposition of carboxylic functional groups. In the range of 460 to 500 $^{\circ}\text{C}$, the samples lost 5 and 10% weight, respectively, which is related to the decomposition of oxygenates functional groups, catalyzed by the metal on the surface. The solid treated with sodium hydroxide (CON-CMN) lost more weight. Above 800 $^{\circ}\text{C}$, the samples lost 7% weight, due to decomposition reactions and loss of metals. The total weight loss of each catalysts was around 19%.

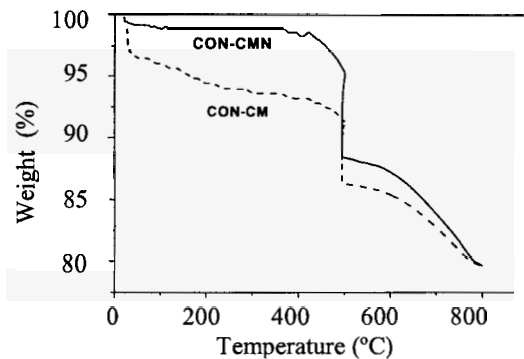


Figure 2. Thermogravimetric curves for fresh catalysts: CON-CM (—) and CON-CMN (---).

Sulfur analysis showed that more than 90% of sulfur was lost during catalyst preparation; the concentration decreased from 7.90 (copolymer) to 0.60% (activated carbon). This remaining sulfur is supposed to stabilize carbon, during carbonization, while most of surface sulfur is eliminated by thermal decomposition.

Fig. 3 shows the thermoprogrammed decomposition (TPD) spectra of the catalysts. The copper and magnesium containing sample (CON-CM) showed an intense peak between 100 and 400 °C that can be attributed to carboxylic groups [2]. The activated carbon (CON sample) presented several low intensity peaks, assigned to carboxylic groups [2]. Two peaks at 450 and 630 °C were detected for CON sample, attributed to lactones, carboxylic acids and anhydride groups [16]. All oxygenates groups were removed from the CON sample at 950 °C and at 1000 °C from the CON-CM sample, indicating that the metal stabilizes the functional groups on the surface. The different kind of these groups on carbon surface and their different decomposition temperatures can be explained by different carbon gasification mechanisms [2]. It can be noted that the metals also stabilize the carboxylic and quinone groups shifting the peak from 859 to 950 °C for CON-CM sample.

The peaks of carboxylic and ethers, between 100 and 400 °C for CON sample, can have been modified by other functional groups due to temperature effect and to the metals and then did not appeared in the CON-CM spectrum. It is known [17] that the acidic groups of polyaromatics rings are susceptible to mesoisomerization and rearrangements, producing more stable groups such as anhydrides and lactones. In fact, the CON-CM sample showed an intense peak between 700 and 1000 °C, which is assigned to anhydrides and lactones.

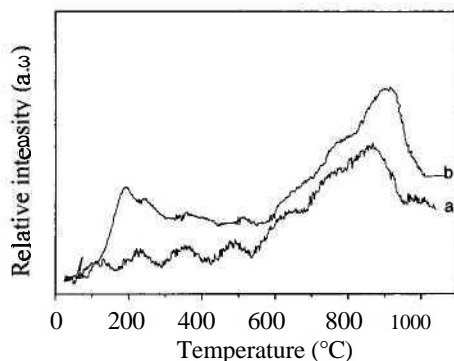


Figure 3. TPD spectra for (a) CON and (b) CON-CM samples.

Fig. 4 shows the scanning electron microscopy images of CON-CM samples before and after reaction. It can be seen that there was not any damage to the samples during reaction and the spheres were not broken and not have any fissure.

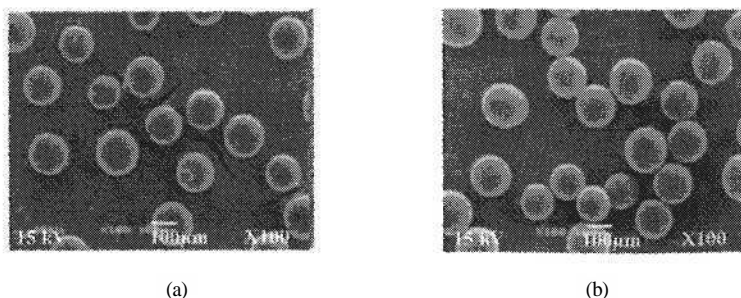


Figure 4. Scanning electronic micrographs of CON-CM sample (a) before and (b) after the ethylbenzene dehydrogenation.

The ethylbenzene conversions as a function of time reaction are shown in Fig. 5. The values for the activated carbon (PAC sample) and the oxidized activated supported carbon (CON) were similar and around 12 %. On the other hand, the copper containing sample (CON-C) showed values quite different, around 68% in the beginning of reaction and around 60% after 90 min of reaction. The addition of magnesium led to a decrease of conversion which reached values of around 18% at the end of reaction. The treatment of this catalyst with a sodium hydroxide solution caused a large increase of the conversion in the beginning, but the catalysts strongly deactivated during reaction, reaching values of around 20 min after 240 min of reaction.

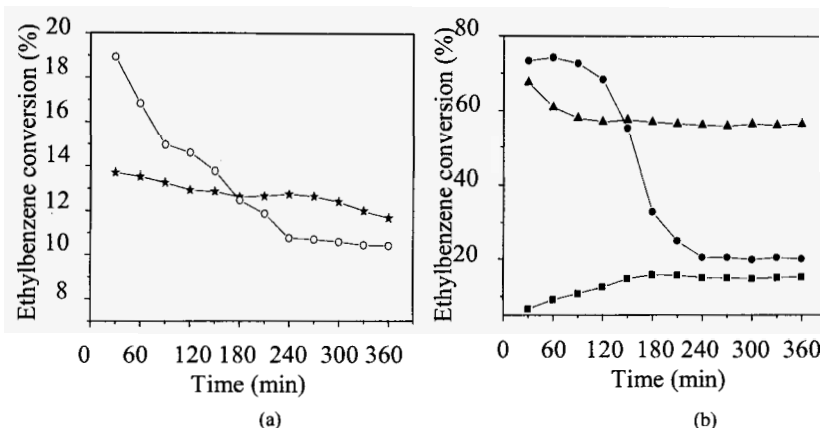


Figure 5. Ethylbenzene conversion as function of reaction time. (a) PAC (ξ) and CON samples (—); (b) CON-C (\blacktriangle), CON-CM (\blacktriangleleft) and CON-CMN (\bullet) samples.

Both the activated carbon (PAC) and the oxidized activated supported carbon (CON) showed selectivities to styrene decreasing with time reaction (Fig. 6), a fact which can be related to the transformations of surface groups during reaction, producing less selective ones. The magnesium and copper containing catalyst showed a similar behavior but the deactivation was slighter, indicating that the metals were able to stabilize the surface groups, which are selective to styrene. On the other hand, the copper containing catalyst did not show any drop in selectivity, which remained in low values since the beginning of reaction. The treatment with the sodium hydroxide solution (CON-CMN) caused a large increase of selectivity during reaction, as we can see in Fig. 6. This can be related to the neutralization of residual functional groups, transforming the carboxylic groups (highly active to ethylbenzene dehydrogenation but poorly selective to styrene) to anhydrides and lactones groups, less active but highly selective to styrene [17]. This also explained the drop in the conversion during the reaction on this catalysts, as shown in Fig. 5.

4. Conclusions

The polymeric activated carbon, obtained from styrene-divinylbenzene copolymer, is a promising catalyst for catalyzing the ethylbenzene dehydrogenation with carbon dioxide, to produce styrene. Its activity and selectivity are attributed to acidic functional groups (carboxylic acids, anhydrides and lactones) on the carbon surface. Copper can be adsorbed on the oxidized activated carbon, increasing the activity and the selective and also the

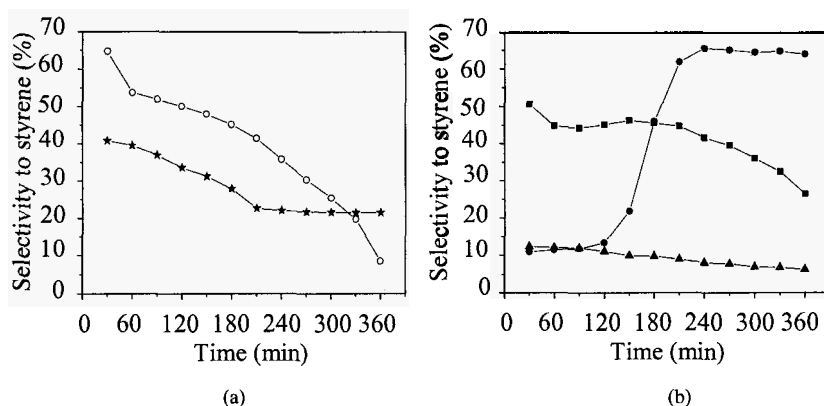


Figure 6. Selectivity to styrene of the catalysts as a function of reaction time (a) PAC (ξ) and CON samples (–); (b) CON-C (\blacktriangle); CON-CM (\diamond); and CON-CMN samples (\circ).

stability of the catalyst during reaction. The addition of magnesium decreased the activity, but increased the selectivity. This can be assigned to the neutralization of the functional groups, transforming the carboxylic groups (highly active to ethylbenzene dehydrogenation but poorly selective to styrene) to anhydrides and lactones groups, less active but highly selective to styrene. The treatment of this catalyst with a sodium hydroxide solution increased this effect even more and less active and more selective catalyst can be obtained.

Acknowledgments

The authors thank the CNPq, FINEP for the financial support and the Dr. Nester Escalon (Facultad de Chemical Cadencies, Universidad de Concepción, Chile) for the TPD spectra.

References

1. M. Sugino; H. Shimada; T. Turuda; H. Miura; N. Ikenaga; T. Suzuki. *Appl. Catal.* 121, **125** (1995).
2. J. L. Figueiredo, M.F.R. Pereira, M.M.A. Freitas and J.J.M. Órfão; *Carbon* **37**, 1379 (1999).
3. Y. Ohishi, T. Kawabata, T. Shishido, K. Takaki, Q. Zhang, Y. Wang, K. Nomura and K. Takehira. *Appl.Catal. A: Gen.* **288**, 220 (2005).
4. E. H. Lee, *Catal. Rev.* **8**, 285 (1963).
5. Y. Sakurai, T. Suzaki, K. Nakagawa. N. Ikenaga, H. Aota and T. Suzuki. *J. Catal.* **209**, 16 (2002).
6. G. C. Grunewald and R. S. Drago, *J. Molec. Catal.* **58**, 227 (1990).

7. R. A. Guerrero and R. I. Rodríguez, *Carbon* **32**, 23 (1994).
8. B. Li, Y. Ren, Q. Fan, A. Feng and W. Dong, *Carbon* **42**, 2669 (2004).
9. S.R. Tennison, *Appl. Catal. A: Gen.* **173**, 289 (1998).
10. A. Gierak, *Mater. Chem. Phys.* **41**, 28 (1995).
11. M. Kocírk, J. Brych and J. Hradil, *Carbon* **39**, 1919 (2001).
12. K. László, A. Bota and I. Dékány, *Carbon* **41**, 1205 (2003).
13. M. A. Fraga, E. Jordão, M.J. Mendes, M.M.A. Freitas, J.L. Faria and J.L. Figueiredo, *J. Catal.* **209**, 355 (2002).
14. H. P. Bohem, *Carbon* **32**, 759 (1994).
15. S.B. Oliveira, D.P. Barbosa, A.P.M. Monteiro, D. Rabelo and M.C. Rangel; *Catal. Today* (2007) (*in press*).
16. C. Subrahmanyam, A. B. Dmitri and L. K. Minsker. *Appl. Catal. B: Environm.* **61**, 98 (2005).
17. G. Puente, J. J. Pis, J. A. Menéndez and P. Grange. *J. Anal. App. Pyrolysis*, **43**, 125 (1997).

IRON OXIDE MAGNETIC NANOPARTICLES CONFINED IN MESOPOROUS SILICA AND CARBON MATERIALS

SHER ALAM, SUJIT K. MONDAL, JONATHAN P. HILL, AND AJAYAN VINU*

WPI Center for Materials Nanoarchitectonics, National Institute for Materials Science, 1-1, Namiki, Tsukuba, 305-0044, Japan, Email: vinu.ajayan@nims.go.jp

Here we demonstrate the fabrication of magnetic iron oxide nanoparticles in SBA-15, hexagonally ordered mesoporous carbon (CMK-3) [15], and carbon nanocage [16] and their unusual magnetic properties. The effect of the nature, structure, and the textural parameters of the mesoporous supports on the magnetic properties has been clearly demonstrated. It has been found that the interaction between the iron oxide nanoparticles, nature of the mesoporous supports, and the size of the nanoparticles play a critical role in controlling their magnetic properties. Among the mesoporous supports studied, carbon nanocage is found to be superior over both CMK-3 and SBA-15. Typical saturation magnetization for magnetic nanoparticles confined to CNC, CMK-3, and SBA-15 are 25, 20, and 8.2 emu/g respectively.

1. Introduction

The fabrication of metal and metal oxide nanoparticles has received considerable attention in the recent years because of their potential application in many areas including adsorption, catalysis, sensors, and nanotechnologies. [1-5]. However, the preparation of nanoparticles with a very small size has never been easy because of their large surface area which enhances the aggregation or coalescence of the individual particles. These problems can be overcome by fabricating the nanoparticles on the solid support, which is highly critical for obtaining stable nanoparticles. Consequently, researchers tried to use the porous materials with very high surface area and large pore diameter as the supports for obtaining the composite materials encapsulated with the nanoparticles, which inhibit the agglomeration and enhance the stability of the metal and metal oxide nanoparticles [1-6]. This is highly essential for preserving the excellent properties of the nanoparticles. Among the nanoparticles, iron oxide nanoparticles with small size are very interesting [1-5] because of their special catalytic and magnetic properties, and promising applications in several fields such as sensors, catalysis, and biomedicine [1-7].

Mesoporous materials have received a significant attention because of their promising applications in many fields such as catalysis, selective adsorption,

sensors, and nanotechnologies owing to their excellent textural parameters such as huge surface area, large pore volume, large pore diameter, and interesting morphologies and topologies [8-13]. Among the mesoporous materials, mesoporous carbon with nanoscale pore sizes are very useful materials, due to their versatility, adaptability, and chemical inert nature and potential applications such as size and shape-selective adsorption media, chromatography separation systems, catalysts, nanoreactors, battery electrodes, capacitors, energy storage devices, and biomedical devices [8-13]. Very recently, Vinu et al. have reported the preparation of well-ordered cage type mesoporous carbon materials, carbon nanocages, which exhibit very high surface area, pore volume, and tunable pore diameters, and are found to be excellent adsorbents for proteins, dyes, and tea components, such as catechin and tannic acid [14-18]. These excellent properties make them available as the support for the fabrication of nanoparticles. There have been several reports on the fabrication of iron oxide nanoparticles inside the pore channels of one and three dimensional mesoporous materials [19-20]. However, the reports on the fabrication of iron oxide nanoparticles inside the carbon nanocage materials and their magnetic properties have not been reported in the open literature so far. Moreover, the magnetic properties of the iron oxide nanoparticles in mesoporous silica such as SBA-15 [21], MCM-41, and hexagonally ordered mesoporous carbon materials [22] have been scarcely reported.

Here we demonstrate the fabrication of magnetic iron oxide nanoparticles in SBA-15, hexagonally ordered mesoporous carbon (CMK-3) [22], and carbon nanocage [14-18] and their unusual magnetic properties. The effect of the nature, structure, and the textural parameters of the mesoporous supports on the magnetic properties has been clearly demonstrated. It has been found that the interaction between the iron oxide nanoparticles, nature of the mesoporous supports, and the size of the nanoparticles play a critical role in controlling their magnetic properties.

2. Experimental Section

2.1 Preparation of Iron Oxide Nanoparticles over Mesoporous Supports

The procedure to prepare the mesoporous supports employed in the manuscript, such as SBA-15, CMK-3, and carbon nanocage can be found elsewhere [14-18,21,22]. The preparation of iron oxide nanoparticles in mesoporous supports was prepared by wet impregnation method and the procedure is as follows: 1.07 ml of 0.5 M solution of $\text{Fe}(\text{NO}_3)_3 \cdot 9 \text{H}_2\text{O}$ in ethanol

was mixed with the – 100 mg of required template materials in 10 ml of ethanol solution. The resultant mixture was stirred at room temperature for 24 hours. Subsequently, the ethanol was evaporated by raising the temperature of the hot plate to 80 °C under stirring. The iron oxide-mesoporous nanocomposites were obtained by oxidizing the above resultant mixture in the presence of controlled oxygen flow at 300 °C for 4 hours. The samples were denoted as 30%Fe₂O₃-x where x denotes the name of the template.

0.5 M solution of Fe (NO₃)₃ 9 H₂O in ethanol was prepared. This solution was mixed with the required template materials [such as SBA-15, CMK-3, or CNC] in 10 ml of ethanol solution. The resultant mixture was stirred for 24 hours at room temperature. Subsequently the ethanol was evaporated using a hot plate. The residue is oxidized at 300°C for 4 hours in the presence of controlled oxygen flow.

2.2. Characterization of the Materials

Powder X-ray diffraction patterns were collected on a Rigaku diffractometer using CuK α ($\lambda = 0.15406$ nm) radiation, operated at 40 kV and 40 mA. The diffractograms were recorded in the 2θ range of 0.7 to 80 ° with a 2θ step size of 0.01 ° and a step time of 1 second. The HRTEM images were obtained with TEM JEOL JEM-2000EX2. The preparation of samples for HRTEM analysis involved sonication in ethanol for 5 min and deposition on a copper grid. The samples were imaged at an accelerating voltage of 200 kV. The dc magnetization measurements were performed with a SQUID magnetometer (MPMSXL, Quantum Design). Zero-field cooling (ZFC) measurements were carried out in the following way: first at zero field cooling down temperature from 300 to 7K, then applying a fields of 100, 500, 1000, 5000 and 10000 Oe, and finally measuring the sample from 7 to 300 K in the fields. Field cooling (FC) measurements were performed immediately after ZFC measurement from 300 to 7K under the said fields. The Hysteresis measurements were conducted at 5, 15, and 25 K between -5 and 5 T and also under the influence of smaller Magnetic Field of ± 2.5 T.

3. Results and Discussion

The lower angle powder XRD diffraction patterns of 30%Fe₂O₃-CMK-3 and 30%Fe₂O₃-SBA-15 in comparison to their parent materials are shown in Figures 1A and 1B, respectively. The wide angle XRD patterns for the above samples are shown in the Figure 1 (inset). As can be seen in Figure 1, the lower angle XRD pattern of SBA-15 and CMK-3 show a sharp peak with several higher

order peaks, which can be indexed to (100), (110) and (200) reflections of the hexagonal space group $p6mm$. This is indicative of hexagonally ordered pore structure.

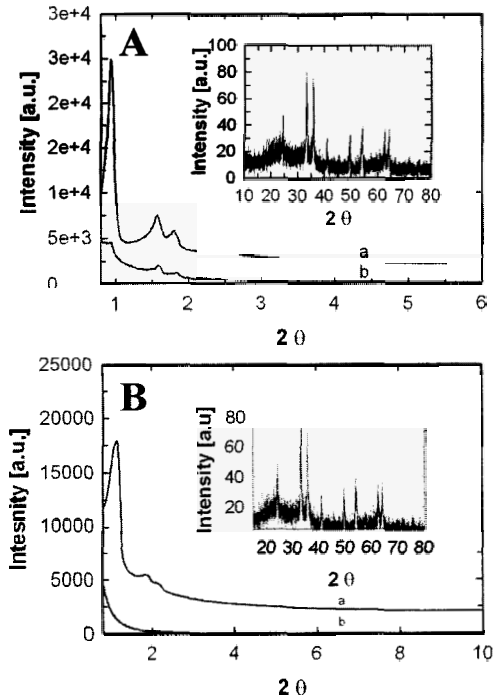


Figure 1: Powder XRD patterns of (A) pure SBA-15 (a) and 30wt%Fe₂O₃-SBA-15 (b) and (B) pure CMK-3 (a) and 30wt%Fe₂O₃-CMK-3 (b). Insets show (A) wide angle XRD patterns of 30wt%Fe₂O₃-SBA-15 and (B) 30wt%Fe₂O₃-CMK-3.

However, intensity of the peak at the lower angle is significantly decreased after the iron oxide immobilization for 30%Fe₂O₃-SBA-15. The large difference in the intensity of the (100) peaks before and after the iron oxide immobilization may not be interpreted as complete damage to the structural order, but it is likely that larger contrast in density between the silica walls and the open pores relative to that between the silica walls and iron oxide particles. On the other hand, the lower angle peak is completely diminished for 30wt%Fe₂O₃-CMK-3 which is attributed to the complete filling of the iron oxide nanoparticles inside the mesoporous channels because the pore diameter of the later is smaller as compared to that of the SBA-15. Interestingly, the wide angle XRD patterns of

both the 30wt%Fe₂O₃-CMK-3 and 30wt%Fe₂O₃-SBA-15 show several higher angle peaks which are quite similar to that of pure iron oxide nanoparticles, confirming that the iron oxide nanoparticles are indeed formed inside the mesoporous channels of the supports.

Figure 2 shows the representative HRTEM micrograph of 30wt%Fe₂O₃-SBA-15 taken with JEOL 200 kV machine. It can be clearly seen from the picture the presence of iron oxide particles with diameters in the range 1-7nm. The sample shows a linear array of pores with the regular intervals, confirming that the structure order of the mesoporous support is retained even after the immobilization of higher amount of iron oxide nanoparticles.

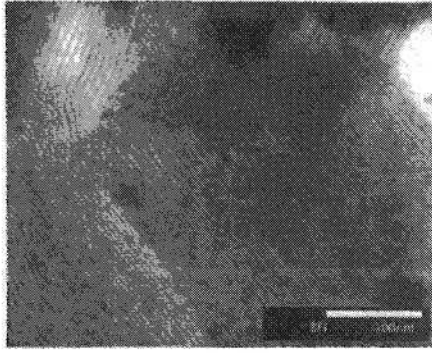


Figure 2: The TEM image of 30wt%Fe₂O₃-SBA-15

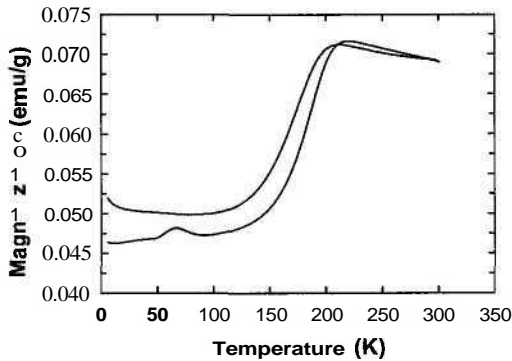


Figure 3: The ZFC/FC magnetization curves for pure iron-oxide nanoparticles, the applied field is 1000 Oe.

It is also instructive and useful to see the explicit effect of the mesoporous matrix, on the magnetic properties of the iron-oxide nanoparticles. To this end we have measured the zero field cool/field cool (ZFC/FC) for the pure iron-

oxide particles, and results are displayed in Figure 3. The results are taken under an applied field of 1000 Oe. This result provides a useful reference and as an aid in understanding the effect of silica or carbon mesoporous matrix on the magnetic properties of iron-oxide particles.

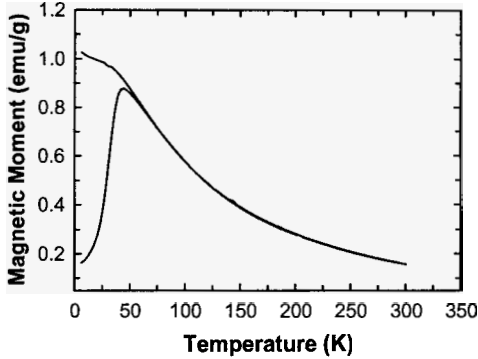


Figure 4: Example of ZFC/FC data, for SBA-15(100). The field is 1000 Oe, The Fe content is 30% by weight and the pore diameter is 9 nm.

Figure 4 illustrates the ZFC/FC behavior of the iron-oxide nano-particles confined in the SBA-15 prepared at 100 °C. It can be clearly seen from Figures 3 and 4 that the magnetization has been enhanced by an order of magnitude by confining iron-oxide nanoparticles in SBA-15(100). Moreover the blocking temperature is 50 K for silica confined nanoparticles which implies a size of roughly 3.5 nm, using Eq. 1 below.

The blocking temperature [T_B] is related to the particle size by the simple relationship [23]:

$$T_B = \frac{KV}{25k_B} \quad (1)$$

Here K is the anisotropy constant $1.2 \times 10^6 \text{ erg/cm}^3$, and k_B Boltzmann constant, $1.38 \times 10^{-16} \text{ erg/K}$. This relationship can also be used to estimate the radius of the nanoparticle [r], assuming for simplicity a spherical shape for the particles. Next we consider the magnetization versus temperature results for CMK-3(100) matrix confining 30% by weight of iron nanoparticles, for the case when oxygen flow is low. The results are displayed in Figure 5.

Figure 5 shows that the iron-oxide particles yield significantly higher magnetization as compared to that of pure iron oxide nanoparticles [Figure 3], and about the same order of magnitude as that of silica SBA-15 [Figure 4].

When the oxygen content is increased there is dramatic increase in magnetization as is vividly demonstrated in Figure 6.

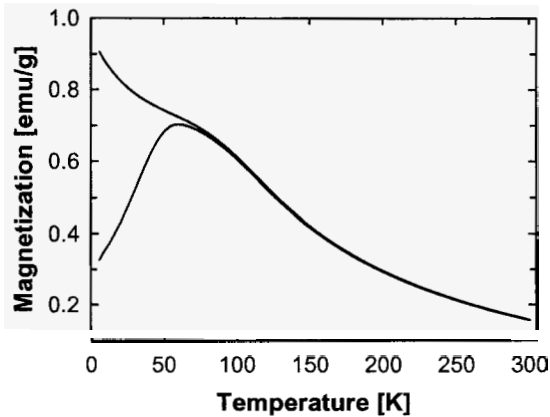


Figure 5: Example of ZFC/FC data, for 30%Fe₂O₃-CMK-3. The field is 1000 Oe, and the pore diameter is 4 nm. This case is for low oxygen content.

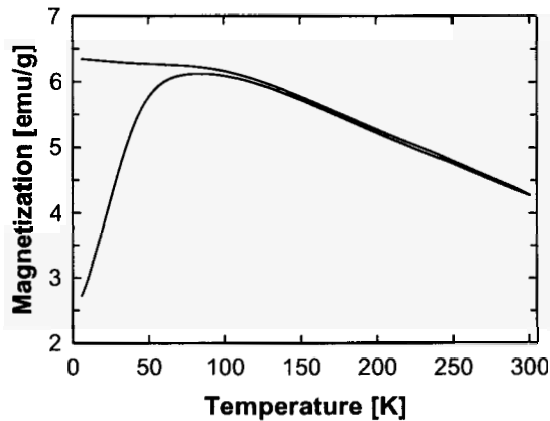


Figure 6: Example of ZFC/FC data, for 30%Fe₂O₃-CMK-3. The field is 1000 Oe and the pore diameter is 4nm. This case is for optimal oxygen content.

The magnetization jumps by an order of magnitude compared to the case when the oxygen content is low [Figure 5], and also for the case of silica [Figure 4]. Compared to the pure case the increase is two orders of magnitude. The blocking temperature is roughly 75K, and the width of the ZFC curve is rather broad [Figure 6].

To study the effect of the structure of carbon supports, the nanoparticles were encapsulated over CNC, which possesses three dimensional cage type structure with very high surface area and large pore volume. Figure 7 shows the ZFC/FC data of 30%Fe₂O₃-CNC measured at 1000 Oe. It is interesting to note that the 30%Fe₂O₃-CNC registered much higher magnetization than that of the other supports employed in this study. Moreover, the sample also registers the highest blocking temperature among the supports studied which is around 100 K, and the width of ZFC is also extremely broad.

It is worthwhile to note that the FC part of the curve, for both 30%Fe₂O₃-SBA-15, Figure 4, and 30%Fe₂O₃-CMK-3 with low oxygen content, Figure 5, rise sharply compared to that of 30%Fe₂O₃-CMK-3 prepared with high flow oxygen and 30%Fe₂O₃-CNC (Figures 6 and 7 respectively), as low temperature region is approached. In the later case it levels out. This further confirms that the overall magnetization is lower in the previous case as compared to that of the later.

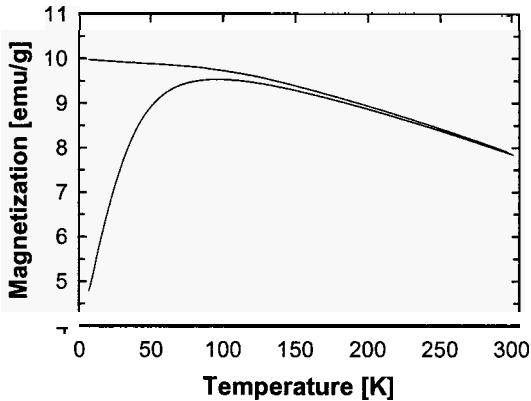


Figure 7: Illustrative example of ZFC and FC data, for 30%Fe₂O₃-CNC, the field is 1000 Oe, and pore diameter is 5.2 nm.

The irreversibility temperature in [where the ZFC and FC curves split] in Figures 6, and 7 is much larger than those in Figures 4 and 5, as expected. We have also measured in detail the hysteresis, but results will be reported elsewhere. These measurements yield the values of saturation magnetization in the range 8.2-25 emu/g, for the 30% of Fe by weight samples.

In order to put our results in perspective, and facilitate comparison with some results reported in the literature [2], and choose to concentrate on our SBA-15 sample, Figure. 4. It should be noted that our magnetization in emu/g, is

greater by more than an order of magnitude [> 100 in most of the temperature range and by factor of 10 at room temperature] than those reported in the literature [2], after correcting for Magnetic Field, i.e. since we have given here the results for 1000 Oe, whereas those in reported in [Ref. 2] are for 500 Oe, we must divide our results by a factor of roughly 2. This could be mainly due to the fact that the size of the iron oxide particles which are grown inside the nanochannels of SBA-15 porous matrix is very small and is almost close the pore diameter of the SBA-15 template. This clearly demonstrates that SBA-15 is highly effective in increasing the magnetization of the iron-oxide nanoparticles. Moreover it is also very encouraging to note that, the size of nanoparticles in our case follows a very narrow distribution. The size distribution fits in a tight range of 3.14-3.54 nm, according to our Magnetic Measurements. This is in sharp contrast to the size distribution of 5-8 nm by pipette drop method, and 3-5 nm for the piezoelectric nozzle method [2]. Thus we can conclude for the first time that SBA-15 can act as a nano-factory for making small magnetic iron-oxide nanoparticles with good magnetization and a very narrow size distribution.

4. Conclusions

We have reported on the magnetic properties of nanoparticles confined in silica and carbon mesoporous matrices, restricting our discussion to one example each, SBA-15 and CMK-3, for silica and carbon cases respectively. The geometry for the considered cases is 2D-hexagonal with space-group $p6mm$. It has been found that the magnetization of super-paramagnetic particles strongly depends on the oxygen treatment. In general, and remarkably it is found that the magnetization of iron-oxide nanoparticles embedded in mesoporous silica is much lower as compared to that of the corresponding mesoporous carbon materials, however the silica templates leads to particles with narrower size distribution. We have achieved large values of magnetization, for example, typical saturation magnetization for magnetic nanoparticles confined to 30% Fe_2O_3 -CNC, 30% Fe_2O_3 -CMK-3, and 30% Fe_2O_3 -SBA-15 are 25, 20, and 8.2 emu/g, respectively. In summary, we demonstrated for the first time the fabrication of super-paramagnetic iron oxide nanoparticles in mesoporous matrix using a simple technique, which are known to have favorable properties such as low cost, low toxicity, and chemical stability.

References

1. R.D. Zysler, D. Fiorani and A.M. Testa, *J. Magn. Magn. Mater.* **224**, 5 (2001).

2. J.-R. Jeong, S.-J. Lee, J.-D. Kim and S.-C. Shin *Phys. Stat. Sol(b)* **241**, 1593 (2004).
3. D.K. Yi, S.T. Selvan, S.S. Lee, G.C. Papaefthymiou, D. Kundaliya and J.Y. Ying, *J. Am. Chem. Soc.* **127**, 4990 (2005).
4. V. Salgueirino-Maceira, M.A. Correa-Duarte, M. Spasova, L.M. Liz-Marzan and M. Farle *Adv. Funct. Mater.* **16**, 509 (2006).
5. K. Simeonidis, S. Mourdikoudis, M. Moulla, C. Martinez-Boubeta, M. Angelkeris, C. Dendrinou-Samara and O. Kalogirou, *J. Magn. Magn. Mater.* **316**, e1-e4 (2007).
6. D. L. Huber, *Small* **1**, 482 (2005).
7. Q. A. Pankurst, J Connolly, S K Jones and J Dobson, *J. Phys. D: Appl. Phys.* **36**, R167 (2007).
8. R. Ryoo, S. H. Joo and S. Jun, *J. Phys. Chem. B* **103**, 7743 (1999).
9. S. H. Joo, S.J. Choi, I. Oh, J. Kwak, Z. Liu and R. Ryoo, *Nature* **412**, 169 (2001).
10. A. Vinu, V. Murugesan and M. Hartmann, *J. Phys. Chem. B* **108**, 7323 (2003).
11. K. Lu and D. D. D. L. Chung, *Carbon* **37**, 427 (1997).
12. M. Kawaguchi, S. Yagi and H. Enomoto, *Carbon* **42**, 345 (2004).
13. Y. Qiu and L. Gao, *Chem. Commun.*, 2378 (2003).
14. A. Vinu, M. Miyahara, V. Sivamurugan, T. Mori and K. Ariga, *J. Mater. Chem.* **15**, 5122 (2005).
15. A. Vinu, M. Miyahara, T. Mori and K. Ariga, *J. Porous. Mater.* **13**, 379 (2006).
16. K. Ariga, A. Vinu, M. Miyahara, J. Hill and T. Mori, *J. Am. Chem. Soc.* **129**, 11022 (2007).
17. A. Vinu, M. Miyahara and K. Ariga, *J. Nanosci. Nanotechnol.* **6**, 1510 (2006).
18. P. Srinivasu, V. V. Balasubramanian, L. Kumaresan, D. P. Sawant, X. Jin, S. Alam, K. Ariga, T. Mori and A. Vinu, *J. Nanosci. Nanotechnol.* **7**, 3250 (2007).
19. H. Huwe and M. Froba, *Carbon* **45**, 304, (2007).
20. N. A. Fellenz, S. G. Marchetti, J.F. Bengoa, R. C. Mercader and S. J. Stewart, *J. Magn. Magn. Mater.* **306**, 30-34 (2007).
21. A. Vinu and M. Hartmann, *Langmuir* **18**, 8010 (2002).
22. A. Vinu, C. Streb, V. Murugesan and M. Hartmann, *J. Phys. Chem. B* **107**, 8297 (2003).
23. B. D. Cullity, *Introduction to Magnetic Materials*, pp. 410-418, (Addison-Wesley, Reading MA, 1972).

FUNCTIONALIZED MESOPOROUS MATERIALS FOR GOLD CATALYSIS

ZHEN MA, HAOGUO ZHU, WENFU YAN, STEVEN H. OVERBURY, SHENG DAI*

*Chemical Sciences Division, Oak Ridge National Laboratory
Oak Ridge, Tennessee 37831, USA*

Recent activities of our group in synthesizing functionalized mesoporous materials for gold catalysis are briefly reviewed. These activities include the synthesis of Au/mesoporous SiO₂, Au/TiO₂/mesoporous SiO₂, Au/mesoporous TiO₂-SiO₂, and Au/MnO_x/mesoporous carbon *via* one-pot co-synthesis, surface-sol-gel coating, and electroless deposition, etc. The assembly of gold nanoparticles in the channels of mesoporous materials furnishes new possibilities for chemical catalysis.

1. Introduction

Mesoporous materials are an important family of materials containing pores with diameters between 2 and 50 nm. Since the invention of mesoporous SiO₂ (e.g., MCM-41 and SBA-15) in the 1990s [1,2], a great deal of attention has been paid to the functionalization of these materials for specific applications such as catalysis, sorption, gas sensing, and optics [3,4]. In catalysis, mesoporous materials can be used as hosts for the preparation of supported metal and metal oxide catalysts and anchored metal complexes [5,6]. Pure and substituted mesoporous materials may also exhibit catalytic activities for acid-base catalysis and redox reactions.

Since Haruta and coworkers found in the late 1980s that supported gold nanoparticles are very active for CO oxidation below room temperature [7,8], catalysis by gold nanoparticles has attracted much attention [9-11]. Because the nanometer sizes of gold particles are essential for achieving high activity in typical reactions, it is expected that mesoporous materials could provide ideal hosts for assembling these gold nanoparticles and the mesopores can become nano-reactors for many chemical reactions. Unfortunately, it turns out that the synthesis of supported Au/mesoporous SiO₂ is not an easy task [12-20].

Our group has been interested in the rational design of novel supported gold catalysts from a synthetic point of view [21-34]. We have loaded gold nanoparticles onto various commercial or synthesized supports, often with complicated interfacial structures, and have tested their catalytic performance in

CO oxidation and other reactions. In the process we have learned how to create and stabilize gold nanoparticles on SiO_2 supports. In this contribution, we specifically summarize our recent effort in the synthesis of functionalized mesoporous materials for gold catalysis. We show that *via* proper materials synthesis techniques, gold nanoparticles can be assembled into the pore channels of mesoporous materials while keeping the mesostructures undestroyed. In addition, these mesostructured catalysts show excellent catalytic activities in CO oxidation, with other applications to be explored in the future.

2. Au/Mesoporous SiO_2 : Initial Attempts



Figure 1. Dark-field TEM image of aggregated large gold particles on mesoporous SiO_2 (SBA-15) [22]. The sample was prepared by deposition-precipitation of $\text{Au}(\text{OH})_x\text{Cl}_{4-x}^-$ directly on SBA-15. Reproduced with permission of the American Chemical Society from Supporting Information of W. F. Yan, B. Chen, S. M. Mahurin, E. W. Hagaman, S. Dai and S. H. Overbury, *J. Phys. Chem. B* 108, 2793 (2004).

SiO_2 is widely used as a support for making metal catalysts owing to its high surface area, thermal stability, mechanical strength, and non-reducibility, but the application of SiO_2 in synthesizing active gold catalysts is a challenge. Impregnation of SiO_2 with HAuCl_4 leads to big gold particles that are not very active for CO oxidation. The presence of chloride in the as-synthesized catalysts facilitates the sintering of gold particles upon calcination. Au/SiO_2 prepared by deposition-precipitation has low gold content because under basic conditions

used to hydrolyze HAuCl_4 to the negatively charged $\text{Au}(\text{OH})_4^-$, the SiO_2 surface is also negatively charged due to the low isoelectric point of SiO_2 (IEP ~ 2). Figure 1 shows a TEM image of Au/mesoporous SiO_2 (SBA-15) synthesized *via* deposition-precipitation method [22]. The population of gold particles is small, and these gold particles are too big to be catalytically active.

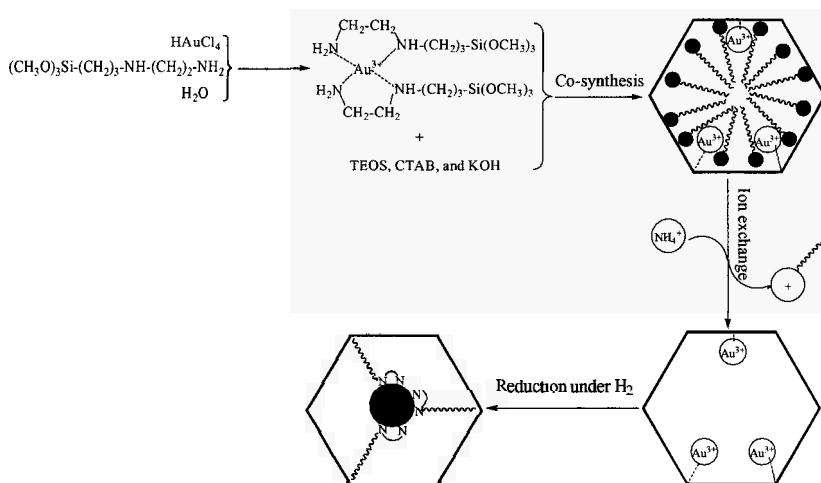


Figure 2. Schematic representation of the synthesis of Au/mesoporous SiO_2 *via* a one-pot co-synthesis approach and its subsequent treatment in H_2 to form reduced gold nanoparticles [21]. Reproduced with permission of the American Chemical Society from H. G. Zhu, B. Lee, S. Dai and S. H. Overbury, *Langmuir* **19**, 3974 (2003).

To get around the issues associated with impregnation and deposition-precipitation methods, we adopted an one-pot co-synthesis method to synthesize Au/mesoporous SiO_2 (Au/MCM-41) [21]. The key idea is to perform regular template-mediated synthesis of mesoporous SiO_2 in the presence of both Au^{3+} as the gold source and $(\text{CH}_3\text{O})_3\text{Si}(\text{CH}_2)_3\text{NH}(\text{CH}_2)_2\text{NH}_2$ as a bifunctional ligand to interact with Au^{3+} and SiO_2 matrix (Figure 2) [21]. The as-synthesized Au/mesoporous SiO_2 was ion-exchanged with NH_4Cl to remove template, and reduced in H_2 . Although small gold particles were confined in the pore channels (Figure 3), the Au/mesoporous SiO_2 synthesized that way was not particularly active for CO oxidation [35]. These examples show how tricky it is to prepare active Au/ SiO_2 catalysts.

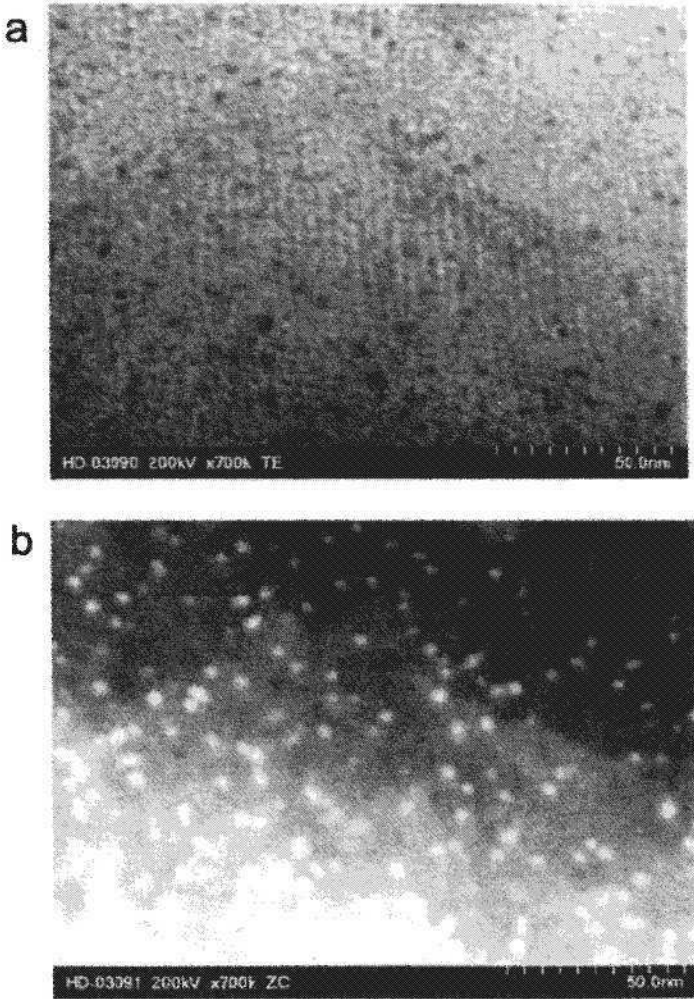


Figure 3. (a) Bright-field and (b) dark-field TEM images recorded on the same area for gold-containing mesoporous SiO₂ (Au/MCM-41) obtained by the removal of surfactants by ion-exchange reaction [21]. Reproduced with permission of the American Chemical Society from H. G. Zhu, B. Lee, S. Dai and S. H. Overbury, *Langmuir* **19**, 3974 (2003).

3. Au/TiO₂/Mesoporous SiO₂

As stated above, the failure of using deposition-precipitation method to synthesize active Au/SiO₂ is due to the low isoelectric point of SiO₂. Thus, one idea to circumvent this constraint is to introduce a metal oxide with a high isoelectric point onto the SiO₂ support. Some metal oxides have higher isoelectric points than SiO₂. They include TiO₂ (IEP ~ 6), CeO₂ (IEP ~ 6), Fe₂O₃ (IEP ~ 8), and Al₂O₃ (IEP ~ 9).

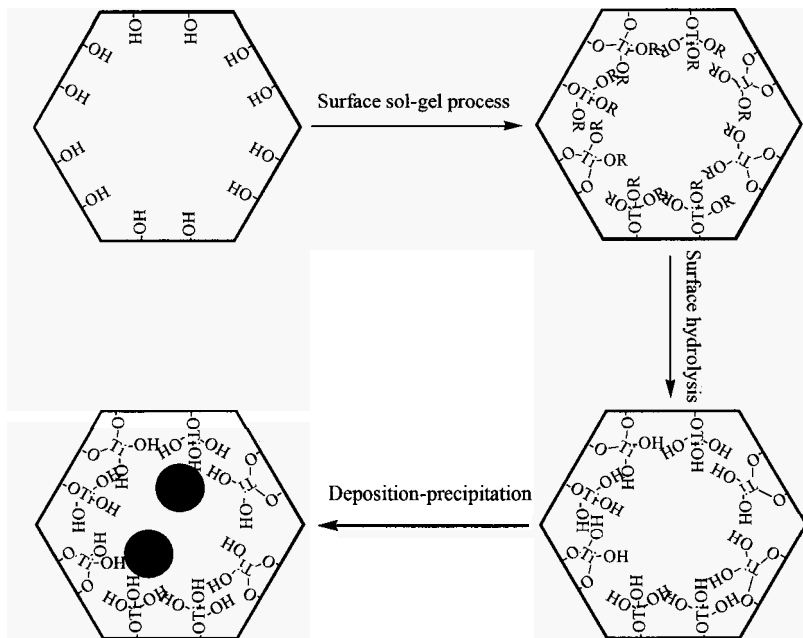


Figure 4. Schematic representation for the surface-sol-gel modification of mesoporous SiO₂ (SBA-15) by amorphous TiO₂ followed by loading gold nanoparticles [22]. Reproduced with permission of the American Chemical Society from W. F. Yan, B. Chen, S. M. Mahurin, E. W. Hagaman, S. Dai and S. H. Overbury, *J. Phys. Chem. B* **108**, 2793 (2004).

We communicated a surface-sol-gel method for modification of mesoporous SiO₂ (SBA-15) with amorphous TiO₂ for assembling gold nanoparticles (Figure 4) [22]. SBA-15 was used as a starting material because its large pore channels (~ 7.4 nm) can allow for the transport of Ti(OC₄H₉)₄ and for the confinement of small gold particles. To synthesize Au/TiO₂/mesoporous SiO₂, a pre-dried SBA-15 material was evacuated and purged with N₂, and Ti(OC₄H₉)₄ dissolved in

methanol and toluene was injected. After reaction, the organic solution was removed *via* vacuum filtration, and unreacted $\text{Ti}(\text{OC}_4\text{H}_9)_4$ was washed off by methanol. After drying the sample *via* vacuum evacuation, deionized water was injected to hydrolyze the anchored $\text{Ti}(\text{OC}_4\text{H}_9)_3$ groups to form amorphous TiO_2 . The resulting $\text{TiO}_2/\text{mesoporous SiO}_2$ support is suitable for loading gold because the presence of titania coating increases the isoelectric point of the support. The catalytic activity of $\text{Au}/\text{TiO}_2/\text{mesoporous SiO}_2$ in CO oxidation was much higher than that of $\text{Au}/\text{mesoporous SiO}_2$. The enhanced activity is not only due to the higher gold loading of $\text{Au}/\text{TiO}_2/\text{mesoporous SiO}_2$, but also due to the presence of active $\text{Au}-\text{TiO}_2$ interface. Similar grafting methods were used to synthesize $\text{Au}/\text{TiO}_2/\text{mesoporous SiO}_2$ ($\text{Au}/\text{MCM-48}$) [36] and $\text{Au}/\text{TiO}_2/\text{amorphous SiO}_2$ [26,37,38] catalysts active for CO oxidation.

4. Au/Mesoporous $\text{TiO}_2\text{-SiO}_2$

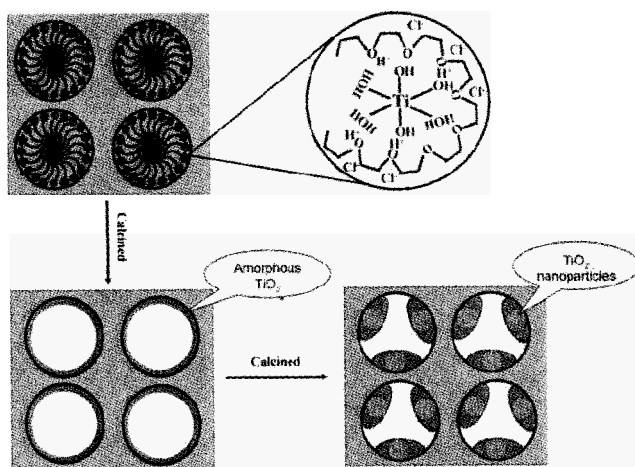


Figure 5. Schematic representation for the synthesis of mesoporous $\text{TiO}_2\text{-SiO}_2$ for assembling gold nanoparticles [23]. Reproduced with permission of the American Chemical Society from H. G. Zhu, Z. W. Pan, B. Chen, B. Lee, S. M. Mahurin, S. H. Overbury and S. Dai, *J. Phys. Chem. B* **108**, 20038 (2004).

As shown above, amorphous TiO_2 dispersed on mesoporous SiO_2 facilitates the uptake of gold and its dispersion. Therefore, in principle, mixed $\text{TiO}_2\text{-SiO}_2$ matrix should also have that effect. This idea was tested by synthesizing

mesoporous $\text{TiO}_2\text{-SiO}_2$ monolith with a large pore diameter using a block copolymer ($\text{EO}_{130}\text{PO}_{60}\text{EO}_{130}$) as the structure-directing agent (Figure 5) [23]. The titania source was titanium ethoxide, the silica source was tetraethyl orthosilicate, and acidic synthesis conditions were adopted. Gold was subsequently loaded onto mesoporous $\text{TiO}_2\text{-SiO}_2$ via deposition-precipitation.

As shown in Figure 6, gold nanoparticles with sizes less than 3 nm were homogeneously distributed on the support surfaces [23]. As a result, these gold catalysts showed high activities in CO oxidation below room temperature. Such mixed oxide mesoporous materials integrate the high thermal stability and excellent mechanical strength of SiO_2 and the active support properties of TiO_2 .

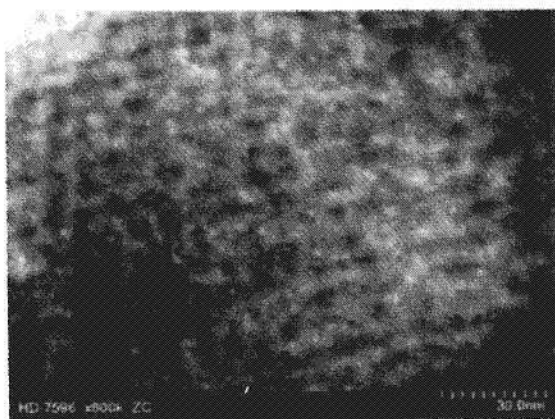


Figure 6. TEM image of gold supported on mesoporous $\text{TiO}_2\text{-SiO}_2$ ($\text{Si/Ti} = 5.5$) calcined at 600°C [23]. Reproduced with permission of the American Chemical Society from H. G. Zhu, Z. W. Pan, B. Chen, B. Lee, S. M. Mahurin, S. H. Overbury and S. Dai, *J. Phys. Chem. B* 108, 20038 (2004).

5. Au/Mesoporous SiO_2 Revisited

We have shown above that the introduction of certain metal oxides onto SiO_2 can make the resulting gold catalysts more active. We now turn to the question of whether one may deposit gold onto neat SiO_2 and obtain catalysts that are active for CO oxidation. Supports for loading gold are classified into two groups in the literature: TiO_2 and Fe_2O_3 are "active" supports because they are reducible and can active and store oxygen; on the other hand, Al_2O_3 and SiO_2 are "inert" supports because they do not supply reactive oxygen for CO oxidation [39].

Nevertheless, gold on "inert" supports can also be active for CO oxidation, as the case with Au/Al₂O₃ [40,41]. This active-inactive classification has been challenged since Okumura et al. reported that Au/SiO₂ prepared *via* gas-phase grafting of dimethyl gold acetylacetonate exhibited high activity in CO oxidation [42,43]. Other researchers have shown that the grafting of alkylammonium [16] or aminosilane [17] onto mesoporous SiO₂ could facilitate the interaction between the gold complex and the grafted SiO₂ surface, resulting in active catalysts. Alternatively, gold particles capped with alkanethiol and alkoxy silane groups could polymerize with tetraethyl orthosilicate to form a metal-organic-inorganic composite active for CO oxidation after calcination [44].

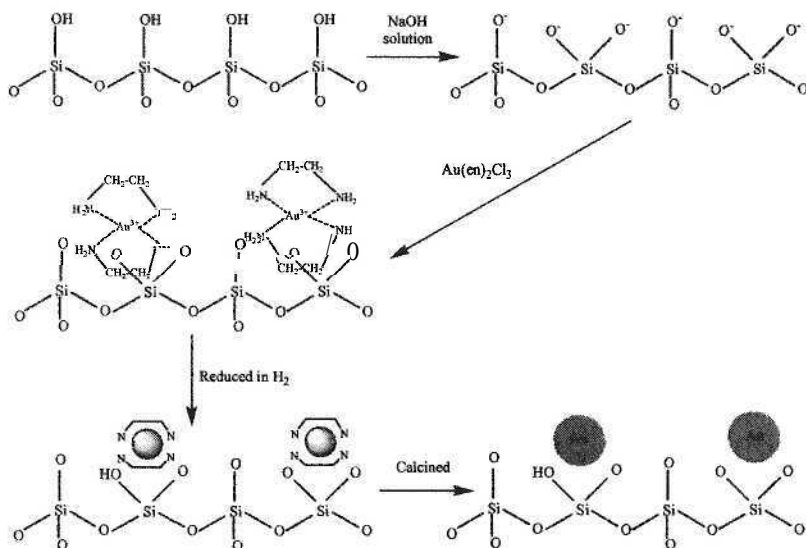


Figure 7. Schematic representation for the preparation of catalytically active Au/mesoporous SiO₂ using Au(en)₂Cl₃ as the gold precursor [30]. Reproduced with permission from H. G. Zhu, Z. Ma, J. C. Clark, Z. W. Pan, S. H. Overbury and S. Dai, *Appl. Catal. A* 327, 226 (2007).

We recently reported the preparation of highly active and stable Au/mesoporous SiO₂ (Au/SBA-15) using Au(en)₂Cl₃ (en = ethylenediamine) as the precursor (Figures 7 and 8) [29]. One of the key observations is that the catalytic activity of Au/SBA-15 was highly dependent on the pH value of deposition solutions: only Au/SiO₂ synthesized under pH > 8.0 was very active for CO oxidation below room temperature. UV-Vis was used to monitor Au(en)₂Cl₃ solutions with different pH value, and it was found that one hydrogen

from the Au(en)_2^{3+} cation was deprotonated above pH of 8.0. It was also found by elemental analysis that the gold loading increased with the solution pH value, whereas the Cl/Au ratio decreased with the solution pH value. These pieces of evidence led to the conclusions that: (1) the formation of $[\text{Au(en)(d-en)}]^{2+}$ is necessary for stable deposition; (2) the concentration of $[\text{Au(en)(d-en)}]^{2+}$ and surface Si-O^- groups both increased with pH, thus facilitating the loading of cationic gold; and (3) Cl^- in the gold precursor, detrimental to gold catalysis, could be further displaced by OH^- with the increase of pH. During the course of this research [29], we used another mesoporous SiO_2 (MCM-41), and found that $\text{Au}/\text{MCM-41}$ synthesized using $\text{Au(en)}_2\text{Cl}_3$ was also active for CO oxidation below room temperature (Figure 9).

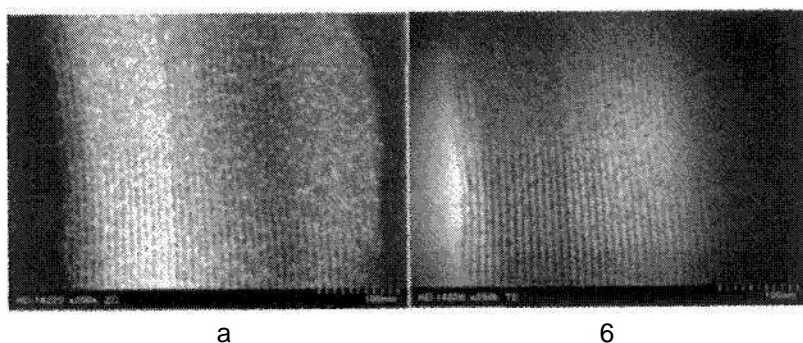


Figure 8. TEM images (a: dark field, and b: bright field) of $\text{Au}/\text{mesoporous SiO}_2$ (SBA-15) using $\text{Au(en)}_2\text{Cl}_3$ as the gold precursor [29]. The catalyst was synthesized at pH of 9.6 and reduced at 150°C . The particle size distribution is 2.9 ± 0.6 nm. Reproduced with permission of the American Chemical Society from H. G. Zhu, C. D. Liang, W. F. Yan, S. H. Overbury and S. Dai, *J. Phys. Chem. B* 110, 10842 (2006).

A similar deposition method was simultaneously developed by Zanella and coworkers to prepare gold particles supported on Aerosil fumed SiO_2 [45]. They systematically studied the influence of solution pH value and adsorption time on gold loading and gold particle size of the resulting Au/SiO_2 samples, but the catalytic activities of these Au/SiO_2 samples in CO oxidation were not investigated [45]. Subsequently we have loaded gold onto fumed SiO_2 (Cab-O-Sil) and have investigated the effects of the catalyst pretreatment *via* reduction and calcination, effect of gold loading, post treatment in acidic and basic media, catalyst deactivation, storage, regeneration, and effect of surface modification by other metal oxides [30]. These Au/SiO_2 catalysts showed excellent activity even after high-temperature pretreatment (e.g., $400\text{--}700^\circ\text{C}$).

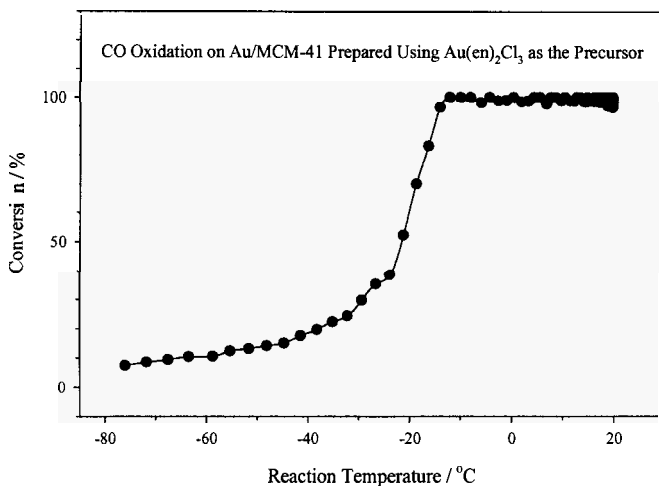


Figure 9. CO oxidation on Au/mesoporous SiO₂ (Au/MCM-41) synthesized using Au(en)₂Cl₃ as the precursor. The catalyst was reduced in 4% H₂ (balance Ar) at 150°C, and 50 mg catalyst was put in the reactor and pretreated in 8% O₂ (balance He) at 500°C for 1 h. The catalyst was cooled down by liquid nitrogen-acetone and allowed to warm up to measure the conversion curve. 1% CO (balance air) was flowed through the catalyst at a rate of 37 cm³/min.

6. Au/MnO_x/Mesoporous Carbon

Carbon materials are an important category of materials used as adsorbents, catalyst supports, and electrodes. Ordered mesoporous carbon can be prepared by filling in the pore channels of mesoporous SiO₂ with organic precursors, followed by carbonization and removal of SiO₂ *via* corrosion [46]. Alternatively, mesoporous carbon can also be synthesized by a soft-templating method using appropriate surfactants [47-49]. Nevertheless, virtually no attempt has been made to load gold onto mesoporous carbon because Au/C catalysts are generally not active for CO oxidation. There could be two reasons for the low activity of Au/C. First, reductive carbon surfaces can easily react with the gold precursor to form large gold particles [50]. Second, the carbon support is not able to activate oxygen for gas-phase CO oxidation [51].

Recently, a novel electroless deposition method to modify various carbon materials by MnO_x was reported in the literature [52,53]. The idea is to immerse a carbon material in an aqueous solution of KMnO₄ or NaMnO₄ to allow for the self-limiting reaction on carbon surface ($4 \text{ KMnO}_4 + 3 \text{ C} + 2 \text{ H}_2\text{O} \rightarrow 4 \text{ MnO}_2 +$

3 CO₂ + 4 KOH) [54]. This facile method results in a conformal coating of MnO_x on the topmost surface of carbon. One objective of the research in the literature is to develop high-performance MnO_x/C capacitors as energy-storage devices. Inspired by this materials synthesis technique, we deposited gold nanoparticles on several MnO_x/C supports by deposition-precipitation (Figure 10) [34], and found that Au/MnO_x/C catalysts, including Au/MnO_x/mesoporous carbon, were much more active than Au/C for CO oxidation, and the catalytic activities were fairly stable as a function of reaction time on stream (Figure 11). This catalyst system may open up new possibilities for subsequent electrochemical studies and catalytic studies, taking advantage of the electric conductivity of MnO_x/C and the catalytic functions of gold nanoparticles and MnO_x.



Figure 10. Schematic representation for the synthesis of Au/MnO_x/C catalysts, including Au/MnO_x/mesoporous carbon, active for CO oxidation [34]. The carbon surfaces were decorated by MnO_x via an electroless-deposition method, and gold nanoparticles were subsequently loaded onto MnO_x/C. Reproduced with permission of Elsevier from Z. Ma, C. D. Liang, S. H. Overbury and S. Dai, *J. Catal.* **252**, 119 (2007).

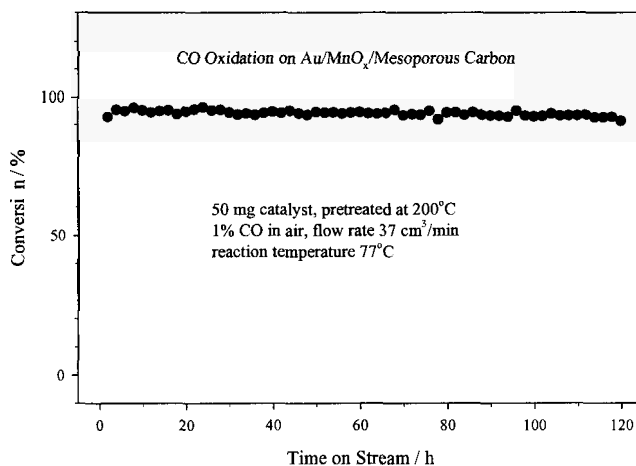


Figure 11. Stability of Au/MnO_x/mesoporous carbon in CO oxidation as a function of time on stream. The mesoporous carbon sample was synthesized by Dr. Chengdu Liang using a soft-templating approach and then graphitized [49]. It should be mentioned that gold on MnO_x-free mesoporous carbon is not active for CO oxidation under the same reaction conditions.

7. Conclusions

In this paper, we have summarized recent advances in our group on the synthesis of gold nanoparticles on mesoporous supports. These catalysts include: (1) Au/mesoporous SiO₂ prepared by a one-pot co-synthesis approach [21]; (2) Au/TiO₂/mesoporous SiO₂ prepared by deposition-precipitation of gold on TiO₂-coated mesoporous SiO₂ [22]; (3) Au/mesoporous TiO₂-SiO₂ prepared involving the control over the different hydrolysis and condensation rates of silicon and titanium alkoxides by complexation of the titanium species to the poly(ethylene oxide) part of a block copolymer; (4) Au/mesoporous SiO₂ prepared using Au(en)₂Cl₃ as the precursor; and (5) Au/MnO_x/mesoporous carbon synthesized by deposition-precipitation of gold on electroless-deposition-derived MnO_x/mesoporous carbon. These new materials show high activities in CO oxidation, and these approaches furnish possibilities for routes to new catalysts.

Acknowledgments

This work was supported by the Office of Basic Energy Sciences, U.S. Department of Energy. The Oak Ridge National Laboratory is managed by UT-Battelle, LLC for the U.S. DOE under Contract DE-AC05-00OR22725. Dr. Chengdu Liang provided mesoporous carbons used in Fig. 11.

References

1. J. S. Beck, J. C. Vartuli, W. J. Roth, M. E. Leonowicz, C. T. Kresge, K. D. Schmitt, C. T. W. Chu, D. H. Olson, E. W. Sheppard, S. B. Mccullen, J. B. Higgins and J. L. Schlenker, *J. Am. Chem. Soc.* **114**, 10834 (1992).
2. D. Y. Zhao, Q. S. Huo, J. L. Feng, B. F. Chmelka and G. D. Stucky, *J. Am. Chem. Soc.* **120**, 6024 (1998).
3. A. Corma, *Chem. Rev.* **97**, 2373 (1997).
4. J. Y. Ying, C. P. Mehnert and M. S. Wong, *Angew. Chem. Int. Ed.* **38**, 56 (1999).
5. D. T. On, D. Desplandier-Giscard, C. Danumah and S. Kaliaguine, *Appl. Catal. A* **253**, 543 (2003).
6. A. Taguchi and F. Schüth, *Micropor. Mesopor. Mater.* **77**, 1 (2005).
7. M. Haruta, T. Kobayashi, H. Sano and N. Yamada, *Chem. Lett.*, 405 (1987).
8. M. Haruta, N. Yamada, T. Kobayashi and S. Iijima, *J. Catal.* **115**, 301 (1989).
9. G. C. Bond and D. T. Thompson, *Catal. Rev.-Sci. Eng.* **41**, 319 (1999).
10. M. Haruta, *Cattech* **6**, 102 (2002).

11. A. S. K. Hashmi and G. J. Hutchings, *Angew. Chem. Int. Ed.* **45**, 7896 (2006).
12. M. Okumura, S. Tsubota, M. Iwamoto and M. Haruta, *Chem. Lett.*, 315 (1998).
13. H. P. Lin, Y. S. Chi, J. N. Lin, C. Y. Mou and B. Z. Wan, *Chem. Lett.*, 1116 (2001).
14. Y. Guari, C. Thieuleux, A. Mehdi, C. Reyé, R. J. P. Corriu, S. Gomez-Gallarado, K. Philippot, B. Chaudret and R. Dutartre, *Chem. Commun.*, 1374 (2001).
15. A. Ghosh, C. R. Patra, P. Mukherjee, M. Sastry and R. Kumar, *Micropor. Mesopor. Mater.* **58**, 201 (2003).
16. C.-M. Yang, M. Kalwei, F. Schüth and K.-J. Chao, *Appl. Catal. A* **254**, 289 (2003).
17. Y.-S. Chi, H.-P. Lin and C.-Y. Mou, *Appl. Catal. A* **284**, 199 (2005).
18. K. K. Zhu, J. C. Hu and R. Richards, *Catal. Lett.* **100**, 195 (2005).
19. C. Aprile, A. Abad, G. A. Hermenegildo and A. Corma, *J. Mater. Chem.* **15**, 4408 (2005).
20. M. T. Bore, H. N. Pham, E. E. Switzer, T. L. Ward, A. Fukuoka and A. K. Datye, *J. Phys. Chem. B* **109**, 2873 (2005).
21. H. G. Zhu, B. Lee, S. Dai and S. H. Overbury, *Langmuir* **19**, 3974 (2003).
22. W. F. Yan, B. Chen, S. M. Mahurin, E. W. Hagaman, S. Dai and S. H. Overbury, *J. Phys. Chem. B* **108**, 2793 (2004).
23. H. G. Zhu, Z. W. Pan, B. Chen, B. Lee, S. M. Mahurin, S. H. Overbury and S. Dai, *J. Phys. Chem. B* **108**, 20038 (2004).
24. W. F. Yan, V. Petkov, S. M. Mahurin, S. H. Overbury and S. Dai, *Catal. Commun.* **6**, 404 (2005).
25. W. F. Yan, S. M. Mahurin, Z. W. Pan, S. H. Overbury and S. Dai, *J. Am. Chem. Soc.* **127**, 10480 (2005).
26. W. F. Yan, S. M. Mahurin, B. Chen, S. H. Overbury and S. Dai, *J. Phys. Chem. B* **109**, 15489 (2005).
27. W. F. Yan, S. Brown, Z. W. Pan, S. M. Mahurin, S. H. Overbury and S. Dai, *Angew. Chem. Int. Ed.* **45**, 3614 (2006).
28. W. F. Yan, S. M. Mahurin, S. H. Overbury and S. Dai, *Top. Catal.* **39**, 199 (2006).
29. H. G. Zhu, C. D. Liang, W. F. Yan, S. H. Overbury and S. Dai, *J. Phys. Chem. B* **110**, 10842 (2006).
30. H. G. Zhu, Z. Ma, J. C. Clark, Z. W. Pan, S. H. Overbury and S. Dai, *Appl. Catal. A* **326**, 89 (2007).
31. H. G. Zhu, Z. Ma, S. H. Overbury and S. Dai, *Catal. Lett.* **116**, 128 (2007).
32. Z. Ma, S. H. Overbury and S. Dai, *J. Mol. Catal. A* **273**, 186 (2007).
33. Z. Ma, S. Brown, S. H. Overbury and S. Dai, *Appl. Catal. A* **327**, 226 (2007).

34. Z. Ma, C. D. Liang, S. H. Overbury and S. Dai, *J. Catal.* **252**, 119 (2007).
35. S. H. Overbury, L. Ortiz-Soto, H. G. Zhu, B. Lee, M. D. Amiridis and S. Dai, *Catal. Lett.* **95**, 99 (2004).
36. M. Bandyopadhyay, O. Korsak, M. W. E. van den Berg, W. Grunert, A. Birkner, W. Li, F. Schüth and H. Gies, *Micropor. Mesopor. Mater.* **89**, 158 (2006).
37. Y. Tai, J. Murakami, K. Tajiri, F. Ohashi, M. Daté and S. Tsubota, *Appl. Catal. A* **268**, 183 (2004).
38. A. M. Venezia, F. L. Liotta, G. Pantaleo, A. Beck, A. Horvath, O. Geszti, A. Kocsonya and L. Guzzi, *Appl. Catal. A* **310**, 114 (2006).
39. M. M. Schubert, S. Hackenberg, A. C. van Veen, M. Muhler, V. Plzak and R. J. Behm, *J. Catal.* **197**, 113 (2001).
40. S.-J. Lee and A. Gavriilidis, *J. Catal.* **206**, 305 (2002).
41. G. M. Veith, A. R. Lupini, S. J. Pennycook, G. W. Ownby and N. J. Dudney, *J. Catal.* **231**, 151 (2005).
42. M. Okumura, S. Nakamura, S. Tsubota, T. Nakamura, M. Azuma and M. Haruta, *Catal. Lett.* **51**, 53 (1998).
43. M. Okumura, S. Tsubota and M. Haruta, *J. Mol. Catal. A* **199**, 73 (2003).
44. G. Budroni and A. Corma, *Angew. Chem. Int. Ed.* **45**, 3328 (2006).
45. R. Zanella, A. Sandoval, P. Santiago, V. A. Basiuk and J. M. Saniger, *J. Phys. Chem. B* **110**, 8559 (2006).
46. R. Ryoo, S. H. Joo and S. Jun, *J. Phys. Chem. B* **103**, 7743 (1999).
47. C. D. Liang, K. L. Hong, G. A. Guiochon, J. W. Mays and S. Dai, *Angew. Chem. Int. Ed.* **43**, 5785 (2004).
48. Y. Meng, D. Gu, F. Q. Zhang, Y. F. Shi, H. F. Yang, Z. Li, C. Z. Yu, B. Tu and D. Y. Zhao, *Angew. Chem. Int. Ed.* **44**, 7053 (2005).
49. C. D. Liang and S. Dai, *J. Am. Chem. Soc.* **128**, 5316 (2006).
50. L. Prati and G. Martra, *Gold Bull.* **32**, 96 (1999).
51. W. C. Ketchie, M. Murayama and R. J. Davis, *Top. Catal.* **44**, 307 (2007).
52. H. Y. Lee, S. W. Kim and H. Y. Lee, *Electrochem. Solid St.* **4**, A19 (2001).
53. M. Q. Wu, G. A. Snook, G. Z. Chen and D. J. Fray, *Electrochem. Commun.* **6**, 499 (2004).
54. X. K. Huang, H. J. Yue, A. Attia and Y. Yang, *J. Electrochem. Soc.* **154**, A26 (2007).

ELECTRODEPOSITION OF GOLD STRUCTURES IN MESOPOROUS TiO₂ SOL-GEL FILMS

INGA BANNAT, KATRIN WESSELS, TORSTEN OEKERMANN, MICHAEL WARK

*Institute of Physical Chemistry and Electrochemistry, Leibniz University Hannover,
Callinstr. 3A, D-30167 Hannover, Germany*

A templated, electrochemical method for the growth of gold structures in mesoporous TiO₂ and SiO₂ films is reported. By applying constant potential spiky disc-like and spherical gold structures in the micrometer region form under or in the thin mesoporous films depending on different interactions between the film and the conductive FTO substrate. The growth of gold exclusively inside the mesopores can be achieved by pulsed electrodeposition. Gold nanowires as a replica of the pore system were formed.

1. Introduction

Titanium^{IV}dioxide (TiO₂) is one of the most popular and promising semiconductors with applications in solar cells [1], photocatalysis [2-3] and as catalyst support [4]. Because of their specific pore system mesoporous thin films of TiO₂ are among the best candidates as a host matrix for stabilizing small metal nanoparticles and nanostructured metal arrays. The resulting nanocomposite materials are of considerable interest due to their optical effects and their photocatalytic and catalytic activity.

Most attempts to enhance the e.g. optical and thus photocatalytic properties of TiO₂ include the modification with noble metals. In particular, gold nanoparticles have been attracting much attention in recent years because of their interesting adjustable optical [5], electrochemical [6], electronic [7] and photoelectrochemical [8] properties which are of great interest for use in catalysts, biosensors and other nanodevices [9]. To fabricate gold structures different procedures have been reported based on electrodeposition [10], electron-beam lithography [11] or nanotemplating [12].

In this paper, we demonstrate the templated electrochemical fabrication of disc-like and spherical gold structures and worm-like gold nanowires by using mesoporous TiO₂ and SiO₂ films as low-cost host materials. The obtained composite structures were characterized by transmission and scanning electron microscopy and studied as photocatalyst in the photooxidation of NO.

2. Experimental Section

2.1. Chemicals and Materials

Fluorine-doped tin oxide coated glass (FTO) with a sheet resistance of $10 \text{ } \Omega/\text{cm}^2$ was purchased from A.I. Glass. Chemical reagents such as titanium (IV) ethoxide ($\sim 95 \%$, Merck), tetraethylorthosilicate (TEOS, $> 98 \%$, Merck), ethanol (99.8 %, Roth), hydrochloric acid (HCl, $> 37 \text{ wt.}\%$, p.a., Riedel-de Haen), hydrogen tetrachloroaurate (III) hydrate ($\text{HAuCl}_4 \cdot x \text{ H}_2\text{O}$, 99.9 %, ABCR) and perchloric acid (HClO_4 , p.a., Acros) were obtained commercially and used as received without further purification. Pluronic P 123 ($\text{EO}_{20}\text{PO}_{70}\text{EO}_{20}$) and Pluronic F 127 ($\text{EO}_{100}\text{PO}_{65}\text{EO}_{100}$) were purchased from BASF and used as typical commercial nonionic templates. Solutions for electrochemistry were prepared using deionised water with a resistivity of greater than 18 MO cm .

2.2. Preparation of Mesoporous Oxide Thin Films

The preparation of thin mesoporous TiO_2 films by a surfactant-templating method using the triblock copolymer Pluronic P 123 as the template is reported elsewhere [13]. In a typical synthesis, 33.6 g titanium (IV) ethoxide were dissolved in 21.6 mL concentrated HCl under vigorous stirring. After 5 min, a solution of 8.0 g Pluronic P 123 in 96.0 g ethanol was added. The resulting sol was subsequently aged at $10 \text{ }^\circ\text{C}$ for 10 min and then used for dip-coating on FTO glass at a constant withdrawal rate of 1 mm s^{-1} . The films were aged for 15 h at $8 \text{ }^\circ\text{C}$.

Preparation of thin mesoporous SiO_2 films was carried out according to a procedure given in [14]. A solution of 16.3 g Pluronic F 127 in 25 mL ethanol was added to a solution of prehydrolyzed TEOS which was prepared by refluxing a solution of 11.18 mL TEOS, 33.3 mL ethanol, 2.2 mL H_2O and 5.0 mL 0.1 M HCl for 1 h. The two solutions were combined and stirred for further 2 h. The films were dip-coated on FTO glass with a withdrawal rate of 1 mm s^{-1} and dried at room temperature.

Both kinds of films were calcined at $400 \text{ }^\circ\text{C}$ for 4 h with a heating rate of $1 \text{ }^\circ\text{C min}^{-1}$.

2.3. Preparation of Au/mesoporous Oxide Thin Films

Gold was deposited from an Ar-saturated aqueous solution containing 70 μM HAuCl_4 and 10 mM HClO_4 in a three-electrode electrochemical cell with a Pt counter and **Ag/AgCl reference electrode** (-0.08 V vs. SCE). The mesostructured films on FTO glass served as **working electrode**. The deposition at constant potential was carried out at 0.3 V for typically 1 h.

For pulsed electrodeposition rectangular reverse pulses of the potential were used (Figure 1). One pulse consist of a potential alternating between -6.0 V hold for 3 s and 0.1 V hold for 1 s. For the deposition of gold 16 pulses were applied.

The obtained films were rinsed with water and dried in air

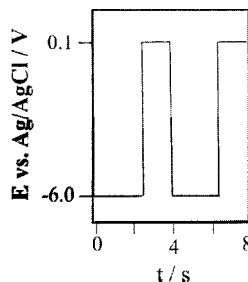


Figure 1: Schematic representation of the rectangular reverse pulses of the potential.

2.4. Instrumentations

Electrochemical deposition was carried out using a potentiostat/galvanostat (Autolab 12, Eco Chemie) with GPES software for collection and analysis of data for pulsed electrodeposition and AMEL instruments 7050 potentiostat for deposition at constant potential.

Scanning electron microscopy (SEM) was employed in a Jeol JSM-6700F field-emission instrument using the secondary electron detector at low acceleration voltages in the range of 0.5 to 2 kV.

Transmission electron microscopy (TEM) was performed at 200 kV on a Jeol JEM-2100F field-emission instrument with an ultra-high resolution pole piece and a spherical aberration constant of $C_s = 0.5$ mm that provides a point-resolution better than 0.19 nm. Moreover, the microscope was equipped with a Gatan GIF 2001 energy filter with a 1k-CCD camera. Specimens from films were prepared for TEM investigations by epoxy agglutination of two film pieces. Furthermore, these samples were first cut into $1.5 \times 1 \times 2$ mm³ pieces, ground and polished on polymer embedded diamond-lapping films to $0.01 \times 1 \times 2$ mm³, approximately. Finally, Ar^+ ion sputtering was employed at 3 kV under an incident angle of 4° until electron transparency was achieved.

The film thickness was measured by a Dektak 6M stylus profilometer. The texture properties of the mesoporous films were determined from Kr adsorption

isotherms carried out at 77 K using a Micromeritics APAS 2010 after outgasing the sample at 150 °C over night.

Photocatalytic oxidation of NO was carried out in an experimental set-up consisting of a gas supply, the photoreactor and a chemiluminescent NO-NO_x analyzer (Horiba ambient monitor APNA-360). To obtain the starting concentration of NO of 100 ppb at the relative humidity of 50 %, a gaseous mixture of dry air (1500 mL min⁻¹), wet air (1500 mL min⁻¹, relative humidity of 100 %) and 50 ppm NO in N₂ (ca. 6 mL min⁻¹) was prepared. The photocatalytic oxidation of NO in the photoreactor was performed with a UV light intensity of 1 mW cm⁻².

3. Results and Discussion

Mesoporous titania films were synthesized by dip coating on FTO substrates, as described in the experimental section. The SEM image of the calcined film (Figure 2, left) show a highly ordered cubic pore arrangement of 8 nm diameter mesopores. The Kr adsorption isotherm for the mesoporous titania film is of type-IV isotherm, typical for mesoporous solids (Figure 2, right). The roughness factor of the film was measured to 103 cm² / cm².

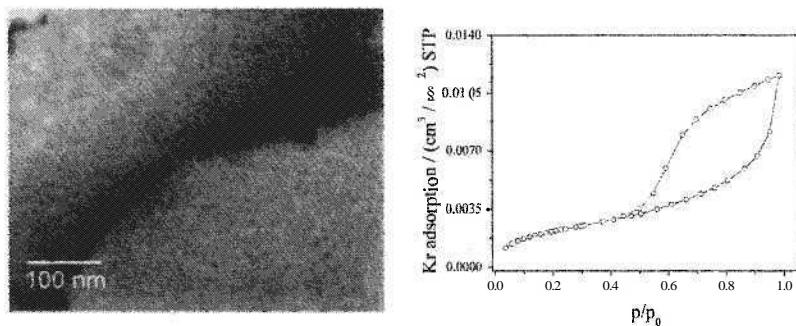


Figure 2: SEM micrograph (left) and Kr adsorption isotherm (right) of a mesoporous TiO₂ film.

Gold was deposited at 0.3 V vs. Ag/AgCl on the mesoporous TiO₂ film from an Ar saturated HAuCl₄ and HClO₄ aqueous solution. During deposition, the mesoporous film became orange colored with a rough surface. The morphology of the electrodeposited gold was characterized by SEM (Figure 3). Flat gold structures with a uniform circular shape and diameters of about 30 μm were observed. These disc-like particles, poorly fixed on the growth surface, easily flake off (Figure 3, right). Their upper sides show a rough surface with

crystalline needles, which corresponds to the orange colored side. This color is the consequence of light scattering effects on the rough surface. The reverse sides of the disc-like particles are very flat (roughness less than ± 250 nm) and show consequently the typical color of gold.

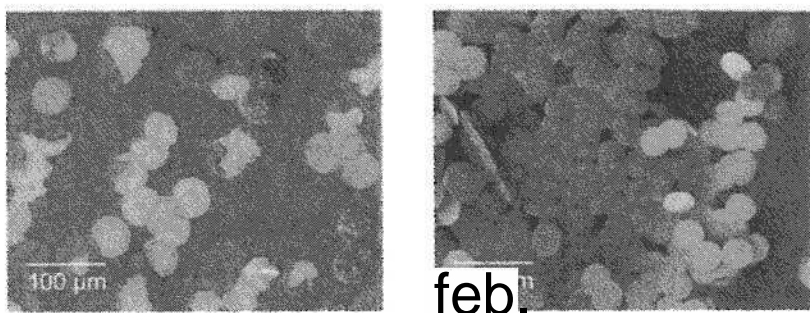


Figure 3: SEM micrographs of the gold structures grown at 0.3 V underneath the mesoporous TiO_2 film; on the substrate (left) and exfoliated fragments (right).

In many places, uprisings underneath the film can be observed (Figure 3 and 4, left). In closer examination, a growth of gold through the mesopores of the TiO_2 film can be excluded (Figure 4). The very bright region in the SEM image corresponds to the gold (Figure 4, right). The higher brightness is a result of the stronger reflection of electrons, a typical effect of elements with high atomic masses. The darker part above the gold, the TiO_2 film, is clearly separated from the gold. Consequently, the growth of the gold takes place underneath the film, which induces the uprisings.

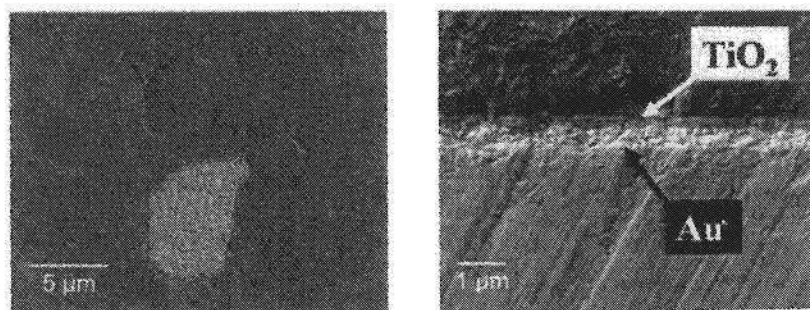


Figure 4: SEM micrographs of the Au/mesoporous TiO_2 film: growth of Au layers underneath the film, at 0.3 V.

Directly after contact of the deposition solution with the film gold ions start to diffuse through the highly porous film to the conductive FTO layer. Because at the applied low potential of 0.3 V the TiO_2 film is not conductive, the reduction of gold-ions takes place only at the FTO. Further deposition occurs on the already deposited gold due to the considerably higher conductivity of the gold. However, instead of growing through the pores, the gold grows two-dimensionally underneath the film because the interaction between the TiO_2 film and the FTO substrate is quite weak. When the mechanical stress of the TiO_2 film becomes too high (Figure 4, left), the film above the growing two-dimensional Au layer cracks and flakes off. Afterwards, gold crystals start to grow three-dimensionally on the circular gold layer and form the rough surface, which can be found on most of the gold particles. By the three-dimensional growth the Au structures become thicker. With increasing thickness of the Au layer the Au-FTO substrate interaction becomes less important in relation to the Au-Au interaction. Mechanical stress then leads to a partial exfoliation of Au platelets from the substrate (Figure 3, right).

A variation of the deposition potential (in the range of -0.7 V to 0.6 V) or deposition time (30 s - 2 h) only results in very similar structures which only slightly differ in their size.

A completely different behavior concerning the deposition of gold can be found by using mesoporous SiO_2 films on FTO as working electrode for the deposition at 0.3 V. Instead of disc-like structures, spherical gold structures with spicular surface and sizes in the range of 5 - 20 μm were observed (Figure 5).

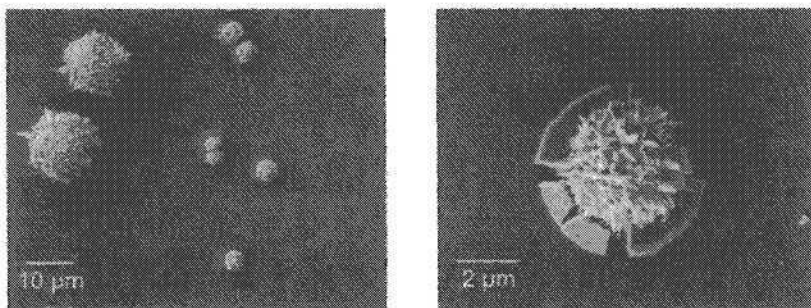


Figure 5: SEM micrographs of mesoporous SiO_2 films with spherical Au structures grown at 0.3 V.

Compared to mesoporous TiO_2 films, a growth of gold underneath the film was not observed. The spherical gold structures suggest an early incipient three-dimensionally growth. The sketch, shown in Figure 6, illustrates the different

formation of gold structures in the two described composites. By using mesoporous TiO_2 as working electrode, gold structures grow underneath the film due to weak interactions between the film and the FTO substrate. A mesoporous SiO_2 film in contrast shows a strong adhesion on the conductive substrate but an only metastable pore structure, which is too weak to withstand the growth of gold. The fast growing Au destroys the mesoporous SiO_2 framework and hence the film finally breaks near the surface.

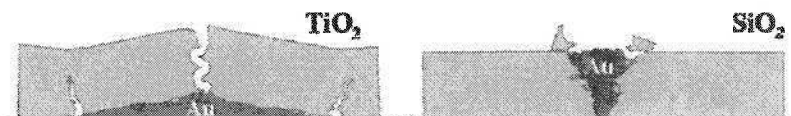


Figure 6: Illustration of the growth mechanism of the gold structures at 0.3 V by using mesoporous TiO_2 and SiO_2 films.

To ensure a growth of gold nanowires exclusively inside the mesopores pulsed electrodeposition can be used (Figure 7). By applying rectangular reverse pulses (Figure 1) the nucleation and growth process of particles is controllable due to alternating potentials (-6.0 V for 3 s, 0.1 V for 1 s). As a result, nanowires were formed as a replica of the cubic pore system with diameters of about 8 nm in accordance with the pore sizes.

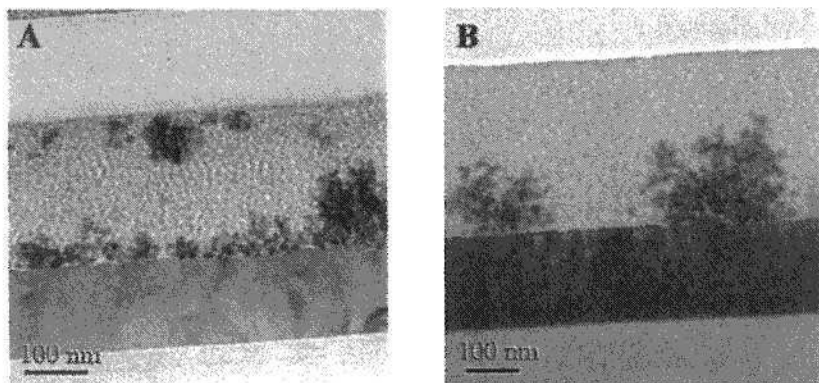


Figure 7: TEM micrographs of mesoporous TiO_2 film with encapsulated Au nanowires and nanoparticles synthesized by pulsed electrochemical deposition by applying 16 pulses at a potential of -6.0 V / 0.1 V (A) and -1.0 V / 0.1 V (B), respectively.

Depending on the applied potentials, gold nanowire growth can start inside the whole film or only from the conductive substrate. If the -6.0 V pulses are applied the TiO_2 framework possess a high conductivity and gold ions can be reduced within the film (Figure 7, A). By decreasing the negative potential in the pulses from -6.0 V to -1.0 V gold nanowires grow exclusively from the conductive FTO substrate through the film (Figure 7, B). As a result, larger aggregates of longer nanowires and less nanoparticles can be obtained.

The densities of the wires inside the pore arrangement can be optimized by increasing the number of pulses. The application of an initial pulse leads not only to seed crystals; instead they start to grow to larger aggregates due to the long pulse duration of 3 s. By increasing the pulse number up to more than 32 pulses a nearly complete filling of the pores is achievable.

A specific property of the obtained films is their color. Different from the bulk, films with encapsulated gold nanowires, formed by applying, for example, 16 pulses, exhibit a blue color. This is a direct consequence of the plasmon resonance of elongated gold nanoparticles, which depends on size, shapes and environment [15].

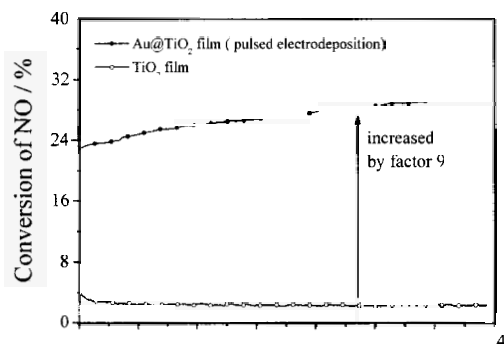


Figure 8: Conversion of NO by investigation of the photocatalytic oxidation of NO.

The photocatalytic properties of the blue gold-loaded TiO_2 films, obtained by pulsed electrodeposition, were investigated in the photocatalytic oxidation of NO (Figure 8). The pure mesoporous TiO_2 films show a low photocatalytic conversion of NO of only 3 % caused by a poor crystallinity of the TiO_2 framework. With encapsulated gold nanowires the activity of the films can be considerably increased by a factor of 9, although the crystallinity of the TiO_2 framework is not altered. The major rate-limiting factor of the photocatalytic

activity of pure TiO_2 is the high degree of recombination between photogenerated electrons and holes. The presence of gold nanowires or nanoparticles leads to a more efficient charge separation of the light generated electron-hole pairs and an increase of their lifetime both explaining the increase of the photocatalytic activity [16,17]. Au particles on TiO_2 are very effective traps for electrons due to the formation of a Schottky barrier at the metal-semiconductor contact. That means the photocatalytically active centers are mainly located near the Au nanowires, and the Au-free parts of the porous TiO_2 matrix ensure a sufficient accessibility for NO to reach the Au/ TiO_2 contacts.

4. Conclusions

Gold structures with uniform disc-like and spherical morphologies were generated by electrochemical deposition of gold at 0.3 V vs. Ag/AgCl on mesoporous TiO_2 and SiO_2 films, dip coated on conductive FTO substrate. The morphologies and sizes of the formed Au particles strongly depend on the conditions of the electrochemical deposition.

Due to the weak film-FTO substrate interaction, gold structures grow two-dimensionally underneath the mesoporous TiO_2 film until the film flakes off followed by a three-dimensionally growth. A growth of gold through the mesopores does not occur.

Spherical gold structures were formed on mesoporous SiO_2 films because of the considerable stronger interaction between film and substrate. The formation starts directly inside the pore and possesses throughout the film, but due to the fast and exoergic growth the only metastable pore structure collapses.

By pulsed electrodeposition Au nanowires were exclusively generate inside the pores of the mesoporous TiO_2 films as a replica of the pore system. The variation of the number of pulses influences the density of the wires in the template. Because Au ion reduction takes place only at negative potential the growth rate of Au can be controlled by applying pulses instead of constant potential. It can be reduced to such a rate, which ensures an energetic relaxation of the system without destroying either the framework or the film-substrate contact.

In the photocatalytic oxidation of NO the presence of Au nanowires in the pores of TiO_2 films leads to an increase of the activity by a factor of up to 9 due to the more efficient charge separation of the light generated electron-hole pairs.

Acknowledgement

The authors thank Dr. J. Rathousky (Heyrovsky Institute of Physical Chemistry in Prague) for recording Kr adsorption isotherms, Dr. D. Bahnemann and J. Tschirch (Institute of Technical Chemistry, Leibniz University Hannover) for providing photocatalytic measurements and Prof. Dr. J. Caro (Institute of Physical Chemistry, Leibniz University Hannover) for fruitful discussions. Financial support by the German Science Foundation (DFG, WA 1116/12-1) in the frame of the priority program SPP 1165 "Nanowires and nanotubes" is gratefully acknowledged.

References

1. B. O'Reagan, M. Grätzel, *Nature* **353**, 737 (1991).
2. L. Zhao, Y. Yu, L. X. Song, X. F. Hu, A. Larbot, *Appl. Surf. Sci.* **239**, 285 (2005).
3. U. Diebold, *Surf. Sci. Rep.* **48**, 53 (2003).
4. E.V. Milsom, H.R. Perrott, L. Peter, F. Marken, *Langmuir* **21**, 6341 (2005).
5. A. C. Templeton, J. Pietron, R. Murray, P. Mulvaney, *J. Phys. Chem. B* **104**, 564 (2000).
6. L. Aldous, D. S. Silvester, C. Villagran, W. R. Pitner, R. G. Compton, M. C. Lagunas, C. Hardacre, *New J. Chem.* **30**, 1576 (2006).
7. X. B. Li, H. Y. Wang, X. D. Yang, Z. H. Zhu, Y. J. Tang, *J. Chem. Phys.* **8**, 126 (2007).
8. K. Yu, Y. Tian, T. Tatsuma, *Phys. Chem. Chem. Phys.* **8**, 5417 (2006).
9. B. Dubertret, M. Calame, A. J. Libchaber, *Nat. Biotechnol.* **19**, 365 (2001).
10. Y. Li, G. Shi, *J. Phys. Chem. B* **109**, 23787 (2005).
11. K. Ueno, V. Mizeikis, S. Juodkazis, K. Sasaki, H. Misawa, *Opt. Lett.* **30**, 2158 (2005).
12. B. M. I. van der Zande, M. R. Böhmer, L. G. J. Fokink, C. Schönenberger, *J. Phys. Chem. B* **101**, 852 (1997).
13. P. C. A. Alberius, K. L. Frindell, R. C. Hayward, E. J. Kramer, G. D. Stucky and B. F. Chmelka, *Chem. Mater.* **14**, 3284 (2002).
14. D. Zhao, P. Yang, N. Melosh, J. Feng, B. F. Chmelka, G. D. Stucky, *Adv. Mater.* **10**, 1380 (1998).
15. J.-E. Park, T. Momma, T. Osaka, *Electrochimica Acta* **52**, 9514 (2007).
16. S. Sakthivel, M. V. Shankar, M. Palanichamy, B. Arabindoo, D. W. Bahnemann, V. Murugesan, *Water Res.* **38**, 7632 (2004).
17. I. M. Arabatzis, T. Stergiopoulos, D. Andreeva, S. Kitova, S. G. Neophytides, P. Falaras, *J. Catal.* **220**, 127 (2003).

MESOPOROUS LAYERS OF TiO₂ AS HIGHLY EFFICIENT PHOTOCATALYSTS FOR CLEAN ENVIRONMENT†

VÍT KALOUSEK, JIRÍ RATHOUSKÝ*

J. Heyrovský Institute of Physical Chemistry of AS CR, v.v.i., Dolejškova 3, 18223 Prague 8, Czech Republic. E-mail:jiri.rathousky@jh-inst.cas.cz.

JESSICA TSCHIRCH, DETLEF BAHNEMANN

Institute of Technical Chemistry, Leibniz University Hannover, Callinstr. 3, D-30167 Hannover, Germany

Mesoporous films of TiO₂ prepared by a template-assisted procedure based on the evaporation-induced self-assembly mechanism were shown to be efficient photocatalysts for the oxidation of nitrogen oxide at high dilution (100 ppb) and in the removal of deposits of oleic acid. Their high photocatalytic activity is explained by a local increase in the partial pressure of NO in the nanopores of the porous film close to the photocatalytically active sites and by the increased diffusion of O₂/H₂O due to the 3D-porosity, which is otherwise hindered by solid or liquid deposits for non-porous TiO₂ films.

1. Introduction

The relatively high concentration of nitrogen oxides (NO_x) in the range of several hundred ppb in the atmosphere of municipal cities and the soiling of the external surfaces of building structures are among the major present environmental issues [1].

Nitrogen oxides are responsible for urban smog because of their photochemical reactions with hydrocarbons. Further, together with sulfur dioxide and sulfur trioxide they are the major contributors to the very harmful acid rain. At present, the technologies for the control of NO_x emissions include combustion modifications, dry and wet processes [2]. Photocatalytic oxidation has gained much attention in the purification of air because it provides an attractive alternative to the more conventional methods [2-4]. The main advantage of photocatalysis over other oxidation treatments results from the

† This work was supported by the Ministry of Education, Youth and Sport of the Czech Republic (project 1M0577).

* Corresponding author.

direct absorption of light, which allows to degrade the pollutants at ambient temperature, pressure, humidity, etc. Additionally, low-concentration and low-flow rate waste streams can be easily processed. Weak UV irradiation of less than 1 mW/cm^2 needed for the photocatalytic conversion is amply provided by the solar light. More over, no extra reactants such as NH_3 or O_3 are required.

Another major environmental issue is the soiling of the external surfaces of buildings and other constructions. The ultimate goal is to provide their surfaces with such a finish, which will render them easy-to-clean or even self-cleaning. One of the promising possibilities is to cover their surface with a photocatalytically active layer. It should be active enough to decompose the solid or liquid deposits or to convert them to such a form, which is easy to remove, typically to smaller oxygenated organic compounds which can be easily washed off.

Due their unique properties, the anatase crystalline films with developed 3D mesoporosity are photocatalysts of choice for the environmental applications. In recent years, a generalized sol-gel procedure for the preparation of large-pore mesoporous films of metal oxides has been developed, which is based on a mechanism that combines evaporation-induced self-assembly (EISA) of a block copolymer with complexation of molecular inorganic species enabling to prepare mesoporous films with good mechanical, optical and transport properties [5-7]. Mesoporous films of TiO_2 are especially effective when the photodecomposition mechanism is based on the surface-adsorbed reactants [8]. The amount of adsorbed substances is increased due to the large surface area, which enhances their decomposition. Further the mesoporosity will ensure fast transport of O_2 and H_2O , which are viable for the photocatalytic degradation of deposits. This transport is often significantly hindered by the compact layer of the dirt. The present communication is aimed at the synthesis of such mesoporous films of TiO_2 with large surface area and the study into their efficiency as photocatalysts in the photooxidation of NO and the degradation of layers of oleic acids, which models typical surface pollutants.

2. Experimental

2.1. Preparation

The sol used for the deposition of the films was prepared according to the following procedure. 5 g of Pluronic P123 (BASF) was dissolved in 56 mL of butan-1-ol and the solution was stirred for 1 hour. 14.4 mL of titanium(IV) ethoxide was mixed with 10.2 mL of concentrated HCl. Afterwards the former

solution was added to the latter one and the mixture stirred for 3 hours. Prior to the deposition, the glass slides were carefully cleaned in diluted HCl, distilled water, ethanol and acetone. The films were deposited by dip-coating the cleaned glass slides at a speed of 1.5 mm/s at relative humidity of 20 %. Afterwards the films were aged at room temperature for 24 hours and calcined in air at 350 °C for 3 hours. In order to obtain thicker films the mentioned procedure was repeated including the dip-coating, aging and finally calcination at 350 °C for 3 hours. All the chemicals were obtained from Sigma-Aldrich (except for the Pluronic template). The non-porous sample was a sample of commercial Aktiv Glass produced by Pilkington.

2.2. Characterization

The morphological properties of the films were studied by combining several techniques. The surface relief of the films was revealed by the atomic force microscopy (AFM) using a Digital Instruments NanoScope apparatus. The details of the surface texture were provided by the high-resolution scanning electron microscopy using a Jeol JSM-6700 F apparatus and the high-resolution transmission electron microscopy (HR-TEM Jeol JEM-2100F UHR). The crystallinity was assessed by the X-ray diffraction using a Siemens D 5005 diffractometer in the Bragg–Brentano geometry using CuK α radiation. The texture properties of the films were determined by the analysis of adsorption isotherms of Kr at 77 K measured with a Micromeritics ASAP 2010 volumetric adsorption unit. The absorption spectra of mesoporous films were obtained with a Perkin Elmer Lambda 19 spectrophotometer.

2.3. Photocatalysis

The experimental set-up for the photocatalytic tests in the gaseous phase consisted of a gas supply part, the photoreactor, and a chemiluminiscent NO-NO $_x$ gas analyzer. (Horiba ambient monitor APNA-360). The gaseous reaction mixture was prepared by mixing streams of dry air (1500 mL/min), wet air (1500 mL/min, relative humidity of 100 %) and 50 ppm NO/N $_2$ (approx. 6 mL/min), in order to obtain a final concentration of NO of 100 ppb at a relative humidity of 50 %. The photoreactor was illuminated by four 8 W black lights, the UV light intensity achieving 1 mW/cm 2 . The conversion of NO equals

$$\text{NO conversion (\%)} = ([\text{NO}]_{\text{inlet}} - [\text{NO}]_{\text{outlet}}) \times 100 / [\text{NO}]_{\text{inlet}}$$

where $[\text{NO}]_{\text{inlet}}$ and $[\text{NO}]_{\text{outlet}}$ are the NO concentration at the inlet and at the outlet of the photoreactor, respectively. Prior to the photocatalytic tests, the photoreactor was purged with the NO/water vapor/air mixture without illumination until a steady outlet NO concentration was achieved. 100% NO conversion is equivalent to a photonic efficiency of $\xi=0.14\%$ assuming a mean irradiation wavelength of 350 nm.

Further the self-cleaning performance of mesoporous TiO_2 films was tested by following the decomposition of a layer of oleic acid. Prior to the photocatalytic tests, the test pieces were purified by a UV light irradiation (2 mW/cm^2) for 24 hours. Oleic acid was deposited by dip-coating from its 10% heptane solution (1 mm/s). Afterwards the films were dried at $70\text{ }^\circ\text{C}$ for 15 min. The samples were illuminated with a UV light (365 nm , 2.0 mW/cm^2), the oleic acid degradation being followed by measuring its contact angle for water.

3. Results and Discussion

3.1. Morphological and structure properties of mesoporous films

The AFM relief of the prepared films is very flat without height variations in excess of ca 10 nm. The pore openings are relatively regularly distributed within the surface with an average size of ca. 8 nm. The TEM image shows more or less regularly ordered pores, whose size ranges from 6 to 10 nm. The pores are separated by walls about 3–4 nm in thickness. Except for the mesoporous structure, no other phases, such as extra-framework nanocrystals or some disordered species, have been detected. The SEM side views provide the film thickness - about 200 and 400 nm for the single- and double-layered films, respectively.

Powder X-ray diffractograms of the mesoporous films show the presence of only one crystalline phase, namely anatase (Fig. 1, bottom). The presence of an X-ray amorphous titania component is the probable reason why the X-ray diffractograms exhibit decreased intensity of reflections due to anatase in comparison with a reference fully crystalline material prepared by the destruction of the mesoporous film by calcination at $600\text{ }^\circ\text{C}$ (in Fig. 1 compare the lower with the upper diffractogram) [9,10].

UV/VIS spectra show that the mesoporous films exhibit some blue shift in the comparison with a bulk TiO_2 (bandgap of 3.2 eV, absorption threshold of 388 nm), the shift being larger for the single-layered (by 53 nm) than for the double-layered film (by 38 nm). The difference in the blue shift is clearly due to

the repeated calcination of the double-layer film, which leads to some increase in the size of the anatase nanocrystals.

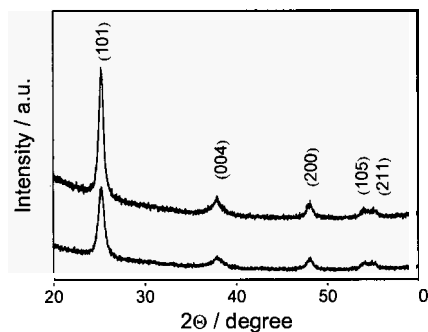


Figure 1. X-ray diffractogram of single-layer films calcined at 350 °C (bottom) and 600 °C (top).

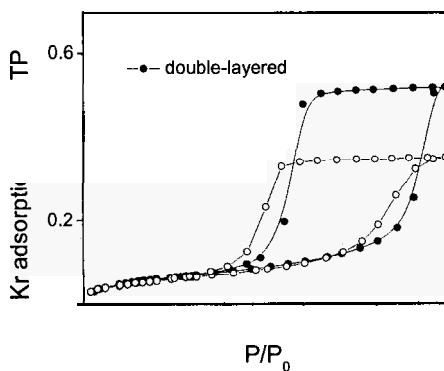


Figure 2. Adsorption isotherms of Kr at 77 K on 1 layer- and 2-layer-film

Adsorption isotherms of Kr on both films are of type IV characterized by a broad hysteresis loop, which proves the presence of mesopores within the films. The long horizontal plateau on the desorption branch for both samples shows that the krypton molecules are firmly held within the pores, which is of importance for the photocatalysis in the gaseous phase. For the calculation of the

texture parameters, the molecular cross-sectional area of krypton of 0.21 nm^2 and the molar volume of solid krypton were used according to the software of the adsorption apparatus producer. The single- and double-layered films exhibit the BET surface area, pore volume and average pore size of 0.35 m^2 , 0.58 mm^3 and ca 6 nm, and 0.50 m^2 , 0.86 mm^3 and ca 6 nm, respectively. The geometrical size of all the films was the same, namely 20 cm^2 .

All the provided experimental data clearly prove that the films exhibit developed mesoporosity with large surface area and more or less regularly ordered pores, whose size equals ca 6 nm and whose pore walls are composed of small anatase nanocrystals (ca 40-60 %) and some amorphous phase.

3.2. Photocatalytic activity

During the photocatalytic oxidation process of NO, adsorbed NO molecules react first with $\text{OH}\cdot$ or $\text{HO}_2\cdot$ radicals to form adsorbed HNO_2 , which is further photooxidized to NO_2 . NO_2 is either desorbed or converted to HNO_3 [2]. The degree of conversion to HNO_3 depends on the residence time of NO_2 in the adsorbed state, which is substantially enhanced by the porosity of the employed photocatalysts, as proven by the krypton adsorption. The surface of the photocatalyst was first equilibrated with the gaseous 100 ppb NO/water vapor/ N_2 mixture. Afterwards, the illumination was started. Fig. 3 (left) shows the characteristic time response – very fast increase in the conversion following immediately after switching on the light, achieving up to 35 % and 41 % (i.e., photonic efficiencies of $\xi = 0.049 \%$ and $\xi = 0.057 \%$, respectively) for the single- and double-layered films, respectively. This fast increase is followed by a decrease in conversion efficiency, the final steady state conversion depending substantially on the thickness of the film – 13% ($\xi = 0.018 \%$) and 23 % ($\xi = 0.032 \%$) for the single- and double-layered films, respectively. The deactivation observed is likely due to the formation and deposition of nitric acid on the surface, as the photocatalytic activity was restored by rinsing the layers with water. However, since this deactivation is a rather fast process, an alternative explanation is the photodesorption of NO that was previously adsorbed during the dark equilibration step. The optimum efficiency was achieved for a double-layered film with a thickness of approx. 400 nm. Further thickness enhancement attained by depositing additional layers of porous TiO_2 is without any beneficial effect. The photocatalytic efficiency of the mesoporous films was compared with that of the commercially available self-cleaning Pilkington Activ Glass, whose activity is practically negligible. The data obtained here clearly support the hypothesis of a confinement effect of the

reactants inside the mesoporous structure, based on an increase in their partial pressure on the active sites [8].

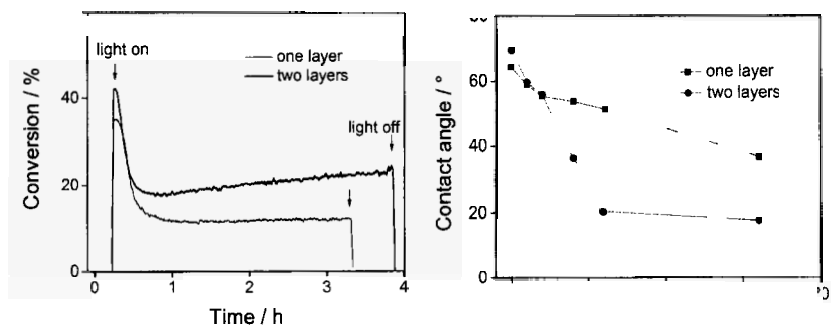


Figure 3. Photocatalytic oxidation of NO (left) and the decomposition of a layer of oleic acid (right) on single-layer and double-layer mesoporous films of TiO_2 .

The photocatalytic decomposition of oleic acid was followed by measuring the decrease in the contact angle for water, which is expected proportional to the degree of its degradation, i.e. its transformation into more hydrophilic compounds, such as acids with shorter chains, aldehydes, alcohols, as well as to gaseous products (CO_2 , H_2O), which leads to the exposure of the hydrophilic TiO_2 surface (Fig. 3, right). The double-layer film exhibits a higher efficiency in comparison with non-porous films, whose activity is often rather restricted due to hindered transport of O_2 and H_2O , which is often rate-determining for the photocatalytic degradation of deposits in the form of compact solid or liquid layers.

4. Conclusions

In summary, mesoporous films of TiO_2 are highly promising photocatalysts for the decomposition of pollutants present at very low concentrations in the gas-phase, as shown for the photooxidation of NO. Their high photocatalytic efficiency can be explained by the local increase in the partial pressure of the compound reacting in the nanopores or cavities of the porous film close to the photocatalytic sites. Krypton adsorption has shown that the adsorbed molecules are firmly held within the porous structure. Further they are highly efficient in the removal of liquid layers deposited on their surface, which is due to the

increased diffusion of O₂/H₂O owing to the 3D-porosity. A commercial non-porous film tested at the same condition exhibited much lower photocatalytic activity. Therefore they are serious candidates for the creation of effective self-cleaning surfaces. Such films can be easily prepared with high reproducibility by a template-assisted procedure, which also enables to effectively control the film thickness and consequently its surface area and pore volume.

Acknowledgements

We are grateful to the Ministry of Education, Youth and Sport of the Czech Republic (project 1M0577) for the financial support. The authors thank A. Feldhoff and I. Bannat (Leibniz University Hannover) for EM images.

References

1. J.H. Seinfeld, S.N. Pandis, *Atmospheric Chemistry and Physics: From Air Pollution to Climate Change*, Wiley, New York, 1998.
2. S. Devahasdin, C. Fan jr., K. Li, D. H. Chen, *J. Photochem. Photobiol. A: Chem.* **156**, 161 (2003).
3. F.-L. Toma, S. Guessasma, D. Klein, G. Montavon, G. Bertrand, Ch. Coddet, *J. Photochem. Photobiol. A: Chem.* **165**, 91 (2004).
4. K. Hashimoto, K. Wasada, N. Toukai, H. Komonami, Y. Kera, *J. Photochem. Photobiol. A: Chem.* **136**, 103 (2000).
5. P. Yang, D. Zhao, D.I. Margolese, B.F. Chmelka, G.D. Stucky, *Nature* **396**, 152 (1998).
6. C.J. Brinker, Y.F. Lu, A. Sellinger, H.Y. Fan, *Adv. Mater.* **11**, 579 (1999).
7. D. Grosso, G.J.A.A. Soler-Illia, F. Babonneau, C. Sanchez, P.-A. Albouy, A. Brunet-Bruneau, A.R. Balkenende, *Adv. Mater.* **13**, 1085 (2001).
8. F. Bosc, D. Edwards, N. Keller, V. Keller, A. Ayril, *Thin Solid Films* **495**, 272 (2006).
9. D. Fattakhova-Rohlfing, M. Wark, T. Brezesinski, B. Smarsly, J. Rathouský, *Adv. Funct. Mater.* **17**, 123 (2007).
10. J. Rathouský, D. Fattakhova Rohlffing, M. Wark, T. Brezesinski, B. Smarsly, *Thin Solid Films* **515**, 6541 (2007).

QUINOLINE-CARBOIMINE PALLADIUM COMPLEX IMMOBILIZED ON MCM-41 AS A VERSATILE CATALYST FOR SONOGASHIRA CROSS-COUPPLING REACTION*

HIDEKI NAKAMURA, KENICHI KOMURA, AND YOSHIHIRO SUGI†

*Department of Materials Science and Technology, Faculty of Engineering,
Gifu University, Gifu, 501-1193, Japan.*

The copper-free Sonogashira cross-coupling reaction of terminal alkynes with aryl halides was studied over palladium complex immobilized on quinoline-carboimine functionalized MCM-41 (Pd-2QC-MCM-41) catalyst. In the reaction of iodobenzene with phenylacetylene, cross-coupling products were successfully obtained by adding base such as piperidine, and the high catalytic activity of Pd-2QC-MCM-41 catalyst was observed in NMP as solvent. The reaction proceeded quantitatively at 80 °C within 3 h. Pd-2QC-MCM-41 catalyst was easily recovered by filtration, and reused without significant loss of catalytic activity.

1. Introduction

Sonogashira cross-coupling reaction of terminal alkynes with aryl halides catalyzed by Pd(0)/Cu(I) is a powerful method for construction of C(sp)-C(sp²) bonds [1,2,3]. Many researches have been reported in both homogeneous and heterogeneous systems, so far [3]. However, with concerning the efficiency of reaction and environmental benign, the heterogeneous catalysts should be promising candidates because the separation of catalyst from reaction products and subsequent reuse of recovered catalyst are quite easier than homogeneous catalysts [4,5]. Recently, the development of Sonogashira cross-coupling reaction has been extended to be more practical; in particular, the copper-free reactions have been attractively investigated. For example, Genêt et al. reported the efficient cross-coupling reaction over water-soluble Pd catalyst [6]. However, only a few potential reports have been reported on the copper-free heterogeneous catalysts in Sonogashira reaction. Macquarrie et al. reported the reaction over N, P-chelated Pd(II) complex immobilized on silica gel under solvent-free condition [7]. Djakovitch et al. reported the modified zeolite

* A part of this work was financially supported by Grant Aid for Scientific Research (B) 16310056 and 19061107, the Japan Society for the Promotion of Science (JSPS).

† Corresponding author. E-mail: ysugi@gifu-u.ac.jp.

catalyst ($[\text{Pd}(\text{NH}_3)_4]^{2+}/(\text{NH}_4)\text{Y}$) [8]. Köhler reported Pd/C as catalyst gave the excellent results by using N-methyl-2-pyrrolidone (NMP) as a solvent and pyrrolidine as an additive [9].

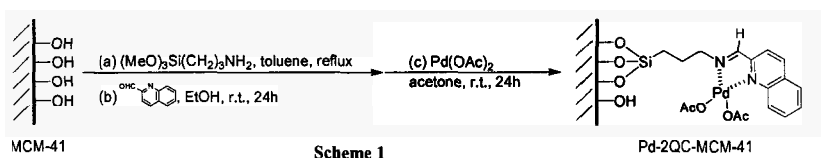
One of the versatile heterogeneous catalysts, the use of mesoporous silica have become attractive since these have a larger surface area and easy to modify their surface for desired purposes. We recently reported the Heck-type vinylation and Suzuki coupling reaction over Pd, Rh, and Pt complexes immobilized on mesoporous silica (FSM-16), and found that quinoline-carboimine functionalized catalyst had the high catalytic performance at even low concentration of metal complex and reusable without loss of catalytic activity due to the negligible leaching of metal species [10,11]. Here, we report the copper-free Sonogashira cross-coupling reaction of terminal alkynes with arylhalides over Pd complex immobilized on quinoline-carboimine functionalized MCM-41 (Pd-2QC-MCM-41) catalyst.

2. Experimental

2.1. Catalyst Preparation

Immobilization of metal complexes on MCM-41 are following steps as illustrated in Scheme 1 [10,11]:

- Surface modification of MCM-41 was carried out by using 3-aminopropyltrimethoxysilane in toluene under azeotropic reflux for 3 h to give an aminopropyl group immobilized on MCM-41 (AP-MCM-41).
- Preparation of quinoline-carboimine ligands on MCM-41 was to use AP-MCM-41 and 2-quinolinecarboxyaldehy in distilled EtOH for 24 h at room temperature (2QC-MCM-41).
- Pd-2QC-MCM-41 catalyst was prepared by 2QC-MCM-41 and PdX_2 ($\text{X} = \text{OAc}, \text{Cl}$) in distilled acetone for 24 h at room temperature.



From the powder XRD measurement, obtained Pd-2QC-MCM-41 was retained its ordered mesoporus structure; however, the decreased intensity of (100) direction was observed comparing with that of calcined MCM-41. N_2

isotherm adsorption of Pd-2QC-MCM-41 elucidated the decrease of surface area ($642 \text{ m}^2 \cdot \text{g}^{-1}$) and pore volume ($0.463 \text{ cm}^3 \cdot \text{g}^{-1}$) comparing with calcined MCM-41 ($950 \text{ m}^2 \cdot \text{g}^{-1}$ in surface area and $0.837 \text{ cm}^3 \cdot \text{g}^{-1}$ in pore volume). This means that the palladium complex was effectively immobilized on MCM-41. Similar observation was also found in our recent report [10, 11]. FT-IR measurements of 2-quinolinecarboimine functionalized MCM-41 (2QC-MCM-41) and Pd-2QC-MCM-41 revealed that the considerable band shift was observed at C=N double bond moiety (1645 cm^{-1} to 1634 cm^{-1} , Figure not shown). This characteristic band shift is due to the complex formation of palladium metal with imine ligand. The Pd content in the catalyst was found in $0.0905 \text{ mmol} \cdot \text{g}^{-1}$ by ICP analysis, and the amount of ligand was estimated as $0.359 \text{ mmol} \cdot \text{g}^{-1}$ by TG analysis.

2.2 Sonogashira Cross-Coupling Reaction

The reaction was carried out by terminal alkyne (1.0 mmol), aryl halide (1.3 mmol), biphenyl (0.2 mmol, internal standard), amine (2.0 mmol), and Pd-2QC-MCM-41 catalyst (0.02 g, 0.0018 mmol based on Pd) in 1-methyl-2-pyrrolidone (NMP, 3.0 ml). The mixture was stirred for 3 h at $80 \text{ }^\circ\text{C}$ under nitrogen atmosphere. The catalyst was separated from reaction mixture by filtration. The filtrate was analyzed by a Shimadzu Gas Chromatograph GC-18 equipped with a Ultra-1 capillary column (Agilent: $25 \text{ m} \times 0.2 \text{ mm}$) to determine the conversion and yield. Isolation of cross-coupling products was carried out by column chromatography using EtOAc/hexane (8/2) as an eluent. The reuse of the recovered catalyst was done in a similar way as the first run.

3. Results and Discussion

3.1. The Influence of Metal Precursors

Table 1 shows the effect of the metal precursors in the cross-coupling reaction of iodobenzene with phenyl acetylene in DMF in the presence of triethylamine. The catalysts, Ru-, Pt-, and Rh-2QC-MCM-41 had no activity for the reaction (entries 1 to 3). However, the Pd catalysts prepared from $\text{Pd}(\text{OAc})_2$ and PdCl_2 showed the good catalytic activity to yield toluene effectively (entries 4 and 5). Because $\text{Pd}(\text{OAc})_2$ is a promising metal precursor to prepare metal complex, we chose over Pd-2QC-MCM-41 catalyst prepared from $\text{Pd}(\text{OAc})_2$ for the further research.

Table 1. The influence of metal precursors in copper-free Sonogashira cross-coupling reaction.^a

Entry	Catalyst ^b	Conversion (%) ^c
1	Ru-2QC-MCM-41(RuCl ₃ ·xH ₂ O)	0
2	Pt-2QC-MCM-41(H ₂ PtCl ₆ ·6H ₂ O)	0
3	Rh-2QC-MCM-41(RhCl ₃ ·xH ₂ O)	0
4	Pd-2QC-MCM-41 (Pd(OAc) ₂)	69.4
5	Pd-2QC-MCM-41 (PdCl ₂)	64.2

^a Reaction conditions; iodobenzene (1.0 mmol), phenyl acetylene (1.4 mmol), catalyst (0.02 g), triethylamine (2.0 mmol), solvent: DMF (3 ml), biphenyl (0.2 mmol, as an internal standard), temperature: 80 °C, period: 7 h. ^b Compounds in parentheses are precursor for the immobilized metal complex. ^c Based on iodobenzene.

Table 2. The influence of the solvent in Sonogashira cross-coupling reaction^a

Entry	Solvent	Conversion (%)
1	DMF	61.5
2	NMP	69.4
3	DMSO	47.3
4	Toluene	53.9
5	1,4-Dioxane	39.1

^a Reaction conditions; iodobenzene (1.0 mmol), phenyl acetylene (1.4 mmol), catalyst (0.02 g), triethylamine (2.0 mmol), biphenyl (0.2 mmol, as an internal standard), solvent (3ml), temperature: 80 °C, period: 7 h. ^b Based on iodobenzene.

3.2. The Influence of Solvent

Table 2 shows the influence of the cross-coupling reaction of iodobenzene with phenyl acetylene. The high conversions of iodobenzene of 69.4% and 61.5% were observed in NMP and DMF, respectively (entries 1 and 2). However, DMSO, toluene, and dioxane gave less conversion (entries 3-5). Our recent report for Heck-type vinylation, we also found the efficiency of NMP as a solvent due to stabilization of active palladium species [11]. Thus, we used the NMP as a solvent for the further research.

3.3. The Influence of Base as Additive

The addition of base is essential for the absorption of hydrogen halide formed by the Pd catalyzed reactions such as Heck and Suzuki couplings. In the

Table 3. The influence of base as additive in Sonogashira cross-coupling reaction^a

Entry	Base	Conversion (%) ^b
1	None	0
2	Triethylamine	69.4
3	Piperidine	98.7
4	Piperidine ^c	67.8
5	Pyridine	0
6	Indoline	0
7	Na ₂ CO ₃	58.0
8	NaOAc	50.2
9	K ₂ CO ₃	3.8

^a Reaction conditions; iodobenzene (1.0 mmol), phenyl acetylene (1.4 mmol), catalyst (0.02 g), base (2.0 mmol), biphenyl (0.2 mmol, as an internal standard), solvent: NMP (3 ml), temperature: 80 °C, period: 7 h. ^b Based on iodobenzene. ^c 1.0 mmol of piperidine was used.

copper-free Sonogashira coupling reaction, the addition of base is quite important to inhibit the homo-coupling reaction of terminal alkyne (Glaser-type reaction) [8]. Table 3 summarizes the influence of base as an additive in the cross-coupling reaction of iodobenzene with phenyl acetylene. Although no reaction occurred in the absence of base (entry 1), the addition of triethylamine accelerated the reaction effectively, resulting in the conversion of 69.4% (entry 2). The quantitative conversion of iodobenzene was observed by using piperidine (entry 3); however, an equimolar amount of piperidine against iodobenzene gave less conversion (entry 4). Organic bases such as pyridine and indoline gave no activities due to their low basicity (entries 5 and 6). The use of inorganic bases such as Na₂CO₃ and NaOAc gave moderate conversions (entries 7 and 8), whereas the addition of K₂CO₃ gave the only low conversion (entry 9). These indicate that organic amines are more suitable than inorganic ones because organic amines can effectively trap the formed hydrogen halide in the reaction medium. Consequently, it is found that the addition of two-fold amount of piperidine was effectively enhanced the reactions to yield the cross-coupling product with high conversion. From these results, piperidine was used as base for the further research.

3.4. The Influence of Reaction Temperature and Period

Figure 1 shows the influence of reaction temperature in the Sonogashira cross-coupling reaction over Pd-2QC-MCM catalyst. The reaction was

performed for 3 h in the presence of piperidine in NMP solvent. The reaction did not occur at 40 °C; however, the catalytic activity increased with increasing the temperature, and the 100% conversion was achieved at 80 °C. Figure 2 shows the influence of the reaction period over Pd-2QC-MCM catalyst at 80 °C. Conversion of iodobenzene reached 100% after 3 h. This excellent catalytic performance of Pd-2QC-MCM can be explained that the active catalytic species is effectively immobilized as ‘palladium complex’ on MCM-41.

3.5. Leaching experiment

The immobilized metal complex catalysts often suffer from leaching of metal species during the reaction. In particular, trace palladium species leaching from the immobilized complex sometimes works as active catalyst in palladium catalyzed organic synthesis. Thus, it is important to clarify the influence of leaching metal against the catalysis behavior. To confirm this issue, reaction mixture was filtrate under hot condition after 30 min reaction (conversion of phenyl acetylene was 43.4% in the filtrate). Then resulting filtrate was heated again to continue the reaction. After 3 h, the 49% conversion of phenyl acetylene was observed. This indicates that leaching of palladium metal may occur to react in homogeneous phase; however, it is negligible. Because reaction did not well proceed after removing the catalyst. Therefore, Pd-2QC-MCM works effectively as a complex during the catalysis.

Table 4. The Sonogashira coupling reaction of phenyl acetylene with various aryl halides over Pd-2QC-MCM-41 catalyst.^a

Entry	Aryl halide	Conversion (%) ^b	Yield (%) ^b
1	Iodobenzene	100	98.8
2	4-Iodotoluene	95.9	93.5
3	4-Iodoanisole	97.3	94.7
4	4-Iodoaniline	94.7	94.1
5	1-Iodonaphthalene	85.2	83.2
6	4-Iodoacetophenone	100	98.7
7	1-Iodo-4-nitrobenzene	100	98.6
8	Bromobenzene	2.7	0
9	4-Bromotoluene	4.7	0

^a Reaction conditions: aryl halide (1.3 mmol), phenyl acetylene (1.0 mmol), piperidine (2.0 mmol), catalyst (0.02 g), biphenyl (0.20 mmol, as an internal standard), NMP (3 ml), temperature, 80 °C, period, 3 h. ^b Based on phenyl acetylene.

3.6. Terminal alkynes with aryl halides

The results of Sonogashira cross-coupling reaction of phenyl acetylene with iodobenzene discussed above indicate that Pd-2QC-MCM-41 catalyst is a versatile catalyst for the cross-coupling reaction. To know the applicability for the organic synthesis, cross-coupling reactions of terminal alkynes, phenyl acetylene, 4-ethynyltoluene and 4-ethynylanisole with various aryl halides were examined over Pd-2QC-MCM-41 catalyst at optimized conditions for phenyl acetylene and iodobenzene: NMP as solvent and piperidine as base at 80 °C for 3 h. Table 4 shows the results of the Sonogashira coupling reaction of phenyl acetylene with various aryl halides over Pd-2QC-MCM-41 catalyst. Iodobenzene gave the quantitative yield of tolane within 3 h (entry 1). Aryl halides having the electron-donating group such as 4-iodotoluene, 4-iodoanisole and 4-iodoaniline also gave coupling products with phenyl acetylene in high

Table 5. The Sonogashira coupling reaction of 4-ethynyltoluene and 4-ethynylanisole with various aryl halides over Pd-2QC-MCM-41 catalyst.^a

Entry	Aryl halide	4-Ethynyltoluene		4-Ethynylanisole	
		Conv. (%) ^b	Yield (%) ^b	Conv. (%) ^b	Yield (%) ^b
1	Iodobenzene	94.5	94.1	100	100
2	4-Iodotoluene	93.8	93.1	100	100
3	4-Iodoanisole	93.1	91.6	100	100
4	4-Iodoaniline	94.1	93.3	100	100
5	4-Iodoacetophenone	99.2	98.8	100	100
6	1-Iodonaphthalene	81.3	79.4	90.3	87.5
7	1-Iodo-4-nitrobenzene	100	100	100	100
8	Bromobenzene	0	—	0	—

^a Reaction conditions; aryl halide (1.3 mmol), alkyne (1.0 mmol), piperidine (2.0 mmol), catalyst, (0.02 g), biphenyl (0.20 mmol, as an internal standard), NMP (3 ml), temperature, 80 °C, period: 3 h. ^b Based on alkyne.

Table 6. Recycling of Pd-2QC-MCM-41 catalyst in Sonogashira coupling reaction.^a

Recycle	1st	2nd	3rd	4th
Yield (%) ^b	100	100	93.4	92.7

^a Reaction conditions; phenyl acetylene (1.0 mmol), iodobenzene (1.3 mmol), catalyst: (0.02 g), piperidine (2.0 mmol), solvent: NMP (3 ml), temperature, 80 °C, period: 3 h. ^b Based on phenyl acetylene.

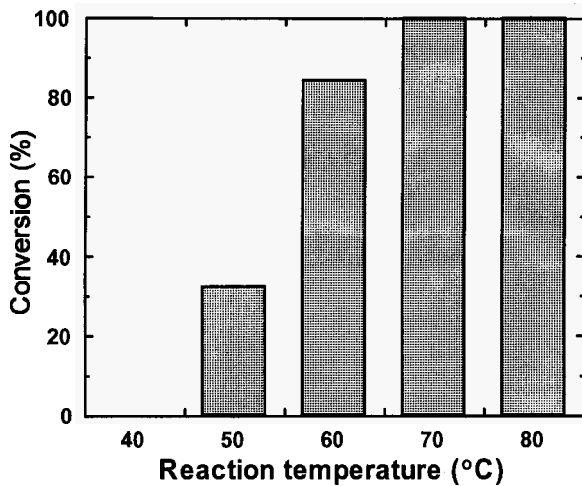


Figure 1. The influence of reaction temperature on the conversion over Pd-2QC-MCM catalyst in the Sonogashira cross-coupling reaction of phenyl acetylene with iodobenzene. Reaction conditions: aryl halide (1.3 mmol), phenyl acetylene (1.0 mmol), piperidine (2.0 mmol), catalyst (0.02 g), solvent: NMP (3 ml). period, 3 h.

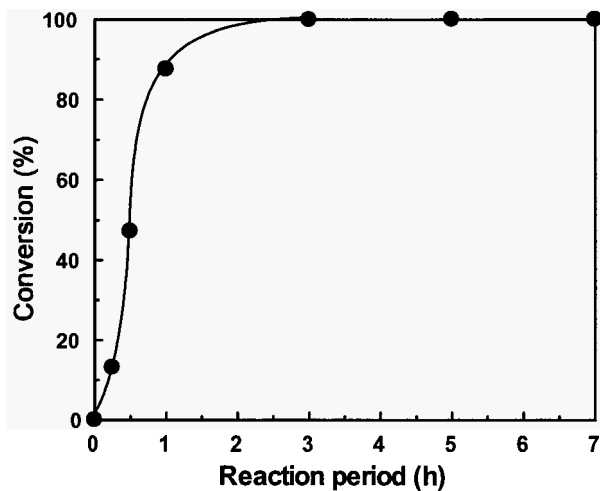


Figure 2. The influence of reaction period on the conversion over Pd-2QC-MCM catalyst in the Sonogashira cross-coupling reaction of phenyl acetylene with iodobenzene. Reaction conditions: see Figure 1

yield and conversions over Pd-2QC-MCM-41 catalyst (entries 2-4), although a trace amount of homo-coupling dialkyne of phenyl acetylene formed via dialkynylpalladium intermediate was obtained as a minor product in all cases. The good yield of cross-coupling product was also obtained from 1-iodonaphthalene (entry 5). 4-Iodoacetophenone and 1-iodo-4-nitrobenzene having electron-withdrawing group gave 100% conversions of phenyl acetylene to form corresponding tolanes in high yields (entries 6 and 7). Less active aryl bromides such as bromobenzene and 4-bromotoluene only gave the trace amount of homo-coupled dialkynes (entries 8 and 9).

The Sonogashira cross-coupling reaction of 4-ethynyltoluene and 4-ethynylanisole with various aryl halides was also examined as shown in Table 5. The cross-coupling product of iodobenzene with 4-ethynyltoluene was obtained in 94.1% yield (entry 1). The excellent conversions of 4-ethynyltoluene were also observed by 4-iodotoluene, 4-iodoanisole, and 4-iodoaniline (entries 2-4). 4-Iodoacetophenone and 1-iodo-4-nitrobenzene gave the cross-coupling compounds in the quantitative conversion and yield (entries 4 and 5). 1-Iodonaphthalene gave a slightly lower conversion, but good yield of cross-coupling product (entry 6). However, bromobenzene gave no cross-coupling products with 4-ethynyltoluene (entry 8). 4-Ethynylanisole gave cross-coupling products in high conversions and yields for most of aryl halides (entries 1-5,7). However, the conversion for 1-iodonaphthalene was slightly lower than the other iodides (entry 6). No product was also detected for bromobenzene (entry 8). These differences of the catalytic activity by changing functional group are due to the electron withdrawing abilities of terminal alkynes associated with acidity.

3.7. Recycling of Pd-2QC-MCM-41 catalyst

One of the most important advantages in the heterogeneous catalyst is the easy separation of the catalyst and reaction mixture and reuse of recovered catalyst for the further reaction. The reaction by using recovered catalyst was investigated to clarify the reusability of Pd-2QC-MCM-41 catalyst (Table 6). The catalyst was recovered by filtration, washed well with acetone, and dried at room temperature. No significant decrease of catalytic activity was observed until 4th reactions. These results indicate that the Pd-2QC-MCM-41 catalyst is the versatile heterogeneous catalyst in the Sonogashira coupling reaction with good reusability. This is because the palladium metal is not leached during the catalysis and work up.

4. Conclusion

The Pd complex immobilized on 2QC-MCM-41 (Pd-2QC-MCM-41) showed the excellent catalytic activity for the copper-free Sonogashira cross-coupling reaction. It found that the addition of piperidine and the use of 1-methyl-2-pyrrolidone (NMP) as a solvent effectively proceeded the coupling reaction to afford the cross-coupling product. The cross-coupling reactions of phenyl acetylene with various aryl halides catalyzed by Pd-2QC-MCM-41 gave toluene derivatives in excellent yields although a small amount of dialkyne, homo-coupling product, was accompanied as a minor product. The alkynes such as 4-ethynyltoluene and 4-ethynylanisole also gave the only cross-coupling products in excellent yields. However, no reaction occurred for less reactive 4-bromobenzene and 4-bromotoluene. The Pd-2QC-MCM-41 catalyst was easily recovered from the reaction mixture and reusable without loss of its catalytic activity. These excellent catalytic performances of Pd-2QC-MCM-41 are due to the effective immobilization of palladium metal as a 'complex', not naked metal.

References

1. K. Sonogashira, Y. Tohda, and N. Hagihara, *Tetrahedron Lett.* **50**, 4467 (1975).
2. K. Sonogashira, *J. Organometall. Chem.* **653**, 46 (2002).
3. J. S. Moore, *Acc. Chem. Res.* **30**, 402 (1997) and references cited therein.
4. B. M. Choudary, S. Madhi, N. S. Chowdari, M. L. Kantam, and B. Sreedhar, *J. Am. Chem. Soc.* **124**, 14127 (2002).
5. N. Kim, M. S. Kwon, C. M. Park, and J. Park, *Tetrahedron Lett.* **45**, 7057 (2004).
6. J. P. Genêt, E. Blart, and M. Savignac, *Synlett*, 715 (1992).
7. M. Bandini, R. Luque, V. Budarin, and D. J. Macquarrie, *Tetrahedron* **61**, 9860 (2005).
8. L. Djakovitch and P. Rollet, *Adv. Synth. Catal.* **346**, 1782 (2004).
9. R. G. Heidenreich, K. Köhler, J. G. E. Krauter, and J. Pietsch, *Synlett*, 1118 (2002).
10. J. Horniakova, T. Raja, Y. Kubota, and Y. Sugi, *J. Mol. Catal. A: Chemical* **217**, 73 (2004).
11. J. Horniakova, H. Nakamura, R. Kawase, K. Komura, Y. Kubota, and Y. Sugi, *J. Mol. Catal. A: Chemical* **233**, 49 (2005).

SOY OIL DEGRADATION OVER HIGHLY ORDERED Al MCM-41

MARCELO J.B. SOUZA, GICELIA RODRIGUES

*Chemical Engineering Department, Federal University of Sergipe,
São Cristóvão, 4910000, SE, Brazil.*

ANTONIO S. ARAUJO, ANNE M.G. PEDROSA, STEVIE H. LIMA

*Chemistry Department, Federal University of Rio Grande do Norte,
Natal, 5907-970, RN, Brazil.*

This work is focused on the synthesis, characterization and application of AlMCM-41 material. AlMCM-41 was prepared using silica gel and pseudoboehmite as silica and aluminum sources, respectively, and surfactant cetyltrimethylammonium bromide as a template. The textural properties of the calcined AlMCM-41 were characterized by powder X-ray diffraction (XRD), transmission electron microscopy (TEM) and nitrogen adsorption measurements. The catalytic activity of AlMCM-41 was evaluated in the soy oil degradation via TG. A comparative study of the thermal and catalytic degradation of soy oil was performed. This study shows a decrease in the activation energy and conversion temperatures of this process when AlMCM-4 is used as a catalyst.

1. Introduction

The silica-based MCM-41 is the main mesoporous material of the M41S family, discovered by researchers in Mobil Oil Corporation [1]. The formation of the MCM-41 phase occurs according to the liquid crystal templating (LCT) mechanism, in which SiO_4 tetrahedra interact with the surfactant template under hydrothermal conditions [1]. A typical preparation of MCM-41 requires a solvent, a template (surfactant molecule) and a silica source, whose nature and molar composition may influence several properties of the resulting materials such as: specific surface area (S_{BET}), pore volume (V_p), unit cell parameter (a_0), pore diameter (D_p) and the silica wall thickness (W_t). For instance, Araujo et al. [2] investigated MCM-41 materials with tailored pore diameter by means of surfactants having different chain lengths. Among MCM-41-type materials those containing Al species are of great importance for catalysis; the presence of tetrahedral Al in the siliceous framework generates Bronsted acid sites and

consequently, makes AlMCM41 an attractive catalyst. However, the synthesis of highly ordered AlMCM-41 is more difficult in comparison to MCM-41, which is purely siliceous material. Some papers have been published providing textural characterization of AlMCM-41 materials obtained by a variety of synthesis routes. In the present work, the synthesis of AlMCM-41 was carried out using pseudoboehmite as alumina source. An extensive characterization of AlMCM-41 has been made using powder X-ray diffraction (XRD), nitrogen adsorption and transmission electron microscopy (TEM). The presence of aluminum in the MCM-41 structure can generate surface acidity, which is necessary in acid catalyzed reactions [3]. Conversion of vegetable oils and animal fats, composed predominantly of triglycerides, via pyrolysis-type reactions represents a promising way for the production of renewable fuels and chemicals [4]. This work is focused on the synthesis, characterization and catalytic applications of AlMCM-41 materials in the pyrolysis of soy oil.

2. Experimental

The AlMCM-41 material was synthesized using silica gel (Merck, 95.5 %), sodium silicate (Riedel de Haeh, 63 % SiO_2 and 18 % Na_2O), cethyltrimethylammonium bromide (CTMABr, VETEC, 98 %), pseudoboehmite (Vista, 70 % Al_2O_3) and distilled water. These chemicals were mixed in order to obtain a synthesis gel with the following molar composition: 4.58SiO_2 : $0.485\text{Na}_2\text{O}$: 1 CTMABr: $0.057\text{Al}_2\text{O}_3$: $200\text{H}_2\text{O}$.

Typically, to obtain ~1.3 g of dry product the recipe involving the following amounts of reagents was used: (i) 0.861 g of silica, 0.787 g of sodium silicate and 8.362 g of distilled water were placed into a 50 mL Teflon beaker and stirred at 60 °C for 2 h; (ii) 0.026 g of pseudoboehmite was placed in 2.0 g of distilled water and stirred at 60 °C for 1 h. The solution (ii) was added to the solution (i) and stirred at 60 °C for 30 minutes. A solution (iii) prepared from 1.751 g of cethyltrimethylammonim bromide and 6.362 g of distilled water was added to the (i) + (ii) mixture and stirred for 1 h at room temperature. The hydrogels were placed into 45 mL teflon-lined autoclaves and heated at 100 °C for 1-4 days. The resulting material was filtered, washed with water and dried at 100 °C in an oven for 2 hours.

The as-prepared material was calcined at 450 °C for 1 h in N_2 atmosphere and then for 1 h in air at same temperature using dynamic flow of 100 mL min^{-1} . The temperature was increased from room temperature to 450 °C at a heating rate of 5 °C min^{-1} [3].

XRD measurements were carried out using CuK α radiation in the 2θ angle range from 1 to 10° with step of 0.02° , on Shimadzu XRD 6000 X-ray equipment. The specific surface area was determined from nitrogen adsorption isotherm according to the Brunauer-Emmett-Teller (BET) method [5] in the relative pressure range from 0.1 to 0.3. Pore size distributions were calculated according to Barrett-Joyner-Halenda (BJH) algorithm [6]. TEM measurements were performed using a Joel 2010 instrument with an electron beam accelerating voltage of 200 kV; the sample was dispersed ultrasonically in 2-propanol, and a drop of the suspension was deposited on a holey carbon copper grid.

Soy oil degradation experiments were performed on Mettler equipment, TGA/SDTA-851 model, using nitrogen as a carrier gas flowing at 25 mL min^{-1} . The samples (pure soy oil and pure soy oil + AlMCM-41 in 3:1 mass ratio) were heated from room temperature up to 900°C , at a heating rate of 5, 10 and $20^\circ\text{C min}^{-1}$. The model-free kinetics [3] was used to evaluate the kinetic parameters of thermal and catalytic soy oil decomposition.

3. Results and Discussion

XRD analysis of the AlMCM-41 sample (see Figure 1) revealed characteristic diffraction peaks for this material; namely (100), (110), (200), (210) and (300). The main interplanar spacing (d_{100}) was used to obtain the unit cell parameter a_0 . The value of a_0 represents the sum of the pore diameter (D_p) and the silica wall-thickness (W_s). The a_0 value evaluated on the basis of (100) XRD reflection was 4.75 nm. Nitrogen adsorption-desorption isotherm data were used to determine the specific surface area, pore volume and pore size distribution. The surface area has been obtained from adsorption data in the range of relative pressures from 0.05 to 0.3 by the Brunauer-Emmett-Teller (BET) method.

Nitrogen adsorption-desorption isotherm for the calcined AlMCM-41 sample are shown in Figure 2a. Type IV isotherm according to the IUPAC classification [7] was obtained indicating mesoporous structure of the sample studied. The isotherm represents three stages: adsorption at low pressures ($P/P_0 < 0.20$) accounts for a monolayer adsorption of nitrogen on the walls of the mesopores; this process is followed by multilayer formation and capillary condensation take place. As the relative pressure increases, the isotherm rises steeply (at a relative pressure of about 0.28), which is characteristic for the capillary condensation of nitrogen within mesopores, having a narrow pore size distribution. At higher relative pressures ($P/P_0 > 0.4$) multilayer adsorption on the outer surface of the particles (as well as capillary condensation in textural mesopores) occurs. The total surface area of the synthesized AlMCM-41,

calculated according to the BET method, was $870 \text{ m}^2 \text{ g}^{-1}$. The pore size distribution determined from the adsorption isotherm by the BJH method covered the pore diameter range of 20-600 Angstroms. As can be seen from Figure 2b, a very narrow distribution was obtained for the AIMCM-41 material, with a medium pore diameter of 3.14 nm and a mesopore volume of 0.51 cc/g.

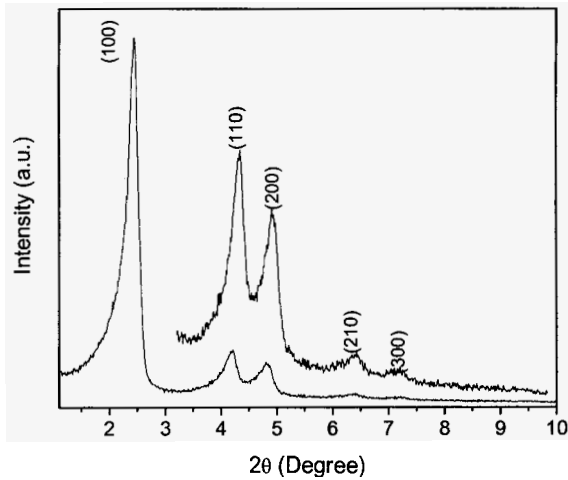


Figure 1. XRD powder patterns of the calcined AIMCM-41 material

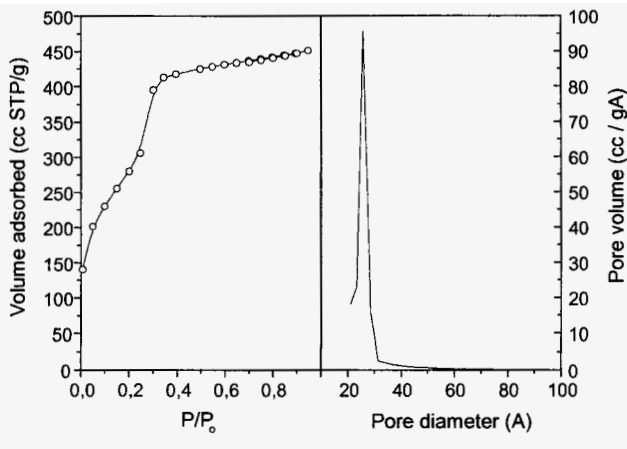


Figure 2. Nitrogen adsorption isotherm and the corresponding pore size distribution for the AIMCM-41 material studied.

Figure 3 shows a transmission electron microscopy image of the calcined AlMCM-41 sample. This image and XRD pattern show that the mesopores are hexagonally ordered. On the other hand, the uniform porosity revealed by TEM analysis is in line with a narrow pore size distribution determined from N₂ adsorption isotherm.

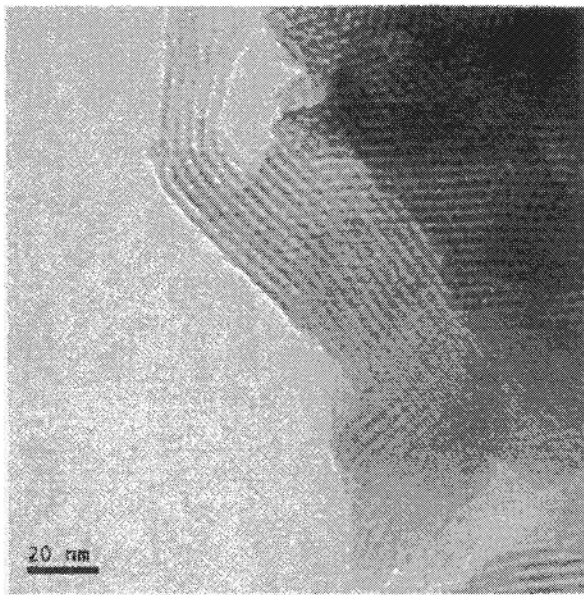


Figure 3. TEM image showing hexagonally ordered mesopores in the AlMCM-41 sample.

Figure 4 shows the comparative conversion curves obtained from thermogravimetric (TG) profiles of the thermal soy oil degradation and catalytic soy oil degradation over AlMCM-41. As can be seen from this figure the presence of AlMCM-41 decreased the temperature of oil degradation by ca. 50 °C. Typically, the catalysts used for this type of processes are acid oxide and molecular sieve-type catalysts. The reaction products are heavily dependent on the type of catalyst and reaction conditions; they can range from diesel-like fractions to gasoline-like fractions. The activation energy was evaluated by the model-free kinetics model, which gave apparent activation energy values of 250 and 190 kJ/mol for the thermal and catalytic degradation of soy oil, respectively.

This study shows that thermogravimetric technique is a simple and attractive technique to study the kinetics of catalyzed degradation of various organics.

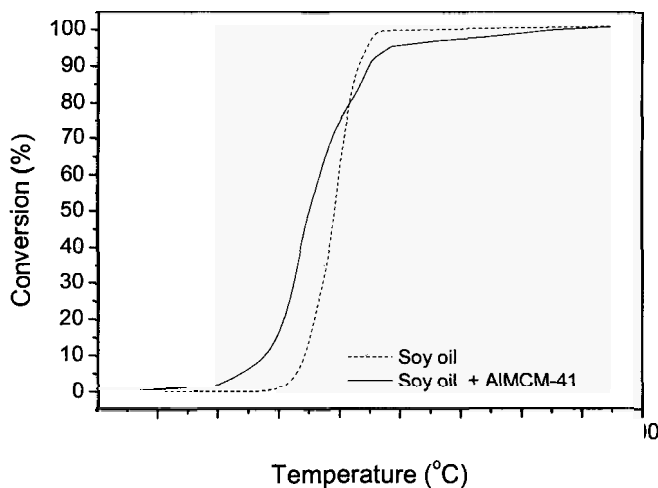


Figure 4. Conversion as of soy oil at different temperatures.

Acknowledgments

The authors acknowledge the support from Conselho Nacional de Desenvolvimento Científico e Tecnológico (Edital Universal, Proc. 472111/2006-0 / MCT/CNPq).

References

1. J. S. Beck, J. C. Vartuli, W. J. Roth, M. E. Leonowicz, C. T. Kresge, K. D. Schmitt, C. T. W. Chu, D. H. Olson, E. W. Sheppard, S. B. McCullen, Y. B. Higgins, I. L. Schelenker, *J. Am. Chem. Soc.* **114**, 10843 (1992).
2. A. S. Araujo, M. Jaroniec, *Thermochim. Acta* **345**, 173 (2000).
3. A. S. Araujo, V. J. Fernandes Jr., M. J. B. Souza, A. O. S. Silva, J. M. F. B. Aquino, *Thermochim. Acta* **413**, 235 (2004).
4. K. D. Maher, D. C. Bressler, *Biores. Technol.* **98**, 2351 (2007).
5. S. Brunauer, P. H. Emmett, J. Teller, *J. Am. Chem. Soc.* **60**, 309 (1938).
6. E. P. Barret, L. J. Joyner, P. Halenda, *J. Am. Chem. Soc.* **73**, 373 (1951).
7. K. S. Sing, D. H. Everett, R. A. W. Haul, L. Moscow, R. Apierotti, T. Rouquerol, T. Siemienew-ska, *Pure Appl. Chem.* **57**, 603 (1985).

BIODIESEL PRODUCTION BY HETEROGENEOUS CATALYSIS IN THE PRESENCE OF CaO SUPPORTED ON MESOPOROUS SILICA

MÔNICA C. G. ALBUQUERQUE, DIANA C. S. AZEVEDO,
CÉLIO L. CAVALCANTE JR.

*Grupo de Pesquisas em Separações por Adsorção (GPSA)
Dept. Eng. Química, Universidade Federal do Ceará –UFC Campus do Pici, bl. 709,
60455-760, Fortaleza-CE, Brazil*

INMACULADA JIMÉNEZ URBISTONDO, JOSÉ SANTAMARÍA GONZALEZ,
JOSEFA M. MÉRIDA ROBLES, ENRIQUE RODRÍGUEZ CASTELLON,
ANTONIO JIMENEZ LOPEZ, PEDRO MAIRELES TORRES

*Departamento de Química Inorgánica, Cristalografía y Mineralogía, Facultad de
Ciencias, Universidad de Málaga, Campus de Teatinos, 29071, Málaga, Spain*

In this work, a series of catalysts based on calcium oxide supported on mesoporous SBA-15 silica has been synthesized, characterized and evaluated in transesterification processes. Their textural and structural characterization has been carried out by using XRD, XPS, CO₂-TPD and N₂ adsorption. The catalytic activity was previously evaluated in the transesterification of ethyl butyrate with methanol, and then the most active catalyst was tested in the biodiesel production from castor oil. This family of basic catalysts is stable against lixiviation in the reaction medium.

1. Introduction

As energy demands increase and fossil fuel reserves are limited, research is increasingly directed towards alternative fuels that are environmentally more acceptable. Biofuels are liquid or gaseous fuels derived from renewable resources. The development and utilization of biofuels is promoted in several countries in order to decrease the emission of carbon dioxide from fossil fuels and mitigate air pollution, as well as to reduce the dependence upon imported energy, thus favoring domestic resources [1,2]. In this context, biodiesel is a clean and renewable fuel that consists of fatty acid methyl esters (FAME) or fatty acid ethyl esters (FAEE), derived from the transesterification of vegetable oil or fat with a monohydric alcohol in the presence of a catalyst.

Castor oil possesses an important potential among the available raw materials for biodiesel production [3]. Besides the advantage of being a native

growing plant in Brazil, castor plant is versatile concerning the climate and ground types. Castor oil is composed mainly of triglycerides of ricinoleic acid (90%) and oleic and linoleic acids (10%), the latter being non-hydroxylated fatty acids. Due to this particular chemical composition, castor oil becomes highly interesting for industrial purposes. Castor seeds are poisonous to humans and animals because they contain ricin, ricinine and certain allergens that are toxic [4].

The transesterification reaction can be catalyzed by strong liquid acid and soluble base catalysts. Typical biodiesel production involves an alkali-catalyzed process, but this brings undesired effects for lower cost high free fatty acid feed stocks, such as soap formation, thus requiring purification steps which are costly and technically difficult [5,6].

The use of heterogeneous catalysts in the transesterification would simplify greatly the technological process by facilitating the separation of the post-reaction mixture. Therefore, conventional homogeneous catalysts are expected to be replaced in the near future by environmentally friendly heterogeneous catalysts, mainly due to environmental constraints and simplifications in the existing process. At the laboratory scale, many different heterogeneous catalysts have been developed to catalyze the transesterification of vegetable oils [7-18].

Classic heterogeneous base catalysts, which contain either Lewis or Brønsted basic sites, have been the most extensively tested for the transesterification reactions of triglycerides, mainly alkaline earth metal oxides, hydroxides and alkoxides. Thus, Peterson and Scarrah [19] studied the use of CaO, ZnO and those loaded on Al₂O₃, SiO₂ and MgO in the methanolysis of rapeseed oil. Recently, several studies [16,20] have demonstrated the partial leaching of calcium oxide in the reaction medium, which could require additional steps to remove metal ions from biodiesel.

A significant progress in the field of mesoporous materials was the synthesis of SBA-15 [21], which is receiving increasing attention mainly due to its higher pore diameter and thermal stability associated to thicker pore walls, which allow its use in catalytic processes demanding high temperatures for catalyst activation or reaction [21-25]. CaO has also been incorporated to mesoporous silica to generate basic sites [26,27].

In the present study, a series of CaO supported on SBA-15 materials with different CaO loadings was prepared by using the incipient wetness impregnation method, characterized by X-ray diffraction, N₂ adsorption at 77 K, X-ray photoelectron spectroscopy and CO₂ temperature-programmed desorption (CO₂-TPD), and tested as catalysts in the transesterification of ethyl butyrate with

methanol. Finally, the most active catalyst was used in the biodiesel production from castor oil.

2. Experimental

2.1. Catalyst preparation

Chemicals were supplied by Aldrich and used as received. For the synthesis of SBA-15, 5 g of EO20-PO70-EO20 (Pluronic 123 from Aldrich) polymer was dissolved in 200 mL of a 0.4 M H₂SO₄ aqueous solution and stirred at room temperature for 1 day. Then, 0.2 g of NaOH and 197.3 mL of a sodium silicate aqueous solution were added, under vigorous stirring. The resulting solution was aged at room temperature for 5 days. The solid was filtered, washed with water, dried at 333 K, and calcined at 823 K for 6 h [28].

The SBA-15 support was impregnated with different amounts of calcium acetate by using the incipient wetness method in aqueous solutions. The amount of calcium oxide incorporated to the support, after drying in air at 333 K and calcination at 873 K for 6 hours, was ranged between 4 and 20 wt.%. Catalysts were labeled as SBA-nCaO, where n is the weight percentage of supported calcium oxide, as determined by ICP-AES.

2.2. Catalyst characterization

Powder XRD measurements were performed on a Siemens D5000 automated diffractometer, over a 2 θ range with Bragg-Brentano geometry using the Cu K α radiation and a graphite monochromator.

X-ray photoelectron spectroscopy (XPS) studies were performed with a Physical Electronics PHI 5700 spectrometer equipped with a hemispherical electron analyzer (model 80-365B) and a Mg-K α (1253.6 eV) X-ray source. High-resolution spectra were recorded at 45° take-off-angle by a concentric hemispherical analyzer operating in the constant pass energy mode at 29.35 eV, using a 720 mm diameter analysis area. Charge referencing was done against adventitious carbon (C 1s 284.8 eV). The pressure in the analysis chamber was kept lower than 5·10⁻⁶ Pa. PHI ACCESS ESCA-V6.0 F software package was used for data acquisition and analysis. A Shirley-type background was subtracted from the signals. Recorded spectra were always fitted using Gauss-Lorentz curves in order to determine more accurately the different binding energies.

N₂ adsorption-desorption isotherms at 77 K of catalysts calcined at 1073 K were obtained using an ASAP 2020 model of gas adsorption analyzer from Micromeritics, Inc., and samples were outgassed at 473 K and 1·10⁻² Pa, overnight before adsorption.

The basicity of catalysts was studied by temperature-programmed desorption using CO₂ as probe molecule. Catalysts (100 mg) were pretreated under a helium stream at 1073 K for 1 h (20 K min⁻¹, 100 mL min⁻¹). Then, temperature was decreased down to 373 K, and a flow of pure CO₂ (50 mL min⁻¹) was subsequently introduced into the reactor during 1 h. The TPD of CO₂ was carried out between 373 and 1073 K under a helium flow (10 K min⁻¹, 30 mL min⁻¹), and CO₂ was detected by an on-line gas chromatograph (Shimadzu GC-14A) provided with a TCD, after passing by an ice-NaCl trap to eliminate any trace of water.

2.3. Catalyst activity

Prior to the study of castor oil transesterification, the catalysts were evaluated in the transesterification of ethyl butyrate (Aldrich) with methanol (ultra pure, Alfa Aesar), for which several reaction parameters were optimized. This reaction was performed in a glass batch reactor with a water-cooled condenser, controlled temperature (333 K) and inert atmosphere (N₂). Before the reaction, the catalysts were activated at 1073 K for one hour (heating rate, 10 K/min) under a He flow. After cooling, the catalyst was quickly added to the reaction mixture. The reaction was stopped by submerging the reactor in an ice bath. The catalyst was separated by filtration, and the reaction products were analyzed in a gas chromatograph (Shimadzu GC model 14A) equipped with FID and a capillary silica fused SPB1 column. The catalytic activity was determined from the ethyl butyrate:methyl butyrate areas ratio.

Then, the most active catalyst was tested in the biodiesel production from castor oil, at a reaction temperature of 333 K, by using different methanol:oil molar ratio and catalyst concentration. The mixture was kept under an inert atmosphere of nitrogen. This three-phase system was stirred vigorously (1250 rpm) and refluxed. By the same procedure, the reaction was stopped by submerging the reactor in an ice bath. And the catalyst was separated by filtration. The conversion in the transesterification reaction was the parameter used to evaluate the catalyst activity. It was calculated by the mono, di and triglycerides production determinate by using a gas chromatograph (Varian GC model CP-3800), equipped with FID and a capillary CP-WAX 52CB column.

3. Results and Discussion

3.1. Catalysts characterization

The choice of a SBA-15 silica as support is due to its thick pore walls and long-range ordered structure, which give rise to a high thermal stability, as

evidenced by the presence in the XRD pattern, after calcination at 1073 K, of an intense reflection together with several low intensity peaks at low angle (Figure 1). The main diffraction peak is preserved after the incorporation of calcium oxide, indicating that the mesoscopic order is maintained after impregnation and thermal activation. Calcium oxide could be stabilized by acid-base interaction with the acidic surface of the SBA-15 silica, thus avoiding drastic structural transformations.

In the high angle region, the SBA-nCaO catalysts calcined at 1073 K show in their powder XRD patterns the typical reflections of cubic CaO (Figure 2). If the catalysts are not calcined at this temperature, the corresponding XRD patterns evidence the presence of calcite phase, CaCO_3 , and calcium hydroxide (inset of Figure 2). The narrow peaks observed in the XRD patterns point to the existence of large crystallites on the surface of the mesoporous support.

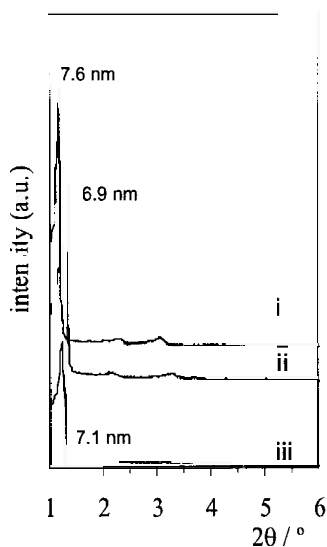


Figure 1. XRD patterns of a) SBA-15 calcined at (i) 823 K, (ii) 1073 K and (iii) the SBA-14CaO catalyst.

The CaO crystallite sizes determined from the Scherrer equation applied to the XRD data are in all cases higher than 50 nm. Therefore it is obvious that these large CaO particles are located outside of the mesopores, since the average pore diameter obtained from the N_2 adsorption-desorption isotherm is 4.2 nm (Table 1).

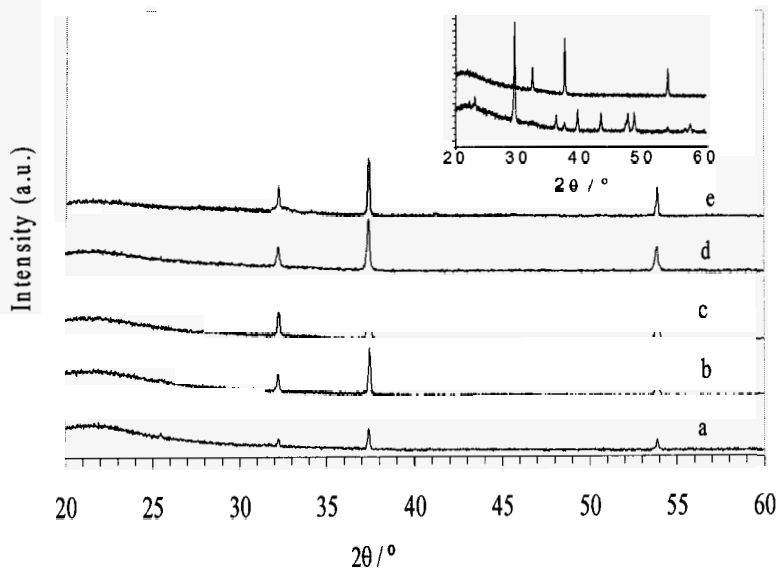


Figure 2. Powder X-ray diffraction patterns of CaO-supported SBA-15 catalysts calcined at 1073 K: (a) SBA-4CaO, (b) SBA-6CaO, (c) SBA-8CaO, (d) SBA-14CaO and (e) SBA-20CaO (inset: SBA-14CaO calcined at 823 (bottom) and 1073 K (top))

The XPS technique has been employed to get information about the surface characteristics of the CaO-based catalysts. In the C 1s region, signals are observed at 284.8, 287.2 and 289.6 eV, which can respectively be assigned to C-H, C-O and CO_3^{2-} groups, confirming the presence of calcium carbonate. Moreover, no significant variation of the binding energy (BE) values with the CaO loading were observed, pointing to a similar interaction between the active phase and the support along this series of catalysts. Moreover, this technique has allowed evaluating the degree of dispersion of the calcium species, not only on the silica surface but also in the inner region by performing a depth profile analysis after etching with an Ar^+ gun. The difference between the surface (XPS) and bulk Si/Ca atomic ratio (ICP-AES) values becomes more significant as the loading of CaO is lowered (more than 100% for SBA-4CaO), whereas they are very close for the samples with higher loadings. In the case of SBA-14CaO, both values are identical. This fact points to that CaO is uniformly distributed on the silica support, as corroborated from the analysis of different regions of the catalysts which give rise to similar surface Si/Ca atomic ratio, except for the samples with lower loading. The depth profile analysis of samples SBA-8CaO

and SBA-14CaO performed by etching with an Ar^+ gun reveals that calcium oxide is also filling the mesoporous network, as can be deduced from the evolution of the Si and Ca atomic concentrations as a function of the etching time (Figure 3). The data indicate that Ca percentages are barely modified after 10 minutes of treatment (40 nm of depth), and therefore it can be stated that the distribution of Ca into the siliceous SBA-15 support is uniform.

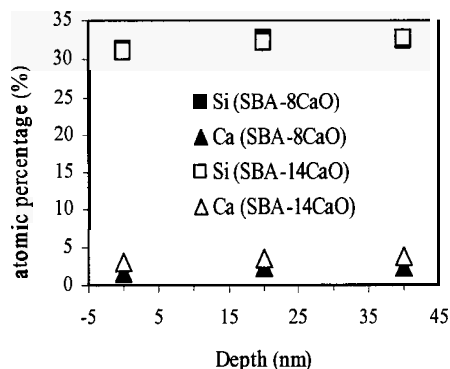


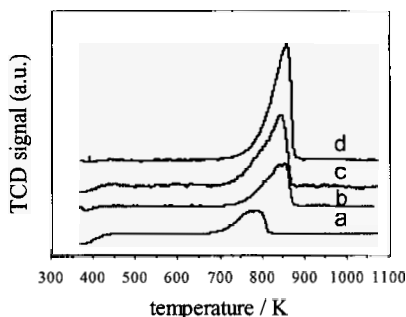
Figure 3. Evolution of the Ca and Si atomic concentrations as a function of the depth, after Ar etching.

The textural characteristics of the SBA-15 support and catalysts have been evaluated from the N_2 adsorption-desorption isotherms (Table 1). There are a drastic reduction of both specific surface area and pore volume values after the incorporation of calcium oxide on the SBA-15 support. This fact could be explained not only by the partial blocking of the porous network by the presence of large CaO crystallites, already detected by XRD, but also by the partial filling of pores as deduced by XPS. However, the destruction of the siliceous framework by both effects, interaction with the calcium species and thermal treatment at 1073 K, can be ruled out because the supported phase, CaO, can be completely removed from the catalyst by treatment with HCl aqueous solution. After this acid treatment, the typical XRD peaks of the SBA-15 support and its textural characteristics are observed again.

Thus, the catalyst with the lowest CaO loading, SBA-4CaO, shows a broad CO_2 desorption band extending from 700 until 800 K. By increasing the amount of CaO on the catalysts, this band becomes more intense and the more clearly defined desorption maximum is shifted towards higher temperatures, thus confirming the highest basicity of the SBA-14CaO catalyst.

Table 1. Textural parameters of the SBA-15 support and catalysts calcined at 1073 K

Catalyst	S_{BET} (m^2/g)	V_{p} (cm^3/g)	d_{p} (av) (nm)
SBA-15	413	0.370	4.2
SBA-4CaO	34.0	0.038	3.0
SBA-6CaO	24.2	0.028	3.0
SBA-8CaO	21.8	0.042	4.8
SBA-14CaO	7.4	0.019	5.4

Figure 4. Temperature-programmed desorption profiles of CO_2 over (a) SBA-4CaO, (b) SBA-6CaO, (c) SBA-8CaO, (d) SBA-14CaO catalysts.

The CO_2 temperature-programmed desorption plots are displayed in Figure 4. In all cases, a broad desorption band is observed between 700 and 900 K, which intensity and temperature depend on the CaO content.

The activity in transesterification reactions of calcium oxide supported on SBA-15 has been evaluated by initially choosing the reaction of ethyl butyrate with methanol as model reaction. The experimental conditions were: reaction temperature: 333 K, inert atmosphere (nitrogen), stirring rate of 1250 rpm and 1 h reaction time.

The study of the catalytic performance in the transesterification of ethyl butyrate with methanol of SBA- n CaO catalysts as a function of the CaO loading reveals that an increment until 20 wt% does not increase the transesterification activity (Figure 5). This fact could be explained by the formation of larger CaO particles, without increasing the surface of the active phase accessible to reactants, as indicated from the data obtained by CO_2 -TPD, where the highest desorption value is found for SBA-14CaO. It has been previously pointed out that a thermal treatment at 1073 K is necessary to transform the CaCO_3 into CaO. Without activation, all catalysts are inactive in the transesterification of ethyl butyrate with methanol, and the maximum conversion is attained after activation at 1073 K.

Concerning the reaction temperature, it is found that an increase in temperature favours the conversion of ethyl butyrate, and taking into account that the boiling point of methanol is 337.7 K, a temperature slightly lower than this, 333 K, has been chosen to carry out all experiments. Moreover, a stirring rate of 1250 rpm rules out the existence of external transport limitations, since lower values give rise to lower conversion and a value of 1500 rpm does not increase the activity (Figure 5).

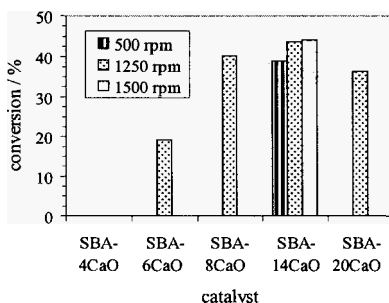


Figure 5. Conversion in the transesterification of ethyl butyrate (BE) with methanol as a function of the CaO loading and the stirring rate (SBA-14CaO) (activation temperature= 1073 K, amount of catalyst= 62 mg, methanol:ethyl butyrate molar ratio= 4:1, reaction temperature= 333 K, reaction time= 1 h).

A key aspect of the present work was to evaluate the degree of lixiviation of the active phase in this family of CaO-based catalysts since previous studies have shown that a fraction of bulk calcium oxide is dissolved in the methanolic solution [16,20], and the objective of using supported CaO catalysts was to stabilize this active phase. The experimental procedure employed to evaluate the contribution of the homogeneous process due to the presence of CaO in solution consisted in putting in contact the catalyst with methanol for 1 h at 333 K under nitrogen. Then, the catalyst was removed by filtration and methanol was added to ethyl butyrate and maintained at the same temperature, 333 K, for 1 h. If catalyst lixiviation takes place, conversion will be observed due to the homogeneous contribution.

The conversion values for the different supported CaO catalysts were in all cases negligible, thus pointing to the stabilization of the active phase on the SBA-15 siliceous support, which prevents its lixiviation. However, when bulk CaO is used, a conversion of 8.5% was measured.

The study of biodiesel production from castor oil was accomplished by using SBA-14CaO, which has demonstrated to be the most active catalyst in the transesterification of ethyl butyrate with methanol.

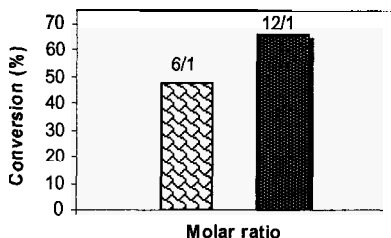


Figure 6. Conversion of the SBA-14CaO in the transesterification of castor oil with methanol for two different methanol : castor oil molar ratio (activation temperature= 1073 K, stirring rate= 1250 rpm, amount of catalyst= 1%, reaction temperature= 333 K, reaction time= 1 h).

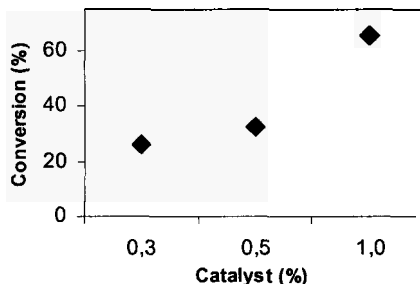


Figure 7. Conversion of the SBA-14CaO in the transesterification of castor oil with methanol with different catalyst amount (methanol : castor oil molar ratio=12/1, activation temperature= 1073 K, stirring rate= 1250 rpm, reaction temperature= 333 K, reaction time= 1 h).

Firstly, the influence of the methanol:castor oil molar ratio on the conversion was evaluated (Figure 6). Two values, 6:1 and 12:1, were tested, and according to the literature [29,30], the largest conversion to methyl esters (ME) was obtained for the highest methanol:triglyceride (TG) molar ratio used (12:1), i.e. four times the stoichiometric ratio, since 1 mole of TG reacts with 3 moles of methanol to give 3 moles ME. Thus, under the same experimental conditions (activation temperature= 1073 K, stirring rate= 1250 rpm, amount of catalyst= 1 wt.%, reaction temperature= 333 K, reaction time= 1 h), the best conversion was observed for a molar ratio of 12:1 (Figure 6).

Finally, the amount of catalyst was also varied, and it is seen in Figure 7 that an increase in conversion is achieved when 1 wt% of catalyst is employed, by using a methanol:TG molar ratio 12:1, catalyst activation temperature 1073 K, stirring rate 1250 rpm and reaction temperature 333 K. Thus, the maximum biodiesel yield from castor oil was 66%.

4. Conclusions

In the present study, catalysts based on calcium oxide supported on mesoporous SBA-15 silica have been synthesized, characterized and tested as basic catalysts in transesterification processes for the synthesis of methyl esters, such as those presented in biodiesel. This family of basic catalysts is stable against lixiviation in methanol. The catalyst that showed the best performance in the transesterification of ethyl butyrate with methanol, chosen as a model reaction, SBA-14CaO, was used in the transesterification of castor oil for biodiesel production. Several parameters, such as catalyst concentration and methanol:castor oil molar ratio, have been optimized in order to achieve the maximum biodiesel yield.

In the methanolysis of vegetable oil, the molar ratio is a determinant parameter, and the highest conversion (66%) was obtained with a catalyst concentration about 1 wt.% and a 12:1 molar ratio. Therefore, this family of CaO-based catalysts is very promising for biodiesel production from castor oil, under a pure heterogeneous catalytic process.

Acknowledgments

The authors are grateful to financial support from Spanish Ministry of Education and Science (ENE2006-15116-C04-02 project), Junta de Andalucía (PO6-FQM-01661) and to the Brazilian Ministry of Education by CAPES/MECD 084/05, for the financial support to M.C.G. Albuquerque.

References

1. B.K. Barnwal, M.P. Sharma, *Renew Sust Energ Rev.* **9**, 363 (2005).
2. D. Fabbri, V. Bevoni, M. Notari, F. Rivetti, *Fuel* **86**, 690 (2007).
3. P.M. Ndiaye, E. Franceschi, D. Oliveira, C. Dariva, F.W. Tavares and J. V. Oliveira, *J. Supercritical Fluids* **37**, 29 (2006).
4. D.S. Ogunniyi, *Bioresource Technology* **97**, 1086 (2006).
5. A. Demirbas, *Energy Convers. Manage* **44**, 2093 (2003).
6. F.R. Ma and M.A. Hanna, *Bioresour. Technol.* **70**, 1 (1999).
7. D.E. López, K. Suwannakarn, D.A. Bruce and J.G. Goodwin Jr., *J. Catal.* **247**, 43 (2007).
8. S. Furuta, H. Matsuhashi and K. Arata, *Chem. Commun.* **5**, 721 (2004).
9. E. Lotero, Y. Liu, D.E. López, K. Suwannakarn, D.A. Bruce and J.G. Goodwin Jr., *Ind. Eng. Chem. Res.* **44**, 5353 (2005).
10. S. Gryglewicz, *Bioresour. Technol.* **70**, 249 (1999).
11. L. Bournay, D. Casanave, B. Delfort, G. Hillion and J.A. Chodorge, *Catal. Today* **106**, 190 (2005).

12. D.G. Cantrell, L.J. Gillie, A.F. Lee and K. Wilson, *Appl. Catal. A* **287** 183 (2005).
13. W. Xie and H. Li, *J. Mol. Catal. A* **255**, 1 (2006).
14. C.R.V. Reddy, R. Oshel and J.G. Verkade, *Energy Fuels* **20**, 1310 (2006).
15. W. Xie, X. Huang and H. Li, *Bioresour. Technol.* **98**, 936 (2007).
16. M.L. Granados, M.D.Z. Poves, R. Mariscal, F.C. Galisteo, R.M. Tost, J. Santamaría and J.L.G. Fierro, *Appl. Catal. B* **73**, 327 (2007).
17. E. Leclercq, A. Finiels and C. Moreau, *J. Am. Oil Chem. Soc.* **78**, 1161 (2001).
18. G.J. Suppes, K. Bockwinkel, S. Lucas, J.B. Mason and J.A. Heppert, *J. Am. Oil Chem. Soc.* **78**, 139 (2001).
19. G. R. Peterson and W. P. Scarrah, *J. Am. Oil Chem. Soc.* **61**, 1593 (1984).
20. H. Zhu, Z. Wu, Y. Chen, P. Zhang, S. Duan, X. Liu and Z. Mao, *Chinese J. Catal.* **27**, 391 (2006).
21. D. Zhao, J. Feng, Q. Huo, N. Melosh, G.H. Fredrickson, B.F. Chmelka and G.D. Stucky, *Science* **279** (1998) 548.
22. Y. Segura, P. Cool, P. Kustrowski, L. Chmielarz, R. Dziembaj and E.F. Vansant, *J. Phys. Chem. B* **109** (2005) 12071.
23. Y.M. Wang, Z.Y. Wu, Y.L. Wei and J.H. Zhu, *Micropor. Mesopor. Mater.* **84** 127 (2005).
24. Y.F. Han, F. Chen, Z.Y. Zhong, K. Ramesh, E. Widjaja and L.W. Chen, *Catal. Commun.* **7**, 739 (2006).
25. D.P. Sawant, A. Vinu, S.P. Mirajkar, E. Lefebvre, K. Ariga, S. Anandan, T. Mori, C. Nishimura and S.B. Halligudi, *J. Mol. Catal. A* **271** (2007) 46.
26. Z.Y. Wu, Q. Jiang, Y.M. Wang, H.J. Wang, L.B. Sun, L.Y. Shi, J.H. Xu, Y. Wang, Y. Chun and J.H. Zhu, *Chem. Mater.* **18**, 4600 (2006).
27. Z. Gabelica, M. Shibata, H. Hotta, T. Suzuki and S. Valange, *Studies in Surface Science and Catalysis* **140**, 279 (2001).
28. M. Gómez-Cazalilla, J.M. Mérida-Robles, A. Gurbani, E. Rodríguez-Castellon and A. Jimenez-Lopez, *J. Solid State Chem.* **180**, 1130 (2007).
29. B. Fredman, E.H. Pryde and T.L. Mounts, *J. Am. Oil Chem. Soc.* **61**, 1638 (1984).
30. G. Vicente, A. Coteron, M. Martinez and J. Aracil, *Industrial Crops and Products* **8**, 29 (1998).

POLYMERIC ACTIVATED CARBON-SUPPORTED VANADIUM AND MAGNESIUM OXIDES FOR STYRENE PRODUCTION

RAPHAEL DIAS HOLTZ, MARIA DO CARMO RANGEL *

*Grupo de Estudos em Cinética e Catálise, Instituto de Química, Universidade Federal da Bahia. Campus Universitário de Ondina, Federação. 40 170-280. Salvador-BA, Brazil.
E-mail: mcarmov@ufba.br*

SÉRGIO BOTELHO DE OLIVEIRA

*Grupo de Estudos em Cinética e Catálise, Instituto de Química, Universidade Federal da Bahia. Campus Universitário de Ondina, Federação. 40 170-280. Salvador-BA, Brazil.
Departamento de Química, Centro Federal de Educação Tecnológica de Goiás. 74055-110, Goiânia, Goiás, Brazil*

The preparation and characterization of activated carbon obtained from sulfonated styrene-divinylbenzene copolymer were described in this work. The effect of vanadium and magnesium on their activity and selectivity towards styrene was also studied to find new catalysts for ethylbenzene dehydrogenation carried out without steam, to produce styrene. It was found that the samples were more active and selective than a commercial hematite based catalyst. Both magnesium and vanadium improved the catalysts but vanadium is a more efficient promoter than magnesium. This metal alone is able to improve the activity and selectivity of the catalyst and produced the most efficient catalyst. This was related to its dehydrogenation function.

1. Introduction

Styrene is one of the most important monomers of the modern petrochemical industry [1], being used in the production of polystyrene, acrylonitrile-butadiene-styrene resin (ABS) and of a great variety of polymers [2]. Another important application is in the styrene-butadiene latex production [1].

The main industrial route used for styrene production is the ethylbenzene dehydrogenation, responsible for more than 90% of the world production [3]. The process consumes great amount of energy and is carried out under overheated steam excess [4,5]. The reaction is performed industrially on iron oxide base catalysts (hematite) containing cerium, chromium and potassium

* To whom correspondence should be addressed.

oxides. The commercial catalyst presents several advantages, such as resistance against impurities and low cost, but deactivates with time due to the loss of potassium that migrates to the pellet center or goes out from the reactor [5,6]. Moreover, this catalyst contains chromium, which can cause damages to human health and to the environment.

A promising alternative is the use of activated carbon based catalysts. These materials have been widely studied for the oxidative dehydrogenation of ethylbenzene and showed high performance due to their textural properties [7] and to the surface composition that presents functional groups, mainly quinones, responsible for its catalytic activity [8].

Activated carbons with high surface area and pore volume can be produced from a large variety of carbonaceous materials. Among them the spherical polymeric activated carbon, prepared from the polymer pyrolysis at high temperatures and controlled atmosphere, is particularly attractive [9]. This material can be obtained in the form of regular spheres with high surface specific area, high adsorption capacity, abrasion resistance and adequate mechanical properties [10]. Other advantages of activated carbons include their acid-base properties and low diffusional resistance to liquids and gases, when used in fixed bed reactors. Moreover, these solids allow the easy metal incorporation on their surface as well as on the surface of precursor resin [11].

On the other hand, some studies about the ethylbenzene dehydrogenation in carbon dioxide presence showed high conversion of ethylbenzene and selectivity to styrene over vanadium and magnesium based catalysts [12,13].

In this context, this work describes the synthesis of activated-carbon supported vanadium and magnesium catalysts and the evaluation of their catalytic activity in ethylbenzene dehydrogenation for styrene synthesis in steam absence. The activated carbon was produced by pyrolysis of the sulfonated styrene-divinylbenzene copolymer.

2. Experimental

2.1. Preparation of the catalysts

The styrene-divinylbenzene copolymer was synthesized through polymerization in aqueous suspension. Inert diluents were used (heptane and toluene) for pores formation, leading to a macroporous type structure.

In the preparation of the aqueous phase, a mixture of gelatin, hydroxiethylcellulose and sodium chloride was used as suspension agent. After the dissolution of the two agents of suspension, the solutions were mixed and the

sodium chloride was added to them. The ratio of aqueous to organic phase was kept at 4:1 (v/v).

In the preparation of the organic phase, the benzoin peroxide was dissolved in a mixture of styrene and divinylbenzene with a molar ratio of 15/85 (organic phase) at room temperature, under stirring. Toluene and heptane were then added and kept under stirring.

The organic phase was added to a balloon equipped with magnetic stirrer, reflux condenser, nitrogen injector and thermometer, containing the aqueous phase under agitation at room temperature. The emulsion was kept under stirring for 10 min. The reaction mixture was then heated up to 60 °C, under stirring (500 rpm) for 24 h, being later cooled and the copolymer spheres were separated for filtration. The copolymer was transferred to a beaker containing distilled water, rinsed and heated at 50 °C, for 1 h and filtered. This procedure was repeated using ethanol until the solvent filtered was completely soluble in water. After that, the resin was dried at 70 °C, for 24h. Only the spheres with size range between 125 - 250 μm were used in this work.

In the sulfonation of the styrene-divinylbenzene copolymer, the dry resin was placed in contact with concentrated sulfuric acid in a beaker and the mixture was heated up to 70 °C, for 30 min. Dichloroethane was then added to the mixture. After 4 h, the resin was washed with the reaction mixture diluted with 2% of distilled water. The ratio of dilution was increased gradually, starting at 2% followed by 5, 10, 20, 30% up to 100% dilution.

The thermal treatment consisted of heating the sulfonated copolymer at 300 °C at room atmosphere for 2 h, followed by carbonization at 900 °C under nitrogen flow, for 3 h. The activation was carried out at 800 °C for 2 h, under flow of nitrogen saturated with steam (AC Sample). All heatings were carried out at a rate of 10 °C min⁻¹, intercalated with cooling until room temperature.

In the adsorption of vanadium and magnesium, aqueous solutions of ammonium metavanadate in oxalic acid (5 g.L⁻¹ of vanadium) and magnesium nitrate (0.5 g.L⁻¹ of magnesium) were used. The activated carbon (Sample AC) was dispersed in the metallic solutions and kept for 24 h at room temperature, thus generating samples with different metals. After that, the samples were filtered and heated at 60 °C. The solids obtained were calcined 600 °C under nitrogen flow for 1 h, at a rate of 10 °C min⁻¹. The nominal concentrations of the metals were 0.5% Mg and 5%V.

2.2. Characterization of the catalysts

The scanning electronic microscopy analysis of the samples was performed using JEOL T 330 equipment connected to EDS detection system. The thermal stability of activated carbon was evaluated on the basis of thermogravimetric curves obtained for Sample AC using Mettler Toledo TGA/SDTA 851E equipment.

The concentration of vanadium and magnesium in the catalysts was determined by atomic absorption spectrometry in a Perkin-Elmer 306 apparatus. Around 0.1 g sample was heated in an erlenmeyer containing 10 mL of concentrated nitric acid and boiled for 1 h. The sample was, then, filtered, transferred to a 100 mL volumetric balloon and filled with distilled water, being analyzed later.

The crystalline structure of vanadium and magnesium in the samples was characterized by X-ray diffraction, in a Shimadzu XRD6000 equipment, in a range of $2\theta = 10$ to 80 degrees. The textural properties and the specific surface area (BET) were measured by nitrogen adsorption at $-196\text{ }^{\circ}\text{C}$ using Micromeritics ASAP 2020 equipment. In each analysis, 0.15 to 0.20 g of the sample was used. After the removal of the water present in the pores, using vacuum heating, the solid was placed in contact with gaseous nitrogen for the determination of the adsorption/desorption isotherms.

2.3. Evaluation of the catalysts

In the catalytic evaluation of solids, around 0.300 g of the material was conditioned in a microreactor of fixed stream bed, operating the $530\text{ }^{\circ}\text{C}$ and 1 atm. The reactor with the catalyst was heated under nitrogen flow (85 mL/min) up to the reaction temperature. The nitrogen flow was, then, deviated for the saturator with ethylbenzene at $77\text{ }^{\circ}\text{C}$. The stream from the saturator was then fed to the reactor. The effluent gaseous formed was continuously monitored collecting fractions at intervals of 30 min, in a condenser at $0\text{ }^{\circ}\text{C}$. The organic phase was analyzed by gaseous chromatography, using a Varian chromatograph 3600-X with flame ionization and thermal conductivity detectors.

3. Results and Discussion

The catalysts showed particles as regular spheres, with sizes which vary from 50 to 200 μm , as shown in Fig. 1(a). The decrease in the particle size is due to the volume contraction caused by successive thermal treatments. The scanning electronic microscopy analysis of V-Mg/AC sample did not show any metallic

agglomerate on the surface. From the thermal analysis, Fig. 1(b), it was verified that the polymeric activated carbon showed a small weight loss (1 %) at low temperatures and high thermal stability at higher temperature up to around 600 °C. Therefore, the active carbon is stable at the reaction temperature (530 °C).

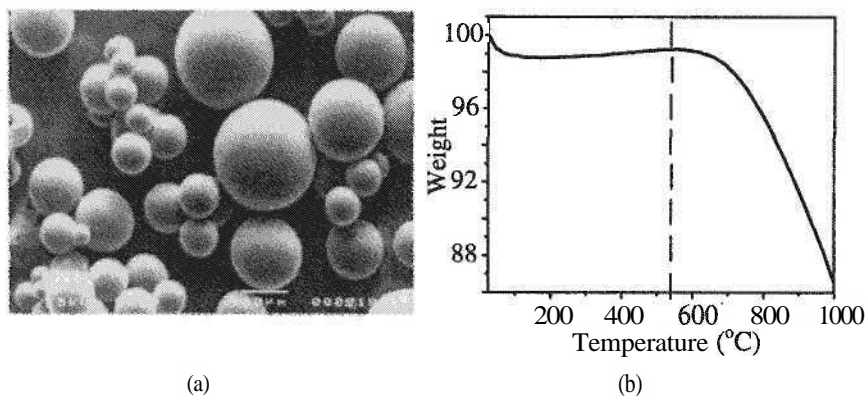


Figure 1. (a) Scanning electron micrograph of the V-Mg/AC sample (150 x); (b) Thermogravimetric curve of the AC sample obtained by pyrolysis of sulfonated styrene-divinylbenzene copolymer.

The amounts of vanadium and magnesium were close to the expected values, as shown in Table 1. However, no diffraction peak related to magnesium compound was noted, probably due to its low concentration in solids. The two amorphous halos at $2\theta = 22$ and 43° , characteristic of the activated carbon [14], were shown in the samples diffractograms without significant alterations (Fig. 2). All samples containing vanadium showed X-ray diffraction peaks typical of vanadium trioxide [15]. The V/AC sample showed the peak at $2\theta = 48^\circ$, while in the V-Mg/AC curve it appeared at $2\theta = 36^\circ$. All samples showed broad peaks which are typical of activated carbon.

Table 1. Concentrations of vanadium and magnesium in the solids.

Sample	V (% m/m)	Mg (% m/m)
AC	-	-
V/AC	5.03	-
Mg/AC	-	0.44
V-Mg/AC	4.56	0.42

The specific surface area and pore volume of AC sample decreased with the adsorption of vanadium or magnesium (Table 2) and this effect was stronger in the vanadium-containing samples. This can be assigned to the higher amount of vanadium as compared to magnesium. The micropore area, as well as the

micropore volume, also showed reduction due to the metals adsorption while the pore diameter did not suffer significant variation.

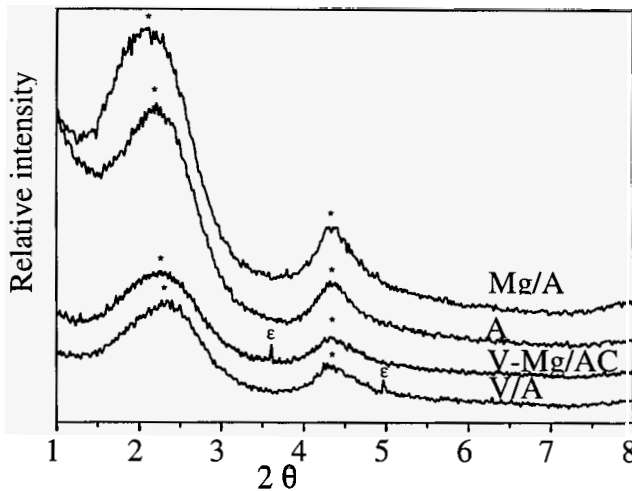


Figure 2. X-ray diffractograms of the samples. (*) activated carbon and (ϵ) V_2O_3 phase.

Table 2. Textural properties of the activated carbon before and after the metallic adsorption.

Sample	Sg_{BET} ($m^2 \cdot g^{-1}$)	Sg_{micro} ($m^2 \cdot g^{-1}$)	Pore volume BJH ($cm^3 \cdot g^{-1}$)	Micropore volume (<i>t</i> -plot) ($cm^3 \cdot g^{-1}$)	Pore diam. (nm)
AC	611	437	0.60	0.23	13
V/AC	450	312	0.46	0.16	13
Mg/AC	587	421	0.56	0.22	13
V-Mg/AC	432	309	0.43	0.16	14

Figure 3 shows the adsorption isotherms of the AC containing or not vanadium and magnesium. It was noticed that the curves are similar to II or IV Type with associated micropores [16]. The isotherms were similar among themselves, indicating that the incorporation of vanadium and magnesium, and the further heating, had not significantly modified the porous structure of the material. The curves of pores distribution, presented in Fig. 4, showed mesoporous domain between 10 and 30 nm, not only for the activated carbon (AC Sample) but also for solids containing metals. These curves indicate that the addition of vanadium and/or magnesium, followed by calcination at 600 °C under nitrogen flow for 1 h, did not modify the average solid pore size. It was verified that the higher the concentration of the metal added in the activated carbon, the lower average pore

volume. These results suggest that the added metal oxides are present outside the porous system of the activated carbon and serves as ballasts decreasing both the specific surface area and the pore volume of the catalysts.

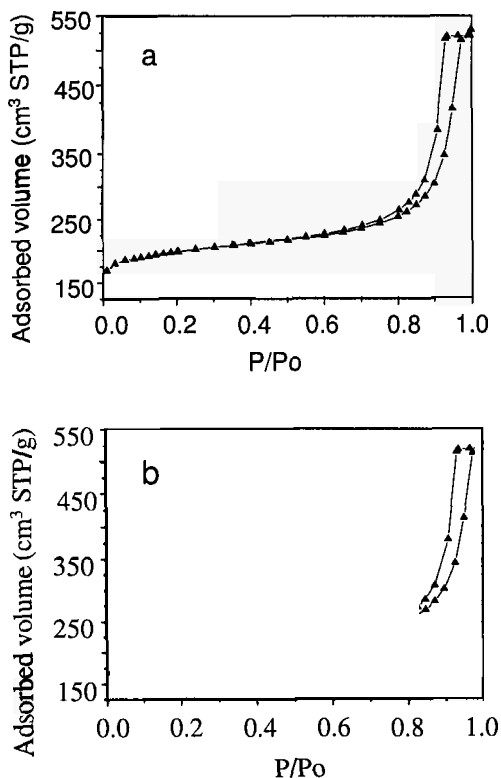


Figure 3. Adsorption and desorption isotherms of nitrogen at $-196\text{ }^{\circ}\text{C}$: (a) Sample AC; (b) Mg/AC (●), V/AC (■) e V-Mg/AC (○).

The ethylbenzene conversion and styrene selectivity, after 7:30 h of reaction, are presented in Table 3. Figure 5 represents the curves of ethylbenzene conversion as a function of reaction time. A commercial hematite based catalyst, doped with potassium and chromium oxides, showed an ethylbenzene conversion of 5% after 7:30 h during the reaction carried out in steam absence. The same catalyst carried out in steam presence showed a conversion of 12%. All the synthesized catalysts presented conversion higher than the commercial catalyst while the selectivity values were similar. The activated carbon (AC sample)

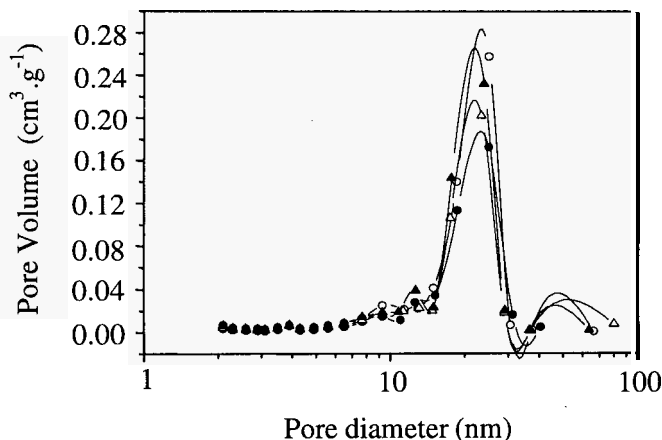


Figure 4. Pore distribution curves of the obtained catalysts: (○) AC; (▲) Mg/AC; (Δ) V/AC and (●) V-Mg/AC.

Table 3. Ethylbenzene conversion and styrene selectivity on the catalysts after 7:30 h reaction.

Catalysts	Conversion (%)	Selectivity (%)
AC	17	95
V/AC	35	98
Mg/AC	22	97
V-Mg/AC	32	99
Commercial (steam absence)	5	98
Comercial (steam presence)	12	98

showed the lowest value of selectivity, probably due to the presence of acidic sites on the solid surface, mainly quinones [9], which are active in the ethylbenzene dehydrogenation, however presenting low selectivity to styrene. The addition of magnesium in the activated carbon caused a small increase in the values of conversion and selectivity, probably due to neutralization of the acidic sites of the solid surface.

On the other hand, the addition of vanadium improved the catalytic properties of activated carbon, by increasing the activity and the selectivity to styrene. The increase on the activity can be assigned to a catalytic action of vanadium, a well-known dehydrogenation catalyst [12] while the increase of the selectivity can be associated to the coverage of some acidic sites by this metal.

From these results it can be concluded that there is no advantage in using magnesium in these catalysts, since vanadium alone is able to produce highly active and selective catalysts. The V/AC sample led to the highest value of

ethylbenzene conversion, around 35%, after 7:30 h reaction working in steam absence. This corresponds to three times the value of conversion showed by the commercial catalyst in steam presence, representing a great economy to the process energy. The fact that the catalyst with lower amount of vanadium and magnesium absence (V/AC) presents the highest conversion values is an advantage, besides the synthesis of the catalyst to be most economic.

4. Conclusions

Activated carbon, obtained from pyrolysis of the sulfonated styrene-divinylbenzene copolymer, is presented as a promising catalyst to ethylbenzene dehydrogenation to produce styrene, due its textural and catalytic properties. It

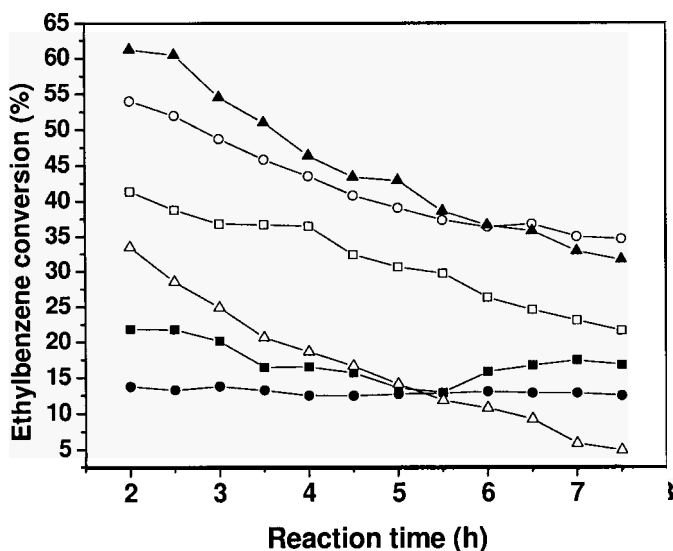


Figure 5. Ethylbenzene conversion as function of reaction time in ethylbenzene conversion at 530 °C on the catalysts: (■) AC; (□) Mg/AC; (○) V/AC; (▲) V-Mg/AC; (△) Commercial water vapor absence and (●) Commercial with water vapor.

is more active than a commercial catalyst, based on iron oxide. The addition of vanadium improved the catalyst even more, by increasing the activity and the selectivity to styrene. This can be assigned to an action of vanadium by

catalyzing the reaction and also by covering the acidic sites of the activated carbon, which are active to benzene and toluene, the main subproducts.

The vanadium-containing catalyst led to 35% of ethylbenzene conversion, about three times the value showed for the commercial catalyst evaluated in the steam presence, thus being the most promising one. Besides the fact that all the synthesized catalysts presented higher conversions than the commercial catalyst, the process do not use heated steam, which represents a great energy economy to the process.

Acknowledgements

RDH acknowledges CAPES for his fellowship. The authors acknowledge CAPES and CNPq for the financial support.

References

1. G. R Meima; P. G. Menon. *Applied Catal. A* 212, 239–245 (2001).
2. M. Baghalha; O. Ebrahimpour. *Applied Catal. A* 326, 143–151 (2007).
3. A. Kotarba; W. Rozek; I. Serafim; Z. Sojka. *Journal of Catalysis* 247, 238–244 (2007).
4. M. Sugino; H. Shimada; T. Turuda; H. Miura; N. Ikenaga; T. Suzuki. *Applied Catal.*, 121, 125 (1995).
5. Lee, E. H.; *Catal. Rev.*, 8, 285 (1963).
6. Li, W. Y.; Lettman, C.; Maier, W.F. *Catal. Lett.*, 69, 181 (2000).
7. M. F. R. Pereira; J. J. M. Orfão; J. L. Figueiredo. *Colloids Surf. A* 241(1-3), 165 (2004).
8. M. F. R. Pereira; J. L. Figueiredo; J. J. M. Órfão; P. Serp; P. Kalck; Y. Kihn. *Carbon*, 42, 2807 (2004).
9. K. Laszló, A. Bota, L. G. Nagy. *Carbon* 38, 1965-1976 (2000).
10. M. F. R. Pereira; J. J. M. Órfão; J. L. Figueiredo. *Carbon* 40, 2393–2401 (2002).
11. B. Li; Y. Ren; Q. Fan; A. Feng; W. Dong. *Carbon* 42, 2669 (2004).
12. Y. Sakurai; T. Suzaki, N. Ikenaga, T. Suzuki. *Applied Catal. A* 192, 281–288 (2000).
13. Y. Sakurai; T. Suzaki; K. Nakagawa; N. Ikenaga; H. Aota; T. Suzuki. *Journal of Catalysis* 209, 16–24 (2002).
14. A. Oya; H. Marsh. *Journal of Material Science* 17, 309–322 (1982).
15. *JCPDS 84-0319* (1997).
16. P. A. Webb and C. Orr, *Analytical Methods in Fine Particle Technology*, Micromeritics Instruments Cooperation, Norcross, p. 58 (1997).

TWO-STEP SYNTHESIS PROCEDURE OF BETA ZEOLITES: MESOPOROSITY AND PERFORMANCE AS ACID CATALYSTS

SAULO DE TARSO FIGUEIREDO GRECCO, PAULO SÉRGIO SANTANA NOBRE
*Grupo de Estudos em Cinética e Catálise, Instituto de Química, Universidade Federal da
Bahia, Campus Universitário de Ondina, Federação. 40170-290. Salvador, Ba, Brazil*

ERNESTO ANTÔNIO URQUIETA-GONZÁLEZ
*Departamento de Engenharia Química, Universidade Federal de São Carlos.
13565-905 São Carlos, São Paulo, Brazil*

MARIA DO CARMO RANGEL*
*Grupo de Estudos em Cinética e Catálise, Instituto de Química, Universidade Federal da
Bahia, Campus Universitário de Ondina, Federação. 40170-290. Salvador, Bahia,
Brazil. *E-mail: mcarmov@ufba.br*

The reactions of toluene with trimethylbenzene are important routes to produce benzene and xylenes, which are high value chemicals used as starting materials for many industrial processes. The commercial process uses large pore zeolites which, however, deactivate with time, mainly due to coke formation. In order to find new catalysts for these reactions, beta zeolites with different SAR were synthesized by a two-step procedure and evaluated in the reaction of the toluene with 1,2,4-trimethylbenzene. It was verified that the used procedure allowed to prepare beta catalysts, which were more active and stable than a commercial mordenite catalyst. In a first step the synthesis conditions led to the formation of crystalline beta seeds, which subsequently were mesostructured in the presence of CTAB. During mesostructuring the surfactant micelles hamper the seed growing and consequently generating a solid constituted by a poor ordered mesophase and small beta crystals, responsible for the interparticle mesoporosity determined by nitrogen sorption measurements.

1. Introduction

Benzene and xylenes are raw materials in the production of intermediate products for several petrochemical and fine chemical applications, such as the production of synthetic fibers, plastic and resins. Although nowadays those products have been produced through naphtha reforming, new environmental friendly products have been developed at low costs, such as toluene disproportionation and transalkylation with trimethylbenzenes [1-4]. These

reactions are also important for using the toluene and trimethylbenzene excess from naphtha reforming and gasoline pyrolysis [1, 3].

The transalkylation reactions occur in equilibrium with disproportionation, dealkylation and isomerization reactions of aromatics such as xylenes, trimethylbenzenes and others [1-3]. The desired product can be obtained through the control of kinetic parameters, aromatic hydrocarbon reactivity, nature of catalytic sites, morphology and texture of the catalyst used which affect the reaction balance. Therefore, these factors determine the occurrence of disproportionation or transalkylation reactions [3-6].

Those reactions are important alternative routes for the production of benzene and xylenes and can be carried out in the presence of several acid catalysts but due to environmental restrictions a great variety of acid solids have been investigated. Among them, zeolites are the most active and selective catalysts for the reactions but they are easily deactivated due to coke formation which blocks the active sites in the solid channels [5-7]. Therefore, much work has been done in order to obtain materials with zeolitic characteristics and higher pore diameters than the zeolite ones.

Mesoporous aluminosilicates have been shown as versatile catalysts, especially in the conversion of bulky molecules, but they have lower acidity, as compared to zeolites, which limits their catalytic applications [8-12]. Recently, mesostructured mesoporous aluminosilicates have been produced which, due to their properties, join the advantages of zeolites and mesoporous materials, mainly the high acidity and mesoporosity [8-10]. Those properties make them promising materials for many catalytic applications such as disproportionation or transalkylation reactions. High catalytic activity is usually obtained with an increase of aluminum content, once the acidity in the aluminosilicates can be controlled by manipulating the silicon to aluminum ratio making it possible to obtain materials with Brönsted acidity comparable to sulfuric acid [13-15].

Considering those aspects, this work describes the preparation and characterization of catalysts based on beta zeolite with different SAR, using different mesostructuring time. The catalysts were evaluated in the reaction of toluene with 1,2,4-trimethylbenzene, with the aim of producing benzene and xylenes.

2. Experimental

2.1. Synthesis of beta zeolites seeds and mesostructuring

The catalysts were prepared from mesostructuring of beta zeolite seeds [9]. Three samples were obtained: (i) with silica to alumina ratio (SAR)=15 and

mesostructuring time of 48 or 96 h (samples B48-15 and B96-15); (ii) SAR= 9 and 48 h of mesostructuring (B48-9). The beta zeolite seeds were prepared by mixing sodium aluminate, sodium hydroxide, tetraethylammonium hydroxide and silica in water and heating the mixture at 140 °C for 192 h. The seeds were then mesostructured in the presence of cetyltrimethylammonium bromide (CTAB), adjusting the pH to 9.5 and keeping it at 140 °C for 48 or 96 h. Then, the samples were centrifuged, rinsed and dried at 60 °C. The ion exchange was then carried out by use of ammonium chloride, followed by filtration, rinsing and drying at 60 °C and at 110 °C. The obtained materials were calcined at 550 °C for 620 min so the catalysts based on beta zeolite in the acid form were produced.

2.2. Characterization of the samples

The fresh catalysts were characterized by differential thermal analysis (DTA), thermogravimetry (TG), porosity measurements, Fourier transform infrared spectroscopy (FTIR) and X-ray diffraction (XRD). The spent catalysts were characterized by X-ray diffraction and by chemical analysis (carbon amount).

The thermograms were obtained in a TGA/SDTA 851 Mettler Toledo equipment, using 0.005 g of the sample which was put in a sampler and underwent heating from room temperature to 1000 °C, under air flow. The specific surface area and porosity measurements were performed in an AZAP 2020 Micromeritics apparatus, using around 0.15 g of the sample previously heated at 200 °C for 2 h, under nitrogen flow.

The absorption spectra in the infrared region were obtained in the range of 4000 to 400 cm^{-1} , in a Spectrum One Perkin Elmer spectrophotometer, using samples in discs diluted in potassium bromide. The X-ray diffraction measurements were performed in a XRD 6000 Shimadzu device, using CuK α radiation generated at 40 kV and 30 mA and using a nickel filter. The carbon content in the spent catalysts were determined in a CS-200 LECO equipment, using a ceramic crucible with 0.20 g of the sample, 1.25 g of tungsten compound (Lecocel) and 1.25 g of accelerator to help the combustion.

2.3. Catalytic evaluation

The reaction of toluene with trimethylbenzene was carried out for 8 h, in a stainless steel microreactor at 470 °C and 1 atm, using a reaction mixture with 98% toluene and 2% 1,2,4-trimethylbenzene, $\text{H}_2/\text{hydrocarbon}$ (molar)=4 and $\text{WHSV}=1.0 \text{ h}^{-1}$. Before the reaction, the samples (0.5 g) were activated in situ under nitrogen flow at 470 °C, for 1 h. The reaction effluents were analyzed on

line by a ThermoFinnigan Trace CG gas chromatograph using a FFAP capillary column and thermal conductivity and flame ionization detectors.

3. Results and discussion

The TG curves of the samples, shown in Fig. 1(a), displayed three stages of weight loss, in agreement with Kleitz et al [16].

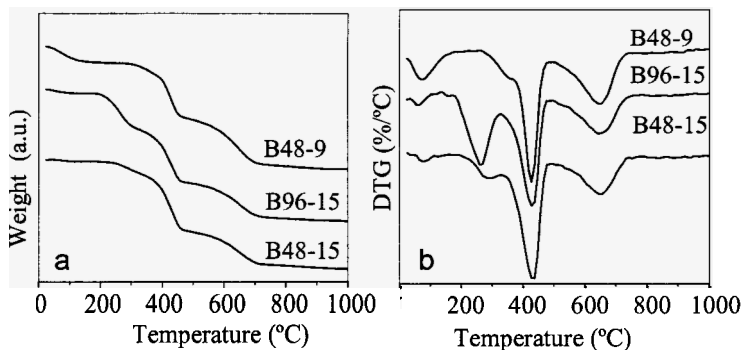


Figure 1. Mass loss curves of the synthesized materials as a function of the temperature: (a) thermogravimetry and (b) derivative thermogravimetry (DTG).

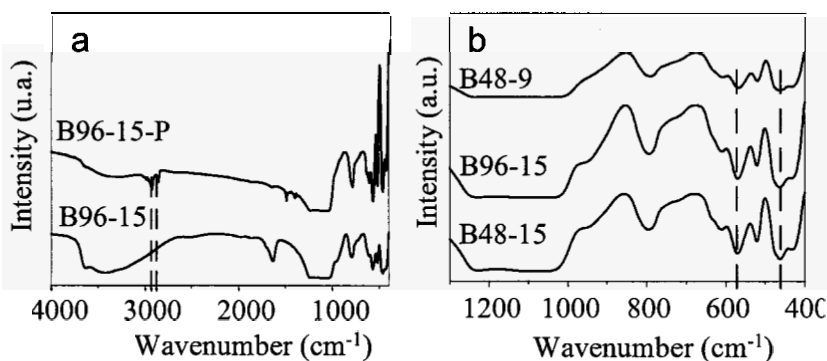


Figure 2. (a) FTIR spectra of as synthesized B96-15 (P) and after calcination. (b) Enlargement of the FTIR spectra of the calcined samples from 1300 to 400 cm⁻¹.

The first stage occurs at temperatures below 200 °C and corresponds to the removal of volatile materials adsorbed on the solid; the second one, between 200 and 450 °C, refers to the decomposition and combustion of the microstructure and mesostructure of templates, while the third one occurs around 600 °C and is

attributed to the dehydroxylation of silanols and to the combustion of the residual coke. Those events can be better understood in the mass loss derivative curve (DTG), shown in Fig. 1(b).

The decomposition and the removal of the templates from the samples during calcination were also followed through FTIR. The spectrum of sample B 96-15, before calcination (Fig. 2a) show deformation bands of C-H bonds of CH₂ template groups (2926 and 2855 cm⁻¹). After calcination, those bands disappeared, indicating that the calcination process was efficient for the template removal [17].

Fig. 2 (b) shows the spectra enlargement in the wavenumber range from 1400 to 400 cm⁻¹ in order to facilitate the visualization of the characteristic bands of amorphous and crystalline materials. It can be observed that the spectra show a band nearby 460 cm⁻¹, which is characteristic of amorphous materials such as MCM-41 [11,12]. Besides, the spectra exhibit an absorption band at 550 cm⁻¹, indicating the presence of a ring-like structure with five members of siloxan bond, T-O-T (T= Si, Al), typical of beta zeolite seeds [11,12].

Regarding the spectra of samples synthesized with different SAR (Fig. 2b), it can be seen a shoulder at around 940 cm⁻¹, which is characteristic of silica, silica gel and several siliceous zeolites and corresponds to the stretching vibration of Si-O bond which belongs to SiO tetrahedron not coupled to a hydroxyl group [14]. Coherently, the absorption is less intense in the lower siliceous B48-9 spectra when compared to B48-15 and B96-15 samples.

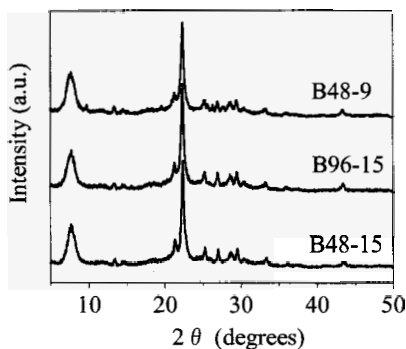


Figure 3. X ray diffractograms of the synthesized samples.

The X-ray diffraction patterns of the synthesized samples (not shown), performed in the low angle region (1 to 10° 2θ), did not show any reflections peaks, thus evidencing that not well ordered mesophase was formed [8-12].

Otherwise, well resolved X ray diffractions patterns (Fig. 3), corresponding to the BEA structure were obtained, evidencing that the two crystallization steps (during seeds formation and mesostructuring) lead to the formation of highly crystalline beta zeolites [8,9].

As shown in Fig. 4, all solids show isotherms, which are intermediates of type I (microporous materials) and type IV (mesoporous materials). As above discussed, the presence of microporous are related with the structure of highly crystalline beta zeolites. Otherwise, the presence of mesoporous (Table 1) could be related with the formation of a poor ordered mesophase during the step of mesostructuring in the presence of CTAB and principally from mesopores formed between the particles (nitrogen adsorption at high relative pressure). This behavior shows that the synthesis of beta zeolites with the two step procedure used here results in a solid formed by small zeolite crystals between amorphous silica particles. In the first step, the synthesis conditions allow the formation of beta zeolite seeds, which in the second step are hampering to continue growing due to the presence of the micelles formed in the presence of CTAB.

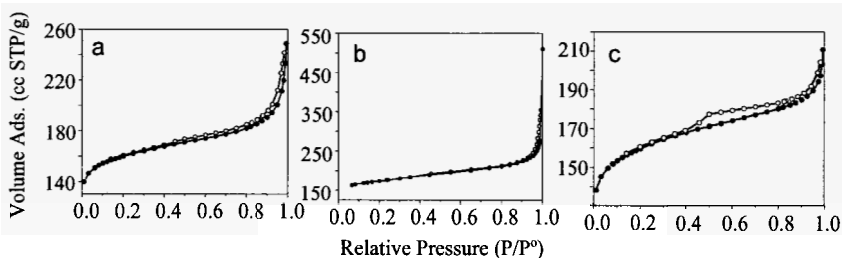


Figure 4. Nitrogen isotherms of calcined beta zeolites: (a) B48-15; (b) B96- 15; (c) B48-9. Symbol: -●- Adsorption; -○- Desorption.

Table 1. Textural properties of calcined beta zeolites: specific surface area (S_g), micropore volume (V_{mi}) and average pore diameter (D).

Samples	S_g , BET ($m^2 \cdot g^{-1}$)	V_{mi} t-plot ($cm^3 \cdot g^{-1}$)	D (nm)
B48-9	492	0.1863	4.71
B48-15	491	0.1933	7.43
B96-15	589	0.1962	11.22

All samples were catalytically active in the reaction of toluene with 1,2,4-trimethylbenzene, as shown in Table 2 which shows the values after 8 h reaction. Figure 5 shows the conversion as a function of time. In general, the catalysts showed high selectivity to benzene, followed by xylenes and ethylbenzene,

indicating that the toluene disproportionation occurred in higher extension than transalkylation and that most of the xylenes produced were disproportionate later in order to produce benzene. All catalysts were more active than a commercial catalyst based in mordenite and were more selective to benzene. Consequently, beta catalyst were more efficient, leading to higher yield of xylenes and benzene and showing low decrease in conversion during reaction (Table 2).

Table 2. Toluene conversion (C), selectivity (S) to aromatics (BZ=benzene, X=xylenes), yield (Y) to xylenes and benzene, conversion decrease (ΔC) and coke on the spent catalysts.

Sample	C (%)	S _{BZ} (%)	S _X (%)	Y _X (%)	Y _{BZ} (%)	ΔC (%)	Coke (%)
Commercial	16	52	11	2.0	8.0	20	2.2
B48-9	28	63	9	2.5	18	--	14.5
B48-15	26	56	14	3.6	14	2	15.1
B96-15	25	62	8	2.0	16	15	14.5

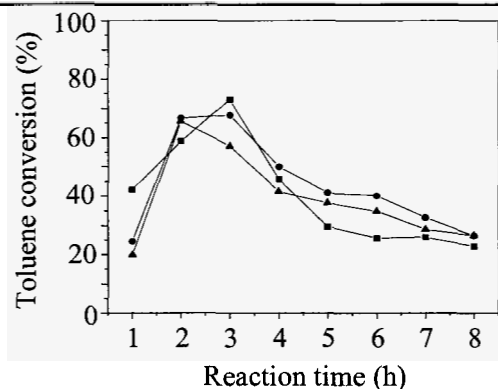


Figure 5. Toluene conversion in the reaction of toluene with 1,2,4-trimethylbenzene as a function of time on stream at 470 °C. -●- B48-15; -□- B96-15; -▲- B48-9.

Table 2 also contains the amount of coke on the spent catalysts after reaction. It can be seen that beta zeolite based materials produced more coke than the commercial one based on mordenite catalyst. However, as the synthesized beta catalysts have a tridimensional micropore structure and interparticle mesoporosity, they were, compared with mordenite, which has a monodimensional micropore structure, more stable during the reaction.

4. Conclusions

It was verified that the used two step synthesis procedure allowed to prepare beta catalysts, which were more active and stable than a commercial mordenite in the

reaction of toluene with 1,2,4-trimethylbenzene. In a first step the synthesis conditions lead to the formation of crystalline beta seeds, which subsequently were mesostructured in the presence of CTAB. During mesostructuring the surfactant micelles hamper the seed growing and consequently generating a solid constituted by a poor ordered mesophase and small beta crystals, responsible for the interparticle mesoporosity determined by N₂ sorption measurements.

Acknowledgments

STFG acknowledges PIBIC/CNPq for his scholarship. This work was supported by CNPq and FINEP.

References

1. J.M. Serra, E. Guillon and A. Corma, *J. Catal.* **227**, 459 (2004).
2. J. Cejka, J. Kotrla and A. Hrejci, *Appl. Catal. A: Gen.* **277**, 191 (2004).
3. T.C. Tsai, S.B. Liu and I. Wang, *Appl. Catal. A: Gen.* **181**, 355 (1999).
4. V. Mavrodinova, M. Popova, R.M. Mihályi, G. Pál-Brbély and C.J. Minchev, *J. of Molec. Catal. A: Chem.* **220**, 239 (2004).
5. T.C. Tsai, *Appl. Catal. A: Gen.* **301**, 292, (2006).
6. T.C. Tsai, W.H. Chen, C.S. Lai, S.B. Liu, I. Wang, and C.S. Ku, *Catal. Today* **97**, 297 (2004).
7. M.C. Rangel, A. Valentini, A.S. Oliveira, J.M. David, J.M. Britto, S.M. Domingues, and P. Reyes, *Quim. Nova*, **26** (3), 305 (2003).
8. W. Guo, L. Huang, P. Deng, Z. Xue, and Q. Li, *Micropor. and Mesopor. Mater.*, **44-45**, 427 (2001).
9. W. Guo, C. Xiong, L. Huang and Q. Li, *J. Mater Chem.* **11**, 1886 (2001).
10. A. Ungureanu, T.V. Hoang, D.T. On, E. Dimitriu and S. Kaliaguine, *Appl. Catal.* **294**, 92 (2005).
11. S. Wang, T. Dou, Y. Li, Y. Zhang, X. Li and Z. Yan, *J. of Solid State Chem.* **177**, 4800 (2004).
12. P.C. Shih, J.H. Wang and C.Y. Mou, *Catal. Today*, **93-95**, 365 (2004).
13. D.T. On, D. Desplandier-Giscard, C. Danumah and S. Kaliaguine, *Appl. Catal. A: Gen.* **253**, 545 (2003).
14. R. Dimitrova, G. Gunduz, L. Dimitrov, T. Tsoncheva, S. Yialmaz, and E.A. Urquieta-Gonzalez, *J. of Molec. Catal. A: Chemical* **214**, 265 (2004).
15. A. Corma, *J. Catal.* **298**, 312 (2003).
16. F. Kleitz, W. Schmidt and F. Schüth, *Micropor. and Mesopor. Mater.*, **65**, 1 (2003).
17. M. Selvaraj, A. Pandurangan, K.S. Seshadri, P.K. Sinhá and K.B. Lal, *Appl. Catal. A: Gen.* **242**, 347 (2003).

ACTIVATED CARBON-SUPPORTED COPPER-DOPED IRON OXIDE FOR ETHYLBENZENE DEHYDROGENATION

DANNS PEREIRA BARBOSA, MARIA DO CARMO RANGEL^{*}

GECCAT Grupo de Estudos em Cinética e Catálise, Instituto de Química, Universidade Federal da Bahia, Campus Universitário de Ondina, Federação, 40170-280 Salvador, Bahia, Brazil. E-mail: mcarmov@ufba.br

DENILSON RABELO

Instituto de Química, Universidade Federal da Bahia, Campus Samambaia Goiânia, Goiás, Brazil

The polymeric activated carbon is a suitable catalytic support due to its purity, reproducibility, physical form and structure. In order to find new catalysts to produce styrene by ethylbenzene dehydrogenation in the presence of steam, the preparation of copper-doped iron oxide supported on polymeric activated carbon was described in this work. All catalysts were more active than a commercial sample, regardless the presence of steam. There was a loss of specific surface area during reaction due to coke deposition but the steam was able to minimize this effect. The best performance was shown by the iron oxide based catalyst, which showed the highest activity, selectivity and stability during reaction. This catalyst is able to work without steam showing high activity and selectivity.

1. Introduction

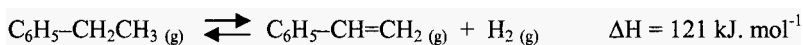
Due to its pore structure and high specific surface area, activated carbon shows a considerable adsorption capacity of organic and inorganic compounds in liquid or gaseous phase. Therefore, these materials find wide applications as adsorbents, batteries electrodes, biomedical engineering and catalytic supports [1]. Regarding catalysis, the activated carbon is an attractive option once it shows thermostability, acid and basic properties, easy interaction with metals and allows the control of porous structure and surface chemical properties as required by catalytic applications [2,3]. Although these advantages, it has inconveniences such as significant levels of impurities which is a consequence of precursor used (wood, coal and others), low physical resistance and limited physical form to grains or dust [3]. A way to surpass this problem is the use of

^{*} To whom the correspondence should be addressed

polymeric precursor which allows the pureness control, the reproducibility, the physical form and the structure through the polymer characteristics [3,4]. Other advantages of the polymeric precursors are the high specific surface area and homogeneous structure of carbon. Moreover, this method makes possible to obtain the material in form of spheres which shows low resistance to the diffusion of liquids and gases in fixed bed catalytic reactors, as a result of homogeneous piling [2,4]. Researchers have directed their works to the production of carbon activated from resins of phenol-formaldehyde [5], polyacrylonitrile and polystyrene [6,7]. The styrene-divinylbenzene copolymer is considered an important precursor due its strong acid properties, its homogeneous grain sized distribution and high physical and chemical resistance [7,8].

Among the diverse catalytic applications of activated carbon, its application is detached in the catalytic ethylbenzene dehydrogenation with steam to produce styrene [9]. Several works have shown that this material is catalytically active in this reaction because of the functional groups in the carbon surface [10,11]. Due to the demand for polymer based in styrene it becomes necessary to minimize the cost for production of monomer [12].

The catalytic ethylbenzene dehydrogenation is responsible for about 90% of the world-wide production of styrene. The reaction is industrially carried out in the presence of steam, over catalysts based on iron oxide (hematite, $\alpha\text{-Fe}_2\text{O}_3$), containing cerium, chromium and potassium oxides and consumes great amount of energy [13,14]. The reaction is endothermic and limited by equilibrium [15]:



The commercial catalyst has the advantage of low cost, but goes on fast deactivation due to the loss of potassium, besides being harmful to the human being and the environment due to the toxic chromium compounds. Potassium can migrate to the pellet center or goes out from the reactor, during commercial operations [14,16]. Once the catalysts represent a significant parcel in production costs, the development of free-potassium and chromium solids with high activity and selectivity becomes useful, since it can be more resistant against deactivation and can avoid environmental problems, besides of decreasing the process energy consumption.

In this context, catalysts based iron oxide doped with copper supported on polymeric activated carbon were prepared, characterized and evaluated in ethylbenzene dehydrogenation with and without steam. The study aims to develop catalysts which can work in a low cost condition.

2. Experimental

Copolymer based on styrene (Sty) and divinylbenzene (DVB) was synthesized by polymerization in suspension using heptane and toluene as pore forming agents. The copolymer was rinsed with ethanol and sulfonated at 70°C, under stirring for 4 h, in a sulfuric acid and dichloroethane mixture (15:3 mL.g⁻¹ of copolymer). After this, it was filtered, rinsed with water deionized and dried at 110 °C.

The ions adsorption was carried out at 25 °C using 1 g of sulfonated resin, which was dispersed in the solution of the metallic ions and kept for 15 min, under stirring. In the preparation of solutions copper nitrate (Cu(NO₃)₂) and iron sulfate (FeSO₄.7H₂O) were used. Three solutions of metallic ions with concentration of 0.3 mol.L⁻¹ had been prepared, one of them containing only Fe²⁺ ions and the others containing Fe²⁺ and Cu²⁺ ions (6 and 12% mole, respectively). After the adsorption of metallic ions, the resin was filtered and rinsed with deionized water. It was then added to a solution, previously heated at 90°C, containing 0.410 g of potassium hydroxide and 0.055 g of potassium nitrate. This mixture was stirred for 5 min, then cooled, filtered and rinsed with deionized water. The procedure of metals incorporation and precipitation was repeated four times with each sample to obtain the COP0 (copolymer with iron oxide), COP6 and COP12 (copolymer with iron oxide and 6 and 12% mole of copper, respectively) samples.

These samples (COP0, COP6 and COP12), and the sulfonated copolymer, were heated in air, at 250 °C for 2 h followed by carbonization at 900 °C, under nitrogen for 3 h. Then, the activation was carried out at 900 °C for 3 h, under flow of nitrogen saturated with steam, producing CP0 (COP0 after heating), CP6 (COP6 after heating), CP12 (COP12 after heating) and CA (sulfonated copolymer without metals after heating) samples.

The amount of copper and iron in the catalysts was determined by atomic spectrophotometry absorption in 306 Perkin-Elmer equipment. The sample (0.01 g) was dissolved under heating in hydrochloric acid (2 mL), filtered and completed with deionized water up to 100 mL. The X-ray diffraction was measured in a DRX6000 Shimadzu apparatus. The textural properties were measured by nitrogen adsorption at -196°C in a Micromeritics ASAP 2010 equipment. The thermal stability of the materials was evaluated by thermogravimetry, in a Mettler Toledo TGA/SDTA 851E balance, heating the samples under nitrogen flow, at a rate of 5 °C.min⁻¹, from room temperature up to 1000 °C.

The samples (CP0, CP6, CP12 and CA) and a commercial catalyst (C), constituted of hematite with potassium, chromium and cerium oxides, were evaluated in a fixed bed microreactor containing 0.300g of solid. The reaction was performed at 530 °C and 1 atm, with a ethylbenzene to steam molar ratio of 10. The reactor effluent was collected at each 30 min and analyzed by gaseous chromatography in a CG-37 chromatograph with 5% carbowax in a chromosorb column and a flame ionization detector. The catalysts were also evaluated without steam.

3. Results and Discussion

The copper and iron amounts in the fresh catalysts are shown in Table 1. It can be seen that high amounts of iron were incorporated in catalysts; they correspond to around 25 % catalysts weight. The copper amounts correspond to 1.1 % (CP6) and 3.6 % (CP12) catalysts weight. In all cases, the values obtained were close to the expected ones.

Table 1. Iron and copper amounts in CP0, CP6 and CP12 catalysts before the reaction.

Samples	Fe (mmol g ⁻¹)	Cu (mmol g ⁻¹)
CP0	4.82	--
CP6	4.08	0.18
CP12	4.05	0.57

The diffractograms of the catalysts before the reaction are shown in Fig. 1a. The profiles of all samples are characteristic of magnetite, without any modification of the crystalline phases due to copper introduction. Besides, no copper-containing phase was detected, a fact which can be assigned to the small size of copper particles making them not detectable by X-ray diffraction. In addition, copper could enter the magnetite lattice, as found in previous works [17-19], because of the size of the ionic radius (0.73 Å), which is close to that of Fe²⁺ (0.74 Å). Moreover, Fe⁰ phase was also observed; it could be produced during the reduction reactions that occur in the carbonization and activation of the polymer. During the ethylbenzene dehydrogenation, this phase disappeared, as noted in the X-ray diffractograms of the spent catalysts (Fig. 1b). This can be assigned to the oxidation action of steam during reaction.

The nitrogen adsorption and desorption curves of the fresh and spent catalysts were typical of macro and mesoporosos materials (II type), regardless the presence of steam during reaction. The textural properties of the catalysts

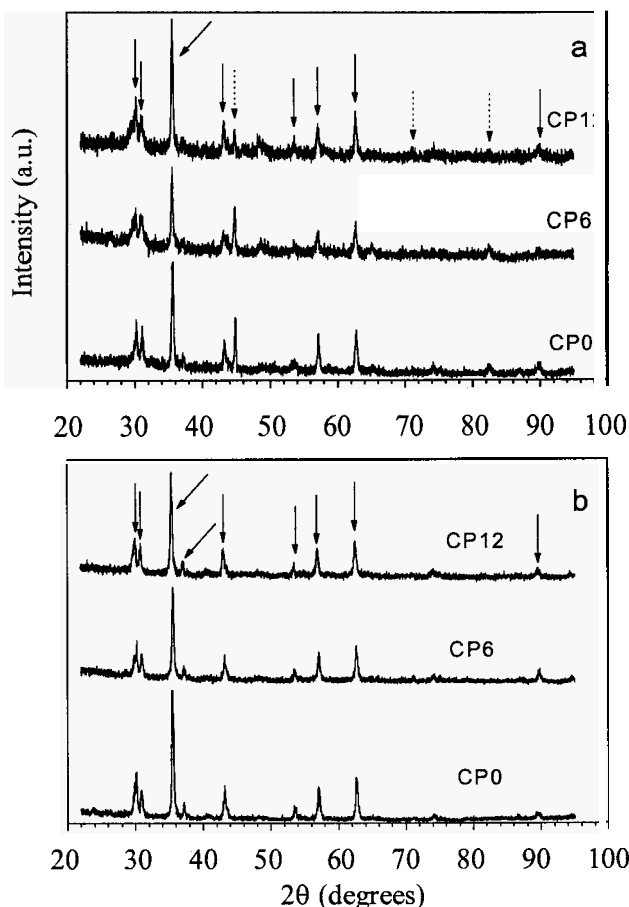


Figure 1. X ray diffractograms of CP0, CP6 and CP12 catalysts (a) before and (b) after reaction with steam. \longrightarrow magnetite; $\cdots\blacktriangleright$ metallic iron.

before and after reaction with and without steam, are shown in Table 2. The metals addition provokes reduction in the specific surface area of activated carbon ($867 \text{ m}^2\cdot\text{g}^{-1}$). There was also a micropore reduction, suggesting the collapse of the structure and/or blockage of the micropores due to the iron and copper presence. During reaction, the textural properties of solids changed depending on the kind of the metal and on the presence of steam. The pure support (CA) kept its porous structure regardless the presence of steam. On the

other hand, in the case of the sample containing iron (CP0), the specific surface area was practically not modified during the reaction in presence of steam, but it diminished in its absence. The same behavior was observed with the sample with the highest content of copper (CP12). In the case of solid with the lowest copper amount (CP6), the area of micropores, volume, diameter of pores and the surface area decreased during reaction. The collapse of the porous structure during reaction can be attributed to the sintering and coke deposition in the catalyst pores. Without steam, this effect increased, since the coke deposits were not oxidized and the pores were easily blocked and/or collapsed.

Table 2. Textural properties of catalysts before (CP0, CP6, CP12 and C) and after reaction. The symbols D and DS indicate the spent catalysts in the reaction with and without steam, respectively.

Samples	S_{BET} (m^2g^{-1})	S_{MIC} (m^2g^{-1})	V_{P} ($\text{cm}^3 \text{g}^{-1}$)	D (nm)
C	16	2.0	0.06	–
CD	9.0	0.7	0.04	–
CDS	10	1.0	0.05	–
CA	867	469	0.80	13.8
CAD	849	576	0.84	13.7
CADS	841	558	0.84	14.1
CP0	87	28	0.18	8.6
CP0D	98	15	0.17	7.6
CP0DS	36	0.5	0.14	8.4
CP6	93	37	0.18	6.8
CP6D	42	3.0	0.12	6.3
CP6DS	29	3.0	0.09	6.6
CP12	124	43	0.22	8.6
CP12D	105	15	0.16	7.0
CP12DS	40	0.3	0.12	7.4

The thermogravimetric curves of the catalysts with metals (CP0, CP6 and CP12) are displayed in Fig. 2. The weight loss at 50-150°C (about 5%) refers to water elimination while those between 700 and 750 °C (about 30%) is related to the polymer chains carbonization. It can be noted that the catalysts are thermally stable at temperature of the ethylbenzene dehydrogenation (530 °C).

The values of ethylbenzene conversion and of selectivity to styrene, after 6 h of reaction with and without steam, are presented in Table 3. In the presence of steam, the support (CA) led to a low conversion, which increased due to the metals; therefore, one can assume that the metal is the active phase in the reaction. The selectivity to styrene also increased because of the metals. In addition, both conversion and selectivity were higher than the commercial sample and thus we can conclude that iron oxide is more active when supported on activated carbon.

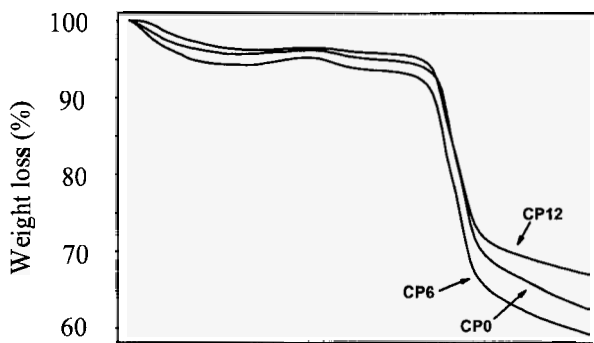


Figure 2. Thermogravimetic curves for the catalysts studied

Table 3. Conversion of ethylbenzene and selectivity to styrene of the commercial catalyst (C), the support (CA) and CP0, CP6 and CP12 catalysts after 6 h of reaction with or without steam.

Ethylbenzene dehydrogenation with steam		
Sample	Conversion (%)	Styrene selectivity (%)
C	13	98
CA	3.0	95
CP0	34	98
CP6	19	98
CP12	21	99
Ethylbenzene dehydrogenation without steam		
Sample	Conversion (%)	Styrene selectivity (%)
C	5.0	97
CA	9.0	96
CP0	24	99
CP6	17	99
CP12	23	99

Without steam, the support was more active than the commercial sample and the introduction of the metals increased the activity even more. The activity of the catalyst containing iron was lower without steam, as compared to the values obtained with steam, probably due to coke formation. On the other hand, the copper-containing catalysts showed high values regardless the presence of steam. In general, the selectivity did not change significantly by the kind and amount of the metal or by the steam presence.

Figures 3 and 4 show the activity curves of the catalysts versus the reaction time, with and without steam. The catalysts were stable under steam, which removes continuously the coke formed on the catalyst surface, in accordance with previous work [15]. Without steam, the activity decreased quickly with time, probably due to the collapse of porous structure by coke deposition.

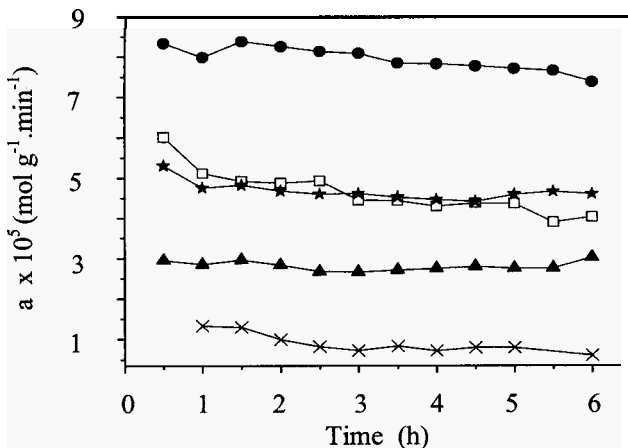


Figure 3. Catalytic activity of the samples as a function of time during the ethylbenzene dehydrogenation with steam: CP0 (●), CP6 (□), CP12 (★) CAD (X) and commercial catalyst (▲).

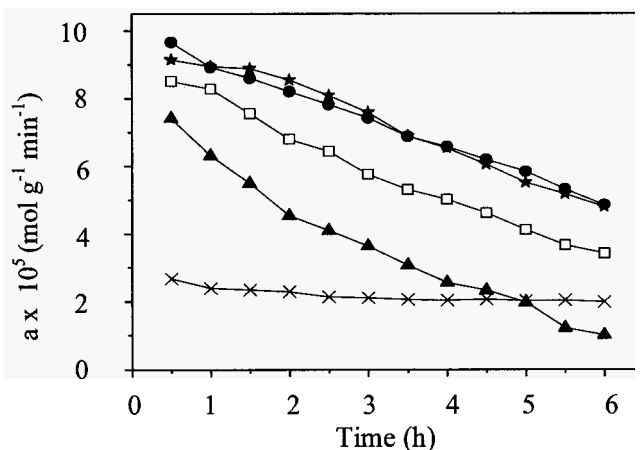


Figure 4. Catalytic activity of the samples as a function of time during the ethylbenzene dehydrogenation without steam: CP0 (●), CP6 (□), CP12 (★) CAD (X) and commercial catalyst(▲).

The activity of the support can be attributed to the presence of oxygenated functional groups in carbon surface (quinones, carbonyls, lactones and anhydrides) which catalyzes the reaction by a redox mechanism [15]. The activity was higher in the reaction without steam and this fact can be explained by the formation of different functional groups during reaction. This is in agreement with other works [20] which showed that these groups can change during heating of activated carbon.

4. Conclusions

Catalysts based on iron oxide doped with copper supported on activated carbon are active in ethylbenzene dehydrogenation to produce styrene, with and without steam. These solids were more active than a commercial catalyst, regardless the presence of steam. In the presence of steam, they are also stable. However, they deactivate without steam, due to the loss of specific surface area during reaction because of the collapse of the porous structure caused by coke deposition. The most promising sample was the catalyst with iron oxide supported on activated carbon, which showed high activity and selectivity in reaction besides resistance against deactivation. This catalyst is able to work without steam showing high activity and selectivity.

Acknowledgments

DPB acknowledges CNPq for his scholarship. The authors thank the Nitriflex and Coremal for donation of monomers and CNPq and FINEP for the financial support. .

Reference

1. S.Y. Karakas, A. Aygün, M. Günes and E. Tahtasakal, *Carbon* **42**, 477 (2004).
2. B. Li, Y. Ren, Q. Fan, A. Feng and W. Dong, *Carbon* **42**, 2669 (2004).
3. S.R. Tennison, *Appl. Catal. A: Gen.* **173**, 289 (1998).
4. K. László, A. Bota and I. Dékány, *Carbon* **41**, 1205 (2003).
5. N. A. Eltekova, D. Berek, I. Novak and F. Belliaro, *Carbon* **38**, 373 (2000).
6. T. Kyotoni, *Carbon* **38**, 269 (2000).
7. S.B Oliveira, D. Rabelo and M.C. Rangel; *Stud.Surf. Sci. Cat.* **156**, 609 (2005).
8. A. Gierak, *Mater. Chem. Phys.* **41**, 28 (1995).
9. M. F. R. Pereira, J. J. M. Órfão, J. L. Figueiredo, *Colloid Surface A.* **241**, 165 (2004).

10. P. Li, T. Li, J. H. Zhou, Z. J. Sui, Y. C. Daí, W-K. Yuan and D. Chen, *Micropor. and Mesopor. Mat.* **95**, 1 (2006).
11. S.B. Oliveira, D.P. Barbosa, A.P.M. Monteiro, D. Rabelo, M.C. Rangel; *Catal. Today* (2007) (*in press*).
12. Y. Sakurai; T. Suzaki; K. Nakagawa; N. Ikenaka; H. Aota; T. Suzuki. *J. Catal.* **209**, 16 (2002).
13. M. Sugino; H. Shimada; T. Turuda; H. Miura; N. Ikenaga; T. Suzuki. *Appl. Catal.* **121**, **125** (1995).
14. E. H. Lee, *Catal. Rev.*, **8**, 285 (1963).
15. J. L. Figueiredo, M.F.R. Pereira, M.M.A. Freitas and J.J.M. Órfão; *Carbon* **37**, 1379 (1999).
16. D. Rabelo, E.C.D. Lima, N. Tavares Filho, F.Q. Soares, L.C. Faria, F. Pelegrini, O. Silva, A.C. Oliveira, V.K. Garg and P. C. Morais. *J Magnetism Magnetic Mater.* **272**, 1205 (2004).
17. M. C. Rangel and A. O. de Souza. *Reac. Kin. and Catal. L.* **79**, 175 (2003).
18. M. C. Rangel and G. C. Araujo, *Catal. Today.* **62**, 201 (2000).
19. M. C. Rangel, A. M. M. Amorim, E. B. Quadro and M. L. Dias, *J. Brazil Chem Soc.*, **10**, 51 (1999).
20. G. Puente, J.J. Pis, J.A. Menezes and P. Grange *J. Anal. Appl. Pyrol.*, **43**, 125 (1997).

CATALYTIC PROPERTIES OF PLATINUM (II) EXCHANGED ZIRCONIUM PHOSPHATE FOR WGSR

ALEXILDA OLIVEIRA DE SOUZA

Departamento de Estudos Básicos e Instrumentais, Universidade Estadual do Sudoeste da Bahia, Praça Primavera 40, Primavera, 45700-000, Itapetinga, Ba, Brazil

MARIA DO CARMO RANGEL*

GECCAT, Instituto de Química, Universidade Federal da Bahia, 40170-280. Salvador, Bahia, Brazil. E-mail: mcarmov@ufba.br

OSWALDO LUIZ ALVES

Instituto de Química, Universidade Estadual de Campinas, Caixa Postal 6154, 13083-970 Campinas, São Paulo, Brazil

Layered zirconium hydrogenphosphate monohydrate, α -ZrP, has been extensively studied in the last years due to its performance as catalyst or catalytic support, besides its use as ionic exchanger. This work reports the study of ionic exchange of α -ZrP samples using platinum, in order to use this material as catalyst in the water gas shift reaction (WGSR), which is an important step in several industrial processes like ammonia synthesis and high purity hydrogen production. It was found that layered zirconium hydrogenphosphate is a promising catalyst and the exchange with platinum increased the activity even more. The catalytic activity results indicated that this property varied as a function of the crystallinity. Increasing the crystallinity the ionic exchange rates decrease but the specific surface areas increase and favor a better catalytic performance. This is ascribed to the lamellar organization, which increases the reactants access to active sites (platinum).

1. Introduction

The study of lamellar materials and the chemistry of their intercalation are in constant development, being a promising field in the solid state chemistry. In this perspective, the α -zirconium (IV) phosphate, usually called α -ZrP, has been the main subject of extensive research during the last years due to the performance of these materials as catalysts or catalytic supports and because of the ion exchange phenomena, intercalation reactions and ionic conductivity. From the catalytic point of view, these compounds are attracting increasing interest due to the thermal and chemical stability, besides the possibility of relating their textural properties with their crystalline structure [1,2]. They are catalytically

active for a great variety of reactions such as dehydrogenation, isomerization, dehydration, hydrogenation and oxidation [3]. It was noted, in several studies, that their catalytic properties depended not only on the preparation conditions and on the thermal treatment used, but also on the presence of other species in the structure. The intercalation with transition metals, for example, modifies the catalytic properties, promoting a better performance of these materials in many processes [4].

In this work the ion exchange properties of the α -ZrP were used for introducing Pt^{2+} ions in the layered structure. This is an alternative route for classical impregnation processes, in order to obtain an adequate methodology for obtaining a -ZP intercalated with platinum. The resulting catalyst was evaluated in water gas shift reaction at high temperatures (HTS, High Temperature Shift).

The water gas shift reaction is an important step for obtaining high purity hydrogen that is carried out by the industry and it is usually conducted on an iron oxide catalytic bed. The catalyst is commercialized in the form of hematite (α - Fe_2O_3) and is reduced in situ to form magnetite (Fe_3O_4), which is the active phase. The formation of metallic iron must be avoided in the reduction process which, besides causing a diminishing of the active sites, can catalyze the undesired production of hydrocarbons [5-7]. In commercial plants, this process is controlled by the injection of high quantities of water vapor to the system which, meanwhile, leads to a great increasing of the operational costs[8]. This justifies the interest for the development of new catalyst that could operate in the presence of smaller quantities of vapor. In this way, the phosphates obtained were evaluated in the HTS reaction, under conditions of low water vapor content, which was much lower than the one used at the industrial processes.

2. Experimental

The samples were obtained by the reaction of 0.5 M zirconium oxychloride solution with concentrated phosphoric acid. The material obtained (ZGel) was refluxed during 48 h with phosphoric acid solutions of 0.5, 1.0, 2.3 and 7.5M, producing the Z0.5, Z1, Z2, Z3 and Z7.5 samples, respectively. After being refluxed, the gel was isolated by centrifugation and washed with deionized water until reaching a pH near 4 and then it was dried at 35 °C [9-11]. The solid thus obtained were exchanged with platinum by refluxing for 48 h, in a tetraammineplatinum chloride solution (0.1 M) The materials were heated for 1 h under hydrogen at 500 °C. The samples with platinum were identified by P (Z0.5 P, Z1 P, Z2 P, Z3 P and Z7.5 P samples). The materials were activated

after thermal treatment during 2 hours at 500°C, under hydrogen flux, using a heating rate of 10°C/min and a feed of 100mL/min.

The zirconium content was determined by gravimetry using the cupferron method [12]. The phosphorus analysis was conducted by spectrophotometry, by the phosphomolibdate method [13], in a visible/UV Hitachi equipment U-200 model. The platinum content was determined by X-ray fluorescence by the fundamental parameters method, in a Tracor model Spectra 5000.

The X-ray diffraction measurements of the powder samples were done in a Shimadzu equipment, XD3A model, with a VG-108R goniometer and a X-ray generating tube, model A-40, using the $\text{CuK}\alpha$ ($\lambda = 1.5418 \text{ \AA}$) radiation and nickel filter. The following conditions were used: 35 kV, 25 mA and the scanning was of 2°/min. A Renishaw Raman Imaging Microscope equipment, System 3000, was used for obtaining the Raman spectra, coupled to an optical microscope with a 1.5 μm resolution and He-Ne ($\lambda = 633 \text{ nm}$) laser.

The specific surface areas were measured in a Micromeritics TPD/TPR 2900 Analyzer. In the experiments, the samples (0.5 g) were heated under nitrogen, at a heating rate of 10° C/min up to 160° C during 1 h. The analysis was then carried out using a 30% N_2/He mixture. The differential thermal analysis was carried out in Shimadzu DSC-50 equipment using about 0.020 g of powder sample, in an aluminum sample carrier. The measurements were conducted under argon flow (100 mL/min), from 25 up to 600° C.

In the catalytic evaluation experiments, a fixed bed microreactor was used, operating at 370° C and 1 atm. A steam to process gas molar ratio of 0.2 was used, which is a value lower than the one used in industrial processes (0.6). The process gas used was made on a mixture of 10% CO , 10% CO_2 , 40% N_2 and 60% H_2 , which has a composition close to the one used in commercial plants. The catalytic activity of the more organized material without platinum (Z7.5 sample) was also measured as a reference.

3. Results and Discussion

From X-ray diffractograms of the $\alpha\text{-ZrP}$, Fig. 1(a), we can see that the gel reflux with solutions of different phosphoric acid concentrations produced materials with different crystallinities. There was an evolution of the lamellar structure organization with the increase of the acid solution concentration. This effect is due to a dissolution and re-precipitation mechanism known as Ostwald Ripening [14]. It can be noticed, from the diffractograms obtained for the phosphates exchanged with platinum, Fig. 1(b), that the exchange with platinum did not change the diffraction pattern for the semicrystalline samples,

while for the non-crystalline phosphates some reflections were noticed, indicating the lamellar organization at $2\theta = 12^\circ$. It means that the structure did not collapse due to platinum incorporation.

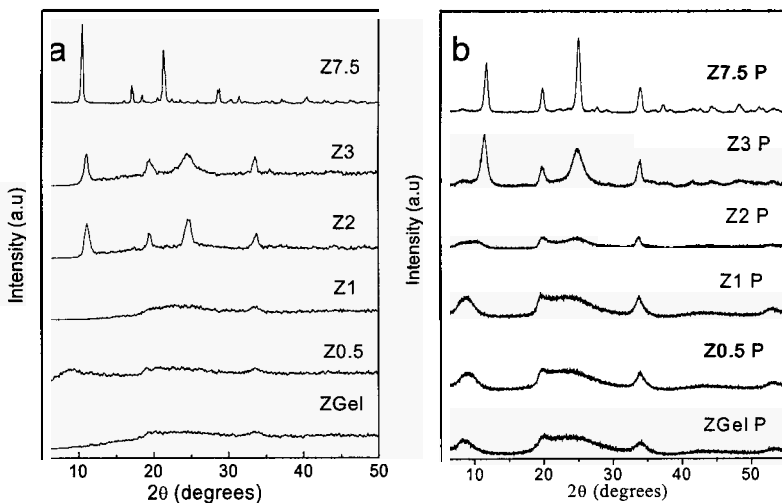


Figure 1. X-ray diffractograms of the solids. (a) ZGel, Z0.5, Z1, Z2, Z3 and Z7.5 samples. (b) ZGelP, Z0.5P, Z1P, Z2P, Z3P and Z7.5P samples.

The chemical analysis results are shown in Table 1. The non-crystalline zirconium phosphates showed a P/Zr ratio lower than 2 (stoichiometric value), while the ratio was near to the stoichiometric value for the semi-crystalline solids. These results indicate that materials with different stoichiometry were obtained: (i) solids with P/Zr ratio $\cong 2$ corresponding to the formula $ZrH(PO_4)_2 \cdot nH_2O$ and (ii) solids with P/Zr ratio deviating from the stoichiometric relation (varying between 1.53 and 1.58). This phase can be described as a hydroxyphosphate of the $Zr(OH)_{2x}(HPO_4)_{2-x} \cdot nH_2O$ type, where n is a number between 0 and 1.5.

It was verified, from the results shown in Table 1 that the crystallinity influenced the ion exchange process, which was decreasing, step by step, while the materials structure was getting organized. This is in accordance with previous studies [15] and is ascribed to the free energy variation, which becomes more positive at materials showing a more organized structure.

Fig. 2 shows the Raman spectra related to the original phosphates and the ones exchanged with platinum. All platinum-free samples showed a band related to P-O bond ($1150-1000 \text{ cm}^{-1}$) centered at 1080 cm^{-1} . This band was becoming

slighter and intense for the samples exposed to reflux with more concentrated phosphoric acid solutions, confirming the results of X-ray diffraction, which indicated the evolution of organization within the structure of these materials. The semicrystalline materials showed a band centered at 283 cm^{-1} indicating the structural organization of the lattice.

Table 1. Chemical analysis results of phosphorous, zirconium, platinum and phosphorus to zirconium (P/Zr): ZGel P, Z0.5 P, Z1 P, Z2 P, Z3 P and Z7.5 P samples with platinum.

Sample	P (%) ± 0.02	Zr (%) ± 0.04	P/Zr (molar)	Exchanged platinum amount (meq/g)
ZGel P	16.00	30.96	1.53	0.09
Z0.5 P	16.48	30.94	1.56	0.09
Z1 P	16.70	31.12	1.58	0.09
Z2 P	18.78	28.63	1.93	0.08
Z3 P	18.90	28.45	1.97	0.07
Z7.5 P	19.15	28.18	2.06	0.07

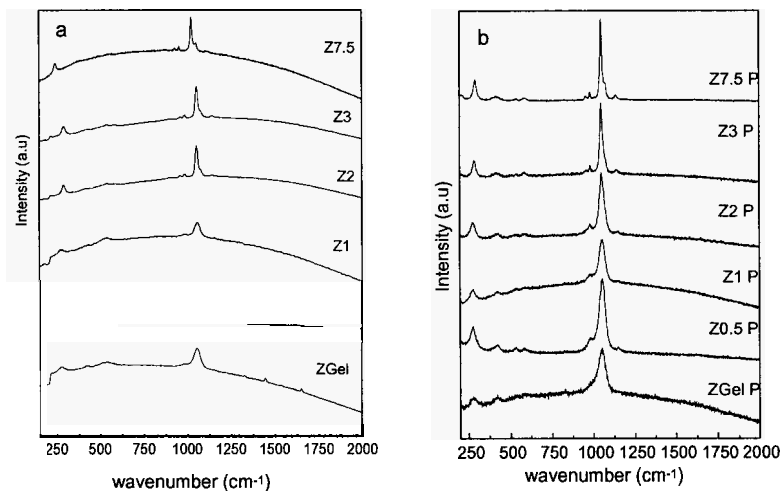


Figure 2. Raman spectra of the solids. (a) ZGel, Z0.5, Z1, Z2, Z3 and Z7.5 samples.. (b) ZGelP, Z0.5P, Z1P, Z2P, Z3P and Z7.5P samples.

The Raman spectra of the amorphous materials showed narrow bands at 1080 cm^{-1} and another at 280 cm^{-1} , after the ion exchange with platinum, indicating that the introduction of $[\text{Pt}(\text{NH}_3)_4]^{2+}$ ion promoted an organization of the phosphates structure, confirming the X-ray diffraction results.

The DSC curves of the samples, displayed in Fig. 3, indicated differences for the thermal behavior depending on the crystallinities of the solids. The

amorphous solids exhibited a wide endothermic peak due to the loss of water at about 165° C, the intensity of this peak depends on the amount of water in the gel. In the case of semicrystalline solids three endothermic peaks were observed in the range of 100 to 250 °C [1]. The first one, with a maximum near 150°C, is associated to the transition phase.



The second endothermic peak has a maximum at 190°C, approximately, which is due to the loss of water. And finally, the third endothermic peak had its maximum at about 230°C where the δ phase becomes the η :phase:

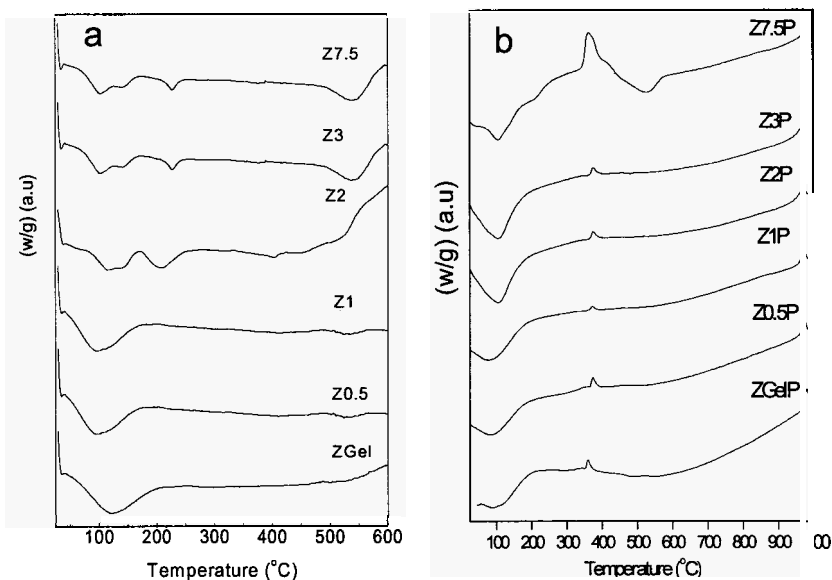


Figure 3. DSC curves of the solids. (a) ZGel, Z0.5, Z1, Z2, Z3 and Z7.5 samples. (b) ZGelP, Z0.5P, Z1P, Z2P, Z3P and Z7.5P samples.

The endothermic peak above the 400° C for the Z1 (525°C), Z2 (403°C) and Z3 (545°C) samples is due to the condensation of the monohydrogen phosphates group to form lamellar pyrophosphate. The absence of this peak, in the platinum-based samples, indicates that higher temperatures are required to condense the monohydrogen phosphates group, when platinum is present.

The differences of intensity and position of the endothermic peaks below 300°C are due to the rates in which hydrating water is lost. It is not possible to

remove water from the crystalline samples at the range of 100-150°C without changing the phase. The shifting to the δ -ZrP (7.41 Å) phase occurs first, because the water molecule has difficulties to be released from the lattice. The definition of the three endothermic peaks was not observed in the range of 100 to 250°C for the semi-crystalline samples exchanged with platinum, indicating that the presence of the $[\text{Pt}(\text{NH}_3)_4]^{2+}$ complex makes the exit of water easier. The bonding NH_3 was removed from the $[\text{Pt}(\text{NH}_3)_4]^{2+}$ complex at temperatures below 300°C, leading to the formation of species of the $[\text{Pt}(\text{NH}_3)_x]^{2+}$ kind until reaching the complex decomposition, which occurs at about 350 °C.

All samples were active in HTS reaction (Fig.4) and the presence of platinum increased the catalytic activity as we can conclude by comparing these values with those obtained with the Z7.5 sample ($2.6 \times 10^{-3} \text{ mol.g}^{-1}.\text{h}^{-1}$). In these samples, α -ZrP acts both as support and as catalyst. Different performances were observed as a function of the crystallinity, this is ascribed to the increasing of the inner surface, due to the lamellas organization on the C direction of the crystallographic planes, making easier the contact between reactants and active sites. All catalysts were stable during reaction. The most crystalline sample and containing platinum displayed a catalytic performance 18 times higher than the last generation HTS catalysts ($2.1 \times 10^{-3} \text{ mol.g}^{-1}.\text{h}^{-1}$) which are iron oxide-based solids doped with chromium and copper oxide. This sample represents a promising alternative for the HTS reaction, in less expensive conditions for industrial operations.

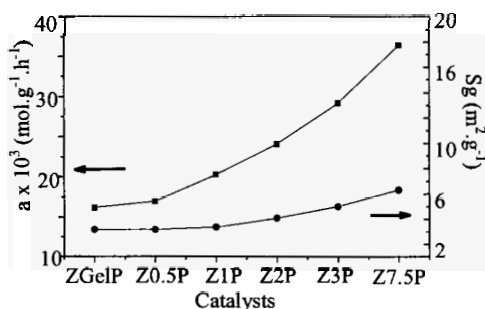


Figure 4. Specific surface area (Sg) and activity (a) of the platinum-containing catalysts: ZGelP, Z0.5P, Z1P, Z2P, Z3P and Z7.5P samples.

4. Conclusions

Layered zirconium hydrogenphosphate is a promising catalyst to water gas shift reaction. The exchange with platinum increased the activity even more. The

catalytic activity results indicate that this property varies as a function of the crystallinity. An increase in the crystallinity caused a reduction of the ionic exchange rates, but increased the specific surface area values and favored a better catalytic performance. This is ascribed to the lamellar organization, which increases the reactants access to active sites (platinum). Thus, the sample more crystalline and with higher specific area showed better catalytic performance.

Acknowledgments

The authors thank to FINEP, CNPq for the financial support.

References

1. G. Alberti, M. Casciola, U. Constantino and R. Vivani, *Adv. Mater.* **8**, 291 (1996).
2. W.H.J. Hogarth, J.C.D. Costa, J. Drennan, and G.Q.Lu, *J. Mater. Chem.* **15**, 754 (2005).
3. D.P. Das, K. Parida and B.R. De, *J. Mol. Catal. A: Chem.* **245**, 217 (2006).
4. A. Ginestra, P. Patrono, M.L Berardelli, P. Galli, C. Ferragina, and M.A. Massucci, *J. Catal.* **103**, 346 (1987).
5. J.S. Campbell, P.Craven and P.W. Young, *Catalyst Handbook*, Wolfe Scientific Books, London, p.97 (1970).
6. H. Bohlbro, *An Investigation on the Kinetics of the Conversion of Carbon Monoxide with Water Vapor Over Oxide based Catalyst*, The Haldor Topsoe Research Laboratory, Verback, p.35 (1969).
7. D.S. Newsome, *Catal. Rev.-Sci.Eng.* **275**, 2192 (1980).
8. G.C. Chichen, R.H. Logan, M.S.Spencer, *Appl.Catal.* **12**, 89 (1984).
9. A. Clearfield, and J. M. Kalnins, *J. Inorg. Nucl. Chem.* **38**, 849 (1976).
10. A. Clearfield and J. A. Stynes, *J. Inorg. Nucl. Chem.* **26**, 117 (1964).
11. S. Ahrland, J.Albertsson, A. Oskarsson and A. Niklasson, *J. Inorg. Nucl. Chem.* **32**, 2069 (1970).
12. P.J.Elving and E. C. Olson, *Anal. Chem.* **27**, 1817 (1955).
13. D.N. Bernhardt and A.R. Wreath, *Anal. Chem.* **27**, 440 (1955).
14. M. Webb, *Ion Exchange Developments and Aplications- Spec. Publ. -R. Soc. Chem.* **182**, 134 (1996).
15. V. Vesely and V. Pekarek, *Talanta* **19**, 219 (1972).
16. J. Novákova, L. Kubelková, L. Brabec, Z. Bastl, N. Jaege. and G. Schulz-Ekloff, *Zeolites* **16**, 173 (1996).
17. A. Clearfield, *Inorganic Ion Exchange Materials*, Editora CRC Press, Boca Raton, Flórida, p.2 (1982).

AMINE-FUNCTIONALIZED SBA-15 SILICA FOR THE ADSORPTION OF CARBON DIOXIDE

H. ŠIKLOVÁ, A. ZUKAL, AND J. CEJKA

J. Heyrovský Institute of Physical Chemistry, v.v.i., Academy of Sciences of the Czech Republic, Dolejškova 3, CZ-182 23 Prague 8, Czech Republic

E-mail: jiri.cejka@jh-inst.cas.cz

V. ZELENÁK

Department of Inorganic Chemistry, Institute of Chemistry, P.J. Safarik University, Moyzesova 11, SK-041 54 Kosice, Slovak Republic

E-mail: vladimir.zelenak@upjs.sk

Functionalization of SBA-15 silica with three ligands differing in amine group basicity, namely 3-aminopropyl, 3-(methylamino)propyl and 3-(phenylamino)propyl ligand was investigated and these materials were tested in CO₂ adsorption. The materials prepared were characterized by nitrogen adsorption at 77 K, X-ray powder diffraction and thermal analysis. Adsorption isotherms of carbon dioxide were measured at 273.2 K; temperature dependence of carbon dioxide adsorption on selected samples was measured in the temperature range from 273.2 to 313.2 K. Isothermic adsorption heats calculated from these data showed the contrast between adsorption behavior of carbon dioxide on the purely siliceous surface and surface grafted with amine groups. The sample containing the highest concentration of aminopropyl ligands showed the steepest carbon dioxide adsorption isotherm. The amount of CO₂ adsorbed on this sample attains 17.8 cm³/g STP at 10 torr in contrast to pure SBA-15 silica, which adsorbs at the same equilibrium pressure 0.9 cm³/g STP only.

1. Introduction

Carbon dioxide is one of the greenhouse gases increasing concentration in the atmosphere of which is assumed to have direct linkage to global climate changes. Therefore, it is important to find an efficient and economic route to entrap and store CO₂ produced during various technological processes. Mesoporous molecular sieves due to their high void volume are promising materials for adsorption of different gases and vapors. Particularly, an addition of amine functional groups to ordered mesoporous silicas offers a possibility to bridge the limits of currently used liquid amine processes for the removal of CO₂.

Functionalization of ordered mesoporous silicas in order to obtain materials for CO₂ adsorption has been extensively examined. Recently, Harlick and Sayari

have published a study with detailed literature review comparing amine-grafted silica-based adsorbents [1]. The most instructive examples of functionalization are shown hereinafter. Pore expanded MCM-41 silica coated with 3-[2-(2-aminoethylamino)ethylamino]propyltrimethoxysilane, exhibited a 117 mg/g adsorption capacity at 298 K and 1 atm for a dry 5 % CO₂ in N₂ feed mixture [1]. By modifying of as-prepared water-washed SBA-15 mesoporous silica with tetraethylenepentamine (TEPA) it was found that the existence of Pluronic P123 template in SBA-15 promotes the capture of CO₂ [2]; the adsorption capacity of such prepared materials attained 144 mg/g at 1 atm and 348 K. The concept called “molecular basket” was explored by Xu et al. [3,4]. The sterically branched polymer polyethylenimine, which has chains with numerous CO₂-capturing aminogroups, was immobilized into the channels of the mesoporous MCM-41 silica. The adsorption capacity attained 133 mg/g at 1 atm and 348 K. Aminopropyl-functionalized MCM-41 silica was reported in the study [5]. Achieved adsorption capacity attained 70 mg/g under 90 % CO₂/Ar mixture (1 atm) at 293 K.

In the present study we have investigated SBA-15 silica functionalized by three amine ligands, namely 3-aminopropyl, 3-(methylamino)propyl or 3-(phenylamino)propyl (PAP) ones. The use of these ligands enabled us to find the influence of the basicity of amine groups both on the shape of CO₂ adsorption isotherms and isosteric adsorption heats of CO₂. The understanding gained through such a study should help to guide future work to improve adsorption properties of functionalized silicas.

2. Experimental

2.1. Materials

SBA-15 silica was prepared according to ref. [6] using poly-(ethylene glycol)-poly-(propylene glycol)-poly-(ethylene glycol) block copolymer Pluronic P123 as a templating agent. Before grafting, the calcined silica was heated at 573 K for 3 h (10 K/min) under vacuum to remove adsorbed water. The batch of 0.5 g of dehydrated SBA-15 was dispersed in 25 cm³ of toluene dried over zeolite sieve 4A. Then 0.5-2.0 mmol of the respective silane (i.e. 3-aminopropyl-trimethoxysilane, 3-(methylamino)propyl-trimethoxysilane and 3-(phenylamino)propyl-trimethoxysilane) were added and the suspension was stirred at ambient temperature for 5 h under argon atmosphere. The solid product was recovered by filtration, repeatedly washed out with toluene and dried at 353 K.

The materials prepared are listed in Table 1. The functionalized samples are labeled with the abbreviations of respective ligands (3-aminopropyl = AP, 3-(methylamino)propyl = MAP, and 3-(phenylamino) propyl = PAP).

2.2. Methods

Adsorption isotherms of nitrogen at 77 K and carbon dioxide in the temperature range from 273.2 to 313.2 K were determined using an ASAP 2020 (Micromeritics) static volumetric apparatus. In order to attain a sufficient accuracy in the accumulation of the adsorption data, the ASAP 2020 was equipped with pressure transducers covering the 133 Pa, 1.33 kPa and 133 kPa ranges. The home-made thermostat maintaining temperature of the sample with accuracy of ± 0.01 K was used for the measurement of carbon dioxide isotherms. Before each adsorption measurement the sample was outgassed under turbomolecular pump vacuum using a special heating program allowing for a slow removal of most preadsorbed water at low temperatures. This was done to avoid potential structural damage of the sample due to surface tension effects and hydrothermal alternation. Starting at ambient temperature the sample was outgassed at 383 K (temperature ramp of 0.5 K/min) until the residual pressure of 0.5 Pa was obtained. After further heating at 383 K for 1 h the temperature was increased (temperature ramp of 1 K/min) until the temperature of 623 K was achieved. This temperature was maintained for 8 h.

X-ray powder diffraction data (not shown) were recorded on a Bruker D8 X-ray powder diffractometer equipped with a graphite monochromator and position sensitive detector (Vântec-1) using CuK α radiation (at 40 kV and 30 mA) in Bragg-Brentano geometry.

The thermal analysis of grafted materials was carried out using STA Netzsch 409PC apparatus up to 1273 K with heating rate 9 K/min under dynamic air atmosphere (20 cm³/min).

3. Results and Discussion

Nitrogen adsorption isotherms at 77 K on the parent SBA-15 silica and functionalized samples are shown in Fig. 1. All the isotherms are characterized by the H1 hysteresis loop, which is typical of the SBA-15 mesoporous structure. Structure parameters of the samples are summarized in Table 1. The BET surface area was calculated from the nitrogen isotherm in the range of relative pressures 0.05 – 0.24. The mesopore volume and mesopore diameter were calculated from the desorption branch of the hysteresis loop using the BJH method. The inspection of structural parameters clearly reveals that the character

of the SBA-15 porous framework is preserved in all functionalized samples. However, owing to the functionalization the surface area decreased from 882.9 m^2/g to 198.3 m^2/g ; the mesopore volume decreased from 1.045 cm^3/g to 0.311 cm^3/g . The mesopore diameter markedly decreased for samples SBA-15/AP3 and SBA-15/PAP from 6.2 to 4.6 and 4.8 nm, respectively (cf. Table 1 and Fig. 1). The decrease in the mesopore volume and mesopore diameter may be attributed to the presence of organic ligands on the mesopore surface. At the same time it may be supposed that ligands contribute to the smoothing of corrugated corona around the mesopores, which causes the decrease in the surface area [7].

To characterize the thermal stability of the grafted materials and to investigate maximum operation temperature, which can be used with the modified materials, the samples were characterized by thermal analysis. Fig. 2 shows TG curves of the samples SBA-15, SBA-15/AP/2, SBA-15/AP/3, SBA-15/MAP and SBA-15/PAP. The weight loss in the temperature range 300 – 440 K corresponds to the thermodesorption of adsorbed moisture. With further heating above 440 K the pyrolysis of amine ligands took place. The onset of the decomposition of AP, MAP and PAP ligands decreased with the increasing molar weight of the ligands. The total weight loss corresponding to the pyrolysis of the organic ligands expressed in wt. % of the dry sample is given in the Table 1. The differences in the mass weight indicate the different amounts of amines grafted on the surface of the SBA-15. Since for carbon dioxide adsorption a concentration of amine groups as adsorption centres is the most important

Table 1. Structural parameters, TG results and adsorption capacities of CO_2 on parent and modified SBA-15 samples.

Sample code	S_{BET} (m^2/g)	V_{ME} (cm^3/g)	D_{ME} (nm)	Weight loss (wt. %)	Loading of ligands (mmol/g)	Adsorption capacity	
						10 torr (cm^3/g STP)	750 torr
(A) SBA-15	882.9	1.045	6.2		0	0.9	34.5
(B) SBA-15/AP1	561.7	0.785	5.8	6.5	1.1	3.6	28.1
(C) SBA-15/AP2	459.9	0.677	5.6	11.5	2	9.7	30.7
(D) SBA-15/AP3	198.3	0.311	4.6	15.3	2.6	17.8	35.4
(E) SBA-15/MAP	445.3	0.672	5.6	19.7	2.7	8.5	29.9
(F) SBA-15/PAP	307.2	0.472	4.8	17.9	1.3	0.7	18.5

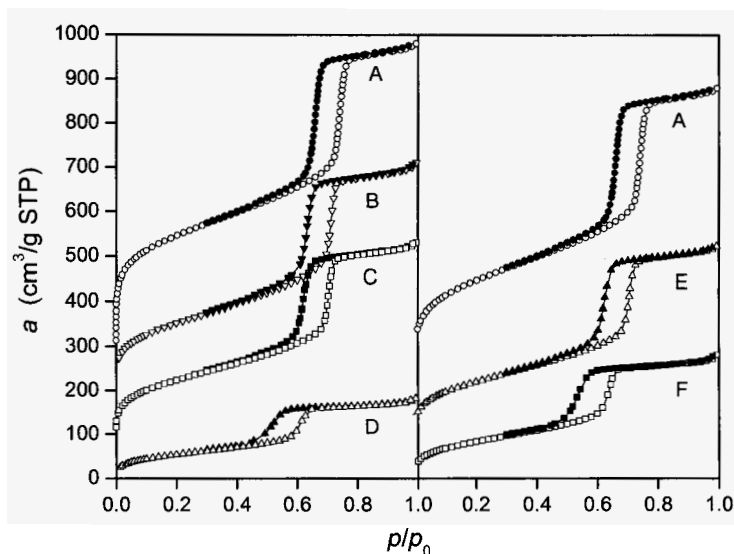


Figure 1. Nitrogen adsorption isotherms for samples (A) SBA-15, (B) SBA-15/AP1, (C) SBA-15/AP2, (D) SBA-15/AP3, (E) SBA-15/MAP, (F) SBA-15/PAP. Except for that on samples SBA-15/AP3 and SBA-15/PAP, isotherms are shifted by 100 cm³/g each. Solid symbols denote desorption.

characteristics, the amount of the amine groups was calculated from thermogravimetric data (Table 1).

Adsorption isotherms of carbon dioxide at 273 K were measured on all prepared samples. These isotherms are shown in Fig. 3; interpolated amounts adsorbed for 10 and 750 torr are listed in Table 1. Both isotherms and interpolated values show distinct differences in the adsorption properties of studied materials. Pure SBA-15 silica does not interact very strongly with CO₂ because the surface hydroxyl groups are not able to induce sufficiently strong interactions and other adsorption sites are missing. With samples with AP ligands the adsorption capacity and steepness of the isotherm strongly increase with increasing amount of amine groups. The sample SBA-15/AP/3 showed the steepest isotherm and the highest adsorption capacity attaining 35.4 cm³/g STP at 750 torr. It should be noted that this capacity expressed in mg CO₂ per 1 g of adsorbent equals to 67.8 mg/g; this value is practically the same as the capacity reported in the ref. [5]. The lower basicity of the MAP and especially PAP

ligands results in the reduced steepness of the CO₂ isotherms and lower adsorption capacities of 29.9 and 18.5 cm³/g STP, respectively, at the same equilibrium pressure.

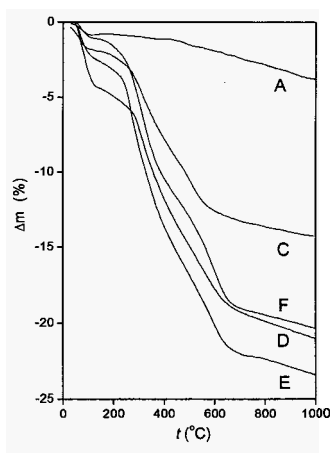


Figure 2. Thermogravimetric curves for samples (A) SBA-15, (C) SBA-15/AP2, (F) SBA-15/PAP, (D) SBA-15/AP3 and (E) SBA-15/MAP.

With samples SBA-15, SBA-15/AP/2, SBA-15/MAP and SBA-15/PAP adsorption isosteres were calculated by means of interpolation adsorption isotherms at 273, 283, 293, 303 and 313 K. Dependences of isosteric adsorption heats q_{st} on amount adsorbed, determined from the slope of the adsorption isosteres, are shown in Fig. 4. The isosteric adsorption heats obtained with SBA-15 change little over the adsorption range measured. Their values of 22-25 kJ/mol are slightly above the molar heat of CO₂ condensation. This indicates a moderate strength of interaction between the adsorbed carbon dioxide molecules and the silica surface. Turning to the functionalized samples containing AP and MAP ligands, very high initial energies of interactions were found in the order of 60-70 kJ/mol. The high values of q_{st} at low surface coverage thus seem to be due to strong interaction between carbon dioxide molecules and amine groups. Once all available amine groups had interacted with the carbon dioxide the gas adsorbed gradually on less reactive surface sites; for this reason, isosteric adsorption heat decreases and approaches values for the siliceous SBA-15. Isosteric adsorption heats determined for CO₂ adsorption on the sample with PAP ligands show that the basicity of ligands plays a decisive role. With accordance of the lower basicity of PAP ligand the maximum isosteric

adsorption heat of 35-37 kJ/mol at low surface coverage quickly decrease to the q_{st} values determined for SBA-15. This dependence of q_{st} on the amount adsorbed indicates a weaker interaction of CO₂ molecule with a PAP ligand.

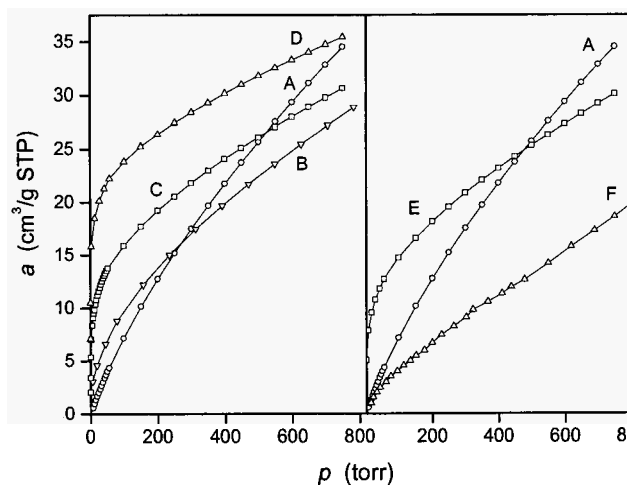


Figure 3. Amounts of adsorbed carbon dioxide for the samples (A) SBA-15, (B) SBA-15/API, (C) SBA-15/AP2, (D) SBA-15/AP3, (E) SBA-15/MAP and (F) SBA-15/PAP.

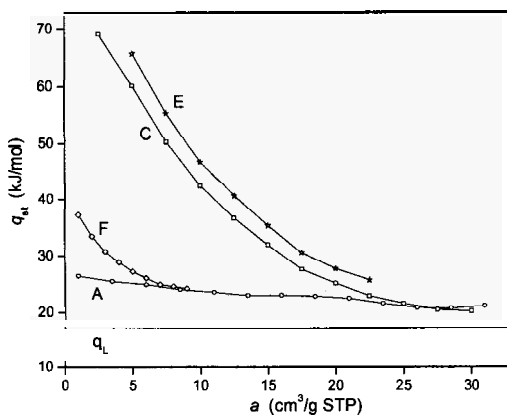


Figure 4. Isothermic heat of adsorption of CO₂ on (A) SBA-15, (C) SBA-15/AP2, (E) SBA-15/MAP and (F) SBA-15/PAP (q_L denotes the molar heat condensation).

4. Conclusion

In this study the effects of post-synthesis amine grafting of SBA-15 silica were investigated. The study of adsorption properties of materials prepared has shown that the steepness of carbon dioxide isotherms and respective adsorption capacities depend on both the amount of amine ligands and their basicity. The steepness of CO₂ adsorption isotherm increases with increasing basicity of amine ligands and their concentration on the surface.

The sample SBA-15/AP3 containing the highest concentration of aminopropyl ligands showed the steepest carbon dioxide adsorption isotherm and the highest adsorption capacity. The respective amounts of CO₂ adsorbed on this sample are 17.8 and 35.4 cm³/g STP at 10 and 750 torr, respectively. Such material can be of potential interest to recover trace amounts of CO₂ due to very strong interaction of carbon dioxide with aminopropyl ligands at low surface coverage.

Acknowledgements

The authors thank EU for financial support of the project (DeSSANS, SES6-CT-2005-020133). JC and AZ thank the Academy of Sciences of the Czech Republic (KAN100400701).

References

1. P.J.E. Harlick and A. Sayari, *Ind. Eng. Chem. Res.* **46**, 446 (2007).
2. M.B. Yue, Y. Chun, Y. Cao, X. Dong and J.H. Zhu, *Adv. Funct. Mater.*, **16**, 1717 (2006).
3. X. Xu, C. Song, J.M. Andresen, B.G. Miller and A.W. Scaroni, *Energy & Fuels*, **16**, 1463 (2002).
4. X. Xu, C. Song, J.M. Andresen, B.G. Miller and A.W. Scaroni, *Microporous Mesoporous Mater.*, **62**, 29 (2003).
5. G.P. Knowles, J.V. Graham, S.W. Delaney and A.L. Chaffe, *Fuel Processing Technol.*, **86**, 1435 (2005).
6. D. Zhao, Q. Huo, J. Feng, B.F. Chmelka and G.D. Stucky, *J. Am. Chem. Soc.* **120**, 6024 (1998).
7. G.A. Zickler, S. Jähnert, W. Wagermaier, S.S. Funari, G.H. Findenegg and O. Paris, *Phys. Rev. B*, **73**, 184109 (2006).

ADSORPTION OF VOLATILE ORGANIC COMPOUNDS ON PORE EXPANDED MESOPOROUS MATERIALS

RODRIGO SERNA-GUERRERO and ABDELHAMID SAYARI

Centre for Catalysis Research and Innovation (CCRI), Department of Chemical Engineering and Department of Chemistry, University of Ottawa, Ottawa, Canada, K1N6N5

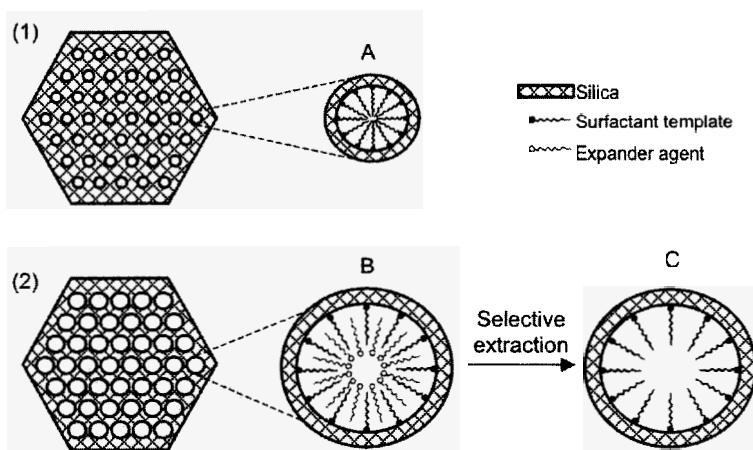
Among the various characteristics that make ordered nanoporous materials potential candidates for adsorption and catalytic applications, the possibility to tailor their structural properties in a relatively easy manner is particularly attractive. In the present work, surfactant-laden nanoporous silica (PE-MCM-41E) was synthesized by means of a pore expansion hydrothermal post-synthesis treatment of as-synthesized MCM-41 followed by selective extraction of the expander agent. This unique material offers the hydrophobic characteristics of the organic surface layer while maintaining significant porosity. PE-MCM-41E was evaluated as an adsorbent of representative volatile organic compounds. For comparison, purely siliceous mesoporous materials before and after pore expansion by hydrothermal treatment (referred to as MCM-41 and PE-MCM-41C, respectively) were also studied. PE-MCM-41E exhibited strong interactions with chlorinated hydrocarbons in terms of heat of adsorption (ΔH_a) and adsorption efficiency in the presence of water vapor. PE-MCM-41E maintained 89% of its capacity in dry streams for dichloromethane while MCM-41 maintained only 80%. Purely siliceous nanoporous materials exhibited strong compatibility with aromatic compounds. In the case of adsorption in the presence of humidity, MCM-41 adsorbed 87% of its capacity for dry benzene compared to 84% for PE-MCM-41C and 81% for PE-MCM-41E.

1. Introduction

Volatile organic compounds (VOCs) represent a wide range of chemical species whose use and production are essential for the chemical industry nowadays. Unfortunately, VOCs are known to be pollutants that contribute to global warming and the ozone layer depletion. Furthermore, some of them are known to be toxic to humans, animals and vegetation alike. Due to their volatile nature, they mix easily with atmospheric air and are easily lost due to fugitive emissions. For these reasons it is imperative to innovate technologies to minimize the release of VOCs to the environment in an efficient and economic manner.

Adsorption separation technologies have gained attention recently due to their working capacity in a wide range of fluid concentrations and their

relatively low energetic demand compared with other alternatives like liquid absorption or incineration. In the quest of the most appropriate adsorption technologies, researchers have synthesized and studied several novel materials with promising characteristics as adsorbents for VOCs. The recently developed family of ordered mesoporous materials (OMMs) exhibit features that make them a good alternative for the objective hereby pursued [1, 2]. OMMs exhibit high surface area and a highly ordered porous structure, but it is the possibility to tailor their surface properties and structure that makes them particularly attractive.



Scheme 1. Representation of the surfactant-layered mesoporous materials with and without pore expansion post-synthesis treatment.

To target non-polar organic molecules, some authors tried to enhance the hydrophobicity of mesoporous materials by attaching hydrophobic molecules (either during synthesis or by means of a post-synthesis treatment) on the silica surface [3-5], since it is widely accepted that non-polar molecules interact more strongly with hydrophobic adsorbents [6]. A less costly procedure consists of retaining the surfactant molecules used as template during the mesoporous silica synthesis inside the silica pores, hence producing surfactant laden mesoporous silica, as represented schematically by Material "A" in Scheme 1 [7,8]. Although some of these surfactant-containing adsorbents reported in the literature exhibited attractive features as adsorbents for VOCs, these materials have a low porosity. This is a major drawback since adsorption separation is a

surface phenomenon and it is known that most of the surface area of porous materials is found precisely inside the pores.

To overcome such problem, the present work proposes the use of a post-synthesis treatment to increase the pore size of an ordered mesoporous silica type MCM-41 with a subsequent selective extraction of the expander agent, thus producing a surfactant laden mesoporous silica with significant porosity (represented by Material C in Scheme 1). Hereby, the performance of this novel mesoporous material is evaluated as adsorbent for chlorinated and aromatic hydrocarbons. The heat of adsorption (ΔH_a) and adsorption capacity (q) were determined in both dry and humid environments. Additionally, purely siliceous MCM-41 before and after post synthesis pore-expansion is investigated for comparison.

2. Experimental

2.1. *Synthesis of Materials*

The adsorbents used were prepared as described previously for MCM-41 [9], PE-MCM-41C [10] and PE-MCM-41E [11]. A solution containing 578.6 g of TMAOH 25% in 5500 g of water was prepared under vigorous stirring at ambient temperature in an 8 L stainless steel vessel. Cetyl-trimethylammonium bromide (820 g) was subsequently added, and stirred for 15 minutes. Finally, 328.4 g of Cab-O-Sil fumed silica was added, producing a mixture with the following composition 1.0 SiO₂:0.343 TMAOH:0.41 CTAB:57 H₂O. The resulting gel was placed in an oven and stirred at 100 °C under autogeneous pressure for 40 h. The material obtained was thoroughly washed with water, filtered and dried at ambient conditions. A sample of this material was calcined for 5 hours at 550 °C, under nitrogen flow during the temperature ramp then under flowing air when the temperature reached 550 °C. This template-free material was labeled MCM-41.

To produce pore-expanded MCM-41, an emulsion was prepared by adding 437.5 g of DMDA in 5250 g of water under vigorous stirring at ambient temperature. Subsequently, 350 g of as-synthesized MCM-41 (i.e. before calcination) was added and the mixture was kept under stirring for 15 more minutes. The resulting suspension was heated in a stainless steel closed vessel at 120 °C under continuous stirring for 72 h. After this time, the product was washed with water, filtered and dried in ambient air. Subsequently, DMDA was selectively extracted by washing the material with ethanol twice using a ratio of 18.5 ml and 9.7 ml per gram of as synthesized MCM-41 in the first and second

extractions, respectively. The material was subsequently filtered and dried in air and was labeled “PE-MCM-41E” where “PE” and “E” indicate that the material was pore-expanded and selectively solvent-extracted. A sample of the material obtained after pore expansion was calcined at 550 °C for 5 h under air flow to remove both expander and template surfactants and was labeled “PE-MCM-41C” with “C” to indicate that the pore-expanded material was calcined.

2.2 Characterization

To determine the surface properties of the materials, nitrogen adsorption isotherms at 77 K were measured using a Micromeritics ASAP 2020 automated volumetric instrument. Before each analysis, the adsorbents were evacuated at high vacuum (1×10^{-5} torr) at 100 °C. In the particular case of PE-MCM-41E the pretreatment temperature was maintained at 50 °C to avoid thermal degradation of the surfactant molecules on its surface. The surface area was determined using the widely accepted Brunauer-Emmet-Teller method. The pore size distribution was estimated with the Kruk-Jaroniec-Sayari (KJS) method [12], which was developed from the Kelvin equation to fit mesoporous materials.

In addition, dichloromethane and benzene adsorption isotherms at ambient temperature (i.e. 25 °C) were determined for the three adsorbents under study using a TA Instruments Q-500 thermogravimetric analyzer (TGA). To generate each point of the isotherm, a stream of nitrogen with known concentration of VOC was directed to the TGA sample chamber. The amount adsorbed was measured at the moment when the sample weight was constant and hence equilibrium could be assumed.

2.3. Heat of adsorption

ΔH_a and Henry's law constants (k) at different temperatures were estimated by the pulse chromatographic method [13] using nitrogen as carrier gas. Using a two-position six-way valve, a 0.025 ml pulse of VOC loaded nitrogen was directed to a stainless steel fixed bed column packed with 1.3 ml of adsorbent and kept at a constant temperature using an electric furnace. The column outlet was continuously monitored with the use of a flame ionization detector (FID). The FID response was recorded in real time using National Instruments Data Acquisition software and hardware.

According to the work of Schneider and Smith [13], the mean retention time of the adsorbate inside the fixed bed column can be approximated by the first absolute moment of the profile of concentration at the column outlet versus time:

$$\mu_1 = \frac{\int (t - \mu_D) C_A dt}{\int C_A dt}$$

where μ_1 is the mean retention time, t is time, μ_D is the mean dead time of the fluid in the experimental setup and C_A is the concentration of the adsorbate at the column downstream. From the first absolute moment, a dimensionless form of Henry's law constant can be calculated:

$$\mu_1 = \frac{L}{u} \left[1 + \frac{(1-\varepsilon)}{\varepsilon} K \right]$$

where L is the length of the column, u is the fluid interstitial velocity, ε is the bed porosity and K is a dimensionless form of Henry's law constant. By determining Henry's law constant values at different temperatures, an Arrhenius type plot of $\ln K$ versus T^{-1} can be generated in which the slope of the curve is proportional to the heat of adsorption [13-16]:

$$\ln K_p = \ln A - \frac{\Delta H_a}{R} (T)^{-1}$$

where K_p is the dimensional form of Henry's law constant, and R is the universal gas constant.

2.4. Adsorption capacity in dynamic processes

To calculate q for single components in a dry environment, breakthrough curves analysis [5] was performed by feeding a continuous stream of VOC at a partial pressure of 0.10 to a fixed bed column monitored with a FID at its outlet. To generate the humid environment a second stream of nitrogen was bubbled into a glass saturator containing water at a constant temperature of 5 °C ($P_{\text{vap}} = 8.7 \times 10^{-3}$ bar) and subsequently mixed with the single VOC containing stream before entering the fixed bed column. The adsorption capacity (q) was determined from the breakthrough profile using a constant flow rate and mass of adsorbent:

$$q = \frac{F_A t_q}{W}$$

where F_A is the flow rate of adsorbate, and W is the mass of adsorbent in the column. In this case, t_q is the stoichiometric time, which is calculated from the breakthrough profile with [17]:

$$t_q = \int_t \left(1 - \frac{C_A}{C_0} \right) dt - t_D$$

where C_0 is the adsorbate concentration at the column inlet and t_D is the experimental setup dead time for breakthrough experiments.

3. Results and Discussion

3.1 Characterization

The adsorption isotherms determined experimentally for the three materials hereby studied are presented in Figure 1. It can be seen that all materials present a Type IV isotherm according to the IUPAC classification, which is characteristic of mesoporous materials. The absence of hysteresis loop for MCM-41 has been well documented previously in mesoporous materials with pore diameters of less than 4 nm [7, 8]. This is in agreement with the estimated pore size distribution of MCM-41, which is very narrow with maxima at 3.5 nm. With respect to PE-MCM-41C and PE-MCM-41E, the nitrogen adsorption isotherms exhibited a shift of the condensation step to higher partial pressures and a hysteresis loop. These two phenomena can be directly related to an effective pore expansion after the post-synthesis treatment.

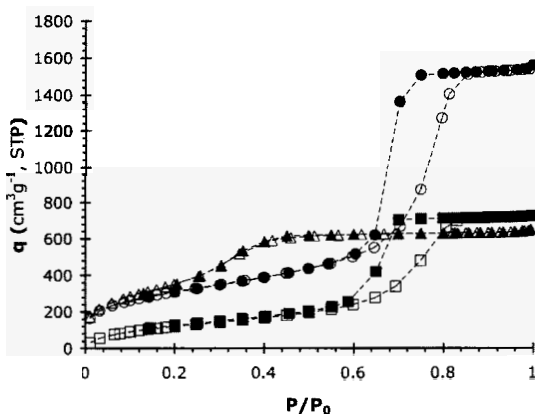


Figure 1. Nitrogen adsorption (open symbols) and desorption (closed symbols) isotherms for MCM-41 (triangles), PE-MCM-41E (squares) and PE-MCM-41C (circles). Dotted lines included are for clarity purposes only

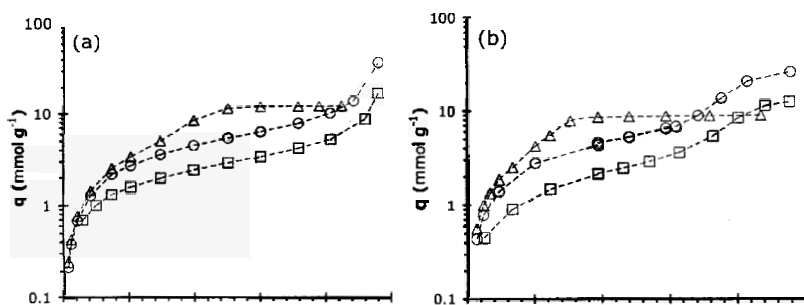
The pore size distributions determined for the pore-expanded materials effectively show a maxima at larger pore diameters than that of MCM-41 (i.e. 7 nm for PE-MCM-41E and 9 nm for PE-MCM-41C) while maintaining a relatively narrow distribution. Although both PE-MCM-41E and PE-MCM-41C were subjected to the same post-synthesis treatment, each one presented a particular pore size and nitrogen adsorption isotherm. It can be inferred that such difference is a result of the space occupied by the occluded surfactant inside the expanded mesopores, suggesting that the synthesis route followed to produce

PE-MCM-41E effectively produced a material functionalized with surfactant molecules and significant void space inside the channels.

Table 1. Structural parameters of mesoporous silicas determined by nitrogen adsorption measurements at 77 K

	S_A ($m^2 g^{-1}$)	V_p ($cm^3 g^{-1}$)	d_p (nm)	ρ_p ($g cm^{-3}$)	ρ_b ($g cm^{-3}$)
MCM-41	1086	0.86	3.5	2.29	0.55
PE-MCM-41E	379	0.83	7.7	1.44	0.80
PE-MCM-41C	1119	2.35	9.2	2.54	0.37

In addition to the nitrogen adsorption measurements, adsorption isotherms at ambient temperature for two VOCs were determined and are presented in Fig. 2. In both cases, it is seen that MCM-41 presents a higher capacity at equilibrium at low VOC concentrations, which is a result of its smaller pore diameter. It can also be seen that at high concentrations of benzene and dichloromethane, there is a sharp increase in adsorption capacity by the pore-expanded materials resulting in a significantly higher total capacity. This can be a result of the larger pore size and volume of the pore-expanded adsorbents, which would accommodate a larger number of VOC molecules inside their pores.



3.2 Heat of adsorption

Figure 3 presents the Arrhenius type plots from which values of ΔH_a were estimated. The surfactant-containing silica (PE-MCM-41E) exhibited the strongest interaction with dichloromethane (DCM) having a $-\Delta H_a$ of 57 kJ/mol.

To corroborate this tendency, experiments were performed using a second chlorinated molecule, i.e. chloroform. As seen in Figure 3a, PE-MCM-41E presented once again the strongest interaction while the non-expanded MCM-41 offered the lowest $-\Delta H_a$, replicating the tendency observed with DCM. This can be a result of an enhanced compatibility between the organic adsorbents and the hydrophobic layer on PE-MCM-41E's surface.

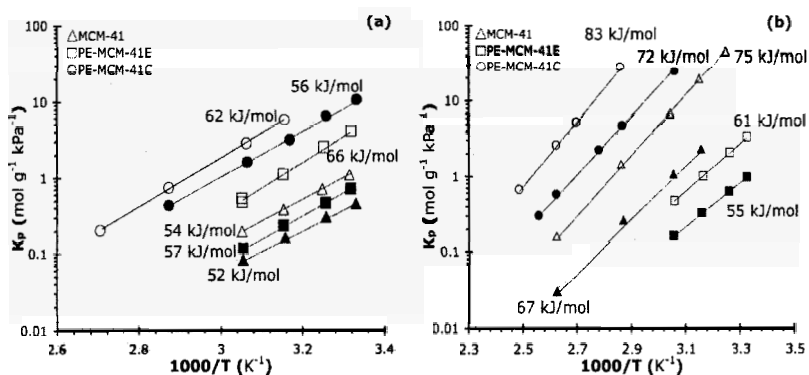


Figure 3. Van't Hoff plots for the adsorption of (a) dichloromethane (closed symbols) and chloroform (open symbols) and (b) benzene (closed symbols) and toluene (open symbols). The values presented in the plot correspond to the heat of adsorption estimated from the closest set of data

The observed tendency in chlorinated hydrocarbons did not occur in the case of aromatic compounds. As seen in Figure 3b, in the case of benzene, PE-MCM-41C presented the highest $-\Delta H_a$ followed closely by MCM-41. It can also be observed that the values of $-\Delta H_a$ of PE-MCM-41E are significantly lower than that of its purely siliceous counterparts. This is attributed to a chemical bonding between the π -electrons in the aromatic hydrocarbons and the hydroxyl groups present in the silica surfaces as reported by other workers [18]. This effect was corroborated using a second aromatic molecule as adsorbate: toluene. As seen in the results from Figure 3b, the purely siliceous materials exhibited once again extremely strong interactions with toluene while the surfactant layer in PE-MCM-41E inhibited the aforementioned chemical interaction. This is evidence of the change in surface chemistry produced by using different post-synthesis treatment routes in the synthesis of each adsorbent even though they were all produced from the same parent mesoporous silica.

3.3 Adsorption Capacity

The values of q estimated with breakthrough curves analysis are summarized Table 2. For the case of dichloromethane in dry streams, the capacities obtained were in the order MCM-41 > PE-MCM-41C > PE-MCM-41E. This tendency is in agreement with the adsorption capacity at equilibrium observed in Figure 2 at low concentrations. However, PE-MCM-41E showed the best efficiency for dichloromethane with a q_{humid} of 89% with respect to dry streams, corroborating its compatibility with this type of VOCs.

For aromatic hydrocarbons, the order obtained was MCM-41 > PE-MCM-41C > PE-MCM-41E once again replicating the equilibrium capacity measurements at low concentration (Figure 2). In humid streams, MCM-41 exhibited the best efficiency, adsorbing 87% of the amount adsorbed under dry conditions. These results demonstrate that the organically modified PE-MCM-41E presents high compatibility with halogenated hydrocarbons while the purely siliceous MCM-41 and PE-MCM-41EC exhibit stronger interactions with aromatic compounds.

Table 2. Adsorption capacity of mesoporous silicas for selected VOCs at a relative pressure of $P/P_0 = 0.10$ in mmol per gram of silica (values in parenthesis are expressed in mmol per gram of adsorbent)

Adsorbent	Dichloromethane				Benzene			
	t_q	q	q_h	q_h/q	t_q	q	q_h	q_h/q
MCM-41	289	1.88	1.48	0.80	1331	2.43	2.10	0.87
PE-MCM-41C	160	1.55	1.30	0.84	767	2.07	1.73	0.84
PE-MCM-41E	212	1.76	1.56	0.89	568	1.40	1.13	0.81
		(0.97)	(0.86)			(0.77)	(0.62)	

References

1. J. S Beck, J. C. Vartuli, W. J. Roth; M. E. Leonowicz, C. T. Kresge, K. D. Schmitt, C. T-W. Chu, D. H. Olson, E. W. Sheppard, S. B. McCullen, J. B. Higgins and J. L. Schlenker, *J. Am. Chem. Soc.* **114**, 10834 (1992).
2. C. T. Kresge, M. E. Leonowicz, W. J. Roth, J. C. Vartuli and J. S. Beck, *Nature* **359**, 710 (1992).
3. V. Antochshuk and M. Jaroniec, *Chem. Mater.* **12**, 2496 (2000).
4. J. M. Kisler, M. L. Gee, G. W. Stevens and A. J. O'Connor, *Chem. Mater.* **15**, 619 (2003).
5. A. Matsumoto, H. Misran and K. Tsutsumi, *Langmuir* **20**, 7139 (2005).
6. A. Stein, B. J. Melde and R. C. Schroden, *Adv. Mater.* **12**, 1403 (2000).

7. H. Zhao, K. L. Nagy, J. S. Waples and G. F. Vance *Environ. Sci. Technol.* **34**, 4822 (2000).
8. Y. Miyake, T. Yumoto, H. Kitamura, T. Sugimoto, *Phys. Chem. Chem. Phys.* **4**, 2680 (2002).
9. A. Sayari and Y. Yang *J. Phys. Chem. B.* **104**, 4835 (2000).
10. M. Kruk, M. Jaroniec, V. Antochshuk and A. Sayari, *J. Phys. Chem. B* **106**, 10096 (2002).
11. A. Sayari, S. Hamoudi and Y. Yang, *Chem. Mater.* **17**, 212 (2005).
12. M. Kruk, M. Jaroniec and A. Sayari, *Langmuir*, **13**, 6267 (1997).
13. P. Schneider and J. M. Smith, *AIChE J.* **14**, 762 (1968).
14. T. Kopac, G. Dogu and T. Dogu, *Chem. Eng. Sci.*, **51**, 2201 (1996).
15. P. J. E. Harlick and F. H. Tezel, *Sep. Purif. Technol.*, **33**, 199 (2003).
16. J. Nokerman, X. Canet, P. Mougin, S. Limborg-Noetinger and M. Frère *Meas. Sci. Technol.* **16**, 1802 (2005).
17. A. Claudino, J. L. Soares, R. F. P. M. Moreira and H. J. Jose, *Carbon*, **42**, 1483 (2004).
18. O. Inel, D. Topaloglu, A. Askin and F. Yumsek, *Chem. Eng. J.* **88**, 255 (2002).

REMOVAL OF LOW VAPOUR PRESSURE TOXIC SUBSTANCES BY NANOPOROUS MATERIALS

J.M. MENESES, R. DENOYEL, J. ROUQUEROL

Madirel, Centre de St Jérôme, 13397 Marseille cedex 20, France

Adsorption of methyl salicylate (a simulant for mustard gas) and dimethyl methyl phosphonate (DMMP, a simulant for nerve agents) by various nanoporous adsorbents is studied. These molecules were chosen because their structure, size and functional groups are similar to those of the corresponding toxic molecule. Adsorbents are activated carbon (used as a benchmark), amorphous silica samples used in chromatography and some ordered mesoporous samples (MCM-48 or MCM-41 type). Because these simulant molecules have at room temperature a saturation pressure lower than 1 Torr, it was necessary to make use of specific adsorption equipment which is coupled with a Tian-Calvet type microcalorimeter. The highest affinity, i.e. the steepest adsorption isotherms at very low pressure, is obtained for the activated charcoal, which also gives rise to the highest adsorption enthalpy at low coverage but the adsorption capacity of the MCM-48 sample for DMMP is the highest (since simulant molecules fill the pores). At $p/p^{\circ} = 0.3$ the masses adsorbed are nearly twice higher than on the benchmark carbon. The regeneration of the samples was followed by High Resolution TG coupled with mass spectrometry. This showed an easier regeneration of MCM-48 (completed at 200 °C) than carbon (which requires heating up to 300 °C). The mass spectrometry analysis also shows that the simulant is decomposed at the level of the adsorbent, which means that non toxic fragments are produced by the regeneration. Evaluation of the time requested to achieve adsorption equilibrium was also carried out for each sample. Whatever the conditions, the activated carbon leads to shorter times and faster kinetics in spite of its lower pore ordering. The main conclusion for this application is that ordered materials may bring some improvements thanks to the very high surface that may be produced by ordering. Because the pore size is slightly larger than that of micropores of carbons, their regeneration is easier. Nevertheless, ordering does not bring any advantage at the level of kinetics.

1. Introduction

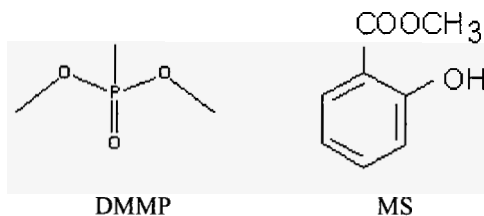
For many years nanoporous adsorbents have been used for removing pollutants either from gas or liquid phases [1]. Their large surface areas and pore volumes give them large adsorbing capacities. Moreover, the pore size, which allows molecular sieving effects, as well as a tailored surface chemistry give rise to selectivity and high affinity (defined as the initial slope of the adsorption isotherm) which are required in the case of toxic molecules elimination.

Activated carbons [2] were historically the first adsorbents used in such application and they are still probably the most used. Recently, new classes of adsorbents were synthesized and are currently known as mesoporous organized materials [3-5]. Prepared by templating methods around surfactants or block copolymers, they reach as high surface areas as activated carbons but with narrower pore size distributions in the mesopore range (2-50 nm according to the IUPAC classification), whereas carbons are often mainly microporous, (0-2 nm).

In this paper the adsorption properties of MCM-41 and MCM-48 type materials are compared to those of a reference activated carbon, in the case of simulant molecules, i.e. methyl salicylate (MS, a simulant for mustard gas) and dimethyl methyl phosphonate (DMMP, a simulant for nerve agents). The samples are compared from three points of view: adsorption thermodynamics, adsorption kinetics and regeneration. One of the main thermodynamic characteristics of these simulant molecules is their very low saturation pressure at room temperature (lower than 1 torr). It was therefore necessary to make use of specific adsorption equipment which is coupled with a Tian-Calvet type microcalorimeter in order to get the main thermodynamic of adsorption characteristics.

2. Experimental

Three adsorbents were used. An MCM-41 sample, provided by F. Fajula (ENSCM, Montpellier, France) with a BET surface area of $600 \text{ m}^2\text{g}^{-1}$, a mean pore size around 3.6 nm and a pore volume of $0.5 \text{ cm}^3\text{g}^{-1}$. An MCM-48 type sample, provided by M. Hudson (Reading University, UK), with a BET surface area of $1000 \text{ m}^2\text{g}^{-1}$, a mean pore size of 2.9 nm and a pore volume of $0.74 \text{ cm}^3\text{g}^{-1}$. An activated carbon, named ASC/T, whose surface area is $825 \text{ m}^2\text{g}^{-1}$, pore volume $0.4 \text{ cm}^3\text{g}^{-1}$ and mean pore size 0.9 nm. The formulas of the two simulant molecules used as adsorbate are given hereafter.



Nitrogen adsorption isotherms at 77K were determined with an ASAP 2010 apparatus from Micromeritics, after outgassing at 150°C. The regeneration of the

adsorbents was studied by High Resolution Thermogravimetry (HRTG) under nitrogen flow. The HRTG analyses were achieved with a TGA Q500 apparatus from TA Instruments coupled with a mass spectrometer (Thermostar from Pfeiffer).

Because of the very low saturation pressure of these simulant molecules (0.6 and 0.11torrs for DMMP and methylsalicylate, respectively), a recently developed apparatus was used [6], whose schematic representation is given in Figure 1.

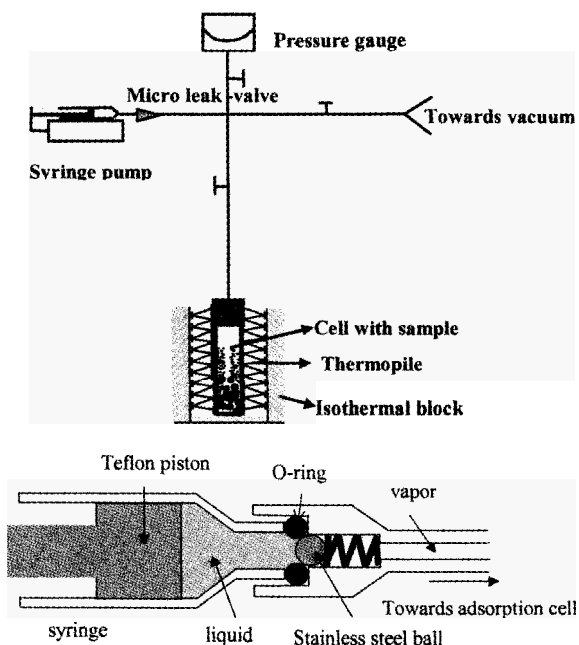


Figure 1. Schematic representation of the vapor adsorption set-up with details of the micro leak-valve.

After being outgassed (and heat-treated at 150°C), the sample cell is placed inside the thermopile of a Tian-Calvet microcalorimeter and connected to the manifold. This latter includes (i) a valve connected to a vacuum pump, (ii) a syringe-pump and (iii) a valve connected to two pressure gauges (MKS Baratron, 1mbar and 100mbar full scale). In order to control an even and low rate of vaporization of the liquid at the outlet of the syringe, a home-made micro

leak-valve is inserted between the syringe and the manifold (see details in figure 1). The liquid is vaporized at the leak-valve outlet. The temperature of the manifold is kept higher than that of the calorimeter. With this set-up, the injection of liquid can be carried out either continuously or stepwise. The linear speed of the syringe-pump (Precidor from Infors, Basel) may be set between 0.001 and 1 mm.min⁻¹, which corresponds to flow rates (in the case of water) ranging between 0.0001 and 1 mg.min⁻¹. The stepwise mode was used in the present case. The amount adsorbed at a given pressure is obtained by comparing the amounts injected to reach that pressure either in the presence or in the absence of a sample. At each step a calorimetric peak is recorded that allows the corresponding adsorption enthalpy to be calculated.

3. Results and discussion

Adsorption isotherms and corresponding differential adsorption enthalpies are given in Figures 2 and 3 for DMMP and MS, respectively. The adsorption isotherms of these vapors on the MCM-41 and MCM-48 samples are quite unusual as compared with standard gas-like nitrogen or with common vapor-like water or with a low molecular weight organic molecule.

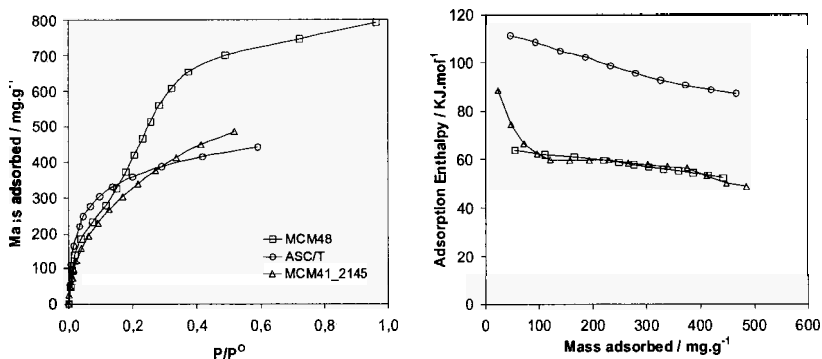


Figure 2: Adsorption isotherms (left) and adsorption enthalpies (right) for DMMP on ASC/T carbon (circles), MCM-41 (triangles) and MCM-48 (squares) at 25 °C.

The mesopore filling is indeed only slightly evidenced by inflection points on the adsorption curve. Nevertheless the filling occurs, as can be concluded from the amounts adsorbed at the highest tested relative pressure which are close to those expected from the pore volume of the adsorbents (determined by nitrogen adsorption) and the liquid density of the adsorbates. This behavior is probably related to the fact that the temperature of adsorption and the relative

size of the molecule and pores are such that these systems are in supercritical conditions [7]. The adsorption isotherms are indeed reversible for nitrogen adsorption which is small as compared to the simulant molecules. The adsorption isotherms should be reversible for simulant molecules (not measured here). It is well known that, as the molecule/pore size ratio increases, the pore filling step occurs at lower pressure and becomes less steep. This is characteristic of a phase transition shifting from first order to second order [8].

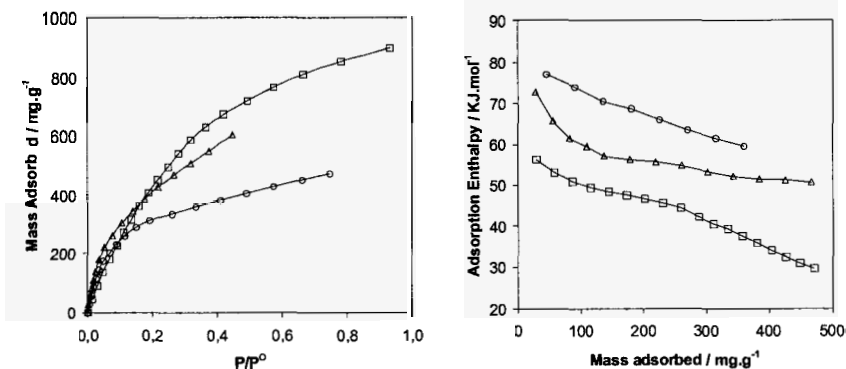


Figure 3: Adsorption isotherms (left) and adsorption enthalpies (right) for MS on ASC/T carbon (circles), MCM-41 (triangles) and MCM-48 (squares) at 25 °C.

The affinity at low pressure is clearly higher for the ASC/T sample in the case of DMMP, whereas for MS the difference is small between ASC/T and MCM-41 (may be the ultimate equilibrium pressure is not reached for the carbon sample). ASC/T is microporous and may present a higher interaction with the adsorbate than pores that can accommodate several molecules. A simple description of molecular interactions in term of Lennard Jones potential (dispersion forces) shows indeed that the adsorption energy should be higher in a pore that can accommodate one molecule [9]. This higher interaction is confirmed by the microcalorimetric results. The differential adsorption enthalpies of both DMMP and MS are clearly higher for the activated carbon than for the two organized silica samples. The difference between the microporous carbon and the silicas is higher for DMMP than for MS. This may be related both to the structure of these molecules and to their accessibility to micropores. For DMMP there is no real difference between adsorption enthalpies of MCM-41 and MCM-48 whereas for MS, they are systematically lower for MCM-48. This may be due to the surface polarity, which depends on the density of silanol groups in the case of silica and influences the adsorption

enthalpies [10]. These adsorption results show that despite a lower affinity for the simulant than microporous carbon at low pressure, the silica samples still have a good affinity for both molecules and show a higher adsorption capacity than the carbon sample over most of the pressure range.

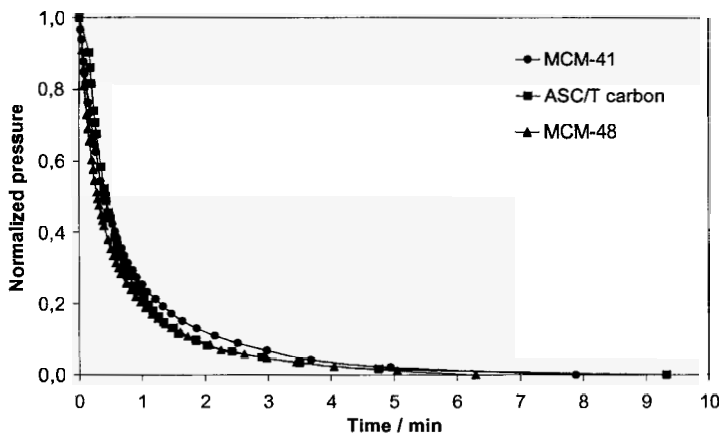


Figure 4: Adsorption kinetics of DMMP at low coverage

The adsorbents were also compared from a kinetic point of view. This comparison is mainly qualitative since the samples were not shaped for such a study in order to eliminate interparticle diffusion contribution. The pressure change above the sample during an adsorption step was indeed simply followed as a function of time. Examples are given in Figures 4 and 5 at two coverages in the case of DMP. The low coverage corresponds to a final equilibrium relative pressure around 0.05, whereas high coverage corresponds to a final equilibrium relative pressure around 0.2. At low coverage 3 min are needed to reach 90% equilibrium in the case of DMMP. For MS, equilibrium times are longer (14, 16 and 25 min for ASC/T, MCM-48 and MCM-41, respectively). At higher coverage, there are large differences between ASC/T and silica samples or both molecules (see Figure 5 for DMMP). The adsorption kinetics is indeed always faster in the case of the charcoal, in spite of its smaller mean pore size.

This surprising result may be due to the way the pores are organized in each sample. Mesoporous organized silicas have larger mean pore size than carbon sample, but on the other hand the latter, which is not organized, may have mesopores or even macropores reaching the center of particles then insuring the transport of molecules. This disadvantage of too well organized samples

concerning transport properties as compared with standard disorganized porous solids has already been observed in the case of chromatographic applications [11].

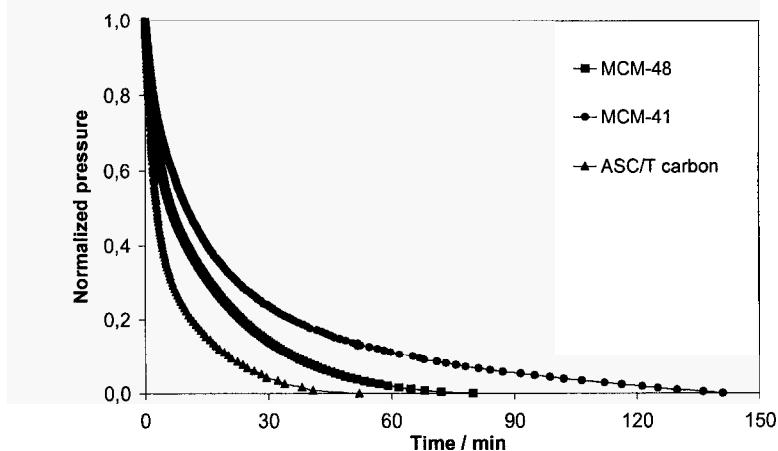


Figure 5. Adsorption kinetics of DMMP at high coverage.

The last aspect of this study deals with the regeneration of the samples. After completion of the calorimetric experiments, the samples filled by the simulant were analysed by HRTG coupled with mass spectrometry. Examples of recording are presented in Figure 6. These curves are obtained after adsorption experiments, but because the system is evacuated at room temperature before removing the sample, an unknown amount of adsorbate is removed before HRTG analysis. These curves then are characteristics of the fraction of molecules that are strongly attached to the surface or are slowly diffusing inside pores.

A clear advantage of MCM-48 over the carbon is its easier regeneration completed at 200 °C instead of 300 °C, notably in the case of MS. This result is in agreement with the lowest adsorption enthalpies obtained on the MCM type samples. The degradation products were analyzed by mass spectroscopy on line with HRTG. A recording is given in Figure 7 in the case of MCM-48.

Only small fragments are detected by the mass spectrometer, indicating that the molecules are mainly decomposed at the level of the adsorbent, which is an interesting result, for safety reasons, if it can be extended to the original, toxic, substances (mustard gas and nerve agent).

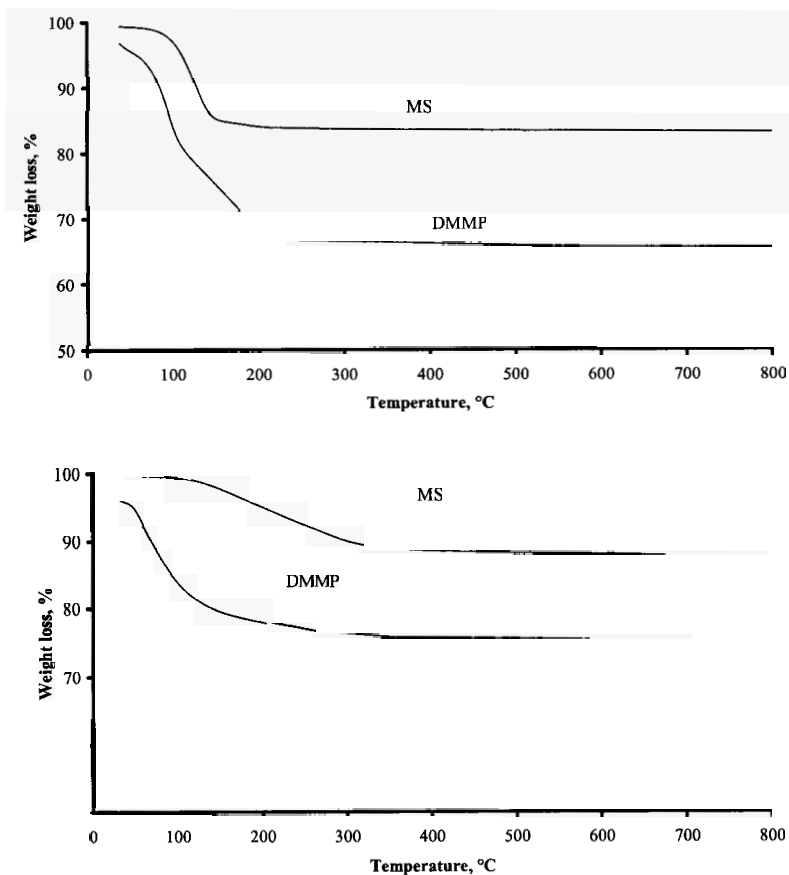


Figure 6: HRTG analysis of simulant desorption from MCM-48 (upper graph) and ASC/T (lower graph).

4. Conclusions

The main conclusion for this application is that ordered mesoporous materials may show very high adsorption capacities thanks to the high surface area produced by ordering. Because their pore size is slightly larger than that of the micropores of carbons (leading to smallest adsorption enthalpies), their regeneration is easier. Nevertheless, ordering does not bring any advantage at the level of kinetics.

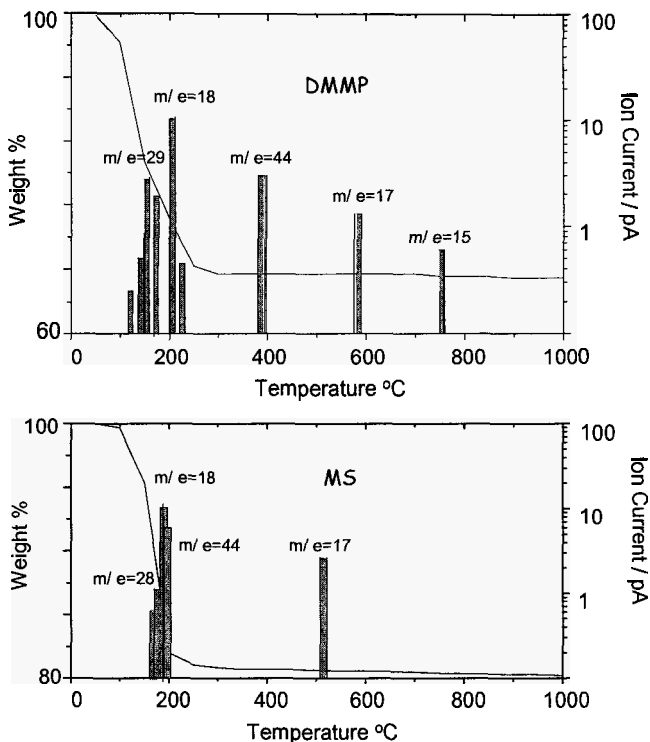


Figure 7. Thermodesorption-Mass-Spectrometry of DMMP and Methyl Salicylate from MCM-48.

Acknowledgements

Authors thank the European Commission for funding this work under the GROWTH-INORGPORE program (project G5RD-CT-2000-00317). They also wish to specially thank Dr. Jessica Ward and Dr. Chris Hindmarsh from DSTL (UK) for valuable discussions.

References

1. J. Rouquerol, *Impact of Science on Society*, **157**, 5-15 (1990)
2. R.P. Bansal, J.P. Donnet, F. Stoeckli, in *Active Carbon*, Marcel Dekker, New York (1988).
3. J.S. Beck, J.C. W.J. Vartuli, Roth, Leonowicz, M. E. C. T. Kresge, K.D. Schmitt, C.T.-W. Chu, D.H. Olson, E.W. Sheppard, S.B. McCullen, J.B. Higgins, J.L. Schlenker, *J. Am. Chem. Soc.*, **114**, 10834 (1992)

4. D. Zhao, P. Yang, Q. Huo, B.F. Chmelka, G.D. Stucky, *Current Opinion in Solid State and Materials Science*, **3**, 111 (1998).
5. F. Di Renzo, A. Galarneau, P. Trens, F. Fajula, *Handbook of Porous Materials*, Ed. F. Schüth, K. Sing, J. Weitkamp, Wiley-VCH, p1311 (2002).
6. R. Denoyel, I. Beurroies and D. Vincent, , *J. Therm. Anal. and Calorimetry*, **70**, 483-492 (2002).
7. K. Morishige and M. Shikimi, *J. Chem. Phys.*, **108**, 7821 (1998).
8. L.D.Gelb, K.E.Gubbins, R. Radhakrishnan and M. Sliwinska-Bartkowiak, *Rep. Prog. Phys.*, **62**, 1573-1659 (1999).
9. D.H.Everett, J.C. Powl, *J. Chem. Soc. Faraday Trans.I*, **72**, 619 (1976).
10. Y. Grillet, P.L.L. Llewellyn, in "The Surface Properties of Silica", Legrand A.P. ed., John Wiley and Sons, Chichester, 23-81 (1998).
11. J. Iapichella, J.-M. Meneses, I. Beurroies, R. Denoyel, Z. Bayram-Hahn, K. Unger and A. Galarneau, *Microporous and Mesoporous Mat.*, **102**, 111-121 (2007).

IMPROVEMENT OF MESOPOROUS SILICA AS AN ADSORBENT FOR NITROSAMINES BY DEVELOPMENT OF HIERARCHICAL STRUCTURE

FANG NA GU, JING JIA WEN, TING TING ZHUANG, JIA HUI XU, WEI HUANG,
CHUN FANG ZHOU, JIAN HUA ZHU*

Key Laboratory of Mesoscopic Chemistry of MOE, School of Chemistry and Chemical Engineering, Nanjing University, Nanjing 210093, China. E-mail: jhzhu@nju.edu.cn

In order to improve the efficiency of mesoporous silica in adsorption of nitrosamines in solution, two strategies are tried. One is to incorporate the hierarchical structure and another is to load the metal species inside of the channel of the porous host, enhancing the adsorption of the target through the geometric confinement and electrostatic interaction, respectively. The microporous structure was introduced into the mesoporous silicas and their adsorption capacities were evaluated through the gaseous or liquid adsorption of nitrosamines, demonstrating the importance of hierarchical structure in the adsorbent for removal of nitrosamines in environment.

1. Introduction

Reduction of environmental carcinogens is one of the potential applications for zeolites in life sciences. Among harmful constituents present in our environment, nitrosamines are well-recognized teratogens and carcinogens in animals and they are considered potentially carcinogenic in humans [1]. Apart from smoking, a cause of health hazard, there are many other sources of nitrosamines in environment. Beer and other malt beverages contain nitrosamines contamination [2]; foods treated with nitrites for coloring, flavoring and preservation can also contain nitrosamines [3]. Some drugs with amines or *N*-substituted amides can be transformed to nitrosamines in human body to generate nitrosamines [4]. Moreover, nitrosamines are present in exhaust gas and wastewater of chemical or rubber factory. However, the multifarious structure of nitrosamines makes difficult the design and synthesis of an effective adsorbent for those toxic compounds. For instance, adsorption of bulky nitrosamines like tobacco-specific nitrosamines (TSNA) is hindered in zeolites due to the geometric limitations of relatively small pores in these adsorbents. Although mesoporous silicas, SBA-15 and MCM-48, exhibit a better catalytic function than zeolites in adsorption and catalytic reaction of NNN (*N*-nitrosanornicotine), a typical TSNA [5], they are

inferior to adsorb the volatile nitrosamines. Thus, some novel functional materials are required to capture the nitrosamines in environment and the candidates should have a suitable pore size distribution to fit the adsorbate with various molecular diameters and shapes.

To improve adsorption of nitrosamines with various structures and sizes in a mixed system (i.e., a few nitrosamines and/or presence of an interference agent), an adsorbent with hierarchical rather than ordered pore structure is preferred. Development of porosity is an important task in the design and synthesis of any adsorbent [6]. Namely, the synthesis of a material with micro- and mesoporous properties is a promising strategy for achieving desired functionality because molecules are first transported through mesopore channels and then strongly adsorbed in micropores [7, 8], which can be easily formed within ordered mesoporous materials [9,10].

Two strategies can be adopted to prepare the molecular sieve adsorbent with hierarchical structure. One of them is to create mesopores in zeolites through dealumination or desilication [11, 12], which is an efficient way to enhance the ability of HZSM-5 to trap nitrosamines in solution [13]. Another approach is to create micropores in mesoporous adsorbents [9, 10] by using zeolites as synthetic reactants [14] or by varying the synthesis temperature and TEOS/surfactant ratio [7, 8]. Nonetheless, the effect of micropores in mesoporous silicas on adsorption of nitrosamines is unclear up to date. The aim of this paper is to examine the impact of introducing micropores into mesoporous silica such as SBA-15 on the removal of nitrosamines from solutions. For comparison, the CuO/SBA-15 samples prepared by one-pot synthesis and solvent-free methods were also utilized.

2. Experimental

N-nitrosodimethylamine (NDMA) *N*-nitrosopyrrolidine (NPYR) and *N*-nitrosohexamethyleneimine (NHMI) were purchased from Sigma and dissolved in dichloromethane at the volume ratio of 1:19 [14], *N*-nitrosodiphenylamine (NDPA) was synthesized in laboratory [15] and other reagents used here were of AR grade. Zeolite HZSM-5 and amorphous silica are commercially available powder samples [16]. Mesoporous silica SBA-15 and MCM-41 were prepared in laboratory according to recipes in literature [17]. To prepare the V-xC sample, 1 mmol of cationic surfactant, cetyltrimethylammonium bromide (CTAB), and 1 mmol of sodium dodecylsulphonate (SLS) were added into 80 g acidic ethanol-water (1:1 weight ratio) to form a clear solution at 313 K. 3.89 g of tetraethyl orthosilicate (TEOS) was added under stirring and kept for selected times at 313

K. The pH value of synthetic gel could be controlled by the amount of HCl added. The samples were filtrated, washed, dried and calcined in air at 823 K for 6 h [18]. The synthesis of SZ sample [14] and the copper-modified SBA-15 [16] have been reported previously. Another series of CuO/SBA-15 was prepared by use of solvent-free grinding method [19]. For one-step synthesis of the copper-modified MCM-41 [20], 1.49 g of CTAB and $x\text{Cu}(\text{NO}_3)_2$ were dissolved in 51.80 g of water and 8.17 g of 36% HCl followed by addition of TEOS (4.25 g). The resulting samples were filtrated, washed, dried and calcined in air at 823 K for 6 h.

Nitrogen adsorption-desorption isotherms at 77 K were measured on a Micromeritics ASAP 2020 system. The samples were evacuated at 573 K for 4 h in the degas port of the adsorption analyzer. The BET specific surface area (S_{BET}) was calculated using adsorption data and the total pore volume was determined from the amount adsorbed at a relative pressure of about 0.99. The pore diameters were calculated from desorption branch of the isotherm using standard BJH method [16].

Adsorption of volatile nitrosamines such as NPYR was carried out by using gas chromatography (GC) method [15]. The nitrosamines solution was injected with amounts of 2 μl each time and gaseous effluent was analyzed by GC. A decrease in the solute to solvent ratio was utilized to calculate the adsorbed amount [15].

Adsorption of NPYR by zeolite in acidic solution (pH=1) was studied using batch method [13], for which the zeolites samples were added into the 25 ml solution with an initial concentration of 4.4×10^{-4} M in colored cone flasks. The mixtures were shaken in a thermostatic water-bath shaker at 310 K for 1 h, and then centrifuged at 3000 rpm for 15 min to separate the solution and the solid. The concentrations of NPYR in acid solution were determined at different times by using photometric method [21]. Through the similar procedure the liquid adsorption of NDPA was performed. 20 mg absorbent was mixed with the dichloromethane solution of NDPA at 277 K for 24 h, and then the residual nitrosamine in the solution was detected by photometric method [21].

3. Results and Discussion

3.1. Impact of Micropores in Mesoporous Silica on Adsorption of Volatile Nitrosamines

Table 1 lists the structural parameters of the V-xC samples. As reported previously [18], porous silica was synthesized with combined micro- and mesoporosity and large pore volume; this silica material was obtained by self-

assembly of an equimolar composition under acidic conditions. The micropore volume and micro-/mesoporosity ratio was tuned by a simple variation of pH value in the synthetic gel. When the pH value of the synthetic system increased from 1 (V-8C) to 4 (V-32C), the micropore volume of the resulting samples raised from 0.10 to 0.17 cm^3g^{-1} at the expense of mesopore volume; the mesopore distribution was kept quite narrow and uniform with the same pore diameter of 3.9 nm, though the mesopore volume declined obviously. However, for the V-37C sample synthesized in aqueous solution without ethanol, the micropore volume is near zero.

Table 1. Structural parameters of the V-xC samples and other porous adsorbents

Sample	S_{BET} (m^2g^{-1})	V_{total} (cm^3g^{-1})	V_{micro} (cm^3g^{-1})	D_{pore} (nm)
V-8C	978	0.65	0.10	3.9
V-32C	674	0.37	0.17	3.9
V-37C	357	0.31	0	3.9
MCM-41	1342	1.12	0	4.0
SiO_2	250	0.80	-	8.0-10.0 ^a

^a these values represent the pore size range of amorphous silica.

Figure 1 shows adsorption of NHMI, NDMA and NPYR, three typical volatile nitrosamines with carcinogenicity, by porous silica materials at 453 K. All of three nitrosamines have the characteristic group, N-NO, but their molecular diameters are different. NDMA is a chain structure with two methyl groups, and NPYR has a five-member ring so its size reaches 0.56 nm. NHMI possesses a seven-member ring in its structure and its size achieves 0.59 nm [22]. Amorphous silica is inactive in adsorption of three volatile nitrosamines under the conditions used in the experiment, while MCM-41 only exhibits a weak ability to trap NHMI. When the total amount of NHMI accumulated to 0.77 $\text{mmol}\cdot\text{g}^{-1}$, only 0.14 $\text{mmol}\cdot\text{g}^{-1}$ was adsorbed by MCM-41 (Figure 1A). Compared with the huge pore size of MCM-41, the molecular diameter of three adsorbates is relatively small which enables them to enter the channel of MCM-41 very easily. However, absence of cation in MCM-41 leads to lack of electrostatic interaction towards the nitrosamine while the wide pore cannot provide the necessary confinement for the tiny adsorbate hence MCM-41 fails to capture the volatile nitrosamines at 453 K [20]. In contrary, V-xC samples show a high ability to adsorb NHMI at 453 K. When the accumulated amount of NHMI reached 0.77 $\text{mmol}\cdot\text{g}^{-1}$, about half of them (0.36 $\text{mmol}\cdot\text{g}^{-1}$) were trapped by V-37C while 0.52 $\text{mmol}\cdot\text{g}^{-1}$ was adsorbed by V-8C or V-32C (Figure 1A). For NDMA and NPYR whose molecular volumes are smaller than NHMI, V-32C

exhibited a higher adsorptive capability than V-8C but the absolute adsorbed amount of NPYR or NDMA by them is obviously lower than that of NHMI due to the relatively high volatility of the former two nitrosamines. Especially, the adsorption of NDMA by V-32C is difficult to be compared with the other two nitrosamines because NDMA has the highest volatility among three adsorbates.

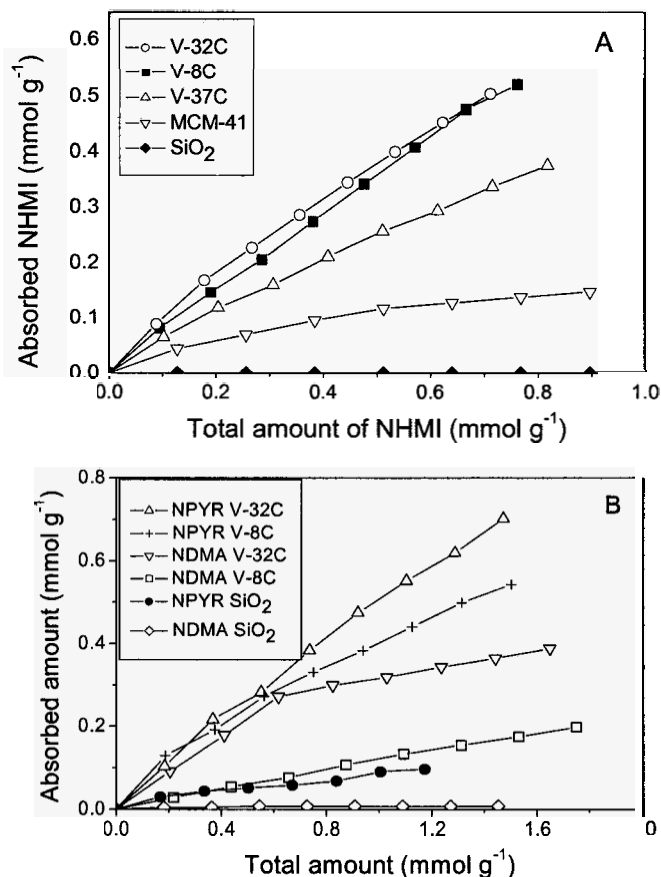


Figure 1. Adsorption of volatile nitrosamines by porous silica samples at 453 K.

The V-32C sample has a smaller surface area ($674 \text{ m}^2 \cdot \text{g}^{-1}$) and pore volume ($0.37 \text{ cm}^3 \cdot \text{g}^{-1}$) than V-8C ($0.65 \text{ cm}^3 \cdot \text{g}^{-1}$ and $78 \text{ m}^2 \cdot \text{g}^{-1}$), but its adsorptive ability towards volatile nitrosamines exceeds V-8C indeed since V-32C possesses a

relatively larger micropore volume ($0.17\text{cm}^3\cdot\text{g}^{-1}$) than V-8C ($0.10\text{cm}^3\cdot\text{g}^{-1}$). This result reflects the importance of micropore in adsorbent on the adsorption of volatile nitrosamines. Moreover, this impact emerges much clear as the molecular size of the volatile nitrosamines becomes small. For instance, when the accumulated amount of nitrosamines reached $0.70\text{mmol}\cdot\text{g}^{-1}$, the capacity of V-32C and V-8C towards NHMI is 0.495 and $0.490\text{mmol}\cdot\text{g}^{-1}$, respectively, they are almost the same within the experimental error; however, their capacities forwards NPYR are 0.364 and $316\text{mmol}\cdot\text{g}^{-1}$, and the difference achieves 13%. For NDMA, their adsorption capacities are 0.283 and $0.083\text{mmol}\cdot\text{g}^{-1}$, and V-32C adsorbs 2.4 times more NDMA than V-8C. These results confirm the important role played by the micropore in adsorption of volatile nitrosamines. Likewise, the impact of micropore can be seen in the adsorption of NHMI where the sequence of adsorptive capacity of three V-xC sample is V-37C > V-8C > V-32C, coincided with the sequence of their micropore volume. It is clear that introducing micropore in mesoporous silica is efficient to enhance its adsorptive ability towards volatile nitrosamines.

3.2. Enhancement of Liquid Adsorption of Nitrosamines by Micropores Present in Mesoporous Silica

Figure 2 displays the adsorption of NPYR in acidic aqueous solution (pH=1) by various porous adsorbents at 310 K. Zeolites exhibit excellent adsorption ability towards NPYR because of their microporous structure, even the adsorbent has different pore size (H-Beta) or different chemical composition (TS-1). Both the aluminum content and acid-basicity of ZSM-5 have a minor effect on the adsorptive ability, and the NaZSM-5 with different Si/Al ratio along with the HZSM-5 exhibit the similar capacity to trap the nitrosamines in solution. In contrary, MCM-41 and SBA-15 exhibit a weak capability to capture the NPYR in the solution (Figure 2). Both of the two mesoporous silica has the pore size many times larger than that of the zeolite used in the experiment, which should be beneficial for accommodation of nitrosamines. However, either SBA-15 or MCM-41 suffers from the lack of cation so that they cannot provide the strong electrostatic affinity to nitrosamines. Besides, the silanol group is the main adsorptive site on the mesoporous silica but it is easily to be occupied by water. The competitive adsorption of the solvent further lowers the adsorption ability of the mesoporous silica in the solution.

To overcome the weakness of mesoporous silica, we introduced the microporous structure into SBA-15 by using zeolite HZSM-5 as the component in the synthesis of the mesoporous silica to obtain the composite of SZ [14]. As

reported previously, SZ sample exhibited three well-resolved diffraction peaks indexed to the (100), (110) and (200) reflections closely matching to the patterns of SBA-15 [14], and there were some residual diffraction peaks of ZSM-5 zeolite remained in the high angle XRD patterns, reflecting the survival of zeolite fragments along with the existence of microporous structure in these fragments. Rather, these fragments consequently possess the Brønst acidity even they are embed in SZ sample [14], which, as explained later, is crucial to accelerate adsorption of nitrosamines in mild conditions. Although SZ possesses a smaller surface area ($545 \text{ m}^2\cdot\text{g}^{-1}$) and pore volume ($0.62 \text{ cm}^3\cdot\text{g}^{-1}$) than SBA-15 ($983 \text{ m}^2\cdot\text{g}^{-1}$ and $1.22 \text{ cm}^3\cdot\text{g}^{-1}$), it can adsorb seven times more NPYR ($5.0 \text{ }\mu\text{mol}\cdot\text{g}^{-1}$) than the parent SBA-15 ($0.6\mu\text{mol}\cdot\text{g}^{-1}$) in acidic solution, which is close to that of HZSM-5 ($4.9 \text{ }\mu\text{mol}\cdot\text{g}^{-1}$) and H-Beta ($5.0 \text{ }\mu\text{mol}\cdot\text{g}^{-1}$).

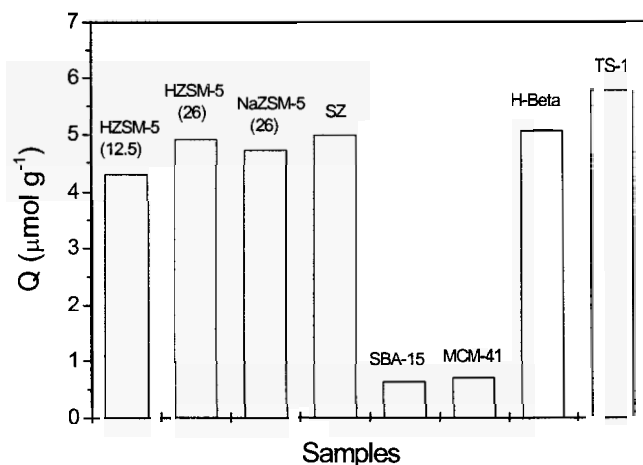


Figure 2. Adsorption of NPYR in acidic aqueous solution by porous adsorbents at 310 K

Clearly the incorporation of zeolite fragments promotes the adsorption of nitrosamines in mesoporous silica, especially due to the remained Brønst acidity in the composite because the protons can form hydrogen bonds with the N atoms of amino-group in nitrosamines, promoting the adsorption and degradation of nitrosamines [21]. A deep investigation on these results reveals another strange phenomenon. There is only half of the siliceous resource coming from the zeolite HZSM-5 in the synthesis of SZ composite, but the composite traps the large amount of nitrosamines same as that by HZSM-5 in the acidic solution. That is to say, the fragment of zeolite HZSM-5 in SZ composite exerts a higher efficiency

in capturing nitrosamines than that in parent zeolite itself. The reason, in our opinion, is the improved geometric microenvironment of the Brønst acid sites within the SZ sample where most of the sites locate in a wilder channel, which enables them to be more accessible for the nitrosamine molecules and to fasten the adsorption process. This discovery implies a new way to design and assemble the special functional materials with desirable chemical and geometric properties, for instance to anchor some microporous guests in the wall of mesoporous host and produce efficient adsorbents.

3.3. Impact of Micropores on Modification of Mesoporous Silica with CuO and the Adsorption of NDPA in Solution

NDPA is a man-made chemical instead of naturally occurring substance; with two rigid phenyls connected with N-N=O functional group, the molecular size of NDPA is significantly larger than that of NDMA or NPYR [15]. Owing to the large molecular size, NDPA is difficult to be adsorbed by many zeolites such as NaA or NaZSM-5. Figures 3 and 4 illustrate the adsorption of NDPA by mesoporous silica or amorphous silica in dichloromethane solution at 277 K. Although these silica samples have the pore size large enough for the accommodation of NDPA, their actual capability is different hence SBA-15 can trap more NDPA than MCM-41 or SiO₂ under the similar experimental conditions.

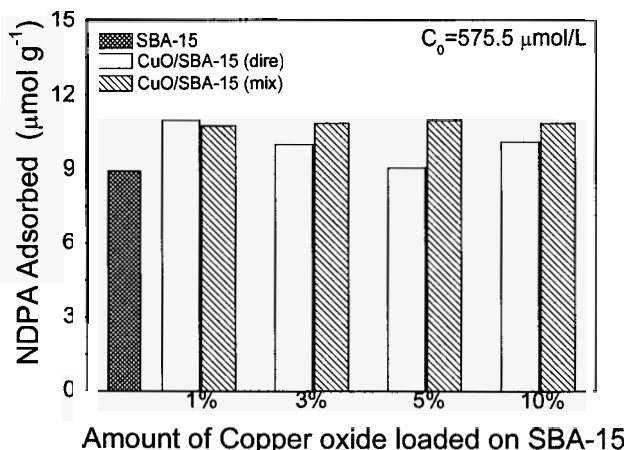


Figure 3. Adsorption of NDPA in dichloromethane solution by SBA-15 samples

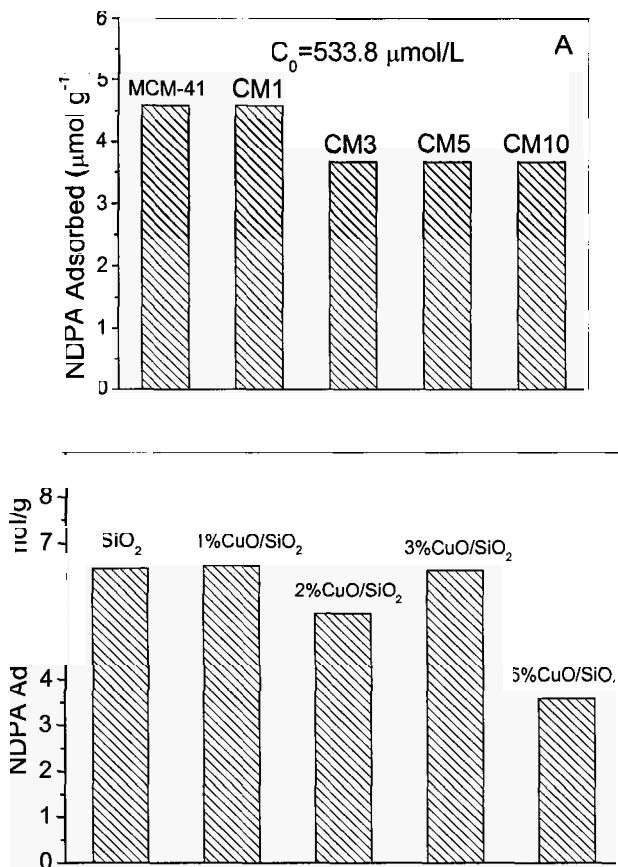


Figure 4. Adsorption of NDPA by (A) MCM-41 and (B) SiO_2 samples in dichloromethane solution

To promote the adsorptive ability of porous silica towards NDPA, all of the three adsorbents are modified with copper oxide through various manners. For SBA-15 both the one-pot synthesis [16] and the solvent-free grinding method [19] are used, while the copper modified MCM-41 is prepared in the one-pot process [20]. Amorphous silica is modified with copper oxide through common impregnation method [23]. As seen in Figure 3, all of the modified SBA-15 samples exhibit the enhanced ability in the adsorption of NDPA in solution, and among them the ground samples display the similar increase from 8.9 to 10.8 $\mu\text{mol/g}$, while the one-pot synthesized samples show different increases, say,

1%CuO/SBA-15 (dir) has a slightly higher ability ($11.0 \mu\text{mol}\cdot\text{g}^{-1}$) than ground samples but 5%CuO/SBA-15 (dir) sample presents the adsorption capacity same as that of parent SBA-15. This difference between two series of sample may result from the different distribution of the copper modifier in the porous host caused by different preparations. The copper oxide cannot be inserted into the framework of SBA-15 during the grinding procedure so that they locate on the surface of SBA-15 to contact with adsorbent. In contrary, some of the guests are wrapped inside the pore wall of SBA-15 host during the one-pot synthesis.

Different from CuO/SBA-15, all copper-containing MCM-41 show a lowered activity in the adsorption of NDPA as seen in Figure 4A. As the loading amount of CuO exceeds 3% (w/w), the composites loss about 10% of the adsorption capacity. At the first glance, different pore size is considered to account for the different adsorptive behaviors of CuO/SBA-15(dir) and CuO/MCM-41 samples. Consequently, amorphous silica is adopted to load copper oxide because it has a continuous pore size distribution over a wide range of pores, i.e., from micropores to macropores. However, the modified SiO_2 also exhibits a declined adsorption capacity in the adsorption of NDPA (Figure 4B). Since MCM-41 has ordered mesoporous structure without micropore, amorphous silica has micropore but lack of ordered porous structure, it is inferred that, even tentatively, the special porous structure of SBA-15 leads to the positive effect of copper modification, not only the relatively large pore size, but also the existence of micropore that has been proven to be crucial for the modification of mesoporous silica with copper oxide [20].

4. Conclusion

This work shows clearly that the development of a hierarchical structure in mesoporous silica can increase its ability to adsorb the volatile nitrosamines in gas stream and solution. Creation of a microporous structure in the pore walls of mesoporous silicas is beneficial for adsorption of nitrosamines and makes these adsorbents attractive for environmental applications.

Acknowledgments

The National Natural Sciences Foundation of China (20373024, 20673053 and 20773061), National Basic Research Program of China (2007CB613301) and the Analysis Center of Nanjing University financially support this research.

References

1. R. Walker. *Food Additives and Contaminants* **7**, 717 (1990).
2. M. Izquierdo-Pulido, J.F. Barbour and R.A. Scanlan. *Food Chem. Toxic.* **34**, 297(1996).
3. W. Lijinsky. *Mutation Research* **443**, 129 (1999).
4. S.S. Mirvish. *Toxicol. Appl. Pharmacol.* **31**, 325 (1975).
5. J.H. Zhu, S.L. Zhou, Y. Xu, Y. Cao and Y.L. Wei. *Chem. Lett.* **32**, 338 (2003).
6. D. R. Rolison, *Science* **299**, 1698 (2003).
7. K. Miyazawa and S. Inagaki. *Chem. Commun.* 2121 (2000).
8. P. Van Der Voort, P. I. Ravikovitch, K. P. De Jong, A. V. Neimark, A. H. Janssen, M. Benjelloun, E. Van Bavel, P. Cool, B. M. Weckhuysen and E. F. Vansant. *Chem. Commun.* 1010 (2002).
9. S. Storck, H. Bretinger and W. F. Mair. *Appl. Catal. A*, **174**, 137 (1998).
10. M. Kruk, M. Jaroniec, C. H. Ko and R. Ryoo. *Chem. Mater.* **12**, 1961(2000).
11. A.H.Janssen, A.J. Koster, K P. De Jong, *Angew. Chem. Int. Ed.* **40**, 1102 (2001).
12. J.C. Groen, L.A.A. Peffer, J.A. Moulijn and J. Perez-Ramirez. *Chem. Eur. J.* **11**, 4983 (2005).
13. X. Dong, C.F. Zhou, M.B. Yue, C.Z. Zhang, W. Huang and J.H. Zhu. *Mater. Lett.* **61**, 3154 (2007).
14. C. F. Zhou, Y. M. Wang, J.H. Xu, T. T. Zhuang, Y. Wang, Z.Y. Wu and J. H. Zhu. *Stud. Surf. Sci. Catal.* **156**, 907 (2005)
15. C.F. Zhou, Z.Y. Yun, Y. Xu, Y.M. Wang, J. Chen and J.H. Zhu. *New J. Chem.* **28**, 807 (2004).
16. Y.M. Wang, Z.Y. Wu, Y.L. Wei and J.H. Zhu, *Microporous Mesoporous Mater.* **84**, 127 (2005).
17. D. Y. Zhao, J. L. Feng, Q. S. Huo, N. Melosh, G. H. Fredrickson, B. F. Chmelka and G. D. Stucky, *Science* **279**, 548 (1998).
18. Y.M. Wang, T.T. Zhuang, Y. Cao, Q. Jiang and J.H. Zhu, *J. Non-cryst. Solids*, **351**, 346 (2005).
19. Y.M. Wang, Z.Y. Wu and J.H. Zhu, *J. Solid State Chem.* **177**, 3815 (2004).
20. J.H. Xu, T.T. Zhuang, Y. Cao, J. Yang, J.J. Wen, Z.Y. Wu, C.F. Zhou, L. Huang, Y. Wang, M.B. Yue and J.H. Zhu. *Chem. Asian J.* **2**, 996 (2007).
21. Y. Xu, J.H. Zhu, L.L. Ma, A. Ji, Y.L. Wei and X.Y. Shang. *Microporous Mesoporous Mater.* **60**,125 (2003).
22. J.H. Zhu, D. Yan, J.R. Xia, L.L. Ma and B. Shen. *Chemosphere* **44**, 949 (2001).
23. Y. Xu, H.D. Liu, J.H. Zhu, Z.Y. Yun, J.H. Xu and Y.L. Wei. *New J. Chem.*, **28**, 244 (2004).

This page intentionally left blank

APPLICATION OF MESOPOROUS ORGANOSILICAS WITH SULFUR- AND NITROGEN-CONTAINING LIGANDS FOR ADSORPTION OF MERCURY IONS

RAFAL M. GRUDZIEN, BOGNA E. GRABICKA, OKSANA OLKHOVYK
MIETEK JARONIEC*

*Chemistry Department, Kent State University,
Kent, OH 44242, USA*

JONATHAN P. BLITZ

*Chemistry Department, Eastern Illinois University
Charleston, IL 61920, USA*

Ordered mesoporous organosilicas (OMOs) with channel-like and cage-like structures such as SBA-15 (*P6mm*), SBA-16 (*Im3m*) and FDU-1 (*Fm3m*) were fabricated by co-condensation (one-pot synthesis) of selected organosilanes and tetraethyl orthosilicate or 1,2-bis(triethoxysilyl) ethane in the presence of amphiphilic block copolymers under acidic conditions. Four types of OMO samples were synthesized: (i) ordered mesoporous silicas (OMSs) with chemically bonded single ureidopropyl and imidazole groups, (ii) OMSs with mixed mercaptopropyl and ureidopropyl surface groups, (iii) OMSs with single disulfide and isocyanurate bridging groups, and (iv) periodic mesoporous organosilica (PMO) with ethane and isocyanurate as primary and secondary bridging groups. Powder X-ray diffraction (XRD), small angle X-ray scattering (SAXS) and nitrogen adsorption studies of these samples confirmed the presence of ordered porosity (*P6mm*, *Im3m* and *Fm3m* symmetry groups), high surface area (440-880 m²/g), accessible pores (7.2-9.0 nm) and high total pore volume (0.53-0.87 cc/g), whereas CHNS elemental analysis and Fourier transform infrared spectroscopy (FT-IR) proved a successful introduction of surface and framework organic groups. The aforementioned one-pot synthesis afforded materials with metal-chelating sites on the pore walls and within the framework having ligand loadings in the range of 0.9-1.27 and 0.76-1.1 mmol/g, respectively. The resulting OMOs were characterized and tested as effective adsorbents for removal of Hg²⁺ ions from aqueous solutions. The adsorption capacity of Hg²⁺ estimated on the basis of spectrophotometric analysis with dithizone as a complexing agent was in the range of 1.66-1.96 and 2.02-3.23 mmol/g for the materials with surface and bridging groups, respectively.

* Corresponding author: Mietek Jaroniec - Tel: 1-330-672 3790, Fax: 1-330-672 3816,
Email: jaroniec@kent.edu

1. Introduction

Various chemicals including toxic heavy metal ions, particularly mercury and lead, discharged from industrial wastes contaminate natural water, and consequently represent a considerable threat to human health and other living organisms [1]. The adsorption-based purification of these species from water, the most abundant and important component of the ecosystem, has become a great concern for researchers working in different disciplines worldwide. Many approaches have been extensively studied and proposed for the removal of harmful metal ions via binding them to insoluble sorbents such as chelating resins and polymers, activated charcoal, zeolites, clays, inorganic oxides and so on. However, these sorbents exhibit several disadvantages including low loading capacities, broad distribution of irregular pores, weak binding constants, and most importantly, low mechanical and thermal stabilities. These issues have stimulated an intensive research on the development of more reliable and selective adsorbents (see review [2] and references therein).

One of the most exciting discoveries in the area of porous materials has been achieved by the development of ordered mesoporous silicas (OMSs) [3,4], which were obtained in the form of insoluble porous solids with narrow pore size distribution, accessible pores, large pore volume and high surface area. Most importantly, these siliceous mesostructures exhibit 2-D (MCM-41 [3] and SBA-15 [4]) and 3-D (SBA-16 [4] and FDU-1 [5,6]) arrangements of ordered cylindrical or spherical pores, respectively, which contain reactive silanols. These silanol groups enable an irreversible surface functionalization (post-synthesis grafting) of the pore walls with varieties of mercury-binding ligands like 1-allyl-3-propylthiourea [7], 1-benzoyl-3-propylthiourea [8] and 2,5-dimercapto-1,3,4-thiadiazole [9]. An alternative way of introducing organic surface groups is co-condensation of organosilanes with tetraethyl orthosilicate (TEOS), which was used to incorporate various ligands such as mercaptopropyl [10], ureidopropyl [11-14], imidazole [15-17] and so on.

A unique class of hybrid materials, known as periodic mesoporous organosilicas (PMOs), has emerged in 1999 [18,19]. In these materials oxygen in a fraction of siloxane bonds is replaced by organic bridging groups. Due to the ease of incorporation of various organic moieties such as cyclam units, crown ethers, thioethers, heterocyclic isocyanurate rings into the silica framework [20-22] and their uniform distribution inside pore walls, PMOs have become very promising materials for adsorption of heavy metal ions (see reviews [2,23] and references therein).

The current work is focused on the design of polymer-templated nanoporous organosilicas with cubic (*Fm3m*, *Im3m*) and hexagonal (*P6mm*) symmetries and various surface and framework organic groups. These materials were prepared from commercially available organosilanes via an easy, effective and environmentally friendly one-pot synthesis, which assures high loadings of organic groups. Introduction of nitrogen and sulfur-containing surface groups such as ureidopropyl and imidazole, as well as bridging groups such as propyl-disulfide and heterocyclic isocyanurate rings afforded efficient adsorbents for the removal of mercury ions from contaminated aqueous solutions.

2. Materials and Methods

2.1. Chemicals

Structure directing agents such as poly(ethylene oxide)-poly(propylene oxide)-poly(ethylene oxide) triblock copolymer Pluronic P123 (EO₂₀PO₇₀EO₂₀) and F127 (EO₁₀₆PO₇₀EO₁₀₆) as well as poly(ethylene oxide)-poly(butylene oxide)-poly(ethylene oxide) B50-6600 triblock copolymer were provided by BASF Corporation and Dow Chemicals, respectively. The precursors for the framework and surface modification such as 1,2-bis(triethoxysilyl)ethane (E), bis(3-(triethoxysilyl)propyl)disulfide (DS), tri[3-(trimethoxysilyl)propyl]isocyanurate (ICS) and ureidopropyltrimethoxysilane (U), (3-mercaptopropyl)trimethoxysilane (SH), *N*-(3-triethoxysilylpropyl)-4,5-dihydroimidazole (IM) were purchased from Gelest, whereas tetraethyl orthosilicate (TEOS, 98%) was from Across Organics; chemical structures of these organosilanes are shown in Table 1. Fuming hydrochloric acid (HCl, 37 %) and ethanol (C₂H₅OH, 95 %) were purchased from Fischer Scientific. Deionized water (DW) used in all synthetic procedures was deionized using in-house Ionpure Plus 150 Service Deionization ion-exchange purification system. All reagents were used as received without further purification.

2.2. Synthesis of OMSs and PMOs

OMSs and PMOs were prepared analogously as reported elsewhere [13,14,17,21,22]. In a typical procedure, functionalized nanoporous materials were synthesized by co-condensation of TEOS (or BTESE [32] in the case of PMO-E-ICS) and suitable organosilanes in order to introduce the surface (U, SH, IM) and framework (DS, ICS) groups in the presence of triblock copolymer templates (P123, F127, B50-6600). In general, triblock copolymer was mixed with 2M HCl, distilled water and sodium chloride (except SBA-15 samples;

OMS-U and PMO-E-ICS) under rapid stirring at 40 °C until a clear solution was obtained. After 4 hours of stirring, TEOS was pipetted dropwise to the polymer solution under vigorous mixing, and then after 15 min organosilane was added to achieve the desired molar composition of both silanes. The slurry was further stirred for 24 h at 40 °C and hydrothermally treated for 48 hours at 100 °C, except FDU-1, which was mixed for 6 h and aged for another 6 h. The powder was washed with DW, filtered and dried at 80 °C overnight. The polymeric template was extracted from as-synthesized samples using 2 ml of 37 wt. % HCl and 100 ml of 95 % ethanol at 70 °C. The template-free mesoporous SBA-15 materials with ureidopropyl surface groups, as well as with ethane and isocyanurate bridging groups were named OMS-U and PMO-E-ICS, respectively. The extracted FDU-1 with mercaptopropyl and ureidopropyl, imidazole and propyldisulfide groups were designated as OMS-U-SH, OMS-IM and PMO-DS, respectively, whereas SBA-16 with isocyanurate group was denoted as PMO-ICS.

2.3. Mercury Adsorption Measurements

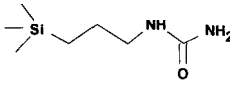
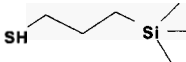
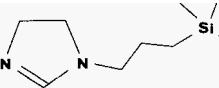
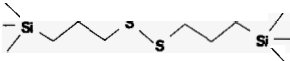
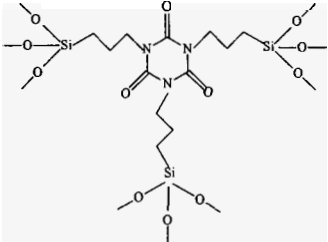
Mercury adsorption was studied under static conditions from aqueous solutions as described elsewhere [8]. All solutions were prepared by dilution of the 0.145N mercury (II) nitrate volumetric standard up to 10 ml. In a typical determination 0.05g of the sample was equilibrated for 40 min with 10 ml of the solution containing mercury nitrate of known concentration (ratio Hg^{2+} :ligand was 3:1). After filtration adsorbent was washed with DW and the filtrate was collected and diluted to 25 ml. Mercury (II) concentration was measured spectrophotometrically with dithizone (diphenylthiocarbazone) as a complexing agent on a Varian Cary 300 UV-Vis spectrophotometer in a 1 cm quartz photocell with 5 ml volume. The amount of mercury was determined from a calibration curve prepared in the range up to 50 μg . The background correction was made against pure chloroform. The remaining Hg (II) ions (non-adsorbed) in all solutions were measured by an absorbance reading at 490 nm.

2.4. Other Measurements

Nitrogen adsorption measurements were performed using ASAP 2010 and ASAP 2020 volumetric analyzers (Micromeritics, Inc., Norcross, GA) at -196 °C. Prior to each adsorption analysis all materials were outgassed under vacuum in the port of the adsorption instrument for at least 2 hour at 110 °C. The specific surface area was evaluated using Brunauer-Emmett-Teller (BET) method [24] in the p/p_0 range of 0.05-0.2. The single-point total pore volume was evaluated by

using the volume adsorbed at $p/p_0 = \sim 0.99$ [25]. The pore size distribution (PSD) was calculated from the adsorption branch of isotherms by using the Kruk-Jaroniec-Sayari (KJS) method [26], which employs the Barrett-Joyner-Halenda (BJH) algorithm [27] but with the statistical film thickness curve and a Kelvin-type relation calibrated for the series of MCM-41 samples. The mesopore diameter, w_{KJS} , was obtained at the peak maximum of the PSD curve. Since the geometry of primary mesopores in FDU-1 and SBA-16 is spherical, this method leads to a systematic underestimation of the mesopore sizes. Therefore, the mesopore diameters were also calculated using the relation between the pore width w_d , unit cell parameter a and the volume of primary mesopores derived for a proper symmetry group [28].

Table 1. Chemical structures of the surface and bridging groups present in the materials studied.

Group	Group name	Organosilane	Formula
U	Ureidopropyl	Ureidopropyl trimethoxysilane	
SH	Mercaptopropyl	(3-mercaptopropyl) trimethoxysilane	
IM	Imidazole	<i>N</i> -(3-(triethoxysilyl)propyl)-4,5-dihydroimidazole	
DS	Propyldisulfide	Bis(3-(triethoxysilyl)propyl)disulfide	
ICS	Isocyanurate	Tri[3-(trimethoxysilyl)propyl]isocyanurate	
E	Ethane	1,2-bis(trimethoxysilyl)ethane	

Powder X-ray diffraction (XRD) measurements were recorded using a PANalytical, Inc. X'Pert Pro (MPD) Multi Purpose Diffractometer with Cu K α radiation, operating voltage of 40 kV, whereas small-angle X-ray scattering (SAXS) measurements were conducted using the NanoSTAR system (Bruker AXS) with pinhole collimation and a two-dimensional detector (HiSTAR), mounted on a micro focus X-ray tube with copper anode and equipped with crossed Göbel mirrors. All measurements were performed at room temperature.

Nitrogen and sulfur contents for all organosilicas were obtained by CHNS analysis on a LECO CHNS-932 elemental analyzer from St. Joseph, MI. Elemental analysis data for nitrogen and sulfur were used to determine the ligand concentrations.

FT-IR spectra were collected using a Digilab FTS-3000 spectrometer equipped with liquid nitrogen cooled mercury-cadmium-telluride detector, operating at 4 cm⁻¹ nominal resolution by co-addition of 64 scans. Diffuse reflectance spectra were obtained using an optical accessory from Harrick Scientific (Ossining, NY, DRA-2CN). Samples were prepared by mixing a 10% (w/w) dispersion of modified silica in dried, pre-ground KCl after adjustment of sample height to obtain the maximum interferogram signal. All spectra were ratioed to that of pure KCl and converted to Kubelka-Munk (KM) units using standard instrument software.

3. Results and Discussion

The structure of the extracted functional materials was studied by either X-ray diffraction (XRD) or small-angle X-ray scattering (SAXS). The unit cell parameters are listed in Table 2. As can be seen from Table 2, the unit cell values are in the range from 11.7 to 18.5 nm. Since the X-ray diffraction patterns are not presented here, Table 2 provides references to the original data. The XRD patterns allowed us to assign the OMO-U and PMO-E-ICS samples to the *P6mm* symmetry group (2D hexagonal arrangement of mesopores), the PMO-ICS sample to the *Im3m* symmetry group, whereas the OMS-U-SH, OMS-IM and PMO-DS samples to the *Fm3m* symmetry group (two latter groups of samples represent 3D cubic structures with spherical cage-like pores).

The adsorption and structural parameters calculated from nitrogen adsorption isotherms measured at -196 °C for the mesoporous materials studied are shown in Table 2. All adsorption isotherms are type IV, which is characteristic for mesoporous materials. As can be seen from Table 2, all organosilicas exhibit accessible pores (5.2-9.3 nm) having volume in the range from 0.38 to 0.87 cc/g and large surface area between 443 and 881 m²/g. Their

pore widths were evaluated according to the KJS (Kruk-Jaroniec-Sayari) method [26], which is applicable for cylindrical pore geometry. Thus, the diameters of the cage-like pores were underestimated. Therefore, Table 2 shows also the pore widths calculated by using the suitable relations reported in [28].

Table 2. Adsorption and structural parameters for the OMSs and PMOs studied.^a

Sample	S_{BET} m ² /g	V_t cc/g	w_{KJS} nm	w_d nm	a nm	Ref #
OMS-U	670	0.87	8.9	8.8	11.7	13
OMS-U-SH	521	0.53	9.0	9.7	17.3	14
OMS-IM	443	0.53	9.3	10.5	18.5	17
PMO-DS	453	0.38	5.2	7.1	14.9	14
PMO-ICS	881	0.56	7.2	10.2	17.2	21
PMO-E-ICS	773	0.85	7.4	8.2	12.8	22

^aNotation: S_{BET} , BET specific surface area; V_t , single-point pore volume; w_{KJS} , mesopore diameter calculated by KJS method [26]; w_d , pore width calculated using the unit cell parameter and pore volume according to the relations derived for the hexagonal $P6mm$ (OMS-U, PMO-E-ICS) or cubic $Im3m$ (PMO-ICS) and $Fm3m$ (OMS-U-SH, OMS-IM, PMO-DS) structures by assuming 2.0 g/cm³ density for all samples [28]; a, unit cell parameter.

A qualitative identification of successful incorporation of the organic groups into the mesostructures studied was confirmed by FT-IR spectroscopy. Figure 1 illustrates the FT-IR spectra of the polymer-free mesostructured silicas with ureidopropyl (Panel A), double mercaptopropyl and ureidopropyl (Panel B), and imidazole surface ligands (Panel C). Two remaining panels show spectra of the organosilicas with disulfide bridges (Panel D) and double isocyanurate and ethane bridges (Panel E). All FT-IR spectra are presented in the range from 4000 and 550 cm⁻¹.

Shown in Figure 1 spectra exhibit characteristic bands (*) attributed to the formation of a condensed silica network at around 1060 cm⁻¹ and 790 cm⁻¹, which relate to asymmetric and symmetric vibrations of Si-O-Si, respectively. A weak absorbance (●) at around 950 cm⁻¹ is typical of non-condensed silica resulting from the asymmetric Si-O stretching mode of Si-O-H group. All spectra exhibit two other bands at about 3200-3500 cm⁻¹ (+) and 1620 cm⁻¹ corresponding to hydrogen-bonded O-H stretching vibrations from silanols and the bending mode of molecularly adsorbed water, respectively [29]. Moreover, all materials also show absorbances in the 2900-3000 cm⁻¹ and 1450 cm⁻¹ regions assigned to the asymmetric stretching and bending C-H vibrations, respectively. The presence of these bands confirms CH groups in SH, U, IM, DS and ICS-functionalized PMOs and OMSs.

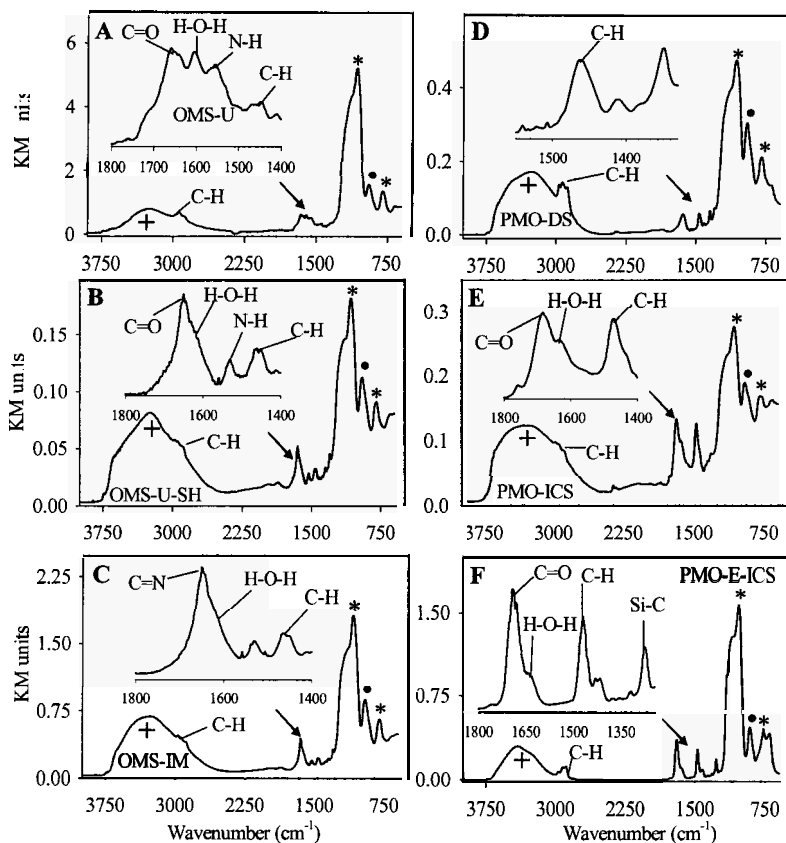


Figure 1. Infrared spectra of the extracted functionalized mesoporous materials with various surface and bridging groups. Panels A and B show spectra for ureidopropyl-functionalized OMS (OMS-U) and bifunctional OMS with ureidopropyl and mercaptopropyl surface groups (OMS-U-SH), whereas the insets present the enlargement of spectra in the carbonyl (C=O) stretching and CH bending regions between 1400 and 1800 cm^{-1} . Panel C shows a spectrum for imidazole-functionalized OMS (OMS-IM) with an inset for the azomethine group (N=C), whereas Panel D represents a spectrum for PMO having disulfide bridges (PMO-DS) with inset for CH bending vibrations. Panels E and F show spectra for isocyanurate-containing PMO (PMO-ICS) and bifunctional PMO with ethane and isocyanurate groups (PMO-E-ICS) with enlarged insets in the C=O stretching and C-H bending regions. Symbols; (+) – refers to hydrogen bonded O-H stretching bands from silanols and surface adsorbed water, (*) – refers to silica network Si-O-Si asymmetric stretching and (●) – represents a Si-OH band.

The vibration at 1650 cm^{-1} in the inset of Panel A showing spectrum of OMS-U is attributed to the carbonyl (C=O) stretching band from $-\text{NHCONH}_2$. The relatively low frequency for this carbonyl stretch is characteristic for an

amidic type carbonyl. The stretching vibrations of NH_2 in the $3380\text{--}3280\text{ cm}^{-1}$ region cannot be separately detected because of the overlap with a broad peak of hydrogen bonded OH stretching bands from silanols and surface adsorbed water. However an N-H bending absorbance is detected at 1550 cm^{-1} [11].

Nitrogen contents obtained by elemental analysis were 1.27 and 0.47 mmol/g for OMS-U and OMS-U-SH, respectively. As regards to mercaptopropyl surface groups in OMS-U-SH (Panel B), the expected S-H stretching vibration at about 2500 cm^{-1} could not be detected due to its weak absorption coefficient [10]. However, the presence of C-H vibrations and elemental analysis of sulfur (1.4 %) confirms mercaptopropyl groups on the pore walls of this mesoporous silica.

The presence of imidazole groups in the pores of OMS-IM is clearly evidenced by C=N stretch at 1650 cm^{-1} (see Panel C) [16]. Elemental analysis showed that the nitrogen content was 0.9 mmol per gram for this sample

The presence of propyldisulfide is evidenced by C-H stretching and bending vibrations in the 2900 cm^{-1} and 1450 cm^{-1} regions. Unfortunately, a C-S bond absorbance, expected at around 1100 cm^{-1} , could not be detected due to overlapping with the intense Si-O-Si asymmetric stretching vibrational mode at the same frequency (Panel D). An evidence for integration of the disulfide bridging groups into the mesostructure is also supported by elemental analysis, which showed about 1.1 mmoles of these groups per gram of PMO-DS.

The spectra of the samples with single isocyanurate groups (PMO-ICS) and double isocyanurate and ethane groups (PMO-E-ICS) are shown in Panels E and F, respectively. As can be seen from these panels, in addition to the CH stretching and bending vibrations, quite intense peaks at slightly less than 1700 cm^{-1} are observed, which originate from carbonyl (C=O) stretching vibrations within the isocyanurate ring. In contrast to PMO-ICS, the PMO-E-ICS sample has much less water adsorbed, as indicated by a relatively low intensity in the O-H stretching region ($3100\text{--}3500\text{ cm}^{-1}$). This results from the presence of ethane moieties in the backbone causing an increased hydrophobicity of the mesopore framework. Furthermore, there are two peaks in the PMO-E-ICS spectrum at about 1260 cm^{-1} and 700 cm^{-1} , which are clearly not seen in the PMO-ICS sample. The former band has been assigned to a Si-C stretch [19], which provides evidence for ethane bridging group and confirms the lack of bond cleavage that could possibly occur during the extraction procedure. Nitrogen elemental analysis of the PMO-ICS and PMO-E-ICS samples showed about 0.76 and 1.04 mmoles of isocyanurate per gram of the material.

The mercury adsorption capacities obtained under Hg^{2+} : ligand ratio = 3:1 estimated under static conditions for the samples studied are collected in Table

3. All adsorbents listed in Table 3 show high adsorption loadings. Among surface-functionalized OMS the OMS-IM sample showed the highest Hg^{2+} uptake (1.96 mmol Hg^{2+} , which corresponds to 0.39 g of Hg^{2+} per gram of the sample). In contrast to multifunctional surface ligands, multifunctional bridging groups possess even higher adsorption capacities, which are equal to 0.4 and 0.45 g of mercury per 1.0 g of PMO-DS and PMO-ICS, respectively. In fact, the maximum adsorption capacity as high as 0.65 g Hg^{2+} /g was obtained for PMO-E-ICS because this sample showed higher concentration of ICS than that in PMO-ICS. It is noteworthy that this material was synthesized exclusively from bridged organosilanes with ethane and isocyanurate groups.

Table 3. Molar composition, elemental analysis and mercury adsorption for the OMSs and PMOs studied.

Sample	X_{lig}	n_t mmole	EA $P_N(P_S)$	C_{lig} mmol/g	Hg^{2+} ads mmol/g	Hg^{2+} ads g Hg^{2+} /g	R
OMS-U	0.15	19.2	3.5	1.27	1.72	0.35	1.3
OMS-U-SH	0.05 0.05	9.96	1.4 (1.4)	0.95	1.66	0.33	1.7
OMS-IM	0.08	19.9	2.5	0.9	1.96	0.39	2.2
PMO-DS	0.11	8.97	7.1	1.1	2.02	0.40	1.8
PMO-ICS	0.08	34.9	3.2	0.76	2.42	0.45	3.2
PMO-E-ICS	0.22	4.65	4.4	1.04	3.23	0.65	3.1

^aNotation: X_{lig} , mole fraction of organic group in the synthesis gel; n_t , total number of moles of TEOS or BTESE (PMO-E-ICS) in the synthesis gel; P_N and P_S , nitrogen and sulfur percentages obtained on the basis of elemental analysis; C_{lig} , total surface coverage of bonded ligands; Hg^{2+} ads, maximum mercury adsorption expressed in mmoles of mercury per gram of adsorbent; R, reflects the ratio of Hg^{2+} to C_{lig} .

The results published by others [23] and herein confirm the advantages of applying modified mesoporous silicas with incorporated bridging moieties for adsorption of heavy metal ions from aqueous solutions. The high adsorption capacities are observed for these materials because of accessible pores, high surface area, large channel-like and cage-like mesopores interconnected by complimentary pores and properly chosen organic ligands that possess multiple active sites.

4. Conclusions

A comparative study is presented for functionalized ordered mesoporous materials with various surface (mercaptopropyl, ureidopropyl and imidazole) and bridging (propyldisulfide and isocyanurate) groups containing sulfur and nitrogen atoms; these materials were synthesized via co-condensation of

appropriate organosilanes and TEOS/BTESE in the presence of triblock copolymers (P123, F127, B50-6600) as templates. The FT-IR and elemental analysis confirmed functionalization of silica mesostructures with organic groups. XRD showed that both OMSs and PMOs exhibited structural ordering of pores, whereas adsorption analysis demonstrated that the samples studied exhibited large mesopores, high surface area and high pore volumes. It was shown that functionalized-OMSs and PMOs possessed high adsorption capacity towards mercury ions due to relatively high loadings of multifunctional groups and fully accessible porous networks. Among the bridging groups studied, the use of isocyanurate rings was beneficial for the preparation of high capacity adsorbents because the ICS moiety can potentially attract three mercury ions per one ICS group giving the mercury capacity of 3.23 mmol/g for the sample with 1.04 mol/g ICS loading. On the other hand, imidazole was a very promising ligand among the surface groups studied, which was shown to be capable of coordinating more than two Hg^{2+} per attached ligand giving mercury adsorption of 1.96 mmol/g for 0.9 mmol/g imidazole loading.

Acknowledgments

This material is based upon work supported by the National Science Foundation under Grant No. CTS-0553014. The authors thank BASF Corporation and Dow Chemicals for providing triblock copolymers, P123, F127 and B50-6600, respectively.

References

1. L. Jaerup, *British Med. Bull.* **68**, 167 (2003).
2. P.K. Jal, S. Patel and B.K. Mishra, *Talanta* **62**, 1005 (2004).
3. C.T. Kresge, M.E. Leonowicz, W.J. Roth, J.C. Vartuli and J.S. Beck, *Nature* **359**, 710 (1992).
4. D. Zhao, J. Feng, Q. Huo, N. Melosh, G.H. Fredrickson, B.F. Chmelka and G.D. Stucky, *Science* **279**, 548 (1998).
5. C. Yu, Y. Yu and D. Zhao, *Chem. Commun.* 575 (2000).
6. R.M. Grudzien and M. Jaroniec, *Chem. Commun.* 1076 (2005).
7. V. Antochshuk and M. Jaroniec, *Chem. Commun.* 258 (2002).
8. V. Antochshuk, O. Olkhovyyk, M. Jaroniec, I.-S. Park and R. Ryoo, *Langmuir* **19**, 3031 (2003).
9. O. Olkhovyyk and M. Jaroniec, *Adsorption* **11**, 205 (2005).
10. X. Wang, S. Cheng and J.C.C. Chan, *J. Phys. Chem. C* **111**, 2156 (2007).
11. Y.J. Gong, Z.H. Li, D. Wu, Y. H. Sun, F. Deng, Q. Luo and Y. Yue, *Microporous Mesoporous Mater.* **49**, 95 (2001).

12. Q. Wei, L. Liu, Z.-R. Nie, H.-Q. Chen, Y.-L. Wang, Q.-Y. Li and J.-X. Zou, *Microporous Mesoporous Mater.* **101**, 381 (2007).
13. R.M. Grudzien, B.E. Grabicka and M. Jaroniec, *Adsorption* **12**, 293 (2006).
14. R.M. Grudzien, B.E. Grabicka, D.J. Knobloch and M. Jaroniec, *Stud. Surface Sci. Catal.* **165**, 443 (2007).
15. C.E. Fowler, S.L. Burkett and S. Mann, *Chem. Commun.* 1769 (1997).
16. T. Kang, Y. Park, K. Choi, J.S. Lee and J. Yi, *J. Mater. Chem.* **14**, 1043 (2004).
17. R.M. Grudzien, B.E. Grabicka, D.J. Knobloch and M. Jaroniec, *Colloids and Surfaces A* **291**, 139 (2006).
18. T. Asefa, M.J. MacLachlan, N. Coombos and G.A. Ozin, *Nature* **402**, 867 (1999).
19. V. Rebbin, M. Jakubowski, S. Potz and M. Froba, *Microporous Mesoporous Mater.* **72**, 99 (2004).
20. O. Olkhovyk and M. Jaroniec, *J. Am. Chem. Soc.* **127**, 60 (2005).
21. R.M. Grudzien, S. Pikus and M. Jaroniec, *J. Phys. Chem. B* **110**, 2972 (2006).
22. R.M. Grudzien, B.E. Grabicka, S. Pikus and M. Jaroniec, *Chem. Mater.* **18**, 1722 (2006).
23. O. Olkhovyk and M. Jaroniec, in: “*Environmental Applications of Nanomaterials*” (G. F. Fryxell and G. Cao, eds), Imperial College Press, London, 2007, pp. 179-212.
24. S. Brunauer, P.H. Emmet and E. Teller, *J. Am. Chem. Soc.* **60**, 309 (1938).
25. K.S. Sing, D.H. Everett, R.A.W. Haul, L. Moscou, R.A. Pierotti, J. Rouquerol and T. Siemieniewska, *Pure Appl. Chem.* **57**, 603 (1985).
26. M. Kruk, M. Jaroniec and A. Sayari, *Langmuir* **13**, 6267 (1997).
27. E.P. Barrett, L.G. Joyner and P.P. Halenda, *J. Am. Chem. Soc.* **73**, 373 (1951).
28. P.I. Ravikovitch and A.V. Neimark, *Langmuir* **18**, 1550 (2002).
29. X.S. Zhao, G.Q. Lu, A.K. Whittaker, G.J. Millar and H.Y. Zhu, *J. Phys. Chem. B* **101**, 6525 (1997).

SEPARATION OF HIGH SURFACE AREA MINERAL SOLIDS FROM SUNCOR COKE FLY ASH

ABDUL MAJID, STEVE ARGUE, DAVID KINGSTON

*Institute for Chemical Process and Environmental Chemistry, National Research
Council of Canada, Ottawa, Ontario K1A 0R9, Canada*

STEPHEN LANG

*Steacie Institute for Molecular Sciences, National Research Council of Canada, Ottawa,
Ontario K1A 0R9, Canada*

JAMES MARGESON

*Institute for Research in Construction, National Research Council of Canada, Ottawa,
Ontario K1A 0R6, Canada*

For the past several years, we have been involved in the development of technically and economically feasible separation techniques for the recovery of by-products from oil sands industry wastes for use as potentially marketable products. The concepts of industrial ecology and an increased societal awareness of waste management continue to provide motivation for the discovery of new applications for these materials, as well as the value-added products that may be derived. In this investigation we have applied a fractionation methodology developed previously to separate high surface area mineral solids from Suncor coke fly ash for potential commercial applications. This fraction has been characterized by EDS elemental analysis, X-ray diffraction, XPS, SEM, solid-state NMR and surface area measurements. The efficiency of separation and the characteristics of the separated mineral fraction from Suncor fly ash have been compared with the data for the mineral solids from Syncrude fly ash reported previously.

1. Introduction

The production of refinery grade oil from the Alberta oil sands deposits as currently practiced by Syncrude and Suncor, generates a substantial amount of waste including, coke, fly ash, coarse sand and fine tailings [1]. Under current production conditions, a plant producing 15,900m³/day (100,000 bbl/day) of synthetic crude oil requires the processing of 100,000 m³/day ore which results in a tailings stream consisting of 100,000 m³ of coarse sand, 2,000 m³ of coke, 100 m³ of fly ash and 20,000 m³ of Mature Fine Tailings (30% solids) [2]. As a result, large inventories of process-affected materials are accumulating. The

major concern regarding these wastes is a question of the volumes involved. The reduction in the volume of the produced wastes by recycling would be economically and environmentally desirable.

The recognition and exploitation of the useful intrinsic properties of waste materials are becoming more important owing to increasing awareness of environmental issues. However, the commercial recycling of oil sands industry wastes is essentially non-existent because of the lack of economical technology, and the absence of compelling incentives in the form of government regulations. It is anticipated that high disposal costs and increased regulatory pressures to minimize landfill disposal options will increase the incentives for development of improved technology and economics for recycling many of the potentially useful components from oil sands mine wastes.

For the past several years, we have been developing separation techniques for the recovery of by-products from oil sands industry wastes [3-11]. The principal objective of this work has been to develop technically feasible separation techniques for potentially marketable products. Recently, we have developed a fractionation methodology for the separation of high surface area mineral solids from oil sands coke fly ash for potential use as polymer reinforcements after surface modification [11]. In this investigation we have applied this methodology to Suncor coke fly ash. The separated mineral fraction has been characterized by EDS elemental analysis, X-ray diffraction, XPS, SEM, solid-state NMR and surface area measurements. The efficiency of separation and the characteristics of the separated mineral fraction from Suncor fly ash have been compared with the data for the mineral solids from Syncrude fly ash reported previously [11].

2. Materials and Methods

2.1. Materials

A sample of Suncor fly ash originating from the burning of coke produced from Athabasca oil sands bitumen, and obtained from Alberta Research Council sample bank in 1983 was used in this investigation. This sample had been characterized previously [12]. All other reagents were obtained from Aldrich and used as received.

2.2. Measurements

^{29}Si NMR spectra were recorded at 40 MHz on a TecMag Apollo series spectrometer. Samples were spun at 4.5 kHz in zirconia rotors in a Doty 7mm

MASS probe. The 90 degree pulse length was 10 micro-seconds. A 10 second delay between pulses was found to be adequate, and spectra were accumulated overnight. ^{27}Al NMR spectra were recorded at 78 MHz on a Bruker AMX-300 spectrometer, using a Doty 5mm mass probe, a 5mm zirconia rotor and 8 to 8.5 kHz MASS. A pulse length of 1 microsecond was used, and 1000 scans were acquired, with a 0.5s delay between scans. A noticeable probe background was subtracted. The chemical shifts of aluminium and silicon were referenced against external 1 M aqueous aluminium nitrate and neat tetra-methyl silane (TMS) respectively.

XPS was performed with a Physical Electronics (Perkin Elmer, Eden Prairie, MN, USA) model 550 instrument. Monochromatic Al K α radiation was used. The dry samples were pressed into indium foil for analysis. Survey spectra were collected using pass energies of 188 eV, while high resolution spectra were recorded with a 22 eV pass energy. An electron flood gun was used to neutralize the charge during the experiment. Binding energies were referenced to the carbon-carbon bond, which was assigned a binding energy of 284.6 eV. Atomic compositions were estimated using a standard program provided with the instrument. During analysis, the pressure inside the instrument was always below 5×10^{-9} torr ($<0.7 \mu\text{Pa}$).

Specific surface areas, pore volumes and pore size distributions were determined using a Micromeritics Gemini III 2375 apparatus, using nitrogen as adsorbent at 77K. The application of the BET equation was used to obtain the adsorption data [13]. The pore-size distribution of the samples was calculated from desorption isotherms, and the BJH method was used for calculations [13-15]. The density of the materials was determined by a Pycnometry measurement with helium using Micromeritics Accupyc 1330 apparatus.

X-ray powder diffraction data were collected between $2\theta = 15^\circ - 70^\circ$ with a scan rate of $2^\circ/\text{min}$ at room temperature on Scintag XDS 2000 with a theta-theta geometry and a copper X-ray tube. The diffractometer had a pyrolytic graphite monochromator in front of the detector. The samples were mounted on a zero background sample holder made of an oriented silicon wafer.

Scanning electron micrographs were recorded using a Hitachi Field Emission Scanning Electron Microscope (SEM) Model S-4800 fitted with an Oxford Inca Energy Dispersive Spectrometer (EDS) used for elemental analysis. It was operated at 1.2keV electron volts and a current of 10 uA. The working distance was 8 mm. Elemental analysis is semi-quantitative and is measured at a working distance of 15 mm with a 20 keV beam energy and 20 uA of current. An average of five determinations was carried out.

Particle size analysis. The particle size distribution of the samples were determined using highly diluted dispersions in 1% aqueous solution of Na_3PO_4 . The measurements were performed using Malvern Zetasizer Model 3000HS particle analyzer, which is based on the principle of laser ensemble light scattering. The particles are introduced to the analyzer beam in a sample presentation cell located in the optical unit. For each sample, the mean value of five replicate determinations were calculated. Values reported are the mean value for two replicate samples.

2.3. Procedures

The procedures used for the separation of mineral solids from Suncor fly ash have been reported previously [11].

3. Results and Discussion

3.1. Effectiveness of leaching process

Representative elemental analyses of the raw and treated ash samples are shown in Table 1. Compared with the Syncrude fly ash sample [11], the acid leaching of the Suncor fly ash was less effective. The treatment of the carbon free sample of fly ash from Suncor, results in only small changes, in the elemental composition of the sample. Ti, V and Ni were not amenable to leaching, which is consistent with the previous investigations [17]. Complete dissolution of sulphur moiety suggests that it may not be part of fly ash matrix. The treatment also selectively removed a smaller amount of other elements including Si and Al. However, the Si:Al ratio remained unchanged.

Table 1. The effect of acid leaching on elemental compositions of ashed fly ash samples

Sample	Elemental composition, W/W%											
	Si	Al	Fe	Mg	Ti	Ca	Na	K	S	V	Ni	Si:Al
untreated	21.0	12.2	7.5	0.7	2.0	1.2	0.7	1.1	3.1	2.7	1.2	1.7
Treated	18.4	10.8	5.9	0.4	2.1	0.5	0.3	0.8	-	2.6	1.2	1.7

Table 2 lists physico-chemical properties of the fly ash samples. The data for a Syncrude fly ash sample is from a previous investigation [11], and has been included for comparison purposes. It is obvious from this data, that the treatment of the two fly ash samples resulted in a significantly different end products. Compared with the Syncrude fly ash sample, the yield of high surface area mineral fraction from Suncor fly ash sample was essentially double. This is because of the higher ash content of Suncor fly ash and the lower leachability of

inorganic salts from the ash matrix. The density of the acid leached Suncor fly ash sample was slightly higher than the corresponding sample from Syncrude. This is because of the higher content and lower leachability of heavy metals in Suncor fly ash samples. The specific surface area of Suncor fly ash increases over 20 times on treatment. However, the surface area of treated Suncor fly ash sample was four time lower than the surface area of Syncrude fly ash sample. Relatively low cost and higher surface area of the treated fly ash samples render these materials as excellent candidates for potential applications in catalysis and/or catalyst support.

Table 2. Physico-chemical characteristics of Suncor Fly Ash samples

Sample ID	Yield	Color	Density (g/cm ³)	Surface Area (m ² /g)	Av. Pore Dia (nm)	Av. particle size (nm)
Untreated ashed Suncor FA	100	Black	2.7	1.7	3.4	870 ± 40
Treated ashed Suncor FA	35.6	Dark brown grey	2.8	35.6	3.4	530 ± 50
Untreated ashed Syncrude FA*	100	Black	2.3	20.6	6.3	1.1 μm
Treated ashed Syncrude FA*	18.4	Light grey	2.6	140.1	3.4	320

* Ref 11

The particle size of the separated mineral solids is significantly smaller than the original fly ash samples (~500 nm vs 5 μm). Removal of un-burnt carbon and admixed as well as surface adsorbed inorganic salts from fly ash may have resulted in the deaggregation of mineral particles. This explains the particle size reduction of the separated mineral solids. Smaller particle size in combination with large specific surface area render these mineral solids as ideal candidates for applications as inorganic fillers for clay-reinforced polymer nanocomposites [18]. The surface modification of these solids may render them compatible with the hydrophobic polymers.

3.2. X-Ray Diffraction

Figure 1 compares the XRD profiles of the Suncor fly ash samples before and after treatment. The mineral composition of the fly ash sample did not change significantly after treatment. Based on the comparison of the reported XRD patterns of similar fly ash samples [19, 20] the major phases identified included mullite, quartz and pseudobrookite. Mineral phases present in smaller amounts included: illite, albite, TiO₂, hematite and hercynite. A minor amount of

kaolinite was also identified in the untreated ashed sample. However, kaolinite was not present in the treated fly ash sample.

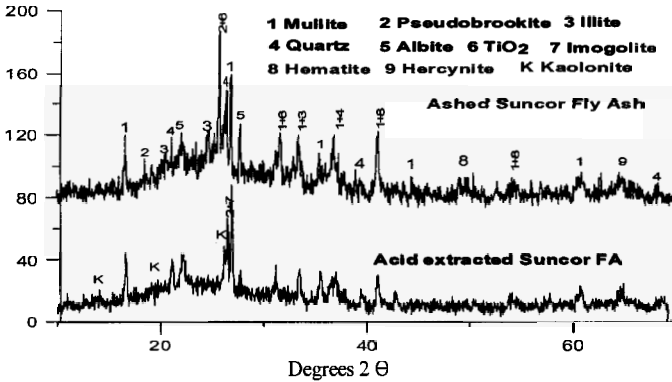


Figure 1. XRD patterns of Suncor Fly ash

3.3. Surface Analysis

The survey spectrum of fly ash samples showed Al, Si, Mg, Ti, V, C and O in both untreated and treated fly ash samples. Iron, potassium, calcium, sodium and sulphur were only detected in the untreated samples. XPS provides information on the top 10 nm of the surface. This suggests that these elements were selectively leached from the surface. The presence of carbon could not be confirmed by Leco combustion analyses, suggesting its presence only on the surface due to the adsorption from atmosphere.

3.4. Scanning Electron Micrography

Figure 2 show scanning electron micrograph (SEM) pictures of untreated and treated Suncor fly ash at various magnifications. Both samples show smooth spherical particles of cenospheres morphology. The diameters of these spheres range from 4-15 μm for the untreated sample and 2-10 μm for the treated sample. These spheres are interdispersed with crystalline inorganic compounds. Spheres in the untreated samples also have adsorbed inorganic matter on them that is removed by acid leaching in the treated sample. The crystalline compounds observed confirmed the presence of mullite and quartz as detected

by XRD. The admixture consists of rods, needles, platlets and porous material in the nm size range.

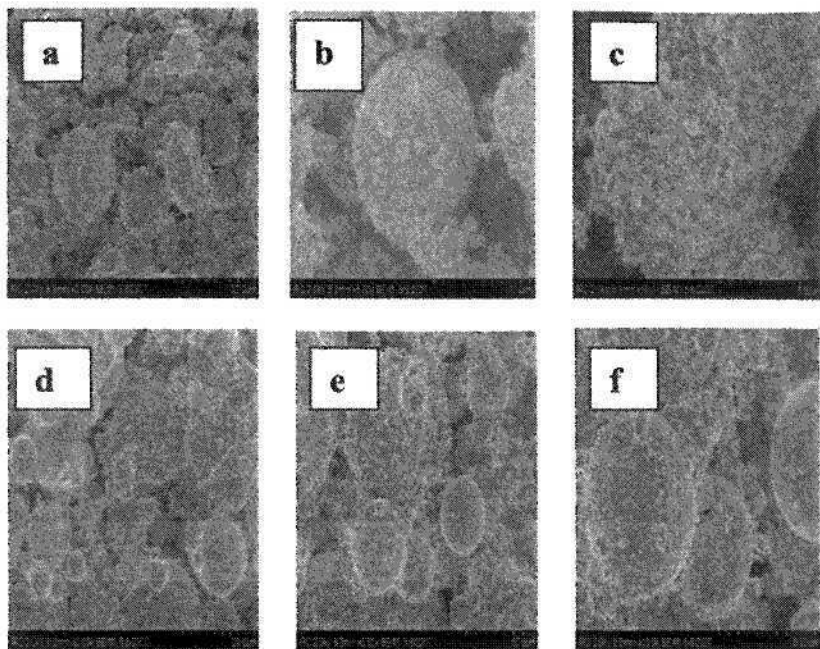


Figure 2. SEM photographs of: 2a-2c. Untreated Suncor fly ash; 2d-2f. Treated FA

3.5. Solid-State NMR Spectroscopy

Nuclear magnetic resonance (NMR) spectroscopy has been shown to be capable of providing considerable information about the structures of aluminosilicates and clay minerals [21-26]. The position of silicon resonance is affected primarily by its degree of polymerization, and by the nature of the nearest neighbor cations, whereas the aluminum resonance is sensitive primarily to the number of atoms in its immediate coordination environment, i.e. to whether the aluminum is four- or six-fold coordinated by oxygen. Solid-state NMR is particularly sensitive to amorphous phases or small crystallites many of which cannot be detected by XRD.

Figure 3 shows ^{29}Si MAS NMR spectrum of the treated sample of Suncor fly ash. The spectrum shows one major broad peak centered at -110 ppm and two shoulders at -104 and -97 ppm. The broad strong peak at the highest field

corresponds to the un-substituted $Q^4(0Al)$ units and is close to those of quartz, cristobalite and perhaps some amorphous silica [27-29]. The lines at -104 and -97 ppm can be assigned to the $Q^4(1Al)$ and $Q^4(2Al)$ units respectively in accordance with the chemical shifts in zeolite type aluminosilicates [29]. These assignments also suggest the presence of feldspars and mullite [30, 31].

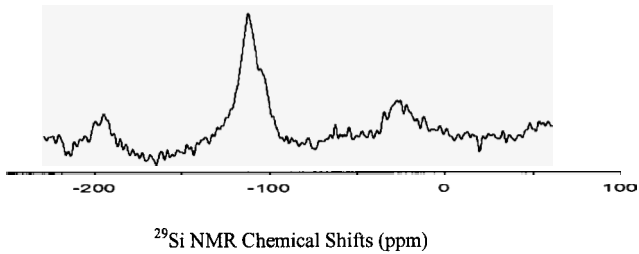


Figure 3. ^{29}Si MAS NMR spectra of treated Suncor Fly Ash

The ^{27}Al -MAS spectra of raw and treated ashed Suncor fly ash samples, are shown in Fig. 4. The spectra contain two major resonances, centered at 50 and 0 ppm, which correspond to four and six coordinate aluminum species respectively [32]. The octahedral component is attributed to the aluminum in the mullite present in the ash [31]. Since ^{29}Si NMR show peaks in the range -97 to -104 attributable to $Q^4(1$ and $2Al)$, it is postulated that the Al^{IV} broad peak centered at 50 ppm arises from the Al atoms in the three dimensional silica framework [28].

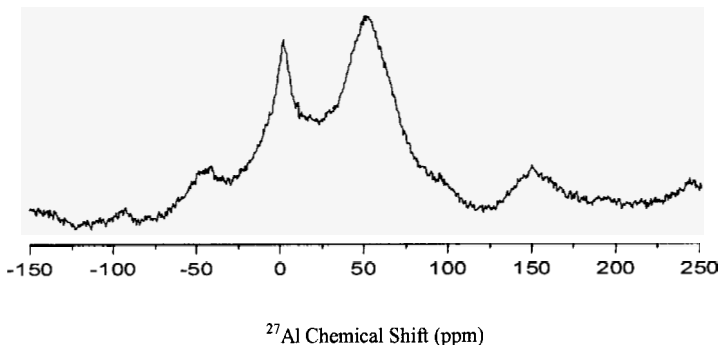


Figure 4. ^{27}Al MAS NMR spectrum of treated Suncor Fly Ash

4. Conclusion

A technically feasible fractionation scheme developed previously for the separation of high surface area mineral solids from fly ash samples was successfully applied to the oil sands coke fly ash sample from Suncor. Suncor coke fly ash was found to be less amenable to acid leaching as compared to the Syncrude coke fly ash. The characteristics of the separated mineral solids such as specific surface area and morphology were also significantly different for the two fly ashes. However, compared with the untreated sample the increase in the specific surface area of the treated Suncor fly ash sample was over 20 times. SEM images for these solids show smooth spherical particles of cenospheres morphology. The particle size of the fly ash also decreased significantly after treatment as a result of leaching of the adsorbed as well as some admixed inorganic salts. Surface area and pore size determine the accessibility to active sites and this is often related to catalytic activity and selectivity in catalyzed reactions. High surface area, relatively low cost and micro-pores render these materials as excellent candidates for potential applications in heterogeneous catalysis. Other potential applications could include: adsorbent, microporous material for example for gas storage after porosity modification, as polymer reinforcements after surface modification, and flattening (mating) agent in the paint and lacquer industry.

References

1. F. W. Camp, "The Tar Sands of Alberta, Canada"; Cameron Engineering Inc.: Denver, 1969.
2. N. R. Morgenstern, A. E. Fair and E. C. McRoberts, *Can. Geochemical J.* **25**, 637 (1988).
3. A. F. Sirianni and J. A. Ripmeester, *Can. J. Pet. Techn.* **79**, 131 (1981).
4. A. Majid and J. A. Ripmeester, *J. Separ. Proc. Techn.* **4**, 20 (1983).
5. A. Kumar, B. D. Sparks and A. Majid, *Separ. Sci. & Tech.* **21**, 315 (1986).
6. A. Majid and J. A. Ripmeester, *3rd UNITAR/UNDP Conf. Proceedings*, 1425 (1985), Richard F. Meyer, Editor.
7. A. Majid, V. P. Clancy and Bryan D. Sparks, *Energy & Fuels* **2**, 651 (1988).
8. A. Majid, B. D. Sparks, and C. A. Hamer, *Fuel* **68**, 581 (1989).
9. R. D. Coleman, B. D. Sparks and A. Majid, *Fuel* **74**, 1156 (1995).
10. A. Majid, S. Argue, V. Boyko, G. Pleizier, P. L'Ecuyer, J. Tunney and S. Lang, *Colloids and Surf. A: Physicochem. Eng. Aspects* **224**, 33 (2003).
11. A. Majid, S. Argue and J. Margeson, *Stud. Surf. Sci. Catal.* **156**, 19 (2005).
12. A. Majid, C. I. Ratcliffe and J. A. Ripmeester, *Fuel Sci. & Tech.* **7**, 879 (1989).

13. K. S. W. Sing, D. H. Everett, R. A. W. Haul, L. Moscou, R. A. Pierotti, J. Rouquerol, and T. Siemieniewska, *Pure Appl. Chem.* **57**, 603 (1985).
14. M. L. Occelli, J. P. Olivier, J. A. Perdigon-Melon and A. Auroux, *Langmuir* **18**, 9816 (2002).
15. G. Leofanti, M. Padovan, G. Tozzola and B. Venturelli, *Catal Today* **41**, 207 (1998).
16. A. Majid and B. D. Sparks, *Fuel* **62**, 772 (1983).
17. L. G. Schneider and Z. M. George, *Extr. Metall. Pap. Symp.* 413 (1981).
18. R. E. Grim, "Clay Mineralogy", McGraw-Hill, London, (1968).
19. H. Jang and T. H. Etsell, *Fuel* **85** 1526 (2006).
20. J. A. Fernandez and A. J. Palomo, *Fuel* **82**, 2259 (2003).
21. N. C. M. Alma, G. R. Hays, A. V. Samoson and E. Lippmaa, *Anal. Chem.* **56**, 729 (1984).
22. P. F. Barron, M. A. Wilson, A. S. Campbell and R. L. Frost, *Nature* **299**, 616 (1982).
23. B. H. W. S. de Jong, C. M. Schramm, and V. E. Parziale, *Geochim Cosmochim. Acta.* **47**, 1223 (1983).
24. J. Klinowski, J. M. Thomas, C. A. Fyfe and J. S. Hartman, *J. Phys. Chem.* **85**, 2590 (1981).
25. E. Lippmaa, M. Magi, A. Samoson, M. Tarmak and G. Engelhardt, *J. Am. Chem. Soc.* **103**, 4992, (1981).
26. R. A. Kinsey, R. J. Kirkpatrick, J. Hower, K. A. Smith and E. Oldfield, *Am. Mineral* **70**, 537 (1985).
27. B. A. Goodman, J. D. Russell, E. Oldfield and R. J. Karkpatrick, *Phys. Chem. Minerals* **12**, 342 (1985).
28. H. He, J. Guo, X. Xie, H. Lin and L. Li, *Clay Minerals* **37**, 337 (2002).
29. E. Lippmaa, M. Magi, A. Samoson, M. Tarmak and G. Engelhardt, *J. Am. Chem. Soc.* **103**, 4992 (1981).
30. E. Lippmaa, M. Magi, A. Samoson, G. Engelhardt and A.-R. Grimmer, *J. Am. Chem. Soc.* **102**, 4889 (1980).
31. A. Fernandez-Jimenez, A. G. de la Torre, A. Palomo, G. Lopez-Olmo, M. M. Alonso and M. A. G. Aranda, *Fuel* **85**, 625 (2006).
32. P. J. Chupas and C. P. Grey, *J. Catal.* **224**, 69 (2004).

DIRECT VISUALIZATION OF ENZYMES ENCAPSULATED IN MESOPOROUS MATERIALS*

SHUN-ICHI MATSUURA[†], TETSUJI ITOH, RYO ISHII, TATSUO TSUNODA,
SATOSHI HAMAKAWA, TAKAAKI HANAOKA, FUJIO MIZUKAMI

*Research Center for Compact Chemical Process,
National Institute of Advanced Industrial Science and Technology (AIST),
Nigatake 4-2-1, Miyagino-ku, Sendai 983-8551, Japan*

The direct visualization technique on the single molecular level was applied to determination of the enzymes encapsulated in the pores of mesoporous materials. As model enzymes, lipase and trypsin modified with fluorescent dyes were encapsulated in folded-sheet mesoporous material (FSM) and SBA-15. As a result of observation using a fluorescence microscope, we found that the individual enzymes were uniformly dispersed in the pores, resulting from the successful incorporation of the two enzymes.

1. Introduction

Artificial assemblies of enzymes have attracted much attention in the bioengineering field due to potential applications to chemical processes such as catalytic reactions [1-3]. Researchers have tried to encapsulate enzymes into silica pores, aiming at an increase in stability and durability to heat, pressure, and chemicals [4-10]. However, the encapsulation of complicated multiple enzymes consisting of several units into the pores is rarely reported. Moreover, the precise dispersion arrangement of the encapsulated enzymes could not be determined based on N₂ adsorption measurements.

Since arrangement of such multiple enzymes is extremely important to express appropriate enzyme activity, it is necessary to evaluate whether the enzymes are encapsulated and aligned in the pores. Thus, direct visualization of encapsulated enzymes (DVEE) on the single molecular level is essential to determine the proper localization of enzymes.

* The research was financially supported by the project of Development of Microspace and Nanospace Reaction Environment Technology for Functional Materials from the New Energy and Industrial Technology Development Organization (NEDO).

Here, we report the direct observation of lipase and trypsin, which are used as model of encapsulated enzymes, in the pores of folded-sheet mesoporous material (FSM) [11, 12] and SBA-15 [13, 14] by fluorescence microscopy. For this purpose, these enzymes were labeled with fluorescence dyes, so that the localization of the enzymes in the pores was visualized under a microscope field. Thus, the presence of the two enzymes in the pores was confirmed by detecting different fluorescent dyes bound to each enzyme. The pore size of FSM-22 and SBA-15 are sufficient to immobilize the two enzymes since both cylindrical enzymes are 4–5 nm long and 3 nm wide. The proposed design of the encapsulation of the fluorescently labeled lipase-trypsin-mesoporous silica conjugate is shown schematically in Figure 1.

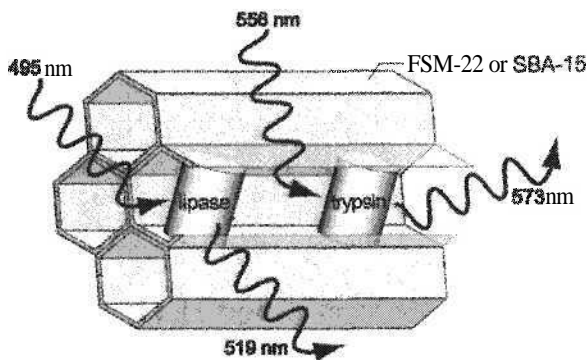


Figure 1. Schematic representation of the fluorescence detection of lipase and trypsin encapsulated in channels of FSM-22 or SBA-15.

2. Materials and methods

2.1. Preparation of FSM-22 and SBA-15

As the capsules for the enzymes, we used a FSM-22 (pore diameter of 4.2 nm) [11, 12] and a SBA-15 (pore diameter of 7.1 nm) [13, 14].

FSM-22 was prepared from kanemite by using dococyltrimethylammonium chloride [$C_{22}H_{45}N(CH_3)_3Cl$]. To 100 mL of water at 70 °C was added 4.24 g of dococyltrimethylammonium chloride, and this mixture was vigorously stirred for 30 min at 70 °C. Five grams of kanemite was added to the mixture and stirred for 3 h at 70 °C. The pH of this mixture was adjusted to 8.5 by slowly adding a 2 mol L⁻¹ HCl aqueous solution during stirring. After the suspension was stirred for 3 h at 70 °C, the solid product was filtered out, washed with 400 mL of

distilled water at 70 °C three times, and dried at 45 °C. The sample was then calcined at 550 °C for 6 h in air.

SBA-15 was synthesized using triblock copolymer, poly(ethylene glycol)-block-poly(propylene glycol)-block- poly(ethylene glycol) (SIGMA-ALDRICH) as template. In a typical synthesis, 10 g of triblock copolymer was dissolved in 300 mL of water and stirred for overnight at 35 °C, and 21.9 g of 12 N HCl and 21.3 g of tetraethyl Orthosilicate (Wako) were added to the above solution. This mixture was stirred for 20 hr at 35 °C. After the stirring, the mixture was aged for 24 h at 80 °C. The solid product was filtered out, washed with 400 mL of distilled water at 70 °C three times, and dried at 45 °C. The sample was calcined in air with a heating rate of 105 °C /h and then held at 550 °C for 10 h.

2.2. Characterization of calcined mesoporous materials

To evaluate pore diameter, pore volume and BET surface area of the calcined mesoporous materials, nitrogen adsorption and desorption measurements at 77 K were carried out on a BELSORP-max (Japan BEL Co. Ltd., Japan). The pore size distributions were determined by analyzing the adsorption branch by the BJH method [15]. Powder X-ray diffraction (XRD) spectra were recorded on a Bruker AXS D8-ADVANCE Vario-1 with 1D-high speed Position Sensitive Detector. Wall thickness was calculated from the average pore diameter and the XRD interplanar d -values. Transmission electron micrographs were obtained using a TEM (JEOL 2010F) with an acceleration voltage of 200 kV.

2.3. Preparation of lipase-trypsin-mesoporous material conjugate

Lipase and trypsin, which were derived from *Phycomyces Nitens* (M_r ~30 kDa, pI 5.9) and from *Porcine pancreas* (M_r 23 kDa, pI 10.8), respectively, were purchased from Wako Pure Chemical Industries. A batch adsorption experiment was carried out by combining 10 mg of the mesoporous material powder (FSM-22 or SBA-15) with 1 mL of appropriate buffer (20 mM sodium acetate buffer (pH 4), 20 mM MES [2-Morpholino- ethanesulfonic acid ($C_6H_{13}NO_4S$)] buffer (pH 6), 20 mM Tris [2-Amino-2-hydroxymethyl-1,3-propanediol ($H_2NC-(CH_2OH)_3$)] buffer (pH 8)) containing an appropriate amount of enzymes (lipase and/or trypsin) and 1 mM PMSF [phenylmethylsulphonyl fluoride ($C_6H_5CH_2-SO_2F$)] as protease inhibitor. The enzyme-mesoporous material mixture dissolved in the buffer solution was gently shaken using a rotator for 20 h at 4 °C in the dark. The conjugate was centrifuged for 5 min at 13,000 rpm and the supernatant was removed after which the conjugate was washed with the buffer. The enzyme concentration of the first supernatant was determined by the

Bradford method using a microplatereader (SpectraMax M2e; Molecular Devices) to check amount of enzyme adsorbed to the silica. The conjugate sample was rinsed by the above washing procedure three times, and resuspended in 1 mL of the buffer.

2.4. *Fluorescent labeling of enzymes*

The fluorescent labeling for direct visualization of the encapsulation was performed on a hetero-enzyme (lipase and trypsin). To visualize the individual enzymes encapsulated in mesoporous material using a fluorescence microscope, the enzymes were chemically modified with amine-reactive fluorescent dyes, Alexa Fluor 488 (Abs/Em = 495 nm/519 nm; Molecular Probes) for lipase and Alexa Fluor 546 (Abs/Em = 556 nm/573 nm; Molecular Probes) for trypsin at positions of some lysine residues. The fluorescent labeling sometimes damages the enzyme seriously because of the binding of the dye to active center of the enzyme. To avoid this problem as much as possible, the enzymes were modified with the degree of labeling at which one dye molecule bound to one enzyme molecule. The labeling reaction was carried out by combining 10 mg of lipase or trypsin powder with 1 mL of 20 mM MES buffer (pH 6) containing an appropriate amount of fluorescent dye, Alexa 488 or 546 dye, respectively. The sample solution was gently shaken using a rotator for 1 h at 4 °C in the dark. The labeled enzyme was purified with gel filtration using a NAP-5 Columns (GE Healthcare) equilibrated with a 20 mM MES buffer (pH 6). The obtained enzyme concentration was determined by the Bradford method with bovine serum albumin as a standard, and the fluorescence intensity with and without mesoporous material was measured using a fluorescence spectrophotometer (F-4500; HITACHI).

2.5. *Microscopic observation by epi-fluorescence and differential interference contrast*

The enzyme-mesoporous material conjugates were observed using an inverted fluorescence microscope (ECLIPSE TE2000-U; Nikon) equipped with a 100x, 1.49 numerical aperture (NA) oil-immersion objective lens. The excitation and emission light were selected with filter sets GFP-BP (suitable for Alexa 488, EX480/40, DM505, BA535/50) and TRITC (suitable for Alexa 546, EX540/25, DM565, BA605/55) produced by Nikon. Fluorescent images of the individual enzymes, which are labeled with fluorescent dyes, were visualized by a high sensitivity EM-CCD camera (ImagEM; C-9100-13, Hamamatsu Photonics) and recorded with an image processor (AQUACOSMOS analysis software;

Hamamatsu Photonics). On the other hand, mesoporous silicas as the capsule for the enzymes were independently observed by differential interference contrast (DIC) using above instrument. After preparing the fluorescently labeled enzyme-mesoporous material conjugates, an aliquot of 10 μl was loaded on a 24 x 60 mm coverslip and covered with an 18 x 18 mm coverslip. The coverslip was put on microscope stage. The observation was carried out at room temperature.

3. Results and discussion

3.1. Characterization of calcined mesoporous materials

Nitrogen adsorption/desorption isotherms, transmission electron micrograph (TEM), and X-ray diffraction (data not shown) data indicate that the mesoporous materials are highly ordered.

Figure 2 shows pore size distribution curves and the corresponding nitrogen adsorption-desorption isotherms (inset) for FSM-22 and SBA-15. As shown in Figure 2 and Table 1, the pore sizes of FSM-22 and SBA-15 were 4.2 nm and 7.1 nm, respectively, which are enough size for encapsulation of lipase and trypsin. The ordered hexagonal arrays and 1D channels of the mesoporous materials were confirmed by TEM observation (Figure 3).

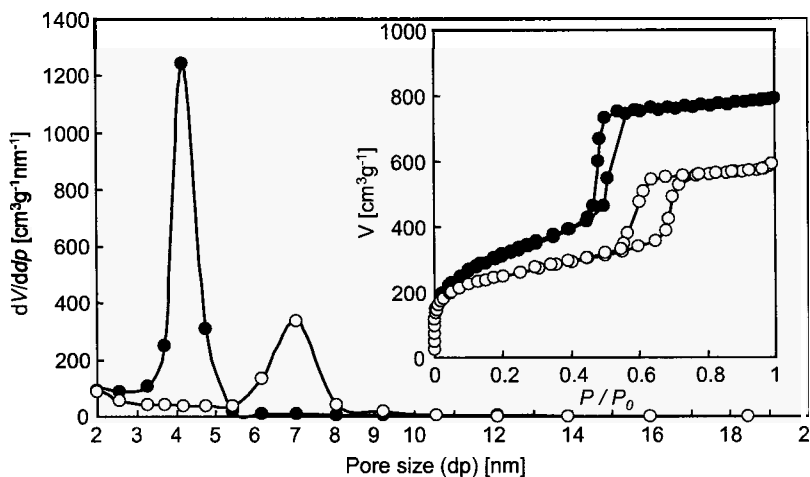


Figure 2. Pore size (dp) distribution curves obtained from the adsorption branch by the Barret-Joyner-Halenda (BJH) method and the corresponding nitrogen adsorption-desorption isotherms (inset) for FSM-22 (filled circles) and SBA-15 (open circles).

Table 1. Physicochemical Properties of mesoporous materials.

	pore diameter [nm]	wall thickness [nm]	specific surface area [m ² /g]	total pore volume [cm ³ /g]
FSM-22	4.2	0.6	1111	1.22
SBA-15	7.1	1.9	866	0.91

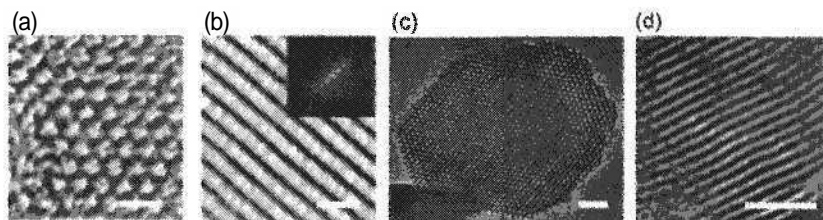


Figure 3. TEM images of the mesoporous materials recorded along the (a) FSM-22 [001], (b) FSM-22 [110], (c) SBA-15 [001], and (d) SBA-15 [110] directions. (b) Inset: electron diffraction pattern. Scale bars are 10 nm (a, b) and 50 nm (c, d).

3.2. Adsorbed amount of the enzymes incorporated into mesoporous materials

The effect of pH on the proportions of two enzymes adsorbed to the mesoporous materials was confirmed (Figure 4). Lipase adsorbed efficiently to both FSM-22 and SBA-15 at pH 6 compared with pH 8 (Fig. 4a and 4b). While the enzyme aggregated heavily at pH 4 and the aggregate did not adsorb to the silica. On the other hand, trypsin adsorbed stably to both FSM-22 and SBA-15 at a pH range from 6 to 8, although the enzyme can be adsorbed to the silica at pH 4 without self-aggregation (Fig. 4c and 4d).

Regarding the saturated adsorption amount of these enzymes, it was found that the adsorbed amount of trypsin is higher than that of lipase in both cases of FSM-22 and SBA-15, attributed to molecular sizes of the enzymes. In addition, both enzymes showed efficient adsorption to FSM-22 compared with SBA-15, suggesting that an electrostatic affinity of silica surface is different between FSM-22 and SBA-15. Interestingly, adsorption behavior of trypsin was different between FSM-22 and SBA-15 (Fig. 4c and 4d). The amount of the trypsin immobilized in FSM-22 was linearly related to the enzyme concentration (Fig. 4C), whereas trypsin-SBA-15 showed loss of adsorbed amount of the enzyme due to self-aggregation at a high concentration (Fig. 4d). These results demonstrate that FSM-22 provides a suitable platform for the immobilization

and dispersion of enzyme in mesopores with disintegration of the aggregate, even at a high concentration of enzyme.

The 20 mM MES (pH 6) proved to be the appropriate buffer for both enzymes. Therefore, the encapsulation of a mixture (weight ratio 1:1) of labeled lipase and trypsin was performed using 20 mM MES as buffer solution (1 mg-enzymes/10 mg-silica). Adsorbed amounts of the labeled enzymes in 20 mM MES were comparable to non-labeled enzymes, indicating that the labeled enzymes retained their adsorption capability after the labeling.

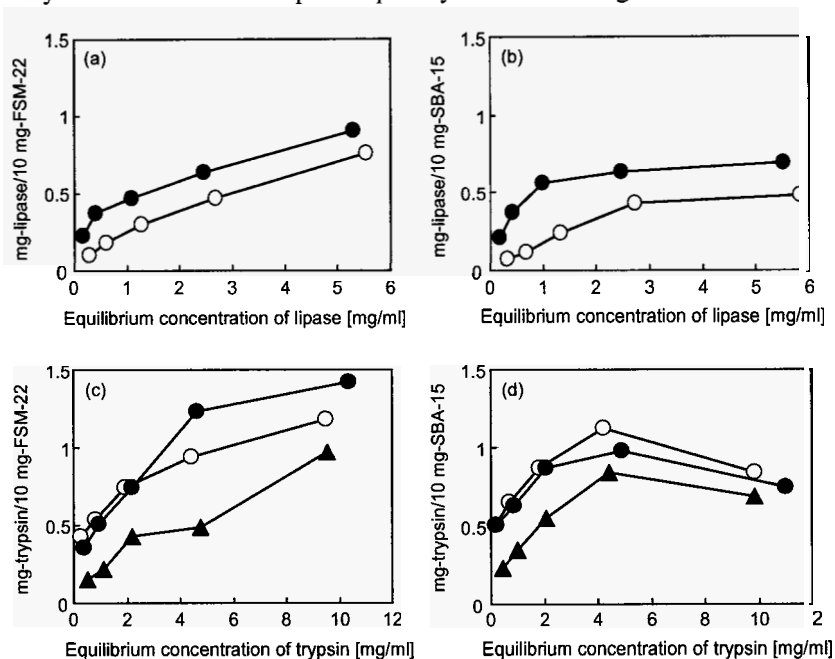


Figure 4. The amounts of lipase (a, b) and trypsin (c, d) adsorbed to the pores of FSM-22 (a, c) and SBA-15 (b, d) were measured spectrophotometrically with respect to the equilibrium concentration of the enzymes. As the buffer, 20 mM sodium acetate buffer (pH 4, filled triangles), 20 mM MES buffer (pH 6, filled circles), and 20 mM Tris buffer (pH 8, open circles) were used for dissolution of enzymes and the adsorption experiment.

In addition, the incorporation of enzymes into pores of mesoporous silicas was evaluated based on nitrogen adsorption measurements of dried samples. The specific surface areas for lipase-FSM-22, trypsin-FSM-22, lipase-SBA-15, and trypsin-SBA-15 were 780, 745, 557, and 600 m^2/g , respectively. These values of surface areas were remarkably low compared with that of FSM-22 (1111 m^2/g)

and SBA-15 (866 m²/g). The decline in surface area results from the incorporation of the enzyme into the mesopores of silica. On the other hand, the pore diameters of enzyme-FSM-22 (3.7 nm) and enzyme-SBA-15 (6.2 nm) were lower than that of FSM-22 (4.2 nm) and SBA-15 (7.1 nm). One possible reason for this is a degradation of the mesoporous framework during the adsorption reaction in the buffer solution.

3.3. Direct observation of two enzyme-mesoporous materials

Figure 5 shows the overlapped fluorescence spectra of Alexa 488 dye-labeled lipase and Alexa 546 dye-labeled trypsin. Since the difference of the two peak wavelengths is approximately 50 nm, these enzymes can be identified readily under a microscopic field.

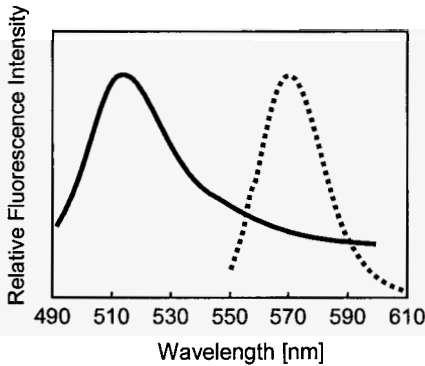


Figure 5. Fluorescence spectra of Alexa 488 dye-labeled lipase (bold line) and Alexa 546 dye-labeled trypsin (dashed line), which were excited at 495 nm and 556 nm, respectively. The spectra were recorded at 490–610 nm. Buffer solution in the samples was 20 mM MES buffer (pH 6).

When the hetero dye-labeled enzyme (lipase and trypsin, weight ratio 1:1) was encapsulated in the silica pores the same two emissions peaks appeared in the fluorescence spectrum and the individual encapsulated enzymes could be directly observed via the fluorescence images (Figure 6). If the fluorescently labeled enzymes were adsorbed mainly on the surface of the silica particles with a smaller pore size, fluorescent enhancement would be obtained from the edge of the particles, as has been reported elsewhere [16]. However, the fluorescence emissions from lipase and trypsin were distributed evenly across the mesoporous silica (Fig. 6b, 6c, 6f and 6g). Moreover, the localization of lipase and trypsin in both silicas was uniform as shown in the fluorescent images superimposed onto

the DIC images of the silicas (Fig. 6d and 6h), resulting from the successful incorporation of the two enzymes into the mesopores of silica.

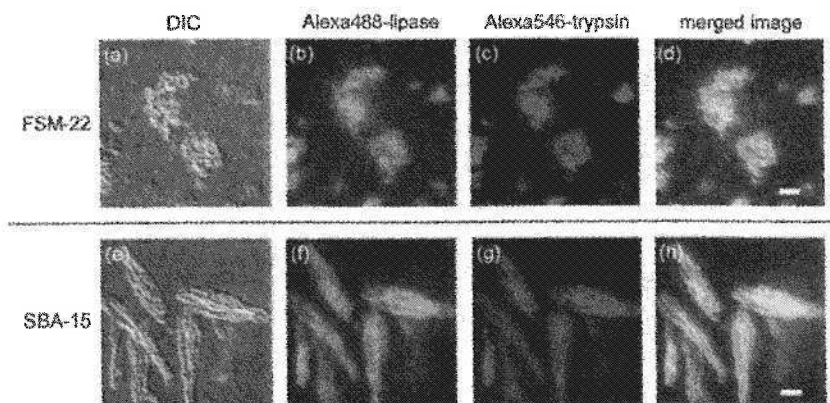


Figure 6. Direct observation of **enzyme-mesoporous silica conjugate**: DIC images of mesoporous materials (a, e), corresponding fluorescence image of Alexa 488-labeled lipase (b, f) and Alexa 546-labeled trypsin (c, g), and their merged image (d, h). The upper half and the lower half indicated enzyme encapsulated in FSM-22 and SBA-15, respectively. Scale bars are 10 μm .

4. Conclusions

We successfully prepared a **hetero-enzyme (lipase and trypsin)-mesoporous material (FSM-22 and SBA-15) conjugates** at a buffer pH range from 6 to 8 and demonstrated the direct visualization of the individual enzymes encapsulated in the silica by a fluorescent microscopy. The fluorescent image of the enzymes merged into DIC image of the silica indicated that the enzymes were distributed all over the pores of the mesoporous materials.

The results suggest that mesoporous silicas are a good host for constructing protein assemblies and single-molecule observation technique permits more precise analysis of molecular localization for an enzyme-mesoporous material. Furthermore, two fluorescent probes used in this study have the relation of donor-acceptor in FRET (fluorescence resonance energy transfer) [17, 18], when they co-exist within several nanometers. Thus, observation of the fluorescently labeled **hetero-enzymes** described in this paper not only suggests a direct evidence of the encapsulation but also opens up a detailed analysis for the intermolecular interaction between hetero-enzymes in mesoporous material by FRET technique.

Acknowledgments

The authors thank Dr. Takako Nagase (National Institute of Advanced Industrial Science and Technology (AIST)) and Mr. Toru Shiomi (Tokyo University of Science) for their help in TEM observation, and Dr. Takayuki Nara (AIST) for skilled technical assistance and valuable discussions.

References

1. Y. Lvov, K. Ariga, I. Ichinose, T. Kunitake, *J. Am. Chem. Soc.* **117**, 6117 (1995).
2. M. Hartmann, *Chem. Mater.* **17**, 4577 (2005).
3. A. Vinu, M. Miyahara, K. Ariga, *J. Nanosci. Nanotechnol.* **6**, 1510 (2006).
4. J. Fan, J. Lei, L. Wang, C. Yu, B. Tu, D. Zhao, *Chem. Commun.* 2140 (2003).
5. A. Katiyar, L. Ji, P. Smirniotis, N. G. Pinto, *J. Chromatogr. A* **1069**, 119 (2005).
6. S. Hudson, E. Magner, J. Cooney, B. K. Hodnett, *J. Phys. Chem. B* **109**, 19496 (2005).
7. I. Oda, K. Hirata, S. Watanabe, Y. Shibata, T. Kajino, Y. Fukushima, S. Iwai, S. Itoh, *J. Phys. Chem. B* **110**, 1114 (2006).
8. T. Itoh, K. Yano, T. Kajino, Y. Inada, Y. Fukushima, *Biotechnol. Bioeng.* **93**, 476 (2006).
9. T. Itoh, R. Ishi, T. Ebina, T. Hanaoka, Y. Fukushima, F. Mizukami, *Bioconjugate Chem.* **17**, 236 (2006).
10. Y. Urabe, T. Shiomi, T. Itoh, A. Kawai, T. Tsunoda, F. Mizukami, K. Sakaguchi, *ChemBioChem* **8**, 668 (2007).
11. T. Yanagisawa, T. Shimizu, K. Kuroda, C. Kato, *Bull. Chem. Soc. Jpn.* **63**, 988 (1990).
12. S. Inagaki, Y. Fukushima, K. Kuroda, *J. Chem. Soc. Chem. Commun.* 680 (1993).
13. D. Zhao, J. Feng, Q. Huo, N. Melosh, G. H. Fredrickson, B. F. Chmelka, G. D. Stucky, *SCIENCE* **279**, 548 (1998).
14. D. Zhao, Q. Huo, J. Feng, B. F. Chmelka, G. D. Stucky, *J. Am. Chem. Soc.* **120**, 6024 (1998).
15. E. P. Barret, L. G. Joyner, P. P. Halenda, *J. Am. Chem. Soc.* **73**, 373 (1951).
16. C. W. Suh, M. Y. Kim, J. B. Choo, J. K. Kim, H. K. Kim, E. K. Lee, *J. Biotechnol.* **112**, 267 (2004).
17. P. R. Selvin, *Methods in Enzymology* **246**, Academic Press, 300 (1995).
18. T. Ha, T. Enderle, D. F. Ogletree, D. S. Chemla, P. R. Selvin, S. Weiss, *Proc. Natl. Acad. Sci. U. S. A.* **93**, 6264 (1996).

UREASE IMMOBILIZATION ON PORE-EXPANDED MESOPOROUS SILICA AND ITS CATALYTIC EFFECT ON HYDROLYSIS OF UREA

KAZI-ZAKIR HOSSAIN AND ABDELHAMID SAYARI*

Centre for Catalysis Research and Innovation (CCRI), Department of Chemistry, University of Ottawa, Ottawa, K1N 6N5, Canada. E-mail: abdel.sayari@uottawa.ca

CARLOS M. MONREAL

*Environmental Health Team, Agriculture and Agri-Food Canada
960 Carling Ave, Ottawa, K1A 0C6, Canada*

Pore-expanded MCM-41 (PE-MCM-41) silica exhibits a unique combination of high specific surface area (ca. 1000 m²/g), pore size (up to 25 nm) and pore volume (up to 3.5 cm³/g). The current study focused primarily on the application of PE-MCM-41 material as suitable host for urease in controlled hydrolysis of urea. Urease adsorbed on PE-MCM-41, regular MCM-41 and silica gel adsorbent (SGA) were used as catalysts for urea hydrolysis reaction. Adsorption studies of urease on these materials from aqueous solution at pH 7.2 revealed that the adsorption capacity of PE-MCM-41 (102 mg/g) is significantly higher than that of MCM-41 (56 mg/g) and SGA (21 mg/g). The equilibrium adsorption data were well fitted using the Langmuir-Freundlich model. Furthermore, the kinetic study revealed that the uptake of urease follows the pseudo-first order kinetics. The *in-vitro* urea hydrolysis reaction on pristine urease and different urease-loaded catalysts showed that the rate of hydrolysis reaction is significantly slower on U/PE-MCM-41 compared to that of bulk urease and urease on MCM-41 and SGA.

1. Introduction

Hydrolysis of urea fertilizer to ammonia and carbon dioxide is catalyzed by urease (a nickel-based metalloenzyme) with a rate approximately 10¹⁴ times the rate of the un-catalyzed reaction [1,2]. Rapid hydrolysis of urea fertilizer by soil-based bacterial urease, results in unproductive nitrogen evolution and in ammonia volatilization and toxicity, hence alkaline-induced crop damage and subsequent greenhouse gas emission [3]. Therefore, a urease inhibitor and/or a means for controlling the rate of the enzymatic hydrolysis of urea can be combined with the urea fertilizer to increase the overall efficiency of nitrogen utilization. The use of urease inhibitors (e.g. phosphoryl amides, quinines, hydroxamic acids) in order to retard the urea hydrolysis has been reported [3].

However, these inhibitors are too expensive and easily decomposed or inactivated to generate any practical benefit [4].

Another possibility to reduce the rate of urea hydrolysis is to immobilize urease within the confined channels of mesoporous silica. Diffusion limitations of the substrate combined with a potential effect of adsorption on the intrinsic activity of the enzyme may bring about significant decrease in the hydrolysis rate. Adsorption-induced immobilization on mesoporous materials has been used for a variety of biologically active species such as amino acids, proteins and enzymes [5-7]. In this process, interactions between the support and the guest molecules are of non-covalent nature, such as hydrogen bonding, electrostatic, van der Waals and hydrophobic or hydrophilic interactions, thus relatively weak. The immobilization techniques, however, could affect their catalytic activity.

Literature reports on urease adsorption by physical immobilization onto solid substrates for the purpose of catalysis and sensing of urea include adsorption onto inorganic support surfaces [8-10], polymeric membranes [11,12], microcapsules [13,14] and sol-gel derived cast films [15,16]. Urease adsorption on activated charcoal for clinical application suffers from particulate release [8], while clay minerals [9] exhibit low adsorption capacity (21.2 mg/g). Urease immobilization on polymeric membranes such as dye attached polyamide membrane [11] by adsorption resulted in an increase of the enzyme thermal stability, while encapsulation in polymeric micro-shells [13,14] through layer-by-layer technique opened up the possibility of preparing a biocatalytic reactor. Urease adsorbed on sol-gel derived films resulted in high thermal and storage stability of the enzyme [15,16]. It is expected that pore-confined adsorption of the enzyme on PE-MCM-41 could increase its stability while decreasing the permeation of the substrate to the active sites of the enzyme, hence reducing its catalytic activity. However, to our knowledge, the immobilization of urease on mesoporous silica and its potential in controlled hydrolysis of urea has not been explored.

Sayari et al. [17,18] reported the preparation of pore-expanded MCM-41 silica (PE-MCM-41) possessing high specific surface area (ca.1000 m²/g), large pore size (up to 25 nm) and pore volume (up to 3.5 cm³/g) via post-synthesis hydrothermal treatment of as-synthesized MCM-41 in the presence of *N,N*-dimethyldecylamine. These materials opened up many opportunities in adsorption and catalytic applications [19-26]. In the present work, we report the adsorption of urease onto a PE-MCM-41 with a specific surface area, pore size and pore volume of ca. 920 m²/g, 10.4 nm and 2.04 cm³/g, respectively, at 25 °C from aqueous solutions at different pHs within the range of 5.0 to 9.0. However, the catalytic effect on urea hydrolysis reaction was investigated using

mesoporous silicas loaded with urease at near neutral pH (7.2). The reason of this particular adsorption condition is associated with the fact that most field crops grow well in a soil with pH ranging from 6 to 8 at ambient temperature [27]. For comparison, regular MCM-41 and silica gel adsorbent (SGA) were also used. This study revealed that the amount of urease adsorbed on PE-MCM-41 was higher as compared to MCM-41 and SGA. However, the catalytic effect of urease-loaded PE-MCM-41 appeared to slow the urea hydrolysis rate much more efficiently than MCM-41 and SGA.

2. Experimental

2.1. Materials

Urease (35 units/mg; from jack bean; M_w 480k Da) was obtained from Fluka. MCM-41 and PE-MCM-41 were synthesized using Cab-O-Sil M5 fumed silica (Cabot Co.) via a two step procedure published earlier [17,18]. Urea (ultra pure), SGA adsorbent (230-400 mesh) and all other chemicals were obtained from Sigma-Aldrich and used as supplied.

2.2. Characterization

To determine the physical characteristics of each material, nitrogen adsorption-desorption isotherms were measured at 77 K on a Coulter Omnisorp 100 gas analyzer. The pure silica materials were degassed at 250 °C under high vacuum (10^{-5} Torr) for 2 h prior to the nitrogen adsorption measurements, while the urease-immobilized samples were degassed at 50 °C for 6 h. The specific surface area was determined from the linear part of the BET plot ($p/p_0 = 0.05$ to 0.15). The average pore size was taken as the peak of the pore size distributions as calculated from the adsorption branch using the KJS (Kruk-Jaroniec-Sayari) method [28]. The total pore volume was determined as the volume of liquid nitrogen adsorbed at p/p_0 of 0.995. Thermogravimetric (TG) analysis of native urease and urease-loaded samples were performed using a TG analyzer (Q 500, TA Instrument) coupled with a mass spectrometer (Pfeiffer ThermoStar) for determining the urease loading and its stability through the weight loss of the material upon heating in the temperature range of 25 to 800 °C, in flowing N_2 .

2.3. Urease Adsorption

A series of urease solutions with concentrations ranging from 0.25 g/L to 10 g/L was prepared by dissolving different amounts of the enzyme in de-ionized water. Adsorption isotherms of urease on various mesoporous adsorbents were

achieved by equilibrating the adsorbents with aqueous solutions of urease with pH 7.2. In each adsorption experiment, 100 mg of the different adsorbents was suspended in 10 mL of the desired urease solution. The suspensions were continuously shaken in a shaking bath at 25 °C until an assumed equilibrium was reached, typically after 24 h and then centrifuged. The urease concentration in the supernatants was measured by UV-Vis spectroscopy at 276 nm (Cary 300, Varian). The urease containing silica materials were recovered from the reaction mixtures by filtration and washed with de-ionized water. The materials were dried at room temperature for 24 h and finally in a vacuum oven at 50 °C for 12 h. Urease-adsorbed samples of MCM-41, PE-MCM-41 and SGA silicas were denoted as U/MCM-41, U/PE-MCM-41 and U/SGA, respectively. The influence of pH on the adsorption of urease onto the mesoporous silica adsorbents was examined as described above with an enzyme concentration of 10 g/L in the pH range 5.0-9.0 using 25 mM phosphate buffer.

2.4. Catalytic Activity in Urea Hydrolysis Reaction

A 5 mM aqueous solution of urea was used to study the catalytic activity of native urease (90 µg/mL) and urease-loaded mesoporous silicas (e.g. U/MCM-41, U/PE-MCM-41 and U/SGA). In each hydrolysis experiment, a determined amount of urease-containing silica catalyst (equivalent to the amount of native urease) was suspended in 50 mL of urea solution at room temperature under gentle stirring and covered to avoid evaporation. A controlled experiment using pristine PE-MCM-41 was performed by using 50 mg of PE-MCM-41 under otherwise the same conditions. The conversion of urea to ammonia was monitored *in-situ* over time using a Benchtop Multimeter (Orion 5-Star, Thermo Electron Co. USA) equipped with an ammonium ion specific electrode (Orion 93-18). Calibration measurements were carried out separately before each set of experiments with ammonium standard solutions of different concentrations.

3. Results and Discussion

Figure 1 shows the nitrogen adsorption-desorption isotherms for MCM-41, PE-MCM-41 and SGA. The isotherm for MCM-41 is of type IV according to the IUPAC classification and exhibits a H1 hysteresis loop, characteristic of periodic mesoporous materials [29,30]. Similarly, PE-MCM-41 exhibits a type IV isotherm with a broad H1 hysteresis loop occurring at higher relative pressure, which is consistent with pore enlargement. Uniformly sized mesopores are evident from the sharp capillary condensation step in the isotherms for both MCM-41 and PE-MCM-41. This is consistent with the narrow pore size

distribution shown in Figure 1 (inset). The mesopores for SGA are devoid of uniformity with very broad pore size distribution as evident in Figure 1 (inset).

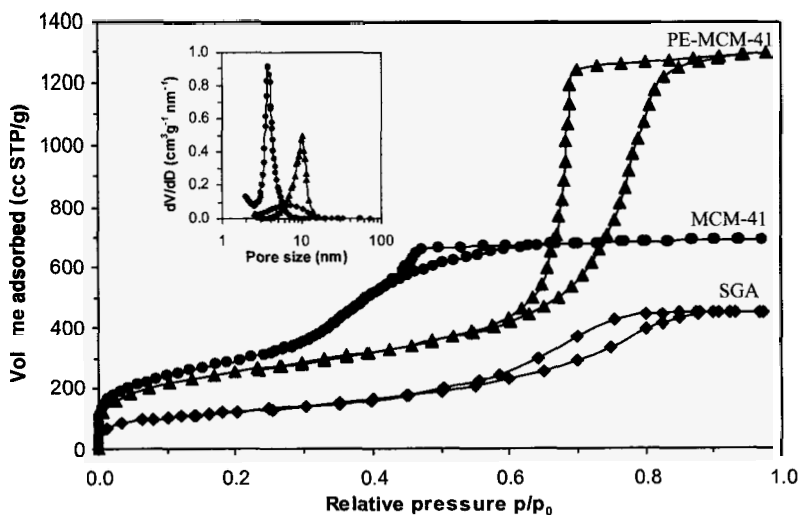


Figure1. Nitrogen adsorption-desorption isotherms for various adsorbents used in this study (Inset: Corresponding KJS pore-size distributions).

The textural properties of the different mesoporous adsorbents are summarized in Table 1. The specific surface areas of MCM-41 and PE-MCM-41 are 1078 and 920 $\text{m}^2 \text{g}^{-1}$, respectively, which are more than double compared to the specific surface area of SGA (443 $\text{m}^2 \text{g}^{-1}$). On the other hand, the pore size of PE-MCM-41 is 10.4 nm, much higher than the pore sizes of MCM-41 (3.8 nm) and SGA (6.5 nm).

Table 1. Textural parameters of various adsorbent and their urease-loaded derivatives from aqueous solution with pH 7.2 at 25 °C.

Materials	Initial conc. (g/L)	Loading (mg/g)	S_{BET} (m^2/g)	Pore size (nm)	V_p (cm^3/g)
PE-MCM-41	-	-	920	10.4	2.14
MCM-41	-	-	1078	3.8	1.08
SGA	-	-	443	6.5	0.71
U/PE-MCM-41	10	102	278	2.1	0.17
U/MCM-41	10	56	491	1.6	0.21
U/SGA	10	21	377	6.4	0.63

Time-resolved uptake of urease over PE-MCM-41, MCM-41 and SGA with initial concentration of 2 g/L (Figure is not shown) revealed that the urease uptake by PE-MCM-41 at the beginning was relatively fast compared to the other adsorbents. PE-MCM-41 with large pore may facilitate the mass transfer inside the channels. However, the adsorption equilibrium is attained for all three adsorbents within 24 h of shaking. The amount of urease adsorbed follows the trend: PE-MCM-41 > MCM-41 > SGA. The adsorption process is well described by the pseudo-first order kinetics [31].

The effect of pH on the adsorption of urease on different mesoporous adsorbents (Figure is not shown) revealed that all three silica adsorbents exhibit similar trends, i.e., the amount of adsorbed urease decreased slowly and linearly as the pH increased from 5.0 to 9.0. The highest adsorption was observed at pH 5, which is close to the isoelectric point (pI) of urease [9]. Near the pI of urease, the net charge of the enzyme is zero and the coulombic repulsive force between the urease molecules is minimal. These phenomena enhance secondary interactions such as hydrogen bonding, van der Waals and hydrophobic-hydrophilic interactions leading to increased urease adsorption. The net negative charges on silica and urease surfaces gradually develop as pH increases which may result in diminishing enzyme adsorption capacity. Nonetheless, the amount of adsorbed urease remained relatively high even on negatively charged silica surface at higher pH.

The equilibrium sorption data obtained was analyzed based on the commonly used Langmuir and Langmuir-Freundlich models [32]. The Langmuir isotherms model is described by the equation

$$q_e = \frac{K_L q_m C_e}{1 + K_L C_e} \quad (1)$$

where q_e (mg/g) is the equilibrium adsorption amount, q_m (mg/g) is the maximum sorption capacity, C_e is the equilibrium concentration of solute (mg/L), K_L is the Langmuir constant. A typical Langmuir-Freundlich model is described by the equation

$$q_e = \frac{K_{LF} q_m C_e^n}{1 + K_{LF} C_e^n} \quad (2)$$

where q_e (mg/g) is the equilibrium adsorption amount, q_m (mg/g) is the maximum sorption capacity, K_{LF} is the Langmuir-Freundlich constant, n is the intensity of the constant. Figure 2 shows the urease adsorption isotherms using equations (1) and (2) and the associated parameters are shown in Table 2. As can be seen from Figure 2, the isotherms are well represented by both Langmuir and Langmuir-

Freundlich models. However, comparing the q_{max} values obtained by the models with the experimental q_{max} values and also the goodness of fit, the adsorption data appears to be following Langmuir-Freundlich model more closely compared to the Langmuir model.

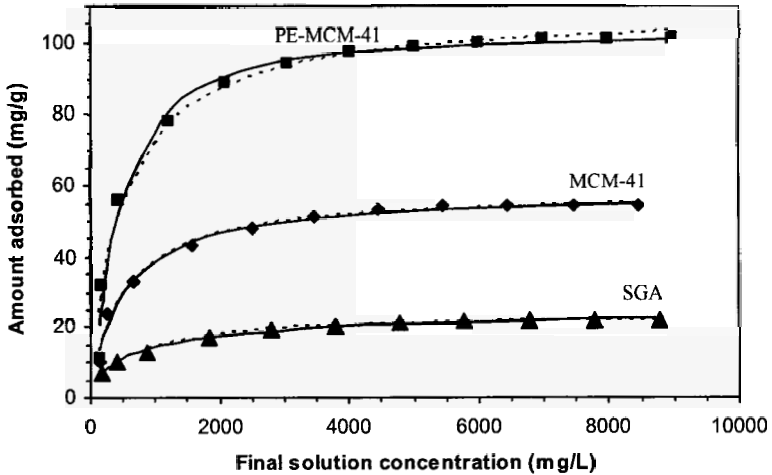


Figure 2. Adsorption isotherms of urease over PE-MCM-41, MCM-41 and SGA. Solid lines represent the data fitted by Langmuir-Freundlich (L-F) and dotted lines for Langmuir (L) model.

The adsorption capacity of the different adsorbents shows the following order: PE-MCM-41 > MCM-41 > SGA, although MCM-41 has higher surface area as compared to the other adsorbents. A reasonable explanation is that the pore sizes of MCM-41 (3.8 nm) and SGA (6.5 nm) are smaller than the dimension of urease (7.5 x 8.0 x 8.0 nm) and not accessible to bulky urease molecules.

Table 2. Adsorption parameters for urease adsorption onto PE-MCM-41, MCM-41 and SGA adsorbents ($C_0 = 10\text{g/L}$).

Adsorbents	q_{max} exp (mg/g)	Langmuir (n = 1)			Langmuir-Freundlich			
		q_{max} cal (mg/g)	$K_L \times 10^3$ (Lg^{-1})	R^2	q_{max} cal (mg/g)	$K_{LF} \times 10^3$ (Lg^{-1})	n	R^2
PE-MCM-41	102	108.6	2.0	0.98	102.9	0.5	1.26	0.99
MCM-41	56	57.8	2.1	0.99	57.6	1.9	1.02	0.99
SGA	21	23.4	1.7	0.99	26.0	8.5	0.71	0.99

In the case of PE-MCM-41, the presence of uniform large pore system (10.4 nm) rather facilitates the diffusion of urease molecules inside the mesopores. Moreover, the mesopore volume of PE-MCM-41 ($2.04 \text{ cm}^3/\text{g}$) is also higher than the MCM-41 and SGA (Table 1) and paves the way for more easily accessible adsorption sites. We can conclude that urease entrapped inside the relatively large pore system of PE-MCM-41, consistent with the larger adsorption capacity of PE-MCM-41 compared to MCM-41 and SGA. The maximum adsorption capacity of urease on PE-MCM-41 was found to be ca. 102 mg g^{-1} which is almost twice as high as the adsorption capacity of MCM-41 (56 mg/g) and 5 times higher than the capacity of SGA (21 mg/g).

Nitrogen adsorption-desorption isotherms for the urease-loaded adsorbents (10 g/L initial concentration) were measured. The isotherms were of type I (Figure is not shown) and the specific surface area, pore diameter and pore volume of all samples were reduced substantially. The results are shown in Table 1. The specific surface area, pore diameter and pore volume of PE-MCM-41 were $920 \text{ m}^2\text{g}^{-1}$, 10.4 nm and $2.04 \text{ cm}^3\text{g}^{-1}$ respectively. These parameters of PE-MCM-41 decreased upon urease loading. For example, the specific surface area of U/PE-MCM-41 was reduced from 920 to $278 \text{ m}^2\text{g}^{-1}$ which represents ca. 70% reduction, while the specific pore volume was reduced from 2.04 to $0.17 \text{ cm}^3\text{g}^{-1}$ corresponding to 91 % decrease. This large reduction of the specific surface area and pore volume were primarily attributed to the adsorption of urease molecule in the mesopore channels of PE-MCM-41.

The stability of urease after adsorption on PE-MCM-41 was ascertained by comparing the TG-DTG plots of PE-MCM-41, native urease and U/ PE-MCM-41 (Figure is not shown). The degradation pattern of the urease changes substantially after adsorption on PE-MCM-41. For example, the weight loss peak of native urease at $152 \text{ }^\circ\text{C}$ (I_u) totally disappeared; the $204 \text{ }^\circ\text{C}$ (II_u) and $238 \text{ }^\circ\text{C}$ (III_u) events moved to higher temperature ($236 \text{ }^\circ\text{C}$ (II_u), $347 \text{ }^\circ\text{C}$ (III_u), respectively). Moreover, the weight loss peak intensities in the U/PE-MCM-41 material decreased significantly compared to the pristine urease. A reasonable explanation to these observations is that the decomposition of the urease adsorbed in PE-MCM-41 is suppressed by the protection of the adsorbent resulting in increased thermal stability. Therefore, it is clear that the urease stability increased upon adsorption onto the PE-MCM-41

Figure 3 shows the hydrolysis of urea by U/MCM-41, U/PE-MCM-41 and U/SGA in comparison to the native urease and pristine PE-MCM-41. The urease-free PE-MCM-41 exhibited negligible conversion of urea to ammonia (0.03%) over 36 h, while pure urease converted 100 % of the urea within 60 min (Figure 3, inset). The catalytic effect of U/MCM-41 and U/SGA exhibited

comparable behaviors as they achieved complete urea conversion within ca. 30 h. However, in the presence of U/PE-MCM-41, urea hydrolysis showed a much slower release of ammonia (e.g. 32 % conversion at 36 h, Figure 3 and 89 % of urea total conversion after 21 days of reaction time, Figure 4).

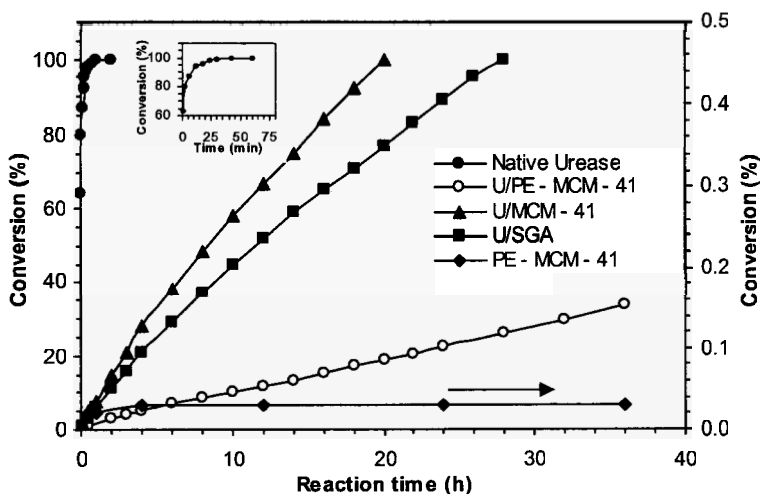


Figure 3. Hydrolysis of urea in aqueous solution to ammonia by U/PE-MCM-41, U/MCM-41, U/SGA and native urease (Inset: Urea hydrolysis to ammonia in the presence of native urease).

These results reveal that the pure silica support material is unable to catalyze the hydrolysis of urea, whereas the free enzyme urease is a too powerful catalyst leading to fast conversion that would prevent the conservation of urea-derived nitrogen in soil. Among the catalysts used in this study, the order of urea hydrolysis reaction rate was as follows: $U \gg U/MCM-41 \sim U/SGA \gg U/PE-MCM-41$. A reasonable explanation of this trend is based on two assumptions: (i) adsorbed urease is inherently less active than pristine urease, and (ii) urease located inside the pore channels is at least apparently, less active than urease adsorbed on the external surface. As mentioned earlier, it is believed that in U/MCM-41 and U/SGA the adsorbed urease is located primarily on the external surface. Thus, though it remained high, their catalytic activity is more than one order of magnitude lower than unsupported urease. On the contrary, in U/PE-MCM-41 urease resides mostly inside the pore channels and shows approximately another order of magnitude decrease in catalytic activity. The lower catalytic activity of U/PE-MCM-41 may be due to either inaccessibility of

urease because of confinement, or slow diffusion of urea inside the now hardly porous material, or a combination thereof. This means of controlling the rate of the enzymatic hydrolysis of urea using PE-MCM-41 could be combined with the urea fertilizer to increase the overall efficiency of nitrogen utilization.

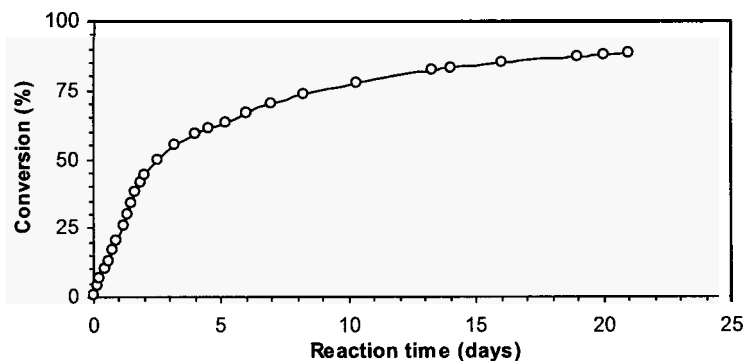


Figure 4. Catalytic performance of U/PE-MCM-41: Slow conversion of urea to ammonia

PE-MCM-41 could be added to agricultural trails few days before the addition of urea fertilizer. Soil based urease may adsorb inside the large pore PE-MCM-41 and limits its activity substantially to hydrolyze the fertilizer as we have shown. Thus, this would allow the fertilizer nitrogen to be released over a longer period of time during the growing season of field crops.

4. Conclusion

In this study, PE-MCM-41, regular MCM-41 and SGA with different textural properties were used to adsorb urease at ambient conditions (25 °C and neutral pH). Adsorption measurements revealed that the amount of urease adsorbed follows the order: PE-MCM-41 > MCM-41 > SGA. This trend of urease adsorption on PE-MCM-41 is due to enhanced mass transfer through the large pores of PE-MCM-41. A maximum urease loading of 102 mg/g on PE-MCM-41 was obtained. Enhanced stability of the urease after adsorption was observed. The urease loaded catalysts were used for *in-vitro* urea hydrolysis reaction. Urease adsorption within the pore system of PE-MCM-41 appears to significantly reduce the rate of urea hydrolysis. Therefore PE-MCM-41 could be used in agricultural soil to reduce the rate of urea hydrolysis process, which may lead to improved management of nitrogen fertilizer for crops nutrition as well as to the reduction of ammonia gas emission from urea fertilizer.

Acknowledgment

A. S. is the Government of Canada Research Chair in *Catalysis by Nanostructured Materials* (2001-2008). We thank the Technology and Innovation program of Natural Resources Canada for financial support.

References

1. E. Jabri, M. B. Carr, R. P. Hausinger and P. A. Karplus, *Science* **268**, 998 (1995).
2. P. A. Karplus, M. A. Pearson and R. P. Hausinger, *Acc. Chem. Res.* **30**, 330 (1997).
3. H. L. T. Mobley and R. P. Hausinger, *Microbiol. Rev.* **53**, 85 (1989).
4. D. F. McCrory and P. J. Hobbs, *J. Environ. Qual.* **30**, 345 (2001).
5. M. Hartmann, *Chem. Mater.* **17**, 4577 (2005).
6. T. J. Pisklak, M. Macias, D. H. Coutinho, R. S. Huang and K. J. Jr. Balkus, *Top. Catal.* **38**, 269 (2006).
7. A. Vinu, K. Z. Hossain, G. S. Kumar and K. Ariga, *Carbon* **44**, 530 (2006).
8. G. Kibarer and G. Akovali, *Biomaterials* **17**, 1473 (1996).
9. L. Gianfreda, M. A. Rao and A. Violante, *Soil. Biol. Biochem.* **24**, 51 (1992).
10. H. Barhoumi, A. Maaref, M. Rammah, C. Martelet, N. Jaffrezic, C. Mousty, S. Vial and C. Forano, *Mater. Sci. Eng. C* **26**, 328 (2006).
11. S. Akgol, Y. Yalcinkaya, G. Bayramoglu, A. Denizli and M. Y. Arica, *Process Biochem.* **38**, 675 (2002).
12. T. Uragami, K. Ueguchi, M. Watanabe, and T. Miyata, *Catal. Today* **118**, 158 (2006).
13. Y. Lvov, A. A. Antipov, A. Mamedov, H. Mohwald and G. B. Sukhorukov, *Nano Lett.* **1**, 125 (2001).
14. Z. Liang, C. Wang, Z. Tong, W. Ye and S. Ye, *React. Funct. Polym.* **63**, 85 (2005).
15. U. Narang, P. N. Prasad and F. V. Bright, *Chem. Mater.* **6**, 1596 (1994).
16. K. Ogura, K. Nakaoka, M. Nakayama, M. Kobayashi and A. Fujii, *Anal. Chem. Acta* **384**, 219 (1999).
17. A. Sayari, M. Kruk, M. Jaroniec and I. L. Moudrakovski, *Adv. Mater.* **10**, 1376 (1998).
18. A. Sayari, *Angew. Chem. Int. Ed.* **39**, 2920 (2000).
19. A. Sayari, S. Hamoudi and Y. Yang, *Chem. Mater.* **17**, 212 (2005).
20. R. S. Franchi, P. J. E. Harlick and A. Sayari, *Ind. Eng. Chem. Res.* **44**, 8007 (2005).
21. P. J. E. Harlick and A. Sayari, *Ind. Eng. Chem. Res.* **45**, 3248 (2006).
22. P. J. E. Harlick and A. Sayari, *Ind. Eng. Chem. Res.* **46**, 446 (2007).
23. D. Das, P. J. E. Harlick and A. Sayari, *Catal. Commun.* **8**, 829 (2006).

24. D. Das and A. Sayari, *J. Catal.* **246**, 60 (2007).
25. J. P. K. Reynhardt, Y. Yang, A. Sayari and H. Alper, *Adv. Funct. Mater.* **15**, 1641 (2005).
26. R. Serna-Guerrero and A. Sayari, *Environ. Sci. Technol.* **41**, 4761 (2007).
27. OMAFRA Staff, Agronomy Guide for Field Crops; Ontario Ministry of Agriculture, Food and Rural Affairs, Canada, 2003. www.Omafra.gov.on.ca/English/products/publicat.html.
28. M. Kruk, M. Jaroniec and A. Sayari, *Langmuir* **13**, 6267 (1997).
29. J. S. Beck, J. C. Vartuli, W. J. Roth, M. E. Leonowicz, C. T. Kresge, K. D. Schmitt, C. T. W. Chu, D. H. Olson, E. W. Sheppard, S. B. McCullin, J. B. Higgins and J. L. Schlenker, *J. Am. Chem. Soc.* **114**, 10834 (1992).
30. C. T. Kresge, M. E. Leonowicz, W. J. Roth, J. C. Vartuli and J. S. Beck, *Nature* **359**, 710 (1992).
31. Y. S. Ho and G. McKay, *Process Biochem.* **34**, 451 (1999).
32. J. H. Choi, S. D. Kim, Y. J. Kwon and W. J. Kim, *Microporous Mesoporous Mater.* **96**, 157 (2006).

ENTRAPMENT OF GLUCOSE OXIDASE INTO MESOSTRUCTURED SILICA

J.L. BLIN, R. BLETA AND M.J. STEBE

*Equipe Physico-chimie des Colloïdes, UMR SRSMC N° 7565 Université Nancy 1/CNRS,
Faculté des Sciences, BP 239
F-54506, Vandoeuvre-les-Nancy cedex, France*

C. CARTERET

*Laboratoire de Chimie Physique et Microbiologie pour l'Environnement UMR7564
Université Nancy 1 / CNRS Faculté des Sciences, BP 239
F-54506, Vandoeuvre-les-Nancy cedex, France*

This work describes the entrapment of glucose oxidase (GOD) into mesostructured silica by physisorption either via a direct one step method or by adsorption. In both cases, the efficiency of the immobilization was revealed by FTIR spectroscopy. The quantity of entrapped enzyme has been determined by solid state UV spectroscopy and it appears that adsorption leads to a lower loading of immobilized GOD. We have also shown that the immobilized enzyme maintains its activity.

1. Introduction

Enzymes are biocatalysts, which exhibit a high selectivity and reactivity under normal conditions, but they are sensitive to denaturation or inactivation by pH, temperature and organic solvents. Moreover, it is usually difficult to recover the active enzymes, thus due to their high costs, their use is limited. One way to overcome these drawbacks consists in immobilizing enzyme onto solid supports. However, the immobilization should be irreversible and stable under potentially adverse reaction conditions. At the same time, high activity, good accessibility to analytes, rapid response times should be kept, while leaching of the biomolecule has to be avoided. Due to its importance in the human metabolism, glucose is the most studied analyte. Indeed, the development of a stable *in vivo* sensor could improve the regulation of glucose concentration and reduce complications related to diabetes. Therefore, many researchers are focused on the immobilization of glucose oxidase (GOD). Among all of the methods of enzyme immobilization, the sol-gel process has been extensively studied [1-3]. The synthesis of a silica matrix by the sol-gel process involves the hydrolysis of

siloxanes, tetramethoxysilane $[\text{Si}(\text{OCH}_3)_4]$ for example, followed by the condensation to yield a SiO_2 network. However, when the gel is dried, evaporation of the pore liquid takes place and substantial shrinkage occurs, involving a pore collapse. From the biomolecule immobilization point of view, this shrinkage and the difficulties to control the pore size distribution of the matrix constitute the main disadvantage of the process. In contrast, owing to their properties such as high specific surface area and uniform pore size distribution, mesoporous materials are excellent candidates as supports for enzymes.

This work describes the immobilization of glucose oxidase (GOD) in mesostructured silica. The enzyme is incorporated into the mesostructured silica framework by physisorption either via a direct one step immobilization method or by adsorption.

2. Materials and Methods

The fluorinated surfactant used, provided by DuPont, had an average chemical structure of $\text{C}_8\text{F}_{17}\text{C}_2\text{H}_4(\text{OC}_2\text{H}_4)_9\text{OH}$, labeled as $\text{R}_8^{\text{F}}(\text{EO})_9$. Glucose oxidase with a molecular mass of 154 kDa (EC 1.1.3.4 type X-S from *Aspergillus niger*, 50 000 units/g) was purchased from sigma and used without any purification.

2.1. Direct one step immobilization

First a micellar solution of $\text{R}_8^{\text{F}}(\text{EO})_9$ at 10 wt.% in water was prepared. The loading of glucose oxidase (GOD), added to the micellar solution, was varied from 0.4 to 7.0 mg per mL of micellar solution, which corresponds to a variation of the GOD concentration from 2.5×10^{-6} to 4.4×10^{-5} mol L^{-1} . Tetramethoxysilane (TMOS), used as the silica source, was added dropwise. The surfactant/silica molar ratio was adjusted to 0.5. The gel obtained was sealed in Teflon autoclaves and heated for 2 days to 60°C . The final products were recovered after ethanol extraction with a soxhlet apparatus for 30 hours

2.2. Adsorption

In a first time a mother solution containing the biomolecule was prepared by mixing the required amount of enzyme with 20 mL of a buffer solution ($\text{pH} = 7$). The loading of enzyme was varied from 1 to 30 mg per mL of solution. Then, after homogenization during 1 hour, 0.25 g of the silica matrix, previously synthesized according to reference 4, were added to 5 mL of the mother solution. The mixture was stirred (300 rpm) at room temperature for 4 hours. The

supernatant was separated from the solid by centrifugation at 5000 rpm during 6 min. The solid was washed 3 times with distilled water and 1 time with acetone before drying it at room temperature in air.

2.3. Characterization

Nitrogen adsorption – desorption isotherms were obtained at $-196\text{ }^{\circ}\text{C}$ over a wide relative pressure range from 0.01 to 0.995 with a volumetric adsorption analyzer TRISTAR 3000 manufactured by Micromeritics. The samples were degassed further under vacuum for several hours at room temperature before nitrogen adsorption measurements. The specific surface area was calculated by the BET (Brunauer, Emmett, Teller) method (molecular cross sectional area = 0.162 nm^2). The pore diameter was determined by the BJH (Barret, Joyner, Halenda) algorithm. The infrared spectra were recorded on a Fourier transform infrared spectrometer Perkin-Elmer 2000, equipped with a KBr beam splitter and a DTGS detector was used. The spectra in diffuse reflectance (DRIFTS) mode were collected using a Harrick DRA-2CI equipment and a Harrick HVC-DRP cell. To perform the analysis, the mesoporous powder was first diluted in a KBr matrix (15 wt.%). Then the sample was kept inside an evacuated chamber (10^{-4} mbar). Reflectances R_s of the sample and R_r of pure KBr, used as a non-absorbing reference powder, were measured under the same conditions. The mesoporous reflectance is defined as $R = R_s/R_r$. The spectra are shown in pseudo-absorbance ($-\log R$) mode. UV-Visible diffuse reflectance spectra were recorded between 200 and 600 nm at 1 nm increments with an integrated sphere attached to a Cary 5G UV-Vis-NIR spectrophotometer.

3. Results and discussion

3.1. Structural and textural features

All the materials characteristics are together in Table 1. When GOD is physisorbed onto the silica matrix, whatever its concentration in the buffer solution, the hexagonal structure is maintained. On the other hand, the immobilization of GOD through the direct one step method leads to well ordered materials only if the GOD concentration is lower than 3.2 mg per mL of micellar solution. Higher loading involves the formation of wormhole-like structures.

As regards the textural characteristics, the immobilization of the enzyme does not affect the shape of the isotherm and a type IV isotherm (not depicted) is obtained by nitrogen adsorption-desorption analysis. Moreover, we can see that the value of the pore diameter remains almost unchanged with the entrapment of

the biomolecule. The main variation that is noted deals with the specific surface area. From Table 1, it is obvious that its value drops when glucose oxidase is incorporated into the silica material. For example if the immobilization is made by adsorption its value varies from 1140 to 445 m²/g, when the concentration of the biocatalyst in the solution is changed from 0 to 30 mg/mL.

Table 1. Materials features : Structure, d-spacing, N₂ specific surface area (S_{BET}) and pore diameter (Ø).

[GOD] in the initial solution (mg/mL)	Structure	d-spacing (nm)	S _{BET} (m ² /g)	Ø (nm)
0	Hexagonal	5.4	1140	3.8
Direct one step method				
0.4	Hexagonal	5.2	962	3.6
1.6	Hexagonal	5.2	879	3.8
3.2	Hexagonal	5.2	869	3.8
3.4	Wormhole	5.4	699	3.7
5	Wormhole	5.3	712	3.9
Adsorption				
1	Hexagonal	5.2	742	3.8
5	Hexagonal	5.2	766	3.8
10	Hexagonal	5.2	705	3.6
15	Hexagonal	5.2	608	3.6
30	Hexagonal	5.2	445	3.4

Moreover, when the entrapment of GOD is performed from the direct one step method, whatever the concentration of GOD the values of d-spacing and pore diameter remain equal to 5.3 and 3.8 nm, respectively (Table 1). If samples are prepared without surfactant, no peak is detected on the SAXS pattern (not shown). This evidences that even if the surfactant is not used to solubilize the enzyme, it plays a key role in the organization of the channel array and it acts also as a pore forming agent.

3.2. Evidence of GOD incorporation and evaluation of the quantity of GOD really immobilized in the silica network

The silica network vibrations are detected on the infrared spectrum below 1800 cm⁻¹ (Fig. 1a). The broad and intense band with a maximum at 1080 cm⁻¹ as well as the shoulder at 1200 cm⁻¹ are characteristic of the antisymmetric stretching vibrational mode of the Si-O-Si siloxane bridges. The less intense absorption at 977 cm⁻¹ is assigned to the Si-O stretching of silanols. Bands detected at 2985,

2939 and 2907 cm^{-1} are assigned to the stretching vibrations of the CH groups of the surfactant, which was not completely removed by the ethanol extraction. However, no evidence of CF absorption is observed on the FTIR spectrum. Thus, the quantity of $\text{R}_8^{\text{F}}(\text{EO})_9$, which remains after extraction is expected very low. The broad absorption around 3550 involves the OH stretching mode of H-bonded silanol groups whereas the sharp band at 3741 cm^{-1} characterizes the free silanols.

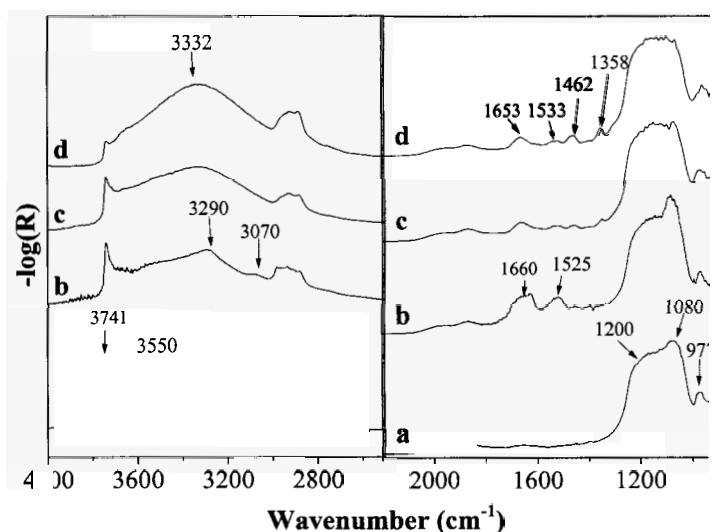


Figure 1. FTIR spectra of a: the silica matrix; b : immobilized GOD by the one step method (5 mg/mL of micellar solution), c: adsorbed GOD (10 mg/mL of solution) and d : adsorbed GOD (30 mg/mL of solution).

In addition to the bands of the silica framework reported above, we observe supplementary vibrations in the spectra of GOD modified silica (spectra 1b-d). These absorptions characteristic of polypeptides were assigned according to results published in the literature [5,6]. It is noteworthy that all analyzed samples were outgassed under vacuum in order to eliminate physisorbed water. Indeed, water absorptions near 1630 cm^{-1} and around 3400 cm^{-1} would prevent clear observation of the polypeptide absorptions. The intense absorption at 3290/3332 cm^{-1} and the weak band at 3070 cm^{-1} are respectively assigned to the amide A (N-H stretching) and amide B (N-H stretching in Fermi resonance with 2 x Amide II) bands. The bands at 1660/1653 and 1525/1533 cm^{-1} are assigned to the amide I and amide II bands. The amide I band originates predominantly from

the C=O stretching vibrations of the peptide bond groups and the amide II band arises from N-H in-plane bending and C-N stretching modes of the polypeptide chains. The amide III band arising from the N-H bending, C-C α and C-N stretching vibration are detected at 1462 and 1358 cm⁻¹. Moreover, we can note that the vibration due to the free silanol (3741 cm⁻¹) strongly vanished upon the adsorption of glucose oxidase (Fig. 1c and d). This means that the adsorption of GOD occurs through hydrogen bonding between NH or C=O groups of enzymes and the surface silanol groups of the mesostructured silica matrix.

Solid state UV spectroscopy was used to evaluate the amount of biocatalyst that is really adsorbed onto the silica matrix. First, in order to make a calibration, various amounts of enzyme (from 2 to 16 mg) were dispersed in 100 mg of pure silica mesoporous molecular sieves. Spectra were recorded, and the pseudo-absorbance of the band at 280 nm versus the amount of enzyme was plotted. Then the silicas containing the enzymes were analyzed.

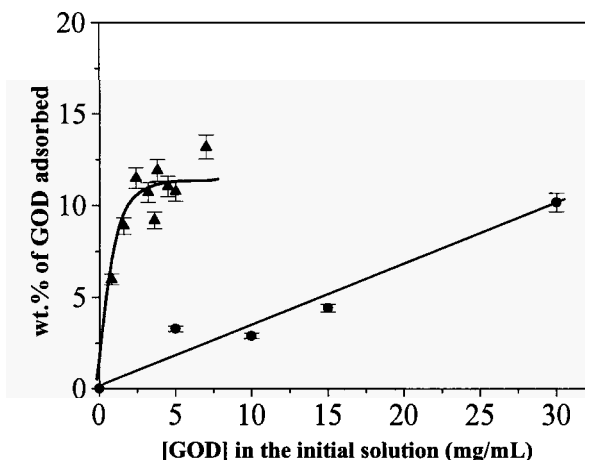


Figure 2. Quantity of immobilized GOD versus the concentration of GOD in the initial solution : GOD was entrapped through the direct one step method (▲) and by adsorption (●).

Concerning the direct one step immobilization method, at first, when the content of GOD varies from 0 to 2.4 mg/mL the percentage of biomolecules that can be incorporated into the silica network increases from 0 to 11 wt.%. For higher concentrations of the enzyme, it reaches a plateau and the added GOD is not incorporated anymore into the mesoporous matrix. By contrast the quantity of GOD that can be physisorbed onto the silica network by adsorption increases with the loading of the biocatalyst in the buffer solution. However, this method

leads to a lower amount of immobilized GOD. This can be related to the leaching of the enzyme during the washing step.

3.3. Activity of the immobilized GOD

The aim of this part is just to check if the immobilized enzyme maintains its activity. Glucose oxidase is a homodimeric enzyme. Each subunit of this protein contains one co-enzyme molecule of Flavine Adenine Dinucleotide (FAD). Each GOD monomer has two distinct domains; one that binds non covalently but very tightly the FAD moiety, and another that binds the β -D-glucose substrate [7]. A colorimetric method was used to test the GOD activity. The system involves two enzymatic reactions (Fig. 3). First, glucose oxidase catalyses, in the presence of molecular oxygen, the oxidation of β -D-glucose to gluconic acid and hydrogen peroxide. The conversion of β -D-glucose into gluconic acid involves the transfer of two protons and two electrons from the substrate to the flavin moiety. In a second step, peroxidase catalyzes the reaction of a dye precursor with hydrogen peroxide to produce a colored dye [8]. First a parent solution was prepared by mixing deionized water (50 mL), D-glucose (0.5 g), 4-aminoantipyrine (0.45g), p-hydroxybenzene (0.47 g) and horseradish peroxidase (0.3 mL).

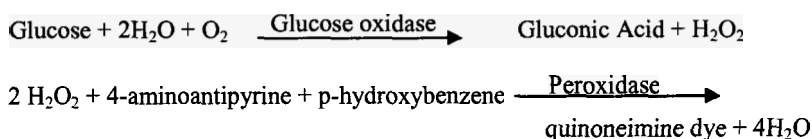


Figure 3. Scheme of the reaction used to evaluate the GOD activity.

The activity of the glucose oxidase is determined by the change of color. Indeed, if 9.6 mg of free GOD are mixed with 3 mL of the parent solution, the mixture obtained turns immediately red. Whatever the method of immobilization, when the silica containing 0.3 mg of glucose oxidase is added to the parent solution, the change of color occurs after about one minute, reflecting the formation of the colored dye and thus the activity of the adsorbed glucose oxidase. The activity was further confirmed by the detection of an adsorption band at 519 nm, which can be attributed to quinoneimine. (Fig 4b,c). No detailed study of the GOD activity has been performed.

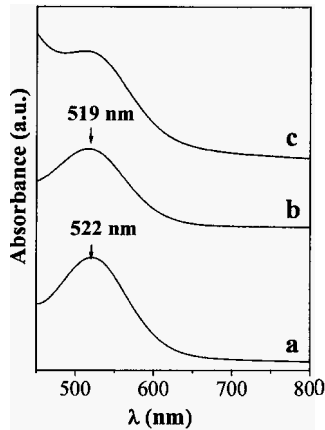


Figure 4. UV spectra showing the activity of the enzyme a : free GOD; b: adsorbed GOD and c : GOD entrapped by the direct one step method.

4. Conclusions

The present study reveals that GOD can be incorporated into silica mesoporous materials via a direct one-step immobilization method or by adsorption. FTIR analysis reveals that the enzyme is truly entrapped into the silica framework. However due to the leaching during the washing step, adsorption leads to a lower amount of incorporated GOD. Nevertheless, whatever the immobilization method, the entrapped enzyme maintained its activity.

References

1. S. Braun, S. Rappoport, R. Zusman, D. Avnir and M. Ottoglenghi, *Mater. Lett.* **10**, 1 (1990).
2. D.J. Blyth, J.W. Aylott, D.J. Richardson and D.A. Russel, *Analyst* **120**, 2725 (1995).
3. K.E. Chung, E.H. Lan, M.S. Davidson, B.S. Dunn, J.S. Valentine and J.I. Zink, *Anal. Chem.* **67**, 1505 (1995).
4. J.L. Blin, P. Lesieur and M.J. Stébé, *Langmuir* **20**, 491 (2004).
5. A. Haouz, C. Twist, C. Zentz, P. Tauc and B. Alpert, *Eur. Biophys. J.* **27**, 19 (1998).
6. F. Caruso, D.N. Furlong, K. Ariga, I. Ichinose and T. Kunitake, *Langmuir* **14**, 4559 (1998).
7. B.E.P. Swoboda, *Biochim. Biophys. Acta* **175**, 365 (1969).
8. S.A. Yamanaka, F. Nishida, L.M. Ellerby, C.R. Nishida, B. Dunn, J.S. valentine and J.I. Zink, *Chem. Mater.* **4**, 495 (1992).

INFLUENCE OF THE PREPARATION METHOD ON THE AMPICILLIN INCORPORATION IN HYDROTALCITE-LIKE COMPOUNDS

RODICA ZAVOIANU, OCTAVIAN DUMITRU PAVEL, ANCA CRUCEANU
MIHAELA FLOREA

University of Bucharest, Faculty of Chemistry, Department of Chemical Technology and Catalysis, Bd. Regina Elisabeta, No. 4-12, S3, Bucharest 030018 Romania

RUXANDRA BÎRJEGA, ANDREI ROTARU

National Institute for Physics of Lasers Plasma and Radiation, Bd. Atomistilor, 409, Bucuresti/Magurele, Romania

CORINA BRADU

University of Bucharest, Faculty of Chemistry, Department of Organic Chemistry and Environmental Protection, Sos. Pandurilor, No90-92, S5, Bucharest, Romania

PETRE ROTARU

University of Craiova, Faculty of Physics Str. A.I. Cuza, No. 1-13, Craiova, Romania

The paper presents a comparison between the chemical and physicochemical properties of three hydrotalcite-like compounds containing ampicillin (HT₃A) prepared by different methods of i.e.: a) impregnation of the dried HT₃ (HT₃AI); b) reconstruction of the HT₃ structure by immersion of the mixed oxide obtained by calcination of HT₃ at 460°C in an aqueous solution of ampicillin sodium salt (HT₃AR); c) direct synthesis at pH 10, using aqueous solutions of Mg and Al nitrates and a base solution of ampicillin (HT₃AS). The obtained results lead to the conclusion that the reconstruction method and the direct synthesis allowed the incorporation of the highest amount of ampicillin. Since both the structure of ampicillin and the hydrotalcite are less altered when using the reconstruction method it was concluded that this preparation technique is more suitable for the sustained release formulation.

1. Introduction

More and more often, hydrotalcite-like compounds (HT) are used as host materials for the creation of inorganic-organic host-guest supramolecular structures with pharmaceutical properties. It is considered that HT have potential for delivery vector, since their cationic layers lead to safe preservation of biofunctional molecules such as drug molecules or genes, and their ion

exchangeability and solubility in acidic media ($\text{pH} < 4$) allow the controlled release of drug molecules. Also, the HT (MgAl-CO_3), facilitates the cellular permeation and it has been used as antacid and antipepsinic agent, or as adsorbent of intestinal phosphates [1]. It has been used as active component of some commercial products such as Almax, Bemolan, Talcid. When ionic exchange is used to obtain these types of solids, sustained release formulation is possible. Recent researches concerning the intercalation of an anticancer drug e.g. methotrexate (MTX), or indomethacin, into hydrotalcite-like compounds with Mg-Al ratio equal to 2 have been reported [2,3]. The studies concerning diclophenac, tolmentin, ibuprofen intercalated in HT by ionic exchange established that the drug content in the solid ranges from 22 to 48% (weight) [3]. Besides relatively numerous articles devoted to drug loaded in hydrotalcite-like compounds we did not find any references on the system HT-ampicillin. The only reference was a recent paper published by M. Catauro et al. [4] investigating the kinetics of the ampicillin release from TiO_2 and $\text{TiO}_2 - 4\text{SiO}_2$ which is actually a quite different system. However, ampicillin has a chemical structure that would allow its intercalation in HT host by ionic exchange. The possibility of controlled release of ampicillin from this type of inorganic host may be interesting for the development of new pharmaceuticals, which could have a longer lasting action. Therefore, in the present paper we investigate the level of ampicillin uptake inside the HT structure depending on the preparation procedure.

2. Experimental

2.1. Preparation of ampicillin –containing hydrotalcite –like compounds

A parent hydrotalcite HT_3 (where 3 is the molar ratio Mg/Al corresponding to the formula $\text{Mg}_3\text{Al}(\text{OH})_8(\text{CO}_3)_{0.5} \times 2\text{H}_2\text{O}$) has been prepared by co-precipitation at low supersaturation and $\text{pH}=10$, using 200 mL aqueous solution of Mg and Al nitrates (0.2 moles $\text{Mg}(\text{NO}_3)_2$; 0.06 moles $\text{Al}(\text{NO}_3)_3$), and 200 mL aqueous solution containing 0.4445 moles NaOH and 0.1778 moles Na_2CO_3 as it was described in our previous publication [5]. The obtained HT_3 was dried at 85°C during 24 hours.

Three hydrotalcite-like compounds containing ampicillin (HT_3A , index 3 stands for Mg/Al ratio and A for ampicillin) have been prepared using different methods i.e.:

1. Impregnation of 2.15 grams of the dried HT_3 with 25mL of an aqueous solution containing 2.5 grams of ampicillin sodium salt (HT_3AI). The excess water has been removed by vacuum evaporation in a ROTAVAP;

2. Reconstruction of the HT₃ structure by immersion of 2.15 grams of the mixed oxide (HT_{3C}), obtained by calcination of HT₃ at 460°C during 24 hours, in 25 mL of an aqueous solution containing 2.5 grams ampicillin sodium salt (HT_{3AR}). The solid was contacted with the ampicillin solution during 24 hours at room temperature in a sealed vessel with mild stirring under nitrogen atmosphere. Afterwards, the solid has been thoroughly washed with decarbonated distilled water and separated by centrifugation;
3. Direct synthesis at pH 10, using aqueous solutions of Mg and Al nitrates and a base solution of ampicillin (HT_{3AS}). For this preparation, the amount of sodium carbonate utilized for the preparation of HT₃ was replaced by an equivalent amount of ampicillin sodium salt, while the amounts of Mg and Al nitrates and sodium hydroxide were kept as in the preparation of HT₃. The obtained precipitate was aged at room temperature, under mild stirring in a sealed vessel under nitrogen during 24 hours, and then it has been washed and separated in the same manner as HT_{3AR} sample.

The samples containing ampicillin have been dried at 40°C during 48 hours.

2.2. Characterization of the ampicillin –containing solids

All the ampicillin–containing samples have been characterized by chemical analysis, X-ray diffraction (XRD), diffuse reflectance infrared Fourier transform spectrometry (DRIFTS), diffuse reflectance UV-Vis spectroscopy (DR-UV-Vis,) and thermogravimetric analysis.

Before the chemical analysis, the samples were dissolved using HCl, (1N) aqueous solution since it does not contain any of the elements that have to be determined in HT_{3A} samples. Al, Mg and Na have been determined by atomic adsorption spectrometry (AAS) and by flame photometry respectively, while S has been determined by potentiometric titration using a Consort C863 Multimeter equipped with ions selective electrode Ag/S. The amount of ampicillin has been calculated based on the content of S since considering the formula of ampicillin anion, $[C_{16}H_{18}N_3O_4S]^-$, this is the only element that is not present during the preparation of the parent HT₃.

The XRD patterns were recorded on a DRON DART UM 2 diffractometer equipped with a monochromator graphite crystal ($\lambda_{CuK\alpha 1} = 1.5406 \text{ \AA}$). The samples were scanned from 5° to 70° (2 θ) in steps of 0.05° with an acquisition time of 2 s at each point. The profile fitting calculations were performed using Jandel Scientific computer software and Voigt functions.

The samples were analyzed by DRIFTS using a Varian 3100 Excalibur spectrometer equipped with diffuse reflectance accessory Harrick Praying

Mantis. DRIFTS spectra averaged over 200 scans were refined by subtracting the spectrum of KBr used as background.

DR-UV-Vis spectra of the samples were collected with Specord 250-222P108 (AnalytikJena) spectrometer, equipped with integration sphere, using MgO as reference. The samples have been scanned in the range 200-900nm, in steps of 1nm, with an integration time of 0.2 s.

The thermogravimetric analysis of the samples was carried out in dynamic air atmosphere, from room temperature to 700 °C, with a heating rate of 10 °C/min using "Diamond Thermogravimetric/Differential Thermal Analyzer" from Perkin Elmer Instruments.

The textural data were determined from the nitrogen adsorption-desorption isotherms using a Micromeritics ASAP 2020 instrument. Prior to each analysis the solids were degassed 2 h at 150 °C under a pressure of 0.1 Pa. The specific surface areas (SSA) were estimated from the adsorption isotherms by Brunauer-Emmett-Teller (BET) method and the corresponding pore size distribution from the adsorption branch by means of a Barrett-Joyner-Halenda (BJH) treatment.

3. Results and Discussions

3.1. Chemical analysis

The results of the chemical analysis presented in Table 1, show higher amounts of incorporated ampicillin for the samples prepared by reconstruction (HT₃AR) and direct synthesis (HT₃AS) compared to the one obtained by impregnation (HT₃AI).

Table 1. Results of the chemical analysis

Sample	Chemical composition (wt. %)					Molar ratios	
	Mg	Al	Ampicillin ^a	Na	H ₂ O ^b	Mg/Al	Ampicillin/Al
HT ₃	24.2	8.9	0	0.02	11.9	3	0
HT ₃ AI	11.2	4.1	50.4	3.0	10.5	3	0.95
HT ₃ AR	11.0	4.2	54.5	1.4	5.6	2.9	1
HT ₃ AS	10.5	4.5	57.6	0.8	6.0	2.6	0.99

^a Calculated based on S content which represents 9.2% wt. of the [C₁₆H₁₈N₃O₄S] molar weight.

^b Calculated based on the loss of weight determined by thermal analysis in the range 105-200°C [6].

Also, it may be seen that the direct synthesis method lead to a lower ratio Mg/Al (e.g., Mg/Al=2.6) in the final product compared to the ratio in the mixture used for the preparation (e.g., Mg/Al=3), while the reconstruction

procedure did not affect significantly the Mg/Al ratio of the product. The sodium content is higher for the sample prepared by impregnation since it has not been removed by washing during this preparation.

3.2. XRD analysis

The XRD spectra of the three samples presented in Figure 1, correspond to a HT-like structure with no diffraction line due to free ampicillin. Amorphous material partially organized in a turbostratic phase (marked with an arrow in figure 1) has been also detected.

Sample HT₃AI spectrum presents a mixture of a HT phase with no significant changes compared to the parent HT structure and an amorphous phase with a pronounced turbostratic characteristic. The slight decrease of the relative basal intensities (I_{003}/I_{110} , I_{006}/I_{110}) marked a low incorporation of ampicillin in the HT's interlayer (Table 2) and therefore, probably, the major part of the total amount of ampicillin incorporated in this sample is entrapped by the turbostratic phase.

Table 2. Structural characteristics of HT₃A samples

Samples	Unit cell parameters		Intensities ratios			FWHM	
	<i>a</i> (nm)	<i>c</i> (nm)	I_{003}/I_{110}	I_{006}/I_{110}	003	006	110
HT ₃	0.307	2.361	4.20	2.45	1.39	1.46	0.80
HT ₃ AI	0.307	2.360	2.83	1.79	1.35	1.41	0.72
HT ₃ AR	0.306	2.398	0.95	1.08	2.35	5.28	0.98
HT ₃ AS	0.304	2.292	1.30	2.72	3.72	6.30	2.02

The XRD pattern of HT₃AR sample indicates the presence of an altered hydroxalcalite phase and an amorphous phase with turbostratic characteristic. The amorphous phase is in a lower amount compared to HT₃AI. The HT phase has an increased *c* parameter value marking an enlargement of the interlayer distance as result of ampicillin incorporation. The effect of ampicillin incorporation is also reflected by the decrease of the relative basal intensities and an enhancement of their degree of disorder expressed by the broadening of the peaks (FWHM, full width at half maximum) showed in Table 2.

The diffraction pattern of the sample prepared by direct synthesis, HT₃AS exhibits the most distorted HT spectrum. The amorphous phase is similar to the turbostratic phase detected in HT₃AR. The HT phase is formed at low *a* value evidencing a higher amount of aluminum incorporated in the brucite-type layer. The increased content of aluminum in the brucite-type layer indicated both by the results of the chemical analysis presented in Table 1 and the relative basal

intensities and extremely broadness of the peaks shown in Table 2, leads to a higher ampicillin amount entrapped in the interlayer space. The intensities inversion between (006) and (003) reflections, e.g higher (006) peaks, is more pronounced than the one observed for HT₃AR suggesting a defective stacking of the layers as a result of ampicillin incorporation. The above-mentioned features allowed us to assume that the highest ampicillin amount has been entrapped in this sample simultaneously to the formation of the HT phase upon precipitation.

These results corroborated with those obtained by chemical analysis account for an increase of the degrees of incorporation of ampicillin in the order: HT₃AI < HT₃AR < HT₃AS.

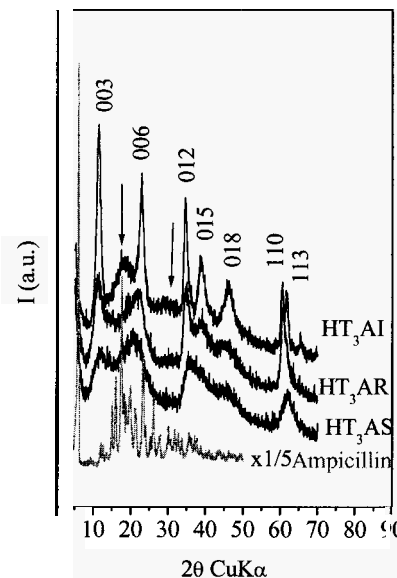


Figure 1. XRD patterns of HT₃A samples.

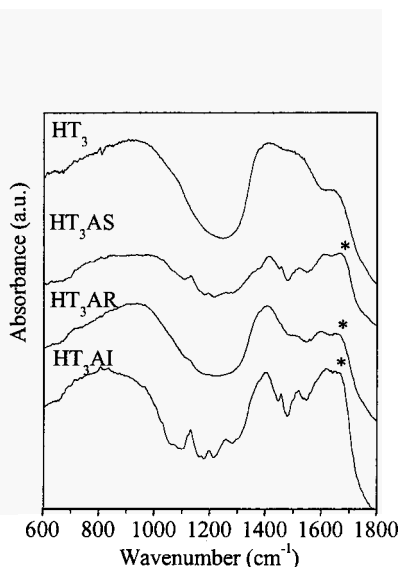


Figure 2. DRIFTS spectra of HT₃A samples.

3.3. DRIFT analysis

The DRIFT spectra of all the ampicillin containing samples (Figure 2) present the main bands at 1760-1800 cm⁻¹ (marked with *) characteristic for the bicyclic thiazolidin-*beta*-lactamic condensed system (also called penam, see Figure 3) in ampicillin [7]. Besides the bands characteristic to the parent hydrotalcite, some other bands associated with the radical (R) of ampicillin are noticed in the spectra of HT₃A samples in the region 1100-1700cm⁻¹. The

intensity of these bands is higher for the sample prepared by impregnation suggesting that in this case the ampicillin is mainly deposited on the external surface of the solid.

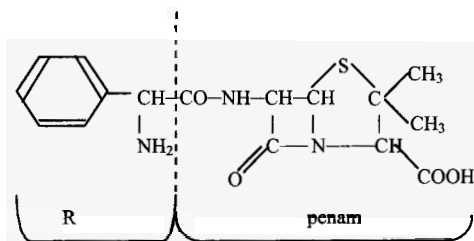


Figure 3. Ampicillin formula.

3.4. DR-UV-VIS analysis

The DR-UV-Vis spectra presented in Figure 4, show only the bands for ampicillin radical (R) at 268, 300 and 325 nm, since the penam unit is not active in UV-Vis region [7]. Since the intensity of the UV-Vis bands is also higher for the sample prepared by impregnation, this result confirms our previous suggestion that in this case there is a higher amount of ampicillin located on the external surface of the solid.

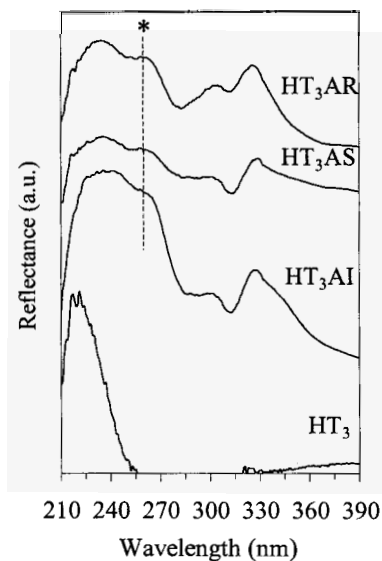


Figure 4. DR-UV-Vis spectra for HT₃A samples.

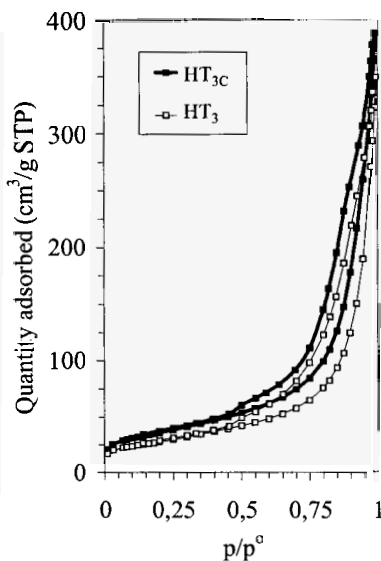


Figure 5. BET isotherms for HT₃ and HT_{3C}.

3.5. Adsorption analysis

The N₂ adsorption-desorption isotherms of the parent HT₃ and the mixed oxide HT_{3C} are presented in Figure. 5. The isotherms are of type IV for which the presence of a hysteresis loop indicates condensation in meso and macropores. The adsorption branch of type IV is similar to type II describing the nitrogen uptake monotonically increase with p/p^0 values due to sorption in the HT mesopores [8]. The shapes of the hysteresis loops describe materials consisting of aggregates or agglomerates of particles forming slit shaped pores (plates or edged particles like cubes), with non-uniform size and/or shape [9]. The volume of micropores is negligible as the t-plots revealed.

Textural data are gathered in table 3. The higher surface area and total pore volume obtained for the mixed oxide HT_{3C}-sample are more likely responsible for the higher amount of ampicillin incorporated via the reconstruction route (HT₃AR) in comparison with the impregnation method (HT₃AI) as the chemical and XRD analysis revealed.

Table 3. Textural data of HT₃ and HT_{3C}

Textural characteristics	HT ₃	HT _{3C}
BET specific surface area (SSA) m ² /g	99	178
Total volume of pores with less than 64.7 nm diameter (cm ³ /g) $p/p^0=0.97$	0.42	0.47
BJH average pore diameter during adsorption (nm)	18.8	16.6
BJH Adsorption cumulative surface area of pores between 1.7-300 nm (m ² /g)	115	195
Adsorption average pore width (4V/A by BET) (nm)	16.9	14.7

3.6. Thermogravimetric analysis

The main differences between the thermal decomposition of, the prepared HT_{3A} samples, the parent HT₃ and the neat ampicillin are illustrated in the TG-DTG curves plotted in Figure 6.

For simplicity of the discussion the temperature ranges where the minimum of the typical peaks appears in DTG curves were pointed out on the figure with consecutive numbers along with the temperature increase. As shown in the thermogram, ampicillin decomposition starts at 221°C. In the temperature range 221-300°C there is a first weight loss of 40.4% and a couple of sharp peaks with low intensity are noticed on the DTG curve. This weight loss corresponds to the decomposition of both R and the methyl groups from the penam unit of the ampicillin formula presented in Figure 3. The decomposition of the penam unit residue occurs in the temperature range 678 - 794°C where the most intense peak of the DTG curve appears.

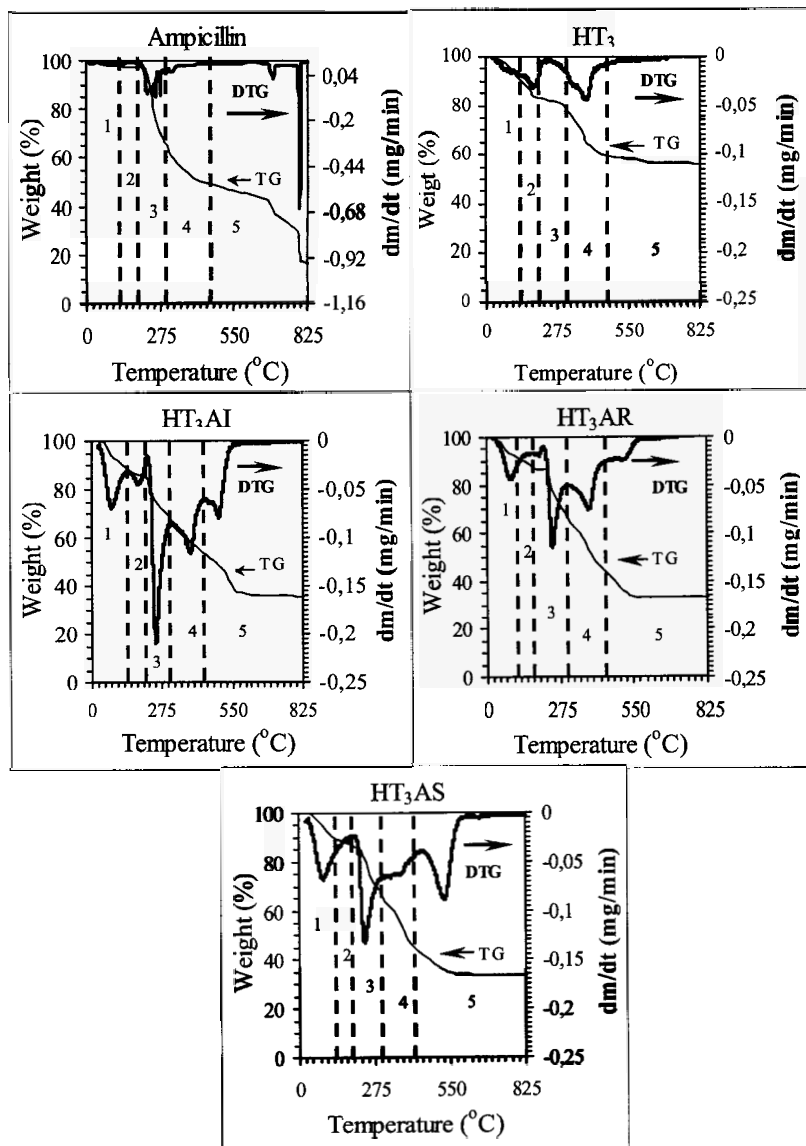


Figure 6. TG-DTG curves of the non-isothermal experiments of Ampicillin, HT₃, HT₃AI, HT₃AR and HT₃AS systems, for the heating rate of 10 $^{\circ}$ C/min.

The thermogram of the parent HT₃ was in line with published data for MgAl hydrotalcites showing a total weight loss (up to 825°C) of 44.7% [6]. It can be noticed that the parent HT₃ is characterized by the presence of two broad peaks, peak 2 at 180°C and peak 4 at 375°C with a shoulder at 350°C. As indicated by several authors, peak 2 is related to the loss of weakly bonded water, while peak 4 and its shoulder are related to the loss of interlayer carbonates and hydroxyls [6, 10, 11].

HT₃A samples had more important losses of weight, which varied between 67.8 – 70.6%, their value increasing with the amount of ampicillin in the sample. Their DTG curves present more peaks than those characteristic for the parent HT₃.

Thus, all three HT₃A samples have the peak 1 at 80°C, which is most probably due to the loss of the superficial humidity since these samples were dried at lower temperature than the parent HT₃ whose DTG curve presents only a shoulder at 80°C. Also, they present two other peaks: peak 3 around 250°C and peak 5 in the temperature range 455-575°C.

Peak 3, is obviously related to the decomposition of ampicillin, since it appears at the same temperature as in the DTG curve of the unsupported ampicillin. It has the highest intensity for the sample prepared by impregnation HT₃AI, which contains the major part of ampicillin deposited on the outer surface. Meanwhile for the samples HT₃AR and HT₃AS, which contain ampicillin incorporated in the interlayer, the intensity of peak 3 is sensibly lower.

Peak 5 is possibly due to the decomposition of a hybrid compound resulted from a chemical reaction between the inorganic support and ampicillin. This assumption is confirmed by the fact that it has the strongest intensity for HT₃AS, prepared by direct synthesis method, which allows the chemical reaction between the inorganic support and ampicillin. The intensity of peak 5 is lower for HT₃AR since in this case the mixed oxide used as support has a poor reactivity and it is less affected by chemical reactions with the ampicillin solution.

The presence of peak 5 in the DTG curve of the sample prepared by impregnation, HT₃AI, indicates that the chemical reaction between the support and the ampicillin solution cannot be excluded in this preparation method. This sample preserves also the characteristics of the parent HT₃ sample, represented by peaks 2 and 4. This is due to the presence of the less affected HT₃ structures, as it was revealed by XRD spectra. However, their intensity is lower due to the low amount of HT₃.

The DTG of HT₃AR preserves only peak 4 of HT₃ without the shoulder, suggesting that it can be related only to the loss of interlayer hydroxyls since no carbonate was present in the mixed oxide used in the reconstruction procedure [12, 13].

For the sample HT₃AS, the intensity of peak 4 is very low due to the lower amount of hydroxyls in the interlayer.

4. Conclusions

The above presented results lead to the conclusion that when preparing ampicillin - containing hydrotalcite-compounds, the reconstruction method and the direct synthesis allowed the incorporation of the highest amount of ampicillin. However, it may be preferable to use the reconstruction method for controlled drug release since this technique preserves better both the structures of ampicillin and of the hydrotalcite.

Acknowledgments

The financial support of this work through Grant CEEX D-11-104/25.10.2006, OXTRANS is gratefully acknowledged.

References

1. B.-P. Yu, J. Sun, M.-Q. Li, H.-S. Luo, J.-P. Yu, *World J Gastroenterol.*, **9**(7), 1427 (2003)
2. M. DelArco, E. Cebadera, S. Gutiérrez, C. Martin, M.J. Montero, V. Rives, J. Rocha and M.A. Sevilla, *J. Pharmaceutical Sciences*, **93**/6, 1649 (2004).
3. J.-M. Oh, M. Park, S. Kim, J.-Y. Jung, Y.-G. Kang and J.-H. Choy, *J. Phys. Chem. of Solids*, **67**, 1024 (2006).
4. M. Catauro, M. G. Raucci, C. Convertito, D. Melisi and M. G. Rimoli, *J. Materials Science: Materials in Medicine*, **17**/5, 413 (2006)
5. R. Bîrjega, O.D. Pavel, G. Costentin, M. Che and E. Angelescu, *Appl. Catal. A: General*, **288**, 185 (2005).
6. F. Cavani, F. Trifiró, A. Vaccari, *Catal. Today*, **11**, 173 (1991).
7. S. Jurcoane, E. Sasarman, A. Rosu, A. Banu, I. Lupescu, R. Berehoiu Tamba, F. Radoi, *Tratat de Biotehnologie, Ed. Tehnica, Bucuresti*, **1**, 270, (2004).
8. M. L. Occelli, J. P. Olivier, A. Auroux, M. Kalwei, and H. Eckert, *Chem. Mater.*, **15**, 4231, (2003).
9. G. Leofanti, M. Padovan, G. Tozzola, B. Venturelli, *Catal. Today*, **41**, 207 (1998).
10. O. Saber, *J. Colloid and Interface Science*, **297**, 182 (2006).

11. V. Rives, M.A. Ulibarri, *Coordination Chemistry Reviews*, **181**, 61 (1999).
12. F. Basile, A. Vaccari, *Layered Double Hydroxides: Present and Future*, Ed. V. Rives, *Nova Science Publisher, New York, USA*, ch. 10, (2001).
13. A. Vaccari, *Appl. Clay Science*, **14**, 161 (1999).

AUTHOR INDEX

A

- Aguado, J. 89
Albuquerque, M. C. G. 577
Alvaro, M. 385
Alves, O. L. 617
Anan, A. 497
Aprile, C. 385
Araujo, A. S. 571
Argue, S. 677
Asefa, T. 497
Azais, T. 457
Azevedo, D. C. S. 577

B

- Bahnemann, D. 553
Balasubramanian, V. V. 37, 47
Bannat, I. 543
Bejblová, M. 477
Bhaumik, A. 235
Bîrjega, R. 717
Blanchard, J. 457
Bleta, R. 709
Blin, J. L. 17, 709
Blitz, I. P. 149
Blitz, J. P. 665
Boekfa, B. 431
Bohaty, A. K. 395
Boissiere, C. 457
Bradú, C. 717
Brinke, G. T. 347
Buckley, R. P. 497

C

- Cao, G. 355, 365
Cao, J. 187
Cao, J.-M. 187, 195
Carmo Rangel, M. 509, 589, 599,
607, 617
Carteret, C. 709
Cavalcante Jr., C. L. 577
Čejka, J. 477, 625
Chang, H. 323
Chaumonnot, A. 457
Cho, S. J. 79
Choomwattana, S. 423, 431
Chun, Y. 487
Cichelli, J. 395
Copley, M. 27
Coppens, M. O. 71
Coupe, A. 457
Cruceanu, A. 717
Czechura, K. 109

D

- Dai, S. 529
Dam, H. M. 497
Darul, M. 203
Davidson, P. 225
Delo, S. A. 377
Denat, F. 129
Denoyel, R. 225, 643
Dias Holtz, R. 589
Do, D. D. 407
Duncan, C. 497

E

Eguchi, T. 445
 Endo, A. 9
 Engelhardt, P. 347
 Etienne, M. 129
 Faust, A.-C. 129
 Feaver, A. M. 365
 Feliczak, A. 203
 Fister, T. T. 365
 Florea, M. 717
 Fujiwara, M. 235

G

Gao, L. 487
 Garcia, B. B. 355, 365
 Garcia, H. 385
 Gaslain, F. 129
 Gies, H. 55
 Gonzalez, J. S. 577
 Gorka, J. 333
 Gorzolnik, B. 225
 Grabicka, B. E. 149, 665
 Grande, D. 225
 Groen, J. C. 71
 Grosso, D. 457
 Grudzien, R. M. 149, 665
 Gu, F. N. 487, 653
 Guo, Q. 99

H

Ha, C.-H. 139
 Hamakawa, S. 687
 Hanaoka, T.-A. 265, 687
 Hanrahan, J. 27
 Hill, J. P. 519
 Hirao, Y. 63
 Holmes, J. 27
 Hossain, K.-Z. 697
 Huang, W. 653

I

Ide, M. 117
 Iida, A. 79
 Ikeda, T. 265
 Ikkala, O. 347
 Inagi, Y. 9
 Inukai, K. 63
 Ishii, R. 265, 687
 Itoh, T. 265, 687

J

Jaroniec, M. 149, 203, 333, 665
 Ji, G.-B. 187
 Jiang, X.-H. 195
 Jiménez Lopez, A. 577
 Joo, S. H. 323
 Justus, J. 37, 47, 313

K

Kalousek, V. 553
 Kawamura, Y. 445
 Keane, D. 27
 Khongpracha, P. 423, 431, 439
 Kim, J. H. 323
 Kim, J. M. 323
 Kim, J.-H. 79
 Kingston, D. 677
 Komura, K. 79, 561
Kondo, J. N. 275
 Kosonen, H. 347
 Kou, J. H. 487
 Krishna, V. 179
 Kurokawa, K. 445

L

Lang, S. 677
 Layek, A. 179
 Lebeau, B. 129
 Lee, H. I. 323

Li, F. 377
 Li, R. 99
 Lima, S. H. 571
 Limtrakul, J. 423, 431, 439
 Limtrakul, P. 431
 Ling, F. 99
 Liu, D.-M. 195
 Liu, J.-S. 187, 195

M

Ma, Z. 529
 Maekawa, T. 63
 Maireles Torres, P. 577
 Majid, A. 677
 Mal, N. K. 235
 Margeson, J. 677
 Marichal, C. 129
 Marschall, R. 159
 Massiot, D. 457
 Matsuura, S.-I. 687
 Meneses, J. M. 643
 Michaux, F. 17
 Mirri, V. 225
 Miyakubo, K. 445
 Mizukami, F. 265, 687
 Mokaya, R. 283, 293
 Mondal, S. A. S. K. 519
 Monreal, C. M. 697
 Moreno, I. 89
 Morris, M. 27

N

Nagle, K. P. 365
 Nakamura, H. 561
 Namuangruk, S. 439
 Nandi, M. 235
 Narkhede, V. 55
 Nishimura, Y. 79
 Nowak, I. 203

Nykänen, A. 347

O

Oekermann, T. 543
 Ohmori, T. 9
Ohta, S. 275
Okubo, T. 275
 Oliveira, S. B. 509, 589
 Olkhovyk, O. 665
 Ookawa, M. 63
 Overbury, S. H. 529

P

Pacula, A. 283
 Pak, C. 323
 Pantu, P. 431
 Park, S. S. 139
 Pavel, O. D. 717
 Pedrosa, A. M. G. 571
 Pega, S. 457
 Penelle, J. 225
 Peral, A. 89
 Pereira Barbosa, D. 509, 607
 Pizarro, P. 89
 Procházková, D. 477

Q

Quilivan, S. 497

R

Rabelo, D. 509, 607
 Ramani, R. 347
 Rathouský, J. 159, 553
 Robles, J. M. M. 577
 Rodrigues, G. 571
 Rodríguez Castellon, E. 577
 Rodríguez, J. M. 89
 Roggenbuck, J. 169
 Rotaru, A. 717

Rotaru, P. 717
 Rouquerol, J. 643
 Rousselin, Y. 129
 Ruokolainen, J. 347

S

Sakthivel, A. 79
 Sanchez, C. 457
 Santana Nobre, P. S. 599
 Sanz, R. 89
 Sawant, D. P. 47, 313
 Sayari, A. 109, 633, 697
 Schepelina, O. 395
 Séguéla, R. 225
 Seidler, G. T. 365
 Selvam, P. 179
 Seo, G. 79
 Sepehri, S. 355
 Serna-Guerrero, R. 633
 Serrano, D. P. 89
 Sharma, K. K. 497
 Šiklová, H. 477, 625
 Soininen, A. 347
 Soldatov, D. V. 213
 Souza, A. O. 617
 Souza, M. J. B. 571
 Srinivasu, P. 47
 Stébé, M. J. 17, 709
 Stein, A. 377
 Sugi, Y. 79, 561
 Sun, L. B. 487
 Sun, W. 99

T

Tao, J. 187, 195
 Tarso Figueiredo Grecco, S. 599
Tatsumi, T. 275
 Tian, B. 245
 Tiemann, M. 169

Tschirch, J. 553
 Tsunoda, T. 687
 Tuomisto, F. 347

U

Ueda, T. 445
 Urbistondo, I. J. 577
 Urquieta-González, E. A. 599

V

Valkama, S. 347
 Van Der Voort, P. 117
 Vathyam, R. 497
 Vercaemst, C. 117
 Verpoort, F. 117
 Vinu, A. 37, 47, 303, 313, 519
 Vlk, J. 477

W

Walcarius, A. 129
 Walczak, K. 203
 Wang, G. 497
 Wang, H.-Y. 187
 Wang, J. 71
 Wang, Y. 487
 Wark, M. 159, 543
Watanabe, R. 275
 Wattanakit, C. 431
 Wen, J. J. 653
 Wessels, K. 543
 Wilhelm, M. 159
 Wongkoblapp, A. 407

X

Xiao, F.-S. 1
 Xie, Y. 497
 Xu, J. H. 653

Y

Yamashita, H. 63
Yan, W. 529
Yang, C. 245, 255
Yang, J. 487
Yang, Z. 293
Yokoi, T. 275
Yokoyama, T. 265
You, D. J. 323
Yue, W. 71

Z

Zăvoianu, R. 717
Zeleňák, V. 625

Zhang, R. 255
Zhang, X. 99
Zhang, Z. 99
Zhao, H.-J. 187, 195
Zhao, Y. 187
Zharov, I. 395
Zheng, M.-B. 187, 195
Zhou, C. F. 653
Zhou, W. 71
Zhu, H. 529
Zhu, J. H. 487, 653
Zhuang, T. T. 653
Zou, Z. G. 487
Zukal, A. 625

This page intentionally left blank

SUBJECT INDEX

A

Activated carbons 509, 589, 607
Acylation reactions 37, 477
Adsorption kinetics 643
Adsorption of VOC 633
Adsorption thermodynamics 643
Air-water interface 139
Alumina 487
Aluminogermanate 63
Aluminosilicate 457, 589
Amine groups 313
Ampicillin intercalation 717
Azobenzene moieties 109

B

Benzene synthesis 599
Biodiesel 571, 577
Bis(methyldichlorosilyl)biphenyl 265

C

Calcium oxide 577
Carbon cryogels 355, 365
Carbon nanotubes 407
Carbonization 293
Carbon-supported copper 509
Carbon-supported magnesium 509
Carboxyl groups 313
Catalysis 37
Chemical vapor deposition 293
Chromatography 27
Clathrates 213
CMK-3 169
CO adsorption 439, 457

Colloidal crystals 377, 395
Composite zeolites 99
Conducting polymers 717
Copper-doped iron oxide 607
Crystal-like wall 139
Crystallization 71
Cyclam moieties 129
Cyclohexene oxidation 203

D

Diblock copolymers 225
Dip impregnation 55
Disassembly 377
Disulfide moieties 149, 665
Dry-gel conversion method 79

E

Electrical conductivity 323
Electrochemical deposition 543
Electrochemical porosimetry 365
Electrochemical supercapacitors 187
Environmental protection 653
Enzyme activity 709
Enzyme silica conjugate 687
Ethene-silica 117
Ethylbenzene dehydrogenation 509,
589, 607
Ethylene adsorption 423
Evaporation induced self-assembly 9

F

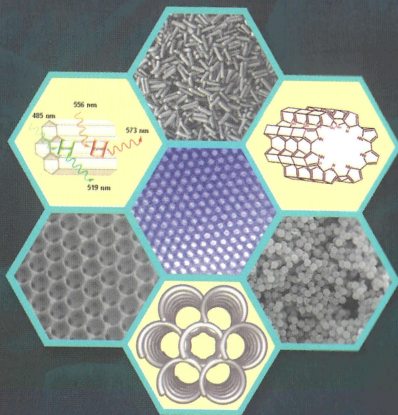
FDU-1 203, 665
Ferroelectric nanocrystals 55

- Fluorescence microscopy 687
Fluorescent labeling 687
Fluorinated surfactant 17, 709
Fly ash 677
Free-standing films 139
Friedel-Crafts alkylation 37
FSM-22 687
Fuel cells 323
Functional mesoporous carbons 313
Functional materials 497, 529
Functional mesoporous polymers 225
Functional nanoparticles 55
- G**
Glucose oxidase 709
Gold catalysts 529
Gold nanostructures 543
Grand Canonical MC simulation 407
- H**
Hard templating 333
H-bonded framework 213
Heavy metal remediation 129, 665
Henry reaction 497
Hierarchical structures 347, 653
Hierarchical zeolites 89
Hollow spheres 293
Hybrid materials 117, 255
Hydrogen storage 283
Hydrolytic degradation 225
Hydrotalcite-like compounds 717
Hydrothermal stability 1
- I**
Ilerite 265
Imidazole groups 665
Immobilization 709
Imogolite 63
Iron oxide 519, 607
- Isocyanurate moieties 665
- K**
KIT-5 47
- L**
Langmuir-Freundlich isotherm 697
Layered zirconium phosphate 617
Lead-zirconia titante 55
Lewis acidity 477
- M**
Magnesium oxide 589
Magnetic nanoparticles 519
MCM-41 55, 126, 129, 159, 179,
477, 561, 571, 633
Mercaptopropyl groups 149, 313
Mercury adsorption 665
Mesoporous aluminosilicate 1, 47, 71
Mesoporous ceria 169
Mesoporous ferrosilicates 37
Mesoporous materials 17, 113, 245,
385, 477, 717
Mesoporous metal oxide 187
Mesoporous nitrides 303
Mesoporous organosilica 129
Mesoporous silica 27, 255, 519,
653, 697
Mesoporous titanosilicates 1, 543
Mesoporous zeolites 1, 89
Mesoporous beta zeolite 599
Mesoporous polypyrrole 235
Metal oxide nanoparticles 385
Metal oxide-phosphate 377
Metal-organic frameworks 431, 445
Methane adsorption 169, 423, 431
Methionine 313
Microcalorimetry 643
Microporous carbons 283

- Microporous materials 265
Microspheres 27
Mineral solids 677
Molecular crystals 213
Molecular motion 445
- N**
N,N-Dimethyldecylamine 27
Nanocasting 169
Nanoclusters 179
Nanocomposites 265
Nanocrystals 71
Nanoparticles 187, 377
Nanoporous catalysts 457, 497
Nanoporous materials 365, 643
Nanoporous niobia 203
Nanotechnology 385
Nanotubes 63
Niobium oxide 203
Nitrogen doped carbons 303
Nitrogen-boron doping 355
Nitrosamine adsorption 653
NO adsorption 439
NO oxidation 543
NO_x 553
- O**
Oligopeptides 213
Ordered mesoporous carbons 275,
293, 323, 333, 519
Ordered mesoporous films 553
Ordered mesostructures 709
Organic zeolites 213
Organofunctionalized seeds 89
- P**
Pd-Quinoline complex 561
Periodic mesoporous organosilicas
109, 117, 129, 149, 198, 665
Phase separation 17
Phase transition 445
Phenolic resin 347
Photocatalysis 203, 553
Photochemistry 385
Photoisomerization 109
Photoresponsive organosilicas 109
Physisorption 709
Platinum doping 617
Platinum nanoparticles 323
Poly(N-isopropylacrylamide) 245
Polyoxometalate 255
Polypyrrole 717
Pore expansion 27, 333, 633, 697
Pore ordering 17
Pore size control 323
Potassium nitrate reduction 487
Proton conductivity 159
Pseudocapacitance 355
Pyrolysis 347
Pyrrole 233, 235
- R**
Recycling 561
Resistors 717
Responsive porous materials 395
- S**
Salt effect 17
SBA-1 37
SBA-15 9, 149, 169, 203, 245, 255,
303, 333, 477, 577, 625, 653,
665, 687
SBA-16 303, 665
Selective nanocatalysts 497
Self-cleaning surfaces 553
Silylation 265
Sodium dodecylsulphate 235
Solid-base catalysts 497

- Solvothermal-annealing synthesis 195
Sonogashira reaction 561
Soy oil 571
Spray drying 9, 457
Structure replication 169
Styrene 589, 607
Styrene-divinylbenzene 509, 589, 607
Sulfonic acid groups 159
Superbasicity 487
Supercapacitor 365
Suppression of NO_x 487
Surface modification 653
Surfactant templating 717
- T**
Template-exchanged method 179
Thermal analysis 445
Thermal degradation 571
Thermal transformation 63
Thermosensitive nanocomposites 245
Titania 543, 553
Tolane 561
Toxic substances 643
Transalkylation reaction 599
Tricobalt tetroxide 195
- Trimethylbenzene 599
- U**
Urea hydrolysis 697
Urease immobilization 697
Ureidopropyl groups 665
- V**
Vacuum gas oil hydrocracking 99
Vanadium oxide 179, 589
Volatile organic compounds 633
- W**
Water adsorption 159, 407
Water gas shift reaction 617
- X**
Xylene 599
- Z**
Zeolite synthesis without NaOH 79
Zeolites as templates 283
Zirconium hydrogenphosphate 617
ZSM-5 71, 89

This page intentionally left blank



Nanoporous Materials

Proceedings of the 5th International Symposium

This proceedings volume contains selected and peer-reviewed original oral and poster contributions to be presented at the 5th International Symposium on Nanoporous Materials, Vancouver, Canada, May 25–28, 2008. It presents recent scientific advances in the area of nanoporous materials, especially those with ordered pores of sizes between 1 and 50 nm, their synthesis, characterization and applications in adsorption, catalysis, bio-related processes, environmental cleanup and nanotechnology. A unique feature of this volume is the wide variety of nanoporous materials covered, ranging from ordered silica nanostructures, silicas with incorporated organic and inorganic species, ordered nanoporous carbons and polymers, metal organic frameworks, nanostructured catalysts to nanoporous films, membranes and monoliths. This proceedings volume reflects the current trends and advances in the field of nanomaterials, which will certainly continue to attract the attention of materials scientists around the globe. It will therefore be a valuable reference for materials scientists, chemists and physicists working in academia, national and industrial laboratories.

World Scientific

www.worldscientific.com

6673 hc

ISBN-13 978-981-277-915-1
ISBN-10 981-277-915-9



9 789812 779151